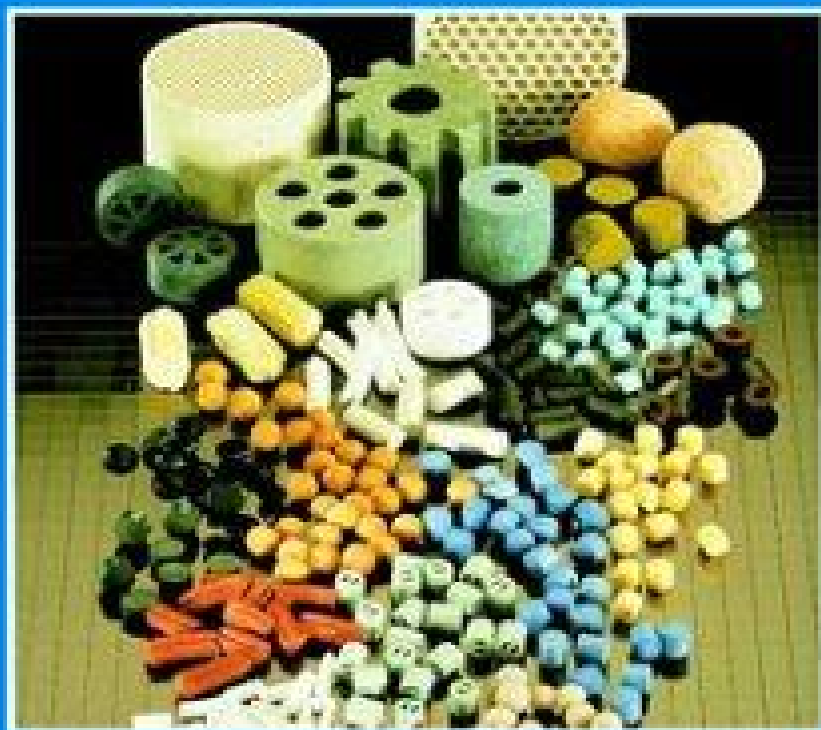


# Preparation of Solid Catalysts

Edited by  
G. Ertl, H. Knözinger, J. Weitkamp



# **Preparation of Solid Catalysts**

Edited by G. Ertl, H. Knözinger, J. Weitkamp

 **WILEY-VCH**



## Further Reading from WILEY-VCH

Gerhard Ertl/Helmut Knözinger/Jens Weitkamp (Eds.)

### **Environmental Catalysis**

1999, 248 pages with 290 figures. Wiley-VCH.

ISBN 3-527-29827-4

Gerhard Ertl/Helmut Knözinger/Jens Weitkamp (Eds.)

### **Handbook of Heterogeneous Catalysis**

5 Volume Set

1997, 2469 pages with 1836 figures and 488 tables. Wiley-VCH.

ISBN 3-527-29212-8

Boy Cornils/Wolfgang A. Herrmann (Eds.)

### **Catalysis from A to Z**

A Concise Encyclopedia

1999, approx. 900 pages with approx. 450 figures and approx. 8 tables. Wiley-VCH.

ISBN 3-527-29855-X

Jens Hagen

### **Industrial Catalysis**

A Practical Approach

1999, 416 pages. Wiley-VCH.

ISBN 3-527-29528-3

John Meurig Thomas/W. John Thomas

### **Principles and Practice of Heterogeneous Catalysis**

1996, 669 pages with 375 figures and 25 tables. Wiley-VCH.

ISBNs 3-527-29239-X (Softcover), 3-527-29288-8 (Hardcover)

R. I. Wijngaarden/K. R. Westerterp/A. Kronenberg

### **Industrial Catalysis**

Optimizing Catalysts and Processes

1998, 268 pages. Wiley-VCH.

ISBN 3-527-28581-4

# Preparation of Solid Catalysts

Edited by G. Ertl, H. Knözinger,  
J. Weitkamp

 **WILEY-VCH**

Weinheim · New York · Chichester · Brisbane · Singapore · Toronto

Prof. Dr. G. Ertl  
Fritz-Haber-Institute  
of the Max Planck Society  
Dept. Physical Chemistry  
Faradayweg 4-6  
D-14195 Berlin  
Germany

Prof. Dr. H. Knözinger  
Ludwig-Maximilian-University  
Institute of Physical Chemistry  
Sophienstr. 11  
D-80333 München  
Germany

Prof. Dr. J. Weitkamp  
University of Stuttgart  
Institute of Technical Chemistry I  
Pfaffenwaldring 55  
D-70569 Stuttgart  
Germany

This book was carefully produced. Nevertheless, authors, editors and publisher do not warrant the information contained therein to be free of errors. Readers are advised to keep in mind that statements, data, illustrations, procedural details or other items may inadvertently be inaccurate.

Title page: Photo courtesy Süd-Chemie AG, Munich, Germany.

Library of Congress Card No. applied for.

A catalogue record for this book is available from the British Library.

Deutsche Bibliothek Cataloguing-in-Publication Data:

A catalogue record for this book is available from the Deutsche Bibliothek

© WILEY-VCH Verlag GmbH, D-69469 Weinheim (Federal Republic of Germany), 1999

Printed on acid-free and chlorine-free paper.

All rights reserved (including those of translation into other languages). No part of this book may be reproduced in any form – by photoprinting, microfilm, or any other means – nor transmitted or translated into a machine language without written permission from the publishers. Registered names, trademarks, etc. used in this book, even when not specifically marked as such are not to be considered unprotected by law.

Composition: Asco Typesetters, Hong Kong  
Printing: Strauss Offsetdruck, D-69509 Mörlenbach  
Bookbinding: J. Schäffer, D-67269 Grünstadt  
Printed in the Federal Republic of Germany

## Foreword

The Handbook of Heterogeneous Catalysis was published in 1997. This book is part of the Handbook, now published as a monograph. Publisher and Editors felt that the Handbook of Heterogeneous Catalysis, which is only available as a full set of five volumes covering almost all aspects of heterogeneous catalysis, might not always be accessible to individuals interested in narrower areas of this field of chemistry. Therefore, the chapters dealing with aspects of preparation of catalysts were selected and put together in this monograph. Catalysis is a rapidly growing field of both academic and technological interest; this Handbook aims to cover the concepts without an encyclopedic survey of the literature, so – although the chapters chosen could not be updated for the present volume – we believe that it will prove most useful to all readers interested in the chemical and physicochemical basis of the preparation of catalysts.

# Contents

<b>1</b>	<b>Introduction .....</b>	<b>1</b>
<b>2</b>	<b>Developing Industrial Catalysts</b> <i>(J. F. LePage)</i> .....	<b>3</b>
<b>2.1</b>	<b>Properties and Characteristics of Industrial Catalysts .....</b>	<b>3</b>
2.1.1	Activity .....	3
2.1.2	Selectivity .....	3
2.1.3	Stability .....	4
2.1.4	Morphology .....	4
2.1.5	Mechanical Strength .....	5
2.1.6	Thermal Characteristics .....	5
2.1.7	Regenerability .....	5
2.1.8	Reproducibility .....	5
2.1.9	Originality .....	6
2.1.10	Cost .....	6
<b>2.2</b>	<b>The Ideal Catalyst and the Optimum Catalyst .....</b>	<b>6</b>
2.2.1	Catalyst Development .....	7
2.2.2	Devising the First Catalytic Formulas .....	8
2.2.3	Optimization of a Typical Catalytic Formula .....	10
<b>3</b>	<b>Bulk Catalysts and Supports .....</b>	<b>11</b>
<b>3.1</b>	<b>Fused Catalysts</b> <i>(R. Schlögl)</i> .....	<b>11</b>
3.1.1	Introduction .....	11
3.1.2	Concept of Fused Catalysts .....	12
3.1.3	Thermodynamic and Kinetic Considerations .....	17
3.1.4	Sulfuric Acid Catalyst .....	19

3.1.5	Metallic Glasses .....	21
3.1.6	Mesostructure of Fused Catalyst Materials .....	25
<b>3.2</b>	<b>Skeletal Metal Catalysts</b> ( <i>M. S. Wainwright</i> ) .....	28
3.2.1	Introduction .....	28
3.2.2	General Aspects .....	29
3.2.3	Skeletal Nickel Catalysts .....	31
3.2.4	Promoted Skeletal Nickel Catalysts .....	34
3.2.5	Skeletal Cobalt Catalysts .....	34
3.2.6	Skeletal Copper Catalysts .....	35
3.2.7	Promoted Skeletal Copper Catalysts .....	37
3.2.8	Skeletal Copper–Zinc Catalysts .....	38
<b>3.3</b>	<b>Metallic Glasses</b> ( <i>A. Baiker</i> ) .....	43
3.3.1	Introduction .....	43
3.3.2	Preparation .....	43
3.3.3	Chemical and Structural Properties .....	44
3.3.4	Metallic Glasses in Catalysis Research .....	46
3.3.4.1	Research on Metallic Glasses in As-Quenched State .....	46
3.3.4.2	Metallic Glasses as Precursors to Catalytically Active Materials .....	49
3.3.5	Case Studies: CO Oxidation Catalysts Prepared from Metallic Glasses .....	50
3.3.5.1	Pd/ZrO <sub>2</sub> Catalysts from Amorphous Pd–Zr Alloys .....	50
3.3.5.2	Promoted Gold–Zirconia Catalysts from Ternary Gold- Containing Glassy Alloys .....	52
3.3.6	Factors Influencing Chemical and Structural Properties of Catalytic Materials Derived from Metallic Glasses .....	53
3.3.6.1	Chemical Composition .....	53
3.3.6.2	Chemical and Structural Homogeneity .....	54
3.3.6.3	Thermal Stability and Crystallization Behavior .....	54
3.3.6.4	Oxidation Behavior .....	55
3.3.6.5	Dissolution of Gases .....	56
3.3.6.6	Segregation Phenomena .....	56
3.3.7	Conclusions and Outlook .....	56
<b>3.4</b>	<b>Precipitation and Coprecipitation</b> ( <i>F. Schüth and K. Unger</i> ) .....	60
3.4.1	Introduction .....	60
3.4.2	General Principles Governing Precipitation from Solutions ...	61
3.4.3	Influencing the Properties of the Final Product .....	69
3.4.4	Prototypical Examples of Precipitated Catalysts and Supports	75

---

<b>3.5</b>	<b>Sol–Gel Process</b>	
	<i>(E. I. Ko)</i> .....	85
3.5.1	Introduction .....	85
3.5.2	Important Parameters in Sol–Gel Preparation .....	85
3.5.3	Advantages of Sol–Gel Preparation.....	91
3.5.4	Catalytic Membranes .....	96
3.5.5	Other Sol–Gel Materials.....	97
3.5.6	Summary .....	97
<b>3.6</b>	<b>Flame Hydrolysis</b>	
	<i>(H. Jacobsen and P. Kleinschmit)</i> .....	99
3.6.1	Manufacture.....	99
3.6.2	Physicochemical Properties of Fumed Oxides .....	101
3.6.3	Preparation of Formed Supports.....	104
3.6.4	Applications .....	107
<b>3.7</b>	<b>Solid-State Reactions</b>	
	<i>(P. G. Menon and B. Delmon)</i> .....	109
3.7.1	Why Solid-State Reactions?.....	109
3.7.2	Description of Preparative Methods .....	117
3.7.3	Conclusions and Prospects.....	136
<b>3.8</b>	<b>High-Surface Transition Metal Carbides and Nitrides</b>	
	<i>(S. T. Oyama)</i> .....	139
3.8.1	General Properties of Transition Metal Carbides and Nitrides.....	139
3.8.2	Thermodynamic Considerations in the Preparation of Carbides and Nitrides.....	139
3.8.3	Survey of Preparative Methods .....	142
<b>3.9</b>	<b>Carbons</b>	
	<i>(R. Schlögl)</i> .....	150
3.9.1	Introduction .....	150
3.9.2	Structural Chemistry of Carbon.....	151
3.9.3	Overview .....	151
3.9.4	Basic Structures.....	153
3.9.5	Loosely Defined Structures .....	157
3.9.6	Formation of Carbon Materials, General Pathways.....	167
3.9.7	Formation of Carbon Materials, Mechanistic Aspects .....	169
3.9.8	Catalytic Formation of Carbon from Molecules .....	171
3.9.9	Carbon on Noble-Metal Catalysts .....	173
3.9.10	Carbon Formation in Zeolites .....	175
3.9.11	Graphitization of Carbons.....	178

3.9.12	Reaction of Oxygen with Carbon .....	180
3.9.13	Surface Chemistry of Carbon .....	188
3.9.14	Non-Oxygen Heteroelements on Carbon Surfaces .....	191
3.9.15	Surface Oxygen Groups .....	195
3.9.16	Carbon as Catalyst Support .....	216
3.9.17	Carbon as Catalyst .....	223
3.9.18	Case Studies of Catalytic Applications .....	224
3.9.19	Catalytic Removal of NO by Carbon .....	225
3.9.20	Removal of Carbon Deposits From Catalyst Materials .....	227
3.9.21	Activation of Oxygen on Carbon Surfaces .....	229
3.9.22	Conclusions .....	234
<b>3.10</b>	<b>Heteropoly Compounds</b> ( <i>K.-Y. Lee and M. Misono</i> ) .....	240
3.10.1	Structure and Catalytic Properties .....	240
3.10.2	Heteropolyacids – Acid Forms in Solid State and in Solution .....	245
3.10.3	Salts of Heteropolyacids – Cation-Exchanged Forms .....	247
3.10.4	Mixed-Coordinated Heteropoly Compounds .....	251
3.10.5	Metal-Coordinated Heteropolyanions .....	253
3.10.6	Heteropolyanions Intercalated in Layered Double Hydroxides .....	256
3.10.7	Supported Heteropoly Compounds .....	257
<b>3.11</b>	<b>Hydrothermal Zeolite Synthesis</b> ( <i>E. J. P. Feijen, J. A. Martens and P. A. Jacobs</i> ) .....	262
3.11.1	Introduction .....	262
3.11.2	Zeolitization in General .....	262
3.11.3	Synthesis of Industrial Zeolites .....	279
<b>3.12</b>	<b>Pillared Clays</b> ( <i>J. J. Fripiat</i> ) .....	284
3.12.1	Introduction .....	284
3.12.2	Pillars .....	290
3.12.3	Pillared Clays .....	296
3.12.4	Catalytic Properties .....	308
3.12.5	Conclusions .....	311
<b>4</b>	<b>Supported Catalysts .....</b>	<b>315</b>
<b>4.1</b>	<b>Deposition of Active Component .....</b>	<b>315</b>
4.1.1	Impregnation and Ion Exchange ( <i>M. Che, O. Clause and Ch. Marcilly</i> ) .....	315



4.1.2	Anchoring and Grafting of Coordination Metal Complexes onto Oxide Surfaces ( <i>C. Louis and M. Che</i> ) .....	341
4.1.3	Heterogenization of Complexes and Enzymes ( <i>W. Keim and B. Driessen-Hölscher</i> ) .....	355
<b>4.2</b>	<b>Supported Metal Cluster Catalysts</b> ( <i>B. C. Gates</i> ) .....	371
4.2.1	Introduction .....	371
4.2.2	Preparation of Supported Metal Clusters .....	373
4.2.2.1	Synthesis of Supported Metal Carbonyl Clusters .....	373
4.2.2.2	Decarbonylation of Supported Metal Carbonyl Clusters .....	374
4.2.2.3	Formation of Metal Clusters in Zeolite Cages by Reduction of Exchange Cations .....	374
4.2.2.4	Deposition of Size-Selected Gas-Phase Metal Clusters .....	375
4.2.2.5	Formation of Nearly Uniform Metal Particles on Supports ...	375
4.2.3	Structural Characterization of Supported Metal Clusters .....	376
4.2.4	Catalysis by Supported Metal Clusters .....	378
4.2.4.1	Catalysis by Supported Ir <sub>4</sub> and Ir <sub>6</sub> Clusters .....	380
4.2.4.2	Catalysis by Clusters of Pt and of Ir in Zeolite LTL .....	385
4.2.5	Summary and Assessment .....	386
4.2.6	Acknowledgment .....	386
<b>4.3</b>	<b>Metal Clusters in Zeolites</b> ( <i>W. M. H. Sachtler</i> ) .....	388
4.3.1	Introduction .....	388
4.3.2	Metal Clusters Versus Macroscopic Metals .....	389
4.3.3	Preparation of Mono- or Bimetallic Clusters in Zeolites .....	390
4.3.4	Interaction of Metal Clusters and Zeolite Protons .....	393
4.3.5	Effects of Zeolite Geometry on Catalysis .....	399
<b>4.4</b>	<b>Zeolite-Entrapped Metal Complexes</b> ( <i>G. Schulz-Ekloff and S. Ernst</i> ) .....	405
4.4.1	Synthesis of Zeolite-Entrapped Metal Complexes .....	405
4.4.2	Characterization .....	411
4.4.3	Catalysis by Zeolite-Entrapped Transition Metal Complexes ..	420
<b>4.5</b>	<b>Supported Catalysts from Chemical Vapor Deposition and Related Techniques</b> ( <i>Y. Iwasawa</i> ) .....	427
4.5.1	Chemical Vapor Deposition Process .....	427
4.5.2	CVD Precursors .....	428
4.5.3	CVD Application .....	430

---

4.5.4	CVD Catalysts.....	430
4.5.4.1	Nickel .....	430
4.5.4.2	Chromium.....	432
4.5.4.3	Copper and Calcium.....	433
4.5.4.4	Iron.....	434
4.5.4.5	Molybdenum .....	434
4.5.4.6	Cobalt.....	439
4.5.4.7	Vanadium .....	442
4.5.4.8	Titanium .....	445
4.5.4.9	Zirconium .....	445
4.5.4.10	Tin .....	447
4.5.4.11	Ruthenium .....	448
4.5.4.12	Palladium Films .....	448
4.5.4.13	Palladium/Zeolites.....	448
4.5.4.14	Bimetals .....	449
4.5.4.15	Mixed Metal Oxides .....	451
4.5.4.16	Silica .....	453
4.5.5	CVD-Related Techniques.....	455
4.5.6	Conclusions.....	456
<b>4.6</b>	<b>Preparation of Supported Catalysts by Deposition-Precipitation</b> ( <i>J. W. Geus and A. J. van Dillen</i> ).....	460
<b>4.7</b>	<b>Solid Superacids</b> ( <i>K. Tanabe and H. Hattori</i> ) .....	487
4.7.1	Sulfate-Treated Metal Oxides, Mixed Oxides, and Those Modified with Platinum.....	488
4.7.1.1	Preparative Methods.....	488
4.7.1.2	Morphology and Surface Properties.....	490
4.7.1.3	Structure of Superacid Sites.....	493
4.7.1.4	Catalytic Properties.....	495
4.7.2	Other Solid Superacids.....	498
<b>4.8</b>	<b>Spreading and Wetting</b> ( <i>H. Knözinger and E. Taglauer</i> ) .....	501
<b>4.9</b>	<b>Redox Methods for Preparation of Bimetallic Catalysts</b> ( <i>J. Barbier</i> ).....	526
<b>5</b>	<b>From the Precursor to the Final Catalyst...</b>	541
<b>5.1</b>	<b>Formation of Final Catalysts</b> ( <i>B. Delmon</i> ).....	541

5.1.1	Introduction and Background.....	541
5.1.2	Activation of Supported Catalysts by Calcination.....	553
5.1.3	Activation of Supported Catalysts by Reduction.....	555
5.1.4	Reduction–Sulfidation.....	565
5.1.5	Other Methods of Activation.....	574
5.1.6	Conclusions.....	574
<b>5.2</b>	<b>Catalyst Forming</b> <i>(J. F. Le Page)</i> .....	579
5.2.1	Forming Microgranules.....	579
5.2.2	Forming Granules.....	583
5.2.2.1	Pelletizing.....	583
5.2.2.2	Extrusion.....	584
5.2.2.3	Pan Granulation.....	586
5.2.2.4	Miscellaneous Forming Operations.....	586
5.2.3	Organizing a Catalyst-Manufacturing Process.....	587
<b>6</b>	<b>Computer-Aided Catalyst Design</b> <i>(M. Baerns and E. Körtling)</i> .....	591
<b>6.1</b>	<b>Introduction</b> .....	591
<b>6.2</b>	<b>Heuristics in Catalyst Design</b> .....	594
6.2.1	Knowledge-Based Systems.....	594
6.2.2	Neural Networks.....	597
<b>6.3</b>	<b>Deterministic Methods in Catalyst Design</b> .....	599
<b>6.4</b>	<b>Chemical Reaction Engineering Aspects</b> .....	601
<b>6.5</b>	<b>Conclusions</b> .....	601
	<b>Index</b> .....	605

# Contributors

M. Baerns  
Institut für Angewandte Chemie  
Berlin-Adlershof e. V.  
Rudower Chaussee 5  
12484 Berlin/Germany

A. Baiker  
ETH Zürich  
Technisch Chemisches Laboratorium  
8092 Zürich/Switzerland

J. Barbier  
Laboratoire de Chimie IV-URA 350  
Université de Poitiers  
40, Avenue du Recteur Pineau  
86022 Poitiers Cedex/France

M. Che  
Laboratoire de Reactivité de Surface  
Université Pierre et Marie Curie  
Tour 54  
4, Place Jussieu  
75252 Paris Cedex 05/France

O. Clause  
Institut Francais du Petrole  
B. P. 311  
92506 Rueil Malmaison/France

B. Delmon  
Unité de Catalyse et Chimie  
des Matériaux Divisés  
Université Catholique de Louvain

Place Croix du Sud, 2  
1348 Louvain-la-Neuve/Belgium

B. Driessen-Hölscher  
Institut für Technische Chemie und  
Petrolchemie  
RWTH Aachen  
Templergraben 55  
52056 Aachen/Germany

S. Ernst  
Fachbereich Chemie  
Technische Chemie  
Universität Kaiserslautern  
Postfach 3049  
67653 Kaiserslautern/Germany

J. P. Feijen  
Centrum voor Oppervlaktechemie en  
Katalyse  
Katholieke Universiteit Leuven  
Kardinaal Mercierlaan 92  
3001 leuven (Heverlee)/Belgium

J. J. Fripiat  
Department of Chemistry  
University of Wisconsin  
P.O. Box 413  
Milwaukee, WI 53211-3029/USA

B. C. Gates  
Department of Chemical Engineering  
University of California  
Davis, CA 95616-5294/USA

J. W. Geus  
Department of Inorganic Chemistry  
University of Utrecht  
Debye Institute  
P.O. Box 80083  
3508 TB Utrecht/The Netherlands

H. Hattori  
Center for Advanced Research of  
Energy Technology  
Hokkaido University  
Kita-ku, Kita 13, Nishi 8  
Sapporo 060/Japan

Y. Iwasawa  
The University of Tokyo  
Department of Chemistry  
School of Science  
Hongo, Bunkyo-ku  
Tokyo 113/Japan

P. A. Jacobs  
Centrum voor Oppervlaktechemie en  
Katalyse  
Katholieke Universiteit Leuven  
Kardinaal Mercierlaan 92  
3001 Leuven (Heverlee)/Belgium

H. Jacobsen  
Degussa AG  
GB Anorganische Chemieprodukte  
Forschung und Entwicklung  
Postfach 1345  
63403 Hanau (Wolfgang)/Germany

W. Keim  
Institut für Technische Chemie und  
Petrochemie  
RWTH Aachen  
Templergraben 55  
52056 Aachen/Germany

P. Kleinschmit  
Degussa AG  
GB Anorganische Chemieprodukte  
Forschung und Entwicklung

Postfach 1345  
63403 Hanau (Wolfgang)/Germany

H. Knözinger  
Institut für Physikalische Chemie  
Universität München  
Butenandt-Str. 5-13, Haus E  
81372 München/Germany

E. I. Ko  
Department of Chemical Engineering  
Carnegie Mellon University  
Pittsburgh, PA 15213-3890/USA

E. Körting  
Institut für Angewandte Chemie  
Berlin-Adlershof e.V.  
Rudower Chaussee 5  
12484 Berlin/Germany

K.-Y. Lee  
Department of Chemical Engineering  
College of Engineering  
Korea University  
5-1 Anam-dong, Sungbuk-ku  
Seoul 136-701/Korea

J. F. Le Page  
Institut Francais du Petrole  
B. P. 311  
92506 Rueil Malmaison/France

C. Louis  
Laboratoire de Reactivité de Surface  
Université Pierre et Marie Curie  
Tour 54  
4, Place Jussieu  
75252 Paris Cedex 05/France

Ch. Marcilly  
Institut Francais du Petrole  
B. P. 311  
92506 Rueil Malmaison/France

J. A. Martens  
Centrum voor Oppervlaktechemie en

Katalyse  
Katholieke Universiteit Leuven  
Kardinaal Mercierlaan 92  
3001 Leuven (Heverlee)/Belgium

P. G. Menon  
Laboratorium voor Petrochemische  
Techniek  
Universiteit Gent  
Krijgslaan 281  
9000 Gent/Belgium

M. Misono  
Faculty of Engineering  
University of Tokyo  
Bunkyo-ku  
00113 Tokyo, Japan

T. S. Oyama  
Department of Chemical Engineering  
Virginia Polytechnic Institute  
Blacksburg, VA 24061-0211/USA

W. M. H. Sachtler  
V. N. Ipatieff Laboratory  
Center for Catalysis and Surface Science  
Northwestern University  
2137 Sheridan Road  
Evanston, Ill. 60208-3000/USA

R. Schlögl  
Fritz-Haber-Institut der  
Max-Planck-Gesellschaft  
Faradayweg 4-6  
14195 Berlin/Germany

F. Schüth  
MPI für Kohlenforschung  
Postfach 10 13 53  
45466 Mülheim Germany

G. Schulz-Ekloff  
Fachbereich 2 (Biologie/Chemie)  
Institut für Angewandte und  
Physikalische Chemie  
Universität Bremen  
Postfach 330 440  
28334 Bremen/Germany

E. Taglauer  
Max-Planck-Institut für Plasmaphysik  
Boltzmannstrasse 2  
85748 Garching/Germany

K. Tanabe  
14-11 Sonomachi, Oasa, Ebetsu-shi  
Hokkaido, 069/Japan

K. Unger  
Institut für Anorganische und  
Analytische Chemie  
Joh.-Joachim-Becher-Weg 24  
Johannes Gutenberg Universität  
55128 Mainz/Germany

A. J. van Dillen  
Department of Inorganic Chemistry  
University of Utrecht  
Debye Institute  
P.O. Box 80 083  
3508 TB Utrecht/The Netherlands

M. S. Wainwright  
Faculty of Engineering  
University of New South Wales  
P.O. Box 1  
Kensington, NSW 2033/Australia

# 1 Introduction

Nature has developed the most efficient and selective catalysts known today. Workers in academia and industry still have a long way to go to reach nature's sophistication in the synthesis of catalysts. For many decades, catalysts were prepared by an empirical approach based on the experience and knowledge of the particular period. Perhaps the best known success story of the development and preparation of a technical solid catalyst by empirical methodologies is that of the ammonia synthesis catalyst by Alwin Mittasch [1–3]. In February 1909 he wrote in his laboratory journal: (i) the search for a suitable catalyst necessitates carrying out experiments with a certain number of elements together with numerous additives; (ii) the catalytic substances must be tested at high pressures and temperatures just as in the case of Haber's experiments; (iii) a very large number of test series will be required [3]. For the optimization of the actual promoted iron catalyst which is still used today, Mittasch ultimately carried out more than 10,000 tests, the number of catalyst formulations exceeding 4,000 [3].

Catalyst preparation lacked a reliable scientific basis until recently and perhaps still does, although catalytic chemists have slowly moved from alchemy to what is now called the science of catalysis. Even in 1940, Raney stated: "It is in the preparation of catalysts that the chemist is most likely to revert to type and to employ alchemical methods. From all evidence, it seems the work should be approached with humility and supplication, and the production of a good catalyst received with rejoicing and thanksgiving" [4, 5].

The catalyst is often, if not always, the heart of a chemical process, and thus, synthesis strategies for technical catalysts are proprietary knowledge of catalyst producers. Therefore, those strategies are either not accessible or protected by patents. This situation, which unfortunately severely hampers the flow of knowledge and information, was strikingly formulated by Richardson: "Catalyst preparation is the secret of achieving the desired activity, selectivity and life time" [6, 7].

Recently combinatorial methodologies were introduced into catalyst development [8, 9]. In this approach, large libraries of materials are synthesized as potential catalysts and examined by microanalysis techniques, and the results are evaluated statistically. This methodology permits an efficient material screening in the case of multi-parameter problems such as the development of solid catalysts. Combinatorial methodologies may be considered as modern versions of Mittasch's approach toward catalyst development that are faster and more cost-efficient than the tradi-

tional methodologies. It seems that potential catalyst formulations can be determined by the combinatorial approach, while technologically important parameters, such as catalyst morphology, texture and forms, mechanical and thermal properties, long-time stability, environmental friendliness, regenerability and disposal of spent catalysts, etc., will still have to be tested independently.

One of the major difficulties in rational preparation of solid catalysts is the fact that catalytic materials are “living” materials, i.e. the active catalyst is often formed from the synthesized precursor material during an induction period under catalytic conditions. Hence, in general the goal of catalyst development must be the synthesis of a suitable catalyst precursor for the chemical process under consideration.

A wealth of information has been accumulated in recent years in various research areas which are relevant to the preparation of bulk and supported solid catalysts. Of high importance for the synthesis of bulk materials is the controlled synthesis of solids including e.g. precipitation and co-precipitation, solid-state reactions, hydrothermal synthesis of zeolites, sol-gel techniques, etc. Great progress has been made in interface chemistry, guest-host interactions, grafting and heterogenization techniques, deposition-precipitation etc., which are extremely important in the synthesis of supported catalysts. This increased understanding of relevant areas of research can now be used as a basis for rational preparation of solid catalysts, and is documented in this monograph. The important parameters of the formation of the final catalysts, catalyst forming and strategies for the development of industrial catalysts are also covered.

## References

1. A. Mittasch, *Geschichte der Ammoniak-Katalyse*, Verlag Chemie, Weinheim, **1951**.
2. A. Mittasch, *Adv. Catal.* **1950**, 2, 81.
3. B. Timm, *Proc. 8. Intern. Congr. Catal.*, Berlin 1984, Verlag Chemie, Weinheim, and Dechema, Frankfurt, **1984**, Vol. 1, p. I-7.
4. M. Raney, *Ind. Eng. Chem.* **1940**, 32, 1199.
5. M. S. Wainwright, in *Handbook of Heterogeneous Catalysis* (Eds.: G. Ertl, H. Knözinger, J. Weitkamp), Wiley-VCH, Weinheim, **1997**, Vol. 1, p. 64.
6. J. T. Richardson, *Principles of Catalyst Development*, Plenum Press, New York, **1989**, p. 134.
7. M. Che, O. Clause, Ch. Marcilly, in *Handbook of Heterogeneous Catalysis* (G. Ertl, H. Knözinger, J. Weitkamp), Wiley-VCH, Weinheim, **1997**, Vol. 1, p. 191.
8. B. Jandeleit, H. W. Turner, T. Uno, J. A. M. van Beck, W. H. Weinberg, *Cattech*, **1998**, 4, 101.
9. R. Schlögl, *Angew. Chem.* **1998**, 110, 2467; *Angew. Chem. Int. Ed. Engl.*, **1998**, 37, 2333.



## 2 Developing Industrial Catalysts<sup>×)</sup>

J. F. LePAGE

Once an active species and perhaps its support have been selected, the task is to construct from precursors of these active species a catalytic structure whose properties and characteristics will meet the demands of an industrial user. One must avoid creating a structure that is only a laboratory curiosity which for technical or economic reasons can not be manufactured on industrial scale.

### 2.1 Properties and Characteristics of Industrial Catalysts

In addition to the fundamental properties that come from the very definition of a catalyst, i.e., activity, selectivity, and stability, industrial applications require that a catalyst be regenerable, reproducible, mechanically and thermally stable, original, economical, and possess suitable morphological characteristics.

#### 2.1.1 Activity

A high activity will be reflected either in high productivity from relatively small reactors and catalyst volumes or in mild operating conditions, particularly temperature, that enhance selectivity and stability if the thermodynamics is more favorable.

#### 2.1.2 Selectivity

High selectivity produces high yields of a desired product while suppressing undesirable competitive and consecutive reactions. This means that the texture of the catalyst (in particular pore volume and pore distribution) should be improved toward reducing limitations by internal diffusion, which in the case of consecutive reactions rapidly reduces selectivity.

---

<sup>×)</sup> Reprinted with permission from J. F. Le Page, *Applied Heterogeneous Catalysis – Design, Manufacture, Use of Solid Catalysts*, Editions Technip, Paris, 1987.

### 2.1.3 Stability

A catalyst with good stability will change only very slowly over the course of time under conditions of use and regeneration. Indeed, it is only in theory that a catalyst remains unaltered during reaction. Actual practice is far from this ideal. Some of the things that lead to a progressive loss of activity or selectivity or mechanical strength are as follows:

- (a) Coke forms on some catalysts through the intervention of parasitic reactions of hydrogenolysis, polymerization, cyclization, and hydrogen transfer.
- (b) Reactants, products or poisons may attack active agents or the support.
- (c) Volatile agents, such as chlorine, may be lost during reactions such as reforming.
- (d) The crystals of a deposited metal may become enlarged or regrouped. A change in the crystalline structure of the support can cause a loss of mechanical strength.
- (e) Progressive adsorption of trace poisons in the feed or products may reduce activity. It has been pointed out that industrial feedstocks are rarely pure products, but mixtures containing portions of impurities that must sometimes be eliminated beforehand so that the catalyst can be used.

### 2.1.4 Morphology

The external morphological characteristics of a catalyst, i.e. its form and grain size, must be suited to the corresponding process. For moving or boiling bed reactors the spherical form is recommended for reducing problems of attrition and abrasion. In a fluid bed, a spherical powder is preferred for limiting attrition, and its grains should have well determined size distributions for obtaining good fluidization. In a fixed bed, beads, rings, pellets, extrudates, or flakes can be used; but their form and dimensions will have an influence on the pressure drop through the bed. Thus for a given equivalent diameter, catalysts can be classified according to the relative pressure drops they cause, as follows:

Rings < beads < pellets < extrudates < crushed

This pressure drop must be high enough to ensure an even distribution of the reaction fluid across the catalytic bed, but it must not be so high as to cause an increase in the cost of compressing and recycling any gases.

Let us point out again that the grain density and especially the filling density are properties that greatly preoccupy the user; and these depend on the morphology in terms of pore volume. The catalyst is bought by weight with the purpose of filling a given reactor, and the cost of the catalyst charge will depend on its filling density. Finally, with respect to morphology, we point out that catalysts in the form of beads lend themselves better to handling, filling and emptying reactors, as well as any sieving that may appear necessary for eliminating fines after a number of regenerations.

### **2.1.5 Mechanical Strength**

The mechanical strength of a catalyst is demonstrated by its resistance to crushing, which enables the catalyst to pass undamaged through all the strains, both foreseen and accidental, that occur within the catalyst bed. Mechanical strength is also demonstrated by the resistance of the grains to attrition through rubbing, which produces fines and can cause an increase in the pressure drop in a catalytic bed. In the case of powdered catalysts destined for fluid or boiling beds, a resistance to abrasion on the walls or to erosion by the fluids is also required.

### **2.1.6 Thermal Characteristics**

For certain catalysts thermal conductivity and specific heat require consideration. High thermal conductivity of the catalytic mass leads to reduced temperature gradients within the grain, as well as in the catalytic bed, for endothermic or exothermic reactions, by improving heat transfer. For other catalysts, the specific heat assumes more importance; a high specific heat permits a catalytic cracking catalyst to carry a large thermal load from the combustion of coke back to the endothermic cracking reaction, where it is usefully consumed. By contrast, catalysts in catalytic mufflers are more efficient when they are quickly carried to a high temperature by the combustion gases, and a low specific heat can be advantageous.

### **2.1.7 Regenerability**

As we have pointed out in relation to stability, it is only in theory that the catalyst is found intact at the end of the reaction. All catalysts age; and when their activities or their selectivities have become insufficient, they must be regenerated through a treatment that will return part or all of their catalytic properties. The most common treatment is burning off of carbon, but scrubbing with suitable gases is also frequently done to desorb certain reversible poisons; hydrogenolysis of hydrocarbon compounds may be done when the catalyst permits it, as well as an injection of chemical compounds. When the treatment does not include burning off carbon deposits, it is often called rejuvenation.

The shorter the cycle of operating time between two regenerations, the more important the regeneration. It becomes apparent that it is not enough for the catalyst to recover its activity and selectivity, it must also preserve its mechanical strength during successive regenerations or rejuvenations.

### **2.1.8 Reproducibility**

Reproducibility characterizes the preparation of a catalyst as much as the catalyst itself; it is of concern to industrial users who want to be assured of the quality of

successive charges of catalyst; and it also preoccupies the various engineers responsible for developing the catalyst from the laboratory on to industrial manufacture. Indeed, the preparation of a catalyst generally takes place in several rather complex stages dependent on a large number of variables difficult to control simultaneously. The result is that it is indispensable to rapidly verify that the reproducibility of the preparation is feasible, as well as to keep in mind that the formula developed in the laboratory should be capable of extrapolation to pilot scale and to industrial scale under acceptable economic conditions.

### **2.1.9 Originality**

It is also important that the catalyst and the process in which it will be used can be exploited legally through licenses. This is only possible either if the catalyst is original, which is rare, or if it belongs to the public domain, which is more frequent. In the first case, it can be protected by fundamental patents; in the second case, the possible patents can apply only to improvements. The greater the originality, the higher the potential royalties associated with the catalyst or with the process for which it is the controlling part.

### **2.1.10 Cost**

Even when a catalyst possesses all the properties and characteristics just enumerated, there remains one last requirement: it must withstand comparison with competitive catalysts or processes with equivalent functions from the point of view of cost; or at least its cost should not place too heavy a burden on the economics of the process for which it will be used.

## **2.2 The Ideal Catalyst and the Optimum Catalyst**

All of the above properties and characteristics are not independent; when one among them is changed with a view to improvement, the others are also modified, and not necessarily in the direction of an overall improvement. As a result, industrial catalysts are never ideal. Fortunately, however, the ideal is not altogether indispensable. Certain properties, such as activity and reproducibility, are always necessary, but selectivity, for example, has hardly any meaning in reactions like ammonia synthesis; and the same holds true for thermal conductivity in an isothermal reaction. Stability is always of interest but becomes less important in processes that include continuous catalyst regeneration, when it is regenerability that must be optimized. Furthermore, originality can be of secondary importance for certain manufacturing situations such as those relevant to national defense.

The goal, therefore, is not an ideal catalyst but the optimum, which may be defined by economic feasibility studies concerning not only the catalyst but also the rest of the process. And when the catalytic process is established and the catalyst in

question must compete as a replacement, the replacement catalyst's cost and method of manufacture predominate in arriving at the optimum formula.

Depending on the use and the economic competition, therefore, the optimization studies establish an hierarchy among the properties and characteristics of a catalyst; and knowledge of this hierarchy helps to better orient the efforts of the research team responsible for creating and developing the catalyst and its process. Even when the hierarchy is not fixed at the start, it can evolve in the course of developing the catalyst, sometimes even after industrialization.

### 2.2.1 Catalyst Development

A real-life solid catalyst is something entirely different to its user, its manufacturer, or its creator.

The user considers the catalyst within the framework of its function of promoting a chemical reaction, and its properties.

The engineer responsible for manufacturing the catalyst considers it from a different point of view, although still recognizing the needs of the user. For this engineer, the catalyst is primarily a chemical product characterized by its composition and its method of preparation, from the nature of its precursor salts of the active agents, through the conditions of various unit operations used for constructing the catalytic solid. All these operations, precipitation, ripening, filtration, washing, forming, drying, impregnation, calcination and activation, need to be meticulously controlled so that at the end of the manufacturing process the catalyst fits the range of specifications guaranteed to the user.

Finally, although the physical chemist who designs a solid catalyst will be interested in the two preceding points of view, he or she will concentrate on defining it in intrinsic physicochemical terms, such as its texture (pore distribution, specific surface of the overall solid, surface of the deposited active agents, structural density and grain density), its crystallographic characteristics (X-ray or electron diffraction examination to precisely determine the presence of a definite compound, a solid solution, or an alloy), its electronic properties (energy levels of the electrons, valence state of certain elements, or the  $d$  character for other elements or metallic alloys), and especially its surface properties either isolated or preferably in its reaction atmosphere (the thermodynamic characteristics of chemisorption, the chemical and electronic modifications of the catalytic surface, state of surface oxidation or reduction, acidity or basicity, and nature of the bonds in the adsorbed phase).

These various aspects of the catalyst are related through cause and effect. The properties sought in the industrial catalyst by the user flow from its intrinsic physicochemical characteristics; and both industrial properties and physicochemical properties closely depend on the method of preparation. Therefore, it is essential that the research team and the engineers in charge of developing a catalyst and its corresponding process be trained for and given the tools for following the development of the catalyst through all its various aspects, economic and legal ones included. Considering this complexity, the approach to an optimum catalyst can only be an experimental procedure advancing step-by-step through trial and error.

### 2.2.2 Devising the First Catalytic Formulas

An initial hierarchy of required qualities arises out of the detailed analysis of the chemical transformation plus the data from exploratory tests to select the catalytic species. This hierarchy depends on general laws of kinetics and chemical engineering, as well as observations of industrial operations that are more or less analogous. The steps of its articulation are as follows:

- Starting with the selected active species in the laboratory, one prepares a family of catalysts that are related through variations in the manufacturing process, such as sequence of the unit operations, of which certain ones are considered *a priori* critical by reason of their influence on the catalyst properties. The catalysts of this initial family are not chosen at random, but on the basis of general knowledge of inorganic chemistry and chemistry of the solid, plus the know-how acquired from analogous catalysts that seem closest to the fixed objective.
- Subsequently one prepares a list of physicochemical characteristics to be determined for the various catalysts of the family. These characteristics will be those most likely to produce meaningful results from correlations with mechanical and catalytic properties or with the conditions of preparation.

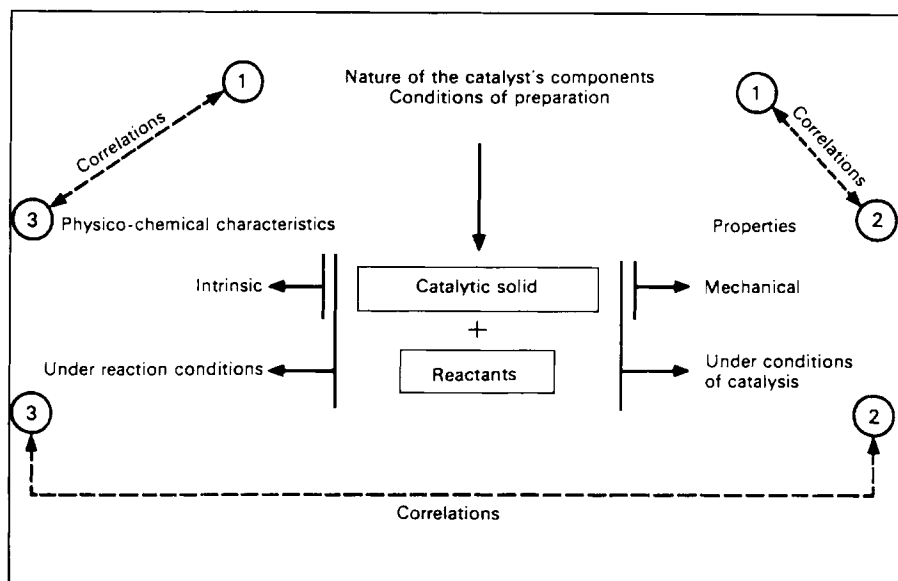
The catalysts of this initial family are then submitted to experiments whose results should permit:

- (a) A good estimation of the predicted performances, the preferred conditions of preparation, and the physicochemical characteristics.
- (b) An identification of critical properties for the catalyst (i.e., those properties most difficult to obtain), as well as the key unit operations (i.e., those essential to the performance of the catalyst), and the physicochemical characteristics on which the performance of the catalyst depends.

Next, a second series of tests is carried out for the purpose of clarifying points shown to be most important at the end of the first series of tests, both in the preparation of the catalysts and in determination of the performance and physicochemical characteristics.

At the end of this second series, and possibly a third, the results should be good enough for the following three partial objectives:

- (a) To establish some correlations between the properties of the catalyst, the intrinsic characteristics of the solid, and the conditions of preparation, as illustrated in Fig. 1. These correlations will provide a basis for perfecting the catalyst, and they can be ultimately used for defining the control tests during industrial manufacture.
- (b) To make an initial selection of some acceptable catalysts to be studied more thoroughly.
- (c) To start using one of the acceptable catalysts for a practical study of the problems of the chemical reaction process. It would be indeed illogical to delay



**Figure 1.** The different aspects of catalysis and their interrelations (adopted from ref [1]).

studying the problems of the overall process for formulation of the optimum catalyst, since according to the economic criteria the idea of an optimum catalyst has meaning only within the framework of the total problems posed by the unit. Thus it is necessary to begin the study of these problems on a catalyst that is judged acceptable, in order to deduce those elements that will orient optimization of the industrial catalyst.

At this stage it is time for a few practical remarks:

- (a) Although the study of catalytic properties can sometimes be made on model molecules for the initial preparation, it is generally preferable to operate with industrially representative feedstocks, and under industrially representative conditions, as early as possible.
- (b) For the initial catalysts, one sometimes omits the study of stability, a property that essentially demands a great deal of time for evaluation. Generally, stability is studied only with formulas that are already acceptable and often after having developed a test for accelerated aging.
- (c) For a catalyst to be regarded as acceptable, a study of its manufacturing process should have been started and advanced to the pilot scale for judging its production feasibility. Indeed, from this point on, experimenting becomes costly, and it is necessary to make sure that the catalyst is not just a laboratory curiosity.
- (d) As soon as the first results from the study of the process are obtained with the initial acceptable formula, an economic analysis and possibly a legal review

should be undertaken for judging more accurately the industrial viability of the proposed process. If the results that one can expect from these reviews deviate too far from commercial requirements, the research project should be abandoned. If the proposed process is shown to be economically viable, one continues on to the optimization of the catalyst, taking into account the problems to be encountered in the course of its use in the proposed process.

### 2.2.3 Optimization of a Typical Catalytic Formula

This optimization is achieved by exploiting to the utmost the correlations established during definition of the initial catalytic formulas. It should not only take into account the problems raised by the study of use but also the need for a simple and economical preparation that can be expanded to industrial scale. Therefore, the problems of extrapolating to industrial scale the various unit operations perfected in the laboratory have to be resolved in the pilot plant. This study consists of:

- (a) Pilot preparation of a certain number of samples whose performances must be tested. Examination of the results makes it possible to specify the operating conditions for each stage of the future industrial operation.
- (b) Forecasting a price for the industrial catalyst.
- (c) Establishing a manufacturing process using existing equipment as far as possible.
- (d) Production of enough catalyst by the manufacturing process for the catalyst to be representative of industrial production.

One must remember that a catalyst optimized in this way represents only a transitory optimum; experience has shown that hardly is any catalyst industrialized before it is subject to improvements, either for correcting deficiencies revealed through the industrial experience or for improving a competitive position. Sometimes it happens that a change occurs in the very nature of the catalytic agent; and at that point it is a veritable matter of catalyst renovation, involving a procedure identical to that which has just been described for the genesis of the initial formula.

Perfecting an industrial catalyst is thus the culmination of a long and complicated process that requires a knowledge as broad as possible of the methods relative to the preparation of catalysts, to the study of catalytic and mechanical properties, and to the determination of the physicochemical characteristics.

## References

- 1. R. Montarnal, and J. F. Le Page, *La catalyse au laboratoire et dans l'industrie*, 1967, Masson, 1967, 231–287.



## 3 Bulk Catalysts and Supports

### 3.1 Fused Catalysts

R. SCHLÖGL

#### 3.1.1 Introduction

A small number of heterogeneous catalysts is prepared by fusion of various precursors. The obvious group of compounds are metal alloy catalysts which are applied in unsupported form like noble metal gauze for the ammonia oxidation to nitric oxide. Melting of the elements in the appropriate composition is the only way to produce bulk amounts of a chemical mixture of the constituent atoms. The process is well-described by thermodynamics and a large database of phase diagrams and detailed structural studies is available. Metallurgy provides the technologies for preparation and characterization of the products [1]. This enables the synthesis of a large number of bulk alloys with well-defined properties. An interesting development in the use of such bulk-phase metallic alloy catalysts is the application of bulk metallic glasses in the form of ribbons with macroscopic dimensions [2–5]. In this class of materials the atomic dispersion in the liquid alloy is preserved in the solid state as a single phase, although the material may be metastable in its composition. This allows the preparation of unique alloy compositions which are inaccessible by equilibrium synthesis. The solidification process by rapid cooling (cooling rates above  $10^4 \text{ K s}^{-1}$ ) creates “glassy” materials with well-defined short range order but without long range order. The difference in free energy between compositional equilibration and crystallization, stored in the metallic glass, can be used to transform the material in an initial activation step from a glassy state into a nano-crystalline agglomerate with a large internal surface interface between crystallites. This still metastable state is the active phase in catalysis and the final transformation into the stable solid phase mix with equilibrium composition terminates the life of such a catalyst.

In oxide materials [2] which are fused for catalytic applications, two additional factors contribute to the unique features of this preparation route. Many oxides in their liquid states are thermodynamically unstable with respect to the oxygen partial pressure present in ambient air, i.e. they decompose into lower-valent oxides and

release molecular oxygen into the gas phase. This process can be fast on the time-scale of the fusion process, such as with vanadium pentoxide or manganese oxides, or may be slow, as with iron oxides. The existence of such decomposition reactions and the control of their kinetics [6] can create a unique quenched solid which is thermodynamically metastable at ambient conditions with respect to its oxygen content. In addition, by controlling the phase nucleation, a local anisotropy of phases, i.e. a mixture of particles of different oxide forms interdispersed with each other, can be obtained. Such oxides exhibit a complex and reactive internal interface structure which may be useful either for direct catalytic application in oxidation reactions or in predetermining the micromorphology of resulting catalytic material when the fused oxide is used as precursor.

The application of the fusion process can lead to a control over structure-sensitive reactions for unsupported catalysts. The prototype example for such a catalyst is the multiply-promoted iron oxide precursor used for ammonia synthesis.

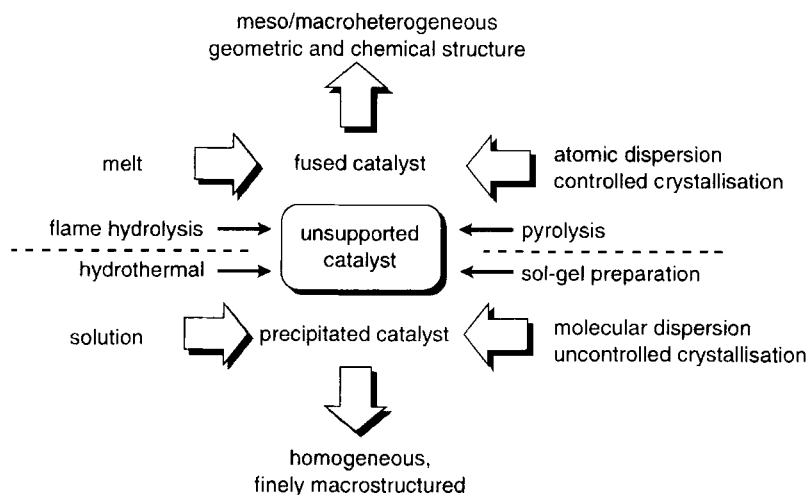
Another feature of fused catalytic compounds can be the generation of a melt during catalytic action. Such supported liquid phase (SLP) catalysts consist of an inert solid support on which a mixture of oxides is precipitated which transform into a homogeneous melt at reaction conditions. These systems provide, in contrast to the case described before, a chemically and structurally homogeneous reaction environment. The standard example for this type of catalyst is the vanadium oxide contact used for oxidation of  $\text{SO}_2$  to  $\text{SO}_3$ .

### 3.1.2 Concept of Fused Catalysts

The preparation of non-supported catalysts by fusion is an expensive and very energy-consuming high-temperature process. It has to compete with the concept of wet chemical preparation by the mixing-precipitating-calcining process which can be used in oxidative and reductive modes to obtain oxides and metals. Sol-gel preparation or flame hydrolysis are derivatives of the general approach. Another unconventional alternative to this important route of catalyst preparation is offered by tribochemical procedures; however, these are still in an early stage of research.

This enumeration shows that the term “fused catalyst” is not synonymous with “unsupported catalyst”, but designates a small subgroup of unsupported catalytic materials. Fused catalysts have passed through the molten state at least once during their preparation. In this respect fused catalyst are fundamentally different from other catalysts prepared at high temperatures, such as carbons which are produced by gas-solid reaction processes with substantially kinetic differences compared to melt-solidification reactions.

Figure 1 summarizes the main differences and objectives between the major preparation strategies. A collection of the major individual reaction steps for the synthesis of unsupported catalysts can be found in Table 1. One fundamental insight from this rather schematic comparison is that differences in the reaction kinetics of the synthesis of a given material will lead to different mesoscopic and macroscopic structures which considerably affect the catalytic performance. It is necessary to control these analytically difficult-to-describe parameters with much the same pre-



**Figure 1.** Principal pathways to generate unsupported catalytic materials. The methods indicated in the centre of the scheme are discussed in other sections of this book. The methods of fusion and precipitation will be discussed more in detail to illustrate the consequences of the different reaction environments on the structural properties of the final products. The dashed line separates solution methods (bottom) from high-temperature reactions (top).

cision as the atomic arrangement or the local electronic structure. Whereas these latter parameters influence the nature of the active site, it is the meso/macrostructure which controls the distribution and abundance of active sites on a given material. It is necessary in certain cases to apply the costly method of fusion as there is no other way to obtain the desired (and in most cases unknown) optimal meso/macrostructure of the final catalyst.

Details of the chemistry in the precipitation process can be found in other sections of this handbook. This section focuses on fused catalysts. The reader may contrast the following discussion with the contents of Table 1.

Fused catalysts allow the combination of compounds and elements in atomic dispersions which do not mix either in solution (e.g. oxides) or in the solid state. Melting provides the necessary means to generate an intimate, eventually atomically disperse distribution; a carefully controlled solidification can preserve the metastable situation in the melt down to operation temperature. In the melt the preformation of “molecules” such as oxo complexes or alloy clusters can occur. The final short-range order of the catalyst is predetermined. Examples are alloys of noble metals with elements located in the main group sections or in the early transition metal groups of the periodic table (E-L TM alloys). In the case of oxides the partial pressure of oxygen has the chance to equilibrate between the gas phase environment of the melting furnace and the liquid oxide. With compounds in high formal oxidation states this can lead to thermochemical reduction, as for iron oxide (reduction of hematite to magnetite and wustite), or for silver oxide which reduces to the metal. Compounds in low oxidation states, such as  $\text{MnO}$ ,  $\text{Sb}_2\text{O}_3$  or  $\text{VO}_2$ , will oxidize to higher oxidation states and thus also change the chemical structure.

**Table 1.** Main reaction steps in precipitation and fusion of catalytic solids.

Step	Wet chemical	Fusion
Mixing of atoms	in solution	in melt
Preformation of compounds	frequently, with solvent ligands	possible for alloys (E-L-TM), always for compounds (oxides)
Compositional modification	frequently, by ligand exchange and incorporation of solvent	possible with volatiles, frequently with compounds by thermochemical reduction
Solidification	precipitation, difficult to control, very fine particles with molecular homogeneity	cooling, very important to control, affects chemical structure (exsolution) and long-range ordering
Calcination	required for ligand removal, complex reaction, difficult to control	not required
Formulation	pressing, extrudation precipitation onto supports	crushing, sieving, production of wires and gauze

The kinetics to reach the equilibrium situation can be quite slow, so that the holding time and mechanical mixing of the melt will crucially affect the extent of the chemical conversion. Early termination of the holding time will lead to metastable situations for the melt with local heterogeneity in the chemical composition of the final product. This can be desirable, as in the case of the iron oxide precursor for ammonia synthesis, or it can be unwanted as in most intermetallic compounds. Also, the dissolution of, for example, one oxide into another, can be a prolonged process and early cooling will lead to a complex situation of disperse binary compounds coexisting with ternary phases. Examples are alumina and calcium oxide promoters in iron oxide melts where ternary spinel compounds can be formed, provided that sufficient trivalent iron is present. This requires the addition of activated forms of the binary oxides in order to dissolve some of the ions before the thermochemical reduction has removed the trivalent iron in excess of that required for the formation of the matrix spinel of magnetite. These examples illustrate that both the starting compounds, their purity and physical form, and the heating program will severely affect the composition and heterogeneity of the resulting material. Scaling-up of such fusion processes is a major problem as heat and ion transport determine, to a significant extent, the properties of the material. Also the gas phase over the melt and its control are of high importance as its chemical potential will determine the phase inventory of the resulting compound.

Besides the complex cases of mixed oxides, there exist more simple problems of oxide and scale formation in alloy production. The detrimental effect of oxide shells around metal particles preventing intermixing is well known. The compositional changes resulting from preferential oxidation of one component have also to be taken into account. Instability of the product and/or drastic changes in the thermochemical properties of the material after shell formation (such as massive increases in the required fusion temperature in noble metal eutectic mixtures) are

common, in particular in small-scale preparations. These effects still set limits to the availability of catalytically desired alloys for practical purposes (e.g. for compounds with Zr, Si, alkali, Mg).

In addition to these more practical problems of catalyst preparation, there are also severe theoretical problems associated with the prediction of the chemistry in the fluid state of a compound. The motion of all structural elements (atoms, ions, molecules) is controlled by a statistical contribution from Brownian motion, by gradients of the respective chemical potentials (those of the structural elements and those of all species such as oxygen or water in the gas phase which can react with the structural elements and thus modify the local concentration), and by external mechanical forces such as stirring and gas evolution. In electric fields (as in an arc melting furnace), field effects will further contribute to nonisotropic motion and thus to the creation of concentration gradients. An exhaustive treatment of these problems can be found in a textbook [6] and in the references therein.

The second step in the process is the cooling of the melt. Slow cooling will result in equilibration of the mix according to the thermodynamic situation. Only in simple cases will this yield the desired compound. In most cases the mixture of structural elements stable in the melt will be metastable at ambient conditions. Techniques of supercooling are applied to maintain the desired composition [7]. Rapid solidification with temperature gradients up to about  $100\text{ K s}^{-1}$  are required to generate metastable crystalline solids. Local heterogeneity (such as concentration gradients or undissolved particles) will disturb the equilibrium formation [8] of crystals and lead to unusual geometries of the grain structure. The crystallite size is also affected by the cooling rate, in particular at temperatures near the solidus point where the abundance of (homogeneous) nuclei is determined. Rapid cooling limits the growth of large crystals as the activation energies for diffusion and dissolution of smaller crystallites is only available for a short time. Annealing of the solid after initial solidification can be used to modify the crystallite size, provided that no unwanted phase transition occurs in the phase diagram at or below the annealing temperature. Knowledge of the complete phase diagram for the possible multi-component reaction mixture is mandatory for the design of a temperature-time profile for a catalyst fusion experiment. In many cases these phase diagrams are not available or not known with sufficient accuracy, so that a series of experiments is required to adjust this most critical step in the whole process. Frequently, empirical relationships between characteristic temperatures in the phase diagram and the critical temperatures for stable-to-metastable phase transformations (e.g. the ratio between an eutectic temperature and the crystallization temperature of a binary system) are used to predict compositions of stable amorphous compounds of metals and metalloids [8, 9].

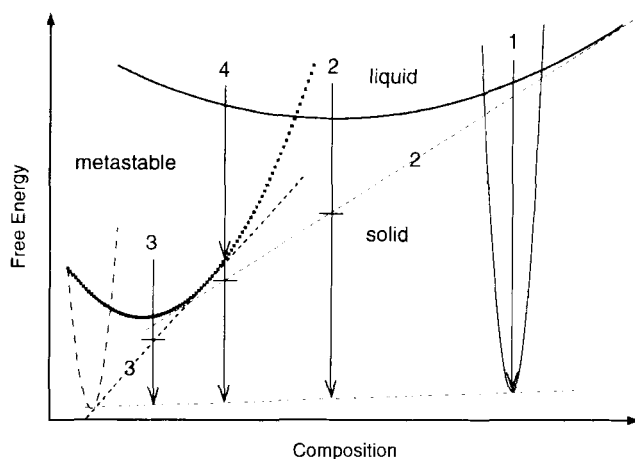
Cooling rates between  $100$  and  $10\,000\text{ K s}^{-1}$  can lead to a modification of the long-range order of the material. Under such rapid solidification conditions the time at which the activation energy for motion of structural elements is overcome is so short that the mean free pathlength reaches the dimension of the structural unit. Then the random orientation of the units in the melt is preserved and the glassy state is obtained. Such solids are X-ray amorphous and contain no grain boundary network and exhibit no exsolution phenomena. They are chemically and structur-

ally isotropic [6]. These solids preserve, however, the energy of crystallization as potential energy in the solid state. It is possible to transform these glasses into cascades of crystalline states, some of which may be also metastable at the crystallization condition as the activation energy, for falling into the state of equilibrium, is not high enough. Glassy materials are thus interesting precursors for the formation of metastable compositions and/or metastable grain boundary structures which are inaccessible by precipitation and calcination. The critical glass-forming temperatures vary widely for different materials, with alkali silicates requiring low cooling rates of several  $100 \text{ K s}^{-1}$  and transition metal oxides and E-L TM alloys rates above  $1000 \text{ K s}^{-1}$ . Pure elements cannot be transformed into the glassy state. By utilizing these differences, composite materials with a glassy phase coexisting with a crystalline phase can be obtained. Examples are amorphous oxide promoter species dispersed between the iron oxides of the ammonia synthesis catalyst precursor.

The third step in the catalyst preparation process is the thermal treatment known as calcination, which is essential in all wet chemical processes. It leads to solvent-free materials and causes chemical reactions between components with the oxidation states of all elements reaching their desired values. All this is already accomplished during preparation of the fluid phase and during precipitation of the fused catalyst, and hence such a step is rarely required for these catalysts. This feature significantly reduces the difference in energy input to the final catalyst, between fusion and precipitation. The fact that the conditioning of the catalytic material occurs in the fluid state for a fused catalyst and in the solid state for the precipitated catalyst has two important consequences. First, the temperature levels of conditioning are different and so is the composition of the resulting material in particular with respect to volatile components. Secondly, the calcination reaction occurs as solid-solid state reaction with diffusion limitations and eventual topochemical reaction control, both giving rise to spatial heterogeneity in large dimensions relative to the particle size. In fused systems the fluid state allows very intimate mixing and hence isotropic chemical reactivity, provided that the composition is either stable during cooling or quenched so rapidly that no demixing occurs. Chemical heterogeneity at any dimensional level can be created or occurs unintentionally with no gradients between particle boundaries if the cooling process is suitably adjusted to allow partial equilibration of the system.

The last step of catalyst preparation is the activation which is required for both types of materials. In this step, which often occurs in the initial stages of catalytic operation, (in situ conditioning) the catalyst is transformed into the working state which is frequently chemically and/or structurally different from the as-synthesized state. It is desirable to store free energy in the catalyst precursor which can be used to overcome the activation barriers into the active state in order to initiate the solid state transformations required for a rapid and facile activation. These barriers can be quite high for solid-solid reactions and can thus inhibit the activation of a catalyst.

A special case is catalysts which are metastable in their active state with respect to the catalytic reaction conditions. In this case a suitable lifetime is only reached if the active phase is regenerated by solid state reaction occurring in parallel to the substrate-to-product conversion. In this case it is of special relevance to store free



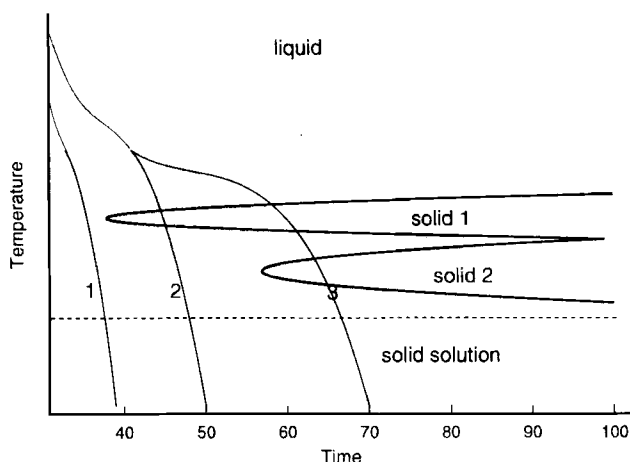
**Figure 2.** The thermodynamic situation upon solidification of a multinary system. The vertical lines designate principal reaction pathways, the dashed tangent lines illustrate the compositional changes arising from an equilibrium solidification at the respective pathways (interrupt lines on the vertical arrows). The narrow areas of existence designate stable phases with a finite phase width, the area designated metastable indicates the existence of a single phase solid which is unstable at ambient conditions.

energy in the catalyst precursor as insufficient solid state reaction rates will interfere with the substrate-to-product reaction cycle. A class of catalyst in which this effect is of relevance are oxide materials used for selective oxidation reactions.

### 3.1.3 Thermodynamic and Kinetic Considerations

The following general considerations are intended to illustrate the potential and complications when a fused catalyst material is prepared. The necessary precondition is that the starting state is a homogeneous phase (the fluid).

Figure 2 shows a general free energy versus composition diagram [10] for a fused catalyst system. The composition coordinate may be a projection [11] through a multinary phase diagram. The melt will solidify in the phase (1) with little compositional variation, if the melt is cooled slowly. This path leads to a stable solid with little problems in its preparation and identification. If the melt is cooled suitably to follow the solidus curve further down in free energy it reaches the eutectic point (2) and can then be rapidly quenched without any compositional variation. This creates a metastable solid with a large amount of free energy stored in the solid state. The resulting material is a characteristic fused catalyst (or precursor). If the cooling is slowed down, the composition will split in a primary crystallization [11] of the supersaturated solution. The melt is then enriched in one component according to the tangent line (2) and the solid is depleted until it reaches the composition of the metastable solid (3). The enriched melt can either crystallize in (1) or react along pathway 3 provided that enough energy of crystallization is released and



**Figure 3.** Kinetics of solidification illustrating how various cooling programmes (pathways 1 to 3) can affect the final inventory of phases which differ in their respective crystallization kinetics. The characteristic times are in the microsecond regime for metallic alloys but extend into the time-scales of days for compounds such as oxides.

the cooling conditions [12] are still adequate. The metastable solid (3) may either be quenched and form a further metastable component of the phase mix or it can undergo equilibration in the same way as system (2) along the tangent line (3). The cooling conditions and eventual annealing intervals will decide over the branching ratio. A further possibility is the formation (4) of a supersaturated solid solution (the metastable solid in Figure 2) directly from the melt followed by either quench cooling to ambient temperature leading to another metastable phase in the mix or by equilibration according pathway (3).

The solidification kinetics and compositional fluctuations in the melt will decide over the crystallization pathway which can be followed by all of the melt. If local gradients in temperature or composition exist in the system the crystallization pathway can be locally inhomogeneous and create different metastable solids at different locations in the macroscopic solidified blocks.

This simple consideration shows that a wide variety of stable and metastable solids can be produced from a homogeneous melt if the solidification conditions are suitably chosen. In this way a complex solid phase mix can be obtained which is inaccessible by the wet chemical preparation route. The metastable phase mix may either contain an active phase or may be used to generate it by a suitable activation procedure at relatively low temperatures. A stable phase which is catalytically useful should be accessible by other less complex and costly ways and is thus not be considered here.

The kinetic situation is generalized in Figure 3. For a fused catalyst system a liquid phase is assumed to coexist with a metastable solid solution. Additional solid phases crystallize with retarded kinetics and form lenses in the time-temperature diagram of Figure 3. Three characteristic cooling profiles are sketched. Rapid



quenching (1) leads to only the solid solution without compositional changes and without mesoscopic heterogeneity. Intermediate quenching (2) passes through the solid 1 area and leads to a branching of the solid products between solid 1 and the solid solution with a modified composition (primary crystallization, path 2 in Figure 2). Cooling with a holding sequence (3) allows preformation of structural units in the melt and leads to the formation of three solids with different compositions. Moving the holding temperature further down into the ranges occupied by the solid phases provides control over the branching of the solid products. It can be seen that rapid cooling of the fused melt leads to a clear situation with respect to the solid as all free energy is transferred into the solid phase and liberated only in solid-solid reactions. If the cooling rate is intermediate or if the cooling rate is not isokinetic in the whole melt, then we obtain complex situations with wide variations in chemical and local compositions of the final solids.

The reduced fused iron oxide for ammonia synthesis is a perfect example illustrating in its textural and structural complexity the merit of this preparation strategy which allows to create a metastable porous form of the element iron. The necessary kinetic stabilization of the metastable solid is achieved by the ex-solution of irreducible oxide phases of structural promoters. Some of them precipitate during solidification, whereas others are liberated from the matrix during activation. A prerequisite for the very important secondary ex-solution species is the intimate phase mixture of ternary iron earth alkali oxides, which cannot be achieved by wet chemical precipitation techniques due to the extremely different coordination chemistry of the various cations in solvent media.

### 3.1.4 Sulfuric Acid Catalyst

The reaction of gaseous  $\text{SO}_2$  with molecular oxygen in the contact process seems to proceed over two independent mechanisms [13] one of which is the direct oxidation of a vanadium pentoxide-sulfur dioxide adduct by oxygen and the other proceeding via a redox cycle involving  $\text{V}^{4+}$  and  $\text{V}^{3+}$  intermediate species [13–15].

The technical catalyst is a supported liquid phase system of vanadium pentoxide in potassium pyrosulfate [16, 17]. Other alkali ions influence the activity [18] at the low-temperature end of the operation range, with Cs exhibiting a particular beneficial effect [13].

It is necessary to work at the lowest possible temperature in order to achieve complete conversion. Only at temperatures below 573 K is the equilibrium conversion of  $\text{SO}_2$  practically complete, with about 99.5% conversion. The binary phase diagram vanadium-oxygen shows the lowest eutectic for a mixture of pentoxide and the phase  $\text{V}_3\text{O}_7$  at 910 K. All binary oxides are stable phases from their crystallization down to ambient temperature. The pyrosulfate promoter is thus an essential ingredient rather than a beneficial additive to the system. Compositions of 33% alkali (equals to 16.5% pyrosulfate) solidify at around 590 K. This temperature is still too high as at around 595 K the activation energy increases sharply, even although the system is still liquid. The liquid state is thought to be essential for the facile diffusion [13, 19] of oxygen to the active sites [13].

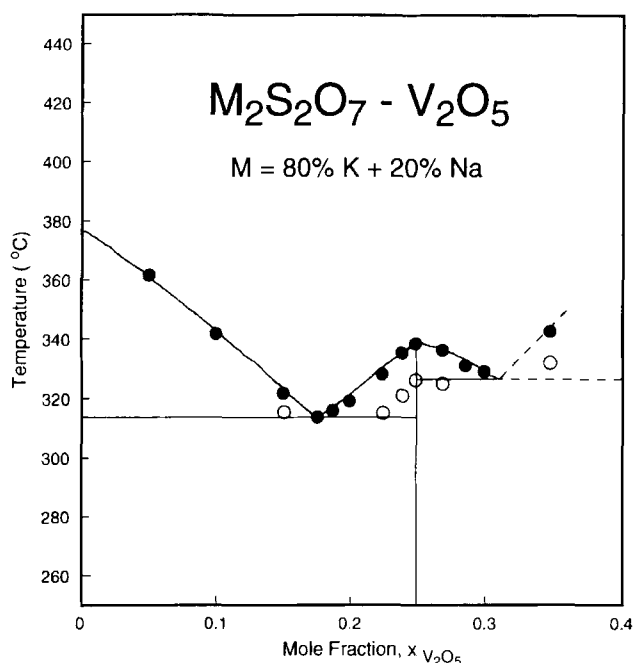
The small mismatch between required and achieved minimum operation temperature has the severe consequence that a special preabsorption stage has to be included in the reactor set-up in order to achieve the essential complete conversion. In this manner the partial pressure of the  $\text{SO}_3$  product is lowered before the last stage of conversion, rendering acceptable incomplete conversion of the overheated catalyst. If the reason why the catalyst does not operate efficiently down to its solidification point could be eliminated one may circumvent the intermediate absorption stage and thus facilitate the reactor design considerably.

Catalyst fusion is essential to bring and keep the pyrosulfate–vanadium oxide system into a homogeneous state which is the basis for operating the system at the eutectic in the ternary phase diagram. The reaction mechanism and the fact that the operation point of the catalyst is at the absolute minimum in the  $\text{V}^{5+}$ – $\text{O}_2$  section of the phase diagram point to the existence of a supersaturated solution of partly reduced vanadium oxides in the melt. The point at which the activation energy for  $\text{SO}_2$  oxidation changes over to a lower (transport-controlled) value marks thus the stage at which crystallization of the supersaturated solution begins under catalytic conditions. This hypothesis could be verified in pioneering studies by Fehrmann and co-workers using electric conductivity measurements and preparative isolation techniques [16, 17]. They isolated crystals of a variety of  $\text{V}^{4+}$  and  $\text{V}^{3+}$  ternary alkali sulfates. These precipitates can be redissolved in a regeneration procedure of the catalyst involving a heat treatment to 800 K under oxidizing conditions [17]. In a rather elegant *in situ* electron paramagnetic resonance (EPR) study the deactivation mechanism was experimentally confirmed on an industrial supported catalyst in which the phase  $\text{K}_4(\text{VO})_3(\text{SO}_4)_5$  was identified as  $\text{V}^{4+}$  deactivating species which could also be redissolved by a high temperature treatment. [20]

The accurate analysis of the problem is complicated as, under reaction conditions (presence of oxygen), all redox equilibria between  $\text{V}^{5+}$  and the lower oxidation states are shifted towards the pentavalent state. The generation of realistic model systems in which, for example, conductivity experiments can be performed, thus requires the exact control of the gas phase in contact with the melt.

The real pseudobinary phase diagram [16] of  $\text{V}_2\text{O}_5/\text{S}_2\text{O}_7\text{M}_2$  with  $\text{M} = \text{K}$  or  $\text{Na}$  is rather complex in the interesting range around the eutectic which is displayed in Figure 4. The formation of a complex salt with the composition  $3\text{M}_2\text{S}_2\text{O}_7 \cdot x\text{V}_2\text{O}_5$  interferes with the eutectic and gives rise to two eutectic points with fusion temperatures of 587 K and of 599 K. It is interesting to note that the chemistry of vanadium pentoxide in molten alkali sulfates is different from the present case with pyrosulfates where no vanadium oxo oligomers are formed. This is an indication of a complex formation between pyrosulfate and vanadium oxide in the sense of preformed molecules in the fused melt. The dashed lines in Figure 4 indicate the estimated continuation of the phase boundaries which are inaccessible experimentally as in this regime glassy oxides with unknown compositions are formed.

These observations on the sulfuric acid catalyst are full in line with the general thermodynamic behaviour of fused catalyst systems. The metastable solid in Figure 2 has to be replaced in this case by a cascade of the partly reduced vanadium ternary sulfates. The processes sketched above occur under thermodynamic control in a quaternary phase diagram, vanadium–oxygen–sulfur–alkali, as illustrated by the



**Figure 4.** Section of the pseudobinary phase diagram of the sulfuric acid SLP catalytic material. The data were taken from Ref. 16. The data points were derived from anomalies of the conductivity versus temperature curves of the respective mixtures. At the high compositional resolution and in the range of the global eutectic, the formation of a vanadate-sulfato complex causes the local maximum in the solidus curve. It is noted that extreme precision in the experimental procedures was necessary to derive this result illustrating the characteristic of fused systems that compound formation can well occur in the molten state.

reversibility of the exsolution of the partly reduced vanadium compounds under suitable partial pressures of oxygen within the melt. This partial pressure is adjusted by the operating temperature. The desired low operation temperature increases the viscosity of the melt and hence increases the diffusion barrier of the gas in the liquid. This in turn facilitates the exsolution of reduced vanadium sulfates which further inhibit the oxygen diffusion.

### 3.1.5 Metallic Glasses

Amorphous metals can be prepared in a wide variety of stable and metastable compositions with all catalytically relevant elements. This synthetic flexibility and the isotropic nature of the amorphous state with no defined surface orientations and no defect structure (as no long-range ordering exists) provoked the search for their application in catalysis [21]. The drastic effect of an average statistical mixture of a second metal component to a catalytically active base metal was illustrated in a model experiment of CO chemisorption on polycrystalline Ni which was alloyed by

Zr as a crystalline phase and in the amorphous state. As CO chemisorbs as a molecule on Ni and dissociates on Zr, it was observed that on the crystalline alloy a combination of molecular and dissociative chemisorption in the ratio of the surface abundance occurred. This additive behavior was replaced by a synergistic effect of the Zr in the amorphous state where molecular adsorption with a modified electronic structure of the adsorbate was observed [22]. This experiment led to the conclusion that with amorphous metals a novel class of catalytic materials with tuneable electronic properties might be at our disposal.

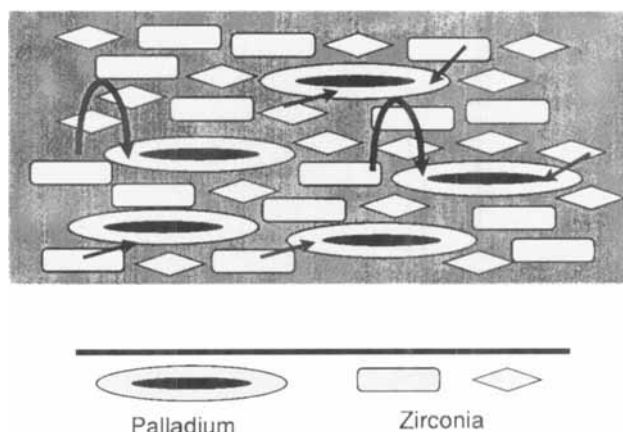
First attempts to check this hypothesis [23] revealed a superior catalytic activity of iron in amorphous iron–zirconium alloys in ammonia synthesis compared to the same iron surface exposed in crystalline conventional catalysts. A detailed analysis of the effect subsequently revealed that the alloy, under catalytic conditions, was not amorphous but crystallized into platelets of metastable epsilon-iron supported on Zr-oxide [24, 25].

This was the first proven example of the operation of the principle that free energy stored in the metastable amorphous alloy can be used to create a catalytically active species which is still metastable against phase separation and recrystallization, but which is low enough in residual free energy to maintain the catalytically active state for useful lifetimes.

In Pd–Zr alloys a different principle of usage for the excess free energy can be found. Amorphous alloys of the composition PdZr<sub>2</sub> were activated in several procedures and compared to a Pd on ZrO<sub>2</sub>-supported catalyst for the activity in CO oxidation applications [26, 27]. In situ activation of the amorphous alloy caused crystallization into small nanocrystalline Pd + O solid solution particles and larger pure Pd particles, which are both embedded into a high interface area of zirconia being present as poorly crystalline phase mix of monoclinic and tetragonal polymorphs. This phase mix is still metastable against formation of large particles of pure Pd and well crystallized large particles of zirconia with little common interface area as it is obtained from conventional impregnation techniques. A detailed analysis of the surface chemistry of the in situ activated amorphous alloy, which is metastable against segregation of a thick layer of zirconia in air, revealed that only under crystallization in the reaction mixture is the intimate phase mix between zirconia and Pd present at the outer surface of the material. It was concluded from kinetic data [26] that the intimate contact between zirconia and Pd should facilitate the spillover of oxygen from the oxide to the metal.

Figure 5 illustrates schematically the advantages of the metastable structure of the active surface. It remains speculative as to whether the beneficial effect is really spillover of oxygen from the oxide through the surface and/or bulk diffusion [26], or whether the structural stabilization of the known [27] oxygen storage phase in the Pd (the solid solution) by the defective zirconia matrix is the reason for the superior catalytic performance.

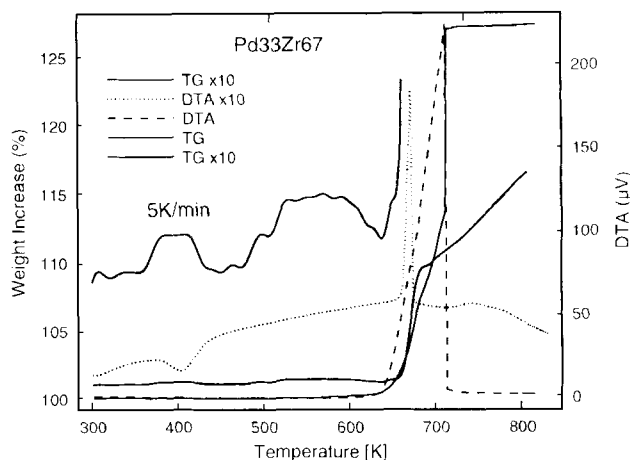
Most relevant for the oxygen transport should be the defective crystal structure of both catalyst components. The defective structure and the intimate contact of crystallites of the various phases are direct consequences of the fusion of the catalyst precursor and are features which are inaccessible by conventional wet chemical methods of preparation. Possible alternative strategies for the controlled synthesis



**Figure 5.** Schematic arrangement of the surface of a partly crystallized E-L TM amorphous alloy such as Pd-Zr. A matrix of zirconia consisting of the two polymorphs holds particles of the L transition metal (Pd) which are structured in a skin of solid solution with oxygen (white) and a nucleus of pure metal (black). The arrows indicate transport pathways for activated oxygen either through bulk diffusion or via the top surface. An intimate contact with a large metal-to-oxide interface volume with ill-defined defective crystal structures (shaded area) is essential for the good catalytic performance. The figure is compiled from the experimental data in the literature [26, 27].

of such designed interfaces may be provided by modern chemical vapor deposition (CVD) methods with, however, considerably more chemical control than is required for the fusion of an amorphous alloy.

The metastable character of amorphous alloys under catalytic conditions is illustrated in Figure 6. Thermogravimetric and differential thermal analysis (TG/DTA) responses are shown for the treatment of a Pd-Zr alloy in reducing and oxidizing atmospheres. In pure hydrogen the formation of hydride intercalation compounds are revealed by the small reversible weight changes in the temperature range between 300 K and 600 K. It is interesting to note that the low-temperature intercalation is an endothermal process (formation of a palladium hydride), whereas the high-temperature intercalation causes no thermal response (formation of a zirconium-hydrogen solid solution). All this does not affect the amorphous character of the alloy which crystallizes in a single exothermic step at 663 K. The concomitant weight gain indicates the extreme reactivity of the fresh zirconium metal surface formed by the segregation and crystal growth leading to a gettering effect of impurities present in the hydrogen gas stream. Their transportation into the bulk of the alloy is reflected by the increasing weight above 680 K. In oxygen the crystallization temperature is the same as in hydrogen, indicating the absence of drastic chemically induced segregation phenomena as cause for the bulk crystallization. The oxidation of Zr metal is a highly exothermic process occurring after the alloy has transformed into a crystalline phase mix. This stepwise conversion with surface and bulk reactivity is reflected in the stepped weight increase. The thermal signal is overloaded by the heat evolution caused by the Zr oxidation so that little structure is seen in the DTA signals. The data show that the amorphous alloy is passivated at



**Figure 6.** Compilation of TG/DTA responses for the crystallization of the amorphous alloy  $\text{Pd}_{33}\text{Zr}_{67}$  which was prepared by the melt-spinning technique. The red data were obtained in hydrogen, the blue data in oxygen. The responses in hydrogen are enlarged by a factor of 10, the enlarged weight curve by a factor of 100 relative to the ordinate scales. A SEIKO instrument was used and gas flows of  $100 \text{ ml min}^{-1}$  were adjusted for sample masses of ca. 4 mg.

room temperature and can be used in oxygen up to the crystallization temperature which breaks the passivation layer due to formation of a new mesostructure causing mechanical stress and strain on the protective coating. However, hydrogen, can penetrate the passivation layer and form hydrides in the amorphous metallic sub-surface regions. The shape of the TG signals indicates transport limitations arising from the nonisothermal experiment. The interaction of the hydrogen with the alloy was not strong enough to overcome the activation barrier for crystallization. Such a diluted palladium catalyst may thus be used up to temperatures of 623 K. The lifetime of the system is not derived by this type of experiment which is too insensitive to detect surface crystallization which would induce slow bulk reactions at lower temperatures than seen in the TG/DTA experiments.

In a study of the application of Pd-Si amorphous alloys as selective hydrogenation catalysts [3] it was found that in situ activation provides a route to active and selective catalysts, whereas ex situ activation caused the crystallization of the system into the thermodynamically stable  $\text{Pd} + \text{SiO}_2$  system, which is indistinguishable in its activity and poor selectivity from conventional catalysts of the same composition. In this study it was possible to show conclusively that all amorphous alloys are not amorphous on their surfaces as they undergo, in reaction gas atmospheres, chemically-induced phase segregation which starts the crystallization process according to Figure 2 (pathway 2).

The function of the fused amorphous alloys is thus to serve as a precursor material for the formation of a metastable active phase characterized by an intimate mixture of phases with different functions. This mixture is preformed during preparation of the metallic melt and preserved by rapid solidification. The micro-morphology consists of quenched droplets allowing subsequent segregation into

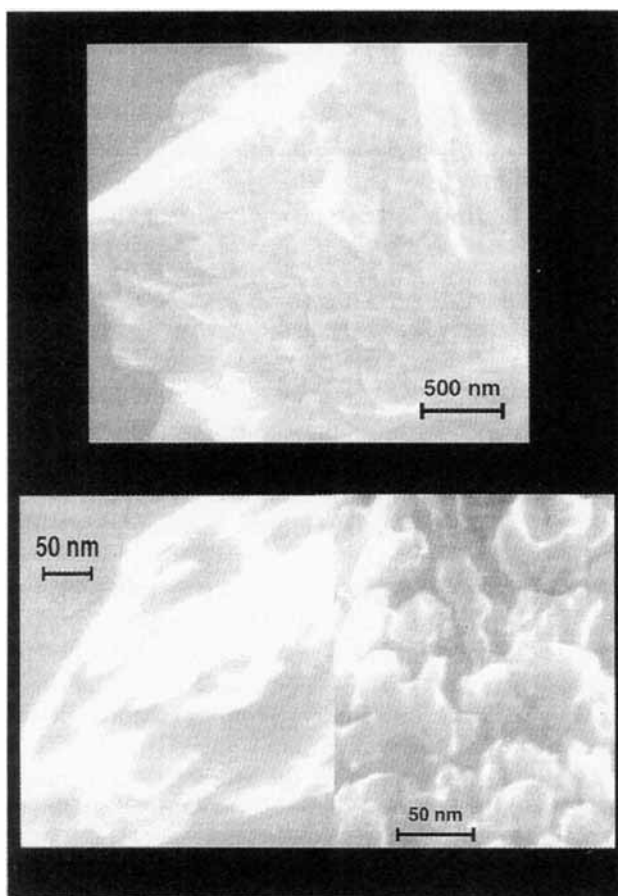
platelets. In situ activation is the method to prevent crystallization in the structure with the global free energy minimum. This activation allows the transformation of the supersaturated solution from the fusion process to only crystallize until the metastable state of the tangent line (2) in Figure 2 is reached. At this stage of transformation the catalytically active state is present. This principle of application of amorphous alloys is also highlighted in review articles [3–5] on the subject which describe a variety of other catalytic applications of this class of fused materials.

### 3.1.6 Mesostructure of Fused Catalyst Materials

The aim of fusion and controlled solidification of a catalytic material is the generation of a metastable catalytic material. The thermodynamic instability can be caused by a nonequilibrium composition, by a nonequilibrium morphology, or by a combination of both. In the case of the SLP catalysts the desired effect is to avoid the formation of solidification in order to maintain a structureless state of the active material.

The detection of metastable phases by spectroscopic and local structure-sensitive methods has been described in case studies [3, 28–31]. The detection of nonequilibrium mesostructures is rather difficult and less frequently carried out due to the fact that the relevant size range is between local atomic microstructural motives and macroscopic crystal morphologies. For this reason conventional scanning electron microscopy as well as transmission electron microscopy (which reveals only two-dimensional projections) are not ideally suited to the study of such mesostructures. High-resolution scanning electron microscopy (SEM) with high-voltage probes and field emission instruments or scanning probe microscopies [25] are suitable techniques to retrieve the information about the metastable mesostructure. This information is of significant catalytic relevance as many reactions are structure-sensitive and thus exhibit different kinetics on different surface orientations. The generation of nonisotropic particles with the consequence of preferred abundancies of selected orientations (i.e. basal planes of platelets) or with large interfaces between different phases in the catalysts are key issues in the process of improving or even tailoring catalytic performance.

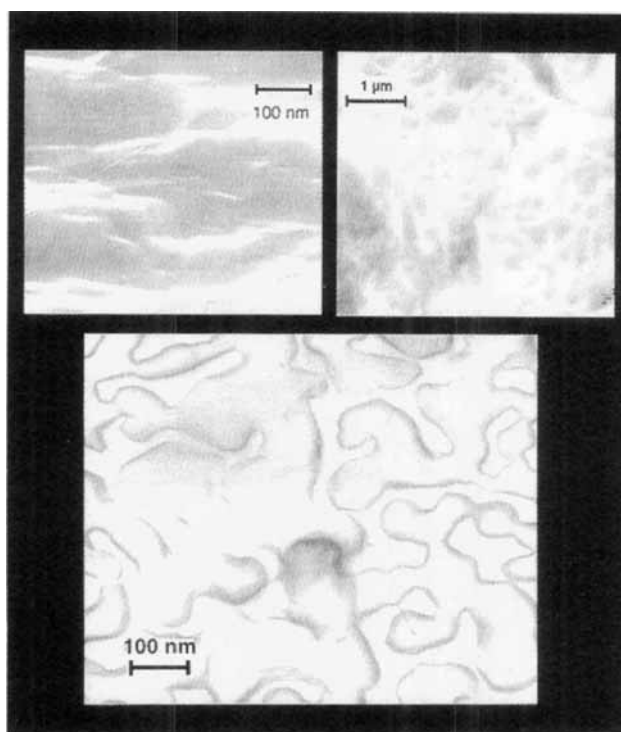
Fused materials provide a viable route to bulk amounts of nonisotropic particles prepared in a controlled yet complex procedure. This is illustrated in the micrographs of Figures 7 and 8 which show metallic iron in nonequilibrium mesostructures generated by fusion processes. Figure 7 shows sections of the activated technical ammonia synthesis catalyst. In the top image the perimeter of an isotropic iron crystallite (a cube) can be seen. The high resolution image reveals, however, that the iron cube is of a spongy structure. The close-up images reveal stacks of platelets with a quite irregular basal plane shape. This irregular shape provides the opportunity to form stacks with irregular edges forming a pore system with a size range of about 10 nm. This pore system is suitable to bring gaseous reactants in the interior of the iron crystal. Only the fusion process of the oxide precursor is responsible for this clearly nonequilibrium mesostructure of a bcc metallic element.



**Figure 7.** High-resolution SEM images of the activated fused iron catalyst for ammonia synthesis. The anisotropic mesostructure and the high internal surface area are visible. The small probe size of a 200 keV electron beam in a JEOL CX 200 instrument was used for backscattering detection of the scanning image from very thin objects.

In Figure 8 typical perspectives of an activated iron-zirconium metallic glass ( $\text{Fe}_{91}\text{Zr}_9$ ) also used for ammonia synthesis [24, 32] can be seen. The top view in the large image shows the formation of a large-area interface between the metallic iron islands and the meandering system of exsolved zirconium oxide. The shape of the pattern is reminiscent of a spilled liquid and is the consequence of the supercooled liquid state of the amorphous precursor. The side views of the two components reveals clearly the different organization of the crystallites in the metallic part, with regular steps of prism faces from platelets for the iron metal, and the spongy porous structure of the zirconia, imaged here in a location with a large oxide patch allowing suitable orientation of the specimen. A similar organization was also shown to be characteristic of the Pd-Zr system used for CO oxidation [27]. The images of





**Figure 8.** SEM surface images of partly crystallized sections of an activated  $\text{Fe}_{91}\text{Zr}_9$  alloy used for ammonia synthesis [23, 24]. The main image reveals the formation of a stepped iron metal structure with a porous zirconium oxide spacer structure. An almost ideal transport system for gases into the interior of the catalyst is created with a large metal–oxide interface which provides high thermal and chemical stability of this structure. The edge contrast in the 200 keV backscattered raw data image arises from the large difference in emissivity between metal and oxide. It is evident that only fusion and segregation–crystallization can create such an interface structure.

Figure 8 illustrate one view of the schematic structure given in Figure 5 for partly crystallized amorphous metals.

## References

1. A. Cottrell, *An Introduction to Metallurgy*, Jesus College, **1975**.
2. *Amorphous Metallic Alloys*, (Ed.: F. E. Luborsky), Butterworths, London, **1983**.
3. K. Noack, C. Rehren, H. Zbinden, R. Schlögl, *Langmuir* **1995**, *11*, 2018–2030.
4. A. Baiker, *Faraday Discuss. Chem. Soc.* **1989**, *87*, 239–251.
5. A. Molnar, G. V. Smith, M. Bartok, *Adv. Catal.* **1989**, *36*, (36), 329–383.
6. *Chemical Kinetics of Solids*, (Ed.: H. Schmalzried), VCH, Weinheim **1995**.
7. D. R. Uhlmann, *J. Non-cryst. Solids* **1972**, *7*, 337.
8. H. A. Davies, B. G. Lewis, *Scripta Met.* **1975**, *9*, 1107–1112.
9. D. Turnbull, *Contemp. Phys.* **1969**, *10*, 473–488.
10. U. Koster, P. Weiss, *J. Non-cryst. Solids* **1975**, *17*, 359.

11. M. von Heimendahl, H. Oppolzer, *Scripta Met* **1978**, *12*, 1087–1090.
12. P. G. Boswell, *Scripta Met.* **1977**, *11*, 701–707.
13. F. J. Doering, D. A. Berkel, *J. Catal.* **1987**, *103*, 126–139.
14. G. K. Borekov, G. M. Polyakova, A. A. Ivanov, V. M. Mastikhin, *Dokl. Akad. Nauk.* **1973**, *210*, 626.
15. G. K. Borekov, A. A. Ivanov, B. S. Balzhinimaev, L. M. Karnatovskaya, *React. Kinet. Catal. Lett.* **1980**, *14*, 25–29.
16. D. A. Karydis, S. Boghosian, R. Fehrmann, *J. Catal.* **1994**, *145*, 312–317.
17. S. Boghosian, R. Fehrmann, N. J. Bjerrum, G. N. Papatheodorou, *J. Catal.* **134**, *119*, 121–134.
18. L. G. Simonova, B. S. Balzhinimaev, O. B. Lapina, Y. O. Bulgakova, T. F. Soshkina, *Kin. Katal.* **1991**, *32*, 678–682.
19. F. P. Holroyd, C. N. Kenney, *Chem. Eng. Sci.* **1971**, *26*, 1971.
20. K. M. Eriksen, R. Fehrmann, N. J. Bjerrum, *J. Catal.* **1991**, *132*, 263–265.
21. R. Schlögl, *Rapidly Quenched Metals*, **1985**, 1723–1727.
22. R. Hauert, P. Oelhafen, R. Schögl, H.-J. Güntherodt, *Rapidly Quenched Metals*, **1985**, 1493–1496.
23. E. Armbruster, A. Baiker, H. Baris, H.-J. Güntherodt, R. Schlögl, B. Walz, *J. Chem. Soc., Chem. Comm.* **1986**, 299–301.
24. A. Baiker, R. Schlögl, E. Armbruster, H.-J. Güntherodt, *J. Catal.* **1987**, *107*, 221–231.
25. R. Schlögl, R. Wiesendanger, A. Baiker, *J. Catal.* **1987**, *108*, 452–466.
26. A. Baiker, D. Gasser, J. Lenzner, A. Reller, R. Schlögl, *J. Catal.* **1990**, *126*, 555–571.
27. R. Schlögl, G. Loose, M. Wesemann, A. Baiker, *J. Catal.* **1992**, *137*, 139–157.
28. H. Yamashita, M. Yoshikawa, T. Funabiki, S. Yoshida, *J. Catal.* **1986**, *99*, 375–382.
29. H. Yamashita, M. Yoshikawa, T. Funabiki, S. Yoshida, *J. Chem. Soc., Faraday Trans. I* **1987**, *83*, 2883–2893.
30. B. Schleich, D. Schmeisser, W. Göpel, *Surf. Sci.* **1987**, *191*, 367–384.
31. P. Oelhafen, M. Liard, H.-J. Güntherodt, K. Berresheim, H. D. Polaschegg, *Solid State Comm.* **1979**, *30*, 641–644.
32. A. Baiker, H. Baris, R. Schlögl, *J. Catal.* **1987**, *108*, 467–480.

## 3.2 Skeletal Metal Catalysts

M. S. WAINWRIGHT

“It is in the preparation of catalysts that the Chemist is most likely to revert to type and to employ alchemical methods. From all evidence, it seems the work should be approached with humility and supplication, and the production of a good catalyst received with rejoicing and thanksgiving” [1].

### 3.2.1 Introduction

Murray Raney graduated as a Mechanical Engineer from the University of Kentucky in 1909 and in 1915 he joined the Lookout Oil and Refining Company in Tennessee with responsibility for installation of electrolytic cells for the production of hydrogen which was used in the hydrogenation of vegetable oils. At the

11. M. von Heimendahl, H. Oppolzer, *Scripta Met* **1978**, *12*, 1087–1090.
12. P. G. Boswell, *Scripta Met.* **1977**, *11*, 701–707.
13. F. J. Doering, D. A. Berkel, *J. Catal.* **1987**, *103*, 126–139.
14. G. K. Boreskov, G. M. Polyakova, A. A. Ivanov, V. M. Mastikhin, *Dokl. Akad. Nauk.* **1973**, *210*, 626.
15. G. K. Boreskov, A. A. Ivanov, B. S. Balzhinimaev, L. M. Karnatovskaya, *React. Kinet. Catal. Lett.* **1980**, *14*, 25–29.
16. D. A. Karydis, S. Boghosian, R. Fehrmann, *J. Catal.* **1994**, *145*, 312–317.
17. S. Boghosian, R. Fehrmann, N. J. Bjerrum, G. N. Papatheodorou, *J. Catal.* **134**, *119*, 121–134.
18. L. G. Simonova, B. S. Balzhinimaev, O. B. Lapina, Y. O. Bulgakova, T. F. Soshkina, *Kin. Katal.* **1991**, *32*, 678–682.
19. F. P. Holroyd, C. N. Kenney, *Chem. Eng. Sci.* **1971**, *26*, 1971.
20. K. M. Eriksen, R. Fehrmann, N. J. Bjerrum, *J. Catal.* **1991**, *132*, 263–265.
21. R. Schlögl, *Rapidly Quenched Metals*, **1985**, 1723–1727.
22. R. Hauert, P. Oelhafen, R. Schögl, H.-J. Güntherodt, *Rapidly Quenched Metals*, **1985**, 1493–1496.
23. E. Armbruster, A. Baiker, H. Baris, H.-J. Güntherodt, R. Schlögl, B. Walz, *J. Chem. Soc., Chem. Comm.* **1986**, 299–301.
24. A. Baiker, R. Schlögl, E. Armbruster, H.-J. Güntherodt, *J. Catal.* **1987**, *107*, 221–231.
25. R. Schlögl, R. Wiesendanger, A. Baiker, *J. Catal.* **1987**, *108*, 452–466.
26. A. Baiker, D. Gasser, J. Lenzner, A. Reller, R. Schlögl, *J. Catal.* **1990**, *126*, 555–571.
27. R. Schlögl, G. Loose, M. Wesemann, A. Baiker, *J. Catal.* **1992**, *137*, 139–157.
28. H. Yamashita, M. Yoshikawa, T. Funabiki, S. Yoshida, *J. Catal.* **1986**, *99*, 375–382.
29. H. Yamashita, M. Yoshikawa, T. Funabiki, S. Yoshida, *J. Chem. Soc., Faraday Trans. I* **1987**, *83*, 2883–2893.
30. B. Schleich, D. Schmeisser, W. Göpel, *Surf. Sci.* **1987**, *191*, 367–384.
31. P. Oelhafen, M. Liard, H.-J. Güntherodt, K. Berresheim, H. D. Polaschegg, *Solid State Comm.* **1979**, *30*, 641–644.
32. A. Baiker, H. Baris, R. Schlögl, *J. Catal.* **1987**, *108*, 467–480.

## 3.2 Skeletal Metal Catalysts

M. S. WAINWRIGHT

“It is in the preparation of catalysts that the Chemist is most likely to revert to type and to employ alchemical methods. From all evidence, it seems the work should be approached with humility and supplication, and the production of a good catalyst received with rejoicing and thanksgiving” [1].

### 3.2.1 Introduction

Murray Raney graduated as a Mechanical Engineer from the University of Kentucky in 1909 and in 1915 he joined the Lookout Oil and Refining Company in Tennessee with responsibility for installation of electrolytic cells for the production of hydrogen which was used in the hydrogenation of vegetable oils. At the

time the industry used a nickel catalyst that was prepared by hydrogen reduction of supported nickel oxide. Raney believed that better catalysts could be produced and in 1921 he formed his own research company. In 1924 he produced a 50% nickel–silicon alloy which he treated with aqueous sodium hydroxide to produce a greyish metallic solid which was tested by hydrogenation of cottonseed oil. He found the activity of his catalyst to be five times greater than the best catalyst then in use and he therefore applied for a patent which was issued on December 1, 1925 [2].

Subsequently Raney produced a nickel catalyst by leaching a 50 wt% Ni–Al alloy in aqueous sodium hydroxide and that catalyst was even more active and a patent application was filed in 1926 [3]. This class of materials is generically called “skeletal” or “sponge” metal catalysts. The choice of an alloy containing 50 wt% Ni and 50 wt% Al was fortuitous and without scientific basis, and is part of the alchemy referred to above. However, it is of interest to note that it is the preferred alloy composition for production of skeletal nickel catalysts currently in use. In 1963 Murray Raney sold his business to the W. R. Grace and Company whose Davison Division produces and markets a wide range of these catalysts. Because Raney® catalysts are protected by registered trademark, only those products produced by Grace Davison are properly called “Raney Ni”, “Raney Cu” etc. Alternatively the more generic “skeletal” is used to refer to catalysts in the following. In addition, “Ni–Al” or “Cu–Al” etc. rather than “Raney alloy” is used to refer generically to the precursor to the catalyst.

Following the development of sponge-metal nickel catalysts by alkali leaching of Ni–Al alloys by Raney, other alloy systems were considered. These include iron [4], cobalt [5], copper [6], platinum [7], ruthenium [8], and palladium [9]. Small amounts of a third metal such as chromium [10], molybdenum [11], or zinc [12] have been added to the binary alloy to promote catalyst activity. The two most common skeletal metal catalysts currently in use are nickel and copper in unpromoted or promoted forms. Skeletal copper is less active and more selective than skeletal nickel in hydrogenation reactions. It also finds use in the selective hydrolysis of nitriles [13]. This chapter is therefore mainly concerned with the preparation, properties and applications of promoted and unpromoted skeletal nickel and skeletal copper catalysts which are produced by the selective leaching of aluminum from binary or ternary alloys.

## 3.2.2 General Aspects

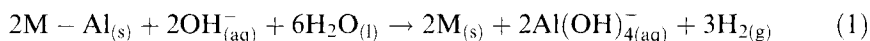
### 3.2.2.1 Alloy Preparation

Alloys are prepared commercially and in the laboratory by melting the active metal and aluminum in a crucible and quenching the resultant melt which is then crushed and screened to the particle size range required for a particular application. The alloy composition is very important as different phases leach quite differently leading to markedly different porosities and crystallite sizes of the active metal. Mondolfo [14] provides an excellent compilation of the binary and ternary phase dia-

grams for aluminum alloys including those used for the preparation of skeletal metal catalysts. Alloys of a number of compositions are available commercially for activation in the laboratory or plant. They include alloys of aluminum with nickel, copper, cobalt, chromium–nickel, molybdenum–nickel, cobalt–nickel, and iron–nickel.

### 3.2.2.2 Activation Using Alkali Leaching

Skeletal catalysts are generally prepared by the selective removal of aluminum from alloy particles using aqueous sodium hydroxide. The leaching reaction is given by



The dissolution of aluminum in aqueous sodium hydroxide may be represented more simply by



The formation of sodium aluminate ( $\text{NaAlO}_2$ ) requires that high concentrations (20–40 wt %) of excess sodium hydroxide are used in order to avoid the formation of aluminum hydroxide which precipitates as bayerite:



and causes blocking of pores and surface site coverage in the sponge metals formed during leaching. The bayerite deposition leads to loss of surface area and hence catalyst activity. Care must be taken during activation of the alloys to vent the large quantities of hydrogen that are produced by reaction in order to prevent explosions and fires.

The temperature used to leach the alloy has a marked effect on the pore structure and surface area of the catalyst. The surface areas of skeletal catalysts decrease with increasing temperature of leaching due to structural rearrangements leading to increases in crystallite size analogous to sintering [15]. Leaching of aluminum from certain alloys can be extremely slow at low temperatures and hence a compromise in the temperature of leaching must be reached in order to produce a catalyst with an appropriate surface area in a reasonable period of time.

A convenient method to produce powdered skeletal catalysts is to use the procedure described by Freel and co-workers [16] for Raney nickel. The same relative proportions of alloy and leachant can be used to maintain the leach reaction relatively isothermal when larger quantities of catalyst are desired. In their method an aqueous solution containing 40 wt % NaOH is added stepwise to 30 g of alloy powder and 150 ml of distilled water in a vessel at 313 K. Alkali additions are made at approximately 2-min intervals. For the first 20-min period the volume of alkali added is 2 ml, and 5-ml additions are made thereafter. A reaction time of around 3 h is sufficient to fully leach 500- $\mu\text{m}$  particles of aluminium–nickel or aluminium–copper alloys at 313 K. After extraction the catalysts are washed with distilled water at ambient temperature, first by decantation and then by water flow in a vessel until the pH is lowered to around 9. The samples can then be stored in a closed vessel under deaerated distilled water to prevent oxidation prior to use.

Activated skeletal catalysts including nickel, copper, cobalt and molybdenum or chromium-promoted nickel are available commercially.

### 3.2.2.3 Storage and Handling

Skeletal metal catalysts are extremely pyrophoric due to the small sizes of the metal crystallites that form during the leaching process. If the catalysts are allowed to dry in air the metal particles rapidly oxidize generating large amounts of heat such that the particles glow red. The heat may cause ignition of combustible materials in the vicinity. It is therefore important that after preparation, the catalysts be properly stored in a liquid. In general, water is used as the storage medium. However, there is the possibility that hydrolysis of any residual sodium aluminate will occur according to Equation 3 leading to the formation of hydrated alumina resulting in catalyst deactivation by surface and pore blocking. For this reason storage under slightly alkaline conditions (pH 9 to 11) is preferred. Studies of storage of catalysts using aliphatic alcohols suggest that isopropanol is a better storage medium than water. However, this does not have significant practical importance.

### 3.2.2.4 Advantages of Skeletal Metal Catalysts

The principal advantage of skeletal catalysts is that they can be stored in the form of the active metal and therefore require no prereduction prior to use as do conventional catalysts which are in the form of the oxide of the active metal supported on a carrier. These catalysts can also be prepared on demand by a simple caustic leaching procedure. They have very high activity since the BET surface area (typically up to  $100\text{ m}^2\text{ g}^{-1}$  for skeletal nickel and  $30\text{ m}^2\text{ g}^{-1}$  for skeletal copper) is essentially the metal surface area. Skeletal catalysts are low in initial cost per unit mass of metal and therefore provide the lowest ultimate cost per unit mass of active catalyst. The high metal content provides good resistance to catalytic poisoning.

Because alloy composition and leaching conditions can be carefully controlled, skeletal catalysts exhibit excellent batch to batch uniformity. The particle size of the catalyst can be easily controlled through crushing and screening. Thus ultrafine powders can be produced for use in slurry-phase reactors whilst large granules can be produced for use in fixed-bed applications. The relatively high densities of skeletal catalysts (particularly nickel) provide excellent settling characteristics compared with supported catalysts when used in slurry-phase reactors. The high thermal conductivity of the all-metal skeletal catalyst is a further advantage.

## 3.2.3 Skeletal Nickel Catalysts

### 3.2.3.1 Skeletal Nickel Catalysts – Alloy Preparation

Skeletal nickel catalysts used industrially are produced from alloys that typically contain 40–50 wt% nickel, with the 50% composition being most commonly used. The alloys are produced by adding molten aluminum to nickel which dissolves by a

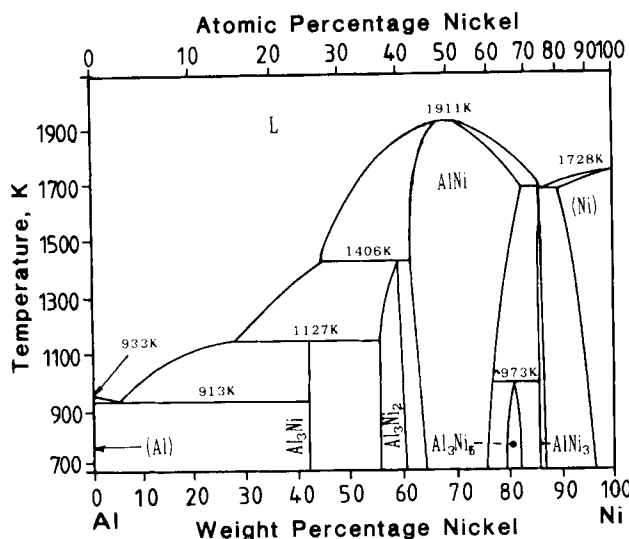


Figure 1. Al-Ni phase diagram.

highly exothermic reaction. For laboratory preparations the use of an induction furnace and graphite crucibles provides a very convenient method of preparation. The melt is rapidly quenched in water leading to alloys with quenched structures consisting of the intermetallics  $\text{Ni}_2\text{Al}_3$ ,  $\text{NiAl}_3$ , and some frozen eutectic. It has been found [17] that the eutectic material leaches more rapidly than  $\text{NiAl}_3$  which leaches much more rapidly than  $\text{Ni}_2\text{Al}_3$ .

The phase diagram for the Al-Ni system is shown in Figure 1. An alloy of composition 42 wt% nickel corresponds to  $\text{NiAl}_3$  whilst  $\text{Ni}_2\text{Al}_3$  contains approximately 60 wt% nickel. A study of the selective leaching of essentially pure  $\text{NiAl}_3$  and  $\text{Ni}_2\text{Al}_3$  intermetallics [17] showed that  $\text{NiAl}_3$  readily leached in 20 wt% aqueous NaOH at temperatures from 274 to 323 K producing porous nickel which was friable and readily disintegrated. On the other hand, at those temperatures  $\text{Ni}_2\text{Al}_3$  was unreactive, requiring temperatures from 343 to 380 K to produce significant extents of leaching. The reaction between  $\text{Ni}_2\text{Al}_3$  and the NaOH solution proceeded in two steps. At first a two-phase mixture of  $\text{Ni}_2\text{Al}_3$  plus Ni was produced and at longer times, nickel alone. It is apparent that the 50 wt% Ni alloy that is commonly used industrially represents a composition that is a compromise between the readily leached  $\text{NiAl}_3$  which produces mechanically weak catalysts and  $\text{Ni}_2\text{Al}_3$  which is more difficult to leach but which forms a strong residual material.

It is not only composition of the melt but also the rate of cooling that determines the metallography of the resulting alloy. In order to produce essentially pure phases it is necessary to undertake very controlled annealing procedures [17]. Freil *et al.* [16] used metallographic techniques to determine the phase compositions of two commercial aluminium-nickel alloys containing 50 wt% Ni and 42 wt% Ni, respectively. They found that the 50 wt% Ni alloy contained 58 vol%  $\text{Ni}_2\text{Al}_3$ , 40 vol%  $\text{NiAl}_3$ , and 2% eutectic, whereas the 42 wt% Ni alloy contained 30 vol%  $\text{Ni}_2\text{Al}_3$ , 45 vol%  $\text{Ni}_2\text{Al}_3$  and 25 vol% eutectic.

**Table 1.** Surface properties of skeletal nickel catalysts produced by leaching a 50 wt % Ni alloy in aqueous sodium hydroxide solution (compiled from refs. 16, 18 and 19).

Activation temp. (K)	BET surface area ( $\text{m}^2 \text{g}^{-1}$ )	Pore volume ( $\text{cm}^3 \text{g}^{-1}$ )	Average pore Diameter (nm)	Crystallite size (nm)	Surface as Ni (%)
323	100	0.064	2.6	3.6	59
380	86	0.125	5.8	5.7	75

### 3.2.3.2 Skeletal Nickel Catalysts – Properties

Skeletal nickel catalysts have BET surface areas typically in the range 50 to  $100 \text{ m}^2 \text{g}^{-1}$ . The theoretical pore volumes for fully leached  $\text{NiAl}_3$  and  $\text{Ni}_2\text{Al}_3$  are  $0.48 \text{ cm}^3 \text{g}^{-1}$  and  $0.17 \text{ cm}^3 \text{g}^{-1}$ , respectively. The large pore volume for the material prepared from  $\text{NiAl}_3$  accounts for its low mechanical strength. Table 1 presents typical characteristics of Raney nickel catalysts produced by leaching a 50 wt % Ni alloy using an  $\text{NaOH} : \text{Al}$  molar ratio of approximately 1.8 : 1. The results in Table 1 show that increased temperature of leaching leads to increased pore diameter, increased crystallite size, and lower total surface area.

A remarkable property of skeletal nickel is its ability to store hydrogen that is produced during the leaching process. It has been shown that the amount of hydrogen present in a freshly prepared sample of skeletal nickel can exceed by an order of magnitude the amount of hydrogen that could be chemisorbed on the surface nickel atoms. There have been a large number of explanations for this phenomenon. Suffice to say, the ability to store hydrogen accounts for the high activity of Raney nickel in a wide range of hydrogenation reactions.

### 3.2.3.3 Skeletal Nickel Catalysts – Uses

Raney nickel catalysts are used in a wide range of organic synthesis reactions including:

- hydrogenation of nitro compounds
- hydrogenation of alkenes
- hydrogenation of carbonyl compounds
- hydrogenation of nitriles
- ammonolysis of alcohols
- hydrogenation of alkynes
- hydrogenation of aromatic compounds
- reductive alkylation
- methanation.

Table 2 lists some typical industrial applications.



**Table 2.** Industrial applications of skeletal nickel catalysts.

Reaction	Reactant	Product
Hydrogenation of nitro compounds	2,4-dinitrotoluene	2,4-toluenediamine
	2-nitropropane	isopropylamine
Hydrogenation of alkenes	sulfolene	sulfolane
Hydrogenation of carbonyl compounds	dextrose	sorbitol
	2-ethylhexanal	2-ethylhexanol
Hydrogenation of nitriles	stearonitrile	stearylamine
	adiponitrile	hexamethylenediamine
Ammonolysis of alcohols	1,6-hexanediol	hexamethylenediamine
Hydrogenation of alkynes	1,4-butyne-1,3-diol	1,4-butanediol
Hydrogenation of aromatics	benzene	cyclohexane
	phenol	cyclohexanol
Reductive alkylation	dodecylamine + formaldehyde	<i>N,N</i> -dimethyl-dodecylamine
Methanation	synthesis gas (CO/CO <sub>2</sub> /H <sub>2</sub> )	methane

### 3.2.4 Promoted Skeletal Nickel Catalysts

The addition of a second component in metal catalysts is widely used in order to enhance activity and/or selectivity. In the case of skeletal nickel catalysts it is a simple procedure to add small amounts of a second metal during the alloy preparation stage. Although other metals have been used in laboratory studies, the most common metals used to promote skeletal nickel catalysts employed industrially are Co, Cr, Cu, Fe, and Mo.

Montgomery [11] has made a detailed study of the functional group activity of promoted Raney nickel catalysts. He prepared catalysts by leaching alloy powders of the type Al (58 wt %)/Ni (37–42 wt %)/M (0–5 wt %), where M = Co, Cr, Cu, Fe, and Mo, in aqueous sodium hydroxide (NaOH/Al (molar) = 1.80) at 323 K. The activities of the catalysts were measured by the rates of hydrogenation of various organic compounds including an alkene, a carbonyl compound, a nitro compound and a nitrile compound. Of the metals tested molybdenum was found to be the most effective promoter. All the metals tested were found to increase the activity of Raney nickel in the hydrogenation of a nitrile compound. It was found that the optimum level of promoter present in the precursor alloy was Cr = 1.5 wt %, Mo = 2.2 wt %, Co = 2.5–6.0 wt %, Cu = 4.0 wt %, and Fe = 6.5 wt %. The effect of promoters was most apparent for the hydrogenation of a nitrile compound. Table 3 summarizes the results of Montgomery [11] showing the catalysts with optimum activity.

### 3.2.5 Skeletal Cobalt Catalysts

Cobalt catalysts have activities in hydrogenation reactions between those of nickel and copper. For example, nickel catalyzes methanation, cobalt catalyzes higher

**Table 3.** Effect of metallic promoters in the hydrogenation of organic compounds using Raney® nickel (compiled from Ref. 11).

Promotor (M)	Alloy composition $\frac{M \times 100}{Ni + M + Al}$	Organic compound	Relative activity <sup>(a)</sup> $\frac{r(M + Ni)}{r(Ni)}$
Mo	2.2	butyronitrile	6.5
Cr	1.5	"	3.8
Fe	6.5	"	3.3
Cu	4.0	"	2.9
Co	6.0	"	2.0
Mo	2.2	acetone	2.9
Cu	4.0	"	1.7
Co	2.5	"	1.6
Cr	1.5	"	1.5
Fe	6.5	"	1.3
Fe	6.5	sodium <i>p</i> -nitrophenolate	2.1
Mo	1.5	"	1.7
Cr	1.5	"	1.6
Cu	4.0	"	1.3
Mo	2.2	sodium itaconate	1.2

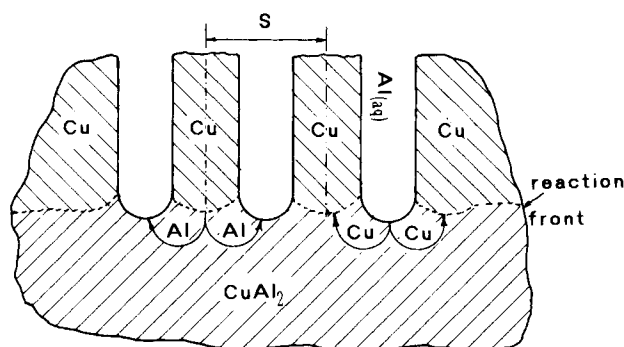
(a) Ratio of reaction rate for promoted catalyst to reaction rate over unpromoted Raney® nickel.

alcohol and low molecular weight hydrocarbon synthesis, whilst copper catalyzes methanol synthesis. Skeletal Co has less activity but greater selectivity than skeletal Ni and is effective in converting nitriles to primary amines in the absence of ammonia. Skeletal cobalt can be readily prepared from a nominal 50 wt % Co alloy. For example, when particles of a 48.8 wt % Co, 51.3 wt % Al alloy were leached in a 40% aqueous sodium hydroxide solution, 97.5% of the Al was leached resulting in porous cobalt with a BET surface area of 26.7 m<sup>2</sup> g<sup>-1</sup> and a bimodal pore size distribution with pore diameter maxima of 4.8 nm and 20 nm [20]. The crystallite size of the extracted catalyst was 4.7 nm. There appears to be scope for considerably more studies of and practical applications for skeletal cobalt catalysts.

### 3.2.6 Skeletal Copper Catalysts

#### 3.2.6.1 Skeletal Copper Catalysts – Alloy Preparation

The earliest study of copper catalysts prepared by the skeletal method was that of Fauconnau [6] who used Devarda's alloy (45 wt % Cu, 50 wt % Al, and 5 wt % Zn) and aluminum bronze (90 wt % Cu and 10 wt % Al). A later study by Stanfield and Robins [21] investigated the influence of the composition of the precursor Cu–Al alloy along with leaching conditions. They found that a catalyst prepared from a 40 wt % Cu, 60 wt % Al alloy was the most active in hydrogenation reactions. The most commonly used alloy has a nominal composition of 50 wt % Cu and 50 wt %



**Figure 2.** Schematic representation of a  $\text{CuAl}_2$ -Cu grain and the alloy-reaction product interface.

**Table 4.** Surface and pore structure data for particles of  $\text{CuAl}_2$  alloy that are fully leached at 293 K (Ref. 22).

Particle size ( $\mu\text{m}$ )	$S_{\text{BET}}$ ( $\text{m}^2 \text{g}^{-1}$ )	Pore diameter $2r_p$ (nm)	Pore volume ( $\text{cm}^3 \text{g}^{-1}$ )	Crystallite size (nm)	Copper rod diameter (nm)
105–180	31.4	23.6	0.214	8.7	20.6
353–420	25.3	31.6	0.203	8.2	28.5
710–850	23.5	34.2	0.197	8.7	31.5
1000–1180	24.0	33.8	0.197	8.5	31.1
1400–1676	23.9	34.2	0.197	8.5	31.5
2000–2360	21.4	38.2	0.195	8.2	35.4

Al which corresponds to an almost pure  $\text{CuAl}_2$  phase with a small amount of Al- $\text{CuAl}_2$  eutectic.

### 3.2.6.2 Skeletal Copper Catalysts – Properties

The temperature and time of leaching has a marked effect on the surface area of skeletal copper catalysts. The surface area decreases with increasing temperature of leaching whilst prolonged contact with caustic solutions leads to structural rearrangements causing significant reductions in surface area [15]. Skeletal copper consists of rods as shown in Figure 2. Leaching of Al takes place at the alloy interface and rods of copper form through the transformation of the parent phase into a highly ordered structure as shown. The products of the leaching process are the copper rods and the sodium aluminate which fills the newly created pores. The spacing  $S$  is the sum of the diameter of the copper rod and the intervening pore.

Table 4 shows the surface properties of skeletal copper catalysts produced by leaching a 50 wt% Cu alloy in aqueous sodium hydroxide solution at 293 K. It shows that the surface area decreases with increasing particle size of the alloy. Table 5 shows the effect of temperature of extraction on the surface area and pore structures of completely leached 1000–1180  $\mu\text{m}$  particles of the 50 wt% Cu alloy. The

**Table 5.** The effect of the temperature of extraction on the surface area and pore structure of completely leached 100–1180  $\mu\text{m}$  particles of  $\text{CuAl}_2$  alloy (Ref. 22).

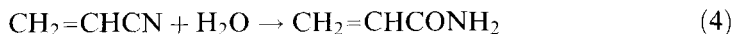
Extraction temperature (K)	$S_{\text{BET}}$ ( $\text{m}^2 \text{g}^{-1}$ )	Pore diameter $2r_p$ (nm)	Crystallite size (nm)	Copper rod diameter (nm)
275	25.4	30.2	7.5	27.5
293	24.0	33.8	8.5	30.8
308	22.6	55.0	11.2	50.1
323	18.5	61.0	12.0	55.6
343	16.9	75.0	13.7	68.3
363	12.7	107.6	14.6	98.0

results show that increased temperature of leaching from 275 to 363 K leads to a steady decrease in surface area from  $25.4 \text{ m}^2 \text{g}^{-1}$  to  $12.7 \text{ m}^2 \text{g}^{-1}$ .

### 3.2.6.3 Skeletal Copper Catalysts – Uses

Skeletal copper catalysts are used in a range of selective hydrogenation and dehydrogenation reactions. For example, they are highly specific for the hydrogenation of the 4-nitro group in 2,4-dinitro-1-alkyl-benzene to the corresponding 4-amino derivative. They are used for hydrogenation of aldehydes to the corresponding alcohols, dehydrogenation of alcohols to aldehydes or ketones, hydrogenation of esters to alcohols, dehydrogenation of methanol to produce methyl formate, and steam reforming of methanol. Thus skeletal copper catalysts can be used in a wide range of gas-phase and liquid-phase hydrogenation and dehydrogenation processes.

A major industrial process that uses skeletal copper catalysts is the liquid-phase hydrolysis of nitriles to produce the corresponding amides. The most important of these reactions is the hydrolysis of acrylonitrile to produce acrylamide [13] according to:



This process is conducted in the liquid phase using fixed beds of skeletal copper catalysts and temperatures from 300 to 400 K. Higher temperatures lead to catalyst fouling by polymerization of the product acrylamide. This deactivation can be reversed by washing the catalyst with caustic soda solution. This regeneration is a positive advantage of skeletal copper over other forms of copper catalysts used in this industrial process.

### 3.2.7 Promoted Skeletal Copper Catalysts

The addition of other metals to promote skeletal catalysts has been the subject of a number of investigations including the use of V, Cr, Mn, and Cd for hydrogenation of nitro compounds [23], Cd in the hydrogenation of unsaturated esters to un-

saturated alcohols [24], and Ni and Zn for the dehydrogenation of cyclohexanol to cyclohexanone. The use of Cr as a promoter is particularly attractive as copper chromite catalysts are used in a wide range of industrial applications. Laine and co-workers [25] have made a detailed study of the structure of chromium promoted skeletal copper catalysts.

### 3.2.8 Skeletal Copper–Zinc Catalysts

#### 3.2.8.1 Skeletal Copper–Zinc Catalysts – Alloy Preparation

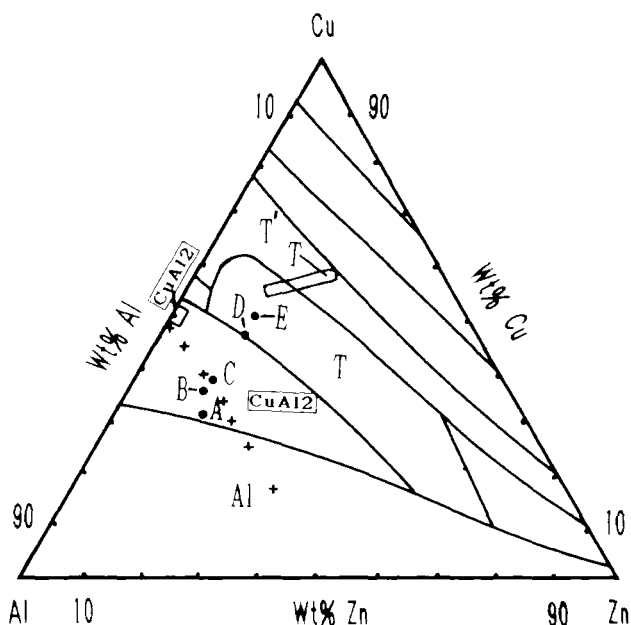
Skeletal Cu–Zn catalysts show great potential as alternatives to coprecipitated CuO–ZnO–Al<sub>2</sub>O<sub>3</sub> catalysts used commercially for low temperature methanol synthesis and water gas shift (WGS) reactions. They can also be used for other reactions such as steam reforming of methanol, methyl formate production by dehydrogenation of methanol, and hydrogenolysis of alkyl formates to produce alcohols. In all these reactions zinc oxide-promoted skeletal copper catalysts have been found to have high activity and selectivity.

Fauconnau [6] was the first to use a skeletal copper catalyst containing zinc. He prepared his catalysts from Devarda's alloy which contained 45 wt% Cu, 50 wt% Al, and 5 wt% Zn. Marsden and co-workers [12] were the first to use skeletal catalysts prepared from Cu–Zn–Al alloys for methanol synthesis. Alloys containing 50 wt% Al and 0–50 wt% Cu with the balance Zn were employed. Optimum activity for low temperature methanol synthesis was found for catalysts prepared by leaching alloys containing 50 wt% Al, 33–43 wt% Cu and 7–17 wt% Zn. Friedrich *et al.* [26] showed that catalysts prepared from alloys containing approximately 50 wt% Al, 30–36 wt% Cu and 14–20 wt% Zn had greatest activity for methanol synthesis. Bridgewater and co-workers [27] made a systematic study to optimize alloy composition and catalyst preparation. The catalysts prepared from alloys containing approximately 38 wt% Cu, 48 wt% Al, and 14 wt% Zn (alloy D in Figure 3) and 47 wt% Cu, 39 wt% Al, and 14 wt% Zn (alloy E in Figure 3) had the highest activities of those tested.

Recently Andreev and co-workers [28] and Mellor [29] have made extensive studies of skeletal Cu–Zn catalysts for the water gas shift reaction. Andreev *et al.* used an alloy of composition 42.2 wt% Cu, 43.5 wt% Al, and 14.3 wt% Zn, whilst Mellor used alloys containing 10–50 wt% Cu, 50 wt% Al, and 0–40 wt% Zn, and 43 wt% Cu, 39 wt% Al, and 18 wt% Zn.

Figure 3 shows the composition of the Cu–Zn–Al alloys used by a number of investigators plotted on the liquidus projection of the Al–Cu–Zn phase diagram [14]. The alloys used by Friedrich *et al.* [26] are shown by the + symbols in this figure. The primary precipitate for alloys containing 0–17 wt% Zn is Cu(Zn)Al<sub>2</sub> which is CuAl<sub>2</sub> containing dissolved Zn. As the Zn content of the melt is increased the Zn content of the Cu(Zn)Al<sub>2</sub> phase increases. For melts containing more than 17 wt% Zn the primary precipitate is an aluminum-based solution. Bridgewater *et al.* [27] showed that alloys containing greater than 39 wt% Cu (compositions D

**Figure 3.** Al–Cu–Zn phase diagram, liquidus projection (Ref. 14): (+) alloys investigated by Friedrich *et al.* [26]; (●) alloys investigated by Bridgewater *et al.* [27].

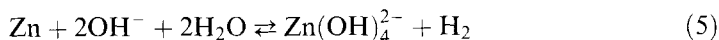


and E in Figure 3) were in the ternary phase region of the liquidus projection and large amounts of this difficult to leach phase were detected in the quenched alloy.

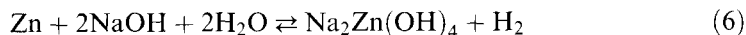
Alloys of Cu–Zn–Al are readily prepared in carbon crucibles heated in an induction furnace as described by Marsden *et al.* [12]. Copper, having the highest melting point, is melted and then aluminum is added. After vigorous stirring with a carbon rod the melt is cooled to below the boiling point of zinc before zinc is added to the melt with stirring. The melt is then rapidly quenched by pouring into cold water or onto a chilled plate. The resulting alloy is then crushed and screened. It has been shown that quenched structures are more readily leached and produce higher surface area catalysts with resultant higher activities.

### 3.2.8.2 Skeletal Copper–Zinc Catalysts – Leaching Studies

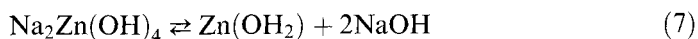
The incorporation of the Zn in Cu–Al alloys complicates the leaching process since the Zn is readily leached by aqueous caustic solutions according to Reaction 5.



If NaOH is the alkali used in the leaching step the dissolution of zinc is given by



When the concentration of NaOH is low the sodium zincate ( $\text{Na}_2\text{Zn}(\text{OH})_4$ ) precipitates as zinc hydroxide according to



It is the reprecipitation of  $\text{Zn}(\text{OH})_2$  in the porous skeletal copper which provides promotion in methanol synthesis, water gas shift, and other reactions. The highly dispersed reprecipitated  $\text{Zn}(\text{OH})_2$  decomposes at around 400 K to form  $\text{ZnO}$  which is an active promoter of copper catalysts.

When leaching aluminum alloys it is generally desirable to use high concentrations of sodium hydroxide in order to remove the Al as  $\text{NaAlO}_2$  and avoid reprecipitation of Al as bayerite ( $\text{Al}_2\text{O}_3 \cdot 3\text{H}_2\text{O}$ ). In the case of leaching of Cu–Zn–Al alloys this is particularly important since bayerite decomposes at around 600 K to form  $\gamma\text{-Al}_2\text{O}_3$  which catalyzes methanol dehydration to form dimethyl ether as a byproduct in methanol synthesis. For this reason a large excess of 40 wt% aqueous NaOH is generally used. Under these conditions much of the Al is washed from the resultant catalyst but sufficient  $\text{Zn}(\text{OH})_2$  remains precipitated on the surface of the porous copper.

More recently Curry-Hyde *et al.* [30] have improved the activity of skeletal Cu–Zn catalysts for methanol synthesis by adding sodium zincate to the sodium hydroxide leach liquor in order to achieve reprecipitation of greater amounts of  $\text{Zn}(\text{OH})_2$  on the surface of the copper. Alloys containing 53 wt% Cu and 47 wt% Al, and 43.2 wt% Cu, 17.7 wt% Zn and 39 wt% Al were leached in 6.1 M aqueous NaOH containing 0.62 M sodium zincate at 274 K and 303 K. They found that the addition of sodium zincate slows the rate of leaching of both alloys leading to increased surface areas. Electron microprobe analysis of the catalysts produced from the Cu–Zn–Al alloy leached in pure 6.1 M NaOH and a solution containing 0.62 M sodium zincate revealed that the ZnO concentration profile was far superior when sodium zincate was added to the leach liquor. Furthermore, when sodium zincate was present in the leachant for the Cu–Al alloy containing no Zn, significant amounts of ZnO were present in the leached catalyst. Mellor [29] has successfully used sodium zincate in the sodium hydroxide leach solution when preparing catalysts from Cu–Zn–Al alloys for the water gas shift reaction.

### 3.2.8.3 Skeletal Copper–Zinc Catalysts – Properties

The properties of skeletal Cu–Zn catalysts depend on the composition of the precursor alloy, the composition of the leach solution, and the temperature and time of leaching. Table 6 shows the properties of catalysts used by Friedrich *et al.* [26]. The leaching conditions used to prepare the catalysts were 323 K, 40 wt% NaOH, and sufficient time for complete reaction of the Zn and Al with the NaOH. Thus, the catalysts were fully leached. Table 6 shows that by replacing copper by zinc in the precursor alloy catalysts with increased BET surface areas, decreased pore volumes, decreased pore diameters, and decreased copper crystallite sizes are produced. It also shows the effect of the precursor alloy composition on the surface and pore properties of the catalysts.

As stated earlier, lower leaching temperatures result in increased surface areas of skeletal catalysts. Furthermore, slowing the leaching process by the addition of

**Table 6.** Properties of skeletal copper–zinc catalysts produced by leaching Cu–Al–Zn alloys in aqueous sodium hydroxide solution at 323 K (Ref. 26).

Sample	Alloy composition (wt%)( <sup>a</sup> )			Catalyst composition (wt%)( <sup>a</sup> )			$S_{\text{BET}}$ ( $\text{m}^2 \text{g}^{-1}$ )	Pore volume ( $\text{cm}^3 \text{g}^{-1}$ )	Pore diameter $2r_p$ (nm)	Copper crystallite diameter (nm)
	Cu	Zn	Al	Cu	Zn	Al				
1	50.6	0	50.2	98.7	0	1.6	17.0	0.385	45.8	11.2
2	44.6	5.3	50.7	98.0	0.8	1.1	18.6	0.242	35.4	11.2
3	39.3	9.8	50.3	97.5	1.4	1.3	21.9	0.241	33.8	10.4
4	36.2	13.6	51.2	96.9	2.1	1.5	24.5	0.239	32.0	—
5	33.5	17.1	49.7	97.1	2.8	1.6	26.8	0.238	28.4	10.4
6	30.5	20.6	50.2	94.5	4.4	2.1	29.4	0.233	27.2	—
7	24.6	26.0	49.8	90.0	8.7	2.0	30.6	0.238	23.0	7.0

(<sup>a</sup>) Compositions of alloys and catalysts were determined by chemical analysis of acid-digested samples. The values in the table have not been normalized.

**Table 7.** Methanol yields at 493 K and 4.5 MPa for skeletal catalysts (produced using different leaching conditions) compared to coprecipitated catalysts tested under the same conditions (Ref. 30).

Catalyst (a)	Space velocity ( $\text{h}^{-1}$ )	Methanol yield ( $\text{kg/l/h}$ )
I	36 000	1.12
I	15 000	0.80
IIa	36 000	0.64
IIb	36 000	0.61
III	12 000	0.60
IV	36 000	0.60
IV	15 000	0.44
V	15 000	0.45

(a) I: Cu–Al–Zn leached in 6.1 M NaOH/0.62 M Na zincate, at 303 K. II: Cu–Al<sub>2</sub> leached in 6.1 M NaOH/0.62 M Na zincate, (a) 274 K (b) 303 K. III: Cu–Al–Zn leaching 6.1 M NaOH, at 274 K. IV and V: Commercial coprecipitated catalysts.

sodium zincate to the leach solution leads to higher surface areas. Thus leaching of CuAl<sub>2</sub> in 6.1 M NaOH containing 0.62 M sodium zincate at 274 K leads to a catalyst of surface area of  $58.1 \text{ m}^2 \text{g}^{-1}$  compared with a surface area of  $28.0 \text{ m}^2 \text{g}^{-1}$  when no sodium zincate is present.

### 3.2.8.4 Skeletal Copper–Zinc Catalysts – Methanol Synthesis

Skeletal Cu–Zn catalysts have activities and selectivities comparable to the best commercially available coprecipitated CuO–ZnO–Al<sub>2</sub>O<sub>3</sub> catalysts. Table 7 shows the comparative performance of skeletal Cu–Zn and commercial catalysts. The skeletal catalysts clearly have great potential for use as methanol synthesis catalysts.



One particular application is in liquid-phase methanol synthesis in which very finely divided powder catalysts are used. This is analagous to the use of finely divided skeletal nickel and skeletal copper in liquid-phase organic syntheses.

### 3.2.8.5 Skeletal Copper–Zinc Catalysts – Water Gas Shift Reaction

Andreev and co-workers [28] and Mellor [29] have prepared catalysts by leaching Cu–Zn–Al in aqueous sodium hydroxide solutions. Their studies have shown that skeletal Cu–Zn catalysts have significantly greater activities than commercial WGS catalysts when operated at temperatures below 573 K.

## Acknowledgments

The author wishes to acknowledge the strong support of the following people and organisations. Professor R. B. (Bob) Anderson who introduced him to the fascinating world of skeletal catalysts in 1977. Dr. S. R. (Stewart) Montgomery who researched skeletal catalysts for Davison Chemical Division of W. R. Grace and Co. has provided him with great insight into the life of Murray Raney along with considerable advice over many years. The many postgraduate students and research fellows who have worked with him on various skeletal catalyst systems and have made outstanding contributions. The financial support of the research into skeletal catalysts over an extended period by the Australian Research Council is gratefully acknowledged.

## References

1. M. Raney, *Ind. Eng. Chem.* **1940**, 32, 1199.
2. M. Raney, *US Patent*, 1563587, **1925**.
3. M. Raney, *US Patent*, 162810-, **1927**.
4. M. Raney, *US Patent*, 1915473, **1933**.
5. B. V. Aller, *J. Appl. Chem.* **1957**, 7, 130.
6. L. Fauconnau, *Bull. Soc. Chim.* **1937**, 4(5), 58.
7. A. A. Vendenypin, N. D. Zubareva, V. M. Akimov, E. I. Klabunovskii, N. G. Giorgadze, N. F. Barannikova, *Izv. Akad. Nauk. SSSR. Ser. Khim.* **1976**, 10, 2340.
8. K. Urabe, T. Yoshioka, A. Ozaki, *J. Catal.* **1978**, 54, 52.
9. T. M. Grishina, L. I. Lazareva, *Zh. Fiz. Khim.* **1982**, 56, 2614.
10. R. Paul, *Bull. Soc. Chim. Fr.* **1946**, 13, 208.
11. S. R. Montgomery in *Catalysis of Organic Reactions* (Ed.: W. R. Moser), Dekker, New York, USA, **1981**, p. 383.
12. W. F. Marsden, M. S. Wainwright, J. B. Friedrich, *Ind. Eng. Chem. Prod. Res. Dev.* **1980**, 19, 551.
13. N. I. Onuoha, M. S. Wainwright, *Chem. Eng. Commun.* **1984**, 29, 1.
14. L. F. Mondolfo, *Aluminium Alloys: Structure and Properties*, Butterworths, London, UK, **1976**.
15. A. D. Tomsett, D. J. Young, M. R. Stambach, M. S. Wainwright, *J. Mat. Sci.* **1990**, 25, 4106.
16. J. Freel, W. J. M. Pieters, R. B. Anderson, *J. Catal.* **1969**, 14, 247.
17. M. L. Bakker, D. J. Young, M. S. Wainwright, *J. Mat. Sci.* **1988**, 23, 3921.

18. J. Freal, S. D. Robertson, R. B. Anderson, *J. Catal.* **1970**, *18*, 243.
19. S. D. Robertson, R. B. Anderson, *J. Catal.* **1971**, *23*, 286.
20. J. P. Orchard, A. D. Tomsett, M. S. Wainwright, D. J. Young, *J. Catal.* **1983**, *84*, 189.
21. J. A. Stanfield, P. E. Robbins, *Actes. Congr. Intern. Catal (2nd)*, Paris, **1960**, *2*, 579.
22. A. D. Tomsett, *Pore Development in skeletal Copper Catalysts*, PhD Thesis, University of New South Wales, Sydney, Australia, **1987**.
23. K. Wimmer, O. Stichnoth, *Ger. Offen.* 875519, **1953**.
24. Kyowa Hakko Kogyo Co. Ltd., *UK Patent* 1029502, **1966**.
25. J. Laine, Z. Ferrer, M. Labady, V. Chang, P. Frias, *Appl. Catal.* **1988**, *44*, 11.
26. J. B. Friedrich, M. S. Wainwright, D. J. Young, *J. Catal.* **1983**, *80*, 1.
27. A. J. Bridgewater, M. S. Wainwright, D. J. Young, J. P. Orchard, *Appl. Catal.* **1983**, *7*, 369.
28. A. Andreev, V. Kafedjiiski, T. Halachev, B. Kuner, M. Kaltchev, *Appl. Catal.* **1991**, *78*, 199.
29. J. R. Mellor, *The Water Gas Shift Reaction: Deactivation Studies*, PhD Thesis, University of Witwatersrand, Johannesburg, South Africa, **1993**.
30. H. E. Curry-Hyde, M. S. Wainwright, D. J. Young, in *Methane Conversion – Studies in Surface Science and Catalysis Volume 36* (Eds.: D. Bibby, C. C. Chang), Elsevier, Amsterdam, The Netherlands, **1988**, p. 239.

## 3.3 Metallic Glasses

A. BAIKER

### 3.3.1 Introduction

Amorphous metal alloys, which are also known as metallic glasses or glassy metals have gained considerable interests in catalysis research due to their unique structural and chemical properties. Most of the research effort made in the past decade have been covered in recent reviews [1–6].

In this chapter, a brief account of the state of the art is given and some important facets of the knowledge gained are discussed. First, we shall consider the preparation of glassy metals and discuss the motivation for their use in catalysis. Then, the two main directions of research, namely studies focusing on the use of glassy metals in as-quenched state (Section 3.3.4.1), and investigations where the glassy metals are used as precursors to catalytically active materials (Section 3.3.4.2), will be considered. Finally, some perspectives will be given in the form of a brief outlook.

### 3.3.2 Preparation

In principle, most of the known preparation methods [1, 2, 7], such as melt quenching, vapor and sputter deposition, and plating, can be used for the production of metallic glasses for catalytic studies. Among these methods melt quenching is the one most widely used. In melt quenching the melt of the constituents is so rapidly

18. J. Freel, S. D. Robertson, R. B. Anderson, *J. Catal.* **1970**, *18*, 243.
19. S. D. Robertson, R. B. Anderson, *J. Catal.* **1971**, *23*, 286.
20. J. P. Orchard, A. D. Tomsett, M. S. Wainwright, D. J. Young, *J. Catal.* **1983**, *84*, 189.
21. J. A. Stanfield, P. E. Robbins, *Actes. Congr. Intern. Catal (2nd)*, Paris, **1960**, *2*, 579.
22. A. D. Tomsett, *Pore Development in skeletal Copper Catalysts*, PhD Thesis, University of New South Wales, Sydney, Australia, **1987**.
23. K. Wimmer, O. Stichnoth, *Ger. Offen.* 875519, **1953**.
24. Kyowa Hakko Kogyo Co. Ltd., *UK Patent* 1029502, **1966**.
25. J. Laine, Z. Ferrer, M. Labady, V. Chang, P. Frias, *Appl. Catal.* **1988**, *44*, 11.
26. J. B. Friedrich, M. S. Wainwright, D. J. Young, *J. Catal.* **1983**, *80*, 1.
27. A. J. Bridgewater, M. S. Wainwright, D. J. Young, J. P. Orchard, *Appl. Catal.* **1983**, *7*, 369.
28. A. Andreev, V. Kafedjiiski, T. Halachev, B. Kuner, M. Kaltchev, *Appl. Catal.* **1991**, *78*, 199.
29. J. R. Mellor, *The Water Gas Shift Reaction: Deactivation Studies*, PhD Thesis, University of Witwatersrand, Johannesburg, South Africa, **1993**.
30. H. E. Curry-Hyde, M. S. Wainwright, D. J. Young, in *Methane Conversion – Studies in Surface Science and Catalysis Volume 36* (Eds.: D. Bibby, C. C. Chang), Elsevier, Amsterdam, The Netherlands, **1988**, p. 239.

## 3.3 Metallic Glasses

A. BAIKER

### 3.3.1 Introduction

Amorphous metal alloys, which are also known as metallic glasses or glassy metals have gained considerable interests in catalysis research due to their unique structural and chemical properties. Most of the research effort made in the past decade have been covered in recent reviews [1–6].

In this chapter, a brief account of the state of the art is given and some important facets of the knowledge gained are discussed. First, we shall consider the preparation of glassy metals and discuss the motivation for their use in catalysis. Then, the two main directions of research, namely studies focusing on the use of glassy metals in as-quenched state (Section 3.3.4.1), and investigations where the glassy metals are used as precursors to catalytically active materials (Section 3.3.4.2), will be considered. Finally, some perspectives will be given in the form of a brief outlook.

### 3.3.2 Preparation

In principle, most of the known preparation methods [1, 2, 7], such as melt quenching, vapor and sputter deposition, and plating, can be used for the production of metallic glasses for catalytic studies. Among these methods melt quenching is the one most widely used. In melt quenching the melt of the constituents is so rapidly

quenched that there is insufficient time for crystallites to nucleate and grow. The common feature of all devices that have been designed to quench molten alloys is that the melt must be converted very rapidly from a jet or stream of droplets into a thin layer in contact with a chill-block to produce thin foil or ribbon of 10–60  $\mu\text{m}$  thickness. In melt spinning, the chill-block is a rapidly spinning copper wheel with which quenching rates of the order of about  $10^6 \text{ K s}^{-1}$  can be achieved.

The combination of the constituents of the various metallic glasses reported in the literature [8] fall into a few well-defined categories:

- (i) glasses based on late transition metal + metalloid;
- (ii) early transition metal + late transition metal or Group IB metal;
- (iii) earth alkali metal + Group IB metal;
- (iv) early transition metal + alkali metal;
- (v) actinide + early transition metal.

Table 1 lists metallic glasses together with the reactions in which they have been used as catalysts. Note that mostly metal–zirconium alloys and Ni, Fe, and mixed Ni–Fe alloys with P and/or B as metalloid have been used in the catalytic studies. Generally, the glassy metals are used in the form of powders or flakes which are prepared from the ribbons by milling or chopping them under liquid nitrogen. Powders can easily be packed into the reactor tube and possess a larger geometrical surface area than the ribbons. However, special care has to be taken that no crystallization occurs during the grinding process.

### 3.3.3 Chemical and Structural Properties

The initial motivation for using glassy metals in catalytic research originated from some of their unique chemical and structural properties [1, 9, 10], which render them interesting materials for catalytic applications. The most attractive properties for catalytic applications are as follows:

- (i) *Surface structure* Ideally, the surface of amorphous materials should be devoid of any long-range ordering of the constituents and exhibit a high density of low-coordination sites and defects. The important role of low-coordination sites in catalysis, such as terraces and steps, has been demonstrated by Somorjai [11] for crystalline materials.
- (ii) *Flexibility in chemical composition* Glassy metals are assumed to possess high flexibility with regard to fine tuning of their electronic properties [12, 13], mainly due to the fact that thermodynamic constraints are less stringent in supercooled liquids than in crystalline materials.
- (iii) *Structural and chemical isotropy* Glassy metals are ideally chemically homogeneous and structurally isotropic.
- (iv) *Reactivity* Glassy metals are highly reactive due to their metastable structure and frequently undergo solid-state reactions more easily than their crystalline

**Table 1.** Reactions investigated on various glassy metal alloys. Compositions of the alloys are given in atomic per cent.

Reactions	Metallic glasses
Ammonia Synthesis	Fe <sub>91</sub> Zr <sub>9</sub> [26, 27], Ni <sub>24</sub> Zr <sub>76</sub> , Ni <sub>64</sub> Zr <sub>36</sub> [28]
Decomposition of NO	Co <sub>65</sub> Zr <sub>10</sub> Pd <sub>25</sub> [29]
Dehydrogenation of:	
Methanol	Cu <sub>67</sub> Ti <sub>33</sub> [30]
2-propanol	Cu <sub>61</sub> Zr <sub>39</sub> [31]
Disproportionation of CO	Pd <sub>33</sub> Zr <sub>67</sub> , Pd <sub>25</sub> Zr <sub>75</sub> [32]
Fischer-Tropsch synthesis	Fe <sub>40</sub> Ni <sub>40</sub> P <sub>16</sub> B <sub>4</sub> [33], Fe-Ni with P and/or B [34], Ni <sub>60</sub> Fe <sub>20</sub> P <sub>20</sub> [35], Fe <sub>20</sub> Ni <sub>60</sub> P <sub>20</sub> , Fe <sub>90</sub> Zr <sub>10</sub> [36], Fe <sub>81</sub> B <sub>13.5</sub> Si <sub>3.5</sub> C <sub>2</sub> [37], Fe <sub>82</sub> B <sub>18</sub> [38, 39], Ni <sub>78</sub> P <sub>19</sub> La <sub>3</sub> , Ni <sub>81</sub> P <sub>19</sub> [40], Fe <sub>80</sub> B <sub>20</sub> , Ni <sub>80</sub> B <sub>20</sub> [41], Fe <sub>40</sub> Ni <sub>40</sub> B <sub>20</sub> [41, 42]
Hydrogenation of:	
(+)-apopinene	Pd <sub>80</sub> Si <sub>20</sub> , Pd <sub>77</sub> Ge <sub>23</sub> [43, 44]
buta-1,3-diene	Ni <sub>81</sub> P <sub>19</sub> [45, 46], Ni <sub>62</sub> B <sub>38</sub> [45], Ni <sub>64</sub> Zr <sub>36</sub> [47], Cu <sub>70</sub> Zr <sub>30</sub> [48], Fe <sub>90</sub> Zr <sub>10</sub> [49]
benzene	Pd <sub>35</sub> Zr <sub>65</sub> , Pd <sub>20</sub> Zr <sub>80</sub> [50]
<i>cis</i> -but-2-ene	Ni <sub>81</sub> P <sub>19</sub> , Ni <sub>62</sub> B <sub>38</sub> [51]
<i>cis</i> -cyclododecene	Pd <sub>80</sub> Si <sub>20</sub> [52], Pd <sub>77</sub> Ge <sub>23</sub> [53]
cyclohexene	Pd <sub>80</sub> Si <sub>20</sub> , (Ni <sub>50</sub> Fe <sub>50</sub> ) <sub>80</sub> B <sub>20</sub> [54], Pd <sub>35</sub> Zr <sub>65</sub> , Pd <sub>20</sub> Zr <sub>80</sub> [50]
ethene	Ni <sub>62</sub> B <sub>38</sub> [55, 56], Ni <sub>36</sub> Zr <sub>74</sub> [57], Cu <sub>70</sub> Zr <sub>30</sub> [58], Cu <sub>62</sub> Zr <sub>38</sub> [59], Ni <sub>81</sub> P <sub>19</sub> , Ni <sub>62</sub> B <sub>38</sub> [51]
ethyne	Fe <sub>44-x</sub> Ni <sub>37</sub> Cr <sub>x</sub> P <sub>15</sub> B <sub>4</sub> ( $x < 10$ ) [60]
<i>n</i> -hexene	Pd <sub>80</sub> Si <sub>20</sub> , (Ni <sub>50</sub> Fe <sub>50</sub> ) <sub>80</sub> B <sub>20</sub> [54]
1-hexene	Pd <sub>80</sub> Zr <sub>20</sub> , Pd <sub>35</sub> Zr <sub>65</sub> , Ni <sub>30</sub> Zr <sub>70</sub> , Ni <sub>40</sub> Fe <sub>40</sub> B <sub>20</sub> , Fe <sub>85</sub> B <sub>15</sub> , Cu <sub>50</sub> Zr <sub>50</sub> [61]
isoprene	Ni <sub>81</sub> P <sub>19</sub> , Ni <sub>62</sub> B <sub>38</sub> [51], Cu <sub>62</sub> Zr <sub>38</sub> [59]
phenylethyne	Pd <sub>80</sub> Si <sub>20</sub> [54, 62], Pd <sub>77</sub> Ge <sub>23</sub> [62], Pd <sub>80</sub> Zr <sub>20</sub> , Pd <sub>35</sub> Zr <sub>65</sub> , Ni <sub>30</sub> Zr <sub>70</sub> , Ni <sub>40</sub> Fe <sub>40</sub> B <sub>20</sub> , Fe <sub>85</sub> B <sub>15</sub> , Cu <sub>50</sub> Zr <sub>50</sub> [61]
propene	Ni <sub>81</sub> P <sub>19</sub> , Ni <sub>62</sub> B <sub>38</sub> [51]
$\alpha$ -pinene	Pd <sub>80</sub> Si <sub>20</sub> , (Ni <sub>50</sub> Fe <sub>50</sub> ) <sub>80</sub> B <sub>20</sub> [54]
1-octyne,4-octyne	Pd <sub>80</sub> Si <sub>20</sub> , Pd <sub>77</sub> Ge <sub>23</sub> [62]
Hydrogenolysis of:	
ethane, cyclopropane	Ni <sub>62</sub> B <sub>38</sub> [55]
Methanation	Ni <sub>67</sub> Zr <sub>33</sub> [63], Ni <sub>64</sub> Zr <sub>36</sub> [64], Pd <sub>35</sub> Zr <sub>65</sub> [65, 66], Au <sub>25</sub> Zr <sub>75</sub> [67], Rh <sub>25</sub> Zr <sub>75</sub> , Pt <sub>25</sub> Zr <sub>75</sub> , Pd <sub>25</sub> Zr <sub>75</sub> , Os <sub>25</sub> Zr <sub>75</sub> , Ir <sub>25</sub> Zr <sub>75</sub> [67] Pd <sub>33</sub> Zr <sub>67</sub> [68]
Methanol synthesis	Au <sub>25</sub> Zr <sub>75</sub> [69], Cu <sub>70</sub> Zr <sub>30</sub> [70, 71], Cu <sub>60</sub> Ti <sub>40</sub> , Cu <sub>64</sub> Hf <sub>36</sub> [71], Cu-Ce-Al [72], Cu <sub>70</sub> Zn <sub>15</sub> Al <sub>15</sub> [73]
Oxidation of:	
carbon monoxide	Pd <sub>33</sub> Zr <sub>67</sub> [74, 75], Pd <sub>25</sub> Zr <sub>75</sub> [76, 77], Au <sub>25</sub> Fe <sub>5</sub> Zr <sub>70</sub> , Au <sub>25</sub> Ag <sub>5</sub> Zr <sub>70</sub> [78]
methane	Pd <sub>25</sub> Zr <sub>75</sub> [79]
xylene	Pd <sub>33</sub> Zr <sub>67</sub> [80]
Reduction of:	
nitric oxide	Ni <sub>91</sub> Zr <sub>9</sub> , Ni <sub>64</sub> Zr <sub>36</sub> , Pd <sub>25</sub> Zr <sub>75</sub> , Rh <sub>25</sub> Zr <sub>75</sub> [81]
<i>trans</i> -2-hexanal,1-tetralone	Pd <sub>25</sub> Zr <sub>75</sub> , Ni <sub>64</sub> Zr <sub>36</sub> [82, 83]
phenol,2- <i>t</i> -butylphenol	Pd <sub>33</sub> Zr <sub>67</sub> , Ni <sub>64</sub> Zr <sub>36</sub> [83]

counterparts. This property is of importance in their use as catalyst precursors (Section 3.3.4.2).

- (v) *Conductivity* Glassy metals exhibit good conductivity for electricity and heat. These properties paired with their excellent corrosion resistance [14] make them particularly interesting for applications in electrocatalysis [15, 16].
- (vi) *Planar morphology* Glassy metals prepared by melt quenching exhibit a planar morphology ideal for investigating with modern surface analytical methods. Their manufacture as foils or small ribbons allows designing new reactor conceptions.

It should be stressed that some of the above properties have been strongly idealized at the origin of the application of metallic glasses in catalysis [1], as will be discussed later on.

Limitations for the application of glassy metals in catalysis originate from their metastable structure and their intrinsically low surface area, corresponding simply to the geometrical area of the as-quenched materials. Furthermore, it should be stressed that ideal glassy metals surfaces, being chemically and structurally isotropic and showing uniform short-range ordering of the constituents, are difficult to produce and are generally not stable under conditions used for catalytic reactions.

### 3.3.4 Metallic Glasses in Catalysis Research

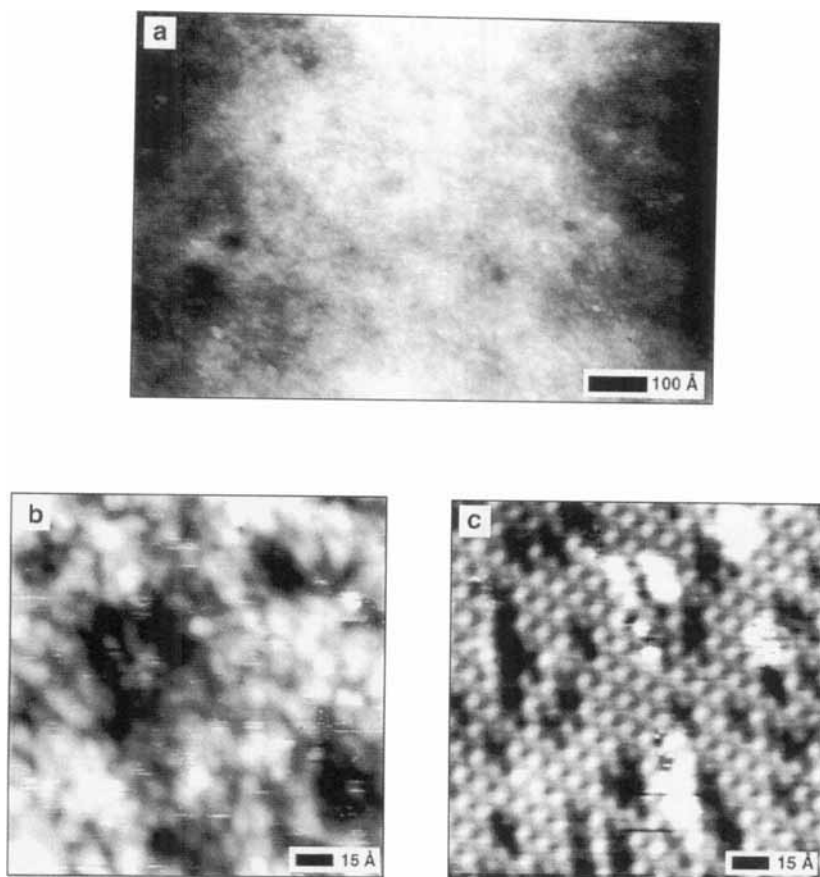
#### 3.3.4.1 Research on Metallic Glasses in As-Quenched State

Metallic glasses have been suggested to be ideal model catalysts for the solution of several important catalytic problems [1], such as

- (i) the role of bi- and multimetallics;
- (ii) the role of surface segregation;
- (iii) the electronic and geometric structure of surface defects;
- (iv) the influence of coordination of surface atoms on activity, selectivity and catalyst lifetime;
- (v) the nature of catalytic sites;
- (vi) the importance of chemical ordering;
- (vii) the effect of amorphization of catalyst components.

However, insufficient knowledge of the surface structure, electronic properties, and surface composition has so far slowed down progress in this field. A major difficulty is the low structural and chemical stability of glassy metal surfaces under conditions suitable for catalytic tests.

Ideally, the surface should be structurally and chemically isotropic and exhibit no long-range ordering of the constituents. Structural investigations using scanning tunneling microscopy (STM) revealed that this ideal surface is difficult to prepare, at least by melt spinning. The surfaces of  $\text{Rh}_{25}\text{Zr}_{75}$  [17],  $\text{Fe}_{91}\text{Zr}_9$  [18],  $\text{Pd}_{84.5}\text{Si}_{15.5}$  [19], and  $\text{Nb}_{40}\text{Ni}_{60}$  [20] alloys were found to be made up of flat areas, identified as



**Figure 1.** Surface structure of melt-spun  $\text{Pd}_{81}\text{Si}_{19}$  in the amorphous state (a and b) and after crystallization (c), investigated using STM. After cleaning the surface by  $\text{Ar}^+$  sputtering, its structure appears rather flat on a large scale ((a) 1000 Å × 646 Å); the gray-scale coding used corresponds to a vertical range of only 12 Å. Images of smaller areas ((b) 150 Å × 150 Å) reveal small objects of typically 5 Å diameter (FWHM) and of ca. 0.1 Å height that probably are due to single surface atoms. Upon crystallization of amorphous  $\text{Pd}_{81}\text{Si}_{19}$  by heating it to ca. 870 K a periodic surface structure is observed ((c) 156 Å × 156 Å). It represents presumably a triclinic crystalline phase (courtesy of T. M. Schaub [21]).

disordered regions, and hill structures, assigned to nanocrystals embedded in the amorphous matrix.

The present state of knowledge on the surface structure of metallic glasses is excellently illustrated by the work of Schaub [21], who investigated melt-spun  $\text{Pd}_{81}\text{Si}_{19}$  in the amorphous state (Figs 1(a) and 1(b)) and after crystallization (Fig. 1(c)). The STM studies provide deeper insight into the structure of the flat areas which were found to be typical for surfaces of metallic glasses. Figure 1(a) depicts the surface structure of amorphous  $\text{Pd}_{81}\text{Si}_{19}$  after cleaning by  $\text{Ar}^+$  sputtering. Note that the surface is rather flat on a relatively large scale.

Generally, the vertical range of the flat areas was smaller than 20 Å. Images of smaller areas (Fig. 1(b)) show small objects (diameter  $\approx 5$  Å, height  $\approx 0.1$  Å) which are probably due to single surface atoms. The mean distance between these objects is about 10 Å which is considerably larger than the expected interatomic distance. It is assumed that this large distance between the objects of atomic size does not correspond to neighboring surface atoms but to atoms (adatoms) located at the periphery of the surface. This assumption is supported by STM investigations [22] and by theoretical calculations of images of single adsorbed atoms [23]. Both methods revealed structures which are comparable to that shown in Fig. 1(b) with regard to shape and size. After crystallization of the amorphous  $\text{Pd}_{81}\text{Si}_{19}$  (Fig. 1(c)), STM revealed periodic surface structures originating from at least two different crystal phases.

The formation of nanocrystals embedded in the flat disordered regions [17, 18] originates mainly from either too low quenching rates or from the presence of contaminants. Surfaces of glassy metals tend to undergo structural relaxation even at temperatures far below the crystallization temperature and the presence of adsorbed reactants is known to enhance this relaxation [24]. Thus, it seems unlikely that the intrinsic catalytic properties of a truly disordered (amorphous) surface of a glassy metal can be probed. In any case, the catalytic reactions would have to be performed at very low temperature. This is a severe limitation, particularly in the light of the intrinsically small surface area of these materials. Only very few catalytic studies are presently available, where the requirements of low temperature and the absence of contaminants have been fulfilled, and these studies indicate clearly that the surfaces reconstruct either during cleaning by sputtering or upon exposure to a reactive atmosphere. Photoemission spectroscopy (XPS and UPS) studies of the adsorption of dinitrogen on amorphous  $\text{Fe}_{91}\text{Zr}_9$  [25] revealed that nitrogen dissociates on such surfaces already at temperatures as low as 79 K and upon hydrogen exposure desorbs, presumably as  $\text{NH}_3$ , leaving nondissociated dinitrogen behind. The results of the UPS and XPS studies, including binding energies and line profiles, agree well with the results of similar investigations carried out on single crystal surfaces of iron. This supports the view that the active component of the amorphous iron–zirconium alloy is elemental iron and that the local electronic structure of the adsorption sites in elemental iron and in the amorphous alloy surface were similar. These studies have clearly demonstrated that the question whether a disordered (amorphous) surface possesses higher intrinsic activity than its crystalline counterpart can hardly be resolved, due to the low stability of the former under reaction conditions.

The possibility of tailoring the electronic properties of glassy metals, and thereby to influence their adsorption behavior, has been illustrated by a UPS investigation of CO chemisorption on various Ni–Zr alloys [26]. The studies showed that the ratio of molecular to dissociative CO chemisorption is not directly related to the ratio of the constituent Ni and Zr on the surface, probably due to zirconium modifying the local electronic structure of the exposed Ni atoms. A striking characteristic of a large number of glass-forming alloys is that they are subject to large hybridization [13].

As concerns the surface composition of glassy metals, ideal chemically isotropic



surfaces hardly exist under reaction conditions or after exposure to air, as will be discussed in Section 3.3.6.2.

Based on the presently available work dealing with catalysis on as-quenched glassy metals carried out at low temperature, we can conclude that the intrinsic activity of a disordered surface could so far not been observed due to the reasons discussed above. This fact makes metallic glasses rather unsuitable for testing surface geometric effects in catalysis. However, this low structural stability leading to high mobility and reactivity of the constituents renders the glassy metals particularly useful as models for studying the segregational behavior (Section 3.3.6.7) of alloy constituents under reaction conditions and as catalyst precursors.

### 3.3.4.2 Metallic Glasses as Precursors to Catalytically Active Materials

Table 1 lists reactions which have been studied on metallic glasses. Note that in the early investigations, the glassy metal alloys were not deliberately used as catalyst precursors. Often it was tacitly assumed that the structural properties of the glassy metal surface are retained under the reaction conditions. The justification for this assumption was disproved in all studies where the surface and bulk structures of the glassy material were carefully analyzed before and after use in catalysis.

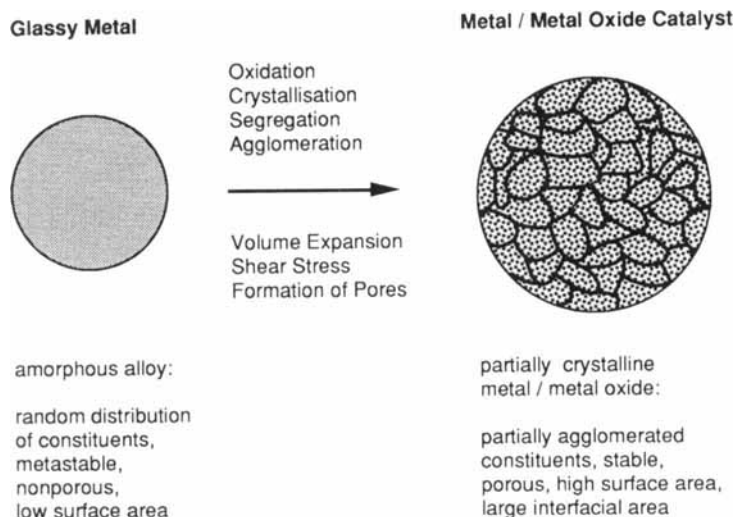
However, even the initial studies indicated that special care has to be taken in pretreating the materials to obtain high catalytic activity. In the simplest case, pretreatment of the as-quenched alloys in a reducing gas atmosphere was necessary to reach high catalytic activities. This behavior is attributed to several reasons, the most important being that the surfaces of metallic glasses exposed to air are often covered with a superficial layer of inactive metal oxides and the low surface area of as-quenched materials ( $<0.1 \text{ m}^2 \text{ g}^{-1}$ ).

Later, the deliberate use of metallic glasses as catalyst precursors opened new routes for the preparation of supported metal catalysts with unusual chemical and structural properties [2–6]. This potential resides mainly in the isotropic nature and high reactivity of these materials compared to their crystalline counterparts.

Several efficient supported metal catalysts [2–6] have been prepared by exposing the precursor alloy to an oxygen-containing gas atmosphere at elevated temperature and subsequent reduction. In situ activation, i.e. the transformation of the precursor alloy to the catalytically active material under reaction conditions [5, 6], has also been applied successfully.

The aim of all these (pre)treatments is to transform the alloy into a supported metal catalyst by oxidizing the more electropositive component(s). In some cases etching in acid solutions (HCl [42],  $\text{HNO}_3$  [40, 43, 51, 55],  $\text{HClO}_4$ , and HF [57, 59]) was also used as a pretreatment procedure, either to remove an inactive oxidic surface layer or to extract selectively components of the alloy (Raney-type catalyst). Figure 2 illustrates these procedures schematically.

Thus-prepared catalysts possess sufficiently large BET (up to  $70 \text{ m}^2 \text{ g}^{-1}$ ) and metal surface areas for technical use. A major difference compared to conventionally prepared supported metal catalysts is that one starts from a solid precursor which ideally contains the constituents homogeneously distributed on an atomic



**Figure 2.** Schematic illustration of the transformation of metal–zirconium alloy to zirconia-supported metal catalyst.

scale. The oxidic support material as well as the active metal particles are formed by gas–solid and solid–solid processes and not by wet chemical processes. This alternative preparation often leads to structural and chemical properties of the resulting catalytic materials which greatly differ from those obtained for similar catalyst preparations using traditional wet chemical procedures.

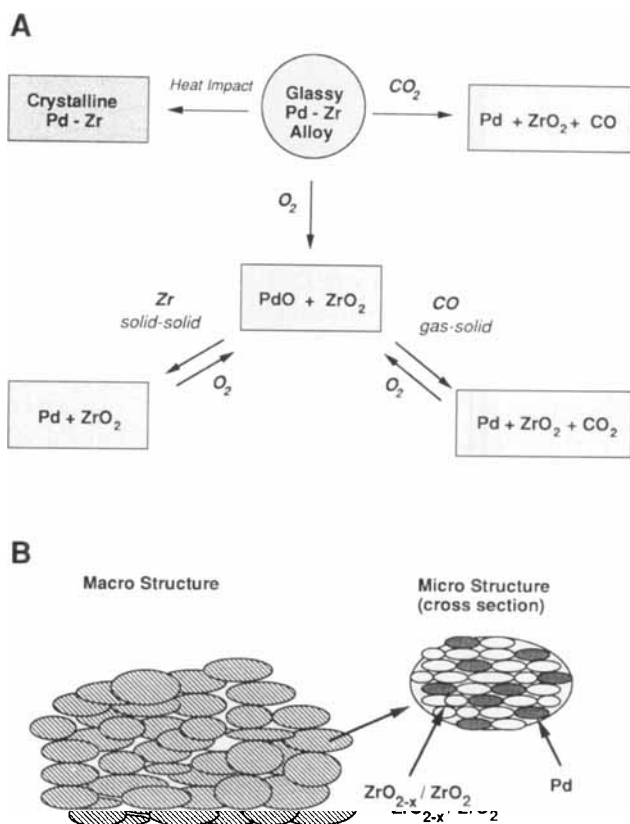
During the pretreatment (activation), the glassy metal alloys undergo a series of structural and chemical changes. Knowledge of the processes occurring in the metallic glass precursor during this pretreatment is a necessary prerequisite for controlling the chemical and structural properties of the final catalyst. For illustration we may consider the preparation of highly active CO oxidation catalysts from zirconium-based metallic glasses.

### 3.3.5 Case Studies: CO Oxidation Catalysts Prepared from Metallic Glasses

#### 3.3.5.1 Pd/ZrO<sub>2</sub> Catalysts from Amorphous Pd–Zr Alloys

The gas–solid and solid–solid reactions relevant for the preparation of Pd/ZrO<sub>2</sub> catalysts from glassy Pd–Zr alloys by either *ex situ* (oxidation in air) or *in situ* activation (oxidation in CO oxidation reaction mixture) are summarized in Fig. 3(A).

By proper control of these processes Pd/ZrO<sub>2</sub> catalysts with unique structural properties and high activity for CO [74–77] and CH<sub>4</sub> [79] oxidation can be prepared. The structural and chemical properties of as-derived catalysts were studied using various techniques, including scanning electron microscopy (SEM), differen-



**Figure 3.** Chemical and structural transformations of metallic Pd–Zr glass precursors and properties of final Pd/ZrO<sub>2</sub> catalysts [74, 75]. (A) Gas–solid and solid–solid reactions occurring during transformation of glassy Pd–Zr alloys to highly active CO oxidation catalysts. The relevance of the different processes depends on the composition of the gas phase, the composition of the alloy, and the temperature of activation. Oxidation in CO<sub>2</sub> is only relevant for in situ preparation, where CO<sub>2</sub> concentrations are sufficiently large. (B) Schematic presentation of structural and chemical properties of catalysts derived from glassy Pd–Zr alloy.

tial thermal analysis (DTA), high resolution transmission electron microscopy (HRTEM), Auger electron spectroscopy (AES), X-ray photoelectron spectroscopy (XPS), and ultraviolet photoelectron spectroscopy (UPS) [74, 75]. The most important structural and chemical features of Pd/ZrO<sub>2</sub> catalysts derived from glassy Pd–Zr alloys are illustrated in Fig. 3(B).

The solid state reactions occurring in metallic glass during in situ activation result in a large increase of the BET surface area from 0.02 m<sup>2</sup> g<sup>−1</sup> up to more than 60 m<sup>2</sup> g<sup>−1</sup> depending on conditions [74, 77]. The final catalysts, exhibiting stable activity, are made up of small intergrown and poorly crystalline domains of palladium and both monoclinic and tetragonal zirconia phases. The resulting large interface between the palladium particles and the oxygen deficient zirconia render this structure capable of storing chemically active oxygen under CO oxidation con-

ditions. Palladium was found to exist predominantly as a metastable intermediate compound ( $\text{Pd} + \text{O}$ ) under reaction conditions, as demonstrated by in situ XPS measurements [75], which showed the binding energy of the  $\text{Pd } 3d_{3/2}$  electrons laying between those of  $\text{PdO}$  and  $\text{Pd}$  metal.

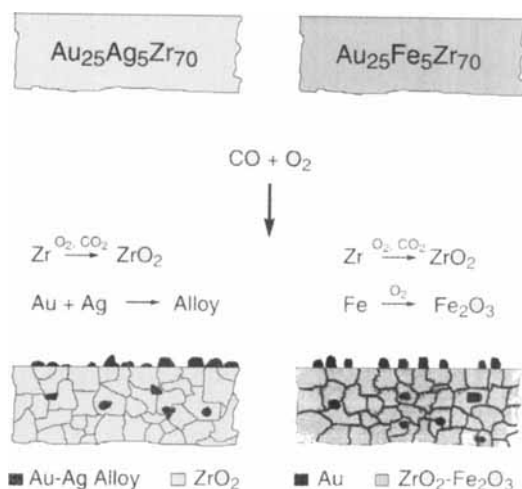
The superior catalytic performance of this system relative to conventionally prepared  $\text{Pd}/\text{ZrO}_2$  catalysts which has been demonstrated for the oxidation of  $\text{CO}$  [74, 77] and the combustion of methane [79] is attributed to the intimate contact of the oxygen storage phase, zirconia, with the active ( $\text{Pd} + \text{O}$ ) phase, which is probably stabilized against reduction to the pure metal by a constant supply of oxygen ions through the bulk of the supporting matrix and the surface of the particle. A similar oxygen transfer is not feasible for the conventionally prepared  $\text{Pd}/\text{ZrO}_2$  catalyst, which is made up of stoichiometric  $\text{ZrO}_2$  and metallic palladium under  $\text{CO}$  oxidation conditions. Another crucial structural difference of these catalysts is the interfacial area between palladium and zirconia. The catalyst derived from glassy  $\text{Pd}$ – $\text{Zr}$  exhibits a large interfacial area between the palladium and zirconia phases, whereas with the conventionally prepared catalyst the interfacial area is relatively small, as shown by electron microscopy [74].

The intrinsic  $\text{CO}$  oxidation activity of palladium contained in a catalyst derived from the  $\text{Pd}$ – $\text{Zr}$  glassy metal precursor was found to be about an order of magnitude higher than that of palladium present in a catalyst prepared by coprecipitation, as demonstrated by comparative kinetic measurements [74]. The stable activity of the catalyst was confirmed in long-term tests of 60 h duration.

### 3.3.5.2 Promoted Gold–Zirconia Catalysts from Ternary Gold-Containing Glassy Alloys

The use of multicomponent glassy metals as catalyst precursors offers further opportunities in catalyst preparation. Potential structural and chemical promoters can already be brought into the melt of the constituents used for the alloy fabrication. Ideally, this leads to an atomic dispersion of these constituents which may be difficult to achieve by conventional preparation techniques. The promotor is randomly distributed in the precursor alloy and can undergo various reactions, which may be controlled by the pretreatment conditions. For illustrating this potential we may consider the preparation of gold–silver/zirconia and gold/zirconia–iron oxide catalysts [78] from corresponding glassy gold–silver–zirconium and gold–iron–zirconium alloys, respectively.

These catalysts, which were found to be most suitable for low-temperature  $\text{CO}$  oxidation, were prepared by in situ oxidation of the glassy metal alloys under  $\text{CO}$  oxidation conditions at 550 K. Figure 4 depicts the relevant transformations and the structural and chemical characteristics of the final active catalysts. In the case of the glassy  $\text{Au}_{25}\text{Ag}_5\text{Zr}_{70}$  alloy, silver forms an alloy (solid solution) with gold resulting in small gold/silver particles which are dispersed on zirconia formed by oxidation of the zirconium component. In contrast, the iron constituent in  $\text{Au}_{25}\text{Fe}_5\text{Zr}_{70}$  is oxidized under  $\text{CO}$  oxidation conditions and distributed in the zirconia matrix affording a catalyst containing gold particles dispersed in a zirconia–iron oxide matrix.



**Figure 4.** Chemical and structural transformations of metallic  $\text{Au}_{25}\text{Ag}_5\text{Zr}_{70}$  and  $\text{Au}_{25}\text{Fe}_5\text{Zr}_{70}$  glass precursors and properties of the final Au–Ag/ $\text{ZrO}_2$  and Au/ $\text{Fe}_2\text{O}_3$ – $\text{ZrO}_2$  catalysts suitable for low-temperature CO oxidation [78].

The zirconia present in both catalysts is made up of a mixture of poorly crystalline monoclinic and tetragonal phases. The catalysts are microporous with BET surface areas of  $30 \text{ m}^2 \text{ g}^{-1}$  (gold/zirconia–iron oxide) and  $45 \text{ m}^2 \text{ g}^{-1}$  (gold–silver/zirconia). This corresponds to a surface area increase due to the structural transformations by more than three orders of magnitude (BET surface area of precursors  $< 0.02 \text{ m}^2 \text{ g}^{-1}$ ). Both catalysts show stable and high CO oxidation activity at ambient temperature.

### 3.3.6 Factors Influencing Chemical and Structural Properties of Catalytic Materials Derived from Metallic Glasses

The gas–solid and solid–solid reactions occurring during pretreatment of the glassy metals are complex and the structure of as-prepared catalysts is influenced by several factors which depend on the intrinsic properties of the metallic glass and the conditions of pretreatment. Relevant intrinsic properties are discussed next.

#### 3.3.6.1 Chemical Composition

The chemical composition [8] influences virtually all the properties mentioned and is therefore a controlling factor in the preparation of catalysts from glassy metals. To date only a limited range of glassy metals have been used in catalysis research (Table 1). This has seriously limited the possible potential of these materials for catalysis. In view of the large number of possible binary or multicomponent metallic systems, the number of alloy melts which can be quenched into the glassy state is still relatively small and by far not as large as one would expect from the fact that thermodynamic constraints are less stringent for metastable solids. Rigorous limitations with regard to the constituents and their concentration ranges have still to

be dealt with. Very different cooling rates are necessary ( $10^2$ – $10^{12}$  K s<sup>-1</sup>) depending on the constituents and their concentration.

The ability of an alloy melt to be quenched into the glassy state with available cooling rates, is determined by energetic and kinetic factors, which are often interdependent [84]. Several different factors influencing the glass-forming ability in metallic melts have been discussed, among them thermodynamics, kinetics, stoichiometry, concentration of valence electrons, atomic sizes of constituents, and electronegativity. Glass formation is generally thermodynamically favored in those systems and concentration ranges for which the free energy of the metastable amorphous state differs as little as possible from that of the corresponding metastable or stable crystalline state. Under these conditions, only small thermodynamic driving forces for crystallization exist for cooling below the liquidus temperature.

### 3.3.6.2 Chemical and Structural Homogeneity

Ideally an amorphous metal alloy should be chemically and structurally isotropic. Isotropic surfaces would be ideal for catalytic applications, since any structural and chemical heterogeneity can impede the selectivity with which a particular chemical reaction is catalyzed. However, several studies [17–19, 38, 39] reveal that the surface of glassy metals prepared by melt-spinning may not be as homogeneous as expected. Structural as well as chemical inhomogeneities have been observed. Chemical and structural anisotropies in the bulk and the surface region not only lower the catalytic selectivity of such materials but also lead to nonuniform propagation of the solid-state reactions occurring during the transformation of the amorphous precursor to the active catalyst. Inhomogeneities are frequently due either to a too slow cooling rate [39], to contamination [39, 85], or to thermally and chemically induced segregation of constituents. All these phenomena greatly impede the control of the structural and chemical properties of the alloy surface, an important requirement for catalytic applications.

### 3.3.6.3 Thermal Stability and Crystallization Behavior

The thermal stability is a severe limitation if the metallic glass is to be used in as-quenched state for catalysis; however, that is not necessarily the case if the glassy alloy is used as a catalyst precursor. The thermal stability is mainly influenced by the chemical composition of the metallic glass and the medium to which it is exposed. It has been shown that the crystallization temperature can be significantly lowered in the presence of a hydrogen atmosphere [49, 68, 70, 86] or an adsorbed organic compound [24].

Glassy metals have been found to crystallize by nucleation and growth processes. The driving force is the difference in free energy between the glass and the appropriate crystalline phase(s). Depending on the composition crystallization may occur by

- (i) primary crystallization, where one crystal phase with a composition different from the amorphous matrix is produced;

- (ii) polymorphic crystallization, where one phase with the same composition as the glass is crystallized (occurs only in concentration ranges near the pure elements or compounds),
- (iii) eutectic crystallization, where two crystalline phases grow concomitantly by a discontinuous reaction.

Most glassy metals can crystallize by two or more different reactions. The route by which crystallization occurs depends not only on the thermodynamic driving force (difference in free energy), but also on the kinetics of the possible routes. In the case of pretreatment of the metallic glass precursor in reactive gas atmospheres, solid–solid and solid–gas reactions are likely to influence the expected crystallization behavior.

An important factor in crystallization is the oxygen content near the surface. Oxygen may stabilize a number of crystalline phases, thus increasing the driving force for crystallization. Selective oxidation of one of the components, e.g. zirconium in binary metal–zirconium glasses is likely to result in excessive crystallization and clustering of the metal (e.g. copper [48, 71, 85], palladium [67, 73], nickel [28, 63] and iron [26, 49]).

#### 3.3.6.4 Oxidation Behavior

The oxidation behavior of glassy metals is of importance in many of their practical applications and particularly in catalysis. In view of this, surprisingly little is known about their oxidation behavior on the fundamental level. Most of the investigations reported in the literature deal with the oxidation of metal–metalloid alloys [39, 86–89] and Group VIII transition metal–zirconium alloys [81, 90–93]. When discussing the oxidation behavior and its influence on the catalytic applications of glassy metals it is meaningful to distinguish between surface and bulk oxidation.

The surface oxidation behavior is particularly important with regard to the use of glassy metals in the as-quenched state. Surface oxidation can occur even at low temperatures and consequently the surface of freshly prepared alloys is often covered with a thin layer of the oxides of their constituents. This phenomenon has contributed to controversy with regard to the catalytic properties of glassy metal surfaces, since in many of the earlier investigations it had been disregarded. Researchers had tacitly assumed that the surface composition resembles the bulk composition of the quenched materials.

Bulk oxidation requires generally the transfer of oxygen from the surface to the bulk and consequently the compactness of the oxide surface layer plays an important role with regard to the bulk oxidation kinetics. Compact oxide surface layers are likely to slow down or even inhibit bulk oxidation due to slow diffusion of oxygen through the dense oxide layer to the unreacted core of the alloy. Frequently, oxidation leads to partial crystallization and phase separation even at temperatures far below the crystallization temperature of the amorphous alloy, due to the removal of the oxidized constituent from the alloy. This is likely to occur if the composition range for glassy metal formation is narrow.

Bulk oxidation generally leads to large stresses in the materials due to the differences in the specific volumes of the unreacted part of the alloy and the oxidized

part. This stress can eventually cause embrittlement of the material, a behavior which has to be accounted for if catalysts are prepared by oxidation of metallic glass precursors.

### 3.3.6.5 Dissolution of Gases

The dissolution of gases in glassy metals frequently differs from that of their crystalline counterparts due to the marked differences in structural and electronic properties. As regards the glassy metals, present knowledge is concentrated mainly on the absorption of hydrogen. Since most glassy metals or catalysts derived from them were exposed to a hydrogen-containing atmosphere, either during reaction or activation, understanding the interaction and solid-state reactions induced by hydrogen is important. Besides its possible direct influence on the catalytic properties of glassy metals as a hydrogen source, the absorption of hydrogen generally enhances the formation of metal hydrides, which have been shown to be crucial intermediates in the preparation of catalysts from amorphous [85] and crystalline [94, 95] metal alloys. Unfortunately, no similar studies are presently available for the solution of other gases in glassy metals.

### 3.3.6.6 Segregation Phenomena

The surface composition of metal alloys is often different from that of the bulk. Major driving forces for surface segregation are different surface free energies of the components, and different heats of chemisorption and reaction of components in the presence of adsorbates. Surface segregation induced by selective oxidation is well known for crystalline and amorphous alloys of the type A–B, where A is an early transition metal or rare earth metal (e.g. Zr, Ti, lanthanides, or actinides), and B a Group VIII (e.g. Ni, Fe, Pd) or Group IB metal (e.g. Cu, Au). Upon exposure of the alloy to oxygen, component A (the more electropositive element) is oxidized and is enriched at the surface [26, 85, 96–100]. As a result phase separation may occur, and the remaining atoms of component B cluster together and precipitate. This phase separation is crucial for the formation of oxide-supported metal particles.

## 3.3.7 Conclusions and Outlook

From the studies reported so far two principle opportunities for the use of glassy metals in catalysis emerge, namely in the *as-quenched* state or as *catalyst precursors*.

The motivation for using them in the *as-quenched* state is based on the surface structure, which ideally should be structurally and chemically isotropic and exhibit no long-range ordering of the constituents, as well as on the ability to tailor the electronic properties. However, the studies available to date indicate that structural relaxation and crystallization phenomena, leading to surface reconstruction, occur even at temperatures far below the crystallization temperature and are enhanced by the presence of adsorbed reactants. Thus, it seems unlikely that the intrinsic cata-



lytic properties of “disordered” (amorphous) surfaces have been uncovered so far. Cleaning and catalytic tests would have to be carried out at conditions where the metastable surface does not undergo reconstruction, which presently seems impossible to achieve. Another problem arises from the intrinsically small surface area of the quenched materials. This problem may be overcome by chemical preparation routes yielding small amorphous alloy particles [101–105].

The use of glassy metals as *catalyst precursors* has opened new routes for the preparation of supported metal catalysts with unusual chemical and structural properties. This potential resides mainly in the high reactivity of these materials compared to their crystalline counterparts. Several efficient supported metal catalysts have been prepared by exposing the precursor alloy to an oxygen-containing gas atmosphere at elevated temperature and subsequent reduction. In situ activation, i.e. the transformation of the precursor alloy to the catalytically active material under reaction conditions, has also been applied successfully. The aim of these (pre)treatments is to transform the alloy into a supported metal catalyst by oxidizing the more electropositive component(s). The structure and morphology of as-prepared catalysts often differs greatly from that of conventionally prepared supported metal catalysts. The oxidic support and the active metal can form intimately intergrown structures and consequently the interfacial area between metal particles and support becomes extremely large leading to maximized metal–support interactions. Such structures are, for most systems, difficult to prepare by conventional methods.

The gas–solid and solid–solid reactions occurring during pretreatment of the glassy metals are complex and the structure of as-prepared catalysts is influenced by several factors, determined by the intrinsic properties of the metallic glass and the conditions of pretreatment. Relevant intrinsic properties are chemical composition, chemical and structural homogeneity, thermal stability, crystallization and oxidation behavior, dissolution of gases, and segregational phenomena. Better understanding of these phenomena is a necessary prerequisite for progress in the use of glassy metals as catalyst precursors.

So far the compositions of glassy metals have rarely been adopted to the special requirements for application in catalysis – in general, amorphous alloys fabricated for other purposes have been used. Considering the importance of the chemical composition for catalysis, this has imposed severe limitations. Careful selection of the alloy composition is at the origin of successful application of these materials and provides significant potential for future developments.

## References

1. C. Yoon, D. L. Cocke, *J. Non-Cryst. Solids* **1986**, 79, 217–245.
2. M. Shibata, T. Masumoto, *Stud. Surf. Sci. Catal.* **1987**, 31, 353–372.
3. A. Molnar, G. V. Smith, M. Bartok, *Adv. Catal.* **1989**, 36, 329–383.
4. A. Baiker, *Faraday Discuss. Chem. Soc.* **1989**, 87, 239–251.
5. A. Baiker in *Advances in Catalyst Design* (Eds: M. Graziani, C. N. R. Rao), Singapore, **1992**, p. 217.
6. A. Baiker, *Topics of Appl. Physics: Glassy Metals III*, (Springer) **1994**, Vol. 72, p. 121.
7. H. J. Güntherodt in *Rapidly Quenched Metals* (Eds: S. Steeb, H. Warlimont), Elsevier, **1985**, Vol. II, p. 1591.

8. Suryanarayana, *Rapidly Quenched Metals: A Bibliography, 1973–1979*, IFI/Plenum, New York, **1980**.
9. F. E. Luborsky, *Amorphous Metallic Alloys*, Butterworths, London, **1983**.
10. R. B. Diegle, *J. Non-Cryst. Solids* **1984**, 61 & 62, 601–612.
11. G. A. Somorjai, *Adv. Catal.* **1977**, 26, 1–68.
12. P. Oelhafen in *Glassy Metals II* (Eds: H. Beck, H. J. Güntherodt) Springer, Berlin, **1983**, p. 283.
13. C. F. Hague, P. Oelhafen, H. J. Güntherodt in *Amorphous Metallic Alloys* (Ed.: F. E. Luborsky), Butterworths, London, **1983**, p. 126.
14. K. Hashimoto, T. Masumoto in *Ultrarapid Quenching of Liquid Alloys* (Ed.: H. Herman), Academic Press, New York, **1981**, p. 29.
15. P. C. Searson, P. V. Nagarkar, R. M. Latanision, *Mod. Aspects Electrochem.* **1990**, 21, 121–161.
16. G. Kreysa, P. Ekdunge, K. Juettnner, *DECHEMA Monogr.* **1990**, 121, 3–13.
17. R. Wiesendanger, M. Ringger, L. Rosenthaler, H. R. Hidber, P. Oelhafen, H. Rudin, H. J. Güntherodt, *Surf. Sci.* **1987**, 181, 46–54.
18. B. Walz, R. Wiesendanger, L. Rosenthaler, H. J. Güntherodt, M. Düggelin, R. Guggenheim, *Mat. Sci. Eng.* **1988**, 99, 501–505; R. Schlögl, R. Wiesendanger, A. Baiker, *J. Catal.* **1987**, 108, 452–466.
19. R. Wiesendanger, M. Ringger, L. Rosenthaler, H. R. Hidber, P. Oelhafen, H. J. Güntherodt, *Z. Phys. Chem. Neue Folge* **1988**, 157, 139–143.
20. L. Scandella, U. Staufer, D. Brodbeck, P. Reimann, H. J. Güntherodt, R. Zehringer, R. Hauert, E. M. Moser, *Mater. Sci. Eng.* **1991**, A133, 601–605.
21. T. M. Schaub, Ph D. Thesis, University of Basle, **1994**.
22. D. M. Eigler, P. S. Weiss, E. K. Schweizer, N. D. Lang, *Phys. Rev. Lett.* **1991**, 66, 1189–1192.
23. N. D. Lang, *Phys. Rev. Lett.* **1986**, 56, 1164–1167.
24. W. Kowbel, W. E. Brower, *J. Catal.* **1986**, 101, 262–267.
25. A. Baiker, H. Baris, R. Schlögl, *J. Catal.* **1987**, 108, 467–479.
26. R. Hauert, P. Oelhafen, R. Schlögl, H. J. Güntherodt, *Solid State Commun.* **1985**, 55, 583–586.
27. A. Baiker, R. Schlögl, E. Armbruster, H. J. Güntherodt, *J. Catal.* **1987**, 107, 221–231.
28. E. Armbruster, A. Baiker, H. J. Güntherodt, R. Schlögl, B. Walz, *Stud. Surf. Sci. Catal.* **1987**, 31, 389–398.
29. M. Komori, H. Habazaki, E. Akiyama, A. Kawashima, K. Asami, K. Hashimoto, *Proc. Symp. on Corrosion, Electrochemistry, Catalysis of Metastable Metals, Intermetallics (Electrochemical Society)* **1993**, Vol. 30, p. 369.
30. H. Yamashita, T. Kaminade, M. Yoshikawa, T. Funabiki, S. Yoshida, *C<sub>1</sub> Mol. Chem.* **1986**, 1, 491–496.
31. T. Katona, Z. Hegedüs, Cs. Kopasz, A. Molnar, M. Bartok, *Catal. Lett.* **1990**, 5, 361–368.
32. M. Maciejewski, A. Baiker, *J. Phys. Chem.* **1994**, 98, 285–290.
33. H. Komiyama, A. Yokoyama, H. Inoue, T. Masumoto, H. Kimura, *Sci. Rep. Res. Inst. Tohoku Univ. Ser.* **1980**, A28, 217–221.
34. A. Yokoyama, H. Komiyama, H. Inoue, T. Masumoto, H. Kimura, *J. Catal.* **1981**, 68, 355–361.
35. A. Yokoyama, H. Komiyama, H. Inoue, T. Masumoto, H. Kimura, *Scr. Metall.* **1981**, 15, 365–368.
36. A. Yokoyama, H. Komiyama, H. Inoue, T. Masumoto, H. Kimura, *ACS Symp. Ser.* **1982**, 196, 237–248.
37. M. Peuckert, A. Baiker, *J. Chem. Soc., Faraday Trans. I* **1985**, 81, 2797–2803.
38. G. Kisfaludi, K. Lazar, Z. Schay, L. Gucci, C. Fetzer, G. Konczos, A. Lovas, *Appl. Surf. Sci.* **1985**, 24, 225–238.
39. G. Kisfaludi, Z. Schay, L. Gucci, G. Konczos, L. Lovas, P. Kovacs, *Appl. Surf. Sci.* **1987**, 28, 111–127.
40. H. Yamashita, M. Yoshikawa, T. Funabiki, S. Yoshida, *J. Catal.* **1986**, 99, 375–382.
41. F. Albertos, B. H. Harij, C. N. Kenney, G. T. Burstein, *Appl. Catal.* **1990**, 65, 85–100.
42. G. Kisfaludi, Z. Schay, L. Gucci, *Appl. Surf. Sci.* **1987**, 29, 367.

43. G. V. Smith, O. Zahraa, A. Molnar, M. M. Khan, B. Rihter, W. E. Brower, *J. Catal.* **1983**, 83, 238–241.
44. A. Molnar, G. V. Smith, M. Bartok, *J. Catal.* **1986**, 101, 540–544.
45. S. Yoshida, H. Yamashita, T. Funabiki, T. Yoezawa, *J. Chem. Soc., Faraday Trans. I* **1984**, 80, 1435–1446.
46. H. Yamashita, M. Yoshikawa, T. Funabiki, S. Yoshida, *J. Chem. Soc., Faraday Trans. I* **1985**, 81, 2485–2493.
47. J. C. Bertolini, J. Brissot, T. Le Mogne, H. Montes, Y. Calvayrac, J. Bigot, *Appl. Surf. Sci.* **1987**, 29, 29–39.
48. A. Baiker, H. Baris, H. J. Güntherodt, *J. Chem. Soc., Chem. Commun.* **1986**, 930–932.
49. H. Yamashita, M. Yoshikawa, T. Funabiki, S. Yoshida, *J. Chem. Soc., Faraday Trans. I* **1987**, 83, 2895–2900.
50. T. Takahashi, Y. Nishi, N. Otsuji, T. Kai, T. Masumoto, H. Kimura, *Can. J. Chem. Eng.* **1987**, 65, 274–279.
51. S. Yoshida, H. Yamashita, T. Funabiki, T. Yonezawa, *J. Chem. Soc., Chem. Commun.* **1982**, 964–965.
52. G. V. Smith, W. E. Brower, M. S. Matyjaszczyk, T. L. Pettit in *Proc. 7th Int. Congr. Catal.* (Eds: T. Seiyama, K. Tanabe), Elsevier, New York, **1981**, Vol. A, p. 355–363.
53. W. E. Brower, M. S. Matyjaszczyk, T. L. Pettit, G. V. Smith, *Nature* **1983**, 301, 497–499.
54. B. C. Giessen, S. S. Mahmoud, D. A. Forsyth, M. Hediger in *Rapidly Solidified Amorphous, Crystalline Alloys* (Eds: B. H. Kear, B. C. Giessen, M. Cohen) Elsevier, New York, **1982**, p. 255.
55. H. Yamashita, M. Yoshikawa, T. Funabiki, S. Yoshida, *J. Chem. Soc., Faraday Trans. I* **1986**, 82, 1771–1780.
56. H. Yamashita, T. Kaminade, T. Funabiki, S. Yoshida, *J. Mater. Sci. Lett.* **1985**, 4, 1241–1243.
57. H. Yamashita, M. Yoshikawa, T. Funabiki, S. Yoshida, *J. Chem. Soc., Faraday Trans. I* **1987**, 83, 2883–2893.
58. A. Baiker, H. Baris, H. J. Güntherodt, *Appl. Catal.* **1986**, 22, 389–393.
59. H. Yamashita, M. Yoshikawa, T. Kaminade, T. Funabiki, S. Yoshida, *J. Chem. Soc., Faraday Trans. I* **1986**, 82, 707–714.
60. G. Carturan, G. Cocco, E. Baratter, G. Navazio, C. Antonione, *J. Catal.* **1984**, 90, 178–181.
61. S. S. Mahmoud, D. A. Forsyth, B. C. Giessen, *Mat. Res. Soc. Symp. Proc.* **1986**, Vol. 58, p. 131.
62. A. Molnar, G. V. Smith, M. Bartok, *J. Catal.* **1986**, 101, 67–72.
63. Y. Shimogaki, H. Komiyama, H. Inoue, T. Masumoto, H. Kimura, *Chem. Lett. (Jpn)* **1985**, 661–664.
64. Ch. Schild, A. Wokaun, R. A. Köppel, A. Baiker, *J. Phys. Chem.* **1991**, 95, 6341–6346.
65. A. Yokoyama, H. Komiyama, H. Inoue, T. Masumoto, H. Kimura, *Chem. Lett. (Jpn)* **1983**, 195–198.
66. A. Yokoyama, H. Komiyama, H. Inoue, T. Masumoto, H. Kimura, *J. Non-Cryst. Solids* **1984**, 61 & 62, 619–624.
67. M. Shibata, N. Kawata, T. Masumoto, H. Kimura, *Chem. Lett. (Jpn)* **1985**, 1605–1608.
68. A. Baiker, D. Gasser, *J. Chem. Soc., Faraday Trans. I* **1989**, 85, 999–1007.
69. R. Köppel, A. Baiker, Ch. Schild, A. Wokaun, *J. Chem. Soc. Faraday Trans. I* **1991**, 87, 2821–2828.
70. D. Gasser, A. Baiker, *Appl. Catal.* **1989**, 48, 279–294.
71. M. Shibata, Y. Ohbayashi, N. Kawata, T. Masumoto, K. Aoki, *J. Catal.* **1985**, 96, 296–298.
72. S. J. Bryan, J. R. Jennings, S. J. Kipling, G. Owen, R. M. Lambert, R. M. Nix, *Appl. Catal.* **1988**, 40, 173–182.
73. A. Coteron, A. N. Hayhurst, *Appl. Catal. A* **1993**, 101, 151–165.
74. A. Baiker, D. Gasser, J. Lenzner, A. Reller, R. Schlögl, *J. Catal.* **1990**, 126, 555–571.
75. R. Schlögl, G. Loose, M. Wesemann, A. Baiker, *J. Catal.* **1992**, 137, 139–157.
76. A. Baiker, M. Maciejewski, S. Tagliaferri, *Ber. Bunsenges. Phys. Chem.* **1993**, 97, 286–292.
77. S. Gredig, S. Tagliaferri, M. Maciejewski, A. Baiker, *Stud. Surf. Sci. Catal.* **1995**, 96, 285–295.
78. A. Baiker, M. Maciejewski, S. Tagliaferri, P. Hug, *J. Catal.* **1995**, 151, 407–419.

79. P. Marti, M. Maciejewski, A. Baiker, *J. Catal.* **1993**, 139, 494–509.
80. L. Borko, Hua Zhu, Z. Schay, I. Nagy, A. Lovas, L. Gucci, *Stud. Surf. Sci. Catal.* **1995**, 96, 297–303.
81. R. Lamprecht, *Ph. D. Thesis*, University of Basel, **1987**.
82. A. Baiker, J. De Pietro, M. Maciejewski, B. Walz, *Stud. Surf. Sci. Catal.* **1991**, 67, 169–178.
83. J. Heveling, E. Armbruster, A. Baiker, *Prepr. Int. Conf. on Catalysis & Catalytic Processing*, Cape Town, South Africa, **1993**, p. 85.
84. F. Sommer in *Rapidly Quenched Metals* (Eds: S. Steeb, H. Warlimont) Elsevier, New York, **1985**, Vol. I, p. 491.
85. A. Baiker, H. Baris, F. Vanini, M. Erbudak in *Proc. 9th Int. Congr. Catal. (Catalysis: Theory, Practice)* (Eds: M. J. Phillips, M. Ternan) Chem. Inst. Canada, **1988**, Vol. 4, p. 1928.
86. P. V. Nagarkar, S. K. Kulkarni, E. Umbach, *Appl. Surf. Sci.* **1987**, 29, 194–222.
87. J. Tamaki, H. Tagaki, I. Imanaka, *J. Catal.* **1987**, 108, 256–258.
88. J. Fusy, P. Pareja, *J. Non-Cryst. Solids* **1987**, 89, 131–142.
89. S. Myhra, J. C. Riviere, L. S. Welch, *Appl. Surf. Sci.* **1988**, 32, 156–172.
90. M. Maciejewski, A. Baiker, *J. Chem. Soc., Faraday Trans. 1* **1990**, 86, 843–848.
91. P. Sen, D. D. Sarma, R. C. Budhani, J. L. Chopra, C. N. R. Rao, *J. Phys.* **1984**, F 14, 565–569.
92. S. Sinha, S. Badrinarayanan, A. P. B. Sinha, *J. Less-Common Met.* **1986**, 125, 85.
93. G. Wei, B. Cantor, *Acta Metall.* **1988**, 36, 167–180.
94. R. M. Nix, T. Rayment, R. M. Lambert, J. R. Jennings, G. Owen, *J. Catal.* **1987**, 106, 216–234.
95. D. L. Cocke, M. S. Owens, R. B. Wright, *Appl. Surf. Sci.* **1988**, 31, 341–369.
96. B. Walz, P. Oelhafen, H. J. Güntherodt, A. Baiker, *Appl. Surf. Sci.* **1989**, 37, 337–352.
97. A. R. Miedema, *Z. Metall.* **1978**, 69, 455–461.
98. F. Vanini, S. Büchler, Xin-nan Yu, M. Erbudak, L. Schlapbach, A. Baiker, *Surf. Sci.* **1987**, 189/190, 1117–1121.
99. L. Schlapbach, *Nato ASI* **1986**, B136, 397.
100. F. Spit, K. Blok, E. Hendriks, G. Winkels, W. Turkenburg, J. W. Drijver, S. Radelaar in *Proc. 4th Int. Conf. Rapidly Quenched Metals* (Eds: T. Masumoto, K. Suzuki) Jpn. Inst. Met., Sendai, **1982**, p. 1635.
101. J. van Wonerghem, S. Morup, S. W. Charles, S. Wells, J. Villadsen, *Phys. Rev. Lett.* **1985**, 55, 410–413.
102. J. van Wonerghem, S. Morup, C. I. W. Koch, S. W. Charles, S. Wells, *Nature* **1986**, 322, 622–623.
103. Deng Jingfa, Zhang Xiping, *Appl. Catal.* **1988**, 37, 339–343.
104. S. Shina, S. Badrinarayanan, A. P. Shina, *J. Less-Common Met.* **1986**, 125, 1179–1190.
105. H. Bönemann, W. Brijoux, T. Joussen, *Angew. Chem.* **1990**, 102, 324–326.

## 3.4 Precipitation and Coprecipitation

F. SCHÜTH AND K. UNGER

### 3.4.1 Introduction

The preparation of catalysts and supports by precipitation or coprecipitation is technically very important [1]. However, precipitation is usually more demanding than several other preparation techniques, due to the necessity of product separa-

79. P. Marti, M. Maciejewski, A. Baiker, *J. Catal.* **1993**, 139, 494–509.
80. L. Borko, Hua Zhu, Z. Schay, I. Nagy, A. Lovas, L. Guzzi, *Stud. Surf. Sci. Catal.* **1995**, 96, 297–303.
81. R. Lamprecht, *Ph. D. Thesis*, University of Basel, **1987**.
82. A. Baiker, J. De Pietro, M. Maciejewski, B. Walz, *Stud. Surf. Sci. Catal.* **1991**, 67, 169–178.
83. J. Heveling, E. Armbruster, A. Baiker, *Prepr. Int. Conf. on Catalysis & Catalytic Processing*, Cape Town, South Africa, **1993**, p. 85.
84. F. Sommer in *Rapidly Quenched Metals* (Eds: S. Steeb, H. Warlimont) Elsevier, New York, **1985**, Vol. I, p. 491.
85. A. Baiker, H. Baris, F. Vanini, M. Erbudak in *Proc. 9th Int. Congr. Catal. (Catalysis: Theory, Practice)* (Eds: M. J. Phillips, M. Ternan) Chem. Inst. Canada, **1988**, Vol. 4, p. 1928.
86. P. V. Nagarkar, S. K. Kulkarni, E. Umbach, *Appl. Surf. Sci.* **1987**, 29, 194–222.
87. J. Tamaki, H. Tagaki, I. Imanaka, *J. Catal.* **1987**, 108, 256–258.
88. J. Fusy, P. Pareja, *J. Non-Cryst. Solids* **1987**, 89, 131–142.
89. S. Myhra, J. C. Riviere, L. S. Welch, *Appl. Surf. Sci.* **1988**, 32, 156–172.
90. M. Maciejewski, A. Baiker, *J. Chem. Soc., Faraday Trans. I* **1990**, 86, 843–848.
91. P. Sen, D. D. Sarma, R. C. Budhani, J. L. Chopra, C. N. R. Rao, *J. Phys.* **1984**, F 14, 565–569.
92. S. Sinha, S. Badrinarayanan, A. P. B. Sinha, *J. Less-Common Met.* **1986**, 125, 85.
93. G. Wei, B. Cantor, *Acta Metall.* **1988**, 36, 167–180.
94. R. M. Nix, T. Rayment, R. M. Lambert, J. R. Jennings, G. Owen, *J. Catal.* **1987**, 106, 216–234.
95. D. L. Cocke, M. S. Owens, R. B. Wright, *Appl. Surf. Sci.* **1988**, 31, 341–369.
96. B. Walz, P. Oelhafen, H. J. Güntherodt, A. Baiker, *Appl. Surf. Sci.* **1989**, 37, 337–352.
97. A. R. Miedema, *Z. Metall.* **1978**, 69, 455–461.
98. F. Vanini, S. Büchler, Xin-nan Yu, M. Erbudak, L. Schlapbach, A. Baiker, *Surf. Sci.* **1987**, 189/190, 1117–1121.
99. L. Schlapbach, *Nato ASI* **1986**, B136, 397.
100. F. Spit, K. Blok, E. Hendriks, G. Winkels, W. Turkenburg, J. W. Drijver, S. Radelaar in *Proc. 4th Int. Conf. Rapidly Quenched Metals* (Eds: T. Masumoto, K. Suzuki) Jpn. Inst. Met., Sendai, **1982**, p. 1635.
101. J. van Wonerghem, S. Morup, S. W. Charles, S. Wells, J. Villadsen, *Phys. Rev. Lett.* **1985**, 55, 410–413.
102. J. van Wonerghem, S. Morup, C. I. W. Koch, S. W. Charles, S. Wells, *Nature* **1986**, 322, 622–623.
103. Deng Jingfa, Zhang Xiping, *Appl. Catal.* **1988**, 37, 339–343.
104. S. Shina, S. Badrinarayanan, A. P. Shina, *J. Less-Common Met.* **1986**, 125, 1179–1190.
105. H. Bönemann, W. Brijoux, T. Jousen, *Angew. Chem.* **1990**, 102, 324–326.

## 3.4 Precipitation and Coprecipitation

F. SCHÜTH AND K. UNGER

### 3.4.1 Introduction

The preparation of catalysts and supports by precipitation or coprecipitation is technically very important [1]. However, precipitation is usually more demanding than several other preparation techniques, due to the necessity of product separa-

tion after precipitation and the large volumes of salt-containing solutions generated in precipitation processes. Techniques for catalyst manufacture thus have to produce catalysts with better performance in order to compensate for the higher cost of production in comparison, for instance, to solid-state reactions for catalyst preparation.

Nevertheless, for several catalytically relevant materials, especially for support materials, precipitation is the most frequently applied method of preparation. These materials include mainly aluminum and silicon oxides. In other systems precipitation techniques are also used, for instance in the production of iron oxides, titanium oxides or zirconias. The main advantages of precipitation for the preparation of such materials is the possibility of creating very pure materials and the flexibility of the process with respect to final product quality.

Other catalysts, based on more than one component, can be prepared by coprecipitation. According to IUPAC nomenclature [2], coprecipitation is the simultaneous precipitation of a normally soluble component with a macrocomponent from the same solution by formation of mixed crystals, by adsorption, occlusion or mechanical entrapment. However, in catalyst preparation technology, the term is usually used in a more general sense in that the requirement of one species being soluble is dropped. In many cases, both components to be precipitated are essentially insoluble under precipitation conditions, although their solubility products might differ substantially. We will therefore use the term coprecipitation for the simultaneous precipitation of more than one component. Such systems prepared by coprecipitation include  $\text{Ni}/\text{Al}_2\text{O}_3$ ,  $\text{Cu}/\text{Al}_2\text{O}_3$ ,  $\text{Cu}/\text{ZnO}$ , and  $\text{Sn-Sb}$  oxides.

Coprecipitation is very suitable for the generation of a homogeneous distribution of catalyst components or for the creation of precursors with a definite stoichiometry, which can be easily converted to the active catalyst. If the precursor for the final catalyst is a stoichiometrically defined compound of the later constituents of the catalyst, a calcination and/or reduction step to generate the final catalyst usually creates very small and intimately mixed crystallites of the components. This has been shown for several catalytic systems and is discussed in more detail later in this article. Such a good dispersion of catalyst components is difficult to achieve by other means of preparation, and thus coprecipitation will remain an important technique in the manufacture of heterogeneous catalysts in spite of the disadvantages associated with such processes. These disadvantages are the higher technological demands, the difficulties in following the quality of the precipitated product during the precipitation, and the problems in maintaining a constant product quality throughout the whole precipitation process, if the precipitation is carried out discontinuously.

To stress the technical relevance of precipitated catalysts, Table I gives an overview of industrially used precipitated catalysts and supports. Since the catalyst compositions, and even less the catalysts preparation procedures for many industrial processes are not disclosed by the companies, this list is by no means comprehensive.

### 3.4.2 General Principles Governing Precipitation from Solutions

Precipitation processes are not only relevant for catalysis, but also for other industries, as for instance the production of pigments. However, in spite of the tremen-

**Table 1.** Some industrially relevant catalysts and supports obtained by precipitation or coprecipitation techniques.

Material	Use	Important examples
Al <sub>2</sub> O <sub>3</sub> (mostly $\gamma$ , in special cases $\alpha$ or $\eta$ )	support, catalyst	Claus process, dehydration of alcohols to alkenes and ethers, support of hydrotreating catalysts, support for three-way catalyst
SiO <sub>2</sub>	support	noble metal/SiO <sub>2</sub> for hydrogenation reactions, Ni/SiO <sub>2</sub> for hydrogenation reactions, V <sub>2</sub> O <sub>5</sub> /SiO <sub>2</sub> for sulfuric acid production
Al <sub>2</sub> O <sub>3</sub> /SiO <sub>2</sub>	catalyst	acid-catalyzed reactions such as isomerizations
Fe <sub>2</sub> O <sub>3</sub>	catalyst, catalyst component	Fischer–Tropsch reactions, major component of catalyst for ethylbenzene reaction to styrene
TiO <sub>2</sub>	support, catalyst, catalyst component	major component of DeNO <sub>x</sub> catalyst
ZrO <sub>2</sub>	catalyst	acid catalyst after sulfate modification
Cu/ZnO	catalyst	methanol synthesis
(VO) <sub>2</sub> P <sub>2</sub> O <sub>7</sub>	catalyst	selective oxidation – for instance butane to maleic anhydride
Cu–Cr oxides	catalyst	combustion reactions, hydrogenations
AlPO <sub>4</sub>	support, catalyst	polymerization, acid-catalyzed reactions
Sn–Sb oxide	catalyst	selective oxidation – for instance isobutene to methacrolein
Bi molybdates	catalyst	selective oxidation – for instance propene to acrolein (mostly supported)

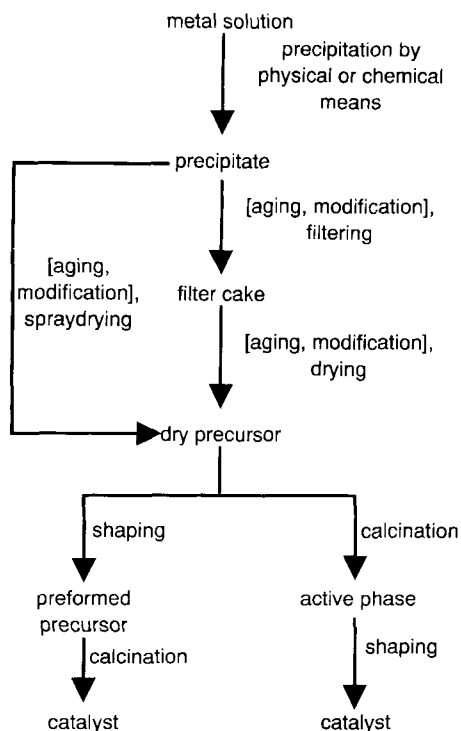
dous importance of precipitation from solution, many basic questions in this field are still unsolved and the production of a precipitate with properties that can be adjusted at will is still rather more an art than a science. This is primarily due to the fact that the key step, nucleation of the solid from a homogeneous solution, is a very elusive one, and is difficult to study using the analytical tools currently available. Spectroscopies using local probes are not sensitive enough to study larger arrangements of atoms on the one hand. Diffraction methods, on the other hand, are not suitable for analysis either, since a nucleus is not large enough to produce a distinctive diffraction pattern. Thus, investigations of crystallization and precipitation processes from solution often have to rely on indirect and theoretical methods. Figure 1 depicts a general flow scheme for the preparation of a precipitated catalyst.

### 3.4.2.1 Physico-Chemical Considerations

In order for a solid to precipitate from homogenous solution, first a nucleus has to form. The formation of a particle is governed by the free energy of agglomerates of the constituents of the solution. The total free energy change due to agglomeration,  $\Delta G$ , is determined by

$$\Delta G = \Delta G_{\text{bulk}} + \Delta G_{\text{interface}} + \Delta G_{\text{others}}$$

where  $\Delta G_{\text{bulk}}$  is the difference of the free energy between solution species and solid

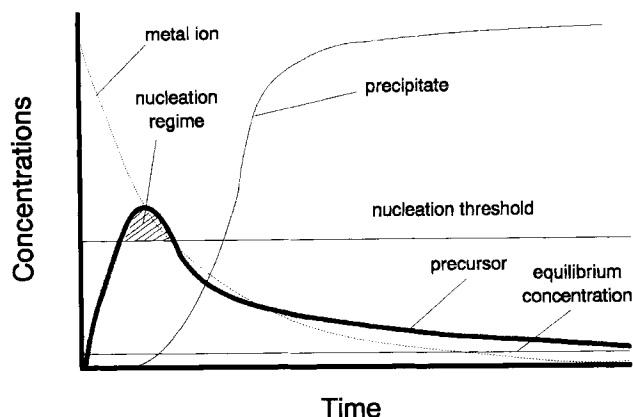


**Figure 1.** Preparation scheme for precipitated catalysts. Optional preparation steps are indicated by square brackets.

species,  $\Delta G_{\text{interface}}$  is the free energy change related to the formation of the interface, and  $\Delta G_{\text{others}}$  summarizes all other contributions, as for instance strain or impurities, which can be neglected here. The agglomeration will be energetically favored if  $\Delta G$  is negative. At supersaturation conditions  $\Delta G_{\text{bulk}}$  is always negative but, to create an interface, energy is needed;  $\Delta G_{\text{interface}}$  is thus positive. For very small particles the total free energy change is positive. If spherical particles are formed,  $\Delta G_{\text{bulk}}$  increases with  $4\pi r^3/3$ , while the interfacial energy only increases with  $4\pi r^2$ . There is thus a critical size  $r$  of the agglomerate, from which on  $\Delta G_{\text{bulk}}$  predominates the total free energy change and the total free energy decreases with the particle size. This critical size is the size of the nucleus.

The general process of the formation of a solid from a solution can be described in a simplified form as indicated in Fig. 2. The most important curve is the nucleation curve which describes the development of the precursor concentration with time. Such a precursor could, for instance, be the hydrolysis product of the metal ions in solution. Only if the precursor concentration exceeds a critical threshold concentration will a nucleus form, and the precipitation begins. The nucleus is defined as the "smallest solid-phase aggregate of atoms, molecules or ions which is formed during a precipitation and which is capable of spontaneous growth" [2]. As long as the concentration of precursor species stays above the nucleation threshold, new particles are formed. As soon as the concentration falls below the critical concentration due to consumption of precursors by nucleation or by the growth pro-





**Figure 2.** Simplified scheme for the formation of a solid product from solution. From the metal ions a precursor species is formed, for instance by hydrolysis or raising the pH. When the concentration of the precursor species exceeds the nucleation threshold, precipitation of the product begins, consuming precursor by nucleation and growth. New nuclei are only formed in the shaded area.

cess, only particle growth of existing particles prevails. Thus, in the framework of this simple concept which was introduced mainly by the work of LaMer in the early 1950s [3] and later used extensively by Matijevic [4] who produced a large number of different monodispersed oxides or hydroxides, particles with a narrow particle size distribution will result from a short nucleation burst, and a wide particle size distribution will result from nucleation over a longer period of time. The size of the particles finally resulting from a precipitation process will be dependent on the area of the shaded section between the nucleation curve and the nucleation threshold. The larger the area, the more particles nucleate and the smaller the resulting particles will be. The nucleation process is strongly temperature dependent, since the rate constant for homogenous nucleation usually does not follow an Arrhenius-type law, but is, for instance, better described by [5]

$$\frac{dN}{dt} = \beta \exp(-A/\ln^2 s)$$

where  $\beta$  is a preexponential term,  $A$  the interfacial energy parameter  $16\pi\sigma^3\Gamma^2/3(kT)^3$ ,  $\sigma$  the solid–fluid interfacial energy,  $\Gamma$  the solid molecular volume,  $s$  the supersaturation. However, this is only one possible expression for the nucleation rate. Several others have been proposed.

Nucleation and growth processes can be described mathematically by sets of differential equations balancing the concentrations of the various species in the system. The most well known approach to this problem is the so-called population balance formalism introduced in the early 1960s [6]. Although such models can give valuable insight into the basic ideas of particle formation from solution, it is an extremely simplified concept. The models are usually only formulated for the formation of a single phase. If more than one phase is possible, the model does not provide information on the nature of the phase eventually formed. According to the Ostwald rule

of successive phase transformation, initially the thermodynamically most unstable phases are formed which then transform to more stable phases. Another factor, which is relatively difficult to implement, is the lack of information on the decisive solution species for many systems. Usually species responsible for nucleation are also considered to be the species contributing to the particle growth. However, the nucleation might involve relatively complex species, while growth – at least of the primary particles – in many cases is assumed to proceed via monomer addition. The model also completely neglects the role of aggregation and agglomeration processes which further contribute to growth and can result in the formation of fewer, but larger particles than predicted for the simple nucleation burst model. Such processes can be of great importance in the formation of technically relevant hydroxides and oxides [7]. However, even if aggregation and agglomeration occurs, narrow particle size distributions, which are often desired, can be obtained. The uniformity in the final particle size distribution can be reached by size dependent aggregation rates [8]. In addition, mechanical agitation or other processes can lead to fragmentation of growing crystals, thus forming secondary nuclei which can alter the particle size distribution.

Another way to induce precipitation without needing a homogeneous nucleation step is the seeding of the solution. Best results are usually obtained if seeding is done with the desired phase. If the solution is seeded, usually no nucleation takes place, since the precursor concentration never exceeds a critical threshold. The precipitation rates in seeded systems normally follow Arrhenius-type rate laws. Precipitation of  $\text{Al}(\text{OH})_3$  in the Bayer process is described by [7]

$$-dc/dt = k \exp(-E/RT) A(c - c_{\text{eq}})^2$$

where  $c$  is the  $\text{Al}_2\text{O}_3$  concentration,  $k$  the rate constant,  $E$  the activation energy (about  $59 \text{ kJ mol}^{-1}$ ),  $R$  the gas constant,  $T$  the temperature,  $A$  the seed surface area and  $c_{\text{eq}}$  the equilibrium concentration. However, here as well, temperature dependencies can be complicated, since the equilibrium concentration might vary strongly with temperature.

From the facts considered above, it is clear that supersaturation of the solution from which precipitation occurs is one of the key factors of the precipitation process. Supersaturation can be reached either by physical means, which is usually cooling down the reaction mixture, or evaporation of the solvent, or by chemical means, i.e. addition of a precipitating agent. The precipitating agent either changes the pH, thus leading to condensation of precursors to form the hydroxides or the oxides, or introduces additional ions into the system by which the solubility product for a certain precipitate is exceeded. The influence of such precipitating agents is discussed in the next section.

If catalysts are prepared by coprecipitation, the relative solubilities of the precipitates and the possibility for the formation of defined mixed phases are essential. If one of the components is much more soluble than the other, there is a possibility that sequential precipitation occurs. This leads to concentration gradients in the product and less intimate mixing of the components. If this effect is not compensated by adsorption or occlusion of the more soluble component, the precipitation

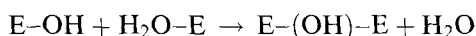
should be carried out at high supersaturation in order to exceed the solubility product for both components simultaneously. Precipitation of the less soluble product will proceed slightly faster, and the initially formed particles can act as nucleation sites for the more soluble precipitate which forms by heterogeneous precipitation. The problem is less crucial if both components form a defined, insoluble species. This is for instance the case for the coprecipitation of nickel and aluminum which can form defined compounds of the hydrotalcite type (see the extensive review by Cavani et al. [9] and the summary by Andrew [10]).

### 3.4.2.2 Chemical Considerations

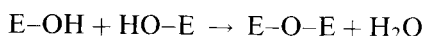
It is generally desirable to precipitate the desired material in such a form, that the counterions of the precursor salts and the precipitation agent, which can be occluded in the precipitate during the precipitation, can easily be removed by a calcination step. If precipitation is induced by physical means, i.e. cooling or evaporation of solvent to reach supersaturation of the solution, only the counterion of the metal salt is relevant. If precipitation is induced by addition of a precipitating agent, ions introduced into the system via this route also have to be considered. Favorable ions are nitrates, carbonates, or ammonium, which decompose to volatile products during the calcination. For catalytic applications usually hydroxides, oxohydrates, oxides (in the following the term “hydroxides” is used in a rather general sense, comprising hydroxides and oxides with different degrees of hydration) are precipitated; in some cases carbonates, which are subsequently converted to the oxides or other species in a calcination step, are formed. Also the precipitation of oxalates as precursors for spinel-type catalysts have occasionally been reported to give good results [11]. If the ions do not decompose to volatile products, careful washing of the precipitate is advisable.

In many cases it has been found advantageous to work at low and relatively constant supersaturation which is achieved homogeneously in the whole solution (precipitation from homogeneous solution, PFHS). This can also be employed for deposition–precipitation processes, see Section 4.6. This can be reached by using a precipitating agent which slowly decomposes to form the species active in the precipitation. The most commonly employed precursor for the liberation of ammonia is urea, which has been used in many precipitation processes [12]. The ammonia is liberated homogeneously over the whole precipitation vessel, thus avoiding higher concentrations at the inlet point which can occur if aqueous ammonia is used. In addition, the carbon dioxide released during the urea hydrolysis can keep the solution essentially oxygen free. These differences can lead to markedly different products [13]. For the preparation of sulfides thioacetamide might be used.

The precipitation of the hydroxides can be performed either starting from an alkaline solution which is acidified, or from acidic solutions by raising the pH. In the first case, the formation of the solid product proceeds via polyanionic species. These polyanionic species undergo condensation reactions, either viaolation reactions



or via oxolation reactions



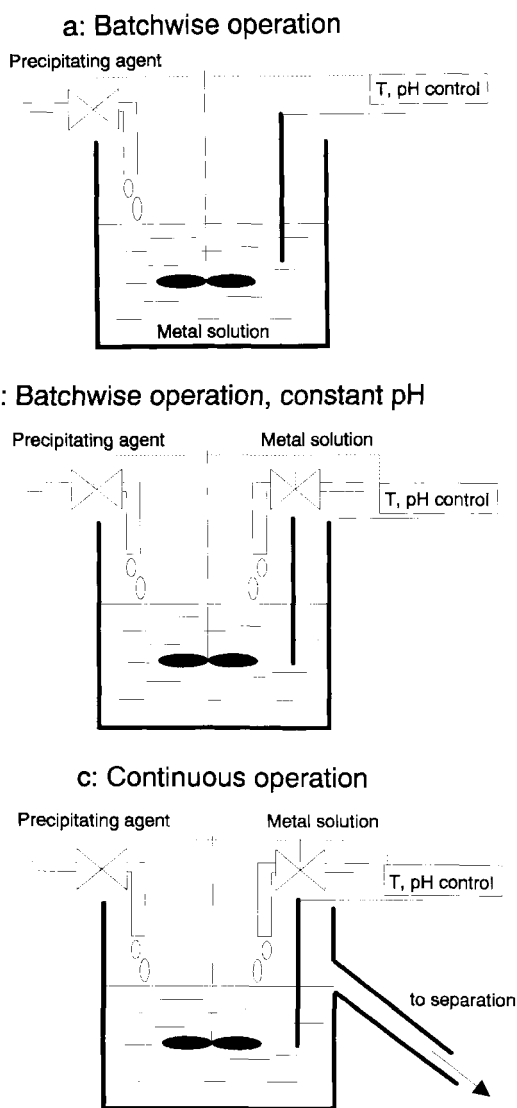
A prototypic example for such precipitation reactions from alkaline solutions is  $\text{SiO}_2$ , which is prepared from silicates, as for instance sodium water glass by acidification. However, most hydroxides for technical applications are precipitated from acidic solutions by the addition of a precipitating agent. Usually ammonia or sodium carbonate are used as the precipitating agent. If other ions do not adversely influence the catalytic performance,  $\text{Ca(OH)}_2$  or  $\text{NaOH}$  can be used. Depending on the metal ion and the precipitating agent, either the hydroxides, carbonates or hydroxycarbonates precipitate. Precipitation from acidic solutions mostly proceeds via polycations and – as in the basic case – by ololation or oxolation reactions. However, intermediate states are not as well known as for the polyanionic species. Only a few defined polycations are known in most cases.

### 3.4.2.3 Process Considerations

There are several ways to carry out the precipitation process (Fig. 3) [14]. The simplest implementation of the precipitation reaction is the batch operation where the solution from which the salt is to be precipitated is usually present in the precipitation vessel and the precipitating agent is added. The advantage of this mode of operation is the simple way in which the product can be obtained; the most severe disadvantage is the variation of batch composition during the precipitation process. This can lead to differences between the product formed during the initial stages of the precipitation and the precipitate formed at the end of the process. If a coprecipitation is carried out this way, it is important to decide which compounds are present in the vessel and which compounds are to be added. If the precipitating agent is present in the precipitator and the mixed metal solutions are added, the product tends to be homogeneous, since the precipitation agent is always present in large excess. If, on the other hand, the precipitating agent is added to a mixed metal solution, the precipitate with the lower solubility tends to precipitate first, thus resulting in the formation of an inhomogeneous product.

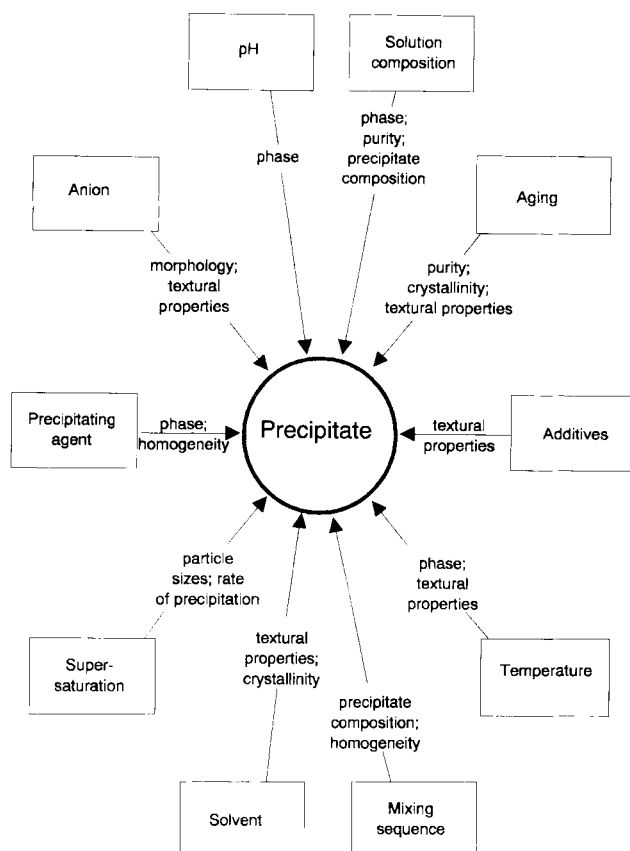
A slightly more complex process is the simultaneous addition of both reagents under strict control of the pH and the reagent ratios. If the precipitation is carried out following this procedure, the ratio of the metal salt and precipitating agent remains constant; all other concentrations, however, change during the process. Homogeneity of the product is usually better than in the first process described, but might still vary between the first precipitate and the precipitate formed last. This is due to the different concentrations of the other ions which are not precipitated and might be occluded in the precipitate to a larger extent during the final stages of the procedure. Moreover, the precipitates first formed are aged for a longer time in the solution. Thus, phase transitions might have already occurred, while fresh precipitates are still formed.

These problems are avoided if a continuous process is employed for the precipitation; however, this makes higher demands on the process control. In a continuous



**Figure 3.** Possible implementations of precipitation processes (after [14]). In the batchwise process (a) the pH and all other parameters except for the temperature change continuously during the precipitation due to consumption of the metal species. Coprecipitation should be carried out in the reversed arrangement by addition of the metal species to the precipitating agent to avoid sequential precipitation. In process (b) the pH is kept constant, but the batch composition and the residence time of the precipitate change continuously. In process (c) all parameters are kept constant.

process all parameters as temperature, concentrations, pH, and residence times of the precipitate can be kept constant or altered at will. Continuous operation is, for instance, used for the precipitation of aluminum hydroxide in the Bayer process. Bayer aluminum hydroxide is the main source for the production of catalytically active aluminas. The precipitation step of the Bayer process is carried out continuously. An aluminum solution supersaturated with respect to  $\text{Al}(\text{OH})_3$ , but not supersaturated enough for homogeneous nucleation, enters the precipitation vessel which already contains precipitate so that heterogeneous precipitation is possible. The nucleation rate has to be controlled very carefully to maintain constant con-



**Figure 4.** Parameters affecting the properties of the precipitate and main properties influenced.

ditions. This is usually done by controlling the temperature of the system to within 2–3 degrees [7].

The continuous process usually allows precipitation at low supersaturation conditions, since seeds are already present in the precipitation vessel. Thus, no homogeneous precipitation, which needs high levels of supersaturation, is necessary, and nucleation occurs heterogeneously with the associated lower supersaturation levels.

### 3.4.3 Influencing the Properties of the Final Product

Basically all process parameters, some of which are fixed and some of which are variable, influence the quality of the final product of the precipitation. Usually precipitates with specific properties are desired. These properties could be the nature of the phase formed, chemical composition, purity, particle size, surface area, pore sizes, pore volumes, separability from the mother liquor, and many more, including the demands which are imposed by the requirements of downstream processes, like drying, pelletizing, or calcination. It is therefore necessary to optimize the parameters in order to produce the desired material. Figure 4 summarizes the parameters

which can be adjusted in precipitation processes and the properties which are mainly influenced by these parameters. The following discussion attempts to give some general guidelines concerning the influence of certain process parameters on the properties of the resulting precipitate. It should, however, be stressed, that the stated tendencies are only trends which might vary in special cases. The exact choice of precipitation parameters is usually the result of a long, empirically driven optimization procedure and a well-guarded secret of catalyst manufacturers or the producers of precursors for catalysts.

### 3.4.3.1 Influence of Raw Materials

As stated above, precursors are usually chosen with counterions that can easily be decomposed to volatile products. These are preferably the nitrates of metal precursors and ammonia or sodium carbonate as the precipitating agent. Also, oxalates have occasionally been employed. If the precipitation is carried out in the presence of ions which can be occluded, repeated washing steps are necessary, if the ions adversely affect the catalytic performance of the later catalyst. Ions as chlorides or sulfates act as poisons in many catalytic reactions. Such ions should therefore be avoided in the precipitation. The problem is reduced if supersaturation is reached by physical means. However, higher degrees of supersaturation, and thus more rapid precipitation and smaller particle sizes, are better achieved by changing the pH.

The nature of the ions present in the precipitation solution can strongly influence the properties of the final product. This was demonstrated effectively by the work of Matijevic who investigated the precipitation of many different metals, primarily as hydroxides [15]. The anions present do not only influence particle morphologies and particle sizes, but can even result in the formation of different phases. One striking example is given by Matijevic [15]: a solution of 0.0315 M  $\text{FeCl}_3$  and 0.005 M  $\text{HCl}$  results in the formation of Hematite,  $\alpha\text{-Fe}_2\text{O}_3$ ; at higher concentrations (0.27 M  $\text{FeCl}_3$  and 0.01 M  $\text{HCl}$ )  $\beta\text{-FeOOH}$  is formed; in the presence of nitrate (0.18 M  $\text{Fe}(\text{NO}_3)_3$ ) and sulfate (0.32 M  $\text{Na}_2\text{SO}_4$ ) ferric basic sulfate ( $\text{Fe}_3(\text{OH})_5(\text{SO}_4)_2 \cdot 2\text{H}_2\text{O}$ ) precipitates; finally, with phosphate (0.0038 M  $\text{FeCl}_3$  and 0.24 M  $\text{H}_3\text{PO}_4$ )  $\text{FePO}_4$  is formed.

The precipitates differ both in the phase formed and also in their morphologies. Depending on the conditions, rather spherical on the one hand, or needle-like crystals on the other hand, can be formed.

Other examples of the influence of the starting materials are the precipitation of  $\text{MoO}_3$  [16] or the preparation of  $\text{AlPO}_4$  [17]. For  $\text{MoO}_3$  small particles with relatively high surface area are formed with  $\text{Na}_2\text{MoO}_4$  as the precursor salt, whereas larger particles with lower surface area precipitate from solutions containing  $(\text{NH}_4)_6\text{Mo}_7\text{O}_{24}$ . In the  $\text{AlPO}_4$  system the type of anion has a strong influence on the recrystallization behavior. Recrystallization to the  $\alpha$ -crystobalite form occurs at 1073 K for  $\text{AlPO}_4$  precipitated from aluminum nitrate. If the sulfate is used, even at calcination temperatures of 773 K, recrystallization to tridymite takes place. The chloride only begins to recrystallize at 773 K; however, at these temperatures large

fractions of amorphous material are present. The phases formed are tridymite and, at temperatures above 1200 K,  $\alpha$ -cristobalite. As in the case of the iron oxides, textural properties can vary drastically.

### 3.4.3.2 Influence of Concentration and Composition

In most cases it is desirable to precipitate at high concentration levels of the metal ions. This increases the space-time yields by decreasing the vessel volume for the same mass of precipitate. Moreover, the higher degrees of supersaturation lead to faster precipitation. Thus, plant investment is reduced. With respect to the quality of the product obtained, smaller particle sizes and higher surface areas are usually achieved at higher concentration levels due to increased nucleation rates at higher supersaturation if homogeneous nucleation takes place. If for some reason the precipitation is carried out at low concentration levels, for instance to produce larger primary particles, the precipitation has to be performed either in continuous systems where seeds are present in the stationary state, or seeds have to be added to the solution.

If catalysts are prepared by coprecipitation, the composition of the solutions determine the composition of the final product. Often the composition of the precipitate will reflect the solution concentrations, as was shown for CuO/ZnO catalysts for methanol synthesis [18], but this is not necessarily the case. For aluminum phosphates it was found that at low P:Al ratios the precipitate composition is identical to the solution composition, but if the P:Al ratio in the solution comes close to and exceeds unity, the precipitate composition asymptotically approaches a P:Al ratio of 1 [19]. Deviations from solution composition in coprecipitation processes will generally occur if solubilities of the different compounds differ strongly and precipitation is not complete or, if in addition to stoichiometric compounds, only one component forms an insoluble precipitate; this the case for the aluminum phosphate.

### 3.4.3.3 Solvent Effects

For economic reasons water is almost exclusively used as the solvent for precipitation processes, at least for bulk catalysts and supports; organic solvents are much more expensive than water. This economic disadvantage is even more severe than would be expected from the price difference, because solubilities for most metal salts are much lower in organic solvents. Thus, to reach the same space-time yield, larger systems usually have to be employed. Moreover, increased environmental problems are associated with the use of organic solvents. However, there are some reports in the literature that organic solvents can be advantageous for the precipitation of certain materials. The low solubilities of the precursor materials may, for instance, result in very low supersaturations, which means slow crystallization. Therefore, particle size distributions can be altered, or phases closer to the equilibrium phases can be formed. The disadvantages of the use of the organic solvents in precipitation



processes have to be compensated by superior product qualities which cannot be achieved by other means.

One of the most important systems which can be prepared advantageously from organic solvents is the  $(\text{VO})\text{HPO}_4 \cdot 0.5 \text{H}_2\text{O}$  precursor for vanadium–phosphorus mixed oxides. This is the best known catalyst for the selective conversion of *n*-butane to maleic anhydride. This system will be discussed in more detail below.

The possibility of obtaining higher surface-area precipitates from organic solvents is described by Desmond et al. [20]; polar compounds such as alcohols, aldehydes, esters, glycols, etc. are used. Due to low solubilities of the precipitating agent (preferably  $\text{Na}_2\text{CO}_3$  or  $\text{K}_2\text{CO}_3$ ) in the organic solvent ( $10^{-1}$ – $10^{-6} \text{ mol L}^{-1}$ ), Group VIIIA, IB and IIB metal oxides can be prepared with higher surface area than from aqueous solutions. This is believed to be due to a constant, low concentration of the precipitating agent which is dissolved as the metal oxide precipitates. The patent claims that different structures can be formed as compared to precipitation from aqueous solutions. Iron oxide, for instance, precipitates as magnetite ( $\text{Fe}_3\text{O}_4$ ) while in water usually hematite ( $\alpha\text{-Fe}_2\text{O}_3$ ) or maghemite ( $\gamma\text{-Fe}_2\text{O}_3$ ) are formed. One of the problems associated with this technique are the long precipitation times of several days. The materials are reported to exhibit surface areas about twice as high as for comparative catalysts prepared from water; the yield in Fischer–Tropsch reactions was about 50% higher than over conventionally prepared catalysts.

In two cases, however, precipitation from organic solvents is used to obtain the catalyst, due to the very nature of the system. This is the hydrolysis of organic precursors and the formation of polymerization catalysts in nonpolar media. In the hydrolysis of organic precursors, alkyls or alkoxides, especially of silicon or aluminum, are hydrolyzed by the action of aqueous bases or water. This process can be carried out in water as the solvent. The reversed system, with the organometallic compound itself as the solvent or an additional solvent have also been described. This process has the advantage that catalyst particles with predetermined shapes, usually spheres, can be formed directly [21]. Moreover, materials resulting from hydrolysis processes are very pure due to the high purity of the starting materials. The aluminum oxide obtained from the hydrolysis of aluminum alcoholates were initially only a byproduct of detergent production but, due to the high quality of the resulting aluminas (for instance PURAL<sup>®</sup>-type aluminas) became the main product of the process. Catalyst production processes based on the hydrolysis of organic precursors are discussed in more detail in a later chapter.

If polymerization catalysts, for instance for alkene polymerization (Ziegler–Natta-type catalysts), are prepared by precipitation methods, they can be formed by precipitation from organic solvents, as claimed in several patents [22]. In these patents the precipitation of titanium–magnesium compounds in THF with hexane as precipitating agent is used for the formation of the catalyst. Many important Ziegler–Natta initiators are solids, and heterogeneous initiator systems seem to be necessary for the production of isotactic polyalkenes [23]. However, not much information on the details of catalyst preparation is available in the open literature.

Summarizing this section, the use of organic solvents for the precipitation of catalysts seems to be of only minor importance. Only in special cases are the higher

costs and problems involved in such processes justified by the superior properties of the final catalyst.

#### 3.4.3.4 Influence on Precipitation of Temperature

As outlined above, nucleation rates are extremely sensitive to temperature changes. Therefore, precipitation temperature is a decisive factor in controlling precipitate properties such as primary crystallite sizes, surface areas, and even the phases formed. However, it is very difficult to state how the precipitation temperature has to be adjusted to achieve a product with specific properties. The optimum precipitation temperature usually is a parameter which has to be determined experimentally.

In general, most precipitation processes are carried out above room temperature, often close to 373 K. One obvious reason for this is that precipitation is more rapid, provided that high levels of supersaturation are maintained.

Depending on the kinetics of the different elementary processes involved in the formation of the precipitate, a temperature increase might lead to an increase in crystallite size, as was observed for the crystallization of pseudoboehmite [24] or iron molybdates [25]. However, in other cases no influence of the precipitation temperature on the crystallite size of the final catalyst was reported [26], or a decrease was reported, as for the ZnO system [27].

For some systems, however, the influence of the temperature on the phase composition can be predicted based on chemical considerations. For instance, the composition of bismuth molybdate catalysts is believed to be determined by the nature of the molybdate anion present in solution [28] which is dependent on the solution temperature. For Ni/SiO<sub>2</sub> catalysts the differences between catalysts prepared at high or low temperatures are explained by the formation of nickel hydro-silicate at high temperatures, while at low temperature the main precipitate is nickel hydroxide [29].

#### 3.4.3.5 Influence of pH

Since the pH directly controls the degree of supersaturation, at least if hydroxides are precipitated, this should be one of the crucial factors in precipitation processes. As for many other parameters, the influence of pH is not a simple one and it has to be investigated experimentally for a specific system. Even in a relatively well-known system such as iron oxide [30] the effect which the precipitation pH has on the properties of the final product is not yet clear. There is no clear relationship between the precipitation pH and the textural and catalytic properties of the precipitate. It is relatively well known what phases are formed under specific conditions, due to the importance of iron oxides as pigments, but the influence of pH with respect to catalytic properties is not well studied.

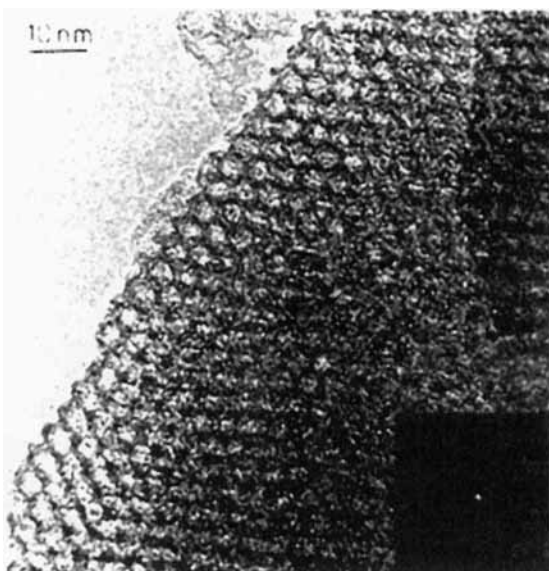
In the aluminum oxide system the precipitation pH is one of the variables which controls the nature of the phase eventually obtained. However, aging conditions of the initially formed amorphous precipitate are at least equally important. In gen-

eral, it can be stated that precipitation above  $\text{pH} = 8$  leads to the formation of bayerite, while precipitation under more acidic conditions favors the subsequent formation of boehmite. Hydrargillite is formed as the product of the Bayer process by seeding a supersaturated alkali containing aluminum solution. The formation of bayerite is strongly facilitated by the presence of alkali cations which stabilize the structure.

### 3.4.3.6 Influence of Additives

The properties of precipitates can be strongly influenced by additives. Additives are substances which are not a necessary ingredient of a precipitation reaction. Thus, although anions of precipitation agents might strongly influence product properties, they are not considered as additives, because they are unavoidable in the precipitation reaction.

The most widely used additives are organic molecules which are added to the precipitate in order to control the pore structure [31]. Such organic molecules can later be removed from the precipitate in a calcination step. A very promising route to the preparation of high surface area oxides (M41S) is the use of surfactants as additives which was introduced in 1992 by scientists of Mobil [32]. The surfactants are able to form liquid crystal-like structures in cooperation with the silicates present in solution [33]. Removing the surfactant by a calcination step leaves a silica negative of the organic liquid crystal with a relatively perfect hexagonal arrangement of pores, the diameters of which can be adjusted between about 2 and 10 nm (Fig. 5). The pore size distribution is very sharp, as can be seen by sorption analysis [34]. In subsequent publications it was shown that the concepts can be generalized



**Figure 5.** Transmission electron micrograph of a mesoporous M41S-type silicate with pore sizes of 4 nm. The regular hexagonal arrangement of the pores can be seen in the micrograph and in the diffraction pattern shown in the inset.

to the preparation of other oxides [35]. BET surface areas can be as high as  $1200\text{ m}^2\text{ g}^{-1}$  for the silicate. A special case is the formation of oxides with anionic surfactants such as alkylsulfates or alkylsulfonates. Decomposition of zirconias or titanias precipitated with such surfactants leads directly to the formation of sulfated zirconias or titanias which exhibit remarkable stabilities and excellent performance in acid-catalyzed reactions [36].

Since the use of additives to control the precipitation of catalysts is a wide field, and is usually treated as trade secrets, this topic cannot be discussed in more detail in the context of this chapter.

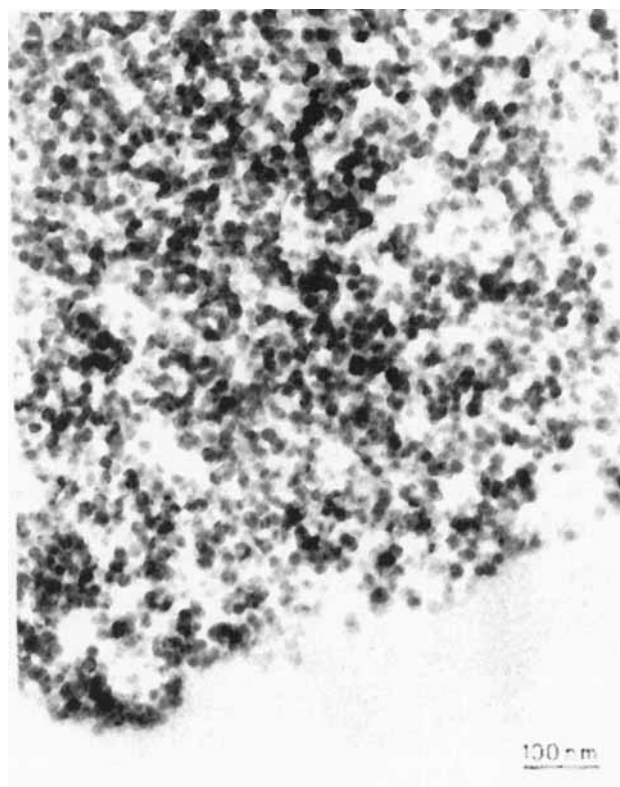
### 3.4.4 Prototypical Examples of Precipitated Catalysts and Supports

This section shows, for four examples of increasing complexity, how precipitates are formed and how the properties of the precipitates are controlled to produce a material suitable for catalytic applications. The first two examples comprise silica, which is primarily used as support material and is usually formed as an amorphous solid, and alumina, which is also used as a catalytically active material, and which can be formed in various modifications with widely varying properties as pure precipitated compounds. The other examples are the results of coprecipitation processes, namely  $\text{Ni}/\text{Al}_2\text{O}_3$  which can be prepared by several pathways and for which the precipitation of a certain phase determines the reduction behavior and the later catalytic properties, and the precipitation of  $(\text{VO})\text{HPO}_4 \cdot 0.5\text{H}_2\text{O}$  which is the precursor of the V/P/O catalyst for butane oxidation to maleic anhydride, where even the formation of a specific crystallographic face with high catalytic activity has to be controlled.

#### 3.4.4.1 Silica as Support Material

Silica applied as a support for catalysts is an X-ray-amorphous form of silicon dioxide [37]. It is manufactured in two steps. First, a silica hydrogel is formed by means of a sol-gel process [38]. Secondly, the silica hydrogel is subjected to aftertreatment followed by dehydration to remove water. The product is a silica xerogel composed of hard porous granules. The granules can be milled to a powder and sized to the desired particle size. Silica beads are obtained in the course of the sol-gel process by dispersing sol droplets into a water-immiscible liquid whereby gelling of the droplets into hydrogel beads occurs [39].

In the sol-gel process sodium silicate (water glass) solution is acidified with sulfuric acid. By decreasing the pH of the water glass solution silicic acids are formed which immediately undergo polycondensation and further growth to colloidal silica particles. Depending on the final pH, the silica concentration, the type and concentration of the electrolyte, the temperature, and other parameters, the dispersion of the colloid particles can be stabilized as a silica sol, or agglomeration of the colloidal particles occurs to silica hydrogel. The silica hydrogel represents a coherent



**Figure 6.** Globular structure of a silica xerogel; magnification  $\times 240\,000$ .

system composed of a three-dimensional network of agglomerated spheres with sodium sulfate solution as dispersing liquid. The pores are preformed by the interstices between the agglomerated nonporous silica globules. The pore structure is thus determined by the size of the globules and their coordination in the agglomerate. Figure 6 visualizes the globular structure of a silica xerogel. The silica hydrogel ages, i.e. it shrinks by expelling water whereby its mechanical strength increases. This process is called syneresis. To convert the hydrogel to the silica xerogel it is washed to remove the salt solution and subjected to drying at about 423–473 K. The drying conditions also affect the specific surface area and the pore structure parameters of the xerogel. When the dried xerogel is exposed to air it adsorbs water to about 5–10 wt% depending on its specific surface area. In the course of aging, washing and drying the hydrogel, a number of procedures can be applied to systematically vary the pore structure, comprised under the term modification. These procedures could be washing with acids or bases, hydrothermal treatment, etc. As a result the pores are enlarged and the specific surface area decreases. This step is important for the preparation of catalyst supports in which transport limitations are minimized.

Large-pore granules of silica xerogel are not suitable as catalyst supports due to the lack of large macropores which are necessary for a good mass transfer and due

to low stability when packed in a fixed-bed reactor. It is advisable to subject the powdered xerogel to pelletization on a rotary plate or to extrudation. In both cases a binder has to be applied to control the porosity and size of macropores and to obtain sufficient mechanical stability (crushing strength and attrition resistance).

Silica beads 2–3 mm in size can be formed in the course of the sol-gel process. The sol passes an orifice where liquid droplets are formed which then settle in a water-immiscible liquid. During settling the liquid droplets solidify to silica hydrogel beads.

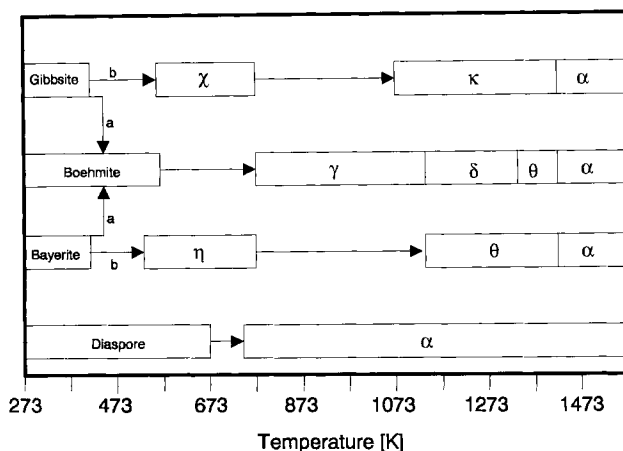
The xerogel contains inorganic impurities which depend on the purity of the water glass and which might affect catalytic performance. Most common are sodium, aluminum, and titanium at concentrations exceeding 1000 ppm. These impurities affect the thermal stability of the xerogel and the catalytic properties of the final catalyst. The silica surface is covered by hydroxyl groups and adsorbed water. At full hydroxylation the concentration of hydroxyl groups amounts to about  $8 \mu\text{mol m}^{-2}$ . There are different types of Brønsted sites, namely isolated (or free), geminal, and vicinal. They can be monitored by  $^{29}\text{Si}$  CP MAS NMR (Cross Polarization Magic Angle Spinning Nuclear Magnetic Resonance) spectroscopy [40], IR spectroscopy [41] and other techniques. The Brønsted sites on the silica surface are weakly acidic ( $\text{p}K_{\text{a}} \approx 7$ ). Dispersed in electrolyte solution, silica xerogel thus acts as a weak cation exchanger which makes it possible to impregnate silicas by equilibration with the ion to be loaded. It is worth noting that silica xerogel is soluble in solutions of  $\text{pH} > 9$ .

One major advantage of silica xerogel over other support materials is the ease of adjustment and control of mean pore diameter, specific surface area and the specific pore volume. Supports for catalytic applications require a sufficiently high specific surface area which is generated by mesopores with mean pore diameters between 5 and 50 nm and a sufficient amount of macropores of a mean pore diameter  $> 50$  nm to ascertain a rapid mass transfer. Also important is a high degree of pore connectivity which requires a high porosity. Enhancing the porosity, however, reduces the mechanical strength of the support particles. Thus, a compromise has to be found. Silica xerogels usually have a specific pore volume between 0.5 and  $1.0 \text{ cm}^3 \text{ g}^{-1}$  which corresponds to a porosity of about 50–70%. Silica xerogels are typical mesoporous adsorbents with a mean pore diameter between 5 and 50 nm and corresponding specific surface areas of between 50 and  $600 \text{ m}^2 \text{ g}^{-1}$ . Macropores of a mean pore diameter of  $> 50$  nm are generated in the course of the formulation and the shaping process.

Silicas are used as supports in a variety of catalytic processes. Typical applications are Ni-, Pd-, or Pt-supported catalysts for hydrogenation reactions and  $\text{V}_2\text{O}_5$ -supported catalysts in the oxidation of  $\text{SO}_2$  in gases from roasting sulfides or sulfur to yield  $\text{SO}_3$ .

#### 3.4.4.2 Active Aluminas

Active aluminas are much more widely used in catalytic applications than silicas, since they are not only excellent support materials, but also very active as catalysts



**Figure 7.** Sequence of phases formed after thermal treatment of aluminum hydroxides and aluminum oxide hydroxides. Pathway (a) is favored by pressures exceeding 1 bar, moist air, heating rates higher than  $1 \text{ K min}^{-1}$  and particle sizes higher than  $100 \text{ }\mu\text{m}$ . Pathway (b) is favored by pressures of 1 bar, dry air, heating rates below  $1 \text{ K min}^{-1}$  and particle sizes below  $10 \text{ }\mu\text{m}$ .

in their own right for several applications. However, the chemistry of aluminas is much more complicated than that of silica, since many crystallographic modifications exist, only few of which are useful as catalysts.

Porous aluminas are manufactured by a controlled dehydration from aluminum hydroxide ( $\text{Al}(\text{OH})_3 = \text{Al}_2\text{O}_3 \cdot 3\text{H}_2\text{O}$ ) or aluminum oxide hydrates ( $\text{AlOOH} = \text{Al}_2\text{O}_3 \cdot \text{H}_2\text{O}$ ). Aluminum hydroxide exists in various crystalline forms as gibbsite (= hydrargillite), bayerite, and nordstrandite [42]. These hydroxides are nonporous. Thermal treatment of gibbsite formed in the Bayer process at about 423 K gives microcrystalline boehmite with a specific surface area of about  $200\text{--}400 \text{ m}^2 \text{ g}^{-1}$ . The best Bayer precursor for the preparation of catalysts is the fine crystalline material deposited as a hard crust on the precipitator wall which is removed periodically from the precipitators. Further treatment between 673 K and 1273 K yields a series of porous crystalline transition aluminas assigned by Greek letters as chi ( $\chi$ ), kappa ( $\kappa$ ), gamma ( $\gamma$ ), eta ( $\eta$ ), theta ( $\theta$ ) and delta ( $\delta$ ). The most important transition oxides for catalytic applications are  $\gamma$ -alumina and the  $\eta$ -alumina. Calcination above 1273 K yields  $\alpha$ -alumina as a crystalline nonporous product. This material is sometimes used as a low surface area support material.

Figure 7 shows the pathways for the formation of different aluminas between  $\text{Al}(\text{OH})_3$  and  $\text{Al}_2\text{O}_3$ .  $\gamma$ -Alumina and  $\eta$ -alumina are also called active aluminas. These materials are seldom phase pure and contain other transition aluminas as impurities. Their properties strongly depend on the type of starting materials, the procedure chosen for thermal treatment, and the operation parameters such as temperature and pressure. Highly active  $\gamma$ -alumina has been prepared by shock calcination followed by rehydration [43].

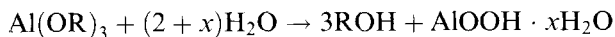
In addition to gibbsite there are other routes to manufacture  $\text{Al}(\text{OH})_3$  and the

**Table 2.** Properties of different precursors used for active alumina preparation.

Property	Bayer hydroxide	Precipitated hydroxides	Ziegler hydroxides
Raw material	bauxite	aluminum salt solutions	aluminum alcoholates
Process	digestion in NaOH and crystallization	neutralization with bases at pH 7–12	hydrolysis
Phase	gibbsite	pseudoboehmite, bayerite, nordstrandite, gibbsite	pseudoboehmite
Size of primary particles (nm)	500–15 000	10–1000	4–10
Main impurity	Na <sub>2</sub> O	chloride, sulfate, nitrate	carbon (very low concentrations)
Weight loss on calcination (wt %)	35	18–40	22–28
Maximum of pore radius distribution (nm)	1.2–2.2	1.2–2.2	3.0–7.5
BET surface area (m <sup>2</sup> g <sup>-1</sup> )	0.5–10	200–400	160–600

consecutive transition oxides. One is the precipitation of Al(OH)<sub>3</sub> from aluminum salts by adjusting the pH between 7 and 12 by adding bases. Precipitation at elevated temperatures and high pH leads to formation of bayerite, whereas at lower pH pseudoboehmite and subsequently boehmite are formed. By heating, these materials can be converted to the active transition aluminas.

A third, very important source of aluminum oxide hydroxides is the hydrolysis of aluminum alcoholates. Due to the high purity of the alcoholate, almost no impurities, except for carbon residues at low concentrations, are present in the product:



where R can vary.

Using such procedures, high purity pseudoboehmite is produced (PURAL<sup>®</sup>, Condea Chemie, Brunsbüttel). With this type of microcrystalline pseudoboehmite spheres of  $\gamma$ -alumina can be manufactured. PURAL can also be extruded to pellets with binders and then subjected to calcination to prepare  $\gamma$ -alumina. The extrudation of various aluminum hydroxides and oxide hydroxides with binders to pellets is covered in Ref. [44]. The properties of the different aluminum hydroxide and oxide hydroxide precursors for the preparation of active aluminas are summarized in Table 2.

The structure of  $\gamma$ -alumina resembles that of the spinel-type MgAl<sub>2</sub>O<sub>4</sub>;  $\eta$ -alumina has a very similar structure. The difference lies in the concentration of stacking faults which is caused by the difference in the structures of the precursors boehmite and bayerite [45]. The concentration of stacking faults is higher in the  $\eta$ -alumina.



$\gamma$ -Alumina exhibits Brønsted acidity, Lewis acidity, and Lewis basicity [46]. Towards electrolytes it acts as a cation and anion exchanger, depending on the pH [47].  $\gamma$ -alumina develops mesoporosity with specific surface areas between 50 and 300 m<sup>2</sup> g<sup>-1</sup> and specific pore volumes up to 0.6 cm<sup>3</sup> g<sup>-1</sup>. Following special procedures, highly porous  $\gamma$ -alumina can be prepared with a specific pore volume up to 0.9 cm<sup>3</sup> g<sup>-1</sup> (Kali Chemie, Hannover, FRG).  $\alpha$ -Alumina (corundum) is nonporous and has a low specific surface area. It is also marketed as a ceramic support with a specific surface area of around 3–5 m<sup>2</sup> g<sup>-1</sup>, a porosity of 50%, and a pellet size of 2–4 mm (Rosenthal Technik AG, Selb, FRG).

Aluminas are used in various catalytic applications.  $\alpha$ -,  $\gamma$ -, and  $\eta$ -aluminas are all used as support materials, the first one in applications where low surface areas are desired, as in partial oxidation reactions. The latter two, and especially  $\gamma$ -alumina, in applications where high surface areas and high thermal and mechanical stability are required. One of the most prominent applications of  $\gamma$ -alumina as support is the catalytic converter for pollution control, where an alumina washcoat covers a monolithic support. The washcoat is impregnated with the catalytically active noble metals. Another major application area of high-surface aluminas as support is in the petrochemical industry in hydrotreating plants. Alumina-supported catalysts with Co, Ni, and/or Mo are used for this purpose. Also, all noble metals are available as supported catalysts based on aluminas. Such catalysts are used for hydrogenation reactions or sometimes oxidation reactions. If high mechanical stability and low surface area of the catalyst support is desired,  $\alpha$ -alumina instead of  $\gamma$ -alumina might be used. This is the case, for instance, for ammonia catalysts which often contain alumina as support material.

$\gamma$ -Alumina is not only used as a support material but also as a catalyst in its native form, for instance in alcohol dehydration reaction, due to the acidic nature of its surface and, most prominently, as the catalyst in the Claus process. Due to the severe conditions of the Claus process, high-stability aluminas have to be employed here.

#### 3.4.4.3 Ni/Al<sub>2</sub>O<sub>3</sub> Catalysts by Coprecipitation

Alumina-supported nickel catalysts are an excellent example for the advantages of and the problems associated with coprecipitation processes for the manufacture of catalysts. Such catalysts are accessible via several pathways, as impregnation, deposition/precipitation, coprecipitation from alumina gels, and more conventional coprecipitation routes. Also, for coprecipitation, different routes are possible, the first examples originating from the 1920s [48]. Starting from the nitrate solutions of nickel and aluminum, there are at least three different routes:

- (i) The most frequently applied route is the precipitation of a hydrotalcite (HTC)-like compound with the general formula  $[M_{1-x}^{II}M_x^{III}(\text{OH})]^{x+}(\text{A}^{n-})_{x/n} \cdot n\text{H}_2\text{O}$  where  $M^{II} = \text{Mg, Ni, Zn, } \dots$ ,  $M^{III} = \text{Al, Fe, Cr, } \dots$ , and  $\text{A}^{n-} = \text{CO}_3^{2-}, \text{SO}_4^{2-}, \text{NO}_3^- \dots$ , using Na<sub>2</sub>CO<sub>3</sub> as the precipitating agent.

The composition of the nickel–alumina hydroxycarbonate (NiAlCO<sub>3</sub>–HTlc)

may thus vary, but an idealized composition is that of the mineral takovite  $\text{Ni}_6\text{Al}_2(\text{OH})_{16}\text{CO}_3 \cdot 4\text{H}_2\text{O}$ . Hydrotalcites as catalytic precursors, amongst them  $\text{NiAlCO}_3\text{--HTlc}$ , are discussed in an excellent recent review [49].

- (ii) Nickel aluminum coprecipitates can be prepared in the complete absence of carbonate ions, for instance by precipitation with  $\text{NaOH}$  in carbonate-free solutions [50]. In this case no mixture of hydroxides is obtained, but nitrates are incorporated and a mixed hydroxynitrate precipitates.
- (iii) The same holds for ammonia solutions, from which the precipitation can be carried out by evaporating the ammonia. If the ammonia is removed without excluding the carbonates, the normal hydroxycarbonate forms. If carbonate is excluded, the hydroxynitrate precipitates [50].

An alternative approach is precipitation by combining an alkaline  $\text{NaAlO}_2$  solution with an acidic nickel nitrate solution [51]. In this case as well, hydrotalcite-like species are probably formed first although, due to the very high nickel contents reported, some nickel hydroxide forms as well. Pure hydrotalcite-like structure are reported to form for  $\text{Ni}:\text{Al}$  atomic ratios between 2 and 3 [52] or 4 [53]; outside this range the hydroxides of the excess species form as additional phases. Rapid precipitation tends to form pure  $\text{Al}(\text{OH})_3$  due to the lower solubility. Aging can lead to recrystallization of some of the pure hydroxides to the hydrotalcite structure as well.

The formation of the hydrotalcite highlights one of the key advantages of coprecipitation techniques. It can provide intimate mixing of the catalyst constituents on an atomic scale at very high loadings. This intimate mixing leads to a very different behavior on calcination and reduction as compared to impregnated catalysts [54]. Whereas impregnated or mechanically mixed catalysts form surface-mixed oxides of the spinel structure at best, which segregate again on reduction to result in the formation of a separate nickel phase on a  $\gamma$ -alumina support, the coprecipitation technique leads to formation of a high surface-area mixed-oxide with varying composition between  $\text{NiO}$  and the spinel-type  $\text{NiAl}_2\text{O}_4$ , depending on the composition of the precursor. On reduction of this oxide, nickel crystallites are formed which exhibit a high degree of "paracrystallinity", i.e. highly defective nickel crystallites with aluminate groups as the defects [55]. The impregnated catalysts are easier to reduce than the coprecipitated materials, as could be expected from the structure of the precursors [56].

The thermal treatment is one of the factors which controls the properties of the final catalyst [56]. The total surface area (in the range between 100 and  $300\text{ m}^2\text{ g}^{-1}$ ) decreases with increasing reduction temperature; however, the nickel surface area (typically  $20\text{--}50\text{ m}^2\text{ g}^{-1}$ ) increases which is probably due to a higher degree of reduction. The best precursor with respect to a high surface area is the hydroxycarbonate. The surface areas of catalysts prepared from hydroxychlorides and nitrates are smaller by about a factor of two. Nickel particle sizes are in the order of 5 nm for such catalysts.

$\text{Ni}/\text{Al}_2\text{O}_3$  catalysts prepared by coprecipitation exhibit excellent sintering stability and can be used in many catalytic reactions. The most important ones are certainly steam reforming and methanation reactions.

The preparation of mixed oxide catalysts from hydroxycarbonates is not restricted

to Ni/Al<sub>2</sub>O<sub>3</sub>, but also possible for several other systems. One example is the technically very important methanol catalyst based on CuO/ZnO. It can be prepared from a hydrotalcite-like precursor as well [57], but mostly a hydrozincite or aurichalcite precursor is used [58]. On reduction of aurichalcite precursors, epitaxial relationships between the copper and the ZnO were observed. Such preferential formation of certain orientations is also the decisive factor in the last example discussed here.

#### 3.4.4.4 V/P/O Catalysts for Butane Oxidation to Maleic Anhydride

The V/P/O ((VO)<sub>2</sub>P<sub>2</sub>O<sub>7</sub>) catalyst is a very specialized material which has a unique activity for the oxidation of *n*-butane to maleic anhydride. Its activity is related to the presence of (100) planes in the catalyst, in which the arrangement of surface atoms ideally matches the geometry of the reacting molecules [59]. Since the cited reviews exist and a very recent review has been given by Cavani and Trifirò [60], only the important findings concerning the preparation of the precursor are reported here, since this example highlights the problems involved in creating high fractions of certain crystallographic faces. In the case of the V/P/O catalyst there exists a pseudomorphic relationship between the precursor (VO)HPO<sub>4</sub> · 0.5 H<sub>2</sub>O and the final catalyst. The equilibrium shape of (VO)<sub>2</sub>P<sub>2</sub>O<sub>7</sub> exhibits only about 32% of the optimum (100) faces. The hemihydrate precursor now is special in that it can be precipitated in a morphology that leads to formation of a much higher (100) fraction, since the (001) of the precursor is structurally related to the (100) of the pyrophosphate.

There are several pathways described for the preparation of the precursor [60]. Usually, V<sub>2</sub>O<sub>5</sub> is reductively dissolved in water or an organic solvent such as alcohols to yield V<sup>IV</sup> species. To this solution phosphoric acid is added and the solid precursor precipitates. Precipitation is often carried out under reflux. There is general agreement that preferentially (001) planes should be exposed in the precursor and that a precursor with a high concentration of stacking faults is superior to more ordered materials. This can best be achieved by precipitation in organic solvents as can be seen by comparison of the X-ray patterns of samples produced either from organic or aqueous media [61].

In a recent study on the precipitation conditions for the hemihydrate [62] the influence of several parameters on the morphology of the precipitate formed was studied. The surface area of the precursors formed was mainly related to the thickness of the crystals. The thicker the crystals (meaning exposure of undesired faces) the lower the surface area. High surface areas could be achieved with a high-boiling alcohol. The conditions favoring the formation of thin, high surface area (VO)HPO<sub>4</sub> · 0.5 H<sub>2</sub>O platelets (H<sub>3</sub>PO<sub>4</sub> 85%, P:V = 1.1–1.2, isobutanol/benzylalcohol, addition of tetraethylorthosilicate) are identical to conditions defined earlier for obtaining the best performing catalyst [63]. The example of the V/P/O catalyst convincingly shows how control of the precipitation conditions, based on a knowledge of the catalytic process, can eventually result in the formation of a highly active catalyst.

## References

1. C. L. Thomas, *Catalytic Processes and Proven Catalysts*, Academic Press, New York, **1970**, Chapters 11 and 14; A. B. Stiles, *Catalyst Manufacture – Laboratory and Commercial Preparations*, Marcel Dekker, New York, **1983**.
2. Recommendations on Nomenclature for Contamination Phenomena in Precipitation from Aqueous Solution, *Pure Appl. Chem.* **1975**, 37, 463–468.
3. V. K. LaMer, R. H. Dinegar, *J. Am. Chem. Soc.* **1950**, 72, 4847.
4. For instance: E. Matijevic, *Acc. Chem. Res.* **1981**, 14, 22.
5. C. J. J. den Ouden, R. W. Thompson, *J. Colloid Interface Sci.* **1991**, 143, 77.
6. A. D. Randolph, M. A. Larson, *AIChE J.* **1962**, 8, 639; the concepts are described in more detail in: A. D. Randolph, M. A. Larson, *Theory of Particulate Processes*, 2nd ed., Academic Press, San Diego, **1988**.
7. For instance: L. K. Hudson, C. Misra, K. Wefers, *Ullmann's Encycl. Ind. Chem.* 5th ed. **1985** Vol. A1, p. 575.
8. G. H. Bogusch, C. F. Zukoski IV, *J. Colloid Interface Sci.* **1991**, 142, 19.
9. F. Cavani, F. Trifirò, A. Vaccari, *Catal. Today* **1991**, 11, 173.
10. S. P. S. Andrew in *Preparation of Catalysts I* (Eds: B. Delmon, P. A. Jacobs, G. Poncelet), Elsevier, Amsterdam, **1976**, p. 429.
11. P. Peshev, A. Toshev, G. Gyurov, *Mater. Res. Bull.* **1989**, 24, 33.
12. For instance: G. Pass, A. B. Littlewood, R. L. Burwell Jr., *J. Amer. Chem. Soc.* **1960**, 82, 6281; M. P. McDaniel, R. L. Burwell Jr., *J. Catal.* **1975**, 36, 384; C. Sivaraj, P. Kantaro, *Appl. Catal.* **1988**, 45, 103; C. Sivaraj, B. R. Reddy, B. R. Rao, P. K. Rao, *App. Catal.* **1986**, 24, 25.
13. K. Tanabe, M. Itoh, K. Morishige, H. Hattori in *Preparation of Catalysts I* (Eds: B. Delmon, P. A. Jacobs, G. Poncelet), Elsevier, Amsterdam, **1976**, p. 65.
14. P. Courty, C. Marcilly, *Stud. Surf. Sci. Catal.* **1983**, 16, 485.
15. E. Matijevic, *Pure Appl. Chem.* **1978**, 50, 1193; identical to: E. Matijevic, *Stud. Surf. Sci. Catal.* **1979**, 3, 555.
16. A. Dalas, C. Kordulis, P. G. Koutsoukos, A. Lycourghiotis, *J. Chem. Soc., Faraday Trans.* **1993**, 89, 3645.
17. J. M. Campelo, A. Garcia, D. Luna, J. M. Marina, *J. Catal.* **1988**, 111, 106.
18. P. Porta, S. de Rossi, G. Ferraris, M. Lo Jacono, G. Minelli, G. Moretti, *J. Catal.* **1988**, 109, 367; G. C. Shen, S. I. Fujita, N. Takezawa, *J. Catal.* **1992**, 138, 754.
19. T. T. P. Cheung, K. W. Wilcox, M. P. McDaniel, M. M. Johnson, *J. Catal.* **1986**, 102, 10.
20. M. J. Desmond, M. A. Pepera, US Patent 4686203, **1987** (Standard Oil Company)
21. T. Kawaguchi, K. Kouhei, *J. Non-Cryst. Solids* **1990**, 121, 383.
22. M. Matura, T. Fujita, Jpn Patent 62257906 A2 871110 Showa (CA 108:76086); M. Kioka, N. Norio, EU Patent 279586 A2 880824 (CA 110:8810); K. Yamaguchi, N. Kanoh, T. Tanaka, E. Toru, N. Enokido, A. Murakami, S. Yoshida, Ger Patent 2515211 751016 (CA 84:74876).
23. A. E. Hamielec, H. Tobita, *Ullmann's Encycl. Ind. Chem.* 5th ed. **1992** Vol. A21, p. 305.
24. D. Damyanov, I. Ivanov, L. Vlaev, *Zh. Prikl. Khim.* **1989**, 62, 486.
25. F. Traina, N. Pernicone, *Chim. Ind. (Milan)* **1970**, 52, 1.
26. A. S. Ivanova, E. M. Moroz, G. S. Litvak, *Kinet. Katal.* **1992**, 33, 1208.
27. A. Vian, J. Tijero, E. Guardiola, *Actas Simp. Iberoam. Catal.*, 9th. Volume 2, Soc. Iberoam. Catal, Lisbon, **1984**, p. 1601.
28. F. Trifirò, H. Hoser, R. D. Scarle, *J. Catal.* **1972**, 25, 12; F. Trifirò, P. Forzatti, P. L. Villa in *Preparation of Catalysts I* (Eds: B. Delmon, P. A. Jacobs, G. Poncelet), Elsevier, Amsterdam, **1976**, p. 147.
29. Y. Nitta, T. Imanaka, S. Teranishi, *J. Catal.* **1985**, 96, 429 and references therein.
30. R. A. Diffenbach, D. J. Fauth, *J. Catal.* **1986**, 100, 466.
31. D. Basmađijan, G. N. Fulford, B. I. Parsons, D. S. Montgomery, *J. Catal.* **1962**, 1, 547.
32. C. T. Kresge, M. E. Leonowicz, W. J. Roth, J. C. Vartuli, J. S. Beck, *Nature* **1992**, 359, 710.
33. A. Monnier, F. Schüth, Q. Huo, D. Kumar, D. Margolese, R. S. Maxwell, G. D. Stucky, M. Krishnamurty, P. Petroff, A. Firouzi, M. Janicke, B. Chmelka, *Science* **1993**, 261, 1299.

34. O. Franke, G. Schulz Ekloff, J. Rathousky, J. Starek, A. Zukal, *J. Chem. Soc., Chem. Commun.* **1993**, 724; P. J. Branton, P. G. Hall, K. S. W. Sing, *J. Chem. Soc., Chem. Commun.* **1993**, 1257; P. L. Llewellyn, H. Reichert, Y. Grillet, F. Schüth, K. K. Unger, *Micropor. Mater.* **1994**, 3, 345; P. J. Branton, P. G. Hall, K. S. W. Sing, H. Reichert, F. Schüth, K. Unger, *J. Chem. Soc., Faraday Trans.* **1994**, 90, 2965.
35. Q. Huo, D. Margolese, U. Ciesla, P. Feng, T. Gier, P. Sieger, R. Leon, P. M. Petroff, U. Ciesla, F. Schüth, G. Stucky, *Nature* **1994**, 368, 317; U. Ciesla, D. Demuth, R. Leon, P. Petroff, G. Stucky, K. Unger, F. Schüth, *J. Chem. Soc., Chem. Commun.* **1994**, 1387.
36. U. Ciesla, T. Suharto, W. Jacobs, F. Schüth, *unpublished results*.
37. R. K. Iler, *The Chemistry of Silica and Silicates*, Wiley, New York, **1979**; D. Barby in *Characterization of Powder Surfaces* (Eds: G. D. Parfitt, K. S. W. Sing), Academic Press, London, **1976**, p. 353; K. K. Unger, *Porous Silica*, J. Chromatogr. Libr. Vol. 16, Elsevier, Amsterdam, **1979**; H. Ferch, A. Kreher, *Chemische Technologie (Winnacker-Küchler)* 4. Aufl. **1983** Bd. 3, Anorgan. Technologie 2, p. 75.
38. J. F. Brinker, G. W. Scherer, *Sol-Gel Science: The Physics and Chemistry of Sol-Gel Processing*, Academic Press, Boston, **1990**.
39. C. W. Higginson, *Chem. Eng.* **1974**, 98.
40. G. Engelhardt, D. Michel, *High Resolution Solid State NMR of Silicates and Zeolites*, Wiley, Chichester, **1987**.
41. B. A. Morrow, *Stud. Surf. Sci. Catal.* **1990**, 57A, 161.
42. K. Wefers, G. M. Bell, *Oxides and Hydroxides of Aluminum*, Alcoa Research Laboratories, Technical Paper No 19, **1972**; K. Bielefeldt, G. Winkhaus, *Chemische Technologie (Winnacker-Küchler)* 4. Aufl. **1983** Bd. 3 Anorgan. Technologie 2, p. 2; L. K. Hudson, C. Misra, K. Wefers, *Ullmann's Encycl. Ind. Chem.* 5th ed. **1985** Vol. A2, p. 575.
43. U. Bollmann, *Habilitationsschrift*, Bergakademie Freiberg, FRG, **1992**.
44. A. Danner, K. K. Unger, *Stud. Surf. Sci. Catal.* **1987**, 31, 343; W. Stoepler, K. K. Unger, *Stud. Surf. Sci. Catal.* **1983**, 16, 643.
45. B. C. Lippens, J. H. de Boer, *Acta Crystallogr.* **1964**, 17, 1312; H. Sallfeld, B. B. Mehrotra, *Naturwissenschaften* **1966**, 53, 128.
46. H. Knözinger, P. Ratnasamy, *Catal. Rev.-Sci. Eng.* **1978**, 17, 31.
47. C. Laurent, H. A. H. Billet, L. de Galaan, *Chromatographia* **1983**, 17, 253.
48. N. Zelinsky, W. Kommarowsky, *Chem. Ber.* **1924**, 57, 667.
49. F. Cavani, F. Trifirò, A. Vaccari, *Catal. Today* **1991**, 11, 173.
50. E. C. Kruissink, L. L. van Reijen, J. R. H. Ross, *J. Chem. Soc., Faraday Trans. I* **1981**, 77, 649.
51. J. Zielinski, *Appl. Catal.* **1993**, A94, 107; J. Zielinski, *J. Mol. Catal.* **1993**, 83, 197; R. Lamber, G. Schulz-Ekloff, *J. Catal.* **1994**, 146, 601.
52. E. C. Kruissink, L. E. Alzamora, S. Orr, E. B. M. Doesburg, L. L. van Reijven, J. R. H. Ross, G. van Veen, *Stud. Surf. Sci. Catal.* **1979**, 3, 143.
53. J. Rathousky, G. Schulz-Ekloff, J. Starek, A. Zukal, *Chem. Eng. Technol.* **1994**, 17, 41.
54. D. C. Puxley, I. J. Kitchener, C. Komodromos, N. D. Parkyns, *Stud. Surf. Sci. Catal.* **1983**, 16, 237.
55. C. J. Wright, C. G. Windsor, D. C. Puxley, *J. Catal.* **1982**, 78, 257.
56. L. E. Alzamora, J. R. H. Ross, E. C. Kruissink, L. L. van Reijen, *J. Chem. Soc., Faraday Trans. I*, **1981**, 77, 665.
57. J. G. Nunan, P. B. Himmelfarb, R. G. Herman, K. Klier, C. E. Bogdan, G. W. Simmons, *Inorg. Chem.* **1989**, 28, 3868.
58. P. Porta, S. De Rossi, G. Ferraris, M. Lo Jacono, G. Minelli, G. Moretti, *J. Catal.* **1988**, 109, 367.
59. J. C. Burnett, R. A. Keppel, W. D. Robinson, *Catal. Today* **1987**, 1, 537; R. M. Contractor, A. W. Sleight, *Catal. Today* **1987**, 1, 587; G. Centi, *Catal. Today* **1993**, 16, 5; G. Centi, *NATO ASI Ser. Ser. C* **1993**, 398, 93.
60. F. Cavani, F. Trifirò, *Stud. Surf. Sci. Catal.* **1995**, 91, 1.
61. L. M. Cornaglia, C. A. Sanchez, E. A. Lombardo, *Appl. Catal. A* **1993**, 95, 117.
62. E. Kesteman, M. Merzouki, B. Taouk, E. Bordes, R. Contractor, *Stud. Surf. Sci. Catal.* **1995**, 91, 707.
63. H. S. Horowitz, C. M. Blackstone, A. W. Sleight, G. Teufer, *Appl. Catal.* **1988**, 38, 193.

## 3.5 Sol–Gel Process

E. I. Ko

### 3.5.1 Introduction

The sol–gel process involves first the formation of a sol followed by that of a gel. A sol, which is a liquid suspension of solid particles ranging in size from 1 nm to 1 micron, can be obtained by the hydrolysis and partial condensation of a precursor such as an inorganic salt or a metal alkoxide. The further condensation of sol particles into a three-dimensional network produces a gel, which is a diphasic material with a solid encapsulating a solvent. Alternatively, a gel can be produced by destabilizing a solution of preformed sols. In either case the materials are referred to aquasol (or aquagel) when water is used as a solvent, and alcosol (or alcogel) when alcohol is used. The encapsulated liquid can be removed from a gel by either evaporative drying or drying with supercritical extraction (supercritical drying for short). The resulting solid products are known as a xerogel and an aerogel, respectively.

The single most important characteristic of the sol–gel preparation of catalytic materials is its *ease of control* that translates into the following advantages:

- (i) the ability to maintain high purity (because of purity of starting materials);
- (ii) the ability to change physical characteristics such as pore size distribution and pore volume;
- (iii) the ability to vary compositional homogeneity at a molecular level;
- (iv) the ability to prepare samples at low temperatures;
- (v) the ability to introduce several components in a single step;
- (vi) the ability to produce samples in different physical forms.

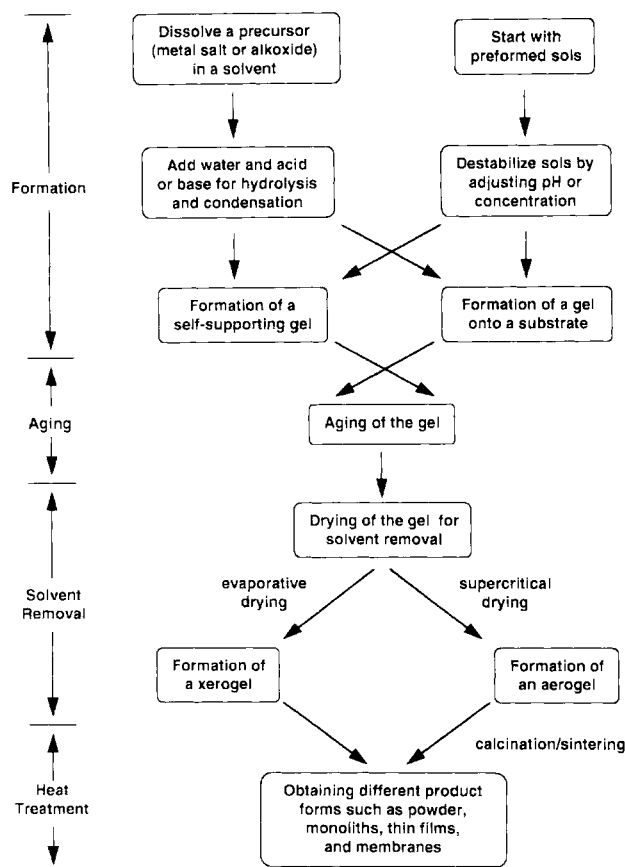
The purpose of this article is to teach catalytic researchers how to realize some of these advantages in their work. To this end we start by identifying the various steps in a sol–gel process and the key parameters in each step that have been shown to impact on the physical and/or chemical properties of the products. We then give selected examples of recent literature results.

### 3.5.2 Important Parameters in Sol–Gel Preparation

Figure 1 shows the four key steps in taking a precursor to a particular product form via sol–gel preparation: formation of a gel, aging of a gel, removal of solvent, and heat treatment. The versatility of this preparative approach lies in the number of parameters that can be manipulated in each of these steps.

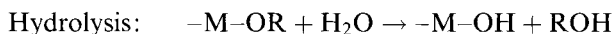
#### 3.5.2.1 Solution Chemistry

The precursor in a sol–gel preparation can either be a metal salt/alkoxide dissolved in an appropriate solvent or a stable colloidal suspension of preformed sols. Metal



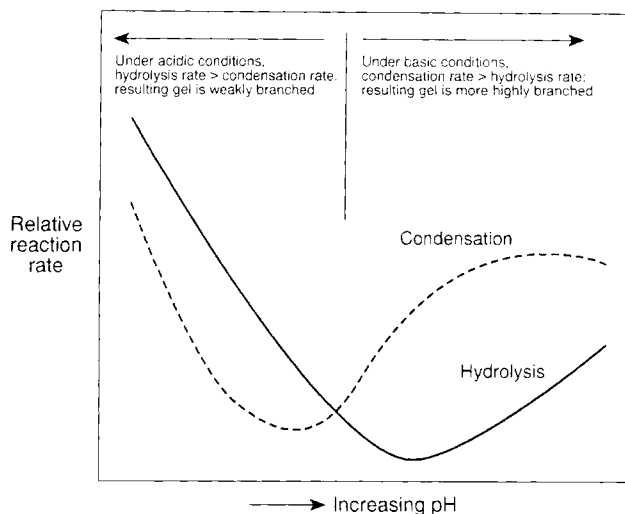
**Figure 1.** Schematic diagram showing the various steps of a sol-gel process.

alkoxides have been the most extensively used because they are commercially available in high purity and their solution chemistry has been documented [1–3]. At its simplest level, sol-gel chemistry with metal alkoxides can be described in terms of two classes of reactions:



where X can either be H or R (an alkyl group).

Such a description oversimplifies the overall process because it does not correctly represent the molecular formulas of the intermediates and end products, nor does it depict the simultaneous occurrence of the two reactions. However, this oversimplification captures the key phenomenological idea that a three-dimensional gel network comes from the condensation of partially hydrolyzed species. Any parameters that affect either or both of these reactions are thus likely to impact on the properties of the product. In fact, Livage et al. [4] pointed out that the important variables are the *relative* rates of hydrolysis and condensation.



**Figure 2.** Schematic diagram showing the variation of hydrolysis and condensation rates of tetraethylorthosilicate with pH, and the effect of relative rate on gel structure.

Figure 2 shows the rates of hydrolysis and condensation of tetraethylorthosilicate (TEOS), which is the most widely studied precursor, vary as a function of pH [5]. Under acidic conditions hydrolysis occurs at a faster rate than condensation and the resulting gel is weakly branched. Under basic conditions the reverse is true and the resulting gel is highly branched and contains colloidal aggregates. Subsequently dried and heat-treated samples have different surface functionalities [6] and pore structures [7].

Because hydrolysis and condensation are both nucleophilic displacement reactions, the reactivity of metal alkoxides is dependent on the positive partial charge of the metal atom and its coordination number [8]. For example, TEOS, with a small positive partial charge on silicon, is the least reactive among the common alkoxides [4]. In general, the longer and bulkier the alkoxide group attached to a particular metal atom, the less reactive that precursor is in hydrolysis and condensation [9]. Changing the type of precursor and/or its concentration are thus effective means of controlling the reaction rates.

The amount of water used in sol–gel preparation and the rate by which it is added also influence gel characteristics. The former is usually expressed in terms of the hydrolysis ratio  $h$ , defined as the moles of water per mole of metal alkoxide,  $M(OR)_m$ . There are three specific regions of interest [4]:

- (i)  $h < 1$ : An infinite network seldom forms due to the low functionality of the precursor towards condensation. Because there are few M–OH groups for cross-linking, gelation or precipitation cannot occur when there is no local excess of water.
- (ii)  $1 < h < m$ : Polymeric gels can form.
- (iii)  $h > m$ : Cross-linked polymers, particulate gels, or precipitates can form when an excess of water is added to the alkoxides.



For a given amount of water, another level of control comes from the rate of addition. Common approaches in adding water slowly are using a micropipette, absorbing moisture from a controlled humidity environment, and generating water in the solution with another chemical reaction.

Two other important sol–gel parameters are temperature and solvent. Both hot and cold plates are commercially available and can be used to increase and decrease the reaction rates, respectively. Varying the temperature is most effective when it can alter the *relative* rates of competing reactions. Solvent can change the nature of an alkoxide through solvent exchange or affect the condensation reaction directly. It is also possible to prepare a gel without a solvent as long as another means, such as ultrasound irradiation [10], is used to homogenize an otherwise immiscible alkoxide/water mixture.

Using preformed sols instead of metal alkoxides as precursors is an attractive alternative in sol–gel preparation because recent advances in inorganic colloidal dispersions allow some control over the characteristics of the starting sols [11]. Often a colloidal suspension of sol particles is stabilized (i.e. prevented from flocculation) by pH adjustment. Thus, pH of the solution, which can be changed by the addition of either acid or base, is the single most important parameter in obtaining a gel from preformed sols. Other parameters that can impact on gel quality are the size and concentration of the starting sol particles.

For any of the sol–gel parameters discussed so far, its effect on gel properties can often be followed by an experimental observable known as *gel time*. Gel time is defined as the time it takes for a solution to undergo a rapid rise in viscosity that corresponds to the transition from a viscous fluid to an elastic gel [9]. At the *gel point* there is a continuous solid phase containing a structure that reflects the formation and branching of particles under specific growth conditions. This particular phase is important because it is the genesis of structural evolution that takes place in all subsequent processing steps [9, 12].

### 3.5.2.2 Aging

Aging represents the time between the formation of a gel and the removal of solvent. As long as the pore liquid remains in the matrix, a gel is not static and can undergo many transformations [9, 12]. For alkoxide-derived gels, condensation between surface functional groups continue to occur after the gel point. This process can actually be desirable because it leads to a more cross-linked network that is mechanically stronger and easier to handle. However, extensive condensation causes the gel to shrink to the point that solvent is actually expelled, in a phenomenon called *syneresis*. Coarsening, or ripening, is a physical process driven by differences in solubility associated with surfaces that have different radii of curvature. Coarsening basically involves the dissolution and reprecipitation of particles, resulting in an increase in the average pore size of the gel and a decrease in its specific surface area.

Parameters that affect these aging processes include temperature, time, and pH of the pore liquid. Common approaches in manipulating these parameters are im-

mersing the gel in or washing it with another liquid, exposing the gel to a different humidity, heating the gel, and using hydrothermal conditions. Even though all these approaches have been demonstrated to change the gel characteristics, an understanding of the cause and effect is at best qualitative at present. For this reason aging is often an overlooked step in the sol-gel preparation of catalytic materials. The recent work of Smith et al. [13], who developed an in situ NMR technique for following the aging process, may open up new opportunities in this area.

### 3.5.2.3 Drying

As the pore liquid is evaporated from a gel network, the capillary pressure associated with the liquid-vapor interface within a pore can become very large for small pores. For example, the capillary pressure with water evaporating from a pore with a radius of 1 nm is on the order of  $1.5 \times 10^8$  pa. With a distribution of pore sizes in a gel, as is commonly the case, the differential pressure across pores of different sizes leads to a collapse in the pore structure. Thus, strategies that are effective in maintaining the integrity of a gel network aim at minimizing either the differential pressure or the capillary pressure itself.

One approach to minimize capillary pressure is to prepare gels containing uniform-sized pores or at least a narrow pore size distribution. This can be done by adding organics such as formamide and glycerol, which are called drying control chemical additives (DCCA), to control the rates of hydrolysis and condensation and in turn the pore size distribution. There are many examples showing that glasses and ceramics prepared with DCCA can better withstand drying due to a more uniform pressure distribution across the gel network [14]. The use of DCCA in preparing catalytic materials has not been common, partly because there are alternatives that do not introduce potential impurities into the system.

The easiest way to understand approaches that are effective in minimizing the capillary pressure directly is to examine the equation

$$P = 2\sigma \cos(\alpha)/r$$

where  $P$  is capillary pressure,  $\sigma$  is surface tension,  $\alpha$  is the contact angle between liquid and solid, and  $r$  is the pore radius. For a given pore size, then, the capillary pressure can be reduced by (i) using a solvent with a lower surface tension or with a contact angle close to  $90^\circ$  and (ii) eliminating the liquid-vapor interface altogether with either supercritical or freeze drying.

Smith and co-workers have aged silica gels in either ethanol or water and subsequently washed them in various aprotic solvents that cover a range of surface tensions [15, 16]. Their results clearly demonstrated the effect of surface tension on microstructure because the resulting xerogels have a wide range of surface area and pore volume. Furthermore, the effect is dependent on the initial network rigidity as acid-catalyzed and base-catalyzed gels respond to the treatment differently. The fact that some of these xerogels have comparable physical properties to aerogels obtained by supercritical drying suggests an attractive alternative in preparing high-surface-area, low-density materials at ambient pressure.

*Supercritical drying* is a high-pressure approach aimed at eliminating the liquid–vapor interface and the accompanying capillary pressure. Since the pioneering work of Kistler [17], the technology of supercritical drying has evolved from a tedious, multistep process to a simpler and safer semicontinuous process [18]. One major advance came from the group of Teichner who used alcoholic solutions of metal alkoxides in preparing gels with a minimal amount of water. In prior preparations that used a large amount of water, tedious washing and solvent exchange steps were necessary because water would dissolve the gel structure at high temperatures [19]. There are now numerous examples showing that aerogels can be prepared to give high porosities, high specific surface areas, low apparent densities, and good textural stability [20]. These advantages can be realized because, in addition to eliminating the liquid–vapor interface, supercritical drying is done at moderate temperatures. In fact, one often overlooked advantage in supercritical drying is its ability to preserve the amorphous structure of an aerogel. For example, it has been reported that a niobia aerogel is slower to crystallize than a xerogel upon further heat treatment and hence better able to retain its high acid strength along with acid site density [21].

Similar to aging, a gel is not static during drying and, for that reason, drying can be viewed as part of the overall aging process. The properties of a product are thus dependent on the drying method and even with a single method, the drying conditions. Most supercritical drying experiments have been done with alcohol because of its use as a solvent in the sol–gel step. But ever since supercritical carbon dioxide was shown to be an effective agent for displacing alcohol [18], many researchers have reported on the effect of drying agent on the properties of aerogels such as silica [14, 15], titania [22], and titania–silica [23]. Because different substances have different critical temperatures, these results can be understood in terms of the accelerated aging of a gel at a higher drying temperature. For example, recently Brodsky and Ko showed that varying the temperature while using a single drying agent, carbon dioxide, can also change the textural and structural properties of calcined titania aerogels [24]. Besides temperature, other parameters that are important in supercritical drying include the path to the critical point, depressurization, and composition of the drying medium [20, 25]. In particular, reduction is prone to occur when an autoclave is filled with hydrogen during drying [20].

One other approach in bypassing a liquid–vapor interface is freeze drying, in which the pore liquid is frozen into a solid that subsequently sublimates to give a product called a cryogel. Data on the characteristics of cryogels are limited because freeze drying has not been used as extensively as supercritical drying in preparing catalytic materials.

#### **3.5.2.4 Calcination/Sintering**

After the removal of pore liquid, further heat treatment is necessary to convert a xerogel or aerogel into a catalytically useful form. Often, heating is done in the presence of a reactive gas (e.g. flowing air, oxygen, or hydrogen) in order to burn off any residual organics or to oxidize (or reduce) the sample. Exposing the sample to a

**Table 1.** Important parameters in the various steps of a sol–gel process.

Step	Purpose	Important parameters
Solution chemistry	to form a gel	type of precursor; type of solvent; pH (acid/base content); water content; precursor concentration; temperature
Aging	to allow a gel to undergo changes in properties	time; temperature; composition of the pore liquid (e.g. pH); aging environment (e.g. humidity)
Drying	to remove solvent from a gel	drying method (e.g. evaporative vs. supercritical vs. freeze drying); temperature and heating rate; pressure and pressurization rate; time
Calcination/sintering	to change the physical/chemical properties of the solid, often resulting in crystallization and densification	temperature and heating rate; time; gaseous environment (e.g. inert vs. reactive gases)

high temperature over an extended period of time leads to sintering and consequently a decrease in surface area. The process can also cause the material to crystallize into different structural forms. Thus, the physical characteristics of a product depend on parameters such as temperature, heating rate, time, and gaseous environment. It is common practice to subject a sample to a more severe heat treatment than it is likely to encounter in a reactor to ensure at least the stability of its textural and structural properties during reaction.

### 3.5.2.5 Summary

Table 1 provides a quick reference to the four key steps in a sol–gel process, the purpose of each step, and the associated experimental parameters that can be varied. Since each of these parameters can potentially affect the properties of a product, literature results on sol–gel preparation should be reported or examined in a similar format to allow a meaningful comparison among different studies. As an example, Table 2 shows the parameters used in the preparation of titania [22] and zirconia [26] aerogels.

### 3.5.3 Advantages of Sol–Gel Preparation

Table 3 is a representative and by no means exhaustive list of reactions that have been catalyzed by sol–gel materials including both xerogels and aerogels. Its pur-

**Table 2.** Examples of sol-gel parameters in the preparation of titania and zirconia aerogels.

Step	Parameter	Final oxide	
		TiO <sub>2</sub> <sup>a</sup>	ZrO <sub>2</sub> <sup>b</sup>
Solution chemistry	precursor	Titanium <i>n</i> -butoxide (Ti(C <sub>4</sub> H <sub>9</sub> O) <sub>4</sub> )	Zirconium <i>n</i> -propoxide (Zr(C <sub>3</sub> H <sub>7</sub> O) <sub>4</sub> )
	solvent	methanol	<i>n</i> -propanol
	nitric acid content	0.125 mol/mol of precursor	0.83 mol/mol of precursor
	water content	4 mol/mol of precursor	2 mol/mol of precursor
	precursor concentration	0.625 mmol/mL of methanol	1.0 mmol/mL of <i>n</i> -propanol
	temperature	room temperature	room temperature
Aging	time	2 h	2 h
	temperature	room temperature	room temperature
	environment	covered beaker	covered beaker
Drying	method	Semicontinuous supercritical	Semicontinuous supercritical
	drying agent	carbon dioxide (CO <sub>2</sub> )	carbon dioxide (CO <sub>2</sub> )
	temperature	343 K	343 K
	pressure	$2.1 \times 10^7$ Pa	$2.1 \times 10^7$ Pa
	time	2 h	2 h
	CO <sub>2</sub> flow rate	85 L h <sup>-1</sup> downstream	85 L h <sup>-1</sup> downstream
Calcination/ sintering	first step	383 K in a vacuum oven for 3 h	383 K in a vacuum oven for 3 h
	second step	523–573 K in a vacuum oven for 3 h	773 K in flowing oxygen for 2 h
	third step	773 K in flowing oxygen (24 L h <sup>-1</sup> ) or 2 h (with a heating rate of 10 K min <sup>-1</sup> from room temperature to 773 K)	

<sup>a</sup> From Ref. 22.<sup>b</sup> From Ref. 26.**Table 3.** Examples of reactions that have been catalyzed by sol-gel materials.

Reaction	Catalyst	Reference
Hydrogenation of phenylacetylene	Pd/SiO <sub>2</sub>	27
Oxidation of CO	Pt/TiO <sub>2</sub>	28
Oxidative dehydrogenation of ethane	Li <sup>+</sup> /MgO promoted by Cl <sup>-</sup>	29
Nitroxidation of alkenes	PbO–ZrO <sub>2</sub> , PbO–Al <sub>2</sub> O <sub>3</sub>	30
Hydrotreating of gas oil	Ni–Mo/TiO <sub>2</sub> –ZrO <sub>2</sub>	31
Selective catalytic reduction of NO by NH <sub>3</sub>	V <sub>2</sub> O <sub>5</sub> , V <sub>2</sub> O <sub>5</sub> –TiO <sub>2</sub> , V <sub>2</sub> O <sub>5</sub> –TiO <sub>2</sub> –SiO <sub>2</sub>	32
Isomerization of 1-butene	Nb <sub>2</sub> O <sub>5</sub> –SiO <sub>2</sub>	33
Fluorination of C <sub>2</sub> Cl <sub>3</sub> F <sub>3</sub> with HF	Cr <sub>2</sub> O <sub>3</sub>	34
Dehydrocyclization of <i>n</i> -heptane	Pt–Sn/Al <sub>2</sub> O <sub>3</sub>	35
Polymerization and co-polymerization of $\alpha$ -alkenes	Transition metal/Al <sub>2</sub> O <sub>3</sub>	36

pose is to demonstrate the potential range of applications and, more importantly, the wide variety of catalytic materials that can be obtained by this preparative approach. Catalysts in this table include supported metals, mixed oxides, promoted oxides, and several three-component systems. This section highlights the advantages sol–gel preparation brings to these different classes of materials.

### 3.5.3.1 Varying the Pore Structure

The classic example of using a sol–gel parameter to vary the pore structure (surface area, pore volume, and pore size distribution) of products is the effect of pH on the properties of silica. As discussed in Section 3.5.2.1 (see also Fig. 2), acid- and base-catalyzed silica gels give rise to products that contain micropores and mesopores, respectively, because of the different extent of branching in the gel. Brinker et al. [37] recently pointed out that other sol–gel parameters, including those in the aging and drying steps, can also significantly change the pore structure of dried gels or films that are made of silicate, multicomponent silicate, and aluminosilicate. In the case of aluminosilicate, changing the alumina content can lead to products having either no porosity, microporosity, or macroporosity. These authors further noted that similar results and concepts should be applicable to nonsilicate systems.

Using preformed sols instead of metal alkoxides as precursors is another effective way to change the pore structure, as recently demonstrated for the sol–gel preparation of zirconia [38]. The two key parameters in this approach are the starting sol size and the intrinsic porosity of the sol particles.

Zou and Gonzalez [39] have varied the pore size distributions of a series of Pt/SiO<sub>2</sub> catalysts by changing the amount of water used in the sol–gel step. The average pore size decreases from 7.5 to 3.5 nm as the hydrolysis ratio, defined as H<sub>2</sub>O:TEOS, increases from 10 to 60. This variation of average pore size is significant because the catalysts are more resistant to sintering in oxygen (up to 948 K for Pt loadings of 0.2–0.3 wt%) when the average pore diameter matches the particle size of Pt.

### 3.5.3.2 Controlling Homogeneity in Mixed Oxides

Mixed oxides, which contain two or more components, are of catalytic interest because they can be used as supports, catalysts, or precursors to other materials. One particularly interesting property that arises by mixing oxides is the generation of strong acidic sites associated with the interface or linkage between the two components [40]. In order to maximize the number of these sites, it is desirable to prepare samples that are homogeneously mixed at a molecular level.

Sol–gel preparation offers excellent control of mixing because of its ability to alter relative precursor reactivity. Qualitatively, we expect good mixing when the two precursors have similar reactivities and poor mixing when they do not. As pointed out in Section 3.5.2.1, both hydrolysis and condensation are nucleophilic

displacement reactions. Effective strategies in matching precursor reactivity thus include:

- (i) using a precursor containing a different alkoxy group;
- (ii) giving a less reactive precursor a head-start by “prereacting” it with water, in a process known as prehydrolysis;
- (iii) slowing down a more reactive precursor by replacing some of its alkoxy groups with different ligands, in an approach known as chemical modification;
- (iv) performing the preparation in a different temperature.

The application of all four strategies to the preparation of zirconia–silica aerogels has recently been reported [41]. On the evidence of 1-butene isomerization activity, Miller et al. concluded that the first three strategies lead to well-mixed samples. Specifically, their results show that in the cogelling of two alkoxides, the reactivities of the two alkoxides must be fairly well matched to achieve homogeneous distribution. If this is not accomplished, then the more reactive component tends to form a “core” onto which the less reactive component attaches. The latter situation is not necessarily bad because the notion of controlling mixing means that one can prepare an inhomogeneous sample if that is what the application calls for. For example, Handy et al. [42] prepared two titania–silica samples as supports for vanadia, one with prehydrolysis to promote mixing and one without prehydrolysis. They found that the former sample is actually less active for the selective catalytic reduction of NO with NH<sub>3</sub>. Apparently the titania crystallites that are present in the less well-mixed sample are necessary to stabilize the active vanadia phase.

The work of Toba et al. [43] is another example showing that better mixing can be accomplished with sol–gel than other preparation methods. These authors prepared alumina–titania samples by complexing-agent-assisted sol–gel (with an ethanol/hexylene glycol solution), coprecipitation, and hydrogel kneading. They concluded that the two oxides are the best mixed (or most homogeneous) in the sol–gel sample because titania resists crystallization the most upon heating and the number of acidic sites, associated with Ti–O–Al bonds, is the highest.

### 3.5.3.3 Changing Dispersion and Stability of Supported Metals

In the sol–gel preparation of supported metals, a metal precursor is usually added directly to the solution prior to gelling. Regardless of whether the metal precursor participates in hydrolysis and/or condensation, it will become part of the network as the gel forms. Thus, any parameters that are important in solution chemistry (Table 1) could affect the properties of the metal upon activation. An example is the work of Zou and Gonzalez [39] cited in Section 3.5. When these authors used water content as a variable to change the pore size distribution of a series of Pt/SiO<sub>2</sub> catalysts, they found that the particle size distribution of reduced Pt (in the form of crystallites) is also dependent on the hydrolysis ratio. The average Pt particle size nearly doubles (from about 1.7 to 3 nm) as the hydrolysis ratio increases from 10 to 60. As noted earlier, the stability of these catalysts, in terms of the resistance of Pt

particles towards sintering, is a function of how well the pore diameter and particle size match.

Lopez et al. [27] prepared Pd/SiO<sub>2</sub> catalysts under both acidic (pH = 3) and basic (pH = 9) conditions in the sol–gel step and reported that an acid medium promotes the formation of small metal crystallites. This finding is consistent with the formation of a microporous silica gel network at a low pH. By comparing samples prepared by the sol–gel method and impregnation, these authors found in the former a stronger metal–support interaction which they ascribed to the square planar palladium complex used as a precursor. Finally, their results showed that the method of preparation as well as the conditions used in each method impact on how these catalysts deactivate in the hydrogenation of phenylacetylene.

In general, the activation and deactivation of metal particles in a sol–gel sample is dependent on how much of the metal is actually occluded (or incorporated) in the support network. In the two examples above, the extent of occlusion is minimal for Pt/SiO<sub>2</sub> and larger for Pd/SiO<sub>2</sub>. A telltale sign of occlusion is when the metal particle sizes determined by chemisorption and transmission electron microscopy (or X-ray diffraction) do not agree and there is no reason to believe that such a difference is caused by electronic effects.

Some occlusion of the metal particles is not necessarily bad. In fact, unlike other methods such as impregnation and ion exchange, sol–gel preparation actually allows a certain amount of control over what fraction of a metal particle is accessible at the support surface. As long as there are exposed metal atoms available for catalysis, a partially buried metal particle may better resist deactivation due to sintering. For example, Lopez et al. [44] found that a Ru/SiO<sub>2</sub> sample prepared by sol–gel is more stable than one prepared by ion exchange. The sol–gel sample, which contains partially occluded Ru particles, does not sinter or volatilize under oxygen treatment at 723 K, whereas the ion-exchange sample does.

#### 3.5.3.4 Preparing Samples in a Single Step

One advantage of preparing supported samples by the sol–gel method is that the supported phase, be it a metal or an oxide, can be introduced *during* instead of *after* the formation of the support. Other than the convenience of saving a step, this feature may introduce unique metal–oxide or oxide–oxide interactions that are inaccessible with other preparation methods. The tradeoff is the activation of the supported phase is likely to be more difficult if it is incorporated within the support structure.

The ability to introduce several components into solution during the sol–gel step makes this approach especially attractive for the preparation of multicomponent oxides and bimetallic catalysts. Of course, the solution chemistry becomes more complex with additional components. But many of the concepts that we have discussed, such as matching relative precursor reactivity and changing the microstructure of the gel network, remain valid in principle. Furthermore, a promoter or an active species can be introduced the same way. There have been recent reports on the one-step preparation of zirconia-sulfate aerogels [45] and Li/MgO catalysts



[46]. These samples are active in the isomerization of *n*-butane and the oxidative coupling of methane, respectively.

Finally, by using preformed sols instead of metal alkoxides as precursors, it is possible to use the sol particles as building blocks and form a gel around them, again in a single step. As discussed in Section 3.5.3.1, this approach offers control over the pore structure and the distribution of active components. For example, the use of a nonporous sol particle effectively prevents incorporation of other species within the particle itself.

### 3.5.4 Catalytic Membranes

Zaspalis and Burggraaf [47] have summarized typical membrane reactor configurations, different membrane/catalyst combinations, and a large number of membrane reactor studies. Their article clearly shows that inorganic membranes prepared by the sol–gel method, with their dual ability in catalysis and separation, have many unique advantages over other product forms. At the same time, it is important to realize that the parameters which affect a membrane's characteristics and the advantages which the sol–gel process offers are similar to what has been presented thus far.

Self-supporting inorganic membranes can be formed with or without a substrate. In either case the precursor sol, consisting of either a colloidal suspension or a polymeric solution, must be formed. To produce a membrane supported on a substrate (i.e. a supported membrane), a preformed porous support is dipped in the precursor sol and a gel forms at the surface of the support typically by the slipcasting method [48]. Another approach is spin coating, in which an excess amount of liquid is deposited onto a substrate and then thinned uniformly by centrifugal force [12]. To produce a non-supported membrane, the liquid is simply poured into a mold of appropriate shape and allowed to dry. All these processes need to be done before the gel point which is accompanied by a large increase in viscosity.

The microstructure of a sol, in terms of the nature and concentration of sol particles, significantly affect a membrane's properties such as average pore diameter and pore size distribution. Other critical parameters are the temperature and rate of evaporation used in the drying and calcination steps. Even though it is economical to obtain the final product form quickly, too rapid a drying rate forms cracks in the membrane. Crack formation is also dependent on thickness of the membrane. The work of Cini et al. [49], who prepared supported microporous  $\gamma$ -Al<sub>2</sub>O<sub>3</sub> membranes as catalyst supports, illustrates many of these effects.

As with other product forms, sol–gel preparation offers excellent control of the chemical composition of catalytic membranes. Again, a second or even a third component can be introduced directly in the solution. Such an approach was used by Xu and Anderson [50], who mixed titanium and zirconium precursors in order to improve the thermal stability of microporous titania and zirconia membranes. Alternatively a second component can be introduced to a preformed membrane. By using the so-called reservoir method, Zaspalis et al. [51] filled the pores of a  $\gamma$ -Al<sub>2</sub>O<sub>3</sub> membrane with a solution of silver nitrate, thereby achieving a high loading of silver

in the top layer of the membrane. These and numerous other examples have demonstrated the feasibility of preparing multicomponent membranes. However, many of the strategies mentioned in Section 3.5.3 (e.g. controlling homogeneity) have yet to be fully explored. Thus, tremendous opportunities exist for researches to exploit the sol–gel process to fine-tune the physical and chemical properties of inorganic membranes.

### 3.5.5 Other Sol–Gel Materials

Due to space limitation, this article has focused primarily on inorganic materials because of their important catalytic applications. But it must be pointed out that some exciting and rapidly developing areas of sol–gel chemistry involve inorganic–organic hybrids [52], gel–entrapped enzymes and proteins [53], and organic gels [54]. The basic principles covered above should enable the readers to learn about these variations of the sol–gel technique and, in turn, to explore the potential applications of a still wider range of materials.

### 3.5.6 Summary

With its versatility and excellent control over a product's characteristics, sol–gel processing has played an important role in catalyst preparation and no doubt will continue to do so. Advances in this area are likely to come from two related fronts. First, it is important to have a better understanding of the chemistry underlying all the processing steps, from gelation to aging to drying. Second, this understanding should be made as quantitative as possible to allow the development of predictive models. As many researchers are actively working towards these goals, it is almost certain that in the next few years we will see many new syntheses, exciting properties, and creative applications of catalytic materials prepared by the sol–gel method and, along with these findings, a better understanding of catalysis itself.

## References

1. D. C. Bradley, R. C. Mehrota, P. D. Gaur, *Metal Alkoxides*, Academic, New York, **1978**.
2. D. C. Bradley, *Chem. Rev.* **1989**, 89, 1317–1322.
3. R. C. Mehrota, *J. Non-Cryst. Solids* **1992**, 145, 1–10.
4. J. Livage, M. Henry, C. Sanchez, *Prog. Solid St. Chem.* **1988**, 18, 259–341.
5. H. D. Gesser, P. C. Goswami, *Chem. Rev.* **1989**, 89, 765–788.
6. J. Y. Ying, J. B. Benziger, *J. Am. Ceram. Soc.* **1993**, 76, 2571–2582.
7. B. Handy, K. L. Walther, A. Wokaun, A. Baiker in *Preparation of Catalysts V* (Eds: P. A. Jacobs, P. Grange, B. Delmon), Elsevier, Netherlands, **1991**, pp. 239–246.
8. J. Livage, C. Sanchez, *J. Non-Cryst. Solids* **1992**, 145, 11–19.
9. L. L. Hench, J. K. West, *Chem. Rev.* **1990**, 90, 33–72.
10. J. Zarzycki in *Ultrastructure Processing of Advanced Materials* (Eds: D. R. Uhlmann, D. R. Ulrich), Wiley, New York, **1992**, pp. 135–148.
11. E. Matijevic, *Langmuir* **1994**, 10, 8–16.

12. C. J. Brinker, G. W. Scherer in *Sol-gel Science: The Physics and Chemistry of Sol-gel Processing*, Academic, New York, **1990**.
13. D. M. Smith, R. Desphande, C. J. Brinker, W. L. Earl, B. Ewing, P. J. Davis, *Catal. Today* **1992**, *14*, 293–303.
14. D. R. Ulrich, *J. Non-Cryst. Solids* **1988**, *100*, 174–193.
15. D. M. Smith, R. Desphande, C. J. Brinker in *Better Ceramics through Chemistry V* (Eds: M. J. Hampden-Smith, W. G. Klemperer, C. J. Brinker), Materials Research Society, Pittsburgh, **1992**, 271, pp. 567–572.
16. R. Desphande, D. M. Smith, C. J. Brinker, *ibid*; pp. 553–558.
17. S. S. Kistler, *Nature* **1931**, *127*, 741.
18. R. J. Ayen, P. A. Iacobucci, *Rev. Chem. Eng.* **1988**, *5*, 157–198.
19. S. J. Teichner, *CHEMTECH* **1991**, *21*, 372–377.
20. G. M. Pajonk, *Appl. Catal.* **1991**, *72*, 217–266.
21. S. M. Maurer, E. I. Ko, *J. Catal.* **1992**, *135*, 125–134.
22. L. K. Campbell, B. K. Na, E. I. Ko, *Chem. Mater.* **1992**, *4*, 1329–1333.
23. M. Beghi, P. Chiurlo, L. Costa, M. Palladino, M. F. Pivini, *J. Non-Cryst. Solids* **1992**, *145*, 175–179.
24. C. J. Brodsky, E. I. Ko, *J. Mater. Chem.* **1994**, *4*(4), 651–652.
25. G. W. Scherer, in *Drying* (Ed.: A. S. Mujumdar), Elsevier, Netherlands, **1992**, pp. 92–113.
26. D. A. Ward, E. I. Ko, *Chem. Mater.* **1993**, *5*, 956–969.
27. T. Lopez, P. Bosch, J. Navarrete, M. Asomoza, R. Gomez, *J. Sol-Gel Sci. & Tech.* **1994**, *1*, 193–203.
28. R. Gomez, T. Lopez, S. Castillo, R. G. Gonzalez, *J. Sol-Gel Sci. & Tech.* **1994**, *1*, 205–211.
29. S. J. Conway, L. H. Lunsford, *J. Catal.* **1992**, *131*, 513–522.
30. R. Tleimat-Manzalji, T. Manzalji, G. M. Pajonk, *J. Non-Cryst. Solids* **1992**, *147/148*, 744–747.
31. J. G. Weissman, E. I. Ko, S. Kaytal, *Appl. Catal. A* **1993**, *94*, 45–59.
32. B. E. Handy, M. Maciejewski, A. Baiker, *J. Catal.* **1992**, *134*, 75–86.
33. S. M. Maurer, E. I. Ko, *Catal. Lett.* **1992**, *12*, 231–238.
34. E. Carlson, J. N. Armor, W. J. Cunningham, A. M. Smith, US Patent 4828 818 **1989**.
35. R. Gomez, V. Bertin, M. A. Ramirez, T. Zamudio, P. Bosch, I. Schifter, T. Lopez, *J. Non-Cryst. Solids* **1992**, *147/148*, 748–752.
36. A. J. Fanelli, A. K. Price, US Patent 3 378 987 **1984**.
37. C. J. Brinker, D. M. Smith, R. Deshpande, P. M. Davis, S. Hietala, G. C. Frye, C. S. Ashley, R. A. Assink, *Catal. Today* **1992**, *14*, 155–163.
38. D. A. Ward, E. I. Ko, *Langmuir* **1995**, *11*, 369–372.
39. W. Zou, R. D. Gonzalez, *Appl. Catal. A* **1993**, *102*, 181–200.
40. K. Tanabe in *Catalysis: Science and Technology* (Eds: J. R. Anderson, M. Boudart), Springer-Verlag, Berlin, **1981**, Vol. 2, pp. 231–273.
41. J. B. Miller, S. E. Rankin, E. I. Ko, *J. Catal.* **1994**, *148*, 673–682.
42. B. E. Handy, A. Baiker, M. Schramel-Marth, A. Wokaun, *J. Catal.* **1992**, *133*, 1–20.
43. M. Toba, F. Mizukami, S. Niwa, Y. Kiyozumi, K. Maeda, A. Annila, V. Komppa, *J. Mater. Chem.* **1994**, *4*(4), 585–589.
44. T. Lopez, L. Herrera, R. Gomez, W. Zou, K. Robinson, R. D. Gonzalez, *J. Catal.* **1992**, *136*, 621–625.
45. D. A. Ward, E. I. Ko, *J. Catal.* **1994**, *150*, 18–33.
46. T. Lopez, R. Gomez, A. Ramirez-Solis, E. Poulain, O. Novaro, *J. Mol. Catal.* **1994**, *88*, 71–84.
47. V. T. Zaspalis, A. J. Burggraaf in *Inorganic Membranes: Synthesis, Characteristics, and Applications*, Van Nostrand Reinhold, New York, **1991**, pp. 177–207.
48. A. J. Burggraaf, K. Keizer, *ibid*, pp. 10–63.
49. P. Cini, S. R. Blaha, M. P. Harold, K. Venkataraman, *J. Membrane Sci.* **1991**, *55*, 199–225.
50. Q. Xu, M. A. Anderson, *J. Am. Ceram. Soc.* **1993**, *76*(8), 2093–2097.
51. V. T. Zaspalis, W. van Praag, K. Keizer, J. G. van Ommen, J. R. H. Ross, A. J. Burggraaf, *Appl. Catal.* **1991**, *74*, 235–248.
52. U. Schubert, N. Hüsing, A. Lorenz, *Chem. Mater.* **1995**, *7*, 2010–2027.
53. D. Avnir, S. Braun, O. Lev, M. Ottolenghi, *Chem. Mater.* **1994**, *6*, 1605–1614.
54. G. C. Ruben, R. W. Pekala, *J. Non-Cryst. Solids* **1995**, *186*, 219–231.

## 3.6 Flame Hydrolysis

H. JACOBSEN AND P. KLEINSCHMIT

### 3.6.1 Manufacture

The term flame hydrolysis describes a process in which a gaseous mixture of a precursor (a metal chloride in many cases), hydrogen and air or oxygen is brought to reaction in a torch installed in a continuously operated flame reactor. The precursor compound is hydrolyzed by the water vapor produced by the oxyhydrogen reaction. Different to this method is the so-called flame oxidation in which the precursor compound is not hydrolyzed but oxidized. The so-called chloride process uses the reaction of  $\text{TiCl}_4$  with oxygen to produce coarser pigment grade  $\text{TiO}_2$  [1]. The reaction is only weakly exothermic and requires a high reaction temperature.  $\text{TiCl}_4$  and oxygen are therefore heated up to  $1000^\circ\text{C}$  before reaction. A related process that has also been the subject of many investigations is spray pyrolysis. Whereas the first two processes describe gas-to-particle processes, spray pyrolysis is an example of a droplet-to-particle process. In many cases spray pyrolysis is used for the manufacture of modern ceramics and high-temperature superconductors. It is common in the literature to use the generic term 'aerosol processes' for gas-to-particle and droplet-to-particle processes. An overall view of aerosol processing of materials in general can be found in Ref. 2.

Of all these processes only flame hydrolysis is used to produce oxides with high surface areas on a large industrial scale. Therefore, the emphasis of this article lies on this subject. In general, this process is suitable for any volatile compound that can be decomposed at a high temperature to form an oxide. Possible precursor compounds that can be used are metal chlorides, carbonyls such as  $\text{Ni}(\text{CO})_4$  or  $\text{Fe}(\text{CO})_5$ , and volatile alcoholates. Reactions that have been studied are, for example, the manufacture of  $\text{Al}_2\text{O}_3$  from  $\text{AlCl}_3$  [3],  $\text{TiO}_2$  from  $\text{TiCl}_4$  [4],  $\text{Fe}_2\text{O}_3$  from  $\text{FeCl}_3$  [5],  $\text{MoO}_3$  from  $\text{MoO}_2\text{Cl}_4$  [6], and  $\text{SiO}_2$  from  $\text{SiCl}_4$  [7]. Alcoholate precursors that have been found to be suitable are titanium propylate and butylate, as well as secondary aluminum butylate [8, 9]. In this case, no flame-generated  $\text{H}_2\text{O}$  is needed for the reaction, and the alcoholates can be decomposed in a hot wall reactor. Certain alkylhalidosilanes such as methyltrichlorosilane are other industrially used sources of silicon, because they are easily accessible byproducts of the silicone industry.

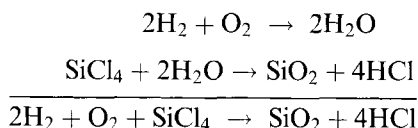
Since the invention of the flame hydrolysis process for the production of  $\text{SiO}_2$  by Degussa [10] many different oxides have been manufactured via this route. Table 1 summarizes the oxides that have been prepared so far [11]. In principle, any mixed oxide that is a combination of the oxides  $\text{SiO}_2$ ,  $\text{Al}_2\text{O}_3$ ,  $\text{TiO}_2$  and  $\text{ZrO}_2$  can be produced as well [12]. On a commercial scale  $\text{SiO}_2$ ,  $\text{Al}_2\text{O}_3$ ,  $\text{Al}_2\text{O}_3/\text{SiO}_2$  mixed oxides,  $\text{TiO}_2$ , and  $\text{ZrO}_2$  are available. Of these, fumed silica is by far the most widely produced oxide [13]. Although fumed silica was originally developed as a reinforcement filler for rubber (white carbon), it has found its way into numerous branches of industry of which catalysis is a comparably new one. The worldwide production

**Table 1.** Oxides produced by flame hydrolysis.

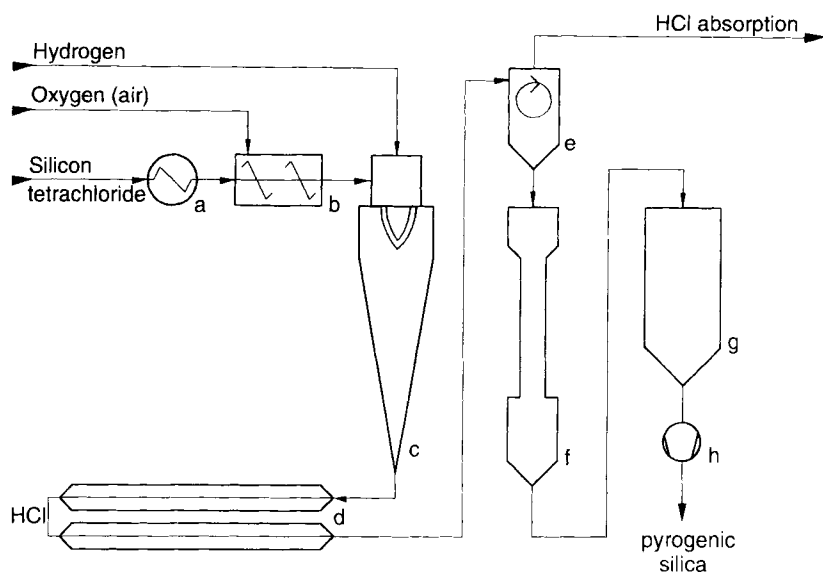
Product	Starting material
Al <sub>2</sub> O <sub>3</sub>	AlCl <sub>3</sub>
AlPO <sub>4</sub>	AlCl <sub>3</sub> /PCl <sub>3</sub>
AlBO <sub>3</sub>	AlCl <sub>3</sub> /BCl <sub>3</sub>
Al <sub>2</sub> O <sub>3</sub> /SiO <sub>2</sub> (mixed oxide)	AlCl <sub>3</sub> /SiCl <sub>4</sub>
Bi <sub>2</sub> O <sub>3</sub>	BiCl <sub>3</sub>
Cr <sub>2</sub> O <sub>3</sub>	CrO <sub>2</sub> Cl <sub>2</sub>
Fe <sub>2</sub> O <sub>3</sub>	Fe(CO) <sub>5</sub> , FeCl <sub>3</sub>
GeO <sub>2</sub>	GeCl <sub>4</sub>
NiO	Ni(CO) <sub>4</sub>
MoO <sub>3</sub>	MoCl <sub>5</sub> , MoO <sub>2</sub> Cl <sub>2</sub>
SiO <sub>2</sub>	SiCl <sub>4</sub>
SnO <sub>2</sub>	SnCl <sub>4</sub> , Sn(CH <sub>3</sub> ) <sub>4</sub>
TiO <sub>2</sub>	TiCl <sub>4</sub>
V <sub>2</sub> O <sub>5</sub>	VOCl <sub>3</sub>
WO <sub>3</sub>	WCl <sub>6</sub> , WOCl <sub>4</sub>
ZrO <sub>2</sub>	ZrCl <sub>4</sub>

capacity for fumed silica was estimated to be approximately 100 000 tons per annum in 1991. Main producers are Degussa (Aerosil®), Wacker (HDK®), Cabot (Cabosil®) and Tokuyama Soda (Reolosil®). The manufacturing process is briefly described below; further details are given in Ref. 14 and the patents and papers cited therein.

SiCl<sub>4</sub> is vaporized, mixed with dry air and hydrogen and then fed into a flame reactor. The SiCl<sub>4</sub> hydrolyzes to SiO<sub>2</sub> and HCl under the influence of the oxy-hydrogen reaction, which includes the formation and reaction of radicals.



The silica so produced can be described as an aerosol of nanometer sized particles. The primary particles coagulate to form aggregates by intergrowth in the flame and further agglomerates by cohesion forces during and after cooling. The formation of this structure is essential for the resulting properties of the product. Filters or cyclones separate the silica from the hydrochloric acid containing off-gas. Residual hydrochloric acid adsorbed on the large surface of the silica can be removed by a steam/air treatment in a fluidized bed reactor. A simplified flow sheet of the flame hydrolysis process is shown in Fig. 1. The size of primary particles and aggregates can be influenced by the flame temperature, the hydrogen to oxygen ratio, the SiCl<sub>4</sub> loading, and the residence time in the flame. Basic research on the flame hydrolysis process itself and on factors influencing the particle formation in flames were published in Refs 15–17.

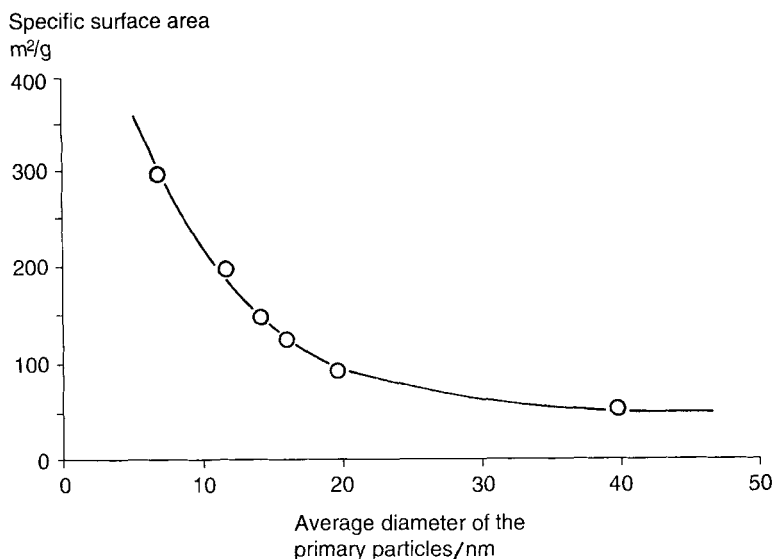


**Figure 1.** Flow sheet of a fumed silica plant: (a) vaporizer, (b) mixing chamber, (c) burner, (d) cooling section, (e) separation, (e) separation, (f) deacidification, (g) hopper, (h) compactor.

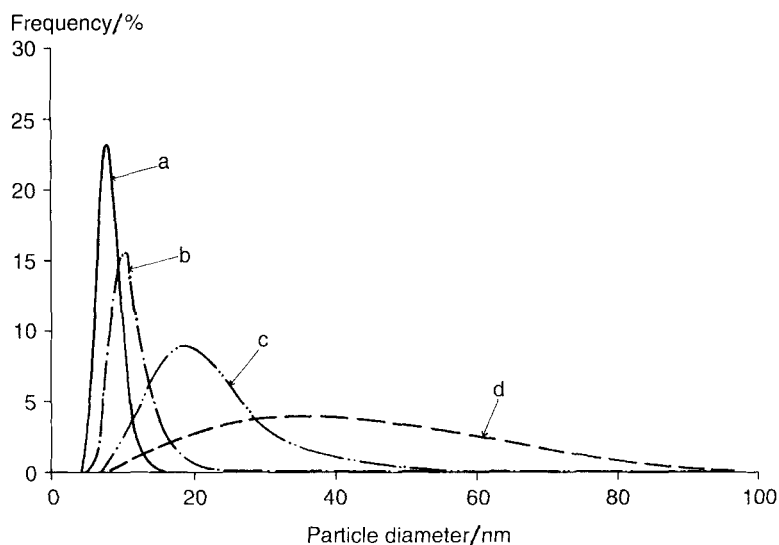
### 3.6.2 Physicochemical Properties of Fumed Oxides

The physicochemical data of fumed oxides are published in a series of documents [18]. The surface area of the fumed oxide is mainly determined by the size of the primary particles. Surface areas range from 25 to  $400 \text{ m}^2 \text{ g}^{-1}$ . In the case of fumed silica products with specific surface areas less than  $300 \text{ m}^2 \text{ g}^{-1}$  the primary particles are dense and have no inner surface. Products with a specific surface area above  $300 \text{ m}^2 \text{ g}^{-1}$  show a certain amount of microporosity instead of further reduced primary particle size. The average particle diameter in the  $300 \text{ m}^2 \text{ g}^{-1}$  product is 7 nm. For comparison, a product with  $50 \text{ m}^2 \text{ g}^{-1}$  has primary particles with diameters of 40 nm. This relationship is shown in Figs 2 and 3.  $\text{TiO}_2$  and  $\text{ZrO}_2$  have a lower specific surface area when compared with  $\text{SiO}_2$  of the same particle size because of their higher density. The structures of two Aerosil types with different particle sizes are shown in the TEM diffraction photographs in Figs 4 and 5. In the TEM photograph of the product with  $300 \text{ m}^2 \text{ g}^{-1}$  it can be seen that a certain number of primary particles of 5–10 nm are aggregated in irregularly shaped arrangements. The  $50 \text{ m}^2 \text{ g}^{-1}$  product consists mainly of isolated primary particles and only a very small number of aggregates. When freshly produced, Aerosil has a bulk density of about  $15 \text{ g L}^{-1}$ . Because this is hard to handle, the product is compacted to 50– $100 \text{ g L}^{-1}$  depending on the application.  $\text{Al}_2\text{O}_3$  (aluminum oxide C with  $100 \text{ m}^2 \text{ g}^{-1}$ , Degussa) is available with an apparent density of  $80 \text{ g L}^{-1}$ .

Fumed silica is always found to be amorphous, and therefore does not cause silicosis. The respective  $\text{Al}_2\text{O}_3$  is crystalline and consists of the thermodynamically

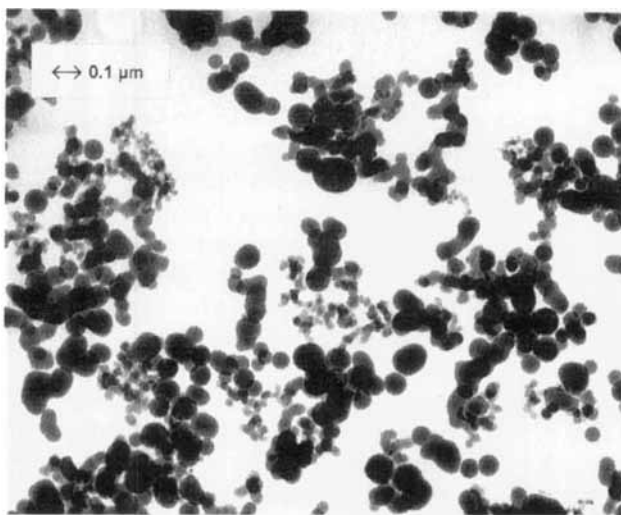


**Figure 2.** Relationship between primary particle size and specific surface area.

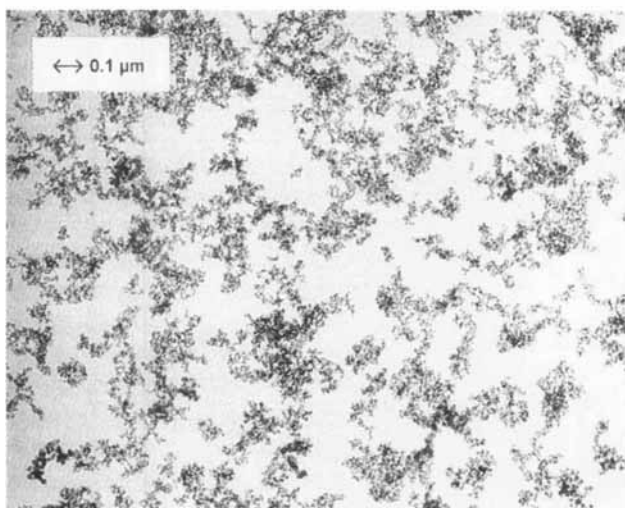


**Figure 3.** Particle size distribution in fumed silicas with different specific surface areas: (a) 300 m² g⁻¹, (b) 200 m² g⁻¹, (c) 90 m² g⁻¹, (d) 50 m² g⁻¹.

metastable  $\delta$  form instead of the stable  $\alpha$  form. It can be transformed to the  $\alpha$ -Al<sub>2</sub>O<sub>3</sub> phase by heating to 1200 °C. This conversion is associated with a loss of surface area and an increase of hardness and abrasiveness. In the commercial TiO<sub>2</sub> obtained by flame hydrolysis, the thermodynamically metastable modification anatase is



**Figure 4.** TEM photograph of a pyrogenic silica with an average particle size of  $\approx 40$  nm and a specific surface area of  $\approx 50 \text{ m}^2 \text{ g}^{-1}$ .



**Figure 5.** TEM photograph of a pyrogenic silica with an average particle size of  $\approx 7$  nm and a specific surface area  $\approx 300 \text{ m}^2 \text{ g}^{-1}$ .

the main phase, with about 30% rutile. The lattice transformation towards higher amounts of rutile becomes notable at temperatures above  $700^\circ\text{C}$ . It is also associated with a decrease of specific surface area. The preference of a high temperature phase is also found in pyrogenic  $\text{ZrO}_2$ , that is obtained in the metastable tetragonal modification instead of the monoclinic room temperature phase. If the freshly produced  $\text{ZrO}_2$  is treated with hot moist air at about  $800^\circ\text{C}$ , in order to reduce the amount of adsorbed hydrochloric acid, a conversion towards higher amounts of the monoclinic phase takes place [19].



Another point concerning the suitability of fumed oxides for catalytic applications, that has to be taken into consideration, is their surface chemistry. Siloxane (Si–O–Si) and silanol groups (Si–OH) occur at the surface of the silica particles. The former are hydrophobic while the latter are hydrophilic and make the pyrogenic silica wettable. The density of silanol groups determined, for example, by reaction with lithium aluminum hydride, is between 2.0 and 2.5 Si–OH nm<sup>-2</sup>. This is significantly lower than the values typically found for precipitated silica. The silanol groups are acidic, which corresponds to an isoelectric point at a pH value of 2. Immediately after production, pyrogenic silica shows mainly isolated silanol groups. In the course of time, adsorbed water reacts with strained siloxane groups and builds further silanol groups. By heating the silica to 400 °C the reaction can be reversed. This can easily be followed by IR spectroscopy [13]. Pyrogenic Al<sub>2</sub>O<sub>3</sub> has basic hydroxy groups at its surface which correspond to an isoelectric point at a pH value of 9. On complete removal of water, aluminum ions are located at the surface which are coordinated by only five oxygen atoms and therefore represent Lewis acid centers. They can add pyridine or again form hydroxy groups through the adsorption of water. The hydroxy groups at the surface of titania are basic or acidic, depending on the surrounding. An isoelectric point at a pH value of 6.5 has been reported [20]. The acidic sites accumulate ammonia and can be esterified with diazomethane. The basic sites can be detected by exchange reactions with certain anions [21]. ZrO<sub>2</sub> has acidic and basic sites at its surface as well, but is more basic than TiO<sub>2</sub>. This corresponds to an isoelectric point at pH 8.2. Compared with the pure oxides, Al<sub>2</sub>O<sub>3</sub>–SiO<sub>2</sub> mixed oxides are strong solid acids. Even stronger acids or superacids are sulphated TiO<sub>2</sub> or ZrO<sub>2</sub>. Due to the above outlined manufacturing process that differs significantly from precipitation or sol–gel processes, the oxides so produced have very special properties, the most important of which have been discussed in this section. The outstanding properties that make pyrogenic oxides so interesting for catalysis are:

- high chemical purity;
- well defined, spherical primary particles;
- practically no internal surface;
- very low drying and ignition loss.

### 3.6.3 Preparation of Formed Supports

Formed supports are much more convenient for commercial-scale processes than powders, especially particles with diameters within the millimeter range are preferred. Unfortunately, fumed oxides are not easy to shape because of their extreme fineness. Several routes to prepare formed supports from pyrogenic powders have been developed. A very simple approach is the use of silica sol and alcohols as binders. SiO<sub>2</sub>, Al<sub>2</sub>O<sub>3</sub> and TiO<sub>2</sub> have been treated in this way. The pyrogenic oxide is mixed with water, silica sol and glycerol, extruded, dried and calcined at 550 °C. The resulting support has not lost much of its original surface area and has a pore

**Table 2.** Typical physicochemical data of a TiO<sub>2</sub> support.

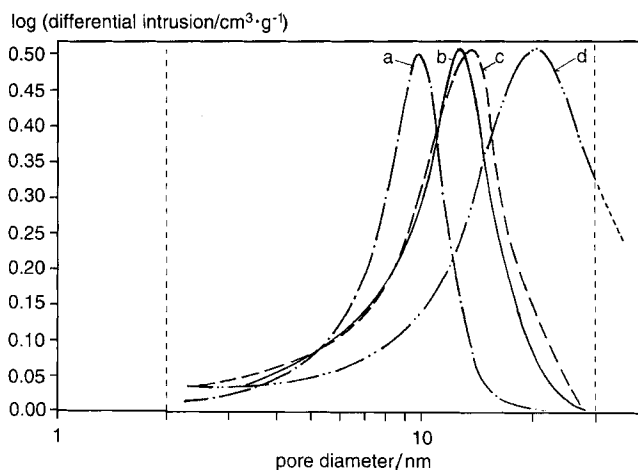
BET surface area (raw oxide)	55 m <sup>2</sup> g <sup>-1</sup>
Composition	99.5% TiO <sub>2</sub> (75% anatase, 25% rutile)
Diameter	4 mm
BET surface area	48 m <sup>2</sup> g <sup>-1</sup>
Pore volume	0.34 cm <sup>3</sup> g <sup>-1</sup>
Pore distribution	no pores below 2 nm, 90% between 2 and 30 nm
Hardness	44 N

volume of 60% which, in the case of silica, corresponds to 0.3 cm<sup>3</sup> g<sup>-1</sup> [22]. The high amount of silica introduced by the use of the silica sol can be a drawback in oxide systems other than silica. This can be avoided by using small amounts of decomposable organic or inorganic acids instead of silica sol as binding agents and small amounts of graphite as a formulation aid. The graphite and the acid can be removed by firing the support. The purity of the support is therefore only determined by the used pyrogenic oxide itself. For example, from pyrogenic TiO<sub>2</sub> with a specific surface area of 48 m<sup>2</sup> g<sup>-1</sup>, supports with 44 m<sup>2</sup> g<sup>-1</sup> and 0.3 cm<sup>3</sup> g<sup>-1</sup> pore volume were produced [23]. If higher pore volumes and crushing strengths are required, the following process can be applied to the above-mentioned pure oxides as well as mixed oxides.

The oxides are mixed with kaolin, graphite, urea and additional water, until a well homogenized paste is obtained. The paste is dried at 100 °C, optionally ground, and then formed by tableting or extruding. The produced pellets or extrudates are then calcined at 800–900 °C [24]. When fumed silica with 200 m<sup>2</sup> g<sup>-1</sup> is used, the resulting supports have a pore volume of 1.2 cm<sup>3</sup> g<sup>-1</sup> and a specific surface area of 195 m<sup>2</sup> g<sup>-1</sup>. If the support itself is used as a catalytically active component as in the case of TiO<sub>2</sub>, the described route is not favorable, because the binder remains on the support and affects the catalytic activity. For TiO<sub>2</sub> it is therefore proposed to use cellulose derivatives (e.g. tylose) as binders and lactic acid as a plasticizer instead of kaolin and graphite. The amount of additives has to be carefully controlled; best results were achieved with 0.3% lactic acid and 1% tylose. Furthermore, a certain amount of water and a well adjusted pH are necessary [25]. Typical properties of so produced supports are listed in Table 2. Some large-scale processes use fixed-bed reactors several cubic meters in volume. In these applications a very high breaking strength is an important requirement for the used supports. Fumed silica pellets with the required increased breaking strength can be produced by using magnesium or aluminum stearate in addition to urea and methyl cellulose. Small amounts of stearate are sufficient for optimal results, therefore again a high purity of the supports is obtained [26]. The physicochemical data of support types made from fumed silica with different surface areas are listed in Table 3. Depending on the surface area and primary particle size of the fumed oxide used, it is possible to manufacture tablets with corresponding pore size distributions, as shown for various fumed silicas in Fig. 6. Oxides with high surface areas result in supports with small pore sizes and vice versa.

**Table 3.** Typical physicochemical data of SiO<sub>2</sub> supports.

Property	BET surface area of raw oxide (m <sup>2</sup> g <sup>-1</sup> )			
	50	130	200	300
Composition (% SiO <sub>2</sub> )	>99	>99	>99	>99
Diameter (mm)	5	6	6	6
BET surface area (m <sup>2</sup> g <sup>-1</sup> )	45	110	160	230
Pore volume (cm <sup>3</sup> g <sup>-1</sup> )	0.6	0.8	0.75	0.8
Pore distribution (nm)	no pores < 8, 90% 10–40	no pores < 7, 90% 10–40	no pores < 6, 90% 10–30	no pores < 4, 90% 7–25
Hardness (N)	125	60	60	80

**Figure 6.** Influence of the surface area of fumed silica on the final pore size distribution after the forming process: (a) 380 m<sup>2</sup> g<sup>-1</sup>, (b) 300 m<sup>2</sup> g<sup>-1</sup>, (c) 200 m<sup>2</sup> g<sup>-1</sup>, (d) 90 m<sup>2</sup> g<sup>-1</sup>.

In general, it can be said that supports on the basis of fumed oxides are in many respects superior to those prepared from other oxides: the high chemical purity is a result of the flame hydrolysis process, in which volatile raw materials purified by rectification are used. Together with the unique particle structure, the high purity leads also to a well defined surface chemistry. The good mechanical properties and the high resistance against sintering have been described [25].

A different approach to make fumed oxides more useful as supports for active compounds is spray granulation. In this process a suspension of fumed oxide in water is fed to a spray drying device. The oxide content of the suspension controls, among other parameters, the size of the resulting particles. A grain size distribution in the submillimeter range is obtainable with this method. The pore size and the pore size distribution can be adjusted by selecting oxides with different particle size

distribution and specific surface area, respectively. Spray granulated supports are mainly needed for catalytic processes using fluidized bed reactors [27].

### 3.6.4 Applications

Because of the unique physicochemical properties of fumed oxides they are attractive for catalytic investigations from several points of view. Pure fumed oxide powders have served as model substances in basic catalysis research. For a review with about a hundred references see Ref. 28. Pyrogenic  $\text{Al}_2\text{O}_3$  has been the subject of an entire series of studies. It serves as a support for catalytically active metals; among the investigated reactions are hydrogenations and polymerizations. The activity of the unloaded oxide has also been tested. The special surface characteristics of pyrogenic  $\text{SiO}_2$  are also of interest to numerous research groups. Emphasis has been laid on  $\text{Ni/SiO}_2$ ,  $\text{Ag/SiO}_2$  and  $\text{Pt/SiO}_2$  with many examples for applications. The oxide as such was also studied, especially with regard to adsorption problems. Interest in titanium oxide has been expanding during recent years, however, it has not yet found many commercial applications in catalysis. A very promising research field is photocatalysis [29, 30].  $\text{TiO}_2$  has been shown to be able to oxidize various organic compounds, when irradiated with sunlight or UV radiation [31, 32]. The activity of pyrogenic  $\text{TiO}_2$  is found to be much higher than pigment grade  $\text{TiO}_2$ . The high photocatalytic activity is used in some environmental processes, for example in the cleaning of waste water from various hazardous chemicals. Other studies on  $\text{TiO}_2$  and especially pyrogenic  $\text{TiO}_2$  report the usefulness in the synthesis of phenol from benzene, nitrate from nitrite, or aldehydes from alcohols [33, 34]. The photoconducting effect of  $\text{TiO}_2$  has been studied in detail in conjunction with the photolysis of water [35–37]. The reaction takes place in a dispersion or colloidal solution of  $\text{TiO}_2$ , to which colloidal ruthenium and colloidal platinum oxide are added. The current generated by UV light in the  $\text{TiO}_2$  is conducted to a platinum layer in which water is split into hydrogen and hydroxy ions. The hydroxy ions are decomposed into oxygen and water at the ruthenium oxide sites. Another catalytic reaction of potential industrial and academic interest is the methanation of carbon dioxide.  $\text{Ru/RuO}_x$  supported on  $\text{TiO}_2$  catalyzes this reaction even at room temperature and ambient pressure [38]. In several patents, catalysts for the Fischer–Tropsch process using various metals on  $\text{TiO}_2$  are described [39]. Furthermore, the use of  $\text{TiO}_2$  in the ammoxidation of aromatics has been reported [40].

For commercial processes, formed supports are more useful. Compared with other supports, fumed oxide supports showed new catalytic effects [41]. Some intensively investigated applications for these supports are abstracted in the following.  $\text{SiO}_2$  pellets have been successfully introduced in a new generation of precious metal supports in vinylacetate monomer production [42]. This resulted in better selectivities and an up to 50% higher space–time yield compared with supports based on natural aluminosilicates. In alkene hydration fumed silica pellets serve as a support for phosphoric acid. In this case, an increased catalyst lifetime and a higher space–time yield were observed [43]. Pyrogenic  $\text{TiO}_2$  powder can be used as a starting

material for the manufacture of monolithic catalysts [44] for the selective reduction of NO<sub>x</sub> with ammonia.

## References

1. P. Woditsch, A. Westerhaus, *Ullmann's Encycl. Ind. Chem.* 5th ed. **1993**, Vol. A20, p. 281.
2. A. Gurav, T. Kodas, T. Pluym, Y. Xiong, *Aerosol Sci. Technol.* **1993**, 19, 411–452.
3. R. Caillat, J. P. Cuer, J. Elston, F. Juillet, R. Pointud, M. Prettre, S. Teichner, *Bull. Soc. Chim. France* **1959**, 152–156.
4. F. Juillet, F. Lecomte, H. Mozzanega, S. J. Teichner, A. Thevenet, P. Vergnon, *Farad. Symp. Chem. Soc.* **1973**, 7, 57–62.
5. P. G. Vergnon, H. B. Landousi, *Ind. Eng. Prod. Res. Dev.* **1980**, 19, 147–151.
6. D. Bianchi, J. L. Bernard, M. Camelot, R. Benali-Chaoui, S. J. Teichner, *Bull. Soc. Chim. France* **1980**, 7–8, 275–280.
7. N. S. Subramanian, Ph.D. Thesis, University of New Hampshire, **1975**.
8. J. L. Gass, S. J. Teichner, *Bull. Soc. Chim. France* **1972**, 6, 2209–2213.
9. J. L. Gass, F. Juillet, S. J. Teichner, *Bull. Soc. Chim. France* **1973**, 2, 429–435.
10. H. Klöpfer German Patent 762 723 **1942** (Degussa).
11. A. T. Liu, P. Kleinschmit, *British Ceramic Proc.* **1986**, 38, 1–10.
12. A. T. Liu, P. Kleinschmit German Patent 3 611 449 **1986** (Degussa).
13. M. Ettlinger *Ullmann's Encycl. Ind. Chem.* 5th ed. **1993**, Vol. A23, pp. 635–642.
14. H. Ferch, H. Fratzscher, *Kautschuk, Gummi, Kunststoffe* **1967**, 20, 578; Degussa AG, Frankfurt am Main, *Technical Bulletin Pigments*, 5th ed., **1993**, p. 11.
15. J. D. Landgrebe, S. E. Pratsinis, *J. Colloid Interface Sci.* **1990**, 139, 63–86.
16. S. E. Pratsinis, *J. Colloid Interface Sci.* **1988**, 2, 416–427.
17. G. D. Ulrich, *Chem. Eng. News* **1984**, 62, 22–29.
18. Degussa AG, Frankfurt am Main, *Technical Bulletin Pigments*, 6th ed., **1993**, p. 56.
19. W. Hartmann, A. T. Liu, D. Peukert, P. Kleinschmit, *Mater. Sci. Eng.* **1989**, A109, 243–246.
20. J. Lyklema, *Chem. Ind.* **1987**, 21, 741.
21. H.-P. Boehm, *Chem.-Ing. Techn.* **1974**, 46, 716.
22. M. Ettlinger, H. Ferch, D. Koth, E. Simon German Patent 3 132 674 **1983** (Degussa).
23. M. Ettlinger, H. Ferch, D. Koth, E. Simon German Patent 3 217 751 **1983** (Degussa).
24. B. Despeyroux, K. Deller, H. Krause, *Chemische Industrie* **1993**, 10, 48–49; K. Deller, R. Klingel, H. Krause German Patent 3 803 894 **1988** (Degussa); K. Deller, R. Klingel, H. Krause German Patent 3 803 895 **1988** (Degussa); K. Deller, R. Klingel, H. Krause German Patent 3 803 897 **1988** (Degussa); K. Deller, M. Ettlinger, R. Klingel, H. Krause German Patent 3 803 898 **1988** (Degussa); K. Deller, R. Klingel, H. Krause, K.-P. Bauer German Patent 3 803 899 **1988** (Degussa).
25. M. Bankmann, R. Brand, B. H. Engler, J. Ohmer, *Catal. Today* **1992**, 14, 225–242; R. Brand, B. Engler, M. Foerster, W. Hartmann, P. Kleinschmit, E. Koberstein, J. Ohmer, R. Schwarz German Patent 4 012 479 **1991** (Degussa).
26. K. Deller, M. Foerster, H. Krause German Patent 3 912 504 **1989** (Degussa).
27. H. Biegler, G. Kallrath German Patent 1 209 108 **1966** (Degussa).
28. D. Koth, H. Ferch, *Chem. Ing. Techn.* **1980**, 52, 628; Degussa AG, Frankfurt am Main, *Technical Bulletin Pigments*, 2nd ed. **1991**, p. 72.
29. M. Formenti, F. Juillet, P. Meriaudeau, S. J. Teichner, P. Vergnon in *Aerosols and Atmospheric Chemistry* (Ed. G. M. Hidy) Academic Press, New York, **1972**, p. 45.
30. M. Formenti, S. J. Teichner, *Catalysis* **1978**, 87–108.
31. Z. Wang, C. Kutal, *Chemosphere* **1995**, 30, 1125–36.
32. J. Papp, S. Soled, K. Dwight, A. Wold, *Chem. Mater.* **1994**, 6, 496–500.
33. H. P. Boehm, *Angew. Chem.* **1966**, 78, 617.
34. M. A. Malati, N. J. Seager, *J. Oil Chem. Assoc.* **1981**, 64, 231.
35. M. Graetzel, *Acc. Chem. Res.* **1981**, 14, 376.

36. V. H. Houlding, M. Graetzel, *J. Am. Chem. Soc.* **1983**, *105*, 5695–5696.
37. M. Graetzel, *Dechema-Monographien*, **1987**, *106*, 189–204.
38. K. R. Thampi, J. Kiwi, M. Grätzel, *Nature* **1987**, *327*, 506–508.
39. R. A. Faito, S. Miseo US Patent 4 749 677 **1988** (Exxon Res. & Eng. Co); C. C. Cherisch, R. A. Fiato, I. E. Wachs US Patent 4 559 365 **1985** (Exxon Res. & Eng. Co); German Patent 2 712 909 **1977**; US Patent 4 042 614 **1977**.
40. H. Beschke, H. Friedrich, J. Helios German Patent 3 107 755 **1982** (Degussa).
41. M. Bankmann, B. Despreyroux, H. Krause, J. Ohmer, R. Brand, *Stud. Surf. Sci. Catal.* **1993**, *75*, 1781–1784.
42. F. Wunder, G. Roscher, K. Eichler German Patent 3 803 900 **1989** (Hoechst); R. Abel, K.-F. Wörner European Patent 634 214 **1995** (Hoechst).
43. G. J. Haining, P. Lusman, A. D. Melville European Patent 578 441 **1994** (BP Chemicals).
44. H. Hellebrand, N. Landgraf, H. Schmelz German Patent 3 938 155 **1990** (Siemens); R. Brand, H. B. Engler, W. Honnen, P. Kleine-Moellhoff, E. Koberstein German Patent 3 740 289 **1989** (Degussa).

## 3.7 Solid-State Reactions

P. G. MENON AND B. DELMON

### 3.7.1 Why Solid-State Reactions?

The methods most commonly used for preparing catalysts are precipitation (Section 3.4) and impregnation (Section 4.1.1). In both of them, the catalytically active material is transferred from a liquid phase, usually an aqueous solution, to a solid. By contrast, other catalysts are obtained from solid precursors. Solid state reactions, namely solid-to-solid reactions in which both the starting material (the catalyst precursor) and the catalyst are solids, offer convenient methods to prepare several industrial catalysts, especially those containing two or more metallic elements or their oxides. The reason of the conspicuous efficiency of these methods to prepare phases containing two or several metallic elements is due to special features of solid-state reactions, compared to liquid-to-solid or gas-to-solid reactions. This section briefly outlines these peculiarities and presents the most frequent types of solid-state processes used in preparing catalysts.

The necessity to have more than one component in a catalyst arises from many needs: those linked to the polyfunctionality often required for the different steps in a reaction, the need to enhance the rate of some reaction steps, inhibition of unwanted side reactions, provision of adequate thermal stability, to take advantage of observed synergetic effects. From a fundamental point of view, the presence of several metal elements in a common structure permits the adjustment of the local electronic properties, imposes well defined coordinations, limits the extent of oxidation–reduction phenomena, and may stabilize the whole catalyst by retarding sintering. Mixed oxide catalysts are used as such, or as precursors of active catalysts, for a

36. V. H. Houlding, M. Graetzel, *J. Am. Chem. Soc.* **1983**, *105*, 5695–5696.
37. M. Graetzel, *Dechema-Monographien*, **1987**, *106*, 189–204.
38. K. R. Thampi, J. Kiwi, M. Grätzel, *Nature* **1987**, *327*, 506–508.
39. R. A. Faito, S. Miseo US Patent 4 749 677 **1988** (Exxon Res. & Eng. Co); C. C. Cherisch, R. A. Fiato, I. E. Wachs US Patent 4 559 365 **1985** (Exxon Res. & Eng. Co); German Patent 2 712 909 **1977**; US Patent 4 042 614 **1977**.
40. H. Beschke, H. Friedrich, J. Helios German Patent 3 107 755 **1982** (Degussa).
41. M. Bankmann, B. Despreyroux, H. Krause, J. Ohmer, R. Brand, *Stud. Surf. Sci. Catal.* **1993**, *75*, 1781–1784.
42. F. Wunder, G. Roscher, K. Eichler German Patent 3 803 900 **1989** (Hoechst); R. Abel, K.-F. Wörner European Patent 634 214 **1995** (Hoechst).
43. G. J. Haining, P. Lusman, A. D. Melville European Patent 578 441 **1994** (BP Chemicals).
44. H. Hellebrand, N. Landgraf, H. Schmelz German Patent 3 938 155 **1990** (Siemens); R. Brand, H. B. Engler, W. Honnen, P. Kleine-Moellhoff, E. Koberstein German Patent 3 740 289 **1989** (Degussa).

## 3.7 Solid-State Reactions

P. G. MENON AND B. DELMON

### 3.7.1 Why Solid-State Reactions?

The methods most commonly used for preparing catalysts are precipitation (Section 3.4) and impregnation (Section 4.1.1). In both of them, the catalytically active material is transferred from a liquid phase, usually an aqueous solution, to a solid. By contrast, other catalysts are obtained from solid precursors. Solid state reactions, namely solid-to-solid reactions in which both the starting material (the catalyst precursor) and the catalyst are solids, offer convenient methods to prepare several industrial catalysts, especially those containing two or more metallic elements or their oxides. The reason of the conspicuous efficiency of these methods to prepare phases containing two or several metallic elements is due to special features of solid-state reactions, compared to liquid-to-solid or gas-to-solid reactions. This section briefly outlines these peculiarities and presents the most frequent types of solid-state processes used in preparing catalysts.

The necessity to have more than one component in a catalyst arises from many needs: those linked to the multifunctionality often required for the different steps in a reaction, the need to enhance the rate of some reaction steps, inhibition of unwanted side reactions, provision of adequate thermal stability, to take advantage of observed synergetic effects. From a fundamental point of view, the presence of several metal elements in a common structure permits the adjustment of the local electronic properties, imposes well defined coordinations, limits the extent of oxidation–reduction phenomena, and may stabilize the whole catalyst by retarding sintering. Mixed oxide catalysts are used as such, or as precursors of active catalysts, for a

Catalyst	Active phases	Industrial processes
Copper chromite	$\text{CuCr}_2\text{O}_4$ , $\text{CuO}$	$\text{CO}$ conversion (low temp) hydrogenation, hydrog hydrogenolysis
Zinc chromite	$\text{ZnCr}_2\text{O}_4$ , $\text{ZnO}$	methanol synthesis (high
Copper/zinc chromite	$\text{Cu}_x\text{Zn}_{1-x}\text{Cr}_2\text{O}_4$ , $\text{CuO}$	methanol synthesis (low p
Iron molybdate	$\text{Fe}(\text{MoO}_4)_3$ , $\text{MoO}_3$	methanol to formaldehyd
Iron oxide/potassium oxide	$\text{KFeO}_2$ , $\text{K}_2\text{Fe}_{22}\text{O}_{34}$	ethylbenzene to styrene
Bismuth molybdate + promoter oxides	mixed molybdates	propene to acrolein propene to acrylonitrile
Zinc ferrite	$\text{ZnFe}_2\text{O}_4$	oxidative dehydrogenatio
Vanadia–molybdena	$\text{V}_2\text{O}_5$ – $\text{MoO}_3$ solid solution	Benzene/butene to maleic
Chromia–alumina	$\text{Cr}_x\text{Al}_{2-x}\text{O}_3$	Dehydrogenation of light
Mixed oxides	perovskite type	catalytic combustion
Barium hexaaluminate	$\text{BaAl}_{12}\text{O}_{19}$	catalytic combustion (sup

whole range of important industrial processes, a representative selection is given in Table 1.

Preparation of atomically homogeneous multicomponent catalysts by conventional methods, however, is often difficult due to three main reasons:

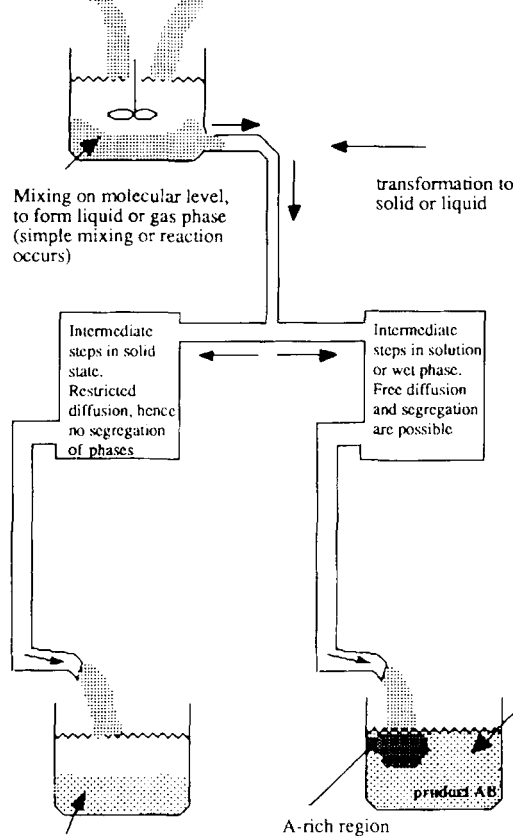
- (i) deposition of active precursors either as a precipitate or onto a support gives separate moieties, instead of a single phase of uniform chemical composition;
- (ii) segregation of the active components can occur during the thermal treatment of the catalyst precursor;
- (iii) the support can selectively interact with one of the active components during the other stage of the formation of the mixed oxide.

A good example of the latter case is the reaction of iron with silicon. On a silica-supported iron molybdate, a fact which made impossible the use of silicon as a support in the case of catalysts used for the oxidation of methanol to formaldehyde. Some of the methods to overcome these difficulties in catalyst preparation are the subject of this section.

This section deals with a small group of solid-to-solid reactions which are relevant to the preparation of certain mixed-oxide catalysts.

In principle, liquids are ideal precursors when atomically homogeneous mixed oxides are desired. The reason is that the ordinary liquid state has no long-range order, and hence permits a statistical repartition of its contents at a molecular level. However, segregation almost invariably occurs when liquids are reprecipitated.





**Figure 1.** Schematic representation of the vital role of solid-state reactions in preparing single-phase catalysts.

complex composition cannot be obtained by a direct reaction, an indirect route can be tried. This is possible if a solid can be obtained of a composition different from the desired solid (e.g. a hydroxide, salts of organic acids, etc.). This solid contains the metallic elements in the proportion required by the catalytic reaction. The reaction is then the solid-state transformation of this hydroxide or salt to the desired oxide. Keeping the material in the solid state throughout the transformation permits powerful control (Fig. 1) which prevents all unwanted atomic rearrangements in the bulk during catalyst preparation. In practice, two goals can be achieved:

- (i) As mentioned above, when specific compositions can be prepared with homogeneity at the molecular level, but in a thermally unstable state (acid hydroxides, complexes, or vitreous compounds), these can be decomposed

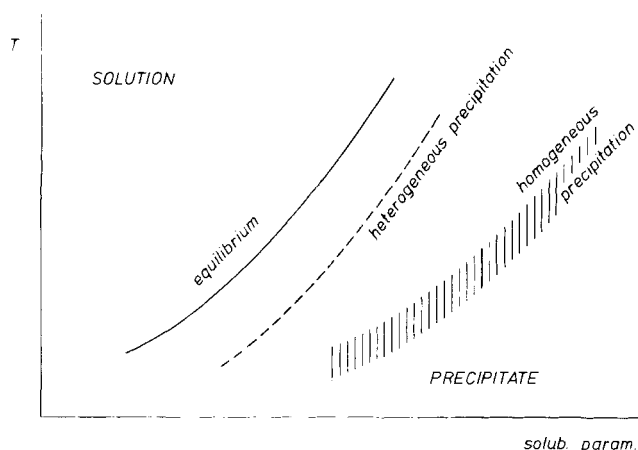
Even more important, for the catalysts considered here, control of the transformation conditions of the precursor to the final catalyst allows, to a certain extent, the preparation of highly dispersed oxides with well defined porosity. This is the main theme of this section. The preparative methods described here are typical cases, selected to highlight how goals (i) and (ii) are achieved in practice in various procedures.

### **3.7.1.1 Some General Concepts and Parameters in Solid-State Reactions**

When multicomponent solid systems are used to prepare a catalyst, homogenization of the precursors (mixing at the molecular level) is extremely important. The activity of the finished catalyst should not differ in the different parts of a catalyst charge, or from batch to batch of it. Two fundamental aspects of solid-state reactions involved in the preparation of catalysts are nucleation and the growth from solution of the nuclei or elementary particles into distinct solid phases in the surrounding liquid medium. Both of these are involved in the preparation of many catalysts and supports as well as in the deposition or dispersion of an active catalyst component on the support surface. The problem is that nucleation is, by essence, a process which favors segregation, thus it goes against the goal of preserving homogeneity at a molecular or atomic scale. Supersaturation of the medium essentially controls both nucleation and growth processes, thus determining ultimately the size, structure, and phases of elementary catalyst particles. The only important fact to remember is that the relative contribution of surface energy in the whole energy context is considerable in small particles of any phase in contact with vacuum or any other phase (gas, liquid, solid) in comparison to that of large particles or flat surfaces (this is expressed by the Gibbs–Thomson law). Nevertheless, nucleation can take place because of statistical fluctuations, whose efficiency in triggering nucleation increases dramatically in a narrow range of supersaturation. The kinetics of nucleation are extremely important when the synthesis of highly dispersed materials is considered. A detailed discussion of these aspects and the relevant literature are given in the reviews by Marcilly [1] and Marcilly and Franck [2]. The importance of nucleation and growth phenomena in solid-state reactions in catalyst preparation will be discussed briefly in the next section. Their vital role and the different ways to control them during the preparation of supported catalysts is discussed in Sections 4.6 and 4.9. General surveys of solid-state reactions involved in catalyst preparation or production can be seen in Courty et al. [3], Courty and Marcilly [4, 5], and Delmon and de Keyser [6]. Several aspects of this subject are also covered and updated in the International Symposia on Scientific Bases for the Preparation of Heterogeneous Catalysts, held in 1975, 1978, and then every 4 years at Louvain-la-Neuve, Belgium [7–12].

The thermodynamics of formation and transformation of a solid phase into another are characterized by two aspects, both of them explaining the difficulty to produce solids of homogeneous composition. The more important of these is nucleation. The other is the tendency of certain components of the solid to diffuse to, or away from, surfaces. These aspects, however, cannot be considered in isola-

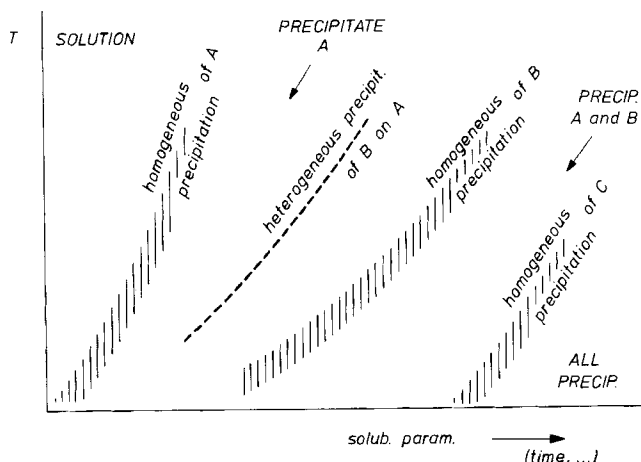
**Figure 2.** Schematic representation of the precipitation conditions for a given compound.



tion. Chemical reactions involve the breaking of bonds and formation of new ones. This involves kinetically limited processes. In many cases, diffusion brings about additional kinetic limitations. The final result is the combination of the effects of all these processes.

Nucleation in solid-state reactions essentially obeys laws similar to those ruling the formation of solids from liquid or gases. The only difference is the enhanced role of diffusion limitations. The simpler case of nucleation from liquids will be sufficient for explaining the problems encountered in the formation of homogeneous solids in all cases.

Figure 2 is a kind of phase diagram with two intensive parameters: here they are the temperature  $T$  and any parameter (indicated as *solub. param.*) on which the solubility or dissociation constant depends. For example this could be the pH or the concentration of a reactant or a precipitating agent. It is also possible to use as coordinates two of these *solub. param.* parameters, holding the temperature constant. This diagram indicates the limits of concentration of a given compound or of a third component (or temperature) for which either a liquid solution or a solution containing a precipitated solid is observed. The line label *equilibrium* corresponds to the exact equilibrium curve separating the monophasic domain (upper left) from the biphasic domain (lower right). The special kinetics of nucleation ensure that, as explained above, the new phase is not formed for a small supersaturation unless a patch of surface of that phase is already formed; in that case, deposition can take place. In the absence of any solid surface, precipitation will only occur in supersaturation conditions represented by the curve "homogeneous precipitation". In truth this is not a curve, but a band, as actual deposition will depend on the rate at which the *solub. param.* changes. The upper left hand border of this band corresponds to so-called critical nucleation conditions, namely those below which no nucleation occurs. The dotted curve represents the conditions where precipitation can occur when a foreign surface is present, i.e. heterogeneous precipitation. The fact that this curve lies at an intermediary position is explained by the fact that the surface energy necessary for forming the precipitate is diminished in comparison to



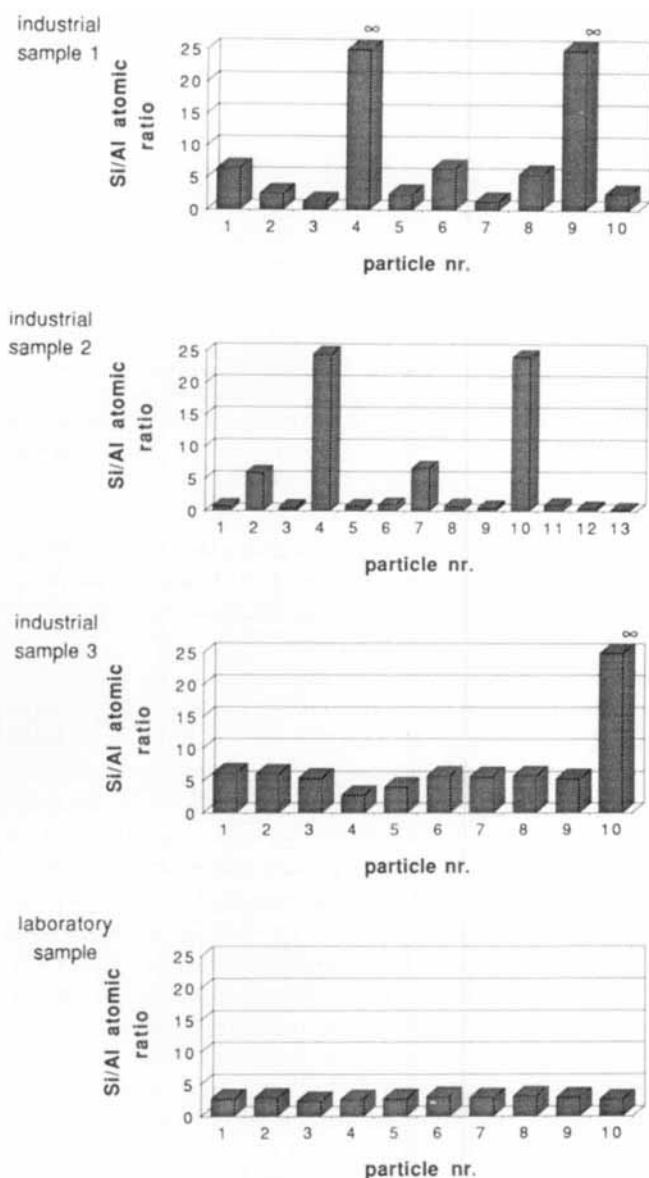
**Figure 3.** Schematic representation of precipitation from a solution containing the compounds A, B, and C.

homogeneous precipitation, but not zero as in the presence of a flat surface of the precipitating compound, i.e. at equilibrium.

Let us now consider a solution containing more than one compound. There will be as many curves of equilibrium, heterogeneous precipitation, and homogeneous precipitation as there are compounds. Figure 3 represents homogeneous precipitation for components A, B and C – a similar figure would represent the situation for the other curves of Fig. 2. The consequence is that the various compounds in a solution precipitate sequentially, namely bring about a segregation and create a solid of heterogeneous composition when the solub. param. changes (e.g. with time, in the direction of the arrow in Fig. 3). This can be very easily seen in coprecipitated silica–alumina, where pure silica is very frequently observed and considerable fluctuations of the Si:Al ratio by factors of 2 to  $\infty$  are measured over a distance of several tens of nanometers for the best, and several micrometers for most samples [13, 14]. Such measurements can be made by analytical microscopy, for example (Fig. 4). This shows that most available silica–aluminas are by no means homogeneous at the atomic scale.

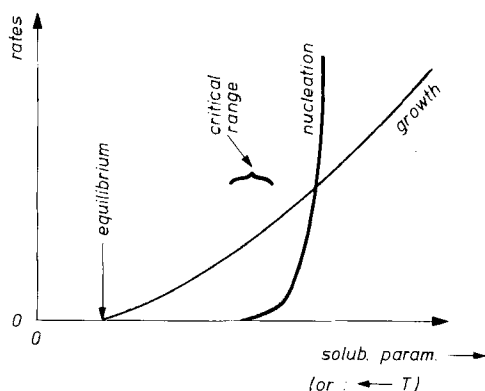
It is possible to increase the homogeneity by taking advantage of the difference in the form of the kinetic laws corresponding to nucleation, on the one hand, and growth of precipitated crystallites, on the other hand. The basis for such attempts is represented schematically in Fig. 5 [15], corresponding to one given compound. On the right of the figure, the rate of nucleation will be very high in comparison to growth, and very tiny particles will be obtained. The situation represented on the left corresponds to large particles and even, below the critical limit for nucleation, to Ostwald ripening. At very high supersaturations of all compounds present in a solution, finely interdispersed particles will be formed. But this will not produce atomically homogeneous solids. Extremely rapid mixing can produce such finely interdispersed phases. Rapid cooling is generally unsuccessful, because diffusion in the liquid phase will considerably perturb the processes leading to nucleation.

When such strategies are used to produce approximately homogeneous solids, the other phenomenon mentioned above can occur, namely *heterogeneous precipitation* of one compound on the surface of the already formed precipitate of another phase.



**Figure 4.** Inhomogeneity of silica–aluminas prepared by various methods. A series of 17 commercial samples of silica–aluminas from seven different producers was submitted to microanalysis. All of them showed considerable fluctuations of composition at the scale of several tens of nanometers to several micrometers. These samples were prepared by coprecipitation or by the sol–gel method. It is not known whether some of these samples were prepared from alkoxides. Smaller but significant fluctuations at the micrometer scale were also observed for two laboratory samples prepared from alkoxides. The samples were dispersed in water with an ultrasonic vibrator. A drop of the resulting suspension was deposited on a thin carbon film supported on a standard copper grid. After drying, the samples were observed and analyzed by transmission electron microscopy (TEM) on a JEOL-JEM 100C TEMSCAN equipped with a KEVEX energy dispersive spectrometer for electron probe microanalysis (EPMA). The accelerating potential used was 100 kV.

First observed was the general aspect of the sample, looking at the whole grid. Then, different points were analyzed (2–3) of various particles (from 10 to 25). The diameter of the static spot was 0.2  $\mu\text{m}$ . The duration of each microanalysis (accumulation) varied between 60 and 240 s [13].



**Figure 5.** Qualitative comparison of the dependency of the rates of nucleation and growth of precipitate particle as a function of the solubility parameter (increasing from left to right) or  $T$  (opposite direction).

This is shown in Fig. 3, for the precipitation of compound B after A has already precipitated. This has given rise to severe misinterpretations of physico-chemical characterization of precipitated solids, especially when surface-sensitive techniques such as X-ray photoelectron spectroscopy (XPS) were used.

As indicated above, elementary thermodynamic considerations show that the creation of a surface is accompanied by a positive free-energy change. This leads to another phenomenon, one which takes place inside an already formed mixed oxide. In order to minimize the positive free-energy change, the solid component with the lowest free energy tends to migrate from the bulk to the surface [16, 17]. Since the migration of a constituent of a solid from its interior to its surface usually involves an activation energy barrier to be overcome, such a process necessarily requires a higher temperature. As a rule of thumb, the Tammann temperature (ca. half the melting temperature) is generally believed to be sufficient to make the atoms or ions in the bulk sufficiently mobile for bulk-to-surface migrations, while the Hüttig temperature (ca. one-third the melting temperature) is enough to make the species, which are already on the surface, sufficiently mobile to undergo agglomeration or sintering. Since working temperatures in catalytic processes often exceed the Hüttig temperatures of metals or oxides used as catalysts, one objective of catalyst preparation is to anchor the active species on to the catalyst/support and thus retard/prevent their free motion or migration under the process conditions. This is why homogeneous compound oxides may be useful for stabilizing the coordination of an oxide element and maintaining dispersion.

### 3.7.1.2 Section Objective

The previous part of this section makes clear that, unless a method is found to directly prepare a catalytic phase (usually an oxide) containing all the wanted metallic elements, and in the required proportions, some more indirect method should be selected. In general, however, direct preparation from the gas or liquid phase will be impossible for the reasons given above. It becomes necessary to resort to a two-step or multiple-step approach using at least one solid precursor.

Several cases need to be distinguished when an atomically homogeneous multi-element catalyst is required:

- (i) Direct preparation by various sorts of reactions (e.g. precipitation). There are very few examples. In practice, this is only possible if an anion, e.g. a molybdate, reacts with a cation to produce the precipitate. The stoichiometry is dictated by the chemistry of the reaction and has little flexibility.
- (ii) A two-step process, through preparation of another type of homogeneous solid of exactly the same composition (e.g. carbonate, hydroxide, oxalate or other precursors, for making finally, in a second step, an oxide) and solid-state reaction of this precursor.
- (iii) Preparation of a solid approximately homogeneous followed by solid-state transformation, hoping that a higher homogeneity will be achieved during this second step.

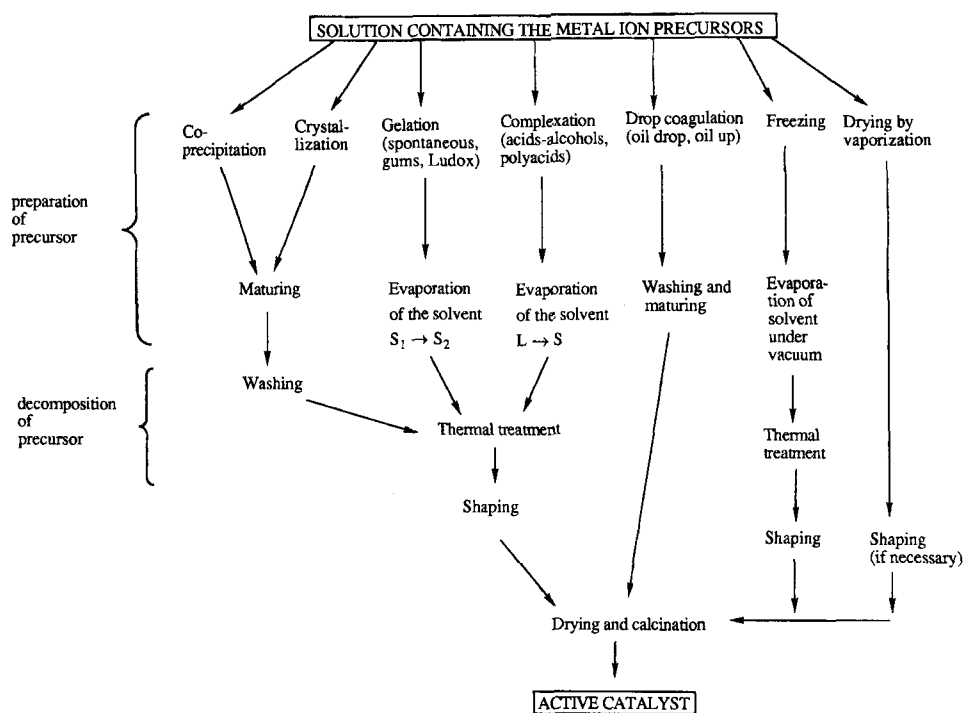
The first category is the subject of Section 3.5. Here, attention is given to the two other categories. Category (ii) corresponds to two different cases, those where the precursor is crystalline, and those where it is amorphous. However, the following discussion is organised according to the technique used, without distinguishing between (ii) and (iii) or whether it is crystalline or not. In each case comments are made on the potential of the technique to produce atomically homogeneous solid precursors.

The details concerning the transformation of the precursors to the final catalysts are mentioned in each case. However, a general comment has to be made here which is that the strategy consisting of starting from a homogeneous solid precursor and transforming it to the desired catalyst is only successful if diffusions in the solid state potentially leading to segregation are made difficult. This requires that only precursors decomposing to the final solid at low temperature, below the Tammann temperatures, be used. On the other hand, for reasons which cannot be presented here in detail, it is advantageous that the solid precursor decomposes with production of large quantities of gases. A coupling between the solid-state transformation and the formation of pores is necessary and the formation of pores is obviously promoted by the evolution of gases. Coupling effects in catalyst preparation are discussed in several articles [18, 19].

In practice, hydroxides, carbonates, hydroxycarbonates, nitrates, and salts of organic acids (oxalates, formates, citrates, etc.) satisfy both requirements. But there are potentially many other possible compounds; some examples are given.

### 3.7.2 Description of Preparative Methods

In very rare cases catalysts can be prepared by dry methods, namely reactions in the solid state. However, the most commonly used methods for preparation of mixed oxide catalysts start from a liquid (Fig. 6). Since complete mixing at the molecular level is possible in solution, a solution of all the concerned salts is often taken as the common starting material. One can essentially distinguish two steps in the proce-



**Figure 6.** General scheme of various methods for the preparation of unsupported catalysts (from Ref. 6).

ture: the preparation of a homogeneous solid precursor and the careful decomposition of this precursor to the oxide. For the first step, it is crucial to avoid the segregation of the oxide species into separate solid phases. This is usually achieved by:

- (i) physical methods such as evaporation to dryness, drying by vaporization, freeze drying, and crystallization – for the reasons explained above, the operation should be extremely rapid;
- (ii) a physico-chemical method like some gelation methods;
- (iii) chemical methods such as precipitation, coprecipitation, oil-drop, oil-up, and complexation. Oil-drop and oil-up involve processes pertaining to categories (ii) and (iii) above.

### 3.7.2.1 Dry Methods

One common method to prepare mixed-oxide catalysts is to grind or ball-mill them together, either dry or in a wet slurry; this is followed by calcination to temperatures of 900–1300 K. The operation may be repeated several times. Catalysts for the styrene process are generally prepared in this way from KOH and oxides of Fe and



**Table 2.** Hydroxycarbonate precursors for Cu/Zn/Cr catalysts.

Phase	Formula
Hydrotalcite-type phase	$M_6^{2+}M_2^{3+}(\text{OH})_{16}\text{CO}_3 \cdot 4\text{H}_2\text{O}$ $M^{2+} = \text{Cu}^{2+}, \text{Co}^{2+}, \text{Zn}^{2+}, \text{Mg}^{2+}$ $M^{3+} = \text{Al}^{3+}, \text{Cr}^{3+}, \text{Fe}^{3+}$
Malachite-type phase (rosasite)	$\text{Cu}_{2-x}^{2+}\text{Zn}_x^{2+}(\text{OH})_2\text{CO}_3$
Copper–zinc hydroxycarbonate (aurichalcite)	$\text{Cu}_{5-x}^{2+}\text{Zn}_x^{2+}(\text{OH})_6(\text{CO}_3)_2$

Cr and other (proprietary) promoter components. The solid–solid reaction during calcination can be accelerated by priming or catalyzing by a little of the product premixed with the reactant oxides. Ammonia synthesis catalysts which are prepared by mixing the components in the molten state does not pertain to this section, strictly speaking. A fluid energy mill, operated with steam injection at 670–970 K and 5–15 bar steam pressure, is applied in some cases. Some other techniques, used only rarely, are dry chemical oxidation of alloys, and electrolytic deposition.

The calcination step can sometimes have a more subtle importance than is generally realized. For instance, at a calcination temperature of 870 K, a promoter such as Li can be mixed to modify a catalyst such as  $\text{TiO}_2$ , whereas at 1200–1300 K it can be incorporated into the lattice structure of  $\text{TiO}_2$ . For the former, optimum performance in the oxidative coupling of methane (OCM) is shown at 17 wt %  $\text{Li}_2\text{O}$  loading and its catalytic activity for OCM dropped by a factor of five after 2 days on stream [20, 21]. For the catalyst calcined at 1200–1300 K, the optimal  $\text{Li}_2\text{O}$  loading was only 1–2 wt %; it is active for OCM at higher temperatures and its stability over several days was much better [22].

In general, the methods described in this subsection give solids with a low surface area.

### 3.7.2.2 Wet Methods

#### A Coprecipitation

The most common method for mixed-oxide catalyst preparation is crystallization or precipitation or coprecipitation in solution of a precursor form (hydroxide, oxide, insoluble salt) of the catalyst. Other specific steps, for example either addition of an extra component or its removal by partial extraction, may sometimes be necessary to adjust the final catalyst composition and ensure homogeneity.

One of the most studied cases, and also the most successful, was that of hydroxycarbonate for preparing catalysts containing copper and zinc or chromium with additional elements (e.g. Co or Al). The reason for these studies was the practical importance of catalysts used for making synthesis gas and methanol. Table 2 [5], which gives the composition of various precursors with their structure, suggests the mixed oxides which could be formed by decomposition. Additional data can be found elsewhere [5, 23–26].

As discussed earlier, precipitation (or simple crystallization) involves two main

steps, nucleation and growth. At the nucleation stage, the first minute crystals of the solid phase are formed; these have a high specific surface area and high surface energy, and hence are unstable. Below a certain critical nuclei size, the free energy of formation of the solid phase is less than its surface energy and the new phase is thermodynamically unstable. Above this critical size, the solid particles can grow. According to the conditions, this growth step is mainly controlled by interface or diffusion phenomena. The first case generally corresponds to the formation of complicated solid structures. The second is more common in the precipitation processes used in catalyst preparation. An overview is given in references given previously [1, 2, 15]. An excellent detailed treatment of nucleation and growth phenomena can be cited [27]. Only more general statements or rules of thumb can be given here.

For nucleation:

- (i) the higher the supersaturation, the higher will be the nucleation rate;
- (ii) any interface may play the role of a heterogeneous nucleus by lowering the surface free-energy of the new phase, and thus increase the rate of nucleation;
- (iii) in general, higher temperatures lower the nucleation rate by increasing the critical size of the nuclei – the upper left boundary of the homogeneous nucleation band reflects this trend.

All this has been represented schematically in Fig. 2.

For growth:

- (i) the higher the supersaturation the higher will be the growth rate, but it is rapidly limited by diffusion processes;
- (ii) since an increase of temperature enhances the diffusion rates, the higher the temperature, the higher will be the growth rate of the new phase.

Combining the above guidelines, and considering Fig. 5, some general rules for obtaining a fine precipitate can be formulated:

- (i) A vigorous stirring of the solution while adding the precipitant is beneficial in two ways: first, each elementary volume of solution reaches rapidly the highest degree of supersaturation; second, it comes into contact several times with the agitator and the walls of the vessel, thereby promoting heterogeneous nucleation also.
- (ii) A rapid addition of the precipitating agent ensures a rapid reaching of the highest degree of supersaturation in the whole volume of the solution, hence a maximum nucleation rate is obtained. For the same reason, the best precipitating agent is the one giving the precipitate with the lowest solubility product.
- (iii) Although the situation may be very different from case to case, precipitation is often advantageously made at the lowest practical temperature, as this often favors nucleation over growth.

In the coprecipitation process, the multi-element product can be of 3 types:

- (i) Metals combined in an insoluble single compound, for instance  $\text{BaTiO}_3$ , can be obtained by precipitation of a hydrated oxalate and subsequent thermal decomposition of this oxalate ( $\text{BaTiO}(\text{C}_2\text{O}_4)_2 \cdot 4\text{H}_2\text{O}$ ). Other instances are precipitations as chromates, molybdates, and tungstates.
- (ii) Some metals precipitate into a single-phase solid solution or a single-phase mixed structure, e.g. precipitation by sodium carbonate of aluminates or hydroxyprecursors of aluminates of Cu, Fe, Ni, Zn, and Mg. Divalent metal oxalates can also be precipitated in this way [28].
- (iii) Some metals precipitate more or less simultaneously, but in separate phases, e.g. metal hydroxides precipitated by NaOH, KOH, and  $\text{NH}_4\text{OH}$ . Normally,  $\text{NH}_4\text{OH}$  is preferable for precipitation, especially when washing off all alkali from the catalyst is a prerequisite for the preparation of the final catalyst. An exception to this is when  $\text{NH}_4\text{OH}$  can form ammino complexes as with transition metals (Ni, Co, Cu, Zn).

Tables 3 to 7 constitute partial lists of mixed salts which have been claimed to be obtained by coprecipitation: dashes join the symbols of elements which can be associated.

### B Spray Drying, Spray Calcination

Spray drying is a versatile method which can produce mixtures of phases with a high degree of interdispersion and a relatively high degree of homogeneity, although there is, in principle, no atomic level homogeneity. This is essentially an improved evaporation method.

Very often, slow evaporation of a homogeneous solution of two precursor salts, e.g.  $\text{MgSO}_4$  and  $\text{Al}_2(\text{SO}_4)_3$ , leads to segregations of the two salts in the solid phase. To prevent this, it is advantageous to eliminate rapidly the solvent, either by spray drying or hot petroleum drying. Spray drying can also be used with the active phase, for removing water. In certain cases, the temperature in the equipment can be raised enough to permit the reaction between the salts to produce an oxide combining two metallic elements. This has been done from solutions of  $\text{MgSO}_4$  and  $\text{Al}_2(\text{SO}_4)_3$  to make highly dispersed  $\text{MgAl}_2\text{O}_4$ . The success of the method, in this case, is the very small size of the crystallites obtained by rapid drying and their excellent interdispersion, this promoting solid-state reactions at the higher temperature.

This technique is used industrially to produce powders for the fabrication of ceramics [29]. Mainly single-metal oxides are made in this way, but it is claimed that  $\text{MnFe}_2\text{O}_4$ ,  $\text{NiFe}_2\text{O}_4$ ,  $\text{NiAl}_2\text{O}_4$ , dopant-stabilized zirconium oxide and titanates can be obtained. Powders of surface area up to  $20 \text{ m}^2 \text{ g}^{-1}$  can be produced. The powder is usually in the form of aggregates of  $0.2\text{--}0.4 \mu\text{m}$  in the best cases, but often of over  $100 \mu\text{m}$  in diameter [29].

By use of this technique, it is possible to prepare fine spherical catalyst particles in the  $10\text{--}100 \mu\text{m}$  diameter range, as are required for typical fluidized-bed catalytic processes. In this technique used for large-scale catalyst manufacture, the feed is generally dilute hydrogel or sol that is sprayed from the top of a tower while hot air is blown in a cocurrent or countercurrent direction to dry the droplets before they reach the bottom of the tower. The fine droplets are produced or atomized by

**Table 3.** Precursors associating elements of identical valency: inorganic compounds (adapted from Ref. 6).

Valency	Hydroxides	Carbonates	Nitrates	Sulphates		
				Simple	Schoenites	Alums
I		Li-Na, Li-K, Na-K, K-Ag	Na-Ag, K-Ag, Ag-Rb, Ag-Tl	Li-Na, Li-K		
II	Mg-Mn-Fe-Co-Ni, Zn-Cd-Sn	Mg-Mn, Mn-Co, Mn-Zn, Mg-Fe-Ni-Zn-Cd, Sn-Pb rare earth		Mg-Mn-Fe-Co-Ni-Cu Zn-Cd rare earth metals, Ce-Th	Mg-Mn-Fe-Co-Ni-Cu	
III	Cr-Fe, Al-Cr-Fe-Tl-Re		Al-Fe, Al-Cr, Cr-Fe			Al-Ti-V-Cr-Mn, Fe-Co-Ga
IV	Ti-Zr-Sn-Ce-Ta-Th			Zr-Ce-Th		
V	Nb-Ta					
VI	Mo-W					



**Table 5.** Precursors associating elements of different valencies: inorganic precursors (adapted from Ref. 6).

Valency	II	III	IV	V	VI
I	carbonates Co-Na, Co-K, Ni-Na, Ni-K nitrates Zn-alkali metals sulphates (schoenites) Mg-Na	carbonates Al-K, Ce-Na nitrates rare earth-alkali metals sulphates (alums) Me <sup>III</sup> -alkali metals	carbonates Ce-alkali metals nitrates Ce-alkali metals sulphates U-alkali metals	alkali metals vanadates	alkali metal chromates, Ag chromate, alkali metal molybdates and tungstates
II		hydroxides Al-Ni nitrates rare earth-Mg, Bi-Mg sulphates Cr-Mg, Cr-Mn, Cr-Fe, Cr-Zn	nitrates Ce-Mg, Ce-Zn	Cu vanadate	alkaline earth chromates, molybdates, and tungstates
III			hydroxides Zr-Nd	Cr vanadate	Fe chromate, rare earth chromates and molybdates, Bi molybdate
IV				uranyl vanadate	Zr chromate, Th chromate, Th molybdate

**Table 6.** Precursors associating elements of different valencies: organic precursors (adapted from Ref. 6).

Valency	II	III	IV	V	VI
I	formates Sn-alkali metals oxal. compl. (Be, Mg)-alkali metals malonates Be-Na, Be-K, Co-K succinates Mg-K, Co-K, Ni-K, Zn-K, Pb-K maleates Cu-K tartrate Fe-Na, Co-Na, Ni- Na, Cu Na, Zn-Na, Pb-Na crystallized citrates	formates Cr-Na, Cr-Ag oxal. compl. M <sup>III</sup> -alkali metals; M <sup>III</sup> = Al, Ti, V, Cr, Fe, Co, Ga malonates Cr-Na, Cr-K, Mn-Li, Mn-Na, Mn-K, Fe-K, Fe-Rb, Fe-Tl, Co-K, Rh-K tartrates Al-K-Na, Cr-K, Mn- Li, Mn-Na, Mn-K, Fe Na, Sb-Ag, Ce-Na, Bi-Na, Bi-K crystallized citrates	formates (Sn or Th)-alkali metals oxal. compl. M <sup>IV</sup> -alkali metals; M <sup>IV</sup> = Zr, Hf, Th or U maleates Zr-K crystallized citrates	malonates VO-alkali metals and Ag tartrates VO-Na, VO-K crystallized citrates	formates Mo-Na, Mo-K malonates U-Na tartrates Mo-Na, Mo-K, W-Na crystallized citrates
II		acetates Cr-Fe, Ca-Au, Pb Au oxal. compl. Al-Mg, Cr-Mg, Fe-Ba malonates Cr-Ba tartrates Al-Ca, Sb-Co, Sb-Ba, Sb-Pb	formates Th-Sr, Th-Ba	malonates VO-Ca, VO-Sr, VO-Ba, VO-Tl, VO-Pb	formates Cr <sup>VI</sup> -Ca acetates U-Fe, U-Ni, U-Zn oxal. compl. Mo-Ba tartrates Mo-Mg crystallized citrates acetates Cr <sup>VI</sup> -Ce
III			crystallized citrates		

**Table 7.** Crystallized mixed citrates (C. Marcilly, unpublished results).

Valency I	II	III
I		
Li <sub>2</sub> Na(C <sub>6</sub> H <sub>5</sub> O <sub>7</sub> )		
Li <sub>2</sub> K(C <sub>6</sub> H <sub>5</sub> O <sub>7</sub> )		
Na <sub>3</sub> K <sub>3</sub> (C <sub>6</sub> H <sub>5</sub> O <sub>7</sub> ) <sub>2</sub> · 6.5H <sub>2</sub> O		
II		
CaAg <sub>2</sub> (C <sub>6</sub> H <sub>4</sub> O <sub>7</sub> ) · 0.5H <sub>2</sub> O	Ca <sub>2</sub> Cu(C <sub>6</sub> H <sub>5</sub> O <sub>7</sub> ) <sub>2</sub> · 9H <sub>2</sub> O	
FeNa(C <sub>6</sub> H <sub>5</sub> O <sub>7</sub> )		
CoK(C <sub>6</sub> H <sub>5</sub> O <sub>7</sub> ) · 4H <sub>2</sub> O		
CoK <sub>4</sub> (C <sub>6</sub> H <sub>5</sub> O <sub>7</sub> ) <sub>2</sub>		
CuK <sub>10</sub> (C <sub>6</sub> H <sub>4</sub> O <sub>7</sub> ) <sub>3</sub> · 12H <sub>2</sub> O		
ZnNa <sub>2</sub> (C <sub>6</sub> H <sub>4</sub> O <sub>7</sub> )		
ZnNa <sub>6</sub> (C <sub>6</sub> H <sub>4</sub> O <sub>7</sub> ) <sub>2</sub>		
III		
2HBO <sub>2</sub> + KC <sub>6</sub> H <sub>7</sub> O <sub>7</sub> + C <sub>6</sub> H <sub>8</sub> O <sub>7</sub>	2HBO <sub>2</sub> + Mg (C <sub>6</sub> H <sub>7</sub> O <sub>7</sub> ) <sub>2</sub>	Ce[Nd(C <sub>6</sub> H <sub>5</sub> O <sub>7</sub> ) <sub>2</sub> ] · 3H <sub>2</sub> O
2HBO <sub>2</sub> + K <sub>2</sub> C <sub>6</sub> H <sub>7</sub> O <sub>7</sub>	HBO <sub>2</sub> + Mg(C <sub>6</sub> H <sub>7</sub> O <sub>7</sub> )	
3HBO <sub>2</sub> + K <sub>3</sub> C <sub>6</sub> H <sub>5</sub> O <sub>7</sub>	6HBO <sub>2</sub> + Mg <sub>3</sub> (C <sub>6</sub> H <sub>5</sub> O <sub>7</sub> ) <sub>2</sub>	
Na <sub>3</sub> H <sub>3</sub> [Fe <sub>2</sub> (C <sub>6</sub> H <sub>4</sub> O <sub>7</sub> ) <sub>3</sub> ]	Ca <sub>3</sub> [La(C <sub>6</sub> H <sub>5</sub> O <sub>7</sub> ) <sub>2</sub> ] <sub>2</sub>	
FeK <sub>6</sub> (C <sub>6</sub> H <sub>5</sub> O <sub>7</sub> ) <sub>3</sub>	Ca <sub>3</sub> [Nd(C <sub>6</sub> H <sub>5</sub> O <sub>7</sub> ) <sub>2</sub> ] <sub>2</sub>	
Fe <sub>2</sub> K <sub>6</sub> (C <sub>6</sub> H <sub>4</sub> O <sub>7</sub> ) <sub>3</sub>		
K <sub>3</sub> [La(C <sub>6</sub> H <sub>5</sub> O <sub>7</sub> ) <sub>2</sub> ]		
Na <sub>3</sub> [Nd(C <sub>6</sub> H <sub>5</sub> O <sub>7</sub> ) <sub>2</sub> ]		
K <sub>3</sub> [Nd(C <sub>6</sub> H <sub>5</sub> O <sub>7</sub> ) <sub>2</sub> ]		
(AsO)Na <sub>3</sub> (C <sub>6</sub> H <sub>5</sub> O <sub>7</sub> ) <sub>2</sub> · 3.5H <sub>2</sub> O		
(AsO)K <sub>3</sub> (C <sub>6</sub> H <sub>5</sub> O <sub>7</sub> ) <sub>2</sub> · 4.5H <sub>2</sub> O		
(SbO)Na <sub>3</sub> (C <sub>6</sub> H <sub>5</sub> O <sub>7</sub> ) <sub>2</sub> · H <sub>2</sub> O		
(SbO)K <sub>3</sub> (C <sub>6</sub> H <sub>5</sub> O <sub>7</sub> ) <sub>2</sub> · 2H <sub>2</sub> O		
NaBi(OH) C <sub>6</sub> H <sub>5</sub> O <sub>7</sub> · 3H <sub>2</sub> O		
KBi(OH) C <sub>6</sub> H <sub>5</sub> O <sub>7</sub> · 3H <sub>2</sub> O		
Na(BiO) <sub>2</sub> C <sub>6</sub> H <sub>5</sub> O <sub>7</sub>		
Bi C <sub>6</sub> H <sub>5</sub> O <sub>7</sub> + 6Na <sub>3</sub> (C <sub>6</sub> H <sub>5</sub> O <sub>7</sub> )		
Na(BiO) <sub>2</sub> (C <sub>6</sub> H <sub>5</sub> O <sub>7</sub> )		
amorphous		
IV		
(NaTiO <sub>2</sub> ) <sub>3</sub> C <sub>6</sub> H <sub>5</sub> O <sub>7</sub>		[Cr <sub>3</sub> (C <sub>6</sub> H <sub>5</sub> O <sub>7</sub> ) <sub>2</sub> ](OH) <sub>2</sub> ] <sub>2</sub> PtCl <sub>6</sub> · 10H <sub>2</sub> O
(TiO)K <sub>2</sub> (C <sub>6</sub> H <sub>6</sub> O <sub>7</sub> ) <sub>2</sub> · H <sub>2</sub> O		
ZrK <sub>3</sub> H (C <sub>6</sub> H <sub>4</sub> O <sub>7</sub> ) <sub>2</sub> · 9.5H <sub>2</sub> O		[Fe <sub>3</sub> (C <sub>6</sub> H <sub>5</sub> O <sub>7</sub> ) <sub>2</sub> ](OH) <sub>2</sub> ] <sub>2</sub> PtCl <sub>6</sub> · 10H <sub>2</sub> O
V		
(VO <sub>2</sub> )Ag <sub>3</sub> C <sub>6</sub> H <sub>4</sub> O <sub>7</sub>		
(VO) <sub>2</sub> Na <sub>4</sub>		
(C <sub>6</sub> H <sub>5</sub> O <sub>7</sub> ) <sub>2</sub> O · 12H <sub>2</sub> O		
(VO) <sub>2</sub> K <sub>4</sub>		
(C <sub>6</sub> H <sub>5</sub> O <sub>7</sub> ) <sub>2</sub> O · 12H <sub>2</sub> O		
[MSb(C <sub>6</sub> H <sub>5</sub> O <sub>7</sub> ) <sub>2</sub> (H <sub>2</sub> O)]		
[M <sub>3</sub> Sb(C <sub>6</sub> H <sub>5</sub> O <sub>7</sub> ) <sub>2</sub> (H <sub>2</sub> O)]		
M = Na or K		
VI		
(MoO <sub>2</sub> )Na <sub>2</sub> (C <sub>6</sub> H <sub>6</sub> O <sub>7</sub> ) <sub>2</sub>	(MoO <sub>2</sub> )Ba(C <sub>6</sub> H <sub>6</sub> O <sub>7</sub> ) <sub>2</sub> · 5H <sub>2</sub> O	
(MoO <sub>2</sub> )K <sub>2</sub> (C <sub>6</sub> H <sub>6</sub> O <sub>7</sub> ) <sub>2</sub>		
(WO <sub>2</sub> )Na <sub>3</sub> H(C <sub>6</sub> H <sub>6</sub> O <sub>7</sub> ) <sub>3</sub> · 0.5H <sub>2</sub> O	(WO <sub>2</sub> ) <sub>2</sub> Ba <sub>3</sub> H <sub>2</sub> (C <sub>6</sub> H <sub>6</sub> O <sub>7</sub> ) <sub>6</sub> · 10H <sub>2</sub> O	
(WO <sub>2</sub> )K <sub>3</sub> H(C <sub>6</sub> H <sub>6</sub> O <sub>7</sub> ) <sub>3</sub> · 0.5H <sub>2</sub> O		



pumping the hydrogel or sol under pressure either through nozzles or onto wheels or discs rotating at a high speed. The method is also convenient to embed crystalline particles of micron or submicron size in an amorphous matrix of 10–100  $\mu\text{m}$  diameter. The best known examples are to embed multicomponent bismuth molybdates in 50% silica matrix for ammoxidation of propylene to acrylonitrile, and to incorporate  $<1\text{--}3\text{ }\mu\text{m}$  zeolite crystallites in amorphous silica-alumina/clay matrix for fluid catalytic cracking (FCC) catalysts. The use of spray drying for making atomically homogeneous mixed oxide does not seem to have gone beyond the development stage.

### **C Hot-Petroleum Drying**

Hot-petroleum drying constitutes an alternative to spray drying. It was developed by Reynen and Bastius [30], initially for small-scale preparations. However, the development of what industry improperly calls the sol–gel method, namely integrated conventional precipitation and gelling, makes it now a large scale preparation method. The principle consists in dropping a fluid material containing the active elements in kerosene. This fluid material may be a gel, a solution in the course of gelling, a stabilized emulsion of a salt solution and kerosene, or an aqueous solution of salts. The temperature of the kerosene bath is maintained at about 440 K. The kerosene bath may be vigorously agitated if necessary. The water evaporates and the powder or, according to processes, the small solid spheres obtained are easily filtered and dried at around 520 K. The product is a free-flowing powder consisting of a homogeneous mixture of salts. The hot-petroleum drying method, contrary to the spray-drying variant (called spray calcination) does not permit the solid-state reactions needed to form the oxides, but the highly dispersed and intermixed salts can be thermally decomposed without phase segregations. Just as spray drying, this method is also dependent on the evaporation of water being faster than the segregation phenomena. The controlling factors are thus the temperature of the hot kerosene and the rate of water evaporation from the droplets. The advantages of this method are the simple setup, the kerosene can be recycled, and the energy consumption is lower than that for spray drying.

### **D Freeze Drying**

Freeze drying corresponds to the same purpose as both above-mentioned methods, but the strategy is different. In order to limit segregation, it is the diffusion process that is slowed down. This can be achieved either by rapid cooling (freeze drying) or by increasing the viscosity of the solution (by some of the methods described below, addition of hydroxycellulose or gums, for example; this increase of viscosity also plays a role in the more elaborate amorphous citrate process described in the next subsection).

Undercooling is the driving force in freeze drying. An aqueous salt solution is introduced dropwise into an immiscible liquid (hexane or a petroleum fraction such as kerosene) cooled below 243 K. The individual droplets are frozen instantaneously and the solid particles are decanted or filtered. The frozen particles are then sublimed in a vacuum to obtain a homogeneous powder of fairly uniform particle size. Important parameters in freeze drying are the final temperature of the salt solution

and the cooling rate. These can be controlled to some extent, but only on a small scale. Hence the method is not very suited for large-scale manufacture of catalysts.

### 3.7.2.3 Chemical Complexation Methods

#### A Crystalline Complex Salts

Oxalates [31], tartates [32], and citrates [33] (Tables 4 and 6) of various metals can form well-crystallized complex salts, e.g.  $\text{Mg}(\text{NH}_4)_4(\text{Al}_x\text{Cr}_{1-x}(\text{C}_2\text{O}_4)_3)_2 \cdot n\text{H}_2\text{O}$ , which on thermal decomposition at moderate temperatures can yield mixed oxides. Although these complex salts permit substitution in large ranges, or even in all proportion in some cases of elements of the same volumes, their stoichiometry is still rather rigid and this imposes a serious limitation on any wide applicability of this method. This limitation is conspicuous when comparing the chemical formulas of crystallized citrates (Table 7) [29] with the very flexible composition of the compounds which will be described in the next subsection. The same remark holds when oxalate complexes are considered:  $\text{M}^{\text{I}}(\text{NH}_4)_4[\text{M}^{\text{III}}(\text{C}_2\text{O}_4)_3]_2 \cdot n\text{H}_2\text{O}$ , where  $\text{M}^{\text{I}}$  and  $\text{M}^{\text{III}}$  both represent a single metal or a mixture of metals or ions (e.g. VO) of the corresponding valency. The problem is further complicated due to the possibility of non-homogenization or phase separation during the chain of downstream unit operations involved in catalyst production. The amorphous complex method, described next, provides an escape from most of these difficulties.

#### B Amorphous Precursor “Citrate” Method: General

The principle of this method consists of preparing a stable amorphous or glassy precursor which, thanks to this amorphous structure, tolerates an enormously wide range of composition. The starting solution is a mixture of metallic salts and a hydroxy acid such as citric, malic, tartaric, lactic, or glycolic acid [3, 34–36]. The metals are preferably in the form of nitrates or ammonium salts, which will not leave any residues on thermal decomposition at a later stage and the decomposition of the nitrate and ammonium ions promotes surface area and porosity, due to the large amount of gas the decomposition evolves. Typical concentrations are 1 g equivalent organic acid per equivalent of total metal content. The solution is concentrated by rapid evaporation under vacuum, for instance in a Rotavapor, until its viscosity exceeds 500 cP at ambient temperature. A very stable syrup is obtained in this way. It can be dehydrated under vacuum at about 350 K to a rigid-foam (meringue) precursor, which is amorphous to X-rays, hygroscopic, and exhibits the color of the metallic ions present. The amorphous precursor appears to be some sort of a three-dimensional polymer in which the multifunctional organic acids are linked to two or more cations. The thermal decomposition of the amorphous mass may proceed more or less continuously or in two distinct steps at 350–370 K and 520–670 K. Because of the danger of violent reactions, this decomposition step is to be carried out very carefully, taking all necessary precautions. The preparation of oxides containing metallic ions highly active in oxidation needs very stringent precautions and is generally not advisable. In particular, the possible detonation of copper and silver salts should be borne in mind. In these cases, the freshly formed

metal particles could be powerful catalysts for some unexpected reactions, e.g. with ammonia. Also, secondary reactions can occur even at room temperature resulting in the formation of a small amount of lethal cyanogen gas. Clearly, this is not a method to be tried by students or inexperienced researchers.

The mechanisms of reactions occurring during preparation of mixed oxides by the citrate methods have been outlined in some detail [37]. In the dehydration under vacuum, extensive loss of nitrate ions (in the form of various nitrogen oxides and ammonium nitrate) occur together with the loss of water. Although easier in the presence of citric acid, the decomposition of nitrate does not involve extensive reaction with the latter below 380 K. The semidecomposed precursor obtained around 410 K is essentially a dehydrated, amorphous, highly porous mixed citrate. The higher temperature decomposition stage, mainly between 500 and 670 K, consists of the burning of citric acid by oxygen. It is facilitated because of the presence of nitrate ions in the initial precursor. As indicated above, this stage is catalyzed by the presence of metals whose oxides are oxidation catalysts. Additional details can be found in Refs 5 and 37.

Mixed oxides obtained by the above method are very lightweight powders of apparent density only  $<0.05 \text{ g cm}^{-3}$ , amorphous to X-rays, free flowing, and consist of aggregates of particles of 20–100 nm. Upon further heating, these oxides crystallize into various well-defined structures depending on the nature and composition of the starting materials: solid solutions, spinels, perovskites, garnets [3]. Variants of the citrate method consist of simply adding citric acid or other hydroxymultifunction acids to solutions used by other methods (precipitation, impregnation, sol–gel, etc.). Although not leading to such excellent results as the original citrate method, the result of such a use of hydroxyacid corresponds to substantial improvement. An improved citrate method has been proposed in which a polyalcohol is added to the initial solution [38]. The polyalcohol is supposed to promote the reticulation in the transformation of the starting solution to the rigid foam. The reticulation or polymer formation is due to the esterification reaction between citric acid and the polyalcohol. This method has been used for the preparation of barium titanates doped by a large variety of ions, but apparently not for preparing catalysts.

Considering the case of crystalline complex salts and the amorphous precursor method, both chemical complexation methods have found important and innovative applications in recent years for the preparation of a wide variety of catalysts and of various perovskite-type catalysts and barium hexaaluminates, as required for high-temperature ( $>1500 \text{ K}$ ) applications such as catalytic combustion. It is therefore worthwhile describing some applications, in the next two subsections.

### C Citrate Method for the Preparation of Perovskite Catalysts

A general introduction to perovskites and their catalytic properties is given in the reviews by Tejuca et al. [39] and Yamazoe and Teraoka [40]. In general, perovskites have been prepared by calcining a solid mixture of constituent metal oxides or carbonates (the method used in the ceramic industry), or by evaporating an aqueous solution of constituent metal nitrates or acetates and by subsequent calcination. The resulting oxides have relatively small surface areas. Some methods which can give higher specific surface areas are listed in Table 8. The guiding principle here is to

**Table 8.** Methods of preparation of high-surface-area perovskites (adapted from Ref. 40).

Description	Preparation method
Control of evaporation (decomposition) process	freeze drying, spray drying, mist decomposition, explosion
Contrivance of precursor materials	coprecipitated oxalate decomposition, amorphous citrate decomposition, decomposition of solid solutions of cyanides and hydroxides

**Table 9.** Specific surface area of  $\text{LaCoO}_3$ , prepared by various methods (adapted from Ref. 40).

Preparation method	Final heat treatment <sup>a</sup>	Surface area ( $\text{m}^2 \text{g}^{-1}$ )
Ceramic methods	1523 K, 48 h	1.7
Oxalate decomposition	1273 K, 12 h	1.6
	1173 K, 15 h	4.5
Acetate decomposition	1123 K, 5 h	2.5
	1123 K, 5 h	2.2
Mist decomposition	973 K <sup>b</sup>	11.8
Citrate decomposition	973 K, 4 h	15.3
	873 K, 2 h	11.3
	973 K, 4 h	8.5
Cyanide decomposition	923 K, 4 h	37.5
Freeze drying	773 K, 10 h	36.2
Explosion	773 K, 10 h	34.6

<sup>a</sup> Temperature and period of calcination in air sufficient for obtaining a single perovskite phase.

<sup>b</sup> A mist of a mixed aqueous solution of cobalt and lanthanum nitrates was treated successively in a flow-type reactor equipped with three furnaces (443 K, 573 K, 973 K), and the residence time in a final furnace (973 K) was about 11 s.

attain as thorough a dispersion as possible, almost to a molecular level, of constituent components in the precursors prior to calcination. Once this is achieved, lower calcination temperatures can convert the precursors to the required perovskite structure of larger surface areas, as shown in Table 9.

Teraoka et al. [41, 42] have applied the amorphous citrate process to prepare unsupported (or neat) and supported perovskites of the type  $\text{LaMn}$ ,  $\text{LaCo}$ ,  $\text{LaMnCu}$ ,  $\text{LaCoFe}$ ,  $\text{LaCaCo}$ ,  $\text{LaCaMn}$ ,  $\text{LaSrMn}$ ,  $\text{LaSrCo}$ ,  $\text{LaSrCoCu}$ , and  $\text{LaSrCoFe}$ . The use of the citrate method for preparing atomically homogeneous oxides on supports has been a very important extension of the citrate method over the years. Nitrates of constituent metals of the required perovskite were dissolved in water and mixed with an aqueous solution of citric acid (molar ratio of citric acid to total metals 1:1). Water was evaporated from the mixed solution using a rotary evaporator at 330–340 K until a sol was obtained. The sol was further dehydrated at the same temperature under vacuum for 5 h. Stabilized alumina of composition  $\text{La}_2\text{O}_3 \cdot 19\text{Al}_2\text{O}_3$  was used as the support for the perovskites. For comparison,

**Table 10.** Specific surface area of perovskite-type catalysts, prepared by the citrate process and the acetate process (adapted from Ref. 41).

Sample	Citrate process		Acetate process	
	Calcination temp. (K)	Surface area (m <sup>2</sup> g <sup>-1</sup> )	Calcination temp. (K)	Surface area (m <sup>2</sup> g <sup>-1</sup> )
LaMnO <sub>3</sub>	923	44.8	1123	7.3
LaCoO <sub>3</sub>	873	11.3	1123	2.2
LaCo <sub>0.4</sub> Fe <sub>0.6</sub> O <sub>3</sub>	823	22.7	1123	3.3
LaMn <sub>0.6</sub> Cu <sub>0.4</sub> O <sub>3</sub>	873	33.0	1123	7.5
La <sub>0.8</sub> Sr <sub>0.2</sub> MnO <sub>3</sub>	873	36.4	1123	8.2
LaCo <sub>0.8</sub> Cu <sub>0.2</sub> O <sub>3</sub>	823	24.7	—	—
La <sub>0.6</sub> Ca <sub>0.4</sub> MnO <sub>3</sub>	873	33.0	—	—
La <sub>0.4</sub> Ca <sub>0.6</sub> CoO <sub>3</sub>	873	14.3	—	—

Teraoka et al. also prepared the above perovskites by an acetate process, instead of by the citrate process. The specific surface areas of the perovskites by the citrate and the acetate processes are compared in Table 10. The amorphous citrate precursor decomposed in three steps, the third decomposition at 820–920 K already inducing crystallization of perovskite-type oxides. The acetate process needed a higher calcination temperature of 1120 K and consequently produced samples the surface areas of which were only 1/3 to 1/7 of those of samples from the citrate process. The higher-area perovskites from the citrate process had higher catalytic activity for methane oxidation. For the preparation of supported perovskite catalysts also, the citrate process was more effective than the acetate process.

An improvement of the oxalate precipitation method for the preparation of LaSrCo perovskites has been reported recently by Chang and Weng [43]. By substituting ethanol for water in the washing of the perovskite precursors, the problems of chemical inhomogeneity and cobalt elution are both eliminated. This method is claimed to be an easier and quicker way to prepare a large variety of perovskites having high surface area, pore volume, and catalytic oxidation activity.

#### D Complex Cyanide Method

Very recently Geus and co-workers [44, 45] have applied another method based on chemical complexes. This is the complex cyanide method to prepare both mono-component (Fe or Co) and multicomponent Fischer–Tropsch catalysts. A large range of insoluble complex cyanides are known in which many metals can be combined, e.g. iron(II) hexacyanide and iron(III) hexacyanide can be combined with iron ions, but also with nickel, cobalt, copper, and zinc ions. Soluble complex ions of molybdenum(IV) which can produce insoluble complexes with metal cations are also known. Deposition precipitation (Section 4.6) can be performed by injection of a solution of a soluble cyanide complex of one of the desired metals into a suspension of a suitable support in a solution of a simple salt of the other desired metal. By adjusting the cation composition of the simple salt solution, with a same cyanide, it is possible to adjust the composition of the precursor from a monometallic oxide

(the case when the metallic cation is identical to that contained in the complex) to oxides containing one or several foreign elements.

Complex metal cyanides decompose at fairly high temperatures. Decomposition in an oxidizing atmosphere (up to 600 K) results in the corresponding oxides, that in an inert or in a reducing atmosphere (up to 900 K) results in the metals or alloys. In either case, reaction of the oxides or of the metals/alloy with the support is minimized. The complex cyanide method can thus establish homogeneity of the constituent ions on a molecular scale and also prevent undesired reactions of the active precursors with the support.

#### **3.7.2.4 Miscellaneous Methods for Obtaining Solid Precursors of Flexible Composition**

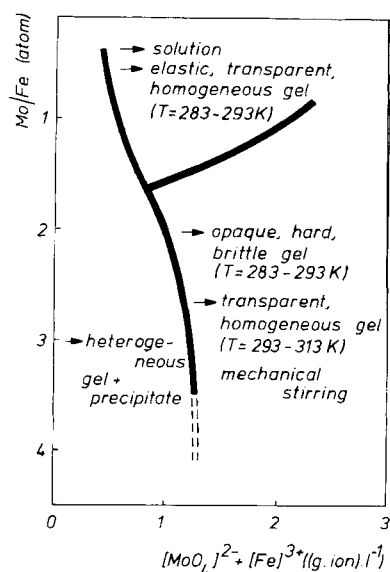
There are still other ways to avoid segregation of phases during the decomposition of a solid precursor to form an oxide.

One such method uses soluble gums or polymers. The principle is the same as in previously described methods. A solution containing all the desired elements is made very viscous by dissolving gums, or functional polymers. Hydroxymethylcellulose and similar structures have been used for this purpose. Usually, the viscous solution can be concentrated (e.g. by evaporation) with little or no crystallization or segregation, and calcined to a mixed oxide containing all the elements finely interdispersed.

Another very interesting method, although of limited application, is a kind of self-gelation. This occurs in the case of amorphous hydrated precipitates with a strong hydrophilic character that favors their interaction with the solution and transformation through tridimensional reticulation to a homogeneous hydrogel retaining the solution in its net. The only well characterized example is iron molybdate gels (pure or with additives) which were developed for the production of catalysts for the oxidation of methanol to formaldehyde [46–51]. Figure 7 [5] shows that gel formation only occurs in a narrow range of composition and operating conditions. The main parameters are the Mo:Fe ratio, the nature of the starting salts, the nature and amount of additives, the temperature, the concentrations, and the intensity of stirring. Aging increases reticulation and homogeneity; the hydrogel becomes hard and brittle (the fractured surfaces exhibit the aspect of glass fractures also commonly found in hydrogels). Depending on the concentrations and Mo:Fe proportions, a precipitate first forms, then partly or totally dissolves to give a gel. A true metastable solution is transiently formed for atomic ratios  $\text{Mo:Fe} \leq 1.5$  [5]. The aged gel is then dried to give a brown transparent, homogeneous xerogel containing less than 1 wt% water which produces the activated catalyst after calcination. This preparation method permits the introduction of many elements as doping agents. The gel may incorporate a large excess of molybdenum compared to the stoichiometry of  $\text{Fe}_2(\text{MoO}_4)_3$ .

It is not known whether this method can be extended to other systems. It could be speculated that all elements giving high molecular weight polyanions could

**Figure 7.** Formation of gels from iron molybdate precipitates [5]. A very fine colloidal precipitate forms in all cases but undergoes different changes suggested by the arrows, according to concentration and Mo:Fe proportions, as well as other conditions mentioned in the figure. In the upper part domain, the colloidal precipitate seems to dissolve to form a solution whose viscosity increases until formation of a gel. In the right-hand domain, the gel directly forms from the colloidal system but can become transparent if the reaction takes place in the temperature range 293–313 K.

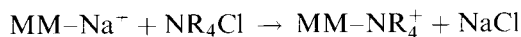


form similar gels when combined with cations carrying three or more positive charges.

### 3.7.2.5 Solid-State Ion Exchange for Zeolite Catalysts

Impregnation and ion-exchange methods for preparation of supported catalysts are discussed in detail in Section 4.1.1. Only ion exchange in the solid state as a novel method to prepare zeolite catalysts is described here.

Modification of zeolite catalysts can be achieved by solid-state reactions between zeolite and other crystalline phases. Thus, alkaline earth, rare earth, and transition metal cations can be introduced into A, X, Y, ZSM-5, beta and mordenite molecular sieves by means of solid-state ion-exchange reactions [52]. Other variations of this approach are solid-state reactions to form host–guest (supramolecular) complexes [53] and the intercalation of polar organic molecules into smectite clays [54, 55]. Still another development is the preparation of organoammonium montmorillonites by room-temperature ion exchange between sodium montmorillonite ( $\text{MM-Na}^+$ ) and solid organoammonium halides [56]:



This methodology has also been extended [57] to high-valent metal cations such as  $\text{Al}^{3+}$  and  $\text{Fe}^{3+}$ : a simple ball-grinding with the corresponding metal nitrate at ambient temperature in air yields the Al- or Fe-exchanged montmorillonite. Such products are interesting acid-clay catalysts, their Brønsted acidity arising mainly

from the dissociation of adsorbed water:



However, the large-scale preparation of such acid-clay catalysts was until recently hampered by two problems:

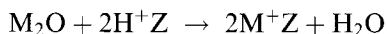
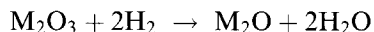
- (i) the tendency of clay suspensions to form gels at clay concentrations above about  $20 \text{ g l}^{-1}$ , which necessitates the use of a large volume of water;
- (ii) the difficulties of large-scale filtering of clay suspensions.

The solid-state ion-exchange reactions, which do not have such limitations, are proving to be an interesting, practical, and low-energy alternative to the preparation of clay catalysts.

Solid-state ion-exchange methods are also suitable for the preparation bifunctional catalysts, containing an acidic as well as a hydrogenation–dehydrogenation function. A typical example is Pd-loaded ZSM-5 [58]. Since a concomitant incorporation of  $\text{Ca}^{2+}$  gave a better catalyst, a two-step solid-state ion exchange could also be carried out, first with  $\text{CaCl}_2$  and then with  $\text{PdCl}_2$ . On subsequent reduction with  $\text{H}_2$ , a catalyst with a mean Pd particle size of about 2 nm was obtained with a strong and stable activity for both hydrogenation and hydroisomerization.

Ga-ZSM-5 catalysts have received considerable attention in recent years ever since the development of the Cyclar process by BP/UOP for aromatization of  $\text{C}_3$ – $\text{C}_4$  alkanes. Kanazirev et al. [59] have shown that this Ga-doping can be achieved by a mechanical mixing of  $\beta$ - $\text{Ga}_2\text{O}_3$  and HZSM-5 in the presence of hydrogen. The solid-state reaction proceeds through  $\text{Ga}_2\text{O}$  as an intermediate, which moves on to the HZSM-5 and gets trapped at the cationic positions in a still lower oxidation state, probably as Ga. This is a new route to high-quality catalyst preparation, without involving any wet-process step.

The above work prompted attempts [60] to incorporate other metals also into ZSM-5 by direct solid-state reactions. Thus, a long-distance transfer and fairly uniform distribution of indium in large ZSM-5 crystals occurs when powdered  $\text{In}_2\text{O}_3$  and ZSM-5 are loosely mixed and then subjected to reduction in hydrogen at a temperature as low as 623 K. Energy dispersive X-ray (EDX) analysis of  $\text{In}_2\text{O}_3$  distribution on ZSM-5 crystals varied between 2.8 and 3.6 wt %, with an average of 3.21 wt %. The reductive solid-state ion exchange with both Ga and In is proposed [60] to proceed as follows ( $\text{M} = \text{Ga}$  or  $\text{In}$ ;  $\text{Z} = \text{HZSM-5}$ ):



### 3.7.2.6 Specific Methods: Example of Hydrotalcite-type Catalysts

The example of hydrotalcite catalyst can serve to illustrate the fact that solids of given structures containing several elements in rather flexible proportions can be



obtained by different techniques. This example will also show that special techniques can be designed for the preparation of specific precursors.

Hydrotalcite (HT) is a clay mineral which on crushing becomes a fine powder, similar to talc. It is a hydroxycarbonate of Mg and Al, of the general formula  $\text{Mg}_6\text{Al}_2(\text{OH})_{16}\text{CO}_3 \cdot 4\text{H}_2\text{O}$ , and occurs in nature in foliated and controlled plates and/or fibrous masses. Anionic clays of the HT type have been of importance in catalysis since 1970. Their interesting properties for catalytic applications are:

- (i) large surface area;
- (ii) basic properties;
- (iii) formation of homogeneous mixtures of oxides with very small crystal size, which on reduction form small and thermally stable metal crystallites;
- (iv) a “memory effect”, which allows reconstruction under mild conditions of the original HT structure when the product of the thermal treatment is contacted with aqueous solutions containing various anions.

Cavani et al. [61], who reviewed this area extensively in 1991, emphasize that all the stages of preparation of a catalyst with a HT-type precursor need precise chemical control to avoid inhomogeneities and chemical segregation.

Three different methods of preparation have been tried so far for HT-type catalysts:

- (i) precipitation (increasing pH method or coprecipitation either at low or at high supersaturation);
- (ii) hydrothermal synthesis and treatments, also ageing;
- (iii) ion-exchange methods.

Since several cases and details for these preparation methods have been given in the review by Cavani et al. [61], only the preparation by Trifiro et al. [62] of a Ni catalyst for steam reforming will be cited here as an illustrative example. The HT-type precursors were prepared by coprecipitation at pH 8 by adding a solution of the nitrates of Mg and Al (or Cr) in the right proportions to a stirred solution of  $\text{NaHCO}_3$ . The precipitate was washed with distilled water till the  $\text{Na}_2\text{O}$  content in it was  $<0.02\%$  and then dried at 363 K. By heating the precipitate in air or vacuum in the range 623–1173 K, various catalysts could be prepared with average Ni crystallite sizes ranging from 2 to 100 nm. These catalysts contained a NiO phase, probably containing traces of  $\text{Al}^{3+}$  ions, a spine-type phase, and an alumina-type phase (doped with small amounts of  $\text{Ni}^{2+}$  ions), probably grafted onto the spinel-type phase. This last phase contributes significantly to the surface area of the catalyst samples, but it has little or no influence on their thermal stability or catalytic activity.

Applications of HT-type catalysts, prepared by the above methods, have been reported in recent years for basic catalysis (polymerization of alkene oxides, aldol condensation), steam reforming of methane or naphtha, CO hydrogenation as in methanol and higher-alcohol synthesis, conversion of syngas to alkanes and alkenes,

hydrogenation of nitrobenzene, oxidation reactions, and as a support for Ziegler–Natta catalysts (Table 2).

### 3.7.3 Conclusions and Prospects

In this section, the main topic has been the use of solid-state transformations to prevent segregation of the composition of solid precursors in a final oxide catalyst. On the whole, crystalline precursors do not permit the desired composition to be achieved, but they can be excellent for some specific cases. Amorphous precursors, especially those using polyfunctional hydroxy acids, of almost any possible composition can be prepared, and can give the corresponding oxides. The initial aim of the method was to prepare solid solutions or oxides of two or several elements in well-defined structures, sometimes containing element substituted within the normal lattice structure. Only one other method has been claimed to offer similar flexibility. This is the sol–gel method (Section 3.5). The two methods have still to be compared in detail. It seems, however, that the kinetics of hydrolysis change very much from one alkoxide to another, with the consequence that the different elements get incorporated in the gel sequentially during gel formation. This phenomenon has the same consequences as the successive precipitation of different elements mentioned above (Fig. 2), namely that the homogeneity of the gel at a molecular scale is not perfect.

When the objective is to prepare an extremely intimate mixture of two or more different oxides, each of them constituted of very small grains or particles, techniques such as spray calcination, oil drop, or freeze drying, the complexation methods (and generally all methods described in Sections B and C above) and the sol–gel method seem to have the same potential in principle. The use of a particular technique is then dictated by other considerations, such as the availability of starting material (especially for alkoxides) or ease of decomposition.

Finally, a word of caution should be added. The successful transformation of the precursors to a homogeneous oxide or a finely interdispersed mixture of oxides demands that diffusion leading to segregation be made as difficult as possible. In particular, the formation of liquid phases during decomposition and calcination of the precursor should be completely avoided. What cannot be avoided is surface contamination.

Another important consideration in preparing mixed-oxide catalysts is the spontaneous monolayer dispersion of oxides and salts onto surfaces of support substrates on calcination. Both temperature and duration of calcination are important here, as discussed in the reviews by Xie and Tang [63] and by Knözinger and Taglauer [64]. If this dispersion step is inadequate or incomplete, the resulting oxide layer, and any reduced metal surface from it, will not be reproducible: from the same catalyst system therefore, one can then have different catalysts prepared at different times and, of course, from one laboratory to another. Spreading and wetting phenomena in preparation of supported catalysts is discussed in Section 4.8.

Heterogeneous catalysts are not just chemicals in the ordinary sense of the word: they are performance chemicals or surface-active materials. Naturally, the perfor-

mance of the catalyst will depend not so much on the initial composition or surface of it as on the real surface, which is formed and stabilized and then changing dynamically under the prevailing process conditions. Here one has to take into account known and controlled process parameters such as temperature, pressure, reactant concentration, and space velocity, as well as variable factors such as feed composition, and unpredictable or unsuspected factors such as impurities and poisons in the feed [65, 66].

## References

1. C. Marcilly, *Rev. Inst. Fr. Petr.* **1984**, 39, 189–208.
2. C. Marcilly, J.-P. Franck, *Rev. Inst. Fr. Petr.* **1984**, 39, 337–364.
3. P. Courty, H. Ajot, C. Marcilly, B. Delmon, *Powder Tech.* **1973**, 7, 21–38.
4. P. Courty, C. Marcilly in *Preparation of Catalysts I* (Eds B. Delmon, P. A. Jacobs, G. Poncelet), Elsevier, Amsterdam, **1976**, pp. 119–145.
5. P. Courty, C. Marcilly in *Preparation of Catalysts III* (Eds G. Poncelet, P. Grange, P. A. Jacobs), Elsevier, Amsterdam, **1983**, pp. 485–519.
6. B. Delmon, N. de Keyser in *Chemical and Physical Aspects of Catalytic Oxidation*, (Eds. J. L. Portefaix, F. Figueras), CNRS, Lyon, **1978**, pp. 491–534.
7. B. Delmon, P. A. Jacobs, G. Poncelet (Eds), *Preparation of Catalysts I*, Elsevier, Amsterdam, **1976**.
8. B. Delmon, P. Grange, P. A. Jacobs, G. Poncelet (Eds), *Preparation of Catalysts II*, Elsevier, Amsterdam, **1979**.
9. G. Poncelet, P. Grange, P. A. Jacobs (Eds), *Preparation of Catalysts III*, Elsevier, Amsterdam, **1983**.
10. B. Delmon, P. Grange, P. A. Jacobs, G. Poncelet (Eds), *Preparation of Catalysts IV*, Elsevier, Amsterdam, **1987**.
11. G. Poncelet, P. A. Jacobs, P. Grange, B. Delmon (Eds), *Preparation of Catalysts V*, Elsevier, Amsterdam, **1991**.
12. G. Poncelet, J. Martens, P. A. Jacobs, P. Grange, B. Delmon (Eds), *Preparation of Catalysts VI*, Elsevier, Amsterdam, **1995**.
13. M. Ruwet, B. Delmon, unpublished results.
14. P. G. Rouxhet, R. E. Sempels, *J. Chem. Soc., Faraday Trans. I* **1974**, 70, 2021–2033.
15. M. Haruta, B. Delmon, *J. Chim. Phys.*, **1986**, 83, 859–868.
16. S. H. Overbury, P. A. Bertrand, G. A. Somorjai, *Chem. Rev.* **1975**, 75, 547–560.
17. G. A. Somorjai, *Chemistry in Two Dimensions: Surfaces*, Cornell University Press, Ithaca, NY, **1981**.
18. B. Delmon in *Reactivity of Solids* (Eds K. Dyrek, J. Haber, J. Nowotny), Elsevier, Amsterdam, and PWN, Warszawa, **1982**, pp. 327–369.
19. B. Delmon, *J. Chim. Phys.*, **1986**, 83, 875–883.
20. A. M. Efstathiou, D. Boudouvas, N. Vamvouka, X. E. Verikios, *J. Catal.* **1993**, 140, 1–15.
21. D. Papagiorgio, A. M. Efstathiou, X. E. Verikios, *Appl. Catal. A* **1994**, 111, 41–62.
22. G. S. Lane, E. Miro, E. E. Wolf, *J. Catal.* **1989**, 119, 161–178.
23. P. Gherardi, O. Ruggeri, F. Trifiró, A. Vaccari, G. Del Piero, G. Manara, B. Notari in *Preparation of Catalysts III* (Eds G. Poncelet, P. Grange, P. A. Jacobs), Elsevier, Amsterdam, **1983**, pp. 723–733.
24. G. Petrini, F. Montino, A. Bossi, F. Garbassi in *Preparation of Catalysts III* (Eds G. Poncelet, P. Grange, P. A. Jacobs), Elsevier, Amsterdam, **1983**, pp. 735–744.
25. E. B. M. Doesburg, R. H. Höppener, B. de Koning, Xu Xiaoding, J. J. F. Scholten in *Preparation of Catalysts IV* (Eds B. Delmon, P. Grange, P. A. Jacobs, G. Poncelet), Elsevier, Amsterdam, **1987**, pp. 767–783.
26. B. S. Rasmussen, P. E. Højlund Nielsen, J. Villadsen, J. B. Hansen in *Preparation of Catalysts*

- IV (Eds B. Delmon, P. Grange, P. A. Jacobs, G. Poncelet), Elsevier, Amsterdam, **1987**, pp. 785–794.
27. W. D. Kingery, *Introduction to Ceramics*, Wiley, New York, **1960**, pp. 291–305.
28. P. K. Gallagher, H. M. O'Bryan, F. Schrey, F. R. Monforte, *Am. Ceram. Soc. Bull.* **1969**, *48*, 1053–1059.
29. W. F. Kladnig, W. Karner, *Ceram. Bull.* **1990**, *69*, 814–817.
30. P. Reynen, H. Bastius, *Powder Metall. Int.* **1976**, *8*, 91.
31. J. Paris, R. Paris, *Bull. Soc. Chim. Fr.* **1965**, 1138–1141.
32. Y. Saikali, J. M. Paris, *Compt. Rend. (C)* **1967**, *265*, 1041–1043.
33. G. Paris, G. Szabo, R. A. Paris, *Compt. Rend. (C)* **1968**, *266*, 554–556.
34. C. Marcilly, B. Delmon, *Compt. Rend. (C)* **1969**, *268*, 1795–1797.
35. P. Courty, B. Delmon, *Compt. Rend. (C)* **1969**, *268*, 1874–1875.
36. C. Marcilly, P. Courty, B. Delmon, *J. Am. Ceram. Soc.* **1970**, *53*, 56–57.
37. B. Delmon, J. Droguest in *Fine Particles, 2nd Intern. Conf.* (Eds W. E. Kuhn, J. Ehretsmann) The Electrochemical Soc., Princeton, **1974**, pp. 242–255.
38. M. P. Pechini, N. Adams, US Patent 3 330 697, **1967**.
39. L. G. Tejuca, J. L. G. Fierro, J. M. D. Tascon, *Adv. Catal.* **1989**, *36*, 237–328.
40. N. Yamazoe, Y. Teraoka, *Catal. Today* **1990**, *8*, 175–199.
41. Y. Teraoka, H-M. Zhang, N. Yamazoe, *Proc. 9th Internat. Congr. Catal., Calgary* **1988**, pp. 1984–1991.
42. H-M. Zhang, Y. Teraoka, N. Yamazoe, *Appl. Catal.* **1988**, *41*, 137–146.
43. C. C. Chang, H. S. Weng, *Ind. Eng. Chem. Res.* **1992**, *31*, 1615–1621.
44. E. Boellaard, A. M. van der Kraan, J. W. Geus, in (Eds G. Poncelet, J. Martens, P. A. Jacobs, P. Grange, B. Delmon) *Preparation of Catalysts VI*, Elsevier, Amsterdam, **1995**, pp. 931–940.
45. E. Boellaard, *Supported Iron (Alloy) Catalysts from Complex Cyanides*, Ph.D. Thesis, Univ. Utrecht, **1994**.
46. Ph. Courty, H. Ajot, B. Delmon, *C. R. Acad. Sc.*, **1973**, *276C*, 1147–1150.
47. Ph. Courty, H. Ajot, B. Delmon (Institut Français du Pétrole), French Patent 1 600 128, **1970**; Belgian Patent 743 578, **1970**.
48. Ph. Courty, H. Ajot, B. Delmon (Institut Français du Pétrole), French Patent 2 031 818, **1970**; Belgian Patent 745 024 **1970**.
49. Ph. Courty, H. Ajot, B. Delmon (Institut Français du Pétrole), German Patent 1 965 176, **1970**.
50. Institut Français du Pétrole: French Patents 2 060 171 **1969**; 2 082 444, **1970**; US Patents 3 716 497, (**1973**); 3 846 341, (**1974**); 3 975 302, (**1976**); 4 000 085, (**1976**); 4 141 861, (**1979**).
51. Ph. Courty, H. Ajot, B. Delmon, unpublished results (1967).
52. S. Beran, B. Wichterlova, H. G. Karge, *J. Chem. Soc., Faraday Trans.* **1990**, *86*, 3033–3037, and references cited therein. See also C. Jia, P. Massiani, P. Beaunier, D. Barthomeuf, *Appl. Catal. A*: **1993**, *106*, L185–L191.
53. F. Toda, K. Nanaka, A. Sekikawa, *J. Chem. Soc., Chem. Commun.* **1987**, 279–280.
54. M. Ogawa, K. Kuroda, C. Kato, *Chem. Lett.* **1989**, 1659.
55. M. Ogawa, T. Hashisume, K. Kuroda, C. Kato, *Inorg. Chem.* **1991**, *30*, 584–585.
56. M. Ogawa, T. Handa, K. Kuroda, C. Kato, *Chem. Lett.* **1990**, 71.
57. M. Crocker, R. H. M. Herold, C. A. Emeis, M. Krijger, *Catal. Lett.*, **1992**, *15*, 339–345.
58. H. G. Karge, Y. Zhang, H. K. Beyer, *Catal. Lett.* **1992**, *12*, 147–156.
59. V. Kanazirev, G. L. Price, K. M. Dooley in *Zeolite Chemistry and Catalysis* (Eds P. A. Jacobs et al.), Elsevier, Amsterdam, **1991**, p. 277–285.
60. V. Kanazirev, V. Valtchev, M. P. Tarassov, *J. Chem. Soc., Chem. Commun.*, **1994**, 1043–1044.
61. P. Cavani, F. Trifiro, A. Vaccari, *Catal. Today*, **1991**, *11*, 173–301.
62. F. Trifiro, A. Vaccari, O. Clause, *Catal. Today*, **1994**, *21*, 185–195.
63. Y. C. Xie, Y. Q. Tang, *Adv. Catal.* **1991**, *37*, 1–43.
64. H. Knözinger, E. Taglauer, *Catalysis*, The Royal Society of Chemistry, Cambridge, **1993**, Vol. 10, 1–40.
65. P. G. Menon, *Catal. Today* **1991**, *11*, 161–172.
66. P. G. Menon, *Chem. Rev.* **1994**, *94*, 1021–1046.

## 3.8 High-Surface Transition Metal Carbides and Nitrides

S. T. OYAMA

### 3.8.1 General Properties of Transition Metal Carbides and Nitrides

The alloying of main group elements, such as C, N, or O, with early transition metals produces a class of materials known as carbides, nitrides, or oxycarbide/nitrides [1–3]. The materials have high melting points ( $> 3300$  K), hardness ( $> 2000$  kg mm<sup>-2</sup>) and strength ( $> 3 \times 10^5$  MPa) [1, 4] and are employed commercially in advanced structural and cutting tool applications. Interestingly, although their physical properties are those of refractory ceramics, their electronic and magnetic properties are typical of metals. Thus, they are good conductors of heat and electricity and have Hall coefficients, magnetic susceptibilities, and heat capacities in the metallic range [1].

The monometallic carbides and nitrides often adopt simple crystal structures (Fig. 1) with the metal atoms arranged in cubic close-packed (ccp), hexagonal close-packed (hcp) or simple hexagonal (hex) arrays. The nonmetallic elements, C, N, and O, occupy interstitial spaces between metal atoms, and for this reason the materials are also known as interstitial alloys.

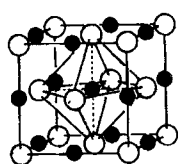
The crystal structures adopted by the binary carbides and nitrides are similar to those found in noble metals. The resemblance is not coincidental, and has been explained using Engel–Brewer valence bond theory [5]. Briefly, the main group elements C and N increase the metal's effective s–p electron count, so that structures and chemical properties of the early transition metals resemble those of the Group 8 metals. This idea was first introduced by Levy and Boudart [6] who noted that tungsten carbide had platinum-like properties.

The carbides and nitrides have been found to be exceptional hydrogenation catalysts [7]. They have activity close to or surpassing those of the Group 8 noble metals for such diverse reactions as methanation [8], ammonia synthesis [9], ammonia decomposition [10], hydrocracking [11], hydrogenation of benzene and cyclohexene [12], and hydroisomerization of *n*-hexane [13], *n*-heptane [14], and methylcyclohexane [15]. Considerable work is also being done in the area of hydroprocessing [16], where the materials have been shown to have high activity for both hydrodesulfurization (HDS) [17, 18] and hydrodenitrogenation (HDN) [19–21].

### 3.8.2 Thermodynamic Considerations in the Preparation of Carbides and Nitrides

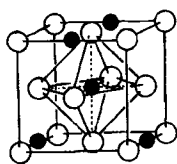
Strategies for preparation are numerous and involve widely differing starting metallic compounds, as well as different carbon and nitrogen sources. It is therefore instructive to consider the thermodynamics [22] of various kinds of transformations.

## Crystal Structures



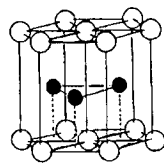
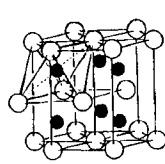
Face-centered cubic

TiC, VC, NbC  
TiN, VN, NbN



Hexagonal close-packed

$\gamma$ -Mo<sub>2</sub>N,  $\beta$ -W<sub>2</sub>N, Re<sub>2</sub>N  
 $\alpha$ -MoC<sub>1-x</sub>,  $\beta$ -WC<sub>1-x</sub>



Simple hexagonal

$\beta$ -Mo<sub>2</sub>C, W<sub>2</sub>C, Re<sub>2</sub>C

WC, MoC  
 $\delta$ -WN

**Figure 1.** Typical crystal structures and compositions of carbides and nitrides (reproduced with permission from Ref. 3).

**Table 1.** Heat and free energy of formation from the elements of transition metal carbides (kJ mol<sup>-1</sup>) calculated from data in Ref. 22.

Transformation	$\Delta H_{298}^0$	$\Delta G_{298}^0$	$\Delta H_{1000}^0$	$\Delta G_{1000}^0$
Ti + C → TiC	-184.5	-181.0	-184.1	-173.6
Zr + C → ZrC	-207.1	-203.7	-208.3	-195.9
Hf + C → HfC	-225.9	-223.0	-225.0	-217.5
V + C → VC	-101.7	-99.08	-103.1	-92.21
Nb + C → NbC	-138.9	-136.9	-136.2	-134.4
Ta + C → TaC	-144.1	-142.6	-142.5	-140.8
Cr + $\frac{2}{3}$ C → $\frac{1}{3}$ Cr <sub>3</sub> C <sub>2</sub>	-85.35	-102.1	-25.17	-182.4
Mo + $\frac{1}{2}$ C → $\frac{1}{2}$ Mo <sub>2</sub> C	-49.45	-58.82	-27.82	-96.11
W + C → WC	-40.58	-39.49	-38.88	-38.48
Mn + $\frac{1}{3}$ C → $\frac{1}{3}$ Mn <sub>3</sub> C	-15.06	-33.24	+29.00	-108.75
Fe + $\frac{1}{3}$ C → $\frac{1}{3}$ Fe <sub>3</sub> C	+25.04	+3.69	+70.53	-83.21

The heats and free energies of formation from the elements at 298 K and 1000 K are presented in Table 1 for carbides and Table 2 for nitrides. For illustration, different transformations to molybdenum carbide are presented at 298 K in Table 3 and at 1000 K in Table 4.

Carbide formation from elemental carbon and transition metals show a number of trends (Table 1). First, the free energy of formation is strongly negative for the early transition metals, and becomes less favorable in going to the Group 8 metals. As temperature is raised, carbide stability decreases slightly among the early transition metals, but increases markedly for the late metals. In general, trends in free

**Table 2.** Heat and free energy of formation from the elements of transition metal nitrides ( $\text{kJ mol}^{-1}$ ) calculated from data in Ref. 22.

Transformation	$\Delta H_{298}^0$	$\Delta G_{298}^0$	$\Delta H_{1000}^0$	$\Delta G_{1000}^0$
$\text{Sc} + \frac{1}{2} \text{C} \rightarrow \text{ScN}$	-313.8	-283.8	-312.0	-213.6
$\text{Y} + \frac{1}{2} \text{N}_2 \rightarrow \text{YN}$	-299.2	-271.5	-296.6	-207.7
$\text{Ti} + \frac{1}{2} \text{N}_2 \rightarrow \text{TiN}$	-338.1	-309.4	-335.4	-243.0
$\text{Zr} + \frac{1}{2} \text{N}_2 \rightarrow \text{ZrN}$	-368.2	-339.6	-365.0	-274.1
$\text{Hf} + \frac{1}{2} \text{N}_2 \rightarrow \text{HfN}$	-373.6	-346.4	-369.8	-284.4
$\text{V} + \frac{1}{2} \text{N}_2 \rightarrow \text{VN}$	-217.2	-191.1	-213.6	-131.2
$\text{Nb} + \frac{1}{2} \text{N}_2 \rightarrow \text{NbN}$	-235.1	-206.0	-231.0	-138.8
$\text{Ta} + \frac{1}{2} \text{N}_2 \rightarrow \text{TaN}$	-252.3	-223.8	-245.0	-160.9
$\text{Cr} + \frac{1}{2} \text{N}_2 \rightarrow \text{CrN}$	-117.2	-92.8	-112.1	-37.97
$\text{Mo} + \frac{1}{4} \text{N}_2 \rightarrow \frac{1}{2} \text{Mo}_2\text{N}$	-40.7	-27.3	-35.8	+1.80
$\text{Fe} + \frac{1}{8} \text{N}_2 \rightarrow \frac{1}{4} \text{Fe}_4\text{N}$	-2.8	+4.37	-5.1	+8.57
$\text{Co} + \frac{1}{6} \text{N}_2 \rightarrow \frac{1}{3} \text{Co}_3\text{N}$	+2.8	+11.46	+3.22	+20.1

**Table 3.** Heat and free energy of reaction of molybdenum carbide at 298 K ( $\text{kJ mol}^{-1}$ ) calculated from data in Ref. 22.

Transformation	$\Delta H_{298}^0$	$\Delta G_{298}^0$
$\text{Mo} + \frac{1}{2} \text{C} \rightarrow \frac{1}{2} \text{Mo}_2\text{C}$	-24.75	-25.2
$\text{Mo} + \frac{1}{2} \text{CH}_4 \rightarrow \frac{1}{2} \text{Mo}_2\text{C} + \text{H}_2$	+12.7	+0.15
$\text{Mo} + \text{CO} \rightarrow \frac{1}{2} \text{Mo}_2\text{C} + \frac{1}{2} \text{CO}_2$	-166.2	-170.0
$\text{MoO}_3 + 3\frac{1}{2} \text{C} \rightarrow \frac{1}{2} \text{Mo}_2\text{C} + 3 \text{CO}$	+388.8	+231.1
$\text{CaMoO}_4 + \frac{1}{4} \text{CaC}_2 + \frac{11}{6} \text{Al} \rightarrow \frac{1}{2} \text{Mo}_2\text{C} + \frac{5}{4} \text{CaO} + \frac{11}{12} \text{Al}_2\text{O}_3$	-786.1	-777.1
$\text{MoO}_3 + 1\frac{1}{6} \text{CH}_4 \rightarrow \frac{1}{2} \text{Mo}_2\text{C} + \frac{2}{3} \text{CO} + 2\frac{1}{3} \text{H}_2\text{O}$	+170.0	+77.41
$\text{Mo}(\text{CO})_6 + \frac{1}{2} \text{H}_2 \rightarrow \frac{1}{2} \text{Mo}_2\text{C} + 5\frac{1}{2} \text{CO} + \frac{1}{2} \text{H}_2\text{O}$	+162.4	-36.70
$\text{MoCl}_6 + \frac{1}{2} \text{CH}_4 + 2 \text{H}_2 \rightarrow \frac{1}{2} \text{Mo}_2\text{C} + 6 \text{HCl}$	-79.7	-192.8
$\text{MoS}_2 + \frac{1}{2} \text{CH}_4 + \text{H}_2 \rightarrow \frac{1}{2} \text{Mo}_2\text{C} + 2 \text{H}_2\text{S}$	+247.7	+200.6

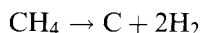
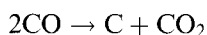
energies are mirrored by values of the heats of reaction but, towards the right in the periodic table, entropic effects are important in stabilizing the compounds.

The thermodynamics of nitride formation from molecular nitrogen and transition metals show similar trends to the carbides. Again, the free energies of formation are strongly negative towards the left in the transition series, and become less favorable on moving to the right. Nitride stability is lower at higher temperatures, and is dominated by the heat of reaction. Entropic effects do not stabilize the late transition metal nitrides as they do the carbides. In general, nitride formation is more favorable than carbide formation in the early transition metals, but this is reversed in the late metals.

**Table 4.** Heat and free energy of reaction of molybdenum carbide at 1000 K ( $\text{kJ mol}^{-1}$ ) calculated from data in Ref. 22.

Transformation	$\Delta H_{1000}^0$	$\Delta G_{1000}^0$
$\text{Mo} + \frac{1}{2} \text{C} \rightarrow \frac{1}{2} \text{Mo}_2\text{C}$	-23.3	-27.2
$\text{Mo} + \frac{1}{2} \text{CH}_4 \rightarrow \frac{1}{2} \text{Mo}_2\text{C} + \text{H}_2$	+21.8	-36.9
$\text{Mo} + \text{CO} \rightarrow \frac{1}{2} \text{Mo}_2\text{C} + \frac{1}{2} \text{CO}_2$	-152.8	-186.8
$\text{MoO}_3 + 3\frac{1}{2} \text{C} \rightarrow \frac{1}{2} \text{Mo}_2\text{C} + 3 \text{CO}$	+374.4	-135.4
$\text{MoO}_3 + 1\frac{1}{6} \text{CH}_4 \rightarrow \frac{1}{2} \text{Mo}_2\text{C} + \frac{2}{3} \text{CO} + 2\frac{1}{3} \text{H}_2\text{O}$	+163.2	-140.1
$\text{Mo}(\text{CO})_6 + \frac{1}{2} \text{H}_2 \rightarrow \frac{1}{2} \text{Mo}_2\text{C} + 5\frac{1}{2} \text{CO} + \frac{1}{2} \text{H}_2\text{O}$	+167.2	-570.4
$\text{MoCl}_6 + \frac{1}{2} \text{CH}_4 + 2 \text{H}_2 \rightarrow \frac{1}{2} \text{Mo}_2\text{C} + 6 \text{HCl}$	-95.7	-449.1
$\text{MoS}_2 + \frac{1}{2} \text{CH}_4 + \text{H}_2 \rightarrow \frac{1}{2} \text{Mo}_2\text{C} + 2 \text{H}_2\text{S}$	+239.1	+95.9

Thermodynamic considerations are useful for determining conditions for carburization and nitridation. For example, in the nitridation of niobium the particular phase of the product (e.g. NbN,  $\beta\text{-Nb}_2\text{N}$ , or  $\gamma\text{-Nb}_4\text{N}_3$ ) will depend on temperature and pressure. This holds true also for carbides. However, for carbides, competing reactions such as



can cause deposition of free carbon. These side reactions can be controlled by properly adjusting gas composition by means of ratios of reactant gases such as  $(\text{CO})/(\text{CO}_2)$  or  $(\text{CH}_4)/(\text{H}_2)^2$ . Examples are given for WC and  $\text{Mo}_2\text{C}$  synthesis (Fig. 2).

The thermodynamic considerations above are useful guides to the preparation of carbides and nitrides, but are not limiting as the syntheses can be carried out at nonequilibrium conditions. For example, in the carburization or nitridation of oxides it is possible to lower the temperature of reaction by sweeping away the product gases [23]:

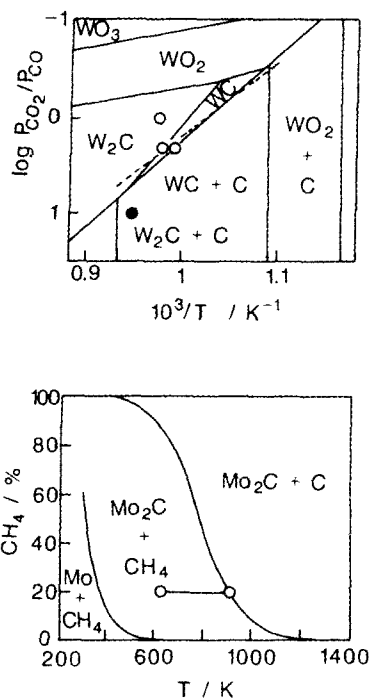


Water vapor produced during reduction is particularly problematic as it can inhibit the reaction or lead to hydrothermal sintering.

### 3.8.3 Survey of Preparative Methods

Many types of preparation are applicable for both carbides and nitrides, and these will be described in this section. General references for this section are Frad [24],





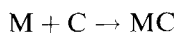
**Figure 2.** Equilibrium curves for the carburization of tungsten and molybdenum. The tungsten diagram shows experimental points for  $W_2C$  (open circles) and  $WC$  (solid circle) [39]. The molybdenum diagram shows the operating line for synthesis with 20%  $CH_4$  in  $H_2$  [11] (reproduced with permission from Ref. 3).

Juza [25], Kosolopova [26], Toth [1], Santhanam [27], and Stoll and Santhanam [28].

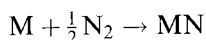
Some of the methods described in this section are employed to produce metallurgical carbides and produce low specific surface area ( $S_g$ ) materials. Nevertheless, some of the compositions have been used in catalytic studies (especially prior to 1980), and their preparation is included in this section.

### 3.8.3.1 Direct Reaction of Metals and Nonmetals

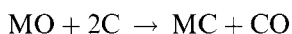
#### A Carbides



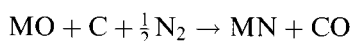
This method of preparation is carried out by contacting metallic powders and solid carbon, sometimes in the presence of gaseous hydrocarbons, at 1500–2300 K. Thermodynamics (Section A.2.1.8.2) indicate that carbide formation from the elements is favorable at lower temperatures, but high temperatures are used to counter solid-state diffusion limitations [26]. Heating is provided by conventional ovens or at higher temperatures in arc furnaces. The latter method is called the Moissan fusion method, after the originator [29, 30]. In the case of the fusion method, the carbides are produced in a molten form and cast shapes can be poured from the melt [31].

**B Nitrides**

Thermodynamic calculations (Table 2) indicate that nitride formation from the elements is favorable, and indeed, many nitrides can be so prepared. For example, TiN, VN, and CrN can be made at 1 bar with molecular nitrogen. As with the carbides, the transformations are diffusion controlled and high temperatures are needed, usually between 1400 K and 1900 K [25]. Elements to the right of molybdenum cannot be nitrified with molecular nitrogen at pressures attainable in conventional facilities.

**3.8.3.2 Reaction of Metal Oxides in the Presence of Solid Carbon****A Carbides**

This transformation is carried out by intimately mixing metal oxide powders with carbon, again as with the pure metals, at temperatures between 1500–2300 K, with or without the presence of a hydrocarbon gas. The reactions of oxides with carbon are thermodynamically favored, but high temperatures are again needed because the transformations are limited by diffusion. The direct transformation of oxides to carbides is economically advantageous over the use of metals since the need to separately reduce the oxide phases is avoided. Wide application is found for the commercial production of carbides of molybdenum, tungsten, and tantalum.

**B Nitrides**

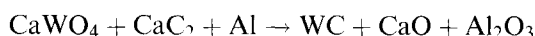
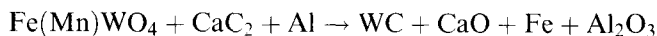
The carbothermal nitridation of oxides is a common method of preparation of nitrides that goes back to the work of Friederich and Sittig [32] in 1925. It is generally applicable to nitrides of high thermal stability such as TiN, VN and CrN. Its main drawback is that it produces impure phases.

**3.8.3.3 Extraction of Carbides from Ferrous Alloys**

This method involves extracting carbide precipitates from solid solution of steels and ferrous alloys. The method is reported by Shimer [33] in 1887 who prepared TiC by dissolving Fe from a titanium-bearing cast iron with hydrochloric acid. Commercial practice involves the use of minerals such as wolframite  $Fe(Mn)WO_4$  or microlite  $Ca_2Ta_2O_7$  in a high-temperature melt of auxiliary (menstruum) metal

with carbon [28]. Carbides of vanadium, chromium, titanium, tantalum, tungsten, and molybdenum for use in machine tools have been produced in this way. Disadvantages of the method are the use of costly acids and the generation of considerable amounts of waste salts.

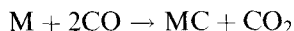
### 3.8.3.4 Reaction of Oxides with Calcium Carbide and Aluminum



Reactions such as the above have been used for the large-scale commercial production of WC by Kennametal, Inc. in a process called the Macro Process [28]. Thermodynamics for the analogous molybdenum reaction show that the reaction is highly exothermic (Table 3). The solid reactants are metered into a carbon-lined kiln to develop a self-sustained exothermic reaction. The reaction occurs in a pool of molten metal at temperatures above 2800 K. At the end of the run the kiln contents solidify into a lower heavy layer of carbide crystals and an upper slag layer of oxides.

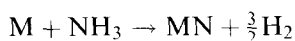
### 3.8.3.5 Reactions of Metals or Metal Oxides with Gas-Phase Reagents

#### A Carbides

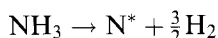


Carburization with gaseous carbon sources such as methane, higher hydrocarbons, and carbon monoxide was initially carried out mainly with metal wires such as tungsten or tantalum, and coarse tungsten powder. Clearly, contacting of the gas and the solid is a problem, and the method is not used commercially. However, it is very useful for the preparation of small-scale laboratory batches. For catalytic applications metals have been carburized with methane and ethane [34], propane [35], and carbon monoxide [36]. One approach to obtain higher surface area carbides has been to maximize the surface area of the precursor [37]. In this manner Palanker et al. [38] optimized the surface area of a tungstic acid precursor to obtain tungsten carbide of  $S_g$  up to  $30 \text{ m}^2 \text{ g}^{-1}$ . Similarly, Lemaître et al. carburized a hydrous oxide precursor with a  $\text{CO}/\text{CO}_2$  mixture to obtain tungsten carbide with  $S_g$  of  $47 \text{ m}^2 \text{ g}^{-1}$  [39].

#### B Nitrides

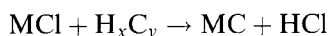


Flowing ammonia has been applied to the synthesis of the nitrides of iron, cobalt, and nickel compounds with very low enthalpies of formation (Table 2). Again, isothermal conditions were employed. Ammonia is preferable over the use of molecular nitrogen to nitride metals or oxides because of the following favorable reaction that produces surface nitrogen,  $N^*$ , and eventually nitride:



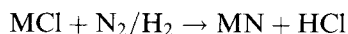
### 3.8.3.6 Decomposition of Metal Halide Vapors

#### A Carbides



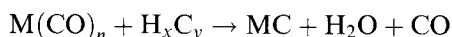
In this method metal chlorides or oxychlorides are made to react with gaseous hydrocarbons in the vicinity of a localized heat source (1400–2100 K). Clearly, the reaction is thermodynamically favorable (Tables 3 and 4). The method was first used by Van Arkel in 1923 with an incandescent tungsten filament to make carbides of tantalum and zirconium [40]. Although the reaction variables have been studied extensively, problems remain with control of the process and with low productivity. Application to catalyst synthesis has been moderate [41].

#### B Nitrides



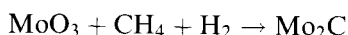
The Van Arkel process can also be used to make metal nitrides. Because of the tendency of  $NH_3$  to decompose at the temperatures needed for nitride formation (1300–1900 K), the gaseous reactant is a mixture of  $H_2$  and  $N_2$ . The nitride forms as a layer around the tungsten wire.

### 3.8.3.7 Decomposition of Gaseous Metal Carbonyls



This method is similar to that employing metal chlorides, except that it uses metal carbonyls. Both methods still receive attention [42]. In the case of the carbonyl compounds the heat of reaction is unfavorable, but the transformation is driven by the release of substantial amounts of carbon monoxide (Tables 3 and 4). The use of carbonyl compounds rather than metal chlorides may have some advantages since the carbon source is already included in the starting material [43]. For example, the reaction of  $WCl_6$  in an isobutane/hydrogen atmosphere produced a WC sample extensively contaminated by surface carbon, as seen by Auger electron spectroscopy. On the other hand, the reaction of  $Mo(CO)_6$  in hydrogen/CO mixtures gave a molybdenum oxycarbide,  $MoO_xC_y$ , with substantially improved surface properties [44], and good activity in ammonia synthesis [45].

### 3.8.3.8 Temperature-Programmed Methods (Carbides and Nitrides)



The temperature-programmed reaction (TPR) method of preparation [46] is a variation of the isothermal method described in Section E. The TPR method consists of treating an oxide precursor in a reactive gas stream while raising the temperature in a uniform manner. By monitoring changes in the exit gas-phase composition, the end of the reaction can be ascertained and the product quenched. Because the synthesis involves the direct transformation of an oxide to a carbide or nitride, it is possible to bypass the metallic state, which is the most prone to sinter (lowest Tammann temperature). In addition, the use of the temperature program allows an optimal balance between synthesis and sintering rates and results in products with high specific surface areas ( $S_g$ ).

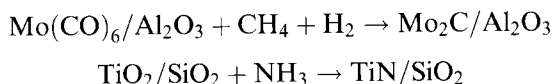
A typical synthesis [47] using the TPR method is exemplified by the preparation of  $\beta$ - $\text{Mo}_2\text{C}$  (hcp) from  $\text{MoO}_3$  using a  $\text{CH}_4/\text{H}_2$  reactant gas mixture. Gas chromatographic traces as a function of temperature and X-ray diffraction indicate that the transformation occurs through a  $\text{MoO}_2$  intermediate. The resulting product  $\beta$ - $\text{Mo}_2\text{C}$  is formed with  $S_g$  increasing from 50 to  $90 \text{ m}^2 \text{ g}^{-1}$  as the  $\text{CH}_4$  concentration is raised from 20 to 100 mol %.

If instead of the  $\text{CH}_4/\text{H}_2$  reactant, a pure  $\text{NH}_3$  stream is used; the product is  $\gamma$ - $\text{Mo}_2\text{N}$  (fcc) of surface area as high as  $225 \text{ m}^2 \text{ g}^{-1}$  [48]. This high value (the equivalent of a silica of  $800 \text{ m}^2 \text{ g}^{-1}$ ) is the result of a solid-state process known as a topotactic transformation [49]. In this process nitrogen replaces oxygen in the lattice with minimal disruption of the molybdenum atoms, so that the product  $\gamma$ - $\text{Mo}_2\text{N}(100)$  planes are produced parallel to the original parent  $\text{MoO}_3(010)$  planes. Because of density differences each original  $\text{MoO}_3$  crystallite of  $\mu\text{m}$  size is transformed into a sponge-like porous agglomerate of  $\gamma$ - $\text{Mo}_2\text{N}$  microcrystals, retaining the original external size and shape of the  $\text{MoO}_3$  parent. This retention of external morphology is known as pseudomorphism. Because of the gradual replacement of oxygen by nitrogen, there is no  $\text{MoO}_2$  intermediate phase but, rather, a continuous transformation through oxynitride compositions.

The same process can be repeated using  $\text{WO}_3$  as the starting material to produce  $\beta$ - $\text{W}_2\text{N}$  (fcc) of up to  $90 \text{ m}^2 \text{ g}^{-1}$ . Interestingly, both the  $\gamma$ - $\text{Mo}_2\text{N}$  and  $\beta$ - $\text{W}_2\text{N}$  can be converted by topotactic transformations to the corresponding carbides, but of the high-temperature cubic structure,  $\alpha$ - $\text{MoC}_{1-x}$  (fcc) and  $\alpha$ - $\text{WC}_{1-x}$  (fcc), with  $x \approx 0.5$ . These phases retain the high surface area of their parent nitrides [50, 51].

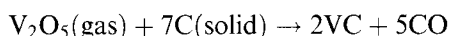
The TPR method has now been applied to  $\text{TiN}_x\text{O}_y$  [52], VN [23], and NbC [53]. Although the TPR method produces high surface area materials, the pore structure of these is usually not controllable. Often, the pores are in the micro-pore regime ( $< 3 \text{ nm}$ ). However, a number of the solid state transformations that lead to carbides and nitrides are topotactic and exhibit pseudomorphism (retention of external particle size and shape). This provides a possible means of engineering the pore structure by preparing oxide precursors with the desired external morphology.

### 3.8.3.9 Utilization of Supports



Highly dispersed carbide phases may be prepared by depositing a precursor on a support and carburizing it. This was demonstrated by Lee et al. [12] for molybdenum carbide using  $\text{Mo(CO)}_6$  deposited onto dehydroxylated alumina from the gas phase. Carburization in a  $\text{CH}_4/\text{H}_2$  stream resulted in a highly dispersed material which X-ray absorption fine structure spectroscopy (EXAFS) confirmed to be  $\beta$ - $\text{Mo}_2\text{C}$ . Supported carbides and nitrides may also be obtained from supported oxide precursors [12, 54, 55], and supported nitrides may be converted to supported carbides [56]. For example, a TiN coating on spherical  $\text{SiO}_2$  particles was prepared by nitriding  $\text{TiO}_2/\text{SiO}_2$  with ammonia [57]. The use of supports offer the advantage of better usage of the active component and higher control of surface area and pore size distribution.

### 3.8.3.10 Reaction Between Metal Oxide Vapor and Solid Carbon



A novel method of preparation of ultrahigh surface area carbides has been developed by the group of Ledoux. It involves the reaction of solid carbon with vaporized metal oxide precursors such as  $\text{MoO}_3$  or  $\text{WO}_2$  [58]. The synthesis uses high specific surface area-activated carbons and the final product appears to retain a “memory” of the porous structure of the starting material. The carbon acts as a skeleton around which the carbides are formed. Catalytically active carbides with surface areas between 100 and  $400 \text{ m}^2 \text{ g}^{-1}$  are generated.

## References

1. L. E. Toth, *Transition Metal Carbides and Nitrides*, Academic Press, New York, **1971**.
2. E. K. Storms, *The Refractory Carbides*, Academic Press, New York, **1967**.
3. S. T. Oyama, *Catal. Today* **1992**, 15, 179.
4. S. T. Oyama, Ed., *The Chemistry of Transition Metal Carbides and Nitrides*, Blackie Academic and Professional, London, **1996**.
5. S. T. Oyama, *J. Solid State Chem.* **1992**, 96, 442.
6. R. B. Levy, M. Boudart, *Science* **1973**, 181, 547.
7. B. Vidick, J. Lemaitre, L. Leclercq, *J. Catal.* **1986**, 99, 439.
8. G. S. Ranhotra, A. T. Bell, J. A. Reimer, *J. Catal.* **1987**, 108, 40.
9. M. Boudart, S. T. Oyama, L. Leclercq, *Proc. 7th Int. Cong. Catal.*, Tokyo, 1980, (Eds: T. Seiyama and K. Tanabe) Kodansha, **1980**, Vol. 1, p. 578.
10. S. T. Oyama, *J. Catal.* **1992**, 133, 358.
11. J. S. Lee, S. T. Oyama, M. Boudart, *J. Catal.* **1987**, 106, 125.
12. J. S. Lee, M. H. Yeom, K. Y. Park, I.-S. Nam, J. S. Chung, Y. G. Kim, S. H. Moon, *J. Catal.* **1991**, 128, 126.
13. M. J. Ledoux, C. Pham Huu, J. Guille, H. Dunlop, *J. Catal.* **1992**, 134, 383.
14. F. H. Ribeiro, M. Boudart, R. A. Dalla Betta, E. Iglesia, *J. Catal.* **1991**, 130, 498.

15. F. H. Ribeiro, R. A. Dalla Betta, M. Boudart, J. Baumgartner, E. Iglesia, *J. Catal.* **1991**, *130*, 86.
16. J. C. Schlatter, S. T. Oyama, J. E. Metcalfe, III, J. M. Lambert, Jr., *Ind. Eng. Chem. Res.* **1988**, *27*, 1648.
17. E. J. Markel, J. W. Van Zee, *J. Catal.* **1990**, *126*, 643.
18. M. Nagai, T. Miyao, *Catal. Lett.* **1993**, *18*, 9.
19. K. S. Lee, H. Abe, J. A. Reimer, A. T. Bell, *J. Catal.* **1993**, *139*, 34.
20. D. J. Sajkowski, S. T. Oyama, *Appl. Catal.* **1996**, *134*, 339.
21. C. W. Colling, L. T. Thompson, *J. Catal.* **1994**, *146*, 193.
22. O. Knacke, O. Kubaschewski, K. Hesselmann, *Thermochemical Properties of Inorganic Substances*, 2nd ed., Springer-Verlag, Berlin, **1991**.
23. R. Kapoor, S. T. Oyama, *J. Sol. St. Chem.* **1992**, *99*, 303.
24. W. A. Frad in *Advances in Inorganic Chemistry and Radiochemistry* (Eds: H. J. Emeléus, A. G. Sharpe), Academic Press, New York, **1968**, Vol. 2, p. 153.
25. R. Jusa in *Advances in Inorganic Chemistry and Radiochemistry* (Eds: H. J. Emeléus, A. G. Sharpe), Academic Press, New York, **1966**, Vol. 9, p. 81.
26. T. Ya. Kosolapova, *Carbides Properties, Production, and Applications*, Plenum Press, New York, **1971**.
27. A. T. Santhanam in *Kirk Othmer, Encyclopedia of Chemical Technology* (Ed.: M. E. Howe-Grant), 4th ed., John Wiley & Sons, New York, **1992**, Vol. 4, p. 848.
28. W. M. Stoll, A. T. Santhanam in *Kirk Othmer, Encyclopedia of Chemical Technology* (Ed.: M. E. Howe-Grant), 4th ed., John Wiley & Sons, New York, **1992**, Vol. 4, p. 861.
29. H. Moissan, *Compt. Rend.* **1893**, *116*, 1225.
30. H. Moissan, *The Electric Furnace* (Translated: A. T. de Mouilpied), Arnold, London, **1904**.
31. P. Schwarzkopf, R. Kieffer, *Refractory Hard Metals*, Macmillan, New York, **1953**.
32. E. Friederich, L. Sittig, *Z. Anorg. Allgem. Chem.* **1925**, *143*, 293.
33. P. W. Shimer, *Chem. News* **1887**, *55*, 156.
34. J. S. Sinfelt, D. J. C. Yates, *Nature Phys. Sci.* **1971**, *229*, 27.
35. M. Saito, R. B. Anderson, *J. Catal.* **1980**, *63*, 438.
36. B. Vidick, J. Lemaître, B. Delmon, *Acta Chim. Acad. Sci. Hungar.* **1982**, *111*, 449.
37. E. A. Mazulevsky, V. Sh. Palanker, E. N. Baybatyrov, A. M. Khisametdinov, E. I. Domanskaya, *Kinet. Katal.* **1977**, *18*, 767.
38. V. Sh. Palanker, D. V. Sokolsky, E. A. Mazulevsky, E. N. Baybatyrov, *J. Power Sources* **1976/1977**, *1*, 169.
39. J. Lemaître, B. Vidick, B. Delmon, *J. Catal.* **1986**, *99*, 415.
40. A. E. Van Arkel, *Physica* **1923**, *3*, 76.
41. L. Leclercq, M. Boudart, US Patent 4 107 282, Aug. 15, **1978**, (Stanford University).
42. J. Hojo, T. Oku, A. Kato, *J. Less-Common Met.* **1978**, *59*, 85.
43. L. Leclercq in *Surface Properties and Catalysis by Non-Metals* (Eds: J. P. Bonnelle, B. Delmon, E. Derouane), Reidel, Dordrecht, **1983**, p. 433.
44. L. Leclercq, K. Imura, S. Yoshida, T. Barbee, M. Boudart in *Preparation of Catalysts II* (Eds: B. Delmon, P. Grange, P. A. Jacobs, G. Poncelet), Elsevier, **1978**, p. 627.
45. M. Boudart, S. T. Oyama, L. Leclercq, *Proc. 7th Int. Cong. Catal.* (Eds: T. Seiyama, K. Tanabe), Kodansha, **1980**; Vol. 1, p. 578.
46. S. T. Oyama, PhD Thesis, Stanford University, **1981**.
47. J. S. Lee, S. T. Oyama, M. Boudart, *J. Catal.* **1987**, *106*, 125.
48. L. Volpe, M. Boudart, *J. Sol. St. Chem.* **1985**, *59*, 332.
49. L. Volpe, M. Boudart, *Catal. Rev.-Sci. Eng.* **1985**, *27*, 515.
50. L. Volpe, M. Boudart, *J. Sol. St. Chem.* **1985**, *59*, 348.
51. J. S. Lee, L. Volpe, F. H. Ribeiro, M. Boudart, *J. Catal.* **1988**, *112*, 44.
52. C. H. Shin, G. Bugli, G. Djega-Mariadassou, *J. Sol. State Chem.* **1991**, *95*, 145.
53. V. L. S. Teixeira da Silva, E. I. Ko, M. Schmal, S. T. Oyama, *Chem. Mat.* **1995**, *7*, 179.
54. L. H. Slaugh, R. J. Hoxmeier, US Patent 4 326 992, **1982**, (Shell Oil Company).
55. D. E. Willis, *J. Catal.* **1983**, *84*, 344.
56. L. H. Slaugh, R. J. Hoxmeier, US Patent 4 325 843, **1982**, (Shell Oil Company).

57. R. E. Partch, Y. Xie, S. T. Oyama, E. Matijevic, *J. Mater. Sci.* **1993**, 8, 2014.  
58. M. J. Ledoux, C. Pham-Huu, S. Marin, M. Weibel, J. Guille, *C. R. Acad. Sci. Paris*, **1990**, 310, Série II, 707.

## 3.9 Carbons

R. SCHLÖGL

### 3.9.1 Introduction

The element carbon plays a multiple role in heterogeneous catalysis. In homogeneous catalysis it occurs as the most prominent constituent of ligand systems and will be treated as such there. Carbon-containing molecules are, in most catalytic applications, the substrates of the process under consideration. Deposits and polymers of carbon often occur as poisons on catalysts. Carbon deposition is the most severe problem in certain zeolite applications. In hydrogenation reactions carbon deposits are thought to act as modifiers of catalyst activity and to provide selectivity by controlling the hydrogenation–dehydrogenation activity of the metal part of the catalyst. Carbon deposits are even thought to constitute part of the active sites in some cases.

Carbon is a prominent catalyst support material as it allows the anchoring of metal particles on a substrate which does not exhibit solid acid–base properties. Carbon is finally a catalyst in its own right, enabling the activation of oxygen and chlorine for selective oxidation, chlorination, and dechlorination reactions.

These multiple roles operate in parallel with a complex structural chemistry giving rise to families of chemically vastly different modifications of the element. It is a special characteristic of carbon chemistry that many of these modifications cannot be obtained as phase-pure materials. This limits the exact knowledge of physical and chemical properties to a few archetype modifications, namely graphite and diamond.

The reason for this poor definition of materials is found in the process of their formation, namely difficult to control polymerization reactions. Such reactions also occur in catalytic reactions with small organic molecules. The nature of carbon deposits therefore reflect all the complexity of the bulk carbon materials. One aim of this article is to describe the structural and chemical complexity of carbon or “soot” in order to provide an understanding of the frequently observed complexity of the chemical reactivity (e.g. in reactivation processes aiming at an oxidative removal of deposits).

The surface chemistry of carbon which determines its interfacial properties is a rich field as a wide variety of surface functional groups are known to exist on carbon. By far the most important family of surface functional groups are those



57. R. E. Partch, Y. Xie, S. T. Oyama, E. Matijevic, *J. Mater. Sci.* **1993**, 8, 2014.  
58. M. J. Ledoux, C. Pham-Huu, S. Marin, M. Weibel, J. Guille, *C. R. Acad. Sci. Paris*, **1990**, 310, Série II, 707.

## 3.9 Carbons

R. SCHLÖGL

### 3.9.1 Introduction

The element carbon plays a multiple role in heterogeneous catalysis. In homogeneous catalysis it occurs as the most prominent constituent of ligand systems and will be treated as such there. Carbon-containing molecules are, in most catalytic applications, the substrates of the process under consideration. Deposits and polymers of carbon often occur as poisons on catalysts. Carbon deposition is the most severe problem in certain zeolite applications. In hydrogenation reactions carbon deposits are thought to act as modifiers of catalyst activity and to provide selectivity by controlling the hydrogenation–dehydrogenation activity of the metal part of the catalyst. Carbon deposits are even thought to constitute part of the active sites in some cases.

Carbon is a prominent catalyst support material as it allows the anchoring of metal particles on a substrate which does not exhibit solid acid–base properties. Carbon is finally a catalyst in its own right, enabling the activation of oxygen and chlorine for selective oxidation, chlorination, and dechlorination reactions.

These multiple roles operate in parallel with a complex structural chemistry giving rise to families of chemically vastly different modifications of the element. It is a special characteristic of carbon chemistry that many of these modifications cannot be obtained as phase-pure materials. This limits the exact knowledge of physical and chemical properties to a few archetype modifications, namely graphite and diamond.

The reason for this poor definition of materials is found in the process of their formation, namely difficult to control polymerization reactions. Such reactions also occur in catalytic reactions with small organic molecules. The nature of carbon deposits therefore reflect all the complexity of the bulk carbon materials. One aim of this article is to describe the structural and chemical complexity of carbon or “soot” in order to provide an understanding of the frequently observed complexity of the chemical reactivity (e.g. in reactivation processes aiming at an oxidative removal of deposits).

The surface chemistry of carbon which determines its interfacial properties is a rich field as a wide variety of surface functional groups are known to exist on carbon. By far the most important family of surface functional groups are those

involving oxygen. Other prominent heteroatoms on the surface are hydrogen and nitrogen. This article focuses on the description and characterization of oxygen surface functional groups.

The final section discusses selected case studies of carbon chemistry in catalysis in order to illustrate characteristic properties of carbon materials as wanted or unwanted components in catalytic systems.

### 3.9.2 Structural Chemistry of Carbon

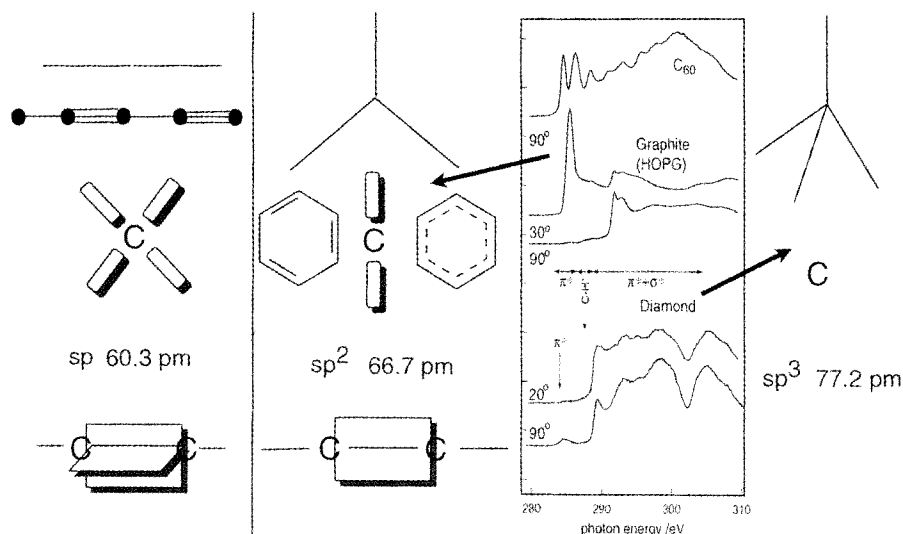
The chemistry of carbon is extremely complex, both in the molecules and in the solid state. The reason for this complexity lies in the pronounced tendency of the element to form homonuclear bonds in three bonding geometries. They can either occur uniformly or in almost unlimited combinations allowing a very large number of homonuclear structures of elemental carbon. The moderate electronegativity of carbon allows for strong covalent interactions with all main group elements. This adds enormously to the complexity of the solid-state chemistry of carbon. In the present context carbon–oxygen bonds will be treated in some detail as they determine to a large extent the stability and reactivity of carbon in typical catalytic environments.

A consequence of the wide choice of bonding situations for carbon atoms is that very few species can be prepared with any degree of purity, thus complicating the determination of structural, chemical, and physical properties. This is illustrated by the fact that even the crystal structure of graphite is only an approximate model [1] as no single crystal with low enough defect concentrations has been found to allow a regular three-dimensional X-ray structure determination. In the context of catalysis it is important to note that “black carbon”, “coke”, “soot” or “carbonaceous deposit” is by no means a graphitic or even homogeneous material with reproducible properties. This leads to the wide variations in application profiles of synthetic carbon blacks (several thousand varieties) and to the difficulties in the determination of oxidation properties of “coke” on catalyst surfaces.

### 3.9.3 Overview

The carbon atom with its  $2s^2$ ,  $2p^2$  electron configuration can form a maximum of four bonds which can be either single, double or triple. As a consequence as three main connectivities result depicted in Fig. 1. The valence orbitals hybridize forming, in the elemental state,  $sp$ ,  $sp^2$  or  $sp^3$  hybrid orbitals. The data in Fig. 1 illustrate that the local bonding geometry and the carbon–carbon bond distances vary significantly with the connectivity as the bond order (and bond strength) increases from the  $sp^3$  to the  $sp$  hybridization state.

The tetrahedral connectivity leads to space-filling carbon polymers which are realized as defect-free ideal structures in diamond. The trigonal connectivity leads to sheets of carbon which are, in the defect-free variety, made up of hexagons leading to so-called graphene layers. The structures of graphite will result if these layers are



**Figure 1.** Connectivities and principle bonding properties of carbon. From top to bottom: connectivity, chemical bonding representation, distribution of  $\pi$  electrons, hybridization symbol, bond length, orientation of the  $\pi$  bonds relative to the carbon skeleton. The spectra represent polarization-dependent carbon 1s XAS data for  $sp^2$  and  $sp^3$  carbons. The angles denote the orientation of the  $E$  vector of the incident light relative to the surface normal of the oriented sample. The assignment of the spectral regions is given and was deduced from the angular dependence of the intensities of each feature. The graphite impurity in the CVD diamond film is less than 0.1 monolayers.

regularly stacked in the third dimension. In the trigonal connectivity the  $sp^2$  hybrid orbitals leave one nonbonding atomic orbital per carbon atom. These orbitals can interact with each other forming so-called weak bonds. These weak bonds can either interact as isolated or conjugated localized double bonds as in alkene molecules or as delocalized aromatic bonds providing metallic properties as in graphite. Any combination between these ideal interactions in defective carbons occurs within areas of double bond character and areas of aromatic character within one carbon sheet. In molecular chemistry this effect of varying degree of double bond localization is referred to as mesomerism. This is rarely observed experimentally (in certain polycyclic aromatic molecules) due to the limited size of organic molecules. A further consequence of the existence of the weak bonds is the action of strong dispersive forces (or van der Waals bonds) in successive layers allowing for the cohesion of graphene layers. These forces provide energy for chemisorption of both polar and nonpolar molecules on graphite surfaces. The bonding strength of the planar connectivity leads to a very poor chemical reactivity of graphene layers which are only reactive at their edges, where the lack of carbon atoms results in dangling bonds.

The trigonal connectivity leads not only to hexagons but enables the incorporation of triangles, pentagons, heptagons and larger cyclic structures as local defects into the basic honeycomb structure. A consequence of these defects is the strong

localization of double bonds around these defects and the deviation of the carbon sheet from planarity. Three-dimensional bends require the incorporation of non-hexagonal units in carbon layers. These form preferred centers of chemical reactivity as the localized double bonds will behave as alkene molecules in organic chemistry, showing pronounced reactivity towards addition and insertion as compared to the typical substitution chemistry of aromatic structures.

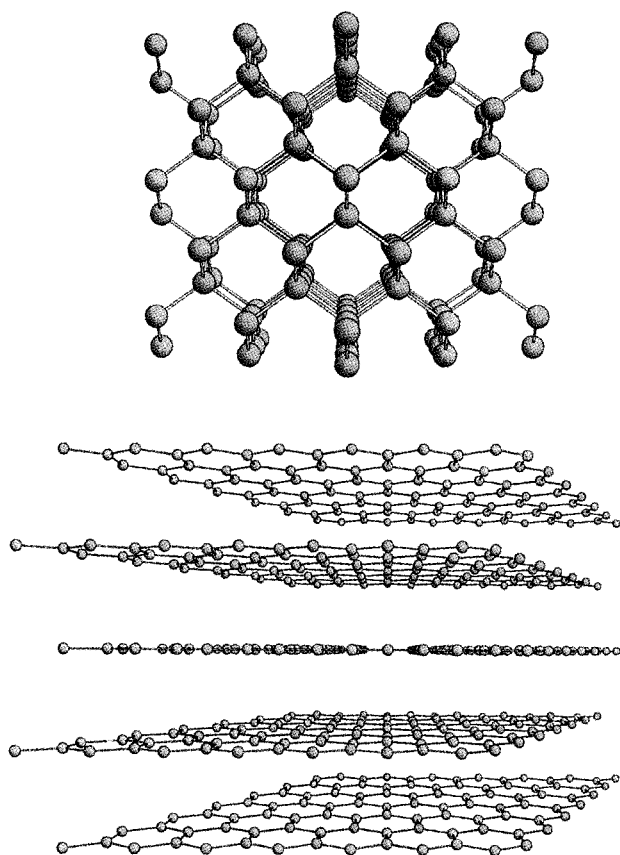
The linear connectivity of  $sp$  hybridization leads to chain-like polymers with conjugated triple bonds formed by the two sets of orthogonal nonbonding orbitals shown in Fig. 1. The resulting structure of cumulated electron density creates high chemical reactivity towards restructuring into the trigonal or tetragonal connectivity and towards addition of heteroatoms. A redistribution of the weakly bonding electrons, as found in molecular ketenes, does not occur in pure carbon materials. The inherent chemical instability of this arrangement causes the materials to occur, under ambient conditions, only rarely in pure form after rapid quenching from high-temperature carbon sources or in meteorites. These phases (e.g. chaotit) are thermodynamically metastable but can occur as part of more complex carbon polymers.

Figure 1 also shows how the different bonding situations are reflected in electron spectroscopy. Depicted are X-ray absorption spectra (XAS) [2] of  $C_{60}$ , graphite and diamond (as CVD film [3], with a trace impurity of graphite). The carbon 1s XAS method is chosen as it resolves clearly the presence of delocalized electrons from the  $\pi$  bonds shown in the connectivity diagrams. For oriented surfaces the polarization dependence of the excitation with synchrotron light allows direct determination of the orientation of the  $\pi$  bond relative to the carbon-carbon backbone bonding which accounts for the high-energy structures. Fullerene and graphite are dissimilar in their spectra mainly because of the molecular character of fullerene, giving rise to discrete bands of weakly interacting molecular orbitals, whereas in graphite a complete overlap of molecular states to broad bands of density of states gives rise to only a few structural features in the spectrum. The ordering of electronic states with energy is, however, very similar for the two carbons with the same connectivity.

### 3.9.4 Basic Structures

The two allotropes of carbon with particularly well defined properties are hexagonal graphite, as thermodynamically stable modification at ambient conditions, and its high-pressure, high-temperature allotrope, cubic diamond. Although both well-crystallised forms with only very rarely be encountered in catalytic systems, it is important to recall some details about their properties as these also prevail in the practical forms of carbon.

The idealized crystal structures are displayed in Fig. 2. The consequences of the different connectivities can be clearly seen. Diamond is an isotropic material consisting of corner-sharing tetrahedra, equivalent to a face-centred close-packed structure of carbon atoms with additional atoms in the centers of every other octant of the cubic unit cell. The ideal tetrahedral arrangement of carbon atoms leads to four equal bonds 154 pm in length. The long-range ordering can be described by



**Figure 2.** Idealized crystal structures of diamond and graphite.

layers of bent carbon hexagons with one additional interlayer bond per carbon atom. The bent hexagons are equivalent to cyclohexane with the in-plane bonds in equatorial and the interlayer bonds in axial positions. The resulting crystals are highly symmetric (space group  $Fd3m$ ) with a preferred (111) cleavage plane. The historical classification of diamond is according to optical absorption properties, which are predominantly controlled by the abundance of substitutional nitrogen and boron atoms.

The structural properties are reflected in the physical properties selected in Table 1. Diamond is a superhard, electrical insulator with an extremely good thermal conductivity. Phase transitions into the liquid state or sublimation occur outside the range of conditions for catalysis (see Table 1). Its chemical reactivity is very limited, occurring mainly through a catalyzed transformation into graphite. From there oxidation and halogenation reactions will occur. An extensive report about structural, morphological and kinetic aspects is available [4].

The trigonal connectivity leads to a planar arrangement of carbon with stronger bonds between the carbon atoms within the planes, as seen from the reduced bond distance of 142 pm. The interplanar distance of 335 pm is significantly larger than the in-plane bonds, leading to a significant reduction of the bulk density of graphite

**Table 1.** Selected properties of hexagonal graphite and cubic diamond. Anisotropic data for graphite are given in directions first parallel to and then perpendicular to the graphene layers.

Property	Graphite	Diamond
Density ( $\text{g cm}^{-3}$ )	2.266	3.514
C–C bond length (pm)	142	154
Enthalpy of sublimation ( $\text{kJ mol}^{-1}$ )	715	710
Enthalpy of oxidation ( $\text{kJ mol}^{-1}$ )	393.51	395.41
Enthalpy of formation ( $\text{kJ mol}^{-1}$ )	0.0	1.90
Melting temperature (K)	2600/9 kbar	4100/125 kbar
Thermal expansion ( $\text{K}^{-1}$ )	$-1 \times 10^{-6} / +29 \times 10^{-6}$	$1 \times 10^{-6}$
Electrical resistivity ( $\Omega \text{ cm}^{-1}$ )	$5 \times 10^{-7} / 1$	$10^{20}$
Mohs hardness	0.5/9	10

as compared to that of diamond (Table 1). All physical properties are strongly anisotropic with a metallic character within the plane directions and an insulator behavior perpendicular to the planes.

The electrical properties are unusual in that a very small band overlap between valence and conduction band of the order of 0.004 eV allows a very small number of carriers (0.02 electrons per C atom) to move freely with extremely small scattering probability. This yields good electrical in-plane conductivity. Perpendicular to the graphene planes the conductivity is of the zero-band semiconductor type with an inverse temperature coefficient as for the metallic in-plane conductivity. As defects increase in the graphene layers the conduction mechanism gradually changes from metallic to semiconducting with only moderate changes in the absolute resistivity, which now cannot be measured as an anisotropic quantity. A high density of defect states on both sides of the Fermi level [5] accounts for this behavior, which makes carbon brushes and carbon filament lamps work. The determination of the temperature dependence of the electrical resistivity is a suitable method with which to determine the degree of graphitic medium range structure in nanocrystalline carbon materials. It also allows the structural effects to be followed of heat treatment during graphitization of nongraphitic precursors.

The interplanar bonding forces are of the order of  $5 \text{ kJ mol}^{-1}$ , and are so weak that small changes in electronic structure of adjacent planes allow swelling of the structure and the incorporation of a very large number of heteroelements and molecular compounds. The electronic changes can be either (i) a weak chemical reduction of the graphene layers by donor compounds such as alkali atoms or (ii) a weak oxidation by bromine, halide salts or mineral acids. All these compounds form intercalation structures with complicated structural and physical properties which have been investigated extensively [6].

In ideal graphite the graphene layers are very large relative to their thickness and are free of intralayer defects. Furthermore, they are stacked in perfect periodicity either in ABAB or in ABCABC stacking sequences giving rise to hexagonal or rhombohedral graphite. Graphite in catalytic situations differs considerably from this ideal structural type – several types of defects give rise to different families of modifications.

Apart from reactivity towards intercalation, graphite is rather inert to other

chemicals, except strong oxidizing agents which form covalent compounds such as graphite fluoride or graphite oxide. Total oxidation of graphite to CO and CO<sub>2</sub> is a highly complex gas–solid reaction which is strongly influenced by the defect structure of the graphite. The reason for this is the chemical inertness of the ideal graphene layer, which cannot be attacked by molecular or atomic oxygen at thermal energies. Reaction thus occurs only at defect sites, such as missing atoms or non-hexagons, and on the perimeter of the graphene layer which collectively form the prism faces of graphite crystal. As these faces occupy less than 0.1% of the graphite crystal faces the number of reactive centers for oxidation in graphite is small. Reactivity thus depends heavily on the additional sites provided by in-plane defects.

In summary, graphite and diamond are two modifications of carbon with similar strong bonds between the carbon atoms (difference in bond length 8.5%). The differing hybridization leads to a different orientation of the covalent interaction. The strong structural anisotropy of graphite as compared to the perfectly isotropic diamond structure gives rise to fundamental physical and structural differences. The differing carbon–carbon bond strengths provide the handle with which to discriminate between the two modifications with a variety of spectroscopic methods. Such methods are of minor importance as long as crystalline materials are under discussion. In catalytic situations, however, multiphase amorphous carbon is frequently encountered which cannot be analyzed convincingly using diffraction techniques.

The fullerenes and carbiners, which are also well-defined forms of carbon, are very rare in their pure forms in catalytic materials. For this reason they will not be treated in detail in this work. Briefly, carbiners are molecular crystals of columns of carbon atoms linked with alternating single and triple bonds. The column length is variable but mass-spectral data suggest lengths of between 10 and 20 carbon atoms. A collection of properties of these silver-white carbons prepared by shock sublimation of graphite which seem stable only at temperatures above 2300 K but survive storage in natural conditions for thousands of years can be found in the literature [7].

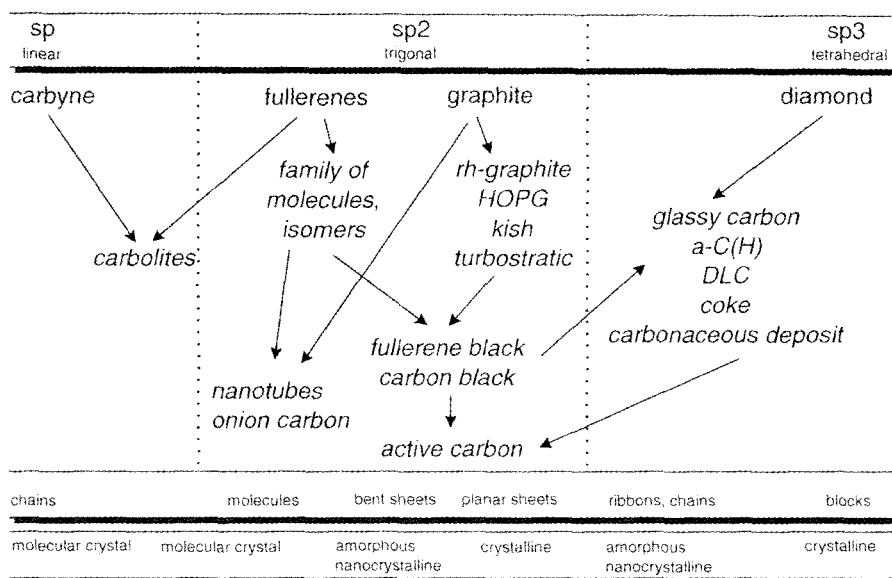
Fullerenes [8, 9] are a large family of molecular carbon cage structures all with carbon atoms in the sp<sup>2</sup> configuration. The three-dimensional structure is made possible by a controlled incorporation of pentagons [8] into the hexagon network. The high symmetry of the resulting ball-shaped molecules is the consequence of certain rules of combination, such as never combining two pentagons and including only 12 pentagons in every molecule. In the frequent event of not following these rules, the bent carbon sheets polymerize to form complex amorphous carbons called fullerene black [10]. It is very important, in the present context, to note that the chemistry of these spherical sp<sup>2</sup> carbons is substantially different from that of the planar allotrope, graphite. The distinction arises from the “strain” in the weak bonds of the fullerenes. The non-planar geometry of the backbone reduces the orbital overlap of the  $\pi$  electrons (Fig. 1) causing localization of the double bonds and an overall chemistry of an electron-poor electrophilic polyalkene [11–13]. One consequence of this is an enhanced reactivity of fullerenes against oxygen compared to graphite [13–15]. Bends in graphene layers are thus the preferred centres of chemical reactivity even without the presence of coordinative under-saturation.

### 3.9.5 Loosely Defined Structures

Figure 3 summarizes some families of carbon materials which are defective variants of the basic allotropes shown in the top line of the scheme. These materials exhibit distinctly different properties compared to the idealized parent structures, so that they are often considered as carbon modifications in their own right. In the bottom lines the long-range ordering types and the crystal types are given for the families of materials.

Carbolites [7] are orange-colored transparent solids with a very low density of  $1.46 \text{ g cm}^{-3}$ . They can be prepared by graphite evaporation under conditions similar to fullerene formation but using argon or argon–hydrogen as quench gas at higher pressures than for fullerene formation. The structural properties are collected in Tables 2 and 3. Models of short chains of carbene structure with assumed interchain cross-links are controversial. The material is rather stable in ambient conditions. High-temperature processes and high temperature gradients are prerequisites for their formation.

The fullerenes [8, 9, 16] are well-defined molecular solids for the smallest compounds mainly for  $\text{C}_{60}$ ,  $\text{C}_{70}$ ,  $\text{C}_{72}$  and  $\text{C}_{84}$  which can be obtained in measurable quantities as purified materials. These molecules are soluble in solvents such as toluene or trichlorobenzene. They form deeply colored solutions which can be purified



**Figure 3.** Families of carbon materials. The top line indicates the connectivity followed by the parent carbon materials representing, according to present knowledge all allotrope phases of carbon. The range of materials in the center of the figure comprises carbons with distinct structural and chemical properties. Whether these are distinct phases or metastable phase mixture is not clear. The arrows mark structural relationships between the materials. The lower lines indicate the shape of the basic structural units and their organization in the solid state.



**Table 2.** Characteristic structural data for various carbon forms.

Carbon	Unit Cell Parameters		
	<i>a</i> axis (pm)	<i>c</i> axis (pm)	$\gamma$ (deg)
Graphite hexagonal	246.2	676.8	120
Carbine	894.0	1536.0	120
Carbine II	824.0	768.0	120
Carbolite	11928	1062	120
Diamond cubic	356.7	—	—

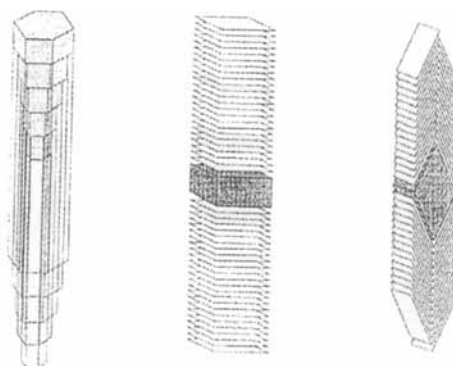
**Table 3.** Raman data.

Carbon	Frequency (cm <sup>-1</sup> )	Appearance
Graphite	1582	sharp
Diamond	1332	sharp
Carbon black	1355	broad
a-CH	1332 + 1500	sharp + broad
Glassy carbon	1359 + 1600	broad + broad
Nanotubes (mixtures)	1566 + 1592	sharp + sharp

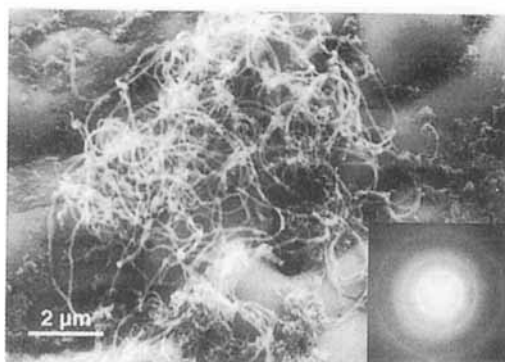
by liquid phase chromatography. The respective molecular solid needs careful sublimation to remove solvent and gas adducts. Fullerenes are air sensitive [17] and light sensitive [11] and decompose slowly by polymerization (becoming insoluble after storage in air).

The large number of predicted larger molecular structures [18] have not been observed as pure compounds, although evidence for the formation of larger cage molecules comes from TEM investigations of the residues of evaporated graphite after extraction of the small soluble fullerenes [19]. Such cage molecules may be present in amorphous carbon materials that have been subjected to sufficiently high temperatures for the skeletal rearrangement. These temperatures are reached in many combustion processes and in understoichiometric oxidation reactions of aromatic and aliphatic hydrocarbons [20]. These studies show that fullerenes can occur in many conventional reactions and not only in graphite evaporation processes which are not frequent in catalytic chemistry.

A class of intermediate compounds between graphite and fullerenes are the nanotube materials. Nanotubes are a special subgroup of graphite fiber materials [21] which can be formed by a wide variety of structure elements. Nanotubes consist of helical twisted [22] sheets of graphite capped with two half-shells of molecular fullerenes. This continuous arrangement of sp<sup>2</sup> carbons exhibits very special electronic properties [23] and is a highly desirable material which is still difficult to obtain in the pure form. Nanotubes frequently contain several layers of graphene sheets wrapped concentrically around each other. In catalytic chemistry this form of tubes or filaments is rather rare. They are very much in contrast to other forms of carbon filaments or tubes which are created under the influence of catalytic con-

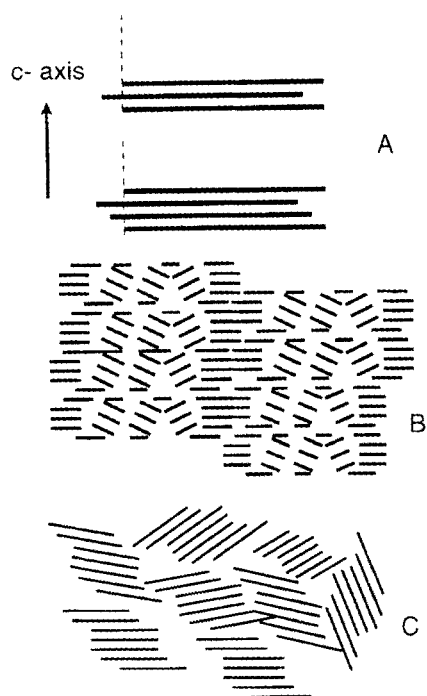


**Figure 4.** Carbon filaments [24] occur in several varieties, differing in the relative arrangement of the graphene units. The orientation is determined by the faceting of the metal catalyst particle (dark). The bottom SEM image shows a spaghetti pile of carbon fibers of tubular orientation. The reaction system was methanol on silver, the catalysts were particulate impurities of metals other than silver. The selected area of electron diffraction pattern shows the ring pattern for turbostratic graphite.



version of hydrocarbons (see below). Figure 4 summarizes common forms of graphitic filaments [24] which all consist of graphene sheets which are stacked together without chemical bonds between the basic structural units [25]. This lack of continuous chemical bonding drastically affects the electronic properties and the chemical reactivity, which are comparable to that of planar graphite. The dark blocks in the figure symbolize the location of the catalyst which is most effective when it contains iron or nickel. A combination of catalytic metals, such as iron or nickel with phosphane impurities, leads to the growth of extremely unusual forms of carbon fibers such as helically wound graphite spirals from acetylene at 975 K [26]. Under catalytic conditions a wide variety of carbon filaments, which may not be linear but resemble spaghetti piles, are possible and may not be recognized as carbon. This is illustrated in Fig. 4 with a silver catalyst used for methanol dehydrogenation with a deposit as spaghetti pile. The identification of carbon was possible by selective area electron diffraction and by energy-dispersive X-ray analysis. From the diffraction pattern it is seen that the internal structure of the fibres is as displayed in the top left schematic drawing.

Onion carbon [27] is also a derivative of graphite which is made from concentric spherical graphene layers which are said to be continuous [28]. A more frequent form of polyhedral graphite particles is made from packages of concentric graphene



**Figure 5.** Stacking variants in graphitic carbon: (A) ideal graphite in ABA and ABCA stacking; (B) partly graphitized carbon with regions of angular inclined graphene stacks between parallel aligned graphene stacks; (C) irregular graphene stacks of nongraphitic  $\text{sp}^2$  carbons.

layers which are bent but not closed by continuous chemical bonds. Such materials occur in graphitization processes of all kinds of precursors and can grow in size to several microns. As it has not been possible to isolate more than milligram quantities of onion carbon little is known about its chemical properties. Its existence in any carbon material indicates, however, a thermal prehistory of graphitization conditions, i.e. temperatures well above 1500 K with reducing or inert gas phase compositions.

A large group of carbon materials represent the disorder varieties of graphite. Figure 5 summarizes stacking schemes along the crystallographic  $c$ -axis. Figure 5(A) shows the stacking of large graphene layers which can be continuous up to lateral sizes of several hundred micrometers. The most frequently observed regular stacking of carbon atoms within the sheets are the hexagonal ABA stacking as in natural graphite and the rhombohedral ABCA stacking. Regular stacking of the graphene layers which are only very weakly bound to each other (by induced dipole moments of the aromatic  $\pi$  electrons) is given by a closest packing of the carbon atom spheres. This gives rise to the following dimensions for ideal hexagonal graphite:

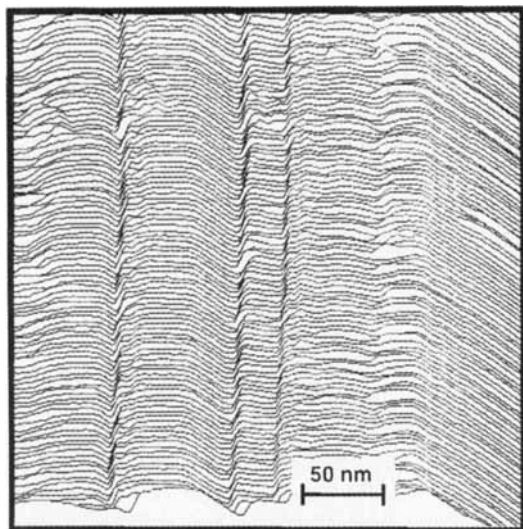
- in-plane distance 142.1 pm
- in-plane lattice constant 246.2 pm
- $c$ -axis lattice constant 670.8 pm
- interlayer distance 353.9 pm

The rhombohedral graphite polymorph is slightly less stable than hexagonal graphite and converts during oxidation or even during mechanical treatment (ultrasonication, milling) into the hexagonal form. It can be discriminated by its powder X-ray diffractogram in the region of the cross-lattice reflections ( $h \neq 0, l \neq 0$ ), which are generally sensitive to the stacking order of a graphite material. The presence of rhombohedral reflections can be used as an absolute criterion with which to identify natural graphite.

As the interlayer bonding in graphite is so weak, it is easy to obtain graphite with little or no regular stacking order, which explains the extreme difficulty of obtaining single crystals of graphite. The interlayer distance increases up to 344 pm as a consequence of the absence of stacking. Even higher values have been reported, which are characteristic for nanocrystalline carbon in which the graphene layers are no longer parallel to each other (see Figure 15). A large number of graphitic materials exists between these two cases, in which the graphene layers become successively smaller and form packages of parallel layer fragments, known as basic structural units (BSUs) [235]. These packages can either be aligned in parallel or may be inclined towards each other. In Fig. 5(B) regular arrays of parallel and inclined stacks of BSUs can be seen. This alignment is characteristic of synthetic graphite used as catalyst support materials. As the chemistry of the edges of the BSU stacks is very different from that of the basal planes, a patterned surface chemistry is observed. The patterning depends on the average angle of inclination. In synthetic graphite which is postannealed after its formation under high temperature and at hydrostatic pressure [29] highly oriented pyrolytic graphite (HOPG; Fig. 3) this angle is as low  $1^\circ$  for top quality samples used as graphite monochromators. At angles of  $5\text{--}30^\circ$  these materials are known as pyrographite. The absence of any preferential alignment is observed between the BSU stacks in pyrocarbons and some carbon black materials. Such a secondary structure is often observed when the process of carbon generation occurs at low temperatures or in large temperature gradients. The surface chemistry of these hard carbons is characterized by a hydrophilic nature, caused by the many terminating oxygen functionalities on these materials.

Kish graphite is a well-ordered variety of synthetic graphite obtained from exsolution of carbon out of liquid iron. Under certain conditions excess carbon, which is insoluble as FeC, crystallizes in a well-ordered platelet morphology and can be isolated by dissolution of the iron matrix in mineral acids. It is the macroscopic variety of the BSU which forms the graphene stacks in filamentous carbon, as shown in Fig. 4. Under certain cooling conditions of the iron melt these flakes can grow to 1 mm in diameter. They represent, by their extraordinarily high degree of ordering, the closest known approximation to graphite single crystals. In catalytic systems the microkish graphite particles are also of highly crystalline, rendering them very resistant to chemical transformation in oxidising or reducing atmospheres.

An example of the lateral anisotropy of the surface chemistry which results from the partial alignment of BSUs according to Fig. 5(B) can be seen in Fig. 6. The STM wide scan shows a system of trenches in HOPG which was oxidized in air at 1000 K for 30 min. Smooth rectangular stripes of hydrophobic graphitic basal planes coexist with almost the same surface area of prismatic faces of the step surfaces. The wedge-shaped contours are imaging artefacts caused by the STM tip. As



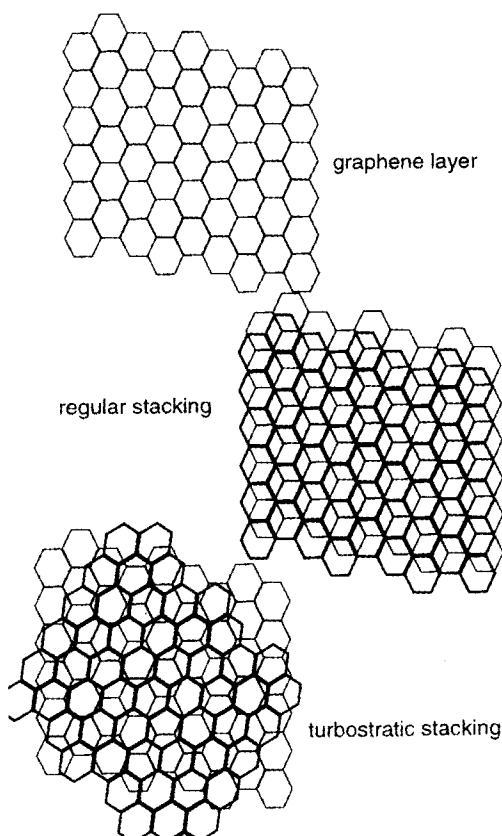
**Figure 6.** Low-resolution STM survey image of a partly oxidized graphite flake. The asymmetric V-shape of the deep trenches is a tip artefact. Conditions: Burleigh ARIS 6000, air, W tip, constant current mode, gap voltage 200 mV.

oxidation proceeds, mainly on the prismatic edges, a pattern results from high recession velocity in the valleys and a low reactivity at the basal planes.

The unidimensional disorder of graphene stacking has a two-dimensional counterpart in the relative angular orientation of the hexagons within adjacent graphene layers. Figure 7 shows schematically the two possibilities of stacking in two-dimensional registry (relative displacement of carbon atoms 0.5 and 0.5 unit cell lengths, hexagonal stacking) and without registry which is referred to as turbostratic disorder. This special state of crystalline disorder is characteristic of layered materials with weak interlayer bonding. Its detection indicates well-developed graphene layers with very little chemical impurity which would force the stacking of layers into a three-dimensional disordered state with no parallel orientation of adjacent BSUs. Nongraphitic carbons frequently exhibit this type of disorder with the consequence that all X-ray diffraction peaks other than the (002) line are absent or very broad.

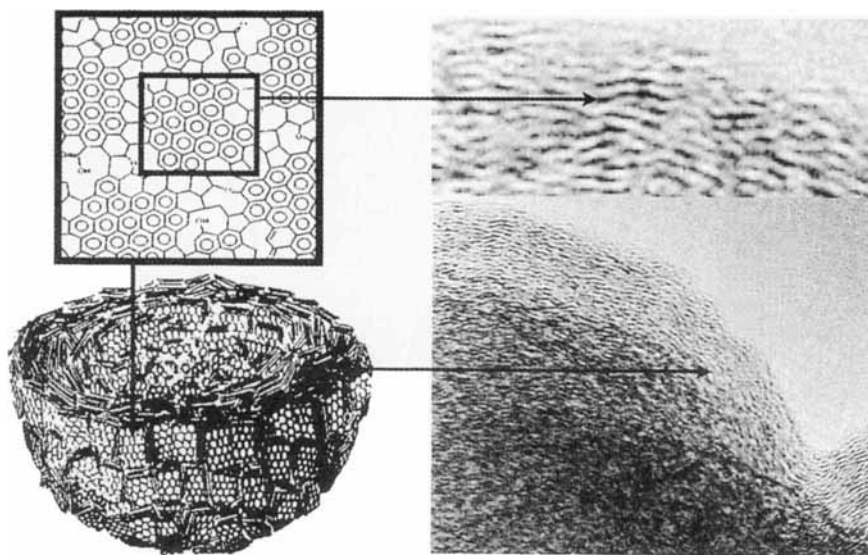
These disordered carbons constitute a transition form, between graphite and carbon blacks, which are turbostratic materials with the additional complication that the lateral size of the BSU becomes very small with typical sizes of below 5 nm. Carbon blacks appear as chainlike aggregates of spherical particles of 10–50 nm diameter [30]. Elemental analysis reveals a significant hydrogen content of  $C_{8-12}H$ . Such materials are referred to as nanocrystalline carbon as the X-ray diffraction mechanism changes from Bragg diffraction to elastic scattering with the different physics of the scattering process [31, 32]. The broad peak in the range of the graphite (002) is no longer a Bragg peak but represents the absolute maximum of the pair correlation function which is dominated by the still parallel arrangement of small graphene layers of sizes comparable to large aromatic hydrocarbons [31].

Figure 8 represents models and high resolution transmission electron microscopy of the secondary structure of carbon blacks forming spherical aggregates. The shell



**Figure 7.** In-plane ordering of graphene layers. The turbostratic case gives rise to Moiré and pseudosymmetric superlattice structures, detectable in STM images. In many cases, however, no correlation exists between the individual layers. The turbostratic ordering has very little effect on the interplanar spacing. Enlarged  $c/2$  parameters arise from defects such as  $sp^3$  centers which accompany the turbostratic graphene layers.

structure of stacks of graphene layers optimizes the interstack interaction, via heteroatoms located at the prism edges of each graphene layer. In many materials the shells are filled by smaller particles or grow around a noncarbon nucleus. The interstack interactions are mediated in many carbon blacks through hydrogen bonds of adjacent OH groups. The outer surface of a black particle also contains significant amounts of OH groups which control the aggregation of the primary spherical particles to fractal larger aggregates, often called the “structure” of carbon black. Modification of the ion strength (for example in aqueous solution) affects the strength of the interaction and influences the aggregation behavior. Thermal activation of the hydroxy groups creates dangling bonds and reorientation of the graphene packages so as to form a covalently cross-linked polymer. The process creates  $sp^3$  bonds and leads to an enormous decrease in chemical reactivity and an increase in mechanical strength. This important aspect of the reactivity of carbons with a high fractional prismatic surface area has the consequence that thermal treatment even under oxidizing conditions can transform the reactive carbon black material into highly stable glassy carbon (see below).

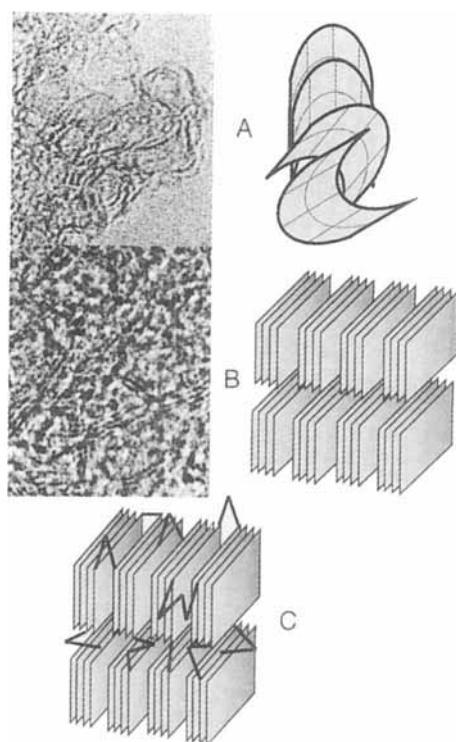


**Figure 8.** Microstructure of carbon black. The nested model is built from planar BSU stacks interconnected by covalent bonds (see top scheme). One BSU (central frame in top scheme) is resolved in high resolution TEM of a real carbon black particle (FW-1, Degussa, Phillips CM 20 FEG, 200 keV). The main image shows a projection through an agglomerate of spherical black particles. The distance between the BSU is 340 pm.

Fullerene black is of a similar constitution and secondary structure as normal carbon black, but with the important difference that its BSUs are composed of non-planar graphene layers. Additionally, the stacks are not straight but curved, giving rise to a more disordered and less dense carbon material. The chemical reactivity is higher as the stability of nonplanar graphene layers is reduced. In addition, the irregular shape of each graphene layer prevents the formation of parallel stacks to a large extent. A fully amorphous array with a large surface fraction of prism faces with result which additionally increase the chemical reactivity.

Figure 9 summarizes these interactions in nanocrystalline carbons which constitute a large fraction of carbonaceous deposits on catalytic materials. It is important to note that these carbons exhibit a high reactivity towards polymerization under weakly oxidizing conditions (inert, vacuum, steam, reducing) and a high reactivity towards total oxidation under strongly oxidizing conditions. Both reactivity patterns are a consequence of the high ratio of prismatic to basal surface area of the carbon stacks. The materials in Figs 9(A) and 9(B) result from weak interactions between the various building blocks. A carbon with  $sp^2$  and  $sp^3$  local bond geometries is formed after polymerization by cross-linking with bonds, atoms or even molecules, as schematically illustrated in Figure 9(C).

The resulting hard carbon black is nongraphitizable by thermal treatment up to 3000 K. The  $sp^3$  bond cannot be rehybridised to  $sp^2$ . These hard carbons are often referred to in catalytic systems as carbonaceous deposit. The material contains some



**Figure 9.** Organization of carbon sheets in nanocrystalline carbons. Case (A) represent bent sheets which are stacked concentrically and randomly. In the high-resolution TEM of fullerene black filamentous structures from carbon macrocycles which did not react to fullerene molecules can also be seen (weak contrasts). Case (B) shows the arrangement of stacks of planar graphene units. Only few of these stacks are oriented with the *a*-axis parallel to the electron beam and can be imaged as illustrated in the sketch, the majority are randomly orientated and give hence an amorphous contrast. Case (C) is the same as (B) with the addition of covalent bonding interactions between the stacks. These bonds are invisible by electron microscopy but influence the graphitizability of the carbon.

heteroatoms (usually hydrogen). It is chemically heterogeneous, structurally amorphous, mechanically hard, and exhibits no graphitic properties, although the large majority of all carbon-carbon bonds are  $sp^2$  hybridized. Higher contents of heteroatoms and the presence of nitrogen, sulfur and oxygen are characteristic properties of coke, the product from carbonization of coal or other hydrocarbon sources with larger molecular constituents. Carbonization is a polymerization process in which small molecules such as methane are liberated. Heteroatoms in the form of ammonia, water and hydrogen disulfide are removed and irregular stacks of small graphene layers (originating from the large organic molecules) are cross-linked by molecular fragments under preservation of the irregular orientation of the stacks (Fig. 9(C)).

In a-CH or diamond-like carbon (DLC) the hydrogen content is as high as  $CH_{0.4}$



and the carbon atoms are arranged in ribbons or chains with no discernible stack structure of graphene layers. Glassy carbon is a technical product made from carbonization of organic polymers and consists of ribbons of  $sp^2$  carbon with a significant contribution of nonhexagonal rings allowing a three-dimensional tangled structure. This creates the high mechanical hardness and the resistance against graphitization lending to this material excellent mechanical stability at high thermal and mechanical load (only under nonoxidizing conditions). Turbostratic stacks of 3 nm width and 10 nm length form the continuously bent BSU of this carbon, which can be formed in catalytic reactions allowing polymerization of molecular precursors followed by carbonisation at around 1000 K (in regeneration cycles for example). The content of  $sp^3$  bonds is low in this material but the hydrogen content which is required to saturate the high specific prismatic surface area of the ribbons, is significant.

Active carbon or charcoal is an important modification of carbon in catalysis. It consists of carbonized biopolymer material which is activated in a second step. This procedure creates a high specific surface area by oxidative generation of micropores of very variable size and shape distribution. A more controlled activation is achieved by the addition of phosphoric acid or zinc chloride to the raw product. The additive is incorporated during carbonization into the hard carbon and is subsequently removed by leaching creating the empty voids in a more narrow pore size distribution as achievable by oxidation. Other activation strategies employ liquid oxidants such as nitric acid to create large pores with a very wide size distribution. Today, many thousands of patents describe numerous ways to structurally activate carbon [33] from mostly natural sources.

A large number of oxygen functional groups are created during the activation process by saturation of dangling bonds with oxygen. This creates a rich surface chemistry which is used for selective adsorption. In addition, it determines the ion exchange properties that are relevant for catalyst loading with active components. A more detailed description of the surface chemical aspects which are most relevant for the catalytic uses of nanocrystalline and activated carbons follows below. The microstructure of activated carbon may be described by the archetypes depicted in Figs 9(B) and 9(C) and may even contain significant amounts of graphitic structure [34], depending on the temperature regime of activation. The micromorphology is often characteristic of the biological origin of the raw material with shapes of cell arrays and even whole plant organs being detectable by SEM imaging. Active carbon contains significant amounts of inorganic matter (iron silicates, silicates, calcium oxides etc.) which is analyzed as ash content after complete combustion. Activated carbons are very heterogeneous materials and are difficult to characterize in microstructure and reactivity. Recent reviews about this class of large-scale technical carbons are available [35, 36].

To summarize, a wide variety of forms of carbon can be found under catalytic conditions. In particular, during deposition and thermal post-treatments a very complex carbon material with unexpected chemical and structural properties can result, causing severe problems in catalyst regeneration and modification of its properties during deactivation. The group of carbons which specifically employed in catalytic systems is summarized in Table 4 together with its most important physi-

**Table 4.** Types of carbon supports and their geometric surface areas.

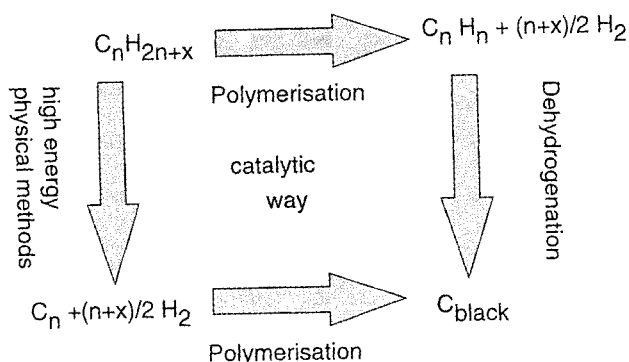
Carbon	Surface area ( $\text{m}^2 \text{g}^{-1}$ )
Natural graphite	0.1–20
Synthetic graphite	0.3–300
Graphitized carbon blacks	20–150
Carbon blacks	40–250
Activated carbon from wood	300–1000
Activated carbon from peat	400–1200
Activated carbon from coal (coke)	200–1000
Activated carbon from coconut shells	700–1500

cal parameter, the specific geometric surface area. The values vary over three orders of magnitude and reach values between geometric surfaces of micron-size particles up to the surface area of the number of carbon atoms in the sample. These latter values are unrepresentative if they are interpreted in terms of a monolayer coverage of the nitrogen probe molecules. Highly porous carbons exhibit pronounced capillary condensation phenomena requiring a full BET isothermal analysis for the determination of the true geometric surface area. Although this is widely known and described in detail in other sections of this handbook, it is still customary to present these very high numbers of BET surface area. Care must be taken in comparing data based on surface area measurements in carbon chemistry as some sources determine the monolayer sorption capacity, whereas others do not. For this reason surface area values determined with various adsorbents, such as nitrogen,  $\text{CO}_2$  or Kr, may also differ significantly as these probe molecules exhibit quite different condensation properties at the conditions of adsorption. The most useful contribution of sorption data to evaluate the nature and size distribution of porosity in carbon materials is not discussed here.

It is noted that in different areas the use of terminology to describe structure and properties of carbons is quite different. Within the carbon-science community a clear system of terminology and definitions was elaborated which is recommended whenever applicable [37, 38].

### 3.9.6 Formation of Carbon Materials, General Pathways

The technical synthesis of graphite, diamond and a variety of other forms of  $\text{sp}^2$  carbons (Fig. 3) is described in a review [39] and is not covered here. As the unintended formation of carbon in deactivation processes and the modification of primary carbon surfaces during chemical treatment (in catalytic service and during oxidative reactivation) and their chemical properties are frequent problems encountered in catalytic carbon chemistry, it seems appropriate to discuss some general mechanistic ideas which mostly stem from the analysis of homogeneous combustion processes (flame chemistry) and from controlled-atmosphere electron microscopy.



**Figure 10.** Reaction pathways from organic molecules to solid carbons. The fundamental processes of dehydrogenation and polymerization occur simultaneously in the catalytic pathway.

The source of all carbon relevant to the present context is the feedstock of hydrocarbon molecules (aliphatic, aromatic, with and without heteroatoms). Figure 10 summarizes the possibilities for their conversion into black carbon. The chemical route comprises polymerization into aromatic hydrocarbons with final thermal dehydrogenation. This process often includes a liquid crystalline phase immediately before final solidification. In this phase large aromatic molecules can self-organize into parallel stacks and form well-ordered precursors for graphitic structures with large planar graphene layers. This phase is referred to as mesophase and can be observed by polarized light optical microscopy.

The physical pathway requires activation of the molecules by high external energy input such as high-temperature flames, projectiles like accelerated and free electrons, or the presence of a plasma source. These conditions can also occur in analytical instruments such as electron spectrometers and microscopes which have the potential to create black carbon during analytical inspection of hydrocarbon layers [27]. In all these cases the molecules are fragmented and dehydrogenated in one process and represent a source of free carbon atoms or small fragments such as  $C_2$  dimers. These fragments condense into chains of carbon atoms which have a strong tendency to form small ring molecules by nucleophilic self-substitution of the end groups. Saturation of the dangling bonds of the primary rings by polymerization leads to graphene layers. These processes occur very rapidly compared to the slow activation along the chemical path. Little time is available for orientation of the rings into stacks, and cross-linking into nonplanar units can easily occur (see Fig. 9). Hard, nongraphitizable carbons are the final products of these processes in which all fullerenes and fullerene blacks are also formed.

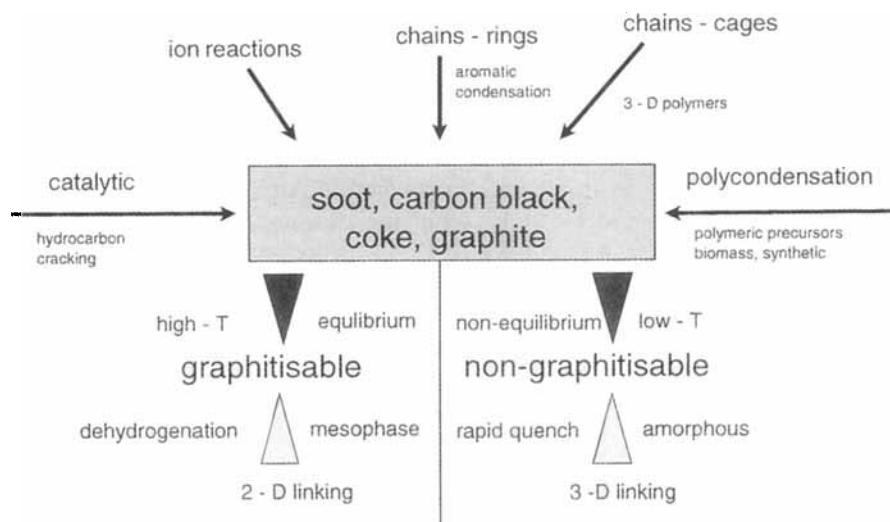
A large number of intermediate pathways are possible when catalytic reactions interfere with the polymerization–dehydrogenation steps. A common scenario is the catalytic dehydrogenation of hydrocarbons on nickel surfaces followed by dissolution of the activated carbon atoms and exsolution of graphene layers after exceeding the solubility limit of carbon in nickel. Such processes have been observed experimentally [40] and used to explain the shapes of carbon filaments. In the most recent synthetic routes to nanotubes [41] the catalytic action of in situ-prepared iron

metal particles was applied to create a catalyst for the dehydrogenation of either ethylene or benzene.

### 3.9.7 Formation of Carbon Materials, Mechanistic Aspects

A schematic correlation between reaction pathways and the principal structural properties of common carbon forms according to the classifications given in Fig. 3 is presented in Fig. 11. The literature [33] is rather controversial [42] allowing only a survey of chemically plausible pathways relevant to the present conditions of possible carbon formation.

Three main synthetic routes to carbon can be identified, none of which produces exclusively one phase or modification of carbon. In all cases, mixtures are produced, as indicated by the central box in Fig. 11. This complexity highlights the generally strong influence that kinetic aspects have on the formation reactions. The realization of a perfect  $sp^2$  local configuration is always energetically favourable and is reached in graphene layers with only hexagonal constituents. The saturation of the peripheral dangling bonds of graphenes can occur either by homonuclear cross-linking (resulting in macroscopic planes or irregular arrays of stacked graphenes) or by heteronuclear bonding (resulting in either polymers or surface functional groups). Metastable configurations contain mixtures of six-membered rings with other ring geometries causing strain in the  $sp^2$  bonds. Nonplanar structures of a wide variety result. These structures are chemically highly reactive and disappear in oxidizing or hydrogenating atmospheres, preferentially over planar structures. This explains an additional strong influence of the gas phase conditions on the distribution of carbon materials.



**Figure 11.** Reaction pathways to the mixed materials with  $sp^2$  connectivity. All these materials occur as either a reactive form (graphitizable) or as a nonreactive final product (see also Fig. 9).

The group of synthesis routes at the top of Fig. 11 combines the chemistry of carbon formation in combustion processes [43, 42]. In high-temperature combustion reactions (above 1200 K) the general reaction occurs via the physical pathway indicated in Fig. 10 with initial fragmentation into neutral species and thermoions (without an additional source of energy).  $C_2$  fragments such as acetylene, or oligomers react to form carbon chains which result in predominantly aromatic molecular fragments (with dangling bonds) and to a lesser extent in combustion atmospheres as three-dimensional cage structures with both  $sp^2$  and  $sp^3$  bonds (becoming a dominant path in fullerene-generating conditions). In cooperation with ionic fragments these secondary building blocks condense to the graphene BSUs with a planar or bent layer structure. In a detailed analysis of the flame chemistry [44–46] a three-zone model of a flame was derived. The elementary building blocks for carbon are formed in the hottest oxidation zone. A surrounding zone with luminous constituents is identified as the location of chain growth into polyalkyne molecules of the form  $C_nH_2$ . In the third dark zone these molecules rearrange into polycyclic hydrocarbons and finally into graphene layers. Ample evidence for this model comes from mass spectral analysis of the gas phase in various types of flames. This diagnostic method gives no indication about the reactive particles, as by the time of their detection they are energetically cold and represent the ground state of a mere species rather than the reaction intermediate. For this reason it is difficult to see that long linear chains could be important intermediates as they are never found in carbon products. A scenario in which these processes are modified by interaction of thermoions [47, 48] and/or aromatic radicals [49] and several independent repair mechanisms for a maximum yield of six-membered condensed rings seems more plausible [42]. The kinetic boundary conditions are of great importance in all these processes as large local temperature gradients are required to allow a significant accumulation of carbons from reactive intermediates. At constant high temperatures the unstable species decomposes effectively back into their constituents. This was studied in detail in several types of combustion reactions [45] and is the guiding principle of all technical processes for carbon black synthesis [39].

Another important aspect is the nature of the hydrocarbon source in relation to the efficiency of carbon formation. The idea that the structure of the molecule should be relevant for the carbon formation (aromatic molecules are better than aliphatic structures) is incorrect in all situations where a pool of primary building blocks is formed (in flames, under oxidative polymerization conditions and under physical activation). However, it is confirmed that a decrease in the average C–C bond energy allows easier chemical fragmentation, which enhances the rate of carbon formation [50].

The growth of carbon particles cannot occur in one synthetic step by condensation of small molecular units. However large an aromatic molecule may become [47–49] it will be too small to create a micron size carbon particle. Three major routes can lead to such large particles. The most unlikely case is a continuous polymerization process at the surface of a fullerene molecule [8]. Both the unfavourable kinetics [51] and the absence of structural evidence that fullerene-like structural elements (identified by characteristic C–C bond lengths) occur in the radial distribution function of black carbon material [31] are strong indicators that

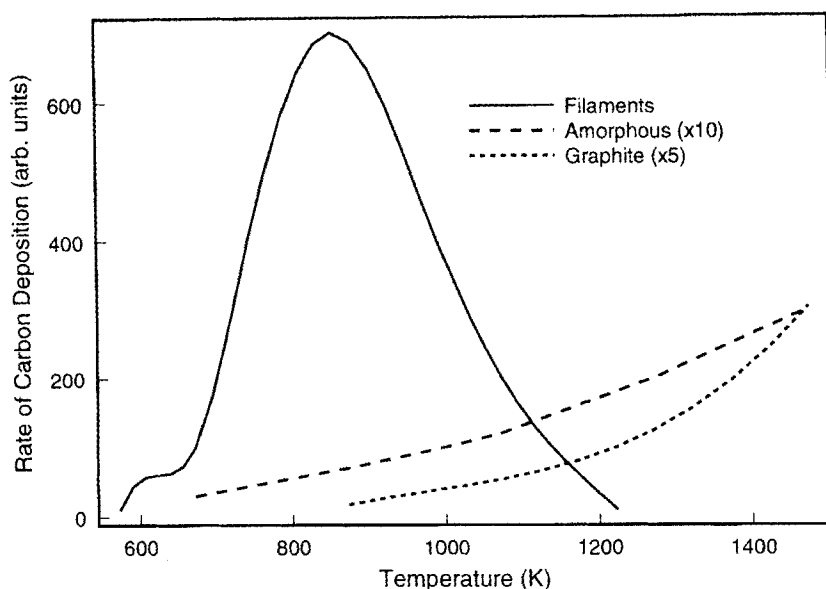
carbon particles, although of spherical morphology, grow in a heterogeneous rather than in a homogeneous way. In a combined kinetic, statistical and microscopic analysis of the growth process [47, 52] a model of surface growth was put forward. According to this, the polyaromatic molecules are dehydrogenated and the dangling bonds are saturated by cocondensation of alkyne units. A mass growth of carbon particles of 90% of the total carbon inventory could be explained in this way, which is in excellent agreement with experimental flame studies [47]. The prediction of this model of a structureless agglomerate of aromatic molecules surrounded by a concentric array of graphene layers [52] is in excellent agreement with all HRTEM observations of homogeneously produced carbon particles. The spherical texture is assumed to be the consequence of droplet formation of aromatic molecules in the initial stages of carbon fragment supersaturation required for homogeneous nucleation. These droplets are not residues from the possible liquid initial fuel, but occur as a consequence of the very rapid initial polymerization of the highly active small carbon fragments.

In summary, all processes which homogeneously generate carbon from molecular precursors and from homogeneous activation lead to spherical particles made from graphene layers (see Figs 8, 9(B) and 9(C)). Spontaneous growth from super-saturated reservoirs of small molecular precursors (chains, alkyne structures, poly-alkynes) of PAH and cocondensation with smaller molecular fragments lead to spherical carbon particles which aggregate to chains of spheres.

Carbons with much larger continuous graphene layers can be obtained from pyrolytic polymerization of prepolymerized hydrocarbons. Synthetic materials such as kapton or polyacrylonitrile (PAN), or biopolymers such as coconut shells, wood coal, rice husks and similar materials, can be used. Carbonization or “coking” involves the chemical removal of all heteroatoms such as nitrogen or sulfur and the cross-linking of the polymeric blocks via the dangling bonds created by the removal of the heteroatoms. In this way the texture of the precursor material is preserved in the final product. As no fragmentation of the precursor is required, this method of carbon generation is much less energy intensive. It leads further to a great variety of structural properties with extreme examples as shown in Figure 9. The possibility of retaining a portion of the heteroatoms, such as silicates in biomass carbon, makes it feasible to produce extra strong carbons (silicate reinforced). These can be useful for anchoring catalytically active metal components such as noble metal particles. The exact chemistry of carbonization is complex and depends on the nature of the precursor and on the gas phase chosen (inert, oxidizing, steam, reducing). For this reason no general description is possible of this difficult to control process, which occurs between 500 K and 1000 K.

### 3.9.8 Catalytic Formation of Carbon from Molecules

The catalytic generation of carbon (Fig. 11, left side) is of significance as the deactivation reaction in many processes involves the presence of hydrocarbons and of transition metal reaction sites. These catalyze dehydrogenation reactions or form solid acid–base centers catalyzing polymerization reactions (see Fig. 10). In a



**Figure 12.** Carbon deposition on metal particles as a function of metal temperature. The dominating form is filamentous carbon, and more conventional forms occur in sizeable quantities only in extremely high-temperature catalytic processes. (After [24]).

review [24] a large amount of kinetic data was compiled about the type of carbon deposited as a function of deposition temperature. Figure 12 shows that the predominant carbon form at most catalytically useful temperatures is filamentous carbon. The carbon source may be CO, methane, acetylene or other hydrocarbons. The metals for which this correlation is valid are either nickel or iron on all kinds of conventional supports and also as binary or Cu alloys. It is important to note that forms of carbon other than filaments rarely grow under the conditions required for steam reforming or Fischer–Tropsch synthesis.

The sequence of events for the growth of these filaments, which can destroy the whole catalyst bed, is now well understood [53–56]. Electron micrographs of the catalyst particles show that they are detached from their support and form either the front or occasionally the centre of a growing carbon filament. In all cases the shape of the particle changes during its operation as the filament growth catalyst. The growth of an anisotropic carbon particle requires structure sensitivity from the process of carbon atom-to-graphite polymerization. Otherwise a shell of graphite would be produced around a core of metal which would then stop acting as a catalyst after completion of the carbon shell. Such morphologies have been observed but are not discussed here as they occur either at high temperatures (see Fig. 12) or under unusual gas phase conditions which are lean in carbon sources. The fact that very little amorphous carbon with uncontrolled polymerization of the BSU is produced further illustrates the relevance of the metal catalyst particle which not only generates the source for the solid carbon formation but also controls the geometry of the polymerization process.

The structure sensitivity of the catalyst is induced in an induction period in which carbon is dissolved into the metal. A flat surface with a subsurface carbide forms, which dissociates the molecular carbon source. The activated atoms diffuse through this layer and migrate to other faces where they exsolve, forming graphene layers. The reconstruction was observed by electron microscopy, revealing a deformation of spherical metal particles into droplet-like conical particles. The base forms the active surface for dissociative adsorption and is always directed away from the surface from which the filament grows. The conical mantels are faceted in various directions and allow the growth of graphene layers with different velocities and orientation. The structures of Fig. 4 result from different abundancies of different facet orientations. Coadsorption of impurities such as oxygen or sulfur strongly affects the growth kinetics by affecting the reconstruction. This sensitivity of the carbon generation process on surface orientation can be used advantageously by controlling the shape and rate of carbon filament growth. Inhibitions as well as enhanced production of carbon filaments can be achieved. Additives in the gas phase (oxygen, sulfides, phosphorus compounds) or the promotion with alkali or boron oxide affect the metal faceting. Additives of alloys of molybdenum, silicon or tungsten influence the migration kinetics and the thermodynamic solubility limits of the carbon atoms in the metal particles (10–300 nm diameter), which is often believed to be the rate-limiting step in the overall process. A number of models differ in the character of the carbide phase, which can be a solid solution or a distinct phase such as cementite in the Fe–C system. An additional source of discrepancy is the origin of the carbon concentration gradient, allowing continuous transport through the metal particle. Thermal gradients were excluded by several independent experiments and convincing circumstantial evidence.

### 3.9.9 Carbon on Noble-Metal Catalysts

In catalytic reactions of hydrocarbon conversions on noble metals (hydrogenation, isomerizations over platinum or rhodium are typical examples) it was found that submonolayer quantities of carbonaceous deposits exert a dominating influence on the sequence of events. This is also known in practical applications where it is noted that a little prereaction time in the hydrocarbon atmosphere is required to obtain a selective performance. The beneficial effect of the carbon overlayer is believed to arise from a moderation of the dehydrogenation activity of noble metal surfaces. Dehydrogenation reactions are the fastest reactions catalyzed by platinum, whereas skeletal rearrangements and hydrogenolysis reactions are about an order of magnitude slower on various single crystal surfaces of platinum at atmospheric pressure and at 573 K [57]. If the hydrocarbon is not adsorbed directly on the metal but is bound instead on a carbon material onto which hydrogen atoms can spill over, it is expected that hydrogenation occurs more selectively relative to all other processes. This idea of an intermediate inert surface with intimate contact to the hydrogen-activating metal, which was developed during the analysis of the coking behavior of supported Ni, Rh, Pd and Pt catalysts [58], requires complete chemical inertness of the carbon against hydrogenation and a suitable electronic structure to permit chemisorption of the organic substrate. In addition, the beneficial effect of structure

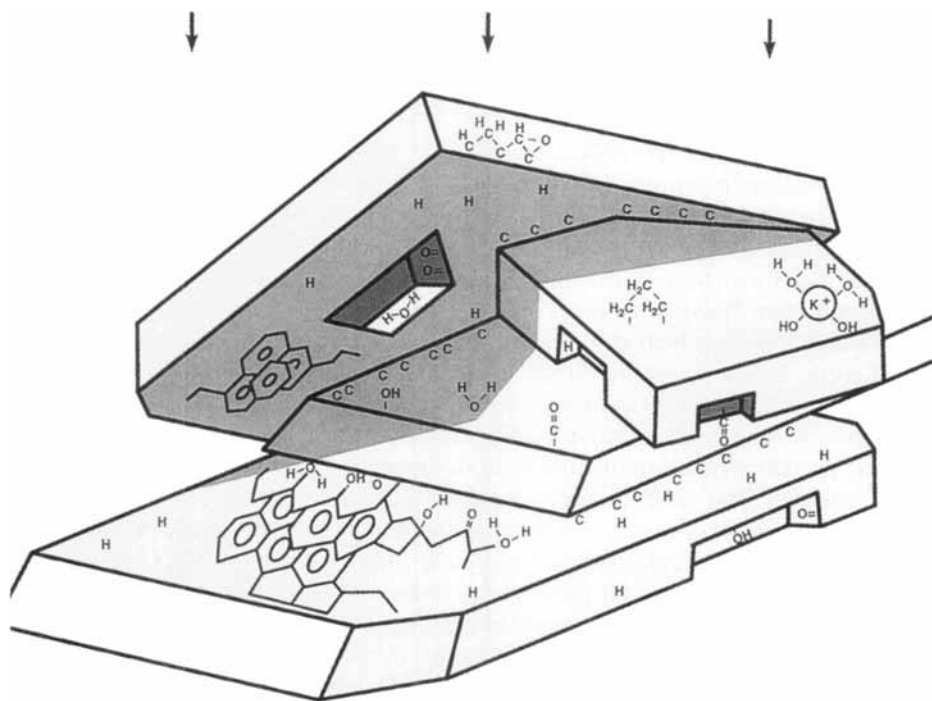


sensitivity, which is prominent in platinum metal catalysis [57], is lost. Combined carbon radiotracer and temperature-programmed desorption experiments on platinum [59] have revealed that up to temperatures of 473 K a carbon species with the composition  $C_nH_{1.5n}$  prevails, which can be removed in excess hydrogen. At higher exposition temperatures the carbon to hydrogen ratio falls sharply to below 1:1 and the resulting carbon is no longer reactive in hydrogen. This more graphitic carbon fulfils the conditions required to act as stable adsorption intermediate. Above 750 K the layer converts into structurally identified graphite which is, however, inactive for hydrogen transfer as was shown by hydrogen isotopic exchange studies [60]. All reaction carried out with hydrocarbons below 473 K require a permanent read-sorption of the hydrogen-rich carbon intermediate, whereas high-temperature treated platinum is permanently modified and passivated for hydrocarbon reactions above 750 K.

The structure of the hydrogen-poor carbon deposit has not been clarified by surface science and is referred to as the carbonaceous overlayer. The structural nature of the hydrogen-rich carbon deposit, however, was amenable to a suite of surface science techniques and the unique structure of alkylidines [61] was derived. These adsorbate species, which have molecular counterparts in organometallic chemistry [62], consist of at least two carbon atoms one of which is bonded to three metal atoms. The other carbon atoms are fully hydrogenated alkyl groups with only C–C single bonds in-between. On reacting platinum surfaces no structure-sensitive effect is expected because 80–95 atom % of all platinum atoms are covered by the carbonaceous deposit, which can be of a different structure. According to the general scheme of Fig. 10 polymerization and dehydrogenation produce hydrogen-poor molecular species with multiple bonds at the surface. The alkylidine species is a well-defined limiting structure occurring instantaneously on clean metal surfaces [63] upon exposure to pure small alkene molecules. With longer residence times and higher temperatures these still hydrogenated species carbonize to form graphene layers which deactivate the metal surface underneath.

Still controversial [64] is the function of the deposit. It could either act as a dynamic cover for nonselective active sites, which is compressed laterally upon substrate adsorption and reexpanded after desorption of the product. The alternative function is to serve as a weakly interacting surface for the substrate adsorption [65].

One way to clarify the role of the adsorbate is the *in situ* investigation of platinum catalysts with electron spectroscopy, which is capable of quantitatively determining the abundance and chemical structure of the carbon species present. This has been done for a platinum black [66] material used after various activation procedures in *n*-hexane conversion reactions. It was found that pristine catalysts are significantly oxidized. These surface oxides are reduced by alkane decomposition into methane, carbon and ethylene. Selectivities to higher hydrocarbons and skeletal isomers of hexane were observed only after an initial induction period. Surface analysis at this stage revealed the presence of Pt metal, of adsorbed OH groups, and a variety of carbon species including carbidic carbon, graphite, amorphous hydrogenated carbon, and several partial oxidation products of this polymer. The total abundance of carbon varied between 15 atom % for purified Pt and 48 atom % after catalysis. This complex situation is summarized in Fig. 13. Only a small fraction of the carbon



**Figure 13.** Schematic representation of the surface coverage of platinum crystallites as they are used in hydrogenation catalysis. The surface analysis instrument detects only the light parts and is affected by shadowing (grey zones; arrows indicate direction of illumination).

deposit is of a graphitic nature. Most carbon species are still in a state before carbonization. The nature of the catalytically active stable, but reactive, carbon deposit may be a layer of amorphous hydrogenated carbon which is sufficiently stable due to its complex network structure but which is still enough polar to provide active centers for hydrocarbon adsorption.

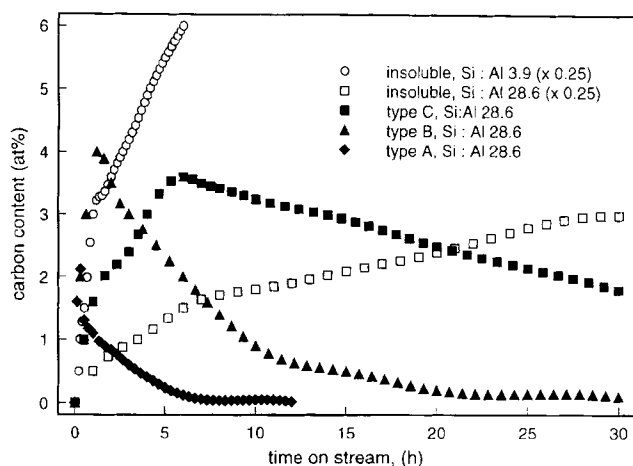
### 3.9.10 Carbon Formation in Zeolites

Zeolites and other oxide-based solid acid catalysts are used in hydrocarbon conversion reactions with enormous economic impact. Their lifetime is, however, very limited due to deposition of carbon which is referred to in the literature as coke formation. The definition of coke in zeolites is very much wider than in the sense of the present article as it is understood that coke is “a carbonaceous deposit which is deficient in hydrogen compared with coke forming molecules” [67]. Two types of coke are discriminated by several techniques amongst which are liquid phase extraction, thermal desorption and spectroscopies like UV-VIS and NMR. One type is white coke which covers naphthalene-type aromatic molecules including derivatives

with alkyl chains and the second type is black coke which covers larger peri-condensed aromatic molecules and alkylated derivatives. This latter type of coke would be referred to in carbon chemistry as a precursor to coke in the sense of Figs 10 and 11.

A significant problem in oxide coke analysis is the determination of the C:H ratio, the most important integral value for a structural characterization. The main problem is the interference of adsorbed or structural water and the structural change occurring during temperature-programmed analysis allowing for carbonisation and the formation of irreversible coke, which is structurally identical with black carbon from polymerization (Fig. 11). In a methodical review [67] the solutions to this problem which contributed a lot to the controversial descriptions of coke on oxide catalysts are described in detail. The absence of large amounts of graphitic carbon in zeolite coke was shown recently by using X-ray absorption spectroscopy at the carbon K-edge [68]. The spectra from an industrial zeolite which was treated with aliphatic and complex aromatic hydrocarbon feedstocks to generate coke showed in both cases the predominant presence of catacondensed aromatic molecules (naphthenes). The independence of the coke properties from the nature of the hydrocarbon feedstock being either methanol (in the MTG process) or small hydrocarbons such as ethylene or propylene or aromatic molecules such as mesitylene or heavy oil fractions, was demonstrated for a technical zeolite sample [69]. This showed that under the influence of the solid acid catalyst the feed is broken into small units from which catacondensed aromatics (with alkyl side chains or as bridging units) are formed. This process, which is similar to carbon formation in homogeneous systems (flames), occurs at comparatively very low temperatures, as low as 475 K. After this polymerization stage, according to the classification of Fig. 10, a step of dehydrogenation up to 700 K follows in which all molecules which can escape the micropore system react into pericondensed polycyclic aromatic molecules. Those molecules that remain in the micropores retain their shape and are not polymerized, which explains the simultaneous presence of both types of coke in zeolites [67]. In subsequent oxidative regeneration steps the pericondensed molecules at the outer surface carbonize and are eventually oxidized giving free all outer surface according to selective adsorption experiments [69]. The catacondensed deposits in the micropores cannot fully carbonize due to spatial constraints and remain partly intact as molecular pore blockers, reducing the micropore accessibility significantly [69].

The sequence of events in coke formation was studied in the model reaction [70] of H-Y zeolite with propene at 723 K. Under these drastic conditions the soluble white coke formed rapidly within 20 min and was converted into insoluble coke within 6 h under inert gas without losing carbon atoms in the deposit. Due to the larger pores in the Y-zeolites compared to the ZSM type zeolites used in the other studies mentioned so far, the structure of the aromatic molecules is somewhat different. The soluble coke in this system consisted of alkyl cyclopentapyrenes ( $C_nH_{2n-26}$ , Type A) as the hydrogen-rich primary product and of alkyl benzoperpylenes ( $C_nH_{2n-32}$ , Type B) and alkyl coronenes ( $C_nH_{2n-36}$ , Type C) as matured components. The temporal evolution of the various products is presented in Fig. 14. It clearly emerges that the soluble coke fractions are precursors for the insoluble



**Figure 14.** Abundance of various types of coke on zeolite H-Y during reaction with propene. The soluble fractions (A–C, black symbols) represent different aromatic structures which form during the first polymerization steps. The insoluble coke is the final product of polymerization which is affected by the solid state acidity of the zeolite, represented here as the Si:Al ratio.

coke and that within the soluble coke fraction the final steps of dehydrogenation–polymerization are very slow compared to the initial formation of smaller aromatic molecules from propene. The sequential formation of precursors with decreasing C:H ratio follows from the shift of the maximum in the abundance of each fraction on the time axis.

The formation of the insoluble coke occurs clearly in several kinetically well discernible stages which can be attributed to initial growth at the outside of the zeolite crystallites and in a slow diffusion-limited growth inside the micropore system. The diffusion limitation will affect the migration of soluble coke molecules rather than the motion of the small precursor molecules. It can be further seen that the acidity of the zeolite is an important controlling parameter, which is summarized here rather crudely as the Si:Al ratio. The more acid sites the faster the kinetics and the higher the absolute amount of coke deposition.

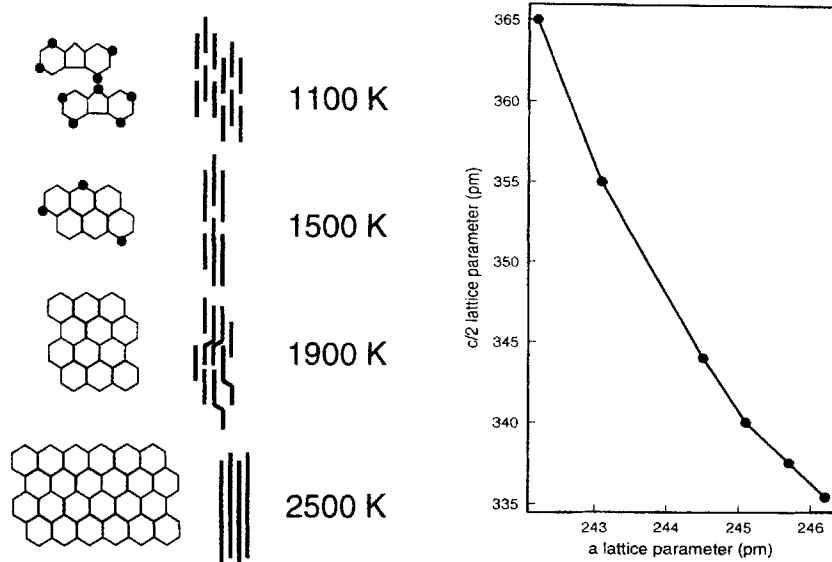
The role of the acid sites may be either catalytic or they are consumed irreversibly during coke formation. In the propene coking study the abundance of coke molecules remained always significantly below the number of supercages in the zeolite which, together with the fact that insoluble coke formation was not saturated within 30 h on stream, points to a catalytic function. This was studied in great detail in a combined catalysis FT-IR study [71] which revealed the constant abundance of Bronsted acid sites in modernite with a Si:Al ratio of 12 during coke formation in ethylbenzene disproportionation. The fact that an IR-active band at  $1600\text{ cm}^{-1}$  can be assigned to coke shows that the structure of zeolite coke is certainly not comparable to coke from coal carbonization. This was incorrectly supposed in a study of coke formation from hexane and hexene in faujasite zeolites [72]. In this study it was found further that alkenic hydrocarbons are much more active than aliphatic

which may, however, be interpreted as inhibition of the initial cleavage of the aliphatic feed molecules which becomes important for long-chain molecules. The ethylbenzene conversion [71] dropped with time on stream and the coke IR band increased proportionally to that without any change in the Bronsted acid band at  $3600\text{ cm}^{-1}$ . Moreover, after complete deactivation of ethylbenzene conversion the acid sites were still active for coke formation with a small precursor molecules as ethylene, which increased the coke band further when fed after ethylbenzene. These results are in line with observations from propene coking but are in conflict with other studies [67] which either claim the involvement of extremely hygroscopic Lewis acid sites (which are hydrolyzed by minute traces of water from hydrocarbon oxidation with lattice oxygen) or the consumption of acid sites during alkene polymerization (which may be an experimental artefact due to the extreme loss in IR transmittance of the samples in these highly reactive coking gas mixtures). It remains an intrinsic disadvantage of this type of study that IR can only detect various forms of soluble coke (the shifts and varying positions of the coke band are a direct consequence of the successive dehydrogenation–polymerization of polyaromatic molecules) and do not indicate the formation, transformation and absolute abundance of insoluble coke which is only detectable in Raman or NMR experiments.

### 3.9.11 Graphitization of Carbons

The various types of carbons obtained by one of the three routes shown in Fig. 11 can be discriminated with respect to their reactivity upon thermal treatment. The lower part of the figure shows the two categories of carbon which will either graphitize (further) upon thermal treatment (annealing) or remain nongraphitic even at temperatures up to 3000 K. The main reason for this distinction of reactivity is the dimensionality of the cross-linking of constituting BSUs. If they are linked in three-dimensional networks then, by thermal treatment, little possibility exists for rearrangement of the cross-linking into the two-dimensional network which is required to form the large planar graphene layers which constitute graphite. The larger the fraction of three-dimensional links in a carbon, the quicker is its formation as there is insufficient time to reach the equilibrium situation of an all  $\text{sp}^2$  carbon connectivity (which excludes three-dimensional networks). Synthesis conditions of rapid quenching from high temperatures are typical for this carbon. Alternatively, the reaction temperature is very low and thus insufficient to provide the activation energy for a rearrangement of the C–C bonds. In catalytic situations charcoals and activated carbons are the usual materials of this class.

Synthesis conditions of high temperatures, with dehydrogenation of hydrocarbons being rate-determining, and the intermediate formations of a liquid phase or even a liquid–crystalline phase (mesophase) of two-dimensional stacking of PAH molecules, are favorable for reaching the equilibrium situation. Pregraphitic structures are then formed which only require annealing for better stacking order and polycondensation of the BSUs by a final dehydrogenation step. The sequence of graphitization events [73] is summarized in Fig. 15. The end of the carbonization process leaves molecular structures consisting of polycyclic aromatic molecules with



**Figure 15.** Graphitization of nanocrystalline graphene precursors (see Fig. 9). Chemical structures (dots represent heteroatoms or methyl groups) and stacking order are given as a function of characteristic temperatures. The polymerization and aromatization are reflected in the average lattice parameters which can be extracted from X-ray diffraction data. The correlation between the axis parameters indicates the shrinking of the cell volume [75].

no heteroatoms other than hydrogen and some alkyl terminating groups. Their alignment is parallel to each other as in van-der Waals crystals of polycyclic molecules. The intermolecular dispersive forces between parallel ring systems are responsible for the alignment. At higher temperatures all non-six-membered structures and most of the alkyl groups are removed. At around 1900 K the large aromatic molecules start condensing to graphene layers. As some of the interconnections are not achieved by pericondensation but by the formations of C–C single bonds, considerably stained sheets with significant buckling will result. This state of graphitization can be observed experimentally by high resolution TEM [73]. The final step, the aromatization of all C–C bonds, occurs only well above 2000 K. Only at such temperatures does the parallel alignment of the graphene layers and the formation of a regular stacking occur, as then the abundance of defective structures within the graphene layers becomes small enough to allow the dispersive forces between the graphene layers to direct the orientation of the BSUs. These sequences of events with the existence of intermediate stages of ordering between graphite and aromatic molecules has been derived conclusively by X-ray diffraction [74, 75]. The evolution of interplanar spacing with carbonization temperature and the kinetics of its equilibration served as tools for the analysis. The aromatization was detectable from a shrinking in the  $a$ -axis parameter, reflecting the shortening of the average C–C bond distance. Both changes lead to a shrinking in the cell volume which is reflected in the relationship between the lattice parameters shown in Fig. 15. The graphiti-

zation reaction proceeds through a series of metastable states [74] with an average change in the carbon–carbon bonding and not via a simple reorientation of turbostratic units into well-stacked units as is frequently assumed.

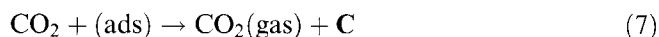
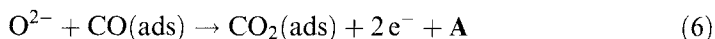
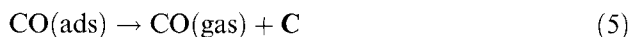
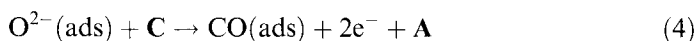
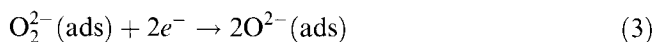
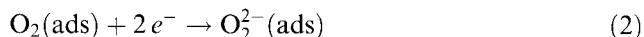
Good candidates for such solid-state phase transformations are carbons produced by polymerization of pitch, tar or other high-boiling fractions of fossil fuels [76]. Pyrocarbons from methane, which are generated under conditions of strongly understoichiometric oxidation, are also suitable candidates for highly ordered synthetic graphitic materials [29]. In catalytic situations most carbonaceous deposits, carbon blacks and synthetic graphite belong to this class of carbons.

The range of temperatures in which graphitization occurs is between 1100 K and 2500 K with significant variations depending on the number and quality of structural defects in the material. In fullerene material the sequence of events of graphitization occurs at temperatures of about 1000 K below that for other carbons [77, 78]. The incorporation of large amounts of potential energy in the form of ring tension by the presence of non-six-membered  $sp^2$  carbon rings lowers the activation energy for the solid structural transformations drastically and allows graphitization at combustion temperatures. A similar low-temperature graphitization is also possible if the carbonaceous deposit on a hydrogenation catalyst has stored chemical energy in form of highly reactive organic molecular structures.

### 3.9.12 Reaction of Oxygen with Carbon

This apparently simple reaction is of multiple relevance in catalytic carbon chemistry. The reaction is used to activate carbon by the increase of surface area due to hole burning. It is further used to create surface functional groups (Section 3.9.5). Finally it is used to remove undesired carbon deposits in regeneration procedures.

The reaction is a gas–solid interface reaction which requires two independent types [79] of electronically different sites. One site should be electron-rich to activate molecular oxygen (site A); the other site should be electron-deficient to react with activated oxygen atoms (site C). A minimal sequence of elementary steps is composed of the following processes:



This sequence of events was suggested by several authors [79, 80] with, however, different assignments to the nature of the two sites ranging from “ionic to covalent”

[79] or to a distribution of sites with varying energy of oxygen chemisorption [81]. In these models it was assumed that the steps (5–7) are rate determining.

Steps 1–3 designate the activation of molecular oxygen into an oxidizing atomic species. This process requires the presence of weakly bound electrons in order to split the dioxygen double bond. Such catalytic sites are available on the basal planes of graphitic carbon. The notion that almost free electrons are also available at structural defect sites [82, 83] is only valid for extremely fast reaction rates, as otherwise stable surface complexes with oxygen, water or hydrogen deactivate such structural defects. The site **A** is thus at graphene planes of sufficient size to exhibit delocalized electrons more weakly bound than in aromatic molecules [84]. The oxygen atoms will diffuse on the surface [85] using their excess dissociation energy until they either recombine and desorb or find a structural defect **C** where they can form a covalent bond to carbon (step 4). This reaction is an oxidation reaction in which the directly bonding carbon atom **C** loses two electrons which flow back into the reservoir of almost free electrons of the graphene layer. It is a matter of ongoing debate to decide on the influence of the diffusion of activated oxygen on the overall kinetics [86]. Due to the extremely different reaction conditions and usually intentionally small conversions, at which experiments are made, it is difficult to decide this question at present. The main problem is the integrating effect of the large number of reactive sites present in an oxidizing carbon sample which precludes the identification of the influence of any particular reaction step, due to the convolution of the elementary step kinetic parameters with the energy distribution of the reactive sites.

The resulting CO complex can either desorb using its energy of formation for activation or survive due to insufficient activation energy. The amount of activation energy depends on the carbon skeleton onto which site **C** is bonded to. It is a structure-sensitive reaction [86, 87]. If the primary CO complex remains long enough at the surface where activated oxygen atoms are available (or if a sufficient flux of activated oxygen is available), then complete oxidation will occur, according to step 6. The desorption of the oxidation product leaves in any case an empty site for a new attack of an oxygen atoms (steps 5 and 7). The oxidation reactions (steps 4 and 6) leave an active site each for oxygen adsorption and dissociation. These sites are, however, not those at which the primary oxygen atoms are formed which changed their positions to diffuse from their location of generation on a graphene layer to the oxidation site.

From this scenario, which was developed from extensive experimental observations [84, 88–92], it is evident that efficient oxidation requires the presence of extended graphene layers for oxygen activation [84, 90] and sufficient defect sites for reaction of the activated oxygen. It was found necessary in an extensive formulation of hypothetical elementary steps to invoke the existence of stationary and mobile initial oxidation products (step 4) in order to explain the varying selectivity between CO and CO<sub>2</sub>. The experimental evidence showed different TDS peaks for carbon–oxygen compounds and not for dioxygen [83, 85, 91, 93] which led the authors to consider only the possibility that reaction products are mobile and not activated oxygen. The process of oxygen activation was assumed to be possible only at the reaction sites themselves (**C** in the reaction scheme). If the activation of molecular

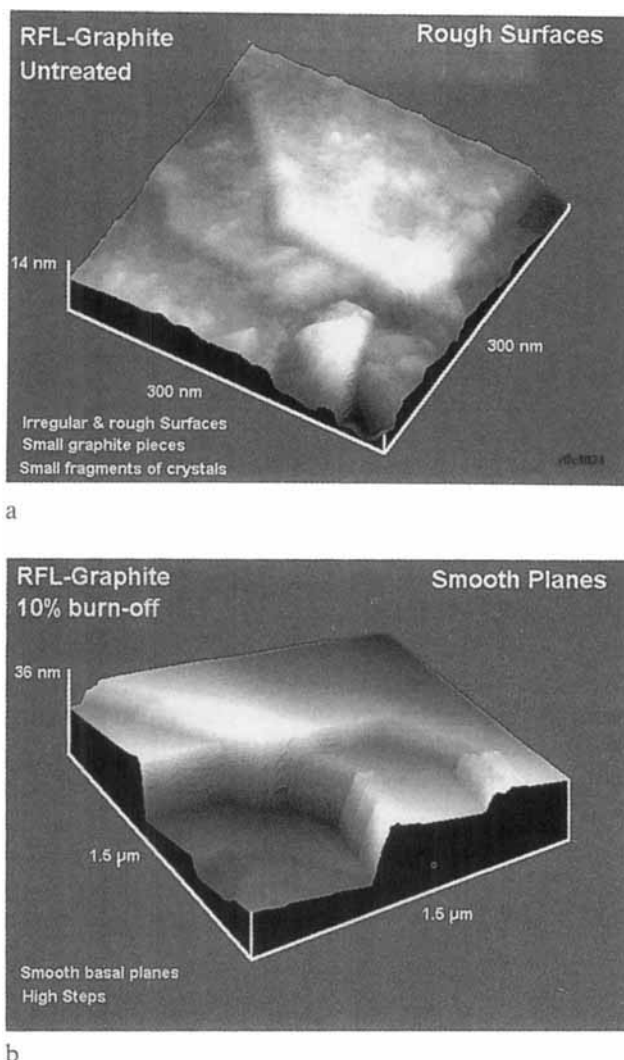


oxygen occurs by nonchemical means (glow discharge [83, 93] or radiolysis [82]) the sensitivity of the overall reaction kinetics to the presence of graphene layers for oxygen activation is lost and a fully structure-insensitive process occurs. In the other extreme of a dioxygen reaction on a perfect graphene layer, reaction of activated oxygen will always occur at the unavoidable external prism surfaces and very efficiently at the few intralayer defects.

One consequence of the reaction mechanism is that carbon burns with molecular oxygen in a layer-by-layer fashion at a decreasing rate as the perimeter of the graphene stack becomes progressively smaller with increasing burn-off. The defects present in variable abundance in each layers contribute significantly to the rate with an increasing tendency towards burn-off as the perimeter of the etch pits enlarges with ongoing reaction. The resulting net rate is an addition of a constant decreasing term and a fluctuating term with an unpredictable overall behavior with burn-off. The unusual dominating role of in-plane defects was established by microscopic studies on graphite oxidation [94, 95]. This effect precludes a definition of reactivity of carbon materials as their average structure is not sufficiently accurately determined to account for the defect distribution in the carbon which controls the activity. This was established recently [96] for a very wide range of carbons containing most of the structural features shown in Fig. 3. A nonlinear compensation effect of the kinetic parameters was discussed. Several groups of carbons with different average structures (graphite, carbon blacks, coals) are differently affected by the rate-enhancing effect of defects which cause simultaneously a decrease in apparent activation energy and an increase in the preexponential factor. The correlation of the kinetic parameters of all carbons results in a nonlinear correlation due to the disregarded structural influence.

Alternative reaction scenarios for the activation of the aromatic graphene layers may be considered. A plausible model with a period of increasing defect creation followed by a period of rapid gasification was discarded by in situ spectroscopic experiments, revealing that the average degree of graphitic chemical bonding does not change with burn-off [2]. The local electronic structure of graphitic  $sp^2$  configurations and the extended structural feature of parallel graphene planes is also not drastically changed with burn-off [2]. Disintegration of the well-ordered surface as preparation for oxidation at every surface site, as found for the reaction of atomic oxygen [83], is not observed with molecular oxygen.

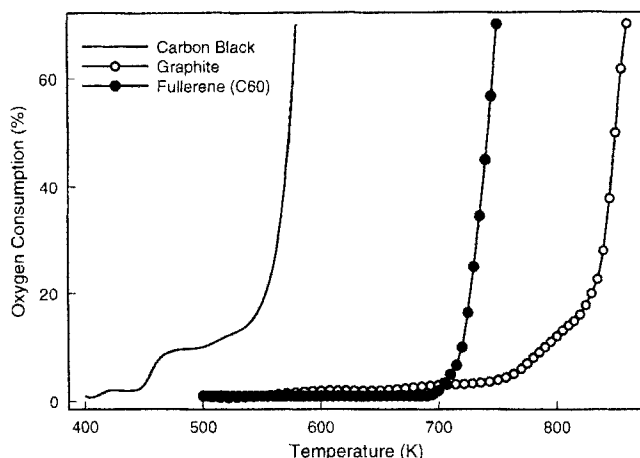
Recent experiments with in situ X-ray diffraction [89, 97] revealed that defective parts of graphite crystals oxidize preferentially, leaving behind a more perfect structure until the total mass loss eliminates the most ordered parts of the crystal. These data are in agreement with the general experience of solid-state chemistry that an increase in defect density creates an increase in gas–solid reactivity. The increase in ordering of the residual graphite surface with progressive oxidation is documented in the STM survey images shown in Fig. 16. The rough surface of a graphite single crystal [89] which is covered by small crystallites [98] becomes smooth after about 10% burn-off with large terraces and few large step structures indicating the grain boundaries of the crystal. Studies at higher resolution show [99] that the terraces are atomically flat, with very few exceptions which are due to certain defects which are more difficult to oxidize than the matrix. A structure with



**Figure 16.** STM images (Burleigh ARIS 6000, air, W tip, constant current mode, 200 mV gap voltage, graphite natural single crystals, oxidation in air at 900 K) of (a) pristine and (b) oxidized graphite surfaces.

sharp needles and small towers results. These observations confirm the complex influence of the defects on the oxidation kinetics which can either accelerate or decelerate by various types of defects. Elemental impurities such as boron are likely candidates for such inhibiting effects as boron compounds are well known for the inhibiting effect on carbon oxidation [100]. Other known inhibiting groups are C–H and certain C–O surface complexes [101].

The in situ X-ray diffraction [89, 97] data further excluded the possibility that oxygen intercalates between the graphene layers and starts the reaction in a three-dimensional way at the internal surface. In-depth oxidation occurs only at structural defects with three-dimensional character such as at grain boundaries and



**Figure 17.** Reactivities of different forms of carbon against oxidation in 5% oxygen in Ar (100%) as function of temperature. The carbon black was FW-1 (Degussa), the graphite natural graphite powder AF (Kropfmühl).

interlayer defects [41, 102]. The contribution of this extra-oxidation activity to the overall rate is small, but severe consequences arise for the mechanical stability of all carbon materials under oxidative load. At very early stages of oxidation they disintegrate and fall into small particles of individual graphitic crystallites. Such mechanical disintegration has important implications for catalyst support materials where the active component falls off at the very beginning of any oxidative load on the system. An extensive review of the uncatalyzed and alkali-ion-catalyzed gasification at defect sites summarizes the present status of research in this highly relevant area [103].

In any practical consideration of carbon application or intended removal (regeneration) the oxidation reactivity is of importance. Figure 17 summarizes results of initial oxidation experiments. Different carbon materials which exhibit all the  $sp^2$  connectivity of carbon atoms exhibit a wide range of oxidation temperatures. The values of these temperatures depend on the definition of reactivity which can be either the first uptake of oxygen, the 50% line of oxygen consumption or even the 50% line of weight loss. Care has to be taken to compare literature values [81, 96, 104] as all these definitions are in use and the differences in temperatures are quite drastic.

The reactivity of the molecular fullerene solid resembles the expected pattern for a homogeneous material. Only a small prereactivity at 700 K indicates that a fullerene-oxygen complex [12] is formed as an intermediate stoichiometric compound [15, 105]. At 723 K the formation of this compound and the complete oxidation are in a steady state [12, 106, 107] with the consequence of a stable rate of oxidation which is nearly independent of the burn-off of the fullerene solid. This solid transforms prior to oxidation into a disordered polymeric material. The process is an example of the alternative reaction scenario sketched above for the graphite oxidation reaction. The simultaneous oxidation of many individual fullerene molecules, leaving behind open cages with radical centers, is the reason for the polymerization.

The molecular nature of this carbon allows the spectroscopic identification [15,

108] of this intermediate and several oxocomplexes serving as precursor compounds [105, 109, 110]. On this basis the reactivity of fullerenes in oxidation is now understood in detail and the reaction scenario is secured by experimental verification [106, 107, 111].

The other two graphitic carbons oxidize, according to the data in Fig. 17, at quite different temperatures and with complex reactivity patterns. They show extensive prereaction activity. A significant oxygen consumption initiates at lower temperatures than the main reaction indicating gasification at extra reactive sites. The spread in temperature of this prereaction activity is very significant. It has been shown recently that the gasification activity at low temperatures is not a surface effect but can lead to a complete combustion of all the carbon [112]. This means for practical applications in catalysis that the minimum corrosion temperature of carbon in oxidative atmosphere can be very much lower than the bulk gasification temperature measured by thermogravimetry, which is too insensitive in most cases to indicate the prereaction activity. The distribution of the prereactivity over reaction temperature is not a characteristic property of a carbon material, but depends in the same way as the main reactivity on the origin, storage and thermal history of the carbon. The oxidation rate as a function of the geometric carbon surface area (total surface area (TSA)) is a sensitive function of extrinsic sample properties [113].

The concept of the existence of an active surface area (ASA) representing a small fraction of the TSA was developed [114] in order to overcome this highly complicated situation. In full analogy with the concept of active sites in catalysis, it was concluded that a surface area measurement with dioxygen under defined conditions should measure the active sites in combustion (C sites in the reaction scheme). This technique allows the detection of the average change of the abundance of active sites with burn-off. The change in ratio between TSA and ASA by over an order of magnitude [114] for a graphitized carbon black highlights the relevance of surface modifications for the oxidation reactivity. A numerical example of the ratio TSA:ASA of  $76:0.24\text{ m}^2\text{ g}^{-1}$  (ratio 316) at the beginning of burn-off and of  $128:2.12\text{ m}^2\text{ g}^{-1}$  (ratio 60) at 35% burn-off of the graphitized carbon black illustrates the accuracy required to obtain meaningful results. This problem of large ratios may be the reason for the deviating numbers for carbon reactivities still quoted by different authors in the literature [86]. The same concept was further very successful in eliminating all the extrinsic influences on the carbon reactivity over ranges of materials with the consequence that a universal rate for the oxidation of  $\text{sp}^2$  carbon was established, deviating for various classes of materials only by a factor of about two [86, 113].

The method of determination of the ASA creates some carbon-oxygen surface complexes which are nonreactive and which cause the still significant dependence of the turn over frequency (TOF) on burn-off or material property. A further improvement of this situation, reducing the dependence of the TOF on burn-off to below 10%, was achieved by introducing the concept of reactive surface area (RSA) [86] or active site density [115]. A simultaneous in situ measurement of rate and abundance of active sites allows the determination of the RSA without any assumptions on reactivity or energy spread of active sites to be incorporated in the

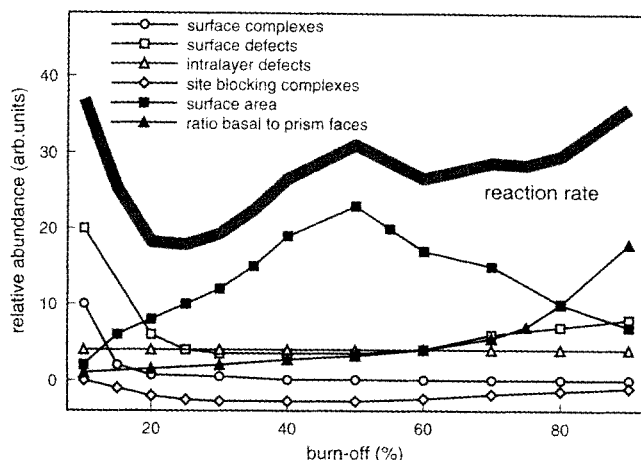
method. The experiment is a transient kinetic measurement as it is well known in catalyst characterization [116].

The oxidation of carbon can also be catalyzed. Two fundamentally different cases should be discriminated. Transition metal oxides and carbides were found to be efficient local sources of atomic oxygen increasing its abundance much above the uncatalyzed case. Streams of diffusing oxygen atoms created decorated pathways of nonselective oxidation of basal plane sites as detected by transmission electron microscopy [117, 118].

Alkali and earth alkaline metal compounds (hydroxides and bicarbonates) were found to be efficient catalysts reducing the 50% weight loss temperature of all kinds of carbon materials by up to 200 K [103]. Two principally different modes of action have been proposed for this technologically and scientifically interesting effect. First, it was assumed that alkali graphite intercalation compounds could form and modify the surface electronic structure of the top graphene layer to enhance the sticking coefficient of molecular oxygen on carbon. This may, however, result from the action of the strong positive point electrostatic charge of a alkali cation residing chemisorbed at the carbon surface. Oxygen molecules still in the gas phase will become polarized which greatly enhances their sticking probability at the surface. The second effect is related to the set of elementary steps required to form a surface oxygen complex. Many of these structures involve the presence of charged oxygen species which require protons as counterions (carboxylic acids, alcohol, phenols etc.). Alkali ions provide ideal counterions in the situation of gasification where few protons are available. In addition, alkali ions do not only accelerate the formation of salts of surface functional groups but they also cannot act as site blockers such as hydrogen, which can form very stable surface hydrogen bonds and reduce the number of active sites. Finally, the alkali salts are all strong Bronsted bases which help desorbing surface functional groups forming during carbon oxidation. Using isotope labeling and other kinetic experiments it was established [119–122] that one very important function in alkali-catalyzed gasification (with  $\text{CO}_2$ ) is to enhance the amount of exchangeable oxygen between gas phase molecules and surface complexes. An alkali–oxygen cluster is envisaged at the active species, which is loaded with oxygen from the gas phase and unloaded by spillover of oxygen to substrate. A fraction of carbon–oxygen–alkali always remains nonexchangeable which is seen as the “backbone” of the system, keeping the alkali at the surface (at high temperatures of about 1000 K where evaporation would be a problem) [103, 123].

A good indicator for the mode of operation of a catalyst in carbon gasification is the ratio of CO and  $\text{CO}_2$  which are formed according to the reaction scheme in independent reactions as simultaneous products. The possible postoxidation of CO to  $\text{CO}_2$  was excluded by a large number of observations and is a basic ingredient in the formulation of the reaction scenario described above. In uncatalyzed gasification reactions the product ratio is about unity with a factor of five deviations for different carbons. The presence of Ca as a catalytic impurity on the carbon from a sooting flame decreased the product ratio to less than 0.01 [81]. A kinetic analysis revealed that the addition of Ca enhanced the rate of  $\text{CO}_2$  formation without affecting CO production. The effect was attributed to a modification of the active sites of reaction step 6 which may be envisaged chemically as a Ca salt formation

**Figure 18.** Schematic representation of the convolution of several influences on the observable oxidation rate as function of carbon burn-off. The broad line for the rate indicates that rapid fluctuations are superimposed on the slow trend.



with a suitable surface complex. The suggested analytical value of the  $\text{CO}:\text{CO}_2$  ratio [81] should, however, be taken with care, as other factors such as the basal:prism surface area ratio also affect the product ratio [86, 87].

The oxidation of graphitic carbon is a complicated gas–solid interaction with the unusual characteristic of a dependence of the reaction rate on conversion. Several independent factors with different dependencies on conversion cooperate in the control of the overall reaction rate. The most difficult part to control is the strong influence of atomic intralayer defects in the graphitic surface. It was made clear by electron microscopy that these unpredictably occurring reaction initiators can dominate the overall reaction rate [95]. The reaction rate expressed as the normalized mass loss per time as a function of burn-off is schematically shown in Fig. 18. In this figure the main controlling factors and their dependencies on burn-off are indicated. The dominating influence is exerted by the changes in TSA and in fractional active prismatic faces surface area of the graphene stacks. In the initial phase of burn-off the removal of surface defects and surface functional groups determines the rate. This was found experimentally by various techniques [89, 124] and is indicated in Fig. 16. The initially strongly changing rate led many researchers to exclude the first 10–20% of the burn-off curve from a kinetic analysis in order not to have to account of this initial effect. For catalytic purposes this effect is highly relevant as the stability of the surface functional groups and surface defects will determine the catalytic reactivity of a carbon sample. In applications where active species are bonded to carbon, the surface structure and its stability determine dispersion and stability of the metal–support system.

All of the effects shown in Fig. 18 are accounted for if the carbon reactivity is given as TOF based on RSA. The only uncontrolled parameter remains the variation in intralayer defect density, which is statistical and not measurable by any reaction-based technique (as the technique modifies the number of intralayer defects). This is symbolized in Fig. 18 by the broad line for the rate which is a slow function of burn-off and a rapidly varying function of the intralayer defect density.

This information shows that the reactivity of a carbon material relevant in catalysis against oxygen (and other oxidizing gases such as  $\text{CO}_2$ ,  $\text{NO}_x$  and water) is not easily defined. As almost no experimental studies have ever applied the RSA–TOF concept it is not surprising that severe inconsistencies about kinetic parameters exist in the literature. A recent review highlights the merits of the transient kinetic technique which is the basis for a unified description of carbon oxidation [125].

The issue of carbon oxidation reactivity is further complicated in all cases where the oxidation of a carbonaceous deposit or a zeolite coke is involved. In these cases the solid carbon oxidation kinetics is superimposed on entirely different oxidation pathways involving organic molecules, and on the kinetics describing the carbonization reaction occurring simultaneously with the gasification reaction. The carbonization reaction system described in Fig. 10 is a sequence of polymerization–dehydrogenation processes which leave essentially pure carbon with widely differing degrees of structural ordering. This carbon, which is responsible for the frequently reported conversion from coke into graphite, is not oxidized at moderate temperatures due to the inhibiting effect of the many surface defects precluding oxygen activation.

### 3.9.13 Surface Chemistry of Carbon

The surface chemistry of carbon is of relevance to all aspects of catalytic carbon chemistry. The two most important heteroelements are hydrogen and oxygen. Each element can undergo a variety of chemically different coordinations which need to be discriminated in analyses of the chemical function of the carbon–heteroatom bond. In the literature the term “surface complex” is often used to describe a group of chemically different bonds which could not be specified in detail.

The local connectivity of surface carbon atoms can be discriminated into  $\text{sp}^3$ , alkenic  $\text{sp}^2$  and aromatic  $\text{sp}^2$  for all kinds of carbon materials of catalytic relevance. Each of the three connectivities can form several types of heterobonds allowing for a broad distribution of carbon heteroatom interactions which coexist on any surface exhibiting structural defects. The surface chemistry of prismatic and basal planes of  $\text{sp}^2$  carbons is fundamentally different, which renders the surface area ratio between the two orientations one of the dominating factors for the description of carbon reactivity. One way of obtaining an estimate for this ratio is to assume that the abundance of hydrophilic sites on a carbon is due to surface functional groups at the prism faces, whereas the basal planes should be hydrophobic. The existence of both properties on a carbon can be verified and quantitatively determined by selective chemisorption of long chain aliphatic molecules ( $n\text{-C}_{32}\text{H}_{66}$ ) or metal salts such as  $\text{HAuCl}_4$  for the hydrophobic sites and alcohol molecules such as  $n$ -butanol for the hydrophilic sites. A practical procedure using microcalorimetry has been developed in the literature [126, 127].

The complexity of carbon materials together with the surface chemical anisotropy and the modifying effects of defects creates a highly complex situation for surface chemistry even when only one heteroelement is considered to be actively

**Table 5.** Heteroatoms in carbon black materials.

Property	Philblack A furnace	Philblack E furnace	Spheron C channel	Spheron 9 channel	Mogul colour
Surface area ( $\text{m}^2 \text{g}^{-1}$ )	45.8	135.1	253.7	115.8	308
Total H (g per 100 g C)	0.35	0.31	0.33	0.62	0.48
Total O (g per 100 g C)	0.58	1.01	3.14	3.49	8.22
CO <sub>2</sub> (g per 100 g C) <sup>a</sup>	0.187	0.401	0.575	0.536	2.205
CO (g per 100 g C) <sup>a</sup>	0.343	0.411	2.00	1.928	4.180
H <sub>2</sub> O (g per 100 g C) <sup>a</sup>	0.00	0.435	0.600	0.710	1.440
H <sub>2</sub> (g per 100 g C) <sup>a</sup>	0.209	0.137	0.152	0.321	0.132
H ( $\mu\text{mol m}^{-2}$ )	38.2	11.5	6.5	26.5	7.7
O ( $\mu\text{mol m}^{-2}$ )	7.9	4.7	7.7	18	16.7
CH <sub>x</sub>	0.48	0.15	0.08	0.33	0.1
CO <sub>x</sub>	0.1	0.06	0.1	0.23	0.21
C <sub>x</sub> R	1.72	4.76	5.55	1.79	3.25
Ratio H : O	4.8	2.5	0.8	1.43	0.48
Ratio CO : CO <sub>2</sub>	1.83	1.02	3.48	3.36	2.04

<sup>a</sup> Integral from thermal desorption up to 1475 K.

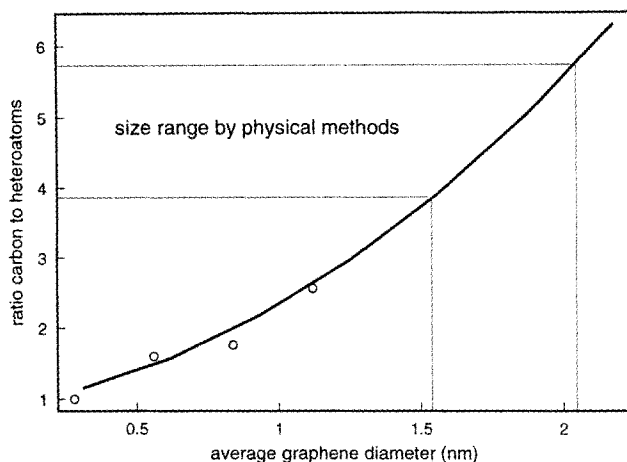
bonded. It is a characteristic of this branch of chemistry to describe surfaces in terms of distributions of properties rather than in sharp numbers.

The greatest attention in the literature has been paid to the carbon–oxygen–hydrogen interaction because of their enormous chemical relevance and the existence of a suite of chemical and physical tools for their characterization. Classes of carbons which are suitable for such studies are carbon blacks. These materials are of high elemental purity (no inorganic impurities) and sufficient specific surface area to allow a quantitative determination of the heteroelement content, which is the basis for any meaningful normalization of surface chemical reactions. In addition, the spectrum of industrial manufacturing processes [39] and the industrial production allows the comparison of data from homogeneous samples with distinctly different (but often unknown) microstructural properties.

A representative collection of surface chemical data of several carbon blacks is compiled in Table 5 which was collected from extensive data [33]. The specific surface area varies by an order of magnitude for the five samples. The total content of heteroatoms (determined by classical microanalytical techniques) amounts to between about 1 and 5 wt% which is a sizeable quantity for a material which is nominally pure carbon.

A technique used often in chemical speciation of the surface functional groups is temperature-programmed desorption (TPD) of all functionalities. The strength of the surface chemical bonds requires maximum temperatures of usually 1273 K with desorption profiles extending from 400 K to the upper limit of heating in inert atmosphere in a quartz tube furnace. Table 5 lists the integral abundance of all possible decomposition products of C–O–H functionalities. The data show that both absolute amounts and product distributions (CO to CO<sub>2</sub> ratios) vary significantly and exhibit no apparent correlation to surface area or synthesis method for the carbon. Reduction of the data per surface area reveals that carbon–hydrogen





**Figure 19.** Calibration curve for the determination of the average size of a graphene unit in nanocrystalline carbon from its content in heteroatoms. The size range seen by physical methods stems from direct electron microscopic observation, from scattering models of X-ray diffraction and from NMR.

functions are abundant heterobonds on carbon black surfaces. Carbon–oxygen functions are always present and in samples 3 and 5 more frequent than hydrogen terminations. The importance of the heteroatoms for the description of the surface properties becomes apparent when the carbon to heteroatom ratios are considered. It occurs that about every other carbon atom exhibits in its connectivity one heteroatom. The ratio of carbon to heteroatom can be used to estimate the size of the basic structural units. Assuming the microstructure of carbon to consist of small graphene platelets with few intralayer defects (Figs 5–9) one may estimate from the topology of pericondensed aromatic structures the ratio of carbon to heteroatoms. These are all located at the prism faces of the graphene layers and saturate the dangling bonds in the carbon  $sp^2$  configurations. This ratio is 1.0 for benzene, 1.25 for naphthalene, 1.6 for perylene, 1.76 for coronene and 2.56 for a  $n = 4$  pericondensed molecule. Such a molecule has a diameter of about 1.2 nm. A coarse correlation between the carbon to heteroatom ratio and the size of hypothetical circular graphene layer is presented in Fig. 19. HRTEM images of carbon blacks exhibit 1.5–2.0 nm as characteristic diameters [130], compatible with  $n = 5$ –8 ring pericondensed structures. Samples 2 and 3 from Table 5 exhibit an abundance of heteroatoms, consistent with a graphene diameter as seen with physical methods. The other samples consist of significantly smaller BSUs which are, however, not observed by microscopy [128, 129]. This discrepancy together with the H:O ratio from Table 5 indicates that more than one heteroatom is bound frequently to one peripheral carbon atom, calling for more complex functional group structures than C–H or C=O terminations. Sample 3 is the best approximation to pure carbon in the selection of Table 5 with a large number of simple carbonyl functions as carbon termination groups (see CO to CO<sub>2</sub> ratio). Sample 4 with the lower surface area and

the same synthesis history exhibits a much richer surface chemistry which could give rise to a strongly underestimated average size of the graphene layers. It is pointed out here that the physical method of determination of graphene layer diameters by X-ray diffraction [33, 39, 130] is critical. Smaller particles than the average do not contribute significantly to the overlapping and diffuse line profiles of the (*hk*) reflections used for the analysis. For this reason it remains valuable to compare physical data with chemical information such as that shown in Fig. 19.

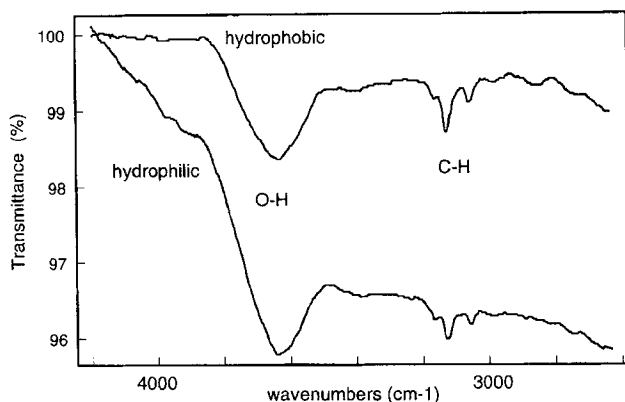
Using refined X-ray diffraction techniques and the extraction of the radial distribution function from molecular X-ray scattering it has been possible to develop a model for a graphene layer [31]. This model is free of the difficulties mentioned above and predicts cluster sizes of between  $n = 3$  and  $n = 5$  for pericondensed rings (coronene, hexaperibenzo coronene) in full agreement with electron microscopic [25] and NMR [131] data which led to construction of Fig. 19. The model material [31] was a coal sample before carbonization containing, as well as the main fraction of  $sp^2$  centres, about 20% carbon atoms in aliphatic connectivity. This one-dimensional structure analysis represents a real example of the scheme displayed in Fig. 9(C).

The data from Table 5 show clearly that a significant fraction of the total carbon surface which is chemically active (prism faces and defect sites) is covered by heteroatoms and many of these sites are not just passivated by C–H bonds. This situation is also characteristic of carbonaceous deposits with  $C_xR$  values of 1.5–2.5 (corresponding to C:H ratios of 0.45–0.65) pointing to truly smaller average diameters of the BSU (see Fig. 19), as was determined by chemical extraction and mass spectrometry [70, 132, 133]. The situation is also typical for carbon materials resulting from dehydrogenation of organic polymers with a large abundance of prism faces and a significant presence of oxygen functional groups. For carbons with larger BSU diameters the dominance of prism sites is gradually reduced and defect sites at crystallite boundaries and intraplane defects become important locations for surface functional groups. The absolute abundance is, however, so much reduced that the accuracy of elemental analytical data as used above is too low to allow a meaningful chemical and structural interpretation.

### 3.9.14 Non-Oxygen Heteroelements on Carbon Surfaces

The most important non-oxygen heteroelement is hydrogen bound to a variety of different reaction sites. Thermal desorption experiments showed that weakly held hydrogen desorbs at 1000 K, and more strongly bound species desorb at 1270 K and 1470 K. Only above 1900 K all hydrogen is released from a carbon material [134]. As this especially stable hydrogen can be as much as 30% of all hydrogen present, it was suggested that this species should be bonded to alkene and alkane link structures within the graphene layers (see Fig. 9(C)) and represents hydrogen bonded to inner surfaces.

The chemical structure of the hydrogen groups is difficult to assess as they can be present either directly bonded to carbon or as protons together with other functional groups. In addition, at low temperatures, all hydrophilic carbons carry a



**Figure 20.** Transmission FT-IR data for two carbon blacks which were pretreated to desorb molecular water films. An in-situ reaction cell with specially prepurified KBr supports were used to accumulate the spectra in dry Ar. All sample handling was carried out in a glove box. A Bruker ISF 66 instrument was used to collect 1000 scans from each sample.

layer of molecular water which needs to be desorbed first to allow a quantitative analysis. Thermal desorption with discrimination of water and carbon oxides can be used to control the desorption the unspecific water layer. It is observed, however, that the water desorption affects the surface chemistry of the carbon, as some labile groups are desorbed and the vacant surface sites can react with water to form C–O–H or C–H bonds [88, 135]. IR spectroscopy can be used to show that even after mild desorption of water from an oxidized carbon black a variety of hydrogen species is present at the surface. Figure 20 shows the corresponding transmission spectrum of two technical carbon blacks with hydrophilic and hydrophobic reaction against liquid water after in situ desorption of molecular water at 573 K. The absorption from carbon–hydrogen and carbon–hydroxy groups overlap to form a complex peak structure. A range of different O–H groups is present (see below) and the C–H frequencies occur also as convolution of signals from isolated C–H functions and shifted components due to C–H groups next to C–O bonds in various configurations. Figure 20 and the TPD experiments from the literature indicate that hydrogen is present not only in strongly bound C–H groups, which coexist with other functional groups, but also in a variety of C–O–H groups which cannot be removed at moderate temperatures up to 675 K. For the hydrophilic sample a broad structure of oligomeric OH group fundamental vibrations causes the strongly falling background at high wavenumbers. After more severe heat treatments the carbon surface is more uniform [136] but is modified in its defect properties and in its chemical reactivity.

The existence of several distinct C–H surface functional groups and the modification of the carbon surface during adsorption of hydrogen has been studied in detail [137]. Four different kinetic regimes of coverage versus reaction time have been identified, indicating the structural heterogeneity of the carbon surface. The material studied (graphon) is a graphitized carbon black with no inorganic im-

purities. This allows the deduction of the heterogeneity of the adsorption sites which was also reproduced by a variation in activation energy for adsorption as an intrinsic effect of the carbon material. The fact that temperatures above 700 K are required to saturate the carbon surface suggests that structural modifications (hydrogen etching) of the surface may significantly contribute to the surface reaction which seems to be more complex than adsorption of hydrogen atoms on (pre-existing) chemisorption sites.

Carbon–nitrogen surface groups are not abundant in carbons made from hydrocarbon precursors. Carbons from nitrogen-containing natural and synthetic polymers contain structural C–N–C groups in aliphatic and aromatic coordination. Surface complexes such as amines, amides, or nitro groups are not very stable and are desorbed during heat treatment (manufacture, activation, precleaning). An extensive body of work has been assembled [135] concerning the intended incorporation of nitrogen from ammonia or cyanides using carbon surfaces prereacted with oxygen or halogens. Several structures of C–N and C–N–H have been identified with physical methods. The stability of the most abundant C–N–H groups is, however, rather limited in temperature.

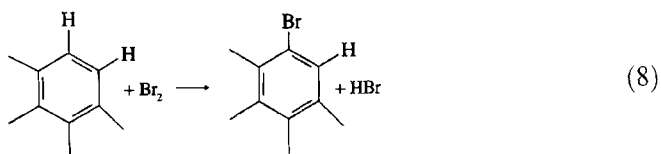
Most significant is the observation that the catalytic behavior of a carbon (from various sources) remains affected by the amination treatment, even when the nitrogen is desorbed from the surface. The explanation was put forward that nitrogen binding (and removal) occurs on defective sites and the nitrogen activation is in fact a mild version of preferential removal of defective surface sites, leaving behind a carbon surface with a more graphitic electronic structure than originally present. Some of the structural nitrogen (pyridine-like incorporation in the graphene layers) is thermally stable up to 1273 K [33, 135] without affecting the catalytic performance of the carbon material. This observation excludes the notion that the heterocyclic substitution injects additional electrons into the conduction band of the semimetal graphite and in doing so enhances its activity in electron transfer reactions (e.g. activation of molecular oxygen in liquid phase oxidation catalysis [138]).

Carbon–sulfur groups are extremely stable surface compounds which cannot be removed by thermal treatment up to 1470 K. Only by a reductive treatment with hydrogen it is possible to clean carbon from sulfur adsorbates. One source of sulfur is the fuel used for the generation of the carbon from which about 90% are covalently bonded to the carbon and 10% are segregated as adsorbate which can be removed by solvent extraction. The abundance of sulfur can amount to several wt%. Removal of the structural sulfur is possible by hydrogen reduction to H<sub>2</sub>S at about 1000 K. A collection of references on this subject is found in the literature [33]. In activated carbons sulfur can also be present in an oxidized form as sulfate or as C–S–O compounds.

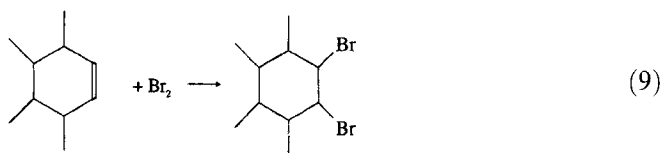
The generation of sulfur functional groups has been investigated in detail in order to prepare anchoring sites on surfaces used in rubber vulcanization (for tyre manufacture). Only those sulfur groups which are not incorporated in the graphene layers can be chemically active for cross-linking polymerization in vulcanization. In a broad study [139], carbon disulfide, hydrogen disulfide, thionyl chloride and sulfur dioxide were used at elevated temperatures to generate sulfided carbon surfaces on

a variety of  $sp^2$  substrates. Structural data revealed in all cases the absence of graphitization phenomena even though the reaction temperatures were up to 1173 K. XPS and IR data indicated that two types of species were formed. One type should be C=S bonded to aromatic rings and the other one a thiolactone.

Carbon-halogen groups are well known to exist for fluorine, chlorine and bromine. These groups can be attached by redox reactions involving the halogen elements either in aqueous solution or in the gas phase. At elevated temperatures bulk reactions occur under intercalation and eventually under formation of bulk covalent carbon-halogen materials ( $CF_{1.1}$  solid,  $CCl_4$  gaseous) [140]. At lower chemical potentials of the halogens, substitution reactions into C-H bonds (reaction 8) or addition reactions onto in situ formed unsaturated bonds (reaction 9) occur. These two reactions are one of the most important analytical tools in describing the chemical reactivity of carbon materials. On the basis of extensive experiments with various carbons [141] the reaction of a carbon with aqueous bromine is suggested to serve as reference experiment for the quantification of the unsaturated carbon atoms which are mostly masked by oxygen surface groups (reaction 9).



The reaction with chlorine occurs, after high-temperature outgassing, directly as addition of halogen on the unsaturated C=C bonds. The strength of the carbon-halogen bonds is determined by using halogen-saturated carbons for halogenation of nucleophiles [33]. It occurs that iodine groups are fully reversibly adsorbed, whereas bromine and chlorine are partly irreversibly adsorbed and can only be removed by high temperature treatments under oxidizing or reducing conditions. This result led to the conclusion that aqueous iodine solutions should be used to determine the surface area of carbon as a selective adsorbent. Reaction with iodine vapor at elevated temperature (600 K) results in the same chemistry as shown in reactions 8 and 9 and is not suitable for carbon selective surface area determination.



Care has to be taken when interpreting results of halogen uptake on carbon at low temperatures, in aqueous solutions or at undefined surface states of the carbon (as received). A large number of reaction involving halogens and oxygen surface functional groups and of course between halogen hydrogen acids and basic functional groups occur simultaneously with the reactions mentioned above. They may thus perturb the analytical data (in particular the amount of HX as measure for reaction

8) to such an extent that no meaningful result can be obtained. The only method is to define the surface chemistry of the carbon by preannealing and treatment in the gas phase or by in situ cooxidation [142], forcing reaction 9 to dominate.

### 3.9.15 Surface Oxygen Groups

The abundance of oxygen atoms on carbons varies over a wide range with a maximum at about  $C_4O$  (see Table 5). The surface chemical and hence many technical properties of carbon materials (including diamond [143]) depend, however, crucially on the carbon–oxygen chemistry which controls adsorption, adhesion and oxidation activities of the surfaces. From the reaction with liquid water acidic and basic surface complexes can be discriminated. Under almost all catalytic conditions both types of oxygen groups are present simultaneously and the pH value of an immersion of carbons in water is the result of protolysis of solid acids and solid base groups. The pH can be as low as weak mineral acids indicating that a significant solid acidity can be present on carbon. The basic reaction is rather more limited and rarely exceeds the value of pH 8. For this reason, an overall good quantitative correlation between pH in aqueous solution and analytical oxygen content for a carbon species has been established [144]. A consequence of the Bronsted acid functionality is that many of the carbon–oxygen groups exhibit a cation exchange capacity and a simultaneous anion exchange capacity (from the basic groups). These functions are most relevant for the application of carbon as catalyst support and provide a method for anchoring metal ions by the same method as used for oxide supports also on carbons. For the special case of protons (exchange on basic groups) the graphene layer in its unperturbed aromatic state is sufficiently basic to allow direct adsorption [145]. In catalytic situations this problem is of limited relevance because for high surface area material the abundance of graphitic surface patches is low and on graphitic materials the surface area is often low, so that a significant interference with the determination of basic functional groups is to be expected only in graphitized carbon blacks. However, when the hydrogen adsorption method is used to determine the dispersion of small metal particles the sorption capacity of the support for activated hydrogen (spill over) has to be taken into account.

The dominating importance of the oxygen functional groups has led to significant efforts to devise preparation routes to obtain only part of the wide  $pK_a$  spectrum on the surface, i.e. to prepare either only acidic or only basic functional groups. This was, however, only partly successful with the result that in all circumstances a spectrum of neutralization equilibria rather than a single  $pK$  value characterized a carbon surface. Basic functional groups can be obtained when carbons are annealed in vacuum or inert gas (Ar, not nitrogen) at 875 K for several hours, cooled down under inert conditions to 300 K and then exposed to air, water or oxygen [146]. The basic reactivity occurs only after contact with water molecules which contribute to the formation of the basic groups.

Predominantly acidic groups are obtained by heating carbon in air or oxygen to 600–900 K with a decrease in acidity with increasing temperature (self-gasification).

Very strongly acidic groups can be obtained with low-temperature liquid phase oxidation using hydrogen peroxide, ozone, chromic acid or aqua regia.

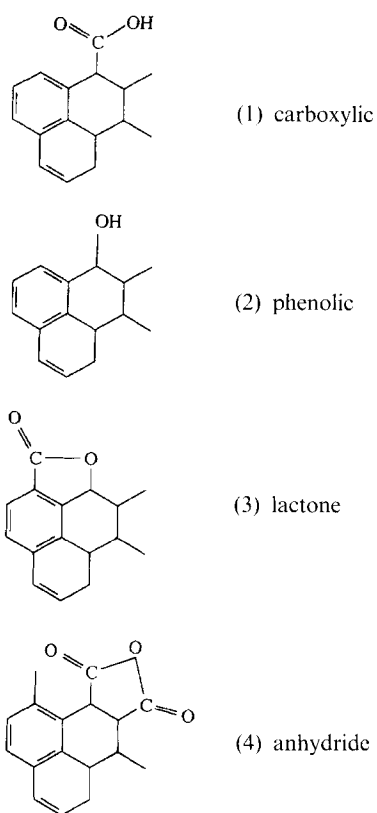
The characterization of the resulting surfaces has been problematic ever since the early attempts [143, 147] by applying chemical means. The advent of many surface physical methods has not contributed significantly more information than that obtained with chemical probe reactions (derivatization as in the early days of organic chemistry). The reason for this is the small abundance of a wide variety of chemically different species. Most surface spectroscopies are too insensitive for the variations in chemical environment. Others require single crystal surfaces which cannot be functionalized. Vibrational spectroscopy is hampered by the strong bulk absorption of light. Nuclear magnetic resonance has relaxation problems with non-hydrogen-carrying surface groups bound to aromatic graphene structures. For these reasons the bulk of our knowledge about the structural details of carbon–oxygen functionalities stems from chemical experiments as collected in several reviews [32, 33, 146, 148–150]. A special series of publications is devoted to structure and reactivity of basic oxygen groups [151–154]. The following description is a critical summary from this large body of information which contains plenty of references to the original work with ample experimental details.

The analysis of the structural chemistry of oxygen groups with chemical methods is limited to stable configurations and misses by definition all metastable configurations which may, however, be present under *in situ* oxidation conditions. Chemical structures of reaction products of the reaction sequence provided by eqs 1–7 may be found in this description, but other less stable configurations may also exit. Care should be taken to transfer the knowledge reported here directly to the actual discussion about the atomic structure of oxidation reaction intermediates [86, 122, 155].

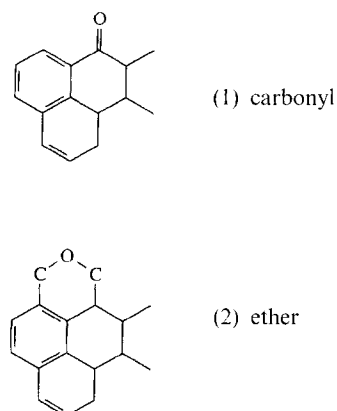
The acidic functional groups can be characterized by their neutralization reactions with a selection of bases differing in their *pK* values. The usual reagents are sodium hydroxide, sodium carbonate, sodium bicarbonate and, for very weak acids, sodium ethoxide in alcohol. An additional dimension of information can be obtained by pretreating the carbon prior to neutralization analysis [156].

Figure 21 shows the representations of the fundamental structures responsible for Brønsted acidity. Only carboxylic and anhydride groups are strictly acidic in water, with the anhydride hydrolyzing to two carboxylic acid functions. These two groups contribute mainly to the reaction with sodium hydroxide but react with all weaker and stronger bases than hydroxide. The lactone groups need to undergo ring opening in a basic medium which can be achieved by 0.05 m sodium carbonate. Phenolic groups are supposed to be frequent due to their structural simplicity (reaction product of eq 4). Their acidity is limited in water and will depend strongly on neighbouring functional groups. Sodium ethoxide is a selective reagent for their detection.

Some oxygen functional groups do not react with water molecules and behave thus as neutral. Their fundamental structures are shown in Fig. 22. Some carbonyl groups can still react with sodium ethoxide. The ether or xanthene structure is fully inactive in aqueous media. Both neutral structures are believed to occur frequently due to their structural simplicity and the fact that in any oxidation reaction these structures have to occur as intermediates in ring destruction sequences. In quanti-



**Figure 21.** Chemical structures of acidic surface groups.

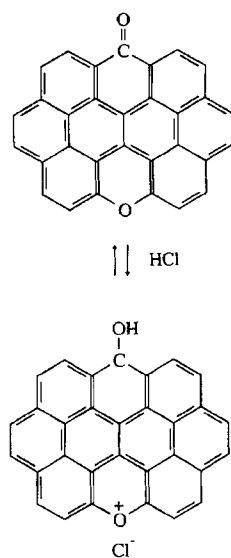


**Figure 22.** Chemical structures of neutral groups (weak acids in nonaqueous media).

tative studies where the oxygen content is compared to the sum of all neutralization reactions a significant excess of chemically unreactive oxygen is stated [149, 146] which is accounted for by these neutral functions.

Bronsted-basic groups are of complicated structure as can be seen from Fig. 23. They consist of two interacting oxygen centres [157], one of which is active in pro-



 $\gamma$ -pyrone

**Figure 23.** Chemical structure of basic functional groups. Both heteroatomic structures are required to explain the neutralization reactivity.

ton adsorption and the other one in anion exchange. The interrelation has been shown in a series of elegant chemical reactions [151–154]. The structure shown in Fig. 23 is tentative, representing the simplest configuration and may have more complicated isomer structures. It is interesting to note that during formation of the basic groups a nonstoichiometric amount of hydrogen peroxide is formed when the oxidized carbon is contacted with moisture or water. This reaction which was also discussed in conjunction with an oxidation of ether structures to chromene groups [157] is reminiscent of the anthraquinone catalysis of technical hydrogen peroxide synthesis. It should be taken into account that in all situations in which dry oxidized carbons are contacted with water a chemically detectable amount of hydrogen peroxide will be formed which may interfere with experimental observations.

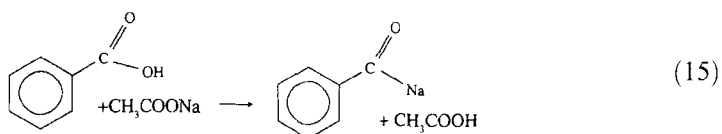
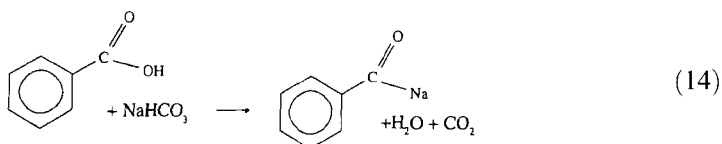
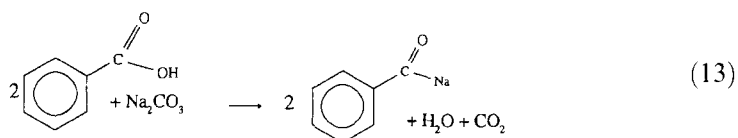
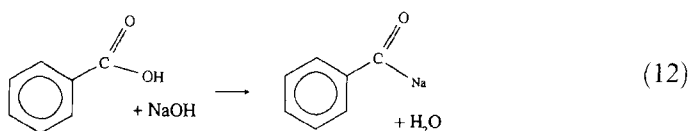
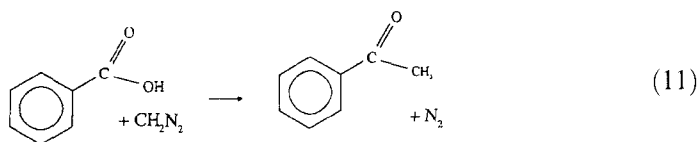
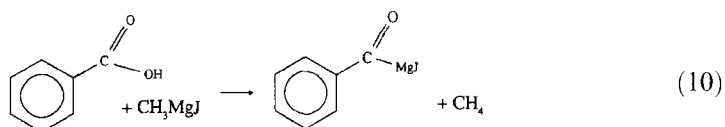
Suitable reactions for the chemical identification of fundamental surface groups are collected in reactions 10–24 which summarize convenient reactions for chemical group identification. A large number of additional reactions with rather special applications can be found in the review literature. When these reactions are used, it is advisable to test the reaction conditions by several different reactions characteristic for the same functional group. It occurs that the neutralization kinetics can be slow, in particular with hydrophobic and porous carbons. Reaction times should not be under 24 h at ambient conditions. However, artefacts such as glass adsorption, reaction with traces of air and the intrinsic problem of conversion of the surface functional groups during chemical reaction limit the reaction time to an optimum for complete but artefact-free determination.

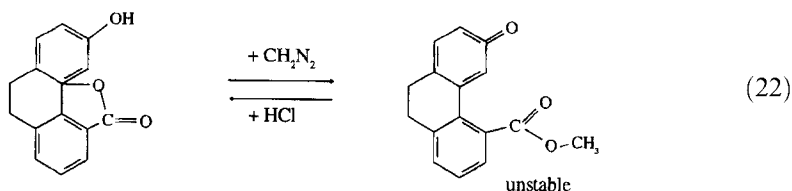
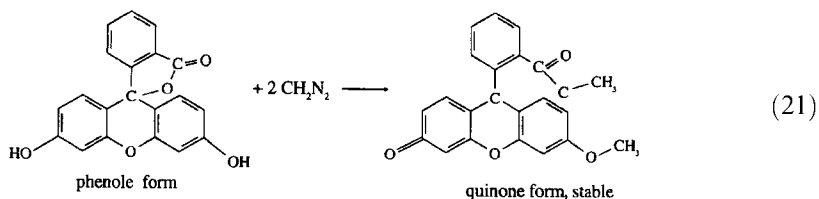
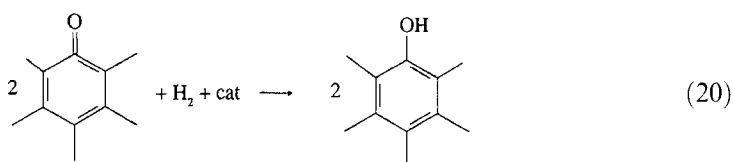
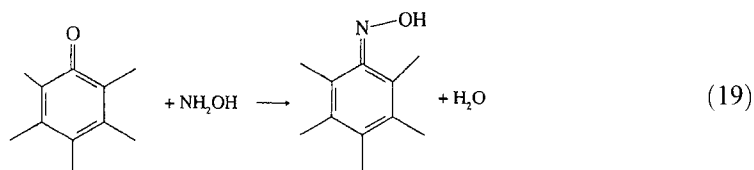
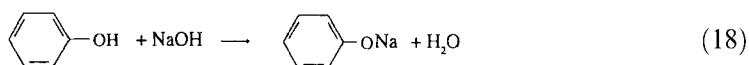
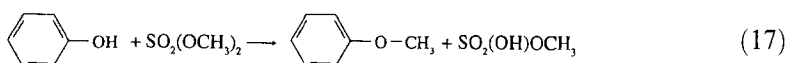
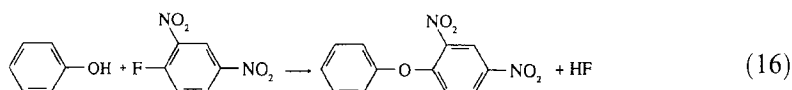
Reactions 12–15 describe the standard neutralization reaction for an organic

carboxylic acid. The discrepancy in neutralization capacity for the different reagents can be used to estimate the  $pK$  distribution [88]. Amounts between 50 and 500  $\mu\text{eq}$  acid per gram of carbon are characteristic values which indicate the high degree of experimental perfection required to determine such surface acidity data. Reactions 10 and 11 form derivatives of the carboxylic acid and can be used to volumetrically detect their presence by monitoring the gaseous reaction products.

Phenol groups are determined by the difference of the neutralization reactions between sodium hydroxide and sodium carbonate which are common for carboxylic and phenolate groups. Oxidized carbons (typically in air at 700 K) contain equal amounts of these two functional groups. Activated carbons contain up to 800  $\mu\text{eq g}^{-1}$  carbon of phenolate groups. The volumetric determinations are also sensitive to both carboxylic and phenolate groups so that specific derivatization processes are needed to reliably discriminate the two types of groups.

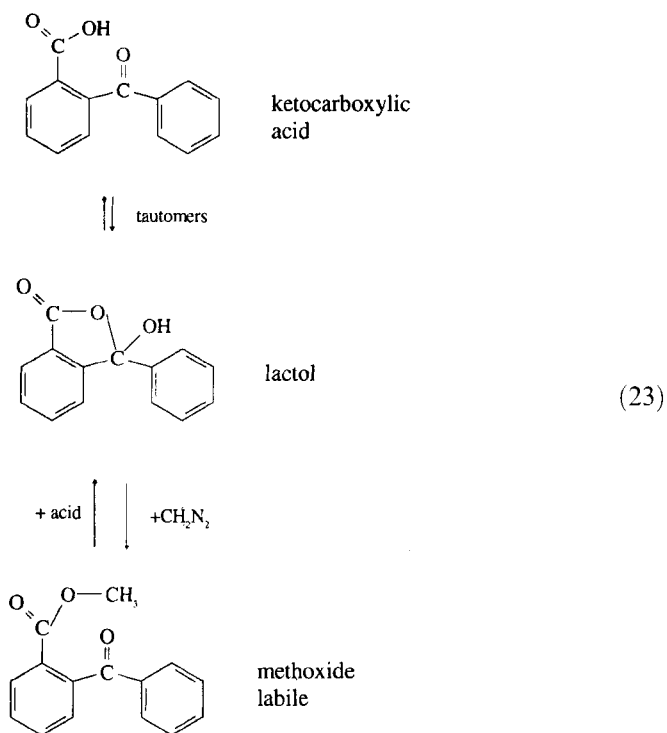
With more complicated structures such as lactones the identification problems





become more complex as the reaction of lactones in water result in the formation of a carboxylic acid group and a neighbouring phenol group. Reactions 23–25 are only characteristic for lactones with the assumption that under the mildest possible reaction conditions the neighbourhood effects of the ring opening reaction will favor the derivation over the same reaction occurring on additionally present non-correlated functional groups.

The complexity of the chemical situation increases further when combinations of

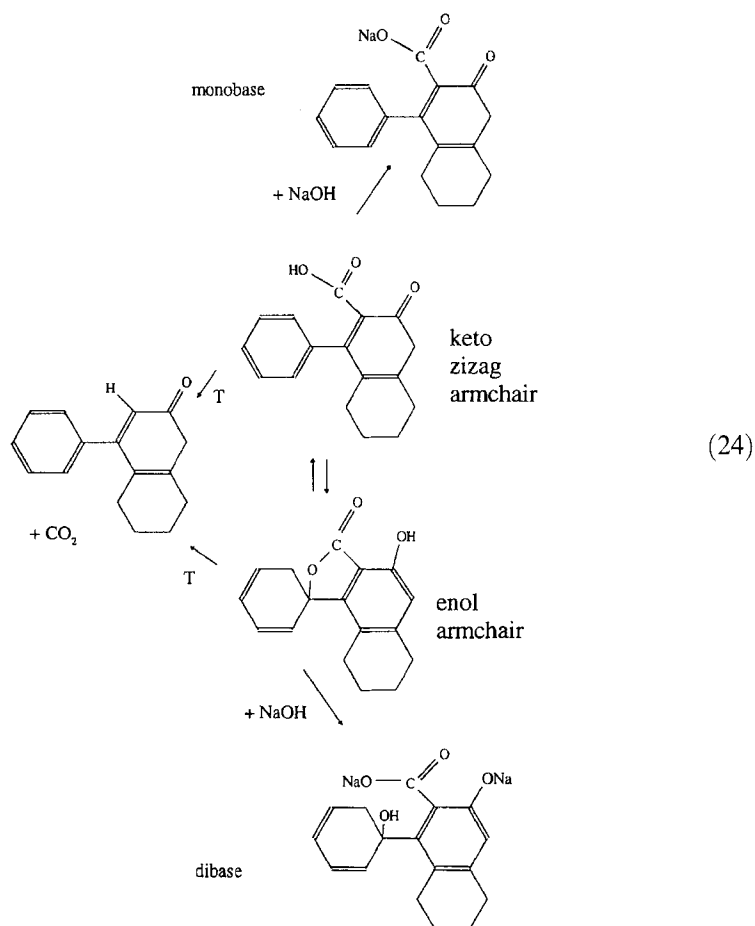


different surface groups start to react with each other. A prominent example is the lactol group originating according to reaction 23 from combination of a carboxyl group and a carbonyl group. This is a situation which is frequent due to the high abundance of both fundamental groups. The resulting structure, representing a complicated example of a coadsorption effect, can undergo a whole spectrum of reactions and interfere with several derivation reactions simultaneously.

Another type of complication arises from the chemical inequivalence of (110) and (110) terminating surfaces, referred to as zigzag and armchair configurations of the graphene layers. In reaction 24 an armchair configuration exhibiting two different functional groups at one six-membered ring is shown. The resulting structure, using the same fundamental groups as for the lactol reaction which are now in 1,2 configuration with respect to each other (1,1 configuration for the lactol), allows tautomerism with the result that upon neutralization either one or two equivalents of base will be consumed. The equilibrium between the two forms depends upon the base concentration of the base used for detection.

Reaction 24 is also a good example for the insensitivity of thermal desorption for such effects because the same molecule results after decarboxylation. Any quantitative correlation between neutralization and thermal desorption thus leads to inconsistencies, which is the historic reason for the intensive investigation into this surface chemical problem [33].

These few examples give an impression about the chemical complexity of the carbon-oxygen surface reaction. They illustrate that surface acidity as a single



number of sample characterization is a very poor representation of the spectrum of reactivity already present in aqueous media. It becomes apparent why in practical applications [130, 150, 158] only poor correlations are observed between such simplified surface chemical parameters and the observed reactivity.

In recent years a simplifying attempt to overcome this complexity was to analyze carbon by TPD and to integrate the total  $\text{CO}$  and  $\text{CO}_2$  emission and to correlate the results with sample pretreatment and chemical reactivity [33]. The limited validity of such an approach is apparent. As is illustrated below, the chemically complex surfaces which are not described by such crude correlations are those with the highest catalytic activity. In applications of carbons as catalyst support it is immediately apparent that the details of the carbon-to-metal interaction depend crucially on such details of surface chemistry. This explains the enormous number of carbon supports commercially used (several thousands). A systematic effort to understand these relationships on the basis of modern analytical capabilities is still missing.

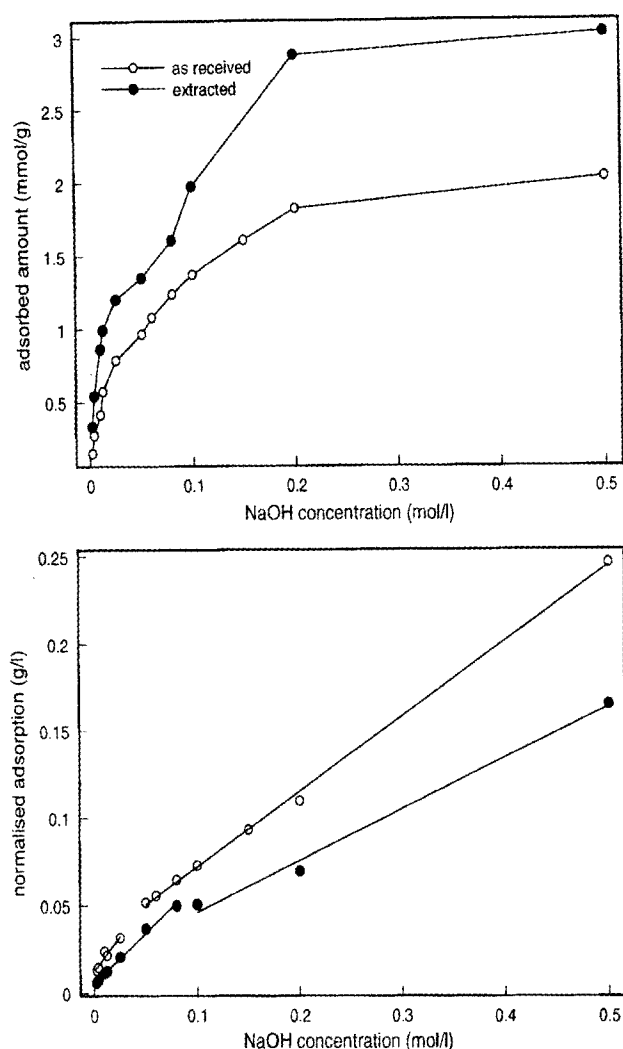
In this situation a variety of techniques can be used to obtain complementary and

if possible quantitative information on the surface chemistry of a given carbon material. High sensitivity and chemical selectivity are characteristic for titration methods of the solid–acid surfaces. The most prominent technique is a one- or two-point titration with two fixed concentrations of e.g. 0.05 N and 0.5 N bases. The titration is usually carried out as back-titration after an adsorption experiment. The results usually differ from each other indicating the distribution of acid sites over one order of magnitude in  $pK$  values. Reactions 12 and 18 are associated with these two values. For a variety of different carbons the characteristic concentrations for the predominant analysis of carboxylic acids and phenols may differ due to variable distributions of local adsorption geometry. This affects, via neighbouring group effects, the dissociation constants of the surface groups and hence modifies the  $pK$  distribution. To avoid the possibly substantial errors, it is recommended practice to determine the adsorption isotherm of the neutralisation reagent on the carbon and to analyze the resulting data in terms of a multiple Langmuir chemisorption model.

The Langmuir model describes, for a uniform surface and a non-self-interacting adsorbate, the relationship between amount adsorbed and exposure concentration. The parameters of the model are the maximum amount adsorbed as a full monolayer and the equilibrium constant for the adsorption–desorption process which indirectly reflects the strength of the adsorbate–substrate interaction. For the present situation the analysis is modified in the following ways:

- it is assumed that several independent site types exist which represent acids with different  $pK$  values;
- the neutralization process is seen as an equilibrium reaction which occurs in an additive way on the different site types;
- no interaction between different site types is assumed (no effects as described in eqn 24),
- no complications with correlated equilibria for generation of the primary sites (e.g. hydrolysis of lactones or anhydrides) are taken into account.

Within these limitations the method supplies information on the absolute abundance of the fundamental solid acid sites and gives a qualitative indication about the  $pK$  average of each site. The procedure works in principle for acid and basic sites [88]. Figure 24 illustrates an example for acid sites on a carbon black sample (FW-1 from DEGUSSA). This sample was selected as the high purity allows an unambiguous assignment of the neutralization to carbon-bonded functional groups and the high surface area provides sufficient chemical heterogeneity for a realistic model. The top panel shows the experimental adsorption isotherms after 24 h equilibration in anaerobic conditions for the as-received sample and an extracted sample. Extraction was done with xylene and ether to remove polycyclic aromatic molecules which are chemisorbed in an abundance of less than a monolayer [39] on the carbon and passivate the genuine carbon surface. The strong effect of the extraction is clearly visible. The shape of the isotherm indicates, at least for the extracted material, some complications as a stepped curvature should not occur from a single Langmuir isotherm. As the reaction should occur in an additive way

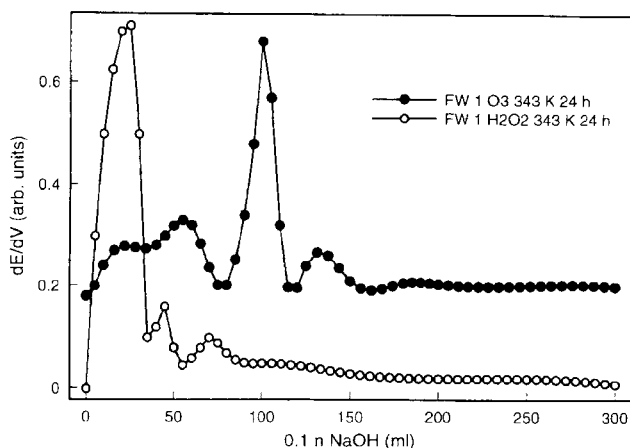


**Figure 24.** Neutralization isotherms (adsorption isotherm of  $\text{OH}^-$ ) for acidic surface groups on a carbon black. The lower plot represents the linearized isotherms according to a modified Langmuir adsorption model.

it is also not expected that the combination of several isotherms should give rise to such a feature, which is absent in the as-received sample. The discontinuity is ascribed to the generation of additional functional groups by chemical reactions between the NaOH with nominally unreactive functional groups during the adsorption–equilibration process.

The lower panel of Fig. 24 shows the analysis of the normalized isotherms. It occurs that two processes are superimposed in each isotherm. The break in the isotherm of the extracted carbon at around 0.1 n concentration indicates that in this regime the extra reactivity which consumes base outside an adsorption has probably occurred. The data can be quantified and provides the following information. The two adsorption sites differ in their acid strengths as can be concluded from the

**Figure 25.** Direct titration of acidic groups on a carbon black. The curves represent the high-resolution first derivatives of the titration curves. The ordinate scales are identical for both experiments (offset).



equilibrium constants ( $K = 14$  (17) for the majority site and  $K = 64$  (107) for the minority sites). The limiting values of coverage are  $2.32 \text{ mmol g}^{-1}$  ( $3.41 \text{ mmol g}^{-1}$ ) and  $1.24 \text{ mmol g}^{-1}$  ( $1.74 \text{ mmol g}^{-1}$ ) for the two species. The data in parentheses give the values for the extracted surface which indicate the sensitivity of the method and the drastic effect of the surface purification process. The purification also has a detectable effect on the acid strength of the sites, which may be explained by the operation of neighbor group effects (adsorbate-adsorbate interaction).

The suitability of this adsorption model to characterize quantitative aspects of surface acidic groups gives no indication, however, about the chemical structure of the reactive sites. Only in combination with the chemical probe reactions is it possible to assign the two types of acid sites to carboxylic acid and hydroxy groups, respectively. It is noted that such an approach can also be used to determine ion exchange capacities for metal ion loading required for the generation of dispersed metal-carbon catalyst systems.

For carbons with large amounts of surface groups per unit weight the method of direct titration can be used. In this method a suitable arrangement for potentiometric titration with slow neutralization, anaerobic conditions and good temperature stability of the experiment, is used to measure directly the titration curve of the solid acid. The first derivative shows the equivalence points of all stages of dissociation. The carbon is considered in this picture as an oligoprotic acid with a series of dissociation equilibria [33, 159]. Figure 25 illustrates the type of information obtained from such a direct titration experiment with a carbon black sample (FW-1) which was oxidized at low temperature in liquid phase to obtain acidic functional groups. Large differences in the abundance (proportional to the peak positions on the abscissa) and in the dissociation constant (peak profile representing the shape of the discontinuity at the equivalence point relative to the strong base  $0.1 \text{ N NaOH}$ ) can be seen for the two oxidizing agents applied under identical conditions to the same carbon material. It is obvious that ozone treatment resulted in the formation of a large amount of very strongly acidic surface functional groups, as seen from the sharp peak in the derivative plot. Three to four other types of functional groups



may be identified with widely varying abundance. Care must be taken in analyzing the derivative profiles, because for weaker acidic systems the effect of incomplete dissociation and the formation of a buffering system which all broaden the derivative peaks must be taken into account.

The direct titration of the parent carbon black which also carries significant amounts of functional groups is not possible. From this, it can be seen that the two alternative chemisorption techniques both have their relevance in carbon chemistry.

Another physical method which became popular in functional group analysis is photoelectron spectroscopy with X-ray excitation. The XPS or ESCA method is used in this context as a fingerprinting tool using empirically derived tables for the chemical shift to analyze the data. Oxygen functional groups can be analyzed either by the oxygen O 1s emission or by the carbon C 1s emission. Due to the much larger shift sensitivity, the carbon 1s range is used in almost all applications. In addition, the presence of a film of molecular water which is not removed in UHV creates a large oxygen 1s signal at 533 eV which overrides many structures in the functional group oxygen spectrum.

The issue of assigning carbon 1s data to chemical structures has been developed extensively in carbon polymer science and is exhaustively reviewed there [160–162]. The principle of the assignment resides on the following assumptions. All  $sp^2$  and  $sp^3$  C–C and C–H bonds give rise to one C 1s signal at 285 eV with a tendency towards lower binding energies for pure graphite which was located for defect-poor samples at 284.6 eV [2, 90, 163]. All carbon heterobonds shift the C 1s signal to higher binding energy. This shift is the larger the more electronegative the hetero-element is relative to carbon. Further increments are brought about by carbon–heteroatom double bonds and by 1,1 substitution of the C–C or C–H bonds. Table 6 reports a critical compilation of literature data on carbon–oxygen-induced shifts for several carbon materials. The table confirms the general trend outlined above. Other tabulations in the literature [33] are physically inconsistent and contain erroneous data. These discrepancies arise from three different sources of inconsistencies:

**Table 6.** Selected carbon 1s chemical shift data for carbon-oxygen groups; common reference is C 1s = 284.6 eV for graphite.

Binding energy (eV)	Assignment	Surface	Reference
285.6	C–O–C	polyvinyl alcohol	234
286.5	C–O–H	polyvinyl alcohol	234
287.8	C=O	polyvinyl alcohol	234
289.2	CO <sub>2</sub> H	polyvinyl alcohol	234
286.2	C–O–R	polyethylene oxidized	174
287.5	C=O	polyethylene oxidized	174
289.0	CO <sub>2</sub> H	polyethylene oxidized	174
286.1	C–O–H	carbon fiber oxidized	172
287.6	C=O	carbon fiber oxidized	172
289.1	CO <sub>2</sub> H	carbon fiber oxidized	172
290.6	carbonate	carbon fiber oxidized	172

- Calibration of the binding energy scale for different experiments (see below).
- Influence of the defect structure on the absolute position of the main line which is often used as internal standard for calibration of the binding energy scale [163].
- Disregard of the asymmetric lineprofile of the graphitic carbon 1s signal. This asymmetry contradicts a physically meaningful spectral deconvolution into a set of Gaussian peaks as mostly done in the literature. The resulting inconsistencies in the positions of contributions and the variable linewidths used in these deconvolution procedures arise from the varying contribution of the line asymmetry to the total spectral weight of the carbon 1s profile. The asymmetry is mainly caused by the coupling of the core hole state created during photoemission to the semi-metallic valence band states of graphite and by the convolution of the primary photoemission with the phonon and plasmon loss spectra [164, 165].
- Disregard of charging effects. Highly functionalized carbons are often not sufficiently metallic conducting to allow the photocurrent to flow through the sample without creating integral potential drops which affect the position of the binding energy scale. In difficult cases the charging up is locally variable (for example with a thick uneven specimen) and prevents correction by recalibration with an internal standard (the C-H + C-C line or the water line).

These three groups of effects shift all or part of the photoemission intensity into the range of the carbon–oxygen chemical shifts and can thus affect the interpretation in an undetected way. The same problems arise when carbon–nitrogen groups are analysed. Nitrogen–oxygen groups (nitrate, nitrite, nitrosyl) are well discernible (403–406 eV binding energy) from nitrogen–hydrogen bonds (around 401–400.5 eV for amino groups) and from carbon–nitrogen bonds (400.0–397 eV). The individual chemical configuration within the groups is, however, difficult to resolve [135]. In a recent publication [166] on the reactivity of nitrogen species with oxidized activated carbons a consistent series of nitrogen chemical shifts falling within the ranges specified above is established. This list of compounds is chemically self-consistent as the modifications used for their generation are fully in line with conventional nitrogen organic chemistry.

The C 1s line is less affected by the less electronegative nitrogen heteroatom and exhibits a much smaller shift range than for oxygen groups. In a recent publication aiming at the XPS analysis of the novel diamond-like  $C_3N_4$  material [167] all these problems are well documented. The authors did not consider charging effects, nor did they account for oxidation of the sputtered surfaces during transfer. In addition, they used Gaussian line profiles and arrived at significantly high carbon 1s chemical shifts for two different C–N bonding geometries which they see as diamond-like (aliphatic) and polypyridine-like (heterocyclic aromatic).

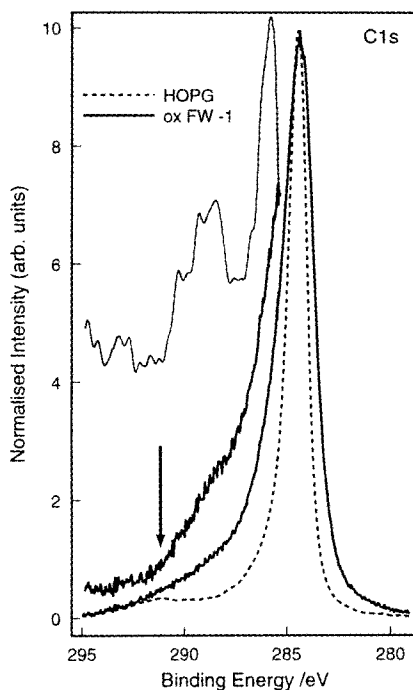
In a very detailed study of the chemical shifts of carbon 1s lines on the nature of the C–C bonding interaction [168] it was found that using the well-determined C 1s value of  $284.6 \pm 0.3$  eV [169] hydrogenated carbons exhibiting a binding energy of  $285.3 \pm 0.05$  eV and carbidic carbon in SiC were found to occur at  $283.4 \pm 0.05$  eV. Diamond and graphite were found to be fully indistinguishable from their shift data, which is in full agreement with a different study using compact [2] rather than film [169] samples. The significant uncertainty which is quoted for the value of

graphite C 1 s photoemission was clarified in a study on the dependence of the carbon 1 s line position on the crystalline quality (nature and abundance of surface defects) [163]. For hydrogenated amorphous carbon films a complex influence of the substrate on the binding energy and probably also on the detailed atomic structure was detected in a study of a-C-H films on various GaAs surfaces. A carbon-rich species with a binding energy of 284.8 eV on GaAs and of 284.6 eV on Si was found in the near interface region of sputtered thin carbon overlayers [170]. These data indicate that a clear speciation of the chemical structure of a carbon species in a catalytic system can be quite ambiguous and that – contrary to chemical intuition – the connectivity of a carbon cannot be inferred from its carbon XPS spectrum. The reason for this failure of the ESCA effect lies in the complex convolution of ground state electronic properties of the carbons (which are all different [2] as expected by intuition) with final state effects [164, 165] (relaxation of the core hole) which produce a diffuse but intense structure in each peak, accounting for their apparent similarity. This became apparent in studies aiming at a discrimination of the KVV Auger spectrum of carbon into s-derived and p-derived valence band states which should be suitable for discrimination of  $sp^3$  and  $sp^2$  carbon connectivities by the Auger lineshape [171].

In summary, care must be taken in interpreting the main component of the carbon 1 s line as fingerprint for the carbon connectivity. In the high binding energy side additional problems arise from plasmon satellites which can occur at 5.6–7.2 eV in  $sp^2$  carbons and at 11.3–12.5 eV in  $sp^3$  carbon above the main line [169]. These broad and weak structures interfere with chemical shift identifications of highly oxidized C–O functional groups [163].

A practical situation is shown in Fig. 26. The carbon 1 s data of HOPG as reference are compared to those of a chemically etched graphitized carbon black sample. The defective graphitized carbon surface exhibits a significantly wider main line at almost the same position as the well-ordered graphite (cleaved and annealed in UHV [90]). It can be seen that the neglect of the line asymmetry invariably causes the erroneous detection of additional lines in the range 1–2 eV above the peak maximum. The difference spectrum is mainly caused by the broadened main line. Only after removing the asymmetric main contribution a small structure (top in Figure 26) can be isolated revealing peaks at 286.0, 287.3, 288.7 and 290.0 eV which can be attributed to surface oxygen functional groups. Only 4.3% of the total intensity is due to the surface groups, in good agreement with 5.5 at% oxygen content. The comparison of these numbers indicates [172] that most functional groups can only carry one oxygen atom per carbon atom and that carboxylic groups, with the largest shift, must be a small minority. The data agree fairly well with those from oxidized carbon fibers [172] and are in agreement with the values from Table 6. A maximum of three different oxygen functionalities can be resolved by XPS. These are the basic chemical structures mentioned in Fig. 21. The more complex cases which were shown to exist with carbon–oxygen single bonds (peak at 286.0 eV in Fig. 26) can also not be resolved by this method with any degree of chemical selectivity.

A significant increase in the chemical specificity of XPS can be achieved when the surface sensitivity of the surface analytical detection is combined with the chemical



**Figure 26.** XPS data in the carbon 1s region for a UHV cleaved graphite reference (HOPG) and a carbon black sample used in the titration experiments of Fig. 25. The arrow marks the position of the graphite surface plasmon. The top section of the modified spectrum in the high-binding energy side reveals several weak peaks for oxygen functional groups after removal of the asymmetric line profile from the main peak.

specificity of the probe reactions discussed above. A highly specific analysis of the chemically reactive surface functional groups can be obtained using heteroatoms such as barium from barium hydroxide, chlorine from HCl or  $\text{SOCl}_2$  [173], or nitrogen and sulfur tags from complex functional reagents [174, 175]. These data reveal that a large number of oxygen functions detected by integral elemental analysis are chemically inert and exhibit no acid–base activity. Such behavior is consistent with keto functions or with oxygen heterocyclic functions (C–O–C in Table 6). From all chemical shift data in the literature and the spectrum in Fig. 26 it appears that the heterocyclic function is the dominating functional group. This accounts for much of the analytical oxygen content without contributing to the low-temperature chemistry. From the sequence of events in carbon oxidation this group is the primary reaction product and has thus also from the mechanistic point of view a high probability of survival in any oxidation treatment as the most abundant reaction intermediate.

At this point a characterization technique with a higher chemical resolution is desirable because such functionalization plus surface analytical combination experiments are extremely difficult to perform in a clean and reproducible way. Vibrational spectroscopy such as FT-IR has been developed into such a tool, after several methodical improvements concerning sample preparation and detector sensitivity. In situ oxidation experiments are still very difficult as heated black carbon is a perfect IR emission source and interferes with any conventional detection in the spectral range of carbon–oxygen fingerprint vibrations.

**Table 7.** Characteristic group frequencies in IR absorption.

Functional group	Absorption frequency ( $\text{cm}^{-1}$ )	Assignment
phenol groups		
O–H	3650–3590	valence
O–H	3500 b	valence polymer
C–OH	1220–1180	valence
C–OH	1350–1100	valence aliphatic
O–H	1390–1330	deformation
keto groups		
C=O	1745–1715	valence aliphatic
C=O	1700–1680	valence aromatic
C=O	1730–1705	valence $\alpha$ -diketo
quinones		
C–O, para	1690–1655	valence, two lines
C–O, ortho	1660	valence, one line
aldehyde groups		
C–H	2920–2880	valence, combined
C=O	1720–1715	valence, combined
carboxylic acids		
C=O (aliphatic)	1735–1700	valence
C=O (aromatic)	1700–1680	valence
C=O (anhydride)	1830, 1750	valence, two lines
O–H	3000–2700	valence
O–H	940–900	deformation
esters, lactones, ethers		
C=O	1730	valence, benzoic
C=O	1740	valence, lactones
C–O–C	1280–1100	valence, ester, lactones
C–O–C	1320–1250	valence, ethers

A compilation of fingerprint vibrations for characteristic carbon–oxygen functions is found in Table 7. Data from a variety of organic molecules from spectra libraries are analyzed and grouped together. Only strong vibrations are tabulated and extreme positions are removed. The compilation shows that several regions of interest exist:

- The  $\text{OH}^-$  valence region which is due to combinations with molecular water is often difficult to resolve.
- The C=O region (1800–1650 wavenumbers).
- The region at 1650 wavenumbers, of C=C vibrations which are isolated from the graphene network (the graphene vibrations are only Raman active, see Table 2).
- The region of C–O single bond vibrations at 1300–1100 wavenumbers with a significant selectivity for different groups when combined with the simultaneously occurring C=O vibrations.

The practical observation of all these vibrations is difficult, as not all of the respective groups are present on a carbon with the same relative abundance. As the

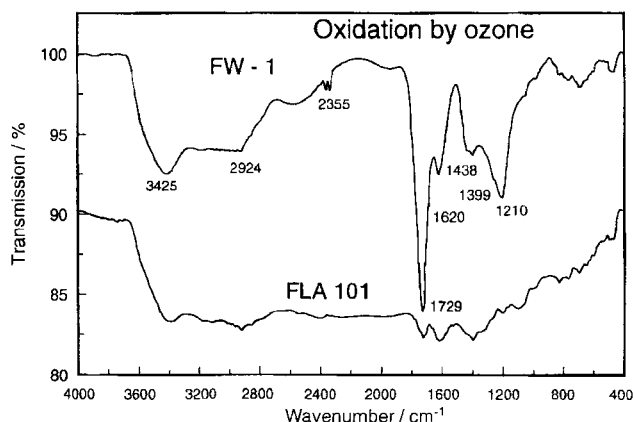
**Table 8.** Observed IR absorption bands for oxidized carbons.

oxidized glassy carbon		oxidized carbon black	
Absorption frequency (cm <sup>-1</sup> )	Assignment	Absorption frequency (cm <sup>-1</sup> )	Assignment
2045	adsorbed CO	3425	C–OH
1780	lactones	2924	C–H aliphatic
1722	carboxylic acids	2355	CO <sub>2</sub> gas phase
1696	aromatic ketones	1760 sh	lactones
1678	quinones	1729	carboxylic acids
1611	isolated C–C bonds	1620	isolated C=C bonds
		1438	O–H deformation
		1399	C–O lactones
		1230 sh	C–O aromatic ether
		1210	C–O phenol

quality of the spectra is generally poor, weak characteristic peaks of a minority group may not be recognized. Strong peaks at 2355 cm<sup>-1</sup> and at about 2045 cm<sup>-1</sup> arise from chemisorbed CO<sub>2</sub> and carbon monoxide during in situ studies [176–178]. The diagnostic value of the data in Table 7 is enhanced by the search for combined absorptions for the more complex functions. Such combinations allow the resolution of the crowded spectral range between 1800 and 1700 cm<sup>-1</sup>. Two oxidized carbon samples are discussed as being representative for the many possible applications of Table 6. The discussion of characteristic IR data on fullerenes and their oxidation products can be found in the literature [105, 106, 108, 111].

Table 8 lists the main absorption frequencies for the two samples. One is a disc of glassy carbon formed under electrochemical oxidation, the other is a powder sample of a high surface area carbon black (FW-1, 235 m<sup>2</sup> g<sup>-1</sup>). The in-situ electrochemical oxidation study [176] allows the tracing of several coexisting species by their respective fingerprints. It can be seen that several groups which remain undetected by chemical adsorption and XPS analysis can be found with the IR technique. No carbon–oxygen single bonds were found in this study. The oxidation potential may have been too high for the accumulation of a significant abundance of these still oxidizable groups. A technical reason may well be the poor spectral quality below 1600 cm<sup>-1</sup>, precluding the detection of any specific absorption besides the extremely strong background. The broad water hydroxy peak from the in situ reaction environment also does not allow the detection of hydrogen groups. For these reasons, not all species are identified. This is required, however, to derive a plausible oxidation mechanism suggested in this paper.

The oxidation reaction by dry ozone at 335 K leads to the formation of a large number of strongly acidic surface groups [179]. A whole spectrum of chemical changes occurs with the treatment leading finally to a breakdown of the carbon into soluble graphene fragments. The ozone reaction is also used to study the oxidation mechanism and its control by micromorphological effects of “hole burning” [180]. Finally, the ozone oxidation is also of influence in atmospheric chemistry, where it



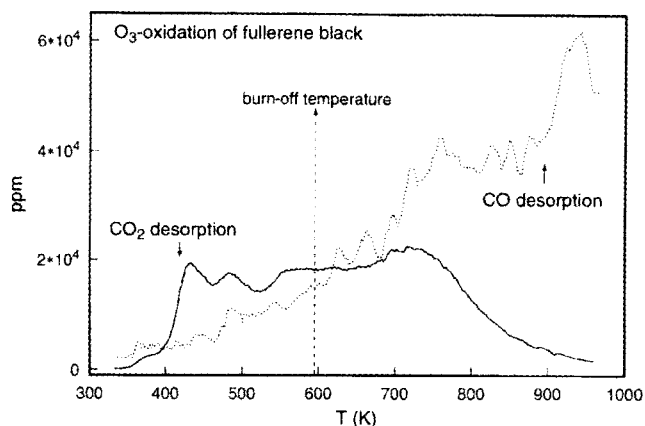
**Figure 27.** FT-IR data of heavily oxidized carbon blacks. The FLA sample is much more graphitic in the stacking order of the BSU and exhibits only 10% of the geometric surface area of the standard FW-1 sample.

modifies carbon black particles which become efficient catalysts for the oxidation of  $\text{SO}_2$  under ambient conditions [181].

The data from Table 8 and the spectra in Fig. 27 indicate that a wide variety of functional groups with single and double oxygen-carbon bonds are formed after mild ozonization at 335 K in aqueous medium. The agreement between the assignments of the absorptions in both samples is quite remarkable and agrees also with the reference data in Table 7. The influence of neighborhood effects on vibrational data and the uncertainty of locating the position of absorptions in broad, overlapping and diffuse bands account for the minor discrepancies in the numerical values of the peak positions. The regions of characteristic absorptions mentioned above can be identified in the top spectrum of Fig. 27. A distribution of absorption band positions for each chemical structure causes the broad envelopes and indicates the structural heterogeneity of the oxidized carbon surface. The sharp double peak of gaseous  $\text{CO}_2$  arises from the large micropore volume of the sample which stores detectable amounts of  $\text{CO}_2$  in relation to the natural abundance of this gas in the ambient air.

The nature of the functional groups seems not to depend on the structure of the carbon substrate, as even on oxidized fullerenes the same bands can be found by IR spectroscopy [108]. The relative abundance is, however, significantly different as can be seen from the comparison of the two carbon black samples used for the data of Fig. 27. The FLA 101 sample is more graphitic with a significantly reduced surface area. The abundance of carbon-oxygen single bonds is greatly reduced with the predominant species being carboxylates after the same treatment which produced the broad variety of functional groups on FW-1. This is full agreement with the published mechanistic picture [180], which correlates velocity and depth of oxidation with microstructure and porosity of the carbon substrate.

Vibrational spectroscopy is a very versatile and, chemically, well-resolved technique for the characterization of carbon-oxygen functional groups. The immense absorption problems of earlier experiments seems to be overcome in present times with modern FT-IR, DRIFTS or photoacoustic detection instruments.



**Figure 28.** Thermal desorption (heating in flowing nitrogen, heating rate  $3 \text{ K s}^{-1}$ ) of  $\text{CO}_2$  and carbon monoxide from heavily oxidized fullerene black (treated in 10% ozone, oxygen at 333 K in water). An IMR-MS detector was used for unperturbed gas analysis and simultaneous detection of other desorption products (see text and Fig. 29). The value for the burn-off temperature is defined as the temperature where a weight loss of 3% had occurred.

The physical technique of desorption spectroscopy of oxygen functional groups is much more frequently used. The conceptually simple experiment using a carrier gas and a nondispersive infrared detector for CO and  $\text{CO}_2$  is not in line with the theoretical complexity of the experiment. One group of complications is of a technical nature and refers to carrier gas purity, mass transport limitations, temperature gradients, nonlinear heating ramps and temperature measurement problems. More severe is the problem that the method is destructive in two ways. First, it removes the functional groups and has to break all adsorbate–substrate bonds in a distribution of local geometries. Second, it is a high-temperature process which activates functional groups to change their structure during the experiment and to interconvert between them. This is particularly complicated in situations with carbon–oxygen single and double bonds located adjacently (see for example lactone decomposition exemplified in reaction 24).

Despite these principal ambiguities the thermal desorption method is a standard characterization technique in carbon surface chemistry. Various examples and data about desorption profiles for a selection of carbon treatments can be found in the literature [88, 90, 155, 182, 183].

The general features of all these data can be discussed using the experiments shown in Fig. 28. A highly reactive carbon with complex amorphous structure was treated with ozone at 335 K in water and the dried product subjected to a temperature-programmed decomposition in flowing nitrogen using a special mass spectrometer (IMR-MS) as detector. This instrument [184] allows the suppression of the nitrogen signal and fully removes any fragmentation of  $\text{CO}_2$  into CO. This is a problem which is significant in conventional mass spectrometers, allowing only crude estimates of changing ratios of CO to  $\text{CO}_2$ . The acid groups (1), (3) and (4) in

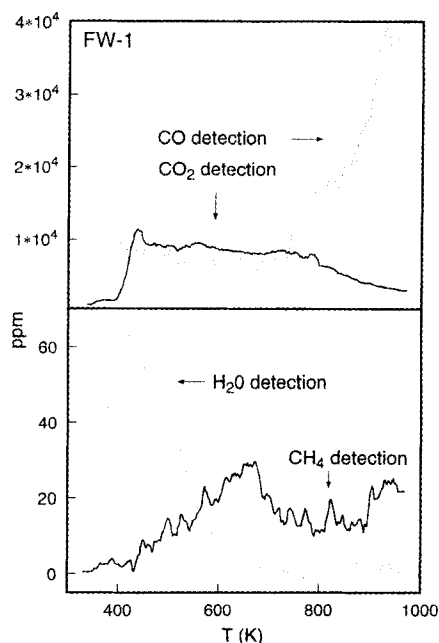


Fig. 21 result in  $\text{CO}_2$  as decomposition products, whereas all other surface groups produce mainly CO during their pyrolysis under non-oxidizing conditions. The more strongly oxidized  $\alpha$ -carbon atoms in acidic groups desorb from the graphene surface at lower temperatures than the CO from the basic groups. This behavior can be recognized in the IMR-MS traces of Fig. 28. The  $\text{CO}_2$  trace shows structures in three broad features with the first peak exhibiting some internal structure which is ascribed to the decomposition of free carboxylic acid groups and structures with other functions next to the acidic group (reaction 24). The poor resolution of the main features indicates significant kinetic effects at a heating rate of  $0.5 \text{ K s}^{-1}$  which points to a distribution of binding energies rather than to one specific desorption event. The occurrence of postdesorption reactions of the  $\text{CO}_2$  acting as oxidant for other functional groups has to be taken into account at temperatures above 650 K [112]. This finds its expression in the crossing-over of the (sensitivity-corrected) desorption traces around 650 K. The increased stability of the basic and neutral functional groups is seen in the high-temperature rise of the CO trace which peaks only above 1000 K. At these temperatures the structural rearrangement of the graphene layers in amorphous carbon becomes an important process, which prevents the observation of the complete desorption of all oxygen functional groups without changing the bulk structure of the substrate. Structural changes in the substrate give rise to the noisy appearance of the CO trace, which indicates eruptions of gas due to the beginning hole-burning process initiated by local concentration maxima of surface oxygen species which terminate quickly due to the lack of oxidant.

The desorption of oxygen functional groups is not correlated with the steady state burn-off of the material in molecular oxygen which begins at temperatures significantly above the desorption of predominantly highly oxidised functional groups.

The relative contributions of the different desorption processes changes with the average surface structure. Comparison of the data in Fig. 28 with those of an analogous oxidation experiment with a different carbon substrate (carbon black FW-1) shown in Fig. 29 reveals that the carbon black contains significantly more basic functional groups than the amorphous fullerene black. This can be traced back to a reduced number of carbon atoms which could be highly oxidized (removed from the aromatic backbone of a graphene BSU) by ozone in the two materials. The presence of five-membered rings in the fullerene black and the organization into stacks of planar graphene units in the carbon blacks are consistent structural explanations. In the carbon black sample, the separation into regimes of stability for acidic and basic functional groups is much less resolved. This indicates a larger structural diversity of the functional groups in the carbon black relative to the pronounced maximum of acidic groups in the fullerene black.

The lower traces in Fig. 29 reveal that other desorption processes occur with the decomposition of oxygen functional groups. The polar oxygen groups bind a layer of water molecules which desorbs above 415 K, after the removal of water multilayers slightly above ambient temperature. The desorption of  $\text{CO}_2$  from acidic groups leaves behind a C–H function. If this function is in an alkenic or aliphatic environment, i.e. in a surface without a closed carbon hexagon termination, then desorption of methane can contribute to a stabilization of the surface by removal of



**Figure 29.** Thermal analysis of a carbon black under the same conditions as used for the experiment in Fig. 28. Note the different scales of the ordinates.

the nonaromatic structures. The missing hydrogen atoms are taken from reactions of water with these defective carbon centres. The respectively small methane signal is displayed in Fig. 29. No higher hydrocarbons are detectable in this experiment. A desorption of molecular hydrogen at temperatures above 900 K from the terminating hydrogen atoms with aromatic carbon structure has been observed [33].

Thermal desorption data can be integrated and may be used to quantify the total number of oxygen functional groups on a carbon surface. When these data are compared with the sum of all chemically detected functional groups a significant excess of the desorption value over the chemical value is found. This excess is confirmation for the existence of chemically neutral oxygen functions which are, in part, strongly bound to the substrate (keto functions, see Fig. 22). These groups act as side blockers in surface reactions and are known in the carbon oxidation literature [86] as “stable complexes” which inhibit the oxidation.

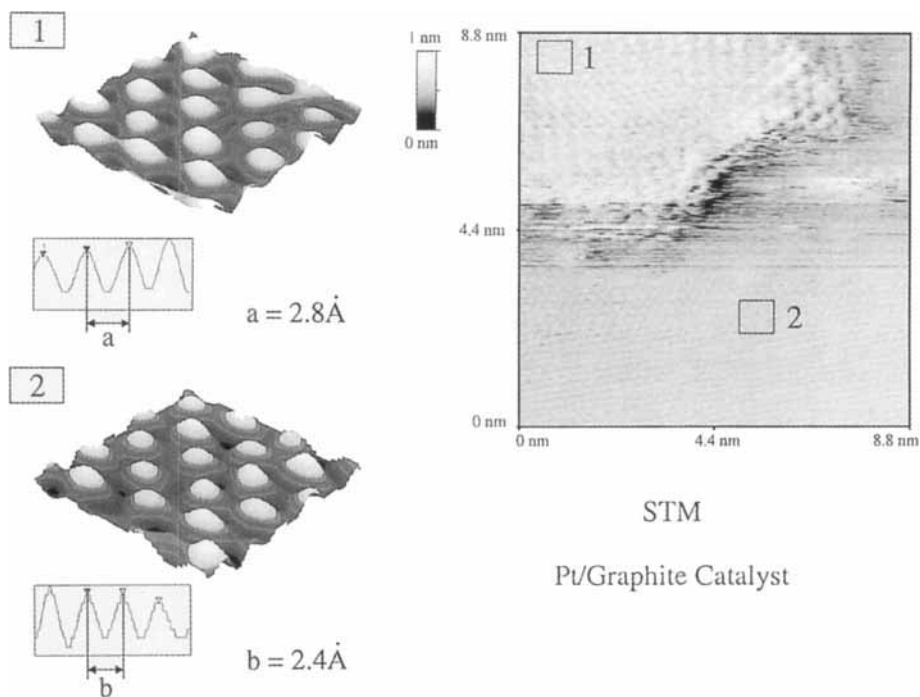
The data in Figs 28 and 29 reveal that it is not possible to fully detect the oxygen desorption without reaching temperatures at which structural changes occur in the substrates. This is a significant problem for hydrocarbon-rich carbons in catalytic deposits. The application of thermal characterization methods has to be regarded with significant reservation, as severe carbonization and dehydrogenation will go along with the “analytical” desorption events. In subsequent adsorption or reaction experiments the presence of a stable graphitic carbon as second phase is stated. The second phase is, in fact, an artefact of the preceding thermal treatment. This feature, which also complicates surface science experiments with oxygen on carbons, has been investigated [88, 90].

### 3.9.16 Carbon as Catalyst Support

The application of carbons in catalysis is mainly as support for active phases in various reactions. Besides a wide variety of noble metal–carbon systems for hydrogenation reactions and fuel cell applications, the large-scale application in the synthesis of vinyl acetate and vinyl chloride are important technical applications [185]. An important application of carbon-supported oxides of silver and copper–chromium, known as whetlerite, is as the active mass in filters for gas masks. The complex chemistry occurring upon oxidation of hazardous gases requires the presence of the carbon surface besides the oxide particles, which is interpreted [186] as indication for a synergistic effect between carbon and oxides for chemisorption of the hazardous gases and simultaneous selective oxidation by activated oxygen. The special field of carbon gasification catalysis is not covered here as in this reaction the carbon is not only the support but also the substrate. The rare case of a desired consumption of the catalyst support creates a special situation [185, 187, 188]. The application of carbon-supported catalysts in synthetic organic chemistry has been reviewed [189].

In all synthetic catalytic applications, carbon is considered as a support with little reactivity towards sensitive molecules with reactive functional groups which would be activated by either Bronsted or Lewis acidity of an oxidic substrate. This so-called weak metal–support interaction was questioned in a comparative study on metal–support interactions for platinum particles [190]. Unfortunately, the preparation conditions were chosen such that gasification of the support had occurred. For a detailed discussion see below. The extremely valuable advantage of an inert substrate consequently has the disadvantage that the active phase is difficult to anchor on the surface. It is hence difficult to create and maintain any useful dispersion of the active phase on carbon. An elegant way around this problem has been suggested [191]. A conventional oxide-supported catalyst may be, after its synthesis, covered with a deliberate carbon contamination layer on the support oxide to shield the free support surface by a carbonaceous deposit. Chemical vapor deposition of carbon from propene on alumina carrying a technical HDS system as active phase was used as demonstrator.

Two more classical ways to anchor the active phase [36] to the substrate are the fixation on oxygen functional groups or on surface defects such as steps in a basal plane of a graphitic structure. In a recent study [192] of the anchoring of the active phase on graphite, the hydrolysis of a platinum complex followed by an in situ reduction at low temperature allowed the grafting of platelets of platinum metal with a highly preferred (111) orientation and with high dispersion on a graphite substrate. It is not yet demonstrated that this attractive arrangement survives catalytic action under useful conditions for useful times. The system was, however, used to study the microstructure of the dispersed platinum. Figure 30 shows an STM image of a raft of platinum (area 1) on graphite (001) (area 2). It can be seen from the atomic resolution insets that both surfaces exhibit the same symmetry, indicating the (111) orientation of the platinum. The distinction between carbon and platinum was made possible by the differing lattice constants. The noise in the graphite image next to the platinum raft is attributed to a contamination of the STM tip



**Figure 30.** STM image of a platinum raft on a graphite powder particle. An organometallic route was used to deposit the metal at low temperatures. The discrimination of metal and graphite with the same lattice geometry is possible by the different lattice parameters.

which was collected from the metal. The thickness of the platinum raft is several metal monolayers, making any accurate analysis difficult due to the imaging artefacts. The genesis of this catalytically highly desirable structure is assumed to start from a molecular anchoring of the precursor at atomic defect sites. These act as nucleation centers for the metal platelets resulting from low-temperature chemical reduction and subsequent coagulation of initially formed metal clusters with no stable anchoring at the basal plane.

The more conventional strategy contains several steps of modification and activation [36, 189]:

- Use of a high surface area graphite with little pore structure in which the active component can be occluded.
- Creation of a maximum amount of acidic surface functional groups with cation exchange capacity.
- Cation exchange of protons by metal ions or hydrolysis of metal complexes by the surface acid groups.
- Chemical reduction of the metal at low temperatures.

This final activation step is often the difficult reaction step as the reduction of the

active component should not reduce the anchoring sites at the carbon. This reduction can occur either chemically by hydrogen atom spill-over or thermally by decarboxylation of the anchoring group. Figure 29 reveals that this decarboxylation can occur at such low temperatures that the stability limit can easily be exceeded by a thermal reduction, with hydrogen for example. The section on surface groups reveals that it is not possible to use stable functional surface groups for anchoring as these groups are chemically inactive and all active groups are thermally unstable.

The inherent problem of limited thermal and chemical stability of metal anchoring sites on carbon limits not only the activation temperature but also the application conditions [185]. In oxidizing environments carbon supports are much less stable than the macroscopic burn-off temperature (see Figs 28 and 17). In order to maintain the dispersion of the active phase, the limiting temperature should be less than the decarboxylation temperature of the anchoring groups. This temperature is equal to the initial CO<sub>2</sub> evolution which sets a margin of stability of the initial dispersion to about 450–500 K. In hydrogenation applications the limiting temperature can be even lower as the active catalyst can produce a stream of active hydrogen which reacts with oxidized anchoring groups under hydrogenolysis/hydrogenation even below 500 K. As, however, most hydrogenation reactions are carried out at temperatures below 373 K to maintain high selectivities, the carbon–metal systems are usually not limited by thermal degradation in the case of hydrogenation reactions.

The reactivity of carbon surfaces without functional groups is low with respect to most elements [193]. Important exceptions are molecular oxygen dihalogens [185] and alkali metals. The redox–amphoteric behavior of sp<sup>2</sup> carbon, which is the basis for the intercalation chemistry [140], allows for a significant charge transfer between adsorbed alkali (or halogen) atoms and even carbon on the graphite (001) surface. Thermodynamic properties of these adsorbates [194] predict that such adlayers with submonolayer coverage should be stable at high temperatures against desorption and should withstand even hydrolysis in liquid water. This is of significant relevance in applications where alkali is needed as catalyst promoter and the carbon substrate serves as reservoir for its storage [195].

Recent experiments [196] with high surface area carbons and iron particles strongly reduced in flowing hydrogen at 1173 K reveal an intimate contact between iron and carbon. It is further shown that an analogous charge transfer between iron and graphite as between alkali and graphite is operative when the iron particles are flat platelets with a high interface area.

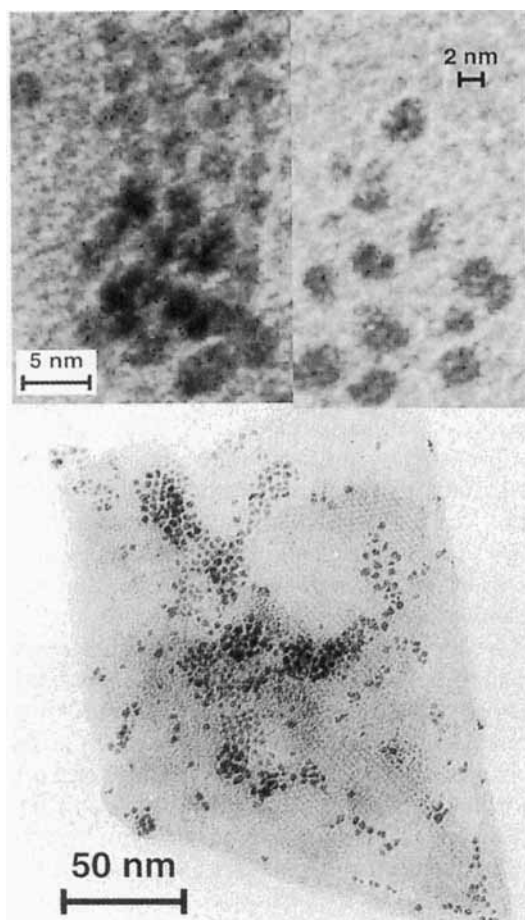
These observations mark a transition from the anchoring strategy to the geometric fixation strategy for fixation of active components on carbon. This strategy relies on the assumption that chemically stable edge sites on carbon act as geometric barriers for the diffusion of catalyst particles at high temperatures where molecular anchors are already unstable. A possible additional chemical anchoring via metal carbon bonds to the dangling bonds of the terminating graphene layer reduces a possible lateral diffusion along the step edge. The best fixation is achieved when the catalyst particle digs a small hole in its fixating geometry where it uniquely fits. Such a selective etching may be achieved by the high temperature reductive treatment mentioned in literature reports about metal carbon catalyst systems [190, 195, 196].

The intuitive assumption that carbon surfaces with a high surface fraction of prismatic faces (110, 100 and higher indexed orientations of graphite) would be suitable to create metal–carbon (carbide) bonds is not supported by experimental evidence. These prismatic faces are chemically too reactive and undergo facile gasification in oxygen or hydrogen. This leads to a geometrically unstable situation for metal particles, which, at reaction conditions, frequently lose their specific adsorption site and become mobile with the chance for agglomeration and deactivation. Successful high-temperature carbon catalysts are always prepared from materials with a smooth and preferentially graphitic surface. Here, the average reactivity of the support is minimized while still providing sufficient structural defects to create mechanical anchoring sites for active metal particles. This has been rationalized by experiments with platinum particles on carbon and by an analysis of the dispersion versus carbon pretreatment [197, 198]. The two studies were carried out with different carbons and using different reaction conditions. Both concluded that the increase in smooth surface area (not in porosity) is an important factor for stabilizing small metal particles. An additional factor of increased surface heterogeneity is given, with different relative importance in both studies. In the present context, this influence is traced back to increasing surface defects allowing direct anchoring. For high temperature preparations (at 723 K) the marked increase in platinum stabilization [198] is traced back to the selective etch process.

The principle of mechanical fixation at step edges is illustrated in Fig. 31 which shows Ru particles on a graphite surface. The single crystalline flake is preferentially (001) oriented but exhibits a system of step structures as revealed by the Moiré fringes (weak line contrast in the main image). The metal particles of a few nm size are platelets which are occasionally stacked above each other (top left plate in Fig. 31). In the main image it can be seen how an almost regular array of particles is formed at step edges of the surface. This geometric arrangement is stable in hydrogen up to 725 K where the particles become efficient methanation catalysts for their substrate. Such geometric arrangements have led to speculations that intercalation compounds between metal and graphite may constitute an active catalyst with the particles seen in Fig. 31 being mechanically bound between adjacent graphene layers. The existence of such geometries is shown by TEM [199]. The investigation of other samples discounts the existence of a fixation by intercalation [200]. The activity of the materials is traced back to particles sitting only at external step edges.

The concept of mechanical fixation of metal on carbon makes catalytic applications at high temperatures possible. These applications require medium-sized active particles because particles below 2 nm in size are not sufficiently stabilised by mechanical fixation and do not survive the high temperature treatment required by the selective etching. Typical reactions which have been studied in detail are ammonia synthesis [195, 201–203] and CO hydrogenation [204–207]. The idea that the inert carbon support could remove all problems associated with the reactivity of products with acid sites on oxides was tested, with the hope that a thermally well-conducting catalyst lacking strong–metal support interactions, as on oxide supports, would result.

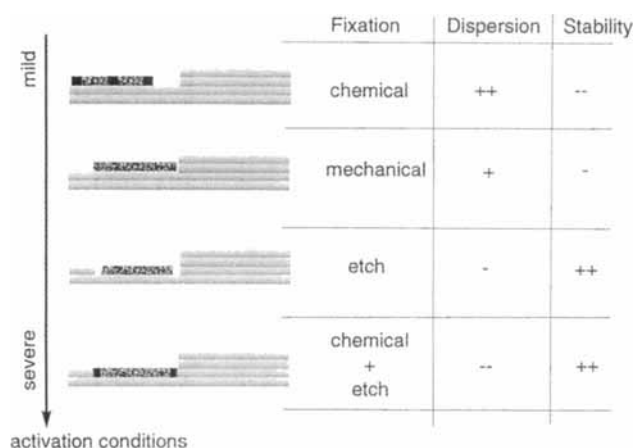
The picture which emerges from the studies of CO hydrogenation is that in addition to this “clean” case of large and active particles, a second class of small



**Figure 31.** Ru metal particles on a flake of natural graphite (TEM, 100 keV).  $\text{Ru}_3\text{CO}_{12}$  was impregnated from toluene and calcined in an inert atmosphere at 375 K. EDX and the beam stability confirmed the metallic character of these particles. Note the regular arrangement at step edges occurring from crystallite edges causing the Moiré contrast in the main image.

particles occurs on less graphitic surfaces. These particles exhibit different activity and more importantly a much more desirable product spectrum with a high alkene to paraffin ratio. These iron particles are superparamagnetic and may be partially oxidized [208]. The electron deficiency which is stated in all studies for the small particles is controversially discussed as pictures of different phases or a specific charge transfer with the carbon substrate.

This raises the question about the metal–support interaction in carbons. The term “wetting” has been used for the carbon–metal interaction [196, 206]. The usual geometry of spherical metal particles, as well as chemical arguments, render the formation of chemical bonds between each metal atom and the carbon substrate less likely. The case of alkali metals is an exception, but only in the limiting case of submonolayer coverages. The images in Figs 30 and 31 support the notion of metal rafts floating on carbon rather than resting as stable compounds. Such wetting interactions should be very stable and are in strong contradiction to the observed

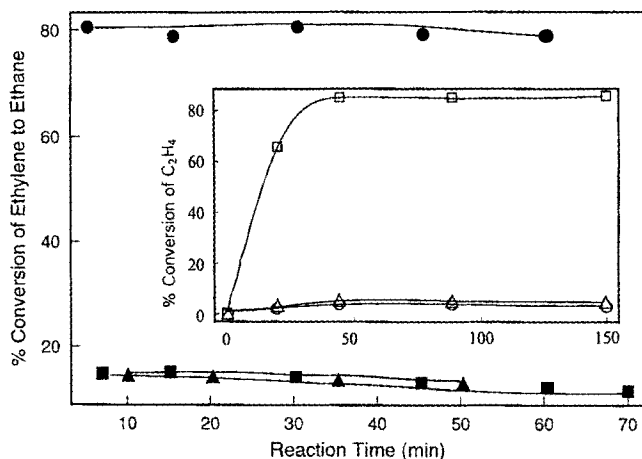


**Figure 32.** Schematic representation of the modes of fixation of metal particles on graphitic surfaces. A stack of graphene layers with a step edge is shown with a metal particle (granite pattern) and surface anchoring groups (black). Nongraphitic carbon deposits are shown in dark grey with fading contrast (bottom sketch).

chemistry of metal–carbon catalysts. The raft structures occur only in cases of mild preparative conditions which allow the agglomeration of primary metal clusters in a predominant two-dimensional fashion. The existence of metal particles with supposed strong interaction [190, 196] is described as always being associated with very severe chemical activation conditions. It is suggested that under these conditions a combination of selective etching with a redeposition of carbon in the interface region between support structure and metal particle occurs in the same way as described above for the carbon filament synthesis. Under these conditions a reactive non-graphitic carbon binder material cements the active particle into the substrate and thus allows for a strong metal–carbon interaction with covalent bonds between the metal and the support mediated by the binder carbon. No microstructural data are available in the literature to support this hypothesis which would explain a large body of partly conflicting results about location and stability of metal–carbon catalysts.

The whole range of carbon interactions with active phases is summarized in Fig. 32. In all cases no strong chemical interaction is assumed between the graphene (001) layers and the metal platelet. The weakest interaction with, however, the highest possible dispersion is obtained with surface anchoring via functional groups. Better stability at low loading with smaller dispersion can be obtained by mechanical fixation. This process requires a flat geometry and thus selective removal of all surface impurities which frequently cover basal planes of graphitic carbons. An example of the application of platinum particles on carbon in selective NO reduction was made [209]. It was concluded from kinetic arguments that the platinum behaves identically to model single crystals with preferred (110) orientation. This can be seen as an indication for the weak metal–support interaction and for the usefulness of non highly dispersed metal–supported systems in selective reactions.



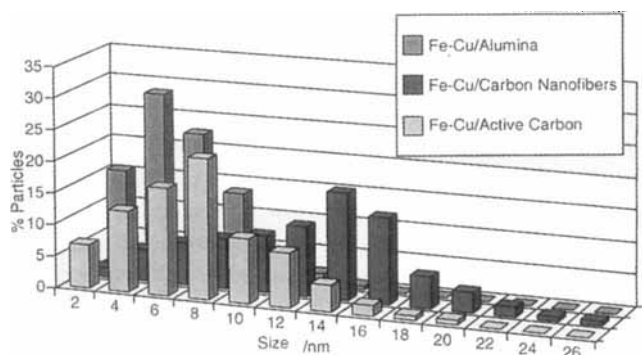


**Figure 33.** Catalytic activity of Fe–Cu bimetallic particles supported on alumina (squares), activated carbon (triangles) and carbon nanofibers (dots). The inset shows the activity of the metal particles on nanofibers in the decomposition of ethylene into solid carbon (squares), ethane (triangles) and methane (dots).

Significantly higher stability is obtained when larger agglomerates are brought into shallow holes (monolayer etch pits) of the basal planes. The generation of such pits can be achieved by reductive gasification under catalytic influence. An alternative to the in situ generation is the strategy of using microporous carbons which involves depositing metal particles at the pore mouths. The usually broad distribution of pore sizes in carbons prevents, however, the complete use of all the metal loaded, as some particles disappear into deeper parts of larger pores and fail to be active in catalysis due to diffusional limitations. Redeposition of carbon from hydrocarbon sources (from either catalytic reactions or the ongoing reductive etching) at the boundary between the metal particle and the carbon substrate occurs. This carbon may not be graphitic but can be of a more reactive connectivity (a-C–H for example) and thus provide chemical bonding between carbon and active particle.

The chemical fixation of metal particles onto carbon via covalent interaction is possible not only via reactive carbon entities as in the latter case but also directly on to a  $sp^2$  surface. This occurs, provided that the electronic structure is locally perturbed transforming the carbon from aromatic into a (poly)alkenic structure. Such a transformation can be achieved by either introducing controlled defect sites or by synthesizing carbons with structurally localized double bonds. Fullerene carbon is an example of the latter case. Oxidized nanotubes or catalytically synthesized carbon nanofibers are examples of the first case. The carbon nanofiber approach has been tested in several reactions [210] and the origin of the different chemical reactivities of the same active metal on planar carbon and on nanofibers was investigated in detail. Figure 33 reveals that the bimetallic iron–copper particles exhibit similar catalytic activities in ethylene hydrogenation on alumina and activated carbon but a considerably higher activity on nanotubes. The inset shows that these bimetallic particles are quite resistant against deactivation by carbon deposition

**Figure 34.** Particle size distributions derived from electron microscopy of the catalysts used for the experiments shown in Fig. 33.



when ethylene is decomposed to carbon filaments and methane plus ethane. The reference catalysts are fully deactivated by the time the nanofiber catalyst has reached a steady state. The most plausible explanation of a different particle size distribution of the bimetallic particles was investigated by TEM. Figure 34 shows the result. It occurs that the widest size distribution by far, with a maximum for the largest particles observed, is found for the most active nanofiber catalyst. The narrowest size distribution with the highest dispersion is achieved on the alumina support, whereas the metal-on-activated carbon catalyst still exhibits a wide distribution of intermediate sized particles. The authors claim the structure shown in Fig. 30 to be responsible for the effects. An epitactic relationship between graphite (001) and the metal close-packed structure is anticipated. The geometric data from Fig. 30 render a strong stabilization of an epitactic relationship surviving the activation step in hydrogen at 673 K less likely. The bonding of a broad spectrum of particles on defects situated or created by reductive etching on the graphene terminations of the discontinuous nanofibers (made by catalytic synthesis and not via the fullerene way) as shown in Fig. 4 seems considerably more plausible.

This example shows that a nonoxidic support can give rise to interesting properties in active particles. The catalytic performance is not simply correlated to size distributions. The experiments presented in this section reveal how few indisputable facts are yet known concerning the metal–support interaction for carbon substrates. Interactions of the type (metal d-states)–(carbon  $sp^3$ )–(carbon  $sp^2$ ) mediated via amorphous accommodation particles (Fig. 32) of intermediate layers should be considered in the prevailing picture of a yet unproved epitaxy between transition metals and graphite (001) surfaces.

### 3.9.17 Carbon as Catalyst

Carbon may also be used as a catalyst without an active component supported on it. This function may overlap with the widespread application of high surface area carbons and sorbents for selective chemisorption processes which are not considered here. The application of carbon as a catalyst in its own right has been reviewed

[211–213]. All applications are based on the simultaneous action of two functions. The first one is the selective chemisorption of an educt at the carbon through either ion exchange via oxygen functions or directly through dispersive forces involving the graphite valence electronic system. The other function is the production of atomic oxygen (or free organic radicals in dehalogenation reactions [211]) occurring on the graphene basal faces of every  $sp^2$  carbon material. Due to its central function in carbon chemistry this process is discussed in detail below. The conjecture that both processes play an important role in catalysis and that, in particular, surface patches with an intact graphene electronic structure act as sinks and sources of electrons in catalytic reaction steps, can be inferred from several observations [34, 135, 211]. The importance of the graphene layers in reactivity is still discussed rather controversially in the literature. The inertness of the basal planes in oxidation frequently dominates the chemical intuition about the stability of an “aromatic” surface.

The fact that carbon is already catalytically active at ambient conditions and in aqueous media has led to considerable efforts in applying carbon as a catalyst in the condensed phase [213]. In many of these application the surface reactivity is given by the ion exchange capacity of the oxygen functional groups binding active ions (instead of particles) and by the simultaneous presence of delocalized electrons acting as redox equivalents. The widespread use of glassy carbon as an electrochemical surface is a special case of the use of this bifunctional property of carbon under mild chemical conditions. The irreversible oxidation under these conditions, and thus the decarboxylation–desorption of surface functional groups, limits drastically the application of carbon catalysts in gas phase reactions. The reactions are, in this case, very slow [214] and allow the extensive use of these functionalities and their broad chemical variation in catalytic applications.

### 3.9.18 Case Studies of Catalytic Applications

The catalytic oxidation of sulphurous acid in aqueous medium to sulphuric acid [138, 84] has been suggested as a probe reaction for the ability of a carbon to activate molecular oxygen at ambient conditions. Besides this remarkable property the reaction is of interest in atmospheric chemistry where it provides a sink for all nonphotochemically oxidized sulfur dioxide [215]. Carbon plays a special role in this environmental application as both pure carbon and active particles (iron oxide [84] for example) anchored to carbon can act as efficient catalysts. The detailed analysis of the reactivity of various types of carbon [138] reveal that basic surface oxides (see Fig. 23) are important to fix the educt  $HSO_3^-$  ion. It was found, in addition, that the activation of molecular oxygen is of kinetic relevance. A variety of surface treatments which did not modify the surface basicity have drastic effects on the reaction kinetics and affect the oxygen activation. The degree of graphitic surface area, the content of nitrogen dopants and the overall electronic structure in terms of the surface perfection are found to be influencing factors. It is suggested [138] that doping of the conduction band of the carbon with free electrons from nitrogen atoms [211] is an important factor.

The selective oxidation of hydrogen disulfide to sulfur with oxygen in the gas

phase at around 400 K is an important side reaction in hydrogen disulfide absorbers used for natural gas treatments. The activated carbons tolerate a high load of elemental sulfur but are eventually deactivated by a full coverage of the activated surface with sulfur. This can be removed by high-temperature steaming. Discussions about this reaction are quite controversial regarding the reaction kinetics [7, 216]. Different carbons with differing pretreatments and different testing conditions were applied. All papers agree on the relevance of the activation details of the carbon for the performance of the catalysts. The variation of the reaction orders between 0 and 1 for each educt makes it difficult to discuss a mode of action for the catalyst. Observations from other reactions make the model presented in a review [216] highly plausible. It is assumed that carbon produces atomic oxygen which oxidises  $\text{HS}^-$  anions present in the aqueous film residing on the polar carbon surface under reaction conditions. The promoters iodine and ferrous ions act to support the chemisorption of  $\text{HS}^-$ . A compensation effect is claimed with a perfect linear relationship between activation energy and preexponential factor. All these details point to a significant impact of kinetic limitations which are not given by the sequence of elementary reactions.

The reaction between phosgene and formaldehyde does not occur as a homogeneous reaction under conventional conditions. It proceeds, however, in the presence of a variety of carbons with ideal selectivity at 445 K [217]. Desorption experiments show that an intermediate adduct between the two educts is the most abundant surface intermediate. The existence of highly polar (acidic) surface groups and the absence of any d-states, which decompose both educts immediately at reaction temperature, are responsible for the success of carbon in this reaction. The reaction involves the selective breaking of a Cl–Cl bond in phosgene and is thus somewhat similar to the well-known action of charcoal in the synthesis of  $\text{SOCl}_2$  from chlorine and  $\text{SO}_2$ . Carbon further catalyzes the synthesis of phosgene from CO and chlorine. It should be mentioned that the existence of surface oxides is not sufficient to explain the reaction as OH groups on oxides do not catalyze the reaction.

The example of selective oxidation of creatinine by activated carbon and air in physiological environments [218] shows again the relationship between catalysis and chemisorption in carbon applications. The creatinine oxidation plays a role as an unwanted side reaction in artificial blood regeneration during dialysis. Creatinine is the ketone to the carboxylic acid creatine which is a heterocyclic nitrogen compound. Whereas the carboxylic acid is only chemisorbed on carbons, the ketone is slowly (time constant one day) oxidized to unknown products which may be toxic. This biologically relevant process occurs only in the presence of molecular oxygen and can be poisoned by chemisorption of thiosulfate. Both indications point again to the operating property of activation of molecular oxygen under very mild conditions.

### 3.9.19 Catalytic Removal of NO by Carbon

One of the most interesting applications of carbon in the future may be the selective reduction of NO with a nonmetallic catalyst. Several highly selective and very active metal oxide catalyst systems exist for this application. They suffer, however,

from lifetime and stability problems in mobile applications such as in advanced car systems. Carbon offers several unique possibilities. First, it exhibits a self-renewing surface in oxidizing and in reducing environments. This removes the problem of catalyst destruction due to sudden instabilities of the gas source. Second, it is less sensitive to irreversible poisoning by metal adsorbates (lead, arsenic, mercury). Finally it may be cultivated as an autoreducing agent and may allow NO removal without a second source of reducing agent, such as ammonia or propene. The technological advantage is that it is cheap and can be produced in large amounts. All this has been demonstrated through research effort, and two kinds of carbon, as SCR (selective catalytic reduction) catalyst [34, 219, 220] and as NO decomposition catalyst [221, 222], have been established. The general problem is to establish sufficient activity in a carbon which is not acting as catalyst support and which is not surface modified. Only then can the advantages of the system over oxide systems be fully exploited. Carbon as catalyst support for copper particles was also tested as a successful alternative to oxide supports [223].

In the SCR application a viable solution has been found [34] by activating the surface such that extremely temperature-resistant surface functional groups with nitrogen atoms are incorporated into the carbon. Complete conversion was achieved at 575 K in the presence of a significant excess of molecular oxygen. The successful modification is obtained from a controlled synthesis of carbons from organic precursors with glucosamine as the nitrogen donor. A variety of carbon samples with other nitrogen donors and carbonization–activation procedures also enhances the SCR activity. There is, however, an unclear correlation between activity and characterization parameters. It is interesting to note that the nitrogen modification results in a change in the interaction of oxygen with the surface. The reaction order is zero with respect to the reductant and positive respect to NO and oxygen. The kinetic data, expressed as a rate constant of NO conversion as function of oxygen partial pressure, reveal a higher reaction order than the square-root dependence on oxygen partial pressure intuitively expected for dissociative activation. Such a square-root dependence was found in earlier experiments for unmodified carbons [138]. A second type of SCR activity is found over unmodified carbons in which the carbon acts only as adsorption platform for the reactants. This is indicated by a negative apparent activation energy [34].

The direct reaction of carbon as graphite or activated carbon [221, 222] with NO in the presence of excess oxygen is a high-temperature process operating with full NO conversion only at about 875 K. The parallel course of the activation curve for NO removal and for oxidation is taken as indication [224] that oxygen etches active sites into the carbon which decompose NO.

Mechanistic studies [225] lead to the conclusion that NO reacts with the carbon to form CO and surface nitrogen groups, which activate the carbon to react with molecular NO under formation of molecular nitrogen and oxygen. The similarity of the relevant nitrogen functional groups in the two reaction channels is striking as well as the importance of additional oxygen to maintain high catalytic activity. This effect is sacrificial in carbon but underlines the operation of a reaction in which defective surfaces are removed and fresh graphitic surfaces are regenerated. The relevance of the surface ordering is in line with the concept of graphene (001) sur-

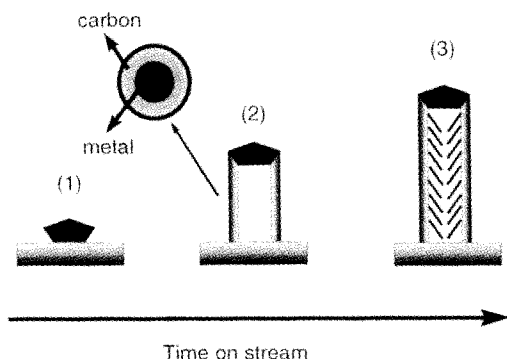
faces acting as electron donor–acceptor sites for redox reactions. This unusual mode of catalyst operation in which no specific surface functional group is the key to activity, but rather the availability of a defect-poor free surface, has been substantiated in several studies with different kinds of carbon materials [226–228]. The question about the catalytic nature of this reaction, which is to a certain extent sacrificial, has been addressed in all studies and answered positively by the determination of a factor  $F$ . This is defined as the fraction of carbon consumed in the  $\text{NO} + \text{O}_2/\text{C}$  reaction. Values from about 0.25 down to 0.09 have been reported for a variety of materials ranging from activated carbon to coke and coal. The reaction is thus clearly a catalytic process. For practical considerations it should be mentioned that with this still “poor” catalysis about 10 ml of solid carbon are sufficient to remove 100 l of gaseous NO in a 5 vol% oxygen–inert atmosphere at ambient pressure.

### 3.9.20 Removal of Carbon Deposits From Catalyst Materials

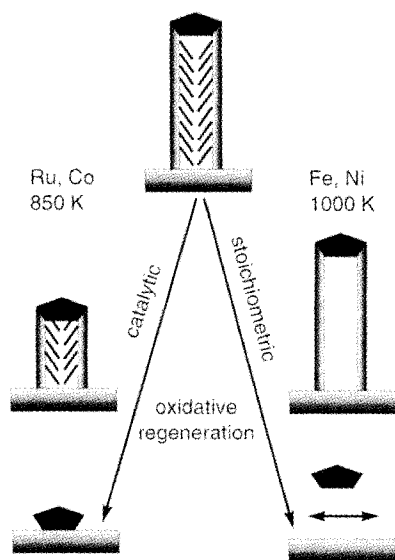
This subject is a special subsection of the carbon–oxygen reaction system and has been treated in some detail above. The present section summarizes observations of the deactivation and possible regeneration of metal–oxide catalyst systems. It has long been rationalized [229] that in oxidative regeneration of carbonized catalysts the transport limitations play a more important role than the chemistry of carbon. The fact that part of the carbon is usually nonremovable under regeneration conditions is indication of the parallel carbonization reaction transforming disordered carbon of  $\text{CH}_x$  stoichiometry into graphitic carbon with much higher resistance to oxidation. To control this interplay between carbonization and oxidation a detailed analysis of the carbon deposit and a specific adjustment of the kinetic details of the regeneration are necessary for each catalytic system.

A second problem of catalyst regeneration is often the modification of the dispersion of the active component. Several studies [24, 230] clarify that carbon deposition originating from hydrocarbons not only covers an active particle but may remove it from its support. This mode of carbonization occurs effectively with metals catalyzing the formation of carbon filaments (see above). Figure 35 summarizes this effect. A metal particle on an oxidic support (stage 1) is removed from it by the solution–exsolution mechanism creating carbon filaments. In the initial growth stage a hollow filament results (stage 2). At later stages (3) the particle restructures under the influence of the carbon–hydrogen dissolved in it and the filament is filled by the formation of graphene layers segregating from the side facets. This oversimplified growth history has been observed in a variety of case studies by electron microscopy [24].

In the later oxidative regeneration two cases of catalytic and stoichiometric gasification [230] have to be discriminated. In Fig. 36 the respective reaction pathways are depicted schematically. The catalytic path leads to a reversal of the filament generation with the effect that at comparatively moderate temperatures the initial stage of a metal particle supported on the oxide is restored. In the stoichiometric case the reaction temperature is higher, leading to a preferential oxidation of the



**Figure 35.** Mode of operation for the removal of a melt particle from an oxidic support by growing a carbon filament. Stage (1) initial saturation of the particle with carbon atoms from dissociation of a hydrocarbon and subsurface dissolution of the resulting free atoms. Stage (2) is after about 1 h on stream: the particle exsolves at the most active faces carbon which grow in a concentric set of graphene bands and remove the particle from the support. Stage (3) after some time on stream: the particle has reshaped such that surfaces within the carbon tube also become active for graphene formation and are deposited as little flakes inside the tube.



**Figure 36.** Oxidative decomposition of the carbon filaments grown in the mode described in Fig. 35. Catalytic metals lower the oxidation temperature and enable reversible removal; noncatalytic metals require higher temperatures which lead to spatial and structural modifications of the metal and finally to deactivation of the catalyst.

inner filler graphene layers according to the layer-by-layer sequence of events described above. During the final stage of tube-wall oxidation the relationship between the metal particle and the carbon fixation is lost with the consequence that the metal particle floats on the support surface and has a chance to agglomerate and move on the support surface. Depending on the catalyst loading this loosening of the metal particle will lead to severe structural deactivation during the first or during subsequent regeneration cycles.

This simple sequence of events can be distilled out of the reviewed observations and detailed microscopic studies available [24, 230]. It is in full agreement with the fundamental aspects of the topochemistry of carbon oxidation and the apparently difficult to understand wide variation of reported sensitivities of metal-oxide catalytic systems in carbon regeneration procedures.

### 3.9.21 Activation of Oxygen on Carbon Surfaces

The process of chemisorption and dissociation of molecular oxygen on carbon is fundamental to almost all aspects of carbon surface chemistry touched on here. It is also the basis of the application of carbon as a selective oxidation catalyst and is an essential part of the carbon gasification reaction (reactions 1–3). Despite this fundamental importance little reliable information is available on the mechanism, adsorption kinetics and sticking coefficient, and on the orientational dependence of such data. This is because reaction conditions and the preparation of well-defined surfaces of carbon are incompatible with conventional UHV systems. Data on polycrystalline samples or on poorly defined surfaces are available. The following cumulative assessment is given from a selection of these data. It is pointed out that similar arguments hold for the diamond surface. Only this interaction has been well researched with UHV surface science methods as the oxygen reaction controls the surface reconstruction of diamond surfaces [231, 232]. Little is known about the oxidation of diamond other than the fact that oxidation and graphitization occur hand in hand.

A set of well defined and quantitative experiments on oxygen chemisorption was carried out on a sample of preheated graphitized carbon black called graphon. This reference material is liberated from surface functional groups by annealing at 1000 K in UHV and subjection to oxygen exposures between 200 K and 550 K in a pressure range of  $10^{-4}$ – $10^2$  mbar [136]. These conditions are suitable for the formation of basic and neutral oxygen functional groups (see Figs 22 and 23). This leads to the conclusion that several chemically inequivalent species are formed. A cumulative analysis of the kinetics of adsorption reveal five inequivalent sorption processes with different time constants and activation energies between  $12 \text{ kJ mol}^{-1}$  and  $50 \text{ kJ mol}^{-1}$ . All species adsorbed are atomic oxygen, as shown by isotope scrambling. Their formation creates CO and CO<sub>2</sub> in the gas phase. The observations can only be rationalized as an indication for the reaction of prism faces with oxygen ending in basic functional groups. The desorption of adsorbed oxygen is only possible by destructive high temperature treatment, releasing CO and CO<sub>2</sub> at 1000 K. The adsorption and activation of molecular oxygen is undetectable because the surface is too reactive to bind the dissociation product atomic oxygen. These findings also mean that molecular oxygen can be dissociated at 200 K on polycrystalline carbon with a small apparent activation energy of  $12 \text{ kJ mol}^{-1}$ .

According to these data no reactive atomic oxygen at low and intermediate oxygen concentrations should be present on carbon, which is in clear contradiction to many chemical facts reported above. Other forms of oxygen activation must co-exist with this immediate functionalization of prismatic faces.

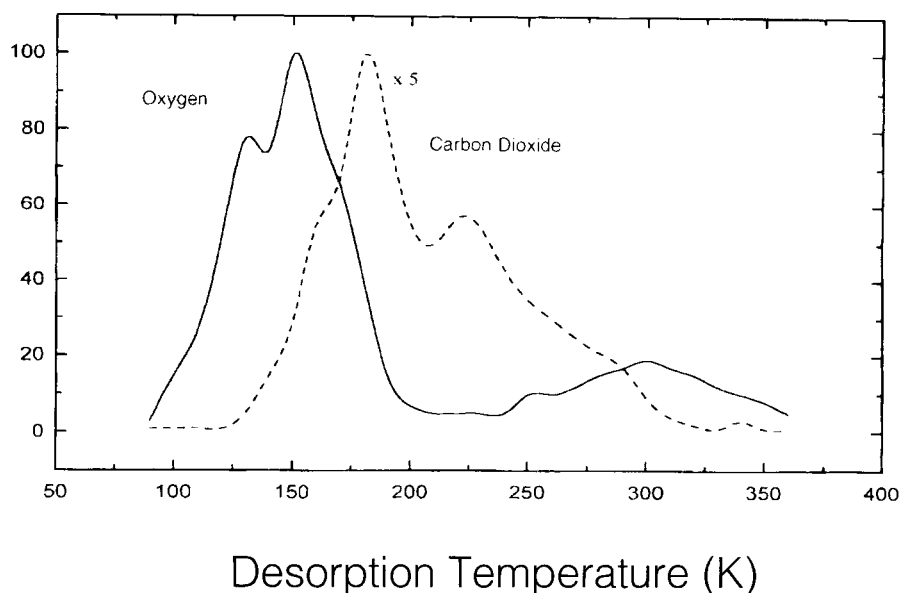


A first XPS spectroscopic study was aimed at the chemisorption of oxygen at 300 K onto graphite (001) [213]. A “very small but unmistakably present” amount of oxygen was detected which we today interpret as oxygen chemisorbed at the surface defects of the sample which was not annealed prior to the experiment. A sticking coefficient for molecular oxygen at 300 K of  $10^{-14}$  is estimated. It is found that cleaning the surface by Ar ion bombardment, which destroys the graphite structure as we know today [163], enhances the sticking coefficient to measurable dimensions of  $10^{-7}$  on the basal plane at 673 K. Kinetic data reveals in analogy to the graphon experiments a variety of “at least four different” species with binding energies between 530 eV and 533 eV. As no C 1s data were reported, it is difficult today to assign these shifts to different species.

The authors [233] later reduced the number of surface species to two and assigned carbonyl and C–O–C species to the XPS lines. It is found that atomic oxygen, generated by a microwave discharge from NO, is effectively chemisorbed at basal planes of graphite giving rise to excessive bulk oxidation. In this study the disruption of the graphite structure upon Ar ion bombardment is demonstrated. The release of implanted Ar by subsequent oxidation is taken as an elegant measure for the oxidation kinetics. Oxidation experiments on natural diamond surfaces can be found in this paper. These surfaces are much more inert in the as-received state and are found to become similar to graphite upon Ar etching. This is explained by ion bombardment-induced graphitization of the diamond.

In a more recent set of experiments [84, 90, 163] a pre-annealed surface of pyrographite with an average (001) orientation was used to perform in situ oxidation experiments which showed measurable conversions at  $10^{-6}$  mbar and 900 K. The oxygen XPS data reveals at higher resolution the same two structures mentioned above. On the basis of the in situ observation it is shown conclusively that carbon–oxygen bonds give rise to several unresolved peaks between 532 eV and 529.9 eV. The structure at 533 eV is found after low-temperature chemisorption of molecular oxygen at 78 K and during in situ gasification at 900 K as a shoulder on the strong peak of carbon–oxygen functions. This high binding energy feature is assigned to a peroxo-like molecular adsorbate species of oxygen weakly bonded to the basal planes of graphitic carbon.

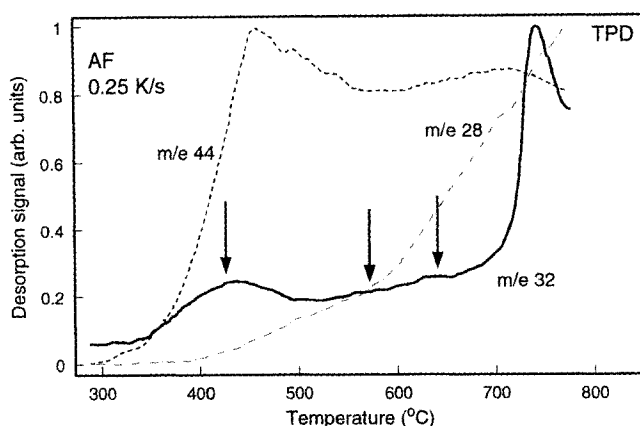
Supporting evidence for the existence of such a weakly held precursor species to carbon–oxygen functions comes from TDS experiments on a well-characterized graphite (001) surface [90]. The material HOPG is not of single crystalline quality and contains an uncharacterized amount of surface defects. It is, however, the best approximation to a single crystal basal surface which technically can be handled. Figure 37 shows the desorption traces for molecular oxygen and CO<sub>2</sub> recorded simultaneously after adsorption of molecular oxygen at 78 K. A structured desorption signal for molecular oxygen is seen at low temperatures which is associated with a chemisorbed molecular species. Variation of the heating rate does not cause a shift of the main peak, indicating a low formal reaction order. The detection of a second signal around ambient temperature exhibiting considerable structure was unexpected. These features are taken to indicate a structural heterogeneity of the adsorption sites, whereas the two peak systems at 150 K and at 300 K represent two chemically different oxygen species. The simultaneously recorded CO<sub>2</sub> emission indicates the following facts:



**Figure 37.** Temperature-programmed ( $10\text{ K s}^{-1}$ ) of molecular oxygen from a cleaved and annealed (001) surface of HOPG graphite. 1000 L oxygen were admitted to the surface at 78 K and  $10^{-6}$  mbar pressure.

- At temperatures as low 180 K oxygen is activated dissociatively and oxidizes (at defect sites) the carbon (001) plane.
- This is shown by a repetition of the experiment shown in Fig. 37 which is impossible on the once-reacted surface. Mechanical cleavage of the sample is required to repeat the experiment.
- No unspecific re-adsorption of oxygen can be detected for all sites from which chemisorbed oxygen in the first experiment was removed by warming to 360 K.
- The desorptions of oxygen and  $\text{CO}_2$  occur partly overlapping and partly alternating.
- The broad structure in  $\text{CO}_2$  desorption indicates the existence of a variety of different reaction sites, compatible with varying local geometries around the defect sites. The participation of prism faces is only possible at step edges as the large prism face area of the geometric sample block is passivated by the very first experiment with the sample. Valence band electronic spectra recorded simultaneously with the desorption experiment [90] reveal the transformation of the semimetallic surface into a fully insulating state, compatible with the creation of many surface defects on the (001) plane.
- Oxygen is activated on patches of relatively electron-rich graphitic structure and reacts at structural defects which are numerous on the mechanically cleaved surface.

These observations imply that no oxygen remains unreacted with carbon above 350 K, which is in line with the catalytic function of carbon exhibiting no oxidation

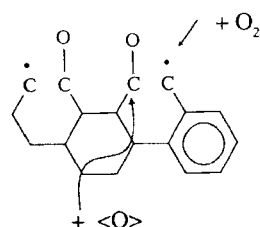
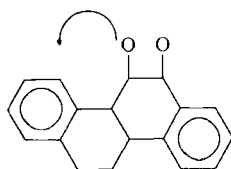
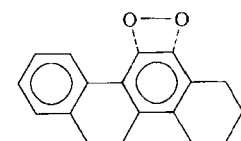
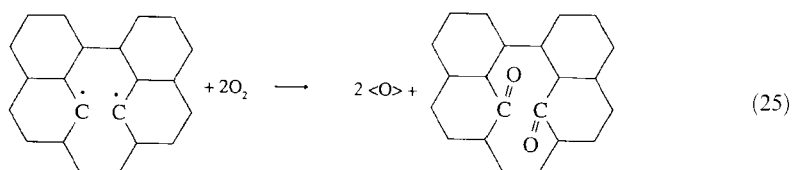


**Figure 38.** Temperature-programmed decomposition ( $0.25 \text{ K s}^{-1}$ ) of oxygen surface functional groups from a graphite powder. The simultaneous mass-spectroscopic analysis reveals the irreversible character of this experiment in which the substrate surface is removed during desorption of the adsorbate.

activity at high temperatures. This precludes, however, the possibility that any of the species detected so far can act as efficient precursors for carbon oxidation which begins with the emission of CO at significantly higher temperatures.

Attempts were made with powdered carbons and enlarged oxygen exposure pressures to detect further species of oxygen by thermal desorption (Fig. 38). The spectra were obtained from a powdered graphite with a low surface area. The arrows mark oxygen desorption peaks from a sample of high surface area carbon black (FW-1, DEGUSSA). It occurs that additional adsorbed species of oxygen exist which exhibit, during their thermal activation, a finite chance to desorb as oxygen rather than the more likely thermally activated reaction with carbon sites. A low-temperature process reacts specifically to acid sites releasing  $\text{CO}_2$ . A broad structure and the sharp high-temperature desorption peak generate increasingly more CO than  $\text{CO}_2$ . Only the high-temperature species has the chance to reach the prism faces and to react with freshly created defect sites. All other species react with very labile surface defects which terminate in their activity after a few reaction cycles. Considering the rough structure of carbon surfaces shown in Fig. 16, this seems likely for carbons with a small degree of total burn-off as is the case with all surface science experiments.

The experimental observations can be summarized in the following scenario of oxygen activation on carbon. Two independent pathways of activation have to be considered. Both require electron-rich adsorption sites for molecular oxygen. The electrons may be either delocalized on graphitic patches or may be localized in dangling bonds at coordinatively unsaturated defects (i.e. free radical centers). These latter sites exist only after high temperature treatment in inert conditions or as short-lived species during steady state gasification. The graphitic surface patches on carbon exist after mild burn-off (see Fig. 16) after the nitrogen activation procedure discussed above and after UHV cleavage and survive in reactive gas atmospheres such as water, air, NO or halogen-containing environments, provided that



the rate of defect formation via “hot” oxygen is low enough not to passivate the graphitic character.

Reaction scheme 25 summarizes the activation of oxygen on a radical center. This is exemplified here as an intralayer defect (one C–C bond missing). Two carbonyl groups are formed, eliminating the radical centers. Two atomic oxygen species O may either subsequently oxidize the former radical centers further to a carboxylic acid site or may diffuse to other sites on the carbon. This depends upon temperature and the local structural environment of the primary radical centers.

Reaction scheme 26 illustrates the chemisorption pathway in which, after a precursor state, first a hyperoxo species and then a peroxo species is formed. The dashed bonds indicate incomplete charge transfer. Only at the final step of dissoci-

ation of the molecular precursor states is the aromatic character of the carbon adsorption site lost. The following steps can then be the diffusion of atomic oxygen, leaving behind a defective carbon site (localized double bonds), or straight reaction of the atomic oxygen with the carbons on which they are chemisorbed. In the boundary condition of high oxygen partial pressure and high temperatures or at very low temperatures, both reaction pathways may cooperate and thus explain the TDS observations discussed above.

Unfortunately, no quantitative data on any of these reaction steps exist, which are obtained under strict control of the experimental variables as in usual surface science experiments with metallic surfaces. Microkinetic modeling which could support in a quantitative way the picture derived so far has to await such well-defined experiments.

### 3.9.22 Conclusions

The surface chemistry of carbon is rather complex. At a single adsorption site several chemically inequivalent types of heteroatom bonds may form. Strong interactions between surface functional groups further complicate the list of surface chemical structures as derived for the most relevant carbon–oxygen system. An additional dimension of complexity is presented by the large variety of substrate structures of carbon which arise from anisotropic covalent bonding rather than by a isotropic metallic interaction.

It is not surprising that a very large body of seemingly conflicting experimental observations has been collected in the literature. A great deal of confusion can be traced back to inadequate analysis of the type of carbon under study, as exemplified by the use of the term “coke” in different fields of chemistry. Another general problem is the insufficient consideration of the reactivity of many carbon species during chemical treatment or even during analytical experiments (temperature-programmed methods). The underlying problem here is the insufficient distinction between thermodynamic phases (allotropes of carbon) and metastable structures. It is a matter of debate how many allotropes of carbon exist besides graphite and diamond. In this ill-defined situation a general description of “the chemistry” of carbon is difficult and is thus not even attempted here. The intention of this compilation of experimental data is to assist the reader in finding an adequate approach with which to analyse the situation for a particular problem with carbon chemistry.

A comprehensive review about particular case studies of carbon as a catalyst [236] provides detailed information and access to the original literature.

## References

1. J. D. Bernal, *Proc. Roy. Soc. A* **1924**, 106, 749–773.
2. F. Atamny, J. Blöcker, B. Henschke, R. Schlögl, T. Schedel-Niedrig, M. Keil, A. M. Bradshaw, *J. Phys. Chem.* **1992**, 96, 4522.
3. T. Schedel-Niedrig, D. Herein, H. Werner, M. Wohlers, R. Schlögl, G. Francz, P. Kania, P. Oelhafen, C. Wild, *Europhys. Lett.* **1995**, 31(8), 461–466.

4. R. Berman, *Physical Properties of Diamond*, Academic Press, Oxford, **1965**.
5. R. Schlögl, *Surf. Sci.* **1987**, 189, 861–872.
6. R. Schlögl in *Graphite Intercalation Compounds II*, (Eds: H. Zabel, S. A. Solin), Springer-Verlag, **1992**.
7. V. I. Kasatochkin, A. M. Sladkov, Y. P. Kudryavtsev, M. M. Popov, J. E. Sterenberg, *Carbon* **1973**, 11, 70–72.
8. H. Kroto, *Science* **1988**, 242, 1139–1145.
9. W. Krätschmer, L. D. Lamb, K. Fostiropoulos, D. R. Huffman, *Nature* **1990**, 347, 354–358.
10. H. Werner, D. Herein, J. Blöcker, B. Henschke, U. Tegtmeier, T. Schedel-Niedrig, M. Keil, A. M. Bradshaw, R. Schlögl, *Chem. Phys. Lett.* **1992**, 134(1–2), 62–66.
11. C. Taliani, G. Ruani, R. Zamboni, R. Danieli, S. Rossini, V. N. Denisov, V. M. Burlakov, F. Negri, *J. Chem. Soc., Chem. Commun.* **1993**, 220.
12. H. S. Chen, A. R. Kortan, R. C. Haddon, M. L. Kaplan, C. H. Chen, A. M. Mujsce, H. Chou, D. A. Fleming, *Appl. Phys. Lett.* **1991**, 59(23), 2956.
13. I. M. K. Ismail, S. L. Rodgers, *Carbon* **1992**, 30(2), 229–239.
14. R. A. Assink, J. E. Schirber, D. A. Loy, B. Morosin, G. A. Carlson, *J. Mater. Res.* **1992**, 7(8), 2136.
15. H. Werner, T. Schedel-Niedrig, M. Wohlers, D. Herein, B. Herzog, R. Schlögl, M. Keil, A. M. Bradshaw, *J. Chem. Soc., Farad. Trans.* **1994**, 90(3), 403–409.
16. H. W. Kroto, A. W. Allaf, S. P. Balm, *Chem. Rev.* **1991**, 91, 1213–1235.
17. H. Werner, D. Buback, U. Göbel, B. Henschke, W. Bensch, R. Schlögl, *Angew. Chem.* **1992**, 104(7), 909–911.
18. J. D. Fitzgerald, G. H. Taylor, L. F. Brunckhorst, L. S. K. Pang, M. H. Terrones, A. L. Mackay, *Carbon* **1992**, 30, 1251–1260.
19. T. Belz, H. Werner, F. Zemlin, U. Klengler, M. Wesemann, B. Tesche, E. Zeitler, A. Reller, R. Schlögl, *Angew. Chem., Int. Ed. Engl.* **1994**, 33(18), 1866–1869.
20. T. Baum, S. Löffler, P. Weilmünster, K.-H. Homann, *Ber. Bunsenges. Phys. Chem.* **1992**, 96(7), 841–857.
21. M. Endo, H. W. Kroto, *J. Phys. Chem.* **1992**, 96, 6941–6944.
22. M. Monthieux, J. G. Lavin, *Carbon* **1994**, 32, 335–343.
23. R. Saito, M. Fujita, G. Dresselhaus, M. S. Dresselhaus, *Mater. Sci. Eng. B* **1993**, B19, 185–191.
24. R. T. K. Baker, *Amer. Chem. Soc., Fuel Chem.* **1996**, 41(2), 521–524.
25. M. Audier, A. Oberlin, M. Coulon, L. Bonnetain, *Carbon* **1981**, 19, 217–224.
26. S. Motojima, I. Hasegawa, S. Kagiya, K. Andoh, H. Iwanaga, *Carbon* **1995**, 33, 1167–1173.
27. W. A. de Heer, D. Ugarte, *Chem. Phys. Lett.* **1993**, 207 (4–6), 480–486.
28. M. S. Zwanger, F. Banhart, *Philosophical Magazine B* **1995**, 72(1), 149–157.
29. A. W. Moore, in *Chemistry and Physics of Carbon* (Eds: P. L. Walker Jr.: P. A. Thrower), Marcel Dekker, New York **1981**, p. 233.
30. H.-P. Boehm, *Z. Anorg. Allg. Chem.* **1958**, 297, 315–322.
31. D. L. Wertz, M. Bissell, *Fuel* **1995**, 74(10), 1431–1435.
32. W. Ruland, *J. Appl. Phys.* **1967**, 38, 5585.
33. J.-B. Donnet; R. Ch. Bansal; M.-J. Wang in *Carbon Black, Science and Technology*, Marcel Dekker, New York, **1993**.
34. L. Singoredjo, F. Kapteijn, J. A. Moulijn, J.-M. Martin-Martinez, H.-P. Boehm, *Carbon* **1993**, 31, 213–222.
35. R. Burmeister, B. Despeyroux, K. Deller, K. Seibold, P. Albers, *Stud. Surf. Sci. Catal.* **1993**, 78, 361–368.
36. D. Richard, P. Gallezot, *Stud. Surf. Sci. Catal.* **1987**, 31, 71.
37. P. B. Weisz, R. D. Goodwin, *Carbon* **1982**, 20, 445–449.
38. P. B. Weisz, R. D. Goodwin, *Carbon* **1983**, 21, 517.
39. O. Vohler, F. von Sturm, E. Wege, H. von Kienle, M. Voll, P. Kleinschmit, *Ullmann's Encycl. Ind. Chem.* **1986**, p. 95–163.
40. M. S. Kim, N. M. Rodriguez, R. T. K. Baker, *J. Catal.* **1991**, 131, 60–73.
41. X. X. Bi, *J. Mater. Res.* **1995**.
42. H. F. Calcote, *Combustion and Flame* **1981**, 42, 215–242.

43. J. Lahaye, G. Prado in *Chemistry and Physics of Carbon* (Eds: P. L. Walker Jr., P. A. Thrower), Marcel Dekker, New York **1978**, p. 167–294.
44. K. H. Homann, H. G. Wagner, *Proc. Roy. Soc. A* **1968**, 307, 141–152.
45. J. H. Kent, H. G. Wagner, *Combustion Science and Technology* **1984**, 41, 245–269.
46. K. H. Homann, H. G. Wagner, *Ber. Bunsenges.* **1965**, 69, 20–35.
47. J. Lahaye, G. Prado, J. B. Donnet, *Carbon* **1974**, 2, 27–35.
48. G. P. Prado, J. B. Howard, in *Advances in Chemistry Series: Evaporation-Combustion of Fuels* (Ed.: J. T. Zung), American Chemical Society, Washington, **1978**, p. 153–166.
49. C. Bertrand, J.-L. Delfau, *Combustion Science and Technology* **1985**, 44, 29–45.
50. F. Takahashi, I. Glassman, *Combustion Science and Technology* **1984**, 37, 1–19.
51. M. Frenklach, L. B. Ebert, *J. Phys. Chem.* **1988**, 92, 563–564.
52. J. Lahaye, *Polymer Degradation and Stability* **1990**, 30, 111–121.
53. R. T. K. Baker, M. A. Barber, P. S. Harris, F. S. Feates, R. J. Waite, *J. Catal.* **1972**, 26, 51–62.
54. I. Alstrup, *J. Catal.* **1988**, 109, 241–251.
55. A. J. H. M. Kock, P. K. de Bokx, E. Boellaard, W. Klop, J. W. Geus, *J. Catal.* **1985**, 96, 468–480.
56. J. R. Rostrup-Nielsen, *J. Catal.*, **1972**, 27, 343–356.
57. G. A. Somorjai, *Proc. 8th International Congress on Catalysis*, Verlag Chemie, Weinheim **1984**, p. 113.
58. G. F. Taylor, S. J. Thomson, G. Webb, *J. Catal.* **1968**, 12, 191–197.
59. S. M. Davis, F. Zaera, B. E. Gordon, G. A. Somorjai, *J. Catal.* **1985**, 92, 240–246.
60. M. Salmeron, G. A. Somorjai, *J. Phys. Chem.* **1982**, 86, 341–350.
61. L. H. Dubois, D. G. Castner, G. A. Somorjai, *J. Chem. Phys.* **1980**, 72(9), 5234–5240.
62. J. R. Fritch, K. P. C. Vollhardt, *Angew. Chem.* **1980**, 92(7), 570–572.
63. B. E. Bent, C. M. Mate, J. E. Crowell, B. E. Koel, G. A. Somorjai, *J. Phys. Chem.* **1987**, 91, 1439–1502.
64. S. M. Davis, F. Zaera, G. A. Somorjai, *J. Catal.* **1982**, 77, 439–459.
65. S. J. Thomson, G. Webb, *J. Chem. Soc., Chem. Commun.* **1976**, 526–527.
66. Z. Paál, R. Schlögl, G. Ertl, *Faraday Trans.* **1992**, 88(8), 1179–1189.
67. H. G. Karge in *Introduction to Zeolite Science and Practice* (Eds: H. van Bekkum, E. M. Flanigen, J. C. Jansen), Elsevier, Amsterdam **1991**, p. 531–570.
68. S. M. Davis, Y. Zhou, M. A. Freman, D. A. Fischer, G. M. Meitzner, J. L. Gland, *J. Catal.* **1992**, 139, 322–325.
69. G. P. Handreck, T. D. Smith, *J. Catal.* **1990**, 123, 513–522.
70. K. Moljord, P. Magnoux, M. Guisnet, *Appl. Catal. A* **1995**, 122, 21–32.
71. H. G. Karge, E. P. Boldingh, *Catal. Today* **1988**, 3, 53–63.
72. D. Eisenbach, E. Gallei, *J. Catal.* **1979**, 56, 377–389.
73. H. Marsh in *Carbon and Coal Gasification* (Eds: J. L. Figueiredo, J. A. Moulijn), Martinus Nijhoff Publishers, Dordrecht **1986**, p. 27.
74. J. Maire, J. Mering, *Chem. Phys. Carbon* **1970**, 6, 125–190.
75. R. W. Henson, W. M. Reynolds, *Carbon* **1965**, 3, 277.
76. H. Marsh, P. L. Walker Jr. in *Chemistry and Physics of Carbon* (Eds: P. L. Walker Jr., P. A. Thrower), Marcel Dekker, New York, **1979**, p. 230.
77. T. Belz, J. Find, D. Herein, N. Pfänder, T. Rühle, H. Werner, M. Wohlers, R. Schlögl, *Ber. Bunsenges. Phys. Chem.* **1997**, 101, 712–725.
78. M. Kanowski, H.-M. Vieth, K. Lüders, G. Buntkowsky, T. Belz, H. Werner, M. Wohlers, R. Schlögl, *Carbon* **1997**, 35, 685–695.
79. G. Blyholder, H. Eyring, *J. Phys. Chem.* **1959**, 63, 1004–1008.
80. S. Ahmend, M. Back, J. M. Roscoe, *Combustion & Flame* **1987**, 70, 1–16.
81. Z. Du, A. F. Sarofim, J. P. Longwell, *Energy & Fuels* **1991**, 5, 214–221.
82. F. S. Feates, *Trans. Faraday Soc.* **1968**, 64, 3093–3099.
83. H. Marsh, T. E. O'Hair, R. Reed, *Trans. Faraday Soc.* **1965**, 61, 285–293.
84. F. Atamny, J. Blöcker, A. Dübotzky, H. Kurt, G. Loose, W. Mahdi, O. Timpe, R. Schlögl, *J. Mol. Phys.* **1992**, 76(4), 851–886.
85. F. J. Vastola, P. J. Hart, P. L. Walker, *Carbon* **1964**, 2, 65–71.

86. L. R. Radovic, H. Jiang, A. A. Lizzio, *Energy & Fuels* **1991**, 5, 68–74.
87. A. A. Lizzio, H. Jiang, L. R. Radovic, *Carbon* **1990**, 28, 7–19.
88. B. Henschke, H. Schubert, J. Blöcker, F. Atamny, R. Schlögl, *Thermochimica Acta* **1994**, 234, 53–83.
89. D. Herein, J. Find, B. Herzog, H. Kollmann, R. Schmidt, R. Schlögl, *ACS Symp. Ser.* **1996**, 148–154.
90. R. Schlögl, G. Loose, M. Wesemann, *Solid State Ionics* **1990**, 43, 183–192.
91. J. M. Ranish, P. L. Walker Jr., *Carbon* **1993**, 31, 135–141.
92. L. E. C. de Torre, J. L. Llanos, E. J. Bottani, *Carbon* **1991**, 29(7), 1051–1061.
93. H. Marsh, T. E. O'Hair, W. F. K. Wynne-Jones, *Trans. Faraday Soc.* **1965**, 61, 274–283.
94. J. M. Thomas, *Chem. Phys. Carbon* **1965**, 1, 121.
95. C. Wong, R. T. Yang, B. L. Halpern, *J. Chem. Phys.* **1983**, 78(6), 3325–3328.
96. A. Cuesta, A. Martínez-Alonso, J. M. D. Tascón, *Energy & Fuels* **1993**, 7, 1141–1145.
97. B. Herzog, D. Bokern, T. Braun, R. Schlögl, *Materials Sci. Forum* **1994**, 166–169, 517–522.
98. A. Kavanagh, R. Schlögl, *Carbon* **1988**, 26(1), 23–32.
99. R. Schlögl, F. Atamny, W. J. Wirth, J. Stephan, *Ultramicroscopy* **1992**, 42–44, 660–667.
100. D. W. McKee in *Fundamental Issues in Control of Carbon Gasification* (Eds: J. Lahaye; P. Ehrburger), Kluwer, Dordrecht, **1991**, p. 484–514.
101. K. J. Hüttinger, J. Adler, G. Hermann, *Carbon and Coal Gasification* Nijhoff, Dordrecht, **1986**, p. 213.
102. S. Amelinkx, P. Delavignette, M. Heerschap, *Chem. Phys. Carbon* **1965**, 1, 2.
103. H. Marsh, N. Murdie, I. A. S. Edwards, H. P. Boehm, *Chem. Phys. Carbon* **1987**, 20, 213.
104. F. M. Lang, P. Magnier, *Chem. Phys. Carbon* **1968**, 3, 121.
105. H. Werner, M. Wohlers, D. Bublak, J. Blöcker, R. Schlögl, *J. Fullerenes Sci. Technol.* **1993**, 1(4), 457–474.
106. M. Wohlers, A. Bauer, T. Rühle, F. Neitzel, H. Werner, R. Schlögl, *J. Fullerenes Sci. Technol.* in press.
107. H. Werner, M. Wohlers, D. Bublak, T. Belz, W. Bensch, R. Schlögl in *Electronic Properties of Fullerenes* (Eds: H. Kuzmany, J. Fink, M. Mehring), Springer, Berlin **1993**, p. 16–38.
108. M. Wohlers, H. Werner, D. Herein, T. Schedel-Niedrig, A. Bauer, R. Schlögl, *Synth. Met.* **1996**, 77, 299–302.
109. K. L. Yeung, E. E. Wolf, *J. Catal.* **1993**, 143(2), 409–429.
110. M. Wohlers, A. Bauer, Th. Belz, Th. Rühle, Th. Schedel-Niedrig, R. Schlögl, *ACS Symp. Ser.* **1996**, 108–112.
111. I. M. K. Ismail, P. L. Walker Jr., *Carbon* **1989**, 27(4), 549–559.
112. R. L. Radovic, P. L. Walker, R. G. Jenkins, *Fuel* **1983**, 62, 849–856.
113. N. R. Laine, F. J. Vastola, P. L. Walker Jr., *J. Phys. Chem.* **1963**, 67, 2030–2034.
114. H. Freund, *Fuel* **1986**, 65, 63–66.
115. P. Biloen, *J. Mol. Catal.* **1983**, 21, 17–24.
116. R. T. Yang, C. Wong, *J. Catal.* **1984**, 85, 154–168.
117. B. Pennemann, R. Anton, *J. Catal.* **1989**, 118, 417–423.
118. F. Kapteijn, O. Peer, J. A. Moulijn, *Fuel* **1986**, 65, 1371.
119. S. R. Kelemen, H. Freund, *J. Catal.* **1986**, 102, 80–91.
120. M. B. Cerfontain, R. Meijer, F. Kapteijn, J. A. Moulijn, *J. Catal.* **1987**, 107, 173–180.
121. J. A. Moulijn, F. Kapteijn, *Carbon* **1995**, 33(8), 1155–1165.
122. R. Schlögl in *Physics and Chemistry of Alkali Metal Adsorption* (Eds: H. P. Bonzel, A. M. Bradshaw, G. Ertl), Elsevier Science, Amsterdam, **1989**, p. 347–377.
123. L. Bonnetain, X. Duval, M. Letort in *Proc. 4th Carbon Conference, Buffalo*, Pergamon Press, **1960**, p. 107–112.
124. F. Kapteijn, R. Meier, S. C. van Eyck, J. A. Moulijn in *Fundamental Issues in Control of Carbon Gasification* (Eds: J. Lahaye, P. Ehrburger), Kluwer, Dordrecht, **1991**, p. 221.
125. A. J. Groszek, S. Partyka, D. Cot, *Carbon* **1991**, 29, 821–829.
126. A. J. Groszek, *Carbon* **1987**, 25, 712–722.
127. F. Atamny, A. Reller, R. Schlögl, *Carbon* **1992**, 1123–1126.
128. F. Atamny, H. Kollmann, H. Bartl, R. Schlögl, *Ultramicroscopy* **1993**, 48, 281–289.
129. E. Koberstein, E. Lakatos, M. Voll, *Ber. Bunsenges.* **1971**, 75(10), 1104–1114.



131. J. A. Franz, R. Garcia, J. C. Lineman, G. D. Love, C. E. Snape, *Energy & Fuel* **1992**, 6, 598–602.
132. M. Spiro, *Catal. Today* **1990**, 7, 167–178.
133. R. C. Bansal, N. Bhatia, T. L. Dhami, *Carbon* **1978**, 16, 65–68.
134. B. R. Puri, R. C. Bansal, *Carbon* **1964**, 1, 451–455.
135. B. Stöhr, H. P. Boehm, R. Schlögl, *Carbon* **1991**, 29(6), 707–720.
136. R. C. Bansal, F. J. Vastola, P. L. Walker Jr., *J. Colloid Interface Sci.* **1970**, 32(2), 187–194.
137. R. C. Bansal, F. J. Vastola, P. L. Walker *Carbon* **1971**, 9, 185–192.
138. M. Zuckmantel, R. Kurth, H. P. Boehm, *Z. Naturforsch.* **1979**, 34b, 188–196.
139. C. H. Chang, *Carbon* **1981**, 19, 175–186.
140. R. Schlögl in *Progress in Intercalation Research, Physics and Chemistry of Materials with Low-Dimensional Structures*, (Eds: Müller-Warmuth), Kluwer, Dordrecht **1994**, p. 83–176.
141. B. R. Puri, R. C. Bansal, *Carbon* **1966**, 3, 533–539.
142. W. O. Stacy, W. R. Imperial, P. L. Walker, *Carbon* **1966**, 4, 343–352.
143. H.-P. Boehm, *Angew. Chem.* **1966**, 78(12), 617–628.
144. M. L. Studebaker, *Rubber Chem. Technol.* **1957**, 30, 1400–1483.
145. C. A. L. Y. Leon, J. M. Solary, V. Calemme, L. R. Radovic, *Carbon* **1992**, 30, 797.
146. H.-P. Boehm, E. Diehl, *Z. Electrochem.* **1962**, 66(8/9), 642–647.
147. U. Hofmann, G. Ohlerich, *Angew. Chem.* **1950**, 62(1), 16–21.
148. H.-P. Boehm, E. Diehl, W. Heck, R. Sappok, *Angew. Chem.* **1964**, 76(17), 742–751.
149. H. P. Boehm, H. Knözinger in *Catalysis, Science and Technology* (Eds: J. R. Anderson, M. Boudart), Springer Verlag, Berlin, **1983**, Chapter 2.
150. H. P. Boehm, *Adv. Catal.* **1966**, 16, 179–274.
151. H.-P. Boehm, M. Voll, *Carbon* **1970**, 8, 227–240.
152. M. Voll, H.-P. Boehm, *Carbon* **1970**, 8, 741–752.
153. M. Voll, H.-P. Boehm, *Carbon* **1971**, 9, 473–480.
154. M. Voll, H.-P. Boehm, *Carbon* **1971**, 9, 481–488.
155. H. Marsh, A. D. Foord, J. S. Mattson, J. M. Thomas, E. L. Evans, *J. Colloid Interface Sci.* **1974**, 49(3), 368–382.
156. G. M. Badger, J. E. Campbell, J. W. Cook, R. P. Ruffael, A. I. Scott, *J. Chem. Soc.* **1950**, 2526.
157. V. A. Garten, D. E. Weiss, *Aust. J. Chem.* **1957**, 10, 309–328.
158. H. P. Boehm, U. Hofmann, A. Clauss in *Third Carbon Conference, Buffalo, New York*, Pergamon Press, Oxford, **1957**, p. 241–247.
159. A. S. Arico, V. Antonucci, M. Minutoli, N. Giordano, *Carbon* **1989**, 27(3), 337–347.
160. D. T. Clark, A. Harrison, *J. Polymer Sci., Polym. Chem. Ed.* **1981**, 19, 1945–1955.
161. D. T. Clark, A. Harrison, *J. Polymer Sci., Polymer Chem. Ed.* **1976**, 14, 533–542.
162. A. Diks in *Electron Spectroscopy, Theory Techniques and Application* (C. R. Brundle, A. D. Baker) **1981**.
163. R. Schlögl, H. P. Boehm, *Carbon*, **1983**, 21(4), 345–358.
164. Y. Baer, *J. Electr. Spectrosc. Rel. Phen.* **1981**, 24, 95–100.
165. P. M. T. M. van Attekum, G. K. Wertheim, *Phys. Rev. Lett.* **1979**, 43, 1896–1898.
166. R. J. J. Jansen, H. V. Bakkum, *Carbon* **1995**, 33, 1021–1027.
167. D. Marton, K. J. Boyd, A. H. Al-Bayati, S. S. Todorov, J. W. Rabalais, *Phys. Rev. Lett.* **1994**, 73(1), 118–121.
168. D. N. Belton, S. J. Schmieg, *J. Vac. Sci. Technol.* **1990**, A8(3), 2353–2362.
169. F. R. McFeely, S. P. Kowalczyk, L. Ley, R. G. Cavell, R. A. Pollak, D. A. Shirley, *Phys. Rev. B* **1974**, 9(12), 5268–5278.
170. D. Ugolini, J. Eitle, P. Oelhafen, M. Wittmer, *Appl. Phys.* **1989**, A48, 549–558.
171. M. A. Smith, L. L. Levenson, *Phys. Rev. B* **1977**, 16(6), 2973–2977.
172. E. Desimoni, G. I. Casellas, A. M. Salvi, T. R. I. Cataldi, A. Morone, *Carbon* **1992**, 30, 527.
173. P. Denison, F. R. Jones, J. F. Watts, *J. Mater. Sci.* **1985**, 20, 4647–4656.
174. L. J. Gerenser, J. F. Elman, M. G. Mason, J. M. Pochan, *Polymer* **1985**, 2026, 1162–1166.
175. R. H. Bradley, E. Sheng, I. S. P. K. Freakley, *Carbon* **1995**, 33(2), 233–241.
176. Y. Yang, Z. G. Lin, *J. Appl. Electrochem.* **1995**, 25, 259–266.

177. A. M. Vassallo, L. S. K. Pang, P. A. Cole-Clarke, M. A. Wilson, *J. Am. Chem. Soc.* **1991**, *113*, (7820–7821).
178. M. Starsinic, Y. Otake, P. L. Walker, Jr., P. C. Painter, *Fuel* **1984**, *63*, 1002–1007.
179. J. B. Donnet, P. Ehrburger, A. Voet, *Carbon* **1072**, *10*, 757.
180. V. R. Deiz, J. L. Bitner, *Carbon* **1972**, *10*, 145.
181. W. R. Cofer, D. R. Schryer, R. S. Rogowski, *Atmosph. Environ.* **1984**, *18*, 243.
182. L. Bonnetain, *J. Chem. Phys.* **1961**, *58*, 34.
183. S. Matsumoto, H. Kanda, Y. Sato, M. Setaka, *Carbon* **1977**, *15*, 299–302.
184. U. Tegtmeier, H. P. Weiss, R. Schlögl, *Fresenius J. Anal. Chem.* **1993**, *347*, 263–268.
185. H. Jüntgen, *Fuel* **1986**, *65*, 1436–1446.
186. M. S. McIntyre, G. R. Mount, T. C. Lipson, B. Harrison, S. Liang, *Carbon* **1991**, *29*, 1071.
187. A. Linares-Solano, M. Almela-Alarcón, C. S.-M. de Lecea, *J. Catal.* **1990**, *125*, 401–410.
188. D. Cazorla-Amoros, A. Linares-Solano, C. S.-M. de lecea, J. P. Joly, *Carbon* **1991**, *29*, 361.
189. R. L. Augustine in *Heterogeneous Catalysis for the Synthetic Chemist*, Marcel Dekker, New York, **1996**.
190. R. T. K. Baker, E. B. Prestridge, R. L. Garten, *J. Catal.* **1979**, *56*, 390.
191. S. L. Butterworth, A. W. Scaroni, *Appl. Catal.* **1985**, *16*, 375–388.
192. F. Atamny, D. Duff, A. Baiker, *Catal. Lett.* **1995**, *34*, 305–311.
193. R. W. Joyner, J. B. Pendry, K. Saldin, S. R. Tennison, *Surf. Sci.* **1984**, *138*, 84–94.
194. C. E. Milstead, A. B. Riedinger, L. R. Zumwalt, *Carbon* **1966**, *4*, 99–106.
195. S. R. Tennison in *Catalytic Ammonia Synthesis: Fundamentals and Practice, Fundamental and Applied Catalysis* (Ed.: J. R. Jennings), Plenum Press, New York, **1991**.
196. E. Hegenberger, N. L. Wu, J. Phillips, *J. Phys. Chem.* **1987**, *91*, 5067–5071.
197. A. Lineares-Solano, F. Rodriguez Reinoso, C. S.-M. de Lecea, O. P. Mahajan, P. L. Walker Jr., *Carbon* **1982**, *20*(3), 177–184.
198. P. Ehrburger, O. P. Mahajan, P. L. Walker Jr., *J. Catal.* **1976**, *43*, 61–67.
199. R. Schlögl, P. Bowen, G. R. Millward, W. Jones, H. P. Boehm, *J. Chem. Soc., Faraday Trans.*, **1983**, *1*(79), 1793–1818.
200. S. Parkash, S. K. Charkrabartup, J. G. Hooley, *Carbon* **1978**, *16*, 231.
201. K. Aika, H. Hori, A. Ozaki, *J. Catal.* **1972**, *27*, 424–431.
202. M. E. Vol'pin, Y. N. Novikov, V. A. Postnikov, V. B. Shur, B. Bayerl, L. Kaden, M. Wahren, L. M. Dmitrienko, R. A. Stukan, A. V. Nefed'ev, *Z. Anorg. Allg. Chem.* **1977**, *428*, 231–236.
203. K. Kalueki, P. W. Morawski, *J. Chem. Tech., Biotechnol.* **1990**, *47*, 357.
204. S. Parkash, J. G. Hooley, *J. Catal.* **1980**, *62*, 187–188.
205. A. Sepúlveda-Escribano, F. Rodriguez-Reinoso, *J. Mol. Catal.* **1994**, *90*, 291–301.
206. A. A. Chen, M. A. Vannice, J. Phillips, *J. Phys. Chem.* **1987**, *91*, 6257–6269.
207. V. K. Jones, L. R. Neubauer, C. H. Bartholomew, *J. Phys. Chem.* **1986**, *90*, 4832–4839.
208. H.-J. Jung, M. A. Vannice, L. N. Mulay, R. M. Stanfield, W. N. Delgass, *J. Catal.* **1982**, *76*, 208–224.
209. K. J. Lim, M. Boudart, *J. Catal.* **1987**, *105*, 263–265.
210. N. M. Rodriguez, M.-S. Kim, R. T. K. Baker, *J. Phys. Chem.* **1994**, *98*, 13108–13111.
211. H. P. Boehm, G. Mair, T. Stoehr, A. R. de Rincón, B. Tereczki, *Fuel* **1984**, *63*, 1061–1063.
212. H. Jüntgen, H. Köhl, *Chem. Phys. Carbon* **1990**, *22*, 145.
213. M. Barber, E. L. Evans, J. M. Thomas, *Chem. Phys. Lett.* **1973**, *18*(3), 423–425.
214. M. Pourbaix, *Atlas of Electrochemical Equilibria in Aqueous Solution*, Pergamon Press, Oxford, **1966**, p. 450–457.
215. O. Timpe, R. Schlögl, *Ber. Bunsenges. Phys. Chem.* **1993**, *97*(9), 1076–1085.
216. J. Klein, K.-D. Henning, *Fuel* **1984**, *63*, 1064–1067.
217. T. A. Ryan, M. H. Stacey, *Fuel* **1984**, *63*, 1101–1106.
218. E. M. Smith, S. Affrossman, J. M. Courtney, *Carbon*, *17*, **1977**, 149–152.
219. T. Okuhara, K. Tanaka, *J. Chem. Soc., Faraday Trans. 1* **1986**, *82*, 3657–3666.
220. H. Yamashita, H. Yamada, A. Tomita, *Appl. Catal.* **1991**, *78*, L1–L6.
221. H. Teng, E. M. Sunberg, J. M. Carlo, *Energy & Fuel* **1992**, *6*, 398.
222. H. Yamashita, A. Tomita, H. Yamada, T. Kyotani, L. R. Radovic, *Energy & Fuel* **1993**, *7*, 85–89.
223. L. Singoredio, M. Slagt, J. van Wees, E. Kapteijn, J. A. Moulijn, *Catal. Today* **1990**, *7*, 157.

226. M. J. Illan-Gomez, A. Linares-Solano, L. R. Radovic, C. S.-M. de Iecea, *Energy & Fuels* **1995**, 9, 97.
227. M. J. Illan-Gomez, A. Linares-Solano, L. R. Radovic, C. S.-M. de Iecea, *Energy & Fuels* **1995**, 9, 104.
228. J. Mochida, S. Kisamori, M. Hironaka, S. Kawano, Y. Matsumura, M. Yoshikawa, *Energy & Fuels* **1994**, 8, 1341.
229. P. B. Weisz, R. D. Goodwin, *J. Catal.* **1963**, 2, 397–404.
230. J. van Doorn, J. A. Moulijn, *Catal. Today* **1990**, 7, 257–266.
231. A. V. Hamza, G. D. Kubiak, R. H. Stulen, *Surf. Sci.* **1990**, 237, 35–52.
232. T. Frauenheim, U. Stephan, P. Blaudeck, D. Porezag, H.-G. Busman, W. Zimmermann-Edling, S. Lauer, *Phys. Rev. B* **1993**, 48(24), 18 189–18 202.
233. S. Evans, J. M. Thomas, *Proc. R. Soc. Lond. A* **1977**, 353, 103–120.
234. S. Akhter, K. Allan, D. Buchanan, J. A. Cook, A. Campion, J. M. White, *Appl. Surf. Sci.* **1988**, 35, 241–258.
235. A. Oberlin, *Chem. Phys. Carbon* **1992**, 22, 2.
236. L. R. Radovic, F. Rodriguez-Reinoso *Chem. Phys. Carbon*, **1997**, 25, 243.

## 3.10 Heteropoly Compounds

K.-Y. LEE AND M. MISONO

### 3.10.1 Structure and Catalytic Properties

Heteropolyanions are polymeric oxoanions (polyoxometalates) formed by condensation of more than two kinds of oxoanions [1]. The term heteropoly compound (HPA) is used for the acid forms and the salts. Other HPA-related compounds are organic and organometallic complexes of polyanions.

Heteropolyanions are composed of oxides of addenda atoms (V, Nb, Mo, W, etc.) and heteroatoms (P, Si, etc.). Various elements which are shown in Table 1 can be the addenda atoms and heteroatoms [2]. The structures are classified into several groups based on the similarity of the composition and structure, for example: Keggin-type,  $\text{XM}_{12}\text{O}_{40}^{n-}$ ; Silverton-type,  $\text{XM}_{12}\text{O}_{42}^{n-}$ ; Dawson-type,  $\text{X}_2\text{M}_{18}\text{O}_{62}^{n-}$ ; Strandberg-type,  $\text{X}_2\text{M}_5\text{O}_{23}^{n-}$ ; Anderson-type,  $\text{XM}_6\text{O}_{24}^{n-}$ ; and Lindqvist-type,  $\text{XM}_6\text{O}_{24}^{n-}$ , where X is heteroatom and M is addenda atom [3]. Structural isomers and lacunary polyanions are also known. Keggin-type anions, of which the catalytic activity has been extensively examined, are the main subject of this chapter. For HPAs in the solid state, the primary structure (polyanions), the secondary (three-dimensional arrangement of polyanions, counter cations, water of crystallization, etc.) and the tertiary structures (particle size, pore structure, etc.) are differentiated (Fig. 1) [4, 5]. Not only the primary and secondary structures, but also tertiary and higher-order structures are influential in the catalytic function. In this respect, the preparation process and resulting structure are very important.

- 226. M. J. Illan-Gomez, A. Linares-Solano, L. R. Radovic, C. S.-M. de Iecea, *Energy & Fuels* **1995**, 9, 97.
- 227. M. J. Illan-Gomez, A. Linares-Solano, L. R. Radovic, C. S.-M. de Iecea, *Energy & Fuels* **1995**, 9, 104.
- 228. J. Mochida, S. Kisamori, M. Hironaka, S. Kawano, Y. Matsumura, M. Yoshikawa, *Energy & Fuels* **1994**, 8, 1341.
- 229. P. B. Weisz, R. D. Goodwin, *J. Catal.* **1963**, 2, 397–404.
- 230. J. van Doorn, J. A. Moulijn, *Catal. Today* **1990**, 7, 257–266.
- 231. A. V. Hamza, G. D. Kubiak, R. H. Stulen, *Surf. Sci.* **1990**, 237, 35–52.
- 232. T. Frauenheim, U. Stephan, P. Blaudeck, D. Porezag, H.-G. Busman, W. Zimmermann-Edling, S. Lauer, *Phys. Rev. B* **1993**, 48(24), 18 189–18 202.
- 233. S. Evans, J. M. Thomas, *Proc. R. Soc. Lond. A* **1977**, 353, 103–120.
- 234. S. Akhter, K. Allan, D. Buchanan, J. A. Cook, A. Campion, J. M. White, *Appl. Surf. Sci.* **1988**, 35, 241–258.
- 235. A. Oberlin, *Chem. Phys. Carbon* **1992**, 22, 2.
- 236. L. R. Radovic, F. Rodriguez-Reinoso *Chem. Phys. Carbon*, **1997**, 25, 243.

## 3.10 Heteropoly Compounds

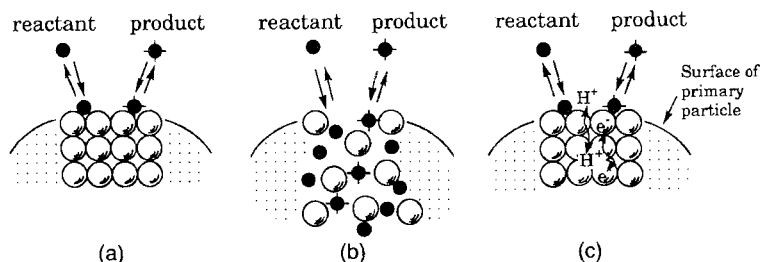
K.-Y. LEE AND M. MISONO

### 3.10.1 Structure and Catalytic Properties

Heteropolyanions are polymeric oxoanions (polyoxometalates) formed by condensation of more than two kinds of oxoanions [1]. The term heteropoly compound (HPA) is used for the acid forms and the salts. Other HPA-related compounds are organic and organometallic complexes of polyanions.

Heteropolyanions are composed of oxides of addenda atoms (V, Nb, Mo, W, etc.) and heteroatoms (P, Si, etc.). Various elements which are shown in Table 1 can be the addenda atoms and heteroatoms [2]. The structures are classified into several groups based on the similarity of the composition and structure, for example: Keggin-type,  $\text{XM}_{12}\text{O}_{40}^{n-}$ ; Silverton-type,  $\text{XM}_{12}\text{O}_{42}^{n-}$ ; Dawson-type,  $\text{X}_2\text{M}_{18}\text{O}_{62}^{n-}$ ; Strandberg-type,  $\text{X}_2\text{M}_5\text{O}_{23}^{n-}$ ; Anderson-type,  $\text{XM}_6\text{O}_{24}^{n-}$ ; and Lindqvist-type,  $\text{XM}_6\text{O}_{24}^{n-}$ , where X is heteroatom and M is addenda atom [3]. Structural isomers and lacunary polyanions are also known. Keggin-type anions, of which the catalytic activity has been extensively examined, are the main subject of this chapter. For HPAs in the solid state, the primary structure (polyanions), the secondary (three-dimensional arrangement of polyanions, counter cations, water of crystallization, etc.) and the tertiary structures (particle size, pore structure, etc.) are differentiated (Fig. 1) [4, 5]. Not only the primary and secondary structures, but also tertiary and higher-order structures are influential in the catalytic function. In this respect, the preparation process and resulting structure are very important.





**Figure 2.** Three types of heterogeneous catalysis for heteropoly compounds: (a) surface type; (b) bulk type I (pseudoliquid); (c) bulk type II.

tween the oxidizing ability of catalyst and the catalytic activity for oxidation in both bulk-type and surface-type reactions. Acid and redox bifunctionality is another characteristic of HPAs. For example, the acidity and oxidizing ability work cooperatively for the oxidation of methacrolein, whereas they function competitively for the oxidative dehydrogenation of isobutyric acid [5]. Interestingly, the former is of surface type and the latter of bulk type.

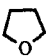
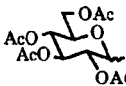
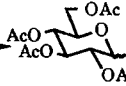
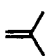
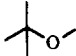
Heteropoly compounds are useful as catalysts due to the following unique characteristics:

- (i) acidic properties and oxidizing ability are systematically controllable;
- (ii) Polyanions are well-defined oxide clusters, hence, catalyst design at the molecular level is possible;
- (iii) Unique reaction environment, such as the pseudoliquid phase, is available, and catalytically useful coordination is possible.


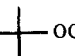

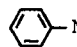
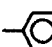
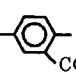
Some HPAs in the solid state are thermally quite stable and suitable for vapor-phase reactions conducted at high temperatures. The thermal stability is in the order  $\text{H}_3\text{PW}_{12}\text{O}_{40} > \text{H}_4\text{SiW}_{12}\text{O}_{40} > \text{H}_3\text{PMo}_{12}\text{O}_{40} > \text{H}_4\text{SiMo}_{12}\text{O}_{40}$  and can be enhanced by the formation of appropriate salts [5–8].

Attempts to utilize HPAs as catalysts have a long history [5]. A bench-scale test was reported for alkylation of aromatics in 1971. The first industrial process using a HPA catalyst was launched in 1972, for the hydration of propene in the liquid phase. The essential role of the Keggin structure for the oxidation of methacrolein was indicated in a patent in 1975. Systematic basic research into heterogeneous catalysis started in the mid 1970s to elucidate the quantitative correlations between the acid–redox properties and catalytic performance of HPAs. Pseudoliquid phase (bulk-type I catalysis) was reported in 1979 and the bulk-type II behavior in 1983 [5]. Similar efforts for homogeneous systems were also carried out in the same period. In the 1980s, several new large-scale industrial processes (e.g. the oxidation of methacrolein, the hydration of isobutene and *n*-butene, and the polymerization of tetrahydrofuran) were initiated by using HPA catalysts [4, 9]. Typical reactions catalyzed by HPAs are shown in Tables 2–6.

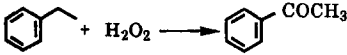
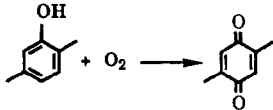
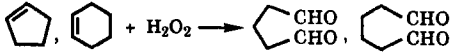
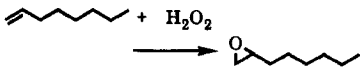
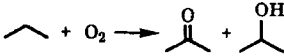
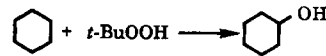
**Table 2.** Homogeneous acid-catalyzed reactions.

Reaction	Catalyst	Remarks	Reference
Hydration of olefins	$\text{H}_3\text{PW}_{12}\text{O}_{40}$	$T = 313\text{--}423\text{ K}$	102(a)
$n$  $\longrightarrow \text{HO} \left[ (\text{CH}_2)_4\text{-O} \right]_n \text{H}$ (PTMG)	$\text{H}_3\text{PW}_{12}\text{O}_{40}$ $n\text{H}_2\text{O}$ $(n = 0\text{--}6)$	$T = 333\text{ K}$ , $\text{MW} \approx 3000$	102(b)
 + ROH $\longrightarrow$ 	$\text{H}_3\text{PW}_{12}\text{O}_{40}$ $\text{H}_6\text{P}_2\text{W}_{18}\text{O}_{62}$	$T = 298\text{ K}$ , $\text{yield} = 60\text{--}98\%$ (2 h) $T = 315\text{ K}$ , $\text{selectivity} \approx 100\%$	102(c) 102(d)
 + $\text{CH}_3\text{OH} \longrightarrow$ 	$\text{H}_3\text{PW}_{12}\text{O}_{40}$ $\text{H}_3\text{PMo}_{12}\text{O}_{40}$	$T = 298\text{ K}$	102(e)
$3\text{ C}_2\text{H}_5\text{CHO} \longrightarrow$ trimer			

**Table 3.** Heterogeneous acid-catalyzed reactions.

Reaction	Catalyst	Remarks	Reference
$\text{CH}_3\text{COOH} + \text{C}_2\text{H}_5\text{OH}$ $\longrightarrow \text{CH}_3\text{COOC}_2\text{H}_5 + \text{H}_2\text{O}$	$\text{H}_3\text{PW}_{12}\text{O}_{40}$	$T = 423\text{ K}$ , $\text{selectivity} = 91\%$ $(90\% \text{ conv.})$	103(a)
Alkylation of aromatics	$\text{H}_3\text{PW}_{12}\text{O}_{40}$	$T = 303\text{--}373\text{ K}$ ,	103(b)
Alkylation of alkanes	$\text{CS}_{2.5}\text{H}_{0.5}\text{PW}_{12}\text{O}_{40}$	$T = 293\text{ K}$ , $P = 5\text{ kg cm}^{-2}$	103(c)
Isomerization of alkanes	$\text{Pd}_{1.5}\text{PW}_{12}\text{O}_{40}$	$T = 483\text{ K}$	103(d)
$\text{CH}_3\text{OH} (\text{CH}_3\text{OCH}_3)$ $\longrightarrow \text{C}_1\text{--C}_6 \text{ Hydrocarbons}$	$\text{H}_3\text{PW}_{12}\text{O}_{40}$ $\text{H}_3\text{PW}_{12}\text{O}_{40}$	$T = 348\text{ K}$ $T = 573\text{ K}$ ,	101, 103(e)
 + $\text{CH}_3\text{OH} \longrightarrow$ 	$\text{CS}_{2.5}\text{H}_{0.5}\text{PW}_{12}\text{O}_{40}$	$T = 563\text{ K}$ , $\text{selectivity} (\text{C}_2\text{--C}_4 \text{ alkenes}) = 74\%$	103(f)
 + $\text{HNO}_3 \longrightarrow$ 	$\text{H}_6\text{P}_2\text{W}_{18}\text{O}_{62}$	$T = 323\text{ K}$	103(g)
 + $(\text{CH}_3\text{CO})_2\text{O} \longrightarrow$ 	$\text{CS}_{1.5}\text{H}_{1.5}\text{PMo}_{12}\text{O}_{40}$ $\text{CS}_{2.5}\text{H}_{0.5}\text{PMo}_{12}\text{O}_{40}$	$T = 413\text{ K}$ , $\text{selectivity} = 97\%$ $(94\% \text{ conv.})$ $T = 573\text{ K}$	103(h) 103(i)

**Table 4.** Homogeneous oxidation reactions.

Reaction	Catalyst	Remarks	Reference
	$\text{H}_3\text{PMo}_{12}\text{O}_{40}$	reflux, selectivity = 100%	104(a)
	$\text{H}_5\text{PMo}_{10}\text{V}_2\text{O}_{40}$	$T = 333 \text{ K}$ , $\text{O}_2 = 1 \text{ atm}$ , yield = 80%	104(b)
	$\text{H}_3\text{PMo}_6\text{W}_6\text{O}_{40}$	$T = 303 \text{ K}$	2(b)
	$\text{H}^+/\text{WO}_4^{2-}/\text{PO}_4^{3-}/\text{QX}$ $(\text{CP})_3\text{PW}_{12}\text{O}_{40}$ CP = cetylpyridinium ion	$T = 343 \text{ K}$ , yield = 82% $T = 333 \text{ K}$ , yield = 76%	104(c) 104(d)
	$\text{H}_7\text{PW}_9\text{Fe}_2\text{NiO}_{37}$	$T = 423 \text{ K}$ , turnover number = 9730 (3 h)	104(e)
	$\text{PW}_{11}\text{CoO}_{39}^{5-}$	$T = 298 \text{ K}$	67(c)

**Table 5.** Heterogeneous oxidation reactions.

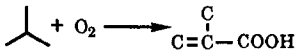
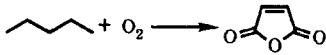
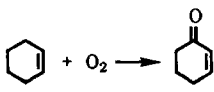
Reaction	Catalyst	Remarks	Reference
$\text{CH}_2=\text{C}(\text{CH}_3)\text{CHO} + \text{O}_2 \longrightarrow \text{CH}_2=\text{C}(\text{CH}_3)\text{COOH}$	$\text{CsH}_3\text{PVMo}_{11}\text{O}_{40}$	$T = 553 \text{ K}$ , selectivity = 80–85%	45, 105(a)
	$\text{H}_3\text{PMo}_{12}\text{O}_{40}$	$T = 623 \text{ K}$ , selectivity = 45%	105(b)
$\text{CH}_3\text{CH}(\text{CH}_3)\text{COOH} \longrightarrow \text{CH}_2=\text{C}(\text{CH}_3)\text{COOH}$	$\text{H}_5\text{PV}_2\text{Mo}_{10}\text{O}_{40}$	$T = 573 \text{ K}$ , selectivity = 72% (52% conv.)	49, 105(c)
	$\text{H}_5\text{PV}_2\text{Mo}_{10}\text{O}_{40}$	$T = 583 \text{ K}$ , selectivity = 55%	105(d)



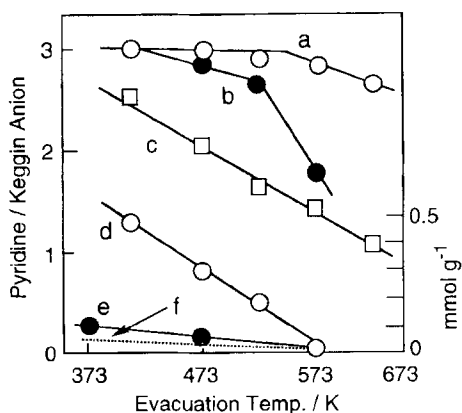
Table 6. Heteropoly-metal multifunctional catalysts.

Reaction	Catalyst	Reference
$\text{RCH=CH}_2 + 1/2\text{O}_2 \longrightarrow \text{RCHOCH}_3$	$\text{PMo}_{12-n}\text{V}_n\text{O}_{40}^{3+n} + \text{PdSO}_4$	13, 60
$\text{C}_6\text{H}_6 + 1/2\text{O}_2 \longrightarrow (\text{C}_6\text{H}_5)_2$	$\text{PMo}_{12-n}\text{V}_n\text{O}_{40}^{3+n} + \text{Pd}(\text{OCOCH}_3)_2$	13, 60
$\text{PhNO}_2 + 3\text{CO} + \text{CH}_3\text{OH} \longrightarrow \text{PhNHCO}_2\text{CH}_3 + 2\text{CO}_2$	$\text{H}_5\text{PMo}_{10}\text{V}_2\text{O}_{40} + \text{PdCl}_2$	63, 106a
	$[(n\text{-C}_4\text{H}_9)_4\text{N}]_5\text{Na}_3[(1,5\text{-cod}) \cdot \text{IrP}_2\text{W}_{15}\text{Nb}_3\text{O}_{62}]$	71
$\text{≡OH} + \text{H}_2 \longrightarrow \text{=OH}$	$\text{Li}_4\text{SiMo}_{12}\text{O}_{40} + \text{RhCl}(\text{PPh}_3)_3$	64
$\text{CH}_3\text{OH} + \text{CO} \longrightarrow \text{CH}_3\text{COOH}$	$\text{RhPW}_{12}\text{O}_{40}/\text{SiO}_2$	106b

### 3.10.2 Heteropolyacids – Acid Forms in Solid State and in Solution

Heteropolyacids are also Brønsted acids in the solid state. Their acidities depend on the constituent elements and their structure.  $\text{H}_3\text{PW}_{12}\text{O}_{40}$  (Keggin type) and its acidic salts are especially strong acids. The color changes of indicators show that solid  $\text{H}_3\text{PW}_{12}\text{O}_{40}$  (anhydrous) is a very strong acid with Hammett acidity function  $H_0 < -8$  [10a], and a superacid,  $H_0 < -13.16$  [10b]. Thermal desorption of pyridine shows that a significant amount of pyridine (equal to the number of protons of the whole bulk) remains for  $\text{H}_3\text{PW}_{12}\text{O}_{40}$  at 573 K, while pyridinium ions adsorbed on  $\text{SiO}_2\text{--Al}_2\text{O}_3$  are completely removed at the same temperature (Fig. 3) [11, 12]. This strong acidity of the heteropolyacid can be attributed to the large size of the polyanion, having a low and delocalizable surface charge density. The acid strength in solution has been measured by various methods and the general trends are  $\text{W}^{6+} > \text{Mo}^{6+} > \text{V}^{5+}$  (for the addenda atom) [13] and  $\text{P}^{5+} > \text{Si}^{4+}$ ,  $\text{Ge}^{4+} > \text{B}^{3+} > \text{Co}^{2+}$  (for the heteroatom or the charge of the polyanion) [14–16]. The latter order is also observed for solid HPAs [17]. Figure 3 shows that  $\text{H}_3\text{PW}_{12}\text{O}_{40}$  is a stronger acid than  $\text{H}_3\text{PMo}_{12}\text{O}_{40}$ . These results indicate that the acid strength can be controlled by the addenda atoms and the heteroatoms. On the other hand, the amount of acidic sites (not the acid strength) on the solid surface is sensitive to the kind of counter cations (Fig. 3) as well as to the resulting tertiary structures (see below).

The heteropolyanion stabilizes protonated intermediates by coordination in solution and the pseudoliquid phase as well as on the surface, thus lowering the activation energy and accelerating reactions. Several protonated intermediates including the protonated ethanol dimer and monomer [18], the protonated pyridine dimer [12, 19], and protonated methanol [20] have been detected in the pseudoliquid phase



**Figure 3.** Thermal desorption of pyridine: (a)  $H_3PW_{12}O_{40}$ , (b)  $H_3PMo_{12}O_{40}$ , (c)  $NaH_2PW_{12}O_{40}$ , (d)  $Na_3PW_{12}O_{40}$ , (e)  $Cs_3PW_{12}O_{40}$ , (f)  $SiO_2-Al_2O_3$ . Pyridine ab(ad)sorbed at 298 K was desorbed at each temperature for 1 h by evacuation.

directly by use of X-ray diffraction (XRD), IR or solid-state NMR. In solid-state  $^1H$  NMR, the chemical shift for the protonated ethanol dimer,  $(C_2H_5OH)_2H^+$  is 9.5 ppm downfield from tetramethylsilane, which lies in the range of superacids reported by Olah et al. [18]. This fact also supports the strong acidity of heteropolyacids.

Heteropolyacids are much more active than mineral acids for several types of homogeneous reactions in both organic solvents and aqueous solution [4, 8]. The enhancement is generally greater in organic solvents. For the hydration of isobutene in a concentrated aqueous HPA solution (above  $1.5 \text{ mol dm}^{-3}$ ), the reaction rate is about 10 times greater than for mineral acids [21]. This rate enhancement is attributed to the combination of stronger acidity, stabilization of protonated intermediates, and increased solubility of alkenes [21]. In this case, the selectivity is also much improved with HPA catalysts.

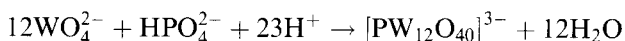
The catalytic behavior of HPA depends on the basicity of reactants [22]. For the decomposition of weakly basic isobutyl propionate, the catalytic activities of the heteropolyacids are 60–100 times higher than those of  $H_2SO_4$  and *p*-toluenesulfonic acid, and the catalytic activity decreases in the order of  $H_3PW_{12}O_{40} > H_4SiW_{12}O_{40} \approx H_4GeW_{12}O_{40} > H_5BW_{12}O_{40} > H_6CoW_{12}O_{40}$ . This is also the order of the acid strength in solution, which increases with the decrease in the negative charge of the polyanion [15, 16, 23, 24]. Izumi et al. [23] indicated that the catalytic activities in nonaqueous solutions were related to the acidity of the heteropolyacid solution and the softness of the polyanion. In dilute aqueous solutions, however, the softness becomes more important, since most heteropolyacids are nearly completely dissociated [23]. For some reactions involving basic molecules such as alcohols, no large differences in activity among these catalysts including  $H_2SO_4$  and *p*-toluenesulfonic acid are observed [22]. This is probably due to the leveling effect.

Heteropolyacids are good multielectron oxidants due to the presence of  $Mo^{6+}$ ,  $W^{6+}$ , and  $V^{5+}$  and the charge delocalizability in the polyanion structure. Generally, the oxidizing ability decreases in the order  $V > Mo > W$ -containing heteropolyanions [13]. The reduction potential decreases linearly with a decrease in the valence of the central atom or an increase in the negative charge of the hetero-

polyanions:  $\text{PW}_{12}\text{O}_{40}^{3-} > \text{GeW}_{12}\text{O}_{40}^{4-} \approx \text{SiW}_{12}\text{O}_{40}^{4-} > \text{FeW}_{12}\text{O}_{40}^{5-} \approx \text{BW}_{12}\text{O}_{40}^{5-} > \text{CoW}_{12}\text{O}_{40}^{6-} > \text{CuW}_{12}\text{O}_{40}^{7-}$  [13, 14]. This property is well reflected in their catalytic activities. For cyclohexene oxidation with hydrogen peroxide, the catalytic activity increased in the order  $\text{B}^{3+} < \text{Si}^{4+} < \text{C}^{4+} \leq \text{P}^{5+}$  [25, 26]. Cetylpyridinium salts of HPA can be used as phase-transfer catalysts and catalyze epoxidation of alkenes very efficiently in a two-phase system comprising aqueous  $\text{H}_2\text{O}_2$  and  $\text{CHCl}_3$  [27].

### 3.10.2.1 Preparation

The typical method for the preparation of heteropolyacids is the acidification of aqueous solutions of oxoanions of addenda atoms and heteroatoms [1b]:



Acidification is generally achieved by the addition of mineral acids. The rates of formation are large, so that the polyanions can be crystallized from stoichiometrically acidified mixtures of the components at room temperature. Although the stoichiometry is often a good guide to the preparation, in some cases an excess heteroatom, the addition of small amount of oxidants, or careful control of temperature and pH is necessary.

The hydrolysis and condensation are usually fast and depend on the pH as well as on the solvent. For example,  $\text{PW}_{12}\text{O}_{40}^{3-}$  starts to decompose above pH 2 and coexists with  $\text{PW}_{11}\text{O}_{39}^{7-}$  and  $\text{PW}_9\text{O}_{34}^{9-}$  [28]. In this respect, pure  $\text{PW}_{12}\text{O}_{40}^{3-}$  should be isolated as free acid by the extraction by ether, the so-called etherate method. If a very acidic solution of the heteropolyanion is shaken with excess diethyl ether, three phases separate: a top ether layer, a middle aqueous layer, and a bottom heteropoly-etherate. The bottom layer is drawn off, shaken with excess ether to remove entrained aqueous solution, and separated again. The etherate is decomposed by the addition of water, the ether is removed, and the aqueous solution of the heteropolyacid is allowed to evaporate until crystallization occurs [1].

By this general method, heteropolyacids containing various kinds of heteroatoms can be prepared:  $\text{H}_3\text{PW}_{12}\text{O}_{40} \cdot 30\text{H}_2\text{O}$  is prepared from  $\text{Na}_2\text{WO}_4 \cdot 2\text{H}_2\text{O}$  and  $\text{Na}_2\text{HPO}_4$  [29];  $\text{H}_4\text{SiW}_{12}\text{O}_{40} \cdot 22\text{H}_2\text{O}$  from  $\text{Na}_2\text{WO}_4$  and  $\text{Na}_2\text{SiO}_3 \cdot 9\text{H}_2\text{O}$  [30];  $\text{H}_4\text{GeW}_{12}\text{O}_{40} \cdot 7\text{H}_2\text{O}$  from  $\text{Na}_2\text{WO}_4 \cdot 2\text{H}_2\text{O}$  and  $\text{GeO}_2$  [22];  $\text{H}_5\text{BW}_{12}\text{O}_{40} \cdot 15\text{H}_2\text{O}$  from  $\text{Na}_2\text{WO}_4 \cdot 2\text{H}_2\text{O}$  and  $\text{H}_3\text{BO}_3$  [31]; and  $\text{H}_6\text{CoW}_{12}\text{O}_{40} \cdot 19\text{H}_2\text{O}$  from  $\text{Na}_2\text{WO}_4 \cdot 2\text{H}_2\text{O}$  and  $\text{Co}(\text{OCOCH}_3)_2 \cdot 4\text{H}_2\text{O}$  [22, 32]. The number of water molecules included in the crystal is variable in all these cases. The structure can be identified by IR, NMR, XRD, etc. [1b, 5].

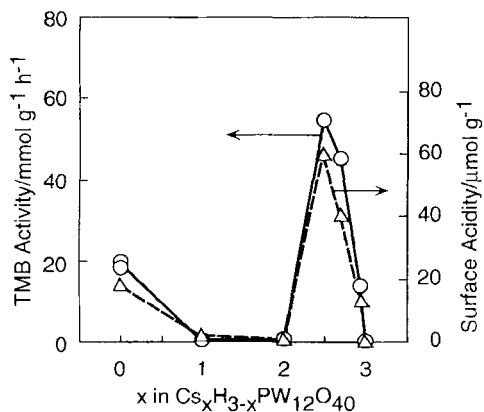
### 3.10.3 Salts of Heteropolyacids – Cation-Exchanged Forms

Salts of heteropolyacids can be divided into two groups according to Niiyama et al. [5, 7]: the salts of small cations such as Na and Cu (group A salts) and salts of large cations like Cs, K, and  $\text{NH}_4$  (group B salts). The behavior of group A salts is similar to that of the acid forms, but is very different in several respects from group B

salts. Group A salts can exhibit pseudoliquid behavior and are very soluble in water and other polar solvents, whereas group B salts are generally insoluble and have high surface areas. Organic salts also exist, but very few studies on their thermal stability and catalytic function have been reported. The thermal stability of group B salts is high (no decomposition occurs below their melting points, for example; the melting points of K and Cs salts of  $\text{H}_3\text{PMo}_{12}\text{O}_{40}$  are reported to be 913 and 963 K, respectively [6]). This is probably due to the absence of protons and water in the lattice of B salts, as the decomposition starts with the formation of water from oxygen of the polyanion and protons (or water) in the lattice.

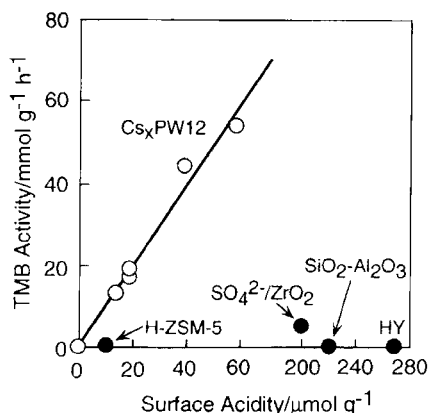
The group B salts of  $\text{H}_3\text{PW}_{12}\text{O}_{40}$  are also strong acids unless they are stoichiometrically neutralized. These salts catalyze various kinds of reactions in the liquid phase as solid catalysts. For the alkylation of 1,3,5-trimethylbenzene with cyclohexene, the activity of  $\text{Cs}_{2.5}\text{H}_{0.5}\text{PW}_{12}\text{O}_{40}$  (abbreviated as  $\text{Cs}_{2.5}\text{W}$ ) is much higher than those of  $\text{SO}_4^{2-}/\text{ZrO}_2$  and Nafion. Here,  $\text{Cs}_{2.5}\text{W}$  is not soluble and the reactions take place on the surface of the solid.

For  $\text{Cs}_x\text{H}_{3-x}\text{PW}_{12}\text{O}_{40}$  (a typical group B salt), the catalytic activity changes dramatically with the extent of neutralization by Cs (Fig. 4).  $\text{Cs}_{2.5}\text{W}$  shows the highest catalytic activity, which is even higher than the acid form. This is in contrast to Na salts (group A salts), where the activity as well as the acidity decreases monotonically with the Na content [33]. The acid strength of  $\text{Cs}_{2.5}\text{W}$  is almost the same as that of  $\text{H}_3\text{PW}_{12}\text{O}_{40}$  according to temperature programmed desorption (TPD) of  $\text{NH}_3$  [34].  $\text{Cs}_{2.5}\text{W}$  consists of very fine particles (particle size 8–10 nm, surface area  $100\text{--}200\text{ m}^2\text{ g}^{-1}$ ). Solid-state  $^{31}\text{P}$  NMR reveals that all protons in the salts are distributed randomly, indicating that nearly uniform acidic salts are formed [4]. The same  $^{31}\text{P}$  NMR spectrum is observed after heat treatment of a sample prepared by the impregnation of  $\text{H}_3\text{PW}_{12}\text{O}_{40}$  on the  $\text{Cs}_3\text{W}$  salt, indicating the formation of the same solid solution by the diffusion of Cs ion and proton. By assuming a uniform distribution of protons, the surface acidity (the number of protons on the surface) of the Cs salts can be estimated from the proton content in the bulk and the specific surface area. When the catalytic activities are plotted against the surface acidity



**Figure 4.** Changes in catalytic activity for the alkylation of 1,3,5-trimethylbenzene (TMB) with cyclohexene and surface acidity (number of protons on the surface) as a function of Cs content in  $\text{Cs}_x\text{H}_{3-x}\text{PW}_{12}\text{O}_{40}$ .

**Figure 5.** Catalytic activity of  $\text{Cs}_x\text{H}_{3-x}\text{PW}_{12}\text{O}_{40}$  for alkylation of 1,3,5-trimethylbenzene (TMB) with cyclohexene as a function of surface acidity. The surface acidity is the number of protons on the surface (external surface for zeolites).

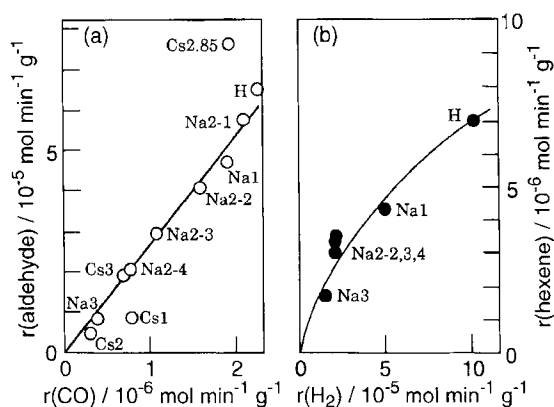


estimated in this way, a good linear correlation is found (Fig. 5) [10b], indicating that the high activity of  $\text{Cs}_{2.5}\text{W}$  is due to its high surface acidity. It is also noteworthy in Fig. 5 that the activities per unit acidity are much greater for Cs salts than for  $\text{SiO}_2\text{-Al}_2\text{O}_3$ ,  $\text{SO}_4^{2-}/\text{ZrO}_2$ , and zeolites. This indicates the presence of additional effects such as acid-base bifunctional acceleration by the cooperation of acidic protons and the basic polyanions.

The acid strength of the acid forms in the solid state usually reflects the one in solution, but the acidic properties of the salts in the solid state are more complicated in general. Five mechanisms are possible for the generation of acidity in metallic salts [5]:

- (i) protons in acidic salts, as for Cs salts as described above;
- (ii) partial hydrolysis of polyanions to form weakly acidic protons;
- (iii) acidic dissociation of water coordinated with multivalent metal ions;
- (iv) Lewis acidity of multivalent metal ions;
- (v) protons formed by the reduction of metal ions with hydrogen.

The redox properties can also be controlled by the formation of salts. However, the relationship between these properties and the catalytic activity for oxidation is not sufficiently clarified. For example, it was reported that the activity order for alkali salts was reversed by the reaction temperature [35]. Nevertheless, good correlations are obtained if the concept of surface- and bulk-type catalysis is appropriately considered [4, 36–38]. The reduction by  $\text{H}_2$  of free acid and group A salts proceeds both on the surface and in the bulk due to the diffusion of protons and electrons, whereas reduction by CO occurs only near the surface. Hence, the rate of reduction by  $\text{H}_2$  represents the oxidizing ability of the catalyst bulk ( $r[\text{H}_2]$ ), while the rate of reduction by CO expresses the oxidizing ability of the surface ( $r[\text{CO}]$ ). Figure 6(a) shows the correlation of the rates of oxidation of acetaldehyde (surface type) with the surface oxidizing ability ( $r[\text{CO}]$ ). In Fig. 6(b), a similar relationship between the rate of oxidative dehydrogenation of cyclohexene (bulk type) and the



**Figure 6.** Correlations between catalytic activity and oxidizing ability: (a) oxidation of acetaldehyde (surface type) and surface oxidizing ability; (b) oxidative dehydrogenation of cyclohexene (bulk type) and bulk oxidizing ability [4, 38] ( $r(\text{aldehyde})$  and  $r(\text{hexene})$  are the rates of catalytic oxidation of acetaldehyde and cyclohexene, respectively).

bulk oxidizing ability ( $r[\text{H}_2]$ ) is presented. Only a poor correlation exists if the former reaction (surface) is plotted against the bulk oxidizing ability. In this way, the catalytic activity and the oxidizing ability of Na salts decrease monotonically with the Na content for both reactions. However, for the oxidations over  $\text{Cs}_x\text{H}_{3-x}\text{PMo}_{12}\text{O}_{40}$ , activity patterns are similar to that in Fig. 4 due to differences in the surface area and secondary structures [4].

Redox properties of  $\text{H}_{3+x}\text{PMo}_{12-x}\text{V}_x\text{O}_{40}$  have been examined by many researchers in relation to selective partial oxidations. However, their oxidizing abilities remain controversial [5]. One reason is that these catalysts are unstable at high temperatures. For example, in the case of oxidative dehydrogenation of isobutyric acid over acidic Cs salts of 12-molybdovanadophosphoric acids ( $\text{Cs}_n\text{H}_{4-n}\text{PMo}_{11}\text{VO}_{40}$ ,  $\text{Cs}_n\text{Mo}_{11}\text{V}$ ),  $\text{Cs}_{2.75}\text{Mo}_{11}\text{V}$  was very efficient: 97% conversion and 78% selectivity to methacrylic acid (MAA) at 623 K, as compared to 40% conversion and 52% selectivity for  $\text{Mo}_{11}\text{V}$  (acid form) [39].  $\text{Mo}_{11}\text{V}$  is significantly decomposed during the pretreatment in  $\text{O}_2$  at 623 K, while  $\text{Cs}_{2.75}\text{Mo}_{11}\text{V}$  decomposes only slightly. The improved thermal stability probably enabled the use of the controlled redox ability.

Noble metal salts of heteropolyacids function in novel ways as catalysts.  $\text{Pd}_{1.5}\text{PW}_{12}\text{O}_{40}$  supported on  $\text{SiO}_2$  catalyzes the skeletal isomerization of hexane in the presence of hydrogen more efficiently than the parent compound  $\text{H}_3\text{PW}_{12}\text{O}_{40}$  [40, 41]. The isomerization rate depends reversibly on the hydrogen partial pressure. The role of hydrogen is thought to be twofold. It dissociates on the surface of metallic palladium and spilled-over hydrogen atoms not only become acidic protons but also suppress coke formation, thus ensuring higher steady activity and longer catalytic life.

Acid sites of  $\text{Ag}_3\text{PW}_{12}\text{O}_{40}$  are generated upon the reduction with hydrogen at 573 K [40, 42]. After the reduction, the catalytic activity (for example, for *o*-xylene isomerization) develops. The generation of acid sites has been confirmed by pyridine adsorption and solid state  $^1\text{H}$  NMR [42].

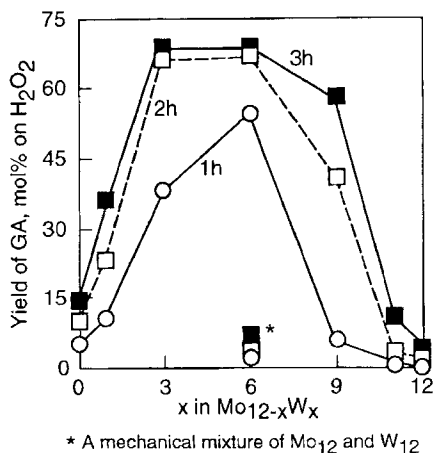
### 3.10.3.1 Preparation

Isolation of the polyanions from solution is generally achieved by the addition of an appropriate counter cation, usually alkali metal, ammonium or tetraalkylammonium ion [1].

Acidic Cs salts of  $\text{H}_3\text{PW}_{12}\text{O}_{40}$  are prepared from aqueous solutions of heteropolyacids and  $\text{Cs}_2\text{CO}_3$ . The compound  $\text{H}_3\text{PW}_{12}\text{O}_{40} \cdot 20\text{H}_2\text{O}$ , which is prepared as described above, is evacuated at 323 K to form  $\text{H}_3\text{PW}_{12}\text{O}_{40} \cdot 6\text{H}_2\text{O}$ . Commercial  $\text{Cs}_2\text{CO}_3$  is dehydrated by evacuation at 693 K for 2 h, prior to use for the preparation of an aqueous solution of  $\text{Cs}_2\text{CO}_3$ . The acidic cesium salts ( $\text{Cs}_x\text{H}_{3-x}\text{PW}_{12}\text{O}_{40}$ ,  $\text{Cs}_x\text{W}$ ) are prepared by the titration of aqueous solution of  $\text{H}_3\text{PW}_{12}\text{O}_{40}$  ( $0.08 \text{ mol dm}^{-3}$ ) with aqueous solution of  $\text{Cs}_2\text{CO}_3$  ( $[\text{Cs}^+] = 0.25 \text{ mol dm}^{-3}$ ), where the aqueous solution of  $\text{Cs}_2\text{CO}_3$  is added dropwise to the  $\text{H}_3\text{PW}_{12}\text{O}_{40}$  solution at room temperature at a controlled rate ( $1 \text{ ml min}^{-1}$ ) [34, 43]. The white colloidal solution obtained is evaporated to solid at 323 K. The surface area changes considerably with the Cs content and the method of preparation. For example, the surface area of  $\text{H}_3\text{PW}_{12}\text{O}_{40}$  is  $5 \text{ m}^2 \text{ g}^{-1}$ , whereas for  $\text{Cs}_x\text{H}_{3-x}\text{PW}_{12}\text{O}_{40}$  prepared as above it is 1, 1, 135, and  $156 \text{ m}^2 \text{ g}^{-1}$  for  $x = 1, 2, 2.5$ , and 3, respectively, after the treatment at 573 K. Just after evaporation,  $\text{Cs}_2\text{W}$  appears to be a mixture of nonacidic  $\text{Cs}_3\text{W}$  covered by the acid form whereas  $\text{Cs}_1\text{W}$  is a mixture of acid form and  $\text{Cs}_2\text{W}$ .  $\text{Cs}_{2.2}\text{W}$  and  $\text{Cs}_{2.5}\text{W}$  have basically the same structure as  $\text{Cs}_2\text{W}$ , except that the amount of acid form covering the  $\text{Cs}_3\text{W}$  surface is much lower for  $\text{Cs}_{2.2}\text{W}$  and  $\text{Cs}_{2.5}\text{W}$ , which brings about the high surface area and unique shape selectivity [44]. As described above, random distribution of  $\text{Cs}^+$  and  $\text{H}^+$  occurs during drying and calcination to form nearly uniform acidic salts.

### 3.10.4 Mixed-Coordinated Heteropoly Compounds

Molybdenum–vanadium mixed-coordinated HPAs are active for several selective oxidations in both homogeneous and heterogeneous systems. The main component of commercial catalysts for the oxidation of methacrolein to methacrylic acid is an acidic Cs salt of  $\text{H}_{3+x}\text{PMo}_{12-x}\text{V}_x\text{O}_{40}$  ( $x = 1-2$ ) [9, 45, 46]. For the oxidative dehydrogenation of isobutyric acid over  $\text{Cs}_{2.75}\text{H}_{0.25+x}\text{PMo}_{12-x}\text{V}_x\text{O}_{40}$ , the activity increased in the order of  $x = 1 > x = 2 > x = 0$  and the methacrylic acid (MAA) selectivity was  $x = 1 \geq x = 2 > x = 0$  [39]. Although various studies of mixed-coordinated HPA catalysts have been reported, their stability and redox properties remain controversial [47–49]. The compound  $\text{Na}_5\text{PMo}_{10}\text{V}_2\text{O}_{40}$ , supported on active carbon, is active for the oxidative dehydrogenation of benzylic alcohols and



**Figure 7.** Synergistic effect of Mo–W mixed-coordinated heteropolyacids for the oxidation of cyclopentene with hydrogen peroxide [26]; 1 h, 2 h, and 3 h are the reaction times. GA = glutaraldehyde

amines without overoxidation of benzaldehyde and benzylamine [50]. The mechanism of the aerobic oxidative dehydrogenation of  $\alpha$ -terpinene to *p*-cymene in solution with mixed-coordinated  $\text{PMo}_{10}\text{V}_2\text{O}_{40}^{5-}$  has recently been reported [51].

Molybdenum–tungsten mixed-coordinated HPA shows a remarkable synergistic effect for, for example, the formation of dialdehydes from alkenes [26, 52]. Compounds of the type  $\text{H}_3\text{PMo}_{12-x}\text{W}_x\text{O}_{40}$  ( $\text{Mo}_{12-x}\text{W}_x$ ,  $x = 0$ –12), prepared by the conventional method, are statistical mixtures of 13 mixed-coordinated heteropolyacids [26, 53]. For the oxidation of cyclopentene by  $\text{H}_2\text{O}_2$  in tri-*n*-butylphosphate solution,  $\text{Mo}_6\text{W}_6$  shows the highest yield of aldehyde, much higher than  $\text{Mo}_{12}$  and  $\text{W}_{12}$  alone or a mechanical mixture of them (Fig. 7). The selectivity of concurrent formation of diol increases with the ratio of W to Mo, reflecting the acidity. The synergistic effect is explained quantum chemically by the increase in the stability of reduced states of mixed-coordinated polyanions [54]. However, there is a possibility that active peroxo species are formed by partial degradation of the starting Keggin anion and the formation is easier with mixed coordinated HPA.

#### 3.10.4.1 Preparation

Reproducible preparation of  $\text{H}_{3+x}\text{PMo}_{12-x}\text{V}_x\text{O}_{40}$  ( $x = 1$ –3,  $\text{Mo}_{12-x}\text{V}_x$ ) was established by Tsigdinos and Hallada [55]. An aqueous solution of  $\text{Na}_2\text{HPO}_4$  and sodium metavanadate is acidified with a concentrated sulfuric acid. To this mixture is added an aqueous solution of  $\text{Na}_2\text{MoO}_4 \cdot 2\text{H}_2\text{O}$ . The detailed procedure is available in the literature. Note that excess sodium metavanadate is used.

Molybdenum–tungsten mixed-coordinated heteropolyacids,  $\text{H}_3\text{PMo}_{12-x}\text{W}_x\text{O}_{40}$ , are prepared from  $\text{Na}_2\text{HPO}_4 \cdot 12\text{H}_2\text{O}$ ,  $\text{Na}_2\text{WO}_4$ , and  $\text{Na}_2\text{MoO}_4 \cdot 2\text{H}_2\text{O}$  solutions. After the solutions are mixed at 353 K for 1 h, hydrochloric acid is added at room temperature. Then the heteropolyacids are extracted with diethyl ether and crystallized at room temperature;  $\text{H}_3\text{PMo}_{12}\text{O}_{40}$  and  $\text{H}_3\text{PW}_{12}\text{O}_{40}$  can also be used as the starting materials. The mixed aqueous solution is held at 353 K for 6 h, followed by



extraction by diethyl ether and recrystallization. The heteropolyacids prepared by these methods are mixtures of mixed-coordinated heteropolyanions having a statistical distribution of  $x$ .

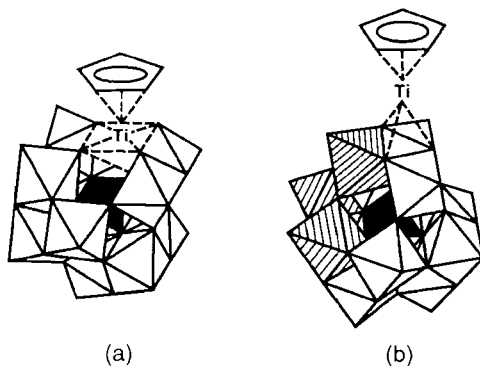
The synthesis of specifically Mo- or V-substituted positional isomers of tungstophosphates is achieved by the method of Massart or Domaille et al., but their catalytic activities are not as high [56, 57]. A requirement for these syntheses is isolation, or the in-place generation, of an appropriate defect polytungstate anion that is subsequently resubstituted with V or Mo: the ion  $[\text{PVW}_{11}\text{O}_{40}]^{4-}$  is derived from in-place generation of  $[\text{PW}_{11}\text{O}_{39}]^{7-}$ ;  $[\alpha\text{-}1,2,3\text{-PV}_3\text{W}_9\text{O}_{40}]^{6-}$  is prepared from preformed  $[\alpha\text{-PW}_9\text{O}_{34}]^{9-}$ ;  $[\beta\text{-}$  and  $\gamma\text{-PV}_2\text{W}_{10}\text{O}_{40}]^{5-}$  are isolated from  $[\text{PW}_{10}\text{O}_{36}]^{7-}$  [57];  $[\alpha\text{-PW}_9\text{Mo}_2\text{O}_{39}]^{3-}$  is prepared from  $[\beta\text{-PW}_9\text{O}_{34}]^{9-}$ ;  $[\alpha\text{-PW}_9\text{Mo}_3\text{O}_{40}]^{3-}$  is derived from  $[\alpha\text{-PW}_9\text{Mo}_2\text{O}_{39}]^{3-}$  [56]. Two important preparative details are emphasized [58]:

- (i) reproducible syntheses require accurate pH readings on a calibrated pH meter;
- (ii) vanadium (V) species are strong oxidants, particularly at low pH, and metallic spatulas are attacked, leaving an intense heteropoly “blue” vanadium (IV) product (ceramic spatulas are recommended).

Product identification relies on  $^{31}\text{P}$  NMR of their solutions. Details of  $^{31}\text{P}$  NMR measurements and preparation methods are available in the literature [59].

### 3.10.5 Metal-Coordinated Heteropolyanions

Metals can be coordinated with a heteropolyanion in three different ways to form metal-coordinated polyanions, which show unique catalytic activities for various reactions. The first method is the simple combination of metal salts with a heteropolyanion. The second is the use of lacunary anion as a ligand for transition metal ions, i.e. transition metal-substituted polyanion (TMSP; Fig. 8(a)). The third is to use a polyanion to support transition metals, i.e. heteropolyanion-supported transition metal (Fig. 8(b)).



**Figure 8.** (a) Transition metal-substituted heteropolyanion  $[\text{PW}_{12}\text{O}_{39}(\text{TiCp})]^{4-}$ ; (b) heteropolyanion-supported transition metal  $[\text{TiCp} \cdot \text{SiW}_9\text{V}_3\text{O}_{40}]^{4-}$  [65]. The hatched octahedra represent  $\text{VO}_6$ , the central phosphate is shown by black tetrahedra,  $\text{Cp} = \text{C}_5\text{H}_5$ .

### 3.10.5.1 Combination of Metal Salts with Heteropolyanions

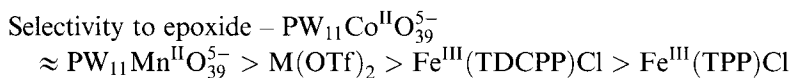
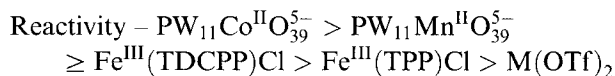
The Wacker-type reaction is a good example in which the heteropolyanion plays a role as a reoxidizing reagent of  $\text{Pd}^0$  in the reaction [60]. It is reported that  $\text{PMo}_6\text{W}_6\text{O}_{40}^{3-}$  is an efficient reoxidant for this reaction and the rate determining step is the reoxidation of  $\text{Pd}^0$  to  $\text{Pd}^{2+}$  [61]. The pH and the concentration of  $\text{Cl}^-$  can be controlled by the use of  $\text{Na}_y\text{H}_{3+x-y}\text{PMo}_{12-x}\text{V}_x\text{O}_{40}$  ( $x = 2, 3$ ), so that the reaction rate and the stability of  $\text{Pd}^{2+}$  increase, and the concentration of  $\text{Cl}^-$  decreases to 1% of that in the conventional ethylene Wacker-type reaction [62]. The anion,  $\text{PMo}_{12-x}\text{V}_x\text{O}_{40}^{(3+x)-}$ , is considered to promote both the solubilization of high concentration of  $\text{V}^{5+}$  and the reoxidation of  $\text{V}^{4+}$  by  $\text{O}_2$ .

Terminal alkenes can be hydrogenated selectively in the presence of  $\text{PdCl}_2$  [63] or  $\text{RhCl}(\text{PPh}_3)_3$  [64] and heteropoly compounds. The catalytic system is also highly active for the production of urethane or isocyanate compounds by the reductive carbonylation of nitrobenzene. It is considered that polyoxometalate coordinating with  $\text{Pd}^{2+}$  in the reduced form is the active species, since easily reducible heteropolyanions are more active [63].

### 3.10.5.2 Transition Metal-Substituted Polyanions (TMSP)

Lacunary Keggin anions,  $\alpha\text{-XM}_{11}\text{O}_{39}^{n-}$ , have a “defect” Keggin structure, in which one addenda atom and one terminal oxygen are missing. These lacunary heteropolyanions, which are formed at relatively high pH, are used as ligands of 3d metal ions. The vacancy is the binding site; for example,  $\text{PW}_{11}\text{O}_{39}^{7-}$  acts as a pentadentate and tetradentate ligand of Co and Cu, respectively [1b, 65, 66]. Complexes of anions such as  $\text{XM}_{11}\text{O}_{39}^{n-}$  ( $\text{X} = \text{P, Si}$ ;  $\text{M} = \text{Mo, W, V, Nb}$ ) with metal ions are used as inorganic analogs of metalloporphyrins (inorganic synzyme) and have important advantages as catalysts, i.e. high resistance to oxidative degradation and thermal stability.

Hill and co-workers have reported that TMSP is effective for the epoxidation of alkenes and the oxygenation of alkanes by use of *t*-BuOOH and PhIO as oxidants [67]. The characteristics of TMSP in alkene epoxidation, compared with those of metalloporphyrins, Schiff base complexes, and triflate salts, are as follows [67]:



(TDCPP = tetrakis-2,6-dichlorophenylporphyrin;  
TPP = tetraphenylporphyrin; OTf = triflate ion)

Thus, the substituted heteropolyanion is stable and active even in the presence of oxidants such as *t*-BuOOH or PhIO. Note that the heteropolyanion is unstable with

respect to hydrogen peroxide. Based on the high stability, TMSP can be used for alkane hydroxylation [67b]. Mansuy et al. have reported that  $\text{P}_2\text{W}_{17}\text{O}_{61}(\text{Mn}^{3+} \cdot \text{Br})^{8-}$  is oxidation resistant and more active for the epoxidation of cyclooctene with PhIO than those containing  $\text{Fe}^{3+}$ ,  $\text{Co}^{2+}$ ,  $\text{Ni}^{2+}$ , or  $\text{Cu}^{2+}$  [68]. The oxygenations of cyclohexane, adamantane, and heptane and the hydroxylation of naphthalene, are also catalyzed by TMSP.

Ruthenium has been used as the catalytic center in TMSP for the oxidations of cyclohexane, adamantane, and styrene with PhIO or *t*-BuOOH [69].

### 3.10.5.3 Heteropolyanion-Supported Metals

The organometallic cations can be supported on reduced heteropolyanions or more negatively charged polyanions such as  $\text{SiW}_9\text{M}_3\text{O}_{40}^{7-}$  and  $\text{P}_2\text{W}_{15}\text{M}_3\text{O}_{62}^{9-}$  ( $\text{M} = \text{V}^{5+}$ ,  $\text{Nb}^{5+}$ ). The latter has three full units of anionic surface charge that enable tight and covalent bonding of transition metals [66].

Finke and co-workers have reported that a  $\text{P}_2\text{W}_{15}\text{-Nb}_3\text{O}_{62}^{9-}$ -supported Ir catalyst,  $[(n\text{-C}_4\text{H}_9)_4\text{N}]_5\text{Na}_3[(1,5\text{-cod})\text{Ir} \cdot \text{P}_2\text{W}_{15}\text{Nb}_3\text{O}_{62}]$  (cod = cyclooctadiene), is active for both hydrogenation [70] and oxygenation [71] of cyclohexene. The turnover frequency is 100 times higher than that of its parent Ir compound,  $[(1,5\text{-cod})\text{IrCl}]_2$ . The supported structure probably remains intact during the reaction, while it is unstable under  $\text{H}_2$  atmosphere [72].

### 3.10.5.4 Preparation

The preparation of TMSPs (Keggin-type and Dawson-type) is described in detail by Walker and Hill [73] and Lyon et al. [74]. The tetrakis(tetra-*n*-butylammonium) salt of  $\text{PMo}_{11}\text{O}_{39}^{7-}$ ,  $(n\text{-Bu}_4\text{N})_4\text{H}_3\text{PMo}_{11}\text{O}_{39}$  (**1**) is prepared and metalated to form the corresponding Keggin-type TMSP.

The compound **1** is prepared as follows:  $\alpha\text{-H}_3\text{PMo}_{12}\text{O}_{40}$  is dissolved in water; the pH of the solution is adjusted to 4.3 with  $\text{Li}_2\text{CO}_3$ ; a precipitate is formed by adding solid  $n\text{-Bu}_4\text{NBr}$  (14 equiv) to the solution with vigorous stirring; the crude product is collected, washed with  $\text{H}_2\text{O}$ , evaporated to dryness, and allowed to air dry overnight at room temperature. In contrast to recrystallization from protic media [75], the light yellow-green crystalline product **1**, can be obtained by repeated recrystallization from organic solvents without decomposition. Recrystallization under nonprotic conditions involves dissolving the crude product in  $\text{CH}_3\text{CN}$  by stirring without heating, followed by slow evaporation of the solvent at room temperature. After three recrystallizations the complex has >99% purity, as confirmed by  $^{31}\text{P}$  NMR [73].

From the lacunary polyanion, for example, the Mn-substituted polyanion,  $(n\text{-Bu}_4\text{N})_4\text{HPMo}_{11}\text{Mn}^{\text{II}}(\text{CH}_3\text{CN})\text{O}_{39}$ , can be prepared [73]: **1** is dissolved in acetonitrile with stirring, and then toluene is added to produce a homogeneous light yellow-green solution; this solution is poured into a separatory funnel to which is added an aqueous solution of  $\text{MnSO}_4 \cdot \text{H}_2\text{O}$  (1.5 equiv); vigorous shaking of the

heterogeneous mixture for  $\approx 1$  min results in an immediate color change of the organic layer to brown indicating that **1** has rapidly extracted the manganese ion into the organic layer; the water layer is drawn off, and the remaining organic layer is placed in a crystallizing dish and allowed to evaporate slowly at room temperature; the crude brown crystalline product is separated by filtration and recrystallized from acetonitrile. Unlike  $\text{Co}^{\text{II}}$ ,  $\text{Mn}^{\text{II}}$ , or  $\text{Cu}^{\text{II}}$ , metalation with  $\text{Zn}^{\text{II}}$  induces the decomposition of **1** [73].

A heteropolyanion-supported metal,  $[(n\text{-C}_4\text{H}_9)_4\text{N}]_5\text{-Na}_3[(1,5\text{-cod})\text{Ir} \cdot \text{P}_2\text{W}_{15}\text{Nb}_3\text{O}_{62}]$  (**2**) is prepared from  $(\text{Bu}_4\text{N})_9\text{P}_2\text{W}_{15}\text{Nb}_3\text{O}_{62}$  and  $[(1,5\text{-cod}) \cdot \text{Ir}(\text{CH}_3\text{CN})_2]\text{BF}_4$  [76]. The choice of the metal–ligand combination  $\text{Ir}(1,5\text{-cod})^+$  and synthesis of  $(\text{Bu}_4\text{N})_9\text{P}_2\text{W}_{15}\text{Nb}_3\text{O}_{62}$  are described in the literature [77, 78]. The synthesis and subsequent storage of **2** require strict oxygen-free conditions. The key to obtaining **2** as a pure solid is the use of mixed  $\text{Bu}_4\text{N}^+/\text{Na}^+$  salts and at least two reprecipitations from paper-filtered homogeneous  $\text{CH}_3\text{CN}$  solution using  $\text{EtOAc}$ .  $\text{Bu}_4\text{NBF}_4$  is very soluble in  $\text{EtOAc}$  and thus is removed by this process. Analytically pure **2** is obtained as a bright yellow, very air-sensitive powder.

### 3.10.6 Heteropolyanions Intercalated in Layered Double Hydroxides

Layered silicate clays intercalated by pillaring polyoxocations are precursors to an important class of microporous catalysts. Smectite clay was the only host structure known to be pillarable by purely inorganic oxo ions. Recently, layered double hydroxides (LDH) pillaring oxo ions were reported by Pinnavaia and co-workers [79, 80].

The pillaring of LDH by Keggin-type heteropolyanions and their lacunary species has been attempted. The gallery heights are reported to be about 10 Å. The reactivity of  $[\text{XM}_{12}\text{O}_{40}]^{n-}$  species for intercalative ion exchange depends strongly on both the net charge and polyhedral framework of the ion [80]. Since the cross-section of a Keggin anion (10 Å diameter) is  $\approx 80 \text{ Å}^2$  and the area per unit positive charge is  $16.6 \text{ Å}^2$  for the layer surface of an LDH,  $[\text{Zn}_2\text{Al}(\text{OH})_6]\text{NO}_3 \cdot 2\text{H}_2\text{O}$ , Keggin ions with a charge less than  $-5$  cannot be electrically balanced by the host LDH [80].

However, more study is needed to establish the catalytic properties, structures and thermal stabilities of the LDH-pillared HPAs.

#### 3.10.6.1 Preparation

The ion-exchange reactions are carried out by dropwise addition of a boiling suspension of  $[\text{Zn}_2\text{Al}(\text{OH})_6]\text{NO}_3 \cdot 2\text{H}_2\text{O}$  to a 40% excess of the polyoxometalates in aqueous solution at room temperature. A nitrogen atmosphere is used to avoid possible reaction of the LDH with atmospheric  $\text{CO}_2$ . The final products are stored under nitrogen [80]. The host LDH is prepared by the reaction of freshly precipitated aluminum hydroxide with an aqueous zinc chloride solution at pH 6.2,

according to the general method of Taylor [81]. The reaction time at 373 K is 7 days.

### 3.10.7 Supported Heteropoly Compounds

Supported heteropoly compounds, where heteropoly compounds are dispersed on the surface of porous solids, are important for applications, since the surface area of heteropolyacids is usually low. The structure, stability, and catalytic properties are very much dependent on the support materials, the extent of loading, and the method of preparation [5, 82]. As supports for heteropoly compounds,  $\text{SiO}_2$ ,  $\text{Al}_2\text{O}_3$ , and  $\text{TiO}_2$ , active carbons, ion-exchange resins, and high surface area salts of HPA have been used. A silane coupling reagent has been tested for binding HPA on oxide support [83]. Insolubility is also an important property when HPA is applied to liquid-phase reactions.

Basic solids such as  $\text{Al}_2\text{O}_3$  and  $\text{MgO}$  tend to decompose HPAs [5, 84, 85], although significant activities have been reported in some cases. On the other hand,  $\text{SiO}_2$  and some carbons are relatively inert. In the cases of  $\text{H}_3\text{PW}_{12}\text{O}_{40}$  and  $\text{H}_3\text{PMo}_{12}\text{O}_{40}$  on  $\text{SiO}_2$ , HPAs are dispersed as thin layers on the support up to a certain quantity of HPA and above that quantity they form thick layers or separate particles [38]. Detailed studies of  $\text{H}_4\text{SiMo}_{12}\text{O}_{40}$  supported on  $\text{SiO}_2$  have been reported [86]. Spectroscopic as well as catalytic tests indicate that the Keggin structure is maintained and catalytic properties corresponding to the parent HPA are revealed at high loading levels [86a,c]. However, at a very low level of loading, strong interactions between the heteropolyacid and surface silanol groups suppress the acidity, and the redox catalysis predominates. It was also shown that the state in solution influences the dispersion after being supported on  $\text{SiO}_2$  [86b]. The thermal stability of HPA on  $\text{SiO}_2$  is usually comparable or slightly lower than the parent HPA [86c, 87], whereas it was reported that  $\text{H}_3\text{PMo}_{12}\text{O}_{40}$  was stable up to 853–873 K when supported on  $\text{SiO}_2$  [88]. Besides decomposition, reformation of the Keggin structure takes place under certain (wet) conditions [5, 89–91]. Silica-bound  $\text{Cs}_{2.5}\text{H}_{0.5}\text{PW}_{12}\text{O}_{40}$ , which is prepared by the hydrolysis of ethyl orthosilicate in the presence of colloidal  $\text{Cs}_{2.5}\text{H}_{0.5}\text{PW}_{12}\text{O}_{40}$  in ethanol, is catalytically more active than Amberlist-15 and H-ZSM-5 with respect to the turnover frequency, as based on the unit acid site [92].

Potassium and cesium salts of HPAs which have high surface areas are useful supports for HPAs. Increased stability as well as improved yield in selective oxidation of acrolein is observed when  $\text{H}_{3+x}\text{PV}_x\text{Mo}_{12-x}\text{O}_{40}$  compounds are supported on  $\text{K}_3\text{PMo}_{12}\text{O}_{40}$  [47, 48]. It was claimed that free acids covered epitaxially the surface of the support, but also the possible formation of a solid solution of  $\text{H}(\text{K}, \text{Cs})_3\text{PW}_{12}\text{O}_{40}$  [93] and  $\text{H}(\text{K}, \text{Cs})_3\text{PMo}_{12}\text{O}_{40}$  [94] due to the diffusion of  $\text{K}^+$ ,  $\text{Cs}^+$  and  $\text{H}^+$  need to be considered.

A certain kind of active carbon is an excellent support of HPAs to make HPAs insoluble [95]. It has been reported that proton transfer from HPAs to the carbon support tightens the binding [96]. High activity was reported for HPAs supported on ion-exchanged resin [97] and HPAs doped in polymers [98, 99].

Polyacetylene can be doped with large anions of  $\text{H}_3\text{PMo}_{12}\text{O}_{40}$ . The doping increases not only the conductivity of the polymer but also the catalytic activity. The HPA is distributed nearly uniformly over the cross-section of the polymer film. For the conversion of ethanol, the catalyst exhibits acid–base activity as well as redox activity. Through the pulse reaction, it has been shown that the rate of formation of ethylene and diethyl ether increased 10 times and the rate of formation of acetaldehyde increased 40 times [98].

Lee and co-workers have shown that the oxidation rate of ethanol was remarkably increased by using a  $\text{H}_3\text{PMo}_{12}\text{O}_{40}$ -blended porous polysulfone (PSF) film [99]. The selectivity for acetaldehyde was high (above 90% selectivity at  $\approx 10\%$  conversion, compared with 40% selectivity at 2% conversion without polymer at 433–463 K).

The coexistence of metal and HPA reveals a unique catalytic bifunctionality. For  $\text{Pt}-\text{Cs}_{2.5}\text{H}_{0.5}\text{PW}_{12}\text{O}_{40}$ , the activity of the *n*-butane isomerization is remarkably enhanced in the presence of  $\text{H}_2$ . The rate of isobutane formation at 573 K is comparable with or higher than those of  $\text{Pt}-\text{H}-\text{ZSM5}$  and  $\text{Pt}-\text{SO}_4^{2-}/\text{ZrO}_2$  while the selectivity of HPA is much higher [100, 101].

### 3.10.7.1 Preparation

Conventional methods such as incipient wetness impregnation are applicable to the preparation of supported HPAs [8].

The doping of polyacetylene with HPAs is performed via chemical oxidation in acetonitrile containing  $\text{H}_3\text{PMo}_{12}\text{O}_{40}$  and minute amount of suitable complexing reagent. Anodic oxidation in an  $\text{H}_3\text{PMo}_{12}\text{O}_{40}$ –acetonitrile electrolyte is also possible using polyacetylene film as the anode. After doping, the films are washed with dry acetonitrile and again vacuum-dried. The samples are stored in vacuum-sealed glass tubes [98].

For blending porous polysulfone (PSF) and HPAs, the choice of solvent is important; dimethylformamide (DMF) has been recommended [99]. A HPA–PSF film is prepared by casting the HPA–PSF–DMF solution on a glass plate, followed by drying in air for 4–5 h and subsequent evacuation for 2 h. The thickness of the HPA–PSF film is usually 0.1 mm [99].

The compound  $\text{Pt}-\text{Cs}_{2.5}\text{H}_{0.5}\text{PW}_{12}\text{O}_{40}$  is prepared as follows [100, 101]: An aqueous solution of  $\text{Pt}(\text{NH}_3)_4\text{Cl}_2$  is added dropwise to an aqueous solution of  $\text{H}_3\text{PW}_{12}\text{O}_{40}$  followed by the addition of an aqueous solution of  $\text{Cs}_2\text{CO}_3$  at 323 K; the resulting suspension is evaporated to solid at 323 K. The molar ratio of  $\text{Pt}^{2+}:\text{Cs}^+:\text{PW}_{12}\text{O}_{40}^{3-}$  is 0.25:2.5:1, where the amount of Pt corresponds to 1.5 wt%, and the surface area is  $112\text{ m}^2\text{ g}^{-1}$ . The palladium analog is obtained from  $\text{Pd}(\text{NO}_3)_2$  in a similar way.

## References

1. (a) G. A. Tsigdinos, *Topics Curr. Chem.* **1978**, 76, 1; (b) M. T. Pope, *Heteropoly and Isopoly Oxometalates*, Springer-Verlag, Berlin, **1983**; (c) M. T. Pope, A. Müller, *Angew. Chem. Int.*

- Ed. Engl.* **1991**, 30, 34; (d) V. W. Day, W. G. Klemperer, C. Schwartz, R.-C. Wang in *Surface Organometallic Chemistry: The Molecular Approach to Surface Science and Catalysis* (Eds: J. M. Bassett, B. C. Gates), Reidel, Dordrecht, **1988**, p. 173.
2. M. Misono, M. Hashimoto, *Shokubai (Catalyst)* **1992**, 34, 152.
  3. Y. Jeannin, M. Fournier, *Pure Appl. Chem.* **1987**, 59, 1529.
  4. M. Misono, *Proc. 10th Int. Congr. Catal.* 1992, Akademiai Kiado: Budapest, **1993**, p.69.
  5. M. Misono, *Catal. Rev. Sci. Eng.* **1987**, 29, 269; **1988**, 30, 339.
  6. K. Eguchi, N. Yamazoe, T. Seiyama, *Nippon Kagaku Kaishi*, **1981**, 336.
  7. H. Niiyama, Y. Saito, S. Yoshida, E. Echigoya, *Nippon Kagaku Kaishi*, **1982**, 569.
  8. Y. Izumi, K. Urabe, M. Onaka, *Zeolite, Clay, and Heteropolyacid in Organic Reactions*, Kodansha, Tokyo, and VCH, Weinheim, **1992**.
  9. M. Misono, N. Nojiri, *Appl. Catal.* **1990**, 64, 1.
  10. (a) M. Otake, T. Onoda, *Shokubai* **1975**, 17, 13; H. Hayashi, J. B. Moffat, *J. Catal.* **1982**, 77, 473; (b) M. Misono, T. Okuhara, *CHEMTECH*, **1993**, Nov., 23.
  11. M. Misono, K. Sakata, Y. Yoneda, W. Y. Lee, *Proc. 7th Int. Congr. Catal.*, 1980, Kodansha, Tokyo, and Elsevier, Amsterdam, **1981**, p. 1047.
  12. M. Misono, N. Mizuno, K. Katamura, A. Kasai, Y. Konishi, K. Sakata, T. Okuhara, Y. Yoneda, *Bull. Chem. Soc. Jpn.* **1982**, 55, 400.
  13. I. V. Kozhevnikov, K. I. Matveev, *Appl. Catal.* **1983**, 5, 135.
  14. J. J. Altenau, M. T. Pope, R. A. Prados, H. So, *Inorg. Chem.* **1975**, 14, 417.
  15. D. E. Katsoulis, M. T. Pope, *J. Am. Chem. Soc.* **1984**, 106, 2737.
  16. T. Okuhara, C. Hu, M. Misono, *Bull. Chem. Soc. Jpn.* **1994**, 67, 1156.
  17. F. Lefebvre, F. X. Liu-Cai, A. Auroux, *J. Mater. Chem.* **1994**, 4, 125.
  18. K. Y. Lee, T. Arai, S.-I. Nakata, S. Asaoka, T. Okuhara, M. Misono, *J. Am. Chem. Soc.* **1992**, 114, 2836.
  19. M. Hashimoto, M. Misono, *Acta Cryst.* **1994**, C50, 231.
  20. J. G. Highfield, J. B. Moffat, *J. Catal.* **1985**, 95, 108; **1986**, 98, 245.
  21. A. Aoshima, S. Yamamatsu, T. Yamaguchi, *Nippon Kagaku Kaishi* **1987**, 976.
  22. C. Hu, M. Hashimoto, T. Okuhara, M. Misono, *J. Catal.* **1993**, 143, 437.
  23. Y. Izumi, K. Matsuo, K. Urabe, *J. Mol. Catal.* **1983**, 18, 299.
  24. L. Barcza, M. T. Pope, *J. Phys. Chem.* **1975**, 79, 92.
  25. N. Mizuno, S. Yokota, I. Miyazaki, M. Misono, *Nippon Kagaku Kaishi* **1991**, 1066.
  26. K. Y. Lee, K. Itoh, M. Hashimoto, N. Mizuno, M. Misono in *New Developments in Selective Oxidation II* (Eds: V. C. Corberán, S. V. Bellón), Elsevier, **1994**, p. 583.
  27. (a) Y. Matoba, H. Inoue, J. Akagi, T. Okabayashi, Y. Ishii, M. Ogawa, *Syn. Commun.* **1984**, 14, 865; (b) Y. Ishii, Y. Kazumasa, T. Ura, H. Yamada, T. Yoshida, M. Ogawa, *J. Org. Chem.* **1988**, 53, 3587; 5549; (c) Y. Ishii, K. Yamawaki, T. Yoshida, T. Ura, M. Ogawa, *J. Org. Chem.* **1987**, 52, 1868; (d) T. Oguchi, Y. Sakata, N. Takeuchi, K. Kaneda, Y. Ishii, M. Ogawa, *Chem. Lett.* **1989**, 2053.
  28. P. Souchay, *Ions Minéraux Condensés*, Masson & Cie, Paris, **1969**.
  29. J. C. Bailar, *Inorg. Synth.* **1939**, 1, 132.
  30. C. Rocchiccioli-Deltcheff, M. Fournier, R. Franck, R. Thouvenot, *Inorg. Chem.* **1983**, 22, 207.
  31. P. Souchay, *Bull. Soc. Chim. Fr.* **1951**, 18, 365.
  32. L. C. W. Baker, T. P. McCutcheon, *J. Am. Chem. Soc.* **1956**, 78, 4503.
  33. T. Okuhara, A. Kasai, N. Hayakawa, Y. Yoneda, M. Misono, *J. Catal.* **1983**, 83, 121.
  34. T. Okuhara, T. Nishimura, H. Watanabe, M. Misono, *J. Mol. Catal.* **1992**, 74, 247.
  35. M. Akimoto, K. Shima, H. Ikeda, E. Echigoya, *J. Catal.* **1981**, 72, 83.
  36. M. Misono, N. Mizuno, T. Komaya, *Proc. 8th Intern. Congr. Catal. Berlin, 1984*, Verlag Chemie-Dechema, **1984**, Vol. 5, p. 487.
  37. N. Mizuno, T. Watanabe, M. Misono, *J. Phys. Chem.* **1985**, 89, 80.
  38. N. Mizuno, T. Watanabe, H. Mori, M. Misono, *J. Catal.* **1990**, 123, 157.
  39. K. Y. Lee, S. Oishi, H. Igarashi, M. Misono, *Catal. Today*, **1997**, 33, 183.
  40. Y. Ono, *Perspectives in Catalysis* (Eds: J. M. Thomas, K. I. Zamaraev), Blackwell: London, **1992**.
  41. S. Suzuki, K. Kogai, Y. Ono, *Chem. Lett.* **1984**, 699.
  42. T. Baba, M. Nomura, Y. Ono in *Acid-Base Catalysis II* (Eds: H. Hattori, M. Misono, Y. Ono), Elsevier, Amsterdam, and Kodansha, Tokyo, **1994**, p. 419.

43. T. Nishimura, T. Okuhara, M. Misono, *Appl. Catal.* **1991**, 73, L7.
44. T. Okuhara, T. Nishimura, M. Misono, *Chem. Lett.* **1995**, No. 2.
45. S. Nakamura, H. Ichihashi, *Proc. 7th Int. Congr. Catal., Tokyo, 1980*, Kodansha, Tokyo, and Elsevier, Amsterdam, **1981**, p. 755.
46. N. Simizu, M. Ueshima, M. Wada, *Shokubai* **1988**, 30, 555.
47. J. B. Black, N. J. Claydon, P. L. Gai, J. D. Scott, E. M. Serwicka, J. B. Goodenough, *J. Catal.* **1987**, 106, 1.
48. K. Bruckman, J. Haber, E. M. Serwicka, *Faraday Disc. Chem. Soc.* **1989**, 87, 173; K. Bruckman, J. Haber, E. M. Serwicka, *Catal. Lett.* **1988**, 1, 35; K. Bruckman, J. Haber, E. M. Serwicka, N. Yurchenko, T. P. Lazarenko, *Catal. Lett.* **1990**, 4, 181.
49. M. Akimoto, H. Ikeda, A. Okabe, E. Echigoya, *J. Catal.* **1984**, 89, 196.
50. R. Neumann, M. Levin, *J. Org. Chem.* **1991**, 56, 5707.
51. R. Neumann, M. Levin, *J. Am. Chem. Soc.* **1992**, 114, 7278.
52. H. Furukawa, T. Nakamura, H. Inagaki, E. Nishikawa, C. Imai, M. Misono, *Chem. Lett.* **1988**, 877.
53. M. A. Schwegler, M. Floor, H. van Bekkum, *Tetrahedron Lett.* **1988**, 29, 823.
54. J. K. Burdett, C. K. Nguyen, *J. Am. Chem. Soc.* **1990**, 112, 5366.
55. G. A. Tsigdinos, C. J. Hallada, *Inorg. Chem.* **1968**, 7, 437.
56. R. Massart, R. Contant, J.-M. Fruchart, J.-P. Ciabrini, M. Fournier, *Inorg. Chem.* **1977**, 16, 2916.
57. P. J. Domaille, G. Watunya, *Inorg. Chem.* **1986**, 25, 1239.
58. P. J. Domaille, *Inorg. Synth.* **1990**, 27, 96.
59. A. Tézé, G. Hervé, *Inorg. Synth.* **1990**, 27, 85.
60. K. I. Matveev, I. V. Kozhevnikov, *Kinet. Katal.* **1980**, 21, 1189.
61. K. Urabe, F. Kimura, Y. Izumi, *Proc. 7th Intern. Congr. Catal. Tokyo, 1980*, Kodansha, Tokyo and Elsevier, Amsterdam, **1981**, p. 1418.
62. J. H. Grate, D. R. Hamm, S. Mahajan, *Preprint distributed at 14th Conference on Catalysis of Organic Reactions*, Albuquerque, NM, April 27–29, **1992**.
63. Y. Izumi, Y. Satoh, H. Kondoh, K. Urabe, *J. Mol. Catal.* **1992**, 72, 37.
64. K. Urabe, Y. Tanaka, Y. Izumi, *Chem. Lett.* **1985**, 1595.
65. N. Mizuno, M. Misono, *J. Mol. Catal.* **1994**, 86, 319.
66. R. K. Ho, W. G. Klemperer, *J. Am. Chem. Soc.* **1978**, 100, 6772.
67. (a) M. Faraj, C. L. Hill, *J. Chem. Soc., Chem. Commun.* **1987**, 1487; (b) C. L. Hill, *Activation and Functionalization of Alkanes*, Wiley, New York, **1989**; (c) C. L. Hill, R. B. Brown, Jr., *J. Am. Chem. Soc.* **1986**, 108, 536.
68. D. Mansuy, J.-F. Bartoli, P. Battioni, D. K. Lyon, R. G. Finke, *J. Am. Chem. Soc.* **1991**, 113, 7222.
69. R. Neumann, C. A.-Gnim, *J. Chem. Soc., Chem. Commun.* **1989**, 1324.
70. D. K. Lyon, R. G. Finke, *Inorg. Chem.* **1990**, 29, 1789.
71. N. Mizuno, D. K. Lyon, R. G. Finke, *J. Catal.* **1991**, 128, 84.
72. M. Pohl, R. G. Finke, *Organometallics* **1993**, 12, 1453.
73. L. A. C.-Walker, C. L. Hill, *Inorg. Chem.* **1991**, 30, 4016.
74. D. K. Lyon, W. K. Miller, T. Novet, P. J. Domaille, E. Evitte, D. C. Johnson, R. G. Finke, *J. Am. Chem. Soc.* **1991**, 113, 7209.
75. M. Fournier, R. C. R. Massart, *Acad. Sci. Paris, Ser. C* **1974**, 279, 875.
76. R. G. Finke, D. K. Lyon, K. Nomiya, S. Sur, N. Mizuno, *Inorg. Chem.* **1990**, 29, 1787.
77. (a) M. Green, T. A. Kuc, S. H. Taylor, *J. Chem. Soc. A* **1971**, 2334; (b) R. R. Schrock, J. A. Osborne, *J. Am. Chem. Soc.* **1971**, 93, 3089.
78. (a) D. J. Edlund, R. J. Saxton, D. K. Lyon, R. G. Finke, *Organometallics* **1988**, 7, 1692; (b) R. G. Finke, D. K. Lyon, K. Nomiya, T. R. J. Weakley, *Acta Crystallogr. C* **1990**, 46, 1592.
79. T. Kwon, G. A. Tsigdinos, T. J. Pinnavaia, *J. Am. Chem. Soc.* **1988**, 110, 3653.
80. T. Kwon, T. J. Pinnavaia, *Chem. Mater.* **1989**, 1, 381.
81. R. M. Taylor, *Clay Miner.* **1984**, 19, 591.
82. K. Tanabe, M. Misono, Y. Ono, H. Hattori, *New Solid Acids and Bases*, Kodansha, Tokyo and Elsevier, Amsterdam, **1989**, p. 170.
83. M. Kamada, Y. Kera, *Chem. Lett.* **1991**, 1831.



84. J. A. R. van Veen, P. A. J. M. Hendricks, R. R. Andrea, E. J. M. Romers, A. E. Wilson, *J. Phys. Chem.* **1990**, *94*, 5282.
85. K. Nowinska, R. Fiedorow, J. Adamiec, *J. Chem. Soc. Faraday Trans.* **1991**, *87*, 749.
86. (a) J.-M. Tatibouet, M. Che, M. Amirouche, M. Fournier, C. Rocchiccioli-Deltcheff, *J. Chem. Soc., Chem. Commun.* **1988**, 1260; (b) M. Fournier, R. Thouvenot, C. Rocchiccioli-Deltcheff, *J. Chem. Soc., Faraday Trans.* **1991**, *87*, 349; (c) C. Rocchiccioli-Deltcheff, M. Amirouche, G. Herve, M. Fournier, M. Che, J.-M. Tatibouet, *J. Catal.* **1990**, *126*, 591.
87. M. J. Bartoli, L. Monceaux, E. Bordes, G. Hecquet, P. Courtine, *Stud. Surf. Sci. Catal.* **1992**, *72*, 81.
88. S. Kasztelan, E. Payen, J. B. Moffat, *J. Catal.* **1990**, *125*, 45.
89. C. R. Rocchiccioli-Deltcheff, M. Amirouche, M. Che, J. M. Tatibouet, M. Fournier, *J. Catal.* **1990**, *125*, 292.
90. A. Ogata, A. Kazusaka, A. Yamazaki, M. Enyo in *Acid-Base Catalysis* (Eds: K. Tanabe, H. Hattori, T. Yamaguchi, T. Tanaka), VCH, Weinheim **1989**, p. 249.
91. Y. Konishi, K. Sakata, M. Misono, Y. Yoneda, *J. Catal.* **1982**, *77*, 169.
92. Y. Izumi, M. Ono, M. Ogawa, K. Urabe, *Chem. Lett.* **1993**, 825.
93. (a) T. Nishimura, H. Watanabe, T. Okuhara, M. Misono, *Shokubai* **1991**, *33*, 420; H. Watanabe, T. Nishimura, S. Nakata, T. Okuhara, M. Misono, *63rd National Meetings of Chem. Soc. Jpn.*, March **1992**; (b) N. Mizuno, M. Misono, *Chem. Lett.* **1987**, 967.
94. M. Misono, N. Mizuno, H. Mori, K. Y. Lee, J. Jiao, T. Okuhara in *Structure-Activity and Selectivity Relationships in Heterogeneous Catalysis*, (Eds: R. K. Grasselli, A. W. Sleight), Elsevier, Amsterdam, **1991**, p. 87.
95. Y. Izumi, K. Urabe, *Chem. Lett.* **1981**, 663.
96. M. A. Schwegler, P. Vinle, M. van der Eijk, H. van Bekkum, *Appl. Catal.* **1992**, *80*, 41.
97. T. Baba, Y. Ono, *Appl. Catal.* **1986**, *22*, 321.
98. J. Pozniczek, I. Kulszewicz-Bajer, M. Zagorska, K. Kruczala, K. Dyrek, A. Bielanski, A. Pron, *J. Catal.* **1991**, *132*, 311.
99. I. K. Song, S. K. Shin, W. Y. Lee, *J. Catal.* **1993**, *144*, 348.
100. K. Na, T. Okuhara, M. Misono, *J. Chem. Soc., Chem. Commun.* **1993**, 1422.
101. K. Na, T. Okuhara, M. Misono, *Chem. Lett.* **1993**, 1141.
102. (a) Y. Onoue, Y. Mizutani, S. Akiyama, Y. Izumi, *Chemtech* **1978**, *8*, 432; A. Aoshima, S. Yamamatsu, T. Yamaguchi, *Nippon Kagaku Kaishi* **1990**, 233; (b) A. Aoshima, S. Tonomura, S. Yamamatsu, *Polymers Advan. Tech.* **1990**, *2*, 127; (c) Eu Patent, EP 263027 (Nippon Fine Chemical Co.); (d) G. Maksimov, I. V. Kozhevnikov, *React. Kinet. Catal. Lett.* **1989**, *39*, 317; (e) S. Sato, C. Sakurai, H. Furuta, T. Sodesawa, F. Nozaki, *J. Chem. Soc., Chem. Commun.* **1991**, 1327.
103. (a) Y. Izumi, R. Hasebe, K. Urabe, *J. Catal.* **1983**, *84*, 402; (b) T. Nishimura, T. Okuhara, M. Misono, *Chem. Lett.* **1991**, 1695; Y. Izumi, N. Natsume, H. Takamine, I. Tamaoki, K. Urabe, *Bull. Chem. Soc. Jpn.* **1989**, *62*, 2159; (c) T. Okuhara, M. Yamashita, K. Na, M. Misono, *Chem. Lett.* **1994**, 1450; (d) Y. Ono, M. Taguchi, Gerile, S. Suzuki, T. Baba, *Stud. Surf. Sci. Catal.* **1985**, *20*, 167; (e) Y. Ono, T. Baba, J. Sakai, T. Keii, *J. Chem. Soc., Chem. Commun.* **1982**, 400; (f) T. Okuhara, T. Hibi, K. Takahashi, S. Tatematsu, M. Misono, *J. Chem. Soc., Chem. Commun.* **1984**, 697; (g) S. Shikata, T. Okuhara, M. Misono, *Sekiyu Gakkaishi* **1994**, *37*, 632; (h) Jpn Patent **1991** 300150; (i) Y. Izumi, M. Ogawa, W. Nohara, K. Urabe, *Chem. Lett.* **1992**, 1987.
104. (a) D. Attanasio, D. Orru, L. Suber, *J. Mol. Catal.* **1989**, *57*, L1; (b) M. Lissel, H. Jansen, R. Neumann, *Tetrahedron Lett.* **1992**, *33*, 1795; (c) C. Venturello, R. D'Aloisio, *J. Org. Chem.* **1988**, *53*, 1553; (d) Y. Ishii, K. Yamawaki, T. Ura, H. Yamada, T. Yoshida, M. Ogawa, *J. Org. Chem.* **1988**, *53*, 3587; (e) J. E. Lyons, P. E. Ellis, Jr., V. A. Durante, *Stud. Surf. Sci. Catal.* **1991**, *67*, 99.
105. (a) M. Ueshima, H. Tsuneki, A. Shimizu, *Hyomen* **1985**, *23*, 69; (b) Jpn Patent **1988** 145249 (Asahi Chem. Ind.); Jpn Patent **1991** 106839 (Sumitomo Chem.); (c) G. B. McGarvey, J. B. Moffat, *J. Catal.* **1991**, *132*, 100; (d) G. Centi, J. L. Nieto, C. Iapalucci, K. Brückman, E. M. Serwicka, *Appl. Catal.* **1989**, *46*, 197.
106. (a) Y. Izumi, Y. Satoh, K. Urabe, *Chem. Lett.* **1990**, 795; (b) R. W. Wegman, *J. Chem. Soc., Chem. Commun.* **1994**, 947.

## 3.11 Hydrothermal Zeolite Synthesis

E. J. P. FEIJEN, J. A. MARTENS AND P. A. JACOBS

### 3.11.1 Introduction

The crystallization of natural zeolites involves geological timescales. Large crystals of zeolite minerals grow in cavities in basic volcanic or metamorphic rocks in the presence of mineralizing solutions. Vast sediments of natural zeolite microcrystallites originate from an alteration of volcanic glass and occur in chemical sedimentary rocks of marine origin. Extensive deposits of natural zeolites are present in all oceans. The natural zeolites find many applications but are less suitable as catalysts due to the presence of impurities which are difficult to eliminate and, in general, synthetic zeolites are preferred for catalytic applications.

In the period from 1940 to 1950, Barrer and his co-workers duplicated the natural zeolite crystallization process under more severe conditions of alkalinity and temperature, and were able to crystallize the first synthetic zeolites in reaction times ranging from hours to days [1]. In the years after the pioneering work of Barrer [2] and Milton [1], many new zeolite types and framework compositions have been synthesized as a result of substantial research activity, especially by oil companies. Since the mid-1970s, much research effort has been devoted to unravel the mechanisms of nucleation and crystal growth of zeolites. The field of synthetic zeolite synthesis has evolved into a mature science. Concepts for tailor-made zeolite crystallizations have been developed, and the 'art' of zeolite synthesis has become a real scientific issue [3].

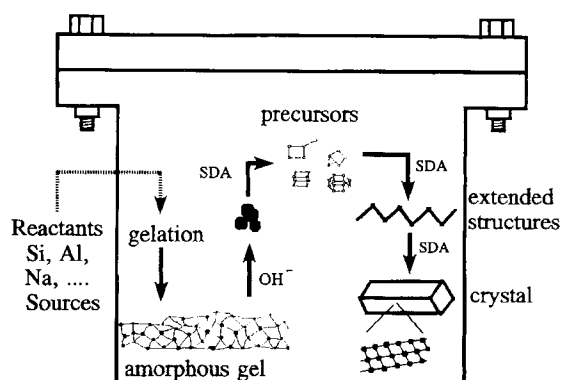
Zeolite synthesis has been treated in several books [2, 4, 5] and symposium proceedings [6]. The literature on the hydrothermal synthesis of zeolites is vast; the references cited here are those that are most appropriate to illustrate this review.

This article explains zeolite synthesis in a broad chemical sense, and illustrates this chemistry with industrial zeolite crystallization processes. Aluminosilicate zeolites and hydrothermal syntheses are the central topic, since these materials and their synthesis conditions cover the majority of industrial zeolite products and manufacturing processes. However, with appropriate changes, the theory presented here is also applicable to zeolites with other framework elements.

### 3.11.2 Zeolitization in General

#### 3.11.2.1 Key Steps in Zeolite Synthesis

The hydrothermal synthesis of aluminosilicate zeolites corresponds to the conversion of a mixture of silicon and aluminum compounds, alkali metal cations, organic molecules and water via an alkaline supersaturated solution into a microporous crystalline aluminosilicate. This complex chemical process called *zeolitization* is schematically depicted in Fig. 1. Common sources of silicon are colloidal silica, waterglass, pyrogenic silica or silicon alkoxides such as tetramethyl and tetraethyl



**Figure 1.** Schematic representation of the zeolite formation process, from reagent sources to the final crystalline product. The process is depicted inside a laboratory-scale autoclave, as used for most experimental zeolite syntheses. (SDA = structure directing agent).

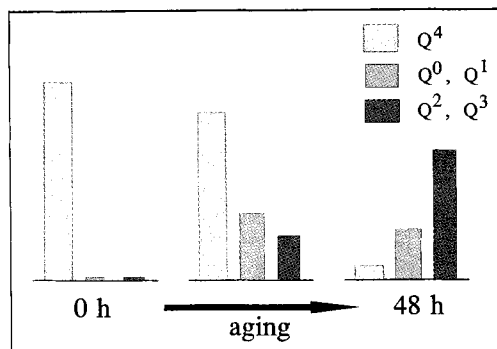
orthosilicate. These raw materials differ with respect to the degree of polymerization of silicon dioxide. Aluminum can be introduced as compounds such as gibbsite, pseudo-boehmite, aluminate salts or the metal powder. Cationic and neutral organic molecules are added as solvents or as structure-directing agents. When the reactants are mixed, they rapidly form an aluminosilicate hydrogel or precipitate. For example, the addition of a solution of sodium aluminate to a silica sol increases the ionic strength of the solution, resulting in immediate gelling, i.e. the destabilization of the sol and formation of a network of colloidal silica particles. Dissolution of this solid phase, mediated by the mineralizing agent, provides the solutions with silicate and aluminate monomers and oligomers, which condense into specific precursor structures, are organized into more extended structures and finally into a crystalline phase.

After the gel point, the hydrogel is aged at room temperature or a slightly increased temperature, remaining below that applied during the crystallization. This treatment of the hydrogel is called the “ageing” or “ripening”. The ageing is often crucial to obtaining the desired crystalline phase and to accelerate the crystallization [7]. After ageing, the hydrogel is heated to the appropriate crystallization temperature, which is most often in the range from 333 to 473 K [2, 8]. The crystallization process is thermally activated and takes place either below or above 370 K. Crystallizations above the boiling point of water require closed systems, allowing a high water vapor pressure to build up. Elevated temperatures allow a high yield of crystals to be achieved in an acceptable period of time.

The crystallization process of a zeolite can be subdivided into the three classic steps, always involved in any type of crystallization, namely *achievement of supersaturation*, *nucleation* and *crystal growth*.

### A Formation of Precursor Species

One of the important reactions occurring during the ripening period is the (partial) depolymerization of the silica sol particles, which is catalyzed by hydroxy ions [2]. This dissolution leads to an increase of the concentration of silica in the liquid phase

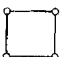

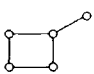




**Figure 2.** Schematic representation of the evolution of the different Si populations during gel aging for the synthesis of zeolite NaY. Non-aged gels clearly show the presence of the colloidal Si source. Upon aging, monomeric Si species are formed, as indicated by the  $Q^0$  lines. Further ageing results in the formation of species with higher connectivity ( $Q_1$ – $Q_3$ ) (after Ref. 9).

of the gel. Ginter et al. [9] studied the evolution of gel ageing in a crystallization of zeolite NaY by liquid-line and  $^{29}\text{Si}$  MAS NMR. They observed a slow dissolution of gel solids at room temperature and acceleration by increasing the temperature. Upon dissolution, the initial products formed are monomeric silicate anions ( $Q^0$ ). After ageing for 24 h, the relative NMR signal intensity of the low connectivity bands  $Q^0$ ,  $Q^1$  and  $Q^2$  was characteristic for sodium silicate solutions with a low silicate ratio ( $\text{SiO}_2 : \text{Na}_2\text{O}$ ), which is tantamount to high alkalinity. Further ageing (from 36 to 48 h) resulted in the formation of silicate species with higher degrees of condensation ( $Q^2$  and  $Q^3$ ), suggesting that the silicate ratio in solution had increased [9]. This evolution is schematically depicted in Fig. 2. After the depolymerization of the silica sol, the monomeric silicate anions released into solution further copolymerize into higher oligomeric species. These oligomers are negatively charged and undergo rapid intramolecular as well as intermolecular exchange of silicate monomers [10, 11]. The condensation and hydrolysis of silicate oligomers occurs through a nucleophilic mechanism catalyzed by hydroxy ions [12]. The acidity (and nucleophilicity) increases with the degree of silicate connectivity in the oligomer ( $Q^3 > Q^2 > Q^1 > Q^0$ ).

In alkaline solutions, aluminum is present as the tetrahedral aluminate anion,  $\text{Al}(\text{OH})_4^-$ . The silicate molecules condense with this monomeric  $\text{Al}(\text{OH})_4^-$  to produce aluminosilicate structures [13, 14]. The condensation rate of silicate oligomers and the aluminate anion increases with increasing silicate ratio, i.e. with increasing oligomerization degree of the silicate [13]. The aluminate anions condense preferentially with the larger silicate species in solution containing the strongest nucleophiles. The preference of aluminum for condensation with large silicate anions is also explained by the low electrostatic repulsion between large silicate species and the  $\text{Al}(\text{OH})_4^-$  anion, since the average negative charge per silicon decreases with the size of the oligomer [15]. Once these aluminosilicate complexes are formed, further polymerization progresses only slowly [15].

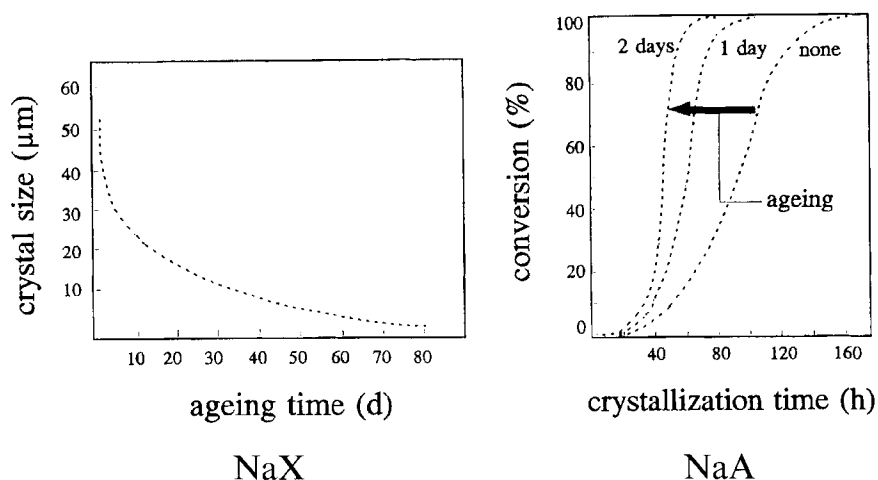
**Table 1.** Examples of secondary building units identified as polysilicate anions in alkaline solutions (from Refs. 10, 13 and 16).

Type	Structure	Type	Structure
4		4-4	
4-1		6-6	
4=1			

The silicate and aluminosilicate polyanion solution chemistry is extremely complex [10, 13, 16]. Silicon 29 and  $^{27}\text{Al}$  NMR spectroscopic techniques have contributed to the identification of these silicate and aluminosilicate polyanion structures [2, 10, 13, 15, 16]. In silicate oligomers, ring- and cage-like structures are more stable than chain-like structures [16]. Among the species which could be identified are a number of the so-called “secondary building units”, (SBU) [2, 16] (see Table 1) which Meier [17] identified as the basic building units of zeolite framework structures. The presence of such units in the liquid phase of hydrogels is rather interesting, for Barrer [2] proposed that the mechanisms of nucleation and crystal growth involve the condensation of specific polyanions rather than monomers [16].

Unfortunately, the  $^{29}\text{Si}$  NMR technique is less suitable for the detection and analysis of silicate species containing more than 12 Si atoms [10]. The identification and characterization of more extended structures would contribute significantly to the understanding of the processes initiating nucleation and crystal growth, as well as of the impact of the various crystallization parameters. Vaughan [18] proposed the formation of “extended sheet and columnar substructures” in aluminosilicate gels containing Na and K, respectively. According to Vaughan’s model, the formation of these extended structures is controlled by the smaller base metal cations (e.g.  $\text{Na}^+$  and  $\text{K}^+$ ), denoted as primary cations, while the larger (secondary) cations govern the condensation mode of these units, and thus the generation of a specific zeolite structure.

Katovic et al. [7] studied the competitive crystallization of zeolite NaX and cubic Na-P (Pc). The crystallization yield and the nature of the zeolite phase obtained depend on the ageing period of the hydrogel. Ageing leads to a shortening of the induction period of the crystallization of both zeolite X and Pc. This is explained by an increase in the number of nuclei formed in solution upon ageing [7]. During polycondensation of the silicate and aluminate precursors, a predominantly amorphous aluminosilicate hydrogel is formed, containing very small semicrystalline particles with a structure resembling that of Pc. The growth of these gel-occluded semicrystalline particles is impeded, however, because the material flux inside the



**Figure 3.** Dependence of crystal size and crystallization kinetics on the ageing period, as demonstrated for the crystallization of NaX and NaA, respectively. The crystallization curves for NaA correspond to non-aged gels and 1 day and 2 day aged gels (after Ref. 21).

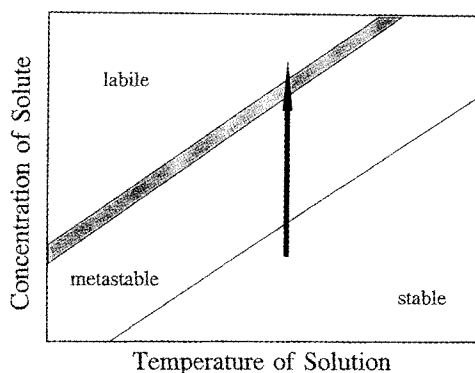
hydrogel matrix is slow [7]. During ageing, structural changes take place in the solid part of the gel, as shown by X-ray diffraction (XRD). The Raman spectra of the gel suggest a slow formation of six-membered aluminosilicate rings, their ordering into sodalite cages and a possible formation of quasicrystalline particles resembling the faujasite structure [19]. Dissolution of the gel during ageing results in the release of these semicrystalline microparticles into the solution. The enhanced yield of crystallization of zeolite NaX from an aged gel can therefore be attributed to the increased number of nuclei formed inside the gel matrix, and explains why zeolite NaX crystallizes from aged gels only [7]. It remains to be explained why in such aged gels the formation of double six-rings (SBU for zeolite NaX) is preferred over that of double four-rings (SBU for zeolite Pc).

The impact of ageing on the crystallization of zeolite NaX and NaA is illustrated in Fig. 3. The crystal size decreases substantially when the gel is aged a longer time. Ageing of the gel enhances the concentration of precursor species, and the concentration of nuclei. The average final crystal size is reduced when a larger number of nuclei develop into crystals. The presence of an increased concentration of nuclei is also reflected in enhanced crystallization kinetics.

## B Three Basic Phases of the Crystallization Process

### (i) Achievement of Supersaturation

A solution with specific concentration and temperature can be in a stable, metastable or labile condition as depicted in Fig. 4. The stable and metastable areas are separated by the normal solubility curve, which determines the normal equilibrium saturation concentration of a component  $c^*$  [20]. The boundary between the metastable and labile region is not always well defined, as indicated by the shaded area.



**Figure 4.** The solubility–supersolubility diagram (reproduced from Ref. 3 with the permission of Elsevier Science).

The degree of supersaturation  $S$  is defined as the ratio of the actual concentration to the normal equilibrium concentration ( $S = c/c^*$ ) [20]. In the stable region, no nucleation nor crystal growth can occur, while in the labile region nucleation as well as crystal growth are possible. In the metastable area, only crystal growth can occur [20].

During ageing, and especially at increased temperatures, the concentration of adequate aluminosilicate precursor species, discussed in section 3.11.2.1 A increases with time by dissolution of the amorphous solid phase and interconversions of dissolved aluminosilicate oligomers in solution. This increasing concentration of solute, occurring usually at a constant temperature, will transform a stable solution into a metastable solution, and finally into a labile one [20]. This transformation is indicated with an arrow in the solubility–supersolubility diagram of Fig. 4.

#### (ii) Nucleation

Primary nucleation from a supersaturated solution can be homogeneous or heterogeneous [20]. The latter is induced by impurities or foreign particles present in the solution, while the former occurs spontaneously. It is evident that heterogeneous nucleation can be suppressed by filtration of the different solutes. Secondary nucleation is induced by crystals and is relevant to the technique of seeding, discussed below.

During the period preceding the formation of viable nuclei, different kinds of germ nuclei (embryos) form by chemical aggregations of the aluminosilicate precursor species and disappear again through depolymerization [2]. As a result of such fluctuations, the germ nuclei will grow in time and form, eventually, different kinds of nuclei with dimensions of the critical size to become viable, i.e. nuclei on which crystal growth occurs spontaneously [2]. The concentration of these species is highest in the boundary layer surrounding the amorphous solid particles, as a result of the enhanced local concentration by dissolution. Presumably, nucleation occurs preferentially in these boundary regions [13].

The net free energy of formation of a nucleus, consisting of  $j$  structural units can be expressed as [8]

$$\Delta g = Aj^{2/3} - Bj \quad (1)$$

in which  $A$  and  $B$  are constants. The term  $Aj^{2/3}$  reflects the interfacial free energy between the nucleus and the solution; it is proportional to the area of the interface between the nucleus and the solution, and has a positive value corresponding to the destabilization of the nucleus. The second term represents the free energy of formation of a nucleus containing  $j$  structural units. According to eq. 1, the nuclei will become viable if  $\delta\Delta g/\delta j = 0$ . Further addition of structural units will decrease  $\Delta g$ , and favor crystal growth [8]. For a spherical nucleus, the free energy of formation depends on the degree of supersaturation  $S$ , the density  $\rho$  and surface energy  $\sigma$  of the nucleus [20]:

$$\Delta g = -\frac{16\pi\sigma^3(MW)^2}{3(RT\rho \ln S)^2} \quad (2)$$

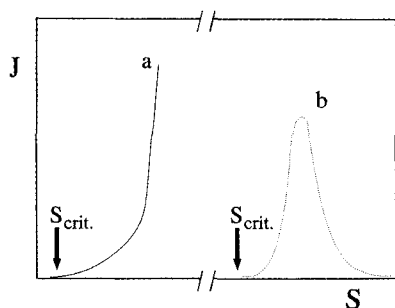
From this equation, it is evident that from a saturated solution ( $S = 1$ ,  $\ln S = 0$ ) no spontaneous nucleation can occur. For a supersaturated solution ( $S > 1$ ),  $\Delta g$  has a finite negative value, and spontaneous nucleation is possible [20].

Nucleation is an activated process, and the nucleation rate  $J$  (the number of viable nuclei formed per unit time) is commonly described as an Arrhenius rate equation [20]:

$$J = A \exp\left(\frac{-\Delta g}{RT}\right) \quad (3)$$

Equation 3 predicts an exponential increase in the nucleation rate with temperature, and consequently, in the degree of supersaturation, since the concentration in solution increases exponentially with temperature. The onset of nucleation occurs at a critical degree of supersaturation,  $S_{\text{crit}}$ . (Fig. 5, line a). The experimentally observed nucleation rates typically exhibit a maximum with increasing degree of supersaturation (Fig. 5, line b). The decrease at high concentrations is caused by the enhanced viscosity of the medium, inhibiting molecular migrations.

The rate of nucleation can be determined from crystal size distribution measurements in the final crystallization product and size increase measurements of the largest crystals in the course of crystallization [21]. During crystallization of NaX, the majority of nuclei are formed at the early stages of the crystallization, i.e. during the autocatalytic stage of the crystallization process, corresponding to the expo-



**Figure 5.** Nucleation rate  $J$  versus degree of supersaturation ( $S$ ): curve a according to the Arrhenius rate equation; curve b experimental observation (reproduced from Ref. 3 with the permission of Elsevier Science).



nential part of the crystallization yield curves (explained in the subsequent section) [21]. As nucleation and crystal growth consume the same precursor species, the nucleation rate is expected to go through a maximum and to decline again after a certain period of time when the consumption of precursor species by crystal growth limits their availability [2, 20].

### (iii) Crystal Growth

Zeolite crystal growth is solution mediated [22]. It occurs at the crystal–solution interface by condensation of dissolved species (secondary building units or more extended species) onto the crystal surface [2, 13]. A direct transition of the solid phase of the gel into crystalline product through solid–solid transformation seems very unlikely [23]. Likewise, nuclei grow to crystals by multiple addition of precursor species. Experimental “crystallization curves” express the yield of crystals against time. These curves usually exhibit an S-shaped profile [2, 20, 21, 23]. The inflection point of these sigmoid curves separates an autocatalytic growth period from a stage of delayed crystal growth owing to a depletion of the solution with precursor species. The autocatalytic nature of the first stage of the crystallization reflects the intrinsic property of self-acceleration of a crystallization process, provided the source of nutrients is not limiting. The experimental crystallization curves can be described by Kholmogorov’s equation [21],

$$Z = 1 - \exp(kt^n) \quad (4)$$

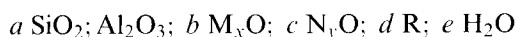
in which  $n$  and  $k$  are constants. Equation 4 describes the evolution of the ratio  $Z$  of the mass of zeolite formed at time  $t$  to the final zeolite mass.

## 3.11.2.2 Key Parameters Governing Zeolitization

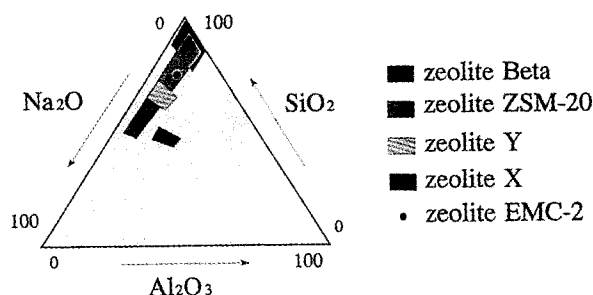
### A Hydrogel Molar Composition

The hydrogel composition is not an independent parameter influencing zeolitization, for it also reflects other parameters indirectly, such as the alkalinity, and the nature and amount of organic templates, the impact of which will be dealt with in more detail later on. The hydrogel composition should be regarded as one of the most important factors determining the outcome of the crystallization, because every zeolite has a specific hydrogel compositional range, which can be very broad or extremely narrow. Such compositional ranges, commonly called crystallization fields, are usually represented graphically in a ternary diagram, such as those illustrated in Fig. 6.

The chemical composition of a specific synthesis hydrogel is usually expressed in terms of molar ratios of oxides:



in which  $M$  and  $N$  stand for (alkali) metal ions,  $R$  for organic template and  $a$ – $e$  are molar ratios. To indicate the crystallization field, the preferred ranges for the relative molar amounts of  $\text{SiO}_2$ ,  $\text{Al}_2\text{O}_3$ ,  $\text{M}_2\text{O}$ ,  $\text{N}_2\text{O}$ ,  $R$  and  $\text{H}_2\text{O}$  can be indicated in the oxide formula. Next to the nature of the templates used, the ratios  $\text{SiO}_2 : \text{Al}_2\text{O}_3$ ,



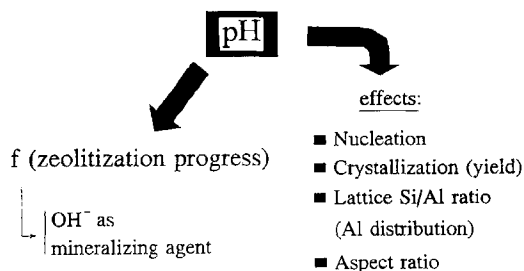
**Figure 6.** Ternary diagram indicating the crystallization fields of different zeolite types (after Ref. 24).

$M_xO(N_yO):SiO_2$ ,  $R:SiO_2$  and  $H_2O:SiO_2$  are often used to characterize a zeolitization. The compositional ratios influence nucleation and crystallization kinetics, the nature of the crystalline phases obtained, the framework composition, Si and Al distribution in the lattice, and the crystal size and morphology [25–31]. For example, the organic-free synthesis of ZSM-5 and mordenite was shown to be dependent on the  $Na_2O:SiO_2$  as well as on the  $SiO_2:Al_2O_3$  ratio: ZSM-5 is preferred at high  $SiO_2:Al_2O_3$  and low  $Na_2O:SiO_2$  ratios in the gel [25].

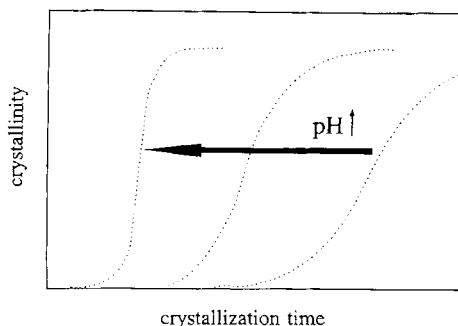
## B Alkalinity

The pH of the alkaline synthesis solution, which is generally between 9 and 13, is of key importance. The  $OH^-$  anions fulfill a crucial catalytic function in the field of inorganic crystallizations designated as the mineralizing (or mobilizing) function. The rates of nucleation and crystallization are influenced by the alkalinity of the medium. Furthermore, the alkalinity has an impact on the Si:Al ratio of the zeolite product, and even on the aspect ratio of the final zeolite crystals. Scheme 1 given an overview of the impact of the alkalinity on the zeolitization process; the pH effects different stages in the process of zeolite formation as well as different product features. The alkalinity itself, however, changes during the zeolitization process.

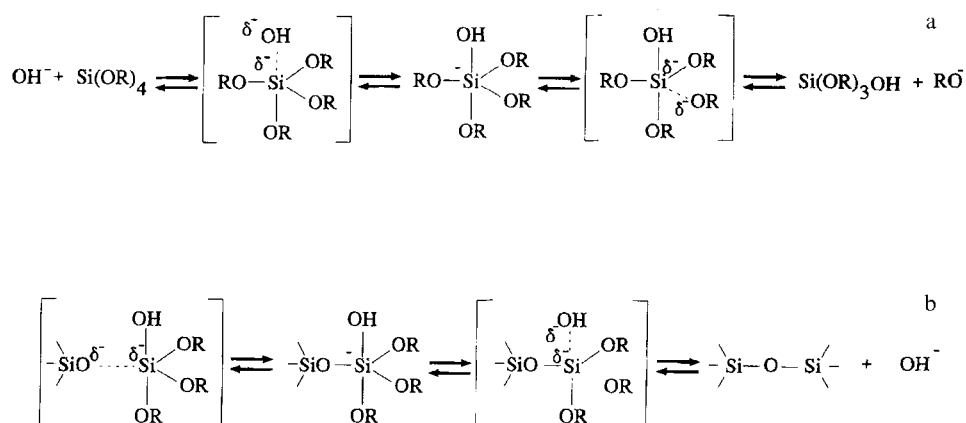
The role of the mineralizing agent is to depolymerize the amorphous aluminosilicate particles at an appropriate rate. Soluble and adequate precursor complexes have  $Si^{IV}$  and  $Al^{III}$  atoms in tetrahedral coordination and contain condensable ligands [22]. The mineralizing agent is indispensable in order to reach a super-saturated state which makes nucleation and crystal growth possible [8, 22]. In general, an increased pH will accelerate crystal growth, and shorten the induction period (the period before formation of viable nuclei) by enhancing the precursor



**Scheme 1**



**Figure 7.** Increasing alkalinity of the synthesis hydrogel reduces the induction period and accelerates crystal growth (increasing the tangent of the steepest part of the crystallization curve; after Ref. 37.)



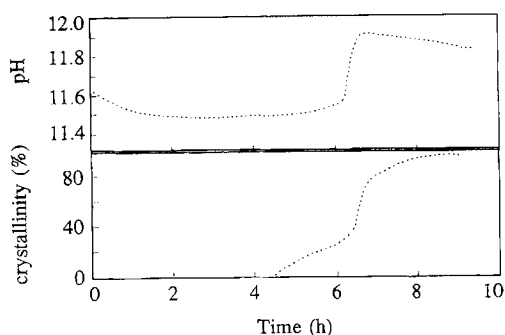
**Scheme 2**

concentration [8]. This alkalinity effect on the crystallization kinetics is schematically explained in Fig. 7.

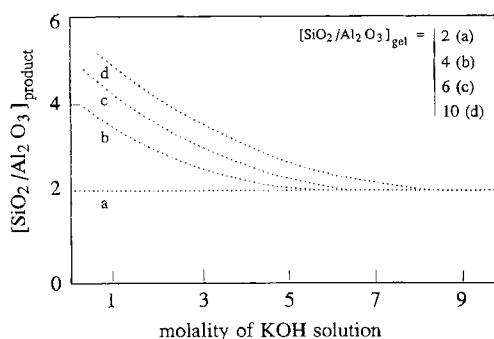
The dissolution of the gel, catalyzed by  $\text{OH}^-$ , proceeds via the nucleophilic  $\text{S}_{\text{N}}2$  mechanism depicted in Scheme 2a. The fivefold coordination state of  $\text{Si}^{\text{IV}}$  in the transition state weakens the siloxane bonds [32]. Condensation occurs via an attack of a nucleophilic deprotonated silanol group on a neutral species, as explained in Scheme 2b [32].

During zeolite crystallization from aluminosilicate gels under basic conditions, there are changes in pH [33, 34]. Figure 8 illustrates this pH variation for the synthesis of EU-1 [33]. First, the pH drops as a result of the hydrolysis of the amorphous aluminosilicate, consuming hydroxy ions. Upon formation of crystals through condensation reactions, the pH increases. During the condensation reaction, hydroxy ligands are expelled upon formation of the oxo ( $-\text{O}-$ ) bridges of the zeolite framework (Scheme 2b). The pH jump coincides with the period of autocatalytic crystal growth (Fig. 8). It is even possible to use this pH change as a simple and rapid method with which to follow the course of crystallization [33].

Another important feature of the alkalinity of aluminosilicate gels is that it



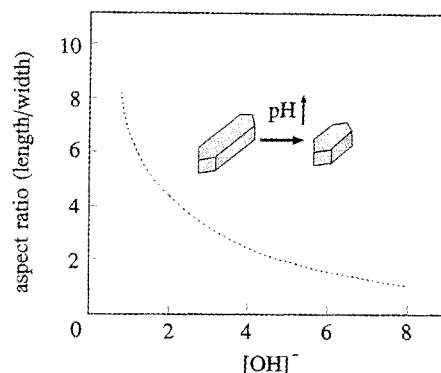
**Figure 8.** pH variation and crystallization curve for the synthesis of zeolite EU-1 (after Ref. 33).



**Figure 9.** Illustration of the influence of the alkalinity of the synthesis hydrogel on the lattice Si:Al ratio of the products formed, for the synthesis of chabazite and edingtonite type zeolites from hydrogels containing various relative amounts of Si and Al (after Ref. 2).

influences the Si:Al ratio of the crystalline product. The average Si:Al ratio in the zeolite shows a tendency to decrease with increasing pH of the synthesis hydrogel [8, 22], as depicted in Fig. 9 for the crystallization of chabazite- and edingtonite-type zeolites from hydrogels with different  $\text{SiO}_2:\text{Al}_2\text{O}_3$  ratios. This is readily explained by a nucleophilic condensation mechanism which involves  $\text{Si-O}^-$  and/or  $\text{Si-OH}$  functions. At increasing pH, the silicate species are more deprotonated. The reaction rate of condensation of silicate species with other silicate species is decreased because the dissociated hydroxy ligands are poor leaving groups. Within the range of effective pH conditions,  $\text{Al}^{\text{III}}$  is present in solution as the aluminate anion  $\text{Al}(\text{OH})_4^-$  and the condensation rate of silicates with the aluminate anion is less influenced by the pH [8, 22]. For faujasite-type zeolites, the very slow linear crystal growth rates for siliceous polytypes (crystallized from inorganic hydrogels) appear to place an upper limit to the Si:Al lattice ratios for the crystals (maximum Si:Al ratio of  $\approx 3.0$ ) obtainable in a reasonable period of time [2]. The lower limit for the lattice Si:Al ratio of aluminosilicate zeolites crystallized in alkaline media is 1.0, as the formation  $\text{Al-O-Al}$  bondings is avoided according to the Löwenstein rule [35]. Aluminosilicate zeolites with an Si:Al ratio of 1.0 are crystallized in very alkaline media where, for kinetic reasons, the silicate monomer only condenses with the aluminate.

The last effect of alkalinity on zeolitization to be discussed is its influence on crystal morphology in general and crystal aspect ratio in particular.

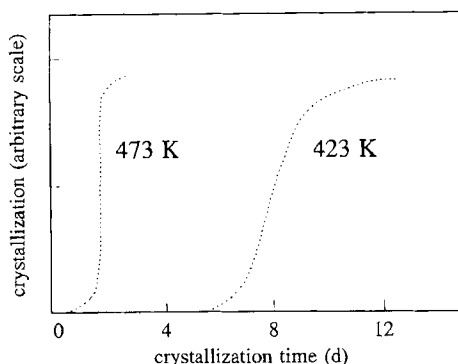


**Figure 10.** Influence of the alkalinity of the hydrogel on the crystal aspect ratio for the synthesis of silicalite-1 crystals (after Ref. 37).

As highly alkaline synthesis gels increase the supersaturation degree and enhance nucleation and crystallization kinetics, fast and massive nucleation is to be expected as well as an increased crystal growth rate. As a result, the crystals usually are morphologically not well defined. At high alkalinity, the crystals sometimes redissolve partially, and this way the crystal morphology can be totally changed. The alkalinity might also alter the shape of the crystals, as is illustrated by its effect on the aspect ratio (length:width) of silicalite-1 crystals in Fig. 10. The aspect ratio drops upon increasing the alkalinity of the solution (the length of the crystals decreases relative to their width).

A separate analysis of the growth rates along the crystal length and width showed that the rate of crystal growth along the  $c$  axis was relatively independent of the hydroxide concentration. The rate of crystal growth, measured along the width ( $a$  and  $b$  crystallographic directions) was found to be strongly dependent on the reaction mixture alkalinity (this rate was found to decrease in a nonlinear fashion with the pH). The role of alkalinity in crystal growth along the  $a$  and  $b$  axes is fundamentally different from that for  $c$  axis growth.

As reaction rates correlate directly with the concentration of precursor species, the difference in growth rate along the different axes may be attributed to different silicate species participating in growth along the different axes. For silicalite-1, the observations were rationalized by a detailed crystallization mechanism [35, 36]. In this model, it is proposed that multiple condensations of double five-ring (d5r) units lead to the formation of so-called pentasil chains, stretching in the  $c$  direction. Crystal growth in the  $c$  direction corresponds to elongation of pentasil chains by addition of d5r units, whereas growth in the other directions involves side-by-side condensation of the chains. After the linking of the chains, some silicate monomers are systematically missing. Completing the structure requires cementing together of the chains with monomeric silicate species. The increased growth rate along the  $a$  and  $b$  axes with increasing  $\text{OH}^-$  concentration can be explained by the increased concentration of monomeric Si units. The constant growth rate along the  $c$  axis points to the existence of a constant concentration of d5r units in solution, independent of the pH.



**Figure 11.** Impact of temperature on crystallization kinetics of zeolite mordenite (after Ref. 2, p. 145).

### C Temperature and Time

In general, as crystallization is an activated process, within certain limits temperature has a positive influence on the zeolitization process. Crystal growth rates are currently expressed as linear growth rates (calculated as  $k = 0.5\delta l/\delta t$  with  $l$  = crystal length). Increasing the temperature results in steeper crystallization curves, shifted towards shorter crystallization times, as illustrated for the synthesis of mordenite in Fig. 11.

The temperature also influences the type of zeolite to crystallize. Increasing temperatures give rise to denser phases, as under hydrothermal synthesis conditions the fraction of water in the liquid phase, which has to stabilize the porous products by filling the pores, becomes lower. Therefore, there exists an upper temperature limit for the formation of each specific zeolite, and of zeolites in general [2, 38]. The use of nonvolatile microvoid filling molecules substituting the water would allow, at least in principle, high-temperature synthesis of open, porous structures [2].

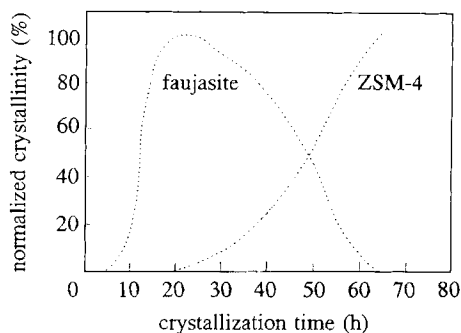
Since in the course of crystallization the solid product is a mixture of zeolite and unreacted amorphous solids, the crystallinity of the product increases with time. However, zeolites are metastable phases and zeolite crystallization is governed by the occurrence of successive phase transformations (Ostwald's rule of successive phase transformations). The thermodynamically least favorable phase crystallizes first, and is successively replaced, in time, by more stable (and often denser) phases [2]. A typical example is the crystallization sequence  $\text{NaY} \rightarrow \text{Na-P}$  (gismondine type) [7, 2], or  $\text{NaY} \rightarrow \text{ZSM-4}$  (Fig. 12) [39].

### D Templates

Templates, sometimes called "structure-directing agents", are agents which in general kinetic and thermodynamic terms contribute to the formation of the zeolite lattice during the zeolitization process in several way:

- (i) They influence the gelation, nucleation and crystal growth processes – the aluminosilicate oligomers are organized into a particular geometry around template molecules and, as a result, provide precursor species for nucleation and growth of the templated structure [10, 40].

**Figure 12.** Example of Ostwald's rule of successive phase transformations: the less stable faujasite phase is replaced in time by the more stable product ZSM-4 (hydrogels containing  $\text{TMA}^+$  cations, after Ref. 39).



- (ii) They lower the chemical potential of the zeolite by lowering the interfacial energy.

Template inclusion in the zeolite micropores contributes to the stability by new interactions (hydrogen bonding, electrostatic and dispersion interactions). It controls the formation of a particular topology through geometrical factors (form and size) [22]. It is evident that changes in the cation density provoked by geometrical or physical properties of the template will be reflected in the chemical composition (Si:Al ratio) of a given topology.

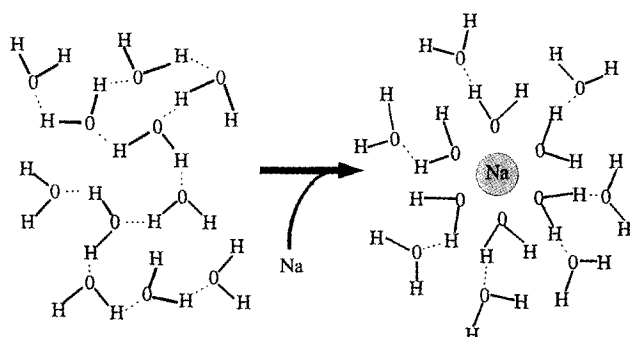
So far, it has not been possible to predict which template is required for a given structure and composition [22]. In selecting possible templates, however, one has to bear in mind some general criteria regarding the templating potential in zeolitization, such as solubility in the solution, stability under synthesis conditions, steric compatibility and possible framework stabilization [22]. The possibility of removing the template without destroying the framework can be an important practical issue [22].

Neutral molecules as well as cations or ion pairs are able to fulfill this structure- and composition-directing function. Each of these three types can be organic or inorganic in nature.

#### *(i) Charged Molecules*

The majority of structure-directing agents used in zeolite synthesis are positively charged molecules. These cations not only function as structure- and composition-directing agents but also positively influence the rate of crystallization [2, 13]. Inorganic as well as organic cations are frequently used and comprise species such as  $\text{Na}^+$ ,  $\text{Li}^+$ ,  $\text{Cs}^+$ ,  $\text{K}^+$ ,  $\text{Rb}^+$ ,  $\text{Ca}^{2+}$ ,  $\text{Sr}^{2+}$ , tetraalkylammonium cations (e.g. tetramethylammonium ( $\text{TMA}^+$ ), tetraethylammonium ( $\text{TEA}^+$ ), tetrapropylammonium ( $\text{TPA}^+$ ) or dihydroxyethyltrimethylammonium), dialkyl and trialkyl amines, and phosphonium compounds [8, 18, 32]. A special case are the crown ethers as these neutral molecules form charged complexes upon complexation of an alkali metal cation in the central cavity [22, 34].

According to Vaughan's extended structure approach already mentioned [18], the nature of the phase(s) that crystallize from aluminosilicate hydrogels depends on the kind of primary ( $\text{Na}^+$  or  $\text{K}^+$ ) and secondary cations present. Primary cations con-



**Figure 13.** Structure-making interaction of a sodium cation and water molecules (dotted lines indicate hydrogen bonds). Note that the first hydration sphere of the (six) water molecules around sodium has an octahedral configuration (reproduced from Ref. 3 with the permission of Elsevier Science).

trol the formation of extended structures, while the secondary cations influence the way in which these extended structures condense. If the primary cation is sodium, layer structures (FAU, EMT and their intergrowths, based on FAU sheets, and MAZ, ECR-1 and MOR, based on MAZ sheets) are generated, while columnar structures (LTL, ERI and OFF, based on LTL-type columns) dominate the potassium aluminosilicate system.

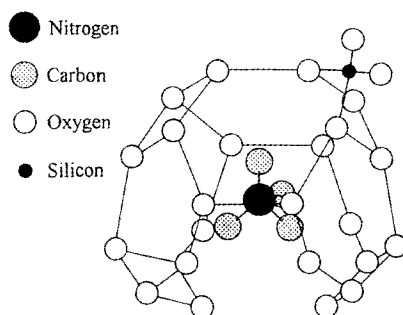
In aqueous solution, cations are known to influence the ordering of water molecules. On the basis of this influence, the cations can be divided into structure-making and structure-breaking agents [10, 13, 41]. Structure-making cations are small cations such as  $\text{Na}^+$  and  $\text{Li}^+$  which interact strongly with water molecules because of their high charge density. As a result of this interaction, the original hydrogen bonds are broken, and the water molecules are strongly organized around the cations [10]. The  $(\text{M}^+ \dots \text{O})$  interaction leads to the formation of a transient network of hydrogen bonded water molecules [13], as illustrated in Fig. 13. Structure-breaking cations are large cations such as  $\text{NH}_4^+$ ,  $\text{K}^+$  and  $\text{Rb}^+$  which interact also with the water molecules, but break the original hydrogen bonds (larger cations would not fit well in the water networks [13]. The interaction of these larger cations with the water molecules is not strong enough to form an organized water cluster [10].

Not all larger cations, however, have a structure-breaking influence on the dynamic molecular water networks. Cations such as tetraalkylammonium organize the water structure [10, 13, 42]. The hydrophobic character of the alkyl chains is responsible for a water-organizing effect. Near the alkyl groups, there is less disruption of the water network [13]. This way, these organic cations tend to be surrounded with many (organized) water molecules in clathrate-like structures [10, 13, 32].

The organized network of water molecules surrounding the cations can be (partially) replaced by silicate and aluminate tetrahedra (the oxygen of silica replaces the oxygen of water) and this way contribute to the formation of cage-like struc-



**Figure 14.** Illustration of water network formation around a  $\text{TMA}^+$  cation; replacement of water molecules by  $\text{SiO}_4$  tetrahedra might result in the formation of sodalite-type cage structures (H atoms are not shown) [13, 41, 43].



tures [13, 32]. An example of the templated formation of a cage by clathrated cations is the formation of sodalite using tetramethylammonium ( $\text{TMA}^+$ ) cations, as illustrated in Fig. 14.

The selective formation (stabilization) of particular silicate structures in quaternary ammonium ion-containing silicate solutions (e.g. cubic octamer at low temperatures) can be inhibited by the presence of alkali metal ions [42]. The disturbed interaction between the organic cations and the water molecules by the hydration of the alkali metals might be responsible for this inhibition [42].

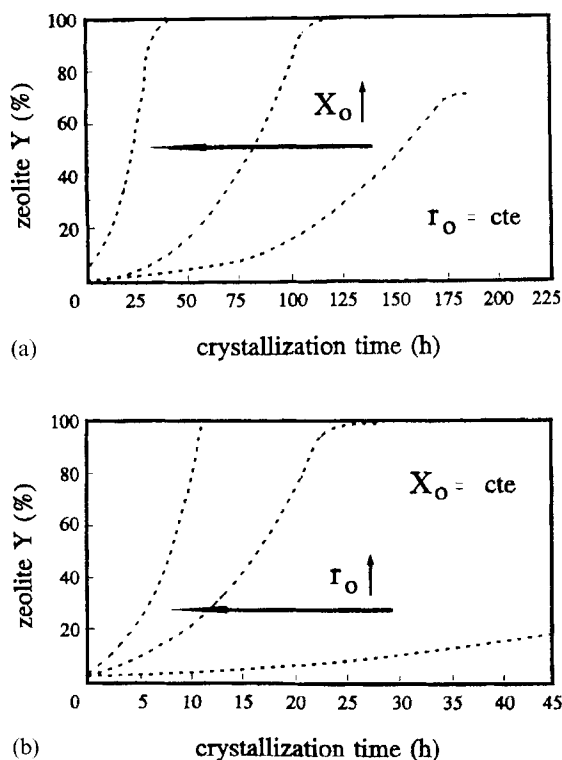
McCormick et al. [44] proposed an additional role for cationic templates. By using  $^{29}\text{Si}$  NMR, they observed an increase in the amount of cage-like structures for alkali metal-containing silicate solutions with increasing cation size. As for a fixed silicate ratio, changes in the alkalinity of the mixture are negligible by using alkali cations with different sizes, this effect was attributed to cation–anion interactions. This interaction was confirmed using NMR spectroscopy by its effect on the chemical shift and the spin-relaxation time of the alkali metal cations. In such solutions, the larger silicate structures interact more selectively with larger cations. The selective cation–anion pair formation is believed to cause a stabilization of particular silicate species, and by this, direct the zeolite synthesis [13, 44].

### (ii) Neutral Molecules

The most important molecule in this class of templating species is the water molecule. Next to its templating effect by interaction with cations, as discussed above, and its solvating and hydrolyzing ability which are of key importance in zeolite synthesis (hydrothermal zeolite synthesis proceeds in aqueous media), it enhances the formation of a zeolitic structure during crystal growth by filling the (micro)pore system, as a guest molecule, thereby stabilizing the porous oxide frameworks [2]. Other neutral templating molecules are amines, ethers and alcohols [22, 32].

### (iii) Ion Pairs

Salts (e.g.,  $\text{NaCl}$ ,  $\text{KCl}$ ,  $\text{KBr}$ ,  $\text{CaF}_2$ ,  $\text{BaCl}_2$ ,  $\text{BaBr}_2$ ) can be occluded as ion pairs (possibly next to water molecules) into the zeolite micropore system, thereby stabilizing the zeolite [8, 2, 22]. As mentioned already, these nonvolatile space-filling species can be used in high-temperature zeolite synthesis applications. When salts



**Figure 15.** The addition of seed crystals (NaX nuclei) affects the crystallization kinetics of NaY: (a) increasing the total amount of seed crystals ( $X_0$ ) with a constant radius ( $r_0$ ) favors crystallization; (b) a constant amount of seed crystals with decreasing radius also enhances the formation of crystalline material (note that next to NaY, NaP was sometimes co-crystallized, after Ref. 23).

are present, and are catalyzing the zeolitization, they may cause the formation of specific zeolites, improve crystallization yield, and even improve crystallinity [8].

### E Seeding

Seeding is a technique in which the supersaturated system is inoculated with small particles of material to be crystallized [20]. These seed particles (crystals) increase in size, as crystalline material is deposited on them [8]. By a seeding operation, the nucleation stage is bypassed and the induction period is eliminated [13].

As the surface area provided by the seed crystals is larger than that provided by fresh nuclei, the seeding technique provides favorable conditions for measuring linear growth rates [2]. Examples of seeds are crystals for the crystallization of NaY-type zeolites, aged hydrogels, and mother liquor from a previous crystallization [2].

Figure 15 illustrates the effect of seeding on the crystallization kinetics of NaY [23]. The impact of the amount of seed crystals added is illustrated in Fig. 15(a). Increasing the amount of seeds clearly enhances crystallization, as demonstrated by the shift of the crystallization curve towards shorter crystallization times. In another set of experiments, a same weight of seed crystals was added, but with a different crystal size (Fig. 15(b)). The zeolitization proceeds faster with the smallest crystals, exposing the largest surface area.

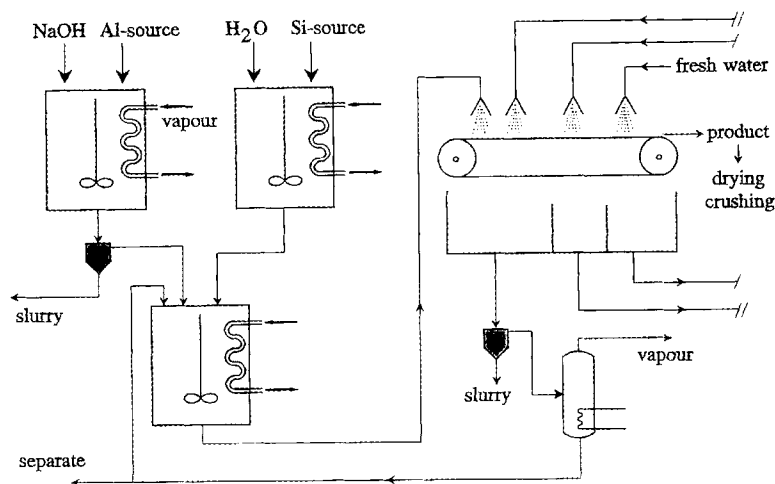
### 3.11.2.3 Zeolitization in Nonaqueous and Acid Media

The choice of a mineralizing agent is not limited to  $\text{OH}^-$  anions. Indeed,  $\text{F}^-$  anions can fulfill this catalytic function as well, allowing zeolitization in acid media. The use of  $\text{F}^-$  anions increases the solubility of certain tri- and tetravalent elements (e.g.  $\text{Ga}^{\text{III}}$  and  $\text{Ti}^{\text{IV}}$ ) through complexation [22, 32]. However, when present in higher concentration,  $\text{F}^-$  anions will inhibit condensation reactions since it is retained in the coordination sphere [32]. According to Guth et al. [22], an increasing  $\text{F}^-$  concentration tends to change the tetrahedral configuration towards an octahedral one for Si and Al complexes. The amount of  $\text{F}^-$  used in zeolite synthesis is limited; generally, no highly supersaturated solutions are involved (avoiding sudden massive nucleation and this way generating a large number of small crystals). Therefore, the crystallization process is more easily controlled (with respect to crystal size and morphology) and the crystals formed in these solutions contain less structural defects. A disadvantage is the longer crystallization period required [22]. Using  $\text{F}^-$  anions, the incorporation of elements such as  $\text{Co}^{\text{II}}$  with a poor solubility in highly alkaline solutions is possible [22]. Examples of fluoride-mediated zeolite crystallizations are those of silica-rich ZSM-5 and ZSM-23 [32].

So far, the use of aqueous media has been very successful for growing zeolites. Nevertheless, it is possible to grow zeolites in other, nonaqueous media such as alcohols (e.g. hydroxysodalite in glycol or ethanol) [32]. The potential use of such solvents in zeolitization is influenced by their viscosity and their relative electric permittivity. This latter property greatly influences the solvating capacity [32]. Recently, a synthesis method for the preparation of giant (millimeter scale!) and morphologically well defined crystals in nonaqueous media was reported by Kuperman et al. [45]. Examples of solvents from which large crystals have been synthesized are pyridine, triethylamine and polyethylene glycol. Next to a mineralizer and optional templating species, water has been added in the stoichiometric amounts necessary for the dissolution of the silicon and aluminum sources. HF-pyridine and HF-alkylamines are claimed to be novel mineralizers by acting as reservoirs for anhydrous HF in the organic solvent, thereby allowing the amount of reactant water to be controlled.

### 3.11.3 Synthesis of Industrial Zeolites

The industrial importance of zeolites can be attributed to their high surface areas in combination with their chemical nature. Indeed, both material features make them suited as cation exchangers (zeolite A in laundry powder), sorbents (zeolite A and X) or as catalysts (ultrastable zeolite Y, ZSM-5 and TS-1). The zeolite types mentioned here are currently prepared on an industrial scale. Figure 16 shows a schematic setup for the industrial preparation of a sodium aluminosilicate zeolite [46]. In a first reactor, a sodium aluminate solution is prepared by mixing an aluminum source (e.g. gibbsite) with a NaOH solution. This alkaline solution is mixed with a silicon-containing solution (e.g. waterglass or colloidal silica). The mixed solution is heated to the crystallization temperature by steam. After crystallization, the zeolite



**Figure 16.** Schematic representation of an industrial sodium aluminosilicate zeolite manufacturing process (after Ref. 46).

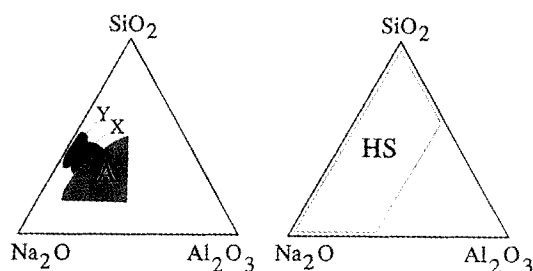
suspension is filtered and washed. The product is finally spray-dried. The alkaline mother liquor is concentrated through heating, and is re-entered into the synthesis process. This way, no byproducts are formed. Zeolites are usually crystallized in batch reactors under one of the following conditions [47]:

- (i) 90–100 °C, atmospheric pressure, pH > 10;
- (ii) 140–180 °C, autogenous water pressure (5–10 bar, closed vessels), pH > 10;
- (iii) 100–180 °C, water + “amine”, autogenous pressure, pH > 10.

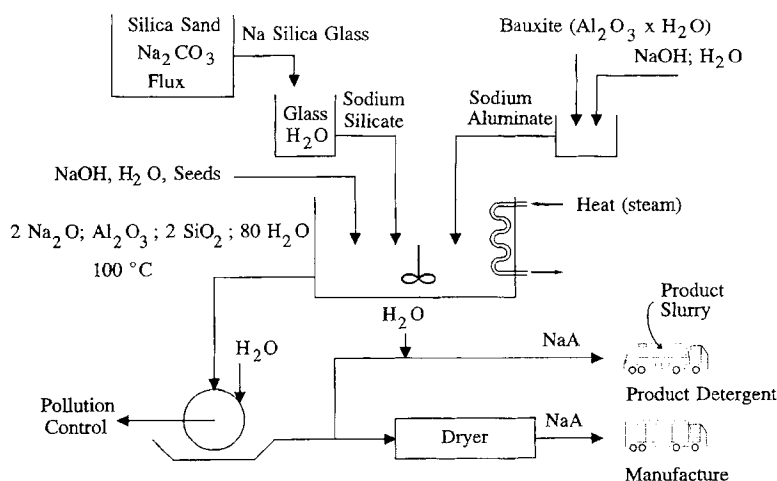
Open tank crystallization reactors and high pressure autoclaves are used, with capacities of up to 38 m<sup>3</sup> and with a volumetric product yield ranging from 10 to 120 kg m<sup>-3</sup> [47, 48].

### 3.11.3.1 Industrial Zeolites Crystallized from the Na<sub>2</sub>O–Al<sub>2</sub>O<sub>3</sub>–SiO<sub>2</sub>–H<sub>2</sub>O System: Zeolites A, X, Y, Mordenite and ZSM-5

The industrially relevant type A, X and Y zeolites crystallize from sodium containing aluminosilicate hydrogels. The molar compositional ranges for the crystallization of these three zeolite types are best illustrated by the compositional diagrams of Fig. 17, where sodium silicate is used as the silicon source [4]. The water content of the gel is between 90 and 98 mol %. The diagrams show that a decreasing aluminum fraction in the gel promotes the formation of zeolite X and eventually zeolite Y instead of zeolite A. Zeolite X and, especially, zeolite Y are indeed known to contain more silicon than zeolite A. The water content in these synthesis hydrogels, or the reactant concentration, is the key to the type of zeolite formed. Figure 17(b) illus-



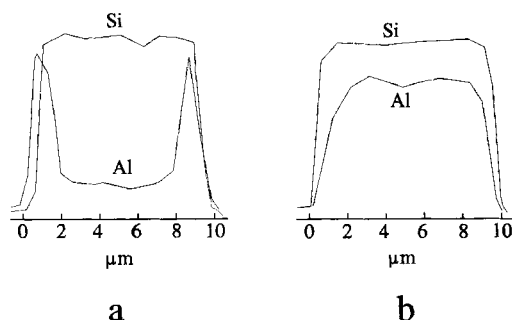
**Figure 17.** Ternary diagram indicating different zeolites crystallized from an inorganic Sodium aluminosilicate gel with a water content of (a) 90–98 mol % and (b) 60–85 mol % (b); Si source is sodium silicate, HS = hydroxysodalite (after Ref. 4).



**Figure 18.** Manufacturing process for type A zeolite (after Ref. 47).

trates the effect of a reduction of the water content to 60–85 mol %. No zeolites are formed, rather, the dense hydroxysodalite phase is formed. In addition to gel composition, the type of zeolite formed is also influenced by the crystallization temperature. The crystallization time for zeolite X, for instance, is reduced from 800 h at 298 K to 6 h at 373 K [4]. At increasing temperatures ( $>423 \text{ K}$ ), the formation of X and Y zeolites is inhibited, and zeolite P becomes the dominant phase [4].

Crystallization is greatly influenced by the nature of the reactants used to make the gel. The use of a colloidal silica sol might provoke the crystallization of zeolite Y from gel compositions which yield zeolite P in the soluble silicate system [4]. In industrial zeolite Y manufacturing processes, the seeding technique is currently applied to facilitate crystallization. Figure 18 schematically shows a typical manufacturing process for the industrially important type A zeolite, which is used in gas drying, the separation of iso and normal alkanes, and detergent water softening



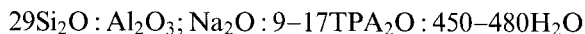
**Figure 19.** Aluminum zoning in MFI-type crystals synthesized in the presence of (a)  $\text{TPA}^+$  and (b) in the absence of any organic molecule (after Ref. 51).

[47]. Zeolites ZSM-5 (MFI type) and mordenite are also crystallized from diluted sodium aluminosilicate gels [5, 49]. Increasing the  $\text{Na}_2\text{O}:\text{SiO}_2$  ratio or decreasing the  $\text{SiO}_2:\text{Al}_2\text{O}_3$  ratio favors the phase transformation  $\text{ZSM-5} \rightarrow \text{mordenite}$  [49]. The production of MFI-type zeolites from inorganic media requires high temperatures ( $>473\text{ K}$ ); the typical framework Si:Al ratio obtained is  $\approx 13$  [50, 51]. Zeolites of the MFI type are most often crystallized in the presence of quaternary ammonium cations or other organic molecules [5], as discussed below.

### 3.11.3.2 Industrial Zeolite Crystallization in the Presence of Organic Compounds: ZSM-5, TS-1

For the preparation of zeolite ZSM-5 (MFI type), the  $\text{TPA}^+$  (tetrapropylammonium) cation is the most popular organic template. Yet, this product is also known to be formed in the presence of  $\text{TEPA}^+$  (triethylpropylammonium) and  $\text{TPMA}^+$  (tripropylmethylammonium) cations as well as with amines, alcohols and many other organic molecules [5].

The MFI-type zeolites crystallized in the presence of  $\text{TPA}^+$  exhibit an Al zoning in the zeolite crystals, opposite to that present in crystals synthesized from inorganic gels [51] (Fig. 19). This aluminum zoning is reflected in the catalytic performances [51]. The typical gel composition according to examples from the original Argauer and Landolt patent [52] is given by



Many gel compositions, however, have been found to yield ZSM-5 type zeolites [5]. In particular, the  $\text{H}_2\text{O}:\text{SiO}_2$  ratio does not seem critical for the crystallization of ZSM-5. Indeed, this ratio has been varied between 7 and 122 [5].

Another important member of the MFI family of materials is a titanosilicate, designated TS-1. This material is applied as a partial oxidation/oxygenation catalyst and is also synthesized in the presence of  $\text{TPA}^+$  cations. The molar gel composition, according to the patent of Taramasso et al. [53], is given in Table 2. The success of a TS-1 preparation is very much dependent on the purity of the source reactants. Indeed, traces of alkali metals present in the reactants impede the insertion of Ti into the silicalite framework [54, 55].

**Table 2.** Molar gel composition and crystallization conditions for the synthesis of zeolite TS-1 [51].

Parameter	Value
SiO <sub>2</sub> :TiO <sub>2</sub>	5–200
OH <sup>−</sup> :SiO <sub>2</sub>	0.1–1.0
H <sub>2</sub> O:SiO <sub>2</sub>	20–200
TPA <sup>+</sup> :SiO <sub>2</sub>	0.4–1.0
Crystallization time	6–30 days
Crystallization temperature	403–473 K

## Acknowledgments

E. J. P. F. acknowledges K. V. Leuven for a postdoctoral fellowship, J. A. M. the Flemish N. F. W. O. for a permanent research position.

## References

1. R. M. Milton *ACS Symp. Ser.*, **1989**, Vol. 398, p. 1.
2. R. M. Barrer, *Hydrothermal Chemistry of Zeolites*, Academic Press, London, **1982**.
3. E. J. P. Feijen, J. A. Martens, P. A. Jacobs *Stud. Surf. Sci. Catal.*, **1994**, 84, 3.
4. D. W. Breck *Zeolite Molecular Sieves: Structure, Chemistry and Use*, Wiley, New York, **1973**.
5. J. A. Martens, P. A. Jacobs *Stud. Surf. Sci. Catal.*, **1987**, 33.
6. M. L. Occelli, H. E. Robson, Eds: *ACS Symp. Ser.*, **1989**, Vol. 398.
7. A. Katovic, B. Subotic, I. Smit, Lj. A. Despotovic, M. Curic, *ACS Symp. Ser.*, **1989**, Vol. 398, p. 124.
8. R. M. Barrer, *Zeolites*, **1981**, 1, 130–140.
9. D. M. Ginter, C. J. Radke, A. T. Bell in *Zeolites: Facts, Figures, Future* (Eds: P. A. Jacobs, R. A. van Santen), Elsevier Science, Amsterdam, **1989**, p. 161.
10. J. P. Gilson *NATO ASI Ser.* **1992**, Vol. 352, p. 19.
11. C. T. G. Knight, R. J. Kirkpatrick, E. Oldfield, *J. Magn. Reson.*, **1988**, 79, 31–40.
12. J. Livage *Stud. Surf. Sci. Catal.*, **1994**, 85, 1.
13. A. V. McCormick, A. T. Bell, *Catal. Rev.-Sci. Eng.*, **1989**, 31, 97–127.
14. J. L. Guth, P. Caullet, P. Jacques, R. Wey, *Bull. Soc. Chim. Fr.*, **1980**, 3–4, 121–126.
15. G. Harvey, L. S. D. Glasser, *ACS Symp. Ser.* **1989**, Vol. 398, p. 49.
16. A. T. Bell, *ACS Symp. Ser.* **1989**, Vol. 398, p. 66.
17. W. M. Meier, *Molecular Sieves*, Society of Chemical Industry, London, **1968**, p. 10.
18. D. E. W. Vaughan, in *Catalysis and Adsorption by Zeolites* (Eds: G. Öhlmann, H. Pfeifer, R. Fricke), Elsevier Science, Amsterdam, **1991**, p. 275.
19. P. K. Dutta, D. C. Shieh, M. Puri, *J. Phys. Chem.*, **1978**, 91, 2332–2336.
20. P. A. Jacobs, *NATO ASI Ser.*, **1992**, Vol. 352, p. 3.
21. S. P. Zhadanov, N. N. Samulevich, in *Proceedings of the 5th International Zeolite Conference* (Ed.: L. V. C. Rees), Heyden, London, **1980**, p. 75.
22. J. L. Guth, P. Caullet, A. Seive, J. Patarin, F. Delprato, *NATO ASI Ser.*, **1990**, Vol. 221, p. 69.
23. H. Kacirek, H. Lechert, *J. Phys. Chem.*, **1975**, 79, 1589–593.
24. Gabelica Z., Dewaele N., Maistriau L., B. Nagy J., Derouane E. G., *ACS Symp. Ser.*, **1989**, Vol. 398, p. 518.
25. F.-Y. Dai, M. Suzuki, H. Takahashi, Y. Saito, in *Proceedings of the 7th International Zeolite Conference*, (Eds: Y. Murakami, A. Iijima, J. W. Ward), Elsevier, Amsterdam, **1986**, p. 223.
26. R. M. Barrer, W. Sieber, *J. Chem. Soc., Dalton Trans.*, **1977**, 1020–1026.
27. M. A. Camblor, A. Mifsud, J. Perez-Pariente, *Zeolites*, **1991**, 11, 792–797.

28. G. Zi, T. Dake, Z. Ruiming, *Zeolites*, **1988**, 8, 453–457.
29. E. J. P. Feijen, K. De Vadder, M. H. Bosschaerts, J. L. Lievens, J. A. Martens, P. J. Grobet, P. A. Jacobs, *J. Am. Chem. Soc.*, **1994**, 116, 2950–2957.
30. U. Mueller, K. Unger, *Zeolites*, **1988**, 8, 154–156.
31. J. Dwyer, K. Karim, W. J. Smith, N. E. Thompson, R. K. Harris, D. C. Apperley, *J. Phys. Chem.*, **1991**, 95, 8826–8831.
32. J. C. Jansen, in *Introduction to Zeolite Science and Practice* (Eds: H. van Bekkum, E. M. Flanigen, J. C. Jansen), Elsevier Science, Amsterdam, **1991**, p. 77.
33. J. L. Casci, B. M. Lowe, *Zeolites*, **1983**, 3, 186.
34. F. Delprato, L. Delmotte, J. L. Guth, L. Huve, *Zeolites*, **1990**, 10, 546–552.
35. W. Löwenstein, *Amer. Mineral.*, **1954**, 39, 92–96.
36. R. A. Van Santen, J. Keijsper, G. Ooms, A. G. T. G. Kortbeek in *Proceedings of the 7th International Zeolite Conference*, (Eds: Y. Murakami, A. Iijima, J. W. Ward), Elsevier, Amsterdam **1986**, p. 169.
37. D. T. Hayhurst, A. Nastro, R. Aiello, F. Crea, G. Giordano, *Zeolites*, **1988**, 8, 416–422.
38. B. Stringham, *Econ. Geol.*, **1952**, 47, 661.
39. F. G. Dwyer, P. Chu, *J. Catal.*, **1979**, 59, 263–271.
40. B. M. Lok, T. R. Cannan, C. A. Messina, *Zeolites*, **1983**, 3, 282–291.
41. R. K. Iler, *The Chemistry of Silica*, Wiley, New York, **1979**.
42. I. Hasegawa, S. Sakka, *ACS Symp. Ser.*, **1989**, Vol. 398, p. 140.
43. R. K. McMullan, T. C. W. Mak, G. A. Jeffrey, *J. Chem. Phys.*, **1966**, 44, 2338–2345.
44. A. V. McCormick, A. T. Bell, C. J. Radke, *ACS Symp. Ser.*, **1988**, Vol. 368, p. 222.
45. A. Kuperman, S. Nadimi, S. Oliver, G. A. Ozin, J. M. Garcés, M. M. Olken, *Nature*, **1993**, 365, 239–242.
46. P. Kripylo, K.-P. Wendlandt, F. Vogt, *Heterogene Katalyse in der Chemischen Technik*, Deutscher Verlag für Grundstoffindustrie, Leipzig, Stuttgart, **1993**.
47. D. E. W. Vaughan, *Chem. Eng. Prog.*, **1988**, 8, 25–31.
48. N. Y. Chen, Th. F. Degnan Jr., C. Morris-Smith, *Molecular Transport and Reaction in Zeolites. Design and Application of Shape Selective Catalysts*, VCH, Weinheim, **1994**, p. 20.
49. F.-Y. Dai, M. Suzuki, H. Takahashi and Y. Saito, *ACS Symp. Ser.*, **1989**, Vol. 398, p. 245.
50. U. Müller, A. Brenner, A. Reich, K. K. Unger, *ACS Symp. Ser.*, **1989**, Vol. 398, p. 346.
51. A. Tissler, P. Polanek, U. Girkbach, U. Müller, K. K. Unger in *Zeolites as Catalysts, Sorbents and Detergent Builders* (Eds: H. G. Karge, J. Weitkamp), Elsevier Science, Amsterdam, **1989**, p. 399.
52. R. J. Argauer, G. R. Landolt, US Patent 3 702 886 **1972** (Mobil Oil).
53. M. Taramasso, G. Perego, B. Notari, US Patent 4 410 501 (**1981**).
54. D. R. C. Huybrechts, R. F. Parton, P. A. Jacobs, *Stud. Surf. Sci. Catal.*, **1991**, 60, 225.
55. G. Bellussi, V. Fattore, *Stud. Surf. Sci. Catal.*, **1991**, 69, 79.

## 3.12 Pillared Clays

J. J. FRIPIAT

### 3.12.1 Introduction

#### 3.12.1.1 Historical Overview

In the history of acid catalysis, clays have played an important role in the past. Acid leaching of natural smectites led to amorphous aluminosilicates with a large acid



28. G. Zi, T. Dake, Z. Ruiming, *Zeolites*, **1988**, 8, 453–457.
29. E. J. P. Feijen, K. De Vadder, M. H. Bosschaerts, J. L. Lievens, J. A. Martens, P. J. Grobet, P. A. Jacobs, *J. Am. Chem. Soc.*, **1994**, 116, 2950–2957.
30. U. Mueller, K. Unger, *Zeolites*, **1988**, 8, 154–156.
31. J. Dwyer, K. Karim, W. J. Smith, N. E. Thompson, R. K. Harris, D. C. Apperley, *J. Phys. Chem.*, **1991**, 95, 8826–8831.
32. J. C. Jansen, in *Introduction to Zeolite Science and Practice* (Eds: H. van Bekkum, E. M. Flanigen, J. C. Jansen), Elsevier Science, Amsterdam, **1991**, p. 77.
33. J. L. Casci, B. M. Lowe, *Zeolites*, **1983**, 3, 186.
34. F. Delprato, L. Delmotte, J. L. Guth, L. Huve, *Zeolites*, **1990**, 10, 546–552.
35. W. Löwenstein, *Amer. Mineral.*, **1954**, 39, 92–96.
36. R. A. Van Santen, J. Keijsper, G. Ooms, A. G. T. G. Kortbeek in *Proceedings of the 7th International Zeolite Conference*, (Eds: Y. Murakami, A. Iijima, J. W. Ward), Elsevier, Amsterdam **1986**, p. 169.
37. D. T. Hayhurst, A. Nastro, R. Aiello, F. Crea, G. Giordano, *Zeolites*, **1988**, 8, 416–422.
38. B. Stringham, *Econ. Geol.*, **1952**, 47, 661.
39. F. G. Dwyer, P. Chu, *J. Catal.*, **1979**, 59, 263–271.
40. B. M. Lok, T. R. Cannan, C. A. Messina, *Zeolites*, **1983**, 3, 282–291.
41. R. K. Iler, *The Chemistry of Silica*, Wiley, New York, **1979**.
42. I. Hasegawa, S. Sakka, *ACS Symp. Ser.*, **1989**, Vol. 398, p. 140.
43. R. K. McMullan, T. C. W. Mak, G. A. Jeffrey, *J. Chem. Phys.*, **1966**, 44, 2338–2345.
44. A. V. McCormick, A. T. Bell, C. J. Radke, *ACS Symp. Ser.*, **1988**, Vol. 368, p. 222.
45. A. Kuperman, S. Nadimi, S. Oliver, G. A. Ozin, J. M. Garcés, M. M. Olken, *Nature*, **1993**, 365, 239–242.
46. P. Kripylo, K.-P. Wendlandt, F. Vogt, *Heterogene Katalyse in der Chemischen Technik*, Deutscher Verlag für Grundstoffindustrie, Leipzig, Stuttgart, **1993**.
47. D. E. W. Vaughan, *Chem. Eng. Prog.*, **1988**, 8, 25–31.
48. N. Y. Chen, Th. F. Degnan Jr., C. Morris-Smith, *Molecular Transport and Reaction in Zeolites. Design and Application of Shape Selective Catalysts*, VCH, Weinheim, **1994**, p. 20.
49. F.-Y. Dai, M. Suzuki, H. Takahashi and Y. Saito, *ACS Symp. Ser.*, **1989**, Vol. 398, p. 245.
50. U. Müller, A. Brenner, A. Reich, K. K. Unger, *ACS Symp. Ser.*, **1989**, Vol. 398, p. 346.
51. A. Tissler, P. Polanek, U. Gierbach, U. Müller, K. K. Unger in *Zeolites as Catalysts, Sorbents and Detergent Builders* (Eds: H. G. Karge, J. Weitkamp), Elsevier Science, Amsterdam, **1989**, p. 399.
52. R. J. Argauer, G. R. Landolt, US Patent 3 702 886 **1972** (Mobil Oil).
53. M. Taramasso, G. Perego, B. Notari, US Patent 4 410 501 (**1981**).
54. D. R. C. Huybrechts, R. F. Parton, P. A. Jacobs, *Stud. Surf. Sci. Catal.*, **1991**, 60, 225.
55. G. Bellussi, V. Fattore, *Stud. Surf. Sci. Catal.*, **1991**, 69, 79.

## 3.12 Pillared Clays

J. J. FRIPIAT

### 3.12.1 Introduction

#### 3.12.1.1 Historical Overview

In the history of acid catalysis, clays have played an important role in the past. Acid leaching of natural smectites led to amorphous aluminosilicates with a large acid

surface able to initiate the carbocation chemistry which has so many diverse applications in catalysis. The original Houdry catalyst was prepared in that manner. Due to the variability in composition of naturally occurring smectites, synthetic aluminosilicates obtained through coprecipitation of aluminum and of silicon salts were substituted for the acid-leached clays as soon as the economic constraints of World War II were released. In the 1960s, the amorphous synthetic aluminosilicates were replaced by zeolites when it was realized that the latter were more active and more stable acid catalysts. The stability is of particular importance in the regeneration process. The unaltered smectites were, however, used as acid catalysts in soft chemistry processes, since the interlayer space (see below) can be kept swollen up to 250 °C by using an adequate solvent. The work of Purnell et al. [1] gives many examples of reactions catalyzed by unpillared clays.

The well recognized problem with smectites is the reversibility of the swelling. For instance, in the presence of water vapor the interlayer distance can reach 6 Å, corresponding to the intercalation of two layers of water on a surface area of about 800 m<sup>2</sup> g<sup>-1</sup>. However, such a hydrated surface is not thermally stable, and the interlayer space starts collapsing above ~ 100 °C.

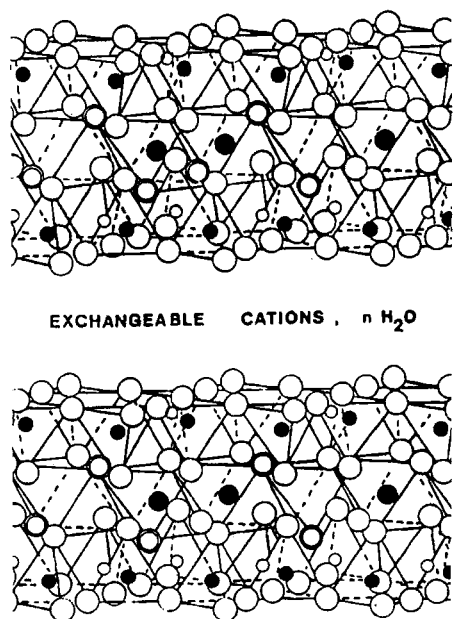
The intercalation of alkylammonium cations, and especially of tetraalkylammonium, as pioneered by Barrer [2] is an easy process, because the clay lattice is negatively charged and a large surface area becomes available in the swollen smectite derivatives. The ammonium cations are not decomposed by moderate heat treatment.

Thus, the use of the beautiful and so flexible architecture of the natural smectites seemed excluded in the harsh conditions of most catalytic reactions involved in petroleum chemistry. Amazingly, the idea to keep the clay layers “permanently expanded” by intercalating robust inorganic pillars came relatively late, and the paternity of the idea is due to Vaughan, Lussier, and Magee [3], and to Brindley and Sempels [4], who, in fact, had combined their efforts. Lahav, Shani, and Shabtai [5] published a pioneering work after the patents were taken but not issued.

Their works were at the origin of a worldwide interest for the so-called pillared clays (PILCS) which have a resemblance to zeolites in the sense that both categories of solids are microporous and can easily be transformed into acid catalysts. To some extent the researchers in the domain of pillared clays were, at least in their early enthusiasm, challenging those in the domain of zeolites. From the theoretical standpoint, large distances between the clay sheets should be obtainable allowing for chemistry of bulky molecules in a large interlayer gallery. This aspect could be an asset for PILCS if heavier oils had to be treated.

So far, it does not appear that such a goal has been achieved. In the meantime, since zeolite chemists have synthesized crystal architectures with larger pores, the future of PILCS is probably restricted to some specialized areas or in areas for which zeolites are too expensive.

A clay is a phyllosilicate made from tetrahedra and octahedra. These building units are organized around at least one (theoretically) infinite tetrahedral layer. Thus, lamellar structures such as double hydroxide and silicic acids are not clays. Only the pillared structures with at least one nonambiguous d001 (X-ray) reflection and a surface area of at least 100 m<sup>2</sup> g after calcination at 200 °C are considered.



**Figure 1.** Basic structure of a smectite. Only two superimposed sheets are shown. Each sheet comprises two layers of tetrahedra “sandwiching” one octahedral layer. Here, two octahedral cavities (●) out of three are occupied (dioctahedral structure). The gallery or interlayer space is the space between sheets where the exchangeable cations are located. The basal 001 plane is made from the oxygen atoms of the tetrahedral layer. The  $c$  axis is perpendicular to 001. (●) and (○) are atoms in the tetrahedral layer in the first and second row, respectively. (○) represents hydroxyls in the octahedral layer.

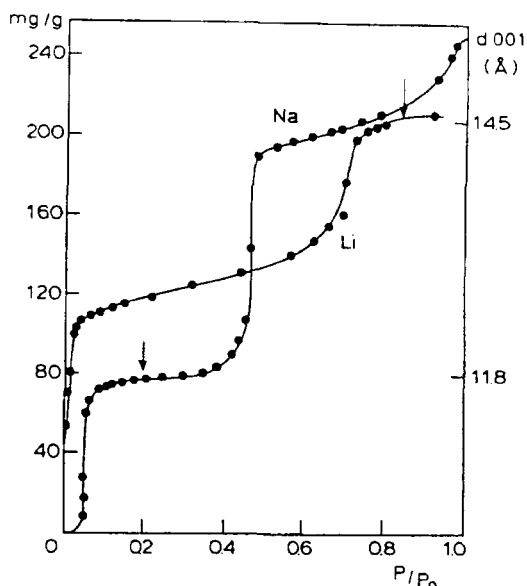
### 3.12.1.2 What are the Clays or Smectites that can be Pillared?

There are excellent books on clay mineralogy that this paragraph does not aim to substitute [6]. However, the further use of mineralogical names and the comprehension of the mechanism of pillaring require a brief summary of the structure of smectites.

All smectites derive from two nonswelling lamellar minerals, namely pyrophyllite or talc (Figure 1). The only structural difference between pyrophyllite and talc is the complete occupation of the octahedral holes in the latter, while in the former two out of three octahedral positions are occupied. For this reason pyrophyllite and talc are called dioctahedral and trioctahedral minerals, respectively, and the clays derived from them keep this distinction. This is not only of academic importance; indeed, trioctahedral minerals are generally more thermally stable than dioctahedral minerals.

As said above, the layers of talc and pyrophyllite cannot be separated. The clay minerals differ from these precursors by the presence of isomorphic substitutions in either the tetrahedral or the octahedral layer or in both. If the substitution intro-

**Figure 2.** Example of the stepwise swelling of a sodium or lithium (Llano) vermiculite upon water adsorption at 25 °C: on the left, weight gain; on the right, d001 spacing. (Reprinted from Ref. 7 with the permission).



duces a cation of lesser valency, a negative charge appears in the lattice which, according to Pauling's principle, must be balanced within the shortest possible distance by a cation. Since clay synthesis occurs in aqueous media in nature, these cations are hydrated. The hydrated cations serve as nuclei for stepwise hydration of the surface as a dehydrated clay is exposed to increasing relative humidity. The successive formation of a single monolayer, or of a two-layer and sometimes of a three-layer hydrate, can be followed by the change in the d001 X-ray spacing, as shown in Figure 2. The thickness of a sheet is about 9.6 Å; the interlayer distance is  $\Delta(\text{Å}) = (d_{001} - 9.6) \text{ Å}$ .

The presence of electric charges in clay lattices, generated by isomorphic substitutions, is at the origin of the cation exchange capacity, just as in zeolites where the charges are created by Si by Al substitutions. In principle, any cation in the interlayer can be replaced by any other, and since the swelling is not limited by a rigid tridimensional architecture as in zeolites, even very bulky complex cations can be used to expand the interlayer gallery over distances which can reach about 2 nm (see below).

Depending upon the nature of the isomorphic substitutions, different clays with more or less charged lattices are obtained. Table 1 gives a short list of the most common ones as well as what is considered as the typical corresponding chemical formula. On the basis of their chemical constitution, mother nature has provided the mineralogist with an endless number of clay family members. If a control of the chemical composition is needed, the synthesis of clays from pure reagents is possible but at a cost larger than the cost of most of the zeolites. The synthesis conditions (temperature and pressure) are more demanding.

In summary, the properties of clays stem from a textural characteristic, the lamellar (or bidimensional) nature of their crystal lattice and from a crystallo-

**Table 1.** Commonly occurring clays.

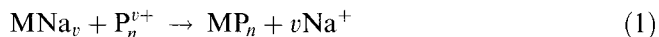
Family	Name	Typical composition
Diocahedral parent: pyrophyllite $x = 0$ mica: muscovite, $K[Si_3, Al]^{IV}[Al_2]^{VI}(OH)_2O_{10}$	$\left\{ \begin{array}{l} \text{montmorillonite} \\ \text{beidellite} \end{array} \right.$	$M_x^+[Si_4]^{IV}[Al_{2-x}R_x^{2+}]^{VI}(OH)_2O_{10}$ $x \approx 1 \quad R^{2+} = Mg^{2+}$ $M_x^+[Si_{4-x}Al_x]^{IV}[Al_2]^{VI}(OH)_2O_{10}$ $x \approx 0.5$
Triocahedral parent: talc $x = y = 0$ mica: phlogophite, $K_x[HSi_{4-x}Al_x]^{IV}[(Mg, Fe^{2+})_3]^{VI}O_{10}(OH, F)_2$	$\left\{ \begin{array}{l} \text{hectorite} \\ \text{saponite} \\ \text{vermiculite} \end{array} \right.$	$M_x^+[Si_4]^{IV}[Mg_{3-x}R_x^{2+}]^{VI}(OH)_{2-y}yFO_{10}$ $x = 0.7, R^+ = Li^+, y = \text{variable}$ $M_x^+[Si_{4-x}Al_x]^{IV}[R_3^{2+}]^{VI}(OH)_2O_{10}$ $x \approx 0.6, R^{2+} = Mg^{2+}, Fe^{2+}$ $M_{x-y}^+[Si_{4-x}Al_x]^{IV}[R_{3-y}^{2+}R_y^{3+}]^{VI}(OH)_2O_{10}$ $x \approx 1, y = \text{variable}$

$M^+$  represents a monovalent exchangeable cation. Superscripts  $^{IV}$  and  $^{VI}$  indicate the tetrahedral and octahedral layers, respectively. The hydration of the clay is not accounted for. In one example pillaring of rectorite is reported. Rectorite is an interstratified mica-smectite with tetrahedral Si by Al substitution. Laponite is a synthetic, poorly crystallized hectorite.

chemical characteristic, the negative charge of the lattice due to isomorphic substitutions. The hydration or complexation of the charge-balancing cation provokes the swelling of the lamellar structure. Note that there is an optimum density of charge for optimal swelling. If the charge is too small ( $<0.5 \text{ meq g}^{-1}$ ), the cation hydration or complexation energy is lower than the adhesion energy between the platelets. (Throughout this section, meq is used to denote 'milliequivalent', i.e.  $10^{-3}$  equivalent charges). If the charge is too large ( $\geq 3 \text{ meq g}^{-1}$ ), the electrostatic attraction between the negative planes and the middle plane containing the exchangeable cations is larger than the swelling force. As far as the two families of clays shown in Table 1 are concerned, the highly charged nonswelling end members are the micas muscovite (diocahedral) or phlogophite (triocahedral). Like pyrophyllite and talc, but for exactly the opposite reasons, micas do not swell unless special treatments are applied. Note that vermiculite, listed as a clay in Table 1, has a lattice charge such that swelling is limited.

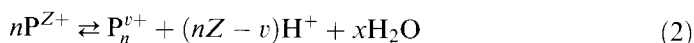
### 3.12.1.3 Basic Pillaring Mechanism

At least at first sight the pillaring mechanism is simple, since it would consist essentially of the exchange of the charge-balancing cation of the clay (preferably  $Na^+$ ) by a cationic oligomer  $P_n^{v+}$  made from  $n$  cations bound by oxo or hydroxo bridges and with a total charge  $v^+$  [8]. If  $M$  is the symbol representing the clay, the following exchange occurs in the gallery:



and the gallery height, or basal spacing  $d_{00l}$  increases by a length somewhat lower than the radius of the oligomer. If the exchange was the only reaction involved in the pillaring mechanism, the experimental procedure would indeed be simple, as is

the case when exchanging sodium by a quaternary alkylammonium, for instance. However, the oligomer itself results from a condensation reaction such as



involving hydroniums and water. Therefore, the overall pillaring reaction necessarily involves reactions 1 and 2, and the chemical properties of the clay surfaces, such as its acidity, play a role.

Finally, if a successful pillaring mechanism has been obtained, as shown by the increase of the d001 reflection in the X-ray pattern of the air-dried pillared material, it remains to create the microporosity. This most important step is performed by removing the hydration water filling the gallery by thermal activation. It will be successful insofar as  $P_n^{v+}$  does not depolymerize, and remains anchored in one way or another to the surface. The nature and the extent of the cross-linking action of  $P_n^{v+}$  on the adjacent microcrystals forming the galleries depend on the nature of both the surface of the clay and that of the pillar. The solid, stabilized in a temperature range between 400 and 500 °C, is the actual pillared clay. Its structure is essentially turbostratic since the long-range crystalline order is only along the *c* axis perpendicular to the layers. There is no long-range order along the *a* and *b* unit cell axes. Since the pillaring oligomers are cationic, it might be assumed that they will be distributed on the surface as far as possible from one another in order to reduce the mutual electrostatic repulsion. Again, the way the pillars are distributed is also a function of an additional factor which becomes apparent when considering the typical composition of the clays shown in Table 1.

In a dioctahedral clay such as montmorillonites, the lattice electric charge results from the substitution of octahedral  $Al^{3+}$  by  $Mg^{2+}$ . Thus, the lattice charge is buried in the octahedral layer and smeared out on the oxygen surface of the 001 plane (see Fig. 1). In such a case, the lattice charge is not localized. On the opposite, in beidellite, for instance, the origin of the lattice charge is the replacement of tetrahedral  $Si^{4+}$  by  $Al^{3+}$ , and the charge is localized in the corresponding tetrahedron, as is the case in zeolites. From  $^{29}Si$  high-resolution solid-state NMR ( $^{29}Si$  MAS NMR) it is known that the distribution of the Al substitutions in layer lattice minerals such as micas and vermiculite is homogeneous [9], bringing them to the largest possible distance from one another. In beidellite and saponite, according to  $^{29}Si$  MAS NMR, it appears that at least the Loewenstein rule applies – the Loewenstein rule is the avoidance rule which states that two tetrahedral Al cannot be next neighbors. The homogeneous dispersion observed for a lamellar structure richer in tetrahedral substitution such as vermiculite is more demanding, since, in addition, it requires the largest possible distance between substitutions.

In lattices with localized electric charges, the distribution of small cations must coincide with that of the tetrahedral isomorphic substitutions. The distribution of the oligomeric cations should be the same and since the homogeneous distribution advocated by Herrero [9] is also that which would minimize the repulsion between pillars, there should be no essential difference between clays with localized and delocalized lattice charges insofar as the pillar distribution is concerned. However, as shown later, the charge localization increases surface reactivity, and it will influence the cross-linking mechanism between the clay platelets.

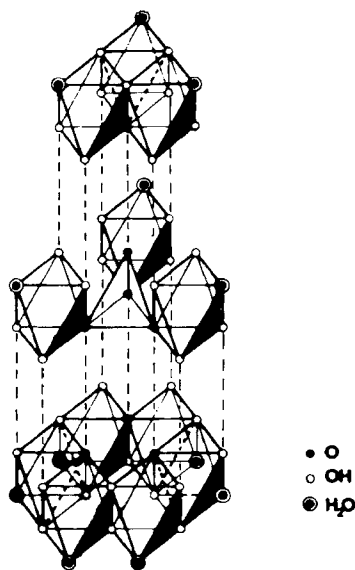


Figure 3. Blown-up structure of the  $\text{Al}_{13}$  cation showing the central Al tetrahedron surrounded by twelve Al octahedra.

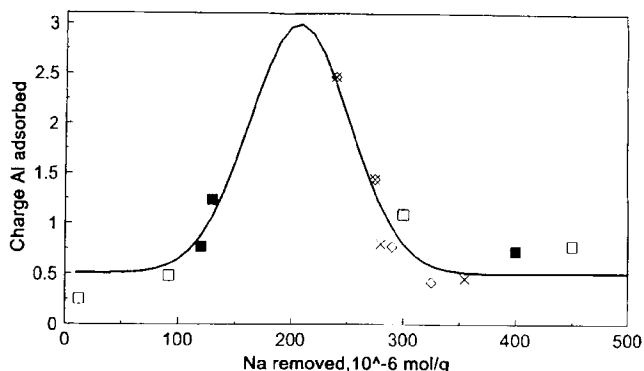
### 3.12.2 Pillars

#### 3.12.2.1 Hydroxyaluminum Polymer

The complexity of the aqueous solution chemistry of  $\text{Al}^{3+}$  and the precipitation of aluminum hydroxide colloids in the smectites interlayer was already a popular subject among clay scientists in the 1960s because of the resemblance of these mixed compounds with natural interstratified minerals. Lahav et al. [5] in 1978 were the first to publish X-ray spectra showing the swelling of montmorillonite up to  $\approx 18 \text{ \AA}$  obtained by mixing an aged suspension of a hydrolyzed aluminum cation with  $R = \text{OH}:\text{Al}$  varying from 1 to 2.3. The total Al content, the  $R$  ratio and the aging time were shown to be important parameters. Prior to the publication by Lahav et al., as mentioned in Section 3.12.1.1, in 1974 a team of scientists at W. R. Grace started studying pillared clays extensively, but it was only in 1980 that Vaughan and Lussier [10a] disclosed their patents dealing with Al, Zr, and Ti pillared clays (see review paper by Vaughan [10b]). In the meantime, progress in analytical techniques afforded a better understanding on the nature of the pillars.

Using the polyhydroxyaluminum polymer as an illustration, it was presumed that the pillar was the so-called  $\text{Al}_{13}$  cation,  $=[\text{Al}_{13}\text{O}_4(\text{OH})_{24}(\text{H}_2\text{O})_{12}]^{7+}$ , whose structure in a hydrated sulfate salt had been determined by Johansson et al. [11] (see Figure 3). As early as 1972 in partially hydrolyzed aluminum solution, Akitt and co-workers [12] had recognized the signature of  $\text{Al}_{13}$  by a NMR peak attributable to fourfold coordinated aluminum ( $\text{Al}^{\text{IV}}$ ) which is typical of the Keggin cation. Since the Keggin cation contains the four planes of oxygen atoms requested to prop apart the clay interlayer by  $\sim 8 \text{ \AA}$ , it was tempting to suggest that pillaring with  $\text{Al}_{13}$  was just a cation exchange process. It was, thus, assumed that the  $\text{Al}_{13}$  polymer

**Figure 4.** Exchange  $\text{Al}_{13}$ -Na in ( $\square$ ) saponite and ( $\blacksquare$ ), ( $\diamond$ ), and ( $\times$ ) hectorite, using a pure  $\text{Al}_{13}$  solution. The charge per Al is the ratio  $\text{Na}^+$  removed : Al uptaken (adapted from Ref. 14).



retains its integrity all through the exchange process, in spite of the fact that  $\text{Al}_{13}$  results from a complex set of reversible hydrolysis reactions [13] which can eventually occur on the clay surface.

The importance of aging the polymer solution, already outlined by Lahav et al. and repeatedly reported by others, had shed some doubt on oversimplifying the pillaring mechanism by a simple cation exchange. Some extremely interesting and recent work by Schoonheydt et al. [14] has shed a new light on the complexity of the phenomena.

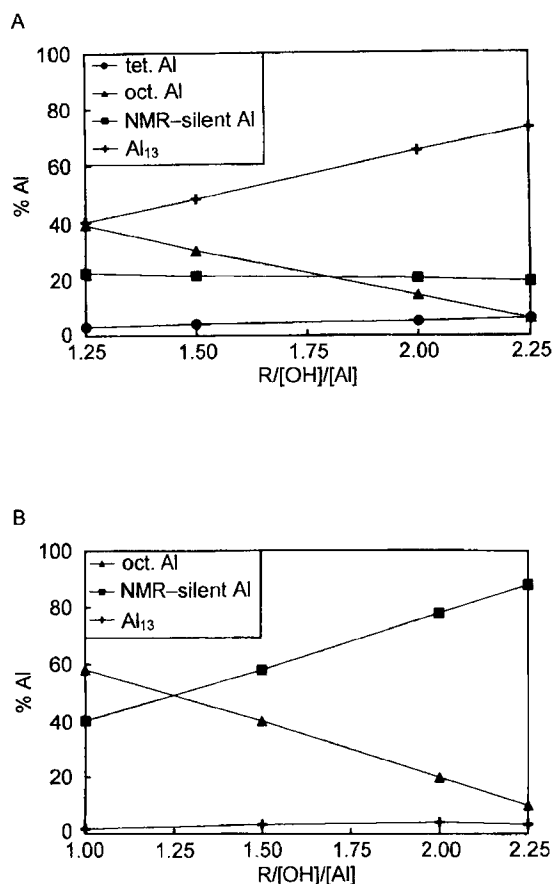
A pure solution of  $\text{Al}_{13}$  chloride was prepared according to the recipe initially proposed by Schönher et al. [15]. From the analysis of the solution by  $^{27}\text{Al}$  NMR, e.g. in measuring quantitatively the intensity of the resonance due to the tetrahedral Al in  $\text{Al}_{13}$ , and the release of sodium, real exchange isotherms were obtained for the first time [14].

Figure 4, calculated from the results displayed in figure 8 of Ref. 14, shows the variation of the average charge per Al adsorbed with respect to the Na released. It is obtained simply as the ratio equiv.  $\text{Na}^+$  released : mol Al fixed. Up to a loading of about 20% of the cation exchange capacities (CEC) which are  $0.55 \text{ meq g}^{-1}$  and  $0.66 \text{ meq g}^{-1}$  for hectorite and saponite, respectively, the charge is lower but not too far from  $+0.55$ . This is the theoretical charge per Al in  $\text{Al}_{13}^{7+}$ . It may be that this first part of the curve shown in Fig. 4 corresponds to the exchange on the external surface.

In the gallery, the exchange is accompanied by a partial, or even total depolymerization of  $\text{Al}_{13}$ . The charge distribution represented by a gaussian function would be random because of a random depolymerization process. As soon as about two-third of the Na content corresponding to the CEC is desorbed, reaggregation of oligomers into  $\text{Al}_{13}$  occurs. The interlayer spacing of about  $8 \text{ \AA}$  is obtained when the  $\text{Al}_{13}$  content exceeds the CEC, which means, of course, that the charge per Al has to decrease. It may be that washing helps further hydrolysis and/or polymerization.

Figure 5 shows the composition of solutions with different OH : Al ratios prepared at room temperature or refluxed for 24 h. In spite of the high relative content in  $\text{Al}_{13}$  of the solution with  $R = 2$  prepared at room temperature, the obtention of the  $1.8 \text{ nm}$  spacing requires aging, washing (eventually by dialysis) and also a pre-





**Figure 5.** Relative quantities of Al species in solution as a function of  $R = \text{OH} : \text{Al}$  in a 0.1 M  $\text{Al}^{3+}$  solution prepared at (A) room temperature, (B) under reflux (reprinted from Ref. 16 with permission).

treatment of the solution at 50 °C in agreement with Plee et al. [17] With a multi-component solution there is obviously a competition of more than one cationic species to replace the  $\text{Na}^+$  (the initial cation) in the interlayer space. The complexity of the pillaring solution is even greater in chlorohydrol solution which has been used successfully as claimed in Refs. 10, 18, and 19. Chlorohydrol is the tradename of the reaction product of Al metal with an aluminum chloride solution. In a chlorohydrol solution with  $R = 1.8$  the amounts of monomeric Al, of  $\text{Al}_{13}$  and of polymeric Al are about one-third [20]. The polymer in question is made from octahedrally coordinated aluminum only.

However, when either a solution of chlorohydrol is used or the refluxed solution with compositions shown in Figure 5(b), the swelling of the clay to 1.8 nm is obtained easily. The main difference between the chlorohydrol or refluxed solution and the solutions obtained at room temperature by partial hydrolysis ( $R \approx 2$ ) is in the small relative abundance in monomeric Al. Meanwhile, it seems that we have also to accept that, on the acid clay surface, the “polymeric” fractions present in the chlorohydrol or in the “refluxed” solution can undergo structural rearrangements

with some reconstruction of  $\text{Al}_{13}$  or of  $\text{Al}_{13}$  polymer, as suggested in Figure 4. Indeed, in the pillared dry material the observed ratio  $\text{Al}^{\text{IV}} : \text{Al}^{\text{VI}}$  is roughly that expected in  $\text{Al}_{13}$  (see Section 3.12.3).

It is interesting that Figueras et al. [21] in what they called competitive adsorption had prepared a pillaring solution containing  $\text{NH}_4^+$  with  $\text{NH}_4^+ : \text{Al}$  ratios as large as 10. Relatively large concentrations of foreign cations decreased the amount of alumina species which were fixed, as expected from simple equilibrium considerations. The addition of ammonium increased the pH ( $\approx 6$ ) and almost completely depleted the concentration in monomeric aluminum. The result was an increased crystallinity of the pillared materials [21]. Recently, Michot and Pinnavaia [22] have improved the crystallinity of alumina-pillared montmorillonite by protecting the  $\text{Al}_{13}$  polymer by a nonionic surfactant. Aging is no longer necessary.

### 3.12.2.2 Gallium and Mixed Gallium Aluminum Hydroxypolymer

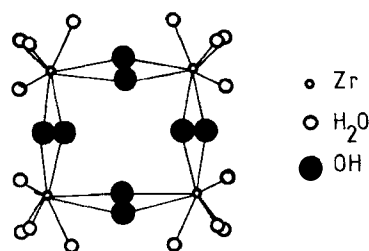
The chemistry of gallium resembles that of aluminum. It has been shown by Bradley et al. [23, 24] that in a pure  $\text{Ga}^{3+}$  solution, the equivalent of the  $\text{Al}_{13}$  polymer is synthesized upon limited hydrolysis. The existence of a mixed (Ga,12Al) polymer [24] where Ga is in tetrahedral coordination has also been noted. The  $^{69}\text{Ga}$  ( $I = 3/2$ ) NMR resonance line is, unfortunately, broader than the  $^{27}\text{Al}$  line, making detailed study of the pillaring mechanism more difficult.

Vierra-Coelho and Poncelet [25] as well as Bradley et al., have shown the Ga or mixed Ga/Al polymeric solutions, prepared as described above for Al polymeric solutions, also have to be aged and the intercalated smectite has to be washed to obtain a successful pillaring, very much as reported for  $\text{Al}_{13}$ .

### 3.12.2.3 Zirconia Hydroxypolymers

Historically, the zirconia hydroxypolymers obtained through the hydrolysis of  $\text{ZrOCl}_2 \cdot x\text{H}_2\text{O}$  were among the first to be used for pillaring clays because they required less optimization than the alumina polymers [10a, b]. The generally accepted structure of the pillaring agent [26] is a  $[(\text{Zr}(\text{OH})_2 \cdot 4\text{H}_2\text{O})_4]^{8+}$  tetramer (Figure 6). This structure is present in solid zirconium chloride [27]. The starting material for producing the polymer is the zirconyl chloride which is hydrolyzed by NaOH and/or  $\text{Na}_2\text{CO}_3$ . An increase in pH increases the degree of polymerization.

Farfan-Torres et al. [8] have used a 0.1 M NaOH solution to produce hydrolysis of either the  $\text{ZrOCl}_2$  solution or the  $\text{ZrOCl}_2$ -clay suspension. As long as the final pH of the pillaring solution was below 2, stable intercalations with 7.4 Å basal spacings were obtained. It is important to note that the clay suspension to which the pillaring solution was added was made from a 1 : 1 mixture of acetone and water. It is evident that at the low pH used for pillaring zirconia, hydronium was a serious competitor for the clay exchange sites and that some acid dissolution of the lattice was likely. Farfan-Torres et al. have measured a residual CEC close to 88% of the initial CEC of an unpillared montmorillonite (Weston-L) after pillaring at pH 1.9



**Figure 6.** Structure of  $[\text{Zr}(\text{OH})_2 \cdot 4\text{H}_2\text{O}]^{8+}$  tetramer (reprinted from Ref. 26 with permission).

and fixation of  $\sim 24$  wt% of  $\text{ZrO}_2$  (or 0.2 mole  $\text{ZrO}_2$ ). The corresponding charge brought by each zirconium in the polymer must be as low as  $0.2^+$ .

The extent of polymerization that the tetramer should undergo to explain such a lowering of the charge is large, and it forces the clay to work as a powerful proton sink. The strong acidity observed by ammonia temperature programmed desorption (TPD) [28] from zirconia-pillared montmorillonite could be partially attributable to the surface protonation.

### 3.12.2.4 Transition Metal Oxide Pillars

The possibility of pillaring clays with transition metal oxides which should exhibit electron transfer properties has been investigated by Pinnavaia and co-workers [29, 30] who studied chromia pillared clay as early as 1985. Chromium nitrate ( $\text{Cr}(\text{NO}_3)_3 \cdot 9\text{H}_2\text{O}$ ) is hydrolyzed by  $\text{Na}_2\text{CO}_3$  and aged for more than one day at  $95^\circ\text{C}$ , the final pH being  $\leq 2$ , the ratio meq  $\text{CO}_3^{2-}$  per mole  $\text{Cr}^{\text{III}}$  being about 2. Accordingly, the  $4\text{A}_{2g} \rightarrow 4\text{T}_{1g}$  and  $4\text{A}_{2u} \rightarrow 4\text{T}_{2p}$  transitions are red shifted, indicating the formation of higher chromia polymer. Aging is essential for obtaining large gallery heights. After calcination at  $500^\circ\text{C}$ , the d001 reflection can still reach about 2.2 nm.

Attempts have been made to pillar smectites by refluxing Cr (III) acetate with a Na–montmorillonite suspension [31]. Linear oligomeric chromium polyhydroxoacetate is believed to be the pillaring agent. However, to get pillared material, calcination under gaseous  $\text{NH}_3$  is necessary, and the crystallinity is not as good as that obtained in the procedure proposed by Pinnavaia et al.

The oligomer resulting from the hydrolysis of chromium nitrate has been identified by X-ray absorption fine-structure spectroscopy (EXAFS) as a tetranuclear species with edge-bridged octahedral chromia [32].

Tantalum pillared clay has been obtained using a pillaring solution obtained through hydrolysis of  $\text{Ta}(\text{OC}_2\text{H}_5)_5$  in an acidified ethanolic solution [33]. The clay is added slowly to this solution.

### 3.12.2.5 Mixed Al–Fe Pillars

Pillaring smectites with iron polyhydroxy polymers which would be similar to those of aluminum is more difficult as far as hydrolysis conditions are concerned. The

base to metal ratio must be about 2, the pH about 1.7, and the reflections are broad and weak (see Table III in Ref. 56). By contrast, mixed Al/Fe<sup>III</sup> pillars have been prepared and the intercalated smectite is thermally stable up to 500 °C, if the Fe:Al ratio is equal to or smaller than 0.2 [34]. The <sup>27</sup>Al NMR spectra in the pillaring solutions with Fe:Al < 0.5 shows the Al<sup>IV</sup> signature of the Keggin cation at 63 ppm [35]. Thus, the pillaring solution would be made from these cations in which Al<sup>3+</sup> would be partially replaced by Fe<sup>3+</sup>. The nature of the substitutions is not known, but in view of the ubiquitous isomorphic replacement of Al by Fe in the octahedral layers of micas, it is likely that some of the octahedral Al are replaced by Fe in the Keggin structure. The pillaring solutions are prepared either (i) by contacting an aged Al<sub>13</sub> solution prepared by the method of Lahav et al. with a 0.1 M FeCl<sub>3</sub> solution at pH between 4 and 4.5 (0.1 M NaCO<sub>3</sub>) or (ii) by cohydrolysis of 0.1 M AlCl<sub>3</sub> to which 0.1 M FeCl<sub>3</sub> is added. The hydrolysis is carried out after the addition of 0.1 M NaCO<sub>3</sub> solution. In both cases, the hydrolysis products are aged 1 week at room temperature and at 120 °C for 4 h before use.

### 3.12.2.6 Titania Pillar

Pillaring smectites with titanium polyhydroxide was among the claim of the original W. R. Grace patents by Vaughan, Lussier, and Magee [3]. The partial hydrolysis of TiCl<sub>4</sub> [36] or alkoxide [37, 38] is performed in HCl solution. Potentiometric titrations suggest the existence of a polynuclear species [(TiO)<sub>8</sub>(OH)<sub>12</sub>]<sup>4+</sup>, the structure of which is unknown [39]. The procedure to get this polymer is a slow hydrolysis of TiCl<sub>4</sub> in 6.0 M HCl until solutions with final concentrations in the range 0.11–1.0 M Ti are obtained [36]. Again, these solutions have to be aged.

The polymer obtained from the hydrolysis of Ti alkoxide is also probably made from octahedra sharing edges [38]. At constant hydrolysis ratio (HCl: Ti alkoxide), the loading in TiO<sub>2</sub> decreases with increasing molecular weight of the alkoxide (from ethoxide to *n*-butoxide), suggesting a simultaneous reduction in the extent of polymerization.

### 3.12.2.7 Silica and Silicate Pillars

As early as 1980 Endo et al. [40] tried to pillar smectite with silica obtained through the decomposition of silicon acetyl acetonate. A spacing corresponding to a single SiO<sub>2</sub> layer was obtained. Fetter et al. [41] have reviewed the various attempts to use organosilicon compounds for obtaining thermally stable pillared smectites. The same paper gives details of the preparation of the pillaring solutions using either 2-(trichlorosilyl)ethylpyridine (TCSEP) or 3-aminopropyltrimethoxysilane (APTMS). A limited hydrolysis was obtained at 0 °C for TCSEP in water or at room temperature for APTMS in methanol and a 16% HCl solution. The hydrolysis product of TCSEP was aged for 3 day, while the aged (27 h) hydrolysis product of APTMS was added to acetone and refluxed for 1 h. It was necessary to store these solutions in the dark before use.

A  $^{29}\text{Si}$  NMR study suggests that the hydrolysis of TCSEP is a complicated process comprising a mixture of compounds such as hydrated monomer, hydrated and trimeric species, and higher polymers with a resonance line near  $-67$  ppm, also observable in the pillared solid.

Moini and Pinnavaia [42] have succeeded in intercalating tubular immogolite in montmorillonite. The synthetic immogolite was brought to a pH higher than the zero point charge, such that it was positively charged and played the role of a supercation.

### 3.12.2.8 Miscellaneous

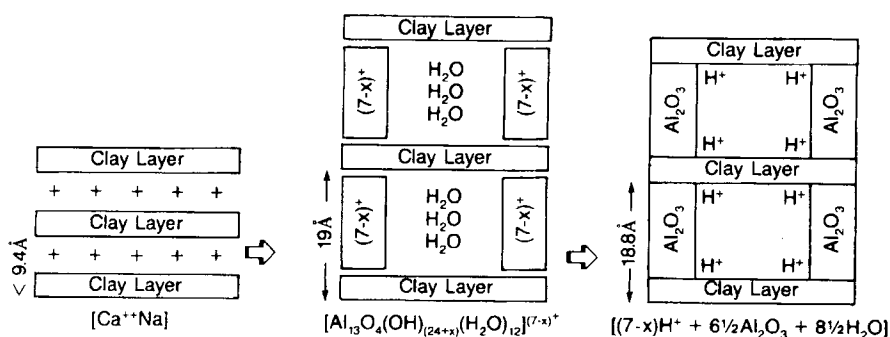
Section 3.12.2, dealing with pillaring solution and pillaring mechanism is restricted to materials in which the nature of the polymer has been investigated. The next section shows that pillars other than those reviewed above have been used successfully. They include binary oxides such as  $\text{LaNiOx}$  [43], lanthanum–aluminum [44], and silicon–titanium [45] pillars.

## 3.12.3 Pillared Clays

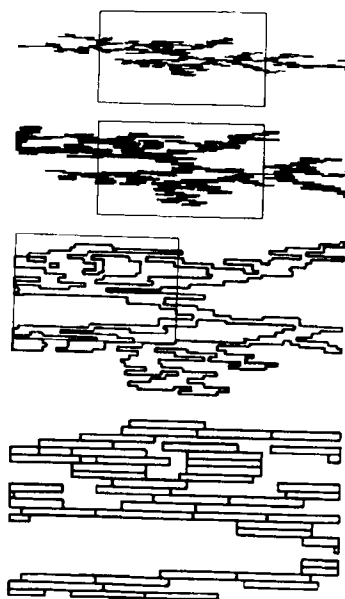
### 3.12.3.1 Preliminary Remarks

From the brief description of the structure of clay (Figure 1) the oversimplified representation of a pillared clay would be that shown in Fig. 7. Such a representation is grossly inaccurate. When air-dried, the vector normal to the clay platelets is scattered by  $\pm 18^\circ$  with respect to the averaged direction of the  $c$  axis [46]. Therefore, there is a significant orientational disorder which can be considered as a distribution of the orientation of tactoids made from a few parallel plates [47, 48]. Moreover, to this orientational disorder must be added a translational disorder, since the turbostratic character is evident from the shape of the  $(hkl)$  X-ray reflection. Thus, the aggregate of platelets to be pillared is more likely to resemble that shown in Figure 8 (see also micrograph in Ref. 50). In brief, the real situation is far from the “rosy” picture in Figure 7. As a consequence, when questions about the specific surface area or of the porosity of PILCS are addressed, the precipitation of the pillaring agent outside the gallery, the contribution to the surface area of the “dangling” sheets, etc. also have to be accounted for.

The coherent scattering domain is always small as evidenced by the observation of three broad 00 $l$  reflections, at the most. From the viewpoint of crystallinity, zeolites and pillared clays belong to two different worlds. Yet, in spite of these remarks which are evident to those who have worked in the field, sometimes one still finds researchers who are amazed by the fact that calculations of microporous volume or of surface area, using a model such as that in Figure 7, do not agree with the experimental results. It is important to stress these points before reviewing the properties of the pillared clay.



**Figure 7.** Early representation of clay pillaring with chlorohydrol (reprinted from Ref. 10(b) with permission).



**Figure 8.** Computer simulation of the formation of clay tactoid by a process of aggregation of  $10^3$  particles. The length: thickness ratio of each particle is 9. In the three topmost diagrams, each rectangle encloses a portion of the tactoid shown enlarged in the diagram immediately below (reprinted from Ref. 49 and 51 with permission).

### 3.12.3.2 Main Physical Characteristics

The d00/ spacing, the pore-size distribution, the specific surface area and its distribution versus the pore radius are the essential physical characteristics of the solid. Since thermal activation is always the necessary final step in the preparation of the pillared clay, the variation of the physical characteristics with the temperature contains important information. A temperature-programmed calcination must be important but it is too rarely investigated.

Whatever the nature of the pillar, the obtention of a pillared clay with a gallery of at least  $\approx 8 \text{ \AA}$  and specific surface area (calculated from the Langmuir isotherm of  $\text{N}_2$  at liquid nitrogen temperature) of at least  $200 \text{ m}^2 \text{ g}^{-1}$  after calcination at  $500^\circ \text{C}$

always requires a critical concentration in pillaring agent. This critical concentration depends upon the nature of the pillaring agent and on the clay. An interesting illustration of this aspect is shown in Fig. 9. Clearly, pillaring *that* montmorillonite (fraction  $< 2$  nm of a Wyoming Na-bentonite) requires more  $\text{Al}_{13}$  polymers (higher  $R = \text{OH} : \text{Al}$ ) than pillaring a synthetic beidellite. Amazingly, the total Al adsorbed is already near saturation (2 mmol Al fixed per g of clay) for an initial  $\text{Al}^{3+}$  content in the solution (the ordinate in Fig. 9) about  $10 \text{ meq g}^{-1}$  of clay. Obviously, at this content the full expansion is not reached in the beidellite while it is in the montmorillonite. Figure 10 represents a good illustration of the large enhancement of the  $\text{N}_2$  adsorption capacity resulting from pillaring beidellite. A strong link between the d001 basal spacing and the surface area has been generally observed for all categories of pillared clays. However, the link between the loading in pillaring agents, the d001 spacing, the surface area, and the porosity is not obvious. As said in section 3.12.3.1, what is pillared is an assembly of tactoids and, consequently, one has to account for the fact that adjacent platelets separated by an interlayer distance  $\Delta$  (for  $\Delta$  d001) are overlapping one another by a variable fraction [51].

The adequate technique of measuring the porosity, the pore-size distribution and the surface area for pillared material is not evident either. The team led by E. F. Vansant and A. Molinard has devoted a great deal of effort to these aspects so important for the separation techniques. Only two recent references [53, 54] are given here and the results in Table 2 are from Ref. 54.

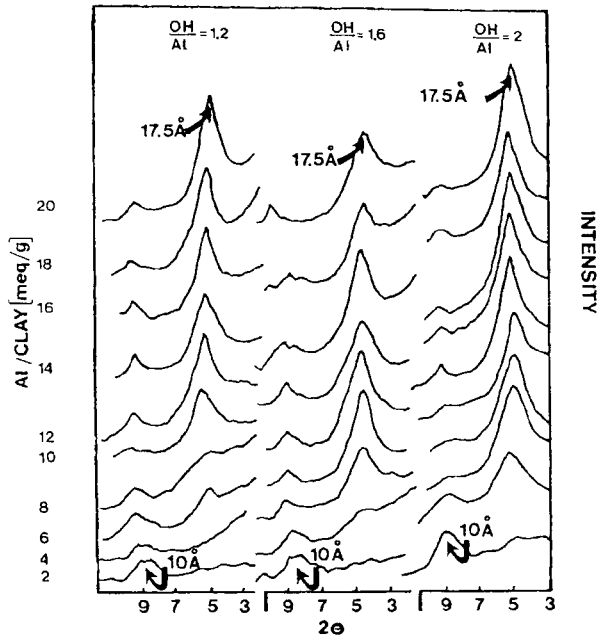
A paper by Yamanaka and Hattori [55] shows that in a montmorillonite pillared with 48 wt%  $\text{Fe}_2\text{O}_3$  an unknown (but not negligible) fraction of the iron oxide is on the external surface. Indeed,  $\text{N}_2$  adsorption isotherms of Brunauer type II are observed instead of the Langmuir isotherm, which would be expected from the observation of an interlayer spacing of  $6.4 \text{ \AA}$ . It is for the same reason that in Fe-pillared montmorillonite in Table 2 it is the BET surface area which is given.

In Table 3, are collected interlayer spacings when the loadings were given. Also, we have skipped the data where the d001 reflection appears as a shoulder on the rapidly decreasing scattering intensity away from the direct X-ray beam.

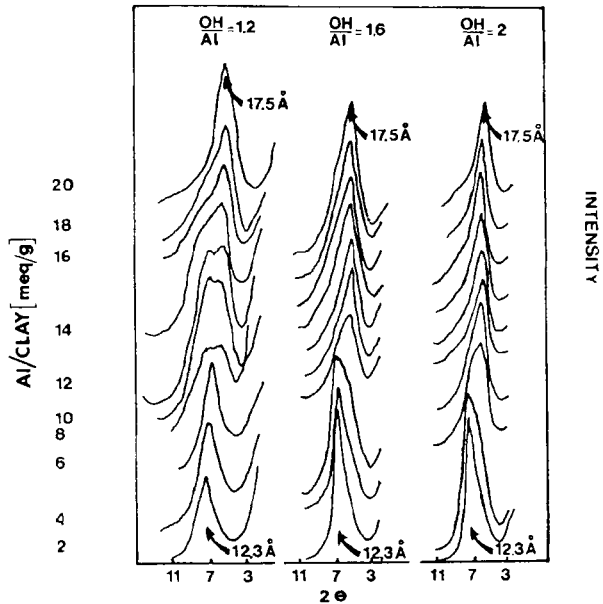
As can be observed, the data obtained with the Al-pillared montmorillonite, beidellite, laponite, and saponite are in good agreement. The mixed aluminum-iron pillar gives spacing close to that of aluminum. The data for iron are more debatable. It looks as though an appreciable fraction of  $\text{Fe}_2\text{O}_3$  is precipitated on the outside surfaces. By contrast, pillaring with chromia and  $\text{Ta}_2\text{O}_5$  leads to less ambiguous results. It should be noted that upon calcination in the air, the interlayer spacing of the chromia-pillared montmorillonite collapses [30]. Saponite with mixed Si-Ti pillar is an example of very good thermal stability.

It should be emphasized that interlayer spacing in the order of  $12\text{--}16 \text{ \AA}$  requires pillars with about six or more oxygen layers. These pillaring species are likely to be nanosized colloidal particles on the positive side of their zero point charge. Some examples of molecular sieving are shown in Table 4. It can be observed that the kinetic molecular diameter, the corresponding amounts of adsorbed molecule, and the interlayer spacing ( $\Delta$  d001) follow the same trend. A fractal analysis of the adsorption process of pillared clays by Van Damme and Fripiat [58] have shown that the values in Table 3 are compatible with an euclidean fractal dimension of 2

**Figure 9(a).** 001 reflection of calcined (500 °C) films of pillared montmorillonite as a function of the initial Al:clay ratio and for  $R = \text{OH} : \text{Al}$  ratios between 1.2 and 2. The composition of such solutions can be found in Fig. 5(a) (reprinted from Ref. 17 with permission).

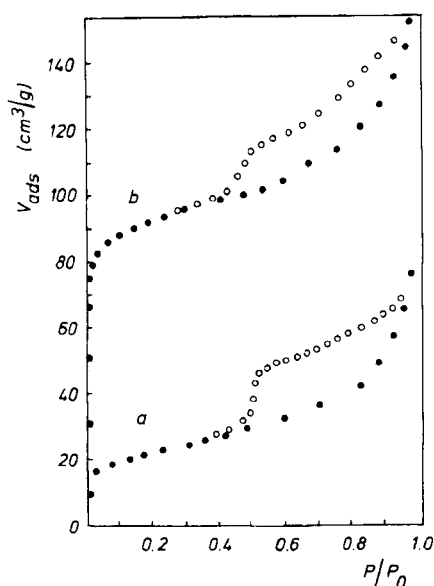


**Figure 9(b).** As Fig. 9(a) except that the smectite is beidellite.



for Al-pillared montmorillonite. It must be emphasized that the preparation conditions of the pillared clay are very critical for the ultimate size of the molecules which have access to the gallery [59].





**Figure 10.** N<sub>2</sub> adsorption (●)–desorption (○) isotherm at 90 K on (a) beidellite and (b) pillared beidellite calcined at 300 °C (reprinted from Ref. 52 with permission).

**Table 2.** Adsorption capacities (mmol g<sup>-1</sup>) at 0.45 bar of various pillared montmorillonites [54].

Gas	Al	Zr	Ti	Fe
<i>At 194 K</i>				
N <sub>2</sub>	0.05	0.09	0.16	0.03
O <sub>2</sub>	0.02	0.03	0.07	0.01
CO <sub>2</sub>	0.95	2.4	1.46	0.29
<i>At 77 K</i>				
N <sub>2</sub>	2.5	3.5	2.8	–
O <sub>2</sub>	3.38	5	5.90	–
Ar	3.04	4.40	5.20	–
<i>Physical Characteristics</i>				
Δd001(Å)	7.8	4.0	16–19	16
Area (Langmuir) m <sup>2</sup> g <sup>-1</sup>	341	280	410	BET = 198

### 3.12.3.3 Chemical Properties

Smectite surfaces are acidic. This results from the high dissociation degree of the cation hydration water [60–62] and is a consequence of the bidimensional structure. The exchangeable cation–clay association is like a cation–anion association, but the “anion”, namely the clay lattice, has an infinite radius of curvature. Thus, the electric field created by the cation strongly polarizes a hydration water molecule in the first coordinate shell. One of the protons is probably delocalized [63] on the network of water filling in the space between the cations, while the remaining OH<sup>-</sup> remains coordinated to the cation. In the pillared clay, there is always a residual

**Table 3.** Observed interlayer spacing  $\Delta = (d_{001} - 9.6) \text{ \AA}$ , nature of the pillar and of the clay. Loading is oxide: clay wt % or clay unit cell, indicated as uc.

Clay <sup>a</sup>	Pillar	Loading	Temp. (°C)	$\Delta$ (Å)	Ref.
Mon	Al	18.7	500	7.8	54
Mon	Al	10	300	8	17
Mon	Al	6	500 <sup>f</sup>	5.7	22
Bei	Al	10	300	8	17
Bei	Al	8.5–34	400	8	52
Sap	Al	10–13.2	400	7.9–8.6 <sup>b</sup>	14
Hec	Al	≈ 11	250	8.6	14,16
Sap	Al	9.2	500	8.2	45
Lap	Al	13	400	7	32
Mon	Zr	16.2–25.1	400	7.4	28
Mon	Zr	19.1	500	4	54
Mon	Ti	20	500	16–19 <sup>c</sup>	54
Mon	Ti	29–49	400	10–12 <sup>b</sup>	38
Mon	Cr	3.5 Cr <sub>2</sub> O <sub>3</sub> /uc	350	13.4	30
Mon	Fe	6–9 Fe <sub>2</sub> O <sub>3</sub> /uc	350	13–15 <sup>d</sup>	56
Mon	Fe	33.2–39.6	350	≈ 18	53
Mon	Ta	17–24	400	13.9–15.9 <sup>b</sup>	33
Mon	Al,Fe	Al <sub>2</sub> O <sub>3</sub> 11.6, Fe <sub>2</sub> O <sub>3</sub> 8.6	400	≈ 7	34
Mon	Al,La	Al <sub>2</sub> O <sub>3</sub> 5, La <sub>2</sub> O <sub>3</sub> 1.7–1.9	autoclave: 120°C	≈ 16 <sup>c</sup>	44
Sap	Ti,Si	TiO <sub>2</sub> 10.6 SiO <sub>2</sub> 9.9	500	22.4	45
Mon	Al,Si	Si: Al ratio, 0.36–0.76, total loading Al + Si ≈ 1.5/uc	500	7.6 <sup>e</sup>	57
Fhec	Al,Si	see above	500	10.2 <sup>e</sup>	57

<sup>a</sup> Mon = montmorillonite; Lap = laponite or synthetic hectorite; Bei = beidellite; Sap = saponite; Fhec = fluorohectorite.

<sup>b</sup> The lowest spacing corresponds to the lowest loading.

<sup>c</sup> Probable interstratification.

<sup>d</sup> Unstable in moist atmosphere.

<sup>e</sup> Sharpness of basal reflection not indicated.

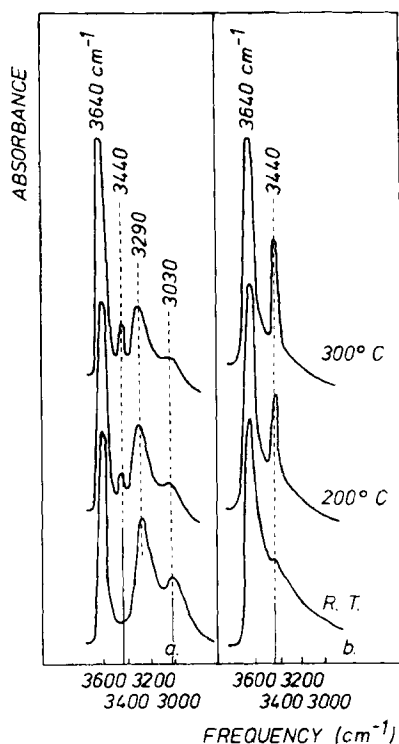
<sup>f</sup> Calcined under vacuum or inert atmosphere.

**Table 4.** Molecular sieving by an Al- and a Cr-pillared clay freeze-dried and calcined at 350°C [19, 30]: amount adsorbed (mmol g<sup>-1</sup> clay) at saturation.

Kinetic diameter (Å) Molec.	4 N <sub>2</sub>	5.8 C <sub>6</sub> H <sub>6</sub>	6.2 (CH <sub>3</sub> ) <sub>4</sub> C	9.2 1,3,5-(C <sub>2</sub> H <sub>5</sub> ) <sub>3</sub> C <sub>6</sub> H <sub>3</sub>	10.2 (F <sub>6</sub> C <sub>4</sub> ) <sub>3</sub> N
Al-pillared <sup>a</sup> 2.87 Al/uc $\Delta d_{001} = 9.5 \text{ \AA}$	2.91	1.61	1.02	0.71	0.43
Cr-pillared <sup>b</sup> 3.53 Cr/uc $\Delta d_{001} = 11.4 \text{ \AA}$	3.63	2.58	1.56	0.91	0.76

<sup>a</sup> BET surface area was 280 m<sup>2</sup> g<sup>-1</sup>.

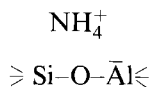
<sup>b</sup> BET surface area was 350 m<sup>2</sup> g<sup>-1</sup>.



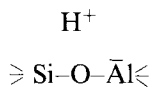
**Figure 11.** IR spectra of (a)  $\text{NH}_4^+$ -beidellite and (b)  $\text{H}_3\text{O}^+$ -beidellite after outgassing at room temperature, 200 °C, and 300 °C (reprinted from Ref. 52 with permission).

cation exchange capacity (CEC), the value of which is dependent on the nature of the pillar and on the loading.

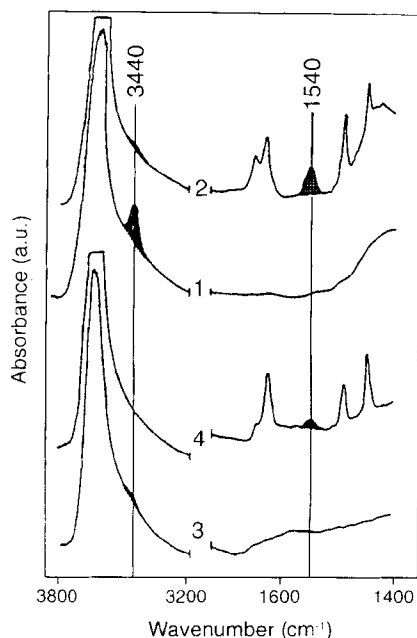
In a dioctahedral clay such as beidellite, Brønsted acid centers can be created, as in Y and other zeolites, by calcining the ammonium exchanged form up to about 400 °C. Upon deammoniating the



cluster in the tetrahedral layer, the acid OH bridge



is obtained as shown by an OH stretching band at  $3440\text{ cm}^{-1}$  in the IR spectra recorded at increasing temperature (Fig. 11). A similar behavior is also observed upon moderate acid leaching. These observations are well in line with the well-established fact that an Al-Si isomorphous substitution is a weak point in a tetrahedral lattice. Therefore, to the Brønsted acidity attributable to the cation hydration water, stronger Brønsted sites can be induced in the 001 plane of dioctahedral



**Figure 12.** IR spectra of (1) Al-pillared beidellite calcined at 400 °C and (3) Al-pillared calcined montmorillonite before the adsorption of pyridine. After adsorption, spectra (2) and (4) are obtained (reprinted from Ref. 64 with permission).

smectites as shown in Fig. 12. These two types of acid sites exist independently from the pillars.

It could have been anticipated that the behavior of a trioctahedral smectite rich in isomorphic substitution, such as saponite, would be similar to that observed for beidellite. It is, indeed, observed that acid leaching [65] produces OH groups not present in the Na-exchanged form but its stretching frequency, instead of being at  $3440\text{ cm}^{-1}$ , is observed at  $3594\text{ cm}^{-1}$ , whereas a band observed in the sodium form at  $3716\text{ cm}^{-1}$  shifts to  $3738\text{ cm}^{-1}$ .

Chevalier et al. [65] have observed that the band at  $3594\text{ cm}^{-1}$  disappears upon pyridine adsorption, but they did not provide information on the thermal stability of the pyridinium.

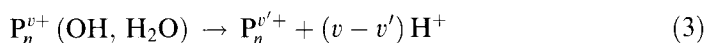
Besides the Brønsted acidity, the exchangeable cation, especially if it is multi-valent and partially dehydrated, is a source of Lewis acidity.

Pillaring the clay will modify the surface acidity in at least two ways, namely (i) the polycationic pillars displace the cations originally present on the surface of the clay and (ii) the pillar's own acidity may create Si–OH–Al bridges in smectites with Al,Si substitutions in the tetrahedral layer. These OH may provide an anchoring point to the pillar. These two remarks are fundamental to the nature of the cross-linking mechanisms.

In clay suspension in contact with the pillaring solution, one may consider that what happens is simply a flocculation provoked by the contraction of the double layer [66]. Such a flocculation process is not likely to markedly change the fundamental texture of the tactoids shown in Figure 8. Once the polycations are within the interlayer space, electrostatic forces are maintaining the clay sheets at the dis-

tance corresponding to the size of the pillars. This, of course, affects the fraction of the platelets facing one another. At that stage cross-linking *per se* is not achieved in the sense that the polycation pillars can be back-exchanged. Actual cross-linking occurs upon thermal activation.

Since thermal activation (i) dehydroxylates the pillars and (ii) activates the eventual attack of the surface by protons and, of course, (iii) removes the clay and pillars hydration water, cross-linking is a complex process. It depends, as shown above, on the nature of the smectites as well as on the nature of the pillars. Hence, several mechanisms of cross-linking must exist. The most trivial mechanism would result from the action of the short-range van der Waals (VdW) forces between pillar and clay surface. Yet, one must not forget that in one way or another the clay lattice charge has to be balanced, irrespective of the residual charge (if any) of the dehydroxylated pillar. If the pillar dehydroxylation is represented by

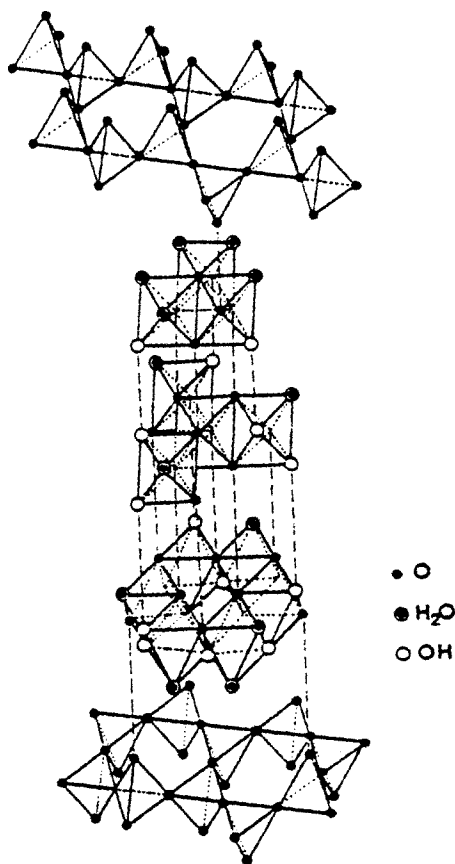


and if  $v'$  is zero, cation back-exchange is impossible.

The protons have (i) to stay on the surface as  $\text{H}_3\text{O}^+$  or (ii) to react with the lattice by opening Si–O–M bridges, as observed for  $\text{M} = \text{Al}$ , or (iii) to disappear into the lattice. It has been observed from the early beginning [10] that the surface charge of an  $\text{Al}_{13}$  cross-linked montmorillonite can be partially restored by calcining in the presence of ammonia. That the initial charge is only partially retrieved is most probably due to a partial dehydroxylation by reaction of the “free” protons with lattice  $\text{OH}^-$ . This explanation is supported by the observation that an ammonium montmorillonite dehydroxylates at least  $100^\circ\text{C}$  lower than a potassium montmorillonite [67]. If the pillar has no charge, the VdW forces alone suffice to explain the structural stability of the pillared material. Such a material appears as a nanocomposite resulting from the dispersion of particles with diameters in the order of 1 nm within the gallery, but there is no cross-linking if we reserve that denomination to covalent (or partially covalent) bonds between elements in the layer and elements in the pillar.

Covalent bonding has been noticed in  $\text{Al}_{13}$  pillared beidellite [68] and fluorophlogophite [69] by observing the  $^{27}\text{Al}$  and  $^{29}\text{Si}$  MAS NMR in the calcined materials. In both cases an inversion of lattice tetrahedron is suggested, the apex oxygen pointing towards the gallery where it binds with the pillar. In the case of the fluorophlogophite studied by Pinnavaia et al. [69] it is, of course, a silicon tetrahedron which is inverted. The  $^{29}\text{Si}$   $\text{Q}^3(\text{Si}-\text{O}-\text{Al})$  line (at  $-92.3$  ppm) splits into two components at  $-93.5$  and  $95.5$  ppm. In the case of beidellite where the cross-linking is most likely initiated by the reaction of the Si–OH–Al bridging hydroxyl on the surface of the clay with an HO–Al group on the pillar, an upfield shift of the  $^{29}\text{Si}$   $\text{Q}^3(\text{Si}-1\text{Al})$  line from  $-90.8$  to  $-92.6$  ppm and been reported [68], but the most noticeable change is the weakening (by  $\approx 50\%$ ) and upfield shift of the line attributable to the fourfold ( $\text{Al}^{\text{IV}}$ ) coordinated aluminum atom in the lattice. This observation prompted Plee et al. [68] to suggest the inversion of a lattice Al tetrahedron and the formation of  $\text{Al}^{\text{IV}}-\text{O}-\text{Al}^{\text{VI}}$  (pillar) linkages, as shown in Fig. 13.

A cross-linking mechanism of another kind was suggested to occur by Tenna-



**Figure 13.** Hypothetical structure of thermally modified alumina pillars sharing three oxygen atoms with three inverted  $\text{Al}^{\text{IV}}$  tetrahedra belonging to two tetrahedral layers of a beidellite (reprinted from Ref. 68, Copyright 1985, American Chemical Society).

koon et al. [70] between alumina pillars and montmorillonite. Based on the absence of perturbation of the  $^{29}\text{Si}$  NMR spectrum of the tetrahedral layer (also emphasized in pillared hectorite in Ref. 68), they suggested that the OH of the octahedral layer would be implied in the formation of a covalent bond with the pillar. Before commenting on this hypothesis, the thermal behavior of  $\text{Al}_{13}$ -pillared montmorillonite and beidellite as revealed by DTA experiments should be summarized.

The maximum endothermic peak resulting from the loss of physically adsorbed water which is observed at about  $100^\circ\text{C}$ , extends up to about  $250^\circ\text{C}$  in unpillared Na-beidellite and montmorillonite [64]. It is followed, in pillared beidellite, by two well-defined endothermic peaks at  $330^\circ\text{C}$  and  $540^\circ\text{C}$  assigned to pillar dehydration and partial dehydroxylation, and to the loss of lattice OH, respectively. In pillared montmorillonite a continuous exothermic effect extends from about  $250^\circ\text{C}$  to  $700^\circ\text{C}$  with maxima at  $330^\circ\text{C}$  and  $630^\circ\text{C}$ . The fact that the pillar and the lattice dehydroxylation temperatures differ by at least  $200^\circ\text{C}$  sheds a serious doubt, from our point of view, on the hypothesis by Tennakoon et al. [70]. In addition, noticeable modification of the  $^{27}\text{Al}$  NMR line attributable to octahedral Al has not been observed.

**Table 5.** NMR data supporting the hypothesis of a lattice Al tetrahedron inversion in Al-pillared saponite.  $R$  is the octahedral Al:tetrahedral Al ratio; in saponite  $\text{Al}^{\text{VI}}$  is only in the pillar (source: Ref. 7).

Sample	Al pillar $\text{mmol g}^{-1}$ clay	Integrated intensity $\text{Q}^3(\text{Si}-1\text{Al})$ (calc. $500^\circ\text{C}$ )	$\text{Al}^{\text{VI}}:\text{Al}^{\text{IV}}$ (uncalc.)
Na-saponite	0.0	29	0.0
D	2.1	21	1.13
A	2.7	14	1.37
C	4.5	7	3.03

A recent work by Lambert et al. [71] on Al-pillared saponites is particularly illuminating as to the question of cross-linking, a (O<sub>2</sub>)y-montmorillonite serving as a reference. They observed (i) a significant decrease of the intensity of the  $^{29}\text{Si}$   $\text{Q}^3(\text{Si}-1\text{Al})$  line but no shift of this line as the pillar density in the gallery increased and (ii) a line assigned to the inverted Al tetrahedron at  $\sim 56$  ppm in double rotation (DOR)  $^{27}\text{Al}$  spectra. Table 5 summarizes some of their findings. They support the conclusion in Ref. 68 concerning the inversion of Al tetrahedra in beidellite.

Similar observations are also reported by Zheng et al. [72] who have pillared rectorite with alumina or silica pillars and by Malla and Komarneni [45]. No splitting of the  $^{29}\text{Si}$  nor appreciable shift are observed in pillared and calcined montmorillonite.

We can summarize the cross-linking question in stating that there is no experimental evidence for the existence of covalent links between the pillars and the 001 surface of the clay lattice, except in the case of clays with tetrahedral substitutions. For experimental reasons the cross-linking mechanism has not been studied for other pillars than Al pillars. It could be predicted, however, that tetrahedral inversion operates in tetrahedrally Al-substituted clay with any pillar, since without exception they all contain OH groups which should react with the clay surface OH groups.

The final question to be developed in this section devoted to the chemical properties is, of course, the modification of the acidity obtained upon pillaring and calcining. As outlined above, the treatment of a pillared clay with ammonia drives the protons resulting from the pillar dehydroxylation from the lattice into the gallery. Thus, Brønsted acidity is potentially present and it should be available to proton acceptor molecules. However, the strength of this acidity is unknown. On the opposite, the surface Si-OH-Al linkages on the surface of pillared beidellite or saponite and of montmorillonite containing a few Al-Si substitutions, in the tetrahedral layer [67], protonate pyridine. As anticipated, pillars such as the zirconia, titania, and alumina pillars are a source of Lewis acidity due to the presence of coordinatively unsaturated sites.

For instance, in alumina pillared saponite, the band near  $1450\text{ cm}^{-1}$  attributable to the pyridine-Lewis site adduct is still observable after desorption at  $520^\circ\text{C}$ , whereas pyridinium disappears after desorption at  $350^\circ\text{C}$  [45]. According to Sun Guida et al. [73] and Del Castillo et al., [38] Ti-pillared montmorillonite has some

Brønsted acidity, as shown by the observation of the IR band at  $1540\text{ cm}^{-1}$  assigned to pyridinium, up to  $250^\circ\text{C}$ . Amazingly, Fetter et al. [41] report a rather strong acidity, indicated by  $\text{NH}_3$  retention up to  $500^\circ\text{C}$  on silica pillared montmorillonite (see Section 3.12.2.7). They attribute its origin to the residual protons, but they do not explain why the acidity of the  $\text{SiO}_2$  pillared clay is larger than that of comparable alumina or zirconia pillared samples. The surface proton or protons removed from the bulk of the lattice may also be at the origin of the Brønsted acidity in titania and zirconia pillared montmorillonites, studied by Farfan-Torres et al. [74]. However, in a recent paper Bodoardo et al. [75] challenged this possibility in suggesting that some of the OH stretching bands observed in pillared montmorillonite can be indicative of acidic  $\text{AlOH}$  or  $\text{SiOH}$ . In particular, a band at  $3660\text{ cm}^{-1}$  which shifts by  $224\text{ cm}^{-1}$  upon adsorbing benzene is assigned to an acidic  $\text{AlOH}$  in the layer or in the pillar.

In these discussions, however, what is too often overlooked is the relative importance of the edge surfaces in the tactoids (Figure 8). On this edge, existence of  $\text{Si-OH-Al}$  bridges resulting either from the condensation of dangling bonds and/or of the reaction of the dangling bonds with components of the pillaring solution could create Brønsted acid sites. A rough estimate of the edge surface area comes to about one-fifth of the gallery area.

#### 3.12.3.4 Chemical Modifications or Functionalization of the Pillaring Species

In this section the modification of a pillar which aims to modify its chemical properties (such as acidity) without affecting in a marked manner the physical properties of the pillared material is reviewed. For instance, the preparation of a titania pillared montmorillonite stable up to  $600^\circ\text{C}$  with a specific surface area of  $\sim 330\text{ m}^2\text{ g}^{-1}$  and a basal spacing of  $22\text{ \AA}$  has been described by Sterte [36]. On the other hand, it is well documented [76] that the sulfate doping of the  $\text{TiO}_2$ ,  $\text{ZrO}_2$ ,  $\text{HfO}_2$ ,  $\text{SnO}_2$ , and  $\text{Al}_2\text{O}_3$  surfaces yields superacids containing, most probably, Brønsted and Lewis acidity. There is also a consensus that the Lewis acidity created by the electron withdrawal power of  $\text{SO}_4$  on the neighbor metallic cation is pre-dominant. The origin of the Brønsted acidity is more controversial.

Among the five oxides cited above three are good pillars and, therefore, it is amazing that only a handful of papers have been devoted to the modification of the pillar acidity by sulfation. Admaiai et al. [77] have added ammonium sulfate to the aged pillaring  $\text{TiCl}_4/\text{HCl}$  solution. Up to 5%  $\text{SO}_4$  can be fixed in that way. The specific surface area of the 2.6%  $\text{SO}_4\text{-TiO}_2$  pillared material is reduced to a constant value of  $\approx 200\text{ m}^2\text{ g}^{-1}$  upon calcination between  $200$  and  $600^\circ\text{C}$ , while the basal spacing decreases from  $\approx 24\text{ \AA}$  to  $22\text{ \AA}$ . The ammonia retention by the sulfated  $\text{TiO}_2$  pillared material calcined at  $600^\circ\text{C}$  is almost double that of the unsulfated pillared clay. From the IR spectra of chemisorbed pyridine, the authors conclude that the acidity enhancement is mainly due to Lewis acidity. Similar results are reported by Boudali et al. [78].

Farfan-Torres and co-workers [74, 79] have prepared sulfated  $\text{ZrO}_2$  pillared clays in a similar way. As for  $\text{SO}_4\text{-TiO}_2$ , an excess of sulfate ( $\text{SO}_4:\text{Zr} \approx 0.7$ ) collapsed

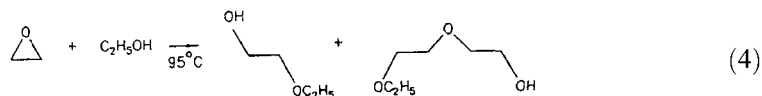


the pillared structure at  $\approx 500^\circ\text{C}$  but the acidity of the sulfated material ( $\text{SO}_4:\text{Zr}=0.35$ ) is also practically doubled, with respect to the unsulfated one. The Brønsted acidity is larger in the  $\text{SO}_4\text{-ZrO}_2$  pillared clay than in the 50%  $\text{TiO}_2$  pillared material, but the unsulfated zirconia pillared clay is also richer in Brønsted sites than the titania analog.

In another vein, one may also consider the introduction of a small amount of alumina in a silica pillar, as a dopant, since it will most probably implement Brønsted sites on the surface of a pillar that would otherwise be neutral. This aspect has been studied by Sterte [80] in pillared montmorillonites and fluorohectorites. In both cases and using a pillar with Si:Al ratio 2.2, the total acidity judged from  $\text{NH}_3$  retention at  $250^\circ\text{C}$  is more than doubled with respect to that measured with alumina pillars.

### 3.12.4 Catalytic Properties<sup>1</sup>

The aim of this last section is to outline the main trends of recent research performed with pillared clays as catalysts. A relatively recent review can be found in Ref. 59. It must be outlined that, as far as we are aware, at the exception of the reaction of ethylene oxide and ethanol producing glycol-ether, described by Atkins, [81] no pilot

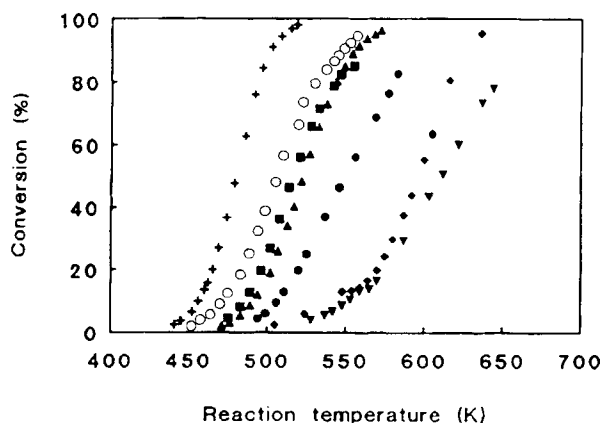


scale application of pillared clays exists. Reaction (4) has been carried out on Al (from chlorohydrol) pillared montmorillonite. This application is far away from the initial goal of the pioneers referred to in Section 3.12.1.1, e.g. the cracking of heavy hydrocarbons. In fact, it is likely that this goal will never be achieved, not because of inferior activity, but because of the lack of thermal and hydrothermal stability of the pillared material, which cannot withstand the severity of the cracking catalysts regeneration treatments.

Molina et al. [82, 83] have compared alumina pillared beidellite (synthetic) and montmorillonites relatively rich in Al  $\rightarrow$  Si substitutions, Si:Al being 13.3 ( $\text{N}_7$  sample) or 19 ( $\text{N}_4$  sample) and 132 (Westone L montmorillonite) in decane hydroisomerization-hydrocracking. In beidellite the Si:Al ratio was 10.9. All samples contain 1 wt % Pt. In addition, two ultrastable Y with Si:Al (framework Al) ratios of 13.5 and 36, respectively, have served as references. A Ga pillared WL montmorillonite was also used for comparison; Fig. 14 shows the conversion versus temperature.

As may be observed, the activity of the pillared beidellite (Si:Al = 10.9) and  $\text{N}_7$  (Si:Al = 13.3) are between the activity of the ultrastable Y CPV-720 (Si:Al = 13.5)

<sup>1</sup> The specific code used by the authors to designate their samples is used here. See corresponding references for further information.



**Figure 14.** Decane conversion versus reaction temperature on Al-pillared clays, Ga pillared montmorillonite GaPW and USY CBV 720 (Si:Al=13.5) (+) and CBV 760 (Si:Al=36) (Δ); (○) Al beidellite; (■) Al N<sub>7</sub>; (●) Al N<sub>4</sub>; (◆) Ga Montmorillonite; (▼) Al Montmorillonite (reprinted from Ref. 82 with permission).

and CPV 760 (Si:Al=36). AlPN<sub>4</sub> (Si:Al=19) and pillared Ga and Al montmorillonite come behind. The order of activity AlPB > AlN<sub>7</sub> > AlN<sub>4</sub> > GaPW ≥ AlPW follows the Brønsted sites content of the clay lattice, that is the number of Si by Al substitutions in the tetrahedral layer. The isomerization selectivity at 60% conversion follows almost the same order, namely, 89.7%, 83.6%, 55.2%, 35.2% (AlPB), and 20.7% (GaPW). This study concluded that USY and Al-pillared beidellite are similar isomerization catalysts. However, on USY (containing 1 wt% Pt) the hydrogenolysis is absent (no CH<sub>4</sub> formed), primary hydrocracking is obtained and the cracked products are essentially branched. On the pillared clay, with 1 wt% Pt also, hydrogenolysis is superimposed on hydrocracking.

A less complex and demanding reaction in terms of acidity, such as isomerization of *m*-xylene has been studied by Molina et al. [82] on similar samples, but without Pt. After 10 h on stream, the conversion on AlPB is about 25%, that is, half of that observed on a USY (with Si:Al=5), but the ratio isomerization on disproportionation was 8 on AlPB and less than 1 on USY. Thus, AlPB is a better isomerization catalyst than USY in the *m*-xylene conversion. In an earlier study of hydrocracking, Ocelli and Renard [84] concluded that pillared montmorillonites are ineffective as such, but if they are used as supports for metals (Mo and Ni) in composite catalysts containing zeolites, they display a good activity. Cumene cracking was carried out at 250 °C as a test reaction for Brønsted acidity on alumina pillared montmorillonite, precalcined between 250 and 500 °C [85]. It was outlined in Section 3.12.3.3 that chemisorbed ammonia is removed from Al-pillared and other pillared montmorillonites between 350 and 400 °C. Interestingly, cumene conversion falls sharply when the pretreatment temperature of the pillared clay is above 400 °C, while the Lewis acidity diminishes slowly with decreasing treatment temperature.

The conversion of cyclohexane to benzene over chromia pillared montmorillonite [30] prerduced at 550 °C in H<sub>2</sub>, is about 100% at 550 °C during 2 h when the con-

tent in chromia is equivalent to 1.24 Cr per unit cell (uc). It drops to half this value on a clay containing 3.53 Cr per uc. The weight hourly space velocity was in the range of  $1\text{--}3\text{ h}^{-1}$ . As compared to chromia dispersed on alumina, the use of the chromia pillared clay does not represent a real advantage.

From this brief review of the use of pillared clays as catalysts in hydrocarbon chemistry it is clear, that at best, one may expect to reach some of the performances of zeolites but not to exceed them.

Surprisingly, the domain of fine chemistry catalysis has not been much explored while it has received a lot of attention for reactions occurring in the interlayer space of unpillared clays [1]. Gutierrez and co-workers [86, 87] have studied the conversion of pinacol **1** and of 2,3-diphenyl-2,3-butanediol **2** into pinacolone **3**, 1,2-diphenyl-2-methyl-1-butanone **4** and 1,2-diphenyl-2-methyl-1-propanone **5**. They used a slurry of calcined Al, Zr, or Cr-pillared montmorillonite in either **1** or **2**. The catalyst: reagent ratio was about 6:1. For **1** the reaction temperature was  $100^\circ\text{C}$  while it was  $160^\circ\text{C}$  for **2**. Both reactions occur in concentrated sulfuric acid. A selectivity higher than 90% is obtained in the transformation of **1**  $\rightarrow$  **2** on zirconia and chromia pillared montmorillonite precalcined at  $400^\circ\text{C}$ , the secondary product being 2,3-dimethyl-1,3-butadiene.

As far as the transformation of **2** is concerned, in concentrated sulfuric acid the yield in **4** about 50%. On calcined Al-pillared and Zr-pillared clay the selectivity toward the ketone **4** is larger than 80% after 2 h, while after 17 h **4** and **5** are obtained in about equal proportions. Gutierrez et al. pointed out that on HY the ketone is a minor component while on acidic Amberlyst 15, **5** is the major component.

Still, in the above example of "soft" chemistry the acidity plays the major role. Work by Rightor et al. [56] and Barrault et al. [34, 88] tested the use of iron or mixed aluminum-iron pillared montmorillonite in the transformation of syngas into light alkenes. The reaction conditions employed by Rightor et al. were as follows:  $\text{H}_2:\text{CO}=2$ , pressure 8.6 bar,  $275^\circ\text{C}$ ,  $\text{GHSV}=2100\text{ h}^{-1}$ . After 21 h on stream the conversion was 1.3%. The Schulz-Flory distribution was obeyed for hydrocarbons from  $\text{C}_1$  to  $\text{C}_6$ . The results of Barrault et al. [34] were quite different on Al-Fe mixed pillars, but the conditions are not comparable. At  $450^\circ\text{C}$ , with a  $\text{H}_2:\text{CO}$  ratio close to 1 and a pressure of 0.1 MPa, the selectivity towards alkenes decreases, but the total conversion increases as the iron content of the pillars increases. The Schulz-Flory law is not obeyed because of an unusual selectivity for the  $\text{C}_2\text{--C}_5$  fraction. This deviation is attributed to a shape selectivity effect.

Choudary et al. [89] have reported the synthesis of chiral sulfoxides on Ti-pillared montmorillonite using diethyltartrate (DET) and *t*-butylhydroperoxide (TBHP) as chiral auxiliary. For instance, Ti-pillared clay is added to dry  $\text{CH}_2\text{Cl}_2 + \text{DET}$ . The prochiral sulfide is added. The mixture is cooled at  $-20^\circ\text{C}$  and azeotropically dried TBHP in toluene is introduced. The reaction is run for 3 h at  $-20^\circ\text{C}$ . Chiral sulfoxide is produced with a yield of 85%. According to Choudary et al. the yield is better in the heterogeneous system (at  $-20^\circ\text{C}$ ) than with the homogeneous catalyst. The enthusiastic reader must be warned that, without apparent reason, only an acid-leached montmorillonite is suitable.

The necessity for better characterization of the catalyst is particularly evident in this last example. Finally, it should be mentioned that pillared clays, such as zeo-

lites, are suitable supports for metal catalyst. An example of selective hydrogenation of 3-butenitrile and 2-butenitrile on palladium supported or Ti-pillared montmorillonite is given in Ref. 89. Apparently, there is no gain in using this catalyst if, for instance, its performance is compared to that of Raney nickel.

### 3.12.5 Conclusions

The pillared clays have an interesting architecture since the distance between the layers can be tuned between  $\approx 6$  and  $\approx 12$  Å and that chemical functions, as for instance Brønsted or Lewis acid sites, can be modified by various techniques. Two main warnings should be addressed to those who are not too familiar with the subject:

- (i) pillared clays are poorly crystallized systems;
- (ii) their thermal stability becomes questionable above 600 °C, when maintained for at least 24 h at this temperature and in the presence of steam.

The field of pillared clays has been much less investigated than that of zeolites, and one may hope that interesting applications have still to be uncovered. From what has been described above it seems that the potentially most interesting domains are in the separation technology and fine chemical catalysis. In hydrocarbon chemistry pillared clays should not compete, but complement zeolites.

### References

1. J. A. Ballantine, M. Davies, I. Patel, J. H. Purnell, M. Rayanakorn, K. J. Williams, J. M. Thomas, *J. Mol. Catal.* **1984**, 26, 37. J. A. Ballantine, J. H. Purnell, M. Rayanakorn, K. J. Williams, J. M. Thomas, *J. Mol. Catal.* **1985**, 30, 373 and references therein.
2. R. K. Barrer, *Phil. Trans. R. Soc. London* **1984**, A311, 333.
3. D. E. W. Vaughan, R. J. Lussier, J. S. Magee, US Patent 3 775 395 **1973**; US Patent 3 838 037 **1974**; UK Patent 1 483 466 **1979**.
4. G. W. Brindley, R. E. Sempels, *Clay Miner.* **1977**, 12, 229.
5. N. Lahav, U. Shani, J. Shabtai, *Clays and Clay Minerals* **1978**, 26, 107.
6. G. Brown, *Phil. Trans. R. Soc. London* **1984**, A311, 221.
7. J. Hougardy, W. E. E. Stone, J. J. Fripiat, *J. Magn. Res.* **1977**, 25, 563 and references therein.
8. C. F. Baes, Jr., R. E. Mesmer, *The Hydrolysis of Cations*, Wiley, New York, **1976**.
9. C. P. Herrero, in *Proc. Int. Clay Conf. 1985*, (Eds: L. G. Schultz, H. Van Olphen, F. A. Mumpton), The Clay Mineral Society, **1987**, p. 24.
10. (a) D. E. W. Vaughan, R. J. Lussier, *Preprints 5th Intern. Conf. on Zeolites*, Naples, Italy, **1980**; (b) D. E. W. Vaughan, *Catal. Today: Pillared Clays*. **1988**, 2, 187.
11. G. Johansson, G. Lundgren, L. G. Sillen, R. Soderquist, *Acta Chem. Scand.* **1960**, 14, 403.
12. (a) J. W. Akitt, W. Greenwood, B. L. Khandelwal, G. R. Lester, *J. Chem. Soc., Dalton Trans.* **1972**, 604; (b) J. W. Akitt, A. Farting, *J. Magn. Res.* **1988**, 32, 345.
13. J. Y. Bottero, D. Tchoubar, J. M. Cases, R. Flessinger, *J. Phys. Chem.* **1982**, 85, 3667.
14. R. A. Schoonheydt, H. Leeman, A. Scorpion, I. Lenotte, P. J. Grobet, *Clays and Clay Minerals* **1994**, 42, 518.
15. S. Schönherr, H. Gorz, D. Muller, W. Gessner, *Z. Anorg. Allg. Chem.* **1981**, 476, 188.

16. R. A. Schoonheydt, J. van den Eynde, H. Tubbax, H. Leeman, M. Stuyckens, J. Lenotte, W. E. Stone, *Clays and Clay Min.* **1993**, 41, 598.
17. D. Plee, L. Gatineau, J. J. Fripiat, *Clays and Clay Min.* **1987**, 35, 81.
18. M. L. Occelli, R. M. Tindwa, *Clays and Clay Min.* **1983**, 31, 22.
19. T. J. Pinnavaia, M. S. Tzou, S. D. Landau, H. R. Raythata, *J. Mol. Catal.* **1984**, 27, 195.
20. J. Sterte, *Catal. Today: Pillared Clays* **1988**, 2, 219.
21. F. Figueras, Z. Klapyta, P. Massiani, Z. Montassir, D. Tichit, F. Fajula, G. Guegen, J. Bousquet, A. Auroux, *Clays and Clay Min.* **1990**, 38, 257.
22. L. J. Michot, T. J. Pinnavaia, *Chem. Mater.* **1992**, 4, 1433.
23. S. M. Bradley, R. A. Kydd, R. Yamdagni, *J. Chem. Soc., Dalton Trans.* **1990**, 413, 2653.
24. S. M. Bradley, R. A. Kydd, R. Yamdagni, *Magn. Res. Chem.* **1990**, 28, 741.
25. A. Vierra-Coelho, G. Poncelet, *Appl. Catal.* **1991**, 77, 303.
26. G. J. J. Bartley, *Catal. Today: Pillared Clays* **1988**, 2, 233.
27. A. Clearfield, P. A. Vaughan, *Acta Cryst.* **1956**, 9, 555.
28. E. M. Farfan-Torres, O. Dedeycker, P. Grange in *Preparation of Catalysts V*, (Eds: G. Poncelet, P. A. Jacobs, P. Grange, B. Delmon), Elsevier Science, **1991**, p. 337.
29. T. J. Pinnavaia, M. S. Tzou, S. D. Landau, *J. Am. Chem. Soc.* **1985**, 107, 2783.
30. M. S. Tzou, T. J. Pinnavaia, *Catal. Today: Pillared Clays* **1988**, 2, 243.
31. A. Jimenez-Lopez, J. Maza-Rodriguez, P. Oliveria-Pastor, P. Mairoles-Torres, E. Rodriguez-Castellon, *Clays and Clay Min.* **1993**, 41, 328.
32. K. Bornholdt, J. M. Corker, J. Evans, J. M. Rommey, *Inorg. Chem.* **1991**, 30, 2.
33. G. Guio, P. Grange, *Mol. Cryst. Liq. Cryst.* **1994**, 245, 221.
34. F. Bergaya, J. Barrault in *Pillared Layered Structures* (Ed.: I. V. Mitchell), Elsevier, **1990**, p. 167.
35. Dongyan Zhao, Guojia Wang, Yashu Yang, Xiexion Guo, Quibin Wang and Jiyau Ren, *Clay and Clay Min.* **1993**, 41, 317.
36. J. Sterte, *Clay and Clay Min.* **1986**, 34, 658.
37. H. Yoneyama, S. Hafa, S. Yamanaka, *J. Phys. Chem.* **1989**, 93, 4833.
38. H. L. Del Castillo, P. Grange, *Appl. Catal. A* **1993**, 103, 23.
39. H. Einaga, *J. Chem. Soc., Dalton Trans.* **1976**, 1971.
40. T. Endo, M. Mortland, T. J. Pinnavaia, *Clays and Clay Min.* **1980**, 28, 105.
41. G. Fetter, D. Tichit, P. Massiani, R. Dutarte, F. Figueras, *Clays and Clay Minerals* **1994**, 42, 161.
42. A. Moini, T. J. Pinnavaia, *Solid State Ionics* **1988**, 26, 119.
43. S. P. Skaribas, P. J. Pomonis, P. Grange, B. Delmon in *Multifunctional Mesoporous Inorganic Solids* (Eds: C. A. C. Sequeira, M. J. Hudson), Kluwer, **1993**, 127.
44. J. Sterte, *Clays and Clay Min.* **1991**, 39, 167.
45. P. V. Malla, S. Komarneni, *Clays and Clay Min.* **1993**, 41, 472.
46. M. Gutierrez-LeBrun, J. M. Gaitte, *J. Magn. Res.* **1980**, 40, 105.
47. A. Banin, N. Lahav, *Israel J. Chem.* **1968**, 6, 235.
48. J. J. Fripiat, J. M. Cases, M. Francois, M. Letellier, *J. Coll. Interf. Sci.* **1982**, 89, 378.
49. H. Van Damme, P. Levitz, J. J. Fripiat, J. F. Alcover, L. Gatineau, F. Bergaya in *Physics of Finely Divided Matter* (Eds: N. Boccara, H. Daoud), Springer Verlag, Berlin, **1985**, p. 24.
50. M. L. Occelli, *Catalysis Today: Pillared Clays* **1988**, 2, 334.
51. J. J. Fripiat, R. Setton, *J. Appl. Phys.* **1987**, 61, 1811.
52. A. Schutz, W. E. Stone, G. Poncelet, J. J. Fripiat, *Clays and Clay Min.* **1987**, 35, 251.
53. I. Heylen, N. Maes, A. Molinard, and E. F. Vansant in *Separation Technology* (Ed.: E. E. Vansant), **1994**, p. 355.
54. A. Molinard, E. F. Vansant, *Adsorption*, Kluwer, Dordrecht, **1994**.
55. S. Yamanaka, M. Hattori, *Catalysis Today: Pillared Clay* **1988**, 2, 261.
56. E. G. Rightor, M. S. Tzou, T. J. Pinnavaia, *J. Catal.* **1991**, 130, 29.
57. J. Sterte, J. Shabtai, *Clays and Clay Min.* **1987**, 35, 429.
58. H. Van Damme, J. J. Fripiat, *J. Chem. Phys.* **1985**, 82, 2785.
59. E. Kikuchi, T. Masuda, *Catalysis Today: Pillared Clays* **1988**, 2, 297.
60. M. M. Mortland, J. J. Fripiat, J. Chaussidon, J. Uytterhoeven, *J. Phys. Chem.* **1963**, 67, 248.
61. M. M. Mortland, K. V. Raman, *Clays and Clay Min.* **1968**, 16, 398.

62. J. J. Fripiat, A. Jelli, G. Poncelet, J. André, *J. Phys. Chem.* **1965**, 69, 2185.
63. R. Touillaux, P. Salvador, C. Vandermeersche, J. J. Fripiat, *Israel J. Chem.* **1968**, 6, 337.
64. D. Plee, A. Schutz, G. Poncelet, J. J. Fripiat in *Catalysis by Acid and Bases* (Eds: B. Imelik, C. Naccache, G. Coudurier, Y. Bentaarit, J. C. Vedrine), Elsevier, Amsterdam, **1985**, p. 343.
65. S. Chevalier, R. Franck, H. Suquet, J. F. Lambert, D. Barthomeuf, *J. Chem. Soc., Faraday Trans.* **1994**, 90, 667.
66. E. J. W. Verwey, J. Th. G. Overbeek, *Theory of the Stability of Lyophobic Colloids*, Elsevier, New York, **1948**.
67. B. Chourabi, J. J. Fripiat, *Clays and Clay Min.* **1981**, 29, 260.
68. D. Plee, F. Borg, L. Gatineau, J. J. Fripiat, *J. Am. Chem. Soc.* **1985**, 107, 2362.
69. T. J. Pinnavaia, S. D. Landau, M. Tzou, I. D. Johnson, M. Lipsicas, *J. Am. Chem. Soc.* **1985**, 107, 7222.
70. D. T. B. Tennakoon, W. Jones, J. M. Thomas, *J. Chem. Soc. Faraday Trans.* **1986**, 82, 3081.
71. J. F. Lambert, S. Chevalier, R. Franck, H. Suquet, D. Barthomeuf, *J. Chem. Soc., Faraday Trans.* **1994**, 90, 675.
72. L. Zheng, Y. Hao, L. Hao, Y. Zhang, Z. Hue, *Zeolites* **1992**, 12, 374.
73. Sun Guida, Yan Fushan, Zhu Huihua, Liu Zhonghui in *Preparation of Catalysts IV* (Eds: B. Delmon, P. Grange, P. A. Jacobs, G. Poncelet), Elsevier, **1987**, p. 649.
74. E. M. Farfan-Torres, E. Sham, P. Grange, *Catal. Today* **1992**, 15, 515.
75. S. Bodoardo, F. Figueras, E. Garrone, *J. Catal.* **1994**, 147, 223.
76. K. Arata, *Adv. Catal.* **1990**, 37, 165 and references therein.
77. F. Admaia, A. Bernier, P. Grange, *New Frontiers in Catalysis*, (Eds: Gucci, F. Solymosi, P. Tetenyi), Proceedings of the 10th Intern. Cong. on Catalysis, Budapest 1992, Elsevier, **1993**, p. 1629.
78. L. K. Boudali, A. Ghorbel, D. Tichit, B. Chiche, R. Dutarte, F. Figueras, *Microporous Materials* **1994**, 2, 525.
79. E. M. Farfan-Torres, P. Grange, *Catalytic Science and Techn.* **1991**, 1, 103.
80. J. Sterte, *New Types of Cracking Catalysts Based on Cross-linked Smectites*, Department of Engineering Chemistry, Chalmers Biblioteks Tryckeri, Göteborg, **1987**, Vol. 1, p. 27.
81. M. P. Atkins, in *Pillared Layered Structures* (Ed.: I. V. Mitchell), Elsevier Applied Science, **1990**, p. 159.
82. R. Molina, S. Moreno, A. Vieira-Coelho, J. A. Martens, P. A. Jacobs, G. Poncelet, *J. Catal.* **1994**, 148, 304.
83. R. Molina, A. Schutz, G. Poncelet, *J. Catal.* **1994**, 145, 79.
84. M. L. Occelli, R. J. Renard, *Catalysis Today: Pillared Clays* **1988**, 2, 309.
85. M.-Y. He, Z. Liu, E. Min, *Catalysis Today: Pillared Clays* **1988**, 2, 321.
86. E. Gutierrez, E. Ruiz-Hitzky, *Mol Cryst. Liq. Cryst.* **1988**, 161, 453.
87. E. Gutierrez, A. J. Aznar, E. Ruiz-Hitsky in *Heterogeneous Catalysis and Fine Chemicals*, (Eds.: Guisnet et al.), Elsevier Science, **1988**, p. 211.
88. J. Barrault, C. Zivkov, F. Bergaya, L. Gatineau, N. Hassoun, H. Van Damme, D. Mari, *J. Chem. Soc., Chem. Commun.*, **1988**, 1403.
89. B. M. Choudary, S. Shobha-Rani, N. Narender, *Catal. Lett.* **1993**, 119, 299.
90. A. Lamesh, H. del Castillo, P. Vanderwegen, L. Daza, G. Jannes, P. Grange, *Heterogeneous Catalysis and Fine Chemicals III*, Elsevier, **1993**, p. 299.

## 4 Supported Catalysts

### 4.1 Deposition of Active Component

#### 4.1.1 Impregnation and Ion Exchange

M. CHE, O. CLAUSE AND CH. MARCILLY

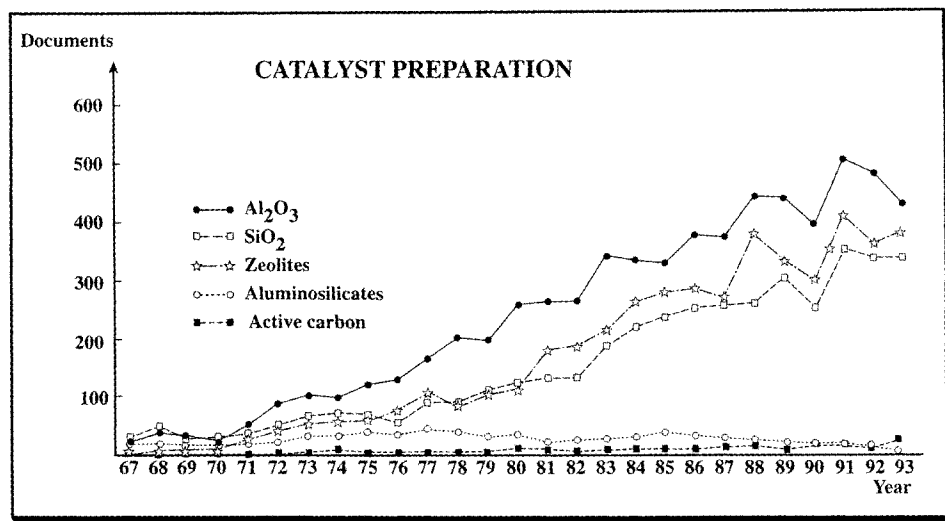
##### 4.1.1.1 Introduction

Many practical catalysts consist of one or several catalytically active component(s) deposited on a high-surface-area support and the present article deals with only such catalysts. The main purpose of using a support is to achieve an optimal dispersion of the catalytically active component(s) and to stabilize it (them) against sintering. However, in a number of reactions, the support is not inert and the overall process is actually a combination of two catalytic functions: that of the active component(s) and that of the support. Fig. 1 gives the number of papers dealing with catalyst preparation involving the supports most frequently studied during the period 1967–1993.

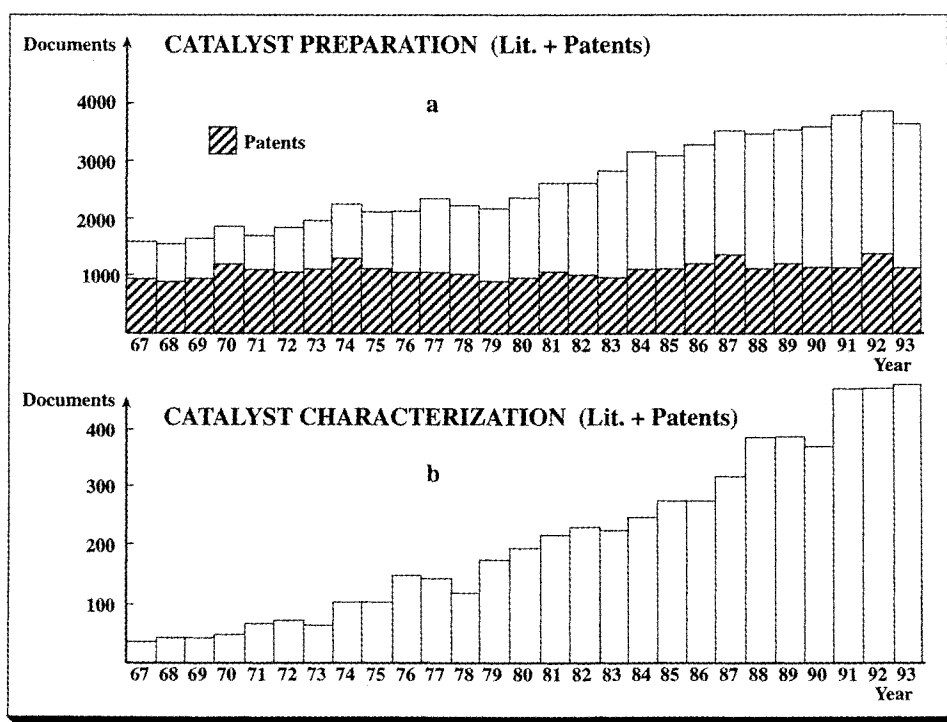
There are many definitions of catalyst preparation but the most revealing one seems to have been given by Richardson [1]: “catalyst preparation is the secret to achieving the desired activity, selectivity and life time”. This definition conveys the idea that catalyst preparation is a strategic procedure which should not be disclosed or, if published, should be protected in the form of patents.

Although the preparation of supported catalysts is one, if not the most, important step in the course of a catalytic process, it is interesting to observe that little attention has been given to this subject in most textbooks written on catalysis. By contrast, the number of documents published on this subject is very large (Fig. 2(a)). This apparent contradiction lies in the fact that most, if not all, papers and patents give preparation procedures rather than rationalizations and concepts, making any synthesis, usually required in textbooks, rather difficult. It is thus no surprise that the term “catalyst design” has been little used.

It is also interesting to observe that while the number of papers steadily increases, the number of patents is, by contrast, almost constant (Fig. 2(a)). It is also important to note (Fig. 2(b)) that the literature on catalyst characterization steadily in-



**Figure 1.** Number of papers concerned with catalyst preparation involving the most frequently used supports during the period 1967–1993.



**Figure 2.** Comparison of the number of papers and patents found in the literature dealing with (a) catalyst preparation and (b) characterization during the period 1967–1993.



creases but remains almost one order of magnitude less abundant than for catalyst preparation, explaining perhaps why our understanding of the latter domain is not satisfactory and is not well rationalized.

For these reasons, there now appears to be a general consensus that one should try to

- (i) investigate the basic aspects of catalyst preparation;
- (ii) identify the elementary steps and the related pertinent parameters so that new sequences of such steps can be proposed, making catalyst architecture possible;
- (iii) establish procedures for choosing the most appropriate method for industrial catalyst preparation.

In recent years, major advances have been made on techniques for physically and chemically characterizing supported catalysts [2] and on the quantitative and qualitative aspects of catalyst preparation [3–12], so that the design of supported catalysts has begun to become a feasible activity.

The term “design” is most appropriate when the precise nature of the active center for a given reaction is known and can be reproduced at the molecular level, including the oxidation state of the catalytically active element, the nature and symmetry of the environment, namely the nature and number of the different ligands (in particular the type of support and number of bonds with the latter, the number and nature of ancillary ligands), and the number of coordination vacancies.

A properly designed catalyst should have the essential attributes of activity, stability, selectivity and regenerability [13]. Such characteristics can be related to the physical and chemical properties of the catalyst, which in turn can be related to the many parameters inherent to the method used to prepare the catalyst. In the past, much of the literature on supported catalysts has not included this information.

There are two main steps in catalyst preparation. The first consists of depositing the active component precursor, as a divided form, on the support, and the second of transforming this precursor into the required active component which, depending on the reaction to be catalyzed, can be found in the oxide, sulfided or metallic state. A large majority of deposition methods involve aqueous solutions and the liquid–solid interface. In some cases, deposition can be also performed from the gas phase and involves the gas–solid interface.

The methods most frequently used to achieve deposition of the active component precursor are impregnation, ion exchange, anchoring, grafting, spreading and wetting, heterogeneization of complexes, deposition–precipitation (homogeneous and redox) and adapted methods in the case of supported bimetallic catalysts. In some cases, the active component (not its precursor form) can be deposited directly on the support.

When a support is put in a solution containing a precursor of the active component, several phenomena can occur among which ion exchange, impregnation, dissolution of the support and formation of surface compounds are the most important. If the experimental parameters are not properly adjusted, there is a fair probability that these phenomena may occur simultaneously. In what follows, we shall therefore discuss, for the sake of simplicity, first ion exchange and then impregnation. We will then consider the problem of oxide dissolution.

### 4.1.1.2 Ion Exchange

Ion exchange consists of replacing an ion in an electrostatic interaction with the surface of a support by another ion species. The support containing ion A is plunged into an excess volume (compared to the pore volume) of a solution containing ion B that is to be introduced. Ion B gradually penetrates into the pore space of the support and takes the place of ion A, which passes into the solution, until an equilibrium is established corresponding to a given distribution of the two ions between the solid and the solution.

#### A Types of Ion Exchangers

Almost all solid mineral supports are oxides. They behave like ion exchangers when their surface bears electric charges. Two categories may be distinguished: (i) natural exchangers and (ii) amphoteric oxides.

Natural exchangers are composed of a framework bearing electric charges neutralized by ions of opposite sign. For zeolites, for example, these charges are negative and are due to the particular environment of aluminum. Aluminum, just like silicon, is effectively situated in the center of a tetrahedron of four oxygen atoms, which provides it with four negative charges, whereas the aluminum itself has only three positive charges. The tetrahedron ( $\text{AlO}_4$ ) is thus an overall bearer of a negative charge distributed over the oxygen atoms, and this charge is neutralized by the presence of various cations,  $\text{Na}^+$ ,  $\text{K}^+$ , etc.

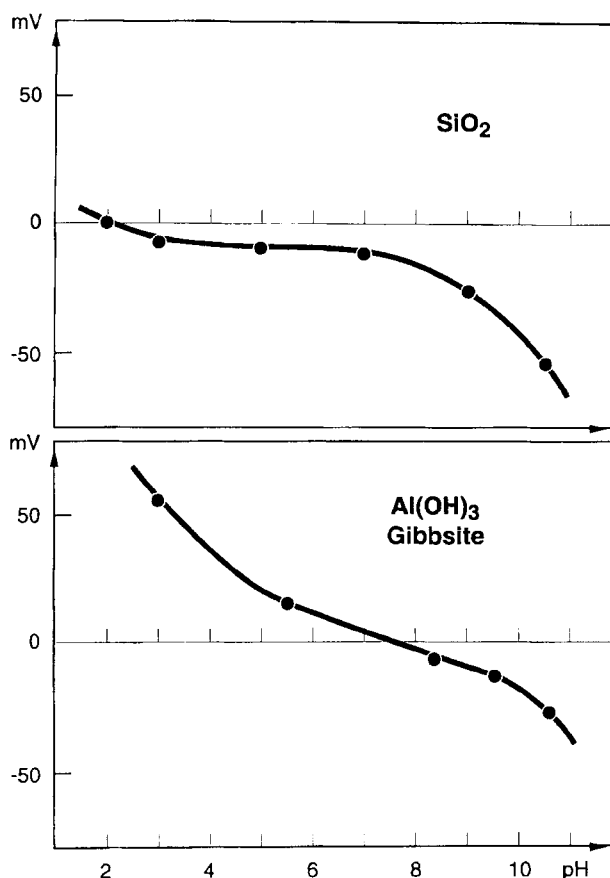
These cations are not definitively linked to the framework but may be replaced by other cations during an ion-exchange operation. Whatever the exchange conditions, and in particular the pH, zeolites are cation exchangers and have a constant number of exchange sites, which is equal to the number of aluminum atoms in their framework.

There are natural ion exchangers other than zeolites. Clays and silicates are cation exchangers, whereas hydrotalcites are anion exchangers. As in the case of zeolites, the number of exchange sites is not pH dependent.

Oxide surfaces contacted with water are generally covered with hydroxy groups which can be schematically represented as  $\text{S-OH}$  where S stands for Al, Si, Ti, Fe etc. Some of these groups may behave as Brønsted acids, whereas other hydroxy groups may behave as Brønsted bases, giving rise to the following equations:



The resulting surface charge which arises from an excess of one type of charged site over the other, is a function of the solution pH. A given value of pH exists for which the particle is not charged overall. This value is characteristic of the oxide and is called the pristine point of zero charge (PPZC or simply ZPC) of the oxide. There is some variation in terminology in the literature in that ZPC sometimes means the isoelectric point (IEP) [14–16]. The ZPC values of oxides frequently used as catalyst supports have been reviewed by Parks [14] and Kung [15]. When oxide particles are suspended in aqueous solutions with  $\text{pH} > \text{ZPC}$ , the oxide particles



**Figure 3.** Variation of the zeta potential of silica and alumina (gibbsite) as a function of pH.

tend to be negatively charged and to adsorb cations. Conversely, at  $\text{pH} < \text{ZPC}$ , anion adsorption is favored [16]. Reported values of the ZPC for  $\gamma$ -alumina range between 7 and 9, depending on thermal activation and impurities. This is illustrated in Fig. 3 which shows the variation of zeta potential as a function of pH for silica and alumina. Thus  $\gamma$ -alumina is amphoteric and may adsorb cations as well as anions. ZPC values for silica range between 1.5 and 3. Silica may only adsorb cations. It should be mentioned that cation adsorption is significant only above pH 7 [16, 17].

Many electrical double-layer and adsorption models have been proposed to account for experimental data dealing with the adsorption of ions on oxides. Stern suggested separation of the solution region near the surface into two parts, the first consisting of a layer of ions adsorbed at the surface (compact layer) and the second consisting of a diffuse Gouy layer [18]. More specifically the compact region can be structured as an inner Helmholtz plane (IHP) located at the surface of the layer of Stern adsorbed ions and an outer Helmholtz plane (OHP), located on the plane of centers of the next layer of ions [19, 20]. Specifically adsorbed ions are located in the

IHP, whereas electrostatically adsorbed ions are located in the OHP (site binding models) [19, 21–26].

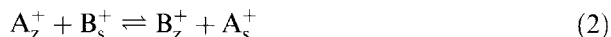
Assumptions underlying the adsorption models are not often discussed in the literature, since the exact nature of the relevant surface complexes or phases is difficult to identify. In particular, lateral interactions between adsorbed ions, site heterogeneity as well as phenomena involving the oxide dissolution or rehydration are not taken into account systematically. The latter phenomena are discussed in section D.d. Lateral interactions between adsorbed ions (ion coadsorption) have been reported [27, 28] and make questionable the use of mass action equations at interfaces. The effect of surface structure, site heterogeneity and surface composition, in particular on the ZPC value, were also pointed out [29, 30].

The adsorption of atomically dispersed ions generally allows for a much better dispersion of the active agent than does simple wetting without exchange [31–33]. Obviously, the high dispersions gained in the precursors have to be kept during the subsequent drying, calcination or reduction operations, which is frequently observed. For example, the metal dispersion on silica resulting from impregnating  $\text{Pt}(\text{NH}_3)_4\text{Cl}_2$  by ion exchange is excellent, even when the platinum loading reaches several weight percent, whereas incipient wetness impregnation with  $\text{H}_2\text{PtCl}_6$  solutions leads to the formation of large metal crystallites after reduction [34].

## B Elementary Background of Single Ion Exchange

We have a single exchange when the solid-solution system makes only two ions intervene: ion  $\text{A}^+$  to be replaced on the solid Z, for instance a zeolite, by ion  $\text{B}^+$  present in the solution.

For the simple case of two monovalent cations, the exchange equilibrium can be written as



in which the subscripts S and Z represent the solution and the solid, respectively.

An exchange is characterized by an isothermal exchange curve representing the variation of the  $C_{\text{BZ}}$  concentration of ion  $\text{B}^+$  in the solid as a function of the  $C_{\text{BS}}$  concentration of  $\text{B}^+$  in the solution. The concentrations  $C_{\text{BZ}}$  and  $C_{\text{BS}}$  are expressed in ion-grams per unit of volume of the solid for the former and of the solution for the latter.

A simple equation between  $C_{\text{BZ}}$  and  $C_{\text{BS}}$  may be obtained by means of various simplifying assumptions. If we take the case of an ideal exchange (both the exchanger and the solution are ideal), and which has only a single category of site, the equilibrium constant  $K_a$  can be written as

$$K_a = \frac{C_{\text{BZ}}C_{\text{AS}}}{C_{\text{BS}}C_{\text{AZ}}} \quad (3)$$

with  $C_{\text{AZ}} + C_{\text{BZ}} = C_Z$  and  $C_{\text{AS}} + C_{\text{BS}} = C_S$ .

With  $C_Z$  and  $C_S$  being the total concentrations of cations in the solid and the solution respectively, it follows that

$$C_{\text{BZ}} = \frac{K_a C_Z C_{\text{BS}}}{C_S + (K_a - 1)C_{\text{BS}}} \quad (4)$$

If the exchange is no longer ideal, eq 4 must be expressed in terms of concentrations and activity coefficients. The problem becomes even more complicated if the ions are not monovalent and if there are several types of sites on the solid surface. In such cases, often encountered in practice, theoretical predictions are no longer possible. It then becomes indispensable to have recourse to experiments to obtain isothermal curves that can be used in predicting the number and conditions of successive exchanges required to replace a given fraction of ions A by ions B.

A simple and standard example of an exchange is that used to replace sodium ions in zeolite NaY by ammonium ions. Zeolite NaY, with the overall formula  $\text{Na}_2\text{O} \cdot \text{Al}_2\text{O}_3 \cdot 5\text{SiO}_2$ , contains 9.9 wt% sodium. Available isothermal exchange curves show that, at room temperature, only about 73% of the sodium ions can be exchanged and that, unless a very large volume of solution is used with an ammonium salt, a single exchange operation is not sufficient to eliminate all of the exchangeable sodium ions. To reach a high exchange degree, we thus adopt either a discontinuous technique, which involves several successive operations, or a continuous technique in which the exchange solution crosses the solid bed and is renewed by the progressive addition of fresh solution with the corresponding drain of the balanced solution.

### C Multiple or Competitive Ion Exchange Involving a Single Metal Ion

This technique, which has been known for a long time with regard to anions [35, 36], was suggested for the first time with regard to cations by Benesi [37]. It proves to be particularly useful when trying to introduce and homogeneously distribute small amounts of a noble metal on a support with a large surface area. This situation is examined in detail by a simple example, that of introducing the ion  $\text{Pt}(\text{NH}_3)_4^{2+}$  by cation exchange into a zeolite  $\text{NH}_4\text{Y}$ .

#### (i) Statement of the Problem

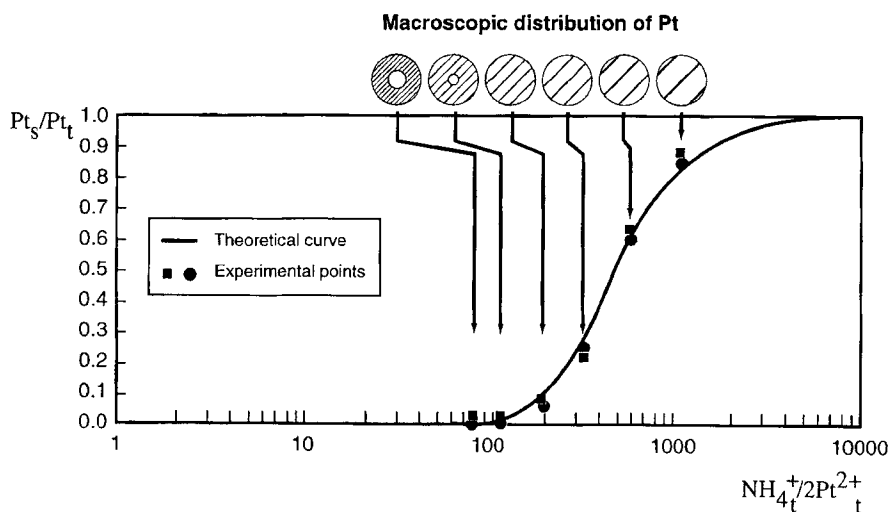
In zeolite  $\text{NH}_4\text{Y}$ , about 73% of the ammonium ions are situated in large cavities and can be replaced by  $\text{Pt}(\text{NH}_3)_4^{2+}$  ions [38–40]. The saturation of all of these exchangeable sites corresponds to the fixing of more than 25 wt% of platinum in relation to the anhydrous zeolite. Yet, for obvious reasons of price, industrial catalysts must contain small amounts of noble metal, less than 1 wt% in relation to the zeolite, and the catalyst manufacturer will try to fix on the zeolite all the metal contained in the solution. This amount of metal contained thus represents 3–4% at the most of the exchangeable sites of the zeolite.

Let us consider a support composed of grains (beads, extrudates or others) several millimeters in diameter and containing a more or less large amount of zeolite Y (20–70 wt%, for example). After impregnation, question arises as to what is:

- the degree of metal fixation by the solid and hence, the residual quantity of metal ions in solution, and
- the macroscopic distribution of the metal inside the support.

The equilibrium between  $\text{NH}_4^+$  and  $\text{Pt}(\text{NH}_3)_4^{2+}$  ions is as follows:





**Figure 4.** Residual fraction of Pt in the solution as a function of the  $\text{NH}_4^+ : 2\text{Pt}_t^{2+}$  ratio of competition between  $\text{NH}_4^+$  and  $\text{Pt}^{2+}$  ions in the whole system.

The isothermal exchange curve between  $\text{NH}_4^+$  ions and  $\text{Pt}(\text{NH}_3)_4^{2+}$  suggests that zeolite Y has a strong affinity for the  $\text{Pt}(\text{NH}_3)_4^{2+}$  ion [39, 40]. Since the exchange velocity is limited by the diffusion inside the grain, tetrammine platinum ions will be quantitatively and strongly fixed on the first sites encountered, i.e. on the periphery of the grains. The concentration of the solution, which is almost the sole driving force behind the diffusion (adsorbed-phase diffusion may be neglected), will thus decrease rapidly. A state of pseudo-equilibrium is obtained which is characterized by a very heterogeneous metal deposit at the macroscopic scale (crust deposit) and which evolves only very slowly towards a state of true equilibrium corresponding to a homogeneous dispersion inside the volume of the grain [39, 40].

The only way of speeding up this evolution towards true equilibrium is to increase the amount of residual metal in solution  $\text{Pt}(\text{NH}_3)_4^{2+}(\text{S})$  or  $\text{Pt}_s$  (obviously while maintaining constant the total amount of platinum  $\text{Pt}_t = \text{Pt}_s + \text{Pt}_z$  in the system) so as to speed up diffusion. This result is obtained, as shown by Fig. 4, by adding an ionic agent, here  $\text{NH}_4^+$ , whose role is to make eq 5 regress towards the left, hence to increase  $\text{Pt}_s$ . Such ionic agents are called “competitors” and the resulting effect the “competition effect.”

*(ii) Thermodynamic Aspect: Fixation Degree of Metal Ions on the Zeolite*

The thermodynamic constant of eq 5 can be written in terms of concentrations of the various ionic species:

$$K_a = \frac{[\text{Pt}]_z [\text{NH}_4]_s^2}{[\text{Pt}]_s [\text{NH}_4]_z^2} \quad (6)$$

If concentrations are replaced by the amounts of the corresponding ions in the

system, for example  $[Pt]_z = Pt_z/V_z$ , eq 6 becomes

$$K_a = \frac{Pt_z(NH_4)_s^2}{Pt_s(NH_4)_z^2} \times \frac{V_z}{V_s} \quad (7)$$

where  $V_z$  and  $V_s$  are the volumes of the zeolite crystals and the solution, respectively. By replacing  $Pt_s$  by  $Pt_t - Pt_z$  and  $NH_{4s}$  by  $NH_{4t} - NH_{4z}$ , eq 7 becomes

$$K_a = \frac{Pt_z}{(Pt_t - Pt_z)} \times \left( \frac{NH_{4t} - NH_{4z}}{NH_{4z}} \right)^2 \times \frac{V_z}{V_s} \quad (8)$$

where  $NH_{4t}$  is the total amount of ammonium ions in the system.

If  $Pt_t$  is small compared to the total number  $N_z$  of exchangeable sites of the zeolite, we can write  $NH_{4z} \approx N_z$ . We can thus express the variation of the fraction of Pt fixed on the zeolite as a function of the total amount  $NH_{4t}$  of the competing ion:

$$\frac{Pt_t}{Pt_z} \approx \frac{1}{K_a} \times \frac{V_z}{V_s} \left( \frac{NH_{4t}}{N_z} - 1 \right)^2 + 1 \quad (9)$$

It can thus be seen that the value of the fixation level  $Pt_z/Pt_t$  can be adjusted to the desired value by adjusting the total amounts of the competing ammonium ion  $NH_{4t}$  in the system.

### (iii) Practical Aspects

The importance of the competition technique lies in the possibility of speeding up the impregnation kinetics and of reaching, within a reasonable length of time, a homogeneous macroscopic distribution of the metal on the support. This is particularly important when the catalyst grains are larger than several millimeters, as would be the case of a Y zeolite-based catalyst in the form of cylindrical pellets about 3 mm in diameter and 2 mm long. In the absence of  $NH_4^+$  ions in the initial solution, the platinum is distributed in a peripheral crown about 0.5 mm thick. Castaing's microprobe shows that, inside this crown, the platinum concentration diminishes strongly from the outside to the inside. The choice of proper amount of  $NH_4^+$  ions per  $Pt^{2+}$  ion in the system must leave less than 5% of the initial platinum in equilibrium in the final solution, but it must also bring about a quasihomogeneous distribution of the metal within a few hours. Proper stirring of the medium is beneficial for the operation. In the absence of stirring, the kinetics is actually limited by diffusion in the bed of solid grains at the bottom of the recipient and of the boundary layer surrounding each grain.

The advantage of the competitive exchange technique is obviously much less evident when the zeolite is exchanged in the form of a fine powder. If no competition is used, various precautions must be strictly respected:

- very effective stirring of the powder;
- progressive addition of the metal ion to the solution (for about an hour);
- an exchange duration longer than or equal to about 5 hours.

Slight competition also speeds up the operation appreciably.

#### 4.1.1.3 Impregnation without Precursor–Support Interaction

Such techniques consist of introducing, into the pore space of a support, a solution of an inert precursor, i.e. one that does not interact with the solid surface. In principle, the precursor thus remains in the dissolved state in the solution and does not become fixed on the surface at this stage of preparation.

Two cases can be distinguished, depending on whether the pore space of the support contains only ambient air at the start or whether it is already filled by the solvent from the impregnation solution (usually water) or by another liquid. Impregnation is said to be capillary in the former case and diffusional in the latter.

##### A Capillary Impregnation

The operation consists of putting into contact with the previously dried support, with a pore volume  $V_p$ , a volume  $V$  of solution containing the precursor selected [41, 42]. In almost all cases,  $V = V_p$ , so that at the end of the operation no excess solution remains outside of the pore space. This is called dry impregnation.

Capillary impregnation is mainly characterized by its exothermicity, by the capillary pressures developed in pores and by the speed with which the pore space is filled.

##### (i) Exothermicity

The replacement of the solid–gas interface by a solid–liquid interface generally causes a considerable decrease in the free enthalpy of the system. This causes a strong release of heat, which often has little effect on the quality of the impregnation, except in the following specific cases:

- The precursor has retrograde solubility and its concentration is about the same as the saturation.
- In a solution containing an unstable mixture of several metal precursors, the temperature rise risks causing the precipitation of a mixed compound poorly distributed on the surface.
- The impregnation solution is aggressive with regard to the support (very acid pH, for example), and an attack of the support surface may then occur, with accelerated alteration of its surface properties.

Solutions exist for avoiding these disadvantages, such as:

- Deactivation of the support by means of superheated steam to form a liquid surface film.
- Stabilization of the precursor(s), for example by complex formation.

##### (ii) Pressures Developed in Pores upon Impregnation

As soon as the support is placed in contact with the solution, the solution is sucked up by the pores [43–48]. Part of the air present in the pore space will be imprisoned and compressed under the effect of capillary forces. The pressures developed inside the imprisoned gas bubbles depend on the radii  $r$  of the curve of the liquid–gas



menisci and may reach several MPa (or tens of bar) when  $r < 100$  nm, as a result of the Young–Laplace law:

$$\Delta P = P - P' = \frac{2\gamma}{r} \quad (10)$$

where  $\gamma$  is the liquid–gas interfacial tension.

Considerable forces will thus be exerted on the portions of the pore walls in contact with these bubbles. The walls that are not strong enough will break down, causing a degradation of the mechanical properties, sometimes even bursting the catalyst grains.

The development of high pressures is a transitory phenomenon. When highly compressed, air becomes dissolved and progressively escapes from the solid. The filling of the pore space is thus far from being instantaneous.

Methods exist for preventing or limiting the bursting of the support upon impregnation, such as operating in vacuum and adding a surfactant to the solution.

### *(iii) Capillary Impregnation Rate*

Oversimplified calculations show that the time taken by the liquid to fill up the pores is of the order of a few seconds [49–53]. In reality, however, determination of impregnation time must take into consideration the imprisonment of air within the porosity and the elimination of this occluded air [48]. The impregnation process will be limited by the dissolution of the imprisoned and compressed air and its migration to the outside of the grain. The Young–Laplace law (eq 10) shows that the last bubbles to disappear are those present in the largest pores, because they are subjected to the lowest pressures.

## **B Diffusional Impregnation**

If the pore space of the support is filled with the same solvent as the impregnation solution, prior to being placed in contact with the latter, the characteristics defined above are valid only for the first phase of saturation by the solvent.

The second phase is generally an immersion phase that consists of plunging the solvent-saturated support into the impregnation solution. This second phase is no longer exothermic and does not cause the development of high pressures inside the pore space. The precursor salt migrates progressively from the solution into the heart of the grains of the support. The driving force at all times is the concentration gradient between the extragranular solution and the advancement front of the soluble precursor in the intragranular solution. The migration time is obviously much longer than for capillary impregnation.

The principle of diffusional impregnation is much simpler than when a precursor–support interaction occurs. Two cases may be distinguished:

- (i) when the concentration of the solution outside the grains remains constant;
- (ii) when this concentration varies from the start to the end of the diffusion process.

The first case has been dealt with by various authors [54–59]. Weisz [56] defines a relaxation time constant  $\tau$  for the system, which is representative of the time re-

quired to be very close to equilibrium (reaching uniform concentration theoretically requires an infinite time):

$$\tau = \frac{R^2}{D} \quad (11)$$

where  $R$  is a length parameter depending on the volume geometry ( $R$  is the radius in the case of a sphere or an extrudate) and  $D$  is the diffusion coefficient of the precursor in the solvent.

When volume  $V$  is occupied by a porous solid, eq 11 is generally made to include a tortuosity coefficient  $\beta$ , the pore fraction  $\varepsilon$  (fraction of the support grain volume occupied by the pore space) and an interaction coefficient  $K$  between the precursor and the support ( $K = 1$  if there is no interaction):

$$\tau = \frac{R^2}{D} \times \frac{\beta}{\varepsilon} \times K = \frac{R^2}{D_{\text{eff}}} \quad (12)$$

where  $D_{\text{eff}} = \varepsilon D / \beta K$  is the effective or apparent diffusion coefficient of the solute in the porous solid.

The values of  $\beta$  are generally between 1.3 and 10, more often between 2 and 6 (values determined from various gases [60]). The values of  $\varepsilon$  are mostly between 0.3 and 0.7 [60]. The values of  $D$  in the liquid phases are generally about  $10^{-5} \text{ cm}^2 \text{ s}^{-1}$  [55–60].

As an example, consider a support made up of beads with radius  $R = 2 \text{ mm}$ , and assume that  $K = 1$ ,  $D = 10^{-5} \text{ cm}^2 \text{ s}^{-1}$  and  $\varepsilon = 0.5$ . Time  $\tau$  calculated from eq 11 is:

$$\begin{aligned} \text{if } \beta &= 1.3, & \tau &\approx 3 \text{ h} \\ \text{if } \beta &= 5, & \tau &\approx 12 \text{ h} \end{aligned}$$

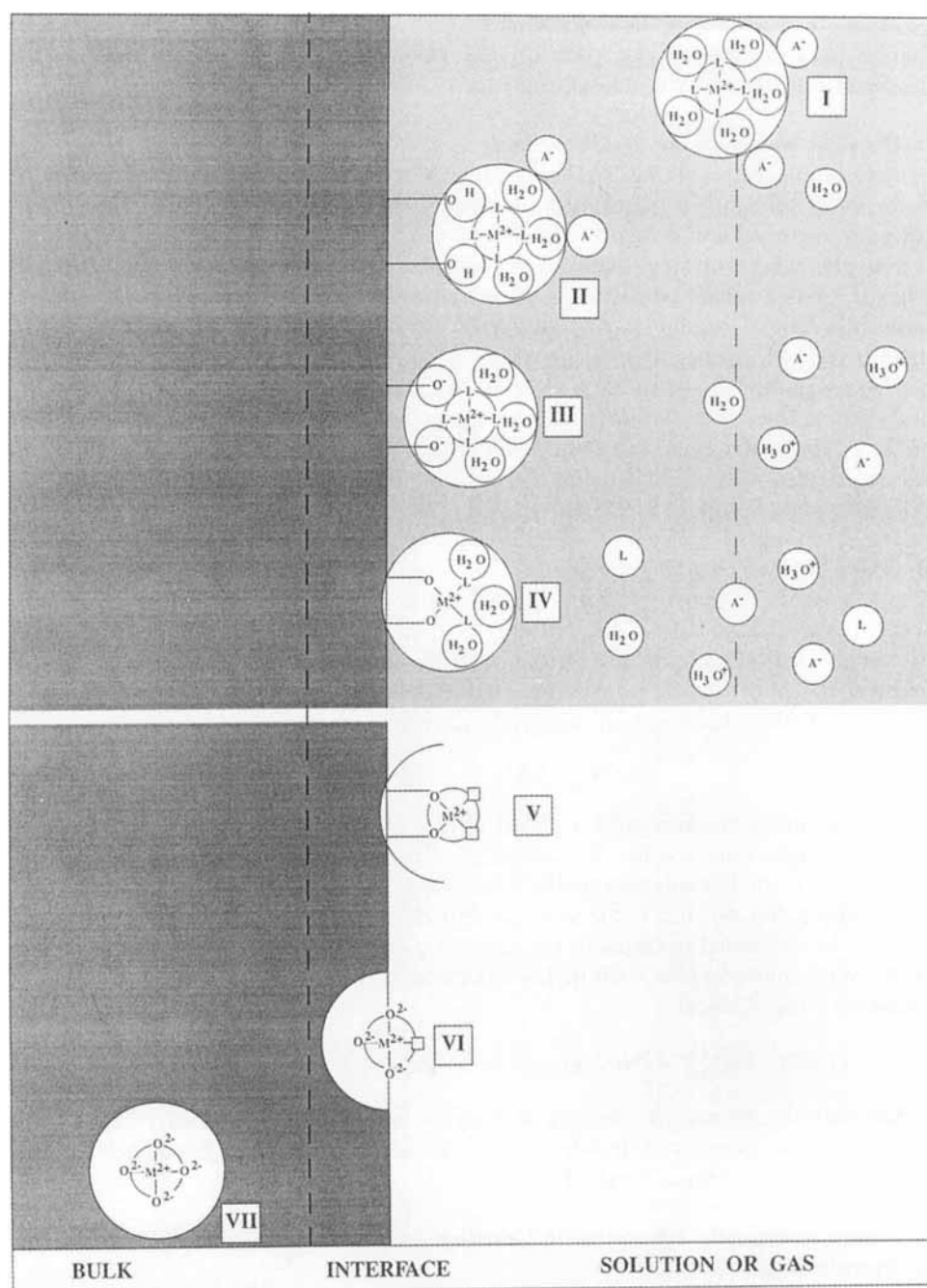
Since the value of  $\tau$  is proportional to the square of the radius, it can be appreciably reduced by diminishing the size of the particles. Thus with beads having a radius of 1 to 0.5 mm, the above value are divided by 4 and 16, respectively.

Diffusional impregnation is almost never used for preparing catalysts when there is no appreciable interaction between the precursor and the support.

#### 4.1.1.4 Role of the Support During the Preparation Steps

Supported transition metal ions (TMI) which often are catalytic sites can also be used to probe the role of the support, via their own interaction with the latter. Because of their partly filled d orbitals, any change in their first coordination sphere immediately affects their optical and magnetic properties and can thus be detected by spectroscopy. In the context of interfacial coordination chemistry [12, 61], the approach has been to use transition metal complexes in aqueous solutions and to investigate the changes, occurring at the liquid–solid interface during deposition, in the interaction between the TMI engaged in the complex and the support.

By a careful control of the preparation parameters, it is possible to obtain the TMI successively in solution (Fig. 5, model I), on the surface in extraframework



**Figure 5.** Interaction models between a TMI of a precursor complex and an oxide support: (top) liquid; (bottom) gas. The left- and right-hand sides represent the solid oxide and fluid phase respectively. The vertical dotted lines represent the width of the interface, as explained in Ref 12.

position (models II–V), then in the surface in framework position (model VI), to finally reach the bulk of the oxide (model VII). Models II–IV are pertinent to the deposition of the active component precursor.

### A Physical Nature of the Oxide Surface

When complexes involving TMI are put in microcontainers, such as the pores of amorphous solids or in the cavities of zeolites, their coordination chemistry is basically not changed and model I (Fig. 5) is applicable.

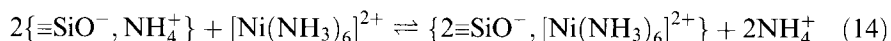
For pHs where surface functions are essentially OH groups, the oxide is able to enter the outer sphere of solvation of the complex in the same way as the solvent molecules (Fig. 5, model I) and thus acts as a solid solvent (Fig. 5, model II). When ligands have electronegative donor atoms (N, O, Cl, F), there can be some hydrogen bonds (model II, assuming  $L = \text{NH}_3, \text{H}_2\text{O}$ ) between the ligands and the OH or/and oxygen ions of the oxide [62]. This aspect, which is little documented, is different from that encountered in zeolites which can act as solid ionic solvents [63] or in solvent oxides where TMIs come to rest after high temperature diffusion to form doped or mixed oxides (Fig. 5, model VII) [64].

### B Oxide Surface as a Counter Ion

The role of the support has been studied further, essentially by diffuse reflectance spectroscopy, in the case of the Ni/SiO<sub>2</sub> system prepared by the competitive cation exchange method using nickel nitrate in water–ammonia solutions [12, 65]. In this method, the silica surface is first contacted with an ammonia solution at a pH above the ZPC of silica, leading to a negatively charged surface (subsection B.a):



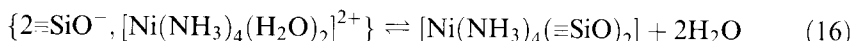
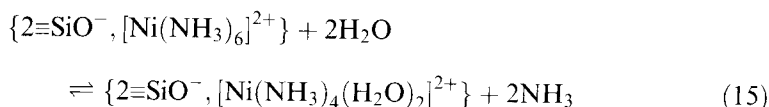
Upon contact of silica with a nickel nitrate ammoniacal solution, one observes that the purple blue colour, characteristic of nickel hexaammine  $[\text{Ni}(\text{NH}_3)_6]^{2+}$ , is transferred from the solution to the silica support, while the diffuse reflectance of the resulting wet powder is the same as that of the initial solution. These phenomena can be explained in terms of the following competitive cation exchange, where ammonium ions compete with nickel hexaammine complexes to occupy the  $\equiv\text{SiO}^-$  exchange sites of silica:



Reaction 14 shows an ion pair is formed with the oxide surface acting as a supramolecular counterion to which the TMI is bonded by ligand-screened electrostatic adsorption (Fig. 5, model III).

### C From Electrostatic Adsorption to Grafting: the Oxide Surface as a Supramolecular Ligand

Upon washing with ammonia solutions, in conditions of pH and NH<sub>3</sub> concentration corresponding to the stability range of the complex  $[\text{Ni}(\text{NH}_3)_4(\text{H}_2\text{O})_2]^{2+}$ , it is suggested that grafting occurs via substitution of two NH<sub>3</sub> molecules by two surface  $\equiv\text{SiO}^-$  ligands according to the successive reactions



The intermediate tetraammine complex has not been detected so far and the actual process can in fact be written as the sum of the two preceding reactions as follows:



It appears that the ligand exchange  $\text{NH}_3/\text{H}_2\text{O}$  in the initial hexaammine complex weakens the coordination sphere making grafting possible via two surface bonds (Fig. 5, model IV), with formation of a neutral *cis*-octahedral complex. It is important to note that the oxide, entering into the coordination sphere of  $\text{Ni}^{2+}$ , becomes a supramolecular bidentate ligand via vicinal  $\equiv\text{SiO}^-$  groups. The latter have been found to be the most probable grafting sites, on the basis of geometrical considerations [12, 65] and by analogy with silicate structure [66]. This also has been confirmed by EXAFS studies [67].

The chelating effect of the surface appears to be the driving force for the formation of the surface *cis*-octahedral complex. Equation 17, which is the sum of eqs 15 and 16, is accompanied by an entropy increase with the release of water molecules and the disappearance of charged species leading to a subsequent disordering of nearby solvent molecules. This aspect is well documented in solution coordination chemistry [68, 69].

Once TMI coming from complexes of the liquid phase (Fig. 5, model I) become bonded to the oxide surface (Fig. 5, model IV), they can remain attached to the support even though the liquid phase is eliminated and the remaining gas–solid system (Fig. 5, model V) heated at higher temperatures. It is then possible to produce vacant coordination sites. The reactivity of such sites towards ligand addition or substitution is the driving force for adsorption and catalysis. This constitutes one of the major differences with coordination compounds in solution [61].

Often, the active oxide forms oligomeric/polymeric species, a monolayer or tri-dimensional oxide particles, with the surface acting as a ligand. In some other cases, intermediate compounds or solid solutions are formed when the support becomes a reactant. This aspect is considered next.

#### D Support as a Chemical Reactant

The impregnations with or without interaction and the ion exchange techniques described in the previous sections involve bringing oxide surfaces in contact with aqueous solutions. The oxide–water system is thermodynamically metastable and evolves slowly towards the oxide precursor, namely the hydrous oxide or hydroxide. Thus, a realistic description of oxide–water interfaces should take into account two phenomena, the oxide rehydration and the oxide dissolution.

On exposure to water, an anhydrous oxide can become hydrated by physical adsorption of water molecules without dissociation, dissociative chemisorption of

water leading to new hydroxy groups, and finally to the formation of superficial oxyhydroxide or hydroxide, such as for MgO [14]. When silica groups are exposed to water for an extended time, their hydroxylation produces polymeric chains of  $-\text{Si}(\text{OH})_2-\text{O}-\text{Si}(\text{OH})_2-\text{OH}$  groups which can link up to form three-dimensional silica gel networks. Around 2 nm thick silica gel layers have been observed on silica surfaces prepared by evaporation of silica on mica which were exposed to humid air [70]. Thus, it may be postulated that surface groups are present not only in a two-dimensional oxide-liquid interface, but also in a bulk phase of finite thickness extending from the surface into the interior of the solid [71].

However, oxide dissolution has often been reported, in particular when impregnations were conducted far from the ZPC of the oxide, which is also the point of minimum solubility of the solid [72]. It is known that alumina dissolves in highly acidic impregnation solutions and that a fraction of dissolved aluminum may be readsorbed during impregnation or drying. Such an effect has been reported during the preparation of alumina-supported platinum [16, 73–76], nickel [77] or palladium [78] catalysts. Silica solubility is constant from pH 2–8, then increases very rapidly in basic medium [16]. For pH 9–10.7 amorphous silica is in equilibrium with the neutral  $\text{Si}(\text{OH})_4$  monomers as well as silicate ions. Above pH 10.7 silica dissolves to form soluble silicates [17]. Silica dissolution in basic media creates new hydroxy groups and hence new sites with chemical affinity for cations, which may explain the observed sharp increase of cation adsorption on silica at pH higher than 10.5 [79, 80].

Interestingly, impurities such as aluminum, calcium, magnesium or zinc were reported to reduce both the rate of dissolution and the solubility of silica at equilibrium. Nitric acid-cleaned silica was immersed in solutions of Al, Be, Fe, Ga or Gd ions at pH from 2 to 9. A drastic reduction of the solubility of silica was observed. In particular, the introduction of Al ions rendered silica insoluble at pH 9. This effect was attributed to the formation of a monolayer of insoluble silicate which lowered the silica solubility to that of the surface compound [17]. Seemingly, silicates involving metal ions are formed even at pH values apparently nonaggressive for silica. However, the amount of metal silicate is not specified and the formation of only a silicate monolayer is purely speculative.

Recently, the formation of layer-type silicates was demonstrated during the impregnation of silica with ammine  $\text{Ni}^{\text{II}}$  ions in the 8–9 pH range [80]. No epitaxy could be identified between the phyllosilicates and the carrier, inferring a monolayer description. This observation is consistent with experiments indicating the weathering at 100 °C of pyrex vessels by aqueous solutions containing  $\text{Ni}^{\text{II}}$  or  $\text{Mg}^{\text{II}}$  salts, leading to the formation of antigorite-type silicates [81, 82]. Likewise, the formation of hydrotalcite-type coprecipitates involving Al ions extracted from the support was observed during impregnation of  $\gamma$ -alumina with  $\text{Ni}^{\text{II}}$ ,  $\text{Co}^{\text{II}}$  and  $\text{Zn}^{\text{II}}$  ions under mild conditions, i.e. pH close to the ZPC, ambient temperature and reasonable contact times [83, 84]. Anions whose presence was required for the electroneutrality of the hydrotalcite-like structures were adsorbed simultaneously with the metal cations. Thus, the oxide supports should not be considered systematically as inert even during impregnations conducted at pH close to the isoelectric point.

The extent of phenomena such as coprecipitate formation during the preparation

of industrial catalysts, i.e. during unit operations such as impregnation, separation, aging or ripening, and drying, needs to be investigated in detail. Spectroscopies allowing coprecipitate determination at the oxide–liquid interface, such as IR, Raman or XAS, should be used for systematic investigations of the role of parameters such as pH, ionic strength, or contact time. It should be realized that there is no need for significant solubility of the support for the formation of surface compounds. The dissolution of the support may be driven by a subsequent coprecipitation with metal ions. Nevertheless, gel-mediated pathways involving the diffusion of metal cations and anions through a hydrous gel layer, by analogy with phenomena occurring during the natural weathering of soils, cannot be excluded [85, 86].

As shown above, the oxide support may play several different roles and those may occur separately or simultaneously, depending on the preparation method [87].

#### 4.1.1.5 Applications

The pertinent key parameters which may influence the interaction of a transition metal complex with an oxide support are first briefly discussed, before examples of important applications of ion exchange and impregnation are given.

##### A Key Experimental Parameters

When dealing with metal complexes in solution and a preformed support, the main problem is to know how to control the interaction (physical or chemical) between the complexes and the support. The discussion above distinguishes five main parameters, which can create or influence the strength of this interaction.

##### *(i) Isoelectric Point (IEP) of the Oxide Support: Influence of Temperature, Impurities and Selective Doping*

This is an essential parameter with which to initiate the electrostatic interaction between the metal complex and the oxide support. A number of papers have been devoted to the problem of regulating the IEP of oxides and the concentration of the charged surface groups. Two methods have been developed. The first one involves the change of temperature of the impregnating solution and the second involves the selective doping of the support surface with various types of ions [88]. Different behaviors were observed depending upon the support. For instance, the IEPs of  $\gamma$ -Al<sub>2</sub>O<sub>3</sub> and TiO<sub>2</sub> were found to increase upon increasing the temperature of the impregnating solution, in contrast to that of SiO<sub>2</sub> which was found to decrease. Selective doping of  $\gamma$ -Al<sub>2</sub>O<sub>3</sub> by very small amounts of Na<sup>+</sup> ions brought about an abrupt increase of IEP, whereas doping with F<sup>-</sup> ions caused a shift to lower IEP values. It should be mentioned that the selective doping method cannot be applied when the dopant leads to catalyst deactivation.

##### *(ii) Cationic and Anionic Metal Complexes*

Metal complexes may exist in essentially two forms: cationic and anionic. Neutral complexes, such as Co(NH<sub>3</sub>)<sub>3</sub>Cl<sub>3</sub>, exist but are relatively rare and would not lead to an electrostatic interaction which requires entities (oxide surface and complex) of

opposite charges. In an earlier review, Brunelle [16] gathered the complexes of metals belonging to Groups 7–11, most frequently used in supported catalysts preparation.

#### *(iii) Solution pH*

The pH appears to be a very versatile and important parameter in the preparation process with which to achieve the desired ion–support interaction. It is worth noting that it influences separately or simultaneously the liquid or/and solid part of the interface.

Qualitatively, the pH allows the sign of the surface charge to be selected as shown by Fig. 3. On the liquid side, it also determines the nature and nuclearity of the complex. For instance, upon decreasing the pH from 14, complexes change from hexaammine to hexaaquametal (III) for many transition metals or from mononuclear  $\text{MoO}_4^{2-}$  to polynuclear  $\text{Mo}_8\text{O}_{26}^{4-}$  [89]. Finally, it controls the solubility of the oxide support. The dissolution of the latter is all the more important as the pH of the solution departs from the IEP [16].

Quantitatively, the pH determines on the solid side the value of the zeta potential related to the concentration of charged surface sites (Fig. 3). On the liquid side, it allows selection of the most abundant metal complex from those coexisting at the same pH. Finally, it controls the amount of monomer produced in the solution upon oxide support dissolution [16].

Having emphasized the importance of the pH parameter, it should be recognized that its measurement is in itself a difficult task [90]. When the surface is charged, the overall ion concentrations are not constant close to the oxide–fluid interface. For instance, above the IEP, i.e. for negatively charged surfaces, there is an increase in cation and proton concentrations at the surface. Therefore, the pH is lower than in the bulk of the solution. The situation is reversed at a pH lower than the IEP. This is a typical compensation effect of the pH.

In colloidal solutions the measurement of the pH is always delicate, since it depends on the average distance between the oxide particles and the pH electrode. This explains why the latter is a function of the stirring rate of the solution. The best measure is the value obtained without stirring, the solid being far from the electrode and deposited at the bottom of the flask (a centrifugation is sometimes necessary). This measure can be considered as the pH of the bulk solution. This latter value, combined with the characteristics of the solution and the IEP of the oxide, allows calculation of the pH profile from the theory developed by Davis et al. [19]. Devices based on fiber-optic sensors [91] are being developed which might help resolve the difficult problem of the determination of pH of oxides in suspension.

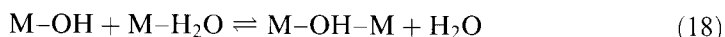
#### *(iv) Ligand Nature*

The ligand type greatly affects both the nature and strength of the metal complex–surface interaction. Several structural and electronic aspects have to be considered for each ligand:

- The type of ligand (neutral molecules or anions) determines the charge of the transition metal complex and hence the conditions such as support nature and pH range, for which ion exchange can occur.



- The bulkiness of the ligand will tend to screen and decrease the electrostatic interaction between the charged surface and the transition metal complex [62].
- When the ligand possesses an appropriate element, such as nitrogen, oxygen or hydrogen, there is a possibility of forming hydrogen bonds with the surface via S–OH groups [62].
- The polydentate nature of the ligand, whether it be the solution mobile ligand such as ethylenediamine, or the rigid surface ( $\equiv\text{SiO}$ )<sub>2</sub>, has a strong entropy effect on the stability of either the initial solution complex or the final grafted complex [61].
- Under conditions where oxide dissolution takes place, the monomers released in solution can react with the molecular species of the precursor component and M–O–M bonds can be formed via ololation and oxolation reactions:



where M is either the metal cation of the support monomer or of the metal complex. The result is that intermediate surface compounds are observed (see subsection 4.1.1.4D) [12, 92]. It is important to note that reactions 18 and 19 can take place because both OH and O are bridging ligands. By contrast, when the ligands of the metal complexes of the precursor component are nonbridging, such as ammonia or ethylenediamine, reactions (18) and (19) cannot occur and isolated grafted complexes are favored.

The understanding of what type of ligand the surface can be identified with, is an important aspect which has some practical consequences. It is well known for instance, that the standard redox potential of TMI can be largely modified depending upon the nature of its surrounding ligands [93]. It is thus expected that different supports will lead, for a given TMI, to different standard redox potentials.

#### (v) *Competitive Ions*

From a practical point of view, the reversibility of adsorption by means of competing ions, as shown by equilibria such as 5 and 14, is very important because it leads to a redistribution of the adsorbed metal complex ions among the charged surface sites, as discussed in subsection 4.1.1.2C. Competitive ions achieve a homogeneous deposition not only on the support surface but also, when pellets are used, throughout the catalyst grain volume [47]. In the latter case, it is possible to control [47, 94, 95] and to model [9] the exchange process and the distribution profile of the active phase along the radius of the grain as a function of time. Some important industrial applications are presented in section E.b.

#### (vi) *Washing*

It is known that washing has to be avoided after the component precursor has been deposited by impregnation. When other deposition methods are involved, the washing step has been reported to have various effects.

The fundamental aspects of washing have not been much studied in the past, although washing can have important consequences. The first is electrostatic in nature

and refers to the oxide support as a charged surface (see subsection D.b). Washing can be accompanied by pH changes so that the surface and the adsorbed species can acquire charges of opposite sign, leading to repulsions [96]. The second consequence rests on the ligand nature of the surface. Here the pH changes accompanying washing may lead to grafting of the component precursor and this aspect has been discussed in section 4.1.1.4C [65]. Yet another consequence of washing is connected with the role of reactant of the oxide support. The oxide dissolution will eventually lead to intermediate compound formation at the surface of the oxide support [80, 92].

## B Application Examples

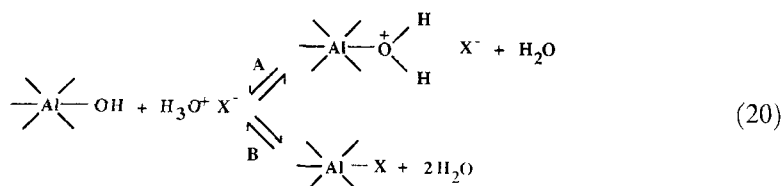
### (i) Preparation of Monometallic Reforming Catalysts

Most conventional reforming catalysts are based on well-dispersed platinum on an alumina promoted by a halogen, usually chlorine. The two main alumina supports used are the two transition aluminas  $\eta$ - and, principally,  $\gamma$ - $\text{Al}_2\text{O}_3$  [75].

The deposition of platinum on alumina is usually carried out by immersing the alumina in an aqueous solution of chloroplatinic acid and hydrochloric acid as a competing agent [34, 75].

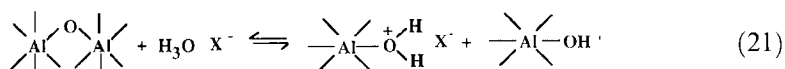
#### a Interactions Between Acid Solutions and the Surface of Alumina

Hydroxy groups present at the surface of a transition alumina behave like bases with respect to the protons of the acids [16, 97]. According to various authors, the reaction is represented by two different mechanisms A and B in eq 20.



In mechanism A, the OH group is protonated and its interaction with the anion is electrostatic [16, 19, 98–101]. In mechanism B [9, 13, 94, 100, 102, 103], the  $\text{X}^-$  anion replaces the  $\text{OH}^-$  group in the complexation sphere of the surface aluminum. Mechanism A is expected to predominate since the surface of the transition aluminas is mainly covered with OH groups [104–107], in presence of water.

Protonation of an oxygen atom of the surface can also occur and lead to the scission of an Al–O bond, according to reaction 21.



According to reactions 20A and 21,  $\text{Al}_2\text{O}_3$  behaves like an anion exchanger. The maximum quantity of anions that the surface can fix, or the anion exchange capacity, is related directly to the number of protonated OH groups [16, 19, 98, 100, 108]. Logically, it depends on the equilibrium constant of reaction 20A. It rises as the pH of the aqueous solution decreases [16, 19, 98, 100, 108, 109]. The process of

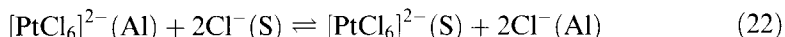
anion fixation on the surface is kinetically very fast [99], and rarely limits the overall kinetics. The rate limiting step is expected to be the diffusion of the ionic species in the pores of the alumina particle.

#### *b Platinum Deposition*

The maximum amount of platinum fixed on alumina from  $\text{H}_2\text{PtCl}_6$  acid, without any significant attack of the support, differs widely according to various authors [16, 34, 35, 73, 95, 108, 110], varying between 2 and about 8 wt%. Most of the values obtained at saturation of  $\gamma$ -aluminas with surface areas ranging between 150 and  $250 \text{ m}^2 \text{ g}^{-1}$  are normally between 2 and about 4 wt% [16, 34, 95, 110]. The platinum content of industrial catalysts is much lower, varying between 0.2 and 0.6 wt%.

Many authors have observed a strong interaction between the chlorinated complex of platinum,  $\text{H}_2\text{PtCl}_6$ , and  $\gamma\text{-Al}_2\text{O}_3$  [16, 34–36, 94, 95, 111]. At impregnation conditions approaching those used for the preparation of reforming catalysts (i.e. small amounts of platinum, generally less than 0.6 wt% of platinum with respect to the support, and low pH, hence high anion exchange capacity), platinum tends to be fixed rapidly and strongly on the first sites encountered. This risk of a heterogeneous macroscopic distribution of platinum on the surface is similar to that described above in the case of the zeolite  $\text{NH}_4\text{Y}$  with  $\text{Pt}(\text{NH}_3)_4^{2+}$  cation.

To obtain homogeneously distributed platinum on alumina, it is necessary to add a competitor ion to the solution. The usual competitor is  $\text{HCl}$  [34, 47, 112] whose role is to act on the equilibrium between the platinum precursor in the solution S and that fixed on the alumina support Al according to the reaction



The quantity of  $\text{Cl}^-$  ions added to the system is usually adjusted to leave a sufficient quantity of  $[\text{PtCl}_6]^{2-}$  in the aqueous solution to ensure easy migration to the center of the grain so that, at the end of the operation, this residual nonadsorbed amount is only a small fraction of the total quantity of platinum involved.

The chemical phenomena in this case are more complicated than in competitive cation exchange on  $\text{NH}_4\text{Y}$  zeolite.  $\text{HCl}$  acts not only as a competitor but also as a stabilizing agent for the coordination sphere of platinum. It has been shown [113, 114] that the  $[\text{PtCl}_6]^{2-}$  anion can lose two to four chloride ligands after a few hours in the absence of hydrochloric acid.

Another level of complexity is caused by the chemical reactivity of the alumina surface, which can be altered in an acidic medium.

#### *c Chemical Alteration of Alumina*

In an acidic media, simultaneously with the protonation reaction 20A of the OH groups, a process of attack and dissolution of the support also occurs [16, 31, 47, 101, 108, 111, 115]. This process occurs below about pH 4, and the solubility of the support rises rapidly with decreasing pH. Reaction 21 probably represents the first step of the formation of soluble compounds of the type  $[\text{Al}(\text{H}_2\text{O})_y(\text{OH})_x]^{(3-x)+}$  with  $x + y = 6$ . This is expected to occur only after reaction 20A is complete. Several experimental observations [31] support these considerations. If alumina beads are

placed in contact with an HCl solution, the following sequence of events occurs: a rapid fixation of the  $\text{Cl}^-$  anion, probably due to reaction 20A; a subsequent slow-down of this fixation; a decrease in the quantity of chloride fixed probably due to the progressive dissolution of the external part of the alumina particle (reaction 21), where the pH is the lowest; and finally a slow fixation of the  $\text{Cl}^-$  anion. If the initial quantity of acid used is small (less than 4–5 wt% Cl), the final event (the slow chloride fixation) resumes after several minutes [31]. This happens because the situation at the particle scale is still far from equilibrium – the pH in the external solution is low but higher in the internal solution near the center of the particle. The pH progressively evolves toward equilibrium, which corresponds to a pH slightly higher than 3. At such a pH, chlorinated aluminum species, which were solubilized at the lower pH during the beginning of the reaction, will be redeposited on the support. Note that, at the concentrations used for the preparation of monometallic reforming catalysts, the solubility of  $\gamma\text{-Al}_2\text{O}_3$  is very low (no more than a few hundred ppm).

*(ii) Metal Concentration Profiles in Supports*

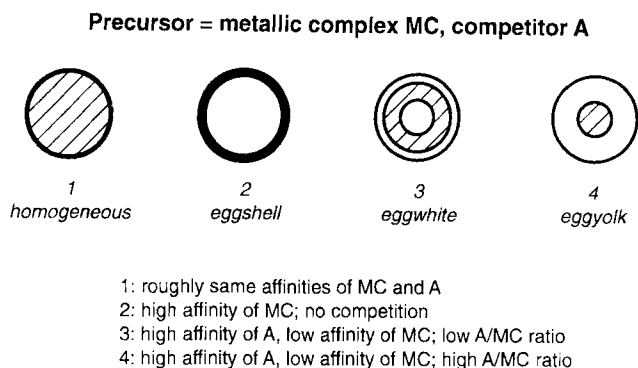
For deposition of chloroplatinic acid on alumina, competitors other than HCl can be used [36, 94, 95, 111, 112, 116–123]. Acids such as  $\text{HNO}_3$  and  $\text{H}_2\text{SO}_4$  are usually more effective than the corresponding salts, such as ammonium, aluminum and sodium nitrates [36]. Nitric acid is about five times more effective than acetic acid [120]. Hydrofluoric acid has a much stronger interaction with alumina than chloroplatinic acid [112] – HF blocks the alumina sites inhibiting the adsorption of the  $[\text{PtCl}_6]^{2-}$  anions. Among the other competitors used are  $\text{CO}_2$  [119], phosphoric acid [117, 118], organic acids such as formic, oxalic, propionic, lactic, salicylic, tartaric and citric acids [94, 116–118, 121–123], miscellaneous salts such as alkaline phosphate [95], alkaline halogenides [95, 118], alkaline benzoate [95], and amines such as monoethanolamine [94].

Some of these competitors, such as monoethanolamine, really act not by a competition effect on adsorption, but rather by a pH effect [94]. In fact a rise in the pH tends to lower the exchange capacity of alumina, causing a more uniform occupation of the surface by the metallic complex.

Careful selection of metal precursors and of competitors helps to obtain a large number of metal distribution profiles on the support surface between the periphery and the grain center [50, 95, 111, 124–127], depending on the strength of their interaction with the support. Four main types of profiles [50, 124–127] serve to describe all the others: uniform, film or eggshell, internal ring or egg white, central or egg yolk (Fig. 6).

Hydrofluoric [112], oxalic, lactic, tartaric [121] and citric acids [121, 128], for example, help to obtain an egg-white or egg-yolk distribution of chloroplatinic acid. These competing agents, which have a high affinity for alumina, become irreversibly fixed on the external sites of the support and force the platinum precursor to migrate farther towards the center of the grain in order to find free sites.

The profile of the macroscopic distribution of the metal on the support depends not only on the competition and time but also on the more or less strong tendency of the metal ion to modify its sphere of coordination or to polymerize. Thus  $[\text{PtCl}_6]^{2-}$  can undergo, in neutral or slightly acid medium, various reactions of



**Figure 6.** The four main categories of macroscopic distribution of a metal within a support. A/MC is the ratio representing competition (with a proportionality factor depending upon the valence of the ions).

aquation and hydrolysis [16, 49, 129–131] which modify the metal environment, the ion charge and thus the affinity of the latter for the support. Molybdc and tungstic ions, present as monomers  $\text{MoO}_4^{2-}$  or  $\text{WO}_4^{2-}$  in basic medium, polymerize when put in neutral or acid medium. The polymerization of tungstic ions, for example, influences the distribution profile [132] via the diffusion rate of these ions. It can also lead to the blocking of part of the pores.

A number of theoretical models of migration and deposition of metallic ions with time in porous supports, with or without the presence of competitor compounds, based on competing liquid-phase diffusion and adsorption mechanisms, have been proposed to account for the experimental results [56–58, 112, 133–138].

#### 4.1.1.6 Conclusions

This short review has tried to emphasize the molecular aspects of catalyst preparation, the role of the support and the different interactions taking place between the metal complex and the support. The case of ion exchange has been presented in more detail, because of the possibilities of varying such interactions in a large domain, ranging from weak physical interactions to stronger chemical interactions.

Although catalyst preparations are usually composed of several successive unit operations (e.g. ion exchange, washing and drying) which are clearly separated, the identification of the elementary steps taking place at the molecular level are far more difficult to detect and to separate. There seems, however, to be some hope, using experimental key parameters, to achieve a better identification and separation so that new sequences can be proposed, making catalyst architecture possible.

## References

1. J. T. Richardson, *Principles of Catalyst Development*, Plenum Press, New York, **1989**, p. 134.
2. B. Imelik, J. C. Védrine (Eds) *Catalyst Characterization: Physical Techniques for Solid Materials*, Plenum Press, New York, **1994**.

3. K. Morikawa, T. Shirasaki, M. Okada, *Adv. Catal.* **1969**, 20, 97–133.
4. L. L. Murrell in *Advanced Materials in Catalysis* (Eds: J. J. Burton, R. L. Garten) Academic Press, New York, **1977**, Chapter 8.
5. D. L. Trimm, *Design of Industrial Catalysts*, Elsevier, New York, **1980**.
6. K. Foger, *Catalysis, Science and Technology*, **1984**, 6, 227–305.
7. Y. Iwasawa in *Tailored Metal Catalysts* (Ed.: Y. Iwasawa), Reidel, Dordrecht, **1986**; Y. Iwasawa, *Adv. Catal.* **1987**, 35, 187–264.
8. B. C. Gates, L. Guzzi, H. Knözinger (Eds) *Metal Clusters in Catalysis*, Elsevier, Amsterdam, **1986**.
9. L. L. Hegedus, R. Aris, A. T. Bell, M. Boudart, N. Y. Chen, B. C. Gates, W. O. Haag, G. A. Somorjai, J. Wei, *Catalyst Design*, Wiley, New York, **1987**.
10. K. I. Tanaka, *Adv. Catal.* **1985**, 33, 99–158.
11. M. Ichikawa, *Adv. Catal.* **1992**, 38, 283–400.
12. M. Che, *Stud. Surf. Sci. Catal.* **1993**, 75A, 31–68.
13. G. J. K. Acres, A. J. Bird, J. W. Jenkins, A. King, *Catalysis (London)* **1981**, 4, 1–30.
14. G. A. Parks, *Chem. Rev.* **1965**, 65, 177–198.
15. H. H. Kung, *Transition Metal Oxides: Surface Chemistry and Catalysis*, Elsevier, Amsterdam, **1989**.
16. J. P. Brunelle, *Pure Appl. Chem.* **1978**, 50, 1211–1229.
17. R. K. Iler, *The Chemistry of Silica*, Wiley, New York, **1979**, p. 56.
18. O. Stern, *Z. Elektrochem.* **1924**, 30, 508–514.
19. J. A. Davis, R. O. James, J. O. Leckie, *J. Colloid Interface Sci.* **1978**, 63, 480–499.
20. A. W. Adamson, *Physical Chemistry of Surfaces*, Wiley, New York, **1982**, 185–231.
21. D. E. Yates, S. Levine, T. W. Healy, *J. Chem. Soc., Faraday Trans. 1* **1974**, 70, 1807–1818.
22. J. A. Davis, J. O. Leckie, *J. Colloid Interface Sci.* **1978**, 67, 90–107.
23. T. W. Healy, L. R. White, *Adv. Colloid Interface Sci.* **1978**, 9, 303–345.
24. J. Westall, H. Hohl, *Adv. Colloid Interface Sci.* **1980**, 12, 265–294.
25. R. Sprycha, *J. Colloid Interface Sci.* **1984**, 102, 173–185.
26. W. H. van Riemsdijk, J. C. M. de Wit, L. K. Koopal, G. H. Bolt, *J. Colloid Interface Sci.* **1987**, 116, 511–522.
27. K. C. Williams, J. L. Daniel, W. J. Thomson, R. I. Kaplan, R. W. Maatman, *J. Phys. Chem.* **1965**, 69, 250–253.
28. N. Spanos, A. Lycourghiotis, *Langmuir* **1993**, 9, 2250–2252.
29. W. H. van Riemsdijk, G. H. Bolt, L. K. Koopal, J. Blaakmeer *J. Colloid Interface Sci.* **1986**, 109, 219–228.
30. C. Contescu, J. Jagiello, J. A. Schwarz, *Langmuir* **1993**, 9, 1754–1765.
31. C. Marcilly, J. P. Franck, *Rev. IFP* **1984**, 3, 337–364.
32. C. N. Satterfield, *Heterogeneous Catalysis in Industrial Practice*, McGraw-Hill, New York, **1991**, Chapter 7.
33. C. Perego, P. Villa in *The Catalytic Process from Laboratory to the Industrial Plant* (Ed.: D. Sanfilippo), **1994**, Chapter 2.
34. J. F. Le Page, *Applied Heterogeneous Catalysis*, Technip, Paris, **1987**, p. 12–122.
35. R. W. Maatman, C. D. Prater, *Ing. Eng. Chem.* **1957**, 49, 253–257.
36. R. W. Maatman, *Ind. Eng. Chem.* **1959**, 51, 913–914.
37. H. A. Benesi, US Patent 3 527 835, **1970**.
38. M. El Malki, J. P. Franck, C. Marcilly, R. Montarnal, *C.R. Acad. Sci. Ser. 2*, **1979**, 288 C, 173–176.
39. F. Ribeiro, C. Marcilly, *Rev. IFP*, **1979**, 34, 405–428.
40. F. Ribeiro, PhD Thesis, University of Poitiers, **1980**.
41. L. I. Kheifets, A. V. Neimark, *Multiphase Processes in Porous Media*, Izd. Khimiya, Moscow, **1982**, p. 320.
42. G. A. Aksel'rud, M. A. Al'tshuler, *Introduction to Capillary-Chemical Technology*, Izd. Khimiya, Moscow, **1983**, p. 264.
43. R. Montarnal, unpublished results, **1973**.
44. M. A. Al'tshuler, *Kolloidny. Zhurnal*, **1961**, 23, 646–651; **1977**, 39, 1142–1144.
45. K. M. Adam, *Water Resources Research* **1969**, 5, 840–870.

46. P. Leroux, unpublished results, **1978**.
47. C. Marcilly in *Catalyse par les Métaux* (Eds: B. Imelik, G. A. Martin, A. J. Renouprez), CNRS, Paris **1984**, p. 121–150.
48. V. V. Veselov, G. A. Chernaja, T. A. Levanjuk, *Kinet. Katal.* **1982**, *20*, 83–87.
49. J. R. Anderson, *Structure of Metallic Catalysts*, Academic Press, London, **1975**, p. 172.
50. A. V. Neimark, L. I. Kheifets, V. B. Fenelonov, *Ind. Eng. Chem., Prod. Res. Dev.*, **1981**, *20*, 439–450.
51. E. W. Washburn, *Phys. Rev.* **1921**, *17*, 273–283.
52. C. H. Bosanquet, *Phil. Mag.* **1923**, *45*, 525–31.
53. M. A. Lauffer, *J. Chem. Educ.* **1981**, *58*, 250–256.
54. J. Crank, *Mathematics of Diffusion*, Clarendon Press, Oxford, **1964**.
55. R. Paterson, *An Introduction to Ion Exchange*, Heyden and Son, London, **1970**.
56. P. B. Weisz, *Trans. Faraday Soc.* **1967**, *63*, 1801–1806.
57. P. B. Weisz, J. S. Hicks, *Trans. Faraday Soc.* **1967**, *63*, 1807–1814.
58. P. B. Weisz, H. Zollinger, *Trans. Faraday Soc.* **1967**, *63*, 1815–1823.
59. J. Crank, G. S. Park, *Diffusion in Polymers*, Academic Press, London, **1984**, Chapter 1.
60. C. N. Satterfield, *Mass Transfer in Heterogeneous Catalysis*, MIT Press, London, **1970**.
61. C. Lepetit, M. Che, *J. Mol. Catal.* **1995**, *100*, 147–160.
62. T. Setoyama, M. Che, unpublished results.
63. J. A. Rabo, P. H. Kasai, *Prog. Solid State Chem.* **1975**, *9*, 1–19.
64. A. Davidson, M. Che, *J. Phys. Chem.* **1992**, *96*, 9909.
65. L. Bonneviot, O. Legendre, M. Kermarec, D. Olivier, M. Che, *J. Colloid Interface Sci.* **1990**, *134*, 534–547.
66. G. W. Brindley, G. Brown, *Crystal Structures of Clay Minerals and their X-Ray Identification*, 2nd edn, Mineralogy Society, London, **1980**, p. 2.
67. L. Bonneviot, O. Clause, M. Che, A. Manceau, H. Dexpert, *Catal. Today* **1989**, *6*, 39–46.
68. K. F. Purcell, J. C. Kotz, *Inorganic Chemistry*, Saunders, Philadelphia, **1977**.
69. F. A. Cotton, G. Wilkinson, *Advanced Inorganic Chemistry*, 4th ed., Wiley, New York, **1980**.
70. G. Vigil, Z. Xu, S. Steinberg, J. Israelachvili, *J. Colloid Interface Sci.* **1994**, *165*, 367–385.
71. J. Lyklema, *J. Electroanal. Chem.* **1968**, *18*, 341–348.
72. G. A. Parks, P. L. de Bruyn, *J. Phys. Chem.* **1962**, *66*, 967–973.
73. R. W. Maatman, P. Mahaffy, P. Hoekstra, C. Addink, *J. Catal.* **1971**, *23*, 105–117.
74. E. Santacesaria, S. Carrà, I. Adami, *Ind. Eng. Chem., Prod. Res. Dev.* **1977**, *16*, 41–44.
75. J. P. Boitiaux, J. M. Devès, B. Didillon, C. R. Marcilly, *Catalytic Naphta Reforming* (Eds: G. J. Antos, A. M. Aitani, J. M. Parera), Marcel Dekker, New York, **1995**, Chapter 4.
76. S. Parkash, S. K. Chakrabartty, T. Koanigawa, N. Berkowitz, *Fuel Process. Technol.* **1982**, *6*, 177–182.
77. S. L. Chen, H. L. Zhang, J. Hu, C. Contescu, J. A. Schwarz, *Appl. Catal.*, **1991**, *73*, 289–312.
78. S. Subramanian, D. D. Obrigkeit, C. R. Peters, M. S. Chattha, *J. Catal.* **1992**, *138*, 400–404.
79. D. W. Fuerstenau, K. Osseo-Asare, *J. Colloid Interface Sci.* **1987**, *118*, 524–542.
80. O. Clause, M. Kermarec, L. Bonneviot, F. Villain, M. Che, *J. Am. Chem. Soc.* **1992**, *114*, 4709–4717.
81. S. Henin, *C.R. Acad. Sci. Ser. 2* **1957**, *244*, 225–227.
82. S. Caillere, S. Henin, H. Besson, *C.R. Acad. Sci.* **1963**, *256*, 208–210.
83. J. L. Paulhiac, O. Clause, *J. Am. Chem. Soc.* **1993**, *115*, 11602–11603.
84. J.-B. d'Espinose de la Caillerie, C. Bobin, B. Rebours, O. Clause, *Preparation of Catalysts VI*, Elsevier, Amsterdam, **1995**, pp. 169–184.
85. W. H. Casey, J. F. Banfield, H. R. Westrich, L. McLaughlin, *Chem. Geol.*, **1993**, *105*, 1–15.
86. W. H. Casey, H. R. Westrich, J. F. Banfield, G. Ferruzzi, G. W. Arnold, *Nature*, **1993**, *366*, 253–256.
87. M. Che, L. Bonneviot, *Stud. Surf. Sci. Catal.*, **1988**, *44*, 147–158.
88. A. Lycourghiotis in *Acidity and Basicity of Solids: Theory, Assessment and Utility*, (Eds: J. Fraissard, L. Petrakis), NATO ASI Series 444c, Kluwer, Dordrecht 1994, pp. 415–444.
89. C. F. Baes, R. E. Mesmer, *The Hydrolysis of Cations*, Krieger, Malabar, **1986**.
90. M. Che, O. Clause, L. Bonneviot in *Proc. 9th Int. Congr. Catal.* (Eds: M. J. Phillips, M. Ternan), Chemical Institute of Canada, Ottawa, **1988**, *4*, pp. 1750–1757 and *5*, pp. 534–537.

91. W. Tan, Z.-Y. Shi, S. Smith, D. Birnbaum, *Science* **1992**, 258, 778–781.
92. M. Kermarec, J. Y. Carriat, P. Burattin, M. Che, A. Decarreau, *J. Phys. Chem.* **1994**, 98, 12008–12017.
93. F. Basolo, R. G. Pearson, *Mechanisms of Inorganic Reactions*, 2nd edn, Wiley, New York, **1967**.
94. A. K. Aboul-Gheit, *J. Chem. Tech. Biotechnol.* **1979**, 29, 480–486.
95. Y.-S. Shir, W. Ernst, *J. Catal.* **1980**, 63, 425–433.
96. C. Louis, and M. Che, *J. Catal.* **1992**, 135, 156–172.
97. E. Borello, G. Dalla Gatta, B. Fubini, C. Morterra, G. Venturello, *J. Catal.* **1974**, 35, 1–10.
98. J. A. Schwarz, *Catal. Today* **1992**, 15, 395–405.
99. M. J. D'Aniello, Jr., *J. Catal.* **1981**, 69, 9–17.
100. A. M. Ahmed, *J. Phys. Chem.* **1969**, 73, 3546–3555.
101. L. J. Jacimovic, J. Stevovic, S. Veljkovic, *J. Phys. Chem.* **1972**, 76, 3625–3632.
102. H. Hohl, W. Stumm, *J. Colloid Interface Sci.* **1976**, 55, 281–288.
103. S. Sivasanker, A. V. Ramaswamy, P. Ratnasamy, *Stud. Surf. Sci. Catal.* **1979**, 3, 185–196.
104. H. Knözinger, P. Ratnasamy, *Catal. Rev.* **1978**, 17, 31–70.
105. J. B. Peri, *J. Phys. Chem.* **1965**, 69, 220–230; *J. Phys. Chem.* **1965**, 69, 211–219; *J. Phys. Chem.* **1965**, 69, 231–239.
106. H. Knözinger, *Adv. Catal.* **1976**, 25, 184–271.
107. Z. Vit, J. Vala, J. Malek, *Appl. Catal.* **1983**, 7, 159–168.
108. E. Santacesaria, D. Gelosa, S. Carra, *Ind. Eng. Chem., Prod. Res. Dev.* **1977**, 16, 45–47.
109. R. Poisson, J. P. Brunelle, P. Nortier, *Catalyst Supports and Supported Catalysts*, (Ed.: A. B. Stiles), Butterworth, Boston, **1987**, pp. 11–55.
110. E. I. Gil'Debrand, *Intern. Chem. Eng.* **1966**, 6, 449–480.
111. Th. Mang, B. Breitschdel, P. Polanck, H. Knözinger, *Appl. Catal.* **1993**, 106, 239–258.
112. L. L. Hegedus, T. S. Chou, J. C. Summers, N. M. Potter, *Stud. Surf. Sci. Catal.* **1979**, 3, 171–183.
113. J. C. Summers, S. A. Ausen, *J. Catal.* **1978**, 52, 445–452.
114. G. Lietz, H. Lieske, H. Spindler, W. Hanke, J. Völter, *J. Catal.* **1983**, 81, 17–25.
115. F. Umland, W. Fischer, *Naturwiss.* **1953**, 40, 439–440.
116. H. Lieske, G. Lietz, H. Spindler, J. Völter, *J. Catal.* **1983**, 81, 8–16.
117. V. Haensel, US Patent 2840 532, **1958**.
118. M. S. Heise, J. A. Schwarz, *Stud. Surf. Sci. Catal.* **1987**, 31, 1–13.
119. C. T. Kresge, A. W. Chester, S. M. Oleck, *Appl. Catal.* **1992**, 81, 215–226.
120. G. N. Maslyanskii, B. B. Zharkow, A. Z. Rubinov, *Kinet. Katal.* **1971**, 12, 699–701.
121. W. Jianguo, Z. Jiayu, P. Li, *Stud. Surf. Sci. Catal.* **1983**, 16, 37–46.
122. T. A. Nuttal, *CSIR Report CENG 182*, CSIR, Pretoria, South Africa, **1977**.
123. E. R. Becker, T. A. Nutall, *Stud. Surf. Sci. Catal.* **1979**, 3, 159–167.
124. M. Komiyama, *Catal. Rev. Sci. Eng.* **1985**, 27, 341–372.
125. E. R. Becker, J. Wei, *J. Catal.* **1977**, 46, 365–381.
126. A. Gavriilidis, A. Varma, *Catal. Rev.* **1993**, 35, 399–456.
127. R. C. Dougherty, X. E. Verykios, *Catal. Rev.* **1987**, 29, 101–150.
128. J. Papageorgiou, *J. Catal.* **1966**, 158, 439–451.
129. W. P. Griffith, *The Chemistry of the Rarer Platinum Metals*, Interscience, London, **1967**.
130. C. M. Davidson, R. F. Jameson, *Trans. Faraday Soc.* **1965**, 61, 2462–2467.
131. G. H. Van Den Berg, H. T. Rijnten, *Stud. Surf. Sci. Catal.* **1979**, 3, 265–277.
132. L. R. Pizzio, C. V. Caceres, M. N. Blanco, *Catal. Lett.* **1995**, 33, 175–192.
133. P. Harriott, *J. Catal.* **1969**, 14, 43–48.
134. R. C. Vincent, R. P. Merrill, *J. Catal.* **1974**, 35, 206–217.
135. M. Komiyama, R. P. Merrill, H. F. Harnsberger, *J. Catal.* **1980**, 63, 35–52.
136. M. Komiyama, R. P. Merrill, *Bull. Chem. Soc. Jpn* **1984**, 57, 1169.
137. S. Y. Lee, R. Aris, *Stud. Surf. Sci. Catal.* **1983**, 16, 35–45.
138. A. A. Castro, O. A. Scelza, E. R. Benvenuto, G. T. Baronetti, S. R. De Miguel, J. M. Parera, *Stud. Surf. Sci. Catal.* **1983**, 16, 47–56.



## 4.1.2 Anchoring and Grafting of Coordination Metal Complexes onto Oxide Surfaces

C. LOUIS AND M. CHE

### 4.1.2.1 Introduction

Many heterogeneous catalysts have been reported in the past to be prepared by anchoring or grafting, processes whereby stable, covalent bonds are formed between an homogeneous transition metal complex and an inert polymer or inorganic support [1–4]. The aim was to combine the potential versatility and selectivity of homogeneous catalysts with the practical advantages of a solid material [5].

According to the recommendations of the International Union of Pure and Applied Chemistry (IUPAC), “deposition involving the formation of a strong (e.g. a covalent) bond between the support and the active element is usually described as grafting or anchoring. This is achieved through a chemical reaction between functional groups (e.g. hydroxyl groups) on the surface of the support and an appropriately selected inorganic, or organometallic compound of the active element [6].” Anchored catalysts are not distinguished from grafted ones either in this definition or in the literature where the situation is made even more complicated since other terms (immobilized, heterogenized, attached, etc.) can be found for the same type of catalysts. Recently, Campbell [7] attempted to distinguish anchoring from grafting as follows: “An anchored catalyst is created by the binding of a species, without substantial change in its structure, to a solid surface. A grafted catalyst is produced when an initial structure bound to the surface is altered considerably by subsequent treatments. Here, the initially bound species is not usually an active catalyst.” Although it is difficult at times to estimate how “substantial” or “considerable” are the changes undergone by a species attached to a surface, we shall nevertheless use Campbell’s definition in what follows. These definitions imply that anchoring will necessarily occur before grafting can take place.

The next few examples are given to illustrate the distinction between anchoring and grafting. By means of Fig. 1, an anchored complex is obtained which is a close analog of *trans*-L<sub>2</sub>Rh(CO)Cl, an active catalyst in the homogeneous hydroformylation reaction [1]. The anchored catalyst also catalyzes hydroformylation.

The example used by Campbell to illustrate grafting concerns oxidation catalysts (Fig. 2) [7]: the formation of the grafted catalyst starts by reacting the silanol groups of a silica previously dehydrated at 473 K with MoCl<sub>5</sub>; an intermediate anchored species is obtained. With subsequent heating to 773 K in oxygen, the remaining chlorines are removed to finally produce a grafted species with terminal molybdenyl bonds [8, 9]. The final surface complex catalyzes methanol oxidation to produce methylformate with a 90–95% selectivity at about 500 K [10].

It is possible to classify the coordination metal complexes used as precursors for anchoring/grafting into three types:

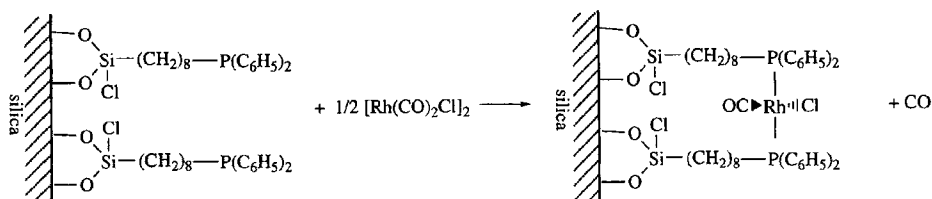


Figure 1. Example for the preparation of an anchored catalyst (from Ref. 1).

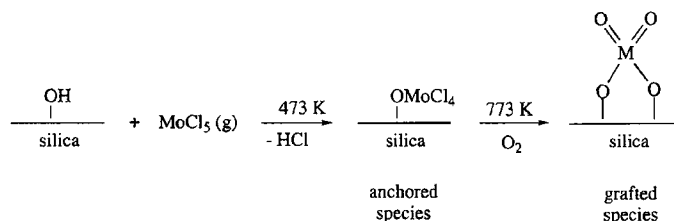


Figure 2. Example for the preparation of a grafted catalyst (from Ref. 7).

- (i) metal halides and oxyhalides;
- (ii) metal alkoxides;
- (iii) organometallics, and especially metal allyls and metal carbonyls.

Only metals in carbonyl complexes are in the zerovalent state and can be polynuclear.

It appears that the first works have been performed to heterogenize transition metal complexes used as homogeneous catalysts of polymerization.

This method is not extensively used for the preparation of industrial catalysts although many patents have been issued. It is mainly developed in research laboratories for the preparation of model catalysts.

The present review deals with the anchoring/grafting of transition metal complexes (mononuclear, dinuclear, or polynuclear) on inorganic supports except zeolites, which are covered in Chapters 4.2 and 4.3. Catalysts with anchored complexes which are the analogs of homogeneous catalysts are described in Chapter 4.4.

#### 4.1.2.2 Preparation: General Principles

The preparation of supported catalysts by anchoring/grafting usually involves several basic steps.

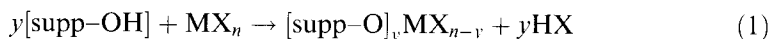
##### A Support Pretreatment

Prior to the reaction, the inorganic oxide support is thermally pretreated to remove physisorbed water and thus avoid spurious reactions which would not lead to

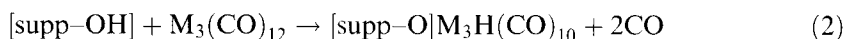
anchoring/grafting. The support can be also dehydroxylated to various extents to control the amount and dispersion of the anchored/grafted species. Different types of hydroxy groups with different reactivities are present on supports. The structure of support surfaces and their reactivity have been extensively described in several reviews ([12–18] and references therein).

### B Anchoring

The chemical reaction usually occurs as soon as the coordination metal complex is in contact with the support. The anchoring involves a condensation reaction between the precursor and the surface OH groups of the support:



The metal oxidation state does not change. In the case of metal carbonyls, the anchoring involves an oxidative addition of a surface OH group to the zerovalent complex (Eq. 2):



The coordination metal complexes are often air-sensitive, so preparations involving nonaqueous and inert solvents or vapor phase reactions (chemical vapor deposition (CVD), Chapter 4.5) are required. The reactions are usually performed between room temperature and a maximum that is limited by the decomposition temperature of the precursor for vapor phase reactions, and the solvent reflux temperature for liquid phase reactions.

As shown in Eq. 1, the support acts as a macroligand for the metal. Depending on the number of bonds between the metal and the support ( $y = 1, 2$  or  $3$ ), the metal can be considered as singly, doubly, or triply bonded to the support. The value of  $y$  may vary with the reactivity, concentration, and nature of both the OH and the coordination metal complex, and also with the reaction temperature.

### C Elimination of Physisorbed Metal Complexes

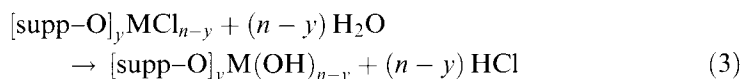
This treatment is obtained by purge under dry and inert gas, for catalysts prepared in the vapor phase, and by washing with pure solvent for catalysts prepared in the liquid phase.

Such anchored complexes with remaining original ligands may be directly used in reactions (Section 4.1.3), such as alkene metathesis (Section 4.1.2.5 below).

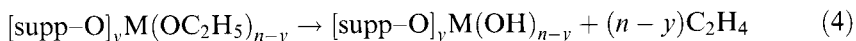
### D Grafting

The remaining initial ligands are eliminated as follows:

- (i) By hydrolysis of the metal–ligand bond (e.g. chloride) of the anchored complex with water (in liquid or vapor phase at various temperatures):



- (ii) By decomposition of the anchored complexes (e.g. alkoxides, organometallics) under mild thermal conditions, for example:



The reaction stoichiometry may be determined from the amount of anchored metal and the number of ligands in the coordination sphere, or the amount of gas evolved (e.g.  $\text{HCl}$  or  $\text{C}_2\text{H}_4$ ) during hydrolysis/decomposition, provided that it does not adsorb on the support.

The anchored/grafted metal species may be characterized by different spectroscopic methods: IR, UV-Vis diffuse reflectance (UV-Vis DRS), electron spin resonance (ESR), X-ray photoelectron (XPS), Raman, X-ray absorption fine-structure (EXAFS), magic angle spinning-nuclear magnetic resonance (MAS NMR), low energy ion scattering (LEIS), etc.

The main advantage of anchoring/grafting over conventional impregnation is the deposition of transition metal elements in various given oxidation states, from zero to high oxidation states. It is theoretically possible to obtain:

- (i) highly dispersed ions with previously partially dehydroxylated supports;
- (ii) a monolayer if the reactive OH groups are close enough to each other.

Theoretically, the amount of metal chemically bonded to the support cannot exceed the monolayer; however, multilayers can be obtained by several cycles of anchoring-hydrolysis or anchoring-decomposition.

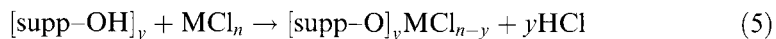
In addition, because of the chemical interaction between transition metal ions and the support established during anchoring, it is possible to prevent migration, sintering and agglomerate formation during subsequent thermal treatments, in contrast with species deposited by mere impregnation which are mainly physically adsorbed.

#### 4.1.2.3 Metal Chlorides and Oxychlorides

The anchoring/grafting may be performed with metal chlorides ( $\text{TiCl}_4$ ,  $\text{VCl}_4$ ,  $\text{MoCl}_5$ ,  $\text{WCl}_6$ ,  $\text{SnCl}_4$ ), and oxychlorides ( $\text{VOCl}_3$ ,  $\text{WOCl}_4$ ). Only grafted complexes are used as catalysts since chlorides must be eliminated before catalytic reactions.

After support dehydration and dehydroxylation, the preparation consists of three steps:

- (i) Anchoring between the (oxy)chloride and the hydroxy groups of the support:



- (ii) Elimination of the physisorbed metal complexes (as described in Section B).
- (iii) Hydrolysis of the M-Cl bond with water (liquid or vapor) to obtain grafted catalysts (see Eq. 3).

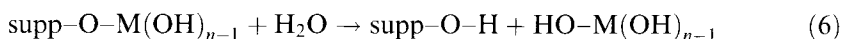
The determination of the stoichiometry of reaction 5 (most often leading to singly

or doubly bonded species) is usually based on the measurement of the amounts of anchored metal and Cl on the catalyst, or HCl evolved during the reaction [19–24].

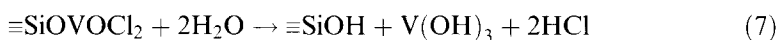
Based on the Cl:V ratio and ESR analysis, Fricke et al. [25] have shown that depending on the pretreatment temperature of the silica (523, 873, 1073K),  $\text{VCl}_4$  can be anchored on silica via three, two or one bonds at 333 K. Haukka and co-workers [26, 27] have also found that the reaction mechanism depends on the reaction temperature. For a reaction between  $\text{TiCl}_4$  and silica at 450 K, the Cl:Ti ratio indicates the presence of species anchored via one and two bonds to titania. The proportion of singly anchored species increases with the increase in the pretreatment temperature of the silica.

The structure of the anchored species may be also deduced from in situ characterization. However, to our knowledge, only a few attempts by ESR and UV–Vis DRS have been reported [8, 19, 24].

It may be also noted that, depending on the systems, the undesirable hydrolysis of the metal–support bond (supp–O–M) may occur:



Hanke et al. [28] and Khalif et al. [29] have shown that the  $\equiv\text{Si-O-V}$  bond is hydrolyzed during chloride hydrolysis of  $\text{VOCl}_3$  anchored on silica:



whereas the  $\text{Ti-O-V}$  bond is retained after anchoring of  $\text{VOCl}_3$  on titania [30]. Fricke et al. [24] show by ESR that reaction 6 also occurs during hydrolysis of  $\text{MoCl}_5$  anchored on silica.

When the supp–O–M bonds are hydrolyzed (Eq. 6), the released species must be removed by washing so as to keep only really anchored species in the catalyst [9, 31]. This washing step can advantageously replace step d of the preparation (Section 4.1.2.2 above) since both hydrolysis and elimination of the released metal species can take place simultaneously. This crucial step is barely mentioned in the literature. This may be the reason why some authors claim that the grafting of chloride complexes does not lead to homogeneously dispersed species on the support surface and forms three-dimensional oxide particles after calcination [29, 32, 33].

Highly dispersed grafted species can be obtained: after grafting of  $\text{MoCl}_5$  [8] or  $\text{SbCl}_5$  [34] on silica, the elimination of the released metal species during washing with ammonia solution and water, respectively, leads to the formation of highly dispersed isolated species.

The amount of grafted metal is usually low, for several possible reasons: low support OH reactivity, chlorination of the surface, and release of metal species during hydrolysis. Bond and Brückman [30] mentioned that it is difficult to obtain a monolayer of vanadium species on  $\text{TiO}_2$  because of the chlorination of the support surface by the HCl evolved during the anchoring of  $\text{VOCl}_3$  at 313 K.

Several cycles of anchoring reaction–hydrolysis can be performed in order to increase the metal loading. However, during the subsequent cycles, the metal chloride complexes can react with the OH groups of both the support and the grafted metal [35], and lead to the formation of two-dimensional or three-dimensional particles.

Hattori et al. [31] mentioned that after three cycles of vapor phase reaction between  $\text{SnCl}_4$  and silica pretreated at 453 K, followed by washing and calcination, the amount of grafted Sn is very close to that required for a monolayer coverage. However, transmission electron microscopy (TEM) and X-ray diffraction (XRD) studies show that not all the silica surface OH groups react with chlorides, and that  $\text{SnCl}_4$  prefers to react with the Sn–OH formed during the hydrolysis. After calcination at 773 K,  $\text{SnO}_2$  particles of 10–15 nm are formed, whereas high and uniform dispersion of  $\text{SnO}_2$  (<2 nm) is obtained for samples prepared by conventional impregnation. The reasons for this are not given in the paper but these results show that grafted catalysts do not always exhibit better characteristics than conventional impregnated samples.

A few authors have mentioned that the use of chloride metal complexes gives a reproducible amount of grafted metal: Benvenutti et al. [34] for the grafting of  $\text{SbCl}_5$  on silica in  $\text{CCl}_4$  at the solvent-reflux temperature, Lindblad and Lindfors [36] for the grafting of  $\text{WOCl}_4$  on silica at 473 K, Haukka and Lakomaa [26] for the grafting of  $\text{TiCl}_4$  on silica at 450 K and 723 K.

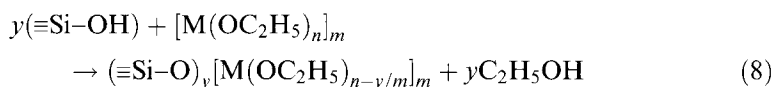
The central ions in (oxy)chloride metal complexes are in a high oxidation state that is preserved during anchoring (Eq. 5) and grafting. Therefore, these grafted catalysts are mainly used to catalyze oxidation reactions, e.g. oxidative dehydrogenation of ethylbenzene [31], oxidation of acrolein [29], methanol [10], and *o*-xylene [30, 37].

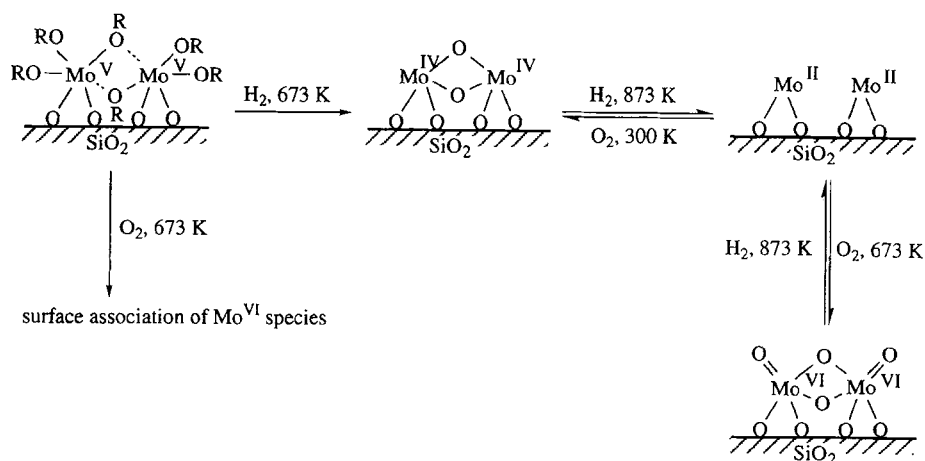
For example, Khalif et al. [29] have observed that the rate of oxidation of acrolein at 593 K per vanadium atom is five times higher with a grafted sample than with an impregnated one because of the higher V dispersion. In the case of Mo/ $\text{SiO}_2$ , Louis et al. [10] have found that the grafted Mo/ $\text{SiO}_2$  exhibits a higher selectivity in methylformate for methanol oxidation than impregnated Mo/ $\text{SiO}_2$ , which is selective in formaldehyde. The differences in the selectivity were explained in terms of the Mo dispersion, which is higher on the grafted samples. Bond and Brückman [30] have shown that the activity and selectivity of V/ $\text{TiO}_2$  in the oxidation of *o*-xylene to phthalic anhydride are highest when the supported vanadium is close to a monolayer.

#### 4.1.2.4 Metal Alkoxides

The principle of preparation is as previously described. The anchoring is often performed in the vapor phase because of the high thermal stability of the alkoxide complexes. The most studied precursors are the ethoxy and acetylacetonate ( $\text{acac} = \text{C}_5\text{H}_7\text{O}_2$ ) complexes.

One of the earlier works using these precursors for catalyst preparation was performed by Kuznetsov et al. [38] and Yermakov et al. [11] with the anchoring of  $[\text{Mo}(\text{OC}_2\text{H}_5)_5]_2$  and  $[\text{Re}(\text{OC}_2\text{H}_5)_3]_3$  on silica:



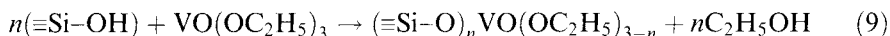


**Figure 3.** Anchoring/grafting of  $[\text{Mo}(\text{OC}_2\text{H}_5)_5]_2$  onto silica support (from Ref. 38).

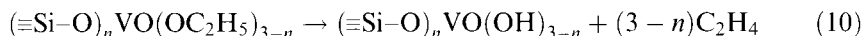
with  $y = 4$  for Mo and  $y = 2$  or 3 for Re. Further thermal oxidation–reduction treatments may take place, leading to the formation of grafted species with different oxidation states, characterized by XPS, EXAFS, ESR (Fig. 3).

The authors [11, 38] mention that the oxidation of anchored ethoxy complexes without preliminary reduction destroys some of the bonds between the metal ions and the silica. This also applies to allyl complexes [11] (see Section E.a below).

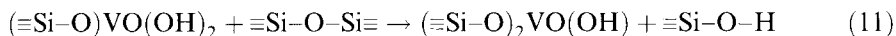
The control of the amount of reactants permits the deposition of highly dispersed species. This can be illustrated by the anchoring of  $\text{VO}(\text{OC}_2\text{H}_5)_3$  from vapor phase onto silica at 423 K, followed by a desorption at 723 K [39]. Singly and doubly anchored V species ( $n = 1$  or 2 in Eq. 9) can be obtained whose ratio depends on the pretreatment temperature of silica:



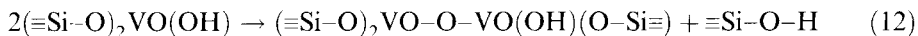
Grafted V is obtained upon thermal decomposition at 523–723 K:



Simultaneously, condensation reactions with other surface sites can also occur, leading to the regeneration of surface OH groups:



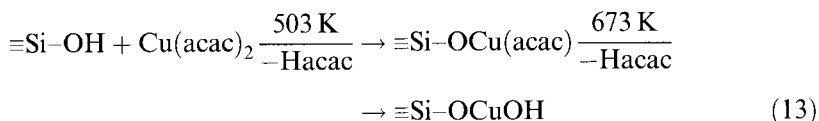
or



Several cycles of anchoring–decomposition may be performed since both the V–OH and the regenerated  $\equiv\text{Si}-\text{O}-\text{H}$  (Eqs 11 and 12) can again react with the precursors; Si–OH can take part in the lateral growth of the vanadium oxide layer along the silica surface, and V–OH in the thickening of the layer. XRD, Raman, EXAFS and XPS reveal that for a 19.4 wt %  $\text{V}_2\text{O}_5$  loading, a thin layer is obtained

with the grafted sample, whereas  $V_2O_5$  crystallites are formed with the impregnated one [39, 40]. The grafted sample is three to four times more active in the reaction of oxidative dehydrogenation of ethanol to acetaldehyde than the impregnated one because of the higher surface area of vanadium oxide [40].

$Cu(acac)_2$  in acetonitrile does not react at room temperature with  $SiO_2$ . Heated at 503 K, the physically adsorbed  $Cu(acac)_2$  reacts with silanol groups and loses one acac per Cu. Subsequent calcination in air at 673 K removes fragments of acac and leaves only OH on the grafted complex [41]:



Anchoring can occur directly when the reaction is performed at higher temperature. Chromium acetylacetonate was found to react from the vapor phase at 473–553 K with the OH of silica, leading to the release of one acac ligand [42]. Depending on the intended use of the Cr/ $SiO_2$  samples, the ligands can be removed either by water vapor at 588 K, which prevents the  $Cr^{III}$  from oxidizing to  $Cr^{VI}$ , or by air treatment at 673 K, which produces  $Cr^{VI}$  species. The same type of study has been made with the  $Ni(acac)_2$ –alumina system at 473 K [43].

It is suggested [41–43] that the steric hindrance due to the size of the anchored complexes determines the maximum amount of metal bonded to the support, and makes them atomically dispersed. The metal loading can be also controlled by the pretreatment temperature of the support which determines the number of OH groups, and by the reaction temperature. The preparations of Cr/ $SiO_2$  and Ni/ $Al_2O_3$  described above give homogeneous and reproducible metal contents.

Several cycles of anchoring–air treatment can be made. It was found with the  $Ni(acac)_2$ –alumina system [44] that the atomically dispersed  $Ni^{II}$  species grafted during the first step act as nuclei for the growth of nickel particles during the subsequent preparation cycles.

#### 4.1.2.5 Organometallics

Organometallic complexes are one of the most common types of precursors used in catalyst preparation by anchoring/grafting. Among them the allyls and the carbonyls are most used, but other ligands such as methyl, *n*-butyl, benzyl, neopentyl ( $\sigma$  ligands), cyclopentadienyl, arene ( $\pi$  ligands) can be also employed.

##### A Metal Allyls

The metal allyls can provide a large variety of anchored/grafted species with different oxidation states after subsequent thermal treatments. They are involved as model catalysts in various catalytic reactions: hydrogenation, oxidation, metathesis, isomerization, or polymerization. The most widely studied metal allyls are Mo and Cr. A list of the metal allyls used as precursors for anchoring/grafting as well as their catalytic applications can be found in Table 5 of Ref. 15.



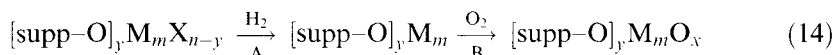
Earlier reviews devoted to the use of metal allyls and other organometallics for the preparation of supported catalysts have been written by Ballard [45], and Candlin and Thomas [46]; extensive work has been performed by Yermakov and co-workers [11, 47–50], and also by Iwasawa and co-workers [15, 16, 51, 52] on difficult-to-reduce elements (e.g. Ti, Zr, Hf, Cr, Mo, W) and, for example, by Basset and co-workers [53–55] on easy-to-reduce elements (e.g. Ni, Pd, Pt).

Typically, the anchoring consists of a reaction between an allyl metal complex, either mononuclear (e.g. Mo, or  $\text{Cr}(\eta^3\text{-C}_3\text{H}_5)_4$ ) or binuclear (e.g.  $\text{Mo}_2$  or  $\text{Cr}_2(\eta^3\text{-C}_3\text{H}_5)_4$ ), and the OH of the support, according to Eq. 1.

A doubly bonded anchored metal complex is usually obtained with Cr, Mo, and W, a singly bonded one with Ni, Pd, and Pt, and either one with Ti, Zr, and Rh (Table 5 of Ref. 15).

The reactions are usually performed at room temperature in pentane, but other solvents can be used, such as toluene. After reaction, the samples are washed several times with pure solvent in order to eliminate unreacted complexes (see Section 4.1.2.2C); this step is not always mentioned in the related papers. Sometimes [54], the precursor may be sublimed under vacuum at room temperature.

The remaining organic ligands can be removed under mild reduction conditions (step A in Eq. 14), so as to lead to grafted metal catalysts.



After step A, the grafted species is in a low oxidation state, and exhibits catalytic activity. For example, the grafted  $\text{Mo}^{\text{II}}$  dimers are more active in 1,3-butadiene hydrogenation at 273 K than the corresponding conventional impregnated Mo catalysts similarly reduced with  $\text{H}_2$  – by two orders of magnitude when grafted on silica and by more than three orders when grafted on alumina [16].

During step A of Eq. 14, hydrides can be formed with Group 4 elements (Ti, Zr, Hf). For example, the anchored  $[\text{Si-O}]_2\text{Zr}^{\text{IV}}(\eta^3\text{-C}_3\text{H}_5)_2$  species is transformed into grafted zirconium dihydride  $[\text{Si-O}]_2\text{Zr}^{\text{IV}}\text{H}_2$  after treatment under hydrogen at 393 K [56]. The anchored  $\text{Zr}^{\text{IV}}$  species is known to be active in ethylene polymerization [45], whereas the grafted zirconium hydrides are found to be the direct precursors of the propagation centers for ethylene polymerization [56]. These hydrides also exhibit high activity in alkene isomerization, especially of 1-butene, with higher rates at 300 K than homogeneous or other heterogeneous catalysts [57].

After oxidation (step B of Eq. 14), grafted oxidized species are obtained with a well-defined structure, characterized for example by EXAFS [16].

Highly dispersed grafted species can be obtained with metal allyls. Figure 4 shows an example of the change in the structure and oxidation state of isolated Mo grafted on silica after different oxidation-reduction treatments [16]. The different species obtained on silica have been characterized by Yermakov and co-workers [11, 47] and on alumina by Iwasawa [15, 16] using techniques such as EXAFS, UV-Vis DRS, and IR. Grafted  $\text{Mo}^{\text{VI}}$  catalysts (species 4) are found to be 11 times more active than the corresponding catalyst obtained by impregnation in the selective oxidation of propene to acrolein [16]. Molybdenum(IV) (species 3) exhibits activity for propene metathesis, but species 1 with allyl ligands is more effective.

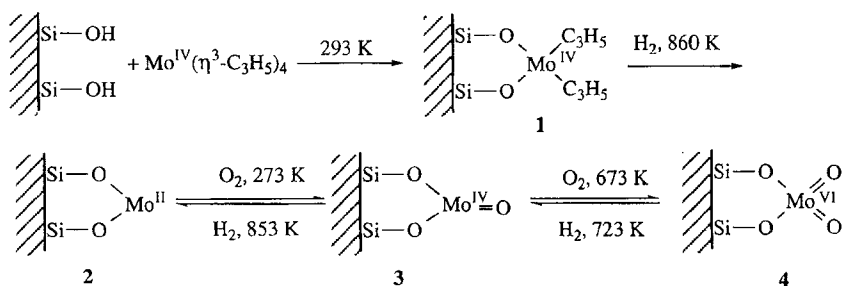


Figure 4. Anchoring/grafting of  $\text{Mo}(\eta^3\text{-C}_3\text{H}_5)_4$  onto silica support (adapted from Ref. 16).

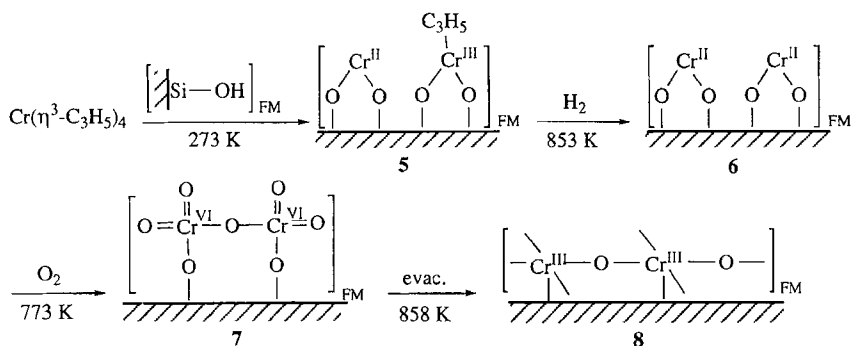


Figure 5. Stepwise transformation of  $\text{Cr}(\eta^3\text{-C}_3\text{H}_5)_3$  anchored onto silica to form a monolayer (from Ref. 15, FM = full monolayer).

A monolayer catalyst can be also obtained. For example, in the case of a reaction between excess  $\text{Cr}(\eta^3\text{-C}_3\text{H}_5)_3$  and a full monolayer of OH groups on silica, a two-dimensional layer of grafted  $\text{Cr}^{\text{III}}$  has been obtained (species 8 in Fig. 5; FM = full monolayer) [15]. After anchoring, the resultant species 5 has about one allyl ligand per two Cr atoms which can be readily removed by  $\text{H}_2$  treatment at 853 K to form a  $\text{Cr}^{\text{II}}$  monolayer 6. The latter is oxidized with  $\text{O}_2$  at 773 K into a  $\text{Cr}^{\text{VI}}$  monolayer 7 which can be transformed into a  $\text{Cr}^{\text{III}}$  monolayer 8 by treatment at 858 K under vacuum. Each  $\text{Cr}^{\text{III}}$  ion is square pyramidal and exhibits one vacant site in its coordination sphere, which makes it more active by two orders of magnitude for the catalytic oxidation of CO at about 473 K than a conventional impregnated Cr catalyst that usually exhibits a three-dimensional  $\text{Cr}_2\text{O}_3$  phase [15].

It is also possible to prepare supported metal catalysts from easy-to-reduce elements. For example,  $[\equiv\text{Supp-O}]\text{Rh}(\eta^3\text{-C}_3\text{H}_5)_2$  (with supp = Al, Si, or Ti) reacts with  $\text{H}_2$  at room temperature to give rhodium metal particles (1.5 nm) [54, 58]. Dialllyl compounds of Group 10 elements (Ni, Pd, Pt), forming species singly anchored onto silica or alumina, are transformed into small metal particles (<1 nm) after reduction under  $\text{H}_2$  at 300–373 K ( $\text{Pt}^0$ ,  $\text{Pd}^0$ ) and 573–673 K ( $\text{Ni}^0$ ) [11, 47, 59].

The metal allyls can be also used to prepare dispersed metal particles stabilized

by the presence of low-valent ions (coming from hard-to-reduce transition elements) and produce bimetallic supported catalysts [47–50, 60] after the following sequence of steps:

- (i) Interaction of benzyl Ti, Hf, allyl Zr (Group 4) or allyl Mo, W complexes (Group 6) with a silica previously calcined at 773–873 K.
- (ii) Reduction at 773–873 K to obtain grafted low-valent ions.
- (iii) Treatment of the reduced catalyst with a solution of allyl Ni, Pd, or Pt complexes (Group 10) in pentane.
- (iv) Reduction with hydrogen.

These mixed catalysts exhibit a higher metal dispersion than monometallic catalysts as well as a stabilization of the metal particles against sintering. Difficult-to-reduce elements (Ti, Hf, Zr, Mo, W) are supposed to act as nucleation sites for the growth of metal particles. Because of the change in the electron density of the metal particles, these catalysts exhibit a higher specific activity than monometallic catalysts in benzene hydrogenation and ethane hydrogenolysis.

## B Metal Carbonyls

Many reviews have been devoted to the use of carbonyl metal complexes for the preparation of supported catalysts [2, 4, 17, 18, 61–67].

The main differences between the carbonyl metal complexes and the metal complexes previously described, are the following:

- (i) The reactivity of metal carbonyls with inorganic oxide surfaces appears more complex; indeed, several types of reaction with the support may be involved, depending on various parameters such as the carbonyl metal complex, the acid–base character of the support, the nature of the carrier gas, the reaction temperature; they lead to different metal complex–support bondings, from Van der Waals to iono-covalent [17, 18, 61, 67]; hence, the anchoring reaction cannot always occur.
- (ii) The metal in the carbonyl complexes is zerovalent; therefore, the anchoring reaction does not involve a condensation reaction with the surface OH groups (Eq. 1) but an oxidative addition of an OH group to the zerovalent complexes (Eq. 2).
- (iii) The complexes can be mononuclear [63], polynuclear, or heteronuclear (carbonyl clusters) [64, 67].

The main reasons for using carbonyl metal complexes as precursors for catalyst preparation are the following:

- (i) Anchored metal carbonyls can be used as heterogeneous analogs of the metal carbonyls used in homogeneous catalysis (see Section 4.1.3).
- (ii) Grafted mononuclear or polynuclear entities can be produced upon decomposition of the anchored carbonyl species.

- (iii) Small metal particles can be easily produced by decomposition or low-temperature reduction of supported metal carbonyls.

A summary of the studies devoted to supported carbonyl metal complexes can be found in Table 2 of Ref. 2.

The anchoring/grafting of carbonyl metal complexes on a support may be ideally described as follows. After thermal pretreatment of the support, the carbonyl metal complex is introduced most often from the vapor phase or via organic solvents such as benzene, cyclohexane, and pentane. At this stage, the complexes are either anchored or physisorbed. When physisorbed, their decomposition as well as the elimination of the excess of physisorbed carbonyl metal complexes occur upon heating the system under vacuum. Upon increasing temperature, ligands may be lost in a stepwise way, leading to subcarbonyl anchored species, and finally to grafted species.

Among monomeric metal carbonyls,  $\text{Mo}(\text{CO})_6$ ,  $\text{Cr}(\text{CO})_6$ ,  $\text{Fe}(\text{CO})_5$ , and  $\text{Ni}(\text{CO})_4$  have been most studied. Their stepwise decomposition on the support may lead to the formation of grafted species. For example,  $\text{Mo}(\text{CO})_6$  is first physically adsorbed onto hydroxylated alumina at room temperature [2, 62, 63, 68]. Thermal decomposition leads to the formation of adsorbed subcarbonyl species such as  $\text{Mo}(\text{CO})_5$  and then  $\text{Mo}(\text{CO})_3$  at 373 K. Complete decarbonylation at 573 K is observed upon oxidative addition of the metal on surface hydroxy groups:

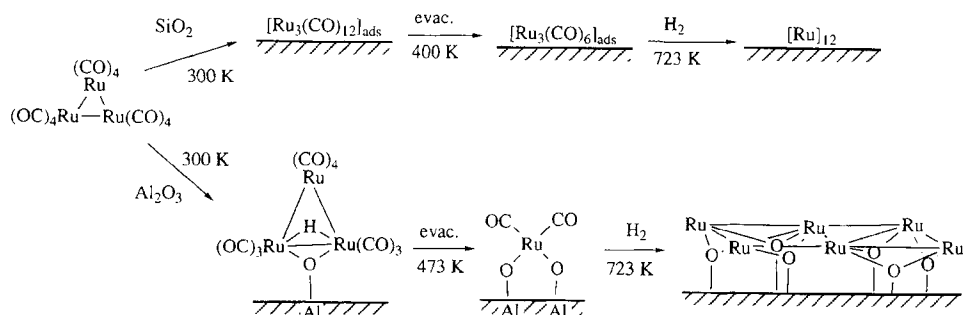


Such grafted catalysts exhibit higher activity in alkene metathesis than conventional catalysts. More details concerning this example can be found in Refs. 2, 62, 63, 68, and references therein.

The deposition of polynuclear carbonyl complexes with metals of Groups 7–9 on oxide supports has been extensively studied as well as that of bimetallic complexes ([64, 67] and references therein). As mentioned above, the pathway leading to anchored/grafted cations or metal particles depends on the nature of the support, i.e. the nature and the amount of surface OH groups. Thus,  $\text{Ru}_3(\text{CO})_{12}$  exhibits stronger interaction with  $\gamma\text{-Al}_2\text{O}_3$  than with  $\text{SiO}_2$  [69, 70]. The EXAFS results show that at room temperature,  $\text{Ru}_3(\text{CO})_{12}$  is physisorbed on silica, whereas it reacts with the OH groups of alumina and forms the anchored  $[\text{HRu}_3(\text{CO})_{10}(\text{O}-\text{Al}\equiv)]$  species (Fig. 6). Upon treatment under vacuum at about 450 K,  $\text{Ru}_3(\text{CO})_{12}$  physisorbed on silica partially decomposes into “adsorbed”  $\text{Ru}_3(\text{CO})_6$  (no Ru–O–Si bonding), whereas Ru anchored on alumina transforms into  $[\text{Ru}(\text{CO})_2(\text{O}-\text{Al}\equiv)_2]$ . Reduction under  $\text{H}_2$  at 723 K leads to small metal particles  $[\text{Ru}]_{12}$  on silica and to grafted oxidized Ru entities  $[\text{Ru}_6(\text{O}-\text{Al}\equiv)_6]$  on alumina (Fig. 6).

This example shows that, in contrast to what is observed with the metal allyls, the formation of metal particles may not involve the formation of anchored species, i.e. cationic species.

It may be noted that other reactions can occur with polynuclear carbonyl complexes, such as oxidative fragmentation [17, 61, 66]. This is observed when  $[\text{HRu}_3(\text{CO})_{10}(\text{O}-\text{Al}\equiv)]$  is transformed into  $[\text{Ru}(\text{CO})_2(\text{O}-\text{Al}\equiv)_2]$  at 473 K (Fig. 6), leading to an oxidation of  $\text{Ru}^{\delta+}$  into  $\text{Ru}^{\text{II}}$ .



**Figure 6.** Transformation of  $\text{Ru}_3(\text{CO})_{12}$  supported on silica and alumina during thermal treatment (from Ref. 69, 70).

#### 4.1.2.6 Conclusion

The anchoring of coordination metal complexes was first used to heterogenize homogeneous catalysts. However, it was soon realized that the resulting anchored complexes exhibited unusual catalytic properties, and that the grafted catalysts could be obtained with controlled dispersion (isolated species, monolayers, multilayers). It appears that the nature of the catalysts obtained depends on many parameters such as the nature of the precursor.

The general problem for using these metal molecular precursors is the necessity of (i) using water- and air-free conditions, and (ii) synthesizing them when they are not commercially available.

In addition, the anchoring reaction does not permit the deposition of metal loadings higher than that corresponding to the monolayer. The metal loading mainly depends on the number of surface OH groups of the support provided that they all can react with the precursor. To get higher loading, i.e. multilayers, it is necessary to perform several cycles of anchoring/decomposition or hydrolysis, which require long and tedious procedures.

Up to now, the most used metal complexes to prepare catalysts by anchoring/grafting have been organometallics, and especially, metal allyls; it appears possible to obtain versatile catalysts containing metal ions with controlled dispersion, various coordination numbers, various ligands, and various but uniform oxidation states, in contrast with impregnated samples.

Metal carbonyls may be used as precursors for anchoring/grafting preparation but their reactivity is much more intricate, and it is uncertain which type of bonding will be predominant and therefore whether anchoring will occur.

Less systematically studied have been chloride metal complexes and those containing alkoxide ligands. Some studies suggest that they are less reliable for obtaining species as well-defined as with allyl precursors. However, recent works [26, 27, 36, 42–44, 71] devoted to the anchoring/grafting in vapor phase (CVD) (see Sections 4.1.2.3 and 4.1.2.4), show that a well-defined supported phase may be obtained when each preparation parameter is carefully controlled and a systematic procedure is used.

However, one must be aware that (oxy)chloride metal complexes are only used for the preparation of grafted ions in a rather high oxidation state whereas alkoxide and allyl precursors can provide ions in various oxidation states (Figs. 3–5).

## References

1. L. L. Murrell in *Advanced Materials in Catalysis*, (Eds.: J. J. Burton, R. L. Garten), Academic Press, New York, **1977**, Chapter 8.
2. D. C. Bailey, S. H. Langer, *Chem. Rev.* **1981**, *81*, 109–148.
3. H. Hirai, N. Toshima in *Tailored Metal Catalysts*, (Ed.: Y. Iwasawa), Reidel, Dordrecht, Holland, **1986**, Chapter 2.
4. B. C. Gates, *Stud. Surf. Sci. Catal.* **1986**, *29*, 415–425.
5. K. G. Allum, R. D. Hancock, S. McKenzie, R. C. Pitkethly, *Catalysis* **1973**, *1*, 477–489.
6. J. Haber, *Pure Appl. Chem.* **1991**, *63*, 1227–1246.
7. I. M. Campbell, *Catalysis at Surfaces*, Chapman & Hall, London, **1988**, p. 64.
8. C. Louis, M. Che, *J. Catal.* **1992**, *135*, 156–172.
9. C. Louis, M. Che, M. Anpo, *J. Catal.* **1993**, *141*, 453–464.
10. C. Louis, J.-M. Tatibouët, M. Che, *J. Catal.* **1988**, *109*, 354–366.
11. Y. I. Yermakov, B. N. Kuznetsov, V. A. Zakharov, *Stud. Surf. Sci. Catal.*, Vol. 8, Elsevier, Amsterdam, **1981**.
12. H. Knözinger, R. Ratnasamy, *Catal. Rev.-Sci. Eng.* **1978**, *17*, 31–70.
13. H.-P. Boehm, H. Knözinger, *Catal. Sci. Technol.* **1983**, *4*, 40.
14. K. Foger, *Catal. Sci. Technol.* **1984**, *6*, 227.
15. Y. Iwasawa in *Tailored Metal Catalysts*, (Ed.: Y. Iwasawa), Reidel, Dordrecht, Holland, **1986**, Chapter 1.
16. Y. Iwasawa, *Adv. Catal.* **1987**, *35*, 187–264.
17. H. H. Lamb, B. C. Gates, H. Knözinger, *Angew. Chem., Int. Ed. Engl.* **1988**, *27*, 1127–1144.
18. A. Zecchina, C. O. Arian, *Catal. Rev.-Sci. Eng.* **1993**, *35*, 261–317.
19. J. C. W. Chien, *J. Am. Chem. Soc.* **1971**, *93*, 4675–4684.
20. S. I. Kol'tsov, V. B. Aleskovskii, *Russ. J. Phys. Chem.* **1967**, *4*, 336–337.
21. S. I. Kol'tsov, V. B. Aleskovskii, *Russ. J. Phys. Chem.* **1968**, *42*, 630–632.
22. S. I. Kol'tsov, A. N. Volkova, V. B. Aleskovskii, *Russ. J. Phys. Chem.* **1970**, *44*, 1272–1274.
23. S. I. Kol'tsov, A. A. Malygin, A. N. Volkova, V. B. Aleskovskii, *Russ. J. Phys. Chem.* **1973**, *47*, 558–560.
24. R. Fricke, W. Hanke, G. Öhlmann, *J. Catal.* **1983**, *79*, 1–12.
25. R. Fricke, H.-G. Jerschkewitz, V. B. Kazanskii, V. A. Shvets, G. Öhlmann, *React. Kinet. Catal. Lett.* **1981**, *18*, 465–471.
26. S. Haukka, E.-L. Lakomaa, A. Root, *J. Phys. Chem.* **1993**, *97*, 5085–5094.
27. S. Haukka, E.-L. Lakomaa, O. Jylhä, J. Vilhunen, S. Hornytzkyj, *Langmuir* **1993**, *9*, 3497–3506.
28. W. Hanke, R. Bienert, H.-G. Jerschkewitz, *Z. Anorg. Allg. Chem.* **1975**, *414*, 109–129.
29. V. A. Khalif, E. L. Aptekar, O. V. Krylov, G. Öhlmann, *Kinet. Katal.* **1977**, *18*, 1055–1059.
30. G. C. Bond, K. Brückman, *Faraday Discuss. Chem. Soc.* **1981**, *72*, 235–246.
31. T. Hattori, S. Itoh, T. Tagawa, Y. Murakami, *Stud. Surf. Sci. Catal.* **1987**, *31*, 113–122.
32. Y. V. Plyuto, J. Stoch, I. V. Babytch, A. A. Chuyko, *J. Non-Cryst. Sol.* **1990**, *124*, 41–47.
33. R. Castillo, B. Koch, P. Ruiz, B. Delmon, *J. Mater. Chem.* **1994**, *4*, 903–906.
34. E. V. Benvenuti, Y. Gushikem, C. U. Davanzo, S. C. de Castro, I. L. Torriani, *J. Chem. Soc. Faraday Trans.* **1992**, *88*, 3193–3196.
35. A. N. Volkova, S. I. Kol'tsov, V. B. Aleskovskii, N. N. Kushakova, *Russ. J. Phys. Chem.* **1977**, *51*, 251–252.
36. M. Lindblad, L. P. Lindfors in *Proceedings of the 10th International Congress on Catalysis*, Budapest, **1992**, (Eds: L. Guzzi, F. Solymosi, P. Téténys), Elsevier Science, Amsterdam, **1992**, Vol. B, p. 1763.
37. G. C. Bond, P. König, *J. Catal.* **1982**, *77*, 309–322.
38. B. N. Kuznetsov, A. N. Startsev, Y. I. Yermakov, *J. Mol. Catal.* **1980**, *8*, 135–145.

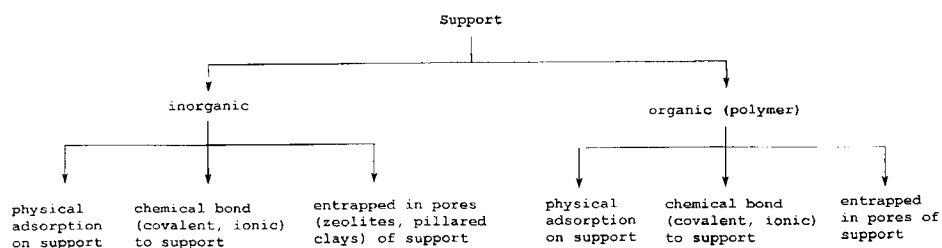
39. K. Inumaru, T. Okuhara, M. Misono, *J. Phys. Chem.* **1991**, 95, 4826–4832.
40. T. Okuhara, K. Inumaru, M. Misono, N. Matsubayashi in *Proceedings of the 10th International Congress on Catalysis*, Budapest, **1992**, (Eds.: L. Guzzi, F. Solymosi, P. Tétényis), Elsevier Science, Amsterdam, **1992**, vol. B, p. 1767.
41. J. C. Kevlin, M. G. White, *J. Catal.* **1991**, 130, 447–458.
42. S. Haukka, E.-L. Lakomaa, T. Suntola, *Appl. Surf. Sci.* **1994**, 75, 220–227.
43. M. Lindblad, L. P. Lindfors, T. Suntola, *Catal. Lett.* **1994**, 27, 323–336.
44. J.-P. Jacobs, L. P. Lindfors, J. G. H. Reintjes, O. Jylhä, H. H. Brongersma, *Catal. Lett.* **1994**, 25, 315–324.
45. D. G. H. Ballard, *Adv. Catal.* **1973**, 23, 263–325.
46. J. P. Candlin, H. Thomas, *Adv. Chem. Ser.* **1974**, 132, 212–239.
47. Y. I. Yermakov, *Catal. Rev.-Sci. Eng.* **1976**, 13, 77–120.
48. Y. I. Yermakov, B. N. Kuznetsov, *Kinet. Katal.* **1977**, 18, 1167–1178.
49. Y. I. Yermakov, Y. A. Ryndin, O. S. Alekseev, V. I. Zaikovskii, A. V. Pashis, *Appl. Catal.* **1986**, 26, 313–326.
50. Y. I. Yermakov, Y. A. Ryndin in *Homogeneous and Heterogeneous Catalysis*, (Eds: Y. I. Yermakov, V. A. Likholobov), VNU Science Press, Utrecht, **1986**, p. 1019.
51. Y. Iwasawa, H. Sato, *Chem. Lett.* **1985**, 507–510.
52. Y. Iwasawa, *Catal. Today* **1993**, 18, 21–72.
53. M. Agnelli, P. Louessard, A. E. Mansour, J. P. Candy, J. P. Bournonville, J. M. Basset, *Catal. Today* **1989**, 6, 63–72.
54. P. Dufour, C. Houtman, C. C. Santini, J.-M. Basset, *J. Mol. Catal.* **1992**, 77, 257–272.
55. S. L. Scott, J.-M. Basset, G. P. Nicolai, C. C. Santini, J.-P. Candy, C. Lecuyer, F. Quignard, A. Choplin, *New J. Chem.* **1994**, 18, 115–118.
56. V. A. Zakharov, V. K. Dudchenko, E. A. Paukshtis, L. G. Karakchiev, Y. I. Yermakov, *J. Mol. Catal.* **1977**, 2, 421–435.
57. J. Schwartz, M. D. Ward, *J. Mol. Catal.* **1980**, 8, 465–469.
58. H. C. Foley, S. J. DeCanio, K. D. Tau, K. J. Chao, J. H. Onuferko, C. Dybowski, B. C. Gates, *J. Am. Chem. Soc.* **1983**, 105, 3074–3082.
59. G. Carturan, G. Cocco, L. Schiffini, G. Strukul, *J. Catal.* **1980**, 65, 359–368.
60. Y. I. Yermakov, B. N. Kuznetsov, Y. A. Ryndin, *Kinet. Katal.* **1978**, 19, 169–179.
61. J. M. Basset, A. Choplin, *J. Mol. Catal.* **1983**, 21, 95–108.
62. J. Phillips, J. A. Dumesic, *Appl. Catal.* **1984**, 9, 1–30.
63. R. F. Howe in *Tailored Metal Catalysts*, (Ed.: Y. Iwasawa), Reidel, Dordrecht, Holland, **1986**, Chapter 3.
64. M. Ichikawa, in *Tailored Metal Catalysts*, (Ed.: Y. Iwasawa), Reidel, Dordrecht, Holland, **1986**, Chapter 4.
65. R. Psaro, R. Ugo, *Stud. Surf. Sci. Catal.* **1986**, 29, 427–496.
66. B. C. Gates, H. H. Lamb, *J. Mol. Catal.* **1989**, 52, 1–18.
67. M. Ichikawa, *Adv. Catal.* **1992**, 38, 283–400.
68. A. Brenner, R. L. Burwell, *J. Catal.* **1978**, 52, 353–363.
69. K. Asakura, K.-K. Bando, Y. Iwasawa, *J. Chem. Soc., Faraday Trans.* **1990**, 86, 2645–2655.
70. K. Asakura, Y. Iwasawa, *J. Chem. Soc., Faraday Trans.* **1990**, 86, 2657–2662.
71. E.-L. Lakomaa, *Appl. Surf. Sci.* **1994**, 75, 185–196.

### 4.1.3 Heterogenization of Complexes and Enzymes

W. KEIM AND B. DRIEBEN-HÖLSCHER

#### 4.1.3.1 Heterogenization of Complexes

In the early 1960s, new processes embracing homogeneous solution catalysis of transition metal complexes emerged. Due to the built-in selectivity advantages



**Figure 1.** How to heterogenize complexes.

and because of its promise to utilize the metals employed up to 100% efficiency – especially for noble metals – homogeneous catalysis advanced rapidly. It soon became obvious that catalyst recycling represented a major hurdle and had to be solved to give homogeneous catalysis a broader industrial future. In the search to combine the advantages of both heterogeneous and homogeneous catalysis, the field of heterogenizing homogeneous transition metal-based catalysts developed. The reasons are obvious: ease of separation of the catalyst from the products; molecular dispersion and accessibility of nearly all metal atoms; achievement of high selectivity; potential for ligand tailoring, mild reaction conditions, use of conventional equipment such as packed-bed or fluidized-bed reactors.

A number of different approaches developed to support homogeneous metal complex catalysts:

- (i) supported liquid-phase catalysis [1, 2];
- (ii) heterogenized metal complexes;
- (iii) porous material entrapped complexes (see Section 4.4);
- (iv) use of membrane filtration;
- (v) use of oligomeric complexes (application of membranes) [3].

Many publications have appeared on the heterogenization of complexes. Reference is given to the reviews, which have appeared in this field over the last two decades [4].

The heterogenization of supported solid phase (SSP) catalysts has attracted considerable attention, and Fig. 1 summarizes the various approaches that have been used.

The chemically bound metal complex catalysts may be further subdivided into covalently attached complexes and those that are ionically bound. In all heterogenized catalysts the main feature of a homogeneous metal-based catalyst, namely ligand coordination and means to tailor-make a catalyst by ligand variation on a molecular level, are given. In this context the immobilization of organometallic compounds or clusters on inorganic supports followed by decomposition, which is used to achieve a high dispersion, must also be mentioned. Examples are chemical vapor deposition (CVD) and the thermal or photochemical decomposition of the complexes (clusters) supported [5]. They are outside of the scope of this chapter.

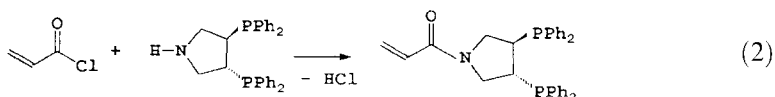
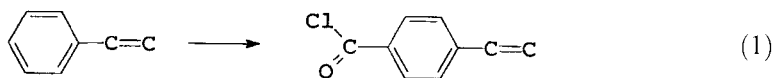


### A Organic Supports

The use of organic supports (macroreticular/macroporous polymers) as carriers for an organometallic complex, which by itself may serve as the catalyst precursor complex, has been widely studied. The polymers must be macroporous, providing a highly accessible internal surface area.

In catalyst preparation the following steps can be distinguished: monomer synthesis  $\rightarrow$  monomer polymerization  $\rightarrow$  functionalization  $\rightarrow$  metal attachment  $\rightarrow$  activation.

In monomer synthesis it is possible to functionalize a monomer selected prior to polymerization, as exemplified in Eqs 1 and 2.



The monomers obtained can be polymerized by themselves or copolymerized with other monomers. The copolymerization route is effective for the synthesis of tailor-made polymer supports with precise control over functionality and other polymer characteristics, but it is laborious and requires specialized skills in polymer synthesis.

To be useful as a catalyst support, the gelular polymers must be swellable, the propensity of which can be controlled by the degree of cross-linking. Polymers can be tailor-made to swell in a particular solvent by appropriate selection of monomer and cross-linking agent.

The functionalization of a polymer can be effected by numerous synthetic procedures and can be achieved chemically or by grafting onto a polymeric material that can, by itself, be used to support metal complexes. Often, the grafting occurs via radiation.

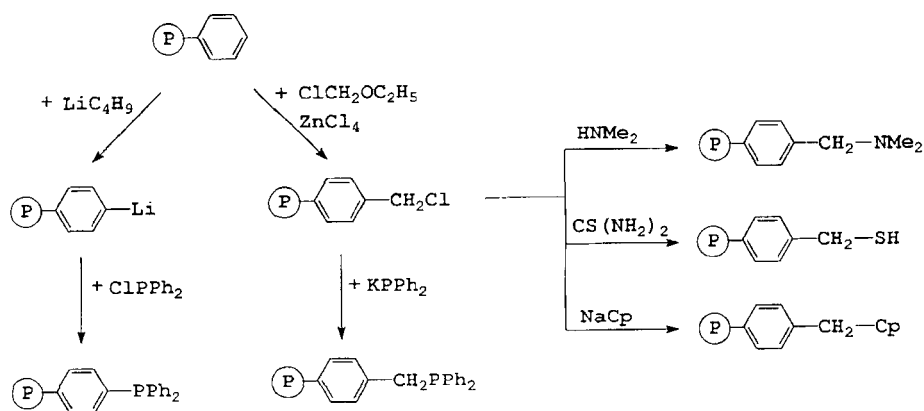
A frequently investigated approach is based on Merrifield's resin, which is a polystyrene polymer [6]. The multiplicity of ways in which to functionalize these resins is shown in Fig. 2.

The functionalization method appears particularly convenient, because underivatized beaded resins of various types and many polymers (such as polyethylene, polystyrene, polyacrylates, polysaccharides, and many others) are commercially available. However, this method suffers from the possibility of side-reactions on the cross-linked polymer, and can yield poorly characterized polymer supports.

Another approach is the use of ion-exchanged resins. Figure 3 illustrates the principle.

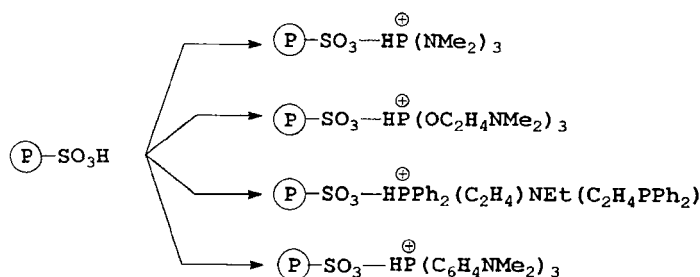
Again P- or P-N-containing polymeric supports are commercially available [6]. They include:

- (i) Polystyrene cross-linked with typically 1–2% divinylbenzene, available with the following functional groups: aminomethyl ( $-\text{CH}_2\text{NH}_2$ ),  $\alpha$ -aminobenzyl



$\text{P}$  = Merrifield's resin

Figure 2. Functionalization of Merrifield's resin.

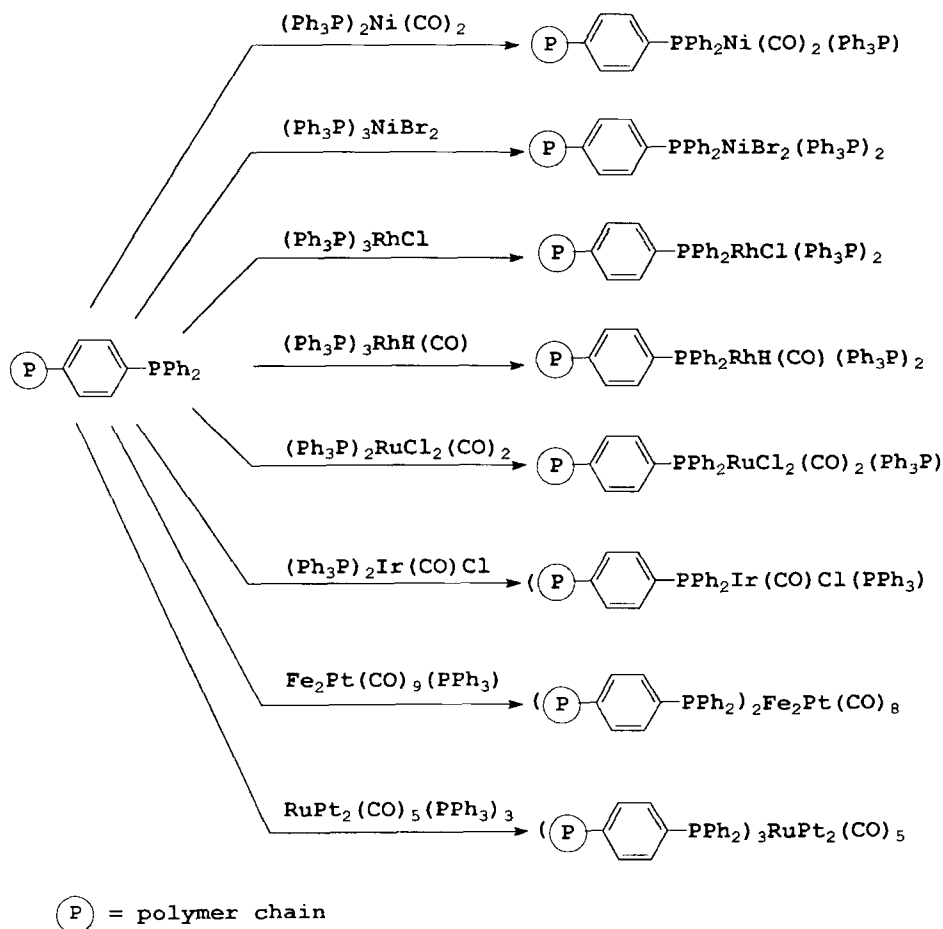


$\text{P}$  = ion - exchanged resin

Figure 3. Ion-exchanged resin as a support.

( $-\text{CH}(\text{NH}_2)\text{C}_6\text{H}_5$ ), chloromethyl ( $-\text{CH}_2\text{Cl}$ ), bromo (Br) and diphenylphosphino ( $-\text{P}(\text{C}_6\text{H}_5)_2$ ).

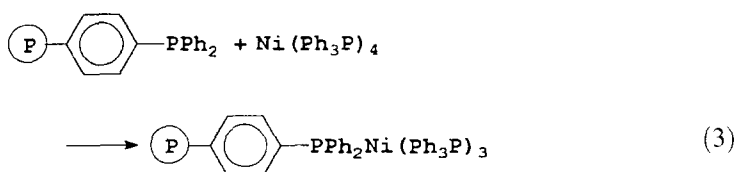
- (ii) Amberlyst resins – macroreticular styrene–divinylbenzene ion-exchange resins (with a high divinylbenzene content) designed for use with organic solvents, functionalized with  $-\text{SO}_3\text{H}$ ,  $-\text{N}(\text{CH}_3)_2$ ,  $-\text{N}(\text{CH}_3)_3^+$ ,  $\text{CH}_3\text{COO}^-$ ,  $\text{CN}^-$ ,  $\text{NO}_2^-$ ,  $\text{SCN}^-$ , and  $\text{BH}_4^-$ .
- (iii) Poly-4-vinylpyridine and pyridinium resins cross-linked with (typically) 2% divinylbenzene. Pyridinium resins are available as the chloride ( $\text{Cl}^-$ ), toluene-4-sulphonate ( $\text{CH}_3\text{C}_6\text{H}_4\text{SO}_3^-$ ), tribromide ( $\text{Br}_3^-$ ), chlorochromate ( $\text{CrClO}_3^-$ ) and dichromate ( $\frac{1}{2}\text{Cr}_2\text{O}_7^{2-}$ ). Poly-4-vinylpyridine resins are available as poly-4-

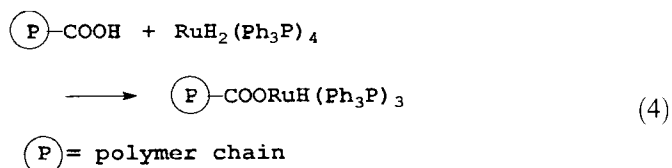


**Figure 4.** Attachment of metals to organic supports.

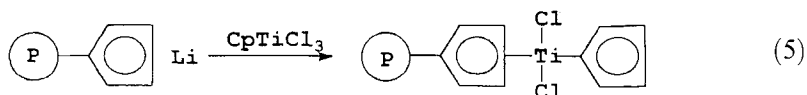
vinylpyridine-sulphur trioxide complex and poly-2-vinylpyridine-borane complex (Nafion) [7].

The functionalized polymers can react in a ligand exchange reaction as shown in Eqs 3 and 4, leading to the corresponding polymer-supported organometallic complexes. Figure 4 illustrates the broad versatility of this approach.





One of the most widely quoted examples of site isolation involves polymer-supported titanocene according to Eq. 5 [8].



Various attempts have been reported in which a complex containing a double bond amenable to polymerization is polymerized: *cis*-[PdCl<sub>2</sub>(CN(CH<sub>2</sub>)<sub>3</sub>-OCO-CH=CH<sub>2</sub>)<sub>2</sub>] [9], vinyl ferrocene, and dimethyl acrylamide [10].

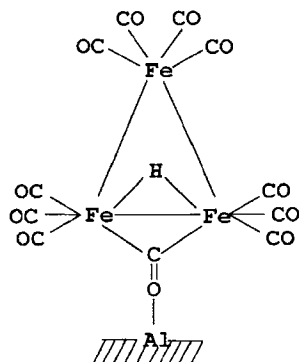
## B Inorganic Supports

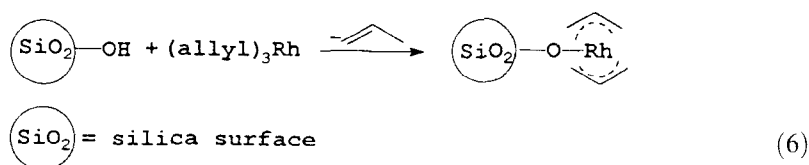
Various approaches to support complexes on inorganic supports are feasible:

- (i) the complexes are adsorbed on surfaces such as SiO<sub>2</sub>, Al<sub>2</sub>O<sub>3</sub>, Al<sub>2</sub>O<sub>3</sub>-SiO<sub>2</sub>;
- (ii) the complexes are fixed by a chemical bond;
- (iii) the complexes are entrapped in cavities of zeolites or pillared clays [2].

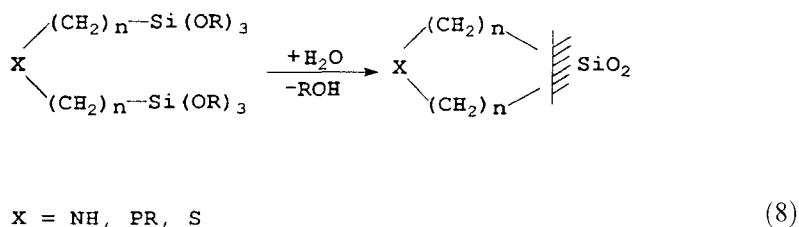
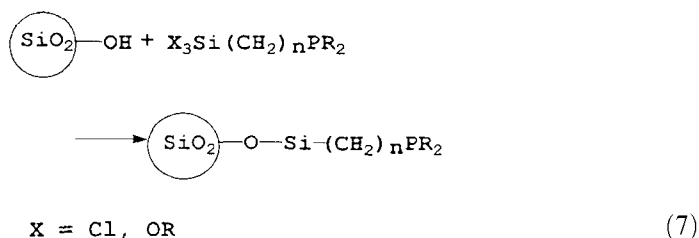
Numerous papers deal with the immobilization of complexes physisorbed/chemisorbed on inorganic supports. In particular, the anchoring of clusters has attracted much attention. For instance, a structure such as **1** was proposed in which the adduct formation is reached by a CO-interaction of the cluster with the Al<sub>2</sub>O<sub>3</sub> surface [11].

The reactive surface hydroxy groups can also react with organometallic compounds as exemplified in Eq. 6 [12].





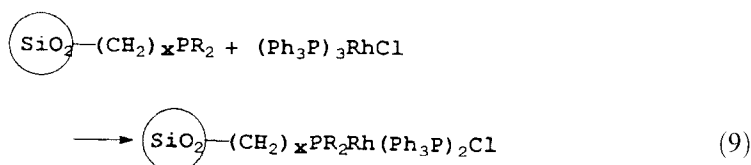
Many authors have investigated the surface organometallic chemistry, which gives rise to a great variety of reaction pathways [13]. A second approach is based on ligand tailoring of inorganic surfaces. Inorganic matrices have reactive surface hydroxy groups, and common practice involves their reaction with organochlorosilanes which either contain the desired functional group according to Eq. 7 or can be subject to subsequent modification [14].

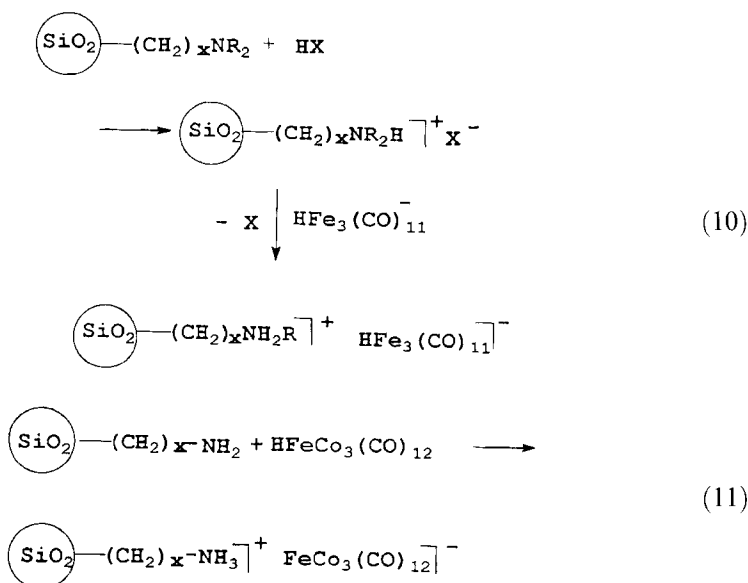


It is also feasible to proceed according to Eq. 8 using hydrolysis of the  $\text{—Si(OR)}_3\text{—}$  units. Catalysts of this type are commercially available under the tradename Deloxan [15]. The silica used can be modified as is well known in heterogeneous catalysis.

Additionally, ion-exchanged structures can be tied to  $\text{SiO}_2$  as in  $[(\text{EtO})_3\text{Si}(\text{CH}_2)_3\text{PBU}_3]^+$ . It is also possible to synthesize a complex such as  $(\text{Ph}_3\text{P})_2\text{R}_2\text{P—4}(\text{CH}_2)_x\cdot\text{Si(OR)}_3\text{RhCl}$  which, upon hydrogenolysis, yields a silica-supported rhodium catalyst.

The metals can be added by various routes: by ligand exchange reactions as in Eq. 9, by ion-exchange as in Eq. 10, or by an acid–base reaction as in Eq. 11 [17].





### C Chemical Reactions

Heterogenized complexes have been used to catalyze a great number of reactions, such as: hydrogenation [18], hydroformylation [19], ethylene oligomerization [20], hydrosilylation [21, 22], polymerization [23], telomerization [24], oxidation [25], oligomerization of monoalkene [26], methanol carbonylation [27], butadiene oligomerization [28], synthesis gas chemistry [29], and isomerization [30].

One of the most attractive fields of homogeneous catalysis is catalysis by chiral transition metal complexes, as the tool for preparing very valuable optically active products from prochiral reactants.

The use of heterogenized complexes looks promising due to the expected fixation of the prochiral reactant in the support matrix. The literature contains some examples, especially in hydrogenation [31], but also in telomerization [32].

To be commercially useful, a catalyst must possess several desirable features. It must exhibit high selectivity, reasonable activity per unit volume of reactor space, and its cost per unit mass of product produced should be low.

The principal disadvantages of organic polymers are their poor heat-transfer ability and in many cases their poor mechanical properties which prevent them from being used in stirred reactors in which they are pulverized. In this regard inorganic supports look more promising. In addition, one of the greatest difficulties in polymer-supported catalysts is their swelling.

One major consequence of confining a catalyst to the surface of a solid is that reagents have a reduced degree of freedom for access to and egress from the site of catalytic activity. Liquid-phase diffusion rates are generally  $\approx 10^{-5} \text{ cm s}^{-1}$ , whereas diffusion rates commonly experienced in polymer matrices are often an order of magnitude lower ( $\approx 10^{-6} \text{ cm s}^{-1}$ ). If the chemical reaction is fast compared with diffusion, the solid catalyst is not used effectively, and a reduced specific activity per

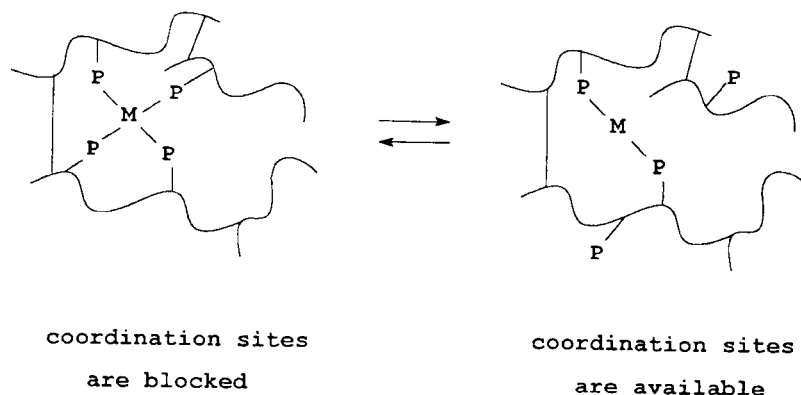


Figure 5. Dissociation of ligands.

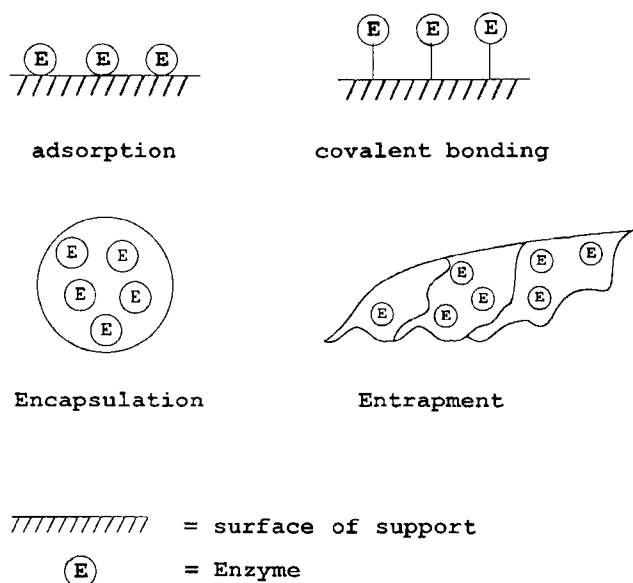
site will be observed. This lower activity is expressed in terms of an effectiveness factor which is defined as the ratio of the observed to the intrinsic rate constants:  $\eta = k_{\text{obs}}/k_{\text{intr}}$ . This phenomenon has been described extensively for catalysis by ion-exchange resins and has also been observed for heterogenized catalysts.

Despite the large amount of work done in the field of support-bound metal catalysis, no important practical application has emerged. One explanation can be the need for a multidisciplinary approach. Various areas of competence in coordination chemistry, polymer science, and engineering must be combined. In addition, the flexible polymer chain can lead to a blocking of free coordination sites needed for catalysis, as shown in Fig. 5. Also metal bleeding represents a great problem. The covalently bond ligands can easily dissociate, thus freeing the metal (Fig. 5).

Everyone working in the respective areas knows about the difficulties in characterizing catalysts and polymers. This certainly becomes no easier in the heterogenization of complexes.

#### 4.1.3.2 Heterogenization of Enzymes

The heterogenization of complexes is directed towards immobilizing the catalytic centers which ensure the high activity and selectivity of the heterogenized complexes. In the case of immobilized enzymes the situation is quite different. Enzymes act in aqueous media under mild conditions very specifically. They are not always ideal catalysts for practical applications, because they are generally unstable and can seldom be used in organic solvents or at elevated temperatures. As one of the methods employed to make enzymes more suitable in biocatalysis, the immobilization of enzymes has been studied since the late 1950s. The number of enzymes known with potential industrial application is impressive, and attempts to heterogenize enzymes have been numerous. Therefore, within the framework of this article, it is impossible to cover all of them, and reference is given to various reviews in this field [33–46].



**Figure 6.** Schematic representation of enzyme immobilization.

There are many advantages when using immobilized enzymes:

- (i) high stability and resistance to sheer stress and contamination;
- (ii) ease of developing continuous processes;
- (iii) fast reaction rate due to high catalyst concentration;
- (iv) easy separation of biocatalysts from fermentation media;
- (v) repetitive use of biocatalysts.

However there are also disadvantages:

- (i) the existence of mass transfer resistances;
- (ii) the necessity of immobilization processes;
- (iii) the additional costs of immobilization reagents.

### A Enzyme Heterogenization Methods

Methods for the immobilization of enzymes – paralleling those for complexes shown in Figure 1 – can be classified into three categories, namely carrier binding, cross-linking, and entrapping methods. Carrier binding is based on linking enzymes to water-insoluble matrices. A further division can be made considering the binding mode: physical adsorption, ionic binding, and covalent binding. Figure 6 exhibits a schematic drawing of the important types of bonding. It is possible to use inorganic, organic, or biological carrier materials.

Adsorption is the bonding of an enzyme to the surface of a carrier, which does not contain a functionalized group for covalent bonding. In theory the adsorption

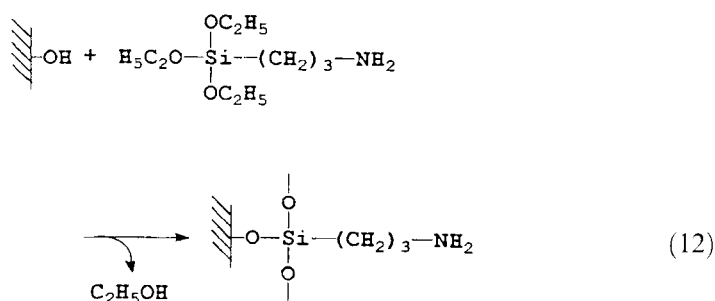


should be reversible, but in practice this is rarely the case. The adsorption is a simple and economic method but highly unreliable. In the following, carrier binding by chemical bonds will be predominantly considered.

#### *Carrier Binding to Inorganic Supports*

Inorganic carrier materials used for chromatography have been applied to covalent enzyme immobilization over the last 25 years [47]. The properties of the support must be adjusted to the enzyme. Several aspects, such as pore morphology, durability in the solvents, handling, compression strength, amount of loading, toleration of maximum pressure drop, and storage must be considered. Inorganic materials have an advantage in that they come as particles of all shapes and sizes as well as in the shape of monolithic porous supports or filter materials. They show no compression even at extremely high pressure drops. Other advantages are that they are not susceptible to microbial attack and that they do not shrink or swell in organic solvents or with pH changes. The most important aspect is their loading capacity which is high enough for a variety of applications.

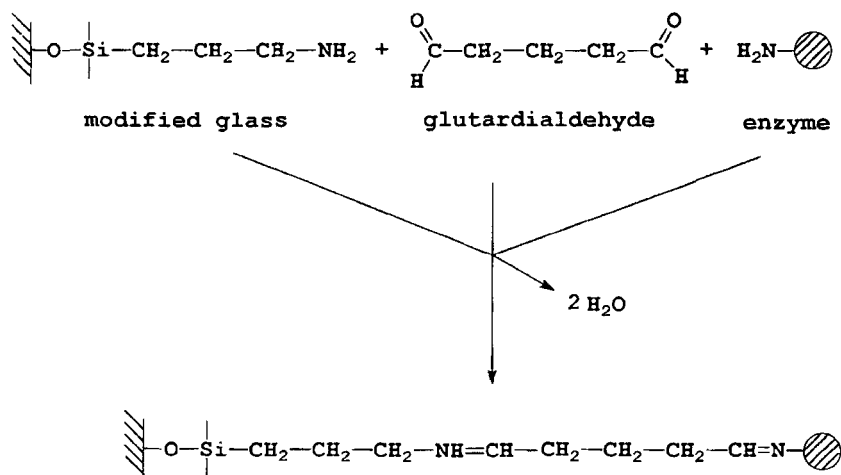
Common industrial inorganic supports are [14] silica, porous glass, alumina, zeolites, ceramics, Aerosil, and glass balls. Prior to its use the porous silica glass, for instance, must be modified as shown in Eq. 12 with amino alkoxy silanes [14].



The amino group can be activated with bifunctional reagents. A commonly applied procedure is the introduction of an aldehyde function by the bifunctional reagent glutaraldehyde. The activated carrier can be used directly for the covalent bonding of the enzyme as shown in Fig. 7. Table 1 summarizes various examples of enzyme immobilization.

#### *Carrier Binding to Organic Supports*

Frequently used organic carrier materials are polymers such as polyacrylamide, polymethacrylamide, polyhydroxyethylmethacrylate, polyamide, vinylacetate-divinylethylene, and polystyrene [66]. Often applied polymers contain hydroxy, amino, oxirane, and anhydride groups. Methods of covalent enzyme bonding [44] are azide, carbodiimide, isothiocyanate, and cyanogen bromide. Polymers with weakly active OH groups must be activated with bifunctional reagents such as

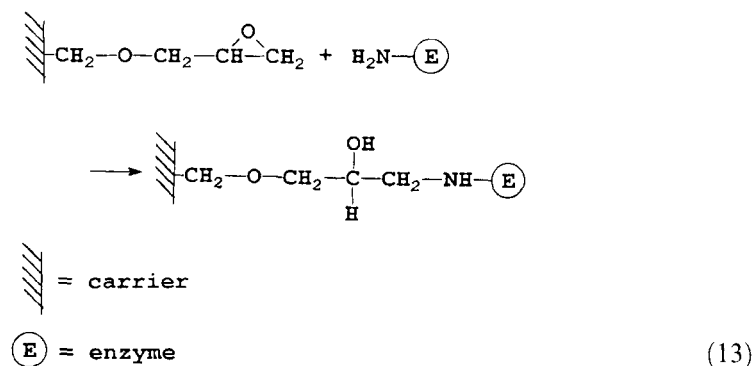


**Figure 7.** Covalent bonding of an enzyme with glutaraldehyde.

**Table 1.** Examples of enzymes covalently coupled to inorganic support materials through silane coupling agents.

Support material	Immobilized component	Reference
Silica	$\beta$ -galactosidase	49
Silica	cellulase	50
Silica	glucose oxidase	51
Porous silica	carbonic anhydrase	52
Porous silica	peroxidase, amyloglucosidase, urease	53
Porous silica	glucose isomerase, $\beta$ -galactosidase, cellulase	54
Silica gel	peroxidase, urease, amyloglucosidase	55
Magnetite	$\beta$ -galactosidase, cellulase	56
Alumina	alkaline protease, glucose oxidase, alcohol dehydrogenase	57
Ca-Ti phosphate	invertase	58
Controlled-pore glass	acetylcholinesterase	59
Controlled-pore glass	amyloglucosidase	60
Controlled-pore glass	glucose oxidase	61
Sintered glass	amyloglucosidase	62
Titanium oxide	hydrogenase	63
		64
		65

cyanogen bromide, trichlorotriazine, tresylchloride, or tosylchloride. Acrylic bead polymers with oxirane groups show preferable properties and immobilization is shown in Eq. 13.



The following list may serve as an introduction to a variety of polymers used [41]: polyacrylamide [67], polyester [68], polyethylene [69], polystyrene [70], Nylon [71].

#### *Carrier Binding to Biological Supports*

Biological materials with OH- and NH<sub>2</sub>- groups for covalent enzyme coupling are agarose, cellulose, alginate, chitosan, dextran, and collagen. The polysaccharides agarose and cellulose, with their hydroxy groups, are widely applicable to the covalent coupling of enzymes. The highly active NH<sub>2</sub>- groups in chitosan can easily be activated with glutardialdehyde in a similar manner to that shown in Fig. 7.

#### *Entrapping/Encapsulation Methods*

Enzymes can be immobilized by physical entrapment without involving any chemical bonding. This route is somewhat more laborious but yields an enzyme that is least altered by the immobilization.

The enzyme can be entrapped into the growing polymer or gel materials or microcapsules (microencapsulation). The retention of enzymes in the reaction vessel can also be achieved by an ultrafiltration membrane. All these immobilization types have in common that the enzymes are not modified and are still acting in their soluble form, so that they should be freely mobile in their "cage". An older but good review of these techniques is given by Tramper [72]. Frequently used matrices for gel entrapment are polyacrylamide and collagen [41]. The membrane inclusion method is a broadly applicable one.

A number of single-enzyme reactions have also been described that function in an enzyme membrane reactor [73].

The main disadvantage is that entrapping methods can often be used for the conversion of low-molecular-weight substrates only, and there is always the possibility for losses of the enzyme to the surrounding environment.

When using the encapsulation method the enzyme is enclosed in a semipermeable membrane. Particles of 1–100 μm diameter are obtained during the immobilization procedure. The encapsulation method, similar to the entrapment method, is suitable only for enzymes acting on low-molecular-weight substrates. Applications of entrapped or encapsulated enzymes are limited.

## B Summary and Prospective Trends

No single immobilization method is best for all enzymes or all applications of any given enzyme. The choice of a given immobilization method, an appropriate matrix, or even the best enzyme to use depends strongly on the application and must be checked from case to case. However, the number of immobilized enzymes with possible industrial application is impressive [74].

One would recommend the use of immobilized enzymes in industry when a novel product can be obtained, when the biotechnological process can compete with a corresponding known chemical process, and when the reaction shows regio- and/or stereo specificity. Developments are expected in the following areas. First, in the synthesis and separation of chiral drugs. One approach could involve a combination of enzyme-catalyzed and chemical asymmetric reactions. Secondly, processes involving enzyme-catalyzed reactions in nonaqueous media will develop further, thus circumventing one of the problems of enzymes associated with limited activity in organic solvents. Thirdly, the coenzyme regeneration may expand to increase the economic feasibility of these rather labile and expensive compounds. Finally, immobilized enzymes can be used for the treatment of waste water, particularly when the water has been polluted by one or more well-characterized contaminants that can be specifically modified or eliminated by enzymes.

An interesting and quite new technique is the treatment of enzyme microcrystals with glutardialdehyde. The cross-linked enzyme crystals obtained remain active in otherwise hostile environments such as prolonged exposure to high temperatures, extreme pH values, or in organic solvents [75].

It can be expected that the use of immobilized enzymes and cells in the food, pharmaceutical, and chemical industries will continue to expand in the future.

## References

1. V. Rao, R. Datta, *J. Catal.* **1988**, *114*, 377–382.
2. L. A. Gerritsen, J. M. Herrmann, J. J. F. Scholten, *J. Mol. Catal.* **1980**, *9*, 241–245.
3. (a) E. Bayer, V. Schurig, *CHEMTECH* **1976**, *5*, 484–487; (b) J. S. Kim, R. Datta, *AIChE J.* **1991**, *37*, 1657–1662; (c) D. E. Bergbreiter, *Functional Polymers*, Plenum Press, New York, **1989**; (d) J. T. Groves, R. Neumann, *J. Am. Chem. Soc.* **1989**, *111*, 2900–2909.
4. (a) Z. M. Michaska, D. E. Weber, *Platinum Met. Rev.* **1974**, *18*, 65–73; (b) B. Delmon, G. Jannes, *Catalysis: Heterogeneous and Homogeneous*, Elsevier, New York, **1975**; (c) J. P. Candlin, H. Thomas, *Adv. Chem. Ser.* **1974**, *132*, 212–239; (d) Y. I. Yermakov, V. Zakharov, *Adv. Catal.* **1975**, *24*, 173–219; (e) Y. I. Yermakov, *Catal. Rev.-Sci. Eng.* **1976**, *13*, 77–120; (f) F. R. Hartley, *Supported Metal Complexes*, Reidel, Dordrecht, **1985**; (g) J. H. Clark, S. R. Cullen, S. J. Barlow, T. W. Bastock, *J. Chem. Soc., Perkin Trans. 2* **1994**, *6*, 1117–1130; (h) G. Braca, *Chimicaoggi* **1988**, *2*, 23–27; (i) J. J. Crowley, H. Rapoport, *Accounts of Chem. Res.* **1976**, *9*, 135–144; (j) F. R. Hartley, P. N. Vezey, *Adv. Organomet. Chem.* **1977**, *15*, 189–234; (k) B. C. Gates, *Catalytic Chemistry*, Wiley, **1991**, p. 182–254; (l) P. Hodge, D. C. Sherrington, *Polymer-Supported Reactions in Organic Synthesis*, Wiley, Chichester, **1980**; (m) G. Luft, *Chem.-Ing.-Tech.* **1991**, *63*, 659–667.
5. (a) H. Knözinger, E. Rumpf, *Inorg. Chim. Acta* **1978**, *30*, 51–58; (b) B. C. Gates, L. Guzzi, H. Knözinger, *Metal Clusters in Catalysis*, Elsevier, Amsterdam, **1986**.
6. (a) R. B. Merrifield, *Angew. Chem. Int. Ed. Engl.* **1985**, *24*, 799; (b) *SMOPTECH*, Artillerigatan 4D, Abo, SF-20520 Finland (Supply Company).

7. K. J. Cavell, *Austr. J. Chem.* **1994**, 47, 769–797.
8. R. H. Grubbs, C. Gibbons, L. C. Kroll, W. Bonds, C. H. Brubaker, *J. Am. Chem. Soc.* **1973**, 95, 2373.
9. B. Corain, M. Zecca, F. O. Sam, G. Palma, L. Silvano, *Angew. Chem., Int. Ed. Engl.* **1990**, 29, 384–386.
10. R. Arshady, B. Corain, S. Lora, G. Palma, U. Russo, F. O. Sam, *Adv. Mater.* **1990**, 2, 412–413.
11. H. Knözinger in *Homogeneous and Heterogeneous Catalysis* (Eds: Y. Yermakov, V. Likholobov), VNU Science Press, Utrecht **1986**, p. 789–818.
12. J. Schwartz in *Homogeneous and Heterogeneous Catalysis* (Eds: Y. Yermakov, V. Likholobov), VNU Science Press, Utrecht **1986**, p. 661–691.
13. (a) J. Evans, B. P. Gracey, *J. Chem. Soc., Dalton Trans.* **1982**, 1123–1129; (b) J. M. Basset, J. P. Candy, A. Choplin, C. Santini, A. Theolier, *Catal. Today* **1989**, 6, 1–26; (c) J. M. Basset, J. P. Candy, A. Choplin, B. Didillon, F. Quignard, A. Theolier in *Perspectives in Catalysis* (Eds: J. M. Thomas, K. I. Zamaraev), Blackwell Scientific, London, **1992**, p. 125–145; (d) B. C. Gates, H. H. Lamb, *J. Mol. Catal.* **1989**, 52, 1–18.
14. M. Capka, *Collect. Czech. Chem. Commun.* **1990**, 55, 2803–2839.
15. U. Deschler, P. Kleinschmit, P. Panster *Angew. Chem.* **1986**, 98, 237–253.
16. I. Tando, *J. Am. Chem. Soc.* **1982**, 104, 6551.
17. R. Hemmerich, W. Keim, M. Röper, *J. Chem. Soc. Chem. Commun.* **1983**, 428.
18. (a) J. M. Brown, H. Molinari, *Tetrahedron Lett.* **1979**, 31, 2933–2936; (b) F. Sanchez, M. Iglesias, A. Corma, C. del Pino, *J. Mol. Catal.* **1991**, 70, 369–379; (c) I. E. Uflyand, V. N. Sheinker, A. V. Bulatov, A. D. Pomogailo, *J. Mol. Catal.* **1989**, 55, 391–395; (d) E. A. Karakhanov, E. B. Neimerovets, A. G. Dedov, *Applied Organomet. Chem.* **1990**, 4, 1–7; (e) R. A. Awe, E. N. Frankel, *J. Am. Oil Chem. Soc.* **1981**, 557–562; (f) T. Okano, K. Tsukiyama, H. Konishi, J. Kiji, *Chem. Lett.* **1982**, 5, 603–606; (g) F. Joo, M. T. Beck, *J. Mol. Catal.* **1984**, 16, 135; (h) A. D. Kini, D. V. Nadkarni, J. L. Fry, *Tetrahedron Lett.* **1994**, 35, 1507–1510; (i) A. El Mansour, J. P. Candy, J. P. Bournonville, O. A. Feretti, J. M. Basset, *Angew. Chem.* **1989**, 101, 360–362; (j) R. J. Card, C. E. Liesner, D. C. Neckers, *J. Org. Chem.* **1979**, 44, 1095–1098.
19. (a) C. Dossi, A. Fusi, L. Garlaschelli, D. Roberto, R. Ugo, *Catal. Lett.* **1991**, 11, 335–340; (b) I. Toth, B. E. Hanson, J. Guo, M. E. Davis, *Catal. Lett.* **1991**, 8, 209–214; (c) W. Junfan, S. Juntan, L. Hong, H. Binglin, *React. Polym.* **1990**, 12, 177–186; (d) L. Alvila, T. A. Pakkanen, T. T. Pakkanen, O. Krause, *J. Mol. Catal.* **1992**, 71, 281–290; (e) S. C. Tang, T. E. Paxson, L. Kim, *J. Mol. Catal.* **1980**, 9, 313; (f) M. E. Ford, A. N., Neogi, *J. Mol. Catal.* **1983**, 9, 99; (g) E. Rode, M. E. Davis, B. E. Hanson, *J. Chem. Soc., Chem. Commun.* **1985**, 1477–1478; (h) G. Schmid, R. Küpper, H. Hess, J.-O. Malm, J.-O. Bovin, *Chem. Ber.* **1991**, 124, 1889–1893; (i) A. Fukuoka, L. F. Rao, N. Kosugi, H. Kuroda, M. Ichikawa, *Appl. Catal.* **1989**, 50, 295–301; (j) M. Ichikawa, *Polyhedron* **1988**, 7, 2351–2367; (k) M. Ichikawa, L. Rao, T. Kimura, A. Fukuoka, *J. Mol. Catal.* **1990**, 62, 15–35; (l) L. A. Gerritsen, A. van Meerkerk, M. H. Vreugdenhil, J. J. F. Scholten, *J. Mol. Catal.* **1980**, 9, 138–155; (m) J. Hjortkjaer, M. S. Scurrel, P. Simonsen, H. Svendsen, *J. Mol. Catal.* **1981**, 12, 179–195.
20. (a) W. Keim, M. Peuckert, *J. Mol. Catal.* **1984**, 22, 289–295; (b) G. A. Nesterov, G. Fink, V. A. Zakharov, *Makromol. Chem., Rapid Commun.* **1989**, 10, 669–673; (c) G. A. Nesterov, V. A. Zakharov, G. Fink, W. Fenzl, *J. Mol. Catal.* **1991**, 66, 367–372; (d) I. E. Uflyand, A. D. Pomogailo, *J. Mol. Catal.* **1989**, 55, 302–310; (e) G. Braca, M. Di Girolamo, A. M. Raspolli Galetti, G. Sbrana, M. Brunelli, G. Bertolini, *J. Mol. Catal.* **1992**, 74, 421–431.
21. B. Marciniak, Z. W. Konetka, W. Urbaniak, *J. Mol. Catal.* **1981**, 12, 221–230.
22. M. Capka, M. Czakoova, J. Hjortkjaer, U. Schubert, *React. Kinet. Catal. Lett.* **1993**, 50, 71–74.
23. (a) V. A. Zakharov, Y. I. Yermakov, *Cat. Rev.-Sci. Eng.* **1979**, 19, 67–103; (b) S. Collins, W. M. Kelly, D. V. Holden, *Macromolecules* **1992**, 25, 1780–1785; (c) G. G. Arzoumanidis, N. M. Karayannis, H. M. Khelghation, S. S. Lee, *Catal. Today* **1992**, 13, 59–71; (d) F. S. Dyachkovskii, A. D. Pomogailo, *J. Polym. Sci. Polym. Symp.* **1980**, 68, 97–108.
24. (a) K. Kaneda, H. Kurosaki, M. Terasawa, T. Imanaka, S. Teranishi, *J. Org. Chem.* **1981**, 46, 2356–2362; (b) J. P. Bianchini, E. Gaydou, B. Wagell, A. Eisenbeis, W. Keim, *J. Mol. Catal.* **1985**, 30, 197–212.

25. (a) T. Yokoyama, M. Nishizawa, T. Kimura, T. M. Susuki, *Chem. Lett.* **1983**, 11, 1703–1706; (b) H. Fischer, G. Schulz-Ekloff, T. Buck, D. Wöhrle, *Erdöl, Erdgas, Kohle* **1994**, 110, 128–135; (c) A. Sorakin, B. Meunier, *J. Chem. Soc., Chem. Commun.* **1994**, 1799–1800.
26. (a) B. M. Trost, J. M. Tour, *J. Am. Chem. Soc.* **1987**, 109, 5268–70; (b) N. Kawata, T. Mizoroki, A. Ozaki, *J. Mol. Catal.* **1975**, 1, 275–283.
27. (a) M. S. Scurell, *La Chimica el Industria* **1979**, 61, 652–655; (b) T.-N. Huang, J. Schwartz, *J. Mol. Catal.* **1984**, 22, 389–93; (c) M. S. Scurell, R. Howe, *J. Mol. Catal.* **1980**, 7, 535–537; (d) P. Gelin, G. Coudurier, Y. Ben Taarit, C. Naccache, *J. Catal.* **1981**, 70, 32–40.
28. (a) C. U. Pittman Jr., S. K. Wu, S. E. Jacobson, *J. Catal.* **1976**, 44, 87–100; (b) U. Schuchardt, E. N. Dos Santo, F. S. Dias, *J. Mol. Catal.* **1989**, 55, 345–352.
29. B. Corain, M. Basato, M. Zecca, G. Braca, A. M. R. Galetti, S. Lora, G. Palma, E. Guglielminotti, *J. Mol. Catal.* **1992**, 73, 23–41.
30. L. C. Po, C. B. Hung, R. H. Grubbs, C. H. Brubaker, *J. Organomet. Chem.* **1981**, 214, 325–37; (b) A. P. Raje, R. Datta, *J. Mol. Catal.* **1992**, 72, 97–116.
31. (a) I. Toth, B. E. Hanson, *J. Mol. Catal.*, **1992**, 71, 365–371; (b) G. L. Baker, S. J. Fritschel, I. R. Stille, J. K. Stille, *J. Org. Chem.* **1981**, 46, 2954–60; (c) A. Corma, M. Iglesias, C. del Pino, F. Sanchez, *J. Organomet. Chem.* **1992**, 431, 233–246; (d) U. Nagel, E. Kinzel, *J. Chem. Soc., Chem. Commun.* **1986**, 14, 1098–1099; (e) H. B. Kagan, T. P. Dang, W. Dumont, J. C. Poulin, *J. Am. Chem. Soc.* **1973**, 95, 8295.
32. W. Keim, D. Schwarzer, D. Vogt, *Chem.-Ing.-Techn.* **1995**, 67, 904.
33. O. R. Zaborsky, *Immobilized Enzymes*, CRC Press, Cleveland, Ohio, **1973**.
34. H. H. Weetall, *Immobilized Enzymes, Antigens, Antibodies and Peptides*, Dekker, New York, **1975**.
35. I. Chibata, *Immobilized Enzymes*, Wiley, New York, **1978**.
36. K. Buchholz, *Charakterization of Immobilized Biocatalysts*, Dechema Monographie 84, Verlag Chemie, Weinheim, **1979**.
37. J. C. Johnson, *Immobilized Enzymes*, Noyes Data Corp., Park Ridge, NJ, **1979**.
38. P. Dunnill, A. Wisemann, N. Blakebrough, *Enzymic and Nonenzymic Catalysis*, Ellis Horwood, Chichester, UK, **1980**.
39. J. F. Kennedy, J. M. S. Cabral, *Solid Phase Biochemistry*, (Ed.: W. H. Scouten), **1983**, Wiley Interscience, New York, p. 253.
40. W. Hartmeier, *Immobilisierte Biokatalysatoren*, Springer Verlag, Berlin, **1986**.
41. K. Mosbach, *Immobilized Enzymes and Cells*, Methods of Enzymology, Vol. 135–137, Academic Press, New York, **1987**.
42. H.-J. Rehm, G. Reed, *Biotechnology*, 2nd ed., VCH, Weinheim, **1993**, 430–466.
43. K. Drauz, H. Waldmann, *Enzyme Catalysis in Organic Synthesis*, VCH, Weinheim, **1994**.
44. B. P. Sharma, L. F. Bailey, R. A. Messing, *Angew. Chem.* **1987**, 94, 836–852.
45. I. Chibata, T. Tosa, T. Sato, *J. Mol. Catal.* **1986**, 37, 1–24.
46. S. Fukui, A. Tanaka, *Ullmann's Encycl. Ind. Chem.* 5th ed. **1987**, Vol. A9, p. 382–388.
47. H. H. Weetall, *Science* **1969**, 166, 615.
48. H. H. Weetall, *Appl. Biochem. Biotechnol.* **1993**, 41, 151–188.
49. A. Kozhukharova, K. Batsalova, Y. A. Popova, N. Kirova, D. Klisurski, D. Simeonov, *Biotechnolo-giya* **1990**, 1, 61.
50. M. Kitaoka, H. Taniguchi, T. Sasaki, *J. Ferment. Bioeng.* **1989**, 67, 182.
51. A. Kojuharova, Y. Popova, N. Kirova, D. Klissurski, D. Simeonov, L. Spasov, *J. Chem. Technol. Biotechnol.* **1988**, 42, 95.
52. J. P. O'Daly, A. L. Crumbliss, R. W. Henkens, *Biotechnol. Appl. Biochem.* **1990**, 12, 11.
53. J. Lobarzewski, A. Wojcik, T. Blaszczyńska, *Acta Biotechnol.* **1989**, 9, 239.
54. J. E. Sorensen, C. Emborg, *Enzyme Microb. Technol.* **1989**, 11, 26.
55. K. Shimizu, M. Ishihara, *Biotechnol. Bioeng.* **1987**, 29, 236.
56. A. Wojcik, J. Lobarzewski, T. Blaszczyńska, J. Fiedurek, *Biotechnol. Bioeng.* **1987**, 30, 983.
57. F. R. H. Dekker, *Appl. Biochem. Biotechnol.* **1990**, 23, 25.
58. A. Garcia, S. Oh, C. R. Engler, *Biotechnol. Bioeng.* **1989**, 33, 321.
59. G. A. Kovalenko, V. D. Sokolovskii, *Biotechnol. Bioeng.* **1992**, 39, 523.
60. T. Suzuki, M. Toriyama, H. Hosonv, Y. Abe, *J. Ferment. Bioeng.* **1991**, 5, 384.
61. S. Kumaran, H. Meier, A. M. Danna, C. Tran-Minh, *Anal. Chem.* **1991**, 63, 1914.

62. F. Janowski, G. Fisher, W. Urbaniak, Z. Foltynowicz, B. Maceniec, *J. Chem. Technol. Biotechnol.* **1991**, 51.
63. M. M. Hossain, D. D. Do, *Biotechnol. Bioeng.* **1985**, 27, 842.
64. J. Fiedurek, J. Lobarzewski, *Starch Staerke* **1990**, 42, 358.
65. P. Cuendet, M. Gratzel, K. K. Rao, D. O. Hall, *Photobiochem. Photobiophys.* **1984**, 7, 311.
66. N. F. Mathur, C. K. Norang, R. W. Williams, *Polymers as Aids in Organic Chemistry*, Academic Press, New York, **1980**.
67. J. K. Imman, H. M. Dintzis, *Biochemistry* **1969**, 8, 4074.
68. R. S. Franek, *Czech. Epidemiol. Mikrobiol. Immunol.* **1978**, 27.
69. T. T. Ngo, K. J. Laider, C. F. Yam, *Can. J. Biochem.* **1979**, 57, 1200.
70. N. Grabhofer, L. Schluth, *Naturwissenschaften* **1953**, 40, 508.
71. W. E. Hornby, L. Goldstein in *Methods in Enzymology* (Ed.: K. Mosbach), **1987**, Vol. 44, p. 118, Academic Press, New York.
72. J. Tramper in *Solid Phase Biochemistry* (Ed.: W. H. Scouten), Wiley Interscience, New York, **1983**, p. 393.
73. U. Kragl, D. Vasic-Racki, C. Wandrey, *Chem.-Ing.-Tech.* **1992**, 64, 499.
74. J. G. Shewale, S. R. Naik, *J. Scientific Ind. Res.* **1991**, 50, 947.
75. N. L. St. Clair, M. Navia, *J. Am. Chem. Soc.* **1992**, 114, 7314–7316. This material is commercially available from Altus Biologies Inc., Cambridge, USA.

## 4.2 Supported Metal Cluster Catalysts

B. C. GATES

### 4.2.1 Introduction

Metals are used widely as catalysts, e.g. for reforming of naphtha, abatement of automobile emissions, hydrogenation of carbon monoxide and hydrogenation of fats. Because the catalytic metal is often expensive, it is usually applied in a finely dispersed form as particles on a high-area porous support (e.g. a metal oxide, zeolite, or carbon), so that a large fraction of the metal atoms are exposed to reactant molecules; the metal may constitute only about 1 wt % of the catalytic material [1–5]. Details of such catalysts are given in Chapter 4.1.1.

Supported metal catalysts used in technology are typically made by impregnation of a porous metal oxide support with an aqueous solution of a metal salt, followed by calcination and reduction in hydrogen. The reduced metal particles are distributed over the internal surface of the support. Because most support surfaces are structurally nonuniform, and because supported metal particles are extremely small and nonuniform in size and shape, the structures of supported metal catalysts are not well understood. This structural complexity is one of the motivations for investigation of supported metals with well-defined structures, which are described in this article.

The average metal particle size in a supported metal catalyst is usually estimated

62. F. Janowski, G. Fisher, W. Urbaniak, Z. Foltynowicz, B. Maceniec, *J. Chem. Technol. Biotechnol.* **1991**, 51.
63. M. M. Hossain, D. D. Do, *Biotechnol. Bioeng.* **1985**, 27, 842.
64. J. Fiedurek, J. Lobarzewski, *Starch Staerke* **1990**, 42, 358.
65. P. Cuendet, M. Gratzel, K. K. Rao, D. O. Hall, *Photobiochem. Photobiophys.* **1984**, 7, 311.
66. N. F. Mathur, C. K. Norang, R. W. Williams, *Polymers as Aids in Organic Chemistry*, Academic Press, New York, **1980**.
67. J. K. Imman, H. M. Dintzis, *Biochemistry* **1969**, 8, 4074.
68. R. S. Franek, *Czech. Epidemiol. Mikrobiol. Immunol.* **1978**, 27.
69. T. T. Ngo, K. J. Laider, C. F. Yam, *Can. J. Biochem.* **1979**, 57, 1200.
70. N. Grabhofer, L. Schluth, *Naturwissenschaften* **1953**, 40, 508.
71. W. E. Hornby, L. Goldstein in *Methods in Enzymology* (Ed.: K. Mosbach), **1987**, Vol. 44, p. 118, Academic Press, New York.
72. J. Tramper in *Solid Phase Biochemistry* (Ed.: W. H. Scouten), Wiley Interscience, New York, **1983**, p. 393.
73. U. Kragl, D. Vasic-Racki, C. Wandrey, *Chem.-Ing.-Tech.* **1992**, 64, 499.
74. J. G. Shewale, S. R. Naik, *J. Scientific Ind. Res.* **1991**, 50, 947.
75. N. L. St. Clair, M. Navia, *J. Am. Chem. Soc.* **1992**, 114, 7314–7316. This material is commercially available from Altus Biologies Inc., Cambridge, USA.

## 4.2 Supported Metal Cluster Catalysts

B. C. GATES

### 4.2.1 Introduction

Metals are used widely as catalysts, e.g. for reforming of naphtha, abatement of automobile emissions, hydrogenation of carbon monoxide and hydrogenation of fats. Because the catalytic metal is often expensive, it is usually applied in a finely dispersed form as particles on a high-area porous support (e.g. a metal oxide, zeolite, or carbon), so that a large fraction of the metal atoms are exposed to reactant molecules; the metal may constitute only about 1 wt % of the catalytic material [1–5]. Details of such catalysts are given in Chapter 4.1.1.

Supported metal catalysts used in technology are typically made by impregnation of a porous metal oxide support with an aqueous solution of a metal salt, followed by calcination and reduction in hydrogen. The reduced metal particles are distributed over the internal surface of the support. Because most support surfaces are structurally nonuniform, and because supported metal particles are extremely small and nonuniform in size and shape, the structures of supported metal catalysts are not well understood. This structural complexity is one of the motivations for investigation of supported metals with well-defined structures, which are described in this article.

The average metal particle size in a supported metal catalyst is usually estimated



from the dispersion (fraction of metal atoms exposed) measured by titration of the metal surface sites by hydrogen or CO chemisorption. Complementary measurements giving structural information are made with transmission electron microscopy and extended X-ray absorption fine structure (EXAFS) spectroscopy, among other techniques. With dispersion data, it is possible to determine the rate of a catalytic reaction per exposed surface metal atom, referred to as a turnover frequency or turnover rate.

The structures of supported metal particles have often been modeled as clusters or crystallites having the symmetries of bulk metals [6]. For example, a six-atom platinum particle may be represented as an octahedron with an edge length of about 0.55 nm and a dispersion of 1. A 20-atom platinum particle with the assumed structure has an edge length of about 1 nm and a dispersion of 0.95, still barely distinguishable from 1. Thus metal dispersions that are determined by chemisorption measurements to be virtually unity indicate metal particles about 1 nm in size or smaller, but the dispersion data do not distinguish particles smaller than about 1 nm.

Supported metals are conveniently classified on the basis of the metal particle size [2]:

1. *Metal particles larger than about 5 nm.* These have surface structures resembling those of chunks of the bulk metal and expose a number of different crystal faces, with the distribution of faces being more or less independent of the particle size. The presence of these relatively large particles in some practical catalysts demonstrates the relevance of single-crystal planes for investigation of catalytic phenomena.
2. *Supported metal particles in the size range 1–5 nm.* These have been regarded as the particles of greatest interest in catalysis because changes in the particle size lead to significant changes in properties for many catalytic reactions; such reactions are classified as structure sensitive [5–8].
3. *Supported metal particles with diameters <1 nm.* These are referred to here as metal clusters to distinguish them from the larger particles. (However, the definition of the term “cluster” is not generally agreed upon in catalysis, and some authors apply it to particles much larger than 1 nm in diameter.) Supported metal clusters are the subject of this review. They are gaining attention because methods have recently been developed to prepare and characterize them and because a catalyst incorporating them (platinum clusters in the pores of LTL zeolite) has found industrial application for selective reforming of naphtha to give aromatics.

A part of the motivation for investigation of supported metal clusters originates from the recognition that there are conceptual links between supported metal clusters and molecular metal clusters, illustrated by metal carbonyls such as  $[\text{Fe}_3(\text{CO})_{12}]$ ,  $[\text{Co}_4(\text{CO})_{12}]$ ,  $[\text{Os}_3(\text{CO})_{12}]$ ,  $[\text{Ir}_4(\text{CO})_{12}]$ , and  $[\text{Pt}_{15}(\text{CO})_{30}]^{2-}$  and by bare metal clusters such as  $\text{Co}_4^+$ ,  $\text{Fe}_4^+$ , and  $\text{Pt}_n$  ( $n = 1\text{--}15$ ), which have been investigated extensively in the gas phase. The practical application of gas-phase clusters as catalysts is appa-

rently not feasible, and the few examples of catalysis by metal carbonyl clusters in solution are neither very well understood nor of practical importance. The prospects of catalysis by ligand-stabilized molecular metal clusters such as metal carbonyls are limited because the more stable of these clusters tend to be unreactive, and the more reactive of these clusters are unstable at the temperatures required for most catalytic reactions.

## 4.2.2 Preparation of Supported Metal Clusters

### 4.2.2.1 Synthesis of Supported Metal Carbonyl Clusters

Metal carbonyl clusters on supports are the most common precursors of structurally simple supported metal clusters. Routes for preparation of molecularly or ionically dispersed metal carbonyl clusters on metal oxide supports include (i) deposition from solution, (ii) reaction with the support surface, and (iii) synthesis from mononuclear precursors on the support surface [9–13]. The first method may not give fully dispersed supported clusters and is usually not preferred. More effective syntheses are illustrated by reactions of precursor metal carbonyl clusters with OH groups of support surfaces. The compound  $[\text{Os}_3(\text{CO})_{12}]$  reacts by oxidative addition with OH groups of  $\text{SiO}_2$  or  $\gamma\text{-Al}_2\text{O}_3$  to give predominantly  $[(\mu - \text{H})\text{Os}_3(\text{CO})_{10} \cdot \{\mu - \text{OM}\}]$ , where  $\text{M} = \text{Si}$  or  $\text{Al}$ , and the braces denote groups terminating the bulk metal oxide [14–18]. Deprotonation of a hydrido metal carbonyl cluster on a basic metal oxide support (such as  $[\text{H}_4\text{Os}_4(\text{CO})_{12}]$  on  $\text{MgO}$  or on  $\gamma\text{-Al}_2\text{O}_3$ ) gives surface ion pairs  $[\text{H}_3\text{Os}_4(\text{CO})_{12}]^- \{\text{M}^{n+}\}$ , where  $\text{M}^{n+}$  is a cation exposed at the surface of the metal oxide support [19].

Metal carbonyl clusters may also be synthesized efficiently from mononuclear metal carbonyl precursors on support surfaces [13]. Yields are often high, but they have not been quantified well. There are parallels between surface and solution chemistry that are predicted roughly by a comparison of surface and solvent properties [13]. For example, syntheses on basic  $\text{MgO}$  surfaces take place as in basic solutions in the presence of reducing agents, and syntheses on  $\text{SiO}_2$  take place as in neutral solvents. For example,  $[\text{Ir}(\text{CO})_2(\text{acac})]$  reacts in the presence of  $\text{CO}$  on  $\text{MgO}$  to give  $[\text{HIr}_4(\text{CO})_{11}]^-$ ,  $[\text{Ir}_8(\text{CO})_{22}]^{2-}$ , or  $[\text{Ir}_6(\text{CO})_{15}]^{2-}$  [20]. Other clusters prepared by surface-mediated synthesis on  $\text{MgO}$  are the following:  $[\text{Os}_5\text{C}(\text{CO})_{14}]^{2-}$  [21],  $[\text{Os}_{10}\text{C}(\text{CO})_{24}]^{2-}$  [21],  $[\text{Rh}_5(\text{CO})_{15}]^-$  [22],  $[\text{Pt}_{15}(\text{CO})_{30}]^{2-}$  [23],  $[\text{Pt}_6(\text{CO})_{12}]^{2-}$  [24],  $[\text{Pt}_9(\text{CO})_{18}]^{2-}$  [24], and  $[\text{Pt}_{12}(\text{CO})_{24}]^{2-}$  [23]. Also,  $[\text{Ir}_4(\text{CO})_{12}]$  has been prepared on  $\gamma\text{-Al}_2\text{O}_3$  [25] and  $[\text{H}_4\text{Os}_4(\text{CO})_{12}]$  on  $\text{SiO}_2$  [26].

The syntheses referred to above take place in zeolite cages, much as they do on surfaces of amorphous metal oxides. Syntheses in the nearly neutral  $\text{NaY}$  zeolite are similar to those occurring on  $\gamma\text{-Al}_2\text{O}_3$ , e.g. those of  $[\text{Ir}_4(\text{CO})_{12}]$  [27] and  $[\text{Ir}_6(\text{CO})_{16}]$  [28] from  $[\text{Ir}(\text{CO})_2(\text{acac})]$ . Syntheses in the more basic  $\text{NaX}$  zeolite are similar to those occurring on  $\text{MgO}$ , e.g. those of  $[\text{HIr}_4(\text{CO})_{11}]^-$  and  $[\text{Ir}_6(\text{CO})_{15}]^{2-}$  [29]. Ship-in-a-bottle syntheses take place when clusters formed in zeolite cages are trapped (and stabilized) there because they are too large to fit through the zeolite apertures.

#### 4.2.2.2 Decarbonylation of Supported Metal Carbonyl Clusters

The preparation of supported metal clusters by decarbonylation of supported metal carbonyl clusters is exemplified by the removal of the CO ligands from the metal frame of  $[\text{Ir}_4(\text{CO})_{12}]$  dispersed on  $\gamma\text{-Al}_2\text{O}_3$ . The decarbonylation of the sample in helium at 473 K, tracked by infrared and EXAFS spectroscopies, takes place with little or no disruption of the tetrahedral metal frame [25]. Details of the chemistry are unknown, but the simple decarbonylation may be relatively unsurprising in view of the indication from electrospray mass spectrometry that CO ligands can be peeled off one by one from a salt of  $[\text{HIr}_4(\text{CO})_{11}]^-$  in the gas phase, giving  $\text{HIr}_4(\text{CO})_{11-x}$  ( $x = 0, 1, 2, \dots, 11$ ) [30]. Similarly, decarbonylation of MgO-supported  $[\text{HIr}_4(\text{CO})_{11}]^-$  [31],  $[\text{Ir}_6(\text{CO})_{15}]^{2-}$  [31],  $[\text{Pt}_{15}(\text{CO})_{30}]^{2-}$  [32], and  $[\text{Os}_{10}\text{C}(\text{CO})_{24}]^{2-}$  [33] also appears to take place without significant changes in the metal framework structures, as indicated by EXAFS spectroscopy.

Decarbonylation of  $[\text{HIr}_4(\text{CO})_{11}]^-$  and of  $[\text{Ir}_6(\text{CO})_{15}]^{2-}$  in NaY zeolite cages occurs similarly [28, 34], and these decarbonylations are reversible [34], in contrast to decarbonylations of the same clusters on MgO [35]. Infrared spectra show that  $[\text{Ir}_4(\text{CO})_{12}]$  (or  $[\text{Ir}_6(\text{CO})_{16}]$ ) was decarbonylated by treatment in  $\text{H}_2$  at 573 K [34]. When CO was adsorbed on the decarbonylated clusters at 77 K and the temperature raised with the sample in CO, mononuclear iridium carbonyls formed at about 240 K. These were converted at about 320 K into  $[\text{Ir}_4(\text{CO})_{12}]$  and at about 400 K into  $[\text{Ir}_6(\text{CO})_{16}]$  [34]. These results show that the reconstruction of the iridium carbonyl clusters involved chemistry more complicated than simple readsorption of CO onto the metal clusters.

#### 4.2.2.3 Formation of Metal Clusters in Zeolite Cages by Reduction of Exchange Cations

Zeolite-supported metal clusters have most commonly been prepared by ion exchange followed by reduction [36–38]. Usually the metals are introduced as cationic complexes, (e.g.  $[\text{Pt}(\text{NH}_3)_4]^{2+}$ ), which replace cations such as  $\text{Na}^+$  in the zeolite and are then decomposed by heating in  $\text{O}_2$  or air and reduced in  $\text{H}_2$ . The metal complex may be introduced instead by impregnation with an aqueous solution. Samples prepared by these methods are typically nonuniform in structure, and therefore only little is written in this section. The synthesis methods may work for zeolites, but they often give larger and less uniform clusters and/or particles of metal when amorphous supports are used. Reduction of metals in zeolites also often leads to nonuniform metal particles, including those that are too large to fit in the cages, resulting in the migration of the metal outside of the intracrystalline pores and/or destruction of the zeolite framework.

Cations of noble metals in zeolites are easily reduced by  $\text{H}_2$ , but proper activation and reduction treatments that give the highest metal dispersions and the most uniform metal clusters are not easily predicted. For example, prior to reduction of a metal ammine complex in  $\text{H}_2$ , it is usually necessary to remove  $\text{NH}_3$  produced by

thermal decomposition, because reduction of metal ions in the presence of evolving  $\text{NH}_3$  leads to formation of agglomerated metal.

Activation of platinum ammine complexes in flowing  $\text{O}_2$  prior to reduction in  $\text{H}_2$  gives highly dispersed platinum clusters in zeolites. The temperature of  $\text{O}_2$  treatment strongly influences the metal dispersion. For example, Dalla Betta and Boudart [39], investigating a sample prepared from  $\text{Pt}(\text{NH}_3)_4\text{Cl}_2$  in CaY zeolite, found that calcination in  $\text{O}_2$  at 623 K followed by treatment in  $\text{H}_2$  at 673 K gave highly dispersed platinum in the zeolite. Ammonia from the platinum complex reduced the platinum; reduced platinum is generally the product of the thermal decomposition (at 573 K or higher temperatures) of platinum amines in Y zeolite, even in air [40]. Highly dispersed platinum (with about six atoms per cluster, on average) in H-mordenite was prepared from  $\text{Pt}(\text{NH}_3)_4(\text{OH})_2$ , with calcination at 623 K and reduction in  $\text{H}_2$  at 623 K [41]. Platinum clusters were prepared in KLTL zeolite by aqueous impregnation with tetraammineplatinum(II) nitrate followed by calcination at 533 K and reduction in  $\text{H}_2$  at 773 K [42]. Alternatively, reduction of platinum (or iridium) ammine complexes in zeolite LTL gave extremely small metal clusters even when the calcination step was omitted [43, 44].

#### 4.2.2.4 Deposition of Size-Selected Gas-Phase Metal Clusters

Beams of gas-phase metal clusters, size selected by a mass spectrometer and allowed to impinge on planar surfaces in an ultrahigh vacuum chamber, give dispersed size-selected clusters on the support. The few such samples are  $\text{Pt}_n$ , where  $n = 1-6$ , on oxidized silicon wafers and on carbon films [45], and  $\text{Pt}_n$  and  $\text{Pd}_n$ , where  $n = 1-15$ , on Ag(110) single crystals [46].

#### 4.2.2.5 Formation of Nearly Uniform Metal Particles on Supports

Most supported metal particles are nonuniform in size and shape, but a few preparations have succeeded in giving nearly uniform particles. Palladium particles with narrow size distributions in the range 1–10 nm were prepared by evaporation of palladium onto a planar support and control of the conditions of nucleation and aggregation of the metal into particles [47–49]. These samples appear to be among the most nearly uniform supported metals in this size range.

The methods applied in the manufacture of microelectronic devices by electron-beam lithography have been used to prepare regular arrays of platinum particles on planar silicon [50]. The samples were made by coating the silicon with a photoresist, exposing it to a narrow electron beam positioned to produce a regular matrix of holes in the photoresist, and then exposure of the sample to platinum vapor. Removal of the photoresist leaves behind a periodic array of uniform platinum particles. A  $1\text{ cm}^2$  silicon wafer was produced with  $2.5 \times 10^9$  platinum clusters, each 50 nm in size and present in a square array with a separation of 150 nm. This is the most nearly uniform sample yet made consisting of supported metal particles. The technology of electron-beam lithography is not available for preparation of regular

arrays of supported metal clusters consisting of only a few atoms because it is not yet possible to prepare sufficiently small holes in the photoresist.

### 4.2.3 Structural Characterization of Supported Metal Clusters

Supported metal clusters pose a challenge in characterization science because they are small, usually nonuniform, and present in only low loadings in solids that are usually amorphous. The most incisive physical methods for identification of dispersed clusters have become available only recently, including, for example, EXAFS spectroscopy, high-resolution electron microscopy,  $^{129}\text{Xe}$  NMR spectroscopy, scanning tunneling microscopy, and atomic force microscopy. These methods, complemented by others, including  $\text{H}_2$  and  $\text{CO}$  chemisorption and wide angle X-ray scattering, have opened the way to investigation of the synthesis and catalytic properties of supported metal clusters.

Size-selected platinum and palladium clusters on planar supports have been investigated with X-ray and ultraviolet photoemission spectroscopy [30, 31]. Each of the clusters  $\text{Pt}_n$  ( $n = 1, 2, \dots, 6$ ) on  $\text{SiO}_2$  [45] has a distinct spectrum. Structural data for the supported clusters are still lacking. Results characterizing  $\text{Pt}_n$  ( $n = 1, 2, \dots, 15$ ) on  $\text{Ag}(110)$  indicate distinct core level binding energies for the different species; the line width was found to increase and then level off for clusters containing more than six platinum atoms [46]. Theoretical calculations suggested chain structures for the smaller clusters on  $\text{Ag}(110)$ .

The relatively new science of metal clusters on supports was almost without a structural foundation before the advent of EXAFS spectroscopy. This technique [51], although still in a stage of rapid development, provides quantitative structure data, most precisely when the clusters contain only a few atoms and are nearly uniform [52]. The technique is limited because it provides only average structural information and relatively imprecise values of coordination numbers; the best data are obtained at low temperatures, typically 77 K.

EXAFS results representing some of the simplest and most thoroughly investigated supported metal clusters are shown in Table 1; the clusters were formed by decarbonylation of metal carbonyls. Supported clusters formed by decarbonylation of  $\gamma\text{-Al}_2\text{O}_3$ -supported  $[\text{Ir}_4(\text{CO})_{12}]$ , which has a tetrahedral metal frame, have an Ir-Ir first-shell coordination number of about 3, the value for a tetrahedron (Table 1). However, the experimental error in this coordination number is as much as  $\pm 20\%$ , and there is no confirming structural information and no technique that easily provides it, although EXAFS data besides the first-shell metal-metal coordination number may provide additional structural information [31].

With these limitations, the structures formed from tetrairidium carbonyls (Table 1) are modeled as  $\text{Ir}_4$  tetrahedra. These are the simplest and best-defined supported metal clusters.

The structures of supported metal clusters depend on the preparation conditions. For example, clusters may be oxidized by traces of  $\text{O}_2$  impurities; increasing hydroxylation of the  $\text{MgO}$  support favors the formation of clusters larger than  $\text{Ir}_4$ , for example [55].

**Table 1.** Supported metal clusters formed by decarbonylation of supported metal carbonyl clusters: characterization by EXAFS spectroscopy.

Support	Precursor	Cluster modeled as	Metal-metal first-shell coordination number	$R$ (nm)	$10^5 \times \Delta\sigma^2$ (nm <sup>2</sup> )	$\Delta E_0$ eV	Ref.
$\gamma$ -Al <sub>2</sub> O <sub>3</sub>	[Ir <sub>4</sub> (CO) <sub>12</sub> ]	Ir <sub>4</sub> tetrahedra	2.9	0.269	3.1	0.83	25
MgO	[HfIr <sub>4</sub> (CO) <sub>11</sub> ] <sup>+</sup>	Ir <sub>4</sub> tetrahedra	3.1	0.269	1.1	1.22	53
MgO	[HfIr <sub>4</sub> (CO) <sub>11</sub> ] <sup>+</sup>	Ir <sub>4</sub> tetrahedra	3.1	0.270	2.3	0.50	54
MgO	[HfIr <sub>4</sub> (CO) <sub>11</sub> ] <sup>+</sup>	Ir <sub>4</sub> tetrahedra	3.0	0.269	4.8	3.9	55
NaY zeolite	[Ir <sub>4</sub> (CO) <sub>12</sub> ] formed from [Ir(CO) <sub>2</sub> (acac)]	Ir <sub>4</sub> tetrahedra	3.4	0.270	3.0	0.06	27
NaX zeolite	[HfIr <sub>4</sub> (CO) <sub>11</sub> ] <sup>+</sup> formed from [Ir(CO) <sub>2</sub> (acac)]	Ir <sub>4</sub> tetrahedra	3.0	0.271	2.9	2.77	29
MgO	[Ru <sub>3</sub> (CO) <sub>12</sub> ]	Ru <sub>3</sub>	1.7	0.264	not stated	not stated	56
$\gamma$ -Al <sub>2</sub> O <sub>3</sub>	[Ru <sub>3</sub> (CO) <sub>12</sub> ]	Ru <sub>6</sub>	3.1	0.264	not stated	not stated	56
$\gamma$ -Al <sub>2</sub> O <sub>3</sub>	[H <sub>3</sub> Re <sub>3</sub> (CO) <sub>12</sub> ]	Re <sub>3</sub>	2.0	0.267	0.86	-3.04	57
Zeolite 5A, Ca form	Pd(NH <sub>3</sub> ) <sub>4</sub> (NO <sub>3</sub> ) <sub>2</sub>	Pd <sub>6</sub>	3.5	not stated	not stated	not stated	58
MgO	[Ir <sub>6</sub> (CO) <sub>16</sub> ] formed from [Ir(CO) <sub>2</sub> (acac)]	Ir <sub>6</sub> in mixture with Ir rafts	2.7	0.272	4	-4.5	31
NaY zeolite	[Ir <sub>6</sub> (CO) <sub>16</sub> ] formed from [Ir(CO) <sub>2</sub> (acac)]	Ir <sub>6</sub>	3.6	0.271	3.5	-2.00	28
MgO	[Pt <sub>15</sub> (CO) <sub>30</sub> ] <sup>2-</sup> formed from Na <sub>2</sub> PtCl <sub>6</sub>	Pt <sub>15</sub>	3.7	0.276	3.3	-0.87	32
MgO	H <sub>2</sub> OsCl <sub>6</sub>	Os <sub>10</sub>	3.8	0.267	0.37	1.2	59

Notes:  $R$  is the average absorber-backscatterer distance,  $\Delta\sigma^2$  the Debye-Waller factor, and  $\Delta E_0$  the inner potential correction. Typical experimental errors in coordination number and  $R$  are as much as  $\pm 20\%$  and  $\pm 2\%$ , respectively. The structures depend on the pretreatment temperatures of the supports and the conditions of decarbonylation, which are stated in the cited references.

The nearly uniform metal clusters on amorphous supports have been prepared either from metal carbonyl precursors or from beams of size-selected bare metal clusters. The only nearly uniform supported metal clusters made by conventional methods are zeolite supported (Table 2). Included in Table 2 are only samples that have been characterized by EXAFS spectroscopy and incorporate extremely small clusters. The synthetic methods used to prepare metal clusters in zeolites are similar to those used for most conventional supported metal catalysts. The zeolites appear to be different from amorphous supports in giving such highly dispersed and nearly uniform metal clusters; the cages and apertures may limit the sizes of the clusters by hindering the migration of species that are mobile and sinter readily on amorphous supports.

It seems likely that zeolite-supported metal clusters made from salts (Table 1) incorporate less uniform clusters than the samples made from metal carbonyl clusters or on planar supports from size-selected metal clusters; however, this suggestion is not yet tested.

Notwithstanding the rapid progress in characterization of supported metal clusters, much remains to be learned. The structures and reactivities of supported metal clusters and the effects of supports on cluster structure and the nature of the cluster–support interface are less than well understood [31]. Powder metal oxide supports are structurally nonuniform, and it has been postulated that clusters reside preferentially at defect sites [62]; experiments with structurally well defined metal clusters on single-crystal metal oxides (or models of these consisting of thin layers of metal oxides on metals) are needed to determine how the support structure affects cluster structure and properties. Assessments of electronic properties of supported clusters are still not consistent with each other. Theoretical chemistry is just beginning to have an impact on the assessment of electronic properties, with calculations having been reported for  $\text{Ir}_4$  and  $\text{Ir}_{10}$  [63], but it is still too early for theories to account reliably for the influence of the support.

In summary, supported metal clusters have been prepared that are nearly uniform in structure, although work is needed to determine structures and properties with greater precision. These samples offer an opportunity to determine the catalytic properties of metal clusters. The first results of such experiments are summarized below.

#### **4.2.4 Catalysis by Supported Metal Clusters**

It is likely that many conventional supported metal catalysts incorporate metal clusters, but because of the difficulty of distinguishing the small clusters from larger metal particles, it has not been possible to identify or define the roles of clusters. Rather, evidence of catalysis by supported metal clusters has arisen only recently, made possible by syntheses that give catalysts containing metal almost exclusively in the form of clusters. The following section is a summary of catalytic results emphasizing supported metal clusters that have been characterized by EXAFS spectroscopy, with the data demonstrating the stability of the clusters and their presence in both the fresh and used catalysts.

Table 2. Zeolite-supported metal clusters formed from salt precursors.

Support	Precursor	Characterization methods <sup>a</sup>	Metal-metal coordination number <sup>b</sup>	Approximate average cluster nuclearity	Comment	Refs
BaKLT zeolite	Pt(NH <sub>3</sub> ) <sub>4</sub> (NO <sub>3</sub> ) <sub>2</sub>	EXAFS, TEM, H <sub>2</sub> chemisorption	3.7	5-6	Sample not calcined after addition of Pt; reduced at 773 K.	43
KLT zeolite	Pt(NH <sub>3</sub> ) <sub>4</sub> (NO <sub>3</sub> ) <sub>2</sub>	EXAFS, H <sub>2</sub> chemisorption, TPD of hydrogen	4.0 ± 0.1	6	Sample not calcined after addition of Pt; reduced at 573 K.	60, 61
KLT zeolite	Pt(NH <sub>3</sub> ) <sub>4</sub> (NO <sub>3</sub> ) <sub>2</sub>	EXAFS, H <sub>2</sub> chemisorption, TPD of hydrogen	4.8 ± 0.2	10	Sample not calcined after addition of Pt; reduced at 773 K.	60, 61
KLT zeolite	Pt(NH <sub>3</sub> ) <sub>4</sub> (NO <sub>3</sub> ) <sub>2</sub>	EXAFS, H <sub>2</sub> chemisorption, TPD of hydrogen	4.9 ± 0.1	12	Sample not calcined after addition of Pt; reduced at 873 K.	60, 61
HLTL zeolite	Pt(NH <sub>3</sub> ) <sub>4</sub> (NO <sub>3</sub> ) <sub>2</sub>	EXAFS, H <sub>2</sub> chemisorption, TPD of hydrogen	4.1 ± 0.1	6	Sample not calcined after addition of Pt; reduced at 573 K.	60, 61
HLTL zeolite	Pt(NH <sub>3</sub> ) <sub>4</sub> (NO <sub>3</sub> ) <sub>2</sub>	EXAFS, H <sub>2</sub> chemisorption, TPD of hydrogen	4.4 ± 0.1	9	Sample not calcined after addition of Pt; reduced at 773 K.	60, 61
HMAZ zeolite	Pt(NH <sub>3</sub> ) <sub>4</sub> (NO <sub>3</sub> ) <sub>2</sub>	EXAFS, H <sub>2</sub> chemisorption	2.9 ± 0.2	4	Sample not calcined after addition of Pt; reduced at 773 K.	60
HMOR zeolite	Pt(NH <sub>3</sub> ) <sub>4</sub> (OH) <sub>2</sub>	EXAFS, TPD of hydrogen	3.7	6	Sample calcined at 623 K after addition of Pt; reduced at 623 K.	41
KHMOR zeolite	Pt(NH <sub>3</sub> ) <sub>4</sub> (OH) <sub>2</sub>	EXAFS, TPD of hydrogen	3.9	6	Sample calcined at 623 K after addition of Pt; reduced at 623 K.	41

<sup>a</sup> Abbreviations: TEM, transmission electron microscopy; TPD, temperature-programmed desorption.<sup>b</sup> Error bounds represent precisions, not accuracies.



#### 4.2.4.1 Catalysis by Supported Ir<sub>4</sub> and Ir<sub>6</sub> Clusters

Catalytic properties of supported clusters identified as primarily Ir<sub>4</sub> or Ir<sub>6</sub> were reported by Xu et al. [30], who investigated structure-insensitive reactions, cyclohexene hydrogenation and toluene hydrogenation. EXAFS spectra showed that the first-shell Ir-Ir coordination numbers characterizing both the fresh and used MgO-supported catalysts made by decarbonylation of supported [Ir<sub>4</sub>(CO)<sub>12</sub>] or [HIr<sub>4</sub>(CO)<sub>11</sub>]<sup>-</sup> are indistinguishable from 3, the value for a tetrahedral metal frame, as in [Ir<sub>4</sub>(CO)<sub>12</sub>] and [HIr<sub>4</sub>(CO)<sub>11</sub>]<sup>-</sup> (Table 3). When decarbonylated, clusters retained this metal frame. EXAFS data show that the decarbonylated Ir<sub>6</sub> clusters had metal frames indistinguishable from the octahedra of the precursor hexairidium carbonyls, indicated by the Ir-Ir coordination number of approximately 4 (Table 3).

Catalytic activities (turnover frequencies) are summarized for these clusters and for conventional (structurally nonuniform) supported catalysts consisting of aggregates of iridium on supports. Turnover frequencies of the latter catalysts are based on the number of surface iridium atoms estimated from hydrogen chemisorption data. The decarbonylated iridium clusters are different in activity from each other and from the supported iridium particles on MgO (Table 4). The clusters represented as Ir<sub>6</sub> are several times less active than those represented as Ir<sub>4</sub>, and both of these are markedly less active than the larger iridium particles.

Changing the support from MgO to  $\gamma$ -Al<sub>2</sub>O<sub>3</sub> to zeolite NaY had little effect on the activities of the decarbonylated clusters (Table 4). The orders of reaction in toluene and in H<sub>2</sub> were found to be approximately 0 and 1, respectively, both for the supported iridium cluster catalysts and the supported iridium particles.

The EXAFS data show that pretreatment in H<sub>2</sub> at 573 K did not lead to a significant change in the metal framework structure of MgO-supported Ir<sub>4</sub> or Ir<sub>6</sub>, but it led to a decrease in their activities for toluene hydrogenation (Table 4). The results suggest that hydrogen bonded to the clusters and inhibited catalysis. However, the effect of hydrogen illustrated by these data is not the same as that observed for Ir<sub>6</sub> in NaY zeolite. The hydrogen pretreatment led to a doubling of the activity of this catalyst without a substantial change in the metal framework structure. The results imply that the different supports are associated with different effects of hydrogen treatment.

Evidence of an influence of the support on the stability of the supported metal clusters is shown by the data for a sample originally containing Ir<sub>4</sub> supported on  $\gamma$ -Al<sub>2</sub>O<sub>3</sub>. Following treatment in H<sub>2</sub> at 573 K, the catalytic activity (per total Ir atom) increased tenfold (Table 4). This increase is explained, at least in part, by the EXAFS result for the used catalyst, which shows that the iridium had aggregated to give clusters with an average of about 20 atoms each (Table 3). Thus the data show that the support significantly affected the stability of the clusters but hardly affected their intrinsic catalytic activity. The results suggest that NaY zeolite helps to stabilize the clusters, perhaps by virtue of entrapment in the supercages.

Although the Ir<sub>4</sub> and Ir<sub>6</sub> clusters catalyze the same reactions as metallic iridium particles, their catalytic character is different, even for structure-insensitive hydrogenation reactions. It is inferred [30] that the clusters are metal-like but not metallic. Thus these data show the limit of the concept of structure insensitivity; this

**Table 3.** EXAFS results characterizing fresh and used supported metal cluster catalysts [64].

Sample number	Catalyst precursor	Support	Treatment/catalysis <sup>a</sup>	$N,^b$ fresh catalyst	$R,^c$ fresh catalyst (nm)	$N,^b$ used catalyst	$R,^c$ used catalyst (nm)	Refs
1	$[\text{HIr}_4(\text{CO})_{11}]^-$	MgO	none	3.2	0.271	—	—	30, 53, 65
2	$[\text{Ir}_4(\text{CO})_{12}]$	$\gamma\text{-Al}_2\text{O}_3$	decarbonylation and catalysis of toluene hydrogenation	2.9	0.269	3.2	0.268	25, 30
3	$[\text{HIr}_4(\text{CO})_{11}]^-$	MgO	decarbonylation and catalysis of toluene hydrogenation	3.2	0.271	2.8	0.269	30, 53, 65
4	$[\text{Ir}_6(\text{CO})_{16}]$	NaY zeolite	decarbonylation and catalysis of toluene hydrogenation	—	—	3.9	0.270	30
5	$[\text{Ir}_6(\text{CO})_{15}]^{2-}$	MgO	decarbonylation, treatment in $\text{H}_2$ at 573 K, and catalysis of toluene hydrogenation	—	—	4.1	0.269	30
6	$[\text{HIr}_4(\text{CO})_{11}]^-$	MgO	decarbonylation, treatment in $\text{H}_2$ at 573 K, and catalysis of toluene hydrogenation	3.1	0.270	3.1	0.270	30
7	$[\text{Ir}_6(\text{CO})_{15}]^{2-}$	MgO	decarbonylation, treatment in $\text{H}_2$ at 573 K, and catalysis of toluene hydrogenation	3.8	0.269	3.7	0.270	30
8	$[\text{Ir}_4(\text{CO})_{12}]$	$\gamma\text{-Al}_2\text{O}_3$	decarbonylation, treatment in $\text{H}_2$ at 573 K, and catalysis of cyclohexene hydrogenation	—	—	5.4	0.267	30
9	$[\text{Ir}_6(\text{CO})_{16}]$	NaY zeolite	decarbonylation, treatment in $\text{H}_2$ at 573 K, and catalysis of cyclohexene hydrogenation	3.6	0.271	4.1	0.269	28, 30
10	$[\text{HIr}_4(\text{CO})_{11}]^-$	MgO	decarbonylation, treatment in $\text{H}_2$ at 573 K, and catalysis of propane hydrogenolysis	—	—	3.3	0.271	30
11	$[\text{HIr}_4(\text{CO})_{11}]^-$	MgO	decarbonylation, treatment in $\text{H}_2$ at 573 K, and catalysis of propane hydrogenolysis	$3.35 \pm 0.15$	$0.2730 \pm 0.0005$	$3.26 \pm 0.23$	$0.2735 \pm 0.0006$	54

Table 3. (cont.)

Sample number	Catalyst precursor	Support	Treatment/catalysis <sup>a</sup>	$N^b$ , fresh catalyst	$R^c$ , fresh catalyst (nm)	$N^b$ , used catalyst	$R^c$ , used catalyst (nm)	Refs
12	$[\text{Os}_{10}\text{C}(\text{CO})_{24}]^{2-}$	MgO	decarbonylation, treatment in $\text{H}_2$ at 573 K, and catalysis of <i>n</i> -butane hydrogenolysis	4.7	0.267	5.0	0.268	59
13	$\text{Pt}(\text{NH}_3)_4(\text{OH})_2$	HMOR zeolite	calcination at 623 K, treatment in $\text{H}_2$ at 623 K, and catalysis of <i>n</i> -hexane isomerization	3.7	0.272	not stated, but nearly 3.7	not stated	41

<sup>a</sup> Conditions of catalysis experiments stated in Table 4. <sup>b</sup>  $N$  is the first-shell metal–metal coordination number; <sup>c</sup>  $R$  is the metal–metal distance, both determined by EXAFS spectroscopy. All error bounds represent precisions, not accuracies.

Table 4. Catalytic activities of supported metal clusters and supported metallic particles [64].

Sample number <sup>a</sup>	Catalyst modeled as	Support	Catalytic reaction <sup>b</sup>	H <sub>2</sub> treatment temperature of catalyst (K)	10 <sup>3</sup> × TOF <sup>c</sup> (s <sup>-1</sup> )	Ref.
1	[HIr <sub>4</sub> (CO) <sub>11</sub> ] <sup>-</sup>	MgO	toluene hydrogenation	no treatment	0.00	30
2	Ir <sub>4</sub>	γ-Al <sub>2</sub> O <sub>3</sub>	toluene hydrogenation	no H <sub>2</sub> treatment	0.94	30
3	Ir <sub>4</sub>	MgO	toluene hydrogenation	no H <sub>2</sub> treatment	0.63	30
4	Ir <sub>6</sub>	NaY zeolite	toluene hydrogenation	no H <sub>2</sub> treatment	0.25	30
5	Ir <sub>6</sub>	MgO	toluene hydrogenation	no H <sub>2</sub> treatment	0.23	30
6	Ir <sub>4</sub>	MgO	toluene hydrogenation	573	0.17	30
7	Ir <sub>6</sub>	MgO	toluene hydrogenation	573	0.03	30
8	aggregates of about 20 atoms each, on average, formed from Ir <sub>4</sub>	γ-Al <sub>2</sub> O <sub>3</sub>	toluene hydrogenation	573	9.9 <sup>d</sup>	30
9	Ir <sub>6</sub>	NaY zeolite	toluene hydrogenation	573	0.52	30
10	Ir <sub>4</sub>	MgO	cyclohexene hydrogenation	573	18	30
11	Ir <sub>4</sub>	MgO	propane hydrogenolysis	573	20	54
12	approximately Os <sub>10</sub>	MgO	<i>n</i> -butane hydrogenolysis	573	not stated; rate influenced by diffusion	59
13	approximately Pt <sub>6</sub> , on average	HMOR zeolite				41
14	Ir crystallites	MgO	<i>n</i> -hexane isomerization toluene hydrogenation	623 773	2.0	30

<sup>a</sup> Sample numbers match those of Table 3. <sup>b</sup> Reaction conditions: each reaction except cyclohexene hydrogenation carried out with vapor-phase reactants in a once-through plug flow reactor operated at atmospheric pressure; cyclohexene hydrogenation carried out with liquid-phase cyclohexene in *n*-hexane solvent saturated with H<sub>2</sub> flowing through the stirred reactor, which was held at atmospheric pressure. <sup>c</sup> TOF (turnover frequency) for toluene hydrogenation at 333 K; for cyclohexene hydrogenation at 298 K; for propane hydrogenolysis at 473 K (turnover frequency) for toluene hydrogenation at 333 K; for cyclohexene hydrogenation at 298 K; for propane hydrogenolysis at 473 K with a H<sub>2</sub>:hydrocarbon molar ratio of 2.5; for *n*-butane hydrogenolysis at 473 K with a H<sub>2</sub>:hydrocarbon molar ratio of 2.5; for *n*-butane hydrogenolysis at 473 K with a *n*-butane:H<sub>2</sub>:He molar ratio of 1:10:9. <sup>d</sup> In contrast to the activities of the other catalysts, the activity of this catalyst is expressed per total Ir atom to facilitate the comparison with the results for sample 2. The comparison shows that the activity, even per total Ir atom, increased as a result of aggregation of the Ir caused by pretreatment of the sample in hydrogen. TOF was calculated on the basis of the assumption that each cluster atom was accessible.

concept pertains only to catalysis by surfaces of structures that are present in three-dimensional particles about 1 nm in diameter or larger. The pattern of structure insensitivity that has been observed for numerous reactions (such as hydrocarbon hydrogenations) catalyzed by particles larger than 1 nm in diameter leads to the suggestion that these particles are metallic in character and the smaller clusters  $\text{Ir}_4$  and  $\text{Ir}_6$  are not metallic, but more nearly molecular in character from the point of view of catalysis [30].

If it is proper to regard supported metal clusters as quasimolecular [30], it follows that the support provides part of a ligand shell, which presumably helps to stabilize the cluster and affects the catalytic activity as ligands affect the catalytic activity of a molecular metal cluster. The lack of a significant support effect on the catalytic activities shown in Table 4 is consistent with the suggestion that all the supports mentioned in the table are metal oxides that are not much different from each other as ligands.

MgO-supported clusters formed by decarbonylation of  $[\text{HIr}_4(\text{CO})_{11}]^-$  were also investigated as catalysts for a structure-sensitive reaction, propane hydrogenolysis [54]. The decarbonylated cluster had an average Ir-Ir coordination number of 3.1, which implies that the tetrahedral metal frame was largely retained after decarbonylation. The catalyst, after use in a flow reactor at 473 K, was characterized by an Ir-Ir coordination number of 3.2, which implies that the cluster structure was largely retained. The lack of a significant change in the average cluster size indicates the stability of the supported catalyst, which is modeled as tetrairidium clusters. The catalyst performance data confirm the stability, indicated by a lack of change in the activity during operation in a flow reactor following a short break-in period.

The turnover frequency of the supported  $\text{Ir}_4$  catalyst (Table 4) was found to be two orders of magnitude less than that of a conventionally prepared MgO-supported iridium catalyst containing iridium particles about 3 nm in average diameter.

The results are consistent with the identification of propane hydrogenolysis as a structure-sensitive reaction, but a reservation must be expressed about this inference – because the supported crystallites are so much more active than the supported clusters, it is difficult to rule out the possibility that a small fraction of the clusters had aggregated on the support surface to give larger species and that these provided the surfaces for the observed catalytic activity. Such a concern for the toluene hydrogenation reaction should not be ruled out, but the likelihood of catalysis by undetected metal particles rather than metal clusters in this reaction is considered less likely than for propane hydrogenolysis because the catalyst preparation, catalysis, and EXAFS experiments were reproduced several times and because the reaction conditions were so mild (333 K, for example). Furthermore, data for cyclohexene hydrogenation are qualitatively in agreement with those for toluene hydrogenation, and the former reaction was carried out at only 298 K [30].

Data for *n*-butane hydrogenolysis catalyzed by MgO-supported clusters formed by decarbonylation of  $[\text{Os}_{10}\text{C}(\text{CO})_{24}]^{2-}$  and modeled as  $\text{Os}_{10}$  are also consistent with the structure sensitivity of hydrogenolysis [59].

#### 4.2.4.2 Catalysis by Clusters of Pt and of Ir in Zeolite LTL

Supported metal clusters as small as those described in the preceding paragraphs are important in catalytic technology, being used for naphtha reforming to give aromatics [66, 67]. The catalysts consist of platinum clusters in zeolite LTL made basic by the presence of  $K^+$  or  $K^+$  and  $Ba^{2+}$  exchange ions [68–70].

In several industrially prepared catalysts of this type, almost all the clusters were confined in the zeolite pores (Table 2). For example, EXAFS spectra determined first-shell Pt-Pt coordination numbers of 4–5, indicating clusters of, on average, about 5–12 atoms. Dark-field electron micrographs [71] lead to a similar conclusion for industrially prepared catalysts.

Catalyst performance is illustrated by data of Lane et al. [72] for conversion of *n*-hexane in  $H_2$  at 603–713 K and atmospheric pressure. Primary products result from both one–six and one–five ring closure, giving benzene and methylcyclohexane, respectively. The catalyst is remarkable for its benzene selectivity, which increases with increasing conversion of *n*-hexane because some of the primary products are further converted into benzene.

Several explanations have been advanced for the unique performance of Pt/LTL zeolite catalysts. Dehydrocyclization is catalyzed by the platinum clusters alone [42, 66, 72], but the support must be nonacidic to prevent yield loss by acid-catalyzed isomerization and hydrocracking [66, 73]. The more basic is the LTL support, the higher is the aromatic selectivity. The interaction of the platinum clusters with the basic support has been suggested to result in an increase in the electron density on platinum and favor the catalysis [74–77]. The steric environment of the platinum clusters may also be important; the one-dimensional pore structure of the LTL zeolite has been suggested to orient the straight-chain alkane parallel to the pore axis, thereby increasing the probability of terminal adsorption [78]. Because well-prepared catalysts incorporate extremely small clusters, with almost no platinum outside the pores, the high selectivity is associated with the low hydrogenolysis activity of platinum clusters smaller than about 1 nm [73]. The small zeolite cavities favor small, stable entrapped clusters.

Iridium clusters in zeolite KLTL, consisting of 4–6 atoms on average, have also been prepared, by reduction of  $[Ir(NH_3)_5Cl]Cl_2$  in  $H_2$  at temperatures exceeding 573 K [44]. Notwithstanding the small cluster size, the basic support environment, and the location in the LTL zeolite pore structure, the clusters were found to be similar to other iridium catalysts for conversion of *n*-hexane and  $H_2$ , having a poor selectivity for aromatization and a high selectivity for hydrogenolysis. Thus the iridium clusters are much less selective than platinum clusters of nearly the same size in the zeolite. The comparison is consistent with the inference that selective naphtha aromatization catalysts require both a nonacidic support and a metal with a low hydrogenolysis activity, such as platinum.

In summary, although the catalysis is complex and not yet fully understood, it is evident that maximization of aromatization selectivity results from the choice of a catalytic metal with a low intrinsic activity for hydrogenolysis (platinum) and optimization of the support alkalinity and steric environment, which favors small

clusters (which are highly selective) and perhaps otherwise favors the desired ring closure.

### 4.2.5 Summary and Assessment

Supported metal clusters are a new class of catalyst made possible by syntheses involving organometallic chemistry on surfaces, gas-phase cluster chemistry, and chemistry in zeolite cages [64]. The synthetic chemistry would not have been possible without the guidance of new characterization science; EXAFS spectroscopy is the technique that has provided the most insight into structures of supported metal clusters. Clusters such as  $\text{Ir}_4$ ,  $\text{Ir}_6$ , and  $\text{Pt}_n$  (where  $n$  is about 6) are small enough to be considered quasimolecular rather than metallic. Their catalytic properties are distinct from those of larger (metallic) particles, even for structure-insensitive reactions.

MgO-supported  $\text{Ir}_4$  and  $\text{Ir}_6$  clusters are stable catalysts, as shown both by EXAFS results indicating retention of the metal framework structures during catalysis (Table 4) and by the lack of significant changes in the catalytic activities during steady-state operation in flow reactors [30, 54]. Thus supported metal cluster catalysts seem to be robust enough for practical application, although questions about their possible regeneration remain to be answered. It may be fruitful to search for reactions for which supported metal clusters have catalytic properties superior to those of conventional supported metals. The catalytic activities of clusters modeled as  $\text{Ir}_4$  and  $\text{Ir}_6$  are less than those of supported iridium particles, at least for hydrocarbon hydrogenation and hydrogenolysis reactions, but the important opportunity in catalysis may be to find reactions for which the activity or selectivity of supported metal clusters is superior to those of conventional supported metals. The high selectivity of Pt/LTL zeolite catalysts for alkane dehydrocyclization appears to be the most persuasive indication of the value of supported metal cluster catalysts. The high selectivity of this catalyst for dehydrocyclization is related to its low selectivity for hydrogenolysis, which may be, at least in part, a consequence of the smallness of the platinum clusters.

### 4.2.6 Acknowledgment

This work was supported by the National Science Foundation (CTS-9300754).

### References

1. J. R. Anderson, *Structure of Metallic Catalysts*, Academic Press, New York, **1975**.
2. M. Boudart, *J. Mol. Catal.* **1985**, 30, 27.
3. J. H. Sinfelt, *Bimetallic Catalysts: Discoveries, Concepts, and Applications*, Wiley, New York, **1983**.
4. M. Boudart, *Adv. Catal.* **1969**, 20, 153.
5. M. Boudart, G. Djéga-Mariadassou, *Kinetics of Heterogeneous Catalytic Reactions*, Princeton University Press, Princeton, NJ, **1984**.

6. O. M. Poltorak, V. S. Boronin, *Russ. J. Phys. Chem.* **1966**, 40, 1436.
7. M. Che, C. O. Bennett, *Adv. Catal.* **1989**, 36, p. 55.
8. G. A. Somorjai, J. Carrazza, *Ind. Eng. Chem. Fundam.* **1986**, 25, 63.
9. B. C. Gates, H. H. Lamb, *J. Mol. Catal.* **1989**, 52, 1.
10. B. C. Gates, L. Guzzi, H. Knözinger (Eds), *Metal Clusters in Catalysis*, Elsevier, Amsterdam, **1986**.
11. Y. Iwasawa, *Catal. Today* **1993**, 18, 21.
12. M. Ichikawa, *Adv. Catal.* **1992**, 38, 283.
13. B. C. Gates, *J. Mol. Catal.* **1994**, 86, 95.
14. R. Psaro, R. Ugo, G. M. Zanderighi, B. Besson, A. K. Smith, J.-M. Basset, *J. Organomet. Chem.* **1981**, 213, 215.
15. M. Deeba, B. C. Gates, *J. Catal.* **1981**, 67, 303.
16. H. Knözinger, Y. Zhao, *J. Catal.* **1981**, 71, 337.
17. R. Psaro, C. Dossi, A. Fusi, R. Ugo, *Res. Chem. Intermed.* **1991**, 15, 31.
18. L.-Y. Hsu, S. G. Shore, L. D'Ornelas, A. Choplin, J.-M. Basset, *J. Catal.* **1994**, 149, 159.
19. T. R. Krause, M. E. Davies, J. Lieto, B. C. Gates, *J. Catal.* **1985**, 94, 195.
20. S. Kawi, B. C. Gates, *Inorg. Chem.* **1992**, 31, 2939.
21. H. H. Lamb, A. S. Fung, P. A. Tooley, J. Puga, T. R. Krause, M. J. Kelley, B. C. Gates, *J. Am. Chem. Soc.* **1989**, 111, 8367.
22. Z. Xu, S. Kawi, B. C. Gates, *Inorg. Chem.* **1994**, 33, 503.
23. J. Puga, R. Patrini, K. M. Sanchez, B. C. Gates, *Inorg. Chem.* **1991**, 30, 2479.
24. Z. Xu, A. L. Rheingold, B. C. Gates, *J. Phys. Chem.* **1993**, 97, 9465.
25. S. Kawi, J.-R. Chang, B. C. Gates, *J. Phys. Chem.* **1993**, 97, 5375.
26. C. Dossi, R. Psaro, D. Roberto, D., R. Ugo, G. M. Zanderighi, *Inorg. Chem.* **1990**, 29, 4368.
27. S. Kawi, J.-R. Chang, B. C. Gates, *J. Phys. Chem.* **1993**, 97, 10599.
28. S. Kawi, J.-R. Chang, B. C. Gates, *J. Am. Chem. Soc.* **1993**, 115, 4830.
29. S. Kawi, B. C. Gates, *J. Phys. Chem.* **1995**, 99, 8824.
30. Z. Xu, F.-S. Xiao, S. K. Purnell, O. Alexeev, S. Kawi, S. E. Deutsch, B. C. Gates, *Nature (London)* **1994**, 372, 346.
31. F. B. M. van Zon, S. D. Maloney, B. C. Gates, D. C. Koningsberger, *J. Am. Chem. Soc.* **1993**, 115, 10317.
32. J.-R. Chang, D. C. Koningsberger, B. C. Gates, *J. Am. Chem. Soc.* **1992**, 114, 6460.
33. H. H. Lamb, M. Wolfer, B. C. Gates, *J. Chem. Soc., Chem. Commun.* **1990**, 1296.
34. T. Beutel, S. Kawi, S. K. Purnell, H. Knözinger, B. C. Gates, *J. Phys. Chem.* **1993**, 97, 7284.
35. F.-S. Xiao, Z. Xu, O. Alexeev, B. C. Gates, *J. Phys. Chem.*, **1995**, 99, 1549.
36. P. Jacobs in *Metal Clusters in Catalysis* (Eds: B. C. Gates, L. Guzzi, H. Knözinger), Elsevier, Amsterdam, **1986**, pp. 357–414.
37. P. Gallezot, *Catal. Rev. – Sci. Eng.* **1979**, 20, 121.
38. P. Gallezot in *Metal Clusters* (Ed.: M. Moskovits) Wiley-Interscience, New York, **1986**, 219.
39. R. A. Dalla Betta, M. Boudart, *Proc. 5th Int. Congr. Catal.* **1973**, Vol. 2, pp. 96–1329.
40. W. J. Reagan, A. W. Chester, G. T. Kerr, *J. Catal.* **1981**, 69, 89.
41. M. M. Otten, M. J. Clayton, H. H. Lamb, *J. Catal.* **1994**, 149, 211.
42. G. S. Lane, F. S. Modica, J. T. Miller, *J. Catal.* **1991**, 129, 145.
43. M. Vaarkamp, J. V. Grondelle, J. T. Miller, D. J. Sajkowski, F. S. Modica, G. S. Lane, B. C. Gates, D. C. Koningsberger, *Catal. Lett.* **1990**, 6, 369.
44. N. D. Triantafillou, J. T. Miller, B. C. Gates, *J. Catal.* **1995**, 155, 131.
45. W. Eberhardt, P. Fayet, D. Cox, A. Kaldor, R. Sherwood, D. Sondericker, *Physica Scripta* **1990**, 41, 892.
46. H. V. Roy, P. Fayet, F. Patthey, W. D. Schneider, B. Delly, C. Massobrio, *Phys. Rev. B* **1994**, 49, 5611.
47. G. Fuchs, D. Neiman, H. Poppa, *Langmuir* **1991**, 7, 2853.
48. H. Poppa, *Catal. Rev. – Sci. Eng.* **1993**, 35, 359.
49. S. Ladas, H. Poppa, M. Boudart, *Surf. Sci.* **1981**, 102, 151.
50. F. H. Ribeiro, G. A. Somorjai, *Recl. Trav. Chim Pays-Bas* **1994**, 113, 419.
51. D. C. Koningsberger, R. Prins (Eds.), *X-ray Absorption: Principles, Applications, Techniques of EXAFS, SEXAFS, and XANES*, Wiley, New York, **1988**.



52. B. C. Gates, D. C. Koningsberger, *CHEMTECH* **1992**, 22, 300.
53. S. D. Maloney, F. B. M. van Zon, D. C. Koningsberger, B. C. Gates, *Catal. Lett.* **1990**, 5, 161.
54. S. Kawi, J.-R. Chang, B. C. Gates, *J. Phys. Chem.* **1994**, 98, 12978.
55. N. D. Triantafillou, B. C. Gates, *J. Phys. Chem.* **1994**, 98, 8431.
56. K. Asakura, Y. Iwasawa, *J. Chem. Soc. Faraday Trans.* **1990**, 86, 2657.
57. A. S. Fung, P. A. Tooley, M. J. Kelley, D. C. Koningsberger, B. C. Gates, *J. Phys. Chem.* **1991**, 95, 225.
58. Z. Zhang, F. A. P. Cavalcanti, W. M. H. Sachtler, *Catal. Lett.* **1992**, 12, 157.
59. H. H. Lamb, M. Wolfer, B. C. Gates, *J. Chem. Soc., Chem. Commun.* **1990**, 1296.
60. M. Vaarkamp, F. S. Modica, J. T. Miller, D. C. Koningsberger, *J. Catal.* **1993**, 144, 611.
61. J. T. Miller, B. L. Meyers, F. S. Modica, G. S. Lane, M. Vaarkamp, D. C. Koningsberger, *J. Catal.* **1993**, 143, 395.
62. S. K. Purnell, X. Xu, D. W. Goodman, B. C. Gates, *J. Phys. Chem.* **1994**, 98, 4076.
63. W. Ravenek, A. P. J. Jansen, R. A. van Santen, *J. Phys. Chem.* **1989**, 93, 6445.
64. B. C. Gates, *Chem. Rev.*, **1995**, 95, 511.
65. S. D. Maloney, M. J. Kelley, D. C. Koningsberger, B. C. Gates, *J. Phys. Chem.* **1991**, 95, 9406.
66. *Oil Gas J.* **1992**, 190, 29.
67. D. Rotman, *Chem. Week* **1992**, 150, 8.
68. J. R. Bernard in *Proc. 5th Int. Zeolite Conf.* (Ed.: L. V. C. Rees), Heyden, London, **1986**, p. 686.
69. T. R. Hughes, W. C. Buss, P. W. Tamm, R. L. Jacobson in *New Developments in Zeolite Science and Technology* (Eds: Y. Murakami, A. Iijima, J. W. Ward), Elsevier, Amsterdam, **1986**, p. 725.
70. G. Larson, G. L. Haller, *Catal. Lett.* **1989**, 3, 103.
71. S. B. Rice, J. Y. Koo, M. M. Disko, M. M. J. Treacy, *Ultramicroscopy* **1990**, 34, 108.
72. P. W. Tamm, D. H. Mohr, C. R. Wilson in *Catalysis 1987* (Ed.: J. W. Ward), Elsevier, Amsterdam, **1988**, p. 335.
73. E. Mielczarski, S. B. Hong, R. J. Davis, M. E. Davis, *J. Catal.* **1992**, 134, 359.
74. C. Besoukhanova, J. Guidot, D. Barthomeuf, M. Breyse, J. R. Bernard, *J. Chem. Soc. Faraday Trans.* **1981**, 77, 1595.
75. W.-H. Han, A. B. Kooh, R. F. Hicks, *Catal. Lett.* **1993**, 18, 193.
76. W.-H. Han, A. B. Kooh, R. F. Hicks, *Catal. Lett.* **1993**, 18, 219.
77. J. T. Miller, F. S. Modica, B. L. Meyers, D. C. Koningsberger, *Prepr., Div. Petrol. Chem., Am. Chem. Soc.* **1993**, 38, 825.
78. S. J. Tauster, J. J. Steger, *J. Catal.* **1990**, 125, 387.

## 4.3 Metal Clusters in Zeolites

W. M. H. SACTLER

### 4.3.1 Introduction

While most industrial applications of zeolite catalysts make use of these materials in their acid mode, zeolites are also excellent supports for metals. These applications are not mutually exclusive; zeolite catalysts containing both acid sites and metal clusters (mono- or multimetallic) act as bifunctional catalysts. Zeolite-supported

52. B. C. Gates, D. C. Koningsberger, *CHEMTECH* **1992**, 22, 300.
53. S. D. Maloney, F. B. M. van Zon, D. C. Koningsberger, B. C. Gates, *Catal. Lett.* **1990**, 5, 161.
54. S. Kawi, J.-R. Chang, B. C. Gates, *J. Phys. Chem.* **1994**, 98, 12978.
55. N. D. Triantafillou, B. C. Gates, *J. Phys. Chem.* **1994**, 98, 8431.
56. K. Asakura, Y. Iwasawa, *J. Chem. Soc. Faraday Trans.* **1990**, 86, 2657.
57. A. S. Fung, P. A. Tooley, M. J. Kelley, D. C. Koningsberger, B. C. Gates, *J. Phys. Chem.* **1991**, 95, 225.
58. Z. Zhang, F. A. P. Cavalcanti, W. M. H. Sachtler, *Catal. Lett.* **1992**, 12, 157.
59. H. H. Lamb, M. Wolfer, B. C. Gates, *J. Chem. Soc., Chem. Commun.* **1990**, 1296.
60. M. Vaarkamp, F. S. Modica, J. T. Miller, D. C. Koningsberger, *J. Catal.* **1993**, 144, 611.
61. J. T. Miller, B. L. Meyers, F. S. Modica, G. S. Lane, M. Vaarkamp, D. C. Koningsberger, *J. Catal.* **1993**, 143, 395.
62. S. K. Purnell, X. Xu, D. W. Goodman, B. C. Gates, *J. Phys. Chem.* **1994**, 98, 4076.
63. W. Ravenek, A. P. J. Jansen, R. A. van Santen, *J. Phys. Chem.* **1989**, 93, 6445.
64. B. C. Gates, *Chem. Rev.*, **1995**, 95, 511.
65. S. D. Maloney, M. J. Kelley, D. C. Koningsberger, B. C. Gates, *J. Phys. Chem.* **1991**, 95, 9406.
66. *Oil Gas J.* **1992**, 190, 29.
67. D. Rotman, *Chem. Week* **1992**, 150, 8.
68. J. R. Bernard in *Proc. 5th Int. Zeolite Conf.* (Ed.: L. V. C. Rees), Heyden, London, **1986**, p. 686.
69. T. R. Hughes, W. C. Buss, P. W. Tamm, R. L. Jacobson in *New Developments in Zeolite Science and Technology* (Eds: Y. Murakami, A. Iijima, J. W. Ward), Elsevier, Amsterdam, **1986**, p. 725.
70. G. Larson, G. L. Haller, *Catal. Lett.* **1989**, 3, 103.
71. S. B. Rice, J. Y. Koo, M. M. Disko, M. M. J. Treacy, *Ultramicroscopy* **1990**, 34, 108.
72. P. W. Tamm, D. H. Mohr, C. R. Wilson in *Catalysis 1987* (Ed.: J. W. Ward), Elsevier, Amsterdam, **1988**, p. 335.
73. E. Mielczarski, S. B. Hong, R. J. Davis, M. E. Davis, *J. Catal.* **1992**, 134, 359.
74. C. Besoukhanova, J. Guidot, D. Barthomeuf, M. Breyse, J. R. Bernard, *J. Chem. Soc. Faraday Trans.* **1981**, 77, 1595.
75. W.-H. Han, A. B. Kooh, R. F. Hicks, *Catal. Lett.* **1993**, 18, 193.
76. W.-H. Han, A. B. Kooh, R. F. Hicks, *Catal. Lett.* **1993**, 18, 219.
77. J. T. Miller, F. S. Modica, B. L. Meyers, D. C. Koningsberger, *Prepr., Div. Petrol. Chem., Am. Chem. Soc.* **1993**, 38, 825.
78. S. J. Tauster, J. J. Steger, *J. Catal.* **1990**, 125, 387.

## 4.3 Metal Clusters in Zeolites

W. M. H. SACHTLER

### 4.3.1 Introduction

While most industrial applications of zeolite catalysts make use of these materials in their acid mode, zeolites are also excellent supports for metals. These applications are not mutually exclusive; zeolite catalysts containing both acid sites and metal clusters (mono- or multimetallic) act as bifunctional catalysts. Zeolite-supported

metals are used for shape-selective hydrogenations [1], hydrodalkylation, isomerization, hydroisomerization, hydrocracking, catalytic reforming [2], CO hydrogenation [3], and other reactions. Details are given in recent reviews [4–6].

This chapter focuses on the chemistry of these catalysts. Zeolites are defined as silica–aluminates having a channel or cage structure capable of accepting gas molecules. The names of individual zeolites are given elsewhere [7]. The word “cluster” describes any multiatomic entity containing less than 100 metal atoms. The word “metal” is used in the restrictive sense to describe a metal element in its *zerovalent* state. Therefore, materials which use heavy metal ions in zeolites, such as the catalysts that convert light alkanes into aromatics [8–10], or the catalysts for NO<sub>x</sub> abatement with copper, cobalt, palladium, or gallium in ZSM-5 or other zeolites [11–15], are not discussed here.

### 4.3.2 Metal Clusters Versus Macroscopic Metals

When a macroscopic metal specimen is divided into clusters of, for example, 50 atoms each, some of the parameters characteristic of a metal undergo dramatic changes, whereas others change only slightly. The first group of parameters can be called *dimension-sensitive*, the second group is almost *dimension-insensitive*.

Obviously, typical collective electronic properties, such as electric conductivity, thermal conductivity, and ferromagnetic susceptibility, are bound to change drastically when the size of the metal entity becomes smaller than the mean free path of the conduction electrons or the ferromagnetic domain. All properties related to the band structure will change for cluster sizes with low state density and discrete energy levels [16, 17]. The energy to remove an electron from a small cluster will be higher than the work function of the bulk metal, but lower than the ionization potential of a metal atom. A striking proof of high dimension sensitivity is provided by results on Rh clusters. Whereas bulk Rh is nonmagnetic, Cox et al., using a modified Stern–Gerlach technique, found a very large magnetic moment for Rh<sub>10</sub> clusters at 195 K [18]. The magnetic moment per Rh atom decreases with cluster size, but the moments of Rh<sub>15</sub>, Rh<sub>16</sub>, and Rh<sub>19</sub> are anomalously large.

Molecular beam data show that for alkali atom clusters certain “magic numbers” characterize clusters that are either very stable or are formed by favorable kinetics. Quantum mechanical calculations by Bonačić-Koutecký et al. predict which geometries lead to stable Na<sub>*n*</sub> clusters for *n* = 3–20 [19]. These structures markedly deviate from those which one would predict on the basis of maximum atom coordination. For instance, the stable clusters Na<sub>5</sub> and Na<sub>6</sub> are planar.

Less is known at present with respect to the most stable shapes of transition metal clusters. As their heats of sublimation are higher than those of alkali metals, it is conceivable that the classical concept of maximizing atom coordination remains valid for these metals. If so, the preferred atom arrangements should be given by the same magic numbers which have been found for rare-gas clusters. For Pt or Rh, for example, the smallest stable cluster would be a 13-atom icosahedron having one atom in the center and 12 atoms in equivalent positions surrounding it, or the isomeric cubooctahedron. However, at the present stage, neither reliable molecular

beam data nor quantum chemical calculations seem to be known to identify the most stable sizes and shapes of such clusters. Moreover, metal clusters in zeolites will differ from those in molecular beams if the interaction with the zeolite walls is significant.

Chemical characteristics and, by implication, catalytic parameters of metal clusters appear less sensitive to sample size than some electronic effects. True quantum jumps in catalytic parameters are expected and observed only when dispersion is brought to the stage that the *ensemble requirements* of some catalytic reactions are no longer fulfilled, or when *isolated metal atoms exist* on a support.

In catalysis, clusters are often considered simply as little pieces of metal, but with highly unsaturated atoms. The energy balance of a chemical process in which a metal reacts with another reactant contains the surface (free) energy of the metal. This term is negligible for macroscopic specimen, but appears as an additional exothermic term for small metal particles. This is usually translated into the language of atomic process by considering the extent of *coordinative unsaturation* of the surface atoms. Atoms involved in chemisorption are coordinatively unsaturated also in macroscopic samples, but the extent of coordinative unsaturation is higher for small clusters. The difference in coordinative unsaturation between clusters and macroscopic metals is comparable to that between crystal faces.

It has been known for decades that chemisorption on metals is often accompanied by atom reconstruction at the surface [20]. For macroscopic samples this reconstruction starts at atomically rough crystal faces and it is more thorough on metal films than on well-sintered single crystals [21, 22]. It thus stands to reason that reconstruction will be very easy when chemisorption and catalysis take place on small metal clusters.

Restricting the dimension sensitivity of clusters in catalysis to the effects of coordinative unsaturation and ease of surface reconstruction might, however, be an oversimplification. Recently, Rosén and co-workers reported measurements on the sticking coefficient  $S$  of several diatomic gases on Rh, Co, Fe, Ni, and Cu clusters in molecular beams [23, 24]. For clusters with less than 10 atoms  $S$  is very low (except for CO on Rh), but it usually reaches a constant, high value for clusters with 25 atoms. For some systems the size dependence of  $S$  is more complicated, reflecting the change in ionization potential with cluster size and the occurrence of closed electron shells.

### 4.3.3 Preparation of Mono- or Bimetallic Clusters in Zeolites

The methods used for depositing metal precursors into the cavities of a zeolite include ion exchange, impregnation of metal salts, deposition of volatile or soluble complexes, [25–29], and solid-state ion exchange [30, 31]. It is possible to combine several of these techniques. For instance, Pt or Rh can be brought into an NaY zeolite by ion exchange, followed by calcination and reduction in  $H_2$ . Subsequent chemical vapor deposition of the volatile carbonyl of a second metal, e.g.  $Fe(CO)_5$  or  $Re_2(CO)_{10}$ , leads to the deposition of the second metal onto the clusters of the

first metal. Physical and catalytic characterization of PtRe/NaY [32] and RhFe/NaY [33] samples indicates predominant formation of bimetallic clusters.

As catalyst preparation has been described extensively in a previous review paper [5], this article merely summarizes the chemistry of the most popular method, namely ion exchange. Three major steps can be discerned.

#### 4.3.3.1 Step 1: Ion Exchange

For the metals of high catalytic activity – Pt, Pd, and Rh – the complexed ions  $[\text{Pt}(\text{NH}_3)_4]^{2+}$ ,  $[\text{Pd}(\text{NH}_3)_4]^{2+}$ , and  $[\text{Rh}(\text{NH}_3)_5(\text{H}_2\text{O})]^{3+}$  in aqueous solution are conveniently exchanged against alkali ions of the zeolite. Because of the rather bulky coordination shell of these ions relative to the pores of the zeolite, the exchange process often requires several days and temperatures above room temperature to achieve completion. If ion exchange is interrupted before equilibrium is reached, a metal ion concentration gradient will exist from the surface to the interior of the zeolite grains. If ion migration to the smaller cages at elevated temperature is not desired, the zeolite can be washed, after ion exchange, with a high pH aqueous solution. This treatment converts transition metal ions to a hydroxygel which is later dehydrated to oxide particles. This procedure is recommended for Ni or Co in NaY, because reduction of oxide particles in supercages can be carried out under rather mild conditions, whereas the reduction of these ions located in the hexagonal prisms is nearly impossible [34].

#### 4.3.3.2 Step 2: Calcination

This is done to remove the water and the ligands from the exchanged ions. The metal ion loaded zeolite is heated in a high flow of air or oxygen. Three phenomena often accompany the elimination of  $\text{H}_2\text{O}$  and  $\text{NH}_3$ :

- (i) *Autoreduction*, i.e. formation of metal clusters and zeolite protons in the reducing atmosphere of (decomposing) ammine ligands. Under calcination conditions, reduction to metal clusters is followed by their growth and the formation of oxide particles. These particles, in turn, can react with protons to form metal ions and water.
- (ii) *Ion migration* to smaller zeolite cages. A driving force for this process is the high negative charge density in small zeolite cages. Ion migration can be prevented by limiting the temperature of calcination. It is possible to initiate ion migration back to large zeolite cavities by offering them an attractive ligand, e.g.  $\text{NH}_3$ . This strategy is at the basis of catalyst rejuvenation [35]. It has also been used to increase the Co content of zeolite supported Pd–Co alloy clusters [36].
- (iii) *Ion hydrolysis* leads to dissipation of positive charge. Multivalent ions, such as  $\text{Rh}^{3+}$ , are converted to monopositive complexes, e.g.  $(\text{RhO})^+$ , and protons.

Each of these can find a location close to a negatively charged  $[\text{AlO}_4/2]^-$  tetrahedron. For zeolites with low Al:(Al + Si) ratios the negative charges may be separated far from each other. Dissipation of the positive ions by hydrolysis lowers the Coulomb energy of the system.

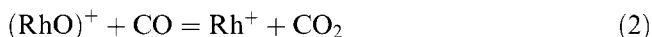
Uncontrolled autoreduction is often undesired, because agglomeration of clusters to larger particles can take place. It can be minimized by carrying out the calcination step in pure oxygen, at a very high flow rate and a very slow temperature ramp, e.g.  $0.5 \text{ K min}^{-1}$  [37]. For Pt and Rh no conditions are known to completely suppress autoreduction.

#### 4.3.3.3 Step 3: Reduction

Reduction is typically carried out in a flow of  $\text{H}_2$ . The process:



creates protons of high Brønsted acidity in addition to metal atoms. If desired, the formation of protons can be minimized by limiting the temperature of calcination, thus keeping a sufficient concentration of  $\text{NH}_3$  within the zeolite. The ligands will neutralize the protons formed during the reduction step. Carbon monoxide, while unable to reduce naked ions, can be used to reduce oxide particles or oxo ions such as



This chemistry is used to discriminate between naked ions and oxygen-containing entities [10, 38, 39]. Temperature programmed reduction (TPR) also helps to identify ions in different locations; analysis of the amount of  $\text{H}_2$  or CO consumed can give the relative quantities in which various reducible species are present. Low  $\text{H}_2$  consumption of metal loaded and freshly calcined samples can indicate a high extent of autoreduction.

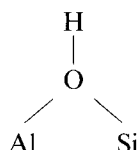
Bimetallic clusters are prepared in a similar way. If ions of metals with widely different reducibility coexist in the same zeolite, the first clusters of the more easily reducible metal serve as nuclei for the less easily reducible metal. TPR results show a pronounced shift of the peak of the latter metal towards lower temperature. The combinations (Pt + Cu) [40], (Pd + Cu) [41], (Pd + Ni) [42], (Pd + Fe) [43], and (Rh + Fe) [44] have been studied in Y zeolite. In all cases, reducibility enhancement leads to formation of bimetallic clusters. The combinations (Pt + Re) and (Rh + Fe) have been prepared by decomposition of a volatile carbonyl of the second element onto the reduced zeolite encaged clusters of the first element. With (Rh + Fe)NaY, Mössbauer spectroscopy shows that  $\text{Fe}^{3+}$  ions are reduced with  $\text{H}_2$  to  $\text{Fe}^{2+}$  and  $\text{Fe}^0$ ; no  $\text{Fe}^0$  clusters are formed, as all  $\text{Fe}^0$  is alloyed to Rh. Magnetic resonance data indicate that  $\text{PdFe}_x$  clusters in NaY give a ferromagnetic resonance signal, even if the cluster contains only one Fe atom [43].

### 4.3.4 Interaction of Metal Clusters and Zeolite Protons

#### 4.3.4.1 Metal Clusters as Lewis Bases

Protons are formed by the reduction of metal ions with  $H_2$ ; a higher proton concentration can be achieved by first exchanging alkali ions against  $NH_4^+$  ions which are converted to protons during calcination. The maximum achievable proton concentration is given by the molar ratio of Al:(Al + Si) in the zeolite.

Although protons in zeolites are Brønsted acid centers, the term “proton” is in fact a linguistic exaggeration; what is meant in the scientific literature on Brønsted acidity of zeolites is the H end of weakly polar O–H groups in which the O stands for an  $O^{2-}$  ion bridging between a  $Si^{4+}$  and an  $Al^{3+}$  centered tetrahedron:



The IR band at  $3610\text{ cm}^{-1}$  in HZSM-5, the bands at  $3560$  and  $3650\text{ cm}^{-1}$  in zeolite HY, and the band at  $3610\text{ cm}^{-1}$  in H-mordenite are assigned to this vibration [45]. Adsorption of alkenes on these sites produces species which are often called chemisorbed carbenium ions but their FTIR signature identifies them as alkoxy groups, i.e. two chemical bonds are formed: a C–H bond with the proton and a covalent bond between one C atom of the alkene and a basic oxygen ion of the zeolite wall. As the nontrivial problem of correctly determining the acid strength of these protons is outside the scope of this article, we merely quote Kazansky's statement: “The only proper way to proceed is to follow the response of hydroxyl groups to their interaction with adsorbed bases” [46]. Solid state NMR and IR spectroscopy are useful methods; for instance, the *change* in the MAS  $^1H$  NMR chemical shift upon adsorbing a weak base is an appropriate measure of the acid strength [47].

Protons are able to form a chemical bond with transition metal atoms. In the resulting metal–proton adducts the transition metal atoms act as Lewis bases. This type of chemical bond was first discovered with zeolite supported metals [48–50], but more recently the same type of chemical interaction has also been observed in metal–organic complexes. The group of van Koten showed by  $^1H$  NMR that hydrogen-bridged Pt configurations with a chemical shift of ca. 20 ppm [51] exist in metal ammine complexes. Molecular orbital calculations were done for Pd complexes; they show that the  $Pd \cdots H-NH_3$  configuration with, formally,  $Pd^{2+}$  is more stable than the tautomeric  $H-Pd \cdots NH_3$  formed with  $Pd^{4+}$ . The structure of zwitterionic complexes with a  $Pt^{2+} \cdots H-N^+$  unit was identified by X-ray diffraction (XRD) [52]. Hydrogen bonding to metal centers of organometallic compounds was also identified by Kazarian et al. [53]. These authors report  $Ir \cdots H-O$  hydrogen bonding between the 18-electron iridium center in  $CP^*Ir(CO)_2$  and a number of fluoroalcohols. In these complexes the Ir atom clearly acts as a proton acceptor. The CO stretching frequency is shifted to higher wavenumbers by amounts in-

creasing with the acid strength of the alcohol; the O–H frequency of the alcohols is broadened and shifted to lower wavenumbers. Complexes have also been detected in which two alcohol molecules are linked to the same Ir atom via C–O–H  $\cdots$  Ir bridges. Complexes of Rh and Co have been found to form similar metal–proton bonds with acidic fluoroalcohols. It can thus be stated that transition metal atoms and their clusters act as Lewis bases towards protons of high acidity, forming chemical bonds  $M \cdots H^+$ .

The formation of metal–proton adducts in zeolites has three important consequences for the use of metal/zeolites in catalysis, which are discussed in this article:

- (i) Protons act as *chemical anchors*, inhibiting metal agglomeration, thus leading to high metal dispersion, even isolated metal atoms.
- (ii) As the partial positive charge of the “zeolite protons” is shared with the metal atoms of the anchored cluster, the cluster becomes *electron-deficient*.
- (iii) The combination in one complex of a metal cluster, capable of dissociatively chemisorbing many molecules, and one or several protons, instrumental in numerous acid-catalyzed reactions, enables metal–proton adducts to act as *collapsed bifunctional sites*.

#### 4.3.4.2 Chemical Anchoring

Numerous examples are known in which zeolite-supported metals, including Pt, Pd or Rh, are formed in higher dispersion on proton-containing zeolites than on proton-free supports. If protons are present, metal dispersion increases with proton concentration. [54]. When the proton anchors are removed, metal clusters become mobile and tend to agglomerate. Three possibilities exist for cutting the chemical anchor:

- (i) *Neutralization of protons* This is conveniently achieved, for instance, by adsorption of ammonia. The resulting large increase in metal particle size is visible by transmission electron spectroscopy (TEM) or extended X-ray absorption fine-structure spectroscopy (EXAFS) [55]. If hydrogen adsorption is to be used for the determination of metal dispersion, a second reduction step is required to remove adsorbed ammonia from the metal clusters.
- (ii) *Displacement of protons* This is often observed upon adding molecules, such as carbon monoxide, which are able to form stronger bonds with the metal. Direct evidence for proton displacement is the ensuing increase in the intensity of IR band for the zeolite O–H groups [56]. If protons are displaced by CO in the stage when metal clusters consist, for example, of three or four atoms, deanchoring of these clusters induces their migration through zeolite channels and their coalescence to larger clusters [57, 58]. At low temperatures, the size of the secondary clusters (formed upon CO admission) is controlled by the diameter of the apertures between zeolite cages [59]. For clusters that are too large to migrate through cage windows at low temperature, removal of some CO



ligands and their replacement by zeolite protons is, however, reversible. With Pd in NaHY it has been demonstrated that mere pumping at room temperature transforms the FTIR spectrum of the pure carbonyl cluster with a Pd<sub>13</sub> core into that of a mixed ligand cluster (H<sup>+</sup> and CO) with the same core. The process is reversible; upon admission of CO, protons are displaced and the original spectrum is restored [48, 60].

- (iii) *Consumption of protons* Alkenes and aromatic molecules form carbenium ions with protons. This process deprives the metal cluster of its chemical anchor. As tertiary carbenium ions are more stable than secondary carbenium ions, metal agglomeration is more severe during catalysis with molecules containing tertiary C atoms. This has been demonstrated in the TEM results from Pd/ZSM-5 catalysts of identical history which were exposed to either cyclopentane or methylcyclopentane in hydrogen. With cyclopentane little growth of the Pd clusters was detected but with methylcyclopentane, which has a tertiary C atom, a rather dramatic growth of the Pd clusters was observed [55].

#### 4.3.4.3 Isolated Metal Atoms

As catalytic activity of metals is essentially confined to surface atoms, much work has been done to achieve high metal dispersion. The non plus ultra in this respect is a metal divided into isolated atoms held by a support, but exposed to the gas phase. This goal has been achieved by combining the applying proton anchoring to a zeolite which contains linear channels with "side-pockets" in which the anchored atoms can be accommodated. The support chosen by Lei and Sachtler [61] and Zholobenko et al. [62] was H-mordenite. At low metal loading and after reduction at low temperature, Pd and Pt were prepared in extremely high dispersions.

For Pt/H-mordenite platinum, the following experimental criteria support the conclusion that a large fraction of the metal is present as Pt-proton complexes with only one Pt atom:

- (i) Pt-Pt coordination of zero, as determined from EXAFS;
- (ii) a CO band in CO-FTIR at higher frequency than all CO bands known hitherto for CO adsorbed on Pt<sup>0</sup>;
- (iii) absence of any frequency shift in this band while the overall coverage with CO was varied;
- (iv) total absence of this band in identical samples after neutralization of the protons;
- (v) a product pattern in the H-D exchange of cyclopentane over these catalysts that deviated significantly from that on all multiatomic Pt catalysts.

The frequency shift (ii) reflects the high electron deficiency of such complexes. Criterion (iii) is conclusive evidence for the absence of adjacent adsorbed CO ligands, as dipole-dipole coupling of neighboring CO<sub>ads</sub> must induce a frequency shift which has always been observed for CO<sub>ads</sub> on multiatomic Pt. Criterion (v) is unique: the H-D exchange of cyclopentane with D<sub>2</sub> has been studied by several

authors on numerous Pt samples [63, 64]; it was always found that the five H atoms at one side of the C<sub>5</sub> ring can be exchanged during one residence of the adsorbed molecule, leading to a partial maximum of the C<sub>5</sub>H<sub>5</sub>D<sub>5</sub> product. A totally different product pattern is observed with Pt/H-mordenite samples with isolated Pt atoms: a binomial distribution of the products shows prevailing stepwise exchange.

#### 4.3.4.4 Electron Deficiency

Electron deficiency of platinum in zeolites was first reported by Dalla Betta and Boudart [65], before the concept of metal–proton adducts was formulated. It is not limited to metal–proton adducts but occurs whenever metal clusters interact with electron acceptors, including Lewis acids and metal ions. Electron deficiency is indicated by several physical data; unfortunately, some of these are not unambiguous. In X-ray absorption the white line, e.g. at the Pt LIII edge, has been interpreted in terms of electron deficiency [66]. However, more recently the signal has been interpreted in terms of the higher ionization potential of small clusters compared to the work function of bulk Pt [67]. Electron deficiency leads to a shift in binding energy in XPS; a shift of the CO vibration frequency observed with FTIR is indicative of a positive charge of the adsorbing metal cluster. Tri et al., using X-ray absorption spectroscopy, observed a correlation between electron deficiency of Pt in zeolites and Brønsted acidity [68]. Blackmond and Goodwin confirmed that the electron-deficient character of the metal increases with the acidity of the support [69].

The results from an FTIR and XPS study of Pd/Y catalysts with varying proton concentrations showed that the shift in the CO frequency [68] and in the Pd binding energy correlates with the proton concentration in the zeolite [50]. Remarkably, the XPS band width remains constant, while the band position shifts. This excludes an equilibrium distribution between coexisting naked metal clusters and metal–proton adducts in the same zeolite. The results suggest a high homogeneity of the metal–proton clusters for any given proton concentration. Where protons are scarce, metal clusters are each linked to one proton, but at high proton concentration every metal cluster appears to be associated to several protons.

Electron deficiency affects the chemisorption and catalytic propensities of metal clusters. Della Betta et al. found that the catalytic activity of 1 nm Pt clusters in NaHY zeolite for neopentane isomerization and hydrogenolysis is 40 times higher than that of Pt/SiO<sub>2</sub> and Pt/Al<sub>2</sub>O<sub>3</sub>. Other authors observed increased activity for hydrogenation [70–73], changes in the competitive hydrogenation of benzene and toluene [74], changes in hydrogenolysis activity [75–77], and high resistance to sulfur poisoning [78–80]. However, recent data show that small clusters stabilized by zeolite protons adsorb little or no hydrogen, which makes the dispersion numbers determined from the H<sub>2</sub> chemisorption data highly questionable. This reduced H<sub>2</sub> adsorption was verified for Ru [81], Pd [82], and Rh [39]. In the conversion of methylcyclopentane, electron-deficient palladium–proton [83] and platinum–proton [84] adducts exhibit not only strongly enhanced activity towards ring enlargement,

but also markedly reduced activity towards ring opening. The former observation is ascribed to the bifunctional character of catalysts containing metal and acid sites, but the latter observation indicates that electron deficiency changes the catalytic propensities of metal clusters. Recent evidence obtained with Rh/NaY and Rh/HY catalysts confirms the same trend: the activity for ring enlargement is higher for Rh/HY, but that for ring opening, the prevailing reaction on Rh/NaY, is strongly suppressed in Rh/HY [85].

Two possible causes have been considered for the experimental fact that linking of zeolite protons to a metal cluster induces significant changes of its catalytic activity. Some authors assume that removing an electron from a metal atom will make this atom more similar to its left neighbor in the Periodic Table. A second hypothesis rejects this alchemistic transmutation of elements [86]; it can be assumed that the protons interact chemically with the adsorbate, transforming it, for instance, into a carbenium-like species which proceeds to interact with the metal.

Results obtained with neopentane as the catalytic probe have been quoted in favor of the former hypothesis, since neopentane is unable to form a carbenium ion in a simple step. The enhanced catalytic activity of Pt [65], Pd [83], and Rh [87] in their electron-deficient state is in agreement with the fact that for each of these three metals the left neighbor in the Periodic Table displays higher catalytic activity. However, other observations, such as the formation of benzene in quantities exceeding the benzene:cyclohexane ratio given by thermodynamics [88], have been ascribed to participation of the adduct protons in the chemisorption complex.

#### 4.3.4.5 Single-Site Bifunctionality

Numerous hydrocarbon conversions require a catalyst that contains both metal and acid sites. An alkane molecule might first be dehydrogenated on a platinum surface; the resulting alkene can subsequently react with a Brønsted acid site and form an adsorbed carbenium ion which might, for instance, isomerize. Repetition of such steps in which intermediates shuttle between acid and metal sites will lead to an alkane isomer, an aromatic molecule, or cracking products, and coke. An excellent description of these kinetic steps in catalytic reforming has been given by Mills et al. [89].

The metal-proton adduct has the potential for combining both catalytic functions into one complex. For instance, chemisorption of an alkane molecule on a metal is dissociative; while the H atom can combine with the proton and leave as H<sub>2</sub>, the positive charge of the remaining complex will, in one canonic form, be localized on the C atom of the alkyl group, thus opening the reaction channel for chemisorbed carbenium ions. For instance, ring enlargement of methylcyclopentane to a six-membered ring becomes possible. In view of the facile dehydrogenation on the metal cluster this adsorbed six-membered ring is free to leave the surface either as a benzene or as a cyclohexane molecule. The result will be similar to classical bifunctional catalysis, but all steps can occur within one residence of the molecule at the metal-proton adduct. Comparison of Pd-proton adduct catalysts and a physi-

cal mixture of the corresponding monofunctional catalysts shows a strong gain in activity by combining protons and metal clusters in the same bifunctional site [83].

#### 4.3.4.6 Metal Oxidation by Protons, Selective Leaching

In equilibrium of eq 1 metal atoms are oxidized to metal ions by zeolite protons at high proton concentration and low  $H_2$  partial pressure. The entropy gain caused by the formation of  $H_2$  favors the reverse of reaction 1 at high temperature even for noble metals such as Pt or Rh [90, 91]. The  $H_2$  release is monitored by TPD; it occurs at a higher temperature than desorption of chemisorbed hydrogen. It is possible to discriminate between the two processes by FTIR because only the oxidation process consumes protons, thus leading to a decrease in the intensity of the characteristic zeolite O–H bands. From eq 1 an equilibrium constant can be defined:

$$K = \frac{a_{M^0}(a_{H^+})^n}{(a_{M^{n+}})(a_{H_2})^{n/2}} \quad (3)$$

where  $a$  stands for the thermodynamic activities. Upon treating the clusters as a solid phase, of which the activity depends on the temperature only, one can include this activity in the equilibrium constant. The activities of the other constituents are replaced by their concentration or gas pressure. For fixed values of  $T$  and  $p_{H_2}$ , the proton concentration and, hence, the extent of reoxidation will increase with metal loading.

For copper and rhodium, carbon monoxide forms stronger bonds with the positive ions than with the zerovalent metal. For these metals, the equilibrium of eq 1 is, therefore, shifted towards the left side when CO is present. This was shown for Rh/NaY by FTIR detection of the  $Rh^+(CO)_2$ , the concomitant emergence of the XPS peak for  $Rh^+$ , and by mass spectroscopy identification of the  $H_2$  evolution upon admission of CO [92]. With Cu/ZSM-5 the oxidation of  $Cu^0$  by zeolite protons and the formation of  $Cu^+(CO)$  was monitored by FTIR as a function of time and temperature [93].

With bimetallic clusters in zeolites, the protons tend to selectively oxidize the less noble alloy constituent. This leaching phenomenon was first observed by Tzou et al. [94]; their EXAFS data showed that in thoroughly reduced (Pt + Cu)/NaY samples some Cu was coordinated to zeolite oxygen; the concentration of this species increased upon heating in He. This suggests that Cu had been leached from Pt–Cu clusters and these Cu ions had migrated into small zeolite cavities. This conclusion was confirmed by Zhang et al. [41] with their study of (Pd + Cu)/NaHY. They made use of the propensity of Pd to form hydrides which are easily identified in TPD by the temperature of their decomposition. As Pd–Cu alloys are unable to form hydrides, leaching of Cu out of the bimetallic clusters restores the cluster propensity to form a hydride. Leaching of Fe from bimetallic Pd–Fe clusters was detected in the same manner [43]. The  $H_2$  release during leaching can be determined with considerable precision; this permits quantitative determination of the number of metal atoms which were initially present in the bimetallic cluster.

### 4.3.5 Effects of Zeolite Geometry on Catalysis

#### 4.3.5.1 Transport and Transition State Restrictions

One cause of the great potential of zeolite-based catalysts in the chemical industry is the stereospecificity that is induced by the peculiar geometry of these systems. Zeolites are molecular sieves which only permit small kinetic diameter molecules to enter their pores. As a result only one component in a mixture might react, while other components are unable to reach the active sites. Likewise, when several isomers are formed in a catalytic process, one of them may escape easily, whereas the other isomers are trapped inside the zeolite cages. These trapped species will leave only after undergoing secondary isomerization or cracking reactions. This phenomenon is exploited for octane upgrading. In catalytic processes where two reaction paths are possible, one involving a monomolecular transition state, the other path requiring a bimolecular complex, the steric constraints of zeolite cavities will strongly favor the less voluminous transition state of the intramolecular process. These effects of zeolite catalysts are not specific for zeolite-supported metals; they have been studied for acidic zeolites and are well described in textbooks [95]. They will, therefore, not be discussed further in this article. However, two effects that are specific to zeolite-encaged metal clusters, namely preoriented collision following collimation, and alteration of diffusion type, by growing metal particles, are discussed below.

#### 4.3.5.2 Collimation of Molecules in Pores

Diffusion of molecules through pores with a diameter comparable to the molecular dimensions is not of the classical Knudsen type. The term “configurational diffusion” was proposed by Weisz for this molecular transport [96]. For nonspherical molecules it will induce an orientation of the molecule with its long axis parallel to the pore axis. The first report that this *collimation* could induce stereospecific catalysis was published by Tauster and Stegar [97]. Once the collimated molecule encounters a metal particle, a head-on collision results, i.e. the molecule will be preferentially adsorbed at its front side. Methylcyclopentane is a nonspherical molecule, its length-to-width ratio being 1.7. When collimated in a narrow pore, it will collide with a metal particle either with its methyl group or with its flat bottom end. Only the latter collision will result in opening of the C<sub>5</sub> ring; 3-methylpentane is the expected product of this reaction. In contrast, for metals on an amorphous support, such as Al<sub>2</sub>O<sub>3</sub> or SiO<sub>2</sub>, the ring-opening products 3-methylpentane (3MP) and 2-methylpentane (2MP) should be formed in the statistical ratio of 2MP:3MP = 2, which is also very close to the thermodynamic ratio. Numerous experimental data by Gault et al. for metals on amorphous supports confirm this expectation [98]. First, indications that the 2MP:3MP ratio was lower in zeolites were obtained with Pt in NaY [99]. A much more pronounced collimation is expected for zeolites with linear, one-dimensional pores; this was indeed confirmed for Pt in zeolite L [100, 101] and in mordenite [102].

The same logic predicts that a collimated molecule moving through a one-dimensional pore should be attacked at its flanks if the metal is present as extremely small clusters in the pore wall. This situation has been realized for Pt in mordenite, as small Pt clusters, even single atoms, can be accommodated in the side-pockets of this zeolite. Only the H form of the zeolite leads to the high metal dispersion needed for this purpose and only at low metal loads are the Pt clusters small enough not to protrude from the side-pockets into the channels to provoke head-on collisions with collimated methylcyclopentane molecules. By varying the size of the Pt clusters it was thus possible to vary the 2MP : 3MP ratio from 1.4 (for large Pt clusters) to 2.8 (for small clusters in side pockets) [102].

#### 4.3.5.3 Types of Pore Diffusion in Zeolites; Effects on Apparent Activation Energy

Metal clusters, like all other sites, are useful in heterogeneous catalysis only if they are accessible to reactants and if the reaction products can leave the catalyst. As for all catalysts, an effectiveness factor  $\eta$  can be defined as the ratio of the actual reaction rate and that of a fictitious catalyst in which the same sites are accessible without any diffusion limitation. In this respect, zeolites can be classified in two groups: materials with cages and intersecting channels, such as zeolite Y, and cage-free zeolites with one-dimensional, nonintersecting narrow channels, e.g. L and Mordenite. For the first group, the ordinary Thiele modulus

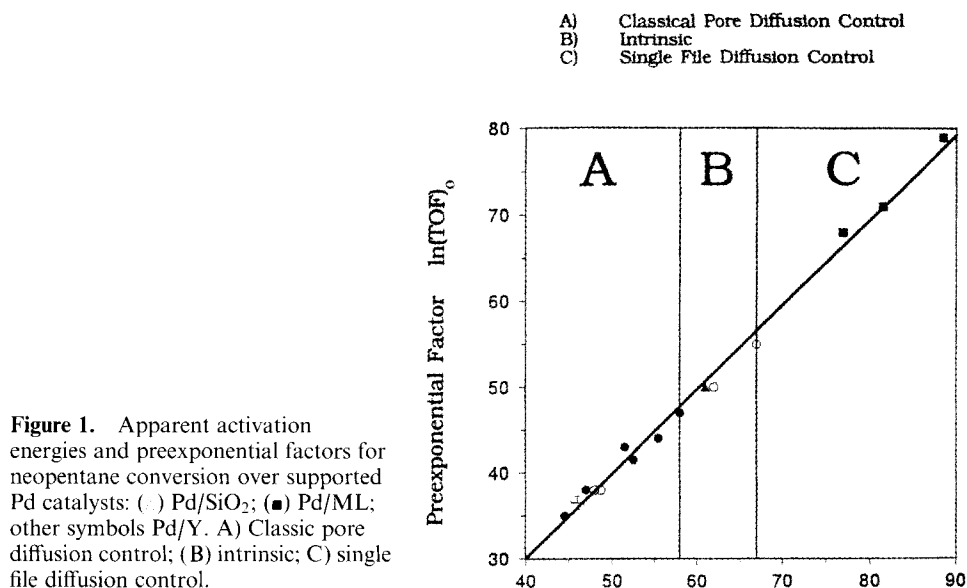
$$\Theta = L/2(k/D)^{1/2} \quad (4)$$

where  $L$  = pore length,  $k$  = intrinsic rate constant and  $D$  = effective diffusion coefficient, can be used to calculate  $\eta$ . Even if channels are largely filled with physisorbed molecules, reactants and products get mixed inside the cages and there are numerous paths connecting each site with the world outside the zeolite.

The situation is fundamentally different for the second group of zeolites, where one-dimensional pores permit molecules to diffuse in and out, but not to pass each other. This so-called *single file diffusion* is reminiscent of the restricted movement of pearls on a string [103]. When the pores are filled with reactant molecules, the reaction products that are formed inside such a pore are effectively trapped. Kärger et al. showed that a Thiele modulus,  $\Theta_{sf}$ , can be defined for single file diffusion; the ratio of  $\Theta_{sf}$  to the ordinary Thiele modulus  $\Theta$  is given by:

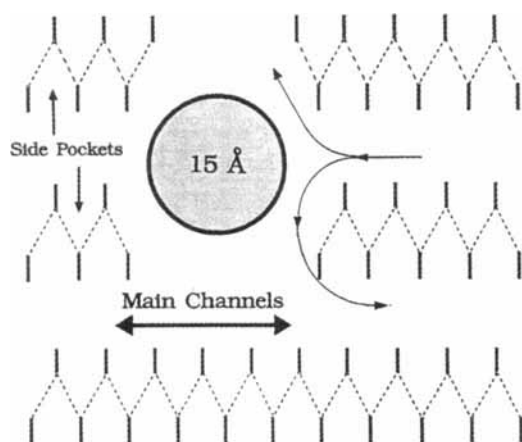
$$\Theta_{sf}/\Theta = N[(3/175)\theta^{3/2}/(1 - \theta)]^{1/2} \quad (5)$$

with  $N$  = number of adsorbing sites per pore and  $\theta$  = degree of their coverage [104]. At high coverage and for typical zeolites with pores of 1  $\mu\text{m}$  length, the Thiele modulus for single file diffusion is two to three orders of magnitude higher than the normal Thiele modulus. The effectiveness factor for single file diffusion is correspondingly lower. Only sites near the pore orifices contribute effectively to the catalytic reaction, as registered by the change in composition of the surrounding



atmosphere. Another consequence of this phenomenon is that the depth of this effective surface zone increases with temperature, as  $\theta$  decreases. In other words, the apparent activation energy for catalysts with single file diffusion will be *higher* than the intrinsic activation energy in the absence of diffusion limitation. This is in contrast to the classical pore diffusion model, which leads to an apparent activation energy *lower* than the intrinsic value. Note that the adsorption sites which have to be considered for single file diffusion will, in general, be different from the catalytically active sites; for instance, it has been found that adsorption of hydrocarbons in zeolites is stronger on Na<sup>+</sup> ions than on protons [105].

The effect of the type of pore diffusion on the apparent activation energy has been studied by Karpiński et al., who used the conversion of neopentane as the probe [106]. A variety of supported palladium catalysts was tested under identical conditions, including Pd/SiO<sub>2</sub>, Pd/NaY, Pd/HY, and a number of Pd/ML catalysts with M = Li, K, and Ca. The study confirmed that for a given zeolite the catalytic activity markedly increased with the concentration of the protons, as expected on the basis of the metal-proton adduct model. More relevant to the present discussion is that a very significant effect of the pore type was found. The activation energy on Pd/SiO<sub>2</sub> is 260 kJ mol<sup>-1</sup>, which is presumably near the intrinsic value. All values for Y-type zeolites are either near this value or lower (184–278 kJ mol<sup>-1</sup>), in agreement with the classic pore diffusion model, but the values for three Pd/ML catalysts, that were all reduced at 400 °C (to eliminate pore blocking by NH<sub>4</sub><sup>+</sup> ions) were higher: Pd/LiL 370 kJ mol<sup>-1</sup>; Pd/KL 325 kJ mol<sup>-1</sup>; Pd/CaL 339 kJ mol<sup>-1</sup>. All activation energies and preexponential factors measured in this study followed a classic compensation line. The data are presented in Fig. 1.



**Figure 2.** Transport paths opened by local destruction of mordenite channels caused by growing platinum particle (from *J. Catal.* **1993**, 144, Fig. 7, p. 7).

#### 4.3.5.4 Beneficial Damage of Zeolite Matrix by Growing Metal Particles

The difference in catalytic effectiveness between one-dimensional and three-dimensional pore systems creates an incentive to introduce some three-dimensionality into zeolites with linear, nonintersecting pores. Several authors have reported that growing metal particles inside zeolite cavities can induce a local destruction of the matrix [107–109]. After reduction at high temperatures, a significant portion of the metal is present as particles that are larger than the zeolite cavities. These particles are located in voids created within the zeolite matrix. This phenomenon was used by Carvill et al. in a study of Pt/H-mordenite catalyst [110]; their XRD data showed a significant loss in zeolite crystallinity when metal reduction was carried out at 500 °C. TEM showed Pt particles larger than the zeolite channels, and metal dispersion was distinctly lower than those samples reduced at 350 °C. With *n*-heptane conversion as the catalytic probe, they found that the sample that was reduced at 500 °C, although having a lower metal dispersion, was twice as active as identical samples reduced at 350 °C [110]. These results clearly show that in the regime of single file diffusion control, catalyst activity can be increased by local destruction of the zeolite matrix, as depicted schematically in Fig. 2.

### Acknowledgement

Financial aid from the Director of the Chemistry Division, Basic Energy Sciences, US Department of Energy, Grant DE-FG02-87ER13654, and from the EXXON Education Foundation is gratefully acknowledged.

### References

1. R. M. Dessau, *J. Catal.* **1982**, 77, 304.
2. F. Ribeiro, C. Marcilly, M. Guisnet, *J. Catal.* **1982**, 78, 275.



3. H. Treviño, W. M. H. Sachtler, *Catal. Lett.* **1994**, 27, 251–258.
4. C. S. John, D. M. Clark, I. E. Maxwell in *Perspectives in Catalysis* (Eds: J. A. Thomas, K. I. Zamaraev), IUPAC, **1992**, p. 387–430.
5. W. M. H. Sachtler, Z. C. Zhang in *Advances in Catalysis* (Eds: D. D. Eley, H. Pines, P. B. Weisz), Academic Press, San Diego **1993**, Vol. 39, p. 129–220.
6. W. M. H. Sachtler, *Accounts of Chemical Research* **1993**, 26, 383–387.
7. W. M. Meier, D. H. Olson, *Atlas of Zeolite Structure Types*, 2nd revsd. ed., Butterworths, London, **1987**.
8. H. Kitagawa, Y. Sendoda, Y. Ono, *J. Catal.* **1986**, 101, 12.
9. M. S. Scurrrell, *Appl. Catal.* **1988**, 41, 88.
10. B. S. Kwak, W. M. H. Sachtler, *J. Catal.* **1994**, 145, 456.
11. M. Iwamoto in *Proceedings 10th Intern. Zeolite Conference*, Garmisch-Partenkirchen, Germany July 1994 (Eds: J. Weitkamp et al.), Elsevier, Amsterdam, **1994**, Part B, p. 1395.
12. Y. Li, J. N. Armor, *Applied Catalysis B*, **1993**, 2, 239.
13. Y. Nishizaka, M. Misono, *Chem. Lett.* **1993**, 8, 1295–8.
14. F. Witzel, G. A. Sill, W. K. Hall, *J. Catal.* **1994**, 149, 229–237.
15. B. S. Kwak, W. M. H. Sachtler, *J. Catal.* **1993**, 141, 729.
16. G. K. Wertheim, *Z. Phys. D* **1989**, 12, 319–326.
17. L. Wöste, *Abstracts 7th Internatl. Symp. Small Metal Particles and Inorg. Clusters*, Kobe, Japan, Sept. 12–16, **1994**, (Eds: S. Sugano et al.), p. 59.
18. A. J. Cox, L. G. Louderback, S. E. Apsel, L. A. Bloomfield, *Phys. Rev. B* **1994**, 49, 12295.
19. V. Bonačić-Koutecký, P. Fantucci, C. Fuchs, J. Koutecký, J. Pittner, *Z. Physik D*, **1993**, 26, 17.
20. A. A. Holscher, W. M. H. Sachtler, *Disc. Faraday Soc.* **1966**, 41, 29.
21. R. Bouwman, W. M. H. Sachtler, *J. Catal.* **1970**, 19, 127.
22. R. Bouwman, G. J. M. Lippits, W. M. H. Sachtler, *J. Catal.* **1972**, 25, 350.
23. J. J. Persson, M. Andersson, A. Rosén, *Z. Phys. D* **1993**, 26, 334–6.
24. M. Andersson, L. Holmgren, A. Rosén, *Surface Review and Letters* **1996**, 3, 683.
25. B. S. Kwak, W. M. H. Sachtler, *J. Catal.* **1993**, 141, 729.
26. Th. Bein, S. J. McLain, D. R. Corbin, R. D. Farlee, K. Moller, G. D. Stuckey, G. Woolery, D. Sayers, *J. Am. Chem. Soc.* **1988**, 110, 1801–1810.
27. C. Dossi, R. Psaro, R. Ugo, Z. C. Zhang, W. M. H. Sachtler, *J. Catal.* **1994**, 149, 92–99.
28. O. C. Feeley, W. M. H. Sachtler, *Applied Catal.* **1991**, 75, 93–103.
29. G. Spoto, A. Zecchina, S. Bordiga, G. Ricchiardi, G. Martra, G. Leofanti, G. Petrini, *Appl. Catal. B* **1994**, 3, 151–72.
30. H. G. Karge, H. K. Beyer in *Zeolite Chemistry and Catalysis*, (Eds: P. A. Jacobs et al.), Elsevier, Amsterdam, **1991**, p. 43.
31. B. Wichterlova, Z. Sobalik, M. Skokanek, *Appl. Catal.* **1993**, 103, 269–80.
32. C. Dossi, J. Schaefer, W. M. H. Sachtler, *J. Mol. Catal.* **1989**, 52, 193.
33. V. Schünemann, H. Treviño, W. M. H. Sachtler, K. Fogash, J. A. Dumesic, *J. Phys. Chem.* **1995**, 99, 1317–1321.
34. M. Suzuki, K. Tsutsumi, H. Takahashi, Y. Saito, *Zeolites* **1988**, 8, 284; 381.
35. O. Feeley, W. M. H. Sachtler, *J. Appl. Catal.* **1990**, 67, 141.
36. Y.-G. Yin, Z. Zhang, W. M. H. Sachtler, *J. Catal.* **1993**, 139, 444.
37. P. Gallezot, *Catal. Rev.-Sci. Eng.* **1979**, 20, 121–154.
38. J. Sárkány, J. L. d'Itri, W. M. H. Sachtler, *Catal. Lett.* **1992**, 16, 241.
39. D. C. Tomczak, V. L. Zholobenko, H. Treviño, G.-D. Lei, W. M. H. Sachtler in *Zeolites and Related Microporous Materials: State of the Art 1994* (Eds: J. Weitkamp, H. G. Karge, H. Pfeifer, W. Hölderich) Studies in Surface Science and Catalysis, Elsevier, **1974**, Vol. 84, Part B, p. 893–900.
40. G. Moretti, W. M. H. Sachtler, *J. Catal.* **1989**, 115, 205–16.
41. Z. Zhang, L. Xu, W. M. H. Sachtler, *J. Catal.* **1991**, 131, 502–512.
42. J. S. Feeley, W. M. H. Sachtler, *J. Catal.* **1991**, 131, 573–581.
43. L. Xu, G. Lei, W. M. H. Sachtler, R. Cortright, J. A. Dumesic, *J. Phys. Chem.* **1993**, 97, 11517–11523.
44. V. Schünemann, H. Treviño, W. M. H. Sachtler, K. Fogash, J. A. Dumesic, *J. Phys. Chem.* **1995**, 99, 1317–1321.

45. L. M. Kustov, V. Yu. Borovkov, V. B. Kazansky, *J. Catal.* **1981**, 72, 149–59.
46. V. B. Kazansky, *Acc. Chem. Research* **1992**, 24, 379.
47. V. Adeeva, J. W. de Haan, J. Jänchen, G. D. Lei, V. Schünemann, L. J. M. van de Ven, W. M. H. Sachtler, R. A. van Santen, *J. Catal.* **1995**, 151, 364–372.
48. L.-L. Sheu, H. Knözinger, W. M. H. Sachtler, *J. Am. Chem. Soc.* **1989**, 111, 8125–8131.
49. W. M. H. Sachtler in *Chemistry and Physics of Solid Surfaces* (Eds: R. Vanselow, R. Howe) Springer Series in Surface Sciences No. 22, Springer, Berlin, **1990**, p. 69–85.
50. W. M. H. Sachtler, A. Y. Stakheev, *Catalysis Today* **1992**, 12, 283–295.
51. I. C. M. Wehman-Ooyevaar, D. M. Grove, P. de Vaal, A. Dedieu, G. van Koten, *Inorg. Chem.* **1992**, 31, 5484–5493.
52. I. C. M. Wehman-Ooyevaar, D. M. Grove, H. Kooijman, p. van der Sluis, A. L. Spek, G. van Koten, *J. Am. Chem. Soc.* **1992**, 114, 9916–9924.
53. S. G. Kazarian, P. A. Hamley, M. Poliakof, *J. Am. Chem. Soc.* **1993**, 115, 9069–9079.
54. L. Xu, Z. C. Zhang, W. M. H. Sachtler, *J. Chem. Soc. Faraday Trans.* **1992**, 88, 2291–2295.
55. Z. Zhang, B. Lerner, G.-D. Lei, W. M. H. Sachtler, *J. Catal.* **1993**, 140, 481–496.
56. Z. Zhang, T. Wong, W. M. H. Sachtler, *J. Catal.* **1991**, 128, 13.
57. Z. Zhang, H. Chen, W. M. H. Sachtler, *J. Chem. Soc. Faraday Trans.* **1991**, 87, 1413–1418.
58. Z. C. Zhang, H. Chen, L.-L. Sheu, W. M. H. Sachtler, *J. Catal.* **1991**, 127, 213–220.
59. Z. C. Zhang, W. M. H. Sachtler, *J. Mol. Catal.* **1991**, 67, 349–357.
60. L. L. Sheu, H. Knözinger, W. M. H. Sachtler, *Mol. Catal.* **1989**, 57, 61–79.
61. G.-D. Lei, W. M. H. Sachtler, *J. Catal.* **1993**, 140, 601–611.
62. V. L. Zholobenko, G.-D. Lei, B. T. Carvill, B. A. Lerner, W. M. H. Sachtler, *J. Chem. Soc. Faraday Trans.* **1994**, 90, 233–238.
63. C. Kemball in *Advances in Catalysis* (Eds: D. D. Eley, P. W. Selwood, P. B. Weisz), Academic Press, San Diego **1959**, Vol. 11, p. 223–262.
64. N. Poole, D. A. Whan, in *Proceedings, 8th International Congress on Catalysis*, Berlin, 1984, Verlag Chemie, Frankfurt, **1985**, Vol. 4, p. 345.
65. R. A. Dalla Betta, M. Boudart in *Proc. 5th Int. Congr. on Catalysis* (Ed: H. Hightower), North-Holland, Amsterdam, **1973**, p. 1329.
66. P. Gallezot, R. Weber, R. A. Dalla-Betta, M. Boudart, *Z. Naturforsch.* **1979**, 34A, 40.
67. M. G. Samant, M. Boudart, *J. Phys. Chem.* **1991**, 95, 4070–4074.
68. T. M. Tri, J. P. Candy, P. Gallezot, J. Massardier, M. Primet, J. C. Védrine, B. Imelik, *J. Catal.* **1983**, 791, 396.
69. D. G. Blackmond, J. G. Goodwin, Jr, *J. Chem. Soc., Chem. Commun.* **1981**, 125.
70. P. Gallezot, J. Datka, J. Massardier, M. Primet, B. Imelik in *Proc. 6th Int. Congr. on Catalysis*, (Eds: G. H. Bond et al.), The Chemical Society, London, **1977**, 696.
71. J. Bandiera, *J. Chim. Phys.* **1980**, 77, 303.
72. V. N. Romannikov, K. G. Ione, L. A. Pedersen, *J. Catal.* **1980**, 66, 121.
73. F. Figueras, R. Gomes, M. Primet, *Adv. Chem. Ser.* **1973**, 121, 480.
74. T. M. Tri, J. Massardier, P. Gallezot, B. Imelik in *Metal Support and Metal Additives Effects in Catalysis* (Ed: B. Imelik), Elsevier, Amsterdam, **1982**, p. 141.
75. C. Naccache, N. Kaufherr, M. Dufaux, J. Bandiera, B. Imelik, in *Molecular sieves-II* (Ed: J. R. Katzer), ACS, Washington, DC, **1977**, p. 538.
76. S. T. Homeyer, Z. Karpiński, W. M. H. Sachtler, *J. Catal.* **1990**, 123, 60.
77. S. T. Homeyer, Z. Karpiński, W. M. H. Sachtler, *Recl. Trav. Chim. Pays-Bas*, **1990**, 109, 81.
78. T. M. Tri, J. Massardier, P. Gallezot, B. Imelik in *Catalysis by Zeolites* (Ed: B. Imelik et al.), Elsevier, Amsterdam **1980**, p. 279.
79. J. A. Rabo, V. Schomaker, P. E. Pickert, in *Proc. 3rd Int. Congr. on Catalysis*, North Holland, Amsterdam, 1965, (Eds: W. M. H. Sachtler et al.), North Holland, **1964**, p. 612.
80. G. D. Chukin, M. V. Landay, V. Kruglikov, D. A. Agievskii, B. V. Smirnov, A. L. Belozerov, V. D. Asrieva, N. V. Goncharova, E. D. Radchenko, O. D. Konovalcherov, A. V. Agofonov, in *Proc. 6th Int. Cong. on Catalysis*, (Eds: G. D. Bond et al.), The Chemical Society, London, **1977**, p. 621.
81. H. T. Wang, Y. W. Chen, J. G. Goodwin, Jr., *Zeolites*, **1984**, 4, 56.
82. L. Xu, Z. C. Zhang, W. M. H. Sachtler, *J. Chem. Soc.; Faraday Trans.* **1992**, 88, 2291–2295.

83. X. L. Bai, H. M. H. Sachtler, *J. Catal.* **1991**, *129*, 121–129.
84. M. Chow, S. H. Park, W. M. H. Sachtler, *Applied Catalysis*, **1985**, *19*, 349–364.
85. T. McCarthy, W. M. H. Sachtler, unpublished results.
86. V. Ponec *Proceedings IX. IVC-ICSS Madrid* **1983**, 121–127.
87. T. T. T. Wong, W. M. H. Sachtler, *J. Catal.* **1993**, *141*, 407–418.
88. B. A. Lerner, B. T. Carvill, W. M. H. Sachtler, *Catal. Lett.* **1993**, *18*, 227–234.
89. G. A. Mills, H. Heinemann, T. H. Millikan, A. G. Oblad, *Ind. Eng. Chem.* **1953**, *45*, 134.
90. M. S. Tzou, B. K. Teo, W. M. H. Sachtler, *J. Catal.* **1988**, *113*, 220–235.
91. T. T. Wong, Z. Zhang, W. M. H. Sachtler, *Catal. Lett.* **1990**, *4*, 365–374.
92. T. T. T. Wong, A. Yu. Stakheev, W. M. H. Sachtler, *J. Phys. Chem.* **1992**, *96*, 7733–7740.
93. J. Sárkány, W. M. H. Sachtler, *Zeolites* **1994**, *14*, 7–11.
94. M. S. Tzou, M. Kusunoki, K. Asakura, H. Kuroda, M. Moretti, W. M. H. Sachtler, *J. Phys. Chem.* **1991**, *95*, 5210–5215.
95. See for instance: B. C. Gates, *Catalytic Chemistry*, Wiley, Chichester, UK, **1992**, p. 285.
96. P. B. Weisz, *Chemtech.* **1973**, *3*, 498.
97. S. J. Tauster, J. J. Steger, *Mater. Res. Soc. Symp. Proc.* **1988**, *111*, 418.
98. F. Gault in *Advances in Catalysis* (Eds: D. D. Eley, H. Pines, P. B. Weisz), Academic Press, San Diego, **1981**, Vol. 30, p. 1–95.
99. G. Moretti, W. M. H. Sachtler, *J. Catal.* **1989**, *116*, 350.
100. W. E. Alvarez, D. E. Resasco, *Catal. Lett.* **1991**, *8*, 53.
101. D. J. Ostgard, L. Kustov, K. R. Poeppelmeier, W. M. H. Sachtler, *J. Catal.* **1992**, *133*, 342–357.
102. B. A. Lerner, B. T. Carvill, W. M. H. Sachtler, *J. Mol. Catal.* **1992**, *77*, 99–108.
103. J. Kärger, M. Petzold, H. Pfeifer, S. Ernst, J. Weitkamp, *J. Catal.* **1992**, *136*, 283–299.
104. J. Kärger, H. Pfeiffer in *Proc. Zeolite Conf. Montreal, 1992* (Eds: R. von Ballmoos et al.), Butterworth-Heinemann, Oxford, **1993**, p. 129–136.
105. P. E. Eberly, Jr, *J. Phys. Chem.* **1963**, *67*, 2404.
106. Z. Karpinski, S. N. Gandhi, W. M. H. Sachtler, *J. Catal.* **1993**, 337–346.
107. N. I. Jaeger, J. Rathousky, G. Schulz-Ekloff, A. Svenson, A. Zukal, in *Zeolites: Facts, Figures, Future*, (Eds: P. A. Jacobs, R. A. van Santen), Elsevier, Amsterdam, **1989**, p. 1005.
108. N. I. Jaeger, A. L. Jaeger, G. Schulz-Ekloff, *J. Chem. Soc., Faraday Trans.* **1991**, *87*, 1251.
109. W. M. H. Sachtler, Z. Zhang, A. Y. Stakheev, J. S. Feeley, in *New Frontiers in Catalysis* (Eds: L. Guzzi, F. Solymosi, P. Tetenyi), Akademiai Kiado, Budapest, **1993**, p. 271.
110. B. T. Carvill, B. A. Lerner, B. J. Adelman, D. C. Tomczak, W. M. H. Sachtler, *J. Catal.* **1993**, *144*, 1–8.

## 4.4 Zeolite-Entrapped Metal Complexes

G. SCHULZ-EKLOFF AND S. ERNST

### 4.4.1 Synthesis of Zeolite-Entrapped Metal Complexes

For the preparation of transition metal complexes in zeolites, a variety of monodentate as well as bi- and polydentate ligands has been used. The early work on monodentate-based complexes has been extensively reviewed by Lunsford [1, 2] and recent updates by Mortier and Schoonheydt [3] and by Ozin and Gil [4] are

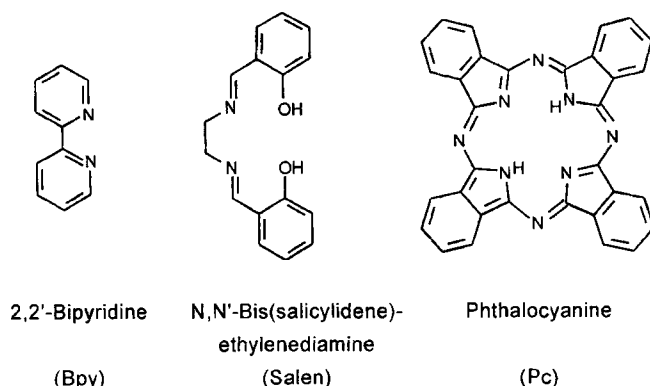
83. X. L. Bai, H. M. H. Sachtler, *J. Catal.* **1991**, 129, 121–129.
84. M. Chow, S. H. Park, W. M. H. Sachtler, *Applied Catalysis*, **1985**, 19, 349–364.
85. T. McCarthy, W. M. H. Sachtler, unpublished results.
86. V. Ponec *Proceedings IX. IVC-ICSS Madrid* **1983**, 121–127.
87. T. T. T. Wong, W. M. H. Sachtler, *J. Catal.* **1993**, 141, 407–418.
88. B. A. Lerner, B. T. Carvill, W. M. H. Sachtler, *Catal. Lett.* **1993**, 18, 227–234.
89. G. A. Mills, H. Heinemann, T. H. Millikan, A. G. Oblad, *Ind. Eng. Chem.* **1953**, 45, 134.
90. M. S. Tzou, B. K. Teo, W. M. H. Sachtler, *J. Catal.* **1988**, 113, 220–235.
91. T. T. Wong, Z. Zhang, W. M. H. Sachtler, *Catal. Lett.* **1990**, 4, 365–374.
92. T. T. T. Wong, A. Yu. Stakheev, W. M. H. Sachtler, *J. Phys. Chem.* **1992**, 96, 7733–7740.
93. J. Sárkány, W. M. H. Sachtler, *Zeolites* **1994**, 14, 7–11.
94. M. S. Tzou, M. Kusunoki, K. Asakura, H. Kuroda, M. Moretti, W. M. H. Sachtler, *J. Phys. Chem.* **1991**, 95, 5210–5215.
95. See for instance: B. C. Gates, *Catalytic Chemistry*, Wiley, Chichester, UK, **1992**, p. 285.
96. P. B. Weisz, *Chemtech.* **1973**, 3, 498.
97. S. J. Tauster, J. J. Steger, *Mater. Res. Soc. Symp. Proc.* **1988**, 111, 418.
98. F. Gault in *Advances in Catalysis* (Eds: D. D. Eley, H. Pines, P. B. Weisz), Academic Press, San Diego, **1981**, Vol. 30, p. 1–95.
99. G. Moretti, W. M. H. Sachtler, *J. Catal.* **1989**, 116, 350.
100. W. E. Alvarez, D. E. Resasco, *Catal. Lett.* **1991**, 8, 53.
101. D. J. Ostgard, L. Kustov, K. R. Poepelmeier, W. M. H. Sachtler, *J. Catal.* **1992**, 133, 342–357.
102. B. A. Lerner, B. T. Carvill, W. M. H. Sachtler, *J. Mol. Catal.* **1992**, 77, 99–108.
103. J. Kärger, M. Petzold, H. Pfeifer, S. Ernst, J. Weitkamp, *J. Catal.* **1992**, 136, 283–299.
104. J. Kärger, H. Pfeiffer in *Proc. Zeolite Conf.* Montreal, 1992 (Eds: R. von Ballmoos et al.), Butterworth-Heinemann, Oxford, **1993**, p. 129–136.
105. P. E. Eberly, Jr, *J. Phys. Chem.* **1963**, 67, 2404.
106. Z. Karpinski, S. N. Gandhi, W. M. H. Sachtler, *J. Catal.* **1993**, 337–346.
107. N. I. Jaeger, J. Rathousky, G. Schulz-Ekloff, A. Svenson, A. Zukal, in *Zeolites: Facts, Figures, Future*, (Eds: P. A. Jacobs, R. A. van Santen), Elsevier, Amsterdam, **1989**, p. 1005.
108. N. I. Jaeger, A. L. Jaeger, G. Schulz-Ekloff, *J. Chem. Soc., Faraday Trans.* **1991**, 87, 1251.
109. W. M. H. Sachtler, Z. Zhang, A. Y. Stakheev, J. S. Feeley, in *New Frontiers in Catalysis* (Eds: L. Guzzi, F. Solymosi, P. Tetenyi), Akademiai Kiado, Budapest, **1993**, p. 271.
110. B. T. Carvill, B. A. Lerner, B. J. Adelman, D. C. Tomczak, W. M. H. Sachtler, *J. Catal.* **1993**, 144, 1–8.

## 4.4 Zeolite-Entrapped Metal Complexes

G. SCHULZ-EKLOFF AND S. ERNST

### 4.4.1 Synthesis of Zeolite-Entrapped Metal Complexes

For the preparation of transition metal complexes in zeolites, a variety of monodentate as well as bi- and polydentate ligands has been used. The early work on monodentate-based complexes has been extensively reviewed by Lunsford [1, 2] and recent updates by Mortier and Schoonheydt [3] and by Ozin and Gil [4] are



**Figure 1.** Selected examples for bi- and tetradentate ligands used to synthesize zeolite-entrapped transition metal complexes.

available. The present chapter will therefore focus on the preparation of zeolite-entrapped transition metal complexes with bi- and polydentate ligands.

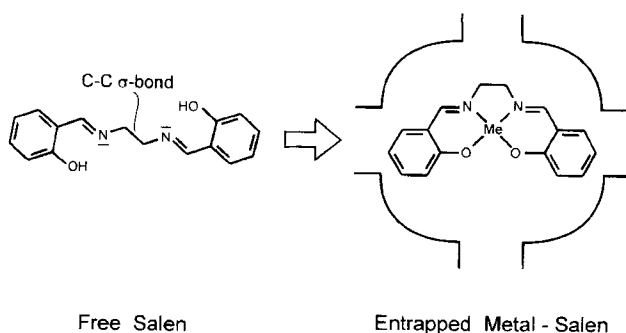
So far, only relatively few bi- and polydentate ligands have been explored for the synthesis of transition metal complexes in zeolites. Among them are ethylenediamine, tetraethylenepentamine, dimethylglyoxime, phenantroline, bi- and terpyridine, various Schiff bases, phthalocyanines, and porphyrins (e.g. [5–9]). From a catalytic point of view, the three ligand types depicted in Fig. 1, viz. the bidentate bipyridine (Bpy), and the tetradentate ligands *N,N'*-bis(salicylidene)ethylenediamine (salen) and phthalocyanine (Pc), have to date attracted by far the most attention. Essentially three methods are currently used to prepare host/guest compounds having these three types of ligands:

- (i) reaction of the preformed ligand with the transition metal previously introduced into the zeolite cages (flexible ligand method);
- (ii) assembling the ligand from smaller species inside the zeolite cavities (ship-in-the-bottle technique);
- (iii) synthesis of the zeolite structure around the preformed transition metal complex (zeolite synthesis method).

These three basic approaches are discussed in more detail in the following.

#### 4.4.1.1 Flexible Ligand Method

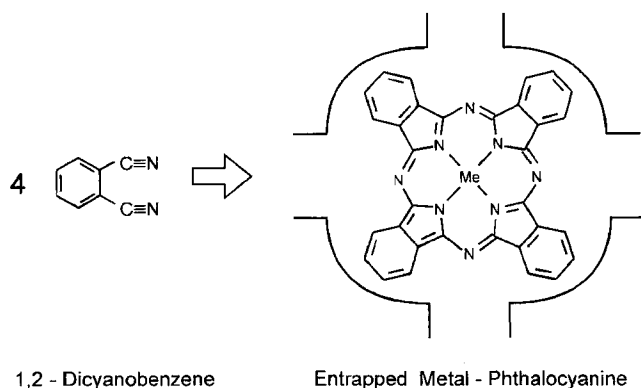
This approach is based on the principle that the free ligand guests can easily enter the cavities of the zeolite host material because they are flexible enough to pass through the restricting windows giving access to the larger cages. As depicted in Fig. 2 for the Schiff base salen as example, the free unfolded ligand is able to enter the pores of the zeolite (in the present case faujasite) due to the possible free rota-



**Figure 2.** Synthesis of zeolite-entrapped metal-salen complexes via the flexible ligand method (adapted from Ref. 10).

tion around the carbon-carbon  $\sigma$ -bond connecting the two salicylidene moieties of the salen molecule. However, once the ligand has entered the zeolite cage and chelated with the previously exchanged transition metal ions, the complex adopts a square-planar configuration which is unable to escape from the zeolite host matrix via the 12-membered ring windows. Hence, the metal-salen complex is physically entrapped in the supercages of faujasite. This principle was first exploited by Herron [11] to prepare cobalt-salen complexes in the supercages of faujasite. Later on, the transition metal ion as well as the structure of the Schiff base ligand were varied extensively [12–19]. The resulting host-guest compounds have been shown to act as oxygen carriers mimicking hemoglobin [12, 16], as selective oxidation catalysts [12, 17, 20] or as catalysts for selective hydrogenations [14, 15, 17] (Section 4.4.3). In addition, they possess interesting electrochemical properties as observed by cyclic voltammetry [19, 21].

The principal experimental approach for preparing zeolite-entrapped transition metal Schiff base complexes is as follows. The  $\text{Na}^+$  form of the selected zeolite is partially exchanged with the envisaged transition metal ion. In order to avoid precipitation of hydrolyzed transition metal species during the exchange or the subsequent high-temperature dehydration, all precautions generally taken during ion exchange of zeolites with transition metal ions should be followed. In particular, dilute exchange solutions of the transition metal salts (e.g.  $5\text{--}20 \times 10^{-3} \text{ mol L}^{-1}$ ) and low heating rates during dehydration should be applied. An alternative to ion exchange in aqueous suspension is solid-state ion exchange [22], especially for those transition metals which easily hydrolyze in water or which do not form water-soluble salts. The ion-exchanged and dried zeolite is mixed in an inert atmosphere (i.e. in a glove box) with the predried Schiff base ( $n_{\text{ligand}}: n_{\text{metal}}$  usually from 2 to 4), filled in a glass tube, evacuated and sealed, and finally heated for several hours at a temperature slightly above the melting point of the ligand (e.g.  $140^\circ\text{C}$  for salen) until a bright color is observed. After the reaction, a soxhlet extraction with acetone, acetonitrile, or dichloromethane is usually applied to purify the zeolite from the uncomplexed ligand. During the complexation step, the Schiff base loses its two ionizable protons to the zeolite framework upon coordination with a divalent transition metal ion. This has two consequences: the resulting transition metal complex is electroneutral, and Brønsted-acid sites are formed inside the zeolite cavities. Therefore, care has to be taken that these acid sites do not interfere in subsequent



**Figure 3.** Ship-in-the-bottle synthesis of zeolite-encaged metal-phthalocyanines (adapted from Ref. 10).

catalytic reactions were they could potentially catalyze undesirable side reactions. Hence, measures have to be taken to remove these acid sites, e.g. via an ion exchange with monovalent metal ions.

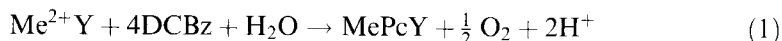
The principal synthetic approach used for the preparation of zeolite-encapsulated Schiff base complexes also holds for the complexation of transition metal ions with bipyridine and has been reviewed in detail recently [9]. By carefully adjusting the ligand-to-metal ion ratio (e.g. 2:1 or 3:1) and the temperature of the synthesis (e.g. 90 °C or 200 °C) the complexation can be easily directed with high selectivity to either the bis- or the tris-coordinated complex [9, 23, 24]. Recently, *cis*-manganese(II)-bis-2,2'-bipyridine complexes encaged in faujasite-type zeolites have found particular interest in industrially relevant catalytic applications, i.e. for selective alkene oxidations (see below) [25, 26].

#### 4.4.1.2 Ship-in-the-Bottle Method

This approach is generally used to synthesize transition metal-phthalocyanines encapsulated in zeolites. This method was first described by Romanovsky and co-workers [27–29]. Its principle is depicted in Fig. 3. It involves the introduction of the metal via ion exchange or preadsorption of a labile metal complex, such as a carbonyl or a metallocene, followed by reaction with 1,2-dicyanobenzene at temperatures from 250 °C to 350 °C. This synthesis principle was later adopted by others to prepare phthalocyanine complexes of, for example, cobalt [30–33], copper [31, 34], iron [35–38], manganese [39], nickel [30, 40], osmium [40], rhodium [41], and ruthenium [40] in the large cavities of faujasite and, more recently, in VPI-5 [38, 42] and zeolite EMC-2 [43].

The introduction of the transition metal ions into the zeolite by ion exchange in aqueous solution requires the same precautions as already described for Schiff base complexes. After loading of the ion-exchanged zeolite with 1,2-dicyanobenzene (DCBz), tetramerization is induced by heating in vacuum at temperatures between ca. 250 °C and 350 °C [30]. It has been demonstrated that differential scanning calorimetry [32, 34] is a useful tool for determining the optimum complexation tem-

perature. The latter obviously varies with the type of transition metal ion and the structure of the zeolite. Complexation occurs according to the stoichiometry given in eq 1 [9, 30].

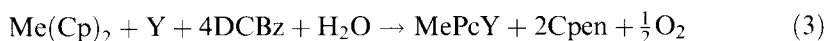


The phthalocyanine precursor has to be reduced for the formation of the transition metal complex. Since it has been found that complexation does not occur if the ion-exchanged zeolite was strongly dehydrated before the complexation step, water is supposed to be the electron source in this process [30]. After complexation, the zeolite is usually purified by three successive soxhlet extractions using acetone, pyridine, or dimethylformamide, and again acetone to dissolve unreacted dicyanobenzene and the side product phthalimide and to remove phthalocyanine or metal-phthalocyanine which was formed on the outer surface of the zeolite crystallites. Typically, the individual extraction steps have to be performed for a period from ca. 2 to ca. 5 days in order to achieve complete extraction. Detailed chemical analyses and mass balances revealed that only a certain fraction of the introduced transition metal ions is complexed, the remainder occupying cation positions in the zeolite [30, 43]. It is to be noted that both Brønsted-acid sites produced in the complexation step and uncomplexed metal ions can interfere in catalytic applications by catalyzing undesirable side reactions.

Another possible method of ship-in-the-bottle synthesis involves the introduction of the transition metal by adsorption of the corresponding carbonyl complex in the zeolite, followed by the synthesis of the phthalocyanine ligand around the transition metal. In this case, two alternatives exist: the carbonyl is first decomposed thermally or photochemically whereby small metal clusters are formed, or a direct ligand exchange of CO by 1,2-dicyanobenzene at lower temperature (e.g. from 100 °C to 200 °C). In both cases, large fractions of the transition metal remain uncomplexed. In the former, the transition metal is present as metal clusters in the supercages of faujasites and only one phthalocyanine complex can be formed per supercage, whereas in the latter case the decomposition of the carbonyl complexes is faster than the rate of complex formation with 1,2-dicyanobenzene. The reaction equation for the "carbonyl route" (eq 2) reveals that no protons and hence no acid sites are produced during complex formation since the valence of the introduced transition metal is zero.



Using metallocenes as the transition metal-supplying agents, again small amounts of water are required during phthalocyanine synthesis (eq 3). In this case, however, the produced protons are not bound as Brønsted-acid sites to the zeolite lattice, but are required to convert the cyclopentadienyl fragments (Cp) of the metallocene to cyclopentadiene (Cpen) [9].



The host-guest compounds produced by the metallocene route have the advantage that they are virtually free from uncomplexed metal species. However, unlike with



the two previously described procedures, large amounts of the free phthalocyanine base are also formed inside the zeolite [38]. Potentially these entrapped free ligands may hinder the diffusion of reactants and/or products in catalytic reactions.

The synthesis of *substituted* metal–phthalocyanines in the supercages of faujasite-type zeolites via the ship-in-the-bottle technique has also been claimed. The incentive to encapsulate substituted complexes is at least twofold:

- (i) to enhance the stability of the complex via bulky substituents which protect the meso-atoms of the phthalocyanine ring;
- (ii) to increase the catalytic activity of the metal by introducing electron-withdrawing groups.

Examples published so far are tetra-*t*-butyl-substituted iron–phthalocyanine [44], perfluorophthalocyanines of iron [45], cobalt [46, 47] copper [46, 47] and manganese [46], and iron–tetranitrophthalocyanine [48]. The starting materials for the in situ ligand synthesis were 4-*t*-butyl-1,2-dicyanobenzene, tetrafluoro-1,2-dicyanobenzene and 4-nitro-1,2-dicyanobenzene, respectively. In the case of the nitro-substituted phthalocyanine it was unambiguously shown that the complex is only formed at the outer surface of the zeolite crystallites [48]. By contrast, there seems to be sufficient experimental evidence for true encapsulation of the perfluorated phthalocyanines [45–47]. Not enough data are available on the tetra-*t*-butyl-substituted system to allow for a final conclusion as to whether or not this very bulky complex is really encapsulated.

The principle of ship-in-the-bottle synthesis was also applied for the in situ preparation of porphyrin-type ligands in the supercages of Y-type zeolites. Nakamura et al. [49] claimed the encapsulation of iron- and manganese–tetramethylporphyrins in the supercages of zeolite NaY by refluxing the transition metal-exchanged zeolite with pyrrole and acetaldehyde in methanolic solution. Unfortunately, however, besides one UV/VIS spectrum no further experimental evidence for true intrazeolitic complex formation were given and the catalytic results obtained with the synthesized materials are poor. The synthesis of encapsulated tetraphenylporphyrins from pyrrole and benzaldehyde has been claimed by Chan and Wilson [50]. No experimental evidence has been presented for true complex encapsulation. Furthermore, there are certainly severe size limitations for these large complexes, at least in the supercages of faujasite-type zeolites. As a whole, the topic of encapsulated porphyrin-type complexes seems to be still in its infancy. Nevertheless, this interesting field deserves further systematic research, in particular in view of the steadily increasing number of large and super-large pore zeolites and molecular sieves which may serve as host matrix.

#### 4.4.1.3 Zeolite Synthesis Method

Incorporation of transition metal complexes by synthesizing the molecular sieve structure around the preformed complexes has also been claimed [51–54]. Prerequisites for this method are the stability of the complex under the conditions of

zeolite synthesis (pH, temperature, hydrothermal conditions) and a sufficient solubility in the synthesis medium to enable random distribution of the complex in the synthesis mixture as well as in the final zeolite. The synthesis of zeolite mordenite from gels containing bipyridine, phenanthroline, or phthalocyanine complexes has been reported by Rankel and Valyocsik [51]. However, encapsulation of the complexes in the final product was neither claimed nor proved. Balkus and co-workers [52–54] claimed that homogeneous encapsulation of transition metal complexes in zeolites is possible by careful design of the zeolite synthesis procedure to avoid aggregation of the complexes in the aqueous synthesis medium. According to these authors, phthalocyanine complexes can be incorporated during crystallization into zeolite X [52] and into the aluminophosphates  $\text{AlPO}_4\text{-5}$  and  $\text{AlPO}_4\text{-11}$  [53]. At least in the two latter cases, formation of mesopores has to be assumed in order to allow for the accommodation of the relatively spacious complexes in the narrow one-dimensional pore systems of  $\text{AlPO}_4\text{-5}$  or even  $\text{AlPO}_4\text{-11}$ . In addition, these two molecular sieves require the presence of further organic templates for their synthesis which have to be removed by calcination before an application in adsorption or catalysis is possible. It is anticipated that during this calcination step the transition metal complex is also destroyed and/or burnt. Hence, the zeolite synthesis method seems to be restricted to those cases, where the synthesis of the zeolite matrix is possible without the use of further organic templates.

## 4.4.2 Characterization

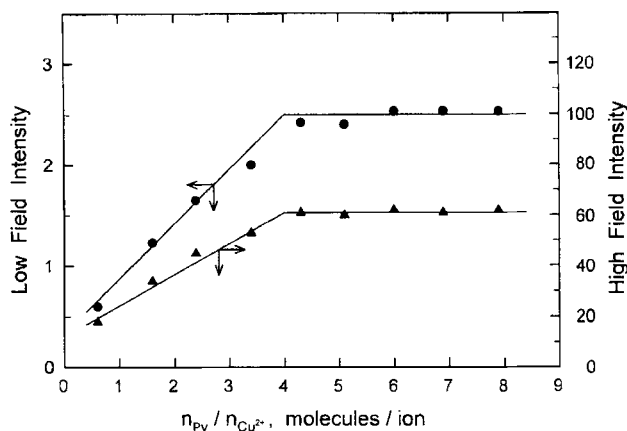
The characterization of zeolite-encapsulated transition metal complexes is carried out with the objective to answer questions about

- (i) the distribution of the complex over the host crystal;
- (ii) the degree of complexation;
- (iii) the type of coordination compared to that in a liquid solvent;
- (iv) the influence of a host–guest interaction on the structure;
- (v) the stability compared to that in the solid or in dissolved states;
- (vi) the ability to exhibit free coordination sites for chemisorption and catalysis.

In the following, methods of characterization are described which have provided largely unambiguous information about these most important questions.

### 4.4.2.1 Electron Paramagnetic Resonance Spectroscopy

Electron paramagnetic resonance (EPR) spectroscopy is a powerful tool for the study of square-planar complexes having  $\text{Co}^{\text{II}}$  as central metal ion due to the low-spin configured doublet ( $S = 1/2$ ) ground states in which the unpaired electron resides in the  $\text{Co } 3d_{z^2}$  orbital, where  $z$  is perpendicular to the chelate plane. The spin Hamiltonian parameters of such ground states are, thus, extremely sensitive to changes in axial ligation. This property can be used to follow the processes of com-

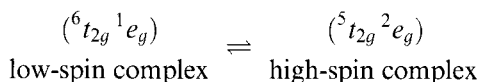


**Figure 4.** Intensity of the  $[Cu^{II}(py)_4]^{2+}$  EPR spectrum vs. the molecules of py adsorbed per  $Cu^{2+}$  ion. Left ordinate: intensity based on the  $m_I = -3/2$  component of the spectrum. Right ordinate: intensity based on the high-field minimum (from Ref. 55).

plexation, hydration, and oxygen bonding by means of a theoretical analysis of the spin Hamiltonian parameters and a comparison of the individual ligand-field effects with the experimental spectra.

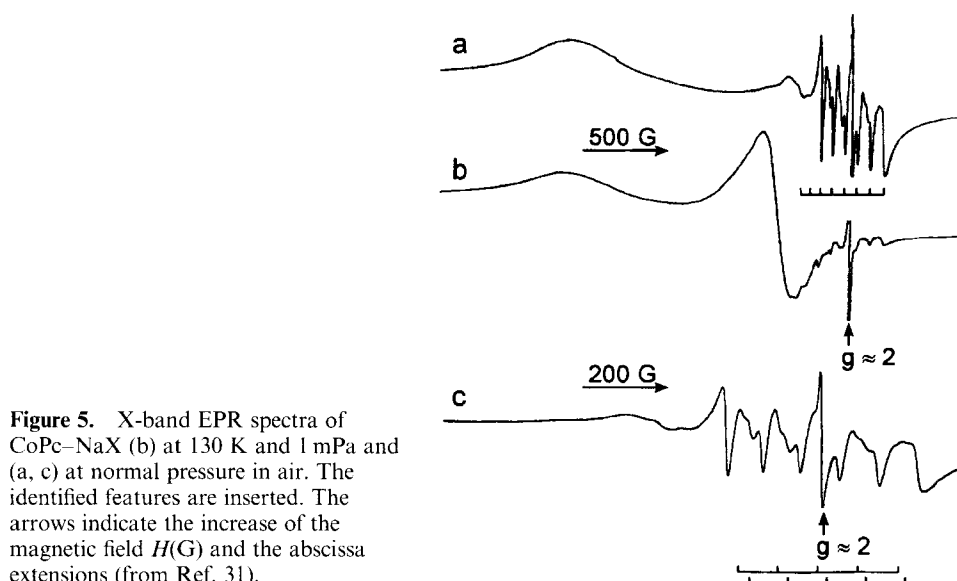
A relatively clear way to follow the complexation process is the evaluation of intensity changes in EPR spectra, as has been demonstrated for the formation of the tetrakis(pyridine)copper(II) complex [55]. The expected stoichiometry  $[Cu^{II}(py)_4]^{2+}$  for the square-planar complex, exhibiting a superhyperfine spectrum, is adjusted in the supercage of the zeolite Y (Fig. 4).

A low-spin state appears in faujasite Y using bipyridine as a ligand for the formation of tris(bipyridine) complexes of  $Co^{II}$ ,  $Fe^{III}$ , or  $Ru^{III}$  [23, 24, 56]. The low-spin state is complete at 77 K, but a temperature-dependent equilibrium conversion into the octahedral high-spin state appears at higher temperatures according to



The multiplicity of the hyperfine structure indicates whether monomeric  $[Co^{III}L_xO_2]^{2+}$  or dimeric  $[Co^{III}L_xO_2-Co^{III}L_x]^{4+}$  complexes are formed from methylamine ligands, since the high-spin state of the latter  $\mu$ -peroxo complex can be converted into the low-spin  $\mu$ -superoxo species  $[Co^{III}L_xO_2-Co^{III}L_x]^{5+}$  by oxidation, e.g. with chlorine or  $H_2O_2$  [57]. The preferential location of the unpaired electron on the oxygen molecule is concluded from the small  $^{59}Co$  hyperfine splitting constants.

From the EPR spectra of a variety of zeolite-entrapped  $Co^{2+}$  Schiff base complexes it could be concluded that planar complexes of  $Co^{2+}$  with tetradentate salen (bis(salicylidene)ethylenediamine) and acacen (bis(acetylacetonyl)ethylenediamine) are only formed in low concentrations in faujasites, but that the pentadentate analogs facilitate the elimination of the zeolite from the primary coordination sphere of the metal ion. In some cases, the spectral characteristics of the entrapped complexes



**Figure 5.** X-band EPR spectra of CoPc–NaX (b) at 130 K and 1 mPa and (a, c) at normal pressure in air. The identified features are inserted. The arrows indicate the increase of the magnetic field  $H$ (G) and the abscissa extensions (from Ref. 31).

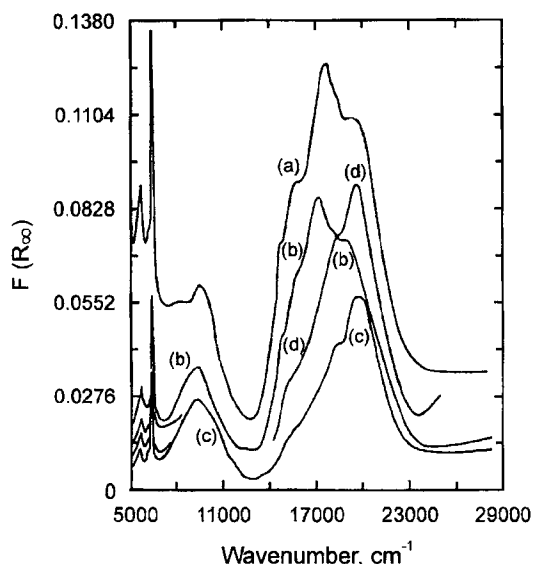
are identical to those of the corresponding solution complexes; in other cases small axial coordination strength is found, presumably due to influences of the zeolite host [17].

Charge-compensating protons, which are formed during the chelating process, have been shown to interact with the pyrrol nitrogen atoms of CoPc, resulting in a nonequivalency of these N atoms [31]. As a consequence, two nitrogen atoms with their nuclear spins  $I = 1$  couple to the low-spin  $\text{Co}^{2+}$  ( $S = 1/2$ ;  $m_S = \pm 1/2$ ;  $m_I = 0, \pm 1, \pm 2$ ;  $M_S = 1$ ;  $M_I = 0$ ). This results in five-component spectra interfering with the octet of the  $^{59}\text{Co}$  hyperfine structure (Fig. 5).

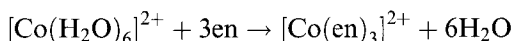
#### 4.4.2.2 Electron Excitation by Ultraviolet/Visible Light

The spectroscopy of ultraviolet and visible light absorption gives information about the d-orbital splitting through the d–d transitions and the ligand–metal interaction through the ligand-to-metal charge-transfer transitions. Information about the coordinative bond is obtained either qualitatively by comparison of the spectra with spectra of known complexes, or quantitatively by ligand field or angular overlap model calculations on the d–d spectrum.

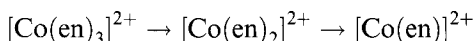
Generally, diffuse reflectance spectroscopy is applied to follow the chelating process in zeolite cages. For example, the formation of the tris(ethylenediamine) in cobalt ion-exchanged faujasite Y is indicated by an increase of the relative intensity of the band at  $20\,650\text{ cm}^{-1}$  (Fig. 6), which is characteristic for a d–d transition of an octahedral complex [58]. Since only relative intensities of the bands, assigned to sixfold coordination, change during the chelate formation the process must occur according to



**Figure 6.** Dynamics of Co chelation by ethylenediamine on hydrated (a) CoNaY. The chelation proceeds by successive removal of water at (b) 329 K, (c) 428 K, and (d) 477 K (from Ref. 58).



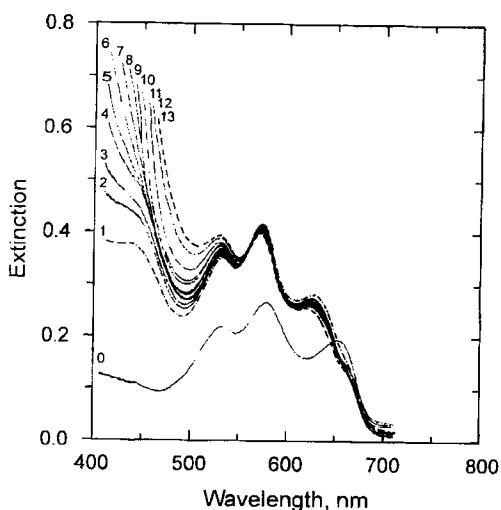
i.e. it represents the replacement of the weaker ligand  $\text{H}_2\text{O}$  by the stronger one. This complex is stable up to 473 K. At higher temperature a stepwise decomposition



proceeds. The intermediate  $[\text{Co}(\text{en})_2]^{2+}$  is identified by an EPR spectrum of the monomeric superoxocomplex exhibiting the presence of a low-spin species, and the monoligand complex is identified by the appearance of charge-transfer bands in the UV region, i.e. above  $20\,000\text{ cm}^{-1}$  [58].

The dynamics of the formation of the dimethylglyoximate-Co(II) complex by uptake of dimethylglyoxime in a cobalt ion-exchanged zeolite NaX single crystal is followed by in situ UV/VIS microscope spectrophotometry in transmission [59]. The temporal changes of the spectra (Fig. 7) indicate the tetrahedral coordination of the starting complex  $[\text{Co}^{\text{II}}(\text{Zeo})_3\text{OH}]^+$  concluded from the band quadrupol between 450 and 700 nm, which originates from the splitting of the transition  $^4F(\Gamma_2) \rightarrow ^4P(\Gamma_4)$  due to  $(L, S)$  coupling effects. The shift of the red band from 655 to 625 nm is due to an increasing distortion of the quasitetrahedral complex, presumably due to the formation of the intermediate  $[\text{Co}^{\text{II}}(\text{Zeo})_3(\text{dmgH})]$ . The formation of a blue double band between 300 and 500 nm indicates a transition  $\Gamma_2(^4F) \rightarrow \Gamma_2(^4P)$  due to a complex of octahedral symmetry  $D_{4h}$ , i.e. the complex  $[\text{Co}^{\text{II}}(\text{dmgH})_2(\text{H}_2\text{O})_2]$ . This model is supported by EPR studies [60].

Using UV/VIS spectroscopy in transmission with large single crystals ( $50\text{ }\mu\text{m}$  size), NaX-entrapped cobalt phthalocyanine complexes have been analyzed [61]. The spectra exhibit a splitting of the Q-band, which is expected for a lowering



**Figure 7.** Dynamics of Co chelation by dimethylglyoxime via vapor-phase deposition in dehydrated (673 K, 5 h) CoNaX at 373 K. Spectrum 0 is pure CoNaX (from Ref. 59).

of symmetry from  $D_{4h}$  to  $D_{2h}$  [62]. Partial protonation of metal-phthalocyanine (MePc) can result in such a lowering to a twofold symmetry [63]. The charge-compensating protons which are generated during the chelate formation are the source of the partial protonation.

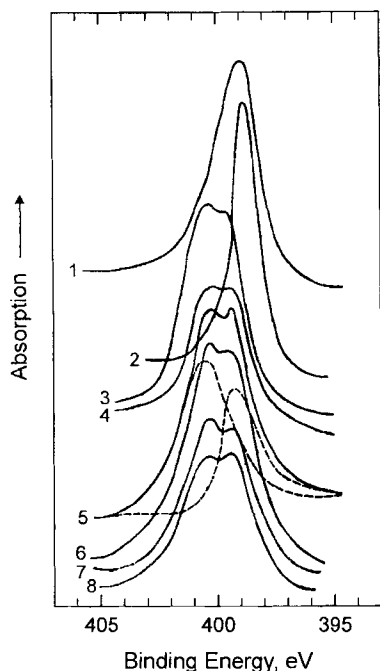
The analysis of luminescence spectra in the UV/VIS region can give information about the distribution of zeolite-encapsulated complexes or can be used as a probe for processes causing acceleration or quenching of emission intensity. For tris(2,2'-bipyridine)ruthenium(II) complexes in zeolite Y, concentration quenching starts at three  $[\text{Ru}^{\text{II}}(\text{bpy})_3]^{2+}$  complexes per unit cell, i.e. at distances of 2–3 nm [23, 24]. Small amounts of water can increase the emission intensity, whereas oxygen acts always as a quencher due to singlet oxygen formation.

For zinc porphyrins incorporated in  $\text{AlPO}_4\text{-5}$  molecular sieves by crystallization inclusion, an average distance for Förster quenching by inductive resonance is found to be 6 nm, i.e. lower than spacings valid for dissolved complexes [64].

#### 4.4.2.3 X-Ray Photoelectron Spectroscopy

X-ray photoelectron spectroscopy (XPS), which can be applied to the analysis of zeolites due to increased electron escape depths, is used to answer questions on

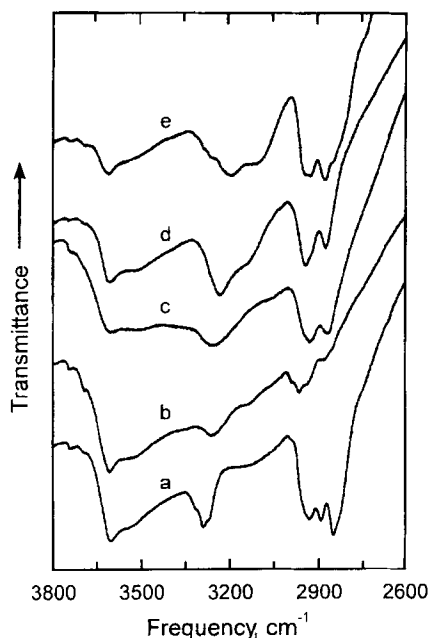
- (i) the homogeneity of the distribution of the encaged complexes, i.e. either uniform throughout the zeolite crystal or enriched in a shell close to the crystal surface;
- (ii) the degree of complexing;
- (iii) the structure of the complex;
- (iv) the interaction with the framework [65–68].



**Figure 8.** XPS spectra of N 1s in MePc-NaY samples and reference spectra: (1) CoPc, (2) NiPc, (3) NiPc-NaY(60), (4) NiPc-NaY(40), (5) NiPc-NaY(30) with spectrum synthesis, (6) CoPc-NaY(60), (7) CoPc-NaY(30), (8) CuPc-NaY(60) (from Ref. 67).

The detailed analysis of Me:Si, Me:Na or N:Si ratios, where Me denotes the complexing metal ion, gives evidence about the preferential location of the complex, i.e. strong deviations from the expected bulk compositions to higher values for these ratios indicate an enrichment at or close to the external surface of the zeolite crystals. High degrees of complexing result in a shift of the binding energy  $E_b$  for the complexing metal to lower values by ca. 1 eV, e.g. for Ni  $2p_{3/2}$  from 855.8 for the nickel ion-exchanged faujasite Y to 854.9 for the zeolite-encaged nickel-phthalocyanine [66]. Another proof for the formation of the phthalocyanine complex is the decrease in the intensity of the satellite shake-up due to the reduction of the magnetic moment, i.e. the decrease of the Ni unpaired spin density in the course of the formation of the diamagnetic NiPc. The degree of binding of the metal ions to the Pc ligand can also be followed via the N:Me ratio, i.e. when the ratio approaches the maximum value of 8 this indicates an increase in the degree of complex formation.

The structure of a zeolite-encaged metal-phthalocyanine can strongly deviate from that of the free complex. This is indicated by a change of the spectra of N 1s (Fig. 8). Instead of a narrow N 1s singlet with  $E_b = 399$  eV and full width of half maximum (FWHM) = 1.9 eV, either strongly broadened peaks (FWHM = 3.5 eV) or poorly resolved doublets are observed. Deconvolution of the N 1s peaks yields two components with binding energies of about 399 and 400.5 eV. Obviously, the eight nitrogen atoms of the Pc molecules are no longer equivalent in the zeolite-encaged state. Presumably, the charge-compensating protons, which are formed



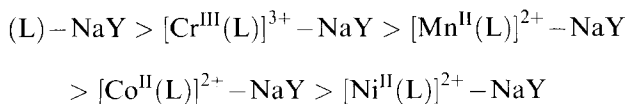
**Figure 9.** High frequency domain of the IR spectra of transition metal complexes of 1,4,8,11-tetraazacyclotetradecane (cyclam) in NaY. a: (cyclam), b:  $[\text{Cr}^{\text{III}}(\text{cyclam})]^{3+}$ , c:  $[\text{Mn}^{\text{II}}(\text{cyclam})]^{2+}$ , d:  $[\text{Co}^{\text{II}}(\text{cyclam})]^{2+}$ , e:  $[\text{Ni}^{\text{II}}(\text{cyclam})]^{2+}$  (from Ref. 17).

during the complex formation from the metal ions and the 1,2-dicyanobenzene, cause a protonation of the pyrrol N atoms and a corresponding shift of the signal.

#### 4.4.2.4 Infrared Spectroscopy

Infrared spectroscopy can give information on whether ligand molecules have coordinated to transition metal cations if different patterns appear in the free or in the chelated state, or if characteristic bands exhibit defined shifts upon chelation.

A striking example, where both conditions are fulfilled, is given for faujasite-hosted transition metal complexes of 1,4,8,11-tetraazacyclotetradecane (cyclam) [17]. The high-frequency domain of the IR spectra shows a shift of the most intense N-H stretching vibration in the order

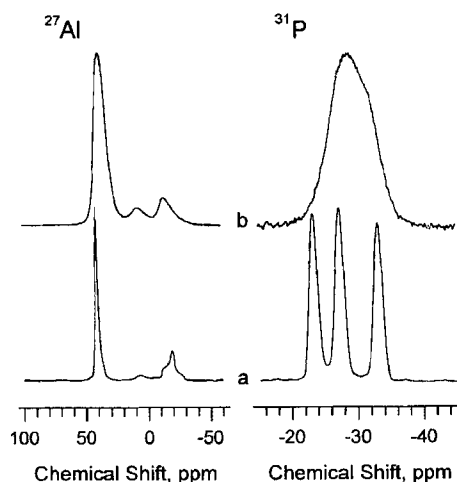


and the shoulders at  $3273$  and  $3321 \text{ cm}^{-1}$  are lost (Fig. 9).

#### 4.4.2.5 Nuclear Magnetic Resonance Spectroscopy

High-resolution magic angle spinning nuclear magnetic resonance spectroscopy (HR MAS NMR) is used to study the interaction of phthalocyanines with the mo-





**Figure 10.**  $^{27}\text{Al}$  DOR NMR and  $^{31}\text{P}$  MAS NMR spectra of VPI-5: (a) as-synthesized and (b) after incorporation of FePc (from Ref. 69).

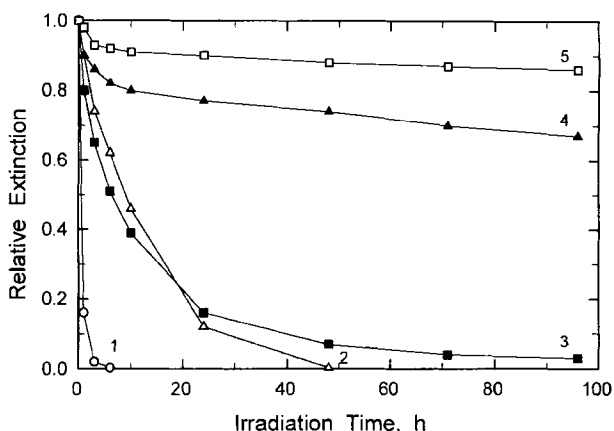
lecular sieve host [69]. For FePc in the aluminophosphate molecular sieve VPI-5,  $^{27}\text{Al}$  double rotation (DOR) spectra and  $^1\text{H}$   $^{27}\text{Al}$  cross polarization (CP) DOR NMR spectra of hydrated and intercalated VPI-5 have been applied (Fig. 10). From the  $^{27}\text{Al}$  line broadening and the CP enhancement of the line intensity in the Pc-intercalated VPI-5 a strong interaction between Al atoms in the pore walls and the protons of encapsulated Pc are deduced. The assumption of a local deformation of the framework by host–guest interaction is supported by the loss of resolution in the  $^{31}\text{P}$  spectrum (Fig. 10).

#### 4.4.2.6 Stability Analysis

The chemical stability of faujasite-encaged metal–phthalocyanines has been studied by thermal analysis under air [70], oxygen, hydrogen, and helium [66]. Under helium the complexes remained stable up to 873 K. Maximum rates of decomposition appear in hydrogen around 700 K, presumably due to catalytically assisted hydrogenolysis, in air around 700 K, related to catalytic self-oxidation, and in oxygen even below 500 K. Consequently, poor stabilities are found in catalytic gas-phase reactions on zeolite-entrapped complexes [70]. In liquid-phase oxidations at relatively low temperatures, e.g. oxidation of ethylbenzene by  $\text{O}_2$  at 409 K, a relatively rapid destruction of the CoPc complex has also been reported [31]. Obviously, oxyfunctionalization reactions of alkanes or alkenes using *t*-butylhydroperoxide or iodosobenzene at room temperature do not significantly affect the stability of zeolite-anchored metal complexes [35, 38].

The strong increase in the photostability of metal–porphyrin compounds upon incorporation into molecular sieves [71] is used to judge on the location of the complex, i.e. at either the external surface or in the voids of the porous mineral crystals (Fig. 11).

**Figure 11.** Stability of zinc(II)-tetrakis(*N*-methylpyridyloxy)-phthalocyanine under irradiation with  $20 \text{ mW cm}^{-2}$  of visible light in air in: (1) DMF, (2) water, (3) adsorbed on the surface of  $\text{AlPO}_4\text{-5}$ , (4) incorporated in  $\text{AlPO}_4\text{-5}$ , and (5) latter sample in vacuum (from Ref. 71).



#### 4.4.2.7 Oxygen Adsorption

Oxygen adsorption is applied to titrate the fraction of  $\text{Co}^{\text{II}}$  ions in the zeolite framework which has been chelated successfully to such complexes exhibiting the capability to bind dioxygen. The oxygen pulse technique has been applied to titrate this fraction for a  $[\text{Co}^{\text{II}}(\text{bipyridine})(\text{terpyridine})]^{2+}\text{-LiY}$  zeolite [72]. Attempts to prepare cobalt complexes of bis(salicylidene)ethylenediamine in faujasite-Y for reversible oxygen uptake [11] failed because the formation of a quadratic-planar chelate is impeded [16]. Reversible uptake of oxygen is successfully realized with cobalt complexes of bis(salicylaldehyde)methyldipropyltriamine (smdpt) in zeolites NaY and NaEMT [16]. The molar ratio bonded  $\text{O}_2$  : total  $\text{Co}^{2+}$  is determined by quantitative evaluation of the EPR signal intensities. Such ratios amounted to 0.25 for  $[\text{Co}^{\text{II}}(\text{smdpt})]\text{-NaEMT}$  and to 0.05 for cobalt complexes of bis(2-pyridinecarboxylaldehyde)ethylendiimide in NaY at room temperature [16, 17]. Presumably, the sorption kinetics is controlled by diffusion processes.

#### 4.4.2.8 Cyclovoltammetry

Recently, cyclovoltammetry was proposed as a method to recognize the preferential location of a zeolite-anchored transition metal complex, i.e. at the external surface of the molecular sieve crystals or encapsulated in the void structure. Moreover, discrimination between different types of accommodation, i.e. physically entrapped or ion-exchanged, is claimed [21]. However, the nature of the electron-transfer processes and the role of the electrolyte cation in the charge compensation are not fully understood and are controversially debated in the literature. Further success in the application of zeolite-encaged complexes for selective electroassisted catalytic reactions requires new strategies to enable ready electron transfer between external electrodes and internal chelates [21].

### 4.4.3 Catalysis by Zeolite-Entrapped Transition Metal Complexes

Zeolite-encapsulated catalytically active transition metal complexes offer a number of advantages over their counterparts in homogeneous solution. General benefits of the heterogenization of homogeneous catalysis are an easy catalyst separation from the reaction medium and the possibility of using a large variety of different solvents and reaction conditions [6–8, 28, 73]. Examples of the advantages introduced by using a microporous zeolite host matrix are the possibility of shape-selective catalysis due to the constrained intrazeolitic environment, a higher catalytic activity, and stability of the encapsulated complexes. The latter arises from the spatial isolation which prevents dimerization of the monomeric complexes and also strongly suppresses an oxidative self-destruction.

Zeolite-encapsulated complexes have also been suggested as model compounds for enzyme mimicking [6, 28]. In this respect, the term “*zeozymes*” (zeolite-based enzyme mimics) has been coined to describe a catalytic system in which the zeolite replaces the protein mantle of the enzyme and the entrapped metal complex (e.g. a metal-phthalocyanine) mimics the active site of the enzyme (e.g. an iron-porphyrin) [6].

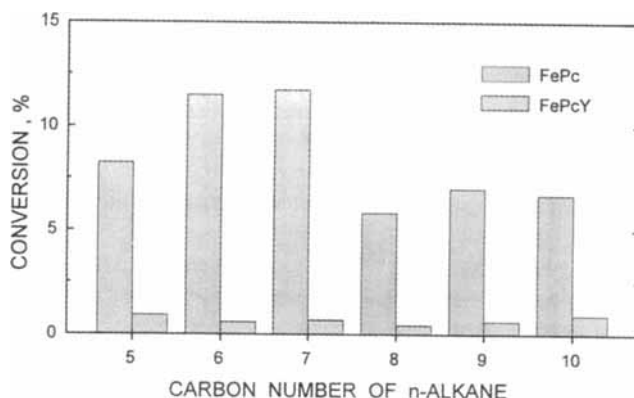
The catalytic properties of zeolite-encapsulated transition metal complexes have been explored in various selective oxidation and hydrogenation reactions. In the former case the choice of the right oxidant was identified as a critical step with respect to catalytic activities and selectivities.

In homogeneously catalyzed oxidations with, for example porphyrins, many different oxygen-supplying reagents have been used (e.g. iodosobenzene, NaClO, KHSO<sub>5</sub>, peracids, perchlorates, organic peroxides, hydrogen peroxide, molecular oxygen) [74]. However, only few of them are useful and practical, especially in combination with zeolite-encapsulated complexes, for the following reasons [7]:

- (i) they are too large to diffuse through the zeolite pores (e.g. certain aromatic peracids);
- (ii) they require a phase-transfer catalyst which, however, is too bulky to enter the pores (as in the case of NaClO);
- (iii) they are too expensive;
- (iv) they are nowadays no longer acceptable under environmental aspects.

For oxidation reactions on zeolite-immobilized complexes, iodosobenzene, organic peroxides (in particular *t*-butylhydroperoxide, TBHP), H<sub>2</sub>O<sub>2</sub>, and O<sub>2</sub> have been used. While iodosobenzene is known as a good oxygen atom donor in homogeneous catalysis because it does not form radicals [74], it has certain disadvantages if used in heterogeneously catalyzed oxidations. The two main drawbacks are reduced reaction rates due to a relatively low mobility in the zeolite pores [12, 35, 36] and the intrazeolitic formation of iodoxybenzene by disproportionation of iodosobenzene [35, 36]. The former leads to relatively fast deactivation of the catalyst due to pore clogging [35, 36]. Therefore, peroxides are nowadays recommended as the preferred oxidants. In this case, however, care has to be taken to minimize the amount of residual (i.e. uncomplexed) metal cations in the zeolite which could induce decomposition of the peroxide [75].

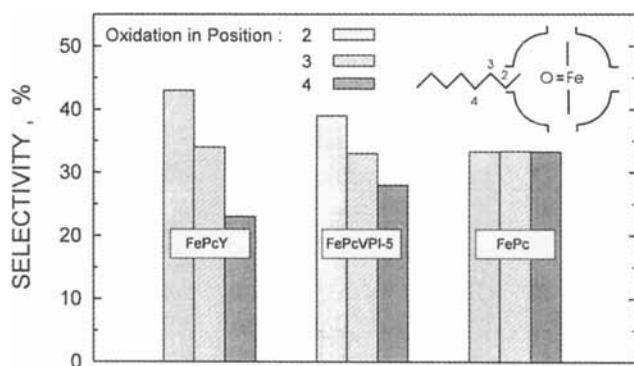
**Figure 12.** Oxidation of the homologous C<sub>5</sub>–C<sub>10</sub> *n*-alkanes on FePc and FePcY under ambient conditions with *t*-butylhydroperoxide as oxygen donor; conversions are given after 2 h of reaction (adapted from Ref. 38).



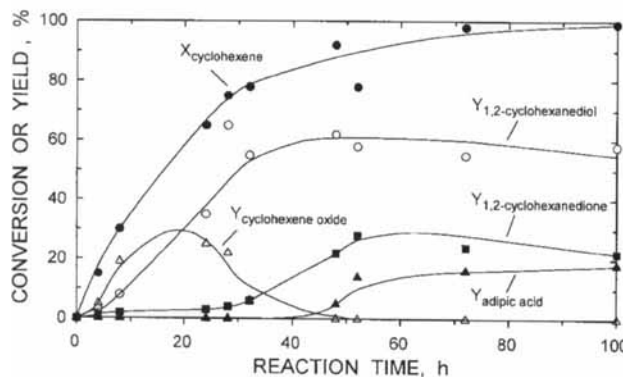
Zeolite-encapsulated iron–phthalocyanine (FePc) complexes are able to catalyze the selective oxidation of alkanes to alcohols and ketones under ambient conditions with iodosobenzene [35, 36] or *t*-butylhydroperoxide [38] as oxygen atom donor. The influence of encapsulation on the catalytic activity of FePc is illustrated in Fig. 12 for the oxidation of a series of homologous *n*-alkanes. It can be seen that free FePc (dissolved in dichloromethane) is much less active than the same complex immobilized in the supercages of zeolite Y. Moreover, whereas the encaged complex remains intact during the reaction, the homogeneous FePc catalyst is completely destroyed, which is indicated by a loss in activity and a colour change from the typical blue-green to light yellow [38]. Turnover numbers (moles of *n*-alkane converted per mol of FePc) between 20 and 30 (depending on the feed alkane) were observed for the free complex, whereas they vary between 180 and 260 for the zeolite-encapsulated FePc. In the latter case, the occurrence of a maximum in activity at C<sub>6</sub>/C<sub>7</sub> has been attributed to an increased reactivity of the alkane with increasing chain length which is superimposed by a decrease of the alkane diffusivity in the zeolite pores [38].

In addition to the differences in activity, interesting selectivity changes are observed upon immobilization of the phthalocyanine complex in a microporous matrix. Examples for reactant shape selectivity, regioselectivity and stereoselectivity have been reported. Herron [36] studied the oxidation of a cyclohexane/cyclododecane (CHx)/(CDo) mixture with iodosobenzene on FePc encaged in zeolite Y. Over free FePc, the bulkier reactant (CDo) is oxidized three times faster than the smaller one (CHx). By contrast, if the complex is encapsulated in zeolite NaY, cyclohexane is preferentially oxidized. This has been attributed to *reactant shape selectivity*: the smaller reactant can reach the encaged complex much more easily than the bulkier cyclododecane, namely the pore size differentiates between molecules of different size. By exchanging the zeolite with cations of increasing size (i.e. K<sup>+</sup>, Rb<sup>+</sup>), the effective pore width is further reduced and the discrimination between reactants of different size is further enhanced [36].

An example of *regioselectivity* is depicted in Fig. 13. Over the free iron–phthalocyanine the oxidation of *n*-octane occurs with equal selectivities in the 2-, 3-, and 4-



**Figure 13.** Regioselectivity in the oxidation of *n*-octane at low conversions over free (FePc) and encapsulated (FePcY and FePcVPI-5) iron-phthalocyanine (after Ref. 76).



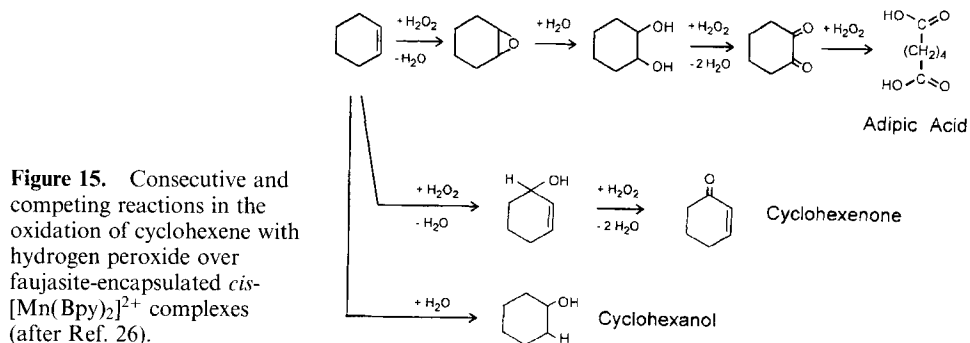
**Figure 14.** Oxidation of cyclohexene with aqueous hydrogen peroxide at 20 °C in the liquid phase on *cis*-[Mn(Bpy)<sub>2</sub>]<sup>2+</sup> encaged in zeolite Y (after Ref. 26).

positions (oxidation in 1-position is not observed) [76]. Encapsulation of the complex in zeolite Y or in the molecular sieve VPI-5 results in the preferred oxidation towards the end of the alkane chain [36, 38, 76]. It is anticipated [36] that the zeolite host structure orients the incoming reactants with respect to the active site in such a manner that oxidation near the end of the chain is favored. This interpretation is supported by the finding that the effect is slightly more pronounced on zeolite Y (cf. Fig. 13) with its smaller window size as compared to the VPI-5 structure.

Examples of *stereoselective oxidations* have been reported by Herron [36]. With either methylcyclohexane or norbornane as reactant, the C–H bond which extends mostly along the molecular axis is preferred for oxidation. In the oxidation of norbornane to norborneols this results in a decrease of the *exo*:*endo* ratio from 9.2 over free FePc to 5.5 on the encapsulated complex. In methylcyclohexane oxidation to 4-methylcyclohexanols, the *trans*:*cis* ratio increases from 1.1 to 2.

Stereoselectivity was also reported in the epoxidation of stilbene. Whereas the *trans* form is preferentially epoxidized over Mnsalen Y [12], FePcY, and Fe(*t*-butyl)PcY [44], *cis*-stilbene is more easily oxidized in homogeneous catalysis.

Other oxidation reactions over zeolite-encapsulated transition metal complexes include the oxidation of CO [77], the direct conversion of methane with oxygen to methanol over ruthenium-, cobalt-, or manganese-phthalocyanines or tetraphen-

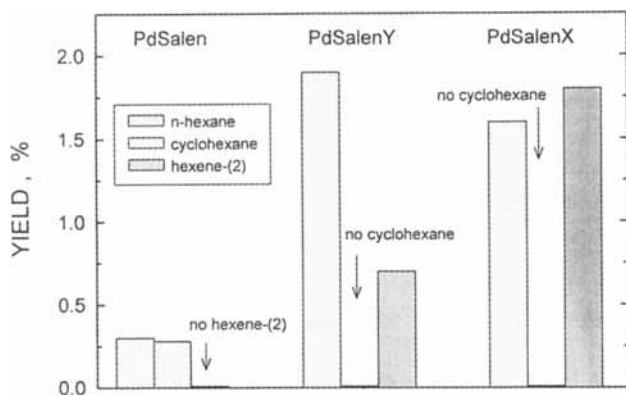


nylporphyrins [50], the oxidation of linear [78, 79] and cyclic [42, 79] alkanes and of hydroquinone to benzoquinone [78] over encapsulated FePc [42, 78] or CoPc [79], oxidation of ethylbenzene in the side chain to 1-phenylethanol and acetophenone over CoPc encaged in zeolites X [31] and EMC-2 [43], and the oxidation of mercaptanes to disulfides over CoPcX [31, 80, 81].

More recently, and from an industrial point of view very attractive, the direct synthesis of adipic acid from cyclohexane or cyclohexene using zeolite-entrapped transition metal complexes was reported. Suitable catalysts are iron-phthalocyanine [82] or *cis*-manganese(II) bis-2,2'-bipyridyl (*cis*-[Mn(Bpy)<sub>2</sub>]<sup>2+</sup>) [26] encapsulated in zeolite Y. Typical experimental results obtained with the latter catalyst in the oxidation of cyclohexene with aqueous hydrogen peroxide are depicted in Fig. 14. The reaction sequence derived from these experiments (Fig. 15) indicates that cyclohexene oxide is the primary oxidation product from cyclohexene. The former is converted by hydration to 1,2-cyclohexanediol and further oxidized to 1,2-cyclohexanedione and adipic acid. In the hydration step as well as in the cleavage of the cyclohexane ring, residual acidity created during the preparation of the encapsulated complex is supposed to assist. Side reactions are the formation of cyclohexenone via allylic oxidation of cyclohexene on uncomplexed Mn<sup>2+</sup> and of cyclohexanol from acid-catalyzed hydration of cyclohexene. Turnover numbers of 460 have been reported for this system [26]. Moreover, the catalyst can be easily regenerated by simple heating to 60 °C. By careful optimization of the catalyst and the reaction conditions, selectivities for adipic acid as high as 80% could be achieved [26]. Although the activity of this catalyst may be still much too low to compete with existing catalytic systems for adipic acid synthesis, it provides interesting prospects for further development.

In an attempt to prepare real zeozymes, an efficient mimic of cytochrome P-450 was successfully developed very recently [83]. It comprises the encapsulation of iron phthalocyanine complexes in the supercages of zeolite Y and embedding this inclusion compound in a polydimethylsiloxane membrane. This system oxidizes alkanes at room temperature at rates comparable to those of the true enzyme. It remains to be seen how this concept can be generalized or transferred to other catalytic systems.

Besides the many examples of oxidation reactions over zeolite-encapsulated transition metal complexes, a few examples of hydrogenation reactions have also



**Figure 16.** Competitive hydrogenation of an equimolar mixture of hexene-1 and cyclohexene over Pd-salen in homogeneous solution and encapsulated in zeolites X and Y (after Ref. 14).

been reported [14, 15, 37, 84, 85]. Shape selectivity effects were observed in the hydrogenation of an equimolar mixture of hexene-1 and cyclohexene over Pd-salen encapsulated in zeolites X and Y [14]. As shown in Fig. 16, both reactants are hydrogenated with comparable rates over the free Pd-salen in homogeneous reaction. Over the encapsulated complex, the linear alkene is still hydrogenated, whereas the cycloalkane is not converted at all. Double-bond isomerization of hexene-1 to hexene-2 occurs over the zeolite catalysts as a side reaction. The effect is more pronounced over the aluminum rich X-type zeolite. Ni-salen encapsulated in zeolite Y was recently reported to also selectively hydrogenate hexene-1 in the presence of cyclohexene [85].

An interesting approach was reported by Kimura et al. [37]. They prepared an electron donor-acceptor complex  $(\text{Na}^+)_4(\text{FePc})^{4-}-\text{NaY}$  from iron-phthalocyanine (FePc) encapsulated in zeolite NaY by reaction with sodium-naphthalene,  $\text{Na}^+$   $(\text{C}_{10}\text{H}_8)^-$ , and this complex gave unusually high ratios of *trans*:*cis*-butene-2 in the selective hydrogenation of butadiene.

Finally, an example of shape selective catalysis in the oligomerization of ethene over certain nickel chelates has been described by Keim [86]. Whereas in homogeneous solution and supported on amorphous carriers much higher carbon numbers are observed, the length of the oligomers could be restricted to  $\text{C}_{20}$  when the complexes were incorporated into a faujasite host matrix.

## References

1. J. H. Lunsford, *Catal. Rev.-Sci. Eng.* **1975**, 12, 137-162.
2. J. H. Lunsford in *Molecular Sieves-II* (Ed.: J. R. Katzer), American Chemical Society Symposium Series, Vol. 40, American Chemical Society, Washington, DC, USA, **1977**, pp. 473-492.
3. W. J. Mortier, R. A. Schoonheydt, *Progr. Solid State Chem.* **1985**, 16, 1-125.
4. G. A. Ozin, C. Gil, *Chem. Rev.* **1989**, 89, 1749-1764.
5. J. H. Lunsford, *Rev. Inorg. Chem.* **1987**, 9, 1-35.
6. R. Parton, D. De Vos, P. A. Jacobs in *Zeolite Microporous Solids: Synthesis, Structure and Reactivity* (Eds: E. G. Derouane, F. Lemos, C. Naccache, F. Ramoa Ribeiro), Kluwer Academic Publishers, Dordrecht, The Netherlands, **1992**, pp. 555-578.

7. D. E. De Vos, F. Thibault-Starzyk, P. P. Knops-Gerrits, R. F. Parton, P. A. Jacobs, *Macromol. Symp.* **1994**, 80, 157–184.
8. B. V. Romanovsky, *Macromol. Symp.* **1994**, 80, 185–192.
9. D. E. De Vos, P. P. Knops-Gerrits, R. F. Parton, B. M. Weckhuysen, P. A. Jacobs, R. A. Schoonheydt, *J. Incl. Phenom.* **1995**, 21, 185–213.
10. J. Weitkamp in *Proceedings from the Ninth International Zeolite Conference* (Eds: R von Ballmoos, J. B. Higgins, M. M. J. Treacy), Butterworth-Heinemann, Boston, **1993**, Vol. 1, pp. 13–45.
11. N. Herron, *Inorg. Chem.* **1986**, 25, 4714–4717.
12. C. Bowers, P. K. Dutta, *J. Catal.* **1990**, 122, 271–279.
13. K. J. Balkus, Jr., A. A. Welch, B. E. Gnade, *Zeolites* **1990**, 19, 722–729.
14. S. Kowalak, R. C. Weiss, K. J. Balkus, Jr., *J. Chem. Soc., Chem. Commun.* **1991**, 57–58.
15. D. E. De Vos, P. A. Jacobs in *Proceedings from the Ninth International Zeolite Conference* (Eds: R. von Ballmoos, J. B. Higgins, M. M. J. Treacy), Butterworth-Heinemann, Boston, **1993**, Vol. 2, pp. 615–622.
16. D. E. De Vos, F. Thibault-Starzyk, P. A. Jacobs, *Angew. Chem., Int. Ed. Engl.* **1994**, 33, 432–433.
17. D. E. De Vos, Ph.D. Thesis, Katholieke Universiteit Leuven, Leuven, Belgium, **1994**.
18. D. E. De Vos, E. J. P. Feijen, R. A. Schoonheydt, P. A. Jacobs, *J. Am. Chem. Soc.* **1994**, 116, 4746–4752.
19. F. Bedioui, L. Roue, J. Devynck, K. J. Balkus, Jr. in *Zeolites and Related Microporous Materials: State of the Art 1994* (Eds: J. Weitkamp, H. G. Karge, H. Pfeifer, W. Hölderich), Studies in Surface Science and Catalysis, Elsevier, Amsterdam, **1994**, Vol. 84B, pp. 917–924.
20. D. E. De Vos, P. P. Knops-Gerrits, D. L. Vanoppen, P. A. Jacobs, *Supramolecular Chemistry*, **1995**, 6, 49–57.
21. F. Bedioui, L. Roué, E. Briot, J. Devynck, S. L. Bell, K. J. Balkus, Jr., *J. Electroanal. Chem.* **1994**, 373, 19–29.
22. H. G. Karge, H. K. Beyer in *Zeolite Chemistry and Catalysis* (Eds: P. A. Jacobs, N. I. Jaeger, L. Kubelková, B. Wichterlová), Studies in Surface Science and Catalysis, Elsevier, Amsterdam, **1991**, Vol. 69, pp. 43–64.
23. W. H. Quale, G. Peeters, G. L. De Roy, E. F. Vansant, J. H. Lunsford, *Inorg. Chem.* **1982**, 21, 2226–2231.
24. W. De Wilde, G. Peeters, J. H. Lunsford, *J. Phys. Chem.* **1980**, 84, 2306–2310.
25. P. P. Knops-Gerrits, D. De Vos, F. Thibault-Starzyk, P. A. Jacobs, *Nature* **1994**, 369, 543–546.
26. P. P. Knops-Gerrits, F. Thibault-Starzyk, P. A. Jacobs in *Zeolites and Related Microporous Materials: State of the Art 1994* (Eds: J. Weitkamp, H. G. Karge, H. Pfeifer and W. Hölderich), Studies in Surface Science and Catalysis, Elsevier, Amsterdam, **1994**, Vol. 84B, pp. 1411–1418.
27. V. Y. Zakharov, B. V. Romanovsky, *Vest. Mosk. Univ., Khim. Ser. 2* **1977**, 18, 143–145.
28. B. V. Romanovsky in *Proc. 8th Int. Congr. Catal.*, Verlag Chemie, Weinheim, **1984**, Vol. 4, pp. 657–667.
29. B. V. Romanovsky, A. G. Gabrielov in *New Developments in Selective Oxidation by Heterogeneous Catalysts* (Eds: P. Ruiz, B. Delmon), Studies in Surface Science and Catalysis, Elsevier, Amsterdam, **1992**, Vol. 72, pp. 443–452.
30. G. Meyer, D. Wöhrle, M. Mohl, G. Schulz-Ekloff, *Zeolites* **1984**, 4, 30–34.
31. G. Schulz-Ekloff, D. Wöhrle, V. Iliev, E. Ignatzek, A. Andreev in *Zeolites as Catalysts, Sorbents and Detergent Builders-Applications and Innovations* (Eds: H. G. Karge, J. Weitkamp), Studies in Surface Science and Catalysis, Elsevier, Amsterdam, **1989**, Vol. 46, pp. 315–325.
32. K. J. Balkus, Jr., J. P. Ferraris, *J. Phys. Chem.* **1990**, 94, 8019–8020.
33. E. Páez-Mozo, N. Gabriunas, F. Lucaccioni, D. D. Acosta, P. Patrono, A. La Ginestra, P. Ruiz, B. Delmon, *J. Phys. Chem.* **1993**, 97, 12819–12827.
34. J. P. Ferraris, K. J. Balkus, Jr., A. Schade, *J. Incl. Phenom.* **1992**, 14, 163–169.
35. N. Herron, G. D. Stucky, C. A. Tolman, *J. Chem. Soc., Chem. Commun.* **1986**, 1521–1522.
36. N. Herron, *J. Coord. Chem.* **1988**, 19, 25–38.
37. T. Kimura, A. Fukuoka, M. Ichikawa, *Catal. Lett.* **1990**, 4, 279–286.



38. R. F. Parton, L. Uytterhoeven, P. A. Jacobs in *Heterogeneous Catalysis and Fine Chemicals II* (Eds: M. Guisnet, J. Barrault, C. Bouchoule, D. Duprez, G. Pérot, R. Maurel, C. Montassier), Studies in Surface Science and Catalysis, Elsevier, Amsterdam, **1991**, Vol. 59, pp. 395–403.
39. Z. Jiang, Z. Xi, *Fenzi Cuihua* **1992**, 6, 467–471; CA 118: 212554p.
40. B. V. Romanovsky, A. G. Gabrielov, *J. Molec. Catal.* **1992**, 74, 293–303.
41. K. J. Balkus, Jr., A. A. Welch, B. E. Gnade, *J. Incl. Phenom.* **1991**, 10, 141–151.
42. R. F. Parton, C. P. Bezoukhanova, F. Thibault-Starzyk, R. A. Reynders, P. J. Grobet, P. A. Jacobs in *Zeolites and Related Microporous Materials: State of the Art 1994* (Eds: J. Weitkamp, H. G. Karge, H. Pfeifer, W. Hölderich), Studies in Surface Science and Catalysis, Elsevier, Amsterdam, **1994**, Vol. 84B, pp. 813–820.
43. S. Ernst, Y. Traa, U. Deeg in *Zeolites and Related Microporous Materials: State of the Art 1994* (Eds: J. Weitkamp, H. G. Karge, H. Pfeifer, W. Hölderich), Studies in Surface Science and Catalysis, Elsevier, Amsterdam, **1994**, Vol. 84B, pp. 925–932.
44. M. Ichikawa, T. Kimura, A. Fukuoka in *Chemistry of Microporous Crystals* (Eds: T. Inui, S. Namba, T. Tatsumi), Studies in Surface Science and Catalysis, Elsevier, Amsterdam, **1991**, Vol. 60, pp. 335–342.
45. A. G. Gabrielov, K. J. Balkus, Jr., S. L. Bell, F. Bedioui, J. Devynck, *Microporous Materials* **1994**, 2, 119–126.
46. F. Bedioui, L. Roué, L. Gaillon, J. Devynck, S. L. Bell, K. J. Balkus, Jr., *Preprints, Div. of Petroleum Chemistry, American Chemical Society* **1993**, 38(No. 3), 529–535.
47. K. J. Balkus, Jr., A. G. Gabrielov, S. L. Bell, F. Bedioui, L. Roué, J. Devynck, *Inorg. Chem.* **1994**, 33, 67–72.
48. R. F. Parton, C. P. Bezoukhanova, J. Grobet, P. J. Grobet, P. A. Jacobs in *Zeolites and Microporous Crystals* (Eds: T. Hattori, T. Yashima), Studies in Surface Science and Catalysis, Elsevier, Amsterdam, **1994**, Vol. 83, pp. 371–378.
49. M. Nakamura, T. Tatsumi, H. Tominaga, *Bull. Chem. Soc. Jpn.* **1990**, 63, 3334–3336.
50. Y.-W. Chan, R. B. Wilson, *Preprints, Div. of Petroleum Chemistry, American Chemical Society* **1988**, 33(3), 453–458.
51. L. A. Rankel, E. W. Valyocsik, US Patent 4 500 503, **1985**, (Mobil Oil Corp.).
52. K. J. Balkus, Jr., S. Kowalak, K. T. Ly, D. C. Hargis in *Zeolite Chemistry and Catalysis* (Eds: P. A. Jacobs, N. I. Jaeger, L. Kubelková, B. Wichterlová), Studies in Surface Science and Catalysis, Elsevier, Amsterdam, **1991**, Vol. 69, pp. 93–99.
53. S. Kowalak, K. J. Balkus, Jr., *Collect. Czech. Chem. Commun.* **1992**, 57, 774–780.
54. K. J. Balkus, Jr., S. Kowalak, PCT Intern. Appl. WO 92/09527, **1992**, (Board of Regents, The University of Texas System).
55. P. S. E. Dai, J. H. Lunsford, *Inorg. Chem.* **1980**, 19, 262–264.
56. K. Mizuno, J. H. Lunsford, *Inorg. Chem.* **1983**, 22, 3483–3486.
57. R. F. Howe, J. H. Lunsford, *J. Am. Chem. Soc.* **1975**, 97, 5156–5159.
58. R. A. Schoonheydt, J. Pelgrims, *J. Chem. Soc. Dalton* **1981**, 914–922.
59. H. Diegruber, P. J. Plath in *Metal Microstructures in Zeolites* (Eds: P. A. Jacobs, N. I. Jaeger, P. Jiru, G. Schulz-Ekloff), Studies in Surface Science and Catalysis, Elsevier, Amsterdam, **1982**, Vol. 12, pp. 23–32.
60. W. Lubitz, C. J. Winscom, H. Diegruber, R. Mösele, *Z. Naturforsch.* **1987**, 42A, 970–986.
61. H. Diegruber, P. J. Plath, *Z. Phys. Chem. (Leipzig)* **1985**, 266, 641–655.
62. L. Edwards, M. Gouterman, *J. Molec. Spectr.* **1970**, 33, 292–310.
63. U. Ahrens, H. Kuhn, *Z. Phys. Chem. (Frankfurt)* **1963**, 37, 1–32.
64. M. Ehrl, F. W. Deeg, C. Bräuchle, O. Franke, A. Sobbi, G. Schulz-Ekloff, D. Wöhrle, *J. Phys. Chem.* **1994**, 98, 47–52.
65. S. V. Gudkov, B. V. Romanovsky, E. S. Shpiro, G. V. Antoshin, Kh. M. Minachev, *Izv. AN SSSR, Ser. Khim.* **1980**, 2448–2451.
66. E. S. Shpiro, G. V. Antoshin, O. P. Tkachenko, S. V. Gudkov, B. V. Romanovsky, Kh. M. Minachev in *Structure and Reactivity of Modified Zeolites* (Eds: P. A. Jacobs, N. I. Jaeger, P. Jiru, V. B. Kazansky, G. Schulz-Ekloff), Studies in Surface Science and Catalysis, Elsevier, Amsterdam, **1984**, Vol. 18, pp. 31–39.
67. Kh. M. Minachev, E. S. Shpiro, *Catalyst Surface: Physical Methods of Studying*, CRC Press, Boca Raton, **1990**, pp. 201–206.

68. J. Strutz, H. Diegruber, N. I. Jaeger, R. Mösel, *Zeolites* **1983**, 3, 102–105.
69. R. F. Parton, C. P. Bezoukhanova, F. Thibault-Starzyk, R. A. Reynders, P. J. Grobet, W. Sun, Y. Wu, P. A. Jacobs, *J. Molec. Catal.*, submitted.
70. H. Diegruber, P. J. Plath, G. Schulz-Ekloff, M. Mohl, *J. Molec. Catal.* **1984**, 24, 115–126.
71. D. Wöhrle, G. Schulz-Ekloff, *Adv. Mater.* **1994**, 4, 875–880.
72. S. Imamura, J. H. Lunsford, *Langmuir* **1985**, 1, 326–330.
73. B. V. Romanovsky, *Acta Phys. Chem.* **1985**, 31, 215–222.
74. B. Meunier, *Chem. Rev.* **1992**, 92, 1411–1456.
75. K.-H. Bergk, F. Wolf, B. Walter, *J. Prakt. Chem.* **1979**, 321, 529–536.
76. R. F. Parton, D. R. C. Huybrechts, Ph. Buskens, P. A. Jacobs in *Catalysis and Adsorption by Zeolites* (Eds: G. Öhlmann, H. Pfeifer, R. Fricke), Studies in Surface Science and Catalysis, Elsevier, Amsterdam, **1991**, Vol. 65, pp. 47–60.
77. B. V. Romanovsky, A. G. Gabrielov, *Mendeleev Commun.* **1991**, 14–17.
78. Á. Zsigmond, F. Notheisz, M. Bartók, J. E. Bäckvall in *Heterogeneous Catalysis and Fine Chemicals III* (Eds: M. Guisnet, J. Barbier, J. Barrault, C. Bouchoule, D. Duprez, G. Pérot, C. Montassier), Studies in Surface Science and Catalysis, Elsevier, Amsterdam, **1993**, Vol. 78, pp. 417–424.
79. E. Pérez-Mozo, N. Gabriunas, R. Maggi, D. Acosta, P. Ruiz, B. Delmon, *J. Molec. Catal.* **1994**, 91, 251–258.
80. U. Hündorf, A. Andreev, L. Petrov, V. Iliev, M. Vassileva, V. Ivanova, A. Elias, L. Prahov, D. Wöhrle, D. Shopov in *Proc. 6th Intern. Symp. Heterog. Catal.* (Eds: D. Shopov et al.), Publishing House of the Bulgarian Academy of Sciences, Sofia, **1987**, Vol. 2, pp. 73–77.
81. G. Schulz-Ekloff, D. Wöhrle, A. Andreev, *Wiss. Z. Technische Hochschule Leuna-Merseburg* **1990**, 32, 649–656.
82. F. Thibault-Starzyk, R. F. Parton, P. A. Jacobs in *Zeolites and Related Microporous Materials: State of The Art 1994* (Eds: J. Weitkamp, H. G. Karge, H. Pfeifer and W. Hölderich), Studies in Surface Science and Catalysis, Elsevier, Amsterdam, **1994**, Vol. 84B, pp. 1419–1424.
83. R. F. Parton, I. F. J. Vankelecom, M. J. A. Casselman, C. P. Bezoukhanova, J. B. Uytterhoeven, P. A. Jacobs, *Nature* **1994**, 370, 541–544.
84. A. N. Zakharov, *Mendeleev Commun.* **1991**, 80–81.
85. D. Chatterjee, H. C. Bajaj, A. Das, K. Bhatt, *J. Molec. Catal.* **1994**, 92, L235–L238.
86. W. Keim in *Homogeneous and Heterogeneous Catalysis* (Eds: Yu. Yermakov, V. Likholobov), VNU Science Press, Utrecht, The Netherlands, **1986**, pp. 499–507.

## 4.5 Supported Catalysts from Chemical Vapor Deposition and Related Techniques

Y. IWASAWA

### 4.5.1 Chemical Vapor Deposition Process

According to IUPAC recommendations [1], deposition taking place by adsorption or reaction from the gas phase is called chemical vapor deposition (CVD). The term CVD is generally used without restriction as to the mode or mechanism of deposition in the field of catalyst precursors. As reviewed in the pioneer work of Powell, Oxley and Blocher [2], the first practical use of CVD was developed in the 1880s in

68. J. Strutz, H. Diegruber, N. I. Jaeger, R. Mösel, *Zeolites* **1983**, 3, 102–105.
69. R. F. Parton, C. P. Bezoukhanova, F. Thibault-Starzyk, R. A. Reyniers, P. J. Grobet, W. Sun, Y. Wu, P. A. Jacobs, *J. Molec. Catal.*, submitted.
70. H. Diegruber, P. J. Plath, G. Schulz-Ekloff, M. Muhl, *J. Molec. Catal.* **1984**, 24, 115–126.
71. D. Wöhrle, G. Schulz-Ekloff, *Adv. Mater.* **1994**, 4, 875–880.
72. S. Imamura, J. H. Lunsford, *Langmuir* **1985**, 1, 326–330.
73. B. V. Romanovsky, *Acta Phys. Chem.* **1985**, 31, 215–222.
74. B. Meunier, *Chem. Rev.* **1992**, 92, 1411–1456.
75. K.-H. Bergk, F. Wolf, B. Walter, *J. Prakt. Chem.* **1979**, 321, 529–536.
76. R. F. Parton, D. R. C. Huybrechts, Ph. Buskens, P. A. Jacobs in *Catalysis and Adsorption by Zeolites* (Eds: G. Öhlmann, H. Pfeifer, R. Fricke), Studies in Surface Science and Catalysis, Elsevier, Amsterdam, **1991**, Vol. 65, pp. 47–60.
77. B. V. Romanovsky, A. G. Gabrielov, *Mendeleev Commun.* **1991**, 14–17.
78. A. Zsigmond, F. Notheisz, M. Bartók, J. E. Bäckvall in *Heterogeneous Catalysis and Fine Chemicals III* (Eds: M. Guisnet, J. Barbier, J. Barrault, C. Bouchoule, D. Duprez, G. Pérot, C. Montassier), Studies in Surface Science and Catalysis, Elsevier, Amsterdam, **1993**, Vol. 78, pp. 417–424.
79. E. Páez-Mozo, N. Gabriunas, R. Maggi, D. Acosta, P. Ruiz, B. Delmon, *J. Molec. Catal.* **1994**, 91, 251–258.
80. U. Hündorf, A. Andreev, L. Petrov, V. Iliev, M. Vassileva, V. Ivanova, A. Elias, L. Prahov, D. Wöhrle, D. Shopov in *Proc. 6th Intern. Symp. Heterog. Catal.* (Eds: D. Shopov et al.), Publishing House of the Bulgarian Academy of Sciences, Sofia, **1987**, Vol. 2, pp. 73–77.
81. G. Schulz-Ekloff, D. Wöhrle, A. Andreev, *Wiss. Z. Technische Hochschule Leuna-Merseburg* **1990**, 32, 649–656.
82. F. Thibault-Starzyk, R. F. Parton, P. A. Jacobs in *Zeolites and Related Microporous Materials: State of The Art 1994* (Eds: J. Weitkamp, H. G. Karge, H. Pfeifer and W. Hölderich), Studies in Surface Science and Catalysis, Elsevier, Amsterdam, **1994**, Vol. 84B, pp. 1419–1424.
83. R. F. Parton, I. F. J. Vankelecom, M. J. A. Casselman, C. P. Bezoukhanova, J. B. Uytterhoeven, P. A. Jacobs, *Nature* **1994**, 370, 541–544.
84. A. N. Zakharov, *Mendeleev Commun.* **1991**, 80–81.
85. D. Chatterjee, H. C. Bajaj, A. Das, K. Bhatt, *J. Molec. Catal.* **1994**, 92, L235–L238.
86. W. Keim in *Homogeneous and Heterogeneous Catalysis* (Eds: Yu. Yermakov, V. Likholobov), VNU Science Press, Utrecht, The Netherlands, **1986**, pp. 499–507.

## 4.5 Supported Catalysts from Chemical Vapor Deposition and Related Techniques

Y. IWASAWA

### 4.5.1 Chemical Vapor Deposition Process

According to IUPAC recommendations [1], deposition taking place by adsorption or reaction from the gas phase is called chemical vapor deposition (CVD). The term CVD is generally used without restriction as to the mode or mechanism of deposition in the field of catalyst precursors. As reviewed in the pioneer work of Powell, Oxley and Blocher [2], the first practical use of CVD was developed in the 1880s in

the production of incandescent lamps to improve the strength of filaments by carbon or metal deposition [2]. In the same decade, the carbonyl nickel process was developed by Mond and others. A number of patents were issued during that period covering the basis of CVD [3].

The technique has grown very rapidly since the mid 1970s and applications of this fabrication process are now key elements in many industrial products, such as semiconductors, optoelectronics, optics, cutting tools, refractory fibers, filters, corrosion applications, and many others [4]. It is a very versatile process also for the production of catalytic materials. CVD is a relatively simple and flexible technology which can accommodate many variations. With CVD, it is possible to deposit target species on the materials with almost any shape of almost any size, and it is also possible to produce almost any metal and nonmetallic material as well as compounds such as oxides, carbides, nitrides, intermetallics and many others [4]. Conversely, CVD has several disadvantages, a major one being the requirement of having chemical precursors with high vapor pressure which are often hazardous and at times extremely toxic. The byproducts of these precursors are also toxic and corrosive and must be neutralized, which may be a costly operation.

The chemical reactions used in CVD, besides adsorption, are numerous and include thermal decomposition (pyrolysis), hydrolysis, disproportionation, reduction, oxidation, carburization, and nitridization. They can be used either singly or in combination [4]. A CVD reaction is governed by both thermodynamics and kinetics. The reaction between gaseous methyltrimethoxysilane and the surface silanol groups on silica was studied in the temperature range 363–493 K, using IR to measure the changes with time in the surface silanol concentration [5], where the OH groups on SiO<sub>2</sub> react monoenergetically. Hexamethyldisilazane is widely used for deactivating gas chromatographic support materials [6]. Material properties affected by CVD are chemical ones such as catalysis, diffusion, corrosion, etc. and physical ones such as surface area, pore size, and pore volume.

### 4.5.2 CVD Precursors

The choice of the proper reactants (the precursors) is very important. These precursors fall into several general major groups which are the halides, carbonyls, organometallics, and hydrides. The choice of a precursor is governed by certain general characteristics which can be summarized as follows [4]:

- (i) stability at room temperature;
- (ii) sufficient volatility at low temperature, to facilitate its transportation to the reactor;
- (iii) capability of being produced in a very high degree of purity;
- (iv) ability to react cleanly on or with the support;
- (v) ability to react without producing side reactions or parasitic reactions.

Typical precursors are listed in Table 1 [4]. The metal carbonyls are a large and very important group of compounds which are used widely in the chemical industry,

**Table 1.** Properties of CVD precursors.

Precursors	m.p. (K)	b.p. (K)	Notes
Co <sub>2</sub> (CO) <sub>8</sub>	324	325(dec)	orange monoclinic crystals
Cr(CO) <sub>6</sub>	437	453(dec)	white octahedral crystals
Fe(CO) <sub>5</sub>	253	376	yellow liquid
Mn <sub>2</sub> (CO) <sub>10</sub>	426	–	stable in air (dark)
Mo(CO) <sub>6</sub>	423	453(dec)	white octahedral crystals
Ni(CO) <sub>4</sub>	248	316	colorless liquid
Os <sub>3</sub> (CO) <sub>12</sub>	403(1.33 Pa; subl.)	–	yellow monoclinic crystals
Re <sub>2</sub> (CO) <sub>10</sub>	443(dec)	343(13.3 Pa)	colorless monoclinic crystals
Ru <sub>3</sub> (CO) <sub>12</sub>	423	dec	orange monoclinic crystals
V(CO) <sub>5</sub>	338	dec	unstable octahedral crystals
W(CO) <sub>6</sub>	442	dec	white octahedral crystals
Ir(CO) <sub>2</sub> Cl <sub>2</sub>	413(dec)	–	colorless needles
Os(CO) <sub>3</sub> Cl <sub>2</sub>	543	553(dec)	colorless crystals
Rh <sub>2</sub> Cl <sub>2</sub> (CO) <sub>4</sub>	373(dec)	353(133 Pa; subl.)	orange-red cubic crystals
RhCl <sub>2</sub> RhO(CO) <sub>3</sub>	398(subl)	–	ruby-red needles
Pt(CO)Cl <sub>2</sub>	468	573(dec)	subl. in CO <sub>2</sub> at 513 K
Pt(CO) <sub>2</sub> Cl <sub>2</sub>	415	483	subl. in CO <sub>2</sub> at 483 K
BCl <sub>3</sub>	166	286	colorless
MoCl <sub>5</sub>	467	541	monoclinic green-black crystals
NbCl <sub>5</sub>	478	527	monoclinic yellow crystals
TiCl <sub>4</sub>	248	409	pale yellow liquid
VCl <sub>4</sub>	245	422	red-brown liquid
ZrCl <sub>4</sub>	710(subl)	604	colorless monoclinic crystals
CrCl <sub>2</sub> O <sub>2</sub>	177	390	dark red powder
VCl <sub>3</sub> O	194	400	yellow liquid
Al(C <sub>2</sub> H <sub>5</sub> ) <sub>3</sub>	215	467	colorless liquid
B(C <sub>2</sub> H <sub>5</sub> ) <sub>2</sub>	285	467	colorless liquid
In(CH <sub>3</sub> ) <sub>3</sub>	361	407	226 Pa/293 K
Sn(CH <sub>3</sub> ) <sub>4</sub>	219	351	colorless
Sb(C <sub>2</sub> H <sub>5</sub> ) <sub>3</sub>	<244	433	colorless liquid
Zn(CH <sub>3</sub> ) <sub>2</sub>	231	319	165 hPa/273 K
Ba(acac) <sub>2</sub>	>593	–	crystalline
Cr(acac) <sub>3</sub>	489	613	red-purple monoclinic crystals
Cu(acac) <sub>2</sub>	503(dec)	473(133 Pa; subl)	blue monoclinic crystals
Fe(acac) <sub>3</sub>	448–456	–	orange powder
Ga(acac) <sub>3</sub>	468	413(133 hPa; subl)	colorless
In(acac) <sub>3</sub>	459	–	cream powder
Ni(acac) <sub>2</sub>	501	–	pale green powder
Sm(acac) <sub>3</sub>	419	–	yellow powder
Pt(acac) <sub>2</sub>	524	–	pale yellow powder
Zr(acac) <sub>4</sub>	445	468(dec)	white crystals
B(OC <sub>2</sub> H <sub>5</sub> ) <sub>3</sub>	188	390	colorless liquid
Sb(OC <sub>2</sub> H <sub>5</sub> ) <sub>3</sub>	–	368(15 hpa)	colorless liquid
Si(OC <sub>2</sub> H <sub>5</sub> ) <sub>4</sub>	196	439	colorless liquid
Ti(OC <sub>2</sub> H <sub>5</sub> ) <sub>4</sub>	–	395(133 Pa)	colorless liquid
Zr(OC <sub>2</sub> H <sub>5</sub> ) <sub>4</sub>	445	508(666 Pa)	white powder
Cu(CH <sub>3</sub> COO)	543(subl)	573(dec.)	colorless monoclinic crystals
Mo <sub>2</sub> (CH <sub>3</sub> COO) <sub>4</sub>	573(subl, vac)	–	yellow crystal
Sn(CH <sub>3</sub> COO) <sub>2</sub>	455	513	colorless rhombic crystals
Fe(C <sub>5</sub> H <sub>5</sub> ) <sub>2</sub>	446	522	subl >393, orange monoclinic crystals
Zr(C <sub>5</sub> H <sub>5</sub> ) <sub>2</sub> Cl <sub>2</sub>	520	423–453(subl)	colorless triclinic crystals
Re <sub>2</sub> O <sub>7</sub>	570	523(subl)	yellow hexagonal crystals

dec = decomposed; subl = sublimed; vac = under vacuum.

particularly in the preparation of heterogeneous catalysts. Although only a few are presently used in CVD, many are being investigated as they constitute an interesting and potentially valuable source of precursor materials. The organometallics are relative newcomers as commercially attractive CVD precursors. A branch of CVD known as metallo-organic (i.e. organometallic) CVD (MOCVD) is used extensively in semiconductor and optoelectronic applications [7]. Snyder et al. developed an impinging jet reactor for MOCVD to deposit cadmium telluride [8].

### 4.5.3 CVD Application

The equipment used for CVD application is relatively simple, does not require ultrahigh vacuum, and can generally be adapted to many process variations. Its flexibility is such that many changes in composition during deposition and codeposition of compounds are readily achieved. A CVD reaction can occur in one of two basic systems: the closed reactor or the open reactor, as shown in Fig. 1. The closed reactor system was the first type to be used for the purification of metals. As the name implies, the chemicals (solid at room temperature) are loaded in a reactor, in which the supports have been pretreated, which is then closed. CVD takes place upon heating to vaporize the chemicals with stirring. More conveniently, vapor precursors are used, which are easier to handle. The precursor vapor is directly interacted with pretreated supports in the reactor. In open reactor CVD or flowing gas CVD, the gaseous reactants are introduced continuously and flow through the reactor at given temperatures.

Many workers have successfully expressed the flow dynamics and mass transport processes mathematically and obtained realistic models that could be used to predict the operational characteristics of a CVD system and assist in the design of reactors [9, 10]. These models define the complex entrance effects and convection phenomena that occur in a reactor and solve the complete equations of heat, mass balance, and momentum. However, such matters are of less importance in the case of catalyst preparation, which also involve the adsorption and reaction of precursors and subsequent chemical treatments.

### 4.5.4 CVD Catalysts

Surface bonding through impregnation is one of the elementary wet techniques for supporting transition metal salts and complexes on inorganic supports. Another preparative method utilizes the volatile nature of metal carbonyls, halides,  $\beta$ -diketonates, alkoxides, acetates, organic complexes, etc. Thus, these precursors may be vapor-deposited or sublimed onto the support at a given temperature in a closed system or in a flow of inert gas.

#### 4.5.4.1 Nickel

The Nickel carbonyl CVD process was the first step in surface fabrication of advanced materials to have an impact in industrial processes [2, 3]. Parkyns proposed

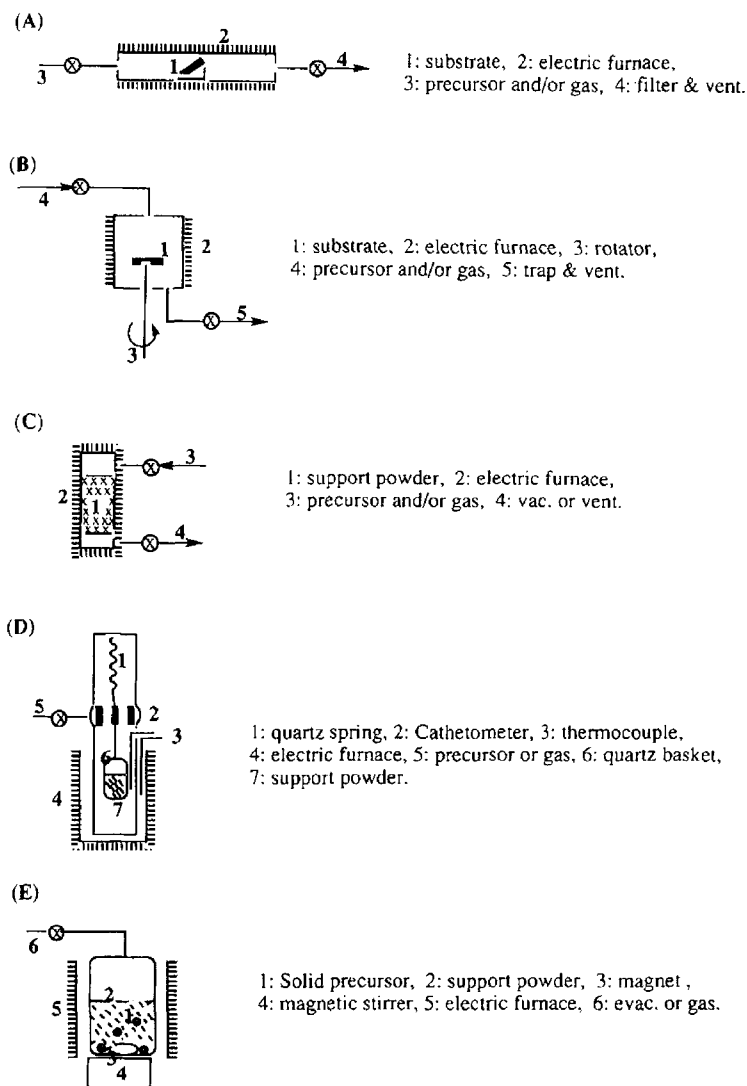


Figure 1. Typical experimental apparatus for CVD.

that, at room temperature  $\text{Ni}(\text{CO})_4$  initially physically adsorbs on alumina, then decomposes upon evacuation to small carbonylated metal clusters [11]. On partially dehydroxylated alumina,  $\text{Ni}(\text{CO})_4$  vapor reacts with the surface to form adsorbed  $\text{Ni}(\text{CO})_3$  at 298–323 K. Subsequent heating of this material to 373 K results in further decarbonylation and agglomeration of nickel. Dispersion of metallic nickel was maximized by isothermally decomposing the carbonyl in vacuo at 623 K followed by passivation in an atmosphere nitrogen with traces of oxygen. Such catalysts were found effective for benzene hydrogenation 333–373 K [12].

$\text{Ni}(\text{CO})_4$  vapor was introduced with  $\text{N}_2$  carrier into a fluidized bed of active car-

bon granules and adsorbed at 323 K or 453 K; it was then decomposed at 523 K in the  $N_2$  atmosphere. The catalysts were subjected to the reaction without any additional treatment. The vapor phase carbonylation of methanol produced mainly methyl acetate. No difference in activity arising from the preparation methods was observed, although the size of nickel metal particles prepared by CVD was much larger than those prepared by impregnation. It is suggested that any nickel loaded on the catalyst was converted into a kind of active species on the surface of active carbon during the reaction [13].

Supported nickel catalysts,  $NiO/SiO_2$ , were prepared by CVD using the system  $NiCl_2 + SiCl_4 + O_2 + H_2$ . The catalysts obtained were applied to methanation and their activity was related to lattice strain of  $NiO$  particles, showing an optimum lattice strain, although the catalytic reaction takes place on  $Ni$  metallic sites [14].

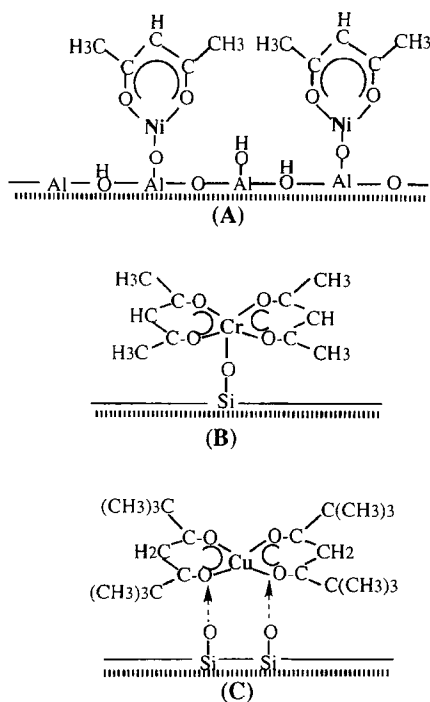
A series of  $Ni/Al_2O_3$  catalysts were prepared from the vapor phase by atomic layer epitaxy (ALE) [15]. ALE was originally a method for growing single crystals and thin films [16]. However, ALE can be classified as a special mode of CVD, since strict demands are made upon the conditions under which the gas–solid reactions are carried out. In ALE the surface is saturated with the volatile reactant, and decomposition and condensation of the reactant are prevented by a suitable choice of reaction conditions [17, 18]. The use of metal halides, oxychlorides,  $\beta$ -diketonates, metal alkoxides, and acetates has been described in ALE catalyst processing [17].

The interaction between  $Ni(acac)_2$  and alumina was restricted to chemisorption by the proper choice of reaction temperature. Nickel, brought into contact with alumina during the first preparation sequence, bonds with the heterogeneous surface (Fig. 2(A)) but retains one acetylacetonate ligand [19]. The size of these species mainly influenced the saturation level [19]. These nickel species, the so-called nucleation centers, are atomically dispersed but catalytically inactive since they interact strongly with the alumina. The chemical nature of the nickel species was changed by removing the ligands with air at elevated temperatures at the end of each sequence. During the 2–4 sequences (5–10 wt %  $Ni$ ), nickel grows on the nucleation centers but also to some extent on unoccupied sites on the support, as characterized by low-energy ion scattering spectroscopy (ISS) and by catalytic activity as a function of the number of preparation sequences. The catalytic hydrogenation of toluene to methylcyclohexane was examined on the  $Ni/Al_2O_3$  catalysts obtained. The reactor was operated at atmospheric pressure and at  $\approx 448$  K at a hydrogen:toluene molar ratio of  $\approx 3:1$  of [15]. During the 6–10 sequences (10–20 wt %) both the ISS signal and the activity remain relatively constant, since nickel is growing on nickel. Thus, the highest activity in the hydrogenation of toluene was obtained at a nickel loading of  $\approx 10$  wt % [15].

#### 4.5.4.2 Chromium

Banks used  $Cr(CO)_6$  on alumina or silica-alumina to polymerize ethene at 394–400 K [20, 21]. Brenner et al. noted that  $Cr(CO)_6/Al_2O_3$  can be used to hydrogenate propene, with maximum activity being observed at 468 K [22].





**Figure 2.** Proposed surface structures of the supported species: (A)  $\text{Ni}(\text{acac})_2$ ; (B)  $\text{Cr}(\text{acac})_3$ ; (C)  $\text{Cu}(\text{DPM})_2$ .

$\text{NaX}$  and  $\text{LiX}$  (57% ion-exchanged) zeolites were used as the support for  $\text{Cr}(\text{CO})_6$ . After evacuation at 673 K for 1 h, zeolite (12–40 mg) in a reactor was exposed to a  $\text{Cr}(\text{CO})_6$  vapor at room temperature of 1 h, giving a  $\text{Cr}(\text{CO})_6$  loading of 2.2 per supercage of zeolite by means of chemical analysis [23]. Tricarbonyl chromium(0) species encaged in  $\text{LiX}$  or  $\text{NaX}$  were found to be highly efficient and stereoselective for the hydrogenation of butadiene above 230 K. A reaction mechanism was proposed in which *cis*-2-butene is formed via  $(\eta^4\text{-C}_4\text{H}_6)\text{Cr}(\text{CO})_3$ , whereas 1-butene forms via  $(\eta^2\text{-C}_4\text{H}_6)\text{Cr}(\text{CO})_3$  and  $(\eta^2\text{-C}_4\text{H}_6)_2\text{Cr}(\text{CO})_3$  [23].

By adsorption measurements and  $^1\text{H}$  MAS NMR,  $\text{Cr}(\text{acac})_3$  was found to be selectively chemisorbed to silica through reaction with isolated OH groups, leading to release of one acac ligand. Surface complex of chromium is proposed in Fig. 2(B) [24]. The mode of interaction of  $\text{Cr}(\text{acac})_2$  with support differs from that of  $\text{Ni}(\text{acac})_2$  and  $\text{Cu}(\text{DPM})_2$  (DPM=dipivaloylmethanate), Fig. 2(C) [25].

#### 4.5.4.3 Copper and Calcium

Copper dipivaloylmethanate  $\text{Cu}(\text{DPM})_2$  or calcium dipivaloylmethanate  $\text{Ca}(\text{DPM})_2$ , were evaporated at 353 K or 483 K, respectively, onto  $\text{SiO}_2$ . The adsorption of the two different metal complexes is similar and the central metal atoms are stable only when the ligand is coordinated. The IR bands of the adsorbed species resemble those of dipivaloylmethane. Thus it was concluded that the ad-

sorption originates from the interaction between the ligand and the surface OH groups, and is not related to the central metal atom (Fig. 2(C)) [25].

#### 4.5.4.4 Iron

Iron carbonyls interact with inorganic oxide surfaces through oxidative addition of acidic or amphoteric OH groups and acid–base reaction through coulombic interaction. The details of this chemistry have been reviewed in the literature [12, 26–29].

Nagy et al. used thermal and photochemical decomposition of  $\text{Fe}(\text{CO})_5$  adsorbed in HY zeolite to form highly dispersed iron particles [30]. Photochemical decomposition gave smaller particles because of the strong carbonyl–surface interaction, arising from electronic excitation of the carbonyl during decomposition.

A new Fe carbonyl cluster  $\text{Fe}_3(\text{CO})_6$  was prepared by CVD of  $\text{Fe}_3(\text{CO})_{12}$  on  $\text{SiR}_x/\text{SiO}_2$  [31]. Modification of the  $\text{SiO}_2$  surface was carried out by reacting  $\text{SiO}_2$  with  $\text{SiCl}_2\text{R}_2$  and  $\text{SiCl}_3\text{R}$  ( $\text{R}=\text{CH}_3$ ,  $\text{C}_6\text{H}_5$ ) at 343 K, followed by heating up to 473 K in vacuum. The samples obtained were exposed to water vapor at 293 K, followed by evacuation at 473 K in order to convert the remaining Si–Cl to Si–OH for condensation among the surface Si species to form Si–O–Si linkages. The modified  $\text{SiO}_2$  supports thus obtained are denoted  $\text{SiR}_x/\text{SiO}_2$ . The amounts of alkyl ligand present were determined by chemical analysis of carbon on  $\text{SiO}_2$ .  $\text{Fe}_3(\text{CO})_{12}$  was deposited onto the  $\text{SiR}_x/\text{SiO}_2$  surface using CVD at room temperature under vacuum. To complete the reaction the sample was further treated at 313 K under vacuum. The deposited Fe species has the composition  $\text{Fe}_3(\text{CO})_6$ , which showed an Fe–Fe distance of 0.273 nm by EXAFS analysis. This is longer than in  $\text{Fe}_3(\text{CO})_{12}$  (0.262 nm) and in Fe metal (0.248 nm). When the  $\text{Fe}_3(\text{CO})_6/\text{SiR}_x/\text{SiO}_2$  catalyst was heated at 368 K in vacuum, the Fe cluster showed a higher activity by a factor of 200 than for the Fe species on  $\text{SiO}_2$ , for propene hydrogenation [31].

#### 4.5.4.5 Molybdenum

##### A Molybdenum Carbonyls

Since the finding of Banks and Bailey in 1964 that  $\text{Mo}(\text{CO})_6/\text{Al}_2\text{O}_3$  activates the metathesis reaction [32, 33], many metal carbonyls have been used to prepare improved catalytic materials [12, 27]. In 1969, Davie et al. presented preliminary results from an IR spectroscopic investigation of the nature of  $\text{Mo}(\text{CO})_6$  surface bonded to alumina [34]. They noted that treatment for 1 h under vacuum at 373 K was required for propene metathesis activity. Howe et al. found that activation of supported  $\text{Mo}(\text{CO})_6$  catalysts involved carbonyl decomposition, the extent of which was a function of the basicity of support hydroxy groups [35]. Brenner and Burwell [36] proposed the species  $\text{Mo}(\text{CO})_5$ ,  $\text{Mo}(\text{CO})_4$ , and  $\text{Mo}(\text{CO})_3$ , obtained in Mo carbonyl decomposition (Scheme 1), the component  $\text{Mo}(\text{CO})_3$  being metathesis-active. This species was found to adsorb one molecule of oxygen at 298 K, ejecting a molecule of carbon monoxide to form adsorbed  $\text{Mo}(\text{CO})_2\text{O}_2$ , a species 15 times more active for metathesis than adsorbed  $\text{Mo}(\text{CO})_3$ . Brenner and Burwell demonstrated

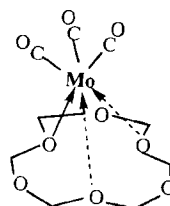
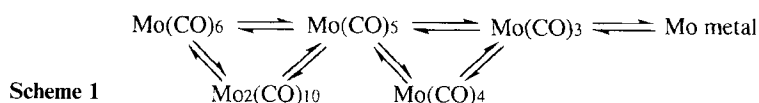
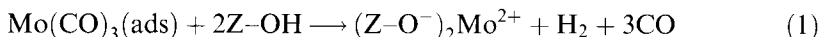


Figure 3. Proposed structure of supported  $\text{Mo(CO)}_3(\text{ads})$  on NaY-zeolite.

that the same subcarbonyl species formed during decarbonylation can react further with surface hydroxy groups ( $\text{Z-OH}$ ) to evolve hydrogen with metal oxidation [37]:



Surface-bonded  $\text{Mo(CO)}_6$  exhibits greater activity for alkene hydrogenation than conventional  $\text{MoO}_3/\text{Al}_2\text{O}_3$  catalysts [22].

Zeolites, among the inorganic oxides, are expected to provide matrices for the formation of uniform catalytic species due to their regular structures. It has been demonstrated that  $\text{Mo(CO)}_6$  encaged in Y-type zeolites show very high activities for a stereoselective hydrogenation of butadiene or *trans*-1,3-pentadiene to the corresponding *cis*-2-alkene [38, 39]. The structure and electronic state of thermally stable molybdenum subcarbonyl species entrapped in Y- and X-type zeolites were studied using EXAFS, XPS, and IR techniques. No Mo–Mo bonding was observed, suggesting a monomeric form. The  $\nu(\text{CO})$  band consists of three peaks at 1911(s), 1790(s), and 1760(sh)  $\text{cm}^{-1}$  for the NaY system. The IR spectra for LiY, CsY, and other NaY zeolites were very similar except for the wavenumbers. The IR peaks suggest a monomeric  $\text{Mo(CO)}_3(\text{OZ})_3$  ( $\text{OZ}$ =zeolite framework oxygen) has a *fac* rather than a *mer* configuration, as shown in Fig. 3 [38, 39].

$\text{Mo(CO)}_6$  entrapped in NaY zeolite was oxidized with molecular oxygen by UV irradiation at room temperature or by thermal treatment at 343–373 K. Both oxidation procedures resulted in the identical molybdenum (VI) oxide, this being a molybdenum dimer species with Mo–Mo distance 0.321 nm. The Mo–Mo bonding of the oxide species was degraded on evacuation at 673 K, while it was considerably stable in the presence of gaseous oxygen [40].

It has been shown that zeolite NaY adsorbs two  $\text{Mo(CO)}_6$  molecules per supercage on exposure to the vapor at room temperature, and that subsequent heating to 473 K causes complete decarbonylation, producing an average loading of two Mo atoms per supercage [39, 41]. EXAFS and  $^{129}\text{Xe}$  NMR data are presented which show that adsorption of  $\text{Mo(CO)}_6$  in zeolite NaY followed by decomposition at 473 K produces uniformly dispersed  $\text{Mo}_2$  clusters in the zeolite supercages. These have an Mo–O distance of 0.21 nm with a coordination number of 1.8, and an Mo–Mo distance of 0.28 nm with a coordination number of 1.0. The Mo–Mo distance only slightly exceeds that in the bulk metal (0.272 nm). XPS measurements

have shown that the Mo 3d binding energy for the product of  $\text{Mo(CO)}_6$  decomposition in NaY is 1.2 eV higher than that of the bulk metal. This binding energy shift was attributed to the small size of zerovalent Mo clusters, but the observation of an Mo–O bond by EXAFS suggests that there may be some charge transfer to zeolite framework oxygen through the chemical bonds. The Mo–Mo coordination number of 1.0 proves conclusively that the initial distribution of two Mo atoms per supercage, determined by the adsorption capacity for  $\text{Mo(CO)}_6$ , is maintained following decarbonylation at 473 K [41].

Molybdenum sulfide catalysts were prepared from  $\text{Mo(CO)}_6$  encaged in zeolites and characterized by XPS, IR and NO adsorption. After evacuation at 673 K for 1–2 h, the powdered zeolite was exposed to  $\text{Mo(CO)}_6$  vapor ( $\approx 8$  Pa) at room temperature for 16 h [42]. The sample was subsequently evacuated at 373 K for 1 h to yield molybdenum subcarbonyl species encaged in the zeolite. Hydrogen sulfide ( $\approx 6.5$  kPa) was introduced to the subcarbonyl species at 373 K for 1 h, followed by evacuation at the same temperature. On contact with  $\text{H}_2\text{S}$ , the orange molybdenum species turned dark brown in color. The sample was then evacuated at 673 K for 1 h. On the basis of IR, TPD, and XPS results, the subcarbonyl species  $\text{Mo(CO)}_3$  was shown to have formed the complex  $\text{Mo(CO)}_3(\text{SH})$ , by reaction with  $\text{H}_2\text{S}$  at room temperature.

The molybdenum catalyst thus prepared was used for the hydrodesulfurization (HDS) of thiophene at 673 K [42]. The CVD catalyst showed a higher catalytic activity per Mo for HDS of thiophene than a molybdenum sulfide catalyst prepared by impregnation procedures. A steady decrease in the turnover frequency (TOF) for the catalysts with similar dispersions as a function of the O(1s) binding energy cannot be interpreted solely in terms of the dispersion. In zeolite systems, diffusion limitations of the reactant and products may operate, in addition to structure effects, because of the small pore size of the zeolite. The low TOF of the Mo/HY zeolite is attributed to strong adsorptions of the reactant and/or products induced by strong acid sites, although it is not ruled out that the TOF is maximized on the LiY or NaY zeolite for some reason [42].

### **B Molybdenum Pentachloride**

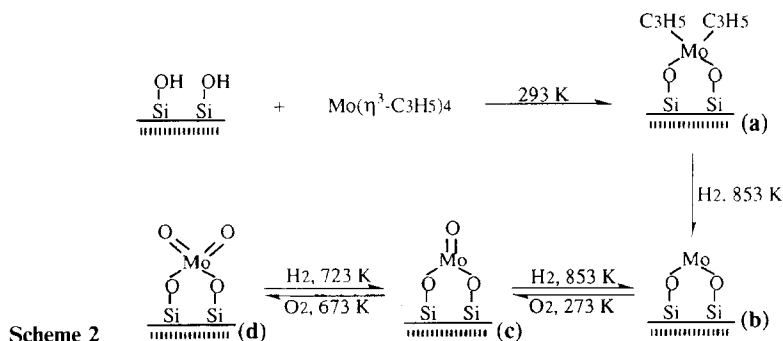
Silica-supported molybdenum catalysts were prepared by the reaction of  $\text{MoCl}_5$  vapor with surface OH groups on  $\text{SiO}_2$  [43]. The samples were then dried in air at  $\approx 350$  K with continuous stirring and calcined in oxygen overnight at 773 K. The catalyst sample was characterized by photoluminescence, which suggests the existence of only one type of tetrahedrally coordinated molybdenum emitting site on the CVD Mo/ $\text{SiO}_2$  oxide catalysts. In contrast, the impregnated Mo/ $\text{SiO}_2$  catalysts contain at least two different types of the tetrahedrally coordinated molybdenum emitting sites with different environments – one on the  $\text{SiO}_2$  surface and the other probably covered with octahedral Mo species that do not luminesce [44]. The CVD Mo/ $\text{SiO}_2$  catalysts showed a higher catalytic activity for photoinduced metathesis of propene than a conventional impregnated Mo/ $\text{SiO}_2$  oxide catalyst. The photoinduced metathesis was suggested to be directly associated with the excitation of the charge-transfer absorption band (around 280–300 nm) upon UV irradiation ( $\lambda > 280$  nm) of the Mo/ $\text{SiO}_2$  catalysts [43]. Propene interacts with the charge

transfer excited triplet state to produce a carbene species which acts as a reaction chain carrier [45].

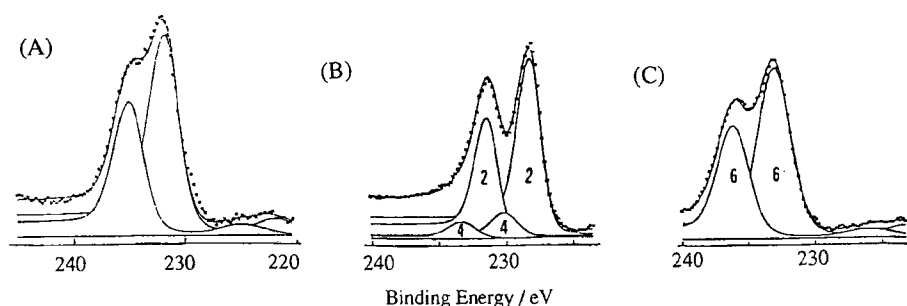
The model of a tetrahedral dioxo Mo species was found to account for the isolated Mo species of the CVD Mo/SiO<sub>2</sub> prepared from MoCl<sub>5</sub>, after oxidizing treatment, on the basis of photoluminescence results [44, 46]. This agreed with the report by Iwasawa et al. using allylmolybdenum-based Mo/SiO<sub>2</sub> and Mo/Al<sub>2</sub>O<sub>3</sub> catalysts, on the basis of in situ EXAFS and photoluminescence studies [29, 47–49]. However, the Raman investigations (Raman shift 994–998 cm<sup>-1</sup>) performed by Wachs and co-workers [50, 51] on Mo/SiO<sub>2</sub> catalysts prepared by different methods (impregnation, MoCl<sub>5</sub>, allylic complex, Mo<sup>III</sup> compound) did not show any evidence for the existence of an isolated tetrahedral dioxomolybdenum species. They observed that the polyoxomolybdates are transformed into isolated octahedral monooxo Mo<sup>VI</sup> cations, using in situ Raman and EXAFS [50, 51], whereas Cornac et al. observed the reverse phenomenon, i.e. the breaking of the Mo–O–X bridge (X = Mo or Si) upon hydration [52]. Desikan et al. [53] also characterized impregnated Mo/SiO<sub>2</sub> samples by in situ Raman spectroscopy (Raman shift 955 and 670 cm<sup>-1</sup>). They found that the isolated surface Mo species present on their dehydrated catalysts is a distorted tetrahedron with C<sub>2v</sub> symmetry, with two short Mo=O bonds and two long Mo–O bonds.

### C Allylmolybdenum

Aigler et al. examined the oxidation states of allyl-based Mo/SiO<sub>2</sub> catalysts by XPS [54]. The MOCVD Mo catalysts were prepared by a dry-mixing and sublimation method, which allowed the allyl complex to be loaded either onto 100–200 mesh particles of the SiO<sub>2</sub> support or onto pressed self-supporting wafers of the same material for XPS work. Typically, 1 g of the support was charged in a quartz reactor, connected to an all-glass BET system and calcined in flowing oxygen at 823 K for 2.5 h and then in vacuum at the same temperature for 2.5 h. The reactor was then transferred, while under vacuum, to a glovebox kept under high-purity nitrogen, where the amount of complex required to produce a 1.7 wt % Mo/SiO<sub>2</sub> catalyst was weighed and placed directly on the support in the reactor. An XPS Mo 3d spectrum was acquired for the Mo/SiO<sub>2</sub> catalyst after adsorption of Mo( $\eta^3$ -C<sub>3</sub>H<sub>5</sub>)<sub>4</sub> onto SiO<sub>2</sub> (structure **a** in Scheme 2). The spectrum obtained showed a Mo 3d peak shape which suggests the presence of one oxidation state (Fig. 4(A)). A variety of



Scheme 2



**Figure 4.** Curve-fitted Mo 3d spectra of the Mo/SiO<sub>2</sub> catalysts following adsorption of Mo( $\eta^3$ -C<sub>3</sub>H<sub>5</sub>)<sub>4</sub> onto SiO<sub>2</sub> (A), reduced at 823 K (B), and oxidized at 573 K (C), corresponding to the structures **a**, **b**, and **d** in Scheme 2.

binding energy values for Mo<sup>4+</sup> complexes have been reported depending on the kinds of ligands associated with the Mo center. Figure 4(B) shows the Mo 3d spectrum obtained by the following reduction of the attached complex at 823 K for 12 h. The Mo 3d envelope shows a major contribution from a single oxidation state (Mo 3d<sub>5/2</sub> binding energy of 228.4 eV), and a minor contribution from Mo<sup>4+</sup> (Mo 3d<sub>5/2</sub> binding energy of 230.2 eV). The Mo 3d<sub>5/2</sub> binding energy value at 228.4 eV is consistent with the presence of Mo<sup>2+</sup>. This is in good agreement with structure **b**, proposed by Iwasawa and co-workers [48, 49]. Figure 4(C) shows the Mo 3d spectrum for the catalyst obtained following oxidation at 573 K. The Mo 3d<sub>5/2</sub> and Mo 3d<sub>3/2</sub> binding energies (233.0 and 236.2 eV) are characteristic of Mo<sup>6+</sup> [54]. In contrast, the conventional impregnation Mo<sup>6+</sup>/SiO<sub>2</sub> catalyst exhibits mixed oxidation states, reflecting a heterogeneous feature.

Work on single crystal oxide surfaces has extended this approach to include technologically interesting complex surfaces not well modeled by single component metallic substrates. Hung et al. reported the use in UHV of organometallic surface deposition, followed by oxidation, to give single crystal models for mixed transition metal oxides under conditions which allow for their structural and compositional characterization [55]. Single crystal Fe(100) was hydroxylated to give a p(2×1) overlayer (exposure to 1.2 L (1 Langmuir:  $1.33 \times 10^{-4}$  Pa·s) of H<sub>2</sub>O at 100 K followed by warming to 243 K). The Fe(100)-OH surface was exposed to Mo( $\eta^3$ -allyl)<sub>4</sub> by vapor-phase dosing as follows. Vacuum-sublimed Mo( $\eta^3$ -allyl)<sub>4</sub> was loaded into a glass sample vial, attached to the sample manifold of the UHV system. The manifold and doser lines were warmed slightly, and the system was exposed to Mo( $\eta^3$ -allyl)<sub>4</sub> vapor in order to passivate the doser lines. Following this treatment, direct measurement of the mass spectrum of the Mo( $\eta^3$ -allyl)<sub>4</sub> vapor in the UHV chamber was consistent with that expected for the intact transition metal complex. The Fe(100)-OH surface was then placed directly in front of the UHV doser and exposed to vapour of the organometallic for 2 min at a measured pressure below  $1.3 \times 10^{-6}$  Pa.

Auger analysis following exposure of the Fe(100)-OH surface to Mo( $\eta^3$ -allyl)<sub>4</sub> indicated a Mo coverage of 0.17 ML (ML: monolayer), consistent with a reaction stoichiometry in which essentially all of the surface hydroxy groups reacted with the

organometallic by protolytic cleavage of allyl ligands to give propene, which is not adsorbed. The residual carbon coverage attributed to a surface bound Mo complex was measured to be 0.61 ML, consistent with a  $\text{Mo(allyl)}_{1-2}$  overlayer stoichiometry [55]. Both  $\text{Mo(allyl)}_1$  and  $\text{Mo(allyl)}_2$  surface-bound species have been reported for reaction of  $\text{Mo(allyl)}_4$  with bulk oxides [29, 47]. The high resolution electron energy loss (HREELS) spectrum of the reaction product between  $\text{Fe(100)-OH}$  and  $\text{Mo}(\eta^3\text{-allyl})_4$  showed reduction in intensity of the  $\nu(\text{OH})$  ( $3400\text{ cm}^{-1}$ ) and  $\nu(\text{Fe-OH})$  ( $475$  and  $785\text{ cm}^{-1}$ ) bands, indicating protolytic cleavage of Mo-allyl units, consistent with results reported using bulk silica or alumina [29, 47]. The new energy loss observed at  $455\text{ cm}^{-1}$  was assigned to overlapping stretching modes of Fe-O and Mo-O bonds of surface Fe-O-Mo species.  $\text{Fe(100)-Mo(allyl)}_2$  was treated at 573 K with  $\text{H}_2$  for 15 min. Allyl ligand-related peaks at 3030, 1465, 1240, and  $915\text{ cm}^{-1}$  were almost entirely lost by this treatment, and the HREELS loss peak assigned to the overlapping Fe-O and Mo-O stretching modes of surface Fe-O-Mo units broadened and shifted to  $440\text{ cm}^{-1}$ . The material was then treated with  $\text{O}_2$  at 573 K. The loss peak assigned to Fe-O-Mo shifted to  $425\text{ cm}^{-1}$  and a new loss peak at  $980\text{ cm}^{-1}$  was assigned to  $\nu(\text{Mo=O})$ , in accord with similar assignments for MoO or  $\text{MoO}_2$  complexes supported on bulk oxides and for soluble species. The O coverage increased to 1.2 ML, consistent with a  $\text{Fe(100)-MoO}_{1-2}$  unit stoichiometry [55].

#### D Molybdenum Trioxide Vapor

Metal oxide vapour synthesis (MOVS) has been developed as a new methodology for the preparation of unsupported and supported heterogeneous metal oxide systems [56]. The reaction vessel encloses a dual resistive evaporation source, heated solvent inlet with shower head, and a tube for product extraction to a Schlenk flask. A rotary pump is used for initial pumpdown and system roughing to 0.13 Pa. An oil diffusion pump increases the vacuum to  $1.3 \times 10^{-5}$  Pa and is protected by a liquid  $\text{N}_2$  trap which prevents the backstreaming of pump oil as well as its contamination by ligand and solvent chemicals used in the synthesis process. A vacuum increases the efficiency of the resistive furnace, which has a practical limit of 1773 K, to generate vapors from metal oxides of low volatility, such as  $\text{Nb}_2\text{O}_5$  (mp 1758 K, bp 3200 K) or  $\text{WO}_3$  (mp 1746 K, bp 2123 K). More volatile metal oxides, such as  $\text{MoO}_3$  (mp 1068 K, bp 1530 K) or  $\text{V}_2\text{O}_5$  (mp 963 K, bp 2325 K), do not require a high vacuum [56]. Throughout vaporization, a continuous flow of solvent is cocondensed with the metal oxide vapors on the sides of the rotating reactor vessel, which is immersed in liquid nitrogen. Supported MOVS catalysts can be readily obtained by introducing a desired support to the MOVS cocondensate product solution extracted from the system. The obtained  $\text{MoO}_3$  vapor-based Mo/ $\text{SiO}_2$  catalyst shows the unique nature and high efficiency in catalytic conversion of methanol to formaldehyde [56, 57].

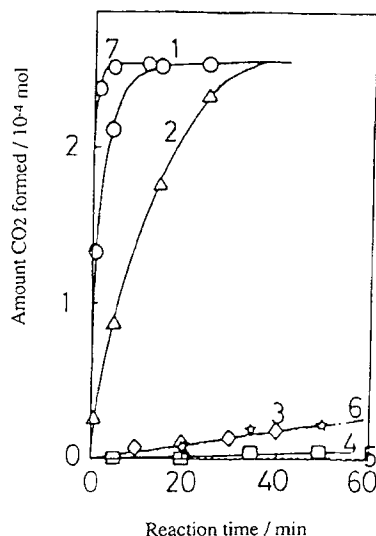
##### 4.5.4.6 Cobalt

A variety of cobalt species with different structures and oxidation states on inorganic oxides can be produced by using  $\text{Co}_2(\text{CO})_8$  as a precursor [29]. Scheme 3

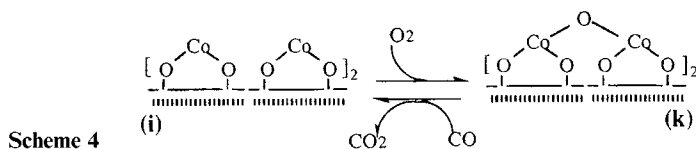


Species **g** is very sensitive to O<sub>2</sub>. It is rapidly oxidized at 298 K to form a new species [CoO]<sub>4</sub> **h**, with simultaneous expansion of the Co–Co bond to 0.321 nm and formation of a new Co–O bond at a distance of 0.202 nm, which is much shorter than the 0.213 nm distance observed for the CoO crystal. On heating to 513 K in vacuo, cluster **h** reacted with the surface OH groups of Al<sub>2</sub>O<sub>3</sub> to form the [Co<sup>II</sup>]<sub>4</sub> assembly **i** of trigonally distorted *T<sub>d</sub>* symmetry, with the accompanying elimination of H<sub>2</sub>O and break of the Co–Co bonds. Treatments of species **e**, weakly adsorbed on SiO<sub>2</sub>, and of species **g** on Al<sub>2</sub>O<sub>3</sub> with O<sub>2</sub> at 773 K produced [Co<sub>3</sub>O<sub>4</sub>]<sub>*n*</sub> (species **j**), characterized by peaks at 450 and 700 nm. The EXAFS analysis showed that the local structure around the Co atom was almost identical to Co<sub>3</sub>O<sub>4</sub> in spinel. The bond distances of Co–O, Co(oct)–Co(oct), Co(oct or tet)–Co(tet), and Co(oct)–Co(oct) were determined to be 0.194, 0.282, 0.339, and 0.491 nm, respectively, compared to 0.190, 0.285, 0.340, and 0.494 nm for a spinel crystal. The [Co<sub>3</sub>O<sub>4</sub>]<sub>*n*</sub> on Al<sub>2</sub>O<sub>3</sub> also takes the spinel-like structure, in which the bond distances of Co–O,





**Figure 5.** CO oxidation with  $O_2$  on various  $\gamma\text{-Al}_2\text{O}_3$  and  $\text{SiO}_2$ -supported cobalt catalysts: 1,  $[\text{Co}_3\text{O}_4]_n/\text{Al}_2\text{O}_3$  **j**; 2,  $[\text{Co}^{\text{II}}]_4/\text{Al}_2\text{O}_3$  **i**; 3,  $[\text{CoO}]_4/\text{Al}_2\text{O}_3$  **h**; 4, impregnated  $\text{Co}_3\text{O}_4/\text{Al}_2\text{O}_3$ ; 5, ion-exchanged  $[\text{Co}(\text{NH}_3)_6]\text{Cl}_3/\text{Al}_2\text{O}_3$  followed by decomposition at 673 K; 6,  $\text{Co}^{\text{II}}/\text{SiO}_2$ ; 7,  $[\text{Co}_3\text{O}_4]_n/\text{SiO}_2$  **j**; catalyst—0.287 g (5 wt% as Co/support).

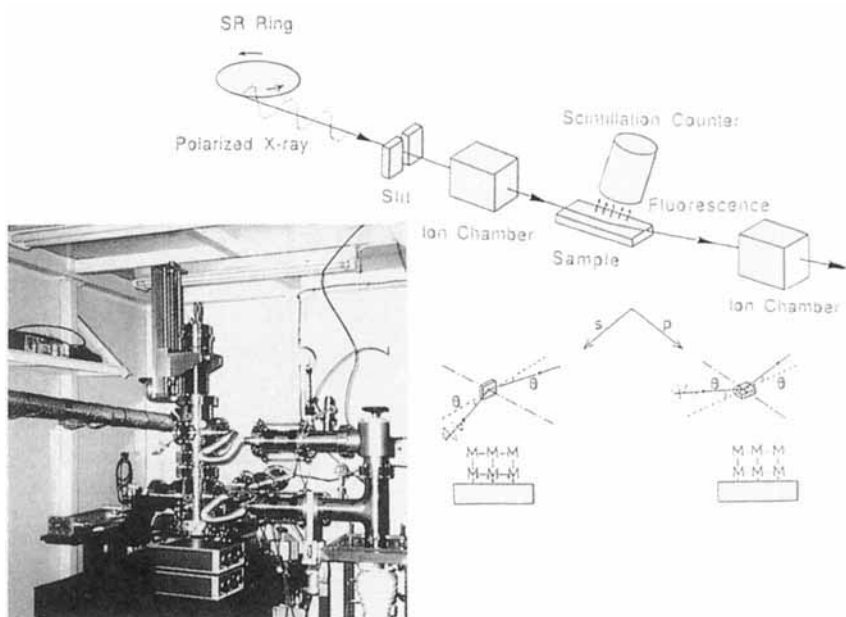


$\text{Co}(\text{oct})\text{--Co}(\text{oct})$ ,  $\text{Co}(\text{oct or tet})\text{--Co}(\text{tet})$ , and  $\text{Co}(\text{oct})\text{--Co}(\text{oct})$  were 0.192, 0.281, 0.336, and 0.488 nm, respectively. The size of  $[\text{Co}_3\text{O}_4]_n$  on  $\text{SiO}_2$  and  $\text{Al}_2\text{O}_3$  is indicated to be a thin, small particle with an average diameter of 1.3 nm and smaller than 1.0 nm, respectively [58].

The  $[\text{Co}_3\text{O}_4]_n$  species **j** on  $\text{SiO}_2$  and  $\text{Al}_2\text{O}_3$  prepared by CVD of  $\text{Co}_2(\text{CO})_8$ , followed by oxidation, were found to be remarkably active for catalytic oxidation of CO with  $O_2$  at 273 K as shown in Fig. 5 [29, 59]. The traditional  $\text{Co}_3\text{O}_4/\text{SiO}_2$  and  $\text{Co}_3\text{O}_4/\text{Al}_2\text{O}_3$  catalysts prepared by the usual impregnation method were almost inactive under similar reaction conditions.

The  $[\text{Co}^{\text{II}}]_4$  species **i** was also active for CO oxidation as shown Fig. 5. EXAFS Fourier transform of the species indicated that the Co assembly exists in a monomer form without any Co–Co bonding [60]. However, the EXAFS Fourier transform measured under 1 bar of  $O_2$  exhibited a small new peak around 0.30 nm. The peak intensity increased under 10 bar  $O_2$ . Curve fitting analysis revealed that the peak is ascribed to a Co–Co arrangement at 0.330 nm. It is likely that the Co–Co peak appears by the linkage of oxygen bridge upon  $O_2$  adsorption, as shown in Scheme 4 [26, 60]. The bridged oxygen linked to two Co atoms reacted almost instantaneously with CO to form  $\text{CO}_2$  at room temperature, leading to the disappearance of Co–Co peak.

More precise characterization of surface multimetal sites prepared by CVD has been performed with single crystal oxide surfaces as catalytic model systems.



**Figure 6.** Set-up of the in-situ polarization-dependent total-reflection fluorescence X-ray absorption fine structure (PTRF XAFS) measurement system.

Polarization-dependent total-reflection fluorescence (PTRF) EXAFS technique enables measurement of EXAFS oscillations of CVD species on oxide surfaces [26]. Figure 6 shows the experimental set-up and a picture of the in-situ PTRF EXAFS technique [61, 62]. This technique provides asymmetric and anisotropic structure analysis on surfaces, that is, bonds parallel (by s-polarization) and perpendicular (by p-polarization) to the surface can be analyzed independently.  $\text{Co}_2(\text{CO})_8$  was supported on  $\alpha\text{-Al}_2\text{O}_3(0001)$  by CVD, followed by calcination at 773 K. The spinel sample on  $\alpha\text{-Al}_2\text{O}_3(0001)$  was also remarkably active for CO oxidation at room temperature [62]. The PTRF EXAFS revealed that  $\text{Co}_3\text{O}_4$  spinel(001) plane with seven layers grew parallel to the  $\text{Al}_2\text{O}_3(0001)$  surface [61, 62].

#### 4.5.4.7 Vanadium

Bond and co-workers found that a  $\text{V}_2\text{O}_5/\text{TiO}_2$  catalyst prepared by the reaction between  $\text{VOCl}_3$  vapor and surface OH groups showed a high selectivity in the oxidation of *o*-xylene to phthalic anhydride [63, 64]. Hydroxy groups on the surface of anatase react with the vapor of  $\text{VOCl}_3$  at room temperature to give a partial monolayer of a vanadium species which, after heating to 670 K, is active for the oxidation of *o*-xylene. Rehydroxylation by  $\text{H}_2\text{O}$  followed by outgassing at 410 K and further treatment with  $\text{VOCl}_3$  leads to improved catalytic properties, and after six such cycles a monolayer catalyst is produced which contains 1.7 wt%  $\text{V}_2\text{O}_5$  and

**Table 2.** Surface V<sub>2</sub>O<sub>5</sub> concentration at monolayer loadings.

Oxide support	Surface area (m <sup>2</sup> g <sup>-1</sup> )	Surface metal (atoms nm <sup>-2</sup> )
SiO <sub>2</sub>	300	0.6
Al <sub>2</sub> O <sub>3</sub>	180	6.8
TiO <sub>2</sub>	55	6.8
ZrO <sub>2</sub>	39	6.4
Nb <sub>2</sub> O <sub>5</sub>	55	6.8

which is superior even to a doubly promoted catalyst prepared by conventional impregnation [64].

CVD of VOCl<sub>3</sub> was applied to prepare V<sub>2</sub>O<sub>5</sub>/Al<sub>2</sub>O<sub>3</sub> [65]. In the CVD of VOCl<sub>3</sub>, it can be expected that the vanadium compound is directly bonded with the support surface through the reaction with OH groups on the support surface, namely,



which are entirely different from the reactions in the wet impregnation method. Thus, the catalyst component may be deposited on different surface sites of the support. An Al<sub>2</sub>O<sub>3</sub> (230 m<sup>2</sup> g<sup>-1</sup>) packed in a Pyrex glass tube was calcined in a flow of dry N<sub>2</sub> for 4 h at 473 K for dehydration, and then subjected to the repeated CVD cycles at 473 K. The sample obtained was calcined at 773 K in O<sub>2</sub> flow for 3 h. The content of supported vanadium was determined by dissolving the V<sub>2</sub>O<sub>5</sub> with sulfuric acid and by titrating the solution with Mohr's solution using sodium diphenylamine sulfonate as an indicator. The CVD catalyst gave a TOF very different from those of impregnated catalysts in the oxidation reactions of hydrogen, ammonia, and benzene [65]. All of these reactions are classified to be structure insensitive. The difference between the CVD and impregnation catalysts may arise from the modification of intrinsic chemical properties of the surface V=O species. At present, the details of the modification are not clear.

Oxide supports such as Al<sub>2</sub>O<sub>3</sub>, TiO<sub>2</sub>, ZrO<sub>2</sub>, and Nb<sub>2</sub>O<sub>5</sub> have a high surface density of reactive surface hydroxy groups and tend to form a close-packed monolayer of the surface metal oxide phase, whereas, oxide supports such as SiO<sub>2</sub> have a lower density of reactive surface hydroxy groups and do not form a close-packed overlayer of the surface vanadium oxide phase. The maximum concentration of the surface vanadium oxide species obtained on the different oxide supports, determined by Raman spectroscopy which readily discriminates between the two-dimensional overlayer and crystallites, is presented in Table 2 [66]. The surface vanadium oxide species on the different oxide supports exhibit a Raman band at 1015–1040 cm<sup>-1</sup> due to the terminal V=O bond of isolated VO<sub>4</sub> species [67, 68]. At low loadings ( $\approx 1$  wt% V<sub>2</sub>O<sub>5</sub>), a single sharp band is present at  $\approx 1030$  cm<sup>-1</sup> which is due to an isolated four-coordinated surface vanadium oxide species containing one terminal V=O bond and three bridging V–O–Ti bonds [69]. At intermediate loadings (2–6 wt%), a second band is present at  $\approx 930$  cm<sup>-1</sup> which has been assigned to a

polymerized, for-coordinated surface vanadium oxide species [69]. At high loadings (>6 wt %), a third sharp band is present at  $994\text{ cm}^{-1}$  due to crystalline  $\text{V}_2\text{O}_5$  which indicates that the close-packed surface vanadium oxide monolayer has been formed and essentially all the reactive surface hydroxy groups consumed. A similar behavior is also observed for the surface vanadium oxide species on other oxide supports [66].

The reactivity of the surface  $\text{V}_2\text{O}_5$  overlayers on the different oxide supports was probed by the methanol oxidation reaction. The reactivity, in terms of TOF, of the surface vanadia species was found to dramatically depend on the specific oxide support and decrease in the following order [66]:

$$\begin{aligned}\text{V}_2\text{O}_5/\text{ZrO}_2(3.3\text{ s}^{-1}) &\approx \text{V}_2\text{O}_5/\text{TiO}_2(2.0\text{ s}^{-1}) \\ &> \text{V}_2\text{O}_5/\text{Nb}_2\text{O}_5(8 \times 10^{-1}\text{ s}^{-1}) \\ &\gg \text{V}_2\text{O}_5/\text{Al}_2\text{O}_3(3.6 \times 10^{-2}\text{ s}^{-1}) \\ &> \text{V}_2\text{O}_5/\text{SiO}_2(3.9 \times 10^{-3}\text{ s}^{-1})\end{aligned}$$

The difference in reactivity may not be a structural factor since the structure is independent of the oxide support. One of the possible factors controlling the reactivity of various supported metal oxide catalysts as a function of oxide support is the difference in the terminal  $\text{V}=\text{O}$  bond or the bridging  $\text{V}-\text{O}$ -support bond. A plot of TOF versus Raman  $\text{M}=\text{O}$  position for supported vanadium oxide, molybdenum oxide, rhenium oxide, and chromium oxide catalysts suggests that no relationship exists between the catalyst reactivity and the terminal  $\text{M}=\text{O}$  bond strength. Wachs et al. proposed that the reactivity may be related to the bridging  $\text{M}-\text{O}$ -support bond [66].

Vanadium oxide overlayers on silica (Aerosil 200) were also prepared by CVD of  $\text{VO}(\text{OC}_2\text{H}_5)_4$  (13.3 Pa) through the reaction with the surface OH groups at 423 K and then thermally decomposed at 723 K. The adsorption-decomposition cycle was repeated several times in a closed CVD reactor [70]. CVD  $\text{V}_2\text{O}_5/\text{SiO}_2$  was 3–4 times more active for oxidative dehydrogenation and dehydration of alcohols than  $\text{V}_2\text{O}_5/\text{SiO}_2$  prepared by impregnation [70, 71].

EXAFS study provided information on the structure of vanadium oxide overlayers on  $\text{MgO}$ ,  $\text{Al}_2\text{O}_3$  and  $\text{SiO}_2$ . On  $\text{MgO}$ , vanadium oxides were present as mixed oxides such as  $\text{Mg}_3\text{V}_2\text{O}_8$ . Vanadium oxides were in the form of thin films on  $\text{Al}_2\text{O}_3$ , regardless of the preparation method. However, three different structures were present on the  $\text{SiO}_2$ : isolated species, crystallites by an impregnation method, and thin films by CVD. The thin films on  $\text{SiO}_2$  were stable even at 773 K in air [72].

Highly dispersed supported vanadium oxide catalysts have been prepared by using the reaction of photochemically activated  $\text{VOCl}_3$  with surface OH groups on Vycor glass at 273 K [73]. Photoactivation of adsorbed  $\text{VOCl}_3$  was carried out by UV excitation of the charge-transfer absorption band of  $\text{VOCl}_3$  at approximately 300–450 nm. The supported vanadium oxides exhibit a higher activity for the photocatalytic isomerization reactions of 2-butene as compared with those obtained for the oxides prepared by a conventional impregnation method.

#### 4.5.4.8 Titanium

The surface or interface of two different metal oxide layers, chemically interacted with each other through covalent bonds, provides a potential way to produce new surface materials. The SiO<sub>2</sub>-attached TiO<sub>2</sub> monolayer was prepared by the CVD reaction between Ti(*i*-OC<sub>3</sub>H<sub>7</sub>)<sub>4</sub> vapor and OH groups of the SiO<sub>2</sub> surface (300 m<sup>2</sup> g<sup>-1</sup>). The SiO<sub>2</sub> was pretreated at 473 K for 2 h in air to control the density of surface OH groups to about five per square nanometer (monolayer). Ti(*i*-OC<sub>3</sub>H<sub>7</sub>)<sub>4</sub> vapor was deposited on the SiO<sub>2</sub> by a CVD method to react with the OH groups of SiO<sub>2</sub> at 353 K for 2 h. The unreacted Ti(*i*-OC<sub>3</sub>H<sub>7</sub>)<sub>4</sub> was removed by evacuation at 473 K. Then, the obtained sample was exposed to water vapor at room temperature to decompose the *i*-OC<sub>3</sub>H<sub>7</sub> ligands, followed by the calcination at 773 K for 2 h. The above procedure was repeated twice to prepare TiO<sub>2</sub> monolayers on SiO<sub>2</sub> [74].

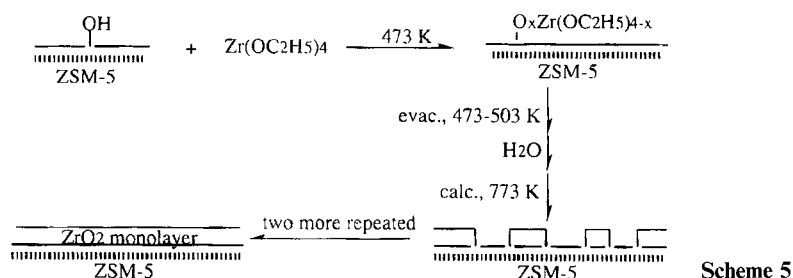
XANES and EXAFS analyses revealed that TiO<sub>2</sub> on SiO<sub>2</sub> exists as the anatase type. The shape of TiO<sub>2</sub> on SiO<sub>2</sub> has been discussed on the basis of the coordination numbers of Ti–Ti bonds. The model which best fits the experimental results, when considering the four model layer structures for the planes (100), (001), (110), and (101), is the monolayer structure with (101) orientation [74].

It has been reported that the highly dispersed TiO<sub>2</sub> particles on SiO<sub>2</sub> are readily reducible with H<sub>2</sub> at 773 K [75]. However, this is not the case of the monolayer catalyst because of the existence of direct Ti–O–Si bonding. Furthermore, no reduction of the TiO<sub>2</sub> monolayer with H<sub>2</sub> at 773 K occurs even in the presence of supported noble metals [74]. Whereas the structure of the TiO<sub>2</sub> layers in Pt/TiO<sub>2</sub>/SiO<sub>2</sub> were not altered by H<sub>2</sub> reduction at 773 K, a remarkable change of the structure of Pd/TiO<sub>2</sub>/SiO<sub>2</sub> was found, in which the anatase structure was transformed to the rutile structure. The bond lengths of Ti–O, Ti–Ti, and Ti–Ti were 0.198, 0.294, and 0.357 nm, respectively, being almost the same as 0.197, 0.294, and 0.357 nm for the corresponding bond lengths in rutile. The TiO<sub>2</sub> overlayer in Pd/TiO<sub>2</sub>/SiO<sub>2</sub> is suggested to have the rutile (110) structure, judging from the coordination numbers of two Ti–Ti bonds. Rutile(110) is known as the most stable plane of rutile.

Highly dispersed TiO<sub>2</sub> supported onto Vycor glass was prepared by CVD using the reaction of TiCl<sub>4</sub> with the surface OH groups, followed by treatment with H<sub>2</sub>O vapor to hydrolyze the supported compounds [76]. CH<sub>4</sub> and CH<sub>3</sub>OH are produced from CO<sub>2</sub> and H<sub>2</sub>O on the CVD TiO<sub>2</sub>/Vycor glass under UV irradiation at 275 K, with a good linear relationship between the yields of these products and the UV irradiation time. ESR studies of the photoreduction of TiO<sub>2</sub> supported on Vycor glass showed that supported samples exhibit only one type of Ti<sup>3+</sup> ion with a low coordination, whereas impregnated catalysts showed several types of Ti<sup>3+</sup> ions, with different coordinations, suggesting the possible formation of uniform Ti sites by CVD [77].

#### 4.5.4.9 Zirconium

A new ZrO<sub>2</sub> monolayer/ZSM-5 catalyst was prepared by CVD of Zr(OC<sub>2</sub>H<sub>5</sub>)<sub>4</sub> on the external surface of ZSM-5 [78]. The CVD catalysts were prepared by taking



advantage of the reaction between  $\text{Zr(OC}_2\text{H}_5)_4$  vapor and the OH groups of ZSM-5 external surface, followed by calcination as shown in Scheme 5.  $\text{Zr(OC}_2\text{H}_5)_4$  vapor (vapor pressure 133 Pa at 473 K) was interacted with 473 K-pretreated ZSM-5 at 473 K. Since the molecular size of  $\text{Zr(OC}_2\text{H}_5)_4$  is larger than the pore size,  $\text{Zr(OC}_2\text{H}_5)_4$  can react with the OH groups located at the external surface and thus they expected to stay at the external surface. After the reaction, unreacted  $\text{Zr(OC}_2\text{H}_5)_4$  was evacuated at 473 K and then the sample was heated to 503 K to complete the reaction. The sample was then exposed to water vapor at room temperature to convert the  $\text{OC}_2\text{H}_5$  ligands to OH groups, followed by calcination at 773 K in air. The loading of  $\text{ZrO}_2$  in the sample thus obtained was determined by X-ray fluorescence by using several standard  $\text{ZrO}_2/\text{ZSM-5}$  samples with known amounts of  $\text{ZrO}_2$ . The coverage of  $\text{ZrO}_2$  deposited by one CVD procedure was estimated to be about 1/3 monolayer, assuming that 1.7 wt % ( $\text{Zr}/\text{ZSM-5}$ ) constitutes a monolayer, based on the external surface area of ZSM-5 ( $15 \text{ m}^2 \text{ g}^{-1}$  and the  $\text{ZrO}_2$  two-dimensional unit cell of size  $0.13 \text{ nm}^2$ ). As a result, a near full-monolayer coverage of  $\text{ZrO}_2$  was obtained by carrying out the CVD procedure three times [78]. A reduction of the pore size and volume of ZSM-5 was not observed after three CVD treatments, judging from the rates of adsorption of toluene, *o*- and *p*-xylenes, and the amounts of adsorbed pentane and benzene.

Table 3 shows the activities and selectivities of the  $\text{ZrO}_2/\text{ZSM-5}$  catalyst for methanol conversion reactions at 1 bar.  $\text{C}_5$  hydrocarbons were found to be selectively produced (88.9%) at 623 K on the  $\text{ZrO}_2$  monolayer/ $\text{ZSM-5}$  catalyst, of which more than 95% was isopentane [78]. This catalytic performance is quite unique, compared with  $\text{ZrO}_2$  double layer/ $\text{ZSM-5}$  and  $\text{ZrO}_2$  triple layer/ $\text{ZSM-5}$ , both of which show similar performances to ZSM-5 itself.

The  $\text{Zr-O}$  (0.206 nm) and  $\text{Zr-Zr}$  (0.369 nm) bond lengths of the  $\text{ZrO}_2$  monolayer were close to those in tetragonal  $\text{ZrO}_2$ , rather than the monoclinic  $\text{ZrO}_2$ , indicating the formation of a tetragonal  $\text{ZrO}_2$ -like structure on the external surface of ZSM-5. The detailed reaction mechanism for the selective formation of isopentane from methanol on the  $\text{ZrO}_2$  monolayer/ $\text{ZSM-5}$  catalyst is not clear, but the  $\text{ZrO}_2$  monolayer may grow epitaxially on the  $\text{ZSM-5}(001)$  plane in the  $[111]$  direction of tetragonal  $\text{ZrO}_2$ . The misfit between the  $\text{ZrO}_2$  overlayer and  $\text{ZSM-5}$  external surface would generate a unique reaction environment for multifunctional catalysis, combining with the acidic properties of the ZSM-5 cage [78].

Scanning tunneling microscopy (STM) and scanning tunneling spectroscopy

**Table 3.** Methanol conversion and product distribution on ZrO<sub>2</sub>/ZSM-5 catalysts.

Catalyst	Temperature (K)	CH <sub>3</sub> OH conversion (%)	Selectivity (%)								
			C <sub>2</sub>	C <sub>3</sub>	C <sub>4</sub>	C <sub>5</sub>	C <sub>6</sub>	C <sub>6</sub> H <sub>6</sub>	<i>p</i> -xylene	Others <sup>a</sup>	Ar <sub>8</sub> <sup>+</sup>
One monolayer ZrO <sub>2</sub> /ZSM-5	573	10.5	3.9	2.8	0.0	88.9	3.0	0.0	0.1	0.5	0.7
	623	13.8	8.4	10.6	0.0	73.5	0.0	0.0	1.7	0.3	5.6
Two monolayers ZrO <sub>2</sub> /ZSM-5	623	30.7	11.5	16.0	11.8	13.5	8.2	0.7	16.6	8.8	14.8
One monolayer SiO <sub>2</sub> /ZSM-5	573	42.2	11.0	16.5	0.0	14.4	12.0	0.8	16.1	7.5	24.3
ZSM-5	573	25.2	17.1	28.3	0.0	13.4	9.8	1.0	14.1	8.6	15.0

Reaction conditions: catalyst = 1.0 g, pressure = 1 bar, argon:CH<sub>3</sub>OH = 2, W/F = 310 g min mol<sup>-1</sup>.

<sup>a</sup>C<sub>6</sub>H<sub>12</sub> + ArMe + *o*-ArMe<sub>2</sub>.

(STS) were used to characterize the structure of a model metal-supported dispersed ZrO<sub>2</sub> on Pd(100) [79]. STM images illustrate changes in the surface morphology of the ZrO<sub>2</sub> resulting from various chemical treatments. The Pd-supported sample was prepared by vapor deposition of Zr(OC<sub>2</sub>H<sub>5</sub>)<sub>4</sub>. Zr(OC<sub>2</sub>H<sub>5</sub>)<sub>4</sub> powder was heated to about 423 K under vacuum and held for 13 h; the vapor was transported to a connecting flask on a vacuum line that held the Pd crystal at room temperature. The single crystal of Pd with the deposited Zr(OC<sub>2</sub>H<sub>5</sub>)<sub>4</sub> was oxidized by treatment in a quartz tube that was open to air; the sample was heated at a rate of approximately 12.5 K min<sup>-1</sup> to 673 K and held for 1 min. The sample was cooled in air to room temperature. The sample was subsequently reduced by H<sub>2</sub> in the quartz tube; it was heated at a rate of 8 K min<sup>-1</sup> to 773 K and held for 1 h. It was then cooled to room temperature in flowing He and transferred under He to a Braun glovebox. When the sample was treated in O<sub>2</sub>, the ZrO<sub>2</sub> appeared as a smooth, featureless overlayer of varying thickness wetting the Pd. After treatment in H<sub>2</sub>, the ZrO<sub>2</sub> formed non-wetting particles on the Pd, with a sharp Pd–ZrO<sub>2</sub> interface [79].

Similar reversible structure transformations of ZrO<sub>2</sub> overlayers have been found with the ZrO<sub>2</sub> overlayer on Pd black by EXAFS [80].

#### 4.5.4.10 Tin

CVD SnO<sub>2</sub>/SiO<sub>2</sub> catalysts were prepared by repeating the following CVD cycle at 453 K: (i) the desiccation of silica gel (240 m<sup>2</sup> g<sup>-1</sup>) in a flow of dry N<sub>2</sub>, (ii) the deposition of SnCl<sub>4</sub> vapor on silica gel surface, (iii) the purge of excess SnCl<sub>4</sub> by flowing dry N<sub>2</sub>, and (iv) the hydrolysis of deposited Sn compound by water vapor [81]. The amount of deposited Sn was controlled by the number of CVD cycles repeated. The resulting materials were washed with 4 mol l<sup>-1</sup> NH<sub>4</sub>OH five times to remove residual chloride ions and with water to remove NH<sub>4</sub>OH, and then dried and calcined at 773 K for 2 h in flowing air.

The activity and selectivity in the oxidative dehydrogenation of ethylbenzene

were measured by the conventional flow reaction [81]. The high selectivity of the resulting CVD catalyst was attributed to moderate acid strength due to the controlled dispersion of  $\text{SnO}_2$  on  $\text{SiO}_2$ .

$\text{Sn}(\text{CH}_3)_4$  vapor has also been CVD-deposited onto Rh particles on  $\text{SiO}_2$ , prepare bimetallic catalysts (see Section 4.5.4.14).

#### 4.5.4.11 Ruthenium

A supported cluster-derived  $\text{Ru}_3(\text{CO})_{12}/2,2'$ -bipyridine/ $\text{SiO}_2$  catalyst has been found to be active both in WGS (water gas shift reaction) [82] and in 1-hexene hydroformylation [83]. The catalyst was prepared by vaporizing  $\text{Ru}_3(\text{CO})_{12}$  at 408 K in a separate sublimation oven and transferring the cluster in CO flow onto the silica bed in a fluidized-bed reactor. Sublimation can be done at low CO pressure, but good mixing is achieved with  $200\text{--}300\text{ ml min}^{-1}$  flow of CO at normal pressure. 2,2'-Bipyridine was either added by a similar technique at 373 K or was mixed with  $\text{Ru}_3(\text{CO})_{12}/\text{SiO}_2$  and activated separately at 373 K in a sealed glass cell under vacuum [84].

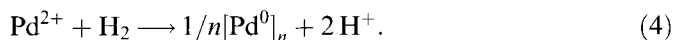
Ruthenocene  $\text{Ru}(\text{C}_5\text{H}_5)_2$  was deposited on Pt particles by CVD to obtain the bimetallic catalyst, which was active for benzene hydrogenation (see Section 4.5.4.14) [85].

#### 4.5.4.12 Palladium Films

Palladium, in the form of thin films, is used in electronics, multilayer magneto-optical data storage, gas sensors, and catalysis. Few precursors have been studied for CVD. The bis(allyl) complexes  $[\text{Pd}(\text{CH}_2\text{CRCH}_2)_2]$  ( $\text{R}=\text{H}, \text{CH}_3$ ) gave palladium thin films with high purity ( $>99\%$ ) by thermal CVD. The complex  $[\text{Pd}(\eta^3\text{-C}_3\text{H}_5)\text{Cp}]$  is more stable but, as often occurs with cyclopentadienyl precursors, the palladium films deposited by thermal CVD contained carbon impurities [86]. The CVD of palladium from  $[\text{Pd}(\text{Cp})_2]$  and  $[\text{Pd}(\text{acac})_2]$  has been patented [87], but films from  $[\text{Pd}(\text{Cp})_2]$  are likely to suffer high carbon contamination and  $[\text{Pd}(\text{acac})_2]$  has rather low volatility [88].  $[\text{Pd}(\eta^3\text{-CH}_2\text{CMeCH}_2)(\text{MeCOCHCOMe})]$  easily prepared by reaction of the sodium  $\beta$ -diketonate with the allylpalladium complex; it is stable in air at room temperature for a long period of time, which is advantageous in handling [88].

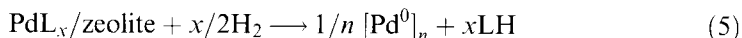
#### 4.5.4.13 Palladium/Zeolites

Acidic sites on reforming catalysts are known to initiate deposition of coke, which is a major cause of catalyst deactivation. In the case of zeolites, ion-exchange of  $[\text{Pd}(\text{NH}_3)_4]^{2+}$  inherently leads to the stoichiometric formation of acid sites (protons) upon reduction of the exchanged cation [89]:





When protons are not desired, they have to be reexchanged against  $\text{Na}^+$  ions in aqueous solution. The development of a one-step preparation of nonacidic Pd/zeolite catalysts would instead rely upon the use of neutral metal precursors of suitable size and reactivity, which could be introduced inside cages without altering the original distribution of positive charges. The use of organopalladium complexes is particularly promising in this sense, since zerovalent metal particles can be obtained through the reductive elimination of volatile ligands:



Its metallic state has been demonstrated by EXAFS with a Pd–Pd bond length of 0.272 nm [89].

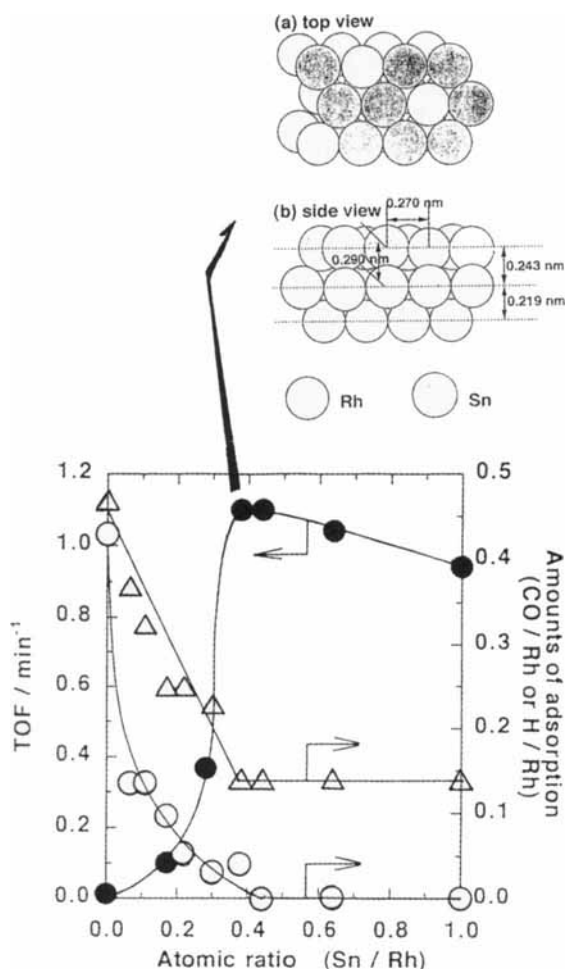
For chemical vapor deposition, both NaY and NaHY zeolites were first placed over a quartz frit in a U-tube reactor, and heated in flowing argon from 298 to 673 K over 2 h. After cooling to room temperature, a weighed amount of  $[\text{Pd}(\eta^3\text{-C}_3\text{H}_5)(\eta^5\text{-C}_5\text{H}_5)]$  was placed at the bottom of the U-tube under argon. Sublimation was carried out overnight in flowing argon ( $10 \text{ ml min}^{-1}$ ) at 298 K [90]. The supported material was heated in a  $\text{H}_2(5\%)/\text{He}$  flow from ambient temperature to 773 K at  $3 \text{ K min}^{-1}$ .

The catalytic results in MCP conversion support the hypothesis of total absence of protons. The Pd/NaY catalyst is 100% selective for the ring-opening reaction of MCP, in agreement with Gault's conclusions that this reaction is the only one catalyzed by the metal function [91]. These catalysts compare well with other nonacidic Pd catalysts; in particular, a lower deactivation rate under catalytic conditions is observed.

#### 4.5.4.14 Bimetals

Preparation of a supported Pd–Cu bimetallic catalyst was examined by vapor deposition.  $\text{Cu}(\text{acac})$  vapor was deposited selectively onto the surface of Pd particles supported on  $\text{Al}_2\text{O}_3$  or  $\text{SiO}_2$  at 353 K [92]. The selective deposition of Cu on Pd, not on the  $\text{Al}_2\text{O}_3$  or  $\text{SiO}_2$  support, was suggested by decrease of CO adsorption on the sample obtained. Supported Pd–Ru catalyst was obtained by exposure of Pd/ $\text{Al}_2\text{O}_3$  to  $\text{Ru}(\text{C}_5\text{H}_5)_2$  vapor. Analysis of the bimetallic catalyst pellet by electron probe microanalysis (EPMA) showed the coincidence of Ru distribution with Pd distribution over the pellet cross-section [92]. The similarly obtained Ru–Pt catalyst was active for benzene hydrogenation [85].

Rh–Sn/ $\text{SiO}_2$  catalysts were prepared by the selective CVD reaction between  $\text{Sn}(\text{CH}_3)_4$  vapor and small metallic particles supported on  $\text{SiO}_2$  [93, 94].  $\text{SiO}_2$  (Aerosil 200) was immersed in a methanol solution of  $\text{RhCl}_3 \cdot 3\text{H}_2\text{O}$ , followed by drying at 373 K for 12 h and reduction with  $\text{H}_2$  at 573 K for 1 h. The Rh particles on the  $\text{SiO}_2$  were then reacted with given amounts of  $\text{Sn}(\text{CH}_3)_4$  vapor ( $<0.6 \text{ kPa}$ ) at 423 K for 15 min in a closed circulating system. The reaction of  $\text{Sn}(\text{CH}_3)_4$  takes place much more rapidly on Rh metal surfaces than with OH groups of  $\text{SiO}_2$ . Thus, most of  $\text{Sn}(\text{CH}_3)_4$  vapor preferentially reacts with Rh particles. The samples were finally reduced with  $\text{H}_2$  at 573 K for 1 h, followed by evacuation in situ before use as



**Figure 7.** The turnover frequency (product molecules per minute per surface Rh atom: ●) for N<sub>2</sub> and N<sub>2</sub>O formation in NO (2.7 kPa)–H<sub>2</sub> (13.3 kPa) reaction at 373 K on Rh/Sn/SiO<sub>2</sub>, the amount of H<sub>2</sub> (○) and CO (Δ) adsorbed on Rh–Sn/SiO<sub>2</sub> at 273 K, and the surface model structure of Rh–Sn bimetallic particles with a fcc(111) surface.

catalysts and also before each run. When Sn(CH<sub>3</sub>)<sub>4</sub> vapor reacted with Rh metal particles, two molecules of CH<sub>4</sub> per Sn(CH<sub>3</sub>)<sub>4</sub> were evolved into the gas phase and no other hydrocarbons were observed. By further reduction at 573 K, two more CH<sub>4</sub> molecules were formed, leaving no residual carbon on the surface [94].

The CVD Rh–Sn/SiO<sub>2</sub> catalysts showed much higher catalytic activities for NO–H<sub>2</sub> reaction and NO dissociation than Rh/SiO<sub>2</sub> and also coimpregnated Rh/Sn/SiO<sub>2</sub> prepared from a methanol solution of RhCl<sub>3</sub> · 3H<sub>2</sub>O and SnCl<sub>2</sub> [93], showing an S-shape dependency on the amount of Sn (Fig. 7) [94]. This type of dependency often indicates the formation of particular bimetallic ensemble sites at the surface of particles which are very active as compared to the monometallic Rh sites. The sharp break in activity at Sn:Rh = 0.4 corresponds to the sharp break in CO adsorption. On the basis of CO adsorption measurements, TEM, and EXAFS, the surface composition of Rh–Sn/SiO<sub>2</sub> at Sn:Rh = 0.4 was estimated to be approximately

$\text{Sn}_s:\text{Rh}_s = 3$ . The model of the bimetallic surface is also shown in Fig. 7, assuming that the surface of particles is fcc (111) as is the case for most surfaces of fcc metal, the morphology of metal particles is a sphere, and that the size of Rh metal particles on which Sn atoms form the surface alloy is 2.5 nm (TEM) [94]. According to the results to the Sn K-edge EXAFS analysis, the bond distance between a Sn atom and the nearest-neighbor atom in the first layer of atoms was 0.270 nm, and the bond distance between a Sn atom and a metal atom in the second layer was 0.290 nm, suggesting a relaxation of the first bimetallic layer.

In situ EXAFS was successfully applied to observe the molecular reaction intermediate for NO-H<sub>2</sub> reaction on highly active Rh-Sn/SiO<sub>2</sub> catalysts. The EXAFS data, with the aid of FTIR, revealed the existence of the bent-type NO with the bond distance of 0.256 nm with Sn atoms (Rh-NO-Sn) on the bimetallic surface under steady-state reaction conditions. The tilted NO was suggested to dissociate to form Sn-O bonds at 0.205 nm [95].

#### 4.5.4.15 Mixed Metal Oxides

Conventionally, terephthalaldehyde has been synthesized from the di- and tetrachlorinated side chain derivatives of *p*-xylene in a liquid-phase process. Palladium deposited on silica gel has also been used as a catalyst to reduce terephthalic chloride in boiling xylene in the Rosemund method. However, these processes are not cost effective because of the limited availability of the starting material and the environmentally undesirable nature of the chlorinated byproducts [96]. Recently, a new commercial process has been developed with a modified ZrO<sub>2</sub> catalyst to produce aromatic, aliphatic, and alicyclic aldehydes via hydrogenation of the corresponding acids [97]. The selective oxidation of an alkyl aromatic to the corresponding aldehyde, especially dialdehyde in the *para* position, is a formidable challenge since acid formation is much more favored [98]. Despite extensive efforts, the low terephthalaldehyde yield per pass, together with a sustainable catalyst stability with low burning, remain a major draw-back for the practical application of the gas-phase oxidation reaction of *p*-xylene. It has been discovered that oxides of iron and molybdenum, interacting with a partially deboronated crystalline borosilicate molecular sieve (DBH) having the MFI crystal structure, Fe/Mo/DBH, are very selective in oxidizing *p*-xylene to terephthalaldehyde and *p*-tolualdehyde in high yields, with sustained catalyst stability [96].

The Fe/Mo/DBH catalyst was prepared by the CVD technique from FeCl<sub>3</sub> and chlorides of molybdenum such as MoO<sub>2</sub>Cl<sub>2</sub>, MoOCl<sub>4</sub>, and MoCl<sub>5</sub> with partially deboronated borosilicate molecular sieve. The preparation procedure involves several steps: NH<sub>4</sub>OAc exchange (remove excess boron) → calcination (reduce Si-OH concentration) → FeCl<sub>3</sub> vapor deposition → cool and wash (remove chloride and boron, and provide Si-OH for Mo CVD) → MoO<sub>2</sub>Cl<sub>2</sub> vapor deposition → calcine → wash or steam (remove chloride) [96]. The first step involves the exchange reaction with ammonium acetate to adjust the silanol content on the surface by removing some boron. The calcined sample was loaded into a horizontally mounted quartz tube with quartz wool plugs securing the sample in place. About 6.0 g of

**Table 4.** Oxidation of *p*-xylene with O<sub>2</sub> to terephthaldehyde over Fe/Mo/DBH (Mo:Fe = 1.8).

Temperature (K)	Gas flow rate (cm <sup>3</sup> min <sup>-1</sup> )	Contact time (s)	WHSV (h <sup>-1</sup> )	O <sub>2</sub> conversion <sup>a</sup> (mol %)	<i>p</i> -Xylene conversion (mol %)	Selectivity (%)			
						Benzaldehyde	<i>p</i> -Tolualdehyde	Terephthaldehyde	CO+CO <sub>2</sub> <sup>b</sup>
673	400	0.15	0.22	11.2	42.0	2.3	30.2	55.8	13.9
683	400	0.15	0.22	14.0	51.0	3.7	27.9	52.1	16.2
693	400	0.15	0.22	17.6	61.0	3.0	27.5	51.8	17.5
703	400	0.15	0.22	22.5	73.9	2.6	26.2	53.7	17.4

<sup>a</sup>(quantity in gas feed) – (quantity in effluent)/(quantity in gas feed).<sup>b</sup>Mainly CO<sub>2</sub>.

WHSV: weight hourly space velocity.

FeCl<sub>3</sub> was placed with additional quartz wool plugs at the end of the reactor in a dry bag which was constantly purged with nitrogen. The reactor was placed back into the tube furnace and a nitrogen line was hooked up to the end close to the FeCl<sub>3</sub> at a flow of about 60 ml min<sup>-1</sup>. The reactor temperature was raised to 733 K in 1 h, and kept at this temperature for 1 h to allow FeCl<sub>3</sub> vapor to pass through the molecular-sieve bed. The bed became uniformly yellow in color. After the resulting yellow iron-deposited solid was unloaded from the reactor, it was added to 800 ml deionized water to form a slurry, washed three times, and oven dried at 393 K. A significant amount of boron was removed (from 1.25% to 0.157%) during the second step. The Fe/DBH sample, 30.9 g, was loaded into the reactor and dried at 673 K under a nitrogen flow, resulting in a final weight of 26.1 g. The same vapor deposition procedure as in the second step was repeated with 6.5 g MoO<sub>2</sub>Cl<sub>2</sub> for 4 h at 473 K and 1.5 h at 473–573 K for the reverse operation. After 6.5 h at 573 K, nitrogen was replaced with air, and the reactor kept at 573 K for an additional 8 h. The reactor temperature was then raised to 923 K, and kept at that temperature for an additional 8 h before it was cooled down to ambient temperature. The resulting Fe/Mo/DBH contained 4.6 wt % Mo and 1.41 wt % Fe, Mo:Fe = 1.9, and was ready for the *p*-xylene oxidation.

The activated catalyst was found to be active for the gas-phase oxidation of *p*-xylene to produce terephthaldehyde in high selectivity with sustained stability under relatively mild conditions, as shown in Table 4 [96]. *P*-Tolualdehyde was also produced. The molar ratio of terephthaldehyde to *p*-tolualdehyde of up to 4:1 with limited burning (less than 10%) was realized under controlled conditions despite the catalyst's large surface area, 250–325 m<sup>2</sup> g<sup>-1</sup>.

Combined use of TEM, analytical EM, Raman, XPS, XRD, and in situ XANES were employed to characterize the catalyst. The ferric molybdate and MoO<sub>3</sub> phases are identified as the major species contributing to the selective oxidation of *p*-xylene to aldehyde. Fe and Mo are deposited into the DBH molecular sieve via two micropore channel systems as defined by the DBH framework, resulting in a uniform dispersion of very small particles of either Fe<sub>2</sub>(MoO<sub>4</sub>)<sub>3</sub> or FeMoO<sub>4</sub> [99]. In the final catalyst, the majority of the Fe<sub>2</sub>(MoO<sub>4</sub>)<sub>3</sub>/FeMoO<sub>4</sub> particles are confined on the DBH molecular sieve crystallites as a separate phase attached on the DBH

framework [100]. The enhancement of activity with the presence of CO<sub>2</sub> in the gas phase was addressed by in situ synchrotron radiation studies. In situ low-temperature CO<sub>2</sub> dosing XANES experiments provided evidence for a strongly chemisorbed CO<sub>2</sub> species on Fe/Mo/DBH at the reaction temperature [100]. A reaction mechanism is postulated based on two different types of active sites, namely the pair sites (2Mo<sup>6+</sup>) for terephthaldehyde and single sites (Mo<sup>6+</sup>) for *p*-tolualdehyde [101].

It was also found on the CVD Fe/Mo/DBH catalyst that a large reactivity gap exists between *p*-xylene and the *ortho* and *meta* isomers due to the *para*-selective nature of the catalyst. *p*-Xylene was preferentially oxidized to terephthaldehyde and *p*-tolualdehyde from the xylene isomer mixture, whereas the rest of the components remained almost intact. By coating the CVD Fe/Mo/DBH catalyst with tetramethylorthosilicate, the preferential oxidation of *p*-xylene over its isomers became even more selective [102]. The CVD Fe/Mo/DBH catalyst also exhibited better catalytic performance for the N<sub>2</sub>O oxidation of benzene to phenol than the impregnated counterpart [99].

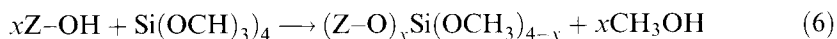
To improve the selective oxidation catalysis of (VO)<sub>2</sub>P<sub>2</sub>O<sub>7</sub>, a V–P–O catalyst was prepared by CVD of VOCl<sub>3</sub> and POCl<sub>3</sub>. The CVD catalyst obtained showed good catalytic performance for the selective oxidation of butane to maleic anhydride, comparable to the (VO)<sub>2</sub>P<sub>2</sub>O<sub>7</sub> catalyst [103].

Composites of ceramics and metals can be prepared by CVD, using suitable precursors, e.g. the heterometallic alkoxide BaSn<sub>2</sub>(OBU)<sub>6</sub> [104]. Decomposition takes place in the temperature range 573–773 K. This temperature is sufficient to decompose the precursor completely and is low enough to prevent carbide formation. The solid material produced reveals a primary structure of ball-shaped particles with the diameters of 20–200 μm, while the diameter of the secondary balls is 200 nm [104].

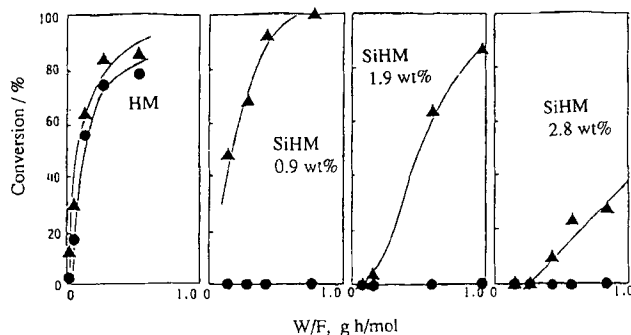
#### 4.5.4.16 Silica

SiO<sub>2</sub> overlayers have been deposited onto the zeolite external surfaces to control the pore-opening size of zeolites. Pore-size control has usually been done by cation exchange. Another method is silanation using SiH<sub>4</sub> [105]. These methods modify the acidity as well as the pore structure, so an undesired change in catalytic activity may be introduced.

CVD of Si(OCH<sub>3</sub>)<sub>4</sub> on the H form of mordenite (HM) has been carried out in order to control the pore-opening size without affecting its acidic properties. Because the molecular size of the alkoxide is larger than the pore size, the alkoxide does not enter the pore and the silicon compound is deposited on the external surface. The initial reaction step may be hydrolysis of the alkoxide:



For highly deposited samples, the CVD procedures were repeated after the evacuation of the gas phase. The sample became gray after the deposition because of coke formation. The deposited samples were then calcined in flowing oxygen at 673 K to remove the carbonaceous deposit. The deposition of the alkoxide does not change



**Figure 8.** Conversion of cracking reactions for octane (▲) and 2,2,4-TMP (●) on HM and SiHM at 573 K; Size: octane (0.43 nm); 2,2,4-TMP (0.62 nm).

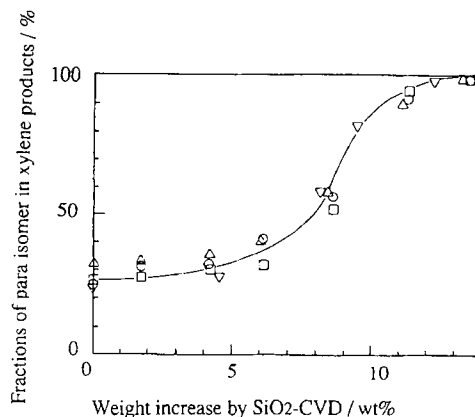
the acidity but reduces the size of the pore openings. The pore size is effectively reduced by  $\approx 0.1$  and  $\approx 0.2$  nm upon formation of 1–2 and 3 monolayers of  $\text{SiO}_2$ , respectively [106].

In Fig. 8, conversion of octane and 2,2,4-trimethylpentane (TMP) on these catalysts are shown as a function of the contact time [107]. Not only octane but also TMP were converted into lower hydrocarbons on HM. However, SiHM of 0.9, 1.9, and 2.8 wt% exhibited high shape-selectivity, since only octane reacted, with 2,2,4-TMP remaining unreacted. The reactant selectivity was thus 100% in any extent of the conversion of octane. Excellent shape-selectivity was observed on SiHM catalyst in the cracking of paraffins. Reactivities of paraffins are distinctive, depending on the molecular size, and the activity of catalyst can be controlled by adjusting the deposition amount. In addition, high shape-selectivity may be related to the deactivation of acid sites at the external surface [107].

The pore-opening size of ZSM-5 is also controlled by CVD of  $\text{Si}(\text{OCH}_3)_4$ . The kinetic diameter of the silicon alkoxide is supposed to be 0.89 nm, much larger than that of the HZSM-5 pore of  $0.54 \times 0.56$  nm. The silica was deposited only on the external surface and narrowed the pore-opening size effectively with the internal structure unaltered. If the deposited silica formed a layer structure, the number of layers could be evaluated from the deposited amount of silica and the cation surface density on ZSM-5. Since the cation site density on the external surface of ZSM-5 is regarded to be  $8.91 \text{ nm}^{-2}$ , the number of silica layers over the modified ZSM-5 is therefore about six on the SiHZSM-5 (12.0 wt%) and four to six on the shape-selectivity improved SiHZSM-5; the fine control of the pore-opening size was tested, exemplified by the conversion of methanol. However, mono- to trilayers are enough for the modification of mordenite. These might be based on the difference in the structure of silica deposited on the external surface [108].

Alkylation of toluene with methanol and toluene disproportionation have been carried out over HZSM-5 modified by CVD of  $\text{Si}(\text{OCH}_3)_4$ . As the silica content increased, the selectivity to *m*- and *o*-xylenes decreased, whereas that to *p*-xylene increased. The fraction of the *para* isomer in xylene increased to more than 98% as shown in Fig. 9 [109]. From adsorption measurements and test reactions, it was found that this modification resulted in the narrowing of the pore-opening size and the inactivation of the external surface. The high *para* selectivity is caused primarily by the narrowing of the pore-opening size.

**Figure 9.** Changes of *para* isomer content in xylene products with increasing silica amounts in toluene alkylation ( $\circ$ ), toluene disproportionation ( $\square$ ), *o*-xylene isomerization ( $\triangle$ ), and methanol conversion ( $\ominus$ ).



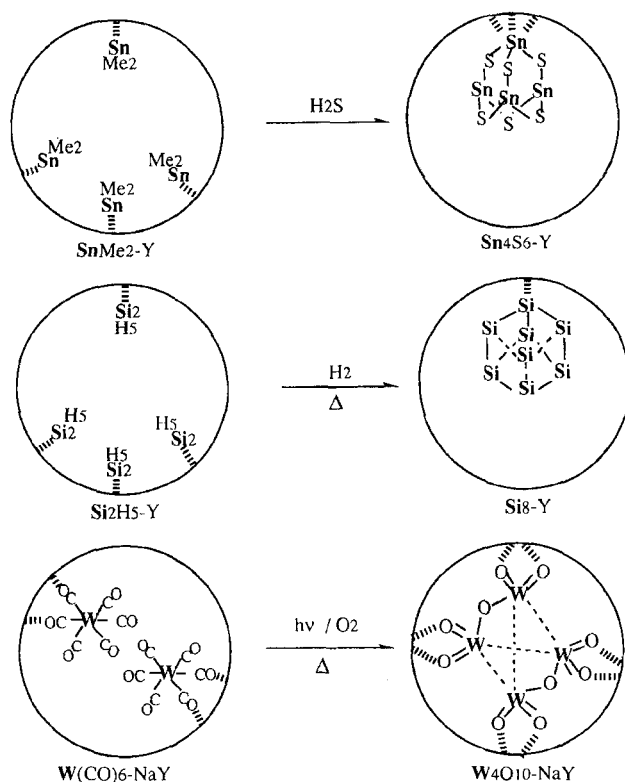
It has been difficult to achieve highly regioselective hydrogenation of unsaturated compounds over heterogeneous catalysts. Platinum-ion-exchanged zeolites coupled with a variety of silicon alkoxides were prepared by CVD [110]. Pt was loaded in zeolite-4A by ion exchange. The CVD treatment was performed in a glass-flow reactor in flowing nitrogen gas; the Pt/zeolite catalyst was treated at 473 K for 3 h with  $\text{Si}(\text{OC}_2\text{H}_5)_4$  ( $1 \text{ mmol h}^{-1}$ ), and at 573 K for 1 h with deionized water (hydrolysis treatment) [111, 112]. This series of treatments was repeated five times and finally the catalyst was treated at 473 K for 1 h without hydrolysis. These catalysts were applied to competitive hydrogenation of terminal and internal alkenes, e.g. 1-octene and *trans*-4-octene, and 1-nonene and *trans*-4-nonene. It was found that the terminal alkene is preferentially hydrogenated [110].

The adsorption and reactions of tetraethoxysilane vapor on clean and water-predosed rutile  $\text{TiO}_2$  (110) have been studied using temperature-programmed desorption (TPD), low-energy electron diffraction (LEED), and X-ray photoelectron spectroscopy (XPS). A distorted  $\text{SiO}_2$  overlayer, made from  $\text{SiO}_4$  tetrahedra, was produced with high probability upon heating to 750 K [113].

### 4.5.5 CVD-Related Techniques

Catalytic CVD is a newly developed plasma-free deposition technique. In the method, deposition gases are decomposed by the catalytic or pyrolytic reactions with a heated catalyzer (e.g. W wire) placed near substrates. Thus films are deposited at low temperatures without help from plasma or photochemical excitation [114, 115].

In plasma CVD, also known as plasma-enhanced or plasma-assisted CVD, the reaction is activated by a plasma. Thermal laser CVD occurs as a result of the thermal energy from the laser coming in contact with and heating an absorbing substrate. In photolytic CVD the chemical reaction is induced by the action of light, specifically ultraviolet radiation, which has sufficient photon energy to break the chemical bonds in the reactant molecules. Fluidized-bed CVD is a special technique



**Figure 10.** Zeolite ligand control over self-assembly.

which is used primarily in the coating of powders. The powder is given quasifluid properties in a flowing gas [116].

### 4.5.6 Conclusions

CVD is no longer a laboratory curiosity and has the potential to become a major technology on par with other disciplines such as conventional wet processing, sol-gel, electrodeposition, etc. The technology still faces many challenges and a large research and development effort is under way in major laboratories in the US, Europe, Japan and other countries, particularly in the semiconductor and engineering industries [1].

Structurally well defined zeolite-entrapped MOCVD and CVD species such as  $\text{W(CO)}_6\text{-Y}$ ,  $\text{Sn(CH}_3)_2\text{-Y}$ ,  $\text{CdCH}_3\text{-Y}$  and  $\text{Si}_2\text{H}_5\text{-Y}$  have been used successfully for the self-assembly and organization of semiconductor nanocluster crystal lattices, including  $\text{W}_4\text{O}_{10}\text{-Y}$ ,  $\text{Sn}_4\text{S}_6\text{-Y}$ ,  $\text{Cd}_6\text{Se}_4\text{-Y}$  and  $\text{Si}_8\text{-Y}$ , as illustrated in Fig. 10 [117]. Materials of this type may have interesting catalytic, electronic, and also luminescent properties.



The method of chemical vapor deposition is now set to open a new area of catalyst preparation. The new materials, structures, and catalysts differ from those offered by other traditional preparation methods may be attractive for application to catalytic processes.

## References

1. J. Haber, *Pure Appl. Chem.* **1991**, 63, 1227–1246.
2. C. F. Powell, J. H. Oxley, J. M. Blocher Jr., (Eds.), *Vapor Deposition*, Wiley, New York, **1966**.
3. L. Mond, US Patent 455 230, **1891**.
4. H. O. Pierson, *Handbook of Chemical Vapor Deposition – Principles, Technology and Applications*, Noyes Publications, New Jersey, **1992**.
5. W. Hertl, *J. Phys. Chem.* **1968**, 72, 1248–1253.
6. W. Hertl, M. L. Hair, *J. Phys. Chem.* **1971**, 75, 2181–2185.
7. J. L. Zilko in *Handbook of Thin-Film Deposition Processes and Techniques* (Ed.: K. K. Shuegraf), Noyes Publications, New Jersey, **1988**.
8. D. W. Snyder, P. J. Sides, E. I. Ko, *J. Crystal Growth* **1992**, 123, 163–173.
9. F. Rosenberger in *Proceedings of the 10th International Conference on CVD* Pennington, **1987**, pp. 193–203.
10. K. F. Jensen in *Proceedings of the 9th International Conference on CVD*, Pennington, **1984**, pp. 3–20.
11. N. D. Parkyn in *Proceedings of the 3rd International Congress on Catalysis*, Amsterdam, **1965**, 2, 914–927.
12. D. C. Bailey, S. H. Langer, *Chem. Rev.* **1981**, 81, 109–148.
13. K. Omata, H. Mazaki, H. Yagita, K. Fujimoto, *Catal. Lett.* **1990**, 4, 123–128.
14. Y. Harano, M. Yano, *Hyomen (Surface)* **1988**, 26, 551–560.
15. J.-P. Jacobs, L. P. Lindfors, J. G. H. Reintjes, O. Jylha, H. H. Brongersma, *Catal. Lett.* **1994**, 25, 315–324.
16. T. Suntola, *Handbook of Crystal Growth* (Ed.: D. T. J. Hurle), Elsevier, Amsterdam, **1993**.
17. E.-L. Lakomaa, *Appl. Surf. Sci.* **1994**, 75, 185–196.
18. S. Haukka, A. Kytokivi, E.-L. Lakomaa, U. Lehtovirta, M. Lindblad, V. Lujala, T. Suntola in *Proceedings of the 6th International Symposium on Scientific Bases for the Preparation of Heterogeneous catalysis*, Belgium, **1995**, 957–966.
19. M. Lindblad, L. P. Lindfors, T. Suntola, *Catal. Lett.* **1994**, 27, 323–336.
20. R. L. Banks, US Patent 3 463 827, **1969**.
21. R. L. Banks, Belgium Patent 633 418, **1963**.
22. A. Brenner, D. A. Hucul, S. J. Hardwick, *Inorg. Chem.* **1979**, 18, 1478–1484.
23. Y. Okamoto, H. Onimatsu, M. Hori, Y. Inui, T. Imanaka, *Catal. Lett.* **1992**, 12, 239–244.
24. S. Haukka, E.-L. Lakomaa, T. Suntola, *Appl. Surf. Sci.* **1994**, 75, 220–227.
25. R. Sekine, M. Kawai, K. Asakura, Y. Iwasawa, in *Proceedings of the Material Research Society Meeting, Anaheim*, **1991**, 222, 333–338.
26. Y. Iwasawa, *Catal. Today*, **1993**, 18, 21–72.
27. R. F. Howe, *Tailored Metal Catalysts* (Ed.: Y. Iwasawa), Reidel, **1986**, pp. 141–182.
28. M. Ichikawa, *Tailored Metal Catalysts* (Ed.: Y. Iwasawa), Reidel, **1986**, pp. 183–263.
29. Y. Iwasawa, *Adv. Catal.* **1987**, 35, 187–264.
30. J. B. Nagy, M. van Eenoo, E. G. Derouane, *J. Catal.* **1979**, 58, 230–237.
31. K. Asakura, K. Ooi, Y. Iwasawa, *J. Mol. Catal.* **1992**, 74, 345–351.
32. R. L. Banks, G. C. Bailey, *Ind. Eng. Chem. Prod. Res. Dev.* **1964**, 3, 170–173.
33. R. L. Banks, *Chem. Tech.* **1986**, 16, 112–117.
34. E. S. Davie, D. A. Whan, C. Kemball, *J. Chem. Soc., Chem. Commun.* **1969**, 1430–1431.
35. R. F. Howe, D. E. Davidson, D. A. Whan, *J. Chem. Soc., Faraday Trans. 1* **1972**, 68, 2266–2280.

36. A. Brenner, R. L. Burwell Jr., *J. Am. Chem. Soc.* **1975**, *97*, 2565–2566.
37. A. Brenner, R. L. Burwell, Jr., *J. Catal.* **1978**, *52*, 353–363; 364–374.
38. Y. Okamoto, T. Imanaka, K. Asakura, Y. Iwasawa, *J. Phys. Chem.* **1991**, *95*, 3700–3705.
39. Y. Okamoto, A. Maezawa, H. Kane, I. Mitsushima, T. Imanaka, *J. Chem. Soc., Faraday Trans. 1* **1988**, *84*, 851–863.
40. Y. Okamoto, Y. Kobayashi, T. Imanaka, *Catal. Lett.* **1993**, *20*, 49–57.
41. J. M. Coddington, R. F. Howe, Y.-S. Yong, K. Asakura, Y. Iwasawa, *J. Chem. Soc., Faraday Trans. 1* **1990**, *86*, 1015–1016.
42. Y. Okamoto, A. Maezawa, H. Kane, T. Imanaka, *J. Mol. Catal.* **1989**, *52*, 337–348.
43. M. Anpo, M. Kondo, Y. Kubokawa, C. Louis, M. Che, *J. Chem. Soc., Faraday Trans. 1* **1988**, *84*, 2771–2782.
44. M. Anpo, M. Kondo, S. Coluccia, C. Louis, M. Che, *J. Am. Chem. Soc.* **1989**, *111*, 8791–8799.
45. C. Louis, M. Che, M. Anpo, *Res. Chem. Intermed.* **1991**, *15*, 81–98.
46. C. Louis, M. Che, M. Anpo, *J. Catal.* **1993**, *141*, 453–464.
47. Y. Iwasawa (Ed.), *Tailored Metal Catalysts*, Reidel, **1986**.
48. Y. Iwasawa, Y. Nakano, S. Ogasawara, *J. Chem. Soc., Faraday Trans. 1* **1978**, *74*, 2968–2981.
49. Y. Iwasawa, S. Ogasawara, *J. Chem. Soc., Faraday Trans. 1* **1979**, *75*, 1465–1476.
50. C. C. Williams, J. G. Ekerdt, J.-M. Jehng, F. D. Hardcastle, A. J. Turek, I. E. Wachs, *J. Phys. Chem.* **1991**, *95*, 8781–8791.
51. M. de Boer, A. J. van Dillen, D. C. Koningsberger, J. W. Geus, M. A. Vuurman, I. E. Wachs, *Catal. Lett.* **1991**, *11*, 227–239.
52. M. Cornac, A. Jeannin, J. C. Lavalley, *Polyhedron* **1986**, *5*, 183–186.
53. A. N. Desikan, L. Huang, S. T. Oyama, *J. Phys. Chem.* **1991**, *95*, 10050–10056.
54. J. M. Aigler, J. L. Brito, P. A. Leach, M. Houalla, A. Proctor, N. J. Cooper, W. K. Hall, D. M. Hercules, *J. Phys. Chem.* **1993**, *97*, 5699–5702.
55. W.-H. Hung, J. Schwartz, S. L. Bernasek, *Langmuir* **1994**, *10*, 2056–2059.
56. E. C. Alyea, K. F. Brown, K. J. Fisher, K. D. L. Smith in *Proceedings of the 10th International Congress on Catalysis*, Budapest (Eds.: L. Guczi, F. Solymosi, P. Tétényi), Elsevier, Amsterdam, **1993**, pp. 503–514.
57. E. C. Alyea, K. F. Brown, K. J. Fisher, *J. Mol. Catal.* **1990**, *63*, L11–L15.
58. Y. Iwasawa, M. Yamada, Y. Sato, H. Kuroda, *J. Mol. Catal.* **1984**, *23*, 95–106.
59. Y. Iwasawa, M. Yamada, *Nikkashi* **1984**, 1042–1049.
60. K. Asakura, Y. Iwasawa, *J. Phys. Chem.* **1989**, *93*, 4213–4218.
61. M. Shirai, K. Asakura, Y. Iwasawa, *Catal. Lett.* **1992**, *15*, 247–254.
62. M. Shirai, T. Inoue, H. Onishi, K. Asakura, Y. Iwasawa, *J. Catal.* **1994**, *145*, 159–165.
63. G. C. Bond, K. Bruckman, *Faraday Discuss., Chem. Soc.* **1981**, *72*, 235–246.
64. G. C. Bond, P. Konig, *J. Catal.* **1982**, *77*, 309–322.
65. T. Hattori, M. Matsuda, K. Suzuki, A. Miyamoto, Y. Murakami, in *Proceedings of the 9th International Congress on Catalysis*, Calgary (Eds.: M. J. Phillips, M. Ternan), The Chemical Institute of Canada, **1988**, pp. 1640–1647.
66. I. E. Wachs, G. Deo, M. A. Vuurman, H. Hu, D. S. Kim, J.-M. Jehng, *J. Mol. Catal.* **1993**, *82*, 443–455.
67. M. A. Vuurman, I. E. Wachs, *J. Phys. Chem.* **1992**, *96*, 5008–5016.
68. G. T. Went, S. T. Oyama, A. T. Bell, *J. Phys. Chem.* **1990**, *94*, 4240–4246.
69. I. E. Wachs, *J. Catal.* **1990**, *124*, 570–573.
70. T. Okuhara, K. Inumaru, M. Misono, N. Matsubayashi in *Proceedings of the 10th International Congress on Catalysis Budapest* (Eds.: L. Guczi, F. Solymosi, P. Tétényi), Elsevier, Amsterdam, **1993**, 1767–1770.
71. K. Inumaru, T. Okuhara, M. Misono, *Chem. Lett.* **1990**, 1207–1210.
72. T. Okuhara, K. Inumaru, M. Misono, *Catal. Lett.* **1993**, *20*, 73–79.
73. M. Anpo, M. Sunamoto, M. Che, *J. Phys. Chem.* **1989**, *93*, 1187–1189.
74. K. Asakura, Y. Iwasawa, *J. Phys. Chem.* **1992**, *96*, 829–834.
75. A. Fernandez, J. Leyrer, A. Z. Gonzalez-Elipse, G. Munuera, H. Knözinger, *J. Catal.* **1988**, *112*, 489–494.
76. M. Anpo, K. Chiba, *J. Mol. Catal.* **1992**, *74*, 207–212.

77. M. Anpo, T. Shima, T. Fujii, S. Suzuki, M. Che., *Chem. Lett.* **1987**, 1997–2000.
78. K. Asakura, M. Aoki, Y. Iwasawa, *Catal. Lett.* **1988**, *1*, 395–404.
79. K. Asakura, Y. Iwasawa, S. K. Purnell, B. A. Watson, M. A. Barteau, B. C. Gates, *Catal. Lett.* **1992**, *15*, 317–327.
80. K. Asakura, Y. Iwasawa, *J. Phys. Chem.* **1992**, *96*, 7386–7389.
81. T. Hattori, S. Itoh, T. Tagawa, Y. Murakami in *Preparation of Catalysts IV* (Eds: B. Delmon, P. Grange, P. A. Jacobs, G. Poncelet), Elsevier, Amsterdam, **1987**, pp. 113–123.
82. U. Kiiski, T. Venalainen, T. A. Pakkanen, O. Krause, *J. Mol. Catal.* **1991**, *64*, 163.
83. L. Alvila, T. A. Pakkanen, O. Krause, *J. Mol. Catal.* **1993**, *84*, 145–156.
84. M. Haukka, T. Venalainen, P. Hirva, T. A. Pakkanen, *Inorg. Chem.* **1995**, *34*, 2931–2936.
85. H. Miura, H. Taguchi, K. Sugiyama, Y. Matsuda, *Shokubai (Catalysts)*, **1988**, *30*, 372–375.
86. J. E. Gozum, D. M. Pollina, J. A. Jensen, G. S. Girolami, *J. Am. Chem. Soc.* **1988**, *110*, 2688–2689.
87. T. Kudo, A. Yamaguchi, Jpn. Patent 62 207 868 **1987**.
88. Z. Yuan, R. J. Puddephatt, *Adv. Mater.* **1994**, *6*, 51–54.
89. C. Dossi, R. Psaro, R. Ugo, Z. C. Zhang, W. M. H. Sachtler, *J. Catal.* **1994**, *149*, 92–99.
90. C. Dossi, R. Psaro, A. Bartsch, A. Galasco, E. Brivio, P. Losi, *Catal. Today*, **1993**, *17*, 527–538.
91. F. Gault, *Adv. Catal.* **1981**, *30*, 1–95.
92. H. Miura, K. Oki, H. Ochiai, J. Kimura, *Shokubai (Catalysts)*, **1989**, *31*, 417–420.
93. K. Tomishige, K. Asakura, Y. Iwasawa, *J. Chem. Soc., Chem. Commun.* **1993**, 184–185.
94. K. Tomishige, K. Asakura, Y. Iwasawa, *J. Catal.* **1994**, *149*, 70–80.
95. K. Tomishige, K. Asakura, Y. Iwasawa, *Chem. Lett.* **1994**, 235–238.
96. J. S. Yoo, J. A. Donohue, M. S. Kleefisch, P. S. Lin, S. D. Elfine, *Appl. Catal.* **1993**, *105*, 83–105.
97. T. Yokoyama, T. Setoyama, N. Fujita, M. Nakajima, T. Maki, K. Fuji, *Appl. Catal. A*, **1992**, *88*, 149–158.
98. W. Partenheimer, *J. Mol. Catal.* **1991**, *67*, 35.
99. J. S. Yoo, A. R. Sohail, S. S. Grimmer, C. Choi-Feng, *Catal. Lett.* **1994**, *29*, 299–310.
100. G. W. Zajac, C. Choi-Feng, J. Faber, J. S. Yoo, R. Patel, H. Hochst, *J. Catal.* **1995**, *151*, 338–348.
101. J. S. Yoo, P. S. Lin, S. D. Elfine, *Appl. Catal. A*, **1993**, *106*, 259–272.
102. J. S. Yoo, J. A. Donohue, M. Kleefisch, *Appl. Catal. A*, **1994**, *110*, 75–86.
103. Y. Takita, T. Hashiguchi, H. Matsunosako, *Bull. Chem. Soc. Jpn.* **1988**, *61*, 3737–3739.
104. M. Veith, S. Kneip, *J. Mater. Sci. Lett.* **1994**, *13*, 335–337.
105. G. Peeters, A. Thys, P. Devievere, E. F. Vansant in *Proceedings of the 6th International Zeolite Conference Reno*, **1983**, s–49.
106. M. Niwa, S. Kato, T. Hattori, Y. Murakami, *J. Chem. Soc., Faraday Trans. 1* **1984**, *80*, 3135–3145.
107. M. Niwa, S. Morimoto, M. Kato, T. Hattori, Y. Murakami in *Proceedings of the 8th International Congress on Catalysis Berlin, DEHEMA, Frankfurt*, **1984**, *IV*, 701–711.
108. M. Niwa, M. Kato, T. Hattori, Y. Murakami, *J. Phys. Chem.* **1986**, *90*, 6233–6237.
109. T. Hibino, M. Niwa, Y. Murakami, *J. Catal.* **1991**, *128*, 551–558.
110. H. Kuno, M. Shibagaki, K. Takahashi, I. Honda, H. Matsushita in *Proceedings of the 10th International Congress on Catalysis Budapest* (Eds.: L. Gucci, F. Solymosi, P. Tétényi), **1993**, pp. 1727–1730.
111. H. Kuno, M. Shibagaki, K. Takahashi, I. Honda, H. Matsushita, *Bull. Chem. Soc. Jpn.* **1991**, *64*, 2508–2512.
112. H. Kuno, M. Shibagaki, K. Takahashi, I. Honda, H. Matsushita, *Bull. Chem. Soc. Jpn.* **1992**, *65*, 1240–1243.
113. L. Gamble, M. B. Hugenschmidt, C. T. Campbell, T. A. Jurgens, J. W. Rogers, Jr., *J. Am. Chem. Soc.* **1993**, *115*, 12096–12105.
114. H. Matsumura, *Jpn. J. Appl. Phys.* **1991**, *30*, L1522–L1524.
115. J. L. Dupuie, E. Gulari, F. Terry, *J. Electrochem.* **1992**, *139*, 1151–1159.
116. J. L. Kaae, *Ceram. Eng. Sci. Proc.* **1988**, *9*, 1159–1168.
117. G. A. Ozin, *Adv. Mater.* **1994**, *6*, 71–76.

## 4.6 Preparation of Supported Catalysts by Deposition–Precipitation

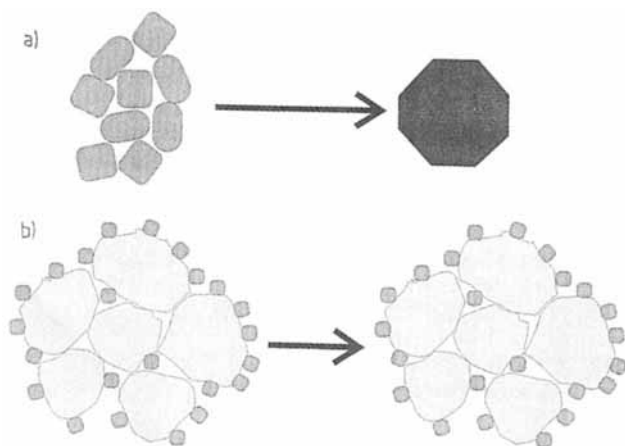
J. W. GEUS AND A. J. VAN DILLEN

### 4.6.1 Introduction

The activity of solid catalysts is usually proportional to the active surface area per unit volume of catalyst. A high activity per unit volume consequently calls for (extremely) small particles. Since most active species sinter rapidly at the temperatures at which the thermal pretreatment and the catalytic reaction are performed [1], small particles of the active species alone do not provide thermostable, highly active catalysts. To provide solid catalysts with the desired thermal stability, a support is therefore generally utilized. A support is a highly porous, thermostable material onto which the active species is dispersed. As indicated in Fig. 1, sintering of small particles leads to a low active surface area; application on a support stabilizes the active surface area.

In view of the favorable bulk density, the price, and its thermal stability, the most frequently used support is alumina. The other supports often used are silica and active carbon. Silica has a lower bulk density, and is more liable than alumina to sintering at temperatures above about 900 K. Furthermore, silica can volatilize at high steam pressures and elevated temperatures. Active carbon supports usually offer very high surface areas. In an environment inert to carbon the thermal stability is extremely high. In an oxidizing environment, however, active carbon will rapidly react with oxygen, and with hydrogen or carbon dioxide, reaction to methane or carbon monoxide, respectively, can proceed. The mechanical strength of carbon supports is, moreover, often insufficient.

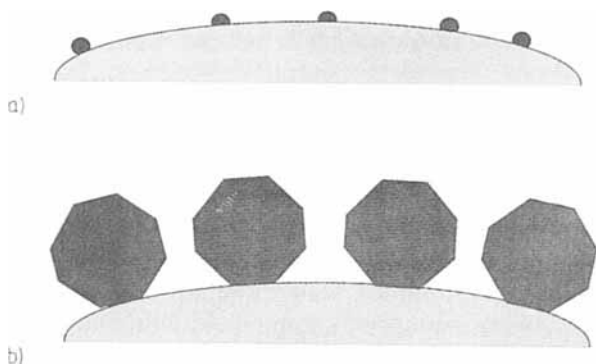
Depending upon the nature of the active component two different types of sup-



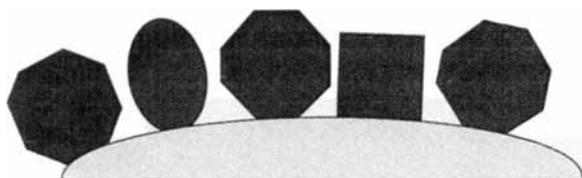
**Figure 1.** (a) Rapid sintering of unsupported active particles. (b) Supported thermostable active material.

ported catalysts can be distinguished [2]. When the active component is highly expensive, as with precious metals, a maximum active surface area per unit weight of active component is aimed at. With less costly active components, such as base metals, base metal oxides, or sulfides, a maximum active surface area per unit volume is most attractive. The reason is that a high active surface area causes a relatively small catalytic reactor volume to be sufficient to achieve a technically satisfactory conversion. When the costs of the reactor dominate the process, a high loading of the support maximizing the active surface area per unit volume will be attractive. Conversely, when the costs of the active component are most important, the maximum active surface area per unit weight of active component is desired. Expensive active components, therefore, will be applied to supports at low loadings leading to small or very small supported active particles, thus providing a high active surface area per unit weight of active component. Since the support is diluting the active component, much higher loadings of the support are generally utilized with base metals or base metal compounds. However, the mobility of the atoms of the active species over the surface of the active component is usually high under the conditions of the catalytic reaction or the thermal pretreatment of the catalyst. As a result, contacting active particles will rapidly decrease their surface area by sintering, which can lead at high loadings to very large bodies of the active component(s) exposing a small active surface area. Contact between the supported active particles must consequently be limited as much as possible. An even and dense distribution of small particles of (the precursor) of the active component over the surface of the support is therefore desired for catalysts containing base metal (compounds) as the active component. Figure 2 schematically indicates a supported precious metal catalyst and an active component consisting of a base metal applied at a high loading on a support.

When the surface area of the support is not affected by the active precursor, the maximum active surface area that can be achieved is of the same order of magnitude as the surface area of the support. A surface of the support thus covered with the active component in a way that the active particles are just not touching will provide an active surface area approaching that of the support. Usually such a coverage calls for small particles of the active component. However, the activity per unit surface area of the active component may vary with the size of the supported



**Figure 2.** (a) Characteristic supported precious metal catalyst. (b) Characteristic supported base metal catalyst.



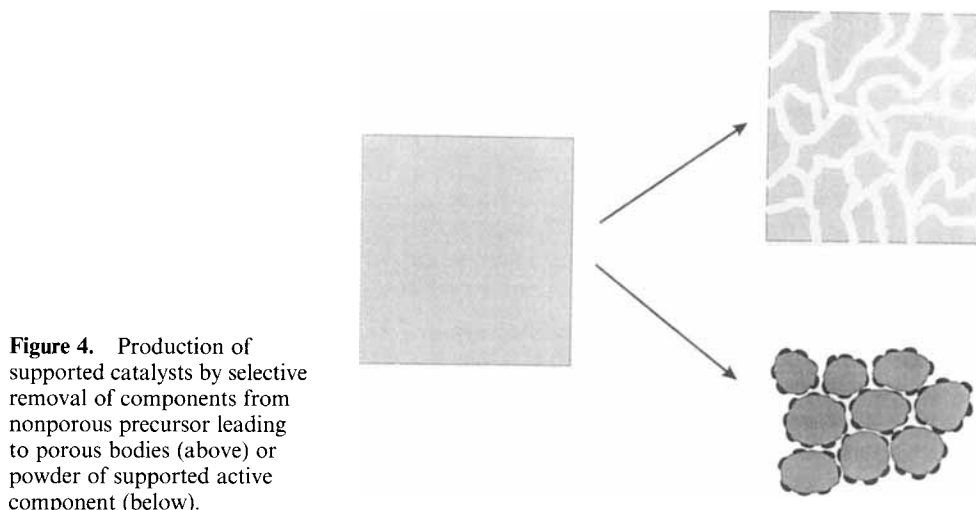
**Figure 3.** Usual supported, highly loaded base metal catalyst.

active moieties. When the activity per unit surface area drops with the size of the active species, the specific activity may be so low that the resulting activity is disappointing, in spite of a high catalytically active surface area per unit volume of catalyst. Reactions for which the surface structure of the catalytically active component is affecting the activity and/or the selectivity are known as structure-sensitive or demanding [3]. With structure-insensitive or facile reactions the structure of the surface of the active component is not affecting the catalytic properties. Small particles may not be favorable when the reaction is structure-sensitive; larger particles may exhibit a higher activity and/or selectivity per unit surface area. Although the active surface area is lower, the higher activity per unit surface area of the active phase results in a higher overall activity. With the selectivity the effect of the size of the active moieties may be even stronger, which causes small supported active particles to be very unfavorable. The most favorable size of supported active particles has, however, only rarely been established. The reason is that it is difficult to vary systematically the size of the active particles deposited on a support while maintaining a narrow particle size distribution. It is consequently desirable to be able to apply the active component(s) uniformly and densely over the surface of the support as particles of controlled size. This is one of the main goals in the preparation of supported catalysts by deposition–precipitation. In Fig. 3 a very highly loaded support surface is schematically indicated – such a loading of a support is difficult to achieve in practice.

After a general discussion of the production of supported catalysts, the theory of nucleation and growth of solids is surveyed. Next the interaction between supports and precipitating precursors of the active components, which is dominating the nucleation with precipitation onto suspended supports, is discussed. This is followed by a review of the loading of powdered supports suspended in an aqueous solution of the active precursor(s) by deposition–precipitation. Highly promising is a technique for the preparation of synthetic clay minerals by deposition–precipitation. A number of embodiments of the procedure are mentioned, including a technically attractive electrochemical precipitation method. Finally, the application of catalytically active precursors into preshaped support bodies is dealt with.

### 4.6.2 Production of Supported Catalysts

The procedures for the production of supported catalysts can be divided into two main groups, namely selective removal of one or more components out of usually nonporous bodies of a compound containing precursors of the support and the active component(s), and application of (a precursor of) the active component(s)



**Figure 4.** Production of supported catalysts by selective removal of components from nonporous precursor leading to porous bodies (above) or powder of supported active component (below).

onto a separately produced support [2]. Both procedures are carried out extensively on a technical scale.

#### 4.6.2.1 Selective Removal of One or More Components

With highly loaded supports, the first procedure, selective removal, is often employed. The most successful example is the technical ammonia synthesis catalyst, which is produced from magnetite ( $\text{Fe}_3\text{O}_4$ ) containing some (up to about 4 wt %) alumina [4]. Selective removal of the oxygen of the magnetite by reduction leads to a highly porous material, in which metallic iron particles of about 40 nm are separated by the remaining alumina. In the reduced catalyst the loading of active component is no less than 96–98 wt %, while the mechanical strength is extremely high. With the copper-based catalysts for the methanol synthesis and for the low-temperature carbon monoxide shift conversion, water, carbon dioxide, and oxygen bonded to the copper are selectively removed from a coprecipitate of copper(II), aluminum(III), and zinc(II). A last example is the removal of water and carbon dioxide from mixed oxalates, as with copper–magnesium or nickel–magnesium oxalates [5]. As shown in Fig. 4, selective removal can result in a porous body, as with the ammonia synthesis catalyst, or in a powder of the support loaded with the active component, as with mixed oxalate precursors.

Although with the selective removal procedure the active component and the support are usually very intimately mixed, it is difficult to control the porous structure and/or the mechanical strength of the resulting catalyst bodies. Nonetheless the procedure is difficult to beat for the production of highly loaded supports. The most well known example of selective removal, the preparation of Raney metals, where aluminum is selectively removed, leaves behind almost exclusively the desired active metal.

#### 4.6.2.2 Application on Separately Produced Supports

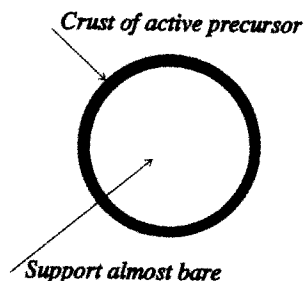
Application of an active precursor onto a separately produced support can be performed with powdered supports and with preshaped support bodies. A powdered support minimizes transport problems during loading with the active component(s), but the subsequent shaping of the loaded support to mechanically strong artifacts may present difficulties. Also, control of the pore structure of the final catalyst can be difficult with loaded, finely divided supports. The most rapid procedure to prepare technical catalysts is to start from commercially available preshaped support bodies of the desired size, shape, porous structure, and mechanical properties. Applying the active component(s) uniformly and finely divided into the support bodies leads immediately to the technical catalyst. However, transport through the long pores of preshaped support bodies can prevent the establishment of a uniform, dense distribution of the active component(s).

*Impregnation of Supports and Drying.* Most obvious is incipient wetness impregnation of a support with a solution of an active precursor and subsequent drying and calcination of the thus loaded support [6]. Incipient wetness or pore-volume impregnation is especially attractive with preshaped support bodies. When the active component has to be in the metallic state, reduction can be carried out after the calcination step. Often, the catalyst is reduced after loading into the reactor to prevent a separate passivation step, in which the surface of the pyrophoric reduced catalyst is carefully oxidized. However, to achieve reproducible catalysts the catalyst manufacturer usually reduces the catalyst and delivers the passivated catalyst, which then only needs a short additional reduction.

It is advantageous if no waste water is produced with impregnation and drying, or if loss of active precursor can be prevented fairly easily. To produce supported precious metal catalysts impregnation and drying is therefore the procedure of choice. For the low loadings usual with precious metals, e.g. 0.5 wt %, adsorption of the precursor on the surface of the support can be used. With alumina, negatively charged precious metal complexes are applied at relatively low pH levels, whereas with silica positively charged ammine complexes are usually employed.

When high loadings are required, pore-volume impregnation is more difficult. First, the solubility of the precursor has to be sufficiently high to allow one to dissolve the required amount of the active component or its precursor in a volume of liquid equal to the pore volume of the support. Often the concentration of the active precursor in the liquid cannot be raised sufficiently. Consequently multiple impregnations are required to achieve the desired loading of the active component. The final distribution of the active component within the support bodies after drying is also often unfavorable. Extensive research has demonstrated that the active precursor is frequently deposited at the external edge of the impregnated support bodies. Boon [7] has shown that for supports with wide pores deposition at the external edge is due to the small crystallites of the active precursor deposited initially at the external edge. The interstices between the small crystallites are more narrow than the pores of the support, which causes a capillary flow of the impregnated liquid from the wide pores of the support to the small crystallites of the active precursor. The result is a porous crust of active precursor, deposited at the external





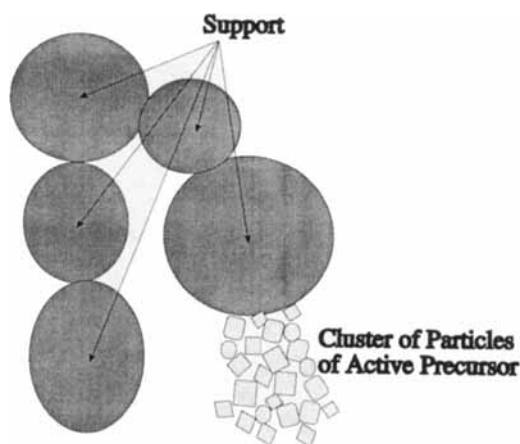
**Figure 5.** Unfavorable distribution of active precursor after impregnation and drying.

edge of the support bodies. Sometimes no active precursor is deposited at all within the internal volume of the support bodies, as indicated in Fig. 5.

With supports having narrow pores, deposition of the active precursor appears to proceed usually at the external edge of the support bodies. The transport of the liquid to the external edge was found to be much faster than the transport of the water vapor through the pores of the support. When the pores of the support are completely filled, capillary flow transports the liquid to the external edge of the support bodies. Furthermore, Knijff [6] and van den Brink [8] have shown that with partly emptied pores the transport of the liquid proceeds through fluid elements capillary-condensed in necks present between the elementary particles of the support. The condition with filled necks bordering the regions of the pore system that have been emptied is known as the funicular state of the impregnated porous solid. As a result the active precursor is mainly deposited at the external edge of the support bodies, where the evaporation of the solvent proceeds and where consequently the concentration is highest.

To prevent migration of the main fraction of the active precursor to the external edge of the support bodies, an active precursor has to be utilized that does not crystallize readily and exhibits a high interaction with the surface of the support, preferably through hydrogen-bridge bonding. Solutions of citrates or ethylenediaminetetraacetic acid (EDTA) complexes have been found to be very effective at preventing deposition of the active precursor exclusively at the external edge of the support bodies [9–12]. With EDTA complexes especially, the pH of the solution being impregnated has to be considered carefully. Much information can be obtained by drying a drop on a microscope slide. If the dissolved material is deposited as a ring, impregnation of a preshaped support and drying is likely to lead to deposition of the precursor on the external edge of the support bodies. If, however, the area of the microscope slide initially covered by the liquid is almost equal to that covered by the dried solid, an even deposition throughout the pores of the support can be expected.

Nevertheless, high loadings often cannot be achieved by pore-volume impregnation, since the required amount of the active precursor cannot be dissolved in the pore-volume of the support. Suspension of the support in a volume of the solution of the active precursor larger than the pore-volume and subsequent drying does not lead to a uniform distribution of the active precursor over the internal surface of the support. The evaporation of the solvent proceeds essentially outside the pore system



**Figure 6.** Clusters of particles of active precursor within support.

of the support and the active precursor is deposited where the solvent evaporates. With a powdered, finely divided support, however, that is continuously and intensively stirred, reasonable results can be obtained. Nonetheless the loading of the support is always inhomogeneous, and the procedure is very difficult to scale up satisfactorily.

*Precipitation onto a Suspended Support.* Precipitation of an active precursor onto a support suspended in a solution of the precursor can provide high loadings, since the compound(s) dissolved in a liquid volume large as compared to the pore-volume of the support are concentrated on the support. Besides coprecipitation of the precursors of the support and the active material and subsequent selective removal of some components, precipitation in the presence of a suspended support is also often carried out to achieve high loadings of the support. The apparatus and the procedures do not differ significantly. However, the precipitation usually proceeds where the precipitating liquid is entering the suspension, and the precipitant necessarily does not enter the suspension within the porous conglomerates of the support. When nucleation and growth of the precipitate of the precursor are rapid, large crystallites of precursor result. With rapid nucleation and slow growth, which is usually encountered with poorly soluble compounds, clusters of small particles of the active precursor outside the pore system of the support are often obtained. At the high concentration at the point where the precipitant enters the suspension, the small particles rapidly and irreversibly flocculate, which leads to the above clusters of small particles. Thus prepared catalysts are liable to rapid deactivation during pretreatment or use at elevated temperatures, since the small elementary particles of the precursor are intimately connected and therefore sinter readily. Figure 6 schematically indicates the type of cluster often found with supported catalysts prepared by precipitation.

The above discussion has indicated that precipitation onto a suspended support is often required to produce catalysts in which the support is highly loaded. Highly loaded supports are especially desirable for catalysts containing (compounds of) base metals as mentioned above. To be able to effect precipitation within the porous

system of a suspended support we have to modify the precipitation process so as to enable the still soluble active precursor to migrate into the pores of the support. Since the diffusion of colloidal particles is fairly slow, we even have to prevent formation of colloidal particles of the active precursor outside the pore system of the support. To obtain the conditions required to achieve transport into the pores of a suspended support, the nucleation of insoluble solids within (aqueous) solution must be considered.

### 4.6.3 Theory of Nucleation

Only a simple review of the theory of nucleation and precipitation [13, 14], to assess the conditions to achieve precipitation exclusively on the surface of the support, is presented here. Consider first the formation of a spherical nucleus in the bulk of the solution. The change in the free enthalpy upon formation of the above nucleus is

$$\Delta G_{\text{tot}} = \Delta G_v - \Delta G_s$$

in which

$$\Delta G_v = \frac{4}{3}\pi r^3(\mu_s - \mu_l) = \frac{4}{3}\pi r^3\Delta\mu_{\text{sl}}$$

$$\Delta G_s = 4\pi r^2\gamma$$

$$\Delta G_{\text{tot}} = \frac{4}{3}\pi r^3\Delta\mu_{\text{sl}} + 4\pi r^2\gamma$$

Here,  $\Delta G_v$  is the volume change in free enthalpy and  $\Delta G_s$  is the interfacial energy of the precipitating solid with the solution,  $2r$  is the diameter of the nucleus of the precipitate,  $\mu_s$  the molecular free enthalpy of the solid precipitate, and  $\mu_l$  of the dissolved solid, while  $\gamma$  is the interfacial energy. The term  $\Delta\mu_{\text{sl}}$ , the difference in molecular free enthalpy between the solid and the dissolved compound, is negative with the bulk solid being stable. For a small change in the size of the nucleus the change in free enthalpy is

$$\frac{d\Delta G_{\text{tot}}}{dr} = 4\pi r^2\Delta\mu_{\text{sl}} + 8\pi r\gamma$$

A maximum in the free enthalpy is obtained when

$$\frac{d\Delta G_{\text{tot}}}{dr} = 0$$

that is

$$4\pi r_c^2\Delta\mu_{\text{sl}} + 8\pi r_c\gamma = 0$$

$$r_c = 2\frac{\gamma}{\Delta\mu_{\text{ls}}}$$

Note that in the latter expression the negative quantity  $\mu_{\text{sl}}$  has been changed for  $\mu_{\text{ls}}$ , a positive value. When the size  $2r$  of the nucleus is greater than  $2r_c$ , the critical size for nucleation, the free enthalpy drops when the size of the nucleus rises. The criti-

cal size of the nucleus corresponds to the maximum in free enthalpy that has to be crossed to arrive at a stable nucleus.  $\Delta\mu_{sl}$  strongly increases with the activity and thus with the concentration of the dissolved compound. The size of the critical nucleus therefore drops rapidly at growing concentration of the dissolved compound.

The rate of nucleation is generally assumed to be proportional to the incidence rate of elementary moieties of the crystallizing species onto the critical nuclei. The rate of nucleation is therefore proportional to the concentration of critical nuclei, which is proportional to

$$\exp\left(-\frac{\Delta G_{\text{tot}}}{RT}\right)$$

Provided that  $r\Delta\mu_{sl} \geq 3\gamma$ , the rate of nucleation is proportional to

$$\exp\left(-\frac{16}{3}\pi\frac{\gamma^2}{\Delta\mu_{ls}^2 RT}\right)$$

Insertion of the earlier derived expression leads to the latter relation to which the density of critical nuclei and, hence, the rate of nucleation is proportional. It can be seen that a higher activity and thus a higher concentration of the precipitating active precursor, which leads to a higher value of  $\Delta\mu_{ls}$ , causes the concentration of critical nuclei to increase exponentially. At a higher concentration the rate of nucleation thus rises sharply.

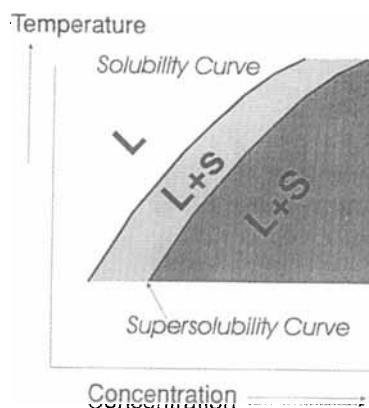
To account for the interaction with the support consider a hemispherical nucleus attached to the support. The change in free enthalpy upon crystallization to form cap-shape nuclei on the support is

$$\Delta G_{\text{tot}} = \frac{3}{2}\pi r^3 \Delta\mu_{sl} + 2\pi r^2 \gamma_{ls} + \pi r^2 \gamma_{ss}$$

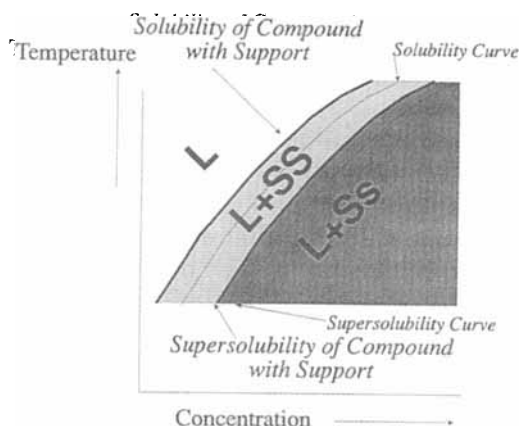
where  $\gamma_{ss}$  is the interfacial energy with the support. The above equations indicate that interaction with the support causing a low value of  $\gamma_{ss}$  can decrease considerably the change in free enthalpy of the formation of a nucleus and hence the concentration of the dissolved active precursor at which a substantial rate of crystallization is exhibited.

We can survey the precipitation in the usual equilibrium diagram, in which the concentration and the temperature of the saturated solutions are represented. Figure 7 schematically indicates the solubility of a solid as a function of the temperature. It can be seen that at increasing temperatures the solubility increases. Since the rate of crystallization or precipitation increases rapidly over a narrow range of concentrations, the concentration as a function of the temperature can be indicated where the precipitation abruptly becomes measurable. The plot of the above concentrations is known as the supersolubility curve, which is also represented in the figure. It is important to note that at concentrations between the solubility and supersolubility curves precipitation within the bulk of the solution does not proceed, although large crystallites of the precursor are stable in the solution.

When the nuclei of the precursor to be precipitated interact significantly with the surface of the support, the rate of precipitation is measurable at much lower concentrations. Accordingly it is possible to perform precipitation exclusively on the



**Figure 7.** Solubility plot also showing the supersolubility curve.

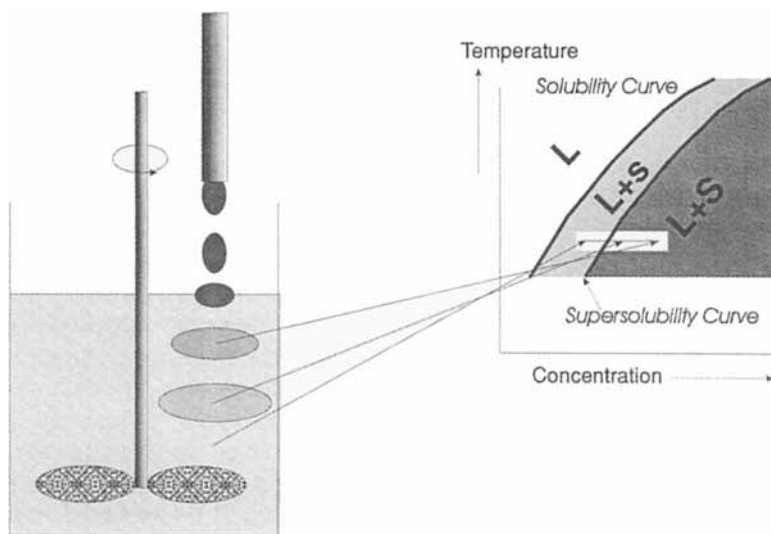


**Figure 8.** Reaction of precipitating active precursor with support to form a less soluble compound.

surface of the support by maintaining the concentration of the precursor between that of the solubility and supersolubility curve. Control of the concentration of catalytically active precursors within the above range is the basis of the deposition–precipitation procedure. With sparingly soluble solids, the concentration difference between the solubility and supersolubility curves is small. The concentration therefore has to be controlled fairly accurately.

Figure 8 shows the case when the active precursor reacts with the surface of the support to yield a compound of a lower solubility. Now both the solubility and the supersolubility curve have been shifted to lower concentrations. We will see that reaction to form a compound with the support often takes place.

With the usual addition of a precipitant to a solution, as schematically represented in Fig. 9, the local concentration rises temporarily above that of the supersolubility curve, which causes rapid nucleation of the precipitate. When after homogenizing the liquid, the final concentration is lower than that of the supersolubility curve, nucleation has already proceeded and the crystallites precipitated are stable. Con-



**Figure 9.** Usual addition of precipitant to suspension of support in solution of active precursor, rapid nucleation outside porous support.

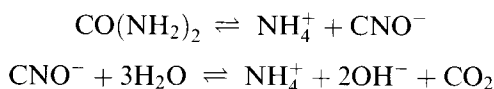
sequently, the concentration has to be maintained continuously below that of the supersolubility curve. With deposition–precipitation this is achieved by performing precipitation from a homogeneous solution [15–17]. A homogeneous solution is most easily obtained by separating the mixing and the generation of the precipitant. This is usually brought about by mixing at a sufficiently low temperature that the reaction generating the precipitant does not proceed markedly, and subsequently raising the temperature to a level where the generation of the precipitant is rapid.

#### 4.6.4 Deposition–Precipitation onto Suspended Finely Divided Supports

As discussed above, sufficiently large interaction between the nuclei of an insoluble active precursor and the surface of a suspended support can bring about precipitation of the precursor exclusively at the surface of the support. Procedures have been developed to achieve deposition–precipitation by changing the pH level, or the valence state of the active precursor, or the concentration of a complexing agent. The complexing agent keeps the active precursor in solution under conditions where the (hydrated) metal ion alone precipitates. To ensure a sufficiently smooth transport of the precipitating species into the pore system of the support, a finely divided support is generally used. When the support after being loaded and separated from the liquid is dried, shaping is usually very easy. The hydroxy groups present in the loaded carrier substantially facilitate the shaping of the support by establishing hydrogen-bridge bonds.

#### 4.6.4.1 Change of pH Level

Precipitation by raising the pH level can be used with the preparation of many catalysts. Especially with tin, nickel and cobalt the procedure is fairly straightforward. The support to be loaded is suspended in a solution of the metal nitrate and a compound is added that is able to consume hydrogen ions. Urea can be utilized to increase the pH of the suspension. Usually the amount of urea is chosen to be 1.5–2.5 times the amount theoretically needed. Urea reacts according to

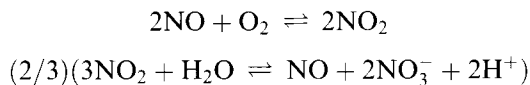


This reaction in which the urea first reacts to produce cyanate and subsequently to ammonium, carbon dioxide, and hydroxy groups, exhibits only a measurable rate at temperatures above about 330 K. It is the first of the above reactions that calls for a temperature of at least 330 K, because ammonium cyanate reacts rapidly at room temperature. Mixing can therefore be carried out at room temperature, while the generation of hydroxy groups proceeds at higher temperatures. When it is desired to perform the precipitation at lower temperatures, ammonium cyanate or a cyanate of an alkali metal can be used. Now, however, mixing has to be done with a suspension kept at about 273 K, to prevent rapid reaction during mixing. An enzyme, urease, has been tried to hydrolyze the urea at low temperatures. However, this enzyme did not work in the presence of usual dissolved catalytically active precursors.

When high loadings of the support have to be applied, the formation of ammonium ions leads to difficulties, because at the higher pH levels required to deposit nickel hydroxide or cobalt hydroxide onto its own lattice, the concentration of ammonium ( $\text{NH}_3$ ) is fairly high. As a result nickel(II) and cobalt(II) redissolve as ammonium complexes. The ammonia can be volatilized by keeping the suspension for a prolonged time at a temperature near 373 K, but then redissolution of nickel or cobalt is difficult to prevent. At high loadings, therefore, it is advantageous to use sodium nitrite, which does not lead to formation of ammonium. Sodium nitrite reacts according to



Oxygen (air) has to be excluded, because oxidation of the NO released leads to the generation of hydrogen ions according to



Consequently the pH changes much less when the nitrogen oxide released can be oxidized by oxygen.

A problem with the use of urea or cyanate can be the production of waste water containing chemically bonded nitrogen, which is difficult to deal with. With the hydrolysis of urea the reaction can be significantly accelerated by performing the reaction at slightly elevated pressures and at temperatures above 373 K. Since

the suspension of the support can be thoroughly mixed at a temperature where the reaction does not proceed, very concentrated solutions can be utilized with urea.

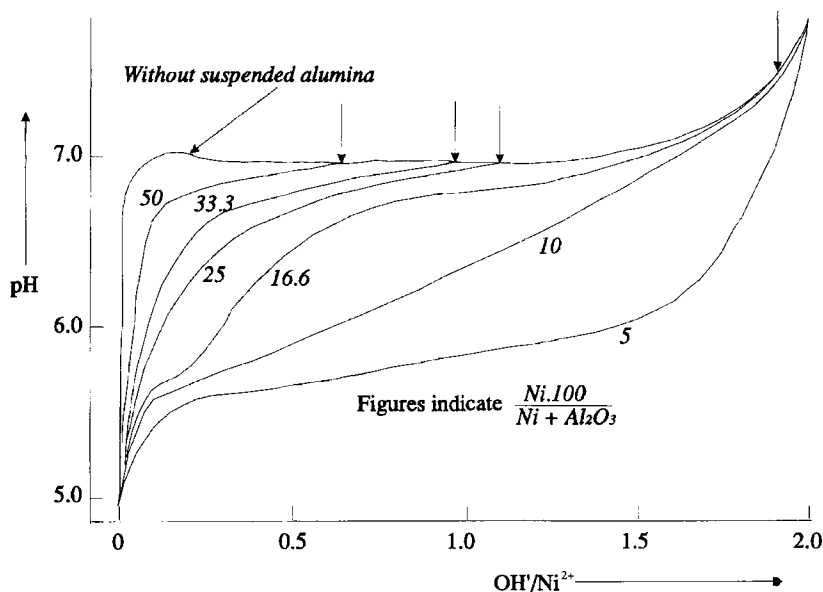
Also the NO released with the disproportionation of nitrite calls for special measures to avoid emission. The environmental problems and the lack of accurate control of the course of the pH level with time has led to the development of an additional deposition–precipitation method, namely the injection procedure. It has been observed that injection of an alkaline solution through a tube ending below the surface of the suspension of the support, avoids locally high concentrations. The reason is that high shear stresses can be established around the end of the injection tube, which is not possible at the surface of the suspension. The injection must be performed slowly and continuously to maintain the solution homogeneous. At a high rate of injection, elements of the solution being injected are brought rapidly in the bulk of the suspension, where the shear stresses are low. Although the injection procedure can be controlled more accurately than the methods using hydroxy ions generating reactants, the procedure calls for much more attention.

Scaling up of the deposition–precipitation procedure does not present any difficulty with urea or sodium nitrite. The preparation of tin oxide on silica catalysts has been scaled up from 1 l to a vessel of 2 m<sup>3</sup> without any difference in the final catalyst. The injection procedure has been scaled up by recirculating the suspension of the support from a large vessel through a small vessel in which the alkaline solution was injected into the vigorously agitated suspension. Provided the flow of the fluid being injected was kept slow and continuous, excellent results have thus been obtained.

Interaction with the support is a prerequisite to achieve the desired dense and uniform coverage of the surface of the support with the precursor of the active component. Precipitation from a homogeneous solution without interaction with the support leads usually to relatively large precipitated crystallites. The interaction with the support can be easily assessed by measuring the pH as a function of time or of the amount of alkali injected both with and without a suspended support. If there is a significant interaction with the support, the level of the pH remains with a suspended support considerably below that of the pH measured without a suspended support. Without a support, the concentration of the supersolubility curve is often apparent from the pH curve passing through a maximum. When the concentration of the supersolubility curve has been attained, nucleation proceeds rapidly and the subsequent growth of the nuclei proceeds faster than the generation or addition of hydroxy ions.

Figure 10 shows the course of the pH during injection of alkali into a nickel nitrate solution kept at 293 K [18]. It can be seen that without a suspended alumina support, the pH passes through the maximum mentioned above. When alumina has been suspended in the solution, the pH remains below the pH level measured with nickel nitrate alone. At a low loading of the support, as with the loading of 5% in Fig. 10, the pH remains considerably below the level exhibited with only nickel nitrate. The low pH level indicates reaction of the surface of the suspended alumina support with nickel(II) ions to a hydrotalcite structure. At higher loadings of the alumina support the nickel ions can no longer be completely accommodated in the surface hydrotalcite and nickel hydroxide grows, which is evident from the pH curve



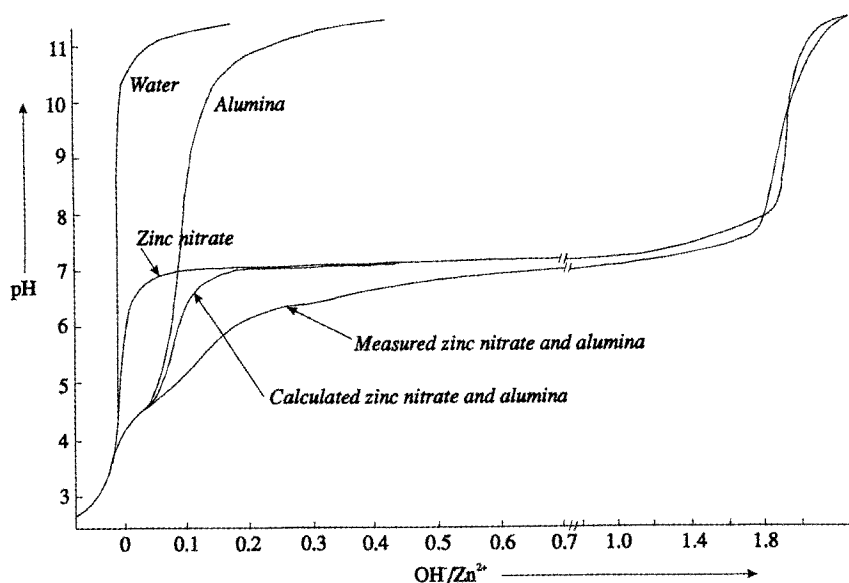


**Figure 10.** Precipitation of nickel(II) from a homogeneous solution by injection of sodium hydroxide at 293 K. A measurement without suspended alumina and measurement with suspended alumina are represented. The final nickel loading is indicated in the figure [18].

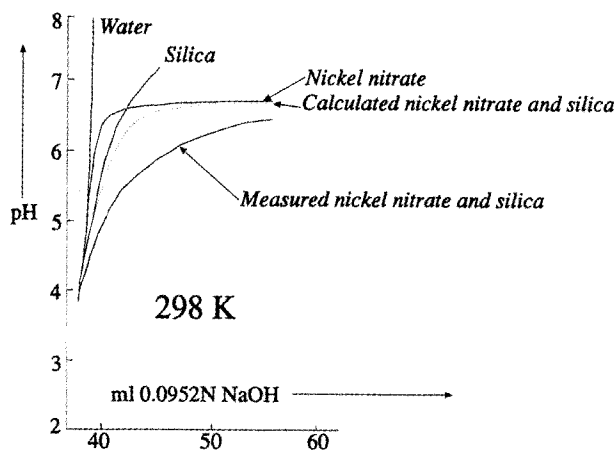
merging the curve measured with nickel nitrate alone. In Fig. 10 a vertical arrow indicates the point where the curve measured with suspended alumina reaches the curve measured with nickel nitrate only. Using temperature-programmed reduction De Bokx et al. [18] demonstrated that the fraction of hydroxy ions consumed at pH levels lower than that observed with nickel nitrate alone measures the fraction of nickel hydroxalcite formed.

Figure 11 shows the course of the pH during the precipitation of zinc(II) with and without suspended alumina [19]. The pH is recorded during addition of alkali to the same volume of water, of a suspension of alumina in water, and of a solution of nickel nitrate. In the figure the curve obtained by addition of the hydroxy ions consumed in the above three measurements is compared with the pH curve experimentally measured with suspended alumina. It is evident that the calculated pH curve runs appreciably above the curve recorded experimentally. The interaction of the precipitating zinc ions with the alumina is evident from the consumption of hydroxy ions at a relatively low pH level.

Analogous experiments with silica as the support indicate the appreciable interaction of precipitating nickel(II) ions with silica [20, 21]. In the experiments represented in Fig. 12 the solutions or the suspension was kept at 298 K. The curve measured with suspended silica runs again considerably below the curve calculated from the curves recorded with water, suspended silica, and nickel nitrate alone. The interaction with the silica support causes a higher consumption of hydroxy ions at a low pH level. Burch and Flambard [22] performed the same experiments with both



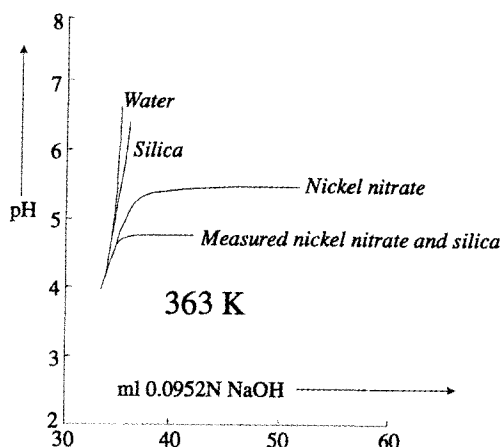
**Figure 11.** Precipitation of zinc(II) from a homogeneous solution by injection of sodium hydroxide at 293 K [19].



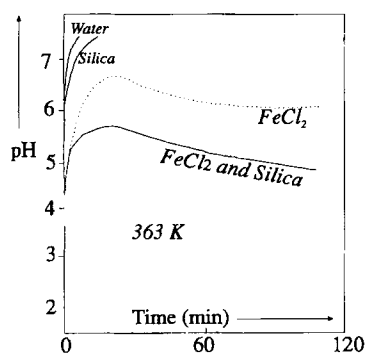
**Figure 12.** Precipitation of nickel(II) from a homogeneous solution by injection of sodium hydroxide at 298 K [20, 21].

silica and titania supports. They observed exactly the same behavior, namely a considerably lower pH level when the precipitation of nickel(II) was carried out in the presence of a silica or titania support.

Figure 13 represents measurements at 363 K with silica as a support. The curve measured with suspended silica in a nickel(II) solution at 363 K remains appreciably below the curve measured with nickel nitrate alone and does not approach the curve measured without suspended silica. The course of the pH with suspended



**Figure 13.** Precipitation of nickel(II) from a homogeneous solution by injection of sodium hydroxide at 363 K [20, 21].

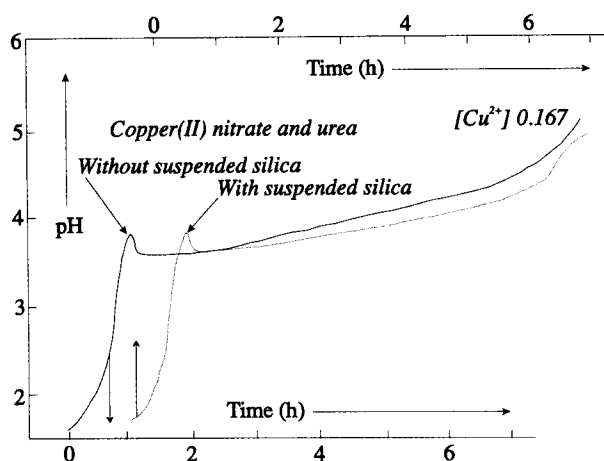


**Figure 14.** Precipitation of iron(II) from a homogeneous solution by injection of sodium hydroxide at 363 K [24].

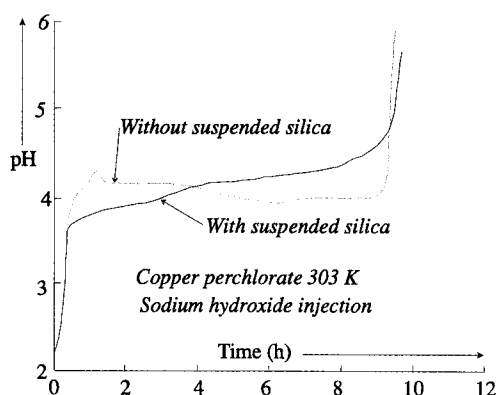
silica indicates formation of a bulk compound with the support, as schematically indicated in Fig. 8. Formation of nickel antigorite (a 1 : 1 clay mineral) or nickel hectorite (a 1 : 2 clay mineral) is evident from X-ray diffraction, electron microscopy, temperature-programmed reduction, and the considerable increase in BET surface area of the silica support after reaction with the nickel ions. Richardson et al. [23] have reported precisely the same results with the precipitation of nickel(II) ions from a homogeneous solution in the presence of a suspended silica (Cabosil) support.

Figure 14 indicates that iron(II) reacts analogously with silica upon precipitation from a homogeneous solution kept at 363 K [24]. Reaction to a new solid phase is also apparent from the maximum exhibited by the pH curve measured with suspended silica. Also with precipitating nickel and suspended silica a maximum in the pH level is often observed when the pH is homogeneously raised at 353 K or at a higher temperature (as shown in Fig. 18).

Figure 15 shows the course of the pH when the pH of a copper(II) nitrate solution is raised by the hydrolysis of urea [20, 25]. Curves with and without suspended silica are represented. Both curves show a distinct maximum and are almost iden-



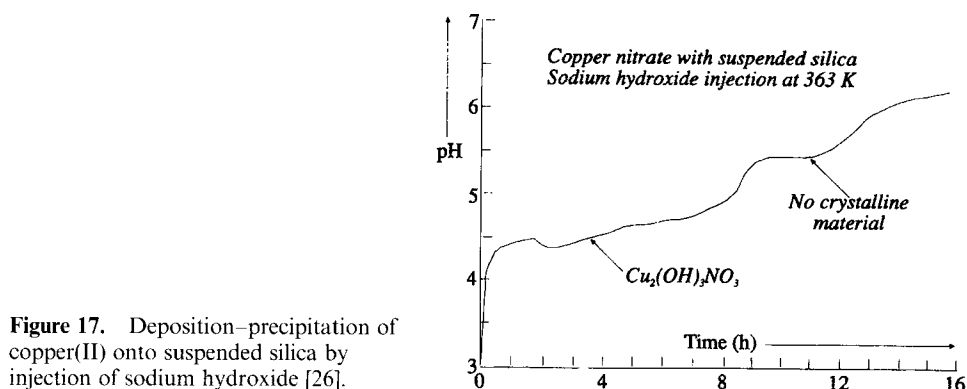
**Figure 15.** Precipitation of copper(II) from a homogeneous solution of copper nitrate by hydrolysis of urea both with and without suspended silica [25].



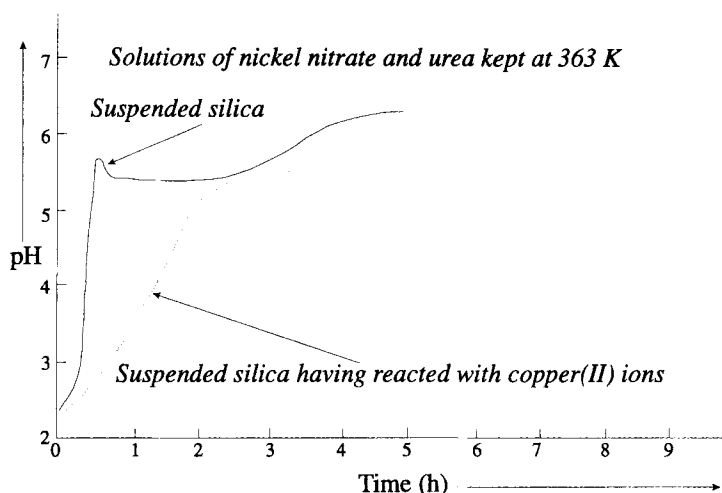
**Figure 16.** Precipitation of copper(II) from a homogeneous solution of copper perchlorate by injection of sodium hydroxide at 303 K [25].

tical. Consequently copper(II) ions precipitating at a pH level below about 4 in the presence of nitrate ions exhibit no interaction with a suspended silica support. During the precipitation of copper(II) from a homogeneous solution of copper nitrate, the copper(II) precipitates as large thin platelets of basic copper nitrate,  $\text{Cu}_2(\text{OH})_3\text{NO}_3$ . Nucleation of the basic copper(II) nitrate and the subsequent rapid growth and consequent rapid consumption of hydroxy ions lead to the pronounced maximum exhibited in the curves of Fig. 15. In the presence of sulfate and chloride ions the corresponding basic salts are precipitating as relatively large crystallites upon precipitation from a homogeneous solution.

With perchlorate ions, which interact less strongly with precipitating copper(II) ions, nucleation of precipitated copper species proceeds at a significantly higher pH level, as can be concluded from Fig. 16. When more alkali has been added, reaction of the basic salt initially precipitated to (brown or black) copper oxide, which is more stable, takes place. Consequently, a drop in pH level is exhibited due to the exchange of perchlorate ions for hydroxy ions. With suspended silica the pH curve



**Figure 17.** Deposition–precipitation of copper(II) onto suspended silica by injection of sodium hydroxide [26].



**Figure 18.** Comparison of deposition–precipitation of nickel(II) ions on silica and on silica having previously reacted with copper(II) ions [27].

runs initially below the level measured without suspended silica. The stabilization of the copper species precipitated by interaction with the support is evident from the fact that now no copper oxide results when more alkali has been added. The loaded support displays still a blue color when the precipitation has finished which is maintained after drying at 383 K.

Figure 17 shows the precipitation of copper(II) at 363 K in the presence of suspended silica when more hydroxy ions are admitted and consequently higher pH levels are obtained [26]. It has been observed that the basic copper nitrate initially precipitated becomes unstable and reacts with the support at higher pH levels. The silica support reacts to a considerable extent with the copper(II) ions to a hydrosilicate, which has a structure analogous to that of the mineral chrysocolla. Nickel hydrosilicate grows without nucleation on silica having reacted with copper(II) ions as is shown in Fig. 18 [27]. When nickel(II) ions are precipitating from homoge-

neous solution by hydrolysis of urea at 363 K in the presence of suspended silica, the pH passes through a maximum as can be seen in Fig. 18. Since the pH level remains much lower than with the precipitation of nickel(II) without suspended silica, nucleation of a nickel hydrosilicate (a clay mineral) is indicated. In the presence of suspended silica that has reacted with copper, the pH remains substantially lower than with pure silica as exhibited in Fig. 18. Accordingly, growth of a mixed hydrosilicate proceeds smoothly with copper(II) hydrosilicate.

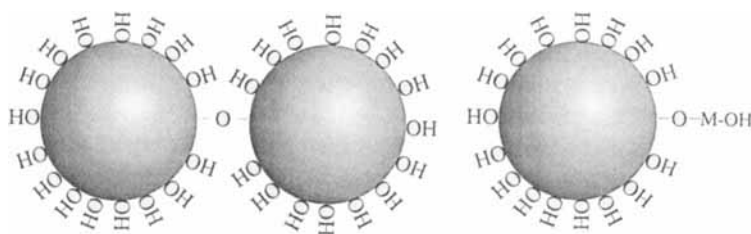
It is important to consider the interaction with the support more closely. Often an electrostatic model has been used to account for the interaction of precipitating species with the support. It has been established that species having an electrostatic charge of the same sign as the support do not deposit onto the support. The isoelectric point of silica is, for instance, about 2, which implies that at lower pH levels the silica is positively charged due to the uptake of hydrogen ions, whereas at higher pH levels ionization of surface hydroxy groups leads to a negative charge:



If an electrostatic interaction alone would determine the interaction of precipitating species with the surface of a suspended support, the interaction with precipitating hydrated iron(III) oxide would be small, whereas the interaction with precipitating copper(II) hydroxide would be considerable. Indeed it was observed that hydrated iron(III) oxide, which reacts to form clusters of very small moieties at pH levels of 2, does not interact significantly with suspended silica. However, the precipitation of copper(II), which also proceeds at a pH level of about 3 with most anions, is not markedly affected by the presence of suspended silica. As shown by the experimental results presented above, copper(II) precipitates with many anions as a basic salt of the anion being present during the precipitation without a significant interaction with the suspended silica support. Actually small silica particles are being supported by large crystallites of the basic copper salts after performing a deposition-precipitation. The above results with copper(II) were measured by Van der Meijden, who extensively studied the precipitation of copper(II) with and without suspended silica [20, 25]. His data show that a pH level above about 4 is required for interaction of precipitating copper(II) with suspended silica. Precipitation from copper(II) perchlorate solutions, which do not readily react to basic copper(II) perchlorate, and which proceeds at higher pH levels, leads to a significant interaction with the silica support.

We therefore feel that besides an electrostatic interaction a chemical interaction between the precipitating species and the support is also required. With colloidal silica solutions a reaction proceeds between the hydroxy groups present on different silica particles. Condensation of water leads to formation of oxygen bridges between the silica particles, which causes gelation of the silica sol. An analogous reaction will proceed between hydroxy groups present on the surface of silica particles and hydroxy groups of partially hydroxylated metal ions. The gelation of silica calls for a pH level of at least about 4, which agrees very well with the pH level at which hydroxylated metal ions are exhibiting interaction with silica. The reaction of the hydroxy groups is schematically indicated in Fig. 19.

Iron consequently has to be applied onto silica from iron(II) solutions, since



**Figure 19.** Schematic representation of the reaction between hydroxy groups on different silica particles leading to gelation of silica sols (left-hand side) and of the hydroxy group(s) on partially hydroxylated metal ions with surface hydroxy groups of silica.

iron(II) precipitates at a much higher pH level than iron(III) [28]. With iron(II) a high interaction with silica supports is observed. With iron(III) a reverse precipitation has to be carried out. An acid iron(III) solution is injected into a suspension of silica, kept at a pH level of about 6 by simultaneous hydrolysis of urea or simultaneous injection of an alkaline solution.

The behavior of copper(II) is interesting. At higher pH levels the initially precipitated basic salt becomes unstable and copper(II) is precipitating onto the suspended silica support. At higher temperatures without suspended silica, black copper(II) oxide results, whereas at lower temperatures without suspended silica blue copper hydroxide is formed. With urea, intermediate formation of malachite, basic copper(II) carbonate, is observed in the absence of suspended silica.

A number of catalytically important metals cannot be applied smoothly on silica, namely metals present in the most stable state as highly charged metal ions forming anions with oxygen. The most important instances of this group of metals are molybdenum, tungsten, and vanadium. The negatively charged  $\text{MoO}_4^{2-}$ ,  $\text{WO}_4^{2-}$ , and  $\text{VO}_3^-$  ions cannot be deposited on silica, which is also negatively charged. The electrostatic charges of the support and of the species to be deposited being opposite is a necessary, but not a sufficient condition to have a sufficient interaction with the support to enable one to perform deposition–precipitation. Vogt et al. [29, 30] have established that decreasing the valence of the metal ions caused the metal ions to be present as hydrated cations in an aqueous solution. Electrochemical reduction of vanadium(V) and molybdenum(VI) to trivalent metal ions can be performed smoothly. Overbeek [31] has carried out the scaling up of the electrochemical reduction and has achieved a very high current efficiency. With the lower valent metal ions the usual deposition–precipitation can be performed by raising the pH of a suspension of silica in a solution of the lower valent metal ion [30, 32, 33].

The behavior of vanadia and molybdena deposited very finely divided on silica is interesting. Vogt showed that vanadia applied as  $\text{V}^{\text{III}}$  and subsequently oxidized to  $\text{V}^{\text{V}}$  by calcination at 623 K for 72 h was deposited on silica as a monolayer; the infrared absorption due to vibrations of hydroxy groups of the silica surface disappeared at a monolayer coverage of vanadia. Apparently the interaction of the precipitating vanadium(III) with the silica surface is strong. De Boer [33] accurately investigated the interaction of molybdena with silica. With molybdena deposited as

$\text{Mo}^{\text{III}}$  and oxidized to  $\text{Mo}^{\text{VI}}$  the vibrations of hydroxy groups of the silica surface did not disappear completely, which indicates that the molybdenum oxide species is not covering the silica surface completely. Low-energy ion scattering, Laser-Raman spectroscopy, and EXAFS have revealed that the molybdena species are present as small hydrated clusters on the silica surface. Upon dehydration, the molybdenum(VI) oxide moieties are spreading over the silica surface and covering the silica surface completely; rehydration leads again to clusters and to some bare silica. When the molybdenum(VI) oxide is finely divided, nucleation of  $\text{MoO}_3$  cannot proceed and the molybdenum oxide is strongly interacting with the silica. The uniform thin layer of molybdenum oxide can only be established by deposition from molybdenum(III) solutions.

The chemical interaction of metal ions precipitating from a homogeneous solution with silica at higher temperatures has been confirmed extensively. With finely divided silica, reaction with synthetic clay minerals has been established. Consequently the reaction is not confined to the surface of silica, but involves also the bulk of small silica particles. Reaction with another solid phase was already concluded from the maximum through which the pH curve often passes during the deposition-precipitation of nickel at a temperature of about 350 K or higher. The complete reaction of the silica particles is also evident from electron micrographs [2], which show a complete disappearance of the silica particles initially present. When the amount of bivalent metal ions is not sufficient to convert the silica completely, growth of platelets of clay minerals out of the silica particles can be easily seen.

By precipitation from homogeneous solution in the presence of suspended silica a procedure for the production of synthetic clay minerals has thus been achieved that is much more favorable than the procedures used in the state of the art, which involves hydrothermal treatment at high temperatures and pressures for prolonged periods of time [34]. The clay minerals from bivalent metal ions are of the hectorite type; the bivalent metal ions are present within the octahedral holes of a central layer, which is covered at both sides by a layer containing  $\text{Si}_2\text{O}_5(\text{OH})$  groups. With magnesium very small platelets exhibiting a surface area of about  $700\text{ m}^2\text{ g}^{-1}$  are obtained, and with zinc much larger platelets having a surface area of about  $200\text{ m}^2\text{ g}^{-1}$ . The surface areas with nickel and cobalt are intermediate. The surface areas are considerably higher than the surface area of the original silica support. The reaction to clay minerals is also evident from the acid groups present within thus loaded silica supports after partial reduction of reducible metal ions, such as, nickel or copper. Addition of tetrahedrally coordinated aluminum during the deposition precipitation leads to reaction to saponite clay minerals, in which a fraction of the silicon ions present in the tetrahedral holes is substituted by aluminum ions. After exchange of the interlayer cations, usually ammonium after the preparation, acid protons are present in the saponite clay minerals. The above preparation procedure yields reproducible clay minerals, the properties of which can be accurately controlled within a wide range, offers interesting possibilities for the technical application of clay minerals in catalytic reactions.

Also, with alumina, reaction of the support to compounds with active precursors can proceed, although the reaction remains generally limited to the surface layer of the alumina. With bivalent metal ions reaction to compounds of a hydrotalcite



structure occurs [18]. Hydrotalcite is a mixed magnesium–aluminum hydroxide ( $\text{Mg}_6\text{Al}_2(\text{OH})_{16}\text{CO}_3 \cdot 4\text{H}_2\text{O}$ ) and takovite ( $\text{Ni}_6\text{Al}_2(\text{OH})_{16}\text{CO}_3 \cdot 4\text{H}_2\text{O}$ ) is the analogous nickel compound. The metal ions are present in the octahedral sites of the brucite structure. Due to the presence of trivalent aluminum ions, the electrostatic charge cannot be compensated by the hydroxy ions only and anions, such as carbonate ions, are accommodated in the interlayer between the hydroxy groups. Reaction to the analogous nickel–aluminum and cobalt–aluminum compounds has been observed with deposition–precipitation of nickel or cobalt on suspended alumina. Actually the reaction to the surface hydrotalcites (or Feitknecht compounds) is unfavorable, since nucleation of spinels of the bivalent metal ions, e.g.  $\text{NiAl}_2\text{O}_4$ , proceeds upon thermal treatment of the surface hydrotalcites.

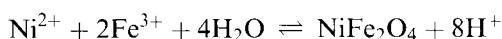
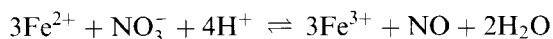
It is notable that when performing reactions within a homogeneous solution, interfacial inorganic reactions often take place that are completely analogous to geochemical reactions. Both the reactions with clay minerals and with hydrotalcites are also well known in geochemistry.

Effecting deposition–precipitation by decreasing the pH level is interesting with metal ions present in the stable state in aqueous solution as anions [35]. With silica no interaction is observed, which has led to the development of the electrochemical reduction procedure. To apply metal ions, such as, molybdenum or vanadium, on alumina, a homogeneous decrease in pH level is interesting. The pH level has been decreased by injection of nitric acid or perchloric acid and electrochemically. However, the rate of crystallization of the hydrated oxides of vanadium(V) and molybdenum(VI) was observed to be fairly low. To prevent dissolution of the alumina supports the pH cannot be decreased to levels below about 3, at which the crystallization of the hydrated metal oxides does not proceed rapidly.

Decreasing the pH levels of suspensions of a suitable support in a solution of an active precursor has therefore been studied much less than raising the pH level.

#### 4.6.4.2 Changing the Valency of Precursor Ions

Precipitation from a homogeneous solution by changing the valence of the metal ions to be precipitated can be performed very smoothly in some cases. An increase in valency has been used with iron and manganese. Iron(II) and manganese(II) are much more soluble than iron(III) and manganese(III) and -(IV). Oxidation with a dissolved oxidizing agent therefore leads to precipitation from a homogeneous solution. With iron(II) the oxidation can be carried out with nitrate ions [28]. Since hydrolysis of the resulting iron(III) ions releases hydrogen ions, the pH must be kept constant by simultaneous injection of an alkaline solution or by hydrolysis of urea. Usually, oxidation of iron(II) from a homogeneous solution leads to precipitation of magnetite,  $\text{Fe}_3\text{O}_4$ . When other suitable bivalent metal ions are present in the solution, other ferrites, such as, nickel or cobalt ferrite, result:



Finely divided magnetite deposited on a support is liable to oxidation and hydrolysis, which leads to hydrated supported iron(III) oxide. To prevent oxidation and hydration, the loaded support has to be dried in an inert gas. After being dried the supported magnetite is fairly stable on exposure to atmospheric air, although reaction to  $\gamma\text{-Fe}_2\text{O}_3$  may proceed.

Precipitation by reduction of metal ions has many applications [36]. Precipitation from a homogeneous solution of chromium by reduction of chromium(VI), which is soluble at pH levels around 7, to chromium(III), which is insoluble at this pH range, has been done. Also, reduction of metal ions, such as, silver, palladium or platinum, to the metallic state can lead to very finely divided metal particles. De Jong and Geus have studied precipitation by reduction of silver ions in the presence of a suspended silica support [37, 38]. A bimodal particle size distribution usually results. The silver complexes adsorbed on the support react with the reducing agent to very small silver particles (about 1 nm), whereas in the bulk of the solution the more difficult nucleation of metallic silver leads to relatively large particles (at least 10 nm). With other precious metals an analogous behavior has been observed. With suspended silica supports that were loaded at pH levels around 7, it was demonstrated that the electrostatic charge of the precursor complexes is determining whether precipitation by reduction to the metal on the support can proceed. Only positively charged complexes, such as the silver ammine complex, resulted in small silver particles deposited evenly over the silica support. The amount of silver complex that can be adsorbed on the silica support, however, was also found to be limited. A higher concentration of silver simply resulted in large silver particles formed in the bulk of the solution.

Controlled growth of previously deposited very small silver particles can also be performed. The procedure involves to establish first the minimum temperature at which reduction of the metal proceeds in the bulk of the solution. With the reduction of silver ammine complexes by formaldehyde, the temperature to effect reduction in the bulk of the liquid is about 310 K. It has been found that metallic silver particles catalyze the reduction of the silver ammine complexes. By suspension of a silica support covered with small silver particles in a solution of  $\text{Ag}(\text{NH}_3)_2^+$  cooling the suspension to 273 K and subsequently injection of formaldehyde, controlled growth of the silver particles can be achieved. It is interesting that the silver particles grow to an elongated shape; apparently the electrostatic repulsion between the positively charged silver complexes brings about an approach from opposite sides. Thermal treatment at a moderate temperature in a reducing gas flow suffices to produce symmetrical metal particles. An analogous procedure can also be carried out with small particles of precious metals, such as platinum or palladium. It is also possible to grow different metals on small metallic nuclei, such as silver, onto platinum particles.

#### 4.6.4.3 Removal of Complexing Agent

The best known procedure in which a complexing agent is removed involves the volatilization of ammonia from ammine complexes. It is important to start from an

insoluble compound and to dissolve the metal ions of the solid compound by complexing with ammonia. An instance is nickel hydroxide, which is dissolved in a mixture of ammonium carbonate and ammonia; removal of the ammonia leads to precipitation of nickel carbonate. It is therefore difficult to achieve a sufficiently high concentration of dissolved nickel. Another problem is the relatively high pH level required to bring the ammonium concentration at the required level to dissolve the nickel completely. At the high pH levels due to the required ammonia concentration, supports such as alumina and silica dissolve.

Procedures have also been developed to oxidize complexing agents, such as EDTA or ethylenediamine. The oxidation was performed with hydrogen peroxide (perhydrol) at a pH level where the uncomplexed metal ions are insoluble [39]. With a number of metal ions, the procedure was successful. With copper, however, cautious operation was required. The oxidation of a copper EDTA complex exhibits an induction period of about 30 min. After this period of time very finely divided copper oxide is deposited onto the support, thus providing a very efficient catalyst for the decomposition of hydrogen peroxide. The hydrogen peroxide rapidly decomposes, releasing a large volume of oxygen, which results in a blowout of the contents of the reactor. To carry out the preparation procedure involving the oxidation of EDTA complexes by hydrogen peroxide on a large scale, a film reactor was utilized to enable the rapid evolution of gas.

#### 4.6.4.4 Electrochemical Deposition–Precipitation

Base metals are generally cheaper than the corresponding metal salts. One reason is that production and transport of the salt, which is heavier per unit weight of metal than the pure metal, can be avoided. With the production of supported catalysts it is therefore often advantageous to start from the metal to be applied onto an appropriate support and not from a salt of the metal. According to the usual procedure the metal has to be dissolved in a suitable acid in the catalyst production plant. To minimize environmental problems hydrochloric acid is often used, although nitric acid can be more easily removed from the catalyst by a thermal treatment. Precipitation of the metal as a hydroxide, hydrated oxide, or basic salt, calls for soda or other alkaline compounds and leads to the production of salts of the alkali metals used, which has to be disposed.

An attractive procedure is possible when a metal is applied without being completely dissolved. Van Stiphout and co-workers have developed a precipitation method in which a metal, such as copper, nickel, or cobalt, can be deposited onto a suspended support by anodic dissolution of the metal [19, 40, 41]. Metal rods or scrap are put into a polymeric basket and connected to an electrode. When the metal is the anode and the voltage for dissolution is lower than the voltage to produce oxygen from water, dissolution of the metal proceeds readily. However, deposition of the metal onto the cathode has to be prevented. At the cathode hydrogen and hydroxy ions should be produced. Van Stiphout and co-workers investigated two methods to prevent deposition of the catalytically active metal onto a platinum cathode. With a polymer membrane capable of a rapid transport of hydrogen ions

and water, slow transport of hydroxy ions and copper, zinc, and cadmium ions, migration of anodically dissolved metal atoms to the cathode can be prevented or impeded. As an alternative, a thin chromia layer can be deposited onto the platinum. Apparently, nucleation of a metal on the chromia proceeds much more slowly than on platinum metal.

The above authors have established that the procedure with the polymeric membrane is not satisfactory. At high current densities, metallic nickel nucleates on the polymeric membrane. Although a reasonable loading of a suspended silica carrier could be achieved, a considerable fraction of the nickel was deposited on the polymeric membrane. The chromia layer method was observed to yield much better results.

Using the electrochemical precipitation procedure silica-supported catalysts having nickel, copper, and copper–nickel as the active components have been prepared. The thus prepared catalysts showed analogous characteristics as the catalysts prepared by deposition precipitation using urea. The copper–nickel catalysts are especially interesting. Measurement of the saturation magnetization and temperature-programmed reduction experiments indicated the formation of copper–nickel alloys after reduction of supports loaded simultaneously or sequentially with copper and nickel. Since the dissolution of nickel or copper is accompanied by the reaction of hydrogen ions to gaseous hydrogen, resulting in the formation of hydroxy ions, the pH level of the suspension does not vary provided that hydroxides or layered silicates containing  $\text{Si}_2\text{O}_5^{2-}$  species are generated. When no suspended silica is present, anodically dissolved copper initially reacts to basic copper salts, which leads to a rapid rise in pH, since the loss of hydrogen ions is not compensated by an equivalent consumption of hydroxy ions. With suspended silica, however, the pH remains virtually constant, except when nitrate ions are present and reaction to nitrite or nitrogen oxide can proceed at the cathode. Both reactions consume hydrogen ions.

Electrochemical procedures can thus be used in the production of solid catalysts for the reduction of higher valent metal ions, usually present as oxyanions, to a lower valent state, where they are less acidic. Also, the above deposition–precipitation method can be extremely well controlled by electrochemical means.

#### 4.6.5 Deposition–Precipitation within Preshaped Support Bodies

Application of one or more precursor(s) uniformly over the internal surface of preshaped support bodies is attractive for the development of industrial catalysts within a short period of time. Since impregnation and drying often leads to deposition more or less exclusively at the external edge of the support bodies, an improved procedure is highly desirable.

Knijff et al. have extensively studied deposition–precipitation within the pore-systems of preshaped support bodies [6, 42]. Impregnation was performed with a solution of the active precursor and urea or ammonium or sodium nitrite. Preferably, the support bodies were evacuated before the impregnating fluid was admitted. To prevent evaporation of the liquid while maintaining the impregnated support bodies at a temperature of about 350 K, their open container was placed in a vessel

with an atmosphere of water saturated at 350 K. With the hydrolysis of urea and with the disproportionation of nitrite, gases are evolved. It is possible that gas bubbles generated within narrow pores push the liquid out of the pores, thus preventing deposition of the active precursor onto the pore walls. Some experiments showed that removal of the liquid out of (part of) the pore system by gas bubbles did not occur. Apparently, dissolution of the gases in the liquid present in the pore system effectively transports the evolved gases out of the pore system of the supports.

Extremely good distributions of the active precursor over the internal surface of the support bodies were obtained. The difficulty, however, is the loading that can be achieved. The limited pore volume of preshaped support bodies and the solubility of the precursor to be deposited and of the agent(s) for deposition–precipitation necessitate multiple impregnations in order to achieve loadings characteristic of base metal (compounds). With urea and simple nitrates, however, highly concentrated solutions can be used, which allows the application of high loadings of the active component. The difficulty here is to fill the pore system completely with the highly viscous concentrated solution. Deposition–precipitation within the pores of preshaped support bodies is therefore attractive for supports with a very high pore volume and calls for additional research when high loadings are desired with supports of a low or intermediate pore volume.

#### 4.6.6 Concluding Remarks

The above procedures for catalyst preparation have generally provided excellent results. Especially important are surface-sensitive reactions. With supported catalysts in which the active components have a narrow particle-size distribution, the optimum particle size for a demanding reaction can be established. Major improvements of supported catalysts, e.g. with respect to carbon deposition and ammonia decomposition, can be achieved by preparing catalysts with a narrow particle-size distribution. Also, the preparation of catalysts in which the active components have a uniform chemical composition is highly important. One instance is the preparation of supported vanadium oxide phosphorus oxide (VPO) catalysts for the selective oxidation of *n*-butane to maleic anhydride, which has been carried out using vanadium(III) deposition onto silica [31].

Technically, the most desirable procedures are those that can use existing equipment for the commercial production of catalysts. Impregnation of preshaped support bodies, drying, and subsequent calcination and/or reduction are therefore attractive, since these techniques can usually be executed in existing equipment. It is interesting that the inorganic chemistry and the techniques to produce advanced catalysts can also be used for the production of magnetic materials, inorganic pigments, and finely divided metals.

Much of the material covered in this review has only been published in the patent literature. Reference is made to the relevant patent literature, since the patents contain accurately described experiments, that nicely exemplify the results dealt with in this review.

## References

1. J. W. Geus in *Sintering and Catalysis* (Ed.: G. C. Kuczynski), Plenum, New York, **1975**, pp. 29–61.
2. J. W. Geus in *Preparation of Catalysts III* (Eds: G. Poncelet, P. Grange, P. A. Jacobs) Elsevier, Amsterdam, **1983**, pp. 1–33.
3. C. N. Satterfield, *Heterogeneous Catalysis in Practice*, McGraw-Hill, New York, **1980**, p. 131.
4. R. Schlögl in *Catalytic Ammonia Synthesis Fundamentals and Practice* (Ed.: J. R. Jennings), Plenum Press, New York, **1991**, p. 19.
5. W. Langenbeck, H. Dreyer, D. Nehring, *Naturwissenschaften* **1954**, *41*, 332; W. Langenbeck, H. Dreyer, D. Nehring, *Z. Anorg. Allgem. Chem.* **1955**, *281*, 90.
6. L. M. Knijff, Ph.D. Thesis, Utrecht University, **1992**.
7. A. Q. M. Boon Ph.D. Thesis, Utrecht University, **1990**.
8. P. J. van den Brink Ph.D. Thesis, Utrecht University, **1992**.
9. US Patent 4 783 434 **1988** (DOW Chemical Company).
10. G. R. Meima, B. G. Dekker, A. J. Van Dillen, J. W. Geus, J. E. Bongarts, F. R. Van Buren, K. Delcour, J. M. Wigman in *Preparation of Catalysts IV* (Eds: B. Delmon, P. Grange, P. A. Jacobs, G. Poncelet) Elsevier, Amsterdam, **1987**, p. 83.
11. P. J. Van den Brink, A. Scholten, A. van Wageningen, M. D. A. Lamers, A. J. van Dillen, J. W. Geus in *Preparation of Catalysts V* (Eds: G. Poncelet, P. A. Jacobs, P. Grange, B. Delmon) Elsevier, Amsterdam, **1991**.
12. G. R. Meima Ph.D. Thesis, Utrecht University, **1987**.
13. A. R. West, *Solid State Chemistry and its Applications*, Wiley, Chichester, **1984**, p. 436.
14. D. Meador, A. Townshend, *Talanta* **1966**, *13*, 1069.
15. H. H. Willard, N. G. Tang, *J. Am. Chem. Soc.* **1937**, *59*, 1190.
16. H. H. Willard, N. G. Tang, *Ind. Eng. Chem., Analytical Edition* **1937**, *9*, 357.
17. P. F. S. Cartwright, E. J. Newman, D. W. Wilson, *The Analyst* **1967**, *97*, 663.
18. P. K. De Bokx, W. B. A. Wasserberg, J. W. Geus, *J. Catal.* **1987**, *104*, 86.
19. P. van Stiphout Ph.D. Thesis, Utrecht University, **1987**.
20. A. J. van Dillen, J. W. Geus, L. A. M. Hermans, J. van der Meijden in *Proceedings of the Sixth International Congress on Catalysis*, London, **1976**, (Eds: G. C. Bond, P. B. Wells and F. C. Tompkins) Chemical Society, Letchworth, England, **1977**, Vol. 2, p. 667.
21. L. A. M. Hermans, J. W. Geus in *Preparation of Catalysts II* (Eds: B. Delmon, P. Grange, P. Jacobs, G. Poncelet) Elsevier, Amsterdam, **1979**, p. 113.
22. R. Burch, A. R. Flambard in *Preparation of Catalysts III* (Eds: G. Poncelet, P. Grange, P. A. Jacobs) Elsevier, Amsterdam, **1983**, p. 311.
23. J. T. Richardson, R. J. Dubus, J. G. Crump, P. Desai, U. Osterwalder, T. S. Cale in *Preparation of Catalysts II* (Eds: B. Delmon, P. Grange, P. Jacobs, G. Poncelet) Elsevier, Amsterdam, **1979**, p. 131.
24. W. J. J. van der Wal Ph.D. Thesis, Utrecht University, **1987**.
25. J. van der Meijden Ph.D. Thesis, Utrecht University, **1981**.
26. J. van Beijnum Ph.D. Thesis, Utrecht University, **1991**.
27. C. N. A. M. Mesters Ph.D. Thesis, Utrecht University, **1984**.
28. J. W. Geus, *Appl. Catal.* **1986**, *25*, 313.
29. E. T. C. Vogt, M. De Boer, A. J. van Dillen, J. W. Geus, *Appl. Catal.* **1988**, *40*, 255.
30. E. T. C. Vogt Ph.D. Thesis, Utrecht University, **1988**.
31. R. A. Overbeek Ph.D. Thesis, Utrecht University, **1994**.
32. M. de Boer, A. J. van Dillen, D. C. Koningsberger, J. W. Geus, M. A. Vuurman, I. E. Wachs, *Catal. Lett.* **1991**, *11*, 227.
33. M. de Boer Ph.D. Thesis, Utrecht University, **1992**.
34. R. J. M. J. Vogels, M. J. H. V. Kerkhoffs, J. W. Geus in *Preparation of Catalysts VI* (Eds: G. Poncelet, J. Martens, P. A. Jacobs, P. Grange) Elsevier, Amsterdam, **1995**, p. 1153.
35. German Patent 1 964 620 **1970** (Stamcarbon).

36. Netherlands Patent 16 777 **1968** (Stamicarbon).
37. K. P. de Jong, J. W. Geus, *Appl. Catal.* **1982**, 4, 41.
38. K. P. de Jong Ph.D. Thesis, Utrecht University, **1982**.
39. German Patent 1 963 827 **1970** (Stamicarbon).
40. P. C. M. van Stiphout, C. R. Bayense, J. W. Geus, *Appl. Catal.* **1988**, 37, 189.
41. P. C. M. van Stiphout, H. Donker, C. R. Bayense, J. W. Geus, F. Versluis in *Preparation of Catalysts IV* (Eds: B. Delmon, P. Grange, P. A. Jacobs, G. Poncelet) Elsevier, Amsterdam, **1987**, p. 55.
42. L. M. Knijff, P. H. Bolt, R. van Yperen, A. J. van Dillen, J. W. Geus in *Preparation of Catalysts V* (Eds: G. Poncelet, P. A. Jacobs, P. Grange, B. Delmon) Elsevier, Amsterdam, **1991**, p. 165.

## 4.7 Solid Superacids

K. TANABE AND H. HATTORI

A solid superacid is defined as a solid material which shows an acid strength higher than the acid strength ( $H_0 = -11.9$ ) of 100% sulfuric acid [1]. The acid strength is measured by use of basic indicators having different  $pK_a$  values [2]. However, this method is not suitable for colored materials and may have some problems when pore sizes of a solid are too small for large molecules of the indicators and if there exist any interactions between the indicators and any sites (basic or redox sites) other than acid sites. The catalytic activity for the skeletal isomerization of *n*-butane is a measure of superacidity, since the reaction does not take place in the presence of 100% sulfuric acid at room temperature. Superacidity can be estimated also by utilizing the temperature-programmed desorption (TPD) method using ammonia or pyridine, provided that the relative value in TPD is related to the absolute value ( $H_0$ ) and the interaction of ammonia or pyridine with basic sites on solid surfaces is confirmed to be negligible.

Recently, various kinds of solid superacids have been developed. The first group is metal oxides and mixed oxides containing a small amount of sulfate ion, and those modified with platinum. The second group is metal oxides, mixed oxides, graphite, metal salts, etc. treated or combined with antimony fluoride or aluminum chloride. The third group is perfluorinated polymer sulfuric acid (Nafion-H). The fourth and fifth groups are H-ZSM-5 and a type of heteropolyacids, respectively. The last group is simply mixed oxides.

The solid superacids of the second group which have a possibility of leaching or evaporating of halogen compounds seem to be environmentally undesirable as catalysts. These superacids and Nafion-H have been extensively reviewed [1–5]. Therefore, the superacids of the first group for which many papers have been contributed recently and the industrial application of which is promising, are mainly described here and the other superacids are dealt with only briefly.

36. Netherlands Patent 16 777 **1968** (Stamicarbon).
37. K. P. de Jong, J. W. Geus, *Appl. Catal.* **1982**, 4, 41.
38. K. P. de Jong Ph.D. Thesis, Utrecht University, **1982**.
39. German Patent 1 963 827 **1970** (Stamicarbon).
40. P. C. M. van Stiphout, C. R. Bayense, J. W. Geus, *Appl. Catal.* **1988**, 37, 189.
41. P. C. M. van Stiphout, H. Donker, C. R. Bayense, J. W. Geus, F. Versluis in *Preparation of Catalysts IV* (Eds: B. Delmon, P. Grange, P. A. Jacobs, G. Poncelet) Elsevier, Amsterdam, **1987**, p. 55.
42. L. M. Knijff, P. H. Bolt, R. van Yperen, A. J. van Dillen, J. W. Geus in *Preparation of Catalysts V* (Eds: G. Poncelet, P. A. Jacobs, P. Grange, B. Delmon) Elsevier, Amsterdam, **1991**, p. 165.

## 4.7 Solid Superacids

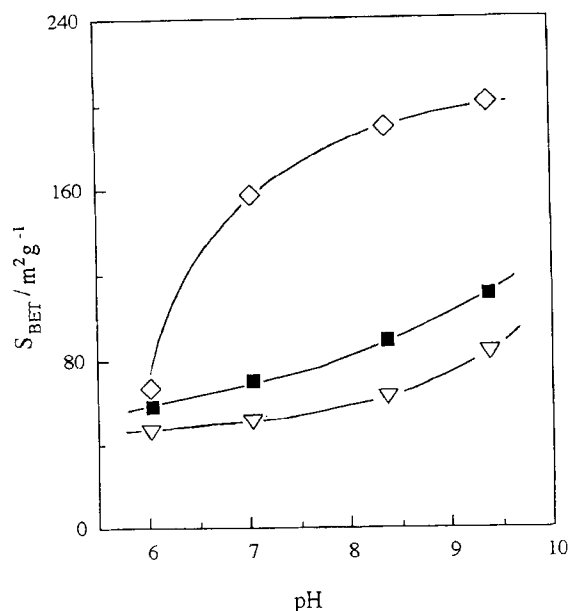
K. TANABE AND H. HATTORI

A solid superacid is defined as a solid material which shows an acid strength higher than the acid strength ( $H_0 = -11.9$ ) of 100% sulfuric acid [1]. The acid strength is measured by use of basic indicators having different  $pK_a$  values [2]. However, this method is not suitable for colored materials and may have some problems when pore sizes of a solid are too small for large molecules of the indicators and if there exist any interactions between the indicators and any sites (basic or redox sites) other than acid sites. The catalytic activity for the skeletal isomerization of *n*-butane is a measure of superacidity, since the reaction does not take place in the presence of 100% sulfuric acid at room temperature. Superacidity can be estimated also by utilizing the temperature-programmed desorption (TPD) method using ammonia or pyridine, provided that the relative value in TPD is related to the absolute value ( $H_0$ ) and the interaction of ammonia or pyridine with basic sites on solid surfaces is confirmed to be negligible.

Recently, various kinds of solid superacids have been developed. The first group is metal oxides and mixed oxides containing a small amount of sulfate ion, and those modified with platinum. The second group is metal oxides, mixed oxides, graphite, metal salts, etc. treated or combined with antimony fluoride or aluminum chloride. The third group is perfluorinated polymer sulfuric acid (Nafion-H). The fourth and fifth groups are H-ZSM-5 and a type of heteropolyacids, respectively. The last group is simply mixed oxides.

The solid superacids of the second group which have a possibility of leaching or evaporating of halogen compounds seem to be environmentally undesirable as catalysts. These superacids and Nafion-H have been extensively reviewed [1–5]. Therefore, the superacids of the first group for which many papers have been contributed recently and the industrial application of which is promising, are mainly described here and the other superacids are dealt with only briefly.





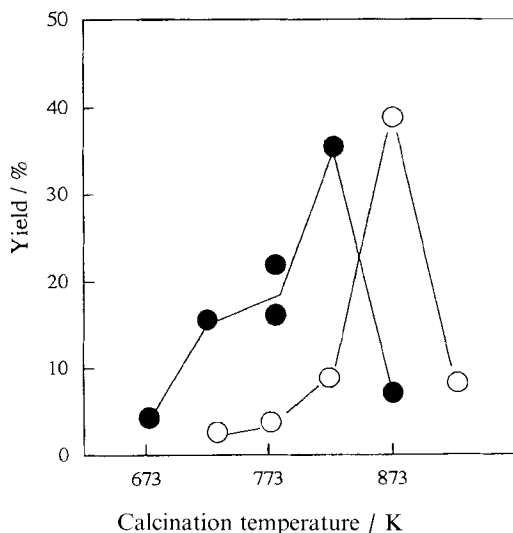
**Figure 1.** Variation of surface area of  $\text{ZrO}_2 \cdot n\text{H}_2\text{O}$  (◇),  $\text{ZrO}_2$  (▽), and  $\text{SO}_4^{2-}/\text{ZrO}_2$  (■) with pH change in precipitation of  $\text{Zr}(\text{OH})_4$ .

### 4.7.1 Sulfate-Treated Metal Oxides, Mixed Oxides, and Those Modified with Platinum

Preparation of these kinds of solid superacids is described first and the effects of the preparation method on the morphology, surface properties, structure of superacid sites, and catalytic performance are discussed.

#### 4.7.1.1 Preparative Methods

The solid superacids such as  $\text{SO}_4^{2-}/\text{ZrO}_2$ ,  $\text{SO}_4^{2-}/\text{TiO}_2$ , and  $\text{SO}_4^{2-}/\text{Fe}_2\text{O}_3$  are easily prepared by impregnating  $\text{Zr}(\text{OH})_4$ ,  $\text{TiO}_2 \cdot n\text{H}_2\text{O}$ , and  $\text{Fe}(\text{OH})_3$ , respectively, with  $(\text{NH}_4)_2\text{SO}_4$  or  $\text{H}_2\text{SO}_4$  followed by calcination at 773–923 K [2, 6]. As an example, the preparation of  $\text{SO}_4^{2-}/\text{ZrO}_2$  is described in more detail. Commercially available  $\text{ZrOCl}_2$ ,  $\text{ZrO}(\text{NO}_3)_2$ , or  $\text{Zr}(\text{NO}_3)_4$  is hydrolyzed with 28% aqueous ammonia and the precipitates formed are washed thoroughly with distilled water and dried at 373 K overnight to obtain  $\text{Zr}(\text{OH})_4$ . The pH in the precipitation of  $\text{Zr}(\text{OH})_4$  strongly influences the surface property, the structure of  $\text{ZrO}_2$ , and the catalytic activity of  $\text{SO}_4^{2-}/\text{ZrO}_2$ . Variation of the surface areas of hydrous and calcined  $\text{ZrO}_2$  and  $\text{SO}_4^{2-}/\text{ZrO}_2$  with pH in the precipitation of  $\text{Zr}(\text{OH})_4$  is shown in Fig. 1 [7]. The higher the pH, the higher the surface area. The time required for precipitation also affects the surface areas. The hydroxide,  $\text{Zr}(\text{OH})_4$ , is immersed into an aqueous solution of  $(\text{NH}_4)_2\text{SO}_4$  or  $\text{H}_2\text{SO}_4$ , and the suspended solution is evaporated to dryness, followed by heat treatment in air or in a vacuum at 773–923 K to obtain



**Figure 2.** Catalytic activities of  $\text{SO}_4^{2-}/\text{ZrO}_2$  prepared by use of  $\text{H}_2\text{SO}_4$  (●) and  $(\text{NH}_4)_2\text{SO}_4$  (○) vs calcination temperature. Yield % of dichlorobenzophenone in acylation of chlorobenzene with *o*-chlorobenzoyl chloride at 403 K in 3 h.

$\text{SO}_4^{2-}/\text{ZrO}_2$ . When  $\text{H}_2\text{SO}_4$  was used, the concentration in aqueous solution affects the catalytic activity of  $\text{SO}_4^{2-}/\text{ZrO}_2$  for the isomerization of *n*-butane [8]. The optimum content of  $\text{SO}_4^{2-}$  in  $\text{SO}_4^{2-}/\text{ZrO}_2$  changes from 1 to 8 wt % depending on the type of reaction. For the isomerization of *n*-butane, maximum activity was observed when the intrinsic sulfur content corresponds to roughly the mondoyer [8]. In the case of acylation of chlorobenzene with chlorobenzoyl chloride, 8 wt % of  $\text{SO}_4^{2-}$  was optimum [9]. Waqif et al. [10] point out that  $\text{ZrO}_2$  and  $\text{TiO}_2$  containing a large amount of sulfate form sulfur complexes different from those in the samples containing a small amount of sulfate.

The optimum temperature of calcination changes, depending on the  $\text{SO}_4^{2-}$  source ( $\text{H}_2\text{SO}_4$  or  $(\text{NH}_4)_2\text{SO}_4$ ), the type of metal oxide in  $\text{SO}_4^{2-}/\text{metal oxides}$ , and the type of reaction. In the acylation reaction, the optimum temperatures are 823 and 873 K for  $\text{H}_2\text{SO}_4$ -treated  $\text{ZrO}_2$  and  $(\text{NH}_4)_2\text{SO}_4$  treated  $\text{ZrO}_2$ , respectively, as shown in Fig. 2 [9]. For the isomerizations of *n*-butane and *n*-pentane, the optimum calcination temperature of  $\text{SO}_4^{2-}/\text{ZrO}_2$  at which the highest acid strength is observed is 923 K, while that of  $\text{SO}_4^{2-}/\text{TiO}_2$  is 773 K [11].

An important point is to use metal hydroxides instead of metal oxides as adsorbents of  $\text{SO}_4^{2-}$ . Since solid superacids lose superacidity by absorbing moisture and carbon monoxide [12], calcination in Pyrex glass tubes and storage in sealed tubes are recommended.

As in the case of  $(\text{NH}_4)_2\text{SO}_4$  or  $\text{H}_2\text{SO}_4$ , the addition of  $\text{SO}_3$  to  $\text{ZrO}_2$ ,  $\text{TiO}_2$ , and  $\text{Fe}_2\text{O}_3$  causes the generation of superacidity [13]. However, the addition of  $\text{SO}_2$  or  $\text{H}_2\text{S}$  (adsorption at 673 K) does not generate superacidity. It is interesting that  $\text{SO}_2/\text{Fe}_2\text{O}_3$  or  $\text{H}_2\text{S}/\text{Fe}_2\text{O}_3$  does not show any acidity, but exhibits superacidity when oxidized with  $\text{O}_2$  at 773 K [14]. On the other hand,  $\text{SO}_4^{2-}/\text{Fe}_2\text{O}_3$  loses its acidity when reduced with  $\text{H}_2$  at 773 K. These facts indicate that oxidation and reduction influence the acidity of sulfur-containing superacids. It should be noted that

the solid superacids cannot be used in the presence of reducing reagents such as hydrogen, alcohols, etc. at high temperatures (above 673 K).

In the preparation of  $\text{Zr}(\text{OH})_4$ , the homogeneous precipitation method using urea can be applied. Namely,  $\text{Zr}(\text{OH})_4$  is prepared by hydrolyzing with an aqueous solution of 10% urea at 368–370 K to precipitate the hydroxide [15]. In the next section the morphology and surface properties are compared with  $\text{Zr}(\text{OH})_4$  prepared by the usual heterogeneous method using aqueous ammonia.

A  $\text{SO}_4^{2-}/\text{TiO}_2\text{--ZrO}_2$  superacid is prepared similarly as  $\text{SO}_4^{2-}/\text{ZrO}_2$  except that  $\text{TiO}_2 \cdot n\text{H}_2\text{O--Zr}(\text{OH})_4$  is obtained from a mixed solution of  $\text{TiCl}_4$  and  $\text{ZrOCl}_2$  by coprecipitation with aqueous ammonia [3]. Fe, Mn,  $\text{SO}_4^{2-}/\text{ZrO}_2$  superacids are prepared by impregnating dried  $\text{ZrO}_2$  with aqueous  $\text{Fe}(\text{NO}_3)_3$ ,  $\text{Mn}(\text{NO}_3)_2$  and  $(\text{NH}_4)\text{SO}_4$ , containing 1.5 wt % Fe, 0.5 wt % Mn and 4.0 wt %  $(\text{NH}_4)_2\text{SO}_4$  and by calcining at 998 K for 1 h [16, 17].

The  $\text{SO}_4^{2-}/\text{ZrO}_2$  modified with Pt is prepared by impregnating  $\text{SO}_4^{2-}/\text{ZrO}_2$  with an aqueous solution of  $\text{H}_2\text{PtCl}_6$ , followed by drying at 383 K and calcining at 873 K in air [18, 19]. For example, the amounts of Pt and S are 0.5 and 1.5 wt %, respectively [18].

The  $\text{SO}_4^{2-}/\text{metal oxides}$  supported on  $\text{SiO}_2$  are prepared as follows. The required amount of  $\text{ZrO}_2$  is mounted on  $\text{SiO}_2$  (surface area =  $299 \text{ m}^2 \text{ g}^{-1}$ , calcined at 773 K) from a methanol solution of  $\text{ZrO}(\text{NO}_3)_2$ , decomposed in air at 673 K and finally activated by admitting  $\text{SO}_3$  gas at room temperature, calcining at 873 K and then oxidizing at 573 K [3, 20]. The  $\text{SO}_4^{2-}/\text{Fe}_2\text{O}_3/\text{SiO}_2$  is obtained by anchoring various iron compounds such as  $[\text{Fe}_3(\text{CH}_3\text{COO})_7\text{OH}]\text{NO}_3$ ,  $\text{Fe}(\text{NO}_3)_3$ ,  $\text{NH}_4\text{Fe}(\text{SO}_4)_2$ , and  $\text{Fe}(\text{CO})_3$  on a  $\text{SiO}_2$  surface and by activating with  $\text{SO}_3$  [21]. The amount of Fe compound is important for generation of strong acidity, about 3 mmol of Fe per gram of  $\text{SiO}_2$  being used.

#### 4.7.1.2 Morphology and Surface Properties

The exothermic peak of  $\text{ZrO}_2$  in a differential thermal analysis profile is shifted from 693 to 813–885 K by  $\text{SO}_4^{2-}$  treatment [15]. Crystallographic phase compositions of various  $\text{SO}_4^{2-}/\text{ZrO}_2$  is shown in Table 1 [22]. It is evident that a metastable tetragonal phase is stabilized when a small amount of  $\text{SO}_4^{2-}$  is present. The development of a monoclinic form in  $\text{ZrO}_2$  and the transformation of tetragonal to monoclinic in  $\text{SO}_4^{2-}$ -promoted  $\text{ZrO}_2$  are almost independent of the preparation method (heterogeneous or homogeneous, with  $\text{H}_2\text{SO}_4$  or  $(\text{NH}_4)_2\text{SO}_4$ . However, the ratio of the tetragonal to the monoclinic phase changes with changes of the pH in the precipitation of  $\text{Zr}(\text{OH})_4$ . When the pH is increased from 6 to 9.4, the percentage of the tetragonal form in  $\text{SO}_4^{2-}/\text{ZrO}_2$  increases from 73 to 100%, although that in pure  $\text{ZrO}_2$  increases from 33 to 70%, only [7].

There is little change in surface area with change of precipitating reagents;  $\text{ZrO}_2\text{--A}$  prepared with ammonia has a slightly larger area than  $\text{ZrO}_2\text{--U}$  prepared with urea as shown in Table 2 [15]. An  $\text{H}_2\text{SO}_4$  treatment caused a considerably lower surface area than in the case of a  $(\text{NH}_4)_2\text{SO}_4$  treatment. The surface area of  $\text{SO}_4^{2-}/\text{ZrO}_2$  changes not only with the pH (Fig. 1), but also with the time of preparation of  $\text{ZrO}_2$ . For example, the surface areas of  $\text{SO}_4^{2-}/\text{ZrO}_2$  in which  $\text{Zr}(\text{OH})_4$

**Table 1.** Crystallographic phase transformation in various  $\text{ZrO}_2$  samples.

Sample	Calcination temperature (K) <sup>a</sup>			
	623	773	923	1073
$\text{ZrO}_2\text{-A}$	<u>M</u>	M	M	M
$\text{H}_2\text{SO}_4/\text{ZrO}_2\text{-A}$	Amor.	<u>T</u>	T	T, <u>M</u>
$(\text{NH}_4)_2\text{SO}_4/\text{ZrO}_2\text{-A}$	Amor.	<u>T</u>	T	<u>T</u> , <u>M</u>
$\text{ZrO}_2\text{-U}$	<u>M</u>	M	M	M
$\text{H}_2\text{SO}_4/\text{ZrO}_2\text{-U}$	Amor.	<u>T</u>	<u>T</u>	T, <u>M</u>
$(\text{NH}_4)_2\text{SO}_4/\text{ZrO}_2\text{-U}$	Amor.	<u>T</u>	<u>T</u>	<u>T</u> , <u>M</u>

<sup>a</sup> Amor. = amorphous; M = monoclinic; M = monoclinic (not well developed); T = tetragonal; T = tetragonal (not well developed);  $\text{ZrO}_2\text{-A}$  = prepared by hydrolysis of  $\text{ZrO}(\text{NO}_3)_2 \cdot 2\text{H}_2\text{O}$  with aqueous ammonia;  $\text{ZrO}_2\text{-U}$  = prepared by hydrolysis of  $\text{ZrO}(\text{NO}_3)_2 \cdot 2\text{H}_2\text{O}$  with urea.

**Table 2.** Surface areas of  $\text{SO}_4^{2-}/\text{ZrO}_2$  (Table 1 gives the definition of  $\text{ZrO}_2\text{-A}$  and  $\text{ZrO}_2\text{-U}$ ).

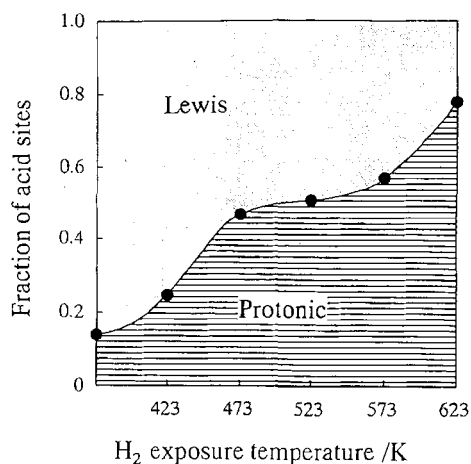
Sample	Surface area ( $\text{m}^2 \text{g}^{-1}$ )
$\text{ZrO}_2\text{-A}$	47.1
$\text{ZrO}_2\text{-U}$	41.7
$(\text{NH}_4)_2\text{SO}_4/\text{ZrO}_2\text{-A}$	119.5
$(\text{NH}_4)_2\text{SO}_4/\text{ZrO}_2\text{-U}$	119.2
$\text{H}_2\text{SO}_4/\text{ZrO}_2\text{-A}$	85.2
$\text{H}_2\text{SO}_4/\text{ZrO}_2\text{-U}$	65.1

was prepared at precipitation times of 0.5, 1, and 8 h at constant  $\text{pH} = 8.3$  were reported to be 92, 127, and  $132 \text{ m}^2 \text{g}^{-1}$ , respectively [7].

The highest *acid strengths* of  $\text{SO}_4^{2-}/\text{ZrO}_2$  and  $\text{SO}_4^{2-}/\text{TiO}_2$  measured in sulfuryl chloride by the indicator method are  $H_0 \leq -16.0$  [22] and  $H_0 \leq -14.5$  [23], respectively, being higher than that of 100%  $\text{H}_2\text{SO}_4$ . However, the acid strength of  $\text{SO}_4^{2-}/\text{ZrO}_2$  was reported to be  $H_0 \leq -13.16$  according to recent study by Ishikawa et al. [24] and  $H_0 \approx -12$  by a spectrophotometric method [25]. The difference may be due to the difference in the preparation method and the measurement method. As mentioned above, the preparation method changes the surface property. Concerning the measurement method using indicators, measurement in a vacuum system [26] seems necessary. Recently, the acid strengths of  $\text{SO}_4^{2-}/\text{TiO}_2$  (73 mol %)- $\text{SiO}_2$  [27] and  $\text{SO}_4^{2-}/\text{ZrO}_2$  (85 mol %)- $\text{SiO}_2$  [28] are reported to be  $H_0 = -14.5$  according to the indicator method in benzene. The acid strengths of  $\text{SO}_4^{2-}/\text{Fe}_2\text{O}_3$  and  $\text{Fe}_2\text{O}_3\text{-MnO}_2\text{-SO}_4^{2-}/\text{ZrO}_2$  cannot be measured by color change of indicators because of their dark colors. However, these are regarded as superacids, judging from their catalytic activities for the isomerization of *n*-butane at room temperature [29, 16]. The  $\text{Fe}_2\text{O}_3\text{-MnO}_2\text{-SO}_4^{2-}/\text{ZrO}_2$  superacid is reported to be about three orders of magnitude more active than  $\text{SO}_4^{2-}/\text{ZrO}_2$  for the isomerization reaction [16]. Its superacidity was ascertained to be higher than that of  $\text{SO}_4^{2-}/\text{ZrO}_2$  on the basis of the TPD data using very weak bases such as benzene, monofluorobenzene, difluorobenzene, etc. and the amount of superacid sites being also larger [17].  $\text{Fe}_2\text{O}_3\text{-}$

**Table 3.** Acid strength of supported solid superacid ( $\text{SO}_3/\text{ZrO}_2/\text{SiO}_2$ ).

Amount of $\text{ZrO}_2$ (mmol g <sup>-1</sup> )	Acid strength in $H_0$ acidity scale <sup>a</sup>			
	-11.4	-13.2	-13.8	-14.5
0.58	+	+	-	-
1.31	+	+	-	-
2.57	+	+	-	-
3.00	+	+	-	-
3.50	+	+	+	+
$\text{SO}_3/\text{SiO}_2$	-	-	-	-

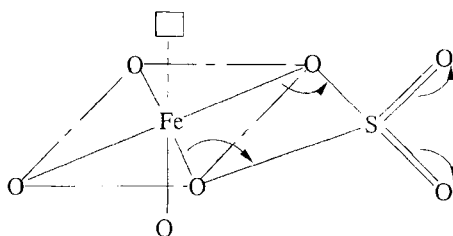
<sup>a</sup> +, present; -, absent.**Figure 3.** Change in fraction of P-Py (proton acid site-pyridine) and L-Py (Lewis acid site-pyridine) caused by exposure to hydrogen at different temperatures.

$\text{MnO}_2\text{-SO}_4^{2-}/\text{ZrO}_2$  shows the highest acid strength among solid superacids containing  $\text{SO}_4^{2-}$ .

The acid strength of  $\text{Pt-SO}_4^{2-}/\text{ZrO}_2$  is determined to be  $H_0 \leq -12.7$  [30]. Sulfated zirconia supported on silica shows superacidity (Table 3) and the amount of  $\text{SO}_4^{2-}$  is important for exhibiting the highest superacidity [20].

The type of superacid sites on  $\text{SO}_4^{2-}$ /metal oxides evacuated at 773 K is only a Lewis type according to the IR absorption bands of adsorbed pyridine [31]. Morterra et al. [32] have shown that pyridine adsorbed on Lewis acid sites dominated the spectra of samples evacuated at 673 K and that the addition of water at 300 K significantly increased the amount of Brønsted acidity. Nascimento et al. [8] report that both Brønsted and Lewis acid sites exist on  $\text{SO}_4^{2-}/\text{ZrO}_2$  treated at 723 K and the ratio of Brønsted to Lewis sites changes with the change of sulfur content. Recently, Lunsford et al. revealed by use of  $^{31}\text{P}$  MAS NMR spectra of adsorbed trimethylphosphine that three types of Lewis acid sites exist on the surface of  $\text{SO}_4^{2-}/\text{ZrO}_2$  treated at 593 K [33].

In the case of  $\text{Pt-SO}_4^{2-}/\text{ZrO}_2$ , molecular hydrogen converts into Brønsted acid sites on the surface with concomitant decrease in Lewis acid sites at temperatures above 423 K, as shown in Fig. 3. Molecular hydrogen in the gas phase seems to



**Figure 4.** Model structure of a superacid,  $\text{SO}_4^{2-}/\text{Fe}_2\text{O}_3$ .

dissociate on platinum to form hydrogen atoms which migrate onto the oxide and lose their electrons at Lewis acid sites to convert into Brønsted acid sites [18].

According to an ESR study, the adsorption of perylene gave the typical signal of its cation radical on  $\text{SO}_4^{2-}/\text{ZrO}_2$ , while no signal was found on  $\text{ZrO}_2$  [15]. This indicates that an oxidizing property (single-electron accepting property) also appears on the solid superacid.

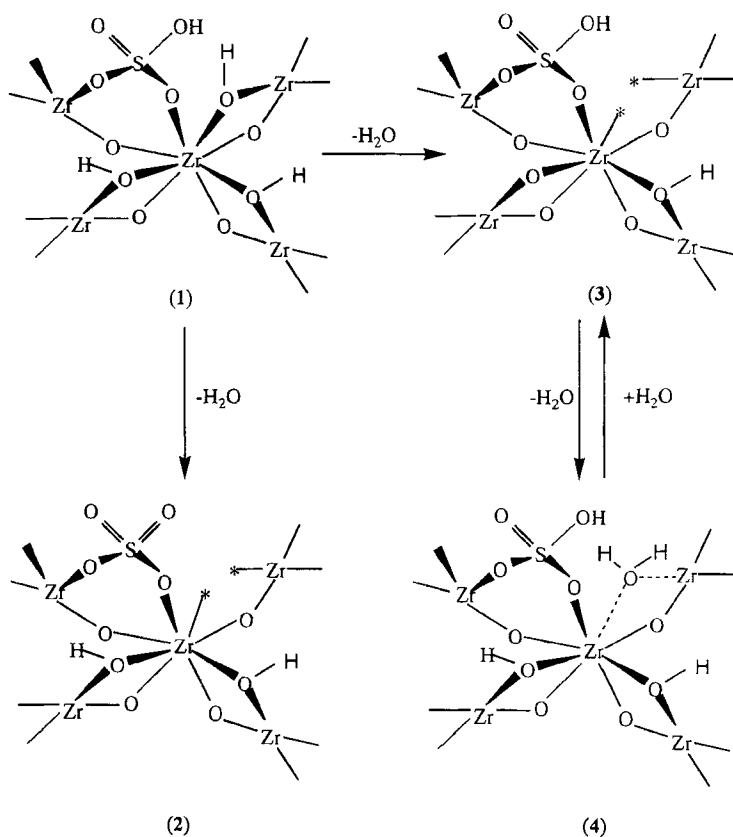
#### 4.7.1.3 Structure of Superacid Sites

Infrared spectroscopic investigation revealed that the  $\text{SO}_4^{2-}/\text{ZrO}_2$ ,  $\text{SO}_4^{2-}/\text{TiO}_2$ , and  $\text{SO}_4^{2-}/\text{Fe}_2\text{O}_3$  gave a common characteristic strong absorption at  $1375\text{--}1390\text{ cm}^{-1}$  which indicates high double bond nature of  $\text{S}=\text{O}$  [31]. This band is missing after hydration and the magnitude of the shift after pyridine adsorption is correlated with catalytic activity; the larger the shift, the higher the catalytic activity.

The X-ray photoelectron spectrum of S  $2\text{P}_{3/2}$  for  $\text{SO}_4^{2-}/\text{Fe}_2\text{O}_3$  showed that the oxidation state of sulfur was  $\text{S}^{6+}$  which is necessary for high catalytic activity of the superacid [34].

From these results, a model structure of the superacid was proposed, which is shown in Fig. 4 [31]. A characteristic feature of the structure is the presence of two  $\text{S}=\text{O}$  bonds. The superacid sites are considered to be metal ions (Lewis acid sites) whose acid strength is enhanced by an inductive effect of  $\text{S}=\text{O}$ . IR spectroscopy of CO adsorbed on  $\text{SO}_4^{2-}/\text{TiO}_2$  also suggests the enhancement of Lewis acid ( $\text{Ti}^{4+}$ ) strength by an inductive effect of the sulfate group [35]. Brønsted acid sites may be generated by the interaction of the Lewis acid sites with water molecules or reacting organic molecules. Whatever the starting materials of sulfur are, once they are oxidized on the metal oxide surfaces, they form the structure shown in Fig. 4 [13].

Saur et al. proposed a sulfite structure having only one  $\text{S}=\text{O}$  which shows a band at  $1180\text{--}1250\text{ cm}^{-1}$  [36]. Recently, Clearfield proposed a model which is shown by structures (1)–(3) in Fig. 5 [37]. The uncalcined  $\text{SO}_4^{2-}/\text{ZrO}_2$  contains protons as bisulfate groups and as hydroxyl groups bridging two zirconium ions. During calcination, water is lost to form (2) and (3). In both structures, Lewis acid sites are formed, but in (3) the bisulfate group remains intact, which results in a Lewis acid site adjacent to an  $\text{S}=\text{O}$  group. These bisulfate groups act as Brønsted acid sites and account for the strong acidity. Lunsford et al. suggest that water acting as a weak Lewis base may be nondissociatively adsorbed via its nonbonding electrons as shown by (4) of Fig. 5 [33] and the strong acidity requires the presence of adjacent



**Figure 5.** A model of superacidity generation on  $\text{SO}_4^{2-}/\text{ZrO}_2$ .

Lewis acid sites, namely, through an inductive effect, electrons are withdrawn from O–H bonds by coordinatively unsaturated zirconium, thus giving rise to more strongly acidic protons. By use of Raman,  $^1\text{H}$  MAS NMR, and IR spectroscopies, Riemer et al. [38] recently proposed a model structure of  $\text{SO}_4^{2-}/\text{ZrO}_2$  calcined at 873 K which is similar to (3) in Fig. 5, namely, the model contains only one S=O group and OH groups linked to the sulfate which develop high Brønsted acidity and zirconium cations which are responsible for Lewis acids. Babou et al. presented several models of sulfated zirconia on the basis of an ab initio quantum mechanical study [39].

The structure containing only one S=O group does not explain the XPS data indicating the existence of  $\text{S}^{6+}$ . The metal oxides which show superacidity by introducing sulfur compounds are considered to have cations of high electronegativity and high coordination number. Also, the importance of coordinative unsaturation of the cations suggests that the cations in Figs 4 and 5 may reside at the edge or corner of the metal oxide surfaces [3].

Platinum on sulfated zirconia remains mostly in a cationic state, even after

hydrogen reduction at 673 K according to the XPS study by Ebitani et al. [40, 41]. Thus, the platinum species in sulfated zirconia do not show typical metallic properties such as high olefin hydrogenation activity and chemisorption of CO [42, 43]. On the basis of XAFS data, however, Ebitani et al. [42] reported that platinum particles on sulfated zirconia are a mixture of platinum metal and platinum oxides and/or sulfide. On the contrary, Sayari and Dicko reported on the basis of X-ray photoelectron spectroscopy (XPS), X-ray diffraction (XRD), and TPR measurements that upon air calcination of  $\text{Pt-SO}_4^{2-}/\text{ZrO}_2$  at 873 K, platinum species were reduced to the metallic state [44]. Zao et al. [45] also reported from XAFS data that platinum species in  $\text{Pt-SO}_4^{2-}/\text{ZrO}_2$  existed in the metallic state following calcination in air at 998 K. There is a controversy on the state of platinum in  $\text{Pt-SO}_4^{2-}/\text{ZrO}_2$ . If the state of platinum were metallic, the catalyst would have shown a high hydrogenation activity and significant chemisorptive property for CO. Careful study of the state of platinum by XRD, X-ray absorption fine-structure spectroscopy (XAFS), and XPS leads to the conclusion that in the core of the particles, metallic platinum exists and in the outer layer of the particles cationic platinum exists in the forms of oxides and/or sulfides.

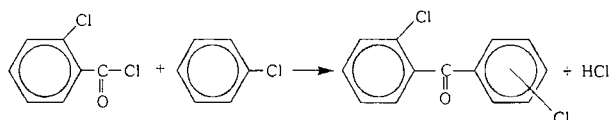
#### 4.7.1.4 Catalytic Properties

The isomerization of *n*-butane is not catalyzed even by 100%  $\text{H}_2\text{SO}_4$  at room temperature. However,  $\text{SO}_4^{2-}/\text{ZrO}_2$  [22],  $\text{SO}_4^{2-}/\text{TiO}_2$  [23],  $\text{SO}_4^{2-}/\text{Fe}_2\text{O}_3$  [23], and  $\text{Fe}_2\text{O}_3\text{-MnO}_2\text{-SO}_4^{2-}/\text{ZrO}_2$  [16] were found to catalyze the isomerization at 293–323 K, the main product being 2-methylpropane. Among these solid superacids, the one which showed the highest catalytic activity and was most stable is  $\text{Fe}_2\text{O}_3\text{-MnO}_2\text{-SO}_4^{2-}/\text{ZrO}_2$  [16, 46]. However, the activities are lowered as the reaction proceeds, mainly due to coke formation. To prevent the catalysts from their deactivation, a  $\text{SO}_4^{2-}/\text{ZrO}_2$  containing a small amount of Pt or Ni was developed. Over a  $\text{Pt-SO}_4^{2-}/\text{ZrO}_2$ , no deactivation was observed in the isomerization of pentane at 413 K under  $20\text{ Kg cm}^{-2}$  of hydrogen pressure, the lifetime being more than 6000 h [47]. Even if Pt is not added, the deactivation of  $\text{SO}_4^{2-}/\text{ZrO}_2$  is reported to be greatly decreased if the hydrogen pressure is high enough [48–50]. The isomerization of alkanes over  $\text{Pt-SO}_4^{2-}/\text{ZrO}_2$  is limited to  $\text{C}_4\text{--C}_6$ , since *n*-hexane isomerizes to isohexanes at 437 K with 99% selectivity, but *n*-heptane isomerization selectivity is only about 50% even at low conversions. Iglesia et al. [51] found that the addition of small amounts of adamantane, a hydride transfer species, to *n*-heptane increased the isomerization rates by a factor of 3 and inhibited undesirable cracking reactions. The intermediates for *n*-butane isomerization catalyzed by liquid superacids such as  $\text{SbF}_5\text{-FSO}_3\text{H}$  and  $\text{SbF}_5\text{-HF}$  are carbonium ions formed by proton transfer from the superacids [52]. Although the mechanisms of *n*-butane isomerization over  $\text{SO}_4^{2-}/\text{ZrO}_2$  are not definite yet, as to whether the carbenium ions or the carbonium ions are involved, Adeeva et al. [53] studied the mechanism of butane isomerization over Fe, Mn-promoted  $\text{SO}_4^{2-}/\text{ZrO}_2$  at 353 K by tracer method in which dual  $^{13}\text{C}$  labeled butane was used. They proposed that the isomerization involves oligomerization and  $\beta$ -fission of a chemisorbed  $\text{C}_8$  carbenium ion to iso- $\text{C}_4$  fragments. On the



**Table 4.** Activities of solid acid catalysts for acylation.

Catalyst	Amount (g)	Reaction time (h)	Yield (%)
ZrO <sub>2</sub>	3.0	3	0
SO <sub>4</sub> <sup>2-</sup> /ZrO <sub>2</sub>	3.0	1	26
SO <sub>4</sub> <sup>2-</sup> /ZrO <sub>2</sub>	6.1	10	100
SiO <sub>2</sub> -Al <sub>2</sub> O <sub>3</sub>	2.5	1	0.2
H-ZSM-5	3.0	3	0
H <sub>2</sub> SO <sub>4</sub>	2 ml	3	0



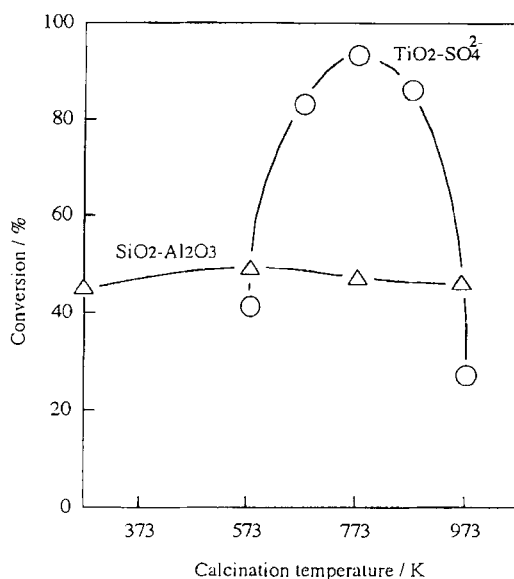
other hand, Garin et al. [54] proposed the monomolecular mechanism for butane isomerization on SO<sub>4</sub><sup>2-</sup>/ZrO<sub>2</sub> at 523 K by tracer study.

Over SbF<sub>5</sub>/metal oxides, it was proposed that *n*-butane isomerization proceeded via carbenium ion intermediates formed by hydride ion transfer from *n*-butane to the Lewis acid sites [55]. The details of sulfated zirconia as a hydrocarbon conversion catalyst have been summarized by Davis et al. [56].

The alkylation of isobutane with 2-butene takes place over SO<sub>4</sub><sup>2-</sup>/ZrO<sub>2</sub> [57, 58] and SO<sub>4</sub><sup>2-</sup>/TiO<sub>2</sub> [58]. The selectivity of a SO<sub>4</sub><sup>2-</sup>/ZrO<sub>2</sub> catalyst for the formation of trimethylpentanes is 91% at 273 K, which is much higher than 16% in the case of zeolite  $\beta$ . The lower selectivity over zeolite  $\beta$  is due mainly to the formation of dimethylhexanes by dimerization of butenes [55]. For alkylation of benzene with propylene at 443 K, the activities of superacids are in the order of SO<sub>4</sub><sup>2-</sup>/TiO<sub>2</sub>-ZrO<sub>2</sub> > SO<sub>4</sub><sup>2-</sup>/ZrO<sub>2</sub> > SO<sub>4</sub><sup>2-</sup>/TiO<sub>2</sub> > SO<sub>4</sub><sup>2-</sup>/Fe<sub>2</sub>O<sub>3</sub> [3]. No activity was observed over TiO<sub>2</sub>-ZrO<sub>2</sub>, ZrO<sub>2</sub>, and TiO<sub>2</sub>. The activities of SiO<sub>2</sub>-Al<sub>2</sub>O<sub>3</sub> and H-ZSM-5 were lower than that of SO<sub>4</sub><sup>2-</sup>/TiO<sub>2</sub>-ZrO<sub>2</sub>, but comparable to SO<sub>4</sub><sup>2-</sup>/ZrO<sub>2</sub>. The alkylation of aromatics and naphthenes with alkanes occurs at 433–523 K in the presence of Pt-SO<sub>4</sub><sup>2-</sup>/ZrO<sub>2</sub> and hydrogen, the products varying with the nature of aromatics and the length of the alkane chain [59].

Acylation of aromatics which had been known to be catalyzed only by AlCl<sub>3</sub> was found to be effectively catalyzed by solid superacids. As shown in Table 4, SO<sub>4</sub><sup>2-</sup>/ZrO<sub>2</sub> exhibited a high activity for the acylation of chlorobenzene with *o*-chlorobenzoyl chloride in the liquid phase. The yield is 100% at 406 K in 10 h, while the yields over H-ZSM-5 and SiO<sub>2</sub>-Al<sub>2</sub>O<sub>3</sub> are 0 and 0.17%, respectively [9].

For the esterification of terephthalic acid with ethylene glycol at 473 K, SO<sub>4</sub><sup>2-</sup>/TiO<sub>2</sub> calcined at 773 K is much more active than SiO<sub>2</sub>-Al<sub>2</sub>O<sub>3</sub> as shown in Fig. 6 [60]. The SO<sub>4</sub><sup>2-</sup>/TiO<sub>2</sub> showed a maximum activity when calcined at 573 K for the esterification of oleic acid with glycerol and of propionic acid with butanol at 403 K [61], where the active sites were attributed to Brønsted acid sites from a correlation between the activity and the Brønsted acidity. The esterification of phthalic anhydride with 2-ethylhexanol to form dioctyl phthalate is also efficiently catalyzed by solid superacids, the selectivity being more than 90% [62]. The catalytic activity



**Figure 6.** Esterification of terephthalic acid with ethylene glycol: reaction temperature 473 K, reaction time 90 min.

**Table 5.** Reactions of CH<sub>4</sub> with C<sub>2</sub>H<sub>4</sub> on solid superacid catalysts.

Catalyst	Product composition (percentage C) <sup>a</sup>						
	C <sub>2</sub>	C <sub>3</sub>	<i>i</i> -C <sub>4</sub>	<i>n</i> -C <sub>4</sub>	<i>i</i> -C <sub>5</sub>	<i>n</i> -C <sub>5</sub>	C <sub>6</sub>
TaF <sub>5</sub> /Al <sub>2</sub> O <sub>3</sub>	13.2	13.8	38.6	6.5	12.7	5.3	–
SO <sub>4</sub> <sup>2-</sup> /ZrO <sub>2</sub> <sup>b</sup>	–	10.9	51.2	–	13.4	–	–

<sup>a</sup> Products excluding CH<sub>4</sub> and C<sub>2</sub>H<sub>4</sub>. <sup>b</sup> Reaction conditions: GHSV = 960, temperature = 573 K, C<sub>1</sub>/C<sub>2</sub> = 2.35 mol mol<sup>-1</sup>, pressure = 1.95 MPa, time on stream = 305 min.

was in the order SO<sub>4</sub><sup>2-</sup>/ZrO<sub>2</sub> > SO<sub>4</sub><sup>2-</sup>/Fe<sub>2</sub>O<sub>3</sub> > HPA (dodecatungstophosphoric acid)/SiO<sub>2</sub> > HPA/Al<sub>2</sub>O<sub>3</sub> > HPA/TiO<sub>2</sub> > HPA/ZrO<sub>2</sub>. The activity of SO<sub>4</sub><sup>2-</sup>/Fe<sub>2</sub>O<sub>3</sub> for the esterification of propionic acid with butanol at 383 K becomes maximum when the catalyst is treated at 573–773 K [63], the catalyst structure being studied by ESR and Mossbauer spectroscopy.

For the activation of methane, SO<sub>4</sub><sup>2-</sup>/ZrO<sub>2</sub> was found to be active for the reaction of methane with ethylene to form C<sub>3</sub>, *i*-C<sub>4</sub>, *i*-C<sub>5</sub> [64]. In Table 5, the product distribution is compared with that of the other solid superacid, TaF<sub>5</sub>/Al<sub>2</sub>O<sub>3</sub> [65]. For the chlorination of methane, the selectivity of SO<sub>4</sub><sup>2-</sup>/ZrO<sub>2</sub> for the formation of methyl chloride exceeds 90% with 30% of chlorine conversion at 473 K and is above 80% with 70–90% conversion at 439 K. The selectivity is enhanced by adding Pt, while Fe<sub>2</sub>O<sub>3</sub>–MnO<sub>2</sub>–SO<sub>4</sub><sup>2-</sup>/ZrO<sub>2</sub> exhibits excellent selectivities (99–100%) at lower conversions [66]. The electrophilic insertion is said to involve electron-deficient metal-coordinated chlorine at the methane C–H bond.

Sulfated zirconia showed the highest activity for the disproportionation of diethyldimethylsilane [67]. For the catalytic combustion of propane at low temperatures, Pt-SO<sub>4</sub><sup>2-</sup>/ZrO<sub>2</sub> and Pt-SO<sub>4</sub><sup>2-</sup>/Al<sub>2</sub>O<sub>3</sub> showed higher activities than Pt/SiO<sub>2</sub>-Al<sub>2</sub>O<sub>3</sub>, Pt/SiO<sub>2</sub>-ZrO<sub>2</sub>, Pt/Al<sub>2</sub>O<sub>3</sub>, Pt/ZrO<sub>2</sub>, etc., the conversion being 100% at 600 K [24]. The SO<sub>4</sub><sup>2-</sup>-doped oxides having higher acid strengths are suggested to be superior support materials for platinum catalyst for low-temperature combustion of propane.

A MoO<sub>3</sub>-SO<sub>4</sub><sup>2-</sup>/TiO<sub>2</sub> catalyst is much more active than MoO<sub>3</sub>/TiO<sub>2</sub> for the reduction of NO with NH<sub>3</sub>. The addition of 0.5 wt % SO<sub>4</sub><sup>2-</sup> increased the conversion from 58 to 84% at 573 K [68]. The higher activity is due to the acidity enhanced by the interaction of TiO<sub>2</sub> with SO<sub>4</sub><sup>2-</sup>. The selective catalytic reduction of NO with NH<sub>3</sub> at higher temperatures (673–798 K) is achieved by use of SO<sub>4</sub><sup>2-</sup>/TiO<sub>2</sub> [69]. The use of MoO<sub>3</sub> or V<sub>2</sub>O<sub>5</sub> causes the oxidation of NH<sub>3</sub> at the high temperatures. For the isomerization of 2-pinene to camphene and tricyclene, SO<sub>4</sub><sup>2-</sup>/TiO<sub>2</sub> showed the highest activity and SO<sub>4</sub><sup>2-</sup>/ZrO<sub>2</sub> the lowest activity, SO<sub>4</sub><sup>2-</sup>/Fe<sub>2</sub>O<sub>3</sub> being intermediate [70]. A SO<sub>4</sub><sup>2-</sup>/Fe<sub>2</sub>O<sub>3</sub> catalyst shows high activities for the reactions such as the dehydration of alcohol, the double-bond isomerization of 1-butene, the isomerization of cyclopropane to propylene [71], and is also active for coal liquefaction [72]. The other reactions, are reviewed elsewhere [4, 6].

## 4.7.2 Other Solid Superacids

Besides sulfated metal oxides and sulfated mixed oxides, there are several kinds of solid superacids as mentioned in introduction.

SbF<sub>5</sub>/SiO<sub>2</sub>-Al<sub>2</sub>O<sub>3</sub>, SbF<sub>5</sub>/SiO<sub>2</sub>-TiO<sub>2</sub>, etc. whose acid strength is in the range from -13.16 to -14.52 are more active than SO<sub>4</sub><sup>2-</sup>/metal oxides for the isomerization of *n*-butane in the gas-phase reaction [26]. In the liquid-phase reaction of pentane, it is confirmed that SbF<sub>5</sub> does not dissolve into the liquid phase at room temperature [73]. In the gas-phase reaction of *n*-butane, SbF<sub>5</sub> is not removed if SbF<sub>5</sub>/metal oxide is preliminarily evacuated at 573 K. Thus, these solid superacids are also promising for the application as catalysts for particular reactions. These types of solid superacid have been described elsewhere [1–4, 6].

AlCl<sub>3</sub>-CuSO<sub>4</sub>, AlCl<sub>3</sub>-CuCl<sub>2</sub>, etc. with H<sub>0</sub> values from -13.16 to -14.52 are active for the isomerization of alkanes, Gatterman-Koch reaction, etc. [2, 4]. These solid superacids have also some disadvantages because they contain halogen atoms.

Nafion-H whose acid strength is -12, is active for diversified organic reactions such as alkylation, isomerization, disproportionation, transalkylation, acylation, nitration, hydration, rearrangement, etc. [1, 5]. Since Nafion-H can be used in aqueous solution, it is a useful catalyst.

A heteropolyacid, H<sub>3</sub>PW<sub>12</sub>O<sub>40</sub>, and its C<sub>2.5</sub> salt calcined at 573 K were found recently to have a superacidity of ≤ -13.16 [74]. The catalytic activities of the heteropolyacids and the other solid superacids for the alkylation of 1,3,5-trimethylbenzene with cyclohexene are in the order Cs<sub>2.5</sub> salt ≫ H<sub>3</sub>PW<sub>12</sub>O<sub>40</sub>, > SO<sub>4</sub><sup>2-</sup>/ZrO<sub>2</sub> > Nafion-H > H-ZSM-5 [75].

A well known zeolite, H-ZSM-5, calcined at 808 K was shown also to have superacidity of -12.70 [74]. The order of acid strength measured by the TPD method

using ammonia is  $\text{SO}_4^{2-}/\text{ZrO}_2 > \text{H}_3\text{PW}_{12}\text{O}_{40}$ ,  $\text{CS}_{2.5}$  salt  $> \text{H-ZSM-5} > \text{SiO}_2\text{-Al}_2\text{O}_3$ . The characteristic of H-ZSM-5 is to stabilize pentacoordinated carbonium ions. Thus, in the case of *n*-hexane reaction, the cracking occurs to form  $\text{H}_2$ ,  $\text{CH}_4$ , etc. [76, 77]. According to the acidity estimation based on the in situ  $^{13}\text{C}$  chemical shift measurement of mesityl oxide, however, the acid strength of H-ZSM-5 is reported to be comparable to that of a solution of 70%  $\text{H}_2\text{SO}_4$  [78].

Some mixed oxides are solid superacids according to measurement by the indicator method.  $\text{WO}_3/\text{ZrO}_2$  calcined at 1073 to 1123 K shows an acid strength of  $\leq -14.5$  and is active for the acylation of toluene with benzoic anhydride at 303 K in liquid phase and the isomerizations of butane and pentane [79]. The mechanism of superacidity generation is said to be similar to that of  $\text{SO}_4^{2-}/\text{ZrO}_2$ , namely, the inductive effect of the double bond of  $\text{W}=\text{O}$  (like  $\text{S}=\text{O}$ ) enhances the acidity of zirconium cation. The acid strength of  $\text{SiO}_2\text{-Al}_2\text{O}_3$  is  $-13.16$  [26] or  $-12.70$  [74]. Very recently,  $\text{SiO}_2\text{-ZrO}_2$  was reported to show superacidity of  $-11.4$  to  $-13.8$ , which changes depending on the composition, although the measurement was made in isooctane [80]. Even  $\text{Al}_2\text{O}_3$  itself is known to show superacidity of  $\leq -14.5$  when prepared by hydrolysis of aluminum isopropoxide followed by calcination at 773 K [81].

Thus, there are now many solid superacids and the term superacidity is no longer unusual. It seems necessary to define solid superacids by judging their reactivities against not only indicators and TPD of ammonia or pyridine, but also test reactions such as the skeletal isomerization of *n*-butane, etc. The controversy concerning the mechanism of superacidity generation needs further research. Some examples have been given which show no correlation between acid strengths of superacids and their catalytic activities. For an interpretation, a concept of concerted acid-base bifunctional catalysis may have to be taken into consideration, since even superacids must have weak basic sites. The geometrical fit between a superacid site and a reacting molecule seems to be another important factor for influencing catalytic activity.

## References

1. G. A. Olah, G. K. S. Prakash, J. Sommer, *Superacids*, Wiley, New York, **1985**.
2. K. Tanabe, M. Misono, Y. Ono, H. Hattori, *New Solid Acids and Bases*, Kodansha, Tokyo, Elsevier, Amsterdam, **1989**.
3. K. Tanabe, H. Hattori, T. Yamaguchi, *Critical Rev. in Surface Chem.* **1990**, 1, 1.
4. T. Yamaguchi, *Appl. Catal. A*, **1990**, 61, 1.
5. G. K. S. Prakash, G. A. Olah, *Acid-Base Catalysis* (Eds: K. Tanabe, H. Hattori, T. Yamaguchi, T. Tanaka), Kodansha, Tokyo, VCH, Weinheim, **1989**, 59.
6. K. Arata, *Adv. Catal.* **1990**, 37, 165.
7. A. Corma, V. Fornes, M. I. Juan-Rajadell, J. M. Lopez Nieto, *Appl. Catal. A*, **1994**, 116, 151.
8. P. Nascimento, C. Akrotopoulou, M. Oszagyan, G. Coudurier, C. Travers, J. F. Joly, J. Vedrine, *Proc. 10th Intern. Congr. Catalysis*, Elsevier, Amsterdam, **1993**, 1185.
9. K. Tanabe, T. Yamaguchi, K. Akiyama, A. Mitoh, K. Iwabuchi, K. Isogai, *Proc. 8th intern. Congr. Catal.*, Berlin, **1984**, Verlag Chemie, Weinheim, 5, 601.
10. M. Waqif, J. Bachelier, O. Saur, J.-C. Lavalley, *J. Mol. Catal.* **1992**, 72, 127.
11. Z. Gao, J. Chen, W. Hua, Y. Tang, in *Acid-Base Catalysis III* (Ed.: H. Hattori, et al.), Kodansha, Tokyo, VCH, Weinheim, **1994**, 26.

12. F. Pinna, M. Signoretto, G. Strukul, G. Cerato, C. Morterra, *Catal. Lett.* **1994**, 26, 339.
13. T. Yamaguchi, T. Jin, K. Tanabe, *J. Phys. Chem.* **1986**, 90, 3148.
14. Y. Nagase, T. Jin, H. Hattori, T. Yamaguchi, K. Tanabe, *Bull. Chem. Soc. Jpn.* **1985**, 58, 916.
15. T. Yamaguchi, K. Tanabe, Y. C. Kung, *Mater. Chem. Phys.* **1986**, 16, 67.
16. C.-Y. Hsu, C. R. Heimbuch, C. T. Armes, B. C. Gates, *J. Chem. Soc., Chem. Commun.* **1992**, 1645.
17. C.-H. Lin, C.-Y. Hsu, *J. Chem. Soc., Chem. Commun.* **1992**, 1479.
18. K. Ebitani, H. Hattori, K. Tanabe, *Langmuir* **1990**, 6, 1743.
19. K. Ebitani, J. Konishi, H. Hattori, *J. Catal.* **1991**, 130, 257.
20. T. Ishida, T. Yamaguchi, K. Tanabe, *Chem. Lett.* **1988**, 1869.
21. T. Yamaguchi, T. Jin, T. Ishida, K. Tanabe, *Mater. Chem. Phys.* **1986**, 17, 3.
22. M. Hino, K. Arata, *J. Chem. Soc., Chem. Commun.* **1980**, 851.
23. M. Hino, K. Arata, *Chem. Lett.* **1979**, 1259; *J. Chem. Soc., Chem. Commun.* **1979**, 1148.
24. A. Ishikawa, S. Komai, A. Satsuma, T. Hattori, Y. Murakami, *Appl. Catal. A* **1994**, 110, 61.
25. B. Umansky, J. Engelhardt, W. K. Hall, *J. Catal.* **1991**, 127, 128.
26. H. Hattori, O. Takahashi, M. Takagi, K. Tanabe, *J. Catal.* **1981**, 68, 132.
27. J. R. Sohn, H. J. Jang, *J. Catal.* **1992**, 136, 267.
28. J. R. Sohn, H. J. Jang, *J. Mol. Catal.* **1991**, 64, 349.
29. K. Arata, M. Hino, *Chem. Lett.* **1979**, 1259.
30. S. Baba, Y. Shibata, H. Takaoka, T. Kimura, K. Takasaka, Japanese Patent, **1986**, 140, 61–153.
31. T. Jin, T. Yamaguchi, K. Tanabe, *J. Phys. Chem.* **1986**, 90, 4794.
32. C. Morterra, G. Cerrato, C. Emanuel, V. Bolis, *J. Catal.* **1993**, 142, 349.
33. J. H. Lunsford, H. Sang, S. M. Campbell, C.-H. Liang, R. G. Anthony, *Catal. Lett.* **1994**, 27, 305.
34. T. Jin, M. Machida, T. Yamaguchi, K. Tanabe, *Inorg. Chem.* **1984**, 23, 4396.
35. F. Lange, K. Hadjiivanov, H. Schmelz, H. Knözinger, *Catal. Lett.* **1992**, 16, 97.
36. O. Saur, M. Bensitel, A. B. Mohammed Saad, J. C. Lavalley, C. P. Tripp, B. A. Morrow, *J. Catal.* **1986**, 99, 104.
37. A. Clearfield, G. P. D. Serrette, A. H. Khazi-Syed, *Catal. Today*, **1994**, 20, 295.
38. T. Riemer, D. Spielbauer, M. Hunger, G. A. H. Mekheimer, H. Knözinger, *J. Chem. Soc., Chem. Commun.* **1944**, 1181.
39. F. Babou, B. Bigot, P. Sautet, *J. Phys. Chem.* **1993**, 97, 11501.
40. K. Ebitani, H. Konno, T. Tanaka, H. Hattori, *J. Catal.* **1992**, 135, 60.
41. K. Ebitani, H. Konno, T. Tanaka, H. Hattori, *J. Catal.* **1993**, 143, 522.
42. K. Ebitani, T. Tanaka, H. Hattori, *Appl. Catal.* **1993**, 102, 79.
43. K. Ebitani, J. Tsuji, H. Hattori, H. Kita, *J. Catal.* **1992**, 135, 609.
44. A. Sayari, A. Dicko, *J. Catal.* **1994**, 145, 561.
45. J. Zhao, G. P. Huffman, B. H. Davis, *Catal. Lett.* **1994**, 24, 385.
46. A. Jatia, C. Chang, J. D. MacLeod, T. Okubo, M. E. Davis, *Catal. Lett.* **1994**, 25, 21.
47. S. Baba, T. Shimizu, H. Takaoka, T. Imai, S. Yokoyama, Preprint of Disc. Meeting of Petrol. Chem. of Jpn. Petrol. Inst., **1986**, No. 2-I-17. Private communication for catalyst life-time.
48. F. Garin, D. Andriamasinoro, A. Abdulsamad, J. Sommer, *J. Catal.* **1991**, 131, 199.
49. F. R. Chen, G. Coudurier, J.-F. Joly, J. Vedrine, *J. Catal.* **1993**, 143, 616.
50. F. Babou, B. Bigot, G. Coudurier, Ph. Sautet, J. C. Vedrine, Preprints of Acid-Base Catalysis II Symposium, Dec. 2–4, 1993, Sapporo, p. 34.
51. E. Iglesia, S. L. Soled, G. M. Kramer, *J. Catal.* **1993**, 144, 238.
52. G. A. Olah, Y. Halpern, J. Shen, Y. K. Mo, *J. Am. Chem. Soc.* **1973**, 95, 4960.
53. V. Adeeva, G. D. Lei, W. M. H. Sachtler, *Appl. Catal. A* **1994**, 118, L-11.
54. F. Garin, L. Seyfried, P. Girard, G. Marire, A. Abdulsamad, J. Sommer, *J. Catal.* **1995**, 151, 26.
55. O. Takahashi, H. Hattori, *J. Catal.* **1981**, 68, 144.
56. B. H. Davis, R. A. Keogh, R. Srinivasan, *Catal. Today* **1994**, 20, 219.
57. A. Corma, M. I. Juan-Rajadell, J. M. Lopez-Nieto, A. Martinez, C. Martinez, *Appl. Catal. A* **1994**, 111, 175.
58. C. Guo, S. Yao, J. Cao, Z. Qian, *Appl. Catal. A* **1994**, 107, 229.
59. J. Hu, K. R. Venkatesh, J. W. Tierney, I. Wender, *Appl. Catal. A*, **1994**, 114, L179.

60. K. Tanabe, H. Hattori, Y. Ban'i, A. Mitsutani, Japanese Patent, **1980**, 55-115570.
61. L. Rongsheng, C. Jingfeng, Z. Wuyang, Y. Hua, Z. Zhiming, W. Quan, *React. Kinet. Catal. Lett.* **1992**, 48, 483.
62. T. S. Thorat, V. M. Yadav, G. D. Yadav, *Appl. Catal. A* **1992**, 90, 73.
63. R.-S. Li, J.-F. Chen, H. Yang, W.-Y. Zhang, *Catal. Lett.* **1993**, 18, 317.
64. M. S. Scurrel, *Appl. Catal.* **1987**, 32, 1.
65. G. A. Olah, *Eur. Pat. Appl.* **1983**, 73673.
66. P. Batamack, I. Bucsí, A. Molnar, G. A. Olah, *Catal. Lett.* **1994**, 25, 11.
67. H. Fujisawa, T. Yamaguchi, *Catal. Lett.* **1993**, 17, 319.
68. S. Okazaki, M. Kumasaka, J. Yoshida, K. Kosaka, K. Tanabe, *Ind. Eng. Chem., Product Res. and Develop.* **1981**, 20, 301.
69. J. P. Chen, R. T. Yang, *J. Catal.* **1993**, 139, 227.
70. R. Ohnishi, T. Morikawa, Y. Hiraga, K. Tanabe, *Z. Phys. Chem. Neue Folge* **1982**, 130, 205.
71. K. Tanabe, A. Kayo, T. Yamaguchi, *J. Chem. Soc., Chem. Commun.* **1981**, 602; A. Kayo, T. Yamaguchi, K. Tanabe, *J. Catal.* **1983**, 83, 99.
72. K. Tanabe, H. Hattori, T. Yamaguchi, S. Yokoyama, J. Umematsu, Y. Sanada, *Fuel* **1982**, 61, 389.
73. O. Takahashi, T. Yamauchi, T. Sakuhara, H. Hattori, K. Tanabe, *Bull. Chem. Soc. Jpn.* **1980**, 53, 1807.
74. T. Okuhara, T. Nishimura, H. Watanabe, M. Misono, *J. Mol. Catal.* **1992**, 74, 247.
75. M. Misono, T. Okuhara, *Chemtech* **1993**, 23, 23.
76. W. O. Haag, R. M. Dessau, *Proc. 8th Intern. Congr. Catalysis*, Dechema, Frankfurt, **1984**, 2, 305.
77. J. A. Lercher, R. A. van Santen, H. Vinek, *Catal. Lett.*, **1994**, 27, 91.
78. J. Sommer, M. Hachoumy, F. Garin, *J. Am. Chem. Soc.*, **1994**, 116, 5491.
79. K. Arata, M. Hino, *Proc. 9th Intern. Congr. Catalysis*, Chem. Inst. Canada, Ottawa, **1988**, 4, 1727.
80. H. J. M. Bosman, E. C. Kruissink, J. V. D. Spoel, F. V. D. Brink, *J. Catal.*, **1994**, 148, 660.
81. K. Tanabe, M. Uchiyama, H. Hattori, *Proc. Symp. Sci. Catalysis. Appl. Ind.*, FPDIL, Sindri, **1979**, Paper No. 46.

## 4.8 Spreading and Wetting

H. KNÖZINGER AND E. TAGLAUER

### 4.8.1 Introduction

Many solid catalysts consist of several (at least two) solid phases which are brought into intimate contact. One of these phases is frequently the support with the catalytically active phases being dispersed on its surface. The most obvious examples of these types of heterogeneous catalysts are supported metals or oxides. Wetting and spreading phenomena frequently occur in such composite materials and may critically influence or determine the structure and morphology of the active phases and hence, their catalytic properties.

Wetting and spreading processes may play an important role in several steps of catalyst syntheses, in catalyst ageing, and rejuvenation. One example are supported

60. K. Tanabe, H. Hattori, Y. Ban'i, A. Mitsutani, Japanese Patent, **1980**, 55-115570.
61. L. Rongsheng, C. Jingfeng, Z. Wuyang, Y. Hua, Z. Zhiming, W. Quan, *React. Kinet. Catal. Lett.* **1992**, 48, 483.
62. T. S. Thorat, V. M. Yadav, G. D. Yadav, *Appl. Catal. A* **1992**, 90, 73.
63. R.-S. Li, J.-F. Chen, H. Yang, W.-Y. Zhang, *Catal. Lett.* **1993**, 18, 317.
64. M. S. Scurrel, *Appl. Catal.* **1987**, 32, 1.
65. G. A. Olah, *Eur. Pat. Appl.* **1983**, 73673.
66. P. Batamack, I. Bucsí, A. Molnar, G. A. Olah, *Catal. Lett.* **1994**, 25, 11.
67. H. Fujisawa, T. Yamaguchi, *Catal. Lett.* **1993**, 17, 319.
68. S. Okazaki, M. Kumasaka, J. Yoshida, K. Kosaka, K. Tanabe, *Ind. Eng. Chem., Product Res. and Develop.* **1981**, 20, 301.
69. J. P. Chen, R. T. Yang, *J. Catal.* **1993**, 139, 227.
70. R. Ohnishi, T. Morikawa, Y. Hiraga, K. Tanabe, *Z. Phys. Chem. Neue Folge* **1982**, 130, 205.
71. K. Tanabe, A. Kayo, T. Yamaguchi, *J. Chem. Soc., Chem. Commun.* **1981**, 602; A. Kayo, T. Yamaguchi, K. Tanabe, *J. Catal.* **1983**, 83, 99.
72. K. Tanabe, H. Hattori, T. Yamaguchi, S. Yokoyama, J. Umematsu, Y. Sanada, *Fuel* **1982**, 61, 389.
73. O. Takahashi, T. Yamauchi, T. Sakuhara, H. Hattori, K. Tanabe, *Bull. Chem. Soc. Jpn.* **1980**, 53, 1807.
74. T. Okuhara, T. Nishimura, H. Watanabe, M. Misono, *J. Mol. Catal.* **1992**, 74, 247.
75. M. Misono, T. Okuhara, *Chemtech* **1993**, 23, 23.
76. W. O. Haag, R. M. Dessau, *Proc. 8th Intern. Congr. Catalysis*, Dechema, Frankfurt, **1984**, 2, 305.
77. J. A. Lercher, R. A. van Santen, H. Vinek, *Catal. Lett.*, **1994**, 27, 91.
78. J. Sommer, M. Hachoumy, F. Garin, *J. Am. Chem. Soc.*, **1994**, 116, 5491.
79. K. Arata, M. Hino, *Proc. 9th Intern. Congr. Catalysis*, Chem. Inst. Canada, Ottawa, **1988**, 4, 1727.
80. H. J. M. Bosman, E. C. Kruissink, J. V. D. Spoel, F. V. D. Brink, *J. Catal.*, **1994**, 148, 660.
81. K. Tanabe, M. Uchiyama, H. Hattori, *Proc. Symp. Sci. Catalysis. Appl. Ind.*, FPDIL, Sindri, **1979**, Paper No. 46.

## 4.8 Spreading and Wetting

H. KNÖZINGER AND E. TAGLAUER

### 4.8.1 Introduction

Many solid catalysts consist of several (at least two) solid phases which are brought into intimate contact. One of these phases is frequently the support with the catalytically active phases being dispersed on its surface. The most obvious examples of these types of heterogeneous catalysts are supported metals or oxides. Wetting and spreading phenomena frequently occur in such composite materials and may critically influence or determine the structure and morphology of the active phases and hence, their catalytic properties.

Wetting and spreading processes may play an important role in several steps of catalyst syntheses, in catalyst ageing, and rejuvenation. One example are supported

metal catalysts which are typically prepared by impregnation from solutions containing suitable salt precursors. Dispersed metal particles are formed during subsequent reduction steps. The growth mechanisms of the metal particles, their sintering during use, and their redispersion during regeneration processes are strongly influenced by the wetting properties between the participating metal and oxide phases. Metal–support interactions can be discussed on the basis of wetting properties. The encapsulation of small metal particles by an overlayer of support oxide which leads to the so-called strong metal–support interaction SMSI [1] is clearly due to the spreading of the support oxide material across the surface of the metal particles. Further, promoter effects are frequently, if not always, due to the formation of an intimate contact between, for example, a metal particle and an oxide promoter. In bimetallic catalysts containing two metals that are immiscible in the bulk (such as Cu and Ru), one metal may still wet the other and thus form an overlayer (Cu on Ru) which may ultimately lead to complete encapsulation [2].

Another example is the synthesis of supported oxide catalysts by spreading of one oxide across the surface of another (support) oxide in physical mixtures. Also, the phenomenon of solid-state ion exchange in zeolites may be discussed within the framework of the wetting and spreading concept.

Despite the significance of wetting and spreading processes in heterogeneous catalysis, they have not been considered very frequently in the catalytic literature. In a recent review [3], Ko argues that this may be due to the fact that the term wetting is attributed to the liquid–solid interface by most researchers and he raises the question as to whether the term wetting in its strictest sense can be used to describe solids that have low atomic mobility at ambient temperature. However, mobility may be induced in solid materials at catalytically relevant temperature conditions, and the general formalism of the thermodynamics of wetting can be applied to solid–solid interfaces [1]. This has been advocated by Haber and co-workers [4–7] in several articles, and the increasing awareness by catalytic chemists of the importance of wetting and spreading phenomena in heterogeneous catalysts is documented in three recent review articles by Xie and Tang [8], by Knözinger and Taglauer [9], and by Ko [3].

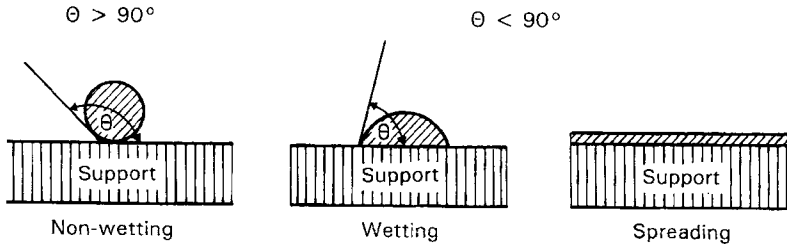
The present chapter first briefly discusses in general terms the formalism of the thermodynamics of wetting and spreading, and the dynamics of the spreading process. Experimental results related to supported metal catalysts including sintering, redispersion, encapsulation of a metal particle by oxide (SMSI) or by another metal are then presented. Finally, the spreading of one oxide on the surface of another oxide is discussed in some detail and solid-state ion exchange in zeolites are mentioned briefly.

## 4.8.2 Theoretical Considerations

### 4.8.2.1 Thermodynamics of Wetting and Spreading

The thermodynamics of wetting of a solid by a liquid is well established and discussed in detail in textbooks on colloid and interface chemistry. A schematic rep-





**Figure 1.** The solid–solid–gas interphase.

representation of wetting and spreading is shown in Fig. 1 where  $\Theta$  is the contact angle between the two phases that are contacting each other.  $\Theta$  is defined by Young's equation,

$$\gamma_{ag} \cos \Theta = \gamma_{sg} - \gamma_{as} \quad (1)$$

where  $\gamma_{ij}$  denotes the specific interface free energy between phases  $i$  and  $j$ , and the subscripts a, s, and g denote active phase, support and gas phases, respectively. If under equilibrium conditions the contact angle is  $\Theta > 90^\circ$ , the supported active phase does not wet the support, whereas wetting occurs for  $\Theta < 90^\circ$ . Spreading of the supported phase across the support surface may occur for the limiting case when  $\Theta$  approaches zero.

When active phase material is brought into contact with a uniform support, the overall change in interfacial energy  $\Delta F$  is given by eq 2

$$\Delta F = \gamma_{ag} \Delta A_a - \gamma_{sg} \Delta A_s + \gamma_{as} \Delta A_{as} \quad (2)$$

The  $\Delta A$  are the changes in surface–interface areas. For spreading to occur of the active phase across the support surface,  $\Delta F$  must be negative. In the opposite case when  $\Delta F > 0$ , islands of the active phase will form on the support which will tend to coalesce into larger particles in order to decrease the free energy of the system.

To fulfil the condition for spreading, namely  $\Delta F < 0$ , the inequality

$$(\gamma_{ag} \Delta A + \gamma_{as} \Delta A_{as}) < \gamma_{sg} \Delta A_s \quad (3)$$

or

$$(\gamma_{ag} + \gamma_{as}) < \gamma_{sg} \quad (4)$$

if  $|\Delta A_a| = |\Delta A_s| = |\Delta A_{as}|$ , must hold.

The interfacial free energy  $\gamma_{as}$  is given by [10–13]

$$\gamma_{as} = \gamma_{ag} + \gamma_{sg} - U_{as} \quad (5)$$

where

$$U_{as} = U_{int} - U_{strain} \quad (6)$$

Here,  $U_{int}$  is the interaction energy per unit interface area between the two phases and  $U_{strain}$  is the strain energy per unit area which is generated by the mismatch of

**Table 1.** Surface free energies, three-dimensional melting points ( $T_{\text{melt}}$ ) and Tammann temperatures ( $T_{\text{Tam}}$ ) of oxides [14].

Oxide	$\gamma$ ( $10^{-6} \text{ J cm}^{-2}$ )	$T^a$ (K)	$T_{\text{melt}}$ (K)	$T_{\text{Tam}}$ (K)
$\text{Al}_2\text{O}_3$	68–70 90	2323 2123	2327	1163
$\text{MgO}$	110–115 110	298 1870	3073	1536
$\text{SiO}_2$	60 39	298 2063	1986	993
$\text{TiO}_2$	28–38	2125–2600	2173 (rutile)	1086
$\text{ZnO}$	90		2248	1124
$\text{ZrO}_2$	59–80 113	1423–2573 < 1423	2988	1494

<sup>a</sup> Temperatures at which surface free energies were measured.

the lattices of the two phases. Combining eqs 4 and 5 gives

$$U_{\text{as}} > 2\gamma_{\text{ag}} \quad (7)$$

i.e.  $U_{\text{as}}$  must be greater than two times the surface free energy  $\gamma_{\text{ag}}$  of the active phase for spreading to occur.

For predictions to be made as to whether or not solid–solid wetting can in principle occur in a given system, surface free energies must be known for the experimental temperature and environmental conditions applied. Surface free energies of metals and pure binary oxides have been compiled by Overbury et al. [14]. The available data are typically measured near the melting point of the material and the temperature coefficients of the  $\gamma$  values (which are of the order of magnitude of  $-10^{-8} \text{ J cm}^{-2} \text{ K}^{-1}$  [14]) are not known in most cases. Surface free energies will also vary with the nature and composition of the gas phase in an unknown form. Therefore, tabulated values can only be used for order-of-magnitude considerations. Surface free energies of several metals and oxides, which bear relevance in heterogeneous catalysis, are summarized in Tables 1 and 2, respectively, together with their bulk melting points  $T_{\text{melt}}$  and Tammann temperatures  $T_{\text{Tam}} \approx 0.5T_{\text{melt}}$ .

The ratio  $U_{\text{as}}/2\gamma_{\text{ag}}$  is considered to be a measure for the tendency toward spreading of phase a across the surface of phase s (eq 7). In a microscopic picture, the same ratio must also be a measure of the relative strengths of interactions between the atoms of phase a and those of phase s in the interface and among the atoms of phase a themselves. The interactions between the two phases are complex in nature and may involve dispersion, polar, and covalent interactions depending on the chemical nature of the two phases.

Van Delft et al. [15, 16] have discussed the tendency of monolayer formation versus crystallite growth of a metal phase a on a substrate s. Deliberately ignoring entropy effects, they calculated the difference  $\Delta E$  in binding energy per atom for an infinite number of adsorbate atoms in either a monolayer or a cubic crystallite:

**Table 2.** Surface free energies and Tammann temperatures of selected metals [113] and their oxides [14].

Metal	$\gamma$ ( $10^{-6}$ J cm $^{-2}$ )	$T^a$ (K)	$T_{\text{Tam}}$ (K)
Cu	135	1356	678
Ir	225	2683	1342
Fe	185	1808	904
Mo	225	2890	1445
Ni	180	1726	863
Pd	150	1827	914
Pt	180	2045	1023
Rh	200	2239	1120
Ru	225	2583	1292
Oxide	$\gamma$ ( $10^{-6}$ J cm $^{-2}$ )	$T^a$ (K)	$T_{\text{Tam}}$ (K)
FeO	59–73	1573–1693	846
	105	1683	
Fe <sub>2</sub> O <sub>3</sub>	36–40	1811	906
MoO <sub>3</sub>	5–7	1068	534
Re <sub>2</sub> O <sub>7</sub>	3–4	600–800	285
V <sub>2</sub> O <sub>5</sub>	8–9	963	482
WO <sub>3</sub>	10	1746	873
ZnO	9		988

<sup>a</sup> Temperature of measurement.

$$\Delta E = \left( \sum_{\text{aa, as}} E_{ij} \right)^{\text{monolayer}} - \left( \sum_{\text{aa}} E_{ij} \right)^{\text{bulk}} \quad (8)$$

If  $\Delta E \leq 0$ , monolayer formation (spreading) will occur, whereas  $\Delta E \gg 0$  predicts the nucleation of crystallites (Volmer–Weber growth mechanism). For a small positive value of  $\Delta E$ , flat islands may be formed. For low coverages (finite number of adsorbate atoms), monolayer formation is favored over crystallite growth, since the crystallite would have a finite size so that the unfavorable contributions of the binding energies of adsorbate atoms at the surface, and particularly at edges and corners of the crystallite, would become relevant [15]. The same authors also proposed that similar considerations may determine whether a layer-by-layer growth (Frank–van der Merwe mechanism) or growth of crystallites on top of a monolayer (Stranski–Krastanov mechanism) will occur. They also pointed out that this simple broken-bond model cannot be applied to systems of ionic solids (oxide–oxide) [16].

It must be noted that the thermodynamic treatment of wetting and spreading given above, is strictly correct only if the thickness of a film produced on a support surface by spreading is large enough to be considered as a bulk phase. As shown by Ruckenstein [17, 18], the free energy change becomes dependent on film thickness when the range of the interaction forces between an atom at the exposed surface of the film and the support is comparable to the thickness of the film. The continuum approach of these authors shows that there exists a critical film thickness for which

the free energy change assumes a maximum negative value, which is typically of the order of interatomic distances and hence corresponds to the thickness of a monolayer.

Ruckenstein [19] also analyzed the stabilities of small crystallites relative to film formation. They showed that there is a minimum crystallite radius  $r_m$  above which the crystallite state is thermodynamically more stable than a film. This minimum radius depends on the contact angle and hence, on the degree of wetting of the support by the active phase:

$$r_m = \frac{h}{1 - \cos \Theta} \quad (9)$$

In eq 9, which is valid for thick films,  $h$  denotes the film thickness. Note that  $r_m$  becomes very large for  $\cos \Theta = 1$  (wetting situation), suggesting that the film is always favored relative to crystallite formation. For situations relevant to supported catalysts, the loading of the support by active phase would generally be small and, hence, the films would be thin. In this case,  $r_m$  becomes dependent on a parameter  $\alpha$ , which is proportional to the difference of two quantities representing the strength of interactions between atoms of the active phase (a–a interactions) and the strength of interactions between a-atoms and s-atoms of the substrate (a–s interactions). For thin films, the minimum crystallite radius  $r_m$  is then given by

$$r_m = \frac{3h}{1 - \cos \Theta + \alpha/h^2 \gamma_{ag}} \quad (10)$$

If the a–a interactions are stronger than the a–s interactions, the parameter will most likely be negative, and if  $h$  is sufficiently small,  $r_m$  can become negative. In this situation, the crystallite state is always thermodynamically favored over the film state. If, however, the denominator of eq 10 becomes positive, when a–s interactions are stronger than a–a interactions, then the radius  $r_m$  can become very large and positive. Under these conditions, the film state may be the thermodynamically preferred situation. For further details, the reader is referred to the detailed treatment by Ruckenstein [19].

Based on his thermodynamic treatment of wetting and spreading, Ruckenstein [20] concluded, that surface-phase transformations may occur. Below a critical loading of the support, a submonolayer of active phase exists on the support. Above the critical loading, large crystallites will form in addition to the submonolayer (or monolayer). It is most likely that submonolayer films always exist in equilibrium with crystallites, although the fractional coverage can be very low. Obviously, these situations are closely related to the growth mechanisms of particles on the support surface.

#### 4.8.2.2 Qualitative Discussion of the Dynamics of Interfacial Processes

The foregoing discussions on the thermodynamics of wetting and spreading are limited to systems which are in their equilibrium state. This is not the case for many solid catalysts and in particular not for supported catalysts in which the support

material is supposed to stabilize small particles of the active phase. Because of the resulting high dispersions and high surface areas, such systems are typically in a state of high surface free energy. During heating and/or during catalytic reactions, these materials therefore have a high tendency to sinter, thereby decreasing the exposed surface area and the surface free energy of the system. Especially, supported metals tend to age via crystallite growth. Under certain conditions and for certain combinations of active phase/support materials, the surface area of the active phase, especially oxides, being exposed to the chemical environment can be increased. Redispersion or spreading may occur. Sintering, redispersion and spreading are dynamic processes which drive a given system toward its equilibrium state. The extent of sintering or dispersion of a given catalytic material depends on several parameters including time of treatment or use, temperature, gas phase composition, presence of additional species on the support surface, and the properties of the support and of the active phase. Here, the surface free energies of the two components and the two-dimensional mobility (surface diffusion coefficients) of atoms, molecules or clusters of the active phase are of special importance.

The formation of highly dispersed particles or crystallites in the synthesis process of, for example, a supported metal catalyst, is governed by nucleation and growth mechanisms (*vide supra*) that have been described in the literature [15, 16, 21–23]. For sintering or redispersion (spreading and film formation) to occur, particles or atoms, molecules or clusters of the active phase must become mobile. As a rule of thumb, the Tammann temperature (in degrees K)

$$T_{\text{Tam}} \approx 0.5T_{\text{melt}}^{\text{bulk}} \quad (11)$$

is considered to be sufficient to make atoms or ions of the bulk of a solid sufficiently mobile for bulk-to-surface migrations, whereas the Hüttig temperature (approximately one-third of the bulk melting temperature) is enough to make the species already located on the surface sufficiently mobile to undergo agglomeration or sintering. Ruckenstein [13, 24] has shown that the enhanced mobility can be associated with the two-dimensional melting of the surface of a solid particle that leads to a liquid-like behavior of the surface layer. A theory of two-dimensional melting has been advanced by Kosterlitz and Thouless [25] which is based on the dislocation pairs model of melting. The two-dimensional melting temperature is given by

$$T_{\text{melt}}^{2\text{-dim}} = (mk/8h^2)a^2\theta_D^2 \quad (12)$$

where  $m$  is the atomic mass,  $k$  the Boltzmann constant,  $h$  Planck's constant,  $a$  the lattice parameter, and  $\theta$  the Debye temperature. It turns out that  $T_{\text{melt}}^{2\text{-dim}}$  as given by eq 12 is proportional to the bulk melting temperature as obtained by Lindemann [26] with the proportionality constant being close to 0.5, the value used in the definition of the Tammann temperature. Values of bulk melting temperatures of catalytically relevant metals and oxides are summarized in Tables 1 and 2, respectively.

Baker [27] observed mobilization of small particles of several metal oxides on graphite at a temperature (the so-called mobility temperature) that was identical to the Tammann temperature. Thus, at least in systems exhibiting relatively weak interactions between active phase and support surface, particle mobility may be

induced at this temperature. The particle migration may perhaps be described as a floating of the active phase particle on the liquid-like surface layer.

For the sintering of small (metal) particles situated on a support surface, several simple mechanisms have been proposed:

- (i) migration of crystallites and their coalescence [28, 29];
- (ii) emission of atoms from small crystallites and their capture by large ones by Ostwald ripening [30–34];
- (iii) a combination of the two previous mechanisms [32].

The theoretical treatment of these various mechanisms has been reviewed by Ruckenstein [35]. The essential features of sintering (of metal particles) can be qualitatively summarized on the basis of these simple processes. Consider a supported metal catalyst with a broad particle-size distribution ranging from single atoms to large particles. Single atoms may migrate across the surface of the support at sufficiently high temperatures and be captured by particles. Simultaneously small particles can migrate across the surface and coalesce when they encounter each other or large ones. This process can be diffusion-controlled if the interaction between two particles in contact are so strong that they form a single particle within a time that is short compared to the time of migration. If, however, the coalescence of two particles into one is slow compared to the diffusion time, the process is said to be coalescence controlled or interface controlled.

The migration rate of particles is size (i.e. mass) dependent. Small particles, being the mobile ones, will therefore tend to be exhausted and further sintering can only occur if the remaining (slow or immobile) particles will emit atoms that migrate from smaller particles to larger ones by which they are captured. It can be shown that there exists a critical radius for the particles [32]. Those particles that have a radius  $r$  smaller than the critical radius  $r_c$  will loose atoms while particles with  $r > r_c$  will gain atoms and grow bigger. This is, of course, the mechanism of Ostwald ripening. As indicated in the previous section, monolayer or submonolayer films can coexist with particles. If there is a particle size distribution with small and large particles being present, atoms will be emitted to the film by the small particles and captured by the larger ones because the film is undersaturated relative to small ones but supersaturated with respect to the large ones. This process can be considered as global ripening and should preferentially be operative at high metal loadings. Alternatively, direct ripening may occur at low metal loadings whereby atoms are transferred directly from small particles to large ones without involving the two-dimensional film of single atoms.

It is clear that the sintering process can be globally dominated by either particle migration or single atom migration. The properties of the support and active phase of the considered catalyst system determine which of the two possible pathways will be dominantly chosen. Ruckenstein and Dadyburjor [32] considered a sintering mechanism in which single atoms and clusters of atoms are emitted from particles, particles of all sizes migrate at size-dependent rates, two particles (including single atoms) that collide, tend to coalesce. The theoretical treatment provided by Ruckenstein and Dadyburjor [32] takes into account the effects of metal loading, two-

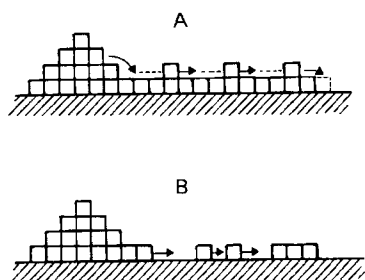
dimensional solubility, diffusional and interfacial processes for all sizes. All these models however, cannot fully describe the mechanisms of sintering because they still disregard the influence of wetting phenomena. Wetting determines the surface contact between support and active phase and therefore affects the migration of the active-phase particles across the support surface. Moreover, the two-dimensional film serving as a pool of single atoms in global ripening must be formed via the spreading of a submonolayer of atoms from the crystallites.

In all the models discussed so far, the support surface was assumed to be flat. In fact, very many case studies, particularly of supported metals, have used flat, low-surface-area substrates. However, Wynblatt and Ahn [36] have demonstrated that surface curvature does affect the surface free energy, the growth of particles (sintering) via particle migration and interparticle transport. Therefore, the sintering process of practical supported catalysts which frequently use high-surface-area, porous supports must be significantly more complex than described by the simple models.

Redispersion processes are very closely related to wetting and spreading phenomena. Inspection of the data accumulated in Table 2 shows that typically the surface free energies of metals are higher than those of the respective oxides. Hence, the thermodynamic condition for spreading (eq 7) on the surface of an oxide support is more likely to be fulfilled for supported metal catalysts in an oxidizing atmosphere, particularly when strong chemical interactions (compound formation) are occurring, thus increasing the value of  $U_{as}$ . It appears that smaller particles spread on the support surface more easily than larger ones do. This phenomenon has been interpreted by Ruckenstein and Chu [37], by introducing a critical radius  $r_c$  for spreading (which obviously is very closely related to the critical radius for particle growth by emission and capture of atoms (*vide supra*)). Smaller particles have a higher dissolution pressure than larger ones, and thus develop a higher tendency towards spreading. Particles with a radius smaller than  $r_c$  can spread completely across the support surface as a monolayer patch.

It is for the above reasons that rejuvenation of supported metal catalysts is typically performed in oxidizing atmospheres. However, redispersion mechanisms may be much more complex than indicated since fragmentation of particles may also occur during the thermal treatments in oxidizing atmospheres (see Section 4.8.3).

Several oxides which are used as active phases in supported oxide catalysts or catalyst precursors are also capable of spreading on typical support materials, such as alumina or titania [3, 8, 9]. Two driving forces may be principally involved in the spreading process. One is the concentration gradient of the active phase which might induce independent atom/molecule diffusion onto the support surface. Haber and co-workers [5, 38], however, argued that surface diffusion should be very slow in oxide systems in the temperature ranges frequently encountered in the solid state synthesis of oxide systems, because of the typically high values of the lattice energies of oxides. Therefore the variation of the surface free energy along the interface of a binary oxide system must be considered as the dominant driving force. The overall surface free energy in such a system can be minimized through the expansion of regions with a low surface free energy and contraction of those with high surface free energy. The gradient of the surface free energy along the surface creates a shear



**Figure 2.** Schematic representation of surface transport processes: (A) unrolling-carpet mechanism; (B) transport by defect diffusion.

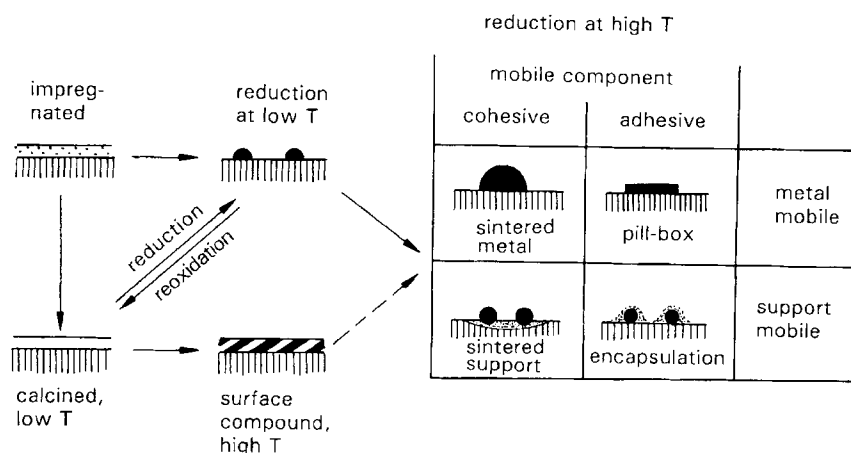
stress on the supported oxide phase and the molecules of this phase may then migrate under the action of this stress from regions of lower to those of higher surface free energy.

As discussed above, surface melting may occur at the Tamman temperature. The mechanism of spreading in powder mixtures of oxides has therefore been described [9] as a migration of species from a liquid-like surface layer of one solid across contact boundaries between grains onto the surface of the support, where they may be immobilized again if the interaction energy  $U_{\text{int}}$  is sufficiently high. A thin film (possibly a single atomic or molecular layer) may thus extend from the contact boundary between the particles onto the support surface. Further transport of the active oxide material can then be envisaged to occur via migration of the active species over the film surface toward the leading edge of the film where they would ultimately be trapped again on the support surface. This process may be described as an unrolling carpet mechanism [39] which is schematically represented in Fig. 2. One may expect that once a monolayer of active material has formed on the support, excess active phase is forming crystallites. Depending on the individual properties of the interacting oxide materials, formation of thick films (several molecular layers) or islands (particles) with finite contact angle may also occur [13] (*vide supra*).

Still another model for the spreading of an active oxide ( $\text{V}_2\text{O}_5$ ) under oxidizing conditions onto the surface of a support (anatase) was proposed by Haber et al. [40]. In this model, the active phase crystallite spreads spontaneously at the beginning of the thermal treatment (hot plate effect) which leads to amorphization of the active phase. Thereafter the spreading is assumed to be diffusion-controlled. Since migration of active phase across the monolayers already formed was found to be highly improbable, it was proposed that spreading in this second stage occurs by diffusion of defects (vacancies) through the monolayer [39], these defects being refilled at the interface between the monolayer and the amorphous active phase (see Fig. 2). Most probably this transport via vacancy diffusion can only occur if the interaction between active phase and support is sufficiently weak for vacancies in the monolayer to be formed under the applied thermal conditions.

It may be interesting to note that Neiman [41] has recently proposed a mechanism for cooperative transport processes in complex oxide materials involving V, Nb, Mo, and W. In this model, it is assumed that the mobile species are  $\text{MeO}_x$  complexes (because of the high covalence of the Me–O bonds) which migrate by





**Figure 3.** Schematic representation of metal-support interactions (adopted from Ref. 16).

rearrangement of the Me–O bonds in regions of local amorphization and quasi-melting of the lattice. It may be speculated that similar processes also occur during spreading of two-dimensional films across the surface of supports.

### 4.8.3 Supported Metal Catalysts

The various stages of the preparation and thermal treatments of supported metal catalysts are very schematically illustrated in Fig. 3. A very similar presentation was earlier given by van Delft et al. [16]. Typically, the support is impregnated with a metal salt (see Section 4.1.1) which serves as the metal precursor and should be well dispersed. Small metal particles may be formed by either direct reduction under mild conditions or by reduction after an intermediate oxidation step. Mild oxidation will lead to thin oxide films spread out on the support or to small oxide particles, where particles and film may also coexist. More severe treatments in oxidative atmospheres can lead to the formation of surface compounds (e.g. spinels) which again may coexist with oxide particles. Continued reduction or thermal treatment in reducing atmosphere under more severe conditions can induce several processes, depending on the nature of the metal and of the support. If the metal is mobile and strong cohesive interactions are operative sintering will occur, whereas the metal particles may spread out and form flat islands (pill-box) if the metal-support interactions are strong. If, in contrast, the support is mobile and strong adhesive interactions come into play, the metal particles can become encapsulated and the so-called SMSI state (strong-metal-support-interaction) may be induced.

It is clear that wetting and spreading phenomena are significantly involved in all steps indicated in Fig. 3. Rather than report on the many studies on sintering and redispersion in practical supported metal catalysts, the following discussion briefly highlights some model studies which have been nicely reviewed by Ruckenstein et al. [1].

#### 4.8.3.1 Sintering and Redispersion

Chen and Ruckenstein [42] have performed a mechanistic study of the sintering of Pd on alumina by transmission electron microscopy (TEM) using model catalysts. These consisted of thin self-supporting and electron-transparent  $\gamma$ -Al<sub>2</sub>O<sub>3</sub> films onto which Pd metal was vacuum evaporated. The resulting thin Pd film was transformed during treatment in flowing H<sub>2</sub> into crystallites in the diameter range 1–7 nm. Starting from this situation, the effects of additional heat treatments in H<sub>2</sub> at various temperatures and for increasing periods of time were studied by TEM. The time sequences of changes in size, shape and position of individual particles at 923 K indicated that the major processes occurring were large-scale crystallite migration and coalescence, because a large number of small crystallites were shown to disappear without change of size with the average diameters of crystallites simultaneously growing. Interestingly, crystallites having diameters as large as 7.5 nm did migrate at 923 K, while some smaller ones appeared to be immobile. Thus, mobilities of crystallites are not only dependent on size. Small crystallites may be trapped in valleys or pits of a rough surface, whereas larger ones, which contact only the tips of the ridges on the surface may travel with greater ease. In addition, the local surface morphologies may affect the interaction forces between particles and support surface. Although the size of small particles did not in general decrease before they disappeared, the possibility of Ostwald ripening could not be excluded. In fact, in localized regions where a few small crystallites were located in close vicinity to larger ones, the former decreased in size and then disappeared. This observation was interpreted as being due to direct ripening (*vide supra*).

Under more severe H<sub>2</sub> treatment, facetting of crystallites larger than 12.5 nm also occurred.

Particle migration (up to 8 nm particles migrated over 25 nm at 773 K) was also observed for Pt on alumina [43]. The two major mechanisms of sintering of supported Pt crystallites appeared to be (i) short-distance, direction-selective migration of particles followed by either collision and coalescence or by direct transfer of atoms between the two approaching particles, or (ii) localized direct ripening between a few immobile, adjacent particles.

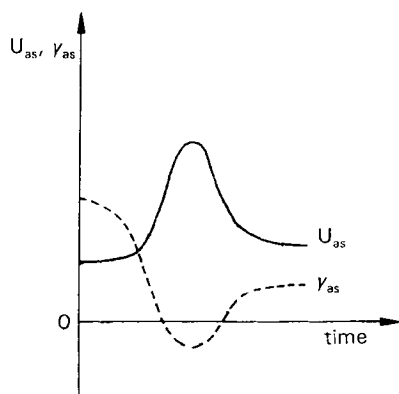
Chen and Ruckenstein [44] also investigated the behaviour of large Pd crystallites on  $\gamma$ -Al<sub>2</sub>O<sub>3</sub> model supports in O<sub>2</sub> atmospheres in the temperature range 623–1193 K. The Pd crystallites are oxidized to form PdO at temperatures below the decomposition temperature of 1143 K. Since the surface free energy of PdO is smaller than that of Pd metal (Table 2), the crystallites extended on the support surface to a smaller wetting angle as expected. Spreading under oxidizing conditions occurs because the surface free energy of the metal oxide  $\gamma_{ag}$  and the interface free energy  $\gamma_{as}$  between the oxidized palladium and the alumina support are smaller. As can be seen from eq 5,  $\gamma_{as}$  is smaller because  $\gamma_{ag}$  is smaller and the interaction energy  $U_{as}$  is larger for the metal oxide than for the metal.

However, additional much more complex phenomena have been observed. Depending on crystallite size and temperature conditions, the formation of porous structures, of torus-like particles, the extension of particles developing irregular leading edges with pits and cavities, and ultimately tearing and fragmentation was observed in 1 bar O<sub>2</sub> over the temperature range mentioned. The pit formation was

explained as a surface tension gradient-driven phenomenon (perhaps enhanced by a wetting-produced stress), and/or as a consequence of crack propagation caused by stress, which was induced by wetting and enhanced by the oxidation of the freshly exposed surface at the tip of the crack. The formation of the torus-like particle was attributed to incomplete oxidation of larger particles at lower temperatures.

It should be noted that, at temperatures higher than the decomposition temperature of bulk PdO in 1 bar O<sub>2</sub>, the palladium particles sintered and formed faceted crystallites.

Very similar phenomena were observed by Ruckenstein and Lee [45] when Ni supported on model alumina films was treated in O<sub>2</sub> atmospheres. Extension of the particles leading to a torus shape during heating was reported, the torus being divided into interlinked subunits and containing small crystallites within the ring. The extension of the oxidized Ni particles is obviously due to the lower surface free energy of NiO and to the lower interfacial free energy between the NiO and the alumina support as outlined above for the Pd-alumina system. However, the interfacial free energy  $\gamma_{as}$  can be extremely small (perhaps even negative under non-equilibrium conditions) when strong chemical interactions or surface compound formation increase the interaction energy  $U_{as}$  in eq 5. In contrast to PdO, NiO has a high tendency toward surface spinel formation in contact with alumina [46, 47], and hence  $U_{as}$  should be large. Therefore, under dynamic oxidation conditions, the large decrease in the dynamic value of  $\gamma_{as}$  and the simultaneous decrease of  $\gamma_{ag}$  can very significantly increase the driving force for spreading. Spinel formation starts at the interface between the NiO particle and the alumina support and propagates into the latter. The surface spinel layer grows until the rate of formation is slowed down by a large diffusional resistance. The interaction energy  $U_{as}$  is only large during the formation of the surface compound and decreases again for the interaction of the NiO with the surface spinel. Therefore, when  $U_{as}$  is plotted against time, it passes through a maximum while, correspondingly,  $\gamma_{as}$  passes through a minimum (which can be negative) as illustrated schematically in Fig. 4. Although there may also be thermodynamic reasons for the appearance of the torus-shaped NiO particles, Ruckenstein and Lee [45] could also explain their formation as a kinetic phenomenon. They suggested that very rapid spreading takes place as soon as the surface spinel starts forming because of the resulting large driving force for wetting, and



**Figure 4.** Time dependence of  $U_{as}$  and  $\gamma_{as}$  (adopted from Ref. 1).

that this may lead to the formation of the torus shape by stress-simulated fracture of the crystallites.

In a similar study, Sushumna and Ruckenstein [48] demonstrated that the composition of gas atmosphere can be of critical importance for the detailed behaviour of Fe supported on alumina catalysts. Even trace impurities of  $O_2$  and  $H_2O$  in  $H_2$  in the ppm range had detectable effects on the sintering behavior of Fe particles.

Industrial regeneration techniques [49] of supported metal catalysts typically involve oxidation/reduction cycles. Redispersion is achieved during thermal treatments in oxidative atmospheres containing  $O_2$ , water, halogens and others [50] often as mixtures since the  $U_{as}$ , interaction energies and, thus, the tendency towards wetting and spreading of the active phase onto the support surface is strongly enhanced under those conditions. As a consequence, highly dispersed metal particles may be formed under subsequent mild reduction conditions.

An interesting case of wetting–nonwetting transition under reaction conditions was recently described by Clausen et al. [51]. By measuring the changes of Cu–Cu coordination numbers by EXAFS for a Cu/ZnO catalyst, these authors inferred that small metallic Cu particles dynamically changed morphology, when the oxidation potential of the  $H_2O/CO/CO_2/H_2$  gas phase was varied by changing the partial pressure of the components. The morphology changes were attributed to wetting–nonwetting phenomena which were due to gas phase-induced changes of the interaction energy between Cu metal and the ZnO support. Essentially no changes of morphology were detected for Cu/SiO<sub>2</sub> catalysts.

#### 4.8.3.2 Strong Metal Support Interactions (SMSI)

As schematically shown in Fig. 3, two extreme situations may occur during thermal treatment at high temperature ( $>773\text{ K}$ ) in reducing atmospheres. If the support is immobile and strong interactions occur between metal particle and support, the metal may spread out on the support surface and form flat islands (pill-box model). If, however, the metal has a high melting point and the support is mobile, then encapsulation of the metal particle may occur by wetting of the metal by support oxide. Since Tauster and co-workers [52, 53] first reported that the chemisorption capacity for  $H_2$  and CO decreased dramatically for supported metal catalysts in the SMSI state, there has been continuing discussion as to whether the phenomenon was caused by electronic or by geometric/morphological effects [1, 54, 55]. The encapsulation or decoration model was proposed because of the failure of the electron transfer models to explain the behavior of large particles supported on titania [56–58]. However, electron transfer effects may also be important contributions for the encapsulation to occur. The phenomenon of encapsulation can be explained in terms of wetting and spreading.

The SMSI effect has been observed for support materials such as  $TiO_2$ ,  $V_2O_5$ ,  $Nb_2O_5$ , and  $Ta_2O_5$ . Inspection of the surface free energies of these oxides (see Table 1), show that they are smaller than those of other supports such as  $SiO_2$ ,  $Al_2O_3$ ,  $ZrO_2$ ,  $MgO$  which do not manifest SMSI. Considering the unrealistic situation of the formation of a thick oxide film on the metal particle, low  $\gamma_{sg}$  values (the support

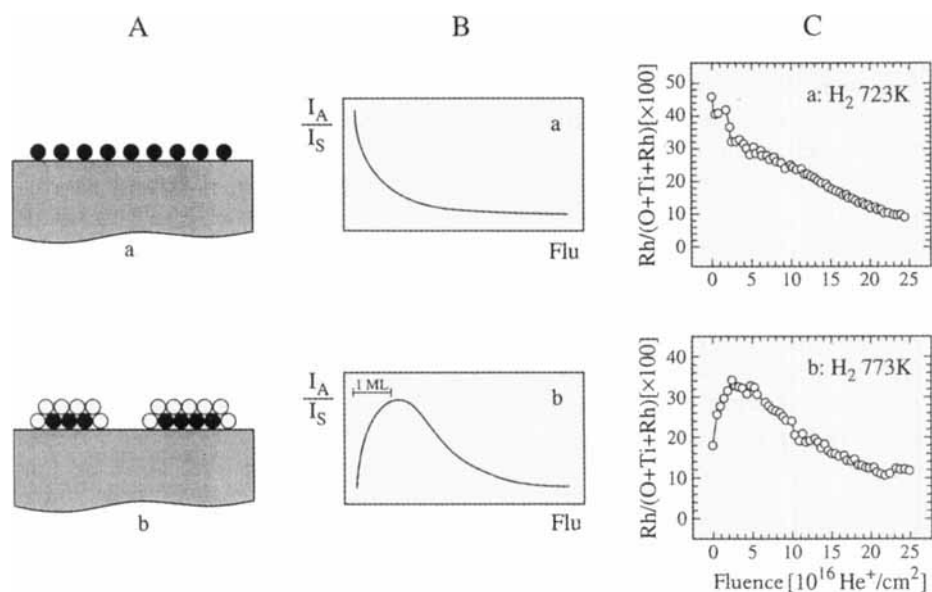
must spread for encapsulation of the metal) would be favorable for spreading as the ratio  $U_{sa}/2\gamma_{sg}$  would increase. The driving force for spreading would even further increase if the interaction energy  $U_{sa}$  between the metal and the support oxide is large. It should be noted that the oxides that manifest SMSI are reducible, and it is generally accepted that partial reduction (possibly catalyzed by the metal) of the support is a prerequisite for encapsulation to occur [1, 54, 55]. Electron transfer from the oxide support to the metal may in fact occur with greater ease if the oxide is in a reduced state. This would increase  $U_{sa}$ , and significantly enhance the driving force for spreading. It should, however, also be noted that the surface free energies of reducible oxides increase if they become oxygen deficient, and that their melting points simultaneously increase. Therefore, the driving force for spreading and the mobility of the oxide decrease in the reduced state. These effects may influence the tendency toward encapsulation, although the enhancement of the interaction term  $U_{sa}$  seems to overcompensate them.

In reality, the strong interactions are short range, and therefore the oxide film forming on the metal particle is expected to be a monolayer or submonolayer film. The driving forces involved are therefore the concentration gradient of the oxide and the gradient of the surface free energy along the metal surface which leads to shear-stress-induced migration of oxide molecules across the metal surface, as already discussed above.

Several studies have been reported in which model  $\text{TiO}_2$  thin films were used as supports, which clearly demonstrated the metal particle encapsulation [59, 60]. Linsmeier et al. [61] and Taglauer and Knözinger [62] have studied the behavior of Rh which was evaporated onto an electrochemically produced  $\text{TiO}_2$  (anatase) film using low energy ion scattering (LEIS) as a surface-sensitive analytical technique. Figure 5(A) shows two models for supported metal catalysts, namely (a) a monolayer of atoms A on the support surface S; and (b) small islands of atoms A which are encapsulated by support S. Figure 5(B) represents the corresponding profiles that are expected for the two models when the scattering intensity ratio  $I_A/I_S$  is plotted versus the fluence (total number of  $\text{He}^+$  ions impinging on the surface). Experimental results for the Rh/ $\text{TiO}_2$  model catalyst after mild  $\text{H}_2$  treatment at 723 K (non-SMSI state) and after severe  $\text{H}_2$  treatment at 773 K (SMSI state) are shown in Fig. 5(C). The experimental profile obtained after low temperature treatment resembles that of a highly dispersed metal film, whereas the profile after high temperature treatment passes through a maximum and clearly indicates the encapsulation of the Rh particles. A rough estimate showed that the fluence at the position of the maximum corresponds to the average value required to sputter one monolayer of oxide. This result nicely relates to the prediction made above for the expected film thickness.

#### 4.8.3.3 Bimetallic Catalysts

Surface segregation phenomena and the surface composition of bimetallic catalysts are controlled by the surface free energies of the constituents of the bimetallic particles. The deposition of metal on metal in relation to bimetallic catalysts has been discussed by Dodson [63].



**Figure 5.** Low energy ion scattering on Rh/TiO<sub>2</sub> model catalysts: (A) structure models; (B) expected intensity profiles; (C) experimental intensity profiles (adopted from Ref. 62).

Particularly interesting systems in the context of wetting are bimetallic supported catalysts containing two metals that are immiscible in the bulk, such as Ru and Cu. Sinfelt and co-workers [64, 65] first reported on a Cu-induced suppression of hydrogen chemisorption for SiO<sub>2</sub>-supported RuCu catalysts; this observation was consistent with the structural model of the bimetallic particles consisting of a Ru core encapsulated by a Cu layer, which was developed by Sinfelt et al. [66] on the basis of EXAFS results. Several surface science studies also demonstrated the formation of Cu films on the surface of Ru single crystal surfaces [67, 68] and infrared studies of CO chemisorption on RuCu/SiO<sub>2</sub> catalysts supported the encapsulation model [69]. The available experimental evidence therefore clearly demonstrates that – although the two metals do not form binary alloys – Cu does wet the Ru. The surface free energy  $\gamma_{\text{Cu}}$  of Cu is relatively small (see Table 2) and lower than that of Ru. Moreover, surface science studies on single crystal model systems [70] and infrared spectra of chemisorbed CO on RuCu/SiO<sub>2</sub> catalysts [69] showed that electron transfer occurs from Cu to Ru. This electron transfer contributes to the strength of interaction between the two metals at the interface and presumably leads to a ratio  $U_{\text{RuCu}}/2\gamma_{\text{Cu}} > 1$ , so that the spreading condition for Cu across the surface of Ru is fulfilled.

#### 4.8.4 Supported Oxide Catalysts

Supported oxides of transition metals, particularly of groups Vb (V), VIb (Cr, Mo, W) and VIIb (Re) are widely used as catalysts or catalyst precursors for various

industrially important reactions. These so-called monolayer-type catalysts are formed when one metal oxide (mobile active phase) is dispersed on the surface of a second metal oxide (immobile support). Typical catalyst supports in industrial applications are transition aluminas, silica, and titania. Inspection of the data summarized in Table 1 indicates, that the surface free energies of these support oxides are higher than those of the mentioned transition metal oxides. Assuming the formation of thick films, the spreading condition of eq 7, namely  $U_{as}/2\gamma_{ag} > 1$ , must be fulfilled. Unfortunately the interaction energies  $U_{as}$  are practically always unknown. However, it has been argued [71] that chemical contributions to  $U_{as}$  should be high if the two components have a tendency to form a ternary oxide via solid-state reactions. In this case the spreading condition should be fulfilled. Based on these arguments, the experimentally observed spreading of  $\text{MoO}_3$  on alumina and titania could be explained [71] since both supports form bulk ternary oxide phases with  $\text{MoO}_3$  ( $\text{Al}_2(\text{MoO}_4)_3$  and  $\text{Ti}(\text{MoO}_4)_2$ , respectively) at higher temperatures, although these are not detected under the spreading conditions. In contrast,  $\text{MoO}_3$  is not known to undergo a solid-state reaction with silica, and consequently spreading of  $\text{MoO}_3$  on the surface of silica was not observed [71].

As already mentioned above, the interaction forces between active phase and support are short range and should be restricted to the interface. Therefore, the driving forces for spreading are expected to decrease significantly once a molecular monolayer is formed. As a consequence, oxide particles or crystallites of the active phase are expected to form when the loading by the active oxide exceeds the theoretical monolayer capacity of the support. Experimental evidence for this situation has in fact been reported in the literature [9].

These principles can be applied for the preparation of supported oxide monolayer catalysts from mechanical mixtures, the advantage of this route being that the handling of solutions for impregnation can be avoided. However, for efficient spreading to occur, the two components of a powder mixture must be brought into intimate contact and optimal mixing is required so as to obtain a homogenous product. Moreover, the active (and mobile) phase must be present as crystallites having diameters below a critical value (see eqs 9 and 10), since otherwise the crystallite state may be thermodynamically more stable than the film. Grinding or milling is therefore usually applied to the powder mixture prior to thermal treatments. Often these processes are not well controlled when powder mixtures are prepared for solid-state synthesis of bulk products or supported catalysts, although they must be expected to influence the reactivity of the powders very significantly.

Grinding will certainly influence the grain sizes and grain-size distributions, and thus the rates of spreading. Also, the two-dimensional melting temperature should be dependent on the grain size (curvature). Several additional phenomena occur in the very complex grinding process that must influence the spreading and reactivity behavior of powder mixtures [72–74]. During grinding, several particles are simultaneously and repeatedly subjected to stress application in the grinding zone. With each stress application, several fractures may occur in each particle. Cracks will be initiated and will propagate; flaw interaction in a particle, secondary breakage, and interaction of particles with each other will occur. The physical and chemical interaction between particles and the grinding environment, and the transport of material through the grinding zone will also affect the nature of the product obtained.

Occasionally material transport between chemically distinct particles may already lead to spreading during the grinding and milling procedure. This may particularly occur when crystallites are involved that have layer structures (e.g.  $\text{V}_2\text{O}_5$ ), so that stress application may lead to exfoliation processes. Even solid-state reactions in bulk phases can be induced by mechanical activation of solid materials and several tribochemical processes have found technological application [75]. For example, Angelov and Bonchev [76] have reported on the formation of a Cu-rich surface layer on  $\text{Co}_3\text{O}_4$  by mechanically treating a powder mixture of CuO and  $\text{Co}_3\text{O}_4$  in a friction grinder. These reactions are believed to occur due to strong local temperature increases which may lead to melting of microscopic zones within contact regions.

The effect of mechanical stress applied to  $\text{MoO}_3$  by grinding in a planetary mill have recently been studied by Mestl and co-workers [77–79]. It was shown that the crystallite sizes decreased from an initial value of about  $1\text{ }\mu\text{m}$  to  $50\text{ nm}$ , with some ultrafine amorphous material also being produced. The BET surface area simultaneously increased from an initial value of  $1.3\text{ m}^2\text{ g}^{-1}$  to  $32\text{ m}^2\text{ g}^{-1}$ . A substoichiometric  $\text{MoO}_{3-x}$  was formed during grinding. The presence of shear defects was indicated by XRD, and  $\text{Mo}^{5+}$  was detected by ESR and optical spectroscopy. When this milled  $\text{MoO}_3$  was gently mixed with alumina without applying additional mechanical stress, and then thermally treated in  $\text{O}_2$  at  $823\text{ K}$  (melting point of bulk  $\text{MoO}_3$  is  $1068\text{ K}$ ), in situ high temperature Raman spectroscopy demonstrated the existence of a surface melt of molybdenum oxide which transformed into a glassy  $\text{MoO}_3$  surface phase on quenching to room temperature [80]. The experiments described by Mestl et al. [80] clearly showed the higher reactivity of the milled  $\text{MoO}_3$  and its more efficient spreading on the alumina surface as compared to the initial low-surface-area material.

Since the reported literature has been summarized in several recent review articles [3, 8, 9], we will only briefly describe a few experimental studies on spreading in oxide mixtures.

#### 4.8.4.1 Molybdenum-based Catalysts

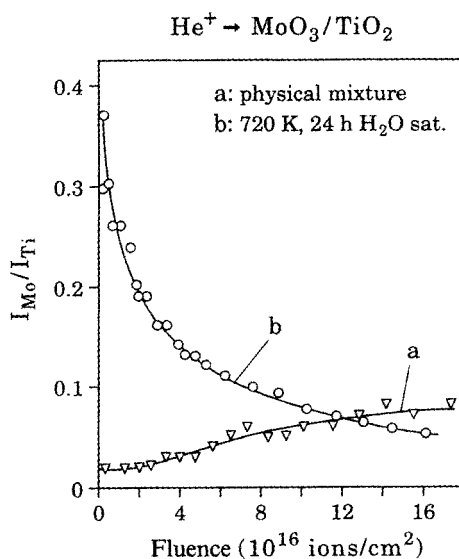
The most thoroughly studied supported oxide systems are those involving molybdenum oxide as the mobile phase. As already mentioned, spreading of  $\text{MoO}_3$  in physical mixtures was observed on the surfaces of aluminas and titania (anatase) but not on silica; the reason for the different behavior of these support oxides was thought to be connected with the interaction energy  $U_{\text{as}}$  between  $\text{MoO}_3$  and the support materials [71]. Highly dispersed molybdenum oxide surface phases were also detected on  $\text{MgO}$  [81, 82] and on  $\text{SnO}_2$  [81]. It is interesting to note that  $\text{MoO}_3$  and  $\text{MgO}$  undergo a solid state reaction to form  $\text{MgMoO}_4$ .

The transport of  $\text{MoO}_3$  across the surface of alumina was demonstrated in several model experiments. Hayden et al. [83] prepared molybdenum oxide on a graphite support. Because of the weak interaction between these two components,  $\text{MoO}_3$  particles were formed. This material was then mixed with  $\text{Al}_2\text{O}_3$  and studied by controlled atmosphere electron microscopy.  $\text{MoO}_3$  particles were mobile on the



graphite surface at 930 K and spontaneously disappeared when they contacted alumina grains. This observation was explained by rapid spreading of the  $\text{MoO}_3$  over the  $\text{Al}_2\text{O}_3$  surface, and related to the higher surface free energy of alumina as compared to graphite. It should, however, be emphasized that the large interaction energy  $U_{\text{as}}$  between  $\text{MoO}_3$  and  $\text{Al}_2\text{O}_3$  is crucial for the large driving force for spreading. Leyrer et al. [84] used model samples which consist of an alumina wafer in contact with a  $\text{MoO}_3$  wafer forming a sharp dividing line. Concentration profiles across the dividing line between the two oxides were measured by Raman microscopy with a lateral resolution of approximately  $20\text{ }\mu\text{m}$ . The results clearly demonstrated that  $\text{MoO}_3$  was in fact transported onto the  $\gamma\text{-Al}_2\text{O}_3$  surface at 800 K in streams of either dry or humid  $\text{O}_2$  whereby the initially sharp concentration profile became diffuse and reached widths of several hundred (up to  $1000\text{ }\mu\text{m}$ ) micrometers after 100 h. It was also shown that the presence of water vapor increased the rate of spreading, and led to the formation of a surface polymolybdate (vide infra). These model experiments also enabled gas phase transport and surface diffusion in a concentration gradient to be discounted as possible mechanisms for the migration of  $\text{MoO}_3$ , since no transport occurred onto a  $\text{SiO}_2$  wafer in an analogous experiment. This result again emphasizes the crucial importance of the interaction energy in fulfilling the spreading conditions given by eq 7.

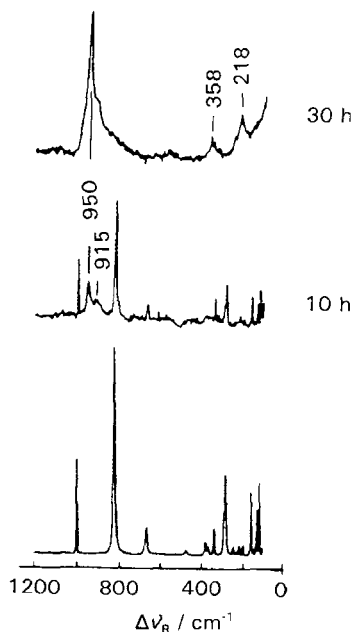
Spreading of polycrystalline  $\text{MoO}_3$  in powder mixtures with  $\gamma\text{-Al}_2\text{O}_3$  and  $\text{TiO}_2$  (anatase) was indicated by the disappearance of the X-ray diffraction pattern of  $\text{MoO}_3$  after thermal treatment, provided that the  $\text{MoO}_3$  content remained below a certain limit [8, 85, 86]. This limiting  $\text{MoO}_3$  content was determined as  $0.12\text{ g MoO}_3$  per  $100\text{ m}^2$  of both alumina and titania, and was interpreted as corresponding to the monolayer capacity. More direct evidence for spreading has been obtained by surface-sensitive techniques such as XPS [8, 9, 85–87] and LEIS [8, 9, 62, 71, 88, 89]. As an example, Fig. 6 shows ion scattering data which clearly support the spreading



**Figure 6.** LEIS intensity profiles for  $\text{MoO}_3/\text{TiO}_2$  catalyst: (a) physical mixture prior to thermal treatment; (b) after thermal treatment for 24 h at 720 K in an  $\text{O}_2$  flow saturated with water vapor.

of  $\text{MoO}_3$  on  $\text{TiO}_2$  during thermal treatment at 720 K. In the figure, the intensity of  $\text{He}^+$  ions backscattered from Mo atoms relative to that of  $\text{He}^+$  backscattered from Ti atoms is plotted against the fluence (=total number of  $\text{He}^+$  ions that have impinged on unit surface area). Profile (a) represents the one characteristic of the physical mixture prior to thermal treatment; the second profile (b) was obtained after thermal treatment of the same mixture at 720 K for 5 h in a flow of oxygen saturated with 32 mbar  $\text{H}_2\text{O}$  vapor. The intensity ratios extrapolated to zero fluence are characteristic of the virgin surface being unaffected by sputtering processes. This value is very low for the starting physical mixture consisting of grains of  $\text{Al}_2\text{O}_3$  and small crystallites of  $\text{MoO}_3$ . Because of the surface sensitivity of the LEIS technique, the Mo/Ti intensity ratio extrapolated to zero fluence is expected to approach infinity if a monolayer of molybdenum oxide is formed on the  $\text{TiO}_2$  surface. Profile (b) indeed steeply rises near zero fluence and thus strongly supports the spreading of  $\text{MoO}_3$  on  $\text{TiO}_2$ . Similar results were obtained with alumina as the support. LEIS experiments also verified that spreading of  $\text{MoO}_3$  on both supports occurred in  $\text{O}_2$  in the presence and in the absence of water vapor.

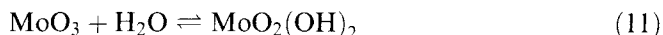
Neither XPS nor LEIS provide structural information of the molybdenum oxide overlayers on the support surfaces. Therefore, laser Raman spectroscopy (LRS) [9, 71, 81, 88–90] and X-ray absorption spectroscopy [91, 92] have been applied to elucidate the structural characteristics of the two-dimensional oxide films. LRS emphasized the role of water vapor for the structure formation. As a representative example, Fig. 7 shows spectra of  $\text{MoO}_3$ – $\text{Al}_2\text{O}_3$  mixtures [89]. The bottom spectrum is characteristic for the oxide mixture prior to thermal treatment and represents



**Figure 7.** Raman spectra of a physical mixture of 9 wt %  $\text{MoO}_3$ – $\text{Al}_2\text{O}_3$  prior to thermal treatment (bottom) and after calcination at 723 K in a stream of  $\text{O}_2$  saturated with water vapour for 10 and 30 h (adopted from Ref. 90).

the signature of polycrystalline  $\text{MoO}_3$ . When the mixture was thermally treated in water-free  $\text{O}_2$ , the same spectrum was obtained for the dispersed oxide film, suggesting that the X-ray-amorphous film still preserved the structural characteristics of  $\text{MoO}_3$ . Figure 7 also shows the spectra of the  $\text{MoO}_3\text{--Al}_2\text{O}_3$  mixture after thermal treatment in humid  $\text{O}_2$  obtained after 10 and 30 h. These spectra demonstrate the chemical transformation of  $\text{MoO}_3$  into a surface heptamolybdate (spectrum after 30 h) with an intermediate monomeric  $\text{MoO}_4^{2-}$  anion being detectable by the characteristic band at  $915\text{ cm}^{-1}$ . These conclusions were supported by X-ray absorption fine structure spectroscopy (EXAFS) [91] for the  $\text{MoO}_3\text{--Al}_2\text{O}_3$  mixture and by the preedge and X-ray absorption near-edge (XANES) structure for the  $\text{MoO}_3\text{--TiO}_2$  system [92].

The chemical transformation of  $\text{MoO}_3$  into a surface polymolybdate on  $\text{Al}_2\text{O}_3$  and  $\text{TiO}_2$  was described as being due to the intermediate formation of  $\text{MoO}_2(\text{OH})_2$ , a reaction which is known to occur under the experimental spreading conditions [93]:



This oxyhydroxide was assumed to react with basic surface hydroxy groups  $[\text{OH}^-]_s$  to yield the monomeric surface molybdate  $[\text{MoO}_4^{2-}]_s$  that was detected by LRS as an intermediate (see Fig. 7):



These intermediates subsequently undergo condensation with formation of the surface polymolybdate if the local concentration of the monomer becomes sufficiently high.

Since gas-phase transport and diffusion in a concentration gradient could be excluded (vide supra), transport of the molybdenum oxide via the unrolling carpet mechanism was proposed [9] (Fig. 2). However, migration via defect diffusion may still be an alternative. Recent in situ LRS studies [80] indicated the presence of a liquid-like layer containing monomers and oligomers of  $\text{MoO}_3$  which might be considered as the migrating species.

#### 4.8.4.2 Vanadium-based Catalysts

The spreading of  $\text{V}_2\text{O}_5$  on alumina and titania has been studied intensely because of the importance of these monolayer-type materials as catalysts for selective catalytic oxidation and for selective catalytic reduction of  $\text{NO}_x$ .  $\text{V}_2\text{O}_5$  has a low melting point, and hence high mobility under mild temperature conditions. It also has a low surface free energy and probably undergoes strong interaction with supports such as alumina since it forms the ternary oxide  $\text{AlVO}_4$ . Thus, the spreading condition  $U_{as}/2\gamma_{ag} > 1$  should be fulfilled. Moreover, in the presence of water vapor, highly volatile and reactive oxyhydroxides such as  $\text{V}_2\text{O}_3(\text{OH})_4$  [94] or  $\text{VO}(\text{OH})_3$  [95] are formed which permit an interpretation of surface chemical transformations of  $\text{V}_2\text{O}_5$ . The many studies on vanadia-based materials have been reviewed [3, 9].

Haber and co-workers [4–6, 38, 40, 96, 97] have demonstrated in several detailed investigations that spreading occurred in  $V_2O_5/TiO_2$  mixtures. They showed in particular [38] that migration of  $V_2O_5$  over the surface of anatase grains led to encapsulation of the latter by a thin overlayer, the properties of which were strongly modified by the interaction with the anatase support. On top of this inner layer on outer layer was detected, its properties being similar to those of  $V_2O_5$ . Centi and co-workers [98, 99] also reported on spreading of  $V_2O_5$  over the surface of titania with formation of an oxide monolayer of  $V^{4+}$  oxide species [98] on top of which amorphous multilayer patches of  $V^{5+}$  oxide were believed to grow [99].

In contrast to Haber and co-workers [4–6, 38], Centi et al. [98, 99] observed the spreading of  $V_2O_5$  not only on anatase but also on the rutile modification. Based on their results, Haber and co-workers [4–6, 38] proposed that spreading was dependent on the crystallographic modification of the support and on the type of crystal plane.

The migration mechanism of  $V_2O_5$  on the surfaces of alumina and titania is not yet understood in detail. As already mentioned, very recent results reported by Haber et al. [40] seem to indicate that a process of defect diffusion through the vanadia monolayer is involved.

#### 4.8.4.3 Tungsten-based Catalysts

The thermodynamic spreading condition may be fulfilled for  $WO_3$  since its surface free energy is relatively low and it definitely forms a ternary oxide  $Al_2(WO_4)_3$  with alumina. However, the Tammann temperature is 873 K, leading to low mobility. Nevertheless, spreading of  $WO_3$  on  $\gamma-Al_2O_3$ , although slow, was observed at 820 K by LEIS [71] and LRS, and EXAFS [100] provided evidence for the formation of a surface polytungstate in the presence of water vapor via an intermediate oxyhydroxide  $WO_2(OH)_2$ . An analogous surface chemistry was also reported for physical mixtures of  $WO_3$  with  $TiO_2$  (anatase) [100].

#### 4.8.4.4 Zeolites as Supports

A few studies involving zeolites and layer silicates as supports for oxides are reported in the literature. Haase et al. [101] have provided experimental evidence for the spreading of  $V_2O_5$  on mordenite. Migration of  $Ga_2O_3$  in H-ZSM-5 zeolites was observed by Mériaudeau and Naccache [102]. Fierro et al. [103] proposed the incorporation of  $MoO_3$  into the intracrystalline cavities of Y-type zeolites by means of vaporization of  $MoO_3$  by reaction with water vapor at 623 K. It was claimed that the zeolite structure was largely retained under these conditions. At higher temperatures, however, a progressive loss of crystallinity was observed. Leyrer and Knözinger [104] have shown that complete degradation of the zeolite structure resulted, when incorporation of Mo into Y-zeolites was attempted via gas-phase transport of  $MoO_2(OH)_2$  at 720 K.

### 4.8.5 Solid-state Ion Exchange of Zeolites

Solid-state ion exchange may be related to phenomena of wetting and spreading in solid-solid systems. Rabo et al. [105–106] first reported that proton-containing samples of zeolite Y reacted with sodium chloride under evolution of HCl. Later, Karge and co-workers [107–111] developed solid-state ion exchange further as a synthetic route for the preparation of alkaline, alkaline earth, rare earth, and transition and noble-metal-containing zeolites starting from parent materials that contain  $H^+$ ,  $NH_4^+$ , or  $Na^+$ . In several cases a 100% cation incorporation could be achieved in a one-step solid-state reaction. Very recently, even the large  $Cs^+$  ions could be driven into  $S_I$  sites of zeolite Y via solid-state ion exchange [112]. Such degrees of exchange are difficult to obtain by conventional methods.

### References

1. S. A. Stevenson, J. A. Dumesic, R. T. K. Baker, E. Ruckenstein, *Metal-Support Interactions in Catalysis, Sintering, and Redispersion*, Van Nostrand Reinhold, New York, **1987**.
2. J. H. Sinfelt, *Bimetallic Catalysts: Discoveries, Concepts and Applications*, Wiley, New York, **1983**.
3. E. I. Ko in *Wettability* (Ed.: J. C. Berg), M. Dekker, New York, **1993**, p. 431.
4. J. Haber in *Surface Properties and Catalysis by Non-Metals* (Eds: J. P. Bonnelle, B. Delmon, E. Derouane), Reidel, Dordrecht, **1983**, p. 1.
5. J. Haber, *Pure Appl. Chem.* **1984**, *56*, 1663.
6. J. Haber, *Proceedings of the 8th International Congress on Catalysis*, Berlin, 1984, Verlag Chemie, Weinheim, **1984**, Vol. 1, p. 85.
7. J. Haber, J. Ziolkowski in *Proceedings of the 7th International Symposium React. Solids*, Bristol, 1972, Chapman and Hall, London, **1972**, p. 782.
8. Y. C. Xie, Y. Q. Tang, *Adv. Catal.* **1990**, *37*, 1.
9. H. Knözinger, E. Taglauer in *Catalysis* (Eds: J. J. Spivey, S. K. Agarwal), Royal Society of Chemistry, Cambridge, **1993**, Vol. 10, p. 1.
10. E. Ruckenstein, S. H. Lee, *J. Catal.* **1987**, *104*, 259.
11. I. Sushumna, E. Ruckenstein, *J. Catal.* **1985**, *94*, 239.
12. S. A. Stevenson, J. A. Dumesic, R. T. K. Baker, E. Ruckenstein, *Metal-Support Interactions in Catalysis, Sintering, and Redispersion*, Van Nostrand Reinhold, New York, **1987**, p. 141.
13. E. Ruckenstein in *Sintering and Heterogeneous Catalysis*, (Eds: G. C. Kuczinski, A. E. Miller, G. A. Sargent), Plenum Press, New York, London, **1984**, p. 199.
14. S. H. Overbury, P. A. Bertrand, G. A. Somorjai, *Chem. Rev.* **1975**, *75*, 547.
15. F. C. M. J. M. van Delft, A. D. van Langeveld, B. E. Nieuwenhuys, *Thin Solid Films* **1985**, *123*, 333.
16. F. C. M. J. M. van Delft, A. D. van Langeveld, B. E. Nieuwenhuys, *Solid State Ionics*, **1985**, *16*, 233.
17. E. Ruckenstein in S. A. Stevenson, J. A. Dumesic, R. T. K. Baker, E. Ruckenstein, *Metal-Support Interactions in Catalysis, Sintering, and Redispersion*, Van Nostrand Reinhold, New York, **1987**, p. 241.
18. E. Ruckenstein, *J. Cryst. Growth*, **1979**, *47*, 666.
19. E. Ruckenstein in S. A. Stevenson, J. A. Dumesic, R. T. K. Baker, E. Ruckenstein, *Metal-Support Interactions in Catalysis, Sintering, and Redispersion*, Van Nostrand Reinhold, New York, **1987**, p. 236.
20. E. Ruckenstein in S. A. Stevenson, J. A. Dumesic, R. T. K. Baker, E. Ruckenstein, *Metal-Support Interactions in Catalysis, Sintering, and Redispersion*, Van Nostrand Reinhold, New York, **1987**, p. 247.

21. G. E. Rhead, M. G. Barthes, C. Argile, *Thin Solid Films* **1981**, 82, 201.
22. E. Bauer, H. Poppa, *Thin Solid Films* **1972**, 12, 167.
23. E. Bauer, H. Poppa, G. Todd, P. R. Davis, *J. Appl. Phys.* **1977**, 48, 3773.
24. E. Ruckenstein in S. A. Stevenson, J. A. Dumesic, R. T. K. Baker, E. Ruckenstein, *Metal-Support Interactions in Catalysis, Sintering, and Redispersion*, Van Nostrand Reinhold, New York, **1987**, pp. 153.
25. J. M. Kosterlitz, D. J. Thouless, *J. Phys. C* **1972**, 5, L 124; **1973**, 6, 1181.
26. F. A. Lindemann, *Z. Phys.* **1910**, 11, 609.
27. R. T. K. Baker, *J. Catal.* **1982**, 78, 473.
28. E. Ruckenstein, B. Pulvermacher, *J. Catal.* **1973**, 29, 224.
29. E. Ruckenstein, B. Pulvermacher, *AIChE J.* **1973**, 19, 356.
30. B. K. Chakraverty, *J. Phys. Chem. Solids* **1967**, 28, 2401.
31. P. C. Flynn, S. E. Wanke, *J. Catal.* **1974**, 33, 233.
32. E. Ruckenstein, D. B. Dadyburjor, *J. Catal.* **1977**, 48, 73.
33. E. Ruckenstein, D. B. Dadyburjor, *Thin Solid Films* **1978**, 55, 89.
34. H. H. Lee, *J. Catal.* **1980**, 62, 129.
35. E. Ruckenstein in S. A. Stevenson, J. A. Dumesic, R. T. K. Baker, E. Ruckenstein, *Metal-Support Interactions in Catalysis, Sintering, and Redispersion*, Van Nostrand Reinhold, New York, **1987**, pp. 156, 187.
36. P. Wynblatt, T. M. Ahn in *Sintering and Catalysis* (Ed: G. C. Kuczynski), Plenum Press, New York, **1975**, p. 83.
37. E. Ruckenstein, Y. F. Chu, *J. Catal.* **1979**, 59, 109.
38. J. Haber, T. Machej, T. Czeppe, *Surf. Sci.* **1985**, 151, 301.
39. P. von Blanckenhagen in *Structure and Dynamics of Surfaces II. Phenomena, Models, and Methods* (Eds: W. Schommers, P. von Blanckenhagen), Springer-Verlag, Berlin, **1987**, p. 73.
40. J. Haber, T. Machej, E. M. Serwicka, I. E. Wachs, *Catal. Lett.* **1995**, 32, 101.
41. A. Ya. Neimann, *Solid State Ionics* **1996**, 83, 263.
42. J. J. Chen, E. Ruckenstein, *J. Catal.* **1981**, 69, 254.
43. I. Sushumna, E. Ruckenstein, *J. Catal.* **1988**, 109, 433.
44. J. J. Chen, E. Ruckenstein, *J. Phys. Chem.* **1981**, 85, 1606.
45. E. Ruckenstein, S. H. Lee, *J. Catal.* **1984**, 86, 457.
46. M. Lo Jacono, M. Schiavello, A. Cimino, *J. Phys. Chem.* **1971**, 75, 1044.
47. Y. Chen, L. Zhang, *Catal. Lett.* **1992**, 12, 51.
48. I. Sushumna, E. Ruckenstein, *J. Catal.* **1985**, 94, 239.
49. E. Ruckenstein, D. B. Dadyburjor, *Rev. Chem. Eng.* **1983**, 1, 251.
50. M. J. D'Aniello, Jr., D. R. Monroe, C. J. Carr, M. H. Krueger, *J. Catal.*, **1988**, 109, 407.
51. B. S. Clausen, J. Schiøt, L. Gråbaek, C. V. Oveson, K. W. Jacobsen, J. K. Nørskov, H. Topsøe, *Topics Catal.* **1994**, 1, 367.
52. S. J. Tauster, S. C. Fung, R. L. Garten, *J. Am. Chem. Soc.* **1978**, 100, 170.
53. S. J. Tauster, S. C. Fung, *J. Catal.* **1978**, 55, 29.
54. G. L. Haller, D. E. Resasco, *Adv. Catal.* **1989**, 36, 173.
55. *Strong Metal Support Interactions* (Eds: R. T. K. Baker, S. J. Tauster, J. A. Dumesic), American Chemical Society, Washington, **1986**.
56. S. Engels, B. Freitag, W. Mörke, W. Röschke, M. Wilde, *Z. Anorg. Allg. Chem.* **1981**, 474, 209.
57. P. Mériaudeau, J. F. Dutel, M. Dufaux, C. Naccache, *Stud. Surf. Sci. Catal.* **1982**, 11, 95.
58. J. Santos, J. A. Dumesic, *Stud. Surf. Sci. Catal.* **1982**, 11, 43.
59. B.-H. Chen, J. M. White, *J. Phys. Chem.* **1983**, 87, 1327.
60. A. D. Logan, E. J. Braunschweig, A. K. Datye, D. J. Smith, *Langmuir* **1988**, 4, 827.
61. Ch. Linsmeier, H. Knözinger, E. Taglauer, *Nucl. Instr. Meth. B* **1996**, 118, 533.
62. E. Taglauer, H. Knözinger, *Phys. Stat. Sol. (b)* **1995**, 192, 465.
63. B. W. Dodson, *Surf. Sci.* **1987**, 184, 1.
64. J. H. Sinfelt, Y. L. La, J. A. Cusumano, A. E. Barnett, *J. Catal.* **1976**, 42, 227.
65. E. B. Prestridge, G. H. Via, J. H. Sinfelt, *J. Catal.* **1977**, 50, 115.
66. J. H. Sinfelt, G. H. Via, F. W. Lytle, *J. Phys. Chem.* **1980**, 72, 4832.
67. K. Christmann, G. Ertl, H. Shimizu, *J. Catal.* **1980**, 61, 397; *Thin Solid Films* **1979**, 57, 247.
68. J. T. Yates, C. H. F. Peden, D. W. Goodman, *J. Catal.* **1985**, 94, 321.

69. R. Liu, B. Tesche, H. Knözinger, *J. Catal.* **1991**, 129, 402.
70. J. E. Houston, C. H. F. Peden, P. J. Feibelman, *Surf. Sci.* **1987**, 192, 457.
71. J. Leyrer, R. Margraf, E. Taglauer, H. Knözinger, *Surf. Sci.* **1988**, 201, 603.
72. P. Somasundaran in *Ceramic Processing before Firing* (Eds: G. Y. Onoda, Jr., L. L. Hench), Wiley, New York, **1978**, p. 78.
73. K. Shinohara in *Powder Technology Handbook* (Eds: K. Jinoya, K. Gotoh, K. Higashitani), M. Dekker, New York, **1991**, p. 481.
74. K. Miyanami in *Powder Technology Handbook* (Eds: K. Jinoya, K. Gotoh, K. Higashitani), M. Dekker, New York, **1991**, p. 595.
75. G. Heinicke, *Tribochemistry*, Akademie-Verlag, Berlin, **1984**.
76. S. A. Angelov, R. P. Bonchev, *Appl. Catal.* **1986**, 24, 219.
77. G. Mestl, B. Herzog, R. Schlögl, H. Knözinger, *Langmuir* **1995**, 11, 3027.
78. G. Mestl, N. F. D. Verbruggen, H. Knözinger, *Langmuir* **1995**, 11, 3055.
79. G. Mestl, T. K. K. Srinivasan, H. Knözinger, *Langmuir* **1995**, 11, 3795.
80. G. Mestl, N. F. D. Verbruggen, F. C. Lange, B. Tesche, H. Knözinger, *Langmuir* **1996**, 12, 1817.
81. S. R. Stampfl, Y. Chen, J. A. Dumesic, C. Niu, C. G. Hill, Jr., *J. Catal.* **1987**, 105, 445.
82. J. M. M. Llorente, V. Rives, *Solid State Ionics* **1990**, 38, 119.
83. T. F. Hayden, J. A. Dumesic, R. D. Sherwood, R. T. K. Baker, *J. Catal.* **1987**, 105, 299.
84. J. Leyrer, D. Mey, H. Knözinger, *J. Catal.* **1990**, 124, 349.
85. Y. Xie, L. Gui, Y. Liu, B. Zhao, N. Yang, Y. Zhang, Q. Guo, L. Duan, H. Huang, X. Cai, Y. Tang in *Proceedings of the 8th International Congress on Catalysis*, Berlin 1984, Dechema, Frankfurt, **1984**, Vol. V, p. 147.
86. Y. Xie, L. Gui, Y. Liu, Y. Zhang, B. Zhao, N. Yang, Q. Guo, L. Duan, H. Huang, X. Cai, Y. Tang in *Adsorption and Catalysis on Oxide Surfaces* (Eds: M. Che, G. C. Bond), Elsevier, Amsterdam, **1985**, p. 139.
87. B. M. Reddy, K. Narsimha, P. Kanta Rao, *Langmuir* **1991**, 7, 1551.
88. R. Margraf, J. Leyrer, E. Taglauer, H. Knözinger, *Surf. Sci.* **1987**, 189/190, 842.
89. R. Margraf, J. Leyrer, E. Taglauer, H. Knözinger, *React. Kinet. Catal. Lett.* **1987**, 35, 261.
90. J. Leyrer, M. I. Zaki, H. Knözinger, *J. Phys. Chem.* **1986**, 90, 4775.
91. G. Kisfaludi, J. Leyrer, H. Knözinger, R. Prins, *J. Catal.* **1990**, 124, 349.
92. L. M. J. von Hippel, F. Hilbrig, H. Schmelz, B. Lengeler, H. Knözinger, *Collect. Czech. Chem. Commun.* **1992**, 57, 2456.
93. O. Glemser, H. G. Wendland, *Angew. Chem.* **1973**, 75, 949.
94. O. Glemser, A. Müller, *Z. Anorg. Allg. Chem.* **1963**, 325, 220.
95. N. L. Yannopoulos, *J. Phys. Chem.* **1968**, 72, 3293.
96. M. Gasior, J. Haber, T. Machej, *Appl. Catal.* **1987**, 33, 1.
97. T. Machej, J. Haber, A. M. Turek, I. E. Wachs, *Appl. Catal.* **1991**, 70, 115.
98. G. Centi, E. Giamello, D. Pinelli, F. Trifiro, *J. Catal.* **1991**, 130, 220.
99. G. Centi, D. Pinelli, F. Trifiro, D. Ghoussoub, M. Guelton, L. Gengembre, *J. Catal.* **1991**, 130, 238.
100. F. Hilbrig, H. E. Göbel, H. Knözinger, H. Schmelz, B. Lengeler, *J. Phys. Chem.* **1991**, 95, 6973.
101. R. Haase, J.-G. Jerschewitz, G. Öhlmann, J. Richter-Mendau, J. Scheve in *Book of Abstracts, 2nd International Symposium on Scientific Bases for the Preparation of Heterogeneous Catalysts*, Louvain-la-Neuve, Belgium, **1978**, paper F5.
102. P. Mériaudeau, C. Naccache, *Appl. Catal.* **1991**, 73, L13.
103. J. L. G. Fierro, J. C. Conesa, A. Lopez Agudo, *J. Catal.* **1987**, 108, 334.
104. J. Leyrer, H. Knözinger, unpublished results.
105. J. A. Rabo, P. H. Kasai, *Progr. Solid State Chem.* **1975**, 9, 1.
106. J. A. Rabo in *Zeolite Chemistry and Catalysis* (Ed: J. A. Rabo), American Chemical Society, Washington, **1976**, p. 332.
107. H. K. Beyer, H. G. Karge, G. Borbély, *Zeolites* **1988**, 8, 79.
108. H. G. Karge, H. K. Beyer, G. Borbély, *Catal. Today* **1988**, 3, 41.
109. H. G. Karge, V. Mavrodinova, Z. Zheng, H. K. Beyer, in *Guidelines for Mastering the Properties of Molecular Sieves* (Eds: D. Barthomeuf, E. G. Derouane, W. Hölderich), Plenum Press, New York, **1990**, p. 157.

110. H. G. Karge, H. K. Beyer, in *Zeolite Chemistry and Catalysis* (Eds: P. A. Jacobs, N. I. Jaeger, L. Kubelková, B. Wichterlová), Elsevier, Amsterdam, **1991**, p. 43.
111. H. G. Karge, B. Wichterlová, H. K. Beyer, *J. Chem. Soc., Faraday Trans.* **1992**, 88, 1345.
112. J. Weitkamp, S. Ernst, M. Hunger, T. Röser, S. Huber, U. A. Schubert, P. Thomasson, H. Knözinger in *Proceedings of the 11. International Congress on Catalysis* (Eds: J. W. Hightower, W. N. Delgass, E. Iglesia and A. T. Bell) Baltimore 1996, Elsevier, Amsterdam, **1996**, p. 731.
113. R. Anderson, *Structure of Metallic Catalysts*, Academic Press, New York, **1975**.

## 4.9 Redox Methods for Preparation of Bimetallic Catalysts

J. BARBIER

### 4.9.1 Introduction

The main problem when preparing bimetallic catalysts is to create close interaction between the two metals [1–5].

The classic co-impregnation or successive impregnation of two metallic salts often proves to be unsatisfactory and new techniques are being tried [6–10]. In all cases these techniques call for the preparation of a monometallic catalyst (i.e. parent catalyst) which is then modified by addition of the second metal. This modification occurs through a selective reaction which takes place solely on the monometallic particles of the parent catalyst.

Metal–metal interactions can result from surface redox reactions occurring in a liquid phase between a reducing agent present or adsorbed on the parent metal and the oxidized form of the second metal [2–10]. The nature of the reductant depends on the various method used:

- (i) preparation of bimetallic catalysts by direct redox reaction – the reductant of the modifier is the parent metal;
- (ii) preparation of bimetallic catalysts by redox reaction of adsorbed reductant – the reductant is preadsorbed on the metallic surface of the parent catalyst (hydrogen is most commonly used);
- (iii) preparation of bimetallic catalysts by catalytic reduction – the catalytic properties of the parent metal are used to improve the rate of the reaction between a reductant and the modifier;
- (iv) preparation of bimetallic catalysts by under-potential deposition – in some cases deposition of adatoms or submonolayers of modifier can occur at a higher potential than the thermodynamic potential required for bulk deposition.



110. H. G. Karge, H. K. Beyer, in *Zeolite Chemistry and Catalysis* (Eds: P. A. Jacobs, N. I. Jaeger, L. Kubelková, B. Wichterlová), Elsevier, Amsterdam, **1991**, p. 43.
111. H. G. Karge, B. Wichterlová, H. K. Beyer, *J. Chem. Soc., Faraday Trans.* **1992**, 88, 1345.
112. J. Weitkamp, S. Ernst, M. Hunger, T. Röser, S. Huber, U. A. Schubert, P. Thomasson, H. Knözinger in *Proceedings of the 11. International Congress on Catalysis* (Eds: J. W. Hightower, W. N. Delgass, E. Iglesia and A. T. Bell) Baltimore 1996, Elsevier, Amsterdam, **1996**, p. 731.
113. R. Anderson, *Structure of Metallic Catalysts*, Academic Press, New York, **1975**.

## 4.9 Redox Methods for Preparation of Bimetallic Catalysts

J. BARBIER

### 4.9.1 Introduction

The main problem when preparing bimetallic catalysts is to create close interaction between the two metals [1–5].

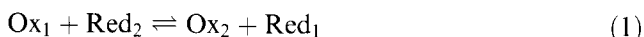
The classic co-impregnation or successive impregnation of two metallic salts often proves to be unsatisfactory and new techniques are being tried [6–10]. In all cases these techniques call for the preparation of a monometallic catalyst (i.e. parent catalyst) which is then modified by addition of the second metal. This modification occurs through a selective reaction which takes place solely on the monometallic particles of the parent catalyst.

Metal–metal interactions can result from surface redox reactions occurring in a liquid phase between a reducing agent present or adsorbed on the parent metal and the oxidized form of the second metal [2–10]. The nature of the reductant depends on the various method used:

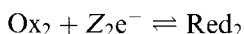
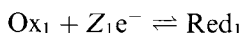
- (i) preparation of bimetallic catalysts by direct redox reaction – the reductant of the modifier is the parent metal;
- (ii) preparation of bimetallic catalysts by redox reaction of adsorbed reductant – the reductant is preadsorbed on the metallic surface of the parent catalyst (hydrogen is most commonly used);
- (iii) preparation of bimetallic catalysts by catalytic reduction – the catalytic properties of the parent metal are used to improve the rate of the reaction between a reductant and the modifier;
- (iv) preparation of bimetallic catalysts by under-potential deposition – in some cases deposition of adatoms or submonolayers of modifier can occur at a higher potential than the thermodynamic potential required for bulk deposition.

### 4.9.2 Preparation of Bimetallic Catalysts by Direct Redox Reaction

A typical redox reaction can be expressed as



The evolution of the overall reaction is defined by comparing the equilibrium potentials of the two half reactions:



These potentials can be calculated from Nernst's law:

$$E_1 = E_1^0 + \frac{RT}{Z_1 F} \ln \frac{a_{\text{Ox}_1}}{a_{\text{Red}_1}} \quad (2)$$

$$E_2 = E_2^0 + \frac{RT}{Z_2 F} \ln \frac{a_{\text{Ox}_2}}{a_{\text{Red}_2}} \quad (2')$$

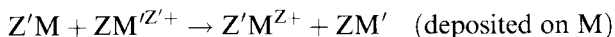
where  $a_{\text{Ox}}$  and  $a_{\text{Red}}$  are the activities of the oxidized and reduced species, respectively, and the other symbols have their usual meanings.

The difference in equilibrium potentials determines the value of the change in the free energy and, therefore, the direction of the overall reaction:

$$\Delta G = -Z_1 Z_2 F (E_1 - E_2) \quad (3)$$

shown here for eq 1 going from left to right. For  $E_1 > E_2$ ,  $\Delta G$  will be negative and the oxidized form  $\text{Ox}_1$  will be reduced by the reductant  $\text{Red}_2$ .

Direct redox reactions can be of great interest for the preparation of bimetallic catalysts, in cases where a parent monometallic catalyst is prepared and is modified by reaction with the oxidized form of a second metal. A typical reaction can be expressed as



where M is the parent metal and M' the modifier.

In practice the preparation of bimetallic catalysts using direct redox reactions can be extensively used for depositing a noble metal with a high standard electrochemical potential onto a non-noble metal with a lower standard electrochemical potential (eq 3).

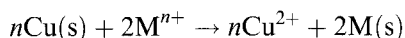
From an experimental point of view a monometallic catalyst is reduced in a reactor, outgassed under a nitrogen flow and then immersed in an aqueous solution. The solution is continuously stirred by a counter-current of nitrogen. The modifier salt, which acts as precursor of the additive, is introduced as a solution. The concentration of the solution is adjusted to equal the number of modifier atoms required for the required composition of the bimetallic phase.

An example of the use of direct redox reactions in the preparation of bimetallic catalysts is the modification of copper catalysts by the addition of ruthenium, plat-

**Table 1.** Standard redox potentials.

Reaction	$E^0$ (V)
$\text{Cu}^{2+} + 2\text{e}^- \rightleftharpoons \text{Cu}$	0.34
$\text{PtCl}_6^{2-} + 4\text{e}^- \rightleftharpoons \text{Pt} + 6\text{Cl}^-$	0.74
$\text{AuCl}_4^- + 3\text{e}^- \rightleftharpoons \text{Au} + 4\text{Cl}^-$	1.00
$\text{Pd}^{2+} + 2\text{e}^- \rightleftharpoons \text{Pd}$	0.99
$\text{Ru}^{3+} + 3\text{e}^- \rightleftharpoons \text{Ru}$	0.38
$\text{ReO}_4^- + 8\text{H}^+ + 7\text{e}^- \rightleftharpoons \text{Re} + 4\text{H}_2\text{O}$	0.37
$\text{PdCl}_4^{2-} + 2\text{e}^- \rightleftharpoons \text{Pd} + 4\text{Cl}^-$	0.62

inum, gold, or palladium [11–14]. Assuming the metallic state for copper atoms on the surface, the redox reaction with the noble metal salts is



where (s) indicates surface location. Comparison of the standard electrochemical potentials (Table 1) shows that three redox reactions can occur.

Chemical analysis of solids and solutions indicate that in all cases metallic ruthenium, platinum, and gold are deposited on copper. Ruthenium, deposit is restricted to approximately 0.33 of the copper surface atoms, demonstrating that the redox reaction between Cu and  $\text{Ru}^{3+}$  can occur only on some special copper sites [11]. With platinum or gold, for the highest amount of modifier introduced ( $\text{M}^{n+}/\text{Cu(s)} > 100$ ), a deposit larger than a monolayer is obtained, indicating that all accessible copper atoms and subsurface copper atoms are involved in the redox reaction [13].

Particles of Raney copper, modified by redox deposition of ruthenium, platinum, or gold were characterized by energy dispersive spectroscopy. Ruthenium is deposited preferentially on the rims of the copper particles while low Miller-index planes are totally free of deposited ruthenium atoms. For platinum or gold the deposition can occur over the whole copper surface [11].

The extent of deposition of a metal M introduced as  $\text{M}^{n+}$  on a Cu catalyst (or on a metal of lower standard potential) depends on the redox reaction equilibrium constant:

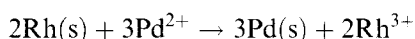
$$2nF \frac{(E_{\text{Cu/Cu}^{2+}}^0 - E_{\text{M/M}^{n+}}^0)}{RT} = \ln \frac{(a_{\text{M}^{n+}})^2 (a_{\text{Cu}})^n}{(a_{\text{M}})^2 (a_{\text{Cu}^{2+}})^n} \quad (4)$$

According to the standard electrochemical potentials (Table 1), with  $\text{Cu/Cu}^{2+}$  and  $\text{Ru/Ru}^{3+}$  couples, the amount of ruthenium deposited on metallic copper will be small, whereas the redox reaction carried out in presence of platinum or gold salts will occur to a large extent. On the other hand, for electrodes of first type (metal immersed in a solution of a salt of that metal), the standard electrochemical potentials as defined by thermodynamics are calculated with regard to a polycrystalline metallic phase of infinite size. However, in the case of small metallic particles,

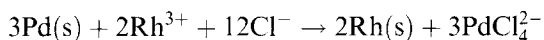
characterized by metallic atoms of different coordination numbers, the notion of a local potential can be introduced. That notion is well known for corrosion reactions which occur preferentially on more oxidizable metal sites, such as faults, and generally on metallic atoms of low coordination numbers.

As a consequence when the difference between equilibrium potentials of the two half redox reactions is low, the modifying metal, during the preparation of a bimetallic catalyst by direct redox reaction, will be deposited selectively on specific sites of the parent metal (i.e. sites that are highly oxidizable such as corners, edges, etc.). However, the equilibrium potentials are defined by Nernst's law which provides facilities to fit the potential values by changing the concentrations of the oxidized and reduced forms (eqs 2 and 2') and so induces selective deposition of the modifier on the parent catalyst.

Finally, the redox properties can be modified by using different ligands which, by chelating metallic ions, alter the standard redox potentials and consequently the equilibrium potentials. As an example, a rhodium catalyst was modified by the surface deposition of palladium obtained when metallic rhodium ( $E_{\text{Rh/Rh}^{3+}}^0 = 0.79 \text{ V}$ ) was exposed to palladium nitrate solution ( $E_{\text{Pd/Pd}^{2+}}^0 = 0.99 \text{ V}$ ); the reaction is given by



However, in the presence of chloride ions which induce a complexation of the palladium ions ( $E_{\text{Pd/PdCl}_4^{2-}}^0 = 0.62 \text{ V}$ ), the overall reaction is reversed and rhodium can be deposited on the surface of a metallic palladium catalyst according to the reaction



Identical results have been obtained with platinum and rhodium couples for preparation of model exhaust gas catalysts.

In summary, the direct redox reactions can be largely used in the preparation of bimetallic catalysts with a close interaction between the metallic constituents. In that case a metal with a high electrochemical potential is deposited on a metal with a lower potential. The applicability of the technique can be extended significantly by using different ligands which, by chelating metallic ions, modify the standard electrochemical potentials.

Finally, under well-defined experimental conditions (essentially the concentrations), the modifying metal can be deposited selectively on specific sites of the parent metal. Such deposition can significantly influence the selectivity of the bimetallic catalysts [12, 14].

### 4.9.3 Preparation of Bimetallic Catalysts by Redox Reaction of Adsorbed Reductant

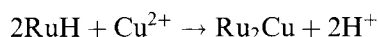
Bimetallic catalysts can be prepared by using a reductant that preadsorbs selectively on the parent metal. The ions of the second metal (additive) are reduced by that

reagent and the two metals interact. This technique was extensively studied by Szabo and co-workers who, using hydrogen as reductant, describe the technique as the "adsorption of metallic ions via ionization of adsorbed hydrogen" [15–19].

A simple example of using preadsorbed hydrogen as reductant was the preparation of a homodispersed Pt/Al<sub>2</sub>O<sub>3</sub> catalyst with increasing particle sizes prepared by platinum returning to the parent Pt/Al<sub>2</sub>O<sub>3</sub> catalyst saturated with irreversibly chemisorbed hydrogen [20].

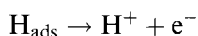
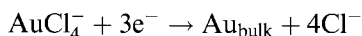
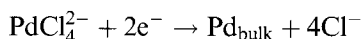
Hydrogen, preadsorbed on noble metals, is commonly used to prepare bimetallic catalysts by redox reaction. This requires the parent metal to chemisorb hydrogen (Pt, Pd, Rh, Ru, etc.) and to introduce a modifier that is reducible by hydrogen (Cu, Re, Ir, Rh, Pd, Pt, Au, etc.). All combinations of these metals have been prepared and characterized. For example, this technique has been used to prepare model Pt–Re reforming catalysts. Also, Pt–Rh and Pd–Rh were prepared to examine the interaction between platinum and rhodium in exhaust gas catalysts [8–10, 15–20, 21].

An interesting example is the preparation of Ru–Cu bimetallic catalysts by the reaction

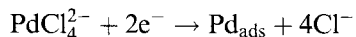
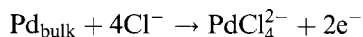


Previously, Cu–Ru was prepared by direct redox reaction, with Ru deposited on Cu. In this case, however, Cu is deposited on Ru. Comparison between the two bimetallic catalysts showed, during D-glucitol transformation that the two bimetallic phases, with same surface compositions, but prepared by two different techniques, had very different catalytic properties [22].

Szabo, Nagy, Margitfalvi, and co-workers [9, 23, 24] investigated the preparation of platinum–gold and platinum–palladium bimetallic catalysts using the ionization of hydrogen preadsorbed on platinum. The first step is the bulk deposition of additive according to the equations



In the presence of chloride ions, the first step is followed by the following spontaneous redistribution of the additive as adsorbed adatoms:



These reactions can also be written for AuCl<sub>4</sub><sup>–</sup>, which suggests that the chloride ions play an important role. Thus, the chelating power of the chloride ions in the transition metal complexes is critical in deposition and redistribution on the parent catalyst surface of the metal additive. If there are few or no chloride ions (that is, in the absence of chloride ions other than those of the precursor or if a chloride-free precursor such as Pd(NO<sub>3</sub>)<sub>2</sub> is used) the bulk deposition–reoxidation reaction is negligible and the deposition of the additive is stable.

Furthermore preparation of Pt–Au bimetallic catalysts using hydrogen pre-

adsorbed on platinum is a complex reaction involving simultaneously reduction of  $\text{AuCl}_4^-$  by hydrogen but also direct oxidation of metallic platinum atoms by  $\text{AuCl}_4^-$  (Table 1) [25].

A kinetic study of reduction of  $\text{AuCl}_4^-$  by hydrogen adsorbed on platinum or by direct oxidation of bare reduced platinum demonstrated that the rate of reduction by hydrogen is 100 times higher than that of the direct redox reaction. Therefore, during preparation of Pt–Au bimetallic catalysts, for low gold coverages (when the quantity of adsorbed hydrogen is sufficient to reduce all the introduced gold ions), gold is reduced by preadsorbed hydrogen; however, for higher gold concentrations, reduction by preadsorbed hydrogen and by direct oxidation of platinum can occur simultaneously.

Different Pt–Au catalysts loaded by different amounts of gold were characterized by energy dispersive spectroscopy which allows the local elemental analysis of the two components [25]. It appeared that, at low gold coverage, the deposition of the additive occurs statistically on the whole surface of platinum. In that case gold is reduced by hydrogen atoms which are adsorbed on all accessible platinum atoms. For higher gold contents the deposition occurs by direct redox reaction and preferentially on high Miller-index planes of platinum particles.

At present considerable research is being carried out to investigate reductants other than hydrogen; the emphasis here is on possible structural sensitivity. For example, hydrazine and aldehydes (such as glucose) at low coverages are selectively adsorbed by particular sites of the basic metal, and can then be used to induce the deposition of additives on those sites [8].

In summary, the preparation of bimetallic catalysts by surface redox reaction using a reductant preadsorbed on the parent monometallic catalyst has been studied in detail. Unfortunately, the method is intricate and time consuming, especially if several successive operations are required. Furthermore, when the modifier has a standard electrochemical potential higher than that of the parent metal ( $\text{AuCl}_4^-$  deposited on  $\text{Pt}^0$ ), the overall reaction is a complex one involving a reduction by adsorbed reductant but also direct oxidation of the metallic parent catalyst. The relative rate of the two parallel reactions determines the catalytic properties of the resulting bimetallic catalyst.

#### 4.9.4 Preparation of Bimetallic Catalysts by Catalytic Reduction

The aim of this technique is to use the catalytic properties of the parent catalyst to increase the rate of reduction of the modifier. Thus the additive is deposited on the catalytic site that is active for the reduction reaction, and the two metals are closely situated.

The catalytic reduction of copper by hydrogen has been investigated on platinum, rhodium, ruthenium, and palladium. Thermodynamics show that  $\text{Cu}^{2+}$  in aqueous solution can be reduced by molecular hydrogen at room temperature. However, a copper solution under a hydrogen flow is perfectly stable because of the slow kinetics of the reaction. Metals such as platinum, palladium, and rhodium, which are able to activate hydrogen, can catalyze the reduction of copper.

The catalytic reduction of  $\text{Cu}^{2+}$  by hydrogen is faster on small platinum particles since the turn over number increases from 0.37  $\text{Cu}^{2+}$  ions reduced per accessible platinum atom per hour to 3.0 when the platinum dispersion increases from 11% to 54% [8]. Thus the catalytic hydrogenation of  $\text{Cu}^{2+}$  ions is a structure-sensitive reaction occurring preferentially on small platinum particles.

Analogous experiments have been performed with rhodium/alumina catalysts [26, 27]. Catalysts (monometallic  $\text{Rh}/\text{Al}_2\text{O}_3$  and modified  $\text{Rh-Cu}/\text{Al}_2\text{O}_3$ ) were characterized by IR spectroscopy using carbon monoxide as a probe molecule. The evolution of the relative intensity gem/linear bonds can be explained by assuming that copper is preferentially deposited on rhodium atoms of low coordination numbers. These results are in agreement with the kinetic study and confirm the view that copper, catalytically reduced by hydrogen, deposits preferentially on high Miller-index planes of the rhodium particles. Similar selective deposition of copper on parent metal particles was achieved by catalytic reduction of  $\text{Cu}^{2+}$  by hydrogen on a  $\text{Pd}/\text{SiO}_2$  catalyst. Such selective deposition of an inactive compound (Cu) on specific active sites of the parent metal (Pt, Rh, Pd, etc.) produces significant modifications of catalytic properties, particularly with regard to selectivity [27, 28].

The technique of catalytic reduction can be extended to reducing agents other than hydrogen. The redox potentials of many organic compounds are well known and the most used system in electrochemistry is the quinone–hydroquinone system. According to Bodnar et al. [29], an organic oxidant–reductant system would irreversibly poison a metallic surface, causing loss of catalytic activity. However, hydrazine and hydroxylamine (in a slightly basic medium) or ascorbic acid were used at a working equilibrium potential less cathodic than hydrogen. Under these conditions, bulk deposition of the additive is limited, thus promoting the generation of submonolayers by underpotential deposition (see next section) [8].

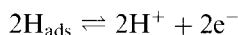
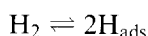
A practical example of using a reductant other than hydrogen is the preparation of  $\text{Rh-Cu}/\text{Al}_2\text{O}_3$  bimetallic catalysts from catalytic reduction of copper by glucose on rhodium. A comparison of the catalytic properties of the two solids (reduction of copper by hydrogen and reduction of copper by glucose), in the conversion of methylcyclopentane shows that the two catalysts perform very differently with regard to hydrogenolysis, yielding low hydrocarbons. These results were explained by assuming that the glucose molecule, to be adsorbed, needs a large ensemble of rhodium atoms and induces deposition of copper on large planes, whereas reduction by hydrogen occurs selectively at the edges and corners of rhodium particles. In conclusion, the catalytic reduction of copper on rhodium is a structure-sensitive reaction which allows deposition of copper onto particular sites, but the structural sensitivity depends on the nature of the reductant [30].

The preparation of bimetallic catalysts by catalytic reduction ensures that the additive is deposited on the metallic site that is active for the reduction reaction. If the additive itself is not catalytically active, only one atom of additive metal would be deposited per active site. In fact, in the case of copper deposition on platinum, using hydrogen as the reducing agent, almost 200 atoms of copper can be deposited per accessible platinum atom. This property was used in the so-called electroless process which allows, for example, the preparation of supported copper catalysts.

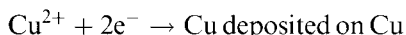
In this case the support is preactivated by impregnation of very low palladium loadings (almost 0.01%). Then the catalytic reduction of copper by hydrogen or formaldehyde, using the catalytic properties of the palladium atoms, yields almost 5% loaded copper catalysts [31].

In bimetallic catalysts prepared by catalytic reduction of copper by hydrogen, copper is deposited as three-dimensional agglomerates which are located, at low copper loadings, on the edges, corners, and rims of the parent metallic particles. The mechanism of deposition can be transferred from that proposed in corrosion and involving a local electrochemical cell:

- (i) the activation of hydrogen can occur on the free platinum surface area:



- (ii) then the reduction reaction, allowed by a transfer of electrons through the metallic phase, can occur on the copper surface:



Finally, at high copper loading (almost 200 copper atoms for one accessible platinum atom), the platinum surface is totally covered and the deposition reaction is terminated.

The additive loading at saturation of the parent catalyst is dependent on the experimental conditions. So, different Pt-Re/Al<sub>2</sub>O<sub>3</sub> bimetallic catalysts were prepared by catalytic reduction of ReO<sub>4</sub><sup>-</sup> by hydrogen.

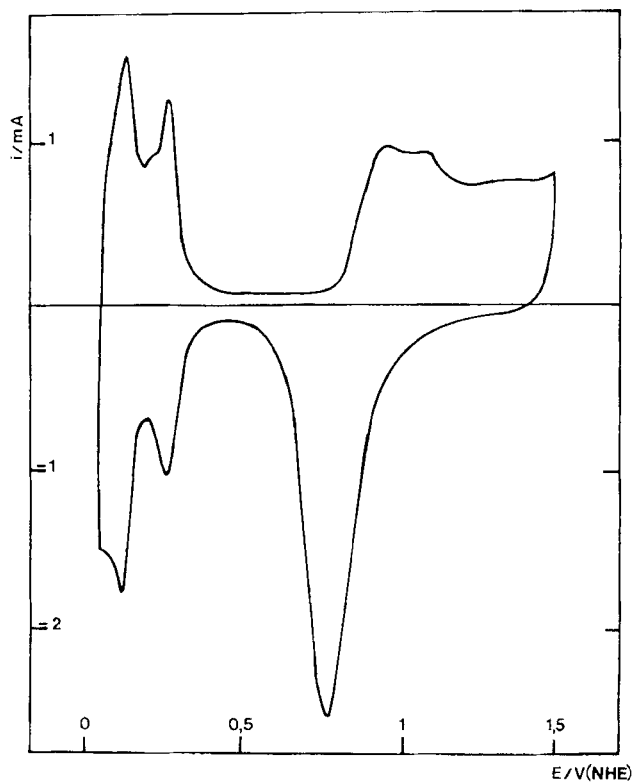
On such bimetallic catalysts the rhenium loading at saturation of a 0.6% Pt/Al<sub>2</sub>O<sub>3</sub> catalyst depends on the hydrogen pressure. From a thermodynamic point of view the quantity of additive deposited at saturation is defined by the equilibrium conditions of the system under consideration. By taking into account the reduction of ReO<sub>4</sub><sup>-</sup> to Re<sup>0</sup> at 303 K (Table 1),

$$0.37 + \frac{0.06}{7} \log \frac{(\text{ReO}_4^-)(\text{H}^+)^8}{\Theta_{\text{Re}}(\text{H}_2\text{O})^4} = \frac{0.06}{2} \log \frac{(\text{H}^+)^2}{p\text{H}_2}$$

where  $\Theta_{\text{Re}}$  is the coverage of platinum by rhenium. This relationship allows the calculation of  $\Theta_{\text{Re}}$  (over Pt) for different concentrations of ReO<sub>4</sub><sup>-</sup>, different pH values, and different hydrogen pressures.

As an example, Fig. 1 introduces the stationary intensity-potential curves of the two redox systems ( $\text{H}_2 \rightleftharpoons 2\text{H}^+$  and  $\text{ReO}_4^- \rightleftharpoons \text{Re}^0$ ) and illustrates the effect of the experimental conditions on the nature of the deposit. It can be seen that at high hydrogen pressure the working point of the system  $E$ , (the potential at which reduction of Re<sup>7+</sup> and oxidation of H<sub>2</sub> occur at the same rate (same intensity)) is close to the reversible potential of hydrogen (almost 300 mV more cathodic than the bulk deposition of Re). At low hydrogen pressure (with lower limiting diffusion intensity) the working potential  $E_2$  is close to the reversible potential of reduction of ReO<sub>4</sub><sup>-</sup>. In electrodeposition it is known that the lower the potential of reduction (more





**Figure 1.** Stationary intensity potential curves: electroreduction of  $\text{ReO}_4^-$ ; electrooxidation of  $\text{H}_2$  (at two values of  $P_{\text{H}_2}$ ).

cathodic) the higher the roughness of the deposit and the higher the extent of a three-dimensional electro-deposit.

In summary, the technique of catalytic reduction for the preparation of bimetallic catalysts can be extensively used with a variety of parent metals and reductants. However, some structure sensitivities of the reduction reactions become apparent and the modifying metal can be selectively deposited on specific sites of the parent-supported metal. Furthermore, such structure sensitivity depends on the nature of the reductant, and a given modifier can be deposited, according to the reductant used, selectively onto different parts of the metallic surface. In fact, a bimetallic catalyst can be tailored to provide the optimum activity, selectivity and lifetime for a given reaction.

#### 4.9.5 Preparation of Bimetallic Catalysts by Underpotential Deposition

For the three techniques previously described, the deposition of the modifier occurs at electrochemical potentials (working potential of the system) which are lower than the equilibrium potential of the modifier (Fig. 1). Under such conditions the depo-

sition of the modifier takes place as a three-dimensional deposit. By contrast, the underpotential deposition (UPD) characteristically forms submonolayer adatom structures [32, 33].

For the electroreduction of  $M'$  the equilibrium potential is

$$M'^{Z'+} + Z'e^- \rightleftharpoons M'$$

$$E_{M'/M'^{Z'+}} = E_{M'/M'^{Z'+}}^0 + RT/Z'F \ln(a_{M'^{Z'+}}/a_{M'})$$

For bulk deposition the activity of the deposited metal,  $a_{M'}$ , is assumed to be constant and equal to one. When the metal  $M'$  is reduced and deposited on a basic metal  $M$  (different to  $M'$ ), the activity of the deposit in the submonolayer is less than one until the coverage of  $M$  by  $M'$  is complete. The following linear relationship is assumed between the activity  $a_{M'}$  of the deposit and the coverage  $\Theta$  of  $M$  by  $M'$  [34–37]:

$$a_{M'} = \gamma_{M'}\Theta \quad (0 \leq \Theta \leq 1)$$

where  $\gamma_{M'}$  is the activity coefficient of  $M'$ . For  $\Theta = 1$ ,

$$a_{M'} = \gamma_{M'} = 1$$

For the deposition of a submonolayer the equilibrium potential is given by

$$E_{M'/M'^{Z'+}}(\Theta) = E_{M'/M'^{Z'+}}^0 + \frac{RT}{Z'F} \ln \frac{a_{M'^{Z'+}}}{\Theta}$$

For  $\Theta < 1$  the equilibrium potential of the submonolayer  $E_{M'/M'^{Z'+}}(\Theta)$  is always more positive than Nernst's potential of bulk deposition  $E_{M'/M'^{Z'+}}$ . As a result, an underpotential deposition of  $M'$  over  $M$  may occur.

The electrochemical potential difference between  $E(\Theta)$  and  $E$  corresponds to a free energy difference:

$$\Delta G = -Z'e_0(E(\Theta) - E) = (\mu_{M'}^\Theta - \mu_{M'}) = Z'e_0\Delta E_p$$

where the chemical potentials of  $M'$  deposited in the submonolayer form and in the bulk are  $\mu_{M'}^\Theta$  and  $\mu_{M'}$ , respectively and where  $e_0$  is the elemental charge of the electron.

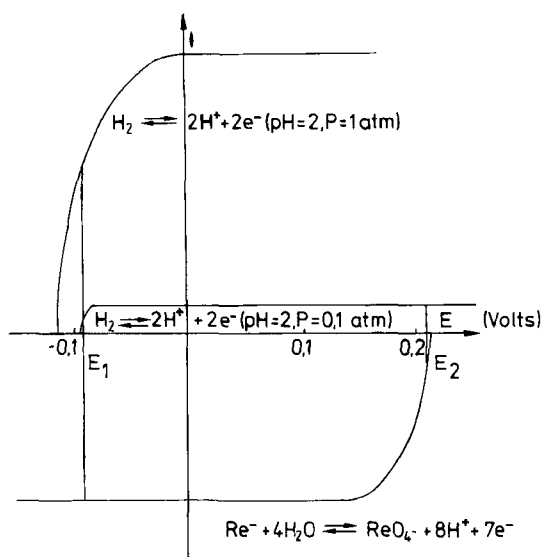
The difference between  $\mu_{M'}^\Theta$  and  $\mu_{M'}$ , is a direct measurement of the difference between the adatom binding energy of  $M'$  deposited on  $M$  and the binding energy of  $M'$  deposited on  $M'$ . Consequently, the potential at which UPD occurs for adatom  $M'$  varies depending on the substrate  $M$ . If  $\Delta E_p$  is known, the binding energy between the substrate  $M$  and the deposited atom  $M'$  can be determined [38–39] (this binding energy is in fact a free energy of chemisorption).

To describe these UPDs quantitatively, Kolb [32] proposed values of  $\Delta E_p$  for a series of substrate–adatom systems. Table 2 gives estimated values of underpotential shifts ( $\Delta E_p$ ) for various metal ions deposited on platinum. Based on these estimated values,  $\Delta E_p$  varies significantly, with the nature of the adatom.

Kolb, Gerischer and co-workers [34–39] showed that the excess energy ( $\Delta E_p$ ) due to UPD varies linearly with the difference between the work functions ( $\Delta\Phi$ ) of the substrate and of the adsorbate:

**Table 2.** Underpotential shifts ( $\Delta E_p$ ) of metal ions deposited on platinum.

Metal ion	Supporting electrolyte	$\Delta E_p$ (V)
Ag <sup>+</sup>	0.5 M H <sub>2</sub> SO <sub>4</sub>	0.44
Cu <sup>2+</sup>	0.5 M H <sub>2</sub> SO <sub>4</sub>	0.41
Sb <sup>3+</sup>	0.5 M H <sub>2</sub> SO <sub>4</sub>	0.64
Ge <sup>4+</sup>	0.5 M H <sub>2</sub> SO <sub>4</sub>	0.75
Pb <sup>2+</sup>	1.0 M HClO <sub>4</sub>	0.87
Bi <sup>3+</sup>	0.12 M HClO <sub>4</sub>	0.59
Cd <sup>2+</sup>	1.0 M HClO <sub>4</sub>	0.96

**Figure 2.** Typical voltammogram of polycrystalline Pt in H<sub>2</sub>SO<sub>4</sub> medium.

$$e_0 \Delta E_p = 0.5 \Delta \Phi$$

Note, however, that the work functions vary with the surface orientation. Thus, the structure of the crystalline metal (M) should lead to the preferential deposition of the additive M' on specific sites of M.

The simplest method to investigate UPD deposit is cyclic voltammetry. This technique, by a linear variation of potential, allows a direct observation of adsorption and desorption peaks of adatoms. As an example Fig. 2 shows a typical voltammogram obtained on polycrystalline platinum electrodes in acidic medium. The first area (between 0 to 0.4 V/RHE (Reference Hydrogen Electrode; the reversible potential of hydrogen at the given pH is taken as reference)) is related to hydrogen adsorption (at negative current, according to the electroreduction of protons:  $H^+ + e^- \rightarrow H_{ads}$ ) and with hydrogen desorption (at positive current, according to

the electrooxidation of adsorbed hydrogen:  $H_{\text{ads}} \rightarrow H^+ + e^-$ ). The potential at zero current is the equilibrium potential corresponding to the redox equilibrium  $H_2 \rightleftharpoons 2H^+ + 2e^-$  and is given by the Nernst's law. At lower potential than this, equilibrium potential evolution of molecular hydrogen takes place, but at higher potential the peaks of hydrogen adsorption can be offered as a first example of underpotential deposition. At least two forms of adsorbed hydrogen are reflected by the two different peaks. These two forms (strongly and weakly bonded) correspond to the chemisorption of hydrogen on different sites of platinum.

The influence of structure on UPD for different metals adsorbed polycrystalline electrodes has been extensively studied in electrochemistry. One general conclusion [35, 37, 40, 49] is that the formation of a submonolayer of adatoms by UPD differs substantially, depending on the substrate structure and the crystal orientation. Indeed, with a heterogeneous polycrystalline surface, the deposition potential can be controlled so that adatoms adsorb preferentially on specific sites of the polycrystal.

In heterogeneous catalysis, the first tests on UPD were performed on bulk catalysts which allows, for the preparation of the bimetallic catalyst, easy control of the electrochemical potential by an external device (potentiostat). In the same way all electrochemical techniques, particularly the control of catalyst potential required for submonolayer deposition, can be extrapolated to metallic catalysts supported on conductive materials such as carbon or carbides [8].

However, in heterogeneous catalysis, metals are usually deposited on nonconducting supports such as alumina or silica. For such conditions electrochemical techniques cannot be used and the potential of the metallic particles is controlled by means of a supplementary redox system [8, 33]. Each particle behaves like a microelectrode and assumes the reversible equilibrium potential of the supplementary redox system in use. For example, with a platinum catalyst deposited on silica in an aqueous solution and in the presence of hydrogen, each particle of platinum takes the reversible potential of the equilibrium  $2H^+ + 2e^- \rightleftharpoons H_2$ , given by Nernst's law as

$$E = \frac{RT}{2F} \ln \frac{(H^+)^2}{P_{H_2}}$$

This potential, adjusted as a function of the pH of the solution and of the hydrogen pressure, is easily fixed between +0.1 V and -0.9 V/NHE (Normal Hydrogen Electrode). The  $H_2/H^+$  couple was used to prepare supported catalysts with platinum, palladium, ruthenium, and rhodium modified with deposits of tin, lead, iron, germanium, and bismuth [50–54]. These catalysts were proposed for their good selectivities for different reactions in specialize organic chemistry.

In fact the UPD technique has been used empirically by specialists of organic chemistry who, in order to increase the selectivity of liquid-phase hydrogenation catalysts, recommended the addition of metallic cations to the hydrogenating reactors. For example, during the selective hydrogenation of ethylenic aldehydes, cations such as  $Co^{2+}$ ,  $Ru^{3+}$ ,  $Ag^+$ ,  $Zn^{2+}$ ,  $Fe^{3+}$ , or  $Fe^{2+}$  were often added to the solvents to promote the selectivity of platinum [55–56]. Under the hydrogenating conditions used, in the presence of hydrogen, and in a protonic solvent, UPD of the additive adatom explains the changes in the selectivity.

Redox systems other than the  $\text{H}_2/\text{H}^+$  couple can be used to monitor the potential of the parent metal particles. For example, the quinone–hydroquinone system can be used to keep the electrochemical potential between 0.5 and 0.0 V/NHE by varying the pH from 0 to 7 for solutions of equal concentrations of quinone and of hydroquinone [57]. UPD clearly opens up a vast field of research since few well-known organic redox systems have used it to date. Note, however, that such surface arrangements may be unstable due to the diffusion of adatoms on the surface or in the bulk of the metal. In some situations, such instability could exclude the use of the catalyst at high temperatures.

In conclusion, as deposition of adatoms can be controlled on well-defined fractions of the parent metal, the UPD technique, by a precise adjustment of the potential, allows a real tailoring of bimetallic catalysts.

#### 4.9.6 Concluding Remarks

Surface redox reactions represent a relatively new approach for preparing supported bimetallic catalysts. Three main techniques have already been identified:

- (i) direct redox reactions between the parent metal and the modifier;
- (ii) redox reactions between a reductant and the modifier – the reductant can be previously adsorbed on the parent metal or introduced as a reagent in the reactor (if no homogeneous reaction can occur between the modifier and the reductant);
- (iii) underpotential deposition.

All these variants are complementary to one another and, by using different experimental conditions, ligands, reductants, and modes of preparation, this approach can apparently be used to prepare any type of bimetallic couple. However, the catalytic properties of the final catalyst will depend strongly on the technique used. The selection of one variant over another depends on the desired structure of the bimetallic phase.

In conclusion, redox reactions allow the surface to be tailored during catalyst preparation, which explains the exceptional catalytic properties, particularly in terms of selectivity, of bimetallic catalysts prepared by these techniques.

#### References

1. V. Ponec, *Catal. Rev. Sci. Eng.* **1975**, *11*, 41.
2. J. H. Sinfelt, *Bimetallic catalysts: Discoveries, concepts and applications*, John Wiley and Sons, New York, **1983**.
3. J. H. Sinfelt US Patent 3 953 368 **1976** Exxon.
4. H. E. Kluksdahl US Patent 3 415 737 **1968** Chevron Corp.
5. J. E. Weisang, P. Engelhard US Patent 3 700 588 **1972** C.F.R.
6. R. Nuzzo, L. Dubois, N. Bowles, M. Tresoske, *J. Catal.* **1984**, *85*, 267.
7. J. P. Candy, O. A. Feretti, G. Mabilon, J. P. Bournonville, A. E. E. Mansour, J. M. Basset, G. Martino, *J. Catal.* **1988**, *112*, 210.

8. J. Barbier, Catalytica Studies Division, *Advances in Catalyst Preparation*, Study number 4191 CP (1992).
9. J. Margitfalvi, S. Szabo, F. Nagy, S. Gobolos, M. Hegedus in *Preparation of Catalysts III* (Eds: G. Poncelet, P. Grange, P. A. Jacos) Elsevier, Amsterdam, **1983**.
10. J. Margitfalvi, S. Szabo, F. Nagy in *Catalytic hydrogenation* (Ed.: L. Lerveny) Elsevier, Amsterdam, **1986**.
11. J. Barbier, J. C. Menez, C. Montassier, J. Naja, G. Del Angel, J. M. Dominguez, *Catal. Lett.* **1992**, 14, 37.
12. J. Barbier, J. P. Boitiaux, P. Chaumette, S. Leporq, J. C. Menez, C. Montassier, EU Patent 380 402 **1990** Institut Français du Pétrole.
13. C. Montassier, J. C. Menez, J. Naja, J. Barbier, J. M. Dominguez, P. Sarrazin, B. Didillon, *J. Mol. Catal.* **1994**, 91, 107.
14. C. Montassier, J. C. Menez, J. Naja, P. Granger, J. Barbier, P. Sarrazin, B. Didillon, *J. Mol. Catal.* **1994**, 91, 119.
15. S. Szabo, F. Nagy, *J. Electroanal. Chem.* **1976**, 70, 357.
16. S. Szabo, F. Nagy, *J. Electroanal. Chem.* **1977**, 84, 93.
17. S. Szabo, F. Nagy, *J. Electroanal. Chem.* **1978**, 87, 261.
18. S. Szabo, F. Nagy, *J. Electroanal. Chem.* **1984**, 160, 299.
19. S. Szabo, I. Bakos, *J. Electroanal. Chem.* **1987**, 230, 233.
20. J. C. Menez, M. F. Denanot, S. Peyrovi, J. Barbier, *Appl. Catal.* **1985**, 15, 353.
21. P. Marecot, J. Barbier, G. Mabilon, D. Durand, M. Prigent EU Patent 929 0516-2 (1992) Institut Français du Pétrole.
22. C. Montassier, J. C. Menez, L. C. Hoang, C. Renaud, J. Barbier, *J. Mol. Cat.* **1991**, 70, 99.
23. I. Bakos, S. Szabo, *J. Electroanal. Chem.* **1993**, 344, 303.
24. S. Szabo, G. Nagy, *J. Electroanal. Chem.* **1977**, 85, 339.
25. J. Barbier, P. Marecot, J. P. Boitiaux, B. Didillon, G. Del Angel, P. Bosch, M. Dominguez, I. Schifter, *Appl. Catal.* **1994**, 116 (1-2).
26. J. Barbier, J. M. Dumas, C. Geron, H. Hadrane, *Appl. Catal.* **1990**, 67, 1.
27. J. M. Dumas, C. Geron, H. Hadrane, P. Marecot, J. Barbier, *J. Mol. Catal.* **1992**, 77, 87.
28. C. Geron, T. Mbang, J. Barbier, V. Bertin, G. Del Angel, *XIV Simposio Iberoamericano de Catalisis* **1994**, 1, 7.
29. Z. Bodnar, T. Mallat, S. Szabo, J. Petro in *Preparation of Catalysts V* (Eds: G. Poncelet, P. Grange, P. A. Jacobs), Elsevier, Amsterdam, **1991**.
30. J. Barbier, *XIV Simposio Iberoamericano de Catalisis* **1994**, 1, VI-1.
31. H. F. Chang, M. A. Saleque, *Appl. Catal.* **1993**, 103 A, 233.
32. D. M. Kolb in *Advances in Electrochemistry and Electrochemical Engineering* (Eds: M. Gerischer, C. N. Tobias), John Wiley and Sons, New York, **1975**.
33. S. Szabo, *Int. Reviews Phys. Chem.* **1991**, 10-12, 207.
34. D. M. Kolb, M. Przasnyski, H. Gerischer, *J. Electroanal. Chem.* **1974**, 54, 25.
35. R. R. Adzic, E. Yeager, B. D. Cahan, *J. Electrochem. Soc.* **1974**, 121, 474.
36. R. R. Adzic, A. V. Tripkovic, R. Atanososki, *J. Electroanal. Chem.* **1978**, 94, 231.
37. R. R. Adzic, A. V. Tripkovic, N. M. Markovic, *J. Electroanal. Chem.* **1980**, 114, 37.
38. H. Gerischer, D. M. Kolb, J. K. Sass, *Adv. Phys.* **1978**, 27, 437.
39. H. Gerischer, D. M. Kolb, M. Przasnyski, *Surf. Sci.* **1974**, 43, 662.
40. A. Hamelin, *J. Electroanal. Chem.* **1979**, 101, 285.
41. A. Hamelin, A. Katayama, *J. Electroanal. Chem.* **1981**, 117, 221.
42. A. Hamelin, A. Katayama, G. Picq, P. Venneereau, *J. Electroanal. Chem.* **1980**, 113, 293.
43. A. M. Abd El Halim, K. Juttner, W. J. Lorenz, *J. Electroanal. Chem.* **1980**, 106, 193.
44. G. Kokkinidis, K. Juttner, *Electrochim. Acta* **1981**, 26, 971.
45. S. Calde, S. Brickenstein, *Anal. Chem.* **1971**, 43, 1858.
46. E. Lamy, J. Barbier, C. Lamy, *J. Chim. Phys.* **1980**, 77 (10), 967.
47. E. Lamy, J. Barbier, *Electrochim. Acta* **1982**, 276, 713.
48. R. Amadelli, J. A. Molla, E. Yeager, *J. Electroanal. Chem.* **1981**, 126, 265.
49. R. Amadelli, J. A. Molla, P. Bindra, E. Yeager, *J. Electroanal. Chem.* **1981**, 128, 2706.
50. J. C. Menez, L. C. Hoang, C. Montassier, J. Barbier, *React. Kinet. Catal. Lett.* **1992**, 46-1, 1.
51. E. Lamy-Pitara, L. El Ouazzani-Benhima, J. Barbier, *J. Electroanal. Chem.* **1992**, 335, 363.

- 52. E. Lamy-Pitara, L. El Ouazzani-Benhima, J. Barbier, *Appl. Catal.* **1992**, A-81, 47.
- 53. I. Bakos, S. Szabo, F. Nagy, T. Mallat, Z. S. Bodnar, *J. Electroanal. Chem.* **1991**, 309, 293.
- 54. S. Szabo, I. Bakos, F. Nagy, T. Mallat, *J. Electroanal. Chem.* **1989**, 263, 137.
- 55. W. F. Tuley, R. Adams, *J. Am. Chem. Soc.* **1925**, 45, 3061.
- 56. G. Cordier, Y. Colleuille, P. Fouilloux (Eds), *Catalyse par les métaux*, CNRS, Paris **1984**.
- 57. M. Kotter, L. Riekert in *Preparation of Catalysts II* (Eds: B. Delmon, P. Grange, P. Jacobs, G. Poncelet), Elsevier, Amsterdam, **1979**.

## 5 From the Precursor to the Final Catalyst

### 5.1 Formation of Final Catalyst

B. DELMON

#### 5.1.1 Introduction and Background

##### 5.1.1.1 Introduction

In most cases, the solids prepared according to the methods described in Section 4.1 are not catalytically active as such. The only exceptions are some grafted catalysts (4.1.2), most heterogenized complexes (4.1.4) and a large proportion of the catalysts prepared by redox methods (4.1.6). In the other cases, the substance deposited on the support must be transformed to a suitable compound (e.g. transformation of hydroxide or oxide to metal or to sulfide) in order to acquire the desired activity.

When a substance is supported on a carrier, its chemical reactivity is fundamentally altered. Comparing reactions of a nonsupported compound with those of the same compound dispersed on a carrier indicates that the kinetics in exactly the same conditions are always altered, and that they may even lead to different products, namely different catalytic materials.

Some of those changes are intuitively expected. This is the case when some chemical reaction has taken place between the active substance and the support. The reactivity then reflects that of the new compound. But other modifications are very often not properly recognized. One of the most common errors results from the ignorance that, beyond a certain threshold, the simple fact that a substance is more highly dispersed may not lead to increased, but rather diminished reactivity.

The present section will examine the phenomena taking place during the last stages of the formation of the active phase, namely calcination, reduction, or sulfidation. These last stages, especially reduction and sulfidation, are usually called activation [1]: activation is defined by IUPAC as the transformation of the precursor solid to the active phase. This is a crucial operation. For a large part it determines or influences all the practical properties of catalysts: activity, selectivity, and resistance to ageing. Only a small proportion of the practical catalysts is used unsupported. Although the activation of such catalysts is important, much more



space has to be allotted to supported precursors. The reason for this importance is the already mentioned fact that the particular behavior of supported phases with respect to chemical transformation is poorly understood in general. Principally, two factors must be taken into account. The first is the state of dispersion of the precursor. The second is the interaction of the precursor with the support. Two sections are devoted to these aspects in what follows.

### 5.1.1.2 Particulars of Chemical Reactions for Supported Substances

#### A General Kinetic Features of Solid-State Reactions

In the transformation of a dispersed supported precursor to its oxide (in calcination), and further to metal or sulfide, various types of reactions take place. It is necessary to recall briefly the different fundamental processes which are involved in such reactions.

In a general way, two main families of reactions involving solids must be distinguished:

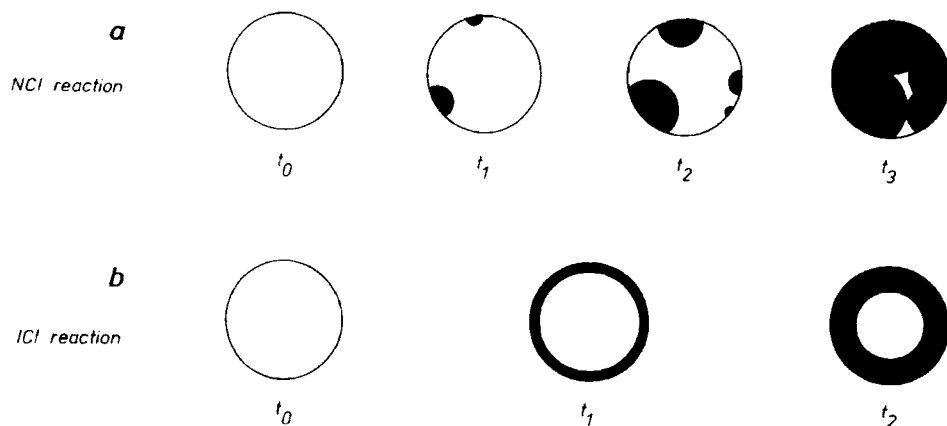
- (i) Reactions taking place as a result of diffusion of a chemical species through the bulk of one of the solids involved (reactant or product). These are *solid-state diffusion* or *ssDC reactions*. Typical examples of such reactions are those of transition metal oxides, such as NiO or Co<sub>3</sub>O<sub>4</sub>, with an alumina support, making a solid solution of the transition metal in  $\gamma$ -Al<sub>2</sub>O<sub>3</sub>, or even leading to the formation of a spinel, NiAl<sub>2</sub>O<sub>4</sub> or CoAl<sub>2</sub>O<sub>4</sub>.
- (ii) Reactions taking place at an interface and kinetically limited by processes occurring at this interface. These are *interface controlled* or *IC reactions*. This corresponds to the case of many dehydroxylations (transformation of hydroxides to oxides), reductions of oxides to metals (NiO to Ni) or reduction-sulfidation processes leading to sulfides (deposited "cobalt molybdate" bilayer, transforming to Co<sub>9</sub>S<sub>8</sub> + MoS<sub>2</sub>).

IC reactions can be of two types. The nucleation of the new phase (e.g. Ni produced by the reduction of NiO) may be rate determining. In that case, separate nuclei of the new phase can be detected (Fig. 1(a)). These are called nucleation-controlled interface or NCI reactions. In other cases, all the surface of the initial solid reacts, and a continuous interface entirely covers the solid reactant. With respect to kinetics, the interfacial process entirely controls the reaction in this last case. This is an ICI reaction (Fig. 1(b)).

For interface-controlled reactions, the rate of reaction at the interface,  $r_i$ , is proportional to the area of the interface  $S_i$ , with a proportionality factor  $k_i$  which is the rate or velocity of interface movement:

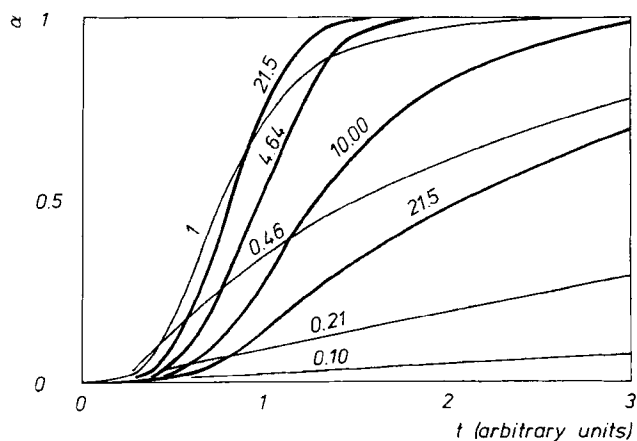
$$r_i = k_i S_i$$

The factor  $k_i$  depends on the experimental conditions. For ICI reactions in constant conditions,  $r_i$  keeps decreasing during the whole reaction. Figure 1(b) suggests that the area of the interface between product (black) and reactant (white) steadily de-



**Figure 1.** Nucleation-controlled interface reaction (NCI) and interface-controlled reaction (ICI) at various times  $t_0$ – $t_3$ .

**Figure 2.** Comparison of the course of reaction (degree of reaction vs. time) of samples composed of identical spherical particles of various diameter. Conventionally, dimension unit is 1 for the curve at the left (adapted from Fig. XI.23, Ref. [7]).



creases. This is not the case for NCI reactions, where  $r_i$  first increases and later decreases: this is suggested in Fig. 1(a) where the interface has considerably shrunk at time  $t_3$ . The overall phenomenon thus depends both on the rate of nucleation  $r_n$  (number of nuclei forming per unit surface area per unit time) and  $k_i$  [2, 3].

It is possible to calculate the variation of the overall rate  $r_i$  due to the convolution of the kinetics of nucleation and interface movement [4–7]. The corresponding variation of the degree of transformation of the solid,  $\alpha$ , can be calculated from  $k_i$  and  $S_i$ . This can be done for different shapes of particles [7], but it is sufficient here to outline the result of calculations made with the assumption of spherical particles of identical diameter. Starting from large particles, a diminution of their size will lead to higher rates of overall reaction. But, contrary to intuitive expectation, the rate will diminish when the particles become very small. This is shown in Fig. 2,

which is a plot of the degree of transformation against time (common scale for all curves) for samples composed of particles of diameter  $d$ ; in this figure, by convention,  $d = 1$  for the sample reacting with the highest rate at the lower  $\alpha$  values. The rate of reaction decreases dramatically by a factor of approximately 20 when the particles are one order of magnitude smaller in diameter. Particles with very different sizes, namely 0.46 and 21.5, surprisingly have comparable reactivities. It should be clear that the parameter governing those changes is the ratio of the rates of nucleation and interface movement; more details can be found in Ref. 7.

It should be noted that this phenomenon has to be taken into account in thermoprogrammed reactions (TPR, TPS, etc.) for correct interpretation. A shift of a reaction peak to higher temperature should not be automatically attributed to a change of chemical composition of the reactant or to the fact that it is less dispersed [8]. The contrary may be true.

### **B Interaction Between Supported Phases and Supports**

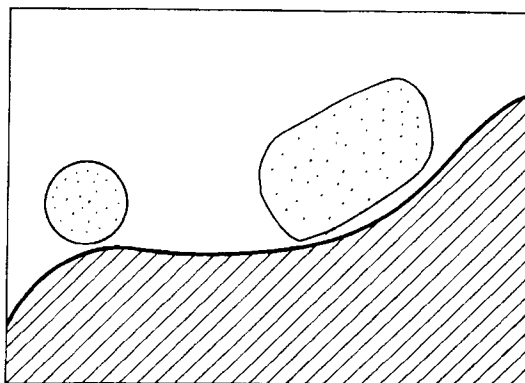
Generally, the observation that activation, or, more generally, the reactions of supported phases, occur differently compared to those of the corresponding pure unsupported material, is generally attributed to interactions between the supported phase and the support. This is of course true phenomenologically. But an essential concept is missing, namely the distinction between two different effects:

- (i) The first effect is merely brought about by the fact that the state of dispersion of the deposited phase is different; this was examined in the previous section.
- (ii) The second effect concerns the nature of the chemical or physico-chemical forces which act between the supported phase and the support and keep the former attached to the latter.

The error in many interpretations in the literature is that this distinction is not clearly made. This may have serious consequences with respect to the understanding of the activation mechanism and the efficient search for experimental parameters permitting the control of activation.

Considering now the chemical or physico-chemical interactions between the supported phase and the support, it is clear that a change of reactivity will be observed if the supported phase reacts chemically with the carrier: for example, nickel can combine with silica to make some hydroxysilicate compound when the deposition–precipitation method is used for preparation. The reactivity of the hydroxysilicate with hydrogen during activation by reduction is very different (actually lower) compared to that of nickel oxide. But careful analysis of the various examples mentioned in literature shows that quite different situations may exist.

Figures 3–10 reflect one way to classify the various categories of precursor–support interaction with emphasis on the chemical or physico-chemical nature of the interaction and the consequence with respect to the structure of the supported phase. Most of the possible situations are represented. Relevant examples can only be found if very different precursors are considered. It should, however, be clear, when considering these figures, that the precursor–support system taken as representative of one category may also correspond in specific cases to other categories.



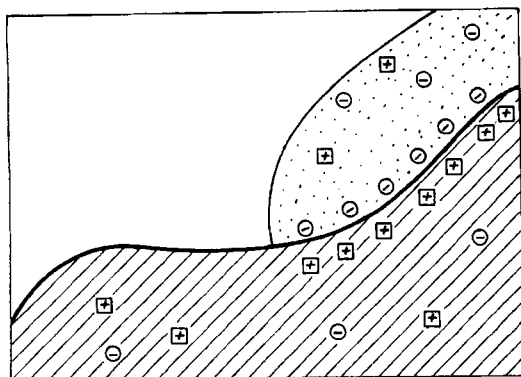
**Figure 3.** Supported phase–support interaction: very weak forces.

The reason is that the structure of a complex solid system depends strongly on the whole succession of phenomena having taken place during the preparation. In spite of the difficulty resulting from this effect, a clear distinction between the different possible situations definitely needs to be made for understanding the multiplicity of behaviors of precursors during activation. The classification presented in the succession of Figs 3–10 and the comments below correspond to increasingly stronger chemical interactions between the supported phase and the support.

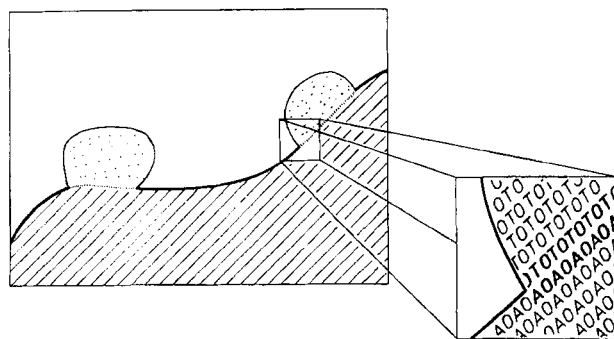
*Case 1: Very weak forces* (Fig. 3). This is the case of Van der Waals forces or hydrogen bonds. Such weak forces are probably insufficient for retaining an active phase attached to the support during an industrial process, but may be sufficient for handling a precursor. Organic precursors deposited from organic solutions are retained on the support by this sort of interaction in most cases. For hydrated salts, hydrogen bonds may also contribute to the attachment of the deposited substance. In both cases, the role of the support is only to disperse the precursor. In principle, weak forces could also be sufficient to bring about some preferential lattice orientation of the crystallites of the precursor. Graphite [9] and, perhaps, sometimes silica [10] could be examples of carriers which exert only a weak action on the supported substance. But care must be taken that carbon may have a functionalized surface and that the hydroxyls of silica can react with a precursor to form Si–O–R bridges (where R may represent many different organic or inorganic moieties: acyl or alkyl species, coordination compounds, etc.).

*Case 2: Electronic interaction* (Fig. 4). In principle, semiconducting or conducting substances deposited on a semiconducting support may form a *junction*, in the electronic sense, with the latter, even if no chemical bond as defined conventionally is formed. Electron transfer across the boundary can, in principle, change the electron density of deposited aggregates. The effect is expected to be more pronounced for small aggregates. This could change the reactivity of the deposited precursor.

*Case 3: Attachment through a thin transition layer* (Fig. 5). In adhesion or attachment of two solids together, by more or less strong forces, a whole spectrum of

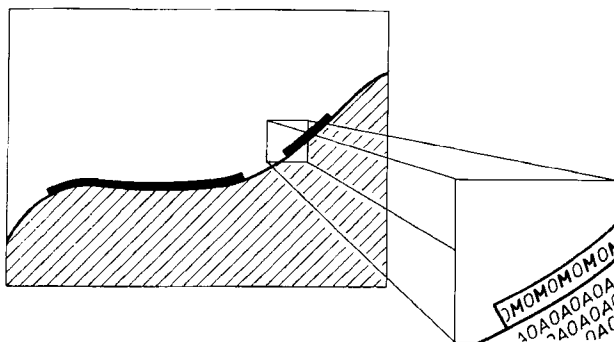


**Figure 4.** Supported phase–support interaction: electronic interaction.



**Figure 5.** Supported phase–support interaction: attachment through a transition layer.

mechanisms may explain the mutual interaction across the interface. However, except for the two cases mentioned above, the existence of a transition layer is always assumed. This transition layer may be a mixed compound of molecular thickness joining together the solids, or involve a thicker layer across which the composition progressively changes from that of one of the solids to that of the other [11]. Figure 5, for simplicity, represents the first situation. The mechanisms permitting adhesion are the same as those which will be discussed in the next cases of interaction (monolayers and bilayers). The main difference is that here the present surface energy of the deposited precursors is higher than the interface energy of the interface with the support, thus favoring the formation of deposited crystallites rather than that of covering layers. There is certainly a whole spectrum of possible situations between the weak or relatively weak interactions discussed above and very strong chemical interactions. This is reflected by the variety of situations observed in practice. A good example of a precursor which corresponds to the present case is cobalt oxide (obtained from nitrate) on silica. In that case, there is a relatively strong interaction, as shown by the partial formation of a monolayer, but the stable situation corresponds to crystallites deposited on silica. The interface probably has the structure of a cobalt silicate but is certainly only a few angströms or nanometers thick. Another example, actually not corresponding to precursors but to the active

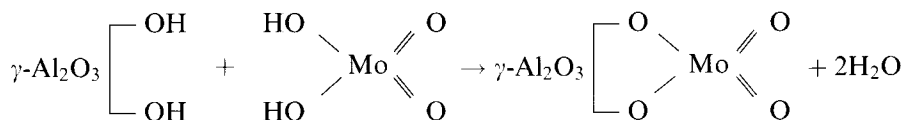


**Figure 6.** Supported phase–support interaction: patches of monolayer (rafts) or complete monolayer.

phase, is  $\text{MoS}_2$  supported on alumina, where a molybdenum oxysulfide makes the transition. This compound may be considered as partly aluminum molybdate, on the alumina side, and molybdenum sulfide, on the other side.

With respect to reactivity in the activation reaction, the situation represented in Fig. 5 suggests that the features of the activation will initially resemble those of the above cases 1 or 2 (Figs 3 or 4), but that new processes will be necessary for making the reaction possible in the final stages. These are expected to be similar to those described for cases 4 through 9.

*Case 4: Chemical interaction: patches of monolayers or complete monolayer* (Fig. 6). This category corresponds to situations where all the atoms or molecules of the supported precursor are exposed on the surface. The upper limit is encountered when the precursor phase combines with the carrier surface as a continuous monolayer. Figure 6 represents a partial coverage with one-molecule-thick patches (also called rafts). A typical example corresponds to the formation of a monolayer of  $\text{MoO}_3$  on the surface of  $\gamma\text{-Al}_2\text{O}_3$  as follows:

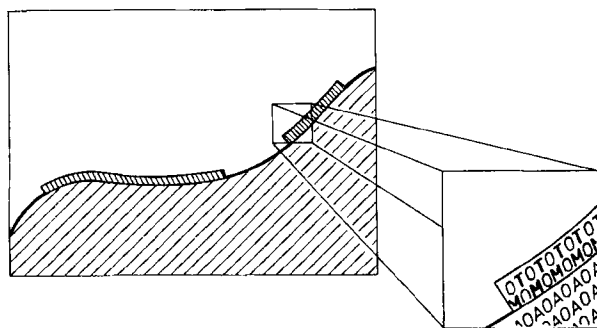


Much evidence of this phenomenon has been presented [12–17]. It is due to a real surface reaction, leading to the formation of a two-dimensional compound with well defined physico-chemical characteristics. The most conspicuous ones are electronic effects [18–24]: a shift of about 0.5 eV towards higher binding energies, of the  $\text{Mo } 3d_{3/2}$  and  $3d_{5/2}$  levels, has been reported.

Special structural features have also been detected using various spectroscopies (see, for example, Ref. 25 and the comprehensive review of Ref. 26). These results have been reproduced very frequently by many authors.

In such a case, one must conclude that a real two-dimensional aluminum molybdate is formed. As long as the quantity of aluminum molybdate corresponds to less than a monolayer, no three-dimensional aluminum molybdate forms.

The reactivity (and all chemical properties) of monolayers are very different from



**Figure 7.** Supported phase–support interaction: formation of bilayers.

those of the pure supported precursor (here  $\text{MoO}_3$ ) or those of the bulk mixed compound of composition similar to the monolayer (here  $\text{Al}_2(\text{MoO}_4)_3$ ) (see Ref. 26).

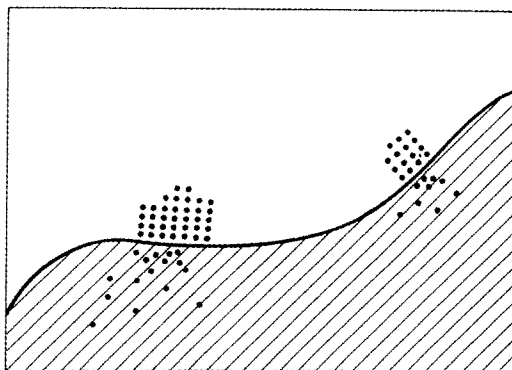
*Case 5: Chemical interaction: formation of bilayers* (Fig. 7). The formation of a two-dimensional compound of molecular thickness is not limited to compounds of a single catalytically active element. The phenomenon also occurs when a precursor contains two elements. The most conspicuous example is that of the cobalt–molybdenum and nickel–molybdenum oxide bilayers on  $\gamma\text{-Al}_2\text{O}_3$  [26–28]. Much of the structure of these bilayers is known [26, 28–30]. They should be considered as two-dimensional cobalt or nickel molybdates; Ion scattering spectroscopy (ISS) studies show that the Group VIII element may, according to circumstances, sit on the outside (exposed to the exterior) or inside (between  $\gamma\text{-Al}_2\text{O}_3$  and the bilayer) [29, 30]. Bilayers have also been the object of innumerable studies reproducing the initial results or sometimes adding particular details.

Comments with respect to reactivity are essentially similar to those made for monolayers. As generally expected with oxides containing two or several metallic elements [44], their reactivity is promoted by the presence of the element most easily reacted (e.g. Co or Ni in Co–Mo or Ni–Mo oxide monolayer with respect to reduction).

*Case 6: Partial formation of solid solutions* (Fig. 8). A more extensive reaction between a precursor and the support is often observed. This can lead to the formation of solid solutions of the supported element in the support. Other compounds of ill-defined stoichiometry can also form between the two partners. This can occur during the precipitation stage, by partial dissolution, and by precipitation, as shown in very recent work [31]. A still more extensive reaction can occur during calcination aimed at producing supported oxide precursors.

Depending on the temperature of calcination, the oxide and the carrier, when their structures are compatible, can dissolve in each other to different extents. The result may range from an ionic exchange confined to the near interface regions, to a multiple layer thick solid solution (or even, ultimately, a homogeneous one). Figure 8 presents a simple case, namely when a precursor, schematically indicated as possessing a well defined structure, can dissolve partially in the support. This is the

**Figure 8.** Supported phase–support interaction: partial formation of solid solutions.



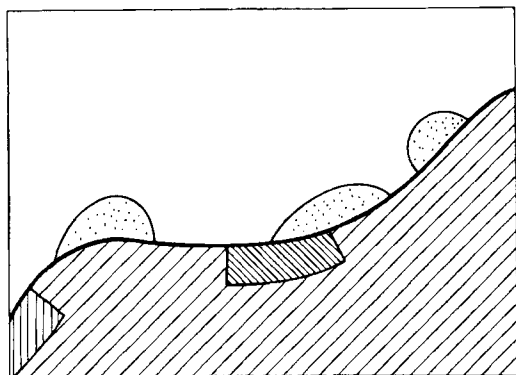
most common case, but the other phenomena mentioned above can also occur. The occurrence of the different situations and their bearing on reactivity have been discussed in a case not related to supported catalysts, but quite illustrative, namely that of the NiO–CuO system [3, 32]. Instances of formation of homogeneous solid solution involving substances used as supports are abundant in literature. For example,  $\text{Cr}_2\text{O}_3$  can react with an alumina support [33] and a similar effect is observed when CoO is contacted with a magnesia support [34]. A technologically very important case is the partial dissolution of cobalt (or nickel) in  $\gamma\text{-Al}_2\text{O}_3$  in HDS catalyst precursors. For cobalt, this is easily explained by the fact that  $\text{Co}_3\text{O}_4$  and  $\gamma\text{-Al}_2\text{O}_3$  both have the spinel structure.

The changes in reactivity which may occur when solid solutions are formed are discussed in detail elsewhere [3]. The support is necessarily very inert with respect to activation conditions. The element trapped in the solid solution will therefore be much less reactive. Consequently, only part of the active element contained in the precursor gets activated. Indeed, the loss of part of cobalt or nickel by reaction with  $\gamma\text{-Al}_2\text{O}_3$  is of concern in hydrotreating reactions; regeneration by calcination, which increases the proportion of the active elements trapped in the support as solid solution, decreases the amount of cobalt or nickel which can play a catalytic role.

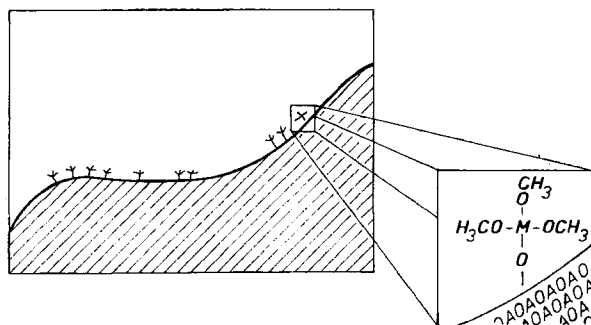
*Case 7: Partial formation of new compounds* (Fig. 9). The formation of a new compound can be either restricted to the near surface domains or extend to the bulk of the solid. It is likely that real spinels, rather than solid solutions (as in the present case) can form when oxide precursors containing transition metal elements such as copper or manganese (and also cobalt or nickel) are submitted to calcination when supported on alumina [35–38]. Other instances correspond unambiguously to the formation of a well defined new phase. Nickel hydroxysilicate is formed in the preparation of the precursor of Ni/SiO<sub>2</sub> catalysts. At high loading of MoO<sub>3</sub> (e.g. 20% MoO<sub>3</sub>) on  $\gamma\text{-Al}_2\text{O}_3$ , for example those used presently for very difficult hydrotreating reactions,  $\text{Al}_2(\text{MoO}_4)_3$  crystallites are formed [39, 40].

The comments concerning reactivity of precursors forming compounds with the support are identical to those of case 6. The general situation is also presented in Ref. 3.





**Figure 9.** Supported phase–support interaction: partial formation of new compounds.



**Figure 10.** Supported phase–support interaction: grafted precursors.

*Case 8: Grafted precursors* (Fig. 10). Organometallic complexes are now very frequently anchored (or grafted) on inorganic surfaces. They may be used as catalysts without any further treatment. However, an increasing number of attempts are made to use these atomically dispersed species as precursors for all sorts of catalysts (oxides, bare metal crystallites, sulfides). This implies that these organometallic complexes also undergo an activation procedure. In parallel with these developments, other molecules attacking the surfaces through a chemical bond are also used. This is the case for chlorides which, by reacting with surface hydroxyls to release HCl, make a bond between the remaining oxygen and the metal. This has been used for dispersing vanadium pentoxide on anatase and for making other highly dispersed catalysts [41–43]. Recently, highly dispersed supported precursors have been successfully prepared using grafted alkoxides as precursors [41–43].

It could be expected that such precursors do not behave as solid reactants, but rather as molecular species. However, the resulting molecular product (bare metal atoms in the zero-valent state, oxide or sulfide monomers) aggregate very rapidly in most cases, leading to the formation of tiny crystallites, so that it is very difficult to clarify mechanisms or even to distinguish general trends. Although the chemical mechanisms concerning grafting are now investigated in detail (Chapters 4.1.2. and 4.1.3.), it seems that the *transformation* for activation of the grafted species has not yet been explored in much detail.

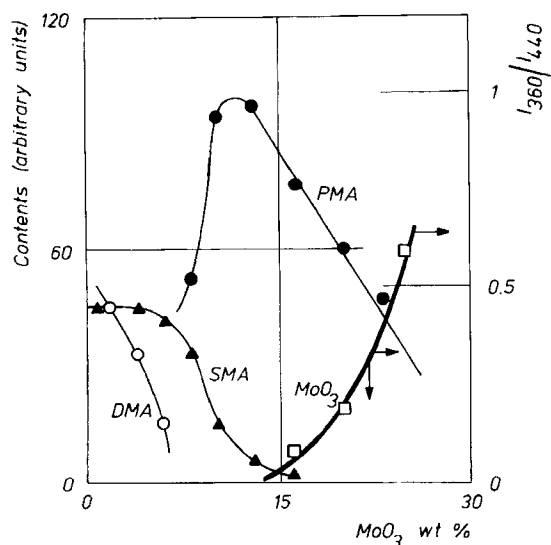
**Table 1.** Behavior of  $\text{MoO}_3$  with respect to various supports or oxides involved in catalysis.

Support	Observed phenomena	References
$\text{Sb}_2\text{O}_4$	detaches completely	45–47
$\text{BiPO}_4$	spontaneous segregation	48
	no $\text{MoO}_3$ or $\text{BiPO}_4$	49
$\text{Co}_3\text{O}_4$	no spreading	50
$\text{SiO}_2$	almost complete monolayer formation	51, 52
	but weak interaction	53–55
	tendency to detach, especially when another ion (e.g. Co, Ni) is present	56, 57
$\text{TiO}_2$	monolayer up to 50% theoretical value	54, 58–61
	spontaneous spreading of $\text{MoO}_3$ on $\text{TiO}_2$	50, 53
	above 50%: amorphous tridimensional and epitaxially grown $\text{MoO}_3$	62
$\text{ZrO}_2$	probably same as $\text{TiO}_2$	54
$\text{MnO}_2$	spontaneous spreading	50
$\text{SnO}_2$	spontaneous spreading	53
$\text{MgO}$	spontaneous spreading	53, 54
$\text{Al}_2\text{O}_3$	extremely stable monolayer (almost complete coverage)	innumerable
	spontaneous spreading	53
	strong modifications of properties of $\text{MoO}_3$	innumerable
$\text{Bi}_2\text{MoO}_6$	reaction to, respectively, $\text{Bi}_2\text{MoO}_7$ and $\text{Bi}_2\text{Mo}_3\text{O}_{12}$ via,	63, 64
$\text{Bi}_2\text{MoO}_7$	probably, strong surface contamination with $\text{MoO}_3$	

*Case 9: Intermediate cases.* There are two major difficulties in describing the supported oxide or, more generally, the precursor (e.g. oxychlorides, salts of various oxides or other compounds) which undergo activation. One is the fact that a same precursor may be involved in different types of interactions according to the nature of the support. The second is that several of the situations described above may coexist in a given catalyst.  $\text{MoO}_3$  offers an excellent illustration of these two difficulties.

Table 1 summarizes the interaction between  $\text{MoO}_3$  and various supports or oxides [44–64]. There is a whole range of situations. At one end is the extremely weak interaction with  $\alpha\text{-Sb}_2\text{O}_4$ . The  $\text{MoO}_3/\alpha\text{-Sb}_2\text{O}_4$  interface energy is weaker than the surface energy of  $\text{MoO}_3$ , so that  $\text{MoO}_3$  detaches spontaneously from  $\alpha\text{-Sb}_2\text{O}_4$ . At the other end stays the  $\text{MoO}_3/\gamma\text{-Al}_2\text{O}_3$  system, with a strong tendency to form a monolayer. Other oxides, such as bismuth molybdates, behave as  $\gamma\text{-Al}_2\text{O}_3$ .

With respect to coexistence of several types of interactions between given partners, this mainly concerns situations 3 through 7 above. This can be illustrated by the case of  $\text{MoO}_3$  dispersed on silica. Silica is generally considered as an inert carrier. It is expected to have only weak interactions with the supported phase and to act merely as a dispersing agent. This is not the case [65, 66]. A series of  $\text{MoO}_3/\text{SiO}_2$  catalysts, prepared by pore volume impregnation, followed by drying at 383 K and calcination at 773 K, show a progressive shift towards higher values of the binding energy (BE) of the  $\text{Si}_{2p}$  line, with increasing active phase loading from 0–20 wt %  $\text{MoO}_3$ , where the positive shift reaches 1 eV [52]. This corresponds to a strong chemical interaction, which is substantiated by the formation of a monolayer [52, 56, 57]. This monolayer structure has limited stability and  $\text{MoO}_3$  crystallites can



**Figure 11.** Product distribution in  $\text{MoO}_3/\text{SiO}_2$  catalysts as determined from acidimetric titrations: ( $\blacktriangle$ ) silicomolybdc acid; ( $\circ$ ) dimolybdates; ( $\bullet$ ) polymolybdates. The estimation of  $\text{MoO}_3$  ( $\square$ ) is derived from the intensity ratio of the reflectance bands at  $360$  and  $440\text{ cm}^{-1}$  [66].

form by spontaneous detachment of the monolayer. As a consequence, the following species are found in  $\text{MoO}_3/\text{SiO}_2$  precursors:  $\text{MoO}_3$ ; dimolybdates (DMA); polymolybdates (PMA); silicomolybdc acid (SMA); molybdenum bound to the surface of the support as a monolayer [14]. As shown in Fig. 11, the proportion of the various species changes according to composition [66].

As a consequence of the coexistence of several species, the  $\text{MoO}_3/\text{SiO}_2$  precursor contains:

- (i) monolayer patches (situation 4 above);
- (ii)  $\text{MoO}_3$  crystallites (situation 3 above);
- (iii) silicomolybdc compounds (situation 7 above).

The situation for the oxidic form of HDS catalysts supported on alumina is still more complicated, as was shown very early [35, 39, 67] and confirmed later by a very large number of authors. The system contains or may contain, according to the situation: free cobalt oxide; cobalt pseudoaluminate or  $\text{CoAl}_2\text{O}_4$ ; free  $\text{MoO}_3$ ; the  $\text{Co}_x\text{—Mo}_y\text{—O}_z$  bilayer; possibly  $\text{Al}_2(\text{MoO}_4)_3$  at high loading.

The temperature of calcination of a support before impregnation understandably modifies the interaction between the precursor and the support, as shown in the above case and that of alumina-supported nickel catalysts [68].

Another additional complication arises when two or several different oxides are deposited on a support, namely the possibility that they combine together. In this respect, cobalt molybdate  $\text{CoMoO}_4$ , although rarely found, can be added to the above list.

The examples selected for supporting the comments on the different types of interactions correspond to samples obtained after calcination. However, it is easy to see that most of these types of interactions can also occur in systems involving a

precursor salt (to be decomposed to a catalytic active oxide) or a metal (e.g. to be sulfided) and a support (oxide or otherwise).

### 5.1.1.3 Article Structure

This article covers the activation of *supported* catalysts. It examines the formation of the final catalysts, as achieved by three categories of treatment: calcination, reduction, and sulfidation (more precisely reduction–sulfidation). Detailed studies of these three categories of processes did not lead to an equally detailed analysis. Outside very general (phenomenological) observations, very little is known concerning the calcination of supported precursors. By contrast, some particular systems have been studied in some detail in reduction (e.g. NiO/support for activation to Ni/support) or sulfidation ( $\text{Co}_x\text{Mo}_y\text{O}_z/\gamma\text{-Al}_2\text{O}_3$  to sulfides).

The discussion is based on the main distinctions between calcination, reduction, sulphidation, and other reactions. Within each of these topics, the unsupported and supported situation will be examined individually if necessary. More emphasis is given to explaining these effects by using typical examples rather than by giving an inventory of the literature. The important point is to understand the general rules, the general trends that are to be observed when the activation parameters are modified, and the various structural and textural changes that activation may bring about.

These subsections will show why activation is such an important process, by demonstrating that it can alter most, probably all, the properties of catalysts.

## 5.1.2 Activation of Supported Catalysts by Calcination

Some catalyst activation processes are extremely important: this is the case for oxides used as catalysts and supports ( $\text{Al}_2\text{O}_3$ ,  $\text{SiO}_2$ ,  $\text{TiO}_2$ ,  $\text{ZrO}_2$ , silica–aluminas), and zeolites. Extremely elaborate procedures are used. This concerns bulk, not supported systems, and is dealt with in Chapter 3. The case of  $\text{SiO}_2$  *mixed* with active phases (e.g. in oxidation) has little relevance to the subject of the present section, as it seems that  $\text{SiO}_2$  does not play the role of a real support, but rather that of a diluent or spacer. An electron microscopy study coupled with microanalysis on a typical oxidation catalyst (propene to acrolein) shows that only a small fraction of the active phases is attached to silica or is situated in its immediate proximity [69]. There are not many cases of truly supported catalysts whose final active form is obtained through calcination. The only notable and important instances are  $\text{V}_2\text{O}_5$ /anatase, used for the oxidation of *o*-xylene to phthalic anhydride, and  $\text{V}_2\text{O}_5$  deposited on  $\text{TiO}_2$  (or various modified supports) used for the selective catalytic reduction of  $\text{NO}_x$ . In all these cases, the literature has given much attention to details of impregnation or grafting, in particular the pretreatment of the support, the influence of support modifiers, and the mechanism by which the active element can be attached to the support (e.g. by grafting, by reaction with surface hydroxyls, etc.). However, only general information on calcination has been given.

Literature does not mention any systematic attempt to analyze the process taking place in the transformation of a supported precursor to the corresponding catalytically active supported oxide. Only scattered and too specific information is available. It is thus only possible to mention general ways which, according to circumstances, could be used to provide a better understanding and control of activation by calcination. This is the object of the following paragraphs.

The overall changes in the transformation of the supported precursor to the supported active oxide should obviously be understood. The supported initial precursor and the supported final oxide each correspond to one of the types of supported phase-support interactions described in Figs 3–9. It is very important to identify changes from one picture to another during calcination. The general tendency will be to reach higher thermodynamic stability through:

- (i) the situation of Fig. 3, corresponding to very weak interaction if the oxide and the support have no affinity to each other. The example (Table 1) is  $\alpha\text{-Sb}_2\text{O}_4\text{-MoO}_3$  where the oxides detach from each other during calcination irrespective of the precursors used;
- (ii) the formation of a monolayer or a bilayer (Fig. 6 or 7);
- (iii) the extensive formation of a solid solution or new compounds. These may contribute to anchor the active oxide crystallites to the support. This is approximately the case of the  $\text{V}_2\text{O}_5$ /anatase catalysts, where one observes very highly dispersed species (perhaps as patches of monolayers), small rafts which are several  $\text{V}_2\text{O}_5$  lattice units thick, and some dissolution of vanadium in anatase. There are good arguments suggesting that the formation of a solid solution or a compound between the support and the active phase keeps the latter in a higher dispersion state (Section 5.1.3).

The simple identification of supported phase-support interaction suggests many ways to control the calcination step: favoring the spreading of the precursor thanks to adequate additives, inhibiting or promoting the formation of solid solutions or new compounds with the support by adequate doping of the latter, ramping increase of temperature or modification of calcination atmosphere (for controlling oxidation states of elements, which in turn modify the interactions with the support), etc.

A second approach to the understanding of calcination is to suppose that there is an analogy between activation of the supported precursor and the decomposition in the presence of oxygen of the corresponding bulk unsupported phase. Thermal decompositions have been the object of very intensive studies since the early 1940s, and rich information can be found in the classic books [2, 3, 70], in the proceedings of the International Symposia on the Reactivity of Solids, and in journals such as *Solid State Ionics* or *Thermochimica Acta*. With respect to the symposia, we give here reference to the 7th, 8th, 9th and 10th [71–74]; the two subsequent ones (1988, 1992) were published in *Solid State Ionics*. When using analogies with the reaction of bulk compounds, the factors mentioned in Section 5.1.1 should be taken into account. These could suggest modifications of the calcination procedure such as previous handling in vacuum or in a reducing atmosphere, or use of a succession of different reaction conditions in order to influence nucleation. The role of water

vapor in the calcination furnace is very important: according to the circumstances, it can be detrimental (in particular to dispersion), or favorable (e.g. if it is wished to introduce vacancies into the activated supported oxide).

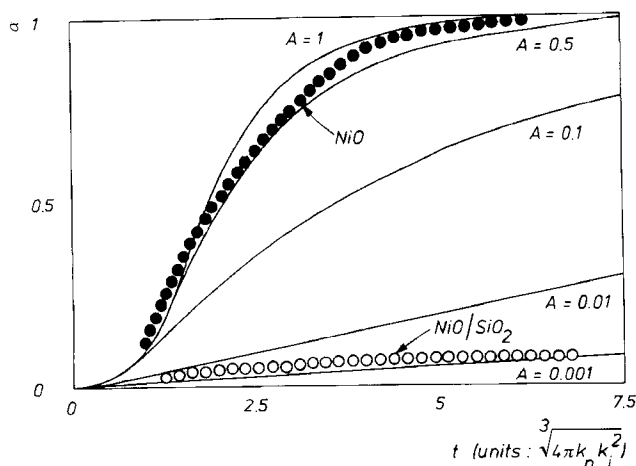
It is also possible to take advantage of studies dealing with the preparation of supported oxide precursors (namely, oxides to be further activated to produce active metals or sulfides by reduction or sulfidation, respectively). Although there is limited information in this field, some scattered information has been published, essentially for  $\text{MoO}_3$  and  $\text{V}_2\text{O}_5$ . Infrared and Raman spectroscopies have provided data concerning various steps in the transformation of precursor salts to oxides.

Summarizing, it is surprising that activation by calcination and, more generally, the calcination of precursor salts to oxides, has not been the object of more systematic studies. For supported catalysts working in the oxide state, the activation step has the same crucial importance as for metals or sulfides. Although the field is mostly unexplored, understanding calcination is certainly possible, on the basis of the general knowledge on reactions of solids, and using analogies with similar reactions of bulk or supported materials. The physico-chemical techniques now available in catalysis laboratories could provide a wealth of useful information, and allow a better control. These are, among others, the spectroscopic techniques (IR, UV, Raman), XPS, electron transmission microscopy and microanalysis with high spatial resolution.

### 5.1.3 Activation of Supported Catalysts by Reduction

In the majority of cases, the last step in the preparation of catalytically active metals is a reduction. The precursor is very frequently an oxide. An oxychloride is the real precursor of active platinum and some noble metals if chlorometal complexes (e.g. chloroplatinic acid) are used. It may be advantageous to use still other precursors and to reduce them directly without any intermediary transformation to oxide. On the other hand, nearly all catalytic metals are used as supported catalysts. The only notable exception is iron for ammonia synthesis, which is a very special case and then the huge body of industrial experience renders scientific analysis of little relevance. The other important metals are Raney nickel, platinum sponge or platinum black, and similar catalysts, but they are obtained by processes other than reduction. This shows the importance of understanding the mechanisms involved in activation by reduction.

Reduction is a typical reaction of a solid. It has been investigated in detail with bulk unsupported materials. The necessary background for the present section, namely that concerning unsupported oxides, can be found in general books [3, 7, 75, 76], the latter for more chemical engineering oriented problems. The backbone of the discussion will be provided by results on the activation of supported nickel catalysts. These catalysts constitute a good example, because the interpretation can benefit from the result of studies dealing with unsupported  $\text{NiO}$ . The reduction of  $\text{NiO}$  has been the object of the most extensive fundamental investigation. In addition, the activation of supported nickel catalysts has also been studied in comparatively more detail than other systems.



**Figure 12.** Quantitative comparison of the reduction ( $\alpha$  = fraction reduced) of bulk and silica-supported NiO at 538 K in a flow of pure  $H_2$  [78]. The parameter  $A$  characterizes the relative rates of nucleation (constant  $k_n$ ) and interface progress (constant  $k_i$ ). Assuming spherical particles,  $A$  corresponds to the average number of nuclei being formed on each NiO particle in the time necessary for the interface to travel a distance equal to the radius  $a$  of the particle [7]:  $A = 4\pi k_n \times k_i^{-1} a^3$ .

We shall examine in succession the effect of the dispersion of the precursor, calcination temperature in the preparation of the precursor, nature and amount of precursor, formation of compounds between precursor and supports, nature of support, effect of modifiers, and activation conditions.

### 5.1.3.1 General: Effect of Precursor Dispersion

The general tendency is clearly that a more dispersed precursor will correspond to a higher rate of reduction and the production of a more dispersed activated metal, provided chemical interactions do not cause side-effects. This is indeed the trend, for all reactions which are not nucleation limited. However, care should be taken that diffusion limitations in the pores may limit activation in the interior of catalyst particles (beads, pellets, tablets).

As previously mentioned, the situation is more complicated in nucleation-limited (NCI) reactions, where extreme dispersion brings about a diminution of reactivity. This effect is illustrated and confirmed by Fig. 12, where the continuous curves correspond to the theory on which Fig. 2 is based and points correspond to experimental data. Electron microscopy data give an average diameter of 500 nm (0.5  $\mu$ m) for bulk NiO [7], and 80–100 nm for NiO/SiO<sub>2</sub> [77]. Figure 12 [78] indicates that the diminution of reactivity of NiO/SiO<sub>2</sub> is due to a reduction of NiO particle size by a factor of about 6 (cube root of the ratio of  $A = 0.5$  for bulk to  $A = 0.002$  for supported NiO). This is about the figure given by electron microscopy (factor of 5–6.3).

The conclusion that nucleation limited the rate of activation by reduction of

NiO/SiO<sub>2</sub> precursor was simultaneously proposed following the above deductions [79] and by Coenen, using an impressive series of converging arguments [80].

### 5.1.3.2 Overall Effects: Influence of Calcination Temperature in Precursor Preparation

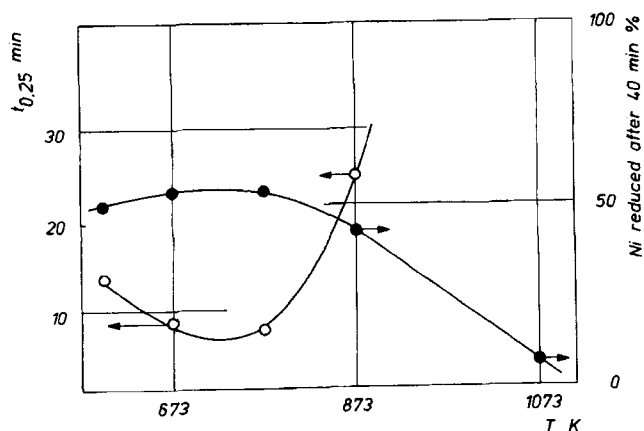
Figure 13 shows the influence of the calcination temperature on the reactivity of NiO supported on silica. The effect is very important [81]. Such effects are often found [82]. These are still more dramatic if the support has not been calcined before impregnation [68].

However, calcination temperature may influence several characteristics of the supported precursor: dispersion, extent of formation of a compound by reaction with the support, etc. The curve giving the fraction of NiO reduced after 40 min suggests the general trends: between 570 and 770 K, dispersion of NiO diminishes and the reaction rate increases as indicated in the previous subsection. Above 770 K, NiO reacts with silica so that the rate of reduction ( $1/t_{0.25}$ ) and the amount reduced decrease.

The various parameters are analyzed separately in the following subsections.

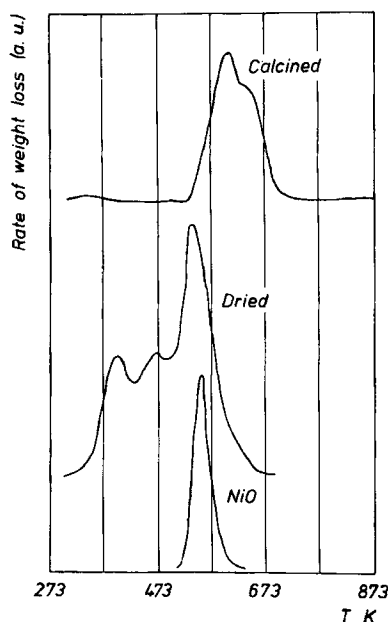
### 5.1.3.3 Role of Precursors

Not surprisingly, the reduction depends on the nature of the precursors, because their overall chemical reactivities are different. Some aspects of the changes, among others, are differences in pure chemical reactivity between compounds (as measured, for example, by rate of interface progress), different states of dispersion, and



**Figure 13.** Influence of calcination temperature on the reduction of NiO/SiO<sub>2</sub> at 598 K by pure H<sub>2</sub> [81]: SiO<sub>2</sub> 334 m<sup>2</sup> g<sup>-1</sup>; 18.9% wt Ni, calcined at 773 K, 5 h;  $t_{0.25}$  is the time necessary to reduce 25% of the NiO; the degree of reduction obtained after 40 min is indicated on the right-hand axis.

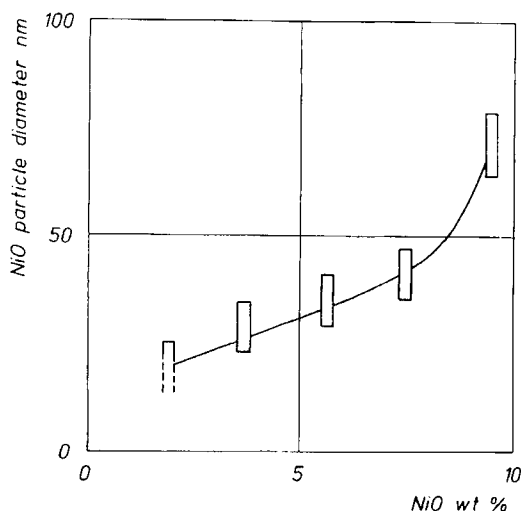




**Figure 14.** Comparison of the TPR profiles of samples of NiO/SiO<sub>2</sub>: SiO<sub>2</sub> surface area 275 m<sup>2</sup> g<sup>-1</sup>; pore volume 0.80 cm<sup>3</sup> g<sup>-1</sup>; pore distribution maximum 8 nm; incipient wetness impregnation by Ni(NO<sub>3</sub>)<sub>2</sub> solution; drying 393 K, 16 h (dried); calcination at 723 K, 16 h (calcined); NiO weight content, on the basis of SiO<sub>2</sub> + NiO, 10.6%; TPR, measured as weight loss, was performed in de-oxygenated, predried H<sub>2</sub>, with a heating rate of 10 K mn<sup>-1</sup>. The two peaks at 403 and 468 K for the dried sample probably correspond, respectively, to dehydroxylation of Ni(OH)<sub>2</sub> and decomposition–reduction of ill-defined compounds containing nitrate ions [83].

intervention or not of rate-limiting nucleation processes. As a consequence, the characteristics of the activated catalysts are also different. An interesting illustration of these changes concerns nickel catalysts prepared by incipient wetness impregnation of silica with an aqueous solution of nickel nitrate. One sample was simply dried at 393 K; the other one calcined at 723 K. In neither of these catalysts was nickel silicate detected, but the calcined sample exhibited very sharp X-ray diffraction peaks of NiO [83]. Figure 14 shows the TPR profiles of these samples, together with those of a bulk NiO. The lower reactivity of supported “calcined” NiO compared to bulk NiO is due to its high dispersion. The temperature programmed reduction (TPR) peak consists of two components, very likely corresponding to two collections of crystallites of different particle size (bimodal size distribution). As shown independently, nickel combined with silica would reduce at temperatures 160–180 K higher [83, 84]. The dried sample reacts 70–90 K lower. The bulk NiO sample used for comparison had been shown to correspond approximately to the maximum reactivity permitted by dispersion (curve 1 of Fig. 2). Nevertheless, the dried sample, with a much higher dispersion than the calcined sample, reacts 25 K lower than bulk NiO (peak at the highest temperature). The dispersion of reduced supported nickel (measured by hydrogen chemisorption, on the assumption of 2

**Figure 15.** Increase in size of crystallites supported on  $\text{SiO}_2$  with increasing amount of  $\text{NiO}$  [83]. The  $\text{SiO}_2$  used had a surface area of  $415 \text{ m}^2 \text{ g}^{-1}$ , pore volume  $1.12 \text{ cm}^3 \text{ g}^{-1}$ . The samples were obtained by pore volume impregnation with an aqueous solution of nickel nitrate. Calcination was at  $773 \text{ K}$  for  $4 \text{ h}$ . The size of the crystallites was determined by electron microscopy.



atoms per  $\text{Ni}$  atom and a surface area of  $6.33 \text{ \AA}^2$  occupied by one  $\text{Ni}$  atom) was 20.1% for the dried sample, and only 2% for the calcined sample, after reduction at  $773 \text{ K}$  for  $6 \text{ h}$ . This result, which concerns samples which are as comparable as possible, dramatically shows the influence of the chemical nature of the precursor.

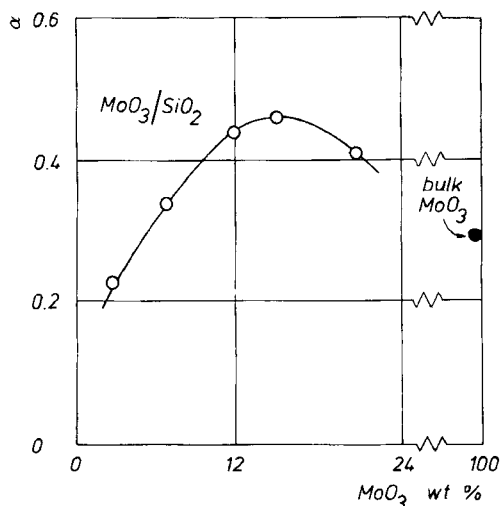
This conclusion prompts two observations. The first underlines the difference of reactivity of  $\text{Ni}(\text{OH})_2$  or partially decomposed  $\text{Ni}(\text{NO}_3)_2$ , on the one hand, and  $\text{NiO}$ , on the other hand, when used as supported precursors. The second suggests that it is advantageous in many cases to start from uncalcined samples for activation by reduction if deeper reduction and higher dispersion are wanted.

The case of cobalt catalysts supported on silica also suggests interesting differences when either the nitrate, acetate or chloride is used [82]. The corresponding study, however, did not isolate the effect on impregnation from that on activation.

#### 5.1.3.4 Influence of the Loading of Deposited Precursor

The influence of the amount of supported precursor is very easy to understand when this precursor mainly forms crystallites. The size of the crystallites tends to increase with the amount deposited (Fig. 15) [68, 79]. The effect on the rate of reduction by hydrogen can easily be inferred from this figure, taking account of Chapter 5.1.3.1.

When the supported phase can form both partial monolayer patches and crystallites, as does  $\text{MoO}_3/\text{SiO}_2$  (case 9), the situation is more complicated, as indicated in Fig. 16. The decrease of reactivity for low loadings is due both to the fact that the reduction of  $\text{MoO}_3$  crystallites to  $\text{MoO}_2$  is nucleation limited (as mentioned in Section A) and that the monolayer patches which coexist with crystallites may have a lower reactivity than the latter. The decrease of reactivity for loadings exceeding 14% is due to the fact that the  $\text{MoO}_3$  crystallites increase in size in a range of di-



**Figure 16.** Degree  $\alpha$  of reduction of  $\text{MoO}_3/\text{SiO}_2$  to  $\text{MoO}_2/\text{SiO}_2$  after 10 h at 673 K,  $\text{H}_2$  pressure 100 kPa [78].

mensions where the role of interface progress is more rate-limiting than nucleation. These effects have been analyzed in some detail [3, 85].

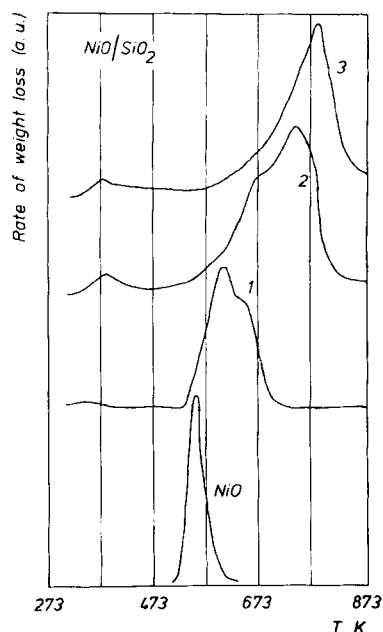
#### 5.1.3.5 Effect of the Formation of Compounds Between the Precursor of the Active Metal and the Support

Impregnation of  $\text{SiO}_2$  by nickel nitrate brings about very little chemical interaction when calcination is made at low temperature (below 770 K). But the necessity to increase dispersion leads to the use of other methods [80, 87], in particular the highly successful deposition–precipitation technique (Chapter 4.6). This brings about the formation of large amounts of nickel hydroxysilicate, which appear as filaments in electron micrography [80, 83, 87]. Compared with Fig. 14, this corresponds to a considerable decrease of reducibility (Fig. 17), as shown by various authors [83, 84].

The reduction of samples impregnated with nickel hexammine  $[\text{Ni}(\text{NH}_3)_6]^{2+}$  also shows a dramatic decrease in the reduction rate and ultimate degree of reduction, compared to the nitrate-impregnated catalysts [79]. The explanation in that case must take into account two factors which have a parallel influence, namely the formation of a small amount of nickel silicate (or hydroxysilicate) and a much higher dispersion: for a  $\text{NiO}$  loading of 9.43%, the ratio of the  $\text{Ni}_{2p}$  to  $\text{Si}_{2p}$  XPS bands is multiplied by a factor of about 14 [79].

#### 5.1.3.6 Nature of the Support

At the end of Chapter 5.1.1.2, we underlined the fact that the state of dispersion and magnitude of the interaction with the support depend strongly on the support.



**Figure 17.** Comparison of TPR profiles of samples of  $\text{NiO}/\text{SiO}_2$  prepared by nitrate impregnation (legend of Fig. 14) or by deposition–precipitation on the same support [83]. The  $\text{NiO}$  loadings were almost identical (10.6 and 10.9 wt%, on the basis of  $\text{SiO}_2 + \text{NiO}$ ): (1) nitrate impregnated, calcined at 723 K (same as in Fig. 14); (2) deposition–precipitation, dried at 393 K for 16 h; (3) same precursor, calcined in the same conditions as the nitrate-impregnated sample. The curve for bulk  $\text{NiO}$  is added.

This has necessarily an influence on activation, as shown by a comparison of  $\text{SiO}_2$ ,  $\text{TiO}_2$ , and  $\text{Nb}_2\text{O}_5$  in the case of nickel [86]. Figure 18, taken from a study of the reduction of  $\text{NiO}$  supported on a range of silica-aluminas [88], illustrates this point. All catalysts were prepared in identical conditions. The reducibility reflects the change in the chemical interaction of  $\text{NiO}$  with the support, as indicated

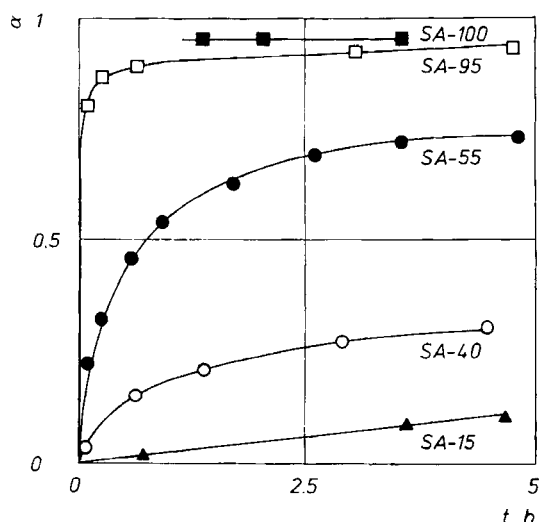
- (i) by UV reflection spectra – the presence of  $\text{Ni}^{2+}$  in an octahedral environment on alumina-rich samples (especially SA-15 and SA-40);
- (ii) by XPS – a strong change in the binding energy of nickel, silicon and surface oxygen.

In addition, the dispersion of nickel oxide on the surface increases as expected when the alumina content increases, as indicated by XPS [88, 89].

### 5.1.3.7 Effect of Modifiers (Promoters)

It can be expected that modifiers considerably alter the course of the activation of catalysts by reduction.

The role of common additives, such as alkali metals used for depressing support acidity, and other additives oppositely promoting acidity, can be inferred from a series of studies using alumina as a support, and cobalt or molybdenum oxide as the supported phase [90–109]. The phenomena are very complex. They result from complicated reactions during its impregnation step, leading to changes of disper-



**Figure 18.** Influence of the nature of the support on the reducibility of NiO. Silica aluminas (SA) containing the percentage of SiO<sub>2</sub> indicated in the designation of the sample (e.g. SA-55: 55 wt% SiO<sub>2</sub>) were impregnated by nickel nitrate using pore volume impregnation; NiO content 10 wt%. The samples were dried for 2 h at 383 K, and calcined at 773 K for 6 h. Reduction in pure H<sub>2</sub> (100 kPa) was carried out at 598 K;  $\alpha$  represents the fraction of NiO reduced [88].

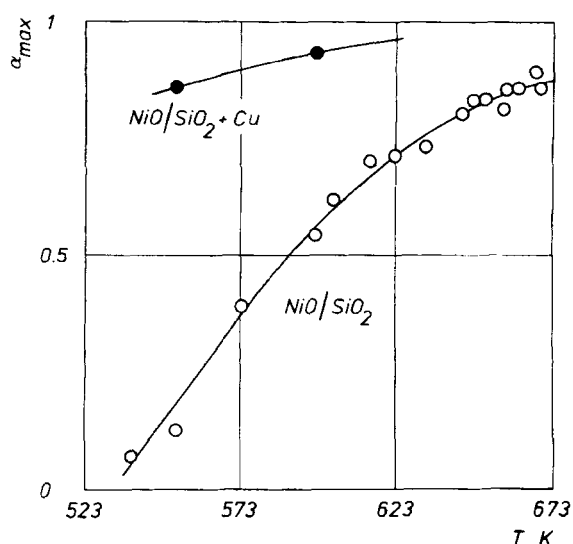
sion, migration of species inside pores, and formation of compounds involving the supported phase and the modifier. This considerably alters the reducibility of the supported precursor and the distribution and dispersion of the reduced metal. To our knowledge, this has only been shown quantitatively but not analyzed in detail. One such example is the role of Ba and La for Ni/ $\gamma$ -Al<sub>2</sub>O<sub>3</sub> [110].

One case deserves special consideration. This is the role of metal additives such as platinum, copper, or donors of spillover hydrogen used in small quantities in comparison with the supported precursor. Figure 19 shows that the maximum degree of reduction,  $\alpha_{\max}$ , of NiO/SiO<sub>2</sub> increases very much when 0.5 wt% copper (as Cu) is added [81]. Platinum and palladium bring about the same kind of effect [81].

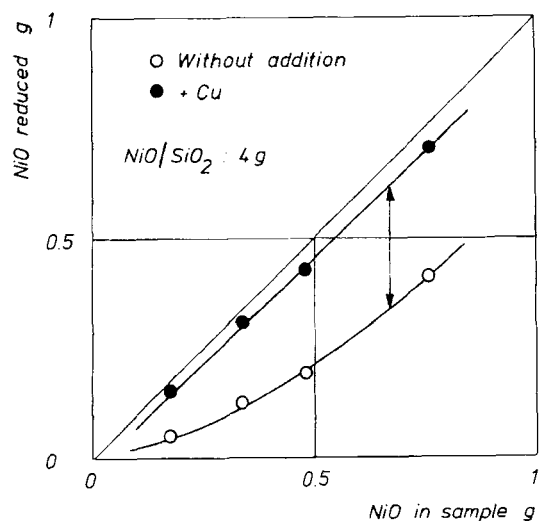
Figure 20 compares the amount of NiO reducible at 598 K without ( $\alpha_{\max}$ ) and with copper, for samples of different NiO loading containing 5.3 wt% Cu on the basis of the Ni content. Copper brings about a substantial increase of ultimate reducibility. The *proportion* of NiO which becomes reducible, thanks to the action of Cu, diminishes as the overall NiO loading increases [81].

The explanation is that Cu (or Pt, or Pd) produces spillover hydrogen which considerably accelerates the nucleation of nickel metal in the reduction conditions. At low loading, the high dispersion of NiO makes that nucleation is rate-limiting if NiO is pure; copper permits nucleation and, consequently, reduction. The effect is proportionally smaller for high NiO loading, because the NiO crystallites are larger and can nucleate more easily (see Sections 5.1.1.2.A and 5.1.2, and Ref. 3).

This effect had been discovered with unsupported oxides. A review of the results obtained is available elsewhere [3, 81, 113], as is more data [81, 113–115]. Some



**Figure 19.** Influence of copper as a promoter on the reduction of NiO/SiO<sub>2</sub>. The NiO/SiO<sub>2</sub> sample is the same as for the experiments of Fig. 13. Part of the sample was subjected to a second impregnation with copper nitrate (total Cu added 0.4 wt% calculated on the total NiO + SiO<sub>2</sub> weight) and calcined at 773 K in air for 5 h. The apparent (or conventional) maximum degree of reduction,  $\alpha_{\max}$ , corresponds to that obtained after 40 min. Reduction in pure hydrogen (100 kPa) [81].



**Figure 20.** Additional reduction of NiO due to copper in NiO/SiO<sub>2</sub> catalysts. Samples of different NiO loadings (wt% of total sample, upper scale; or wt in gram in a 4 g NiO/SiO<sub>2</sub> sample, lower scale) prepared on the same silica and with the same procedure as the samples used for Figs 13 and 19. Copper was introduced as explained in the legend of Fig. 19, in the proportion Cu:Ni = 5.3 wt%. Reduction by pure H<sub>2</sub> (100 kPa) at 598 K. The weight of NiO reduced corresponds to  $\alpha_{\max}$  after 40 min. The double arrow indicates the magnitude of the additional reduction due to copper [81].

publications mention the use of platinum [111, 112] to promote the activation of supported catalysts by reduction.

Let us mention, incidentally, that experiments concerning the influence of other promoters and additives on the reduction of bulk oxide [3, 113–115] can sometimes give pieces of information which are useful for understanding the behavior of supported oxides.

#### 5.1.3.8 Influence of Activation Conditions

Very few systematic studies have been done concerning the influence of the conditions in which the activation by reduction is carried out. Very notable exceptions are two studies concerning NiO/SiO<sub>2</sub> [80, 116].

A higher temperature always brings about a higher degree of reduction [117], as shown in the preceding section. However, this is accompanied by a loss of dispersion, unless this increase permits the reaction of a *compound* of the active metal. For example, nickel from hydroxy silicates is usually more dispersed and less prone to sintering than nickel from NiO. Extremely high reduction temperatures may lead to the so-called strong metal support interaction (SMSI) effect, or alloying of the active metal with the reduced metallic element of the support, e.g. Ni and Si [118, 119].

The overwhelming majority of activation procedures use hydrogen as reducing gas. Other gases (e.g. CO) can indeed produce carbon deposits. There do not seem to have been studies on the influence of hydrogen pressure on activation. The influence of water seems to be always unfavorable [80, 120], and this for two reasons. The first is that water has an inhibitory effect. Working in the presence of water necessitates higher temperatures, with the consequence of an increased danger of loss of metal surface area by purely thermal sintering. The second reason is that water usually promotes sintering for reasons which are not clarified yet.

It is the opinion of the present contributor that some well-selected additives in the reducing gas could favorably modify dispersion and resistance to sintering of the activated metal, but there are no undebatable proofs of such effects.

#### 5.1.3.9 Overall View

The actual activation process is the result of all the factors mentioned above and, consequently, relatively complicated. A short article [121] and another one cited above [81], however, suggest that the fundamental approach presented above is very useful in understanding the overall phenomenon and controlling the activation process. Because of this complexity, no single method can provide all the information necessary for optimizing activation by reduction. Temperature programmed reduction used in previous examples and in many other studies [84, 122] is valuable for providing a first set of data, but it must be completed by techniques adapted to the system (e.g. Mössbauer spectroscopy if Fe is the active phase [123]).

Although nickel catalysts have served as examples, articles dealing with other

metals show that the same concepts apply. This is the case for Co deposition on silica or alumina [82], Cu/ $\gamma$ -Al<sub>2</sub>O<sub>3</sub> [124], and Ag/ $\eta$ -Al<sub>2</sub>O<sub>3</sub> and Ag/TiO<sub>2</sub> [125], for example. The preparation of bimetallic catalysts is more complicated because of possible preferential reduction of one metal before the other, a phenomenon well known with the bulk oxides [3]. A few studies suggest that approaches similar to those mentioned above can also be used in these cases [122].

This section, by focussing on the solid-state aspect of activation by reduction, shows the main parameters which are involved, and hence suggests methods for better control, but many aspects remain unclear. One of the strongest phenomena is the increase of thioresistance of Ni/Al<sub>2</sub>O<sub>3</sub> catalysts thanks to controlled partial reduction [126].

#### 5.1.4 Reduction–Sulfidation

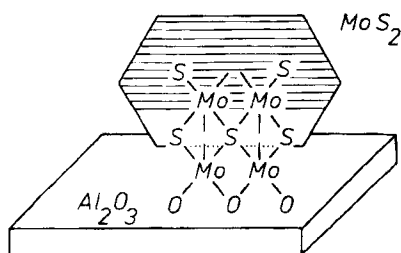
The hydrotreating reactions (hydrodesulfurization, hydrodenitrogenation, hydrodeoxygenation, hydrodemetallation) and some hydrocracking reactions use sulfided catalysts. Until very recently, these catalysts contained, as main active species, molybdenum (or sometimes tungsten). They also contained promoters (cobalt or nickel, or sometimes iron). These are the traditional hydrotreating catalysts. Only very recently have noble metals been used for deep hydrodesulfurization or deep dearomatization. The traditional catalysts are prepared by different techniques which all produce, in a more or less perfect way, bilayers containing active metals (Mo or W) and promoters (Co, Ni or Fe) in the oxide state. This corresponds to the precursor structure shown in Fig. 7. The formation of the active sulfided catalysts necessitates a deep reduction–sulfidation of the oxide precursor. This operation, always called *activation* in the field of hydrotreating, is absolutely crucial. Changes in temperature, rate of temperature increase or composition of the reducing–sulfiding medium can bring about variations of activity by factors exceeding 2 or 3, alter the selectivity, and also extend or diminish catalyst life [127].

In the early days of hydrotreating, the precursors were simply contacted with hydrogen and a sulfur-containing feed, usually an ordinary petroleum fraction to which sulfur-containing compounds were added (a so-called “spiked” feed). Later, the catalysts, charged in the reactor, were treated by a special mixture containing, in addition to hydrogen, either H<sub>2</sub>S or a sulfur-containing compound very easily decomposed to H<sub>2</sub>S in the presence of hydrogen (e.g. dimethyl disulfide or a mercaptan). However, the operation in a large reactor is still difficult to control. For this reason, it seems that presulfidation outside the reactor may be the solution for the future.

Except for a part of the recent attempts to avoid in situ sulfidation, the activation of traditional hydrotreating catalysts always corresponds to the reaction of hydrogen and sulfur-containing compounds with the oxide precursor. Innumerable recipes are proposed for use in industry and have been described in literature. One article, among many, gives a still valuable overview of the possible procedures [128].

The present section deals only with the traditional catalysts, because too little is known presently on catalysts whose formulation includes noble metals. The objec-





**Figure 21.** Schematic representation of a tiny crystallite of  $\text{MoS}_2$  (diameter typically 5–10 nm) attached on the alumina surface in a sulfided hydrotreating catalyst.

tive will be to outline general trends, without attempting the almost impossible task of examining all the various recipes mentioned in the technical or scientific literature. The next section examines some fundamental aspects; subsequent sections outline the influence of various parameters.

#### 5.1.4.1 Fundamental Data

Reduction–sulfidation corresponds to a drastic change of the structure of the active species. The starting bilayer is a two-dimensional oxide adhering to the support (usually alumina) along a continuous interface. The active catalyst is constituted of tiny crystallites attached to this support by small patches of transition interfaces (Fig. 21). The whole reduction–sulfidation reaction involves many simultaneous or successive processes; reduction of  $\text{Mo}^{6+}$  to  $\text{Mo}^{4+}$ , sulfidation of  $\text{Mo}^{4+}$  to  $\text{MoS}_2$ , sulfidation of the Group VIII metal initially in an oxide state to a sulfide, destruction of the bilayer, and formation of crystallites. The Group VI and VIII metals, initially associated in the bilayer, segregate to a large extent in the sulfided state (the extent of segregation is still being debated [129–132]). The existence of strong coupling effects in reactions of solids [3, 133] makes the full analysis of the process difficult, but suggests that many parameters can have a strong influence on the structure and texture of the final sulfided catalyst.

The most striking result of these coupling effects appears at a macroscopic scale, when reduction and sulfidation as a whole are considered.  $\text{MoO}_3$  is reduced at much lower temperatures (sometimes 200 K lower) in a  $\text{H}_2\text{S}/\text{H}_2$  mixture than in pure  $\text{H}_2$  [134, 135]. Starting from already reduced molybdenum, namely  $\text{Mo}^{4+}$  in  $\text{MoO}_2$ , sulfidation takes place at a lower rate than when reduction and sulfidation are simultaneous (namely when starting from  $\text{Mo}^{6+}$ , i.e.  $\text{MoO}_3$ ). The presence of cobalt (or nickel) probably has a slightly promoting effect on the reduction [136–138] because the corresponding oxides are more easily reduced and sulfided than molybdenum (or tungsten).

The explanation of the coupling effect is probably the following. The reduction of  $\text{MoO}_3$  to  $\text{MoO}_2$  is nucleation rate-limited [139]. Spillover hydrogen accelerates the reaction [115, 140, 141]. Because it adsorbs dissociatively on the surface [139, 142],  $\text{H}_2\text{S}$  probably also produces a reactive H species, promoting nucleation of lower Mo oxides at low temperature and, as a consequence, further reduction. The tiny nuclei of the thus-formed suboxide react easily to sulfides because of their high state

of dispersion. In contrast,  $\text{MoO}_2$  produced by separate reduction has a well organized lattice and is much less reactive.

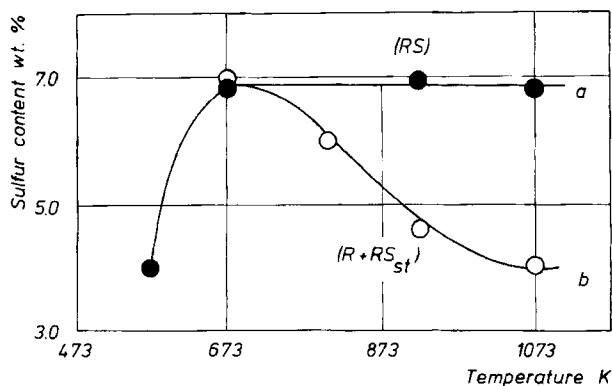
The above conclusions are based on fundamental studies of Steinbrunn and co-workers [139, 143]. The results of these authors also shed some light on the origin of the coupling effect. Upon reduction–sulfidation with pure  $\text{H}_2\text{S}$ , the surface of  $\text{MoO}_3$  is first reduced to  $\text{MoO}_2$ , then sulfided at a much slower rate to  $\text{MoS}_2$  [143]. During reaction with  $\text{H}_2\text{S}/\text{H}_2$  mixtures, a more complicated mechanism sets in, which leads to the formation of highly dispersed  $\text{MoS}_2$  clusters [139, 144].  $\text{MoS}_2$  crystals are formed only at a later stage. The reduction step (to  $\text{MoO}_2$ ) turns out to be slower with  $\text{H}_2\text{S}/\text{H}_2$  than with  $\text{H}_2\text{S}$ . Some refinements were obtained with  $\text{MoO}_3$  thin films [145]. Studies with composite thin films of  $\text{MoO}_3$  evaporated on a freshly cleaned CoO surface indicate that these observations are still valid in the presence of cobalt [146]. The success of the reduction–sulfidation is due to the better balance between reduction and sulfidation rates. Thanks to this better balance, the formation of much smaller  $\text{MoS}_2$  domains (cluster, instead of crystallites) is possible. This is very important for the activation of hydrotreating catalysts, because smaller crystallites of the active phase are finally formed.

A comparison with studies on supported catalysts containing only cobalt or molybdenum [19, 20, 147–149] shows that the simultaneous presence of both elements profoundly alters the processes. This is linked to the existence of the CoMo oxide bilayer, and partly due to the interaction of both elements in the reduction–sulfidation, partly also to the segregation of cobalt from molybdenum in this process. The reduction–sulfidation of cobalt molybdate  $\text{CoMoO}_4$  seems of little relevance [144, 150]; the reason is perhaps that it gets sulfided *before* sufficient reduction, as shown by gravimetry [151].

#### 5.1.4.2 Influence of the Sequence of Steps in Reduction–Sulfidation

The coupling between reduction and sulfidation brings about complex phenomena in the activation of hydrotreating catalysts. A very direct consequence of the above discussion is the different degree of sulfidation reached if the precursor is, on the one hand, simultaneously reduced and sulfided or, on the other hand, reduced first and sulfided afterwards (Fig. 22). Sulfidation of the prereduced catalyst becomes increasingly less efficient as reduction temperature increases. This is presumably due to the growth of  $\text{MoO}_2$  crystallites which become increasingly more refractory to sulfidation. When carried out at low temperature (below about 600 K), a preliminary reduction step is much less harmful. Such a prereduction has even been recommended. The reason is probably that the Group VIII metal gets reduced, segregates and, in the form of sulfide, enhances the production of spillover hydrogen in the subsequent reduction–sulfidation.

The crucial experiment of Fig. 22 can be analyzed in more detail [138].  $\text{Mo}^{5+}$  species can be detected by XPS in series (R + RS), not in series (RS), indicating incomplete reduction. The gain in weight due to sulfidation takes place more rapidly in (RS) than in the (RS) step of (R + RS) experiments. This is paradoxical, as oxygen is removed in (RS), thus partially compensating the weight gain due to the



**Figure 22.** Comparison of the sulfur content of a commercial CoMo catalyst (Procatalyse HR 306) activated by simultaneous reduction–sulfidation (RS) or by reduction followed by sulfidation ( $R + RS_{st}$ ). (a) Simultaneous reduction–sulfidation by a  $H_2S/H_2$  mixture (15%  $H_2S$  by volume). Except for the experiment at 573 K, the samples were first reacted for 4 h at 673 K, then progressively heated to the reaction temperature indicated in the figure and maintained at that temperature for 4 h. (b) Reduction at the indicated temperature for 4 h, followed by sulfidation with the  $H_2S/H_2$  mixture at 673 K for 4 h ( $RS_{st}$  subscript denotes standard temperature) [138].

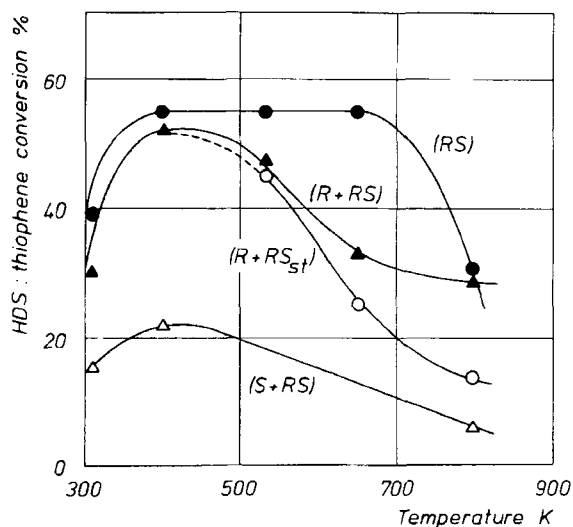
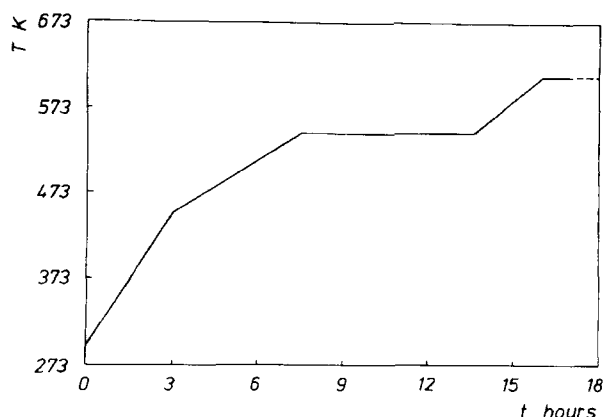
introduction of sulfur by a weight loss. This demonstrates that sulfidation is more rapid when starting from  $Mo^{6+}$  than from reduced forms of molybdenum. NO adsorbed on Mo ions exhibits a special IR band at  $1680\text{--}1700\text{ cm}^{-1}$ , the position of which is characteristic of the reduction state of Mo. After the ( $R + RS$ ) treatment, some deeply reduced Mo ions are present on the surface, whereas in (RS) catalysts only  $Mo^{4+}$  ions are observed. This proves that sulfidation is difficult when starting from  $Mo^{4+}$  ions [134, 138].

#### 5.1.4.3 Influence of Activation Temperature

The changes in activation procedure lead to very large modifications of the activity and selectivity of catalysts, as could be expected from the data of the previous subsection. In view of the previous comments, it is not surprising that activation of HDN or HDS catalysts in the industrial plant must be conducted according to well controlled procedures. The temperature being a major parameter, as suggested by Fig. 22, it is recommended in all in situ activation procedures that the temperature be raised stepwise. Figure 23 is an example of such a temperature vs. time heating procedure. However, the precise procedure to use depends on the catalyst, the nature of the sulfur-containing compound used for sulfidation, and all other operating conditions [128]. The objective of the present discussion is to outline the fundamental phenomena which could justify these procedures.

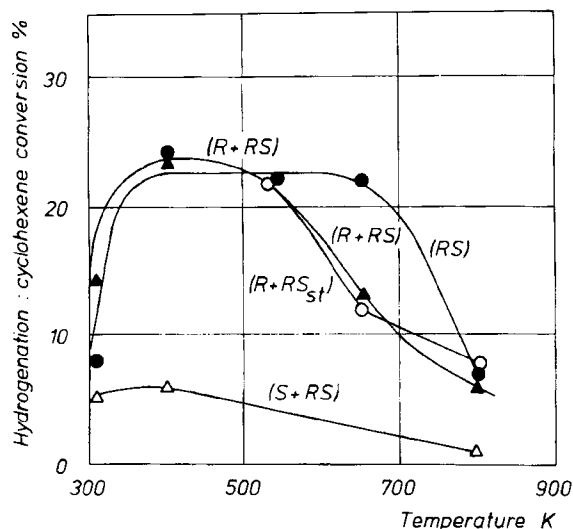
The dramatic influence of temperature is always conspicuous, without consideration of the reduction–sulfidation procedure used. Figures 24 and 25 correspond to activity in hydrodesulfurization and hydrogenation, respectively, where both

**Figure 23.** Typical modification of reactor temperature versus time in the activation of a CoMo/ $\gamma$ -Al<sub>2</sub>O<sub>3</sub> catalyst with a spiked feed.



**Figure 24.** Hydrodesulfurization activity of catalysts (Procatalyse HR 306) activated according to different procedures at different temperatures: (RS) simultaneous reduction–sulfidation (15% H<sub>2</sub>S in H<sub>2</sub>) – except for the experiment at 573 K, the samples were first reacted for 4 h at 673 K, then progressively heated to the temperature indicated in the figure and maintained at this temperature for 4 h; (R + RS) successive reduction in H<sub>2</sub> (4 h) and reduction–sulfidation, as above (4 h), both at the temperature indicated; (R + RS<sub>st</sub>) reduction at the temperature indicated (4 h) followed by reduction–sulfidation at 673 K (4 h) as above; (S + RS) sulfidation by pure H<sub>2</sub>S (4 h) followed by reduction–sulfidation as above (4 h), both steps at the temperature indicated. The reaction with hydrogen with a feed containing 0.5% thiophene and 30% cyclohexene in cyclohexane was made under a total pressure of 3 MPa [138, 152].

reactions (HDS of thiophene and hydrogenation of cyclohexene) occurred simultaneously in a continuous flow equipment under a pressure of 3 MPa [138, 152]. In addition to the procedures used for the results of Fig. 22, samples were also successively reduced and then sulfided at the same temperature (procedure R + RS;



**Figure 25.** Hydrogenation activity of catalysts activated according to different procedures. The experimental conditions are described for Fig. 24 [138, 152].

note that there is here no subscript) or, alternatively, were sulfided by pure  $\text{H}_2\text{S}$  and subsequently reduced-sulfided, at the same temperature ( $\text{S} + \text{RS}$ ). The activities change dramatically. A careful examination of the figure shows that the HDS/hydrogenation selectivity also changes. For the (RS) series, the selectivity varies by a factor larger than 2. Selectivity to HDS is the lowest after activation at 673 K; similar high selectivities are observed for both 573 K and 1073 K [153].

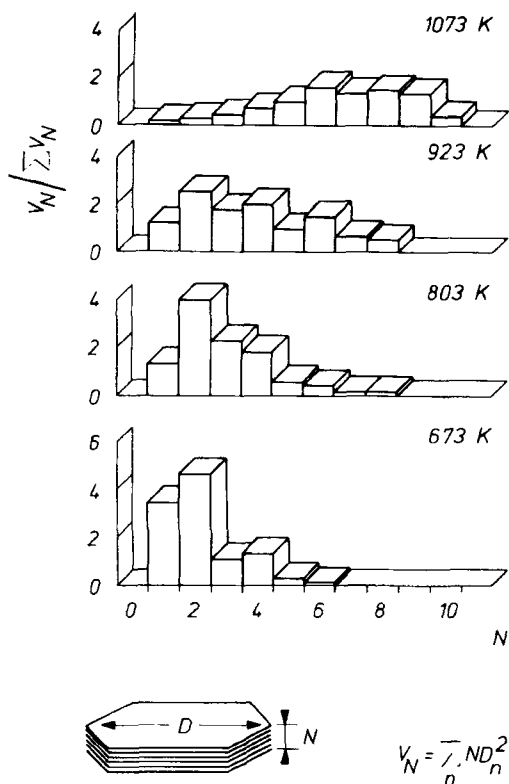
Understandably, the  $\text{MoS}_2$  crystallites grow larger as the activation temperature increases. Electron microscopy shows that the ratio of the total edge plane area to that of the basal planes changes little (by about  $\pm 20\%$ ). The area of the edge planes relative to the volume of the crystallites decreases considerably (by a factor of 5) for activation temperatures growing from 673 to 1073 K [153]. This reflects a proportional change of both the diameter and thickness of the crystallites. Figure 26, which shows the distribution in thickness of the  $\text{MoS}_2$  stacks, indicates how the repartition in size varies with temperature [153]. Infrared studies of adsorbed NO, ISS studies [138, 152, 154] as well as  $^{57}\text{Co}$  Mössbauer emission studies have also been made. When the activation temperature increases, the signal of cobalt pseudoaluminate (or cobalt aluminate-like species) diminishes, indicating that part of the cobalt strongly bound to alumina reacts. The signal attributed to the so-called “Co–Mo–S” phase gets strongly decreased at 923 K, although the catalytic activity remains high (Fig. 27) [152, 155, 156].

Among many studies, three additional systematic studies of the influence of temperature must be cited here [157–159].

#### 5.1.4.4 Influence of the Sulfiding Molecule

It has long been known that the nature of the feed, the spiking of the feed, and the chemical nature of the sulfiding molecules generally, are of considerable importance

**Figure 26.** Variation of the size of the  $\text{MoS}_2$  crystallites on supported CoMo catalyst (Procatalyse HR 306) obtained after activation at different temperatures (procedure RS, see captions for the above figures) as determined by high resolution electron microscopy. The figure considers the collection of crystallites (number  $n$ ) with the same number  $N$  of  $\text{MoS}_2$  layers (thickness  $N$ ). The total volume of each collection can be calculated as indicated in the figure. The fraction in volume (or weight) that each collection represents in the overall sample,  $V_N/\sum V_N$  gives the height of the corresponding bar in the figure [153].

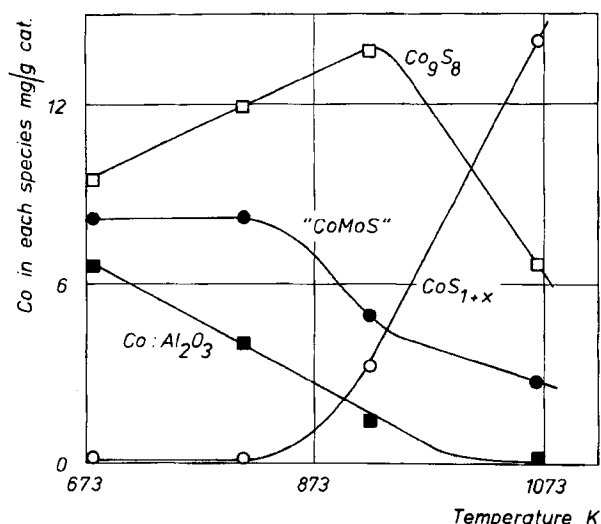


[128, 160, 161]. This is illustrated by Figs 28 and 29 concerning the hydrodesulfurization of thiophene and the hydrogenation of cyclohexene [160]. The optimal temperature for activation is different according to the sulfur containing molecule. As in Figs 24 and 25, it is noteworthy that changing the activating molecule modifies the selectivity.

There is no explanation yet for this effect, except that the very delicate coupling effects between the various elementary reactions mentioned in section 5.1.4.1 are modified when a different source of sulfur is used. The possible formation of highly dispersed carbon in the case of some organic molecules could also explain some differences.

#### 5.1.4.5 Other Results

Other notable data on the reduction-sulfidation of  $\text{CoMo}/\text{Al}_2\text{O}_3$  catalysts can be found in articles not mentioned yet [162, 163]. In a work using supports calcined at various temperatures, incomplete reduction or reduction-sulfidation according to several procedures and characterization of used samples, an attempt has been made to obtain a more in-depth understanding of activation. The merit of the article is to



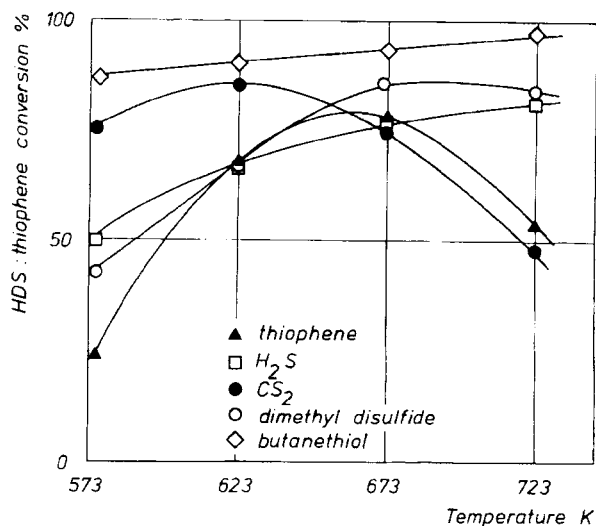
**Figure 27.** Distribution of cobalt among the various species of an activated HDS catalyst, as determined by emission Mössbauer spectroscopy. The catalyst, prepared by impregnation of ammonium heptamolybdate and  $^{57}\text{Co}$  nitrate, was as similar as possible to the commercial one used for obtaining the results presented in the previous figures (3 wt% as  $\text{CoO}$ , 13 wt% as  $\text{MoO}_3$  on  $\gamma$ -alumina). All precautions were taken to avoid possible errors due to noninstantaneous charge compensation in the sequence of nuclear events in  $^{57}\text{Co}$  decay (this has to be taken into account in the nonconducting  $\text{MoS}_2$  matrix) [155, 156].

show that accepted conclusions still hold when the activation is conducted in a wider investigation range than in previous studies [164]. The activation of hydrodesulfurization or hydrodenitrogenation catalysts other than  $\text{CoMo}$  has also been the object of various studies:  $\text{NiMo}$  [165–168],  $\text{NiW}$  [163, 169],  $\text{FeMo}$  [170].

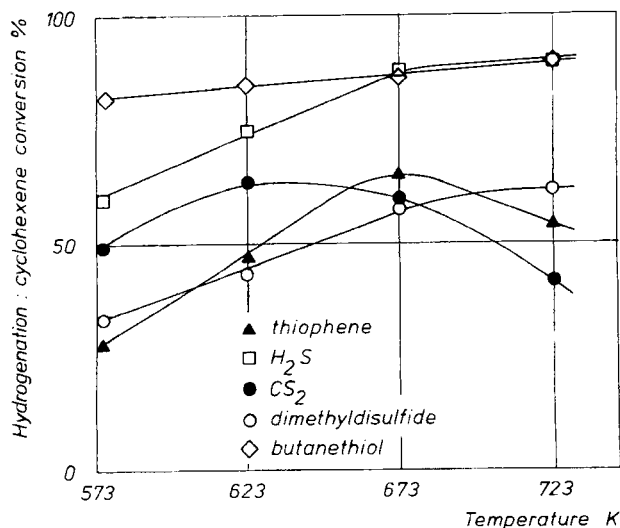
#### 5.1.4.6 Outlook

The tendency at present is to presulfide the catalyst before loading the reactor. This is logical, as it permits a better control of the activation. The control of the activation process is easier in a dedicated plant than in gigantic reactors where temperature control is problematic and uniformity of composition of the sulfiding mixture is practically impossible to achieve.

A new technology is emerging for avoiding the pitfalls of in situ activation. It essentially consists in coating the precursor (oxide) catalyst with a mixture of organic sulfides or polysulfides. The technique had its origin in in situ soaking techniques developed in the late 1970s [128]. Some data are available on some of these new techniques [171]. The effect of this sort of presulfiding with alkylpolysulfides has been discussed [172]. The decomposition of the polysulfides at low temperature



**Figure 28.** Influence of the nature of the sulfiding agent on HDS activity. The catalyst was Pro-catalyse HR 306. The amount of sulfiding agent was calculated in order to obtain a sulfur content of 3 wt% in the charge (hexane). The precursor samples (2 g) were heated in argon ( $36 \text{ L h}^{-1}$ , 3 MPa) up to the desired activation temperature. The argon was then replaced by hydrogen ( $36 \text{ L h}^{-1}$ ) and the feed introduced (liquid hourly space velocity  $42 \text{ h}^{-1}$ ); Activation time was 4 h. Activity measurements were made as explained for Fig. 24 [160].



**Figure 29.** Influence of the nature of the sulfiding agent on hydrogenation activity. Conditions as indicated for Fig. 28 [160].

releases active species which permit sulfidation at low temperature. We speculate that these active species responsible for the efficiency of the process are not only sulfur but also hydrogen.



### 5.1.5 Other Methods of Activation

Some steps at the end of catalyst manufacture are sometimes called activation. This is the case, for example, for the leaching step in the preparation of Raney nickel (Section 3.2); however, this is a special case. A situation which is closer to the topics discussed in the present section is the spontaneous activation which takes place when precursors are contacted with the reacting mixture or feed. It was mentioned in the previous subsection that catalysts were activated in this way in the early development of hydrotreatments. Another example is the activation of vanadium phosphate (VPO) catalysts in the oxidation of butane to maleic anhydride: the fixed-bed VPO catalyst has to be contacted for several days with air-butane mixture before reaching normal activity. This case and that of Raney nickel (both unsupported) fall outside the scope of the present discussion.

### 5.1.6 Conclusions

Although crucial for activity, selectivity, and sustained activity for long periods (catalyst life), the activation of catalysts has not yet been systematically investigated. This article suggests that a methodical study of activation is possible. Scientific interpretation is very often possible and leads to the design of improved procedures. The equipment generally available in most catalysis laboratories, in industry, university, and research institutes, is sufficient for gathering the necessary information. Well established mechanisms explain the phenomena observed. Unfortunately, the science of the reactivity of solids is often ignored, and this hampers proper interpretation and limits the development of improved activation procedures. This article hopefully shows that a better multidisciplinary approach can provide a much clearer picture of the various facets of activation of supported catalysts.

## References

1. J. Haber *Pure Appl. Chem.* **1991**, 63, 1227–1246.
2. A. K. Galwey, *Chemistry of Solids*, Chapman and Hall, London, **1967**, Chapter 5.
3. V. V. Boldyrev, M. Bulens, B. Delmon, *The Control of the Reactivity of Solids*, Elsevier, Amsterdam, **1979**, Chapter 2.
4. W. A. Johnson, R. F. Mehl, *Trans. Amer. Inst. Min. Metall. Engrs.* **1939**, 135, 416–459.
5. K. L. Mampel, *Z. Phys. Chem.* **1940**, A187, 43–57.
6. K. L. Mampel, *Z. Phys. Chem.* **1940**, A187, 235–248.
7. B. Delmon, *Introduction à la cinétique hétérogène*, Ed. Technip, Paris, **1969**, Chapter 11.
8. J. L. Lemaître in *Characterization of Heterogeneous Catalysts* (Ed.: F. Delannay), Marcel Dekker, New York, **1984**, p. 29–70.
9. G. C. Stevens, T. Edmonds in *2nd International Symposium on Preparation of Catalysts* (Eds: B. Delmon, P. Grange, P. A. Jacobs, G. Poncelet), Louvain, la-Neuve, **1978**, 507–517.
10. A. Cimino, B. A. Angelis, *J. Catal.* **1975**, 36, 11–22.
11. B. Delmon in *Interfaces in New Materials* (Eds: P. Grange, B. Delmon), Elsevier, London, **1991**, pp. 1–11.

12. J. Sonnemans, P. Mars, *J. Catal.* **1973**, *31*, 209–219.
13. J. M. J. G. Lipsch, G. C. A. Schuit, *J. Catal.* **1969**, *15*, 174–178.
14. M. Dufaux, M. Che, C. Naccache, *J. Chim. Phys.* **190**, *67*, 527–534.
15. V. H. J. De Beer, T. H. M. van Sint Fiet, J. F. Engelen, A. C. van Haandel, M. V. J. Wolfs, C. H. Hamberg, G. C. A. Schuit, *J. Catal.* **1972**, *27*, 357–368.
16. G. C. A. Schuit, B. C. Gates, *A.I. Che J.* **1973**, *19*, 417–438.
17. W. K. Hall, M. Lojano, in *6th International Congress on Catalysis*, (Eds: G. C. Bond, P. B. Wells, E. C. Tompkins), The Chemical Society, London, **1977**, 246–254.
18. P. Gajardo, R. I. Declerck-Grimée, G. Delvaux, P. Olodo, J. M. Zabala, P. Canesson, P. Grange, B. Delmon, *J. Less-Common Met.* **1977**, *54*, 311–320.
19. R. I. Declerck-Grimée, P. Canesson, R. M. Friedman, J. J. Fripiat, *J. Phys. Chem.* **1978**, *82*, 885–888.
20. R. I. Declerck-Grimée, P. Canesson, R. M. Friedman, J. J. Fripiat, *J. Phys. Chem.* **1978**, *82*, 889–894.
21. P. Canesson, C. Defosse, R. I. Declerck-Grimée, B. Delmon, *5th Ibero-American Symp. on Catalysis*, Lisbon, **1976**, paper A3–8.
22. G. C. Stevens, T. Edmonds in *Chemistry and Uses of Molybdenum* (Eds: P. C. H. Mitchell, A. Seamen), Climax, **1976**, 155–159.
23. A. Miller, W. Atkinson, M. Barber, P. Swift, *J. Catal.* **1971**, *22*, 140–142.
24. A. W. Armour, P. C. H. Mitchell, B. Folkesson, R. Larsson, *J. Less-Common Met.* **1974**, *36*, 361–365.
25. A. Lycourghiotis, C. Defosse, F. Delannay, B. Delmon, *J. Chem. Soc. Faraday Trans. I* **1980**, *76*, 2052–2064.
26. H. Knözinger in *Proceedings 9th International Congress on Catalysis* (Eds: M. J. Phillips, M. Ternan), The Chemical Institute of Canada, Calgary, **1988**, 20–53.
27. B. Delmon, P. Grange, M. A. Apecetche, P. Gajardo, F. Delannay, *C.R. Acad. Sci. Sér. C* **1978**, *287*, 401–403.
28. P. Gajardo, P. Grange, B. Delmon, *J. Catal.* **1980**, *63*, 201–216.
29. F. Delannay, E. N. Haeussler, B. Delmon, *J. Catal.* **1980**, *66*, 469–472.
30. H. Knözinger, H. Jeziorowski, E. Taglauer, *Proc. 7th Intern. Congr. Tokyo* (Eds: T. Seiyama, K. Tanabe), Kodansha and Elsevier, Tokyo and Amsterdam, **1981**, Vol. 1, 604–615.
31. J. B. d'Espinose de la Callère, C. Bobin, B. Rebours, O. Clause in *Preparation of Catalysts VI* (Eds: G. Poncelet, J. Martens, B. Delmon, P. A. Jacobs, P. Grange) Elsevier, Amsterdam, **1995**, 169–184.
32. P. Grange, H. Charcosset, Y. Trambouze, *J. Thermal Anal.* **1969**, *1*, 311–317.
33. Ch. Marcilly, B. Delmon, *J. Catal.* **1972**, *24*, 336–346.
34. A. P. Hagan, C. O. Arean, F. S. Stone, in *Reactivity of Solids* (Eds: J. Wood, O. Lindqvist, C. Helgesson, N. G. Vannerberg), Plenum Press, New York, **1977**, 69–74.
35. M. LoJacono, A. Cimino, G. C. A. Schuit, *Gazz. Chim. Ital.* **1973**, *103*, 1281–1295.
36. M. LoJacono, M. Schiavello, A. Cimino, *J. Phys. Chem.* **1971**, *75*, 1044–1050.
37. M. LoJacono, M. Schiavello, D. Cordischi, G. Mercati, *Gazz. Chim. Ital.* **1975**, *105*, 1165–1176.
38. M. LoJacono, M. Schiavello in *Preparation of Catalysts* (Eds: B. Delmon, P. A. Jacobs, G. Poncelet), Elsevier, Amsterdam, **1976**, 473–484.
39. N. Giordano, J. C. J. Bart, A. Vaghi, A. Castellan, G. Martinotti, *J. Catal.* **1975**, *36*, 81–92.
40. G. N. Asmolov, O. V. Krylov, *Kinet. Katal.* **1970**, *11*, 1028–1033.
41. X. L. Xiong, L. T. Weng, B. Zhou, B. Yasse, E. Sham, L. Daza, F. Gil-Llambias, P. Ruiz, B. Delmon in *Preparation of Catalysts V* (Eds: G. Poncelet, P. Grange, P. A. Jacobs, B. Delmon) Elsevier, Amsterdam, **1991**, p. 537–546.
42. R. Castillo, B. Koch, P. Ruiz, B. Delmon, *J. Mater. Chem.* **1994**, *4*, 903–906.
43. R. Castillo, B. Koch, P. Ruiz, B. Delmon, in *Preparation of Catalysts VI* (Eds: G. Poncelet, J. Martens, B. Delmon, P. A. Jacobs, P. Grange) Elsevier, Amsterdam, **1995**, 291–298.
44. B. Delmon, *J. Mol. Cat.* **1990**, *59*, 179–206.
45. B. Zhou, B. Doumain, B. Yasse, P. Ruiz, B. Delmon in *Proc. 9th Int. Congr. Catalysis* (Eds: M. J. Phillips, M. Ternan), Ottawa, **1988**, *4*, 1850–1857.
46. B. Zhou, E. Sham, P. Bertrand, T. Machej, P. Ruiz, B. Delmon, *J. Catal.* **1991**, *132*, 157–182.

47. L. T. Weng, B. Zhou, B. Yasse, B. Doumain, P. Ruiz, B. Delmon in *Proc. 9th Int. Congr. Catalysis* (Eds: M. J. Phillips, M. Ternan), Ottawa, **1988**, 4, 1609–1616.
48. M. V. E. Rodriguez, B. Delmon, J. P. Damon in *Proc. 7th Int. Congr. on Catalysis* (Eds: T. Seiyama, K. Tanabe), Kodansha and Elsevier, Tokyo and Amsterdam, **1981**, 1141–1153.
49. J. M. D. Tascon, P. Bertrand, M. Genet, B. Delmon, *J. Catal.* **1986**, 97, 300–311.
50. J. Haber, *Pure Appl. Chem.* **1984**, 56, 1663.
51. F. Delannay, P. Gajardo, P. Grange, *J. Microsc. Spectrosc. Electron.* **1978**, 3, 411–426.
52. P. Gajardo, D. Pirotte, C. Defossé, P. Grange, B. Delmon, *J. Electron Spectrosc. Relat. Phenom.* **1979**, 17, 121–135.
53. S. R. Stampfl, Yi Chen, J. A. Dumesic, Chunming Niu, C. G. Gill Jr., *J. Catal.* **1987**, 105, 445–454.
54. DuSung Kim, I. E. Wachs, K. Segawa, *J. Catal.* **1994**, 146, 268–277.
55. M. A. Beñares, Hangchun Hu, I. E. Wachs, *J. Catal.* **1994**, 150, 407–420.
56. P. Gajardo, P. Grange, B. Delmon, *J. Phys. Chem.* **1979**, 83, 1771–1779.
57. P. Gajardo, D. Pirotte, P. Grange, B. Delmon, *J. Phys. Chem.* **1979**, 83, 1780–1786.
58. K. Y. S. Ng, E. Gulari, *J. Catal.* **1985**, 92, 340–354.
59. Y. C. Liu, G. L. Griffin, S. S. Chan, I. E. Wachs, *J. Catal.* **1985**, 94, 108–119.
60. G. C. Bond, S. Flamerz, L. van Wijk, *Catal. Today* **1987**, 1, 229–243.
61. J. G. Eon, E. Bordes, A. Vejux, P. Courtine, in *Proc. 9th Int. Symp. Reactivity of Solids* (Eds: K. Dyrek, J. Haber, J. Nowotny), Cracow, PWN, Warsaw, **1982**, Vol. 2, 603–612.
62. T. Machej, B. Doumain, B. Yasse, B. Delmon, *J. Chem. Soc., Faraday Trans 1* **1988**, 84, 3905–3916.
63. M. El Jamal, PhD Thesis, Université Claude Bernard, Lyon, **1987**.
64. M. El Jamal, M. Forissier, G. Coudurier, J. C. Védrine, in *Proc. 9th Int. Congr. Catalysis* (Eds: M. J. Phillips, M. Ternan), Ottawa, **1988**, 4, 1617–1623.
65. P. Biloen, G. T. Pott, *J. Catal.* **1973**, 30, 169–174.
66. A. Castellan, J. C. J. Bart, A. Vaghi, N. Giordano, *J. Catal.* **1976**, 42, 162–172.
67. V. H. J. De Beer, M. J. M. Van der Aalst, C. J. Machiels, G. C. A. Schuit, *J. Catal.* **1976**, 43, 78–89.
68. S. Narayanan, K. Uma, *J. Chem. Soc Faraday Trans. I* **1985**, 81, 2733–2744.
69. F. Delannay, *Characterization of Heterogeneous Catalysts*, Marcel Dekker, New York, **1984**, 113–115.
70. W. E. Garner, *Chemistry of Solids*, Butterworth, London, **1955**.
71. J. S. Anderson, M. W. Roberts, F. S. Stone, *Reactivity of Solids*, Chapman and Hall, London, **1973**.
72. J. Wood, O. Lindqvist, C. Helgesson, N.-G. Vannerberg, *Reactivity of Solids*, Plenum Press, New York and London, **1977**.
73. K. Dyrek, J. Haber, N. Nowotny, *Proc. 9th Int. Symp. Reactivity of Solids*, Elsevier, Amsterdam, **1982**.
74. P. Barret, L. C. Dufour, *Reactivity of Solids*, Elsevier, Amsterdam, **1985**.
75. P. Barret, *Cinétique hétérogène*, Gauthier-Villars, Paris, **1973**.
76. J. Szekeley, J. W. Evans, Hong Yong Sohn, *Gas-solid reactions*, Academic Press, New York, **1976**.
77. M. Montes, Ph.D. Thesis, Université Catholique de Louvain, **1984**.
78. B. Delmon, M. Houalla in *Preparation of Catalysts II* (Eds: B. Delmon, P. Grange, P. A. Jacobs, G. Poncelet), Elsevier, Amsterdam, **1979**, 439–464.
79. M. Houalla, F. Delannay, I. Matsuura, B. Delmon, *J. Chem. Soc., Faraday Trans. I* **1980**, 76, 2128–2141.
80. J. W. E. Coenen in *Preparation of Catalysts II* (Eds: B. Delmon, P. Grange, P. A. Jacobs, G. Poncelet), Elsevier, Amsterdam, **1979**, 89–111.
81. A. Roman, B. Delmon, *J. Catal.* **1973**, 30, 333–342.
82. M. P. Rosynek, C. A. Polansky, *Appl. Catal.* **1991**, 73, 97–112.
83. M. Montes, Ch. Penneman de Bosscheyde, B. K. Hodnett, F. Delannay, P. Grange, B. Delmon, *Appl. Catal.* **1984**, 12, 309–330.
84. J. A. Moulijn, P. W. N. M. van Leeuwen, R. A. van Santen, *Catalysis*, Elsevier, Amsterdam, **1993**, 355.

85. J. Masson, J. Nechtschein, *Bull. Soc. Chim. Fr.* **1968**, 3933.
86. E. I. Ko, J. M. Hupp, F. H. Rogan, N. J. Wagner, *J. Catal.* **1983**, *84*, 85–94.
87. L. A. M. Hermans, J. W. Geus in *Preparation of Catalysts II* (Eds: B. Delmon, P. Grange, P. A. Jacobs, G. Poncelet), Elsevier, Amsterdam, **1979**, 113–142.
88. M. Houalla, B. Delmon in *Reactivity of Solids* (Eds: K. Dyrek, J. Haber, J. Nowotny), Elsevier, Amsterdam, **1982**, 923–926.
89. M. Houalla, B. Delmon, *J. Phys. Chem.* **1980**, *84*, 2194–2199.
90. M. Houalla, B. Delmon, *C.R. Acad. Sci. Paris, Sér. C.* **1980**, *290*, 301–303.
91. M. Houalla, J. Lemaître, B. Delmon, *J. Chem. Soc., Faraday Trans. I* **1982**, *78*, 1389–1400.
92. M. Houalla, B. Delmon, *C.R. Acad. Sci. Paris, Sér. C.* **1979**, *289*, 77–80.
93. A. Lycourghiotis, C. Defossé, B. Delmon, *Rev. Chim. Minérale* **1979**, *16*, 473–476.
94. A. Lycourghiotis, C. Defossé, F. Delannay, J. Lemaître, B. Delmon, *J. Chem. Soc., Faraday Trans. I* **1980**, *76*, 1677–1688.
95. A. Lycourghiotis, C. Defossé, F. Delannay, B. Delmon, *J. Chem. Soc., Faraday Trans. I* **1980**, *76*, 2052–2064.
96. A. Lycourghiotis, C. Defossé, B. Delmon, *Bull. Soc. Chim. Belg.* **1980**, *89*, 929–935.
97. M. Houalla, F. Delannay, B. Delmon, in *Preprints 7th Canadian Symp. on Catalysis* (Eds: S. E. Wanke, S. K. Chakrabarty), Chemical Institute of Canada, **1980**, 158–165.
98. M. Houalla, F. Delannay, B. Delmon, *J. Phys. Chem.* **1981**, *85*, 1704–1709.
99. J. M. Porto Lopez, S. Ceckiewicz, C. Defossé, P. Grange, B. Delmon, *Appl. Catal.* **1984**, *12*, 331–346.
100. F. M. Mulcahy, M. Houalla, D. M. Hercules, *J. Catal.* **1987**, *106*, 210–215.
101. Ch. Papadopoulou, A. Lycourghiotis, P. Grange, B. Delmon, *Appl. Catal.* **1988**, *38*, 255–271.
102. H. K. Matralis, A. Lycourghiotis, P. Grange, B. Delmon, *Appl. Catal.* **1988**, *38*, 273–287.
103. M. Houalla, B. Delmon, *Appl. Catal.* **1981**, *1*, 285–289.
104. M. Houalla, F. Delannay, B. Delmon, *J. Electron. Spectr. Relat. Phen.* **1982**, *25*, 59–95.
105. H. Lafiteau, E. Néel, C. Clément in *Preparation of Catalysts* (Eds: B. Delmon, P. A. Jacobs, G. Poncelet), Elsevier, Amsterdam, **1976**, 393–404.
106. J. P. R. Vissers, S. M. A. M. Bouwens, V. H. J. de Beer, R. Prins in *Proc. Symp. on Fundamental Chemistry of Promoters and Poisons in Heterogeneous Catalysis*, American Chemical Society, New York, April 13–18, **1986**, 227.
107. A. Stanislaus, M. Absi-Halabi, K. Al-Dolama, *Appl. Catal.* **1988**, *39*, 239–253.
108. P. Atanasova, R. Halachev, *Appl. Catal.* **1988**, *38*, 235–240.
109. M. M. Ramírez de Agudelo, A. Morales in *Proc. 9th International Congress on Catalysis* (Eds: M. J. Phillips, M. Ternan), The Chemical Institute of Canada, Calgary, **1988**, Vol. 1, 42–49.
110. S. Narayanan, K. Uma, *J. Chem. Soc., Faraday Trans. I* **1988**, *84*, 521–527.
111. E. J. Novak, R. M. Koros, *J. Catal.* **1967**, *7*, 50–56.
112. E. J. Novak, *J. Phys. Chem.* **1969**, *73*, 3790.
113. W. Verhoeven, B. Delmon, *Bull. Soc. Chim.* **1966**, 3065–3073.
114. W. Verhoeven, B. Delmon, *Bull. Soc. Chim.* **1966**, 3073–3079.
115. H. Charcosset, B. Delmon, *Ind. Chim. Belg.* **1973**, *38*, 481–495.
116. J. T. Richardson, R. J. Dubus, J. G. Crump, P. Desai, U. Osterwalder, T. S. Cale, in *Preparation of Catalysts II* (Eds: B. Delmon, P. Grange, P. A. Jacobs, G. Poncelet), Elsevier, Amsterdam, **1979**, 131–142.
117. E. B. Doesburg, S. Orr, J. R. H. Ross, L. L. van Rijen, *J. Chem. Soc., Chem. Comm.* **1977**, *20*, 734–735.
118. H. Praliaud, G. A. Martin, *J. Catal.* **1981**, *72*, 394–396.
119. R. Frety, L. Tournayan, M. Primet, G. Bergeret, M. Guenin, J. B. Baumgartner, A. Borgna, *J. Chem. Soc., Faraday Trans.* **1993**, *89*, 3313–3318.
120. G. A. Martin, C. Mirodatos, H. Praliaud, *Appl. Catal.* **1981**, *1*, 367–382.
121. J. Cosyns, M.-T. Chênebaux, J. F. Le Page, R. Montarnal in *Preparation of Catalysts* (Eds: B. Delmon, P. A. Jacobs, G. Poncelet), Elsevier, Amsterdam, **1976**, 459–472.
122. Sun-Hua Chen, Hsiau-Wen Huang, Kuang-Lieh Lu, *Bull. Inst. Chem. Acad. Sinica* **1985**, *32*, 9.
123. B. S. Clausen, H. Topsøe, S. Mørup, *Appl. Catal.* **1989**, *48*, 327–340.
124. J. M. Dumas, C. Geron, A. Kribii, J. Barbier, *Appl. Catal.* **1989**, *47*, L9–L15.

125. L. M. Strubinger, G. L. Geoffroy, M. A. Vannice, *J. Catal.* **1985**, 96, 72–81.
126. D. Duprez, M. Mendez in *Catalyst Deactivation* (Eds: B. Delmon, G. F. Froment), Elsevier, Amsterdam, **1987**, 525–534.
127. D. S. Thakur, M. G. Thomas, *Appl. Catal.* **1985**, 15, 197–225.
128. H. Hallie, *Oil Gas J.*, **1982**, Dec. 20, 69–74.
129. B. Delmon in *Catalysts in Petroleum Refining 1989* (Eds: D. L. Trimm, S. Akashah, M. Absi-Halabi, A. Bishara), Elsevier, Amsterdam, **1990**, 1–40.
130. B. Delmon, *Latin American Appl. Res.*, **1995**, **1996**, 26, 87–97.
131. B. Delmon, *Bull. Soc. Chim. Belg.*, **1995**, 104, 173–187.
132. K. Inamura, R. Prins, *TOCAT2*, Tokyo, August 7–11, **1994**, Abstracts, 111–112.
133. B. Delmon in *Reactivity of Solids* (Eds: K. Dyrek, J. Haber, J. Nowotny), Elsevier, Amsterdam, **1982**, 327–369.
134. J. M. Zabala, P. Grange, B. Delmon, *C.R. Acad. Sc. Paris, Sér. C*, **1974**, 279, 725–728.
135. H. Zahradníková, V. Kárník, L. Beránek, *Coll. Czech. Chem. Comm.* **1985**, 50, 1573.
136. J. M. Zabala, P. Grange, B. Delmon, *C.R. Acad. Sc. Paris. Sér. C* **1974**, 279, 561–563.
137. J. M. Zabala, P. Grange, B. Delmon, *C.R. Acad. Sc. Paris. Sér. C* **1975**, 280, 1129–1132.
138. R. Prada Silvy, J. L. G. Fierro, P. Grange, B. Delmon in *Preparation of Catalysts IV* (Eds: B. Delmon, P. Grange, P. A. Jacobs and G. Poncelet), Elsevier, Amsterdam, **1987**, 605–617.
139. A. Steinbrunn, C. Lattaud, *Surf. Sci.* **1985**, 155, 279–295.
140. D. K. Lambiev, T. T. Tomova, G. V. Samsonov, *Powder Metall. Intern.* **1972**, 4, 17.
141. J. Masson, B. Delmon, J. Nechtschein, *C.R. Acad. Sci. Paris*, **1968**, 266, 428.
142. A. Steinbrunn, J. C. Colson, C. Lattaud, C. G. Gachet, L. de Mourgues, M. Vrinat, J. P. Bonnelle in *Reactivity of Solids* (Eds: P. Barret, L. C. Dufour), Elsevier, Amsterdam, **1985**, 1079–1080.
143. A. Steinbrunn, C. Lattaud, H. Reteno, J. C. Colson in *Physical Chemistry of the solid state: applications in metals and their compounds* (Ed.: P. Lacombe), Elsevier, Amsterdam, **1984**, 551–563.
144. G. L. Schrader, C. P. Cheng, *J. Catal.* **1984**, 85, 488–498.
145. P. A. Spevak, N. S. McIntyre, *J. Phys. Chem.* **1993**, 97, 11031–11036.
146. A. Steinbrunn, M. Bordignon, *Bull. Soc. Chim. Belg.* **1987**, 96, 941–949.
147. R. Thomas, E. M. van Oers, V. H. J. de Boer, J. A. Moulijn, *J. Catal.* **1983**, 84, 275–287.
148. B. Scheffer, P. Arnoldy, J. A. Moulijn, *J. Catal.* **1988**, 112, 516–527.
149. B. Scheffer, N. J. J. Dekker, P. J. Mangnus, J. A. Moulijn, *J. Catal.* **1990**, 121, 31–46.
150. T. I. Korányi, I. Manniger, Z. Paál, O. Marks, J. R. Günter, *J. Catal.* **1989**, 116, 422–439.
151. D. Pirotte, P. Grange, B. Delmon in *Reactivity of Solids* (Eds: K. Dyrek, J. Haber, J. Nowotny), Elsevier, Amsterdam, **1982**, 973–977.
152. R. Prada Silvy, P. Grange, B. Delmon in *Catalysts in Petroleum Refining 1989* (Eds: D. L. Trimm, S. Akashah, M. Absi-Halabi, A. Bishara), Elsevier, Amsterdam, **1990**, 233–260.
153. R. Prada Silvy, F. Delannay, B. Delmon, *Indian J. Technol.* **1987**, 25, 627–638.
154. R. Prada Silvy, J. M. Beuken, J. L. G. Fierro, P. Bertrand, B. Delmon, *Surf. Interf. Anal.* **1986**, 8, 167–172; **1986**, 9, 247.
155. J. Ladrière, R. Prada Silvy, *Hyperfine Interactions* **1988**, 41, 653–656.
156. R. Prada Silvy, Ph.D Thesis, Université Catholique de Louvain, **1987**.
157. V. Stuchly, K. Klusáček, *Appl. Catal.* **1987**, 34, 263–273.
158. Seo Il Kim, Seong Ihl Woo, *Appl. Catal.* **1991**, 74, 109–123.
159. P. J. Mangnus, E. K. Poels, J. A. Moulijn, *Ind. Eng. Chem. Res.* **1993**, 32, 1818–1821.
160. R. Prada Silvy, P. Grange, F. Delannay, B. Delmon, *Appl. Catal.* **1989**, 46, 113–129.
161. T. I. Korányi, I. Manninger, Z. Paál, *Solid State Ionics*, **1989**, 32–33, 1012–1018.
162. M. W. J. Crajé, V. H. J. de Beer, J. A. R. van Veen, A. M. van der Kraan, *J. Catal.* **1993**, 143, 601.
163. P. J. Mangnus, A. Bos, J. A. Moulijn, *J. Catal.* **1994**, 146, 437–448.
164. T. I. Korányi, M. Schikorra, Z. Paál, R. Schlögl, J. Schütze, M. Wesemann, *Appl. Surf. Sci.* **1993**, 68, 307–317.
165. R. Badilla-Ohlbaum, D. Chadwick in *Catal., Proc. 7th Intern. Congress* (Eds: T. Seiyama, K. Tanabe), Kodansha and Elsevier, Tokyo and Amsterdam, **1981**, 2, 1126–1140.

166. J. Abart, E. Delgado, G. Ertl, H. Jeziorowski, H. Knözinger, N. Thiele, X. Zh. Wang, E. Taglauer, *Appl. Catal.* **1982**, 2, 155–176.
167. F. Maugé, J. C. Duchet, J. C. Lavalley, S. Houssenbay, E. Payen, J. Grimblot, S. Kasztelan, *Catal. Today*, **1991**, 10, 561–577.
168. V. L. S. Teixeira da Silva, R. Frety, M. Schmal, *Ind. Eng. Chem. Res.* **1994**, 33, 1692–1699.
169. M. Breysse, M. Cattenot, T. Decamp, R. Frety, C. Gachet, M. Lacroix, C. Leclercq, L. de Mourgues, J.-L. Portefaix, M. Vrinat, M. Houari, J. Grimblot, S. Kasztelan, J.-P. Bonnelle, S. Housni, J. Bachelier, J.-C. Duchet, *Catal. Today*, **1988**, 4, 39–55.
170. W. L. T. M. Ramselaar, M. W. J. Crajé, E. Gerkema, V. H. J. de Beer, A. M. van der Kraan, *Bull. Soc. Chim. Belg.* **1987**, 96, 931–939.
171. S. R. Murff, E. A. Carlisle, P. Dufresne, H. Rabehasaina, *Symp. on Regeneration, Reactivation and Reworking of Spent Catalysts*, Div. Petrol. Chem. ACS, Denver, Preprints, **1993**, 34, 81–86.
172. J. van Gestel, J. Leglise, J.-C. Duchet, *J. Catal.* **1994**, 145, 429–436.

## 5.2 Catalyst Forming\*

J. F. LE PAGE

The order in which the calcining and forming operations are carried out varies from case to case. If calcination causes much textural change, it will destroy the results of an earlier forming operation. This happens with crystallized precursors that are better formed after calcining, and then possibly recalcined after forming to improve mechanical resistance. If calcining does not radically change the texture, it can precede forming. This happens with certain xerogels that are shaped like balls or beads and whose mechanical resistance is enhanced by a well-run calcination.

Two extreme types of forming can be distinguished, depending on whether the desired product is powder microgranules or granules on the order of one to several millimeters 1.

### 5.2.1 Forming Microgranules

Crushing and grinding often serve only to prepare a charge for forming into granules. As a general rule, crushing and grinding is done by generating successive shocks between the product to be crushed and a very hard mass making up the grinder or crusher. The necessary kinetic energy is either furnished by the product, as in cyclone-pulverizers, or more usually by the equipment, as in ball-crushers and mixer-grinders. The lower limit of size for the powder is a few microns. (Such a powder is not usable in fluidized beds because its mechanical resistance is too low).

---

\* Reprinted with permission from J. F. Le Page, *Applied Heterogeneous Catalysis – Design, Manufacture, Use of Solid Catalysts*, Editions Technip, Paris, 1987.

166. J. Abart, E. Delgado, G. Ertl, H. Jeziorowski, H. Knözinger, N. Thiele, X. Zh. Wang, E. Taglauer, *Appl. Catal.* **1982**, 2, 155–176.
167. F. Maugé, J. C. Duchet, J. C. Lavalley, S. Houssenbay, E. Payen, J. Grimblot, S. Kasztelan, *Catal. Today*, **1991**, 10, 561–577.
168. V. L. S. Teixeira da Silva, R. Frety, M. Schmal, *Ind. Eng. Chem. Res.* **1994**, 33, 1692–1699.
169. M. Breyse, M. Cattenot, T. Decamp, R. Frety, C. Gachet, M. Lacroix, C. Leclercq, L. de Mourgues, J.-L. Portefaix, M. Vrinat, M. Houari, J. Grimblot, S. Kasztelan, J.-P. Bonnelle, S. Housni, J. Bachelier, J.-C. Duchet, *Catal. Today*, **1988**, 4, 39–55.
170. W. L. T. M. Ramselaar, M. W. J. Crajé, E. Gerkema, V. H. J. de Beer, A. M. van der Kraan, *Bull. Soc. Chim. Belg.* **1987**, 96, 931–939.
171. S. R. Murff, E. A. Carlisle, P. Dufresne, H. Rabehasaina, *Symp. on Regeneration, Reactivation and Reworking of Spent Catalysts*, Div. Petrol. Chem. ACS, Denver, Preprints, **1993**, 34, 81–86.
172. J. van Gestel, J. Leglise, J.-C. Duchet, *J. Catal.* **1994**, 145, 429–436.

## 5.2 Catalyst Forming\*

J. F. LE PAGE

The order in which the calcining and forming operations are carried out varies from case to case. If calcination causes much textural change, it will destroy the results of an earlier forming operation. This happens with crystallized precursors that are better formed after calcining, and then possibly recalcined after forming to improve mechanical resistance. If calcining does not radically change the texture, it can precede forming. This happens with certain xerogels that are shaped like balls or beads and whose mechanical resistance is enhanced by a well-run calcination.

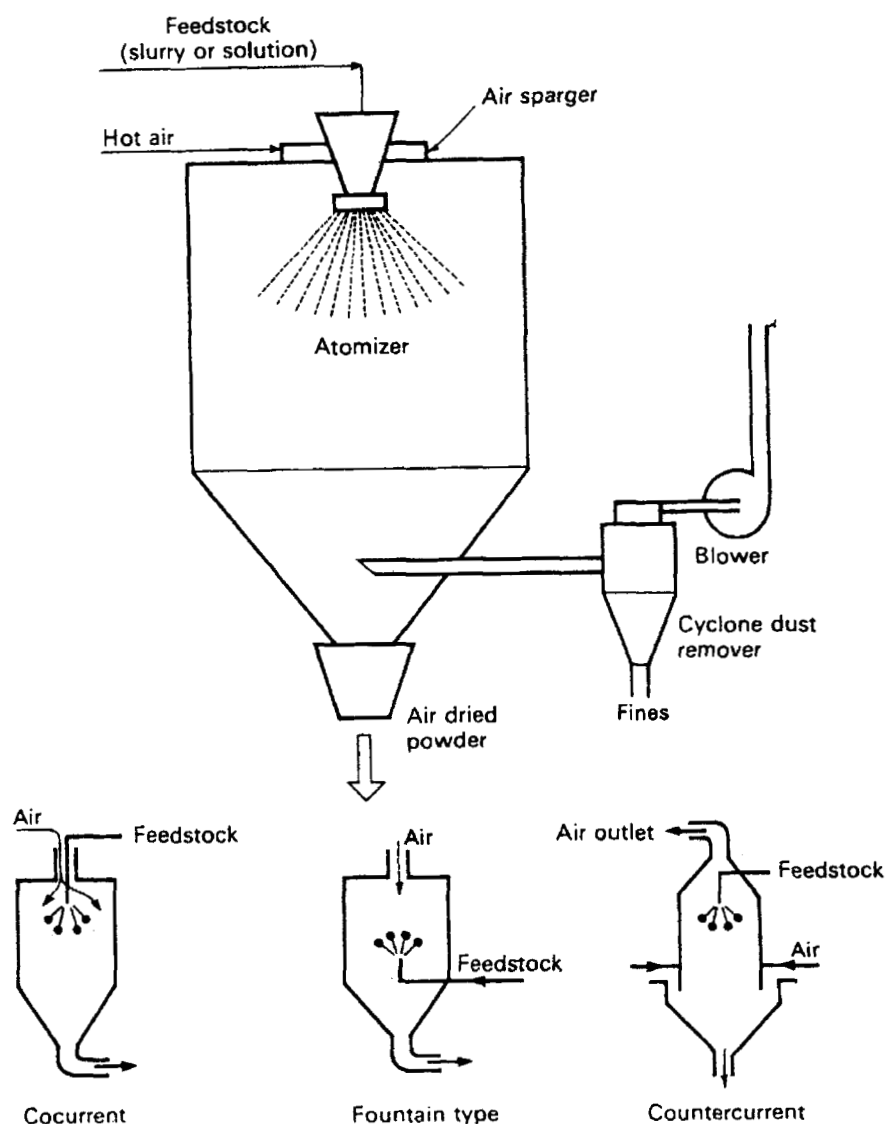
Two extreme types of forming can be distinguished, depending on whether the desired product is powder microgranules or granules on the order of one to several millimeters 1.

### 5.2.1 Forming Microgranules

Crushing and grinding often serve only to prepare a charge for forming into granules. As a general rule, crushing and grinding is done by generating successive shocks between the product to be crushed and a very hard mass making up the grinder or crusher. The necessary kinetic energy is either furnished by the product, as in cyclone-pulverizers, or more usually by the equipment, as in ball-crushers and mixer-grinders. The lower limit of size for the powder is a few microns. (Such a powder is not usable in fluidized beds because its mechanical resistance is too low).

---

\* Reprinted with permission from J. F. Le Page, *Applied Heterogeneous Catalysis – Design, Manufacture, Use of Solid Catalysts*, Editions Technip, Paris, 1987.

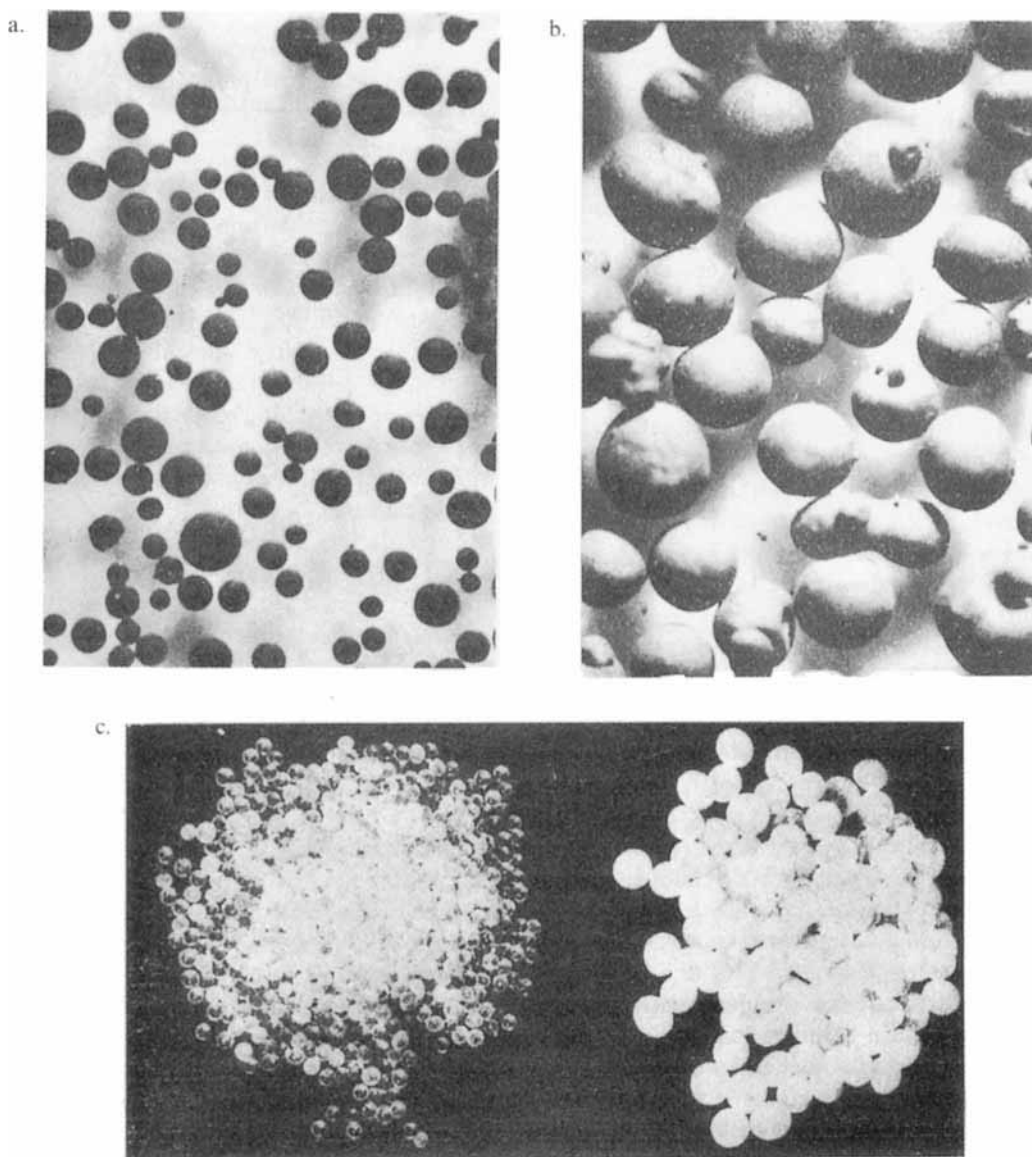


**Figure 1.** A typical air drier system for various flow patterns.

Spray-drying, shown schematically in Fig. 1, accomplishes forming and drying at the same time. It consists of spraying microdroplets of the product to be dried into a hot gas current. It is suitable only for making small-diameter beads (7–700  $\mu\text{m}$ ), because the violence of the treatment provokes local superheating in the solids, leading to difficulty in releasing steam that is suddenly produced, with consequent mechanical degradation of large beads.

Spray drying is used for obtaining cracking catalysts in the form of microbeads

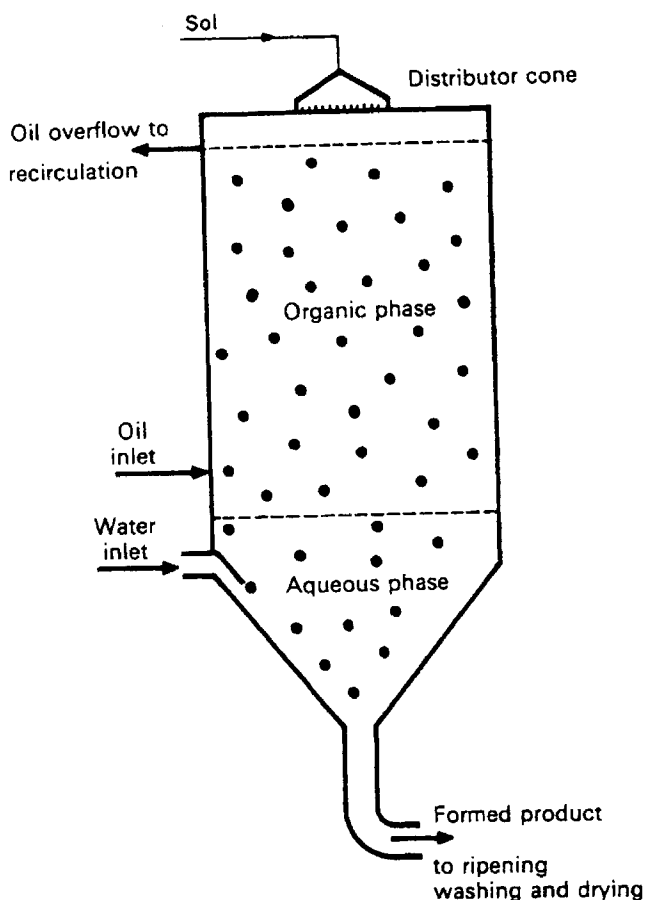




**Figure 2.** Production of micrograins. a. Atomized product 70–160  $\mu\text{m}$ . b. Atomized product 380–570  $\mu\text{m}$ . c. TC catalyst formed in an oil-drop. On the left, after thermal activation,  $d_p = 3 \text{ mm}$ . On the right, before drying,  $d_p = 8\text{--}9 \text{ mm}$ .

(silica–alumina or silica–alumina doped with 5–15% of  $X$  or  $Y$  molecular sieves exchanged with rare earth). Figure 2a and 2b show two different kinds of particle obtained by different atomizations of a given feed to a spray dryer.

Drop coagulation results from metastable sols suspended in a different liquid



**Figure 3.** The oil-drop coagulation system.

phase, and can simultaneously achieve gelling, ripening and forming. Figure 3 illustrates a reactor of the oil-drop type. The aqueous sol is distributed in the form of droplets by a sparger whose orifices are sized to give the desired diameter of bead. The droplets settle through the water-immiscible solvent, whose temperature is raised to around  $100^{\circ}\text{C}$ . The surface tension created on the droplets during passage through the solvent permits formation of gel spheres that must be ripened and ultimately dried. During drying, a contraction of the bead without deterioration is observed as long as the diameter is not too large. Accordingly, this treatment is suitable for producing either microbeads or beads on the order of a few millimeters, such as the silica-alumina beads used in thermofor catalytic cracking (TCC) shown in Fig. 2c.

The operating variables for drop coagulation are: temperature, contact time, sol composition, pH, and the nature of the continuous phase (density, surface tension, etc.). The injection can be done at the top or bottom of the column (oil-drop or oil-up) depending on relative densities.

**Table 1.** Influence of starting material on the choice of a grain-forming process.

Starting material	Process
Monolithic blocks	Crushing and grinding
Powders	Pelletizing
	Granulation
	Extrusion
Pastes, hydrogels	Extrusion
Sols	Drop coagulation
Melted solids	Spray-drying

In drop-coagulation to form beads of alumina hydroxide, the top of a column holding oil and 100 °C is fed with a blend of a sol of aluminium oxychloride and hexamethylene tetramine. Under the influence of the temperature, the amine is decomposed to liberate ammonia, which neutralizes the chloride ions. The product is then ripened, dried, calcined and can be used as a support for reforming catalysts or hydrodesulfurization catalysts [2]. In the same way, a silica sol feeding the bottom of a column of trichloroethylene at around 75 °C permits obtaining silica beads at the top.

## 5.2.2 Forming Granules

The raw material comprises a calibrated powder or paste with suitable rheological properties. No matter what method is to be used, the charge should show properties of fluidity and adhesiveness. Table 1 summarizes methods used for making granules according to the nature of the original charge, whether pelletizing, extrusion, pan granulation, or miscellaneous methods.

### 5.2.2.1 Pelletizing

This consists of compressing a certain volume of usually dry powder in a die between two moving punchers, one of which also serves to eject the formed pellet. Fluidity of the powder is required to assure homogeneous filling of the die; a certain amount of plasticity is desirable in the granules to create the maximum contact between them; and the quality of the intergranular contacts will depend, after compression, on the adhesive properties of the powder.

If a powder does not have all the required qualities, one can add lubricants to aid the sliding and positioning of the microgranules. Such lubricants can be liquid (water, mineral oil) or solid (talc, graphite, stearic acid, and various stearates). Binders are also added to increase the post-compression adhesion, as for example starch is added for pelletizing active carbon. An increase in the adhesive forces due to chemical bonds resulting from contact between the granules can also be achieved by peptizing the microgranules, whose surfaces are thus made more chemically reactive.

Some of the operating variables are characteristic of the equipment (i.e., pressure, rhythm, and frequency of vibration to accelerate the flow of powder into the die), while others depend on the charge and, for a given powder, on the granulometry, the kind and concentration of binders, and the lubricants. The ratio of the diameter of the powder particles to that of the final granules should fall between 1/20 and 1/50.

A conventional industrial pelletizer equipped with around thirty dies can produce 5–10 liter/h of pellets a few millimeters in diameter. Such pellets are usually cylindrical with flat or rounded base surfaces (better distribution of the compression forces); however spheres, hollow cylinders, and toroids can also be obtained.

### 5.2.2.2 Extrusion

Extrusion is a rather general technique applied to pastes; one device forces the paste through a die, while another cuts off the extruded material at the desired length. The ease of extrusion and quality of the product depend on the following properties of the paste:

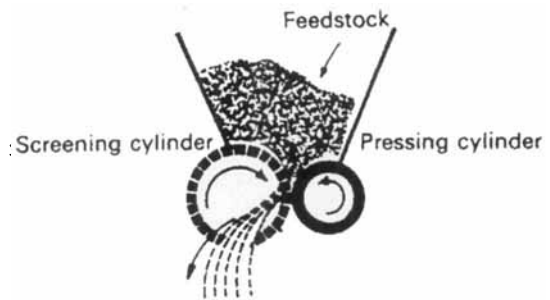
- (a) Viscosity: A non-thixotropic product that is too viscous will block the extruder. A product that lacks in viscosity can not be extruded with a screw and will give extrudates without mechanical resistance when extruded by a press.
- (b) Thixotropy: Certain substances become less viscous under shearing forces, and then recover their initial state after the forces have been released for a time called the relaxation time. The existence of such thixotropic properties is eminently favorable for the flow of a paste and formation of a solid granule at the exit of a die, providing the relaxation time is short enough.
- (c) Stability: Under extrusion conditions, there should be no dynamic sedimentation of the product through exuding water and forming a paste that is too viscous.
- (d) Homogeneity: The paste must be homogeneous to assure that the quality of the product is constant. When necessary, the paste is homogenized in a mixer-kneader under controlled conditions of temperature, time, and pH. An excess of kneading can in fact compact the material and suppress potential macropores. Screw extruders partially knead the paste as it travels along the screw.

Extruding equipment can be classed in one of two categories: press extruders (Fig. 4) and screw extruders (Fig. 5). Press extruders are used principally for pastes that are viscous; screw extruders are preferred for thixotropic products.

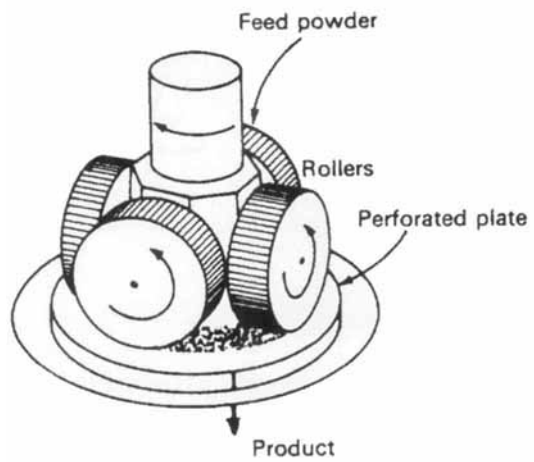
Even for a given charge with specific properties, the operating variables are rather poorly defined and are closely related to the type of equipment. Generally they include: temperature, addition of binders and lubricants to modify viscosity and thixotropy, as for example additions of alginates, starch, kaolinite and montmorillonite.

Extrusion granules generally occur as cylinders 0.5–10.0 mm in diameter. Hollow cylinders can also be obtained with special dies.

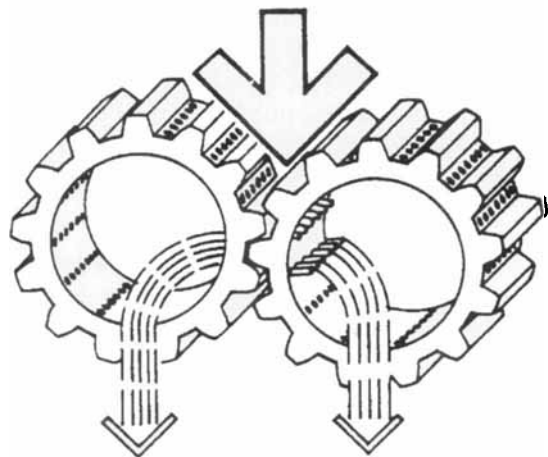
It should be borne in mind that the conditions of extrusion sometimes lend themselves well to certain hydrothermal transformations.



Machine GA65

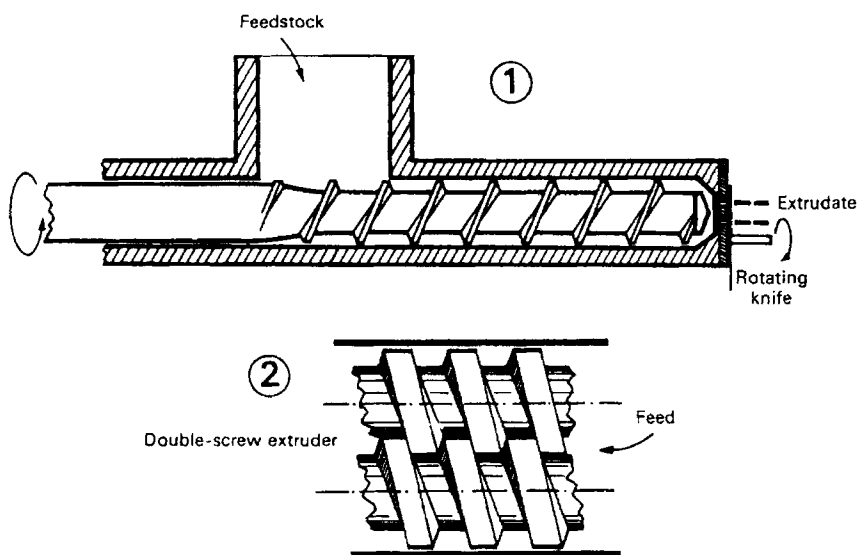


Roller press



Gear press

**Figure 4.** Operating principles of extrusion machines.



**Figure 5.** Operating principles of screw-extruders. (1) Single screw extruder. (2) Double turning screws, which permit a better mix, higher compression, and higher shear.

### 5.2.2.3 Pan Granulation

This consists of agglomerating a powder into beads by moistening it as it rolls about in a rotating pan (Fig. 6). Seed granules are coated with humidified powder under the effect of capillary tensions to give a bead of increasing diameter, by a kind of snow-ball phenomenon. The discharge of the beads in the desired size is accomplished through centrifuging. The granulation operation is followed by a ripening period that starts in the bowl. To achieve good granulation the powder must be rather fine ( $d_p < 50\ \mu\text{m}$ ). For a powder with given internal properties the operating variables are: speed of rotation, inclination of the pan, rate of flow of water, and nature and quantity of the added binders.

Pan granulation is not expensive but has the drawback that the product has a rather wide size distribution, necessitating a screening operation afterwards. The diameter of the beads can vary from 1 mm to 20 mm.

### 5.2.2.4 Miscellaneous Forming Operations

Leaching by chemically dissolving the aluminum from Raney alloys (Ni, Co, Fe, and Cu) can be mentioned here (see chapter 3.2). Melting followed by pulverizing in an air jet comprises a method for preparing certain catalysts for the synthesis of ammonia. As for monolithic supports used particularly in catalytic mufflers, they are produced through special technology such as dry chemical oxidation of aluminum honeycomb, or through the extrusion of mixtures of oxides.

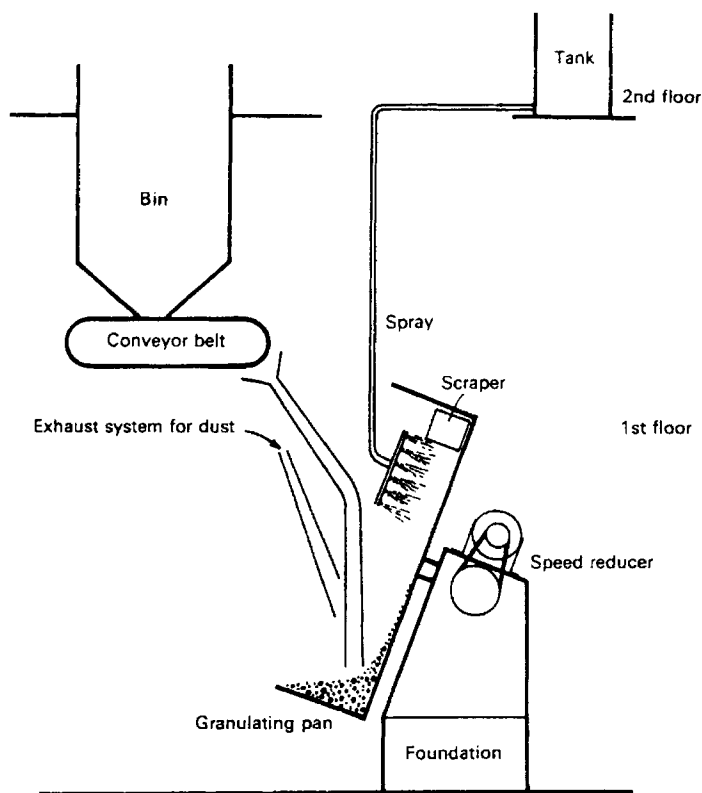


Figure 6. Operating principles of a pan granulator.

### 5.2.3 Organizing a Catalyst-Manufacturing Process

The location of different unit operations in catalyst-manufacturing production lines does not lend itself to debate. Precipitation occurs at the beginning of a fabrication process; calcination then activation, which will be treated later, are the final operations. Certain operations can be repeated in some processes; but the final calcination will come after the last drying. On the other hand, the location of forming operations can vary according to the circumstances; the operation can take place at the beginning (coagulation of sols) or penultimately (pelletizing of dry powders or even colloidal powders). Some of the operations require more than a particular piece of equipment, as often occurs with hydrothermal transformations.

In summary, numerous processes are possible, depending on the starting products, the composition, the structure and texture of the desired product, and frequently on the available equipment in the manufacturing shop. There will often be several processes that can lead to catalysts with very similar characteristics and properties.

Figure 7 illustrates three types of processes corresponding to three different catalysts: a bulk catalyst of iron molybdate for the oxidation of methanol into form-

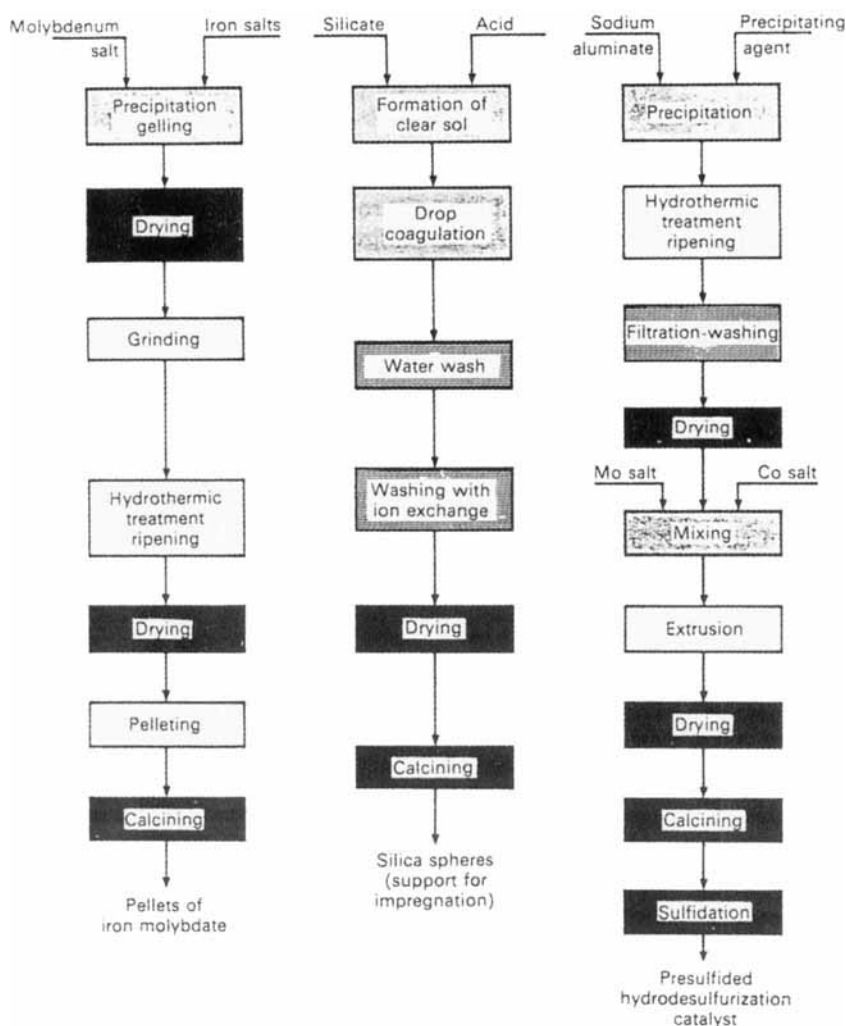


Figure 7. Typical arrangements of the unit operations for manufacturing catalysts.

aldehyde; a support made of silica beads; and a kneaded and coagglomerated hydrosulfurization catalyst based on cobalt and molybdenum on an alumina support. Kneading salts with a xerogel powder having a low water content does in fact correspond to an impregnation operation that will affect the properties of the final catalyst, although the overall process, aside from this operation, remains the same as that which would be used for fabrication of the support alone.

Finally, the importance of choosing the precursor salts and the precipitating agents before any operation should be emphasized; general principles for this cannot be set forth, only some practical suggestions can be made, as follows:

The precursor salts should be decomposable in such a way as to eliminate the



ions or useless constituents through washing or calcination. Use of gelling salts or precipitating agents (binders and lubricants) containing potential poisons of the catalyst must be avoided. Thus it is that in the preparation of catalysts based on copper chromite (used in CO conversion at low temperature) the use of copper chloride or sulfides, which are difficult to reduce and are generators of chlorine and sulfur, must be avoided, because  $\text{Cl}^-$  and  $\text{S}^{2-}$  are catalyst poisons. The same is true for hydrogenation catalysts based on reduced metals. For coprecipitation, compatible salt solutions that give a true coprecipitation must be chosen, and not those that give parallel or consecutive precipitations. Similarly, for certain catalysts obtained from crystallized precursors, one must think about choosing those anions capable of creating the best texture. Apart from these general considerations and certain considerations of economics, one must depend on experimentation for making the best selection of starting chemical compounds.

## References

1. Ph. Courty and P. Duhaut, *Rev. Inst. Française du Pétrole* **1974**, XXIV-6, 861.
2. J. P. Fort and M. Graulier, *Actualité Chimique* **1973**, 2, 7.

## 6 Computer-Aided Catalyst Design

M. BAERNS AND E. KÖRTING

### 6.1 Introduction

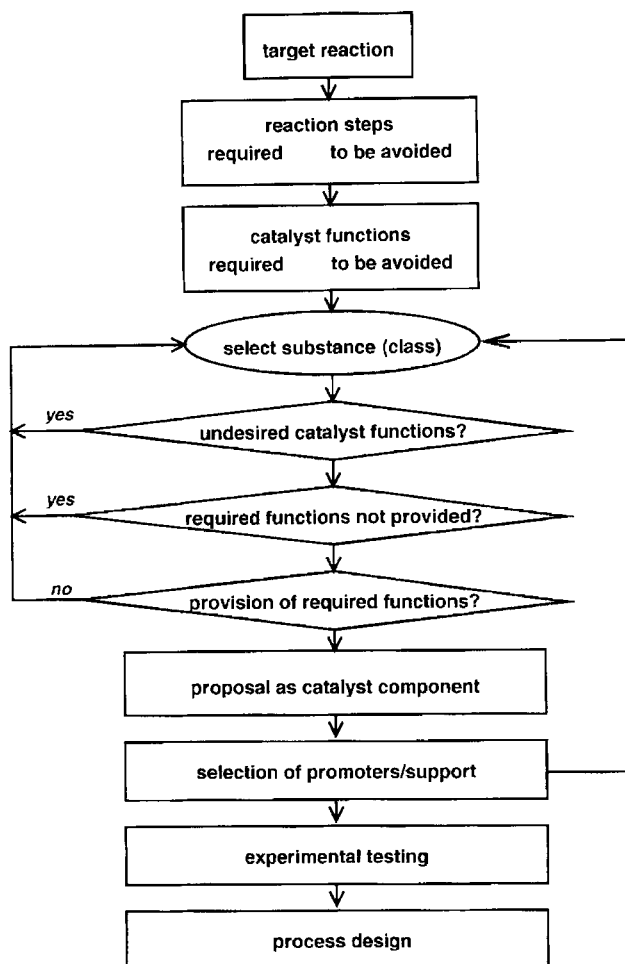
In the past, catalyst design has been mainly based on heuristics; more recently, deterministic methods have started to evolve. Heuristics describes methods by which knowledge is acquired in a logical but nonmathematical manner. In this way also, trial-and-error procedures may be considered to be of the heuristic type as long as they are based on some rational, which is usually the case in catalyst design. Both, heuristic as well as deterministic methods employ computational methods [1, 2]. This article relates to these methods and explains their inherent bases. Before doing so, some necessary definitions and descriptions of the terminology common in computational catalyst design are given.

Heuristic catalyst design is based on a knowledge of:

- catalytic chemistry including inorganic, organic, physical as well as analytical chemistry;
- materials, e.g. their synthesis, characterization, texture and structure;
- chemical reaction engineering principles, i.e. thermodynamic equilibrium and kinetics of the catalytic reaction and of transport processes as well as their interplay; although applicable to deterministic considerations, these qualitative aspects nevertheless affect heuristic searches for an optimum catalyst.

Although some of these aspects are of a quantitative nature, the catalyst expert using his overall knowledge cuts through the complexity in inventing and/or improving a catalyst by handling it in a provisional and intuitive way combining heuristics, experimentation and qualitative modeling. This process is illustrated by Figure 1 which summarizes the various stages of traditional catalyst development.

The reasoning process may be modeled by a computer algorithm (see Chapter 6.2.1). In order to propose catalyst components for a given reaction on a more fundamental basis, reaction steps have to be identified which lead to the desired products or which should be avoided because they are not selective or because they result in deactivation of the catalyst. These reaction steps ought to be elementary reactions steps; however, in the case that such elementary reaction steps are not known, simplified reaction schemes may be useful, too.



**Figure 1.** Modeling the reasoning process of catalyst experts by a computer algorithm.

From experience it is known which types of materials catalyze which reaction steps. It is desirable to relate their activity to solids properties which are measurable or which can be related to measurable quantities. In this way, it is possible to identify substance properties which are required for catalyst components or which should be avoided.

Then, catalyst components can be selected which presumably provide all necessary properties and functions but which do not catalyze undesired reactions or do not lose their activity due to deactivation. For different selection criteria, it will be necessary to find some optimum between possibly contradictory patterns. Since the process is heuristic, no guarantee can be given that the optimum catalyst is found. This is the reason why a set of promising materials has to be prepared and to be tested experimentally; the preselection of catalytic materials may also be based on

different assumptions on elementary reaction steps and required solids properties and catalytic functions. The results of these tests will then be fed back in order to further improve selection criteria. Such an iterative process will also help to better understand the catalytic system in general.

Deterministic catalyst design is slowly supplementing the traditional heuristic approaches, comprising:

- Deriving and applying quantitative relationships for predicting chemical and physico-chemical properties of potential catalytic materials and relating them to the energetic and dynamic interactions of reacting molecules with the catalyst surface.
- Modeling and describing the time course of the catalytic reaction, i.e. their kinetics on an elementary-step basis and relating the reaction scheme and the respective rate constants and activation energies to the physical and chemical properties of the catalytic solid as a basis for further catalyst development [3].
- Combining the kinetics of the catalytic reaction and its interplay with transport phenomena as well as with the hydrodynamics of the chemical reactor to be used as the basis of shaping and operating the final catalyst.
- Relating porosity, pore diffusional processes and kinetics of the catalytic reaction and of the deactivation process to one another with the aim of minimizing apparent catalyst deactivation [4].

In its broadest application deterministic catalyst design will eventually also include molecular dynamics calculations and computer graphics which are both being used for simulating the behavior of molecules on catalytic surfaces and, in particular, on active sites. Although these methods have, in principal, a tremendous potential for predicting and/or improving the catalytic performance of catalytic materials [5–9], they will not be dealt with in detail since their comprehensive application to catalyst design in practice is still in its infancy. Only some selected cases are described.

Very striking results on the interactions of molecules with a catalyst have been recently reported in zeolite catalysis because of the well ordered structure of these materials; it is worth mentioning the subjects of zeolite design [10] and of acidic properties of metallosilicates [11]. In other areas where polycrystalline or even amorphous materials are applied, highly interesting results are now numerous emerging (such as hydrocarbon oxidation on vanadium-based catalysts [12]; location of transition metal cations on Si(100) [13]; CO molecules on MgO surfaces [14]; CH<sub>4</sub> and O<sub>2</sub> interaction with sodium- and zinc-doped CaO surfaces [15]; CO and NO on heavy metal surfaces [16]). An illustration of the computerized visualization of molecular dynamics of Pd clusters on MgO(100) and on a three-dimensional trajectory of Ar in Na mordenite, is the recent publication of Miura et al. [17].

Since chemical reaction engineering considerations apply to nondeterministic as well as deterministic methods they will be briefly dealt with separately. The interaction of chemical kinetics and transport processes and their effect on catalyst activity and selectivity in reaction networks will be emphasized. Some attention will be also paid to catalyst deactivation.

## 6.2 Heuristics in Catalyst Design

Heuristics are relationships between variables of qualitative nature. They may be supported by theoretical concepts, or just rules-of-thumb learned from experience. Since it is up to now impossible to predict the catalytic behavior of a solid only by deterministic methods, the application of heuristics is crucial in catalyst design.

Knowledge-based systems, frequently also called expert systems, for supporting catalyst development belong to the heuristic methods; emphasis is put on the wording “supporting” because such a system is not able to suggest the catalyst from the knowledge stored. (see Chapter 6.2.1). Another application of heuristics are neural networks which have been only very recently introduced as a means of supporting catalyst design (see Chapter 6.2.2).

### 6.2.1 Knowledge-Based Systems

Knowledge-based systems are computer programs which apply knowledge about a specific domain in order to derive new conclusions. These conclusions are on the level of a human expert in this field, but constrained by the field of expertise. Applied to catalysis, the knowledge base contains heuristics about relationships between chemical and physico-chemical properties of solids and their catalytic properties, as well as known properties for such solids which may be used as components of catalysts [2, 18]. An expert system is able to combine this knowledge about different catalyst properties which may be necessary to catalyze the required reaction steps, or which should be avoided because they catalyze side reactions.

Several expert systems of this type have been described in the literature (Table 1). In DECADE (DEsign expert for CAtalyst DEvelopment) Bañares-Alcántara et al. [19] used knowledge processing methods (the expert system shell) of an expert system which was previously used for other problems, and added information about CO hydrogenation catalysis. Proposals for the selection of a catalyst and reaction conditions are reached on different levels of fundamental knowledge:

- (i) on the most abstract level known catalysts are selected for the desired reaction;
- (ii) catalysts are selected which are known to catalyze a reaction which belongs to the same reaction class as the desired reaction;
- (iii) on the most detailed level of knowledge, reaction steps are postulated by for-

**Table 1.** Expert systems for catalyst design.

Approach	Reaction	Name	References
Levels of abstraction	CO hydrogenation	DECADE	19
Standard catalysts	hydrogenation	ESKA	20
Activity patterns	oxidative dehydrogenation	INCAP, INCAP-Muse	21–26
Optimization of catalysts	alcohol synthesis		27, 28
General applicability	different	ESYCAD	29, 30

mal analysis of necessary breaking or formation of bonds, and catalyst components are selected on the basis of knowledge about the ability of different metals for the steps of hydrogen and carbon monoxide dissociation.

The system also provides recommendations for the selection of reaction conditions (pressure, temperature and  $H_2 : CO$  ratio).

The system ESKA (Expert System for Selection and Optimization of Catalysts [20]) was designed at BASF specifically for hydrogenation reactions. The main component of a catalyst is proposed on the basis of activity patterns which describe the applicability of catalysts for different types of hydrogenations. The system also is able to propose secondary catalyst components and, if necessary, a support material which is stable under reaction conditions and does not have any undesired catalytic properties. Based on heuristics for required as well as undesired side reactions and for different catalytically active components, the system also proposes reaction conditions as temperature, pressure, the solvent or the pH.

Kito and Hattori et al. have described INCAP (INtegration of Catalyst Activity Patterns [21–23]), an expert system which rates the applicability of catalyst components for the desired reaction based on known activity patterns for different catalyst properties. The system was successfully applied for the selection of promoter components for the oxidative dehydrogenation of ethylbenzene to styrene. An improved version INCAP-MUSE (INCAP for MUlti-Component catalyst SElection [24–26]) selects as many catalyst components until all required catalyst properties are present. Although the system was successfully applied to oxidation reactions, more recently better results have been obtained by neural network methods (Section 6.2.2).

Hu and co-workers have developed an expert system especially for the optimization of higher alcohol synthesis catalysts [27, 28]. The knowledge base contains data about experimental work and heuristic rules about the relationships between preparation parameters, results of characterization, and higher alcohol selectivity. If the user queries the system for an alcohol catalyst with some required selectivity, starting with the best catalyst, the program proposes modifications, i.e. in composition or operating conditions, in order to improve the performance of the catalyst by application of heuristic rules.

Although the systems described above were designed specifically for one reaction or one reaction class, the system ESYCAD (Expert SYstem for Catalyst Design [29, 30]) has been applied to such different reaction types as CO hydrogenation, acid-catalyzed dehydrogenation of alkanes, or oxidative coupling of methane. The system has recently been extended by incorporating a knowledge acquisition facility which allows the user to enter his own knowledge and to apply the program to catalytic systems of his interest. In order to select catalyst components the system and/or the user proposes reaction steps which are required for a given reaction or which should be avoided as side reactions. Then catalyst properties are determined which are necessary for required reaction steps or which should be avoided because they catalyze undesired reactions or lead to deactivation of the catalyst. On the basis of a database containing chemical and physico-chemical properties of solids, the system selects catalyst components which provide all necessary properties, but

do not catalyze undesired reactions. Optionally, secondary components can be selected (see Fig. 1).

As an illustration, the results of the application of the ESYCAD program to the oxidative coupling of methane are explained. For this reaction, methane may be activated at strong basic sites of the catalyst by heterolytic chemisorption, resulting in methyl anions which may be oxidized to radicals. In the selective reaction, these radicals dimerize to ethane as the primary product. Acid sites or *n*-conductivity should be avoided because they lead to total oxidation. Under reaction conditions the catalyst should be stable, i.e. not be oxidized or reduced or volatilize, which can be checked by thermodynamics.

By doping a primary catalyst component with lower-valent metal cations, additional oxygen vacancies will be created which facilitate the incorporation of electrophilic oxygen species chemisorbed on the surface into the bulk where they will not oxidize adsorbed methyl radicals. Also, the promoter oxide should be basic, not be reducible, oxidizable, or easily volatilizable. It should form a mixed oxide with the main component which may be possible if the ionic radii are similar. According to these rules, the expert system proposes as potential catalyst components combinations of substances with appropriate chemical and physico-chemical properties (Table 2). Many of these systems already have been described in the literature for the oxidative coupling, whereas others have not been tested yet.

### 6.2.1.1 Data Procurement for Knowledge-based Systems

Progress in analytical characterization of catalysts plays an important role in their further development and improvement. Synergistic effects of complimentary characterization tools by which different properties of the catalytic materials are determined are claimed to be beneficial in catalyst design. If this is so, then an expert system for assisting in catalyst selection should be designed in such a way that it accounts for different chemical and physico-chemical properties and their relation to catalytic performance of solid materials.

The catalytic behavior of solid materials is certainly largely governed by the nature of their few topmost atomic layers. However, it can be assumed that these layers are frequently related to the bulk properties of the materials. If one goes along with this preposition, catalytic performance should also be related at least partly to these properties. Then in turn, an expert system should not only incorporate surface but also bulk properties, such as crystallographic structure, lattice parameters, cluster sizes, electronic conductivity and concentration of ion defects.

Against the above background some important questions arise: How should bulk and surface properties be determined for a specific material considered to be a potential catalytic compound? What is the optimum procedure for procuring the required data? This problem is being dealt with in developing a standard Multi-Technique Approach (MTA) and in interpreting the information obtained [31]. To this end the authors emphasize the necessity of a structural model for computer-aided characterization of solid samples by bulk and surface properties. Such a model may then serve as a basis for optimization by selecting the most suitable

**Table 2.** Proposals of the expert system ESYCAD for the oxidative coupling of methane.

primary	secondary	primary	secondary
Li <sub>2</sub> O		Dy <sub>2</sub> O <sub>3</sub> <sup>a</sup>	Na <sub>2</sub> O
MgO <sup>a</sup>	Li <sub>2</sub> O <sup>a</sup>		CaO
CaO <sup>a</sup>	Na <sub>2</sub> O <sup>a</sup>	Tb <sub>2</sub> O <sub>3</sub> <sup>a</sup>	SrO
SrO <sup>a</sup>	Na <sub>2</sub> O		Na <sub>2</sub> O
BaO <sup>a</sup>	Cs <sub>2</sub> O	Gd <sub>2</sub> O <sub>3</sub> <sup>a</sup>	CaO
Y <sub>2</sub> O <sub>3</sub> <sup>a</sup>	Na <sub>2</sub> O		SrO
	CaO <sup>a</sup>		BaO
	SrO <sup>a</sup>	Eu <sub>2</sub> O <sub>3</sub> <sup>a</sup>	Na <sub>2</sub> O
La <sub>2</sub> O <sub>3</sub> <sup>a</sup>	Na <sub>2</sub> O <sup>a</sup>		CaO
	CaO <sup>a</sup>		SrO
	SrO <sup>a</sup>		BaO
	BaO <sup>a</sup>	Sm <sub>2</sub> O <sub>3</sub> <sup>a</sup>	Na <sub>2</sub> O <sup>a</sup>
Yb <sub>2</sub> O <sub>3</sub> <sup>a</sup>	Li <sub>2</sub> O		CaO <sup>a</sup>
	Na <sub>2</sub> O		SrO
	CaO		BaO
	SrO	Tm <sub>2</sub> O <sub>3</sub> <sup>a</sup>	Li <sub>2</sub> O
Er <sub>2</sub> O <sub>3</sub> <sup>a</sup>	Li <sub>2</sub> O		Na <sub>2</sub> O
	Na <sub>2</sub> O		CaO
	CaO		SrO
	SrO	Nd <sub>2</sub> O <sub>3</sub> <sup>a</sup>	Na <sub>2</sub> O
Ho <sub>2</sub> O <sub>3</sub> <sup>a</sup>	Na <sub>2</sub> O		CaO
	CaO		SrO
	SrO		BaO

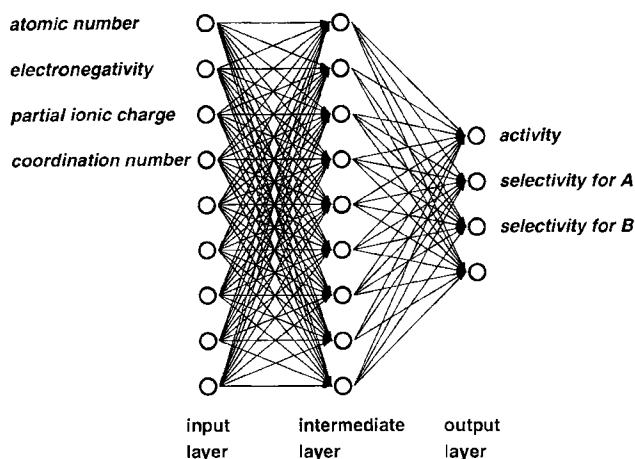
<sup>a</sup> System already known as catalyst.

characterization technique by artificial-intelligence methods. For example, an expert system has been developed for simultaneous interpretation of data gained from XPS and TEM on the surface topology of two-component supported catalysts, i.e. mainly surface-particle size.

## 6.2.2 Neural Networks

The basic idea behind an artificial neural network is a simplified model of the human brain which is said to be able to correlate output data (results) with input data (factors). It is anticipated that neural network technology could also contribute significantly to analyzing, predicting, and optimizing the performance of chemical





**Figure 2.** Modeling relationships between chemical and physico-chemical properties of catalyst components and their catalytical behavior by a neural network.

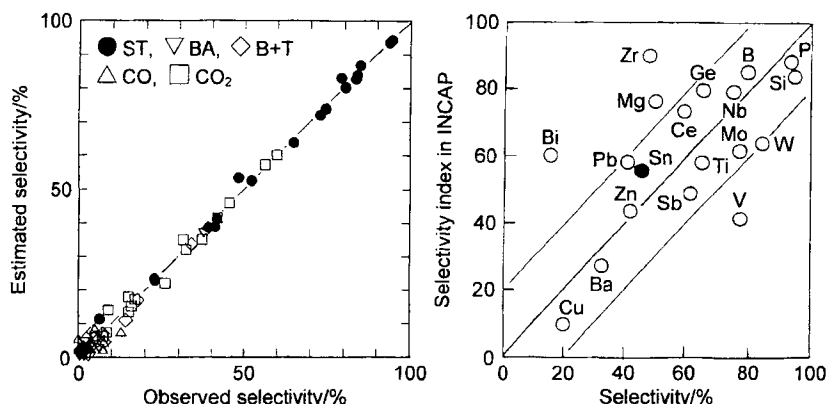
manufacturing units and plants [32]. In the context of predicting the catalytic performance of inorganic solids, neural networks have been applied particularly to estimating or predicting structure–activity relationships and structure–spectrum correlations [33–36].

In heterogeneous catalysis the applicability of this method has been demonstrated. The method is explained below for the acid-catalyzed oxidative dehydrogenation of ethylbenzene as used by Kito et al. [37–41] aiming at maximizing the selectivity to styrene by promoting  $\text{SnO}_2$  with various inorganic compounds.

Applied to catalysis, input data are properties of catalyst components, whereas output data is the observed catalytic performance such as activity and selectivities towards the products. Commonly, an intermediate hidden layer of neurons is included between the input layer and the output layer (Fig. 2), and the artificial neural network is set up this way that the activity of a neuron is calculated as a linear combination of the activity of the neurons of the preceding layer. The artificial neural network is trained with a given set of experimental data, by adjusting the weights for the linear combinations so that it describes the experimental data with a minimum error. The network may be tested if, for learning, one experiment is left out, and the catalytic performance is predicted from the catalyst properties as input data.

When applying a series of promoted and unpromoted  $\text{SnO}_2$  catalysts for the oxidative dehydrogenation of ethylbenzene, the artificial neural network was able to predict the observed selectivities with an average absolute error of only 1.5% (Fig. 3). These results are much better than those obtained by the expert system INCAP (see Chapter 6.2.1), where the average absolute error for the styrene selectivity was about 20%.

In another example, a neural network was applied successfully to the prediction of conversion and yields in the decomposition of NO into  $\text{N}_2$  and  $\text{O}_2$  over Cu/ZSM-5 catalysts [42]. This shows that artificial neural networks are able to describe a complex catalytic system quite well if an appropriate numerical representation is



**Figure 3.** Accuracy of estimation of the selectivities for styrene (ST), benzaldehyde (BA), benzene + toluene (B + T), CO and CO<sub>2</sub> by a neural network (left) in comparison with the selectivity for styrene as estimated by an expert system, INCAP (right) (reproduced by kind permission of T. Hattori).

found for the input and output data. The problem in their application may be the availability of a representative set of experimental data for learning, as well as the interpretation of the weights obtained for neuron interconnections which do not enable direct derivation of guidelines for the optimization of a catalytic system.

## 6.3 Deterministic Methods in Catalyst Design

More recently a hybrid approach to computer-assisted catalyst synthesis, based on a microkinetic analysis of the catalytic reaction, has been put forward which comprises essentially deterministic but also some nondeterministic features. For the synthesis of a catalyst with high activity and selectivity for a given reaction, the application of a microkinetic analysis has been suggested by Dumesic and co-workers [43–45]. The derivation of the microkinetics is not necessarily based on detailed kinetic experimentation but, by analogy, to similarities with other known catalytic processes. In an ideal situation, the microkinetics of a catalytic reaction are completely defined according to Dumesic and his collaborators when:

- all of the chemical species on and above the catalytic surface have been identified unambiguously;
- the elementary reaction steps involving the formation and cleavage of chemical bonds have been established uniquely;
- the rate constants for each elementary reaction have been measured independently;
- the rate constants for each elementary reaction are known as a function of the catalyst formulation.

Unfortunately, these requirements have not yet fully been met for any catalytic reaction, although for some simple catalytic reactions reasonable approaches are

known. Such reactions are the oxidation of CO over a supported Rh catalyst [46, 47], ammonia synthesis over iron [48, 49], and the HCN synthesis over a Pt gauze catalyst. More recently Wolf [50] carried out a microkinetic analysis of the primary reaction steps in the oxidative coupling of methane and also related the rate constants of the various surface steps to different compositions of various  $(\text{CaO})_{1-x} \cdot (\text{CeO}_2)_x$  catalysts and their resulting electronic properties.

In support of catalyst synthesis for a new reaction, a microkinetic simulation is performed using rate constants of the postulated elementary reactions which have been either independently measured or estimated. The applied mechanistic and kinetic models should be consistent with experimentally identified gas-phase products and surface intermediates observed by, for example, infrared spectroscopy. By using these models and kinetic parameters having physical and chemical meaning such as sticking coefficients, surface bond energies, preexponential factors and activation energies for surface reactions, surface bonding geometries, active sites densities and ensemble sizes, the general trend of the kinetic relationships is expected to be in agreement with experimental evidence. By changing the various parameters of the model which are assumed to be related to the catalytic compound(s) used an optimized catalyst composition should eventually evolve.

Dumesic and co-workers have presented various case studies in which they have applied the above concept of microkinetic analysis in order to propose new catalysts or to explain the different catalytic performance of different catalyst formulations for given reactions:

- (i) Oxidation of CO with NO and  $\text{N}_2\text{O}$  decomposition into its elements on Y-zeolites and mordenite exchanged with different first-row transition metals (Cr, Mn, Fe, Co, Ni, Cu).
- (ii) Partial oxidation of methane to methanol and formaldehyde on exchanged Y-zeolites (Cr, Fe/Cu, Co, Mn/Ni).
- (iii) Ethane hydrogenolysis on silica-supported metal catalysts (Fe, Co, Ni, Ru, Rh, Pd, Re, Os, Ir, Pt).

The authors conclude that a coordinated effort involving experimental studies and microkinetic analysis offers an opportunity for determining the factors that limit catalyst performance and for suggesting strategies that alter these limitations. If by microkinetic simulation a similarity is found to a known catalytic system, knowledge about this system may be transferred to the system of interest by analogy [43]. The combination of these ideas with semiempirical correlations of chemical bonding properties with catalyst structure and composition provides directions in the search for new materials.

The microkinetic analysis is certainly a scientifically interesting approach which will contribute to the identification and selection of catalytic compounds even in more complex situations as described above. One problem still to be solved is the experimental procurement and/or estimation of the parameters used in microkinetic simulations, which limits the wide applicability of the method. Providing kinetic parameters for a complex reaction network from kinetic experiments for an "analogous" catalyst is a time-consuming process. Despite the availability of modern

experimental equipment and efficient computers, a complex reaction demands at least one man year of work [51]. The estimation of parameters by *ab initio* or semiempirical methods has to be considered with caution because ideal surfaces are usually assumed.

Nevertheless, *ab initio* or semiempirical quantum chemical calculations, with clusters to represent the catalytic solid material, can help build up a model of the catalytic system and study effects of modifications [52]. Even simulation of the molecular dynamics of the interaction between reactants or intermediates, together with replication of the unit cell of the catalytic solid in a simple force field, may describe observed effects in a catalytic system and may be able to predict the effect of catalyst modifications [53].

## 6.4 Chemical Reaction Engineering Aspects

The preceding discussion has concentrated on the selection of catalytically active components. Although this is an essential task, this is just one aspect of the whole catalytic process, which also includes selection of catalyst support and the design of the overall catalyst in relation to reaction engineering requirements, so that not only activity and selectivity but also mechanical and chemical stability are ensured. For catalyst supports, the design variables are the degree and the form of the dispersion of the catalytic active components, and the porosity of the support.

Deterministic computational methods have been applied to the description of deactivation processes [54]; models also exist for inter- and intraparticle diffusion as well as reactor hydrodynamics. For pore diffusion, which influences catalyst effectiveness and can also influence selectivity, the classical approach which uses equations for the Thiele modulus, relating the rate of chemical reaction to the rate of pore-diffusional processes [55], may be derived in analytical form by Berthelot's network models of randomly interconnected cylindrical pores. Alternatively, Monte Carlo methods may be applied as well for setting up a model of the solid, and for random walk simulation of diffusing reactants and intermediates [56].

Expert systems have been applied to reactor design, design of separation units, and over-all process design. These design tasks conflict with each other. For example the conversion and selectivity of the catalyst have consequences for the separation units, and the shape and mechanical properties of the catalyst are constrained by the reactor type and the operating conditions. Therefore an integrated approach may be useful, where specialized modules are supervised by a general control program, as proposed by Simmrock et al. for process synthesis [57].

## 6.5 Conclusions

The examples given above show that catalyst design requires an integrated approach, which considers heuristic relationships as well as deterministic methods. Computers can help to organize the huge amount of data. Knowledge about one reaction or reaction type and related methods is applicable also to other types of

questions and related reaction classes, where similar reaction steps probably take place and so the same substance properties are involved. In this way a generalization may take place from empirical data about a specific reaction to reaction classes, opening the possibility for reasoning by analogy.

The more surface- and bulk-related properties of solid materials and their relevance to catalysis are incorporated into an expert system for assisting in catalyst design, the more effective such a system will be. Results and experience may be preserved in the knowledge base. Since such information may be applicable to other reaction types, if some reaction steps or relevant material properties are common, knowledge bases describing particular fields of interest may even be licensed to third parties, and so become tradable items.

## References

1. M. Misono, *Catal. Today* **1995**, 23, 301.
2. H. C. Foley, E. E. Lowenthal, *CHEMTECH* **1994**, 24(8), 23.
3. J. A. Dumesic, B. A. Milligan, L. A. Greppi, V. R. Balse, K. T. Sarnowski, C. E. Beall, T. Kataoka, D. F. Rudd, A. A. Trevino, *Ind. Eng. Chem. Res.* **1987**, 26, 1399.
4. S. C. Reyes, E. Iglesia in *Computer Aided Design of Catalysts* (Eds: E. R. Becker, C. J. Pereira), Marcel Dekker, New York, **1993**, Chapter 5.
5. A. Miyamoto, T. Hattori, T. Inui, *Appl. Surf. Sci.* **1992**, 60, 660.
6. A. Miyamoto, T. Hattori, T. Inui, *Physica C* **1991**, 190, 93.
7. A. Miyamoto, T. Hattori, M. Kubo, T. Inui, *Jpn. J. Appl. Phys.* **1992**, 31, 4463.
8. A. Miyamoto, M. Kubo, *J. Jpn. Petrol. Inst.* **1993**, 36, 282.
9. A. Miyamoto, H. Himei, Y. Oka, E. Maruya, M. Katagiri, R. Vetrivel, M. Kubo, *Catal. Today* **1994**, 22, 87.
10. M. E. Davis, *CHEMTECH* **1994**, 24(9), 22.
11. T. Inui, K. Matsuba, Y. Tanaka, *Catal. Today* **1995**, 23, 317.
12. J. Haber, M. Witko, *Catal. Today* **1995**, 23, 311.
13. M. Ishida, M. Yoshida, M. Takashima, K. Sawara, *Catal. Today* **1995**, 23, 341.
14. H. Kobayashi, D. R. Salahub, T. Ito, *Catal. Today* **1995**, 23, 357.
15. N. Zhanpeisov, V. Staemmler, M. Baerns, *J. Molec. Catal.* **1995**, 101, 51.
16. N. Watari, S. Ohnishi, *Catal. Today* **1995**, 23, 371.
17. R. Miura, H. Yamano, R. Yamauchi, M. Katagiri, M. Kubo, R. Vetrivel, A. Miyamoto, *Catal. Today* **1995**, 23, 409.
18. Y. H. Sun, S. W. Li, S. Y. Chen, M. Y. Cheng, S. Y. Peng in *Computer Aided Innovation of New Materials II Part I*, (Eds: M. Doyama, J. Kihara, M. Tanaka, R. Yamamoto), Elsevier, Amsterdam, **1993**, p. 1111.
19. R. Bñares-Alcántara, A. W. Westerberg, E. I. Ko, M. D. Rychener, *Comput. Chem. Engng.* **1987**, 11, 265; **1988**, 12, 923.
20. H. Speck, W. Hölderich, W. Himmel, M. Irgang, G. Koppenhöfer, W.-D. Mroß, *DECHEMA monographs* **1989**, 116, 46.
21. T. Hattori, S. Kito, Y. Murakami, *Chem. Lett.* **1988**, 1269.
22. S. Kito, T. Hattori, Y. Murakami, *Appl. Catal.* **1989**, 48, 107.
23. T. Hattori, H. Niwa, A. Satsuma, S. Kito, Y. Murakami, *Appl. Catal.* **1989**, 50, L11.
24. S. Kito, T. Hattori, Y. Murakami, *Chem. Eng. Sci.* **1990**, 45, 2661.
25. S. Kito, T. Hattori, Y. Murakami in *Catalytic Science and Technology* (Eds: S. Yoshida, N. Takezawa, T. Ono), VCH, New York, **1991**, Vol. 1, p. 285.
26. T. Hattori, H. Niwa, A. Satsuma, S. Kito, Y. Murakami, *Stud. Surf. Sci. Catal.* **1993**, 75, 489.
27. X. D. Hu, H. C. Foley, A. B. Stiles, *Ind. Eng. Chem. Res.* **1991**, 30, 1419.
28. H. C. Foley, E. E. Lowenthal, X.-D. Hu in *Computer Aided Innovation of New Materials II*

- (Eds: M. Doyama, J. Kihara, M. Tanaka, R. Yamamoto), Elsevier, Amsterdam, **1993**, Part 1, p. 1101.
29. E. Körtling, M. Baerns, *Chem.-Ing.-Tech.* **1990**, 62, 365.
  30. E. Körtling, M. Baerns in *Computer Aided Innovation of New Materials II Part 1*, (Eds: M. Doyama, J. Kihara, M. Tanaka, R. Yamamoto), Elsevier, Amsterdam, **1993**, p. 1107.
  31. D. P. de Bruijn, H. P. C. E. Kuipers, *Catal. Today* **1991**, 10, 131.
  32. S. P. Chitra, R. J. Bulson III, D. G. Morell, *CHEMTECH* **1995**, 25(2), 18.
  33. J. Gasteiger, J. Zupan, *CICSJ Bulletin* **1991**, 9, 15.
  34. J. Zupan, G. Gasteiger, *Anal. Chim. Acta* **1991**, 248, 1.
  35. P. C. Jurs, *CICSJ Bulletin* **1991**, 11(5), 2.
  36. J. Zupan, J. Gasteiger, *Neural Network for Chemists*, VCH, Weinheim, **1993**.
  37. S. Kito, T. Hattori, Y. Murakami, *Anal. Sci.* **1991**, 7, 761.
  38. S. Kito, T. Hattori, Y. Murakami, *Ind. Eng. Chem. Res.* **1992**, 31, 979.
  39. S. Kito, T. Hattori, Y. Murakami in *Computer Aided Innovation of New Materials II Part 1*, (Eds: M. Doyama, J. Kihara, M. Tanaka, R. Yamamoto), Elsevier, Amsterdam, **1993**, p. 901.
  40. S. Kito, T. Hattori, Y. Murakami, *Appl. Catal.* **1994**, 114, L173.
  41. T. Hattori, S. Kito, *Catal. Today* **1995**, 23, 347.
  42. M. Sasaki, H. Hamada, Y. Kintaichi, T. Ito, *Appl. Catal. A* **1995**, 132, 261.
  43. D. F. Rudd, J. A. Dumesic, *Catal. Today* **1991**, 10, 147.
  44. M. G. Cardenas-Galindo, L. M. Aparicio, D. F. Rudd, J. A. Dumesic in *Computer Aided Design of Catalysts* (Eds: E. R. Becker, C. J. Pereira), Marcel Dekker, New York, **1993**, Chapter 2.
  45. J. A. Dumesic, D. F. Rudd, L. M. Aparicio, J. E. Rekoske, A. A. Treviño, *The microkinetics of heterogeneous catalysis*, American Chemical Society, Washington, DC, **1993**.
  46. S. H. Oh, G. B. Fisher, J. E. Carpenter, D. W. Goodman, *J. Catal.* **1986**, 100, 360.
  47. G. B. Fisher, S. H. Oh, J. E. Carpenter, C. L. DiMaggio, S. J. Schmieg, D. W. Goodman, T. W. Root, S. B. Schwartz, L. D. Schmidt, *Stud. Surf. Sci. Catal.* **1987**, 30, 215.
  48. P. Stoltze, J. K. Nørskov, *J. Catal.* **1988**, 110, 1.
  49. J. A. Dumesic, A. A. Treviño, *J. Catal.* **1989**, 116, 119.
  50. D. Wolf, *Catal. Lett.* **1994**, 27, 207.
  51. R. W. Wojciechowski, N. M. Rice, *Chem. Eng. Sci.* **1993**, 48, 2881.
  52. H. Kobayashi, *Catal. Today* **1991**, 10, 167.
  53. J. M. Newsam, Y. S. Li, *Catal. Today* **1995**, 23, 325.
  54. R. Christoph, M. Baerns, *Stud. Surf. Sci. Catal.* **1987**, 34, 355.
  55. G. F. Froment, K. B. Bischoff, *Chemical reactor analysis and design*, 2nd ed., Wiley, New York, **1979**.
  56. S. C. Reyes, E. Iglesia in *Computer Aided Design of Catalysts* (Eds: E. R. Becker, C. J. Pereira), Marcel Dekker, New York, **1993**, p. 89.
  57. K. H. Simmrock, B. Fried, A. Fried, *Chem. Ing. Tech.* **1992**, 62, 1018.

## Index

- abrasion, industrial catalysts 5
- acetates 123, 130
- acetylenes 170 f
- acid base centers 171
- acid bifunctionality 242
- acid catalysis, heteropoly compounds 241
- acid sites, zeolites 177
- acid solution, alumina surfaces 334
- acid strengths, solid superacids 491
- acidic dissolution, HPAs 249
- acidic groups, carbons 195, 205
- acidic surfaces, pillared clays 300
- acidity *see*: Bronsted, Lewis etc.
- acids
  - complexation 128
  - zeolites 279
- activation 541 f, 564
  - carbons 217
  - fused catalysts 16
  - pillared clays 304
  - reduction–sulfidation 565 f
  - skeletal nickel catalysts 33
- activation energy, apparent 400
- active aluminas 77
- active carbon, deposition–precipitation 460
- active component deposition 315 f
- active phases, final catalysts 541
- active surface area (ASA) 185
- addende atoms 240
- additives 74
  - bimetallic redox reactions 529
  - carbon formation 173
  - precursor preparation 561
- adipic acid 423
- adsorbed reductants redox reactions 529
- adsorption
  - enzyme heterogenization 356, 364
  - oxide surfaces 328
- aerogel 85, 90
- aerosil 365
- aerosol process, flame hydrolysis 99
- agglomeration 62 f
  - fused catalysts 11
  - metallic glasses 50
  - pan granulation 586
  - supported metal clusters 375
  - zeolite metal clusters 394
- aggregation 65
  - carbons 163
  - pillared clays 297
- aging 5
  - pillars 291
  - sol–gel process 88
  - spreading/wetting 501
  - zeolites 263
- alcogel 85
- alcoholates, volatile 99
- alcohols 33, 277
- aldehyde groups, IR absorption 210
- aliphatic molecules 188
- alkali metal compounds 186
- alkalinity, zeolites 270
- alkanes
  - heteropolyacids 243
  - solid superacids 498
  - zeolite-entrapped metal complexes 423
- alkenes
  - skeletal nickel catalysts 33
  - sol–gel process 92
  - zeolite metal clusters 393
- alkoxides
  - chemical vapor deposition 452
  - precursor–support interactions 550
  - sol–gel process 85, 94
- alkylammonium 285
- alkylation, skeletal nickel catalysts 33
- alkylhalidosilanes 99
- alkylidines 174
- alkynes 33
- allotropes, carbons 153
- alloy preparation, skeletal metal catalysts 29 ff
- allylmolybdenum 437
- allyls 342
- alumina 72
  - active 77
  - deposition–precipitation 460, 480
  - enzyme heterogenization 365
  - precursor preparation 561
- alumina salts 263
- alumina-supported nickel catalysts 80
- alumina surfaces 334
- alumina washcoat 80
- aluminosilicates 262, 271
- aluminum, selective removal 463

- aluminum alloys, skeletal metal catalysts 30
- aluminum chlorides, solid superacids 487
- aluminum dissolution, Raney alloys 586
- aluminum/oxide reactions 145
- amberlyst resin 358
- amines 277
- aminogroups, enzyme heterogenization 365
- aminopropyltrimethoxysilane (APTMS) 295
- ammonia oxidation, fused catalysts 11
- ammonia synthesis
  - deposition–precipitation 463
  - iron–zirconium metallic glasses 26
  - metallic glasses 45
- ammonia TPD, solid superacids 499
- ammonium
  - deposition–precipitation 484
  - heteropolyacids 251
  - zeolites 275
- ammonium salts, complexation 128
- amorphization, metallic glasses 46
- amorphous precursors, citrate 128
- amorphous states, fused catalysts 15
- amphoteric oxides 318
- anatase 515, 550
- anchoring 341 f, 394
- Anderson type structure 240
- anhydride groups 196
- anion exchangers, supported catalysts 318
- annealing
  - Al–Ni system 32
  - carbon graphitization 178
  - fused catalysts 15
- antimony fluorides 487
- applications
  - active component deposition 331
  - carbons 224
  - chemical vapor deposition 430
  - flame hydrolysis 107
  - skeletal catalysts 33, 37
- aquagel 85
- aromatics 243, 496
- aromatic compounds 33
- aromatic radicals 170
- Arrhenius law 64, 268
- ascorbic acid 532
- attachment, thin transition layer 545
- Auger electron spectroscopy (AES) 51
- autoreduction, zeolite metal clusters 391
- beads 321, 556
  - silica 75
  - silica–alumina 582
- beidellite 288, 301
- benzaldehyde 252
- benzene
  - anchoring 352
  - chemical vapor deposition 431
  - metallic glasses 45
  - solid superacids 491
- BET surfaces
  - carbons 167
  - deposition–precipitation 475
  - metallic glasses 49
  - pillared clays 301
  - skeletal catalysts 33 ff, 41
  - titanium oxide supports 105
- bicarbonates 186
- bifunctional catalysts 388
- bifunctional reagents 365
- bifunctionality, single-site 397
- bilayer formation 548
- bimetallic catalysts, spreading/wetting 515
- bimetallic clusters, zeolites 390
- bimetal, CVD 449
- binders, catalyst forming 583
- biocatalysts, enzyme heterogenization 364
- biological supports 367
- bipyridine 406, 412
- black carbon 151
- blocking 31, 363
- boiling bed reactor 4
- bonding 152, 304
- Bronsted acidity
  - carbons 216
  - heteropolyacids 245
  - pillared clays 302
  - solid-state reactions 133
  - solid superacids 492
  - support materials 80
  - zeolite-entrapped metal complexes 409
  - zeolite metal clusters 392
- Bronsted basic groups 197
- Brownian motion 15
- bulk catalysts/supports 11–98
- bulk oxidation, metallic glasses 55
- bulk type heterogeneous catalysis 242
- burn off 5, 182 f, 186, 214, 218
- butane 382, 487, 495
- butane maleic acid system 72, 82
- ball-crushers 579
- barium hexaluminate 110
- basic structural units (BSU) 161, 178, 191
- batch operations, precipitation 67
- bauxite 79
- Bayer process 65 ff, 78
- cages, zeolites 374, 406
- calcination 61, 66, 541
  - fused catalysts 14 f
  - pillared clays 297



- precursor-support interactions 548
- sol-gel process 90
- solid-state reactions 118
- solid superacids 488
- spray 121
- supported catalysts activation 553
- supported metal clusters 371
- surfactants 74
- zeolite metal clusters 391
- calcium 433
- calcium carbide/oxide reactions 145
- capillary impregnation 324
- carbides 139 ff
- carbines 156
- carbolites 157
- carbon 150-235
  - deposition-precipitation 460
- carbon blacks 151, 162 f, 169
- carbon burn-off 5
- carbon-carbon bonds 179 f
- carbon catalysts 223
- carbon deposit removal 227
- carbon dioxide, deposition-precipitation 471
- carbon halogen groups 194
- carbon material formation 167 ff
- carbon monoxide catalysts 50
- carbon monoxide chemisorption on nickel 21
- carbon nitrogen surface groups 193
- carbon-oxygen groups 195 f
- carbon-oxygen bonds 151
- carbon-oxygen-hydrogen interactions 189
- carbon-sulfur groups 193
- carbon surfaces, oxygen activation 229
- carbonaceous deposit 151
- carbonates 66, 122 f
- carbonium 495
- carbonyls
  - chemical vapor deposition 428, 434
  - flame hydrolysis 99
  - high-surface transition metal carbides/nitrides 146
  - oxide surfaces 342, 348
  - skeletal nickel catalysts 33
  - supported metal clusters 372 f
- carboxylic groups 196, 210
- carrier binding 364
- catalysts 3-10
  - bulk 11-98
  - chemical vapor deposition 430
  - forming 579 ff
  - fused 11 ff
  - metal cluster 371 ff
  - mixed oxide 110
  - monometallic reforming 334
  - noble metal 173
  - perovskite 129
  - skeletal metal 28 ff
  - solid acid 175
  - sulfuric acid 19 f
  - supported 315-540
  - zeolite-entrapped metal complexes 420
- Ziegler-Natta 72
- catalytic formulas 8 f
- catalytic membranes 96
- catalytic properties
  - bimetallic catalysts 526
  - heteropoly compounds 240
  - pillared clays 308
  - solid superacids 495
- catalytic reduction, bimetallic catalysts 531
- cation exchange
  - HPA salts 247
  - pillars 291, 302
  - supported catalysts 318
- ceramic methods, perovskite catalysts 130
- ceramics 99, 365
- cesium salts 247 f, 257
- charcoal 166
- charged molecules, zeolites 275
- chemical bonds, enzyme heterogenization 360
- chemical compositions
  - see: compositions*
- chemical interactions, precursor-support 547
- chemical modification
  - pillared clays 307
  - sol-gel process 94
- chemical properties
  - metallic glasses 44, 53
  - pillared clays 300
  - precipitation 62
- chemical reaction engineering 601
- chemical reactivities, precursors 557
- chemical shifts, carbon-oxygen 206 f
- chemical structures
  - see: structures*
- chemical vapor deposition (CVD)
  - fused catalysts 23
  - metal complexes on oxide surfaces 343
  - supported catalysts 427 ff
- chemisorption 229, 372
- chiral sulfoxides 310
- chloride process, flame hydrolysis 99
- chlorides
  - poisoning 70
  - solid superacids 487 f
- chlorination, carbons 150
- chlorine
  - carbons 194
  - solid superacids 497
- chlorobenzene 489
- chlorohydrol 297
- chloroplatinic acid 336

- chromia alumina 110
- chromium
  - chemical vapor deposition 432
  - deposition–precipitation 482
- chromium acetylacetonate 348
- citrates
  - deposition–precipitation 465
  - perovskite catalysts 130
  - valencies 123, 126
- citric acid 128, 336
- Claus process 62, 80
- clay minerals 135
- clays
  - pillared 284 ff
  - supported catalysts 318
- cluster formation
  - metallic glasses 55
  - zeolites 374
- coagulation 581
- cobalt
  - chemical vapor deposition 439
  - precursor–support interactions 549
  - reduction–sulfidation 565
- cobalt catalysts 34
- cobalt chelation 414
- cobalt dioxide 471
- cobalt hydroxide 471
- cobalt–molybdenum oxide bilayers 548
- cobalt oxide, precursor preparation 561
- coimpregnation, bimetallic catalysts 526
- coke 151, 169, 176
- coking behavior, noble metal catalysts 173
- collimation, molecules in pores 399
- colloidal silica, zeolites 262
- colloidal suspension, catalytic membranes 96
- combustion processes, carbons 167 ff
- competitive ions, oxide supports 333
- complex cyanide methods 131
- complexation 118, 128
- complexes, heterogenization 355 f
- complexing agent removal 482
- composite materials, spreading/wetting 501
- compositions
  - Al–Ni system 32
  - fused catalysts 17 f
  - metallic glasses 44, 53
  - precipitation 71
  - zeolites 269, 280 f
- compound formation, precursor preparation 549, 560
- computer aided catalyst design (CAD) 591 ff
- concentration effects, precipitation 71
- concentration profiles, spreading/wetting 519
- condensation
  - heteropolyacids 247 f
  - sol–gel process 86, 93
- conduction band 155
- conductivity, metallic glasses 46
- configurational diffusion 399
- contamination, enzyme heterogenization 364
- cooling
  - Al–Ni system 32
  - fused catalysts 11, 15
- coordination sites, blocking 363
- copper
  - bimetallic catalysts 528 f
  - chemical vapor deposition 433
  - deposition–precipitation 475
  - precursor preparation 562
  - selective leaching 398
  - spreading/wetting 505
- copper-based catalysts 463
- copper catalysts 35 f
- copper chromite 110
- copper–magnesium oxalates 463
- copper–zinc hydrocarbonates 119
- coprecipitation 60 ff
  - active components 330
  - solid-state reactions 119
  - support materials 80
- corundum 80
- costs, industrial catalysts 6
- counter cations 251
- counter current 527
- counter ions, oxide surfaces 328
- coupling agents, enzyme heterogenization 366
- coupling effects, reduction–sulfidation 566
- covalent bonding
  - enzyme heterogenization 356
  - oxide surfaces 351
  - pillared clays 304
- cracking 582
  - spreading/wetting 513
  - zeolite metal clusters 399
- critical nucleation, solid-state reactions 113
- crosslinking, homonuclear 169
- crushing 4, 579
- crystal growth *see*: growth
- crystal structures
  - carbons 153
  - high-surface transition metal carbides/nitrides 139
  - solid superacids 493
  - see also*: structures
- crystalline mixed citrates 126
- crystallite size, skeletal nickel catalysts 33
- crystallization
  - deposition–precipitation 468
  - fused catalysts 13, 18
  - metallic glasses 50, 54
  - zeolites 262
- crystalobalite 70

- cubic diamond 153
- cyanate, deposition–precipitation 471
- cyanide methods, solid-state reactions 130 f
- cyanogen bromide 366
- cyclization, industrial catalysts 4
- cyclohexane 352
- cyclohexene 381, 569
- cyclone pulverizers 579
- cyclopentadiene 409
- cyclopentane 395
- cyclopropane, metallic glasses 45
- cyclovoltammetry 419
  
- dangling bonds 170
- Dawson type structure 240 f
- deactivation
  - precursor–support interaction 324
  - surface blocking 31
- Debye temperature 507
- DECADE 594
- decarbonylation 374 ff
- dechlorination 150
- decomposition
  - carbons 228
  - chemical vapor deposition 428
  - fused catalysts 12
  - high-surface transition metal carbides/nitrides 146
  - metallic glasses 45
  - perovskite catalysts 130
- defects
  - carbons 207
  - metallic glasses 44 f
  - oxygen transport 22
  - spreading/wetting 510
- dehydrogenation
  - carbons 168
  - metallic glasses 45
- Deloxan 361
- deposited precursors 559
- deposition, active components 315
- deposition–precipitation 460 ff
- deposits 151, 157, 216
- desorption 231
- deterministic methods, CAD 599
- developments, industrial catalysts 7 f
- diamond like carbon (DLC) 165
- diamond 57 f, 152, 167
- dicyanobenzene 408
- diethyltartrate (DET) 310
- differential thermal analysis (DTA)
  - fused catalysts 23
  - metallic glasses 50
- diffusion
  - configurational 399
  - internal 3
  - solid-state reactions 542
- diffusional impregnation 325
- dimension sensitive parameters, zeolites 389
- dimers 245
- dimethylformamide (DMF) 258
- dimolybdates 552
- dipivaloylmethanates 433
- dipole–dipole coupling 395
- direct redox reactions, bimetallic catalysts 527
- dispersion
  - chemical vapor deposition 431
  - fused catalysts 13
  - spreading/wetting 502
  - supported materials 94
  - supported metal clusters 372
  - supported phases 544
  - zeolites 275
- displacement, zeolite protons 394
- dissociation
  - carbons 203
  - solid-state reactions 113
- dissolution
  - active components 330
  - aluminium 30
  - catalyst forming 586
  - deposition–precipitation 483
  - enzyme heterogenization 363
  - fused catalysts 14
  - heteropolyacids 249
  - metallic glasses 55
  - precursor–support interactions 549
  - supported catalysts 317
- divinylbenzene, enzyme heterogenization 357
- doping, oxide supports 331
- drop coagulation, catalyst forming 581
- droplet to particle process, flame hydrolysis 99
- drying 580
  - deposition–precipitation 464
  - freeze 127
  - silica supports 76
  - sol–gel process 89
  - solid-state reactions 118
  - spray 121
- drying control chemical additives (DCCA) 89
- dynamics, interfacial processes 506
  
- earth alkaline compounds 186
- electric junctions, precursor–support interactions 545
- electrical properties, carbons 155
- electrochemical deposition–precipitation 483
- electroless process, bimetallic catalysts 532
- electron beam lithography 375
- electron configuration, carbon 151

- electron deficiency, zeolite metal clusters 396
- electron excitation, zeolite-entrapped metal complexes 413
- electron paramagnetic resonance spectroscopy (EPR) 411
- electron probe microanalysis (EPMA) 449
- electronegativity, carbons 151
- electronic interactions, precursor–support 545
- electronic properties 7
  - high-surface transition metal carbides/nitrides 139
  - metallic glasses 44
  - zeolite metal clusters 389
- encapsulation
  - enzyme heterogenization 364 ff
  - spreading/wetting 502, 514
- Engel–Brewer valence bond 139
- entrapping
  - enzyme heterogenization 364 ff
  - metals in zeolites 405 ff
- enzymes
  - deposition–precipitation 471
  - heterogenization 355 f
- ESKA, computer aided catalyst design 594
- esters, IR absorption frequencies 210
- ESYCAD 594
- etching, carbons 218
- ethane 45, 92
- ethanol, HPAs 245
- ethers 210, 277
- ethylbenzene 447
- ethyldiamine, cobalt chelation 414
- ethylenediaminetetraacetic acid (EDTA) 465
- ethylene glycol 496
- eutectic crystallization, metallic glasses 55
- eutectic points, fused catalysts 17 f
- exchange cations, zeolites 374
- exfoliation, spreading/wetting 518
- exothermicity 324
- expert systems, CAD 594
- extended X-ray absorption fine structure spectroscopy (EXAFS)
  - iridium clusters 380
  - spreading/wetting 514, 521
  - supported metal clusters 37, 372, 376
- extrudates 4, 321
- extrusion, catalyst forming 584
- faujasite type zeolites 272
  - carbon formation 177
  - entrapped metal complexes 410
- feedstocks, industrial catalysts 4, 9, 580
- fermentation, enzyme heterogenization 364
- Fermi level 155
- ferrous alloys, carbide extraction 144
- film formation, spreading/wetting 507
- Fischer–Tropsch synthesis 62
  - carbons 172
  - metallic glasses 45
  - solid-state reactions 131
- fixation 219 ff, 321
- flame chemistry 167
- flame hydrolysis 12, 99 ff
- flame oxidation 99
- flexible ligand method 406
- fluid bed reactors 4
- fluidized-bed CVD 455
- formation stages, final catalysts 541 f
- formed supports, preparation 104 f
- formulas 8 f
  - fused catalysts 14
- fragmentation, spreading/wetting 509
- Frank–van der Merwe mechanism 505
- free energy of formation, high-surface transition metal carbides/nitrides 140 f
- freeze drying 118, 127, 130
- fullerene blacks 156, 164
- fullerene-oxide complexes 184
- fullerenes 156 f, 170, 184
- fumed oxides 101 f
- fumed silica plant 101
- functional groups 150, 166, 180, 193
- functionalization
  - enzyme heterogenization 357
  - pillared clays 307
- fused catalysts 11 ff
- fusion, high-surface transition metal carbides/nitrides 143
- gallium hydroxypolymer, pillars 293
- gas dissolution, metallic glasses 55
- gas phase clusters, supported catalysts 372
- gas phase reagents, high-surface transition metal carbides/nitrides 145
- gas to particle process, flame hydrolysis 99
- Gattermann–Koch reaction 498
- gel points
  - zeolites 263
  - sol–gel process 88
- gel time, sol–gel process 88
- gelation, solid-state reactions 118
- gelling, catalyst forming 582
- geometric effects, zeolite metal clusters 390
- gibbsite
  - support materials 78, 319
  - zeolites 263
- glasses, metallic 11, 21 f, 43 f
- glassy carbon 157, 166
- glassy states, fused catalysts 15
- glucose oxidase 366

- 
- glutardialdehyde 366
  - glycolic acids, complexation 128
  - gold 528 ff
  - gold–zirconia catalysts, promoted 52
  - Gouy layer, supported catalysts 319
  - grafted precursors, support interactions 550
  - grafting 328, 341 ff
  - grain boundary structures, fused catalysts 15 f
  - grains 4, 321
  - granules, catalyst forming 579, 583
  - graphene 151, 169
  - graphite 151, 167 ff
    - catalyst forming 583
    - formed supports 105
    - precursor–support interactions 545
  - graphite fiber materials 158
  - graphitization 178
  - grinding
    - catalyst forming 579
    - spreading/wetting 517
  - growth
    - metallic glasses 54
    - precipitation 64
    - solid-state reactions 120
    - spreading/wetting 505
    - zeolites 269
  - halides
    - chemical vapor deposition 428
    - high-surface transition metal carbides/nitrides 146
  - halogenation, carbons 154
  - halogens, spreading/wetting 514
  - Hammett acidity 245
  - handling, skeletal metal catalysts 31
  - hardness
    - carbons 155
    - high-surface transition metal carbides/nitrides 139
  - heat transfer, industrial catalysts 5
  - heat of formation, high-surface transition metal carbides/nitrides 140 f
  - hectorite 288
  - Helmholtz plane 319
  - hematite
    - fused catalysts 13
    - precipitation 70
  - heptane 495
  - heteroatoms
    - carbon blacks 189
  - heterogeneous acid catalysis 243
  - heterogeneous oxidation reactions 244
  - heterogenization, complexes/enzymes 355
  - heteropolyacids (HPA) 240 ff
  - heteropolyanions 240, 255
  - heteropolycompounds 240 ff
  - hexagonal graphite 153
  - hexane
    - faujasite zeolites 177
    - solid superacids 495
    - supported metal clusters 382
  - high resolution transmission electron microscopy (HRTEM) 51
  - high-surface-area support 315
  - high-surface transition metal carbides/nitrides 139 ff
  - high-temperature reactions, fused catalysts 13
  - highly oriented pyrolytic graphite (HOPG) 161
    - surface defects 229
  - homogeneity
    - extrusion 584
    - metallic glasses 54
    - sol–gel process 93
  - homogeneous acid catalysis 243
  - homogeneous catalysis 150
  - homogeneous oxidation reactions, HPAs 244
  - hot-petroleum drying, solid-state reactions 127
  - hot-plate effect, spreading/wetting 510
  - Houdry catalysts 285
  - Hüttig temperature 507
  - hybrid orbitals, carbons 151
  - hydrazine bimetallic catalysts 532
  - hydrides, CVD 428
  - hydrocarbons 158, 172
    - heteropolyacids 243
    - layers 168
  - hydrocracking, reduction–sulfidation 565
  - hydrofluoric acid, alumina surfaces 336
  - hydrogel molar composition, zeolites 269
  - hydrogels 75, 263
  - hydrogen
    - bimetallic catalysts 530
    - precursor preparation 562
    - reducing agent 564
    - supported metal clusters 371
  - hydrogen bonding, zeolites 275
  - hydrogen bridges, deposition–precipitation 470
  - hydrogen disulfide 193
  - hydrogen storage, skeletal nickel catalysts 33
  - hydrogen transfer, industrial catalysts 4
  - hydrogenation
    - enzyme heterogenization 362, 366
    - metallic glasses 45
    - skeletal nickel catalysts 33
  - hydrogenolysis, industrial catalysts 4
  - hydrolysis 64
    - chemical vapor deposition 428
    - heteropolyacids 247 f
    - sol–gel process 86, 93
    - zeolite metal clusters 391
  - hydrosilicates 549

- hydrotalcite
  - coprecipitation 80
  - Cu/Zn/Cr precursors 119
  - deposition–precipitation 472 f, 481
  - supported catalysts 318
- hydrotalcite type catalysts 134
- hydrothermal zeolite synthesis 262 ff
- hydrotreating reactions 565
- hydroxides 66, 79
  - carbons 186
  - solid superacids 488
  - valencies 122
- hydroxy acids, complexation 128
- hydroxy groups
  - deposition–precipitation 470
  - enzyme heterogenization 360
- hydroxyaluminum polymers, pillars 290
- hydroxycarbonate 119
- hydroxyls, precursor–support interactions 545
  
- ideal catalysts 6 ff
- immobilization, enzyme heterogenization 364
- impregnation 315 f
  - bimetallic catalysts 533
  - deposition–precipitation 464
  - precursor–support interaction 324
  - preshaped supports 484
  - solid-state reactions 133
  - solid superacids 488
  - supported metal clusters 371
- impurities, oxide supports 330 f
- INCAP, CAD 594
- industrial catalysts 3–10
- industrial zeolites 279
- inner Helmholtz plane 319
- inorganic compounds, valencies 122
- inorganic supports
  - carrier binding 365
  - enzyme heterogenization 360
- intercalation
  - carbons 218
  - heteropolyanions 255
  - pillared clays 285
- interfaces
  - solid-state reactions 542
  - spreading/wetting 506
- interlayer spacing, pillared clays 301
- intermediate states, precursor–support interactions 551
- internal diffusion, industrial catalysts 3
- iodobenzene 420
- ion exchange
  - solid-state reactions 133
  - spreading/wetting 502
  - supported catalysts 315 ff
  - zeolite metal clusters 391
  - zeolites 523
- ion exchanged resin, enzyme heterogenization 358
- ion pairs, zeolites 277
- ion scattering spectroscopy (ISS)
  - chemical vapor deposition 432
  - precursor–support interactions 548
- ionic binding, enzyme heterogenization 364
- IR spectra
  - beidellite 302
  - carbons 210
  - solid superacids 494
  - zeolite-entrapped metal complexes 417
- iridium, spreading/wetting 505
- iridium carbonyl clusters 376, 380, 385
- iron
  - chemical vapor deposition 434
  - deposition–precipitation 475
  - reduction–sulfidation 565
  - selective leaching 398
  - spreading/wetting 505
  - supported catalysts activation 555
- iron carbonyls 434
- iron molybdate
  - manufacturing processes 587
  - solid-state reactions 110
- iron oxides
  - fused catalysts 12 f
  - precipitation 72
- iron phthalocyanine 421
- iron zirconium alloys 22
- iron–zirconium metallic glasses 26
- isoelectric point (IEP) 318
  - oxide supports 331
  - silica 478
- isolated metal atoms, zeolite metal clusters 395
- isoprene 45
- isotropy, metallic glasses 44
- IUPAC 61, 427, 541
  
- kaolin, formed supports 105
- kapton 171
- Keggin type structure 240 f
- keto groups, IR absorption frequencies 210
- kinetics
  - fused catalysts 17 f
  - solid-state reactions 542
- kish graphite 161
  
- lactic acid 336
- lactones
  - carbons 199
  - IR absorption frequencies 210

- Langmuir isotherm, pillared clays 297  
 Langmuir model 203  
 laponite 301  
 layer by layer growth 505  
 layered double hydroxides (LDH) 256  
 leaching  
   – activation 574  
   – catalyst forming 586  
   – selective 398  
   – skeletal metal catalysts 30, 39  
 Lewis acidity  
   – carbons 216  
   – heteropolyacids 249  
   – solid superacids 492  
   – support materials 80  
 Lewis bases  
   – metal clusters 393  
   – support materials 80  
 ligands  
   – carbons 150  
   – chemical vapor deposition 456  
   – enzyme heterogenization 363  
   – oxide surfaces 328, 332, 348  
   – sol–gel process 94  
   – supported metal clusters 374  
   – zeolite-entrapped metal complexes 405 ff  
   – zeolite metal clusters 395  
 Lindquist type structure 240  
 lithium vermiculite 287  
 loading, deposited precursors 559  
 low energy ion scattering (LEIS) 515, 519  
 Löwenstein rule  
   – pillared clays 289  
   – zeolites 272  
 lubricants, catalyst forming 583
- macroscopic metals, clusters 389  
 macrostructures, fused catalysts 13  
 magnesia clusters, supported 384  
 magnetite 72  
   – deposition–precipitation 463  
   – enzyme heterogenization 366  
   – fused catalysts 13  
 malachite 119  
 maleates 123  
 maleic acids, complexation 128  
 maleic anhydrides 82  
 manganese oxides 12  
 manufacturing 6, 587 f  
   – deposition–precipitation 462  
   – final catalysts 541 ff  
   – flame hydrolysis 99 f  
   – reduction–sulfidation 567  
   – zeolites 281  
 mass transfer, enzyme heterogenization 364
- matrix damage, zeolite metal clusters 402  
 mechanical strength, industrial catalysts 5  
 melting 13 f  
 melting points  
   – carbons 155  
   – high-surface transition metal carbides/nitrides 139  
   – spreading/wetting 504  
 membrane filtration, enzyme heterogenization 356  
 membranes, catalytic 96  
 memory effect, hydrotalcite type catalysts 135  
 Merrifield resin 357  
 mesophases, carbon graphitization 178  
 mesostructures, fused catalysts 13, 25  
 metal additives, precursor preparation 562  
 metal alkoxides, oxide surfaces 342, 346  
 metal alloys  
   – fused catalysts 11  
   – oxide surfaces 348  
 metal carbonyls  
   – high-surface transition metal carbides/nitrides 146  
   – oxide surfaces 342, 351  
   – supported metal clusters 372 f  
 metal chlorides  
   – flame hydrolysis 99  
   – oxide surfaces 344  
 metal cluster catalysts, supported 371 ff  
 metal clusters, zeolites 388 ff  
 metal complexes, oxide supports 331  
 metal concentration profiles, supports 336  
 metal coordinated heteropolyacids 253  
 metal fixation, supported catalysts 321  
 metal halide vapor decomposition 146  
 metal halides 342  
 metal ion exchange, supported catalysts 321  
 metal ligand bonds, grafting 343  
 metal–metal interactions, bimetallic catalysts 526  
 metal–nonmetal reactions, high-surface transition metal carbides/nitrides 143  
 metal oxidation, protons 398  
 metal oxide carbon reactions, high-surface transition metal carbides/nitrides 144, 148  
 metal oxide vapor synthesis (MOVS) 439  
 metal oxides, solid superacids 487 f  
 metal-phthalocyanine 415  
 metal proton adducts, zeolite metal clusters 397  
 metal–salen complexes, zeolite-entrapped metal complexes 407  
 metal salts  
   – complexation 128  
   – heteropolyanions 254  
   – sol–gel process 85  
 metal support interactions, spreading/wetting 511

- metallic glasses 43 ff
  - fused catalysts 11, 21 f
  - quenched states 46, 55
- metallic promoters, skeletal cobalt catalysts 35
- metallo-organic CVD 430
- metalloporphyrins, TMSP 254
- methacrolein 242
- methacrylic acid (MAA) 251
- methanation, skeletal nickel catalysts 33
- methane
  - carbon formation 172
  - solid superacids 497
- methanol 71, 587
  - chemical vapor deposition 447
  - deposition–precipitation 463
  - heteropolyacids 245
  - metallic glasses 45
  - skeletal copper–zinc catalysts 38, 41
  - solid superacids 490
- methyl, oxide surfaces 348
- methylcyclopentane
  - bimetallic catalysts 532
  - zeolite metal clusters 397 f
- microencapsulation 367
- microgranules, catalyst forming 579
- migration
  - deposition–precipitation 465
  - spreading/wetting 508, 512, 521
  - zeolite metal clusters 391
- milling 517
- mixed aluminum iron pillars 294
- mixed-coordinated heteropolyacids 251
- mixed gallium aluminum hydroxypolymers 293
- mixed metal oxides, chemical vapor deposition 451
- mixed oxides
  - solid-state reactions 110
  - solid superacids 487 f
- mixer-grinders, catalyst forming 579
- mixing
  - fused catalysts 14
  - solid-state reactions 117 f
- mobility temperature, spreading/wetting 507
- model molecules 9
- modifier effects, precursor preparation 561
- Moiré fringes 163, 219
- moissan fusion, high-surface TM carbides/nitrides 143
- molar gel compositions 283
- molecule pore collimation 399
- molybdenum
  - chemical vapor deposition 434
  - deposition–precipitation 479
  - spreading/wetting 505, 518
- molybdenum carbides, heats 141
- molybdenum carbonyls 434
- molybdenum oxides 561
- molybdenum pentachloride 436
- molybdenum sulfides 436
- molybdenum trioxides 439
- molybdenum–tungsten mixed-coordinated heteropolyacids 252
- molybdenum–vanadium mixed-coordinated heteropolyacids 251
- monolayers
  - chemical vapor deposition 447
  - precursor–support interactions 547
  - spreading/wetting 517
- monomers, heteropolyacids 245
- monometallic clusters, zeolites 390
- monometallic reforming catalysts 334
- montmorillonite 288, 298 f
- mordenite
  - chemical vapor deposition 452
  - zeolites 274, 280, 399 f
- morphology 4 ff
  - metallic glasses 46
  - solid superacids 490
  - spreading/wetting 501
- Nafion 359
- Nafion-H, solid superacids 487, 498
- nanocrystal formation, metallic glasses 48
- nanotubes 157
- naphthenes 176
- Nernst law 527
- neural networks, computer aided catalyst design 597 f
- neutralization reactions 196
- nickel
  - CO chemisorption 21
  - chemical vapor deposition 430
  - reduction–sulfidation 565
  - spreading/wetting 505
  - supported catalysts activation 555
- nickel alumina hydroxycarbonate, coprecipitation 80
- nickel carbonyl 430
- nickel catalysts
  - skeletal 31 f
  - supported 173
- nickel hydroxide, deposition–precipitation 471
- nickel–magnesium oxalates 463
- nickel–molybdenum oxide bilayers, precursor–support interactions 548
- nickel nitrates, deposition–precipitation 473
- nickel–zirconium alloys, metallic glasses 48
- nitrates
  - carbons 207
  - complexation 128
  - valencies 122



- nitrides, high-surface transition metal 139 ff
- nitriles
  - skeletal nickel catalysts 33
  - carbons 207
  - deposition–precipitation 472
- nitrocompounds, skeletal nickel catalysts 33
- nitrogen 527
- nitrogen oxygen groups 207
- nitrosyl 207
- NO removal, carbons 225
- noble metal carbon systems 216
- noble metal catalysts 173
- noble metal clusters, supported 376
- noble metal gauze, fused catalysts 11
- noble metal salts 250
- noble metals
  - bimetallic catalysts 527 ff
  - enzyme heterogenization 356
  - precursor preparation 562
  - spreading/wetting 505
  - supported catalysts activation 555
  - zeolites 374, 396
- nonaqueous media, zeolites 279
- nonoxygen heteroelements, carbon surfaces 191
- norborneols, zeolite-entrapped metal complexes 422
- normal hydrogen electrode (RHE) 537
- nuclear magnetic resonance (NMR) 417, 494
- nucleation 63
  - controlled interface reactions 542
  - deposition–precipitation 467
  - limited activation reactions 556
  - metallic glasses 54
  - solid-state reactions 112 f, 120
  - spreading/wetting 507
  - suspended supports 466
  - zeolites 267
- nucleophilic displacement, sol–gel process 93
  
- octane upgrading, zeolite metal clusters 399
- olefins 243
- oligomerization, solid superacids 495
- oligomers
  - carbons 170
  - enzyme heterogenization 356
  - zeolites 264
- onion carbon 157 f
- operating conditions 3, 582 f
- optimization, industrial catalysts 6 ff
- orbitals, carbon 151
- organic compounds
  - Raney nickel 35
  - valencies 123
  - zeolites 282
- organic solvents 71
  - anchoring 352
- organic supports
  - carrier binding 365
  - enzyme heterogenization 357
- organometallics
  - chemical vapor deposition 428
  - enzyme heterogenization 361
  - heteropoly compounds 240
  - oxide surfaces 342, 348
- orientation, fused catalysts 15
- Ostwald ripening
  - solid-state reactions 114
  - spreading/wetting 508
- Ostwald rule 64
- outer Helmholtz plane 319
- oxalates
  - perovskite catalysts 130
  - selective removal 463
  - valencies 123
- oxalic acid 336
- oxidation
  - carbons 150
  - heteropolyacids 244
  - metallic glasses 55
- oxide clusters, polyanions 242
- oxide coke analysis 176
- oxide dissolution
  - impregnation 330
  - supported catalysts 317 f
- oxide surfaces
  - chemical vapor deposition 443
  - grafting 341 f
- oxides
  - flame hydrolysis 100
  - precipitation 66
  - supported catalysts 318
- oxoanions 240
- oxobridges, zeolites 271
- oxohydrates 66
- oxolation 67
- oxychlorides
  - oxide surfaces 344
  - supported catalysts activation 555
- oxygen activation, carbon surfaces 229
- oxygen adsorption, zeolite-entrapped metal complexes 419
- oxygen carbon reactions 180
- oxygen functional groups 166
- oxygen transport, fused catalysts 22
- oxyhalides 342
- oxyhydroxides, spreading/wetting 521
  
- palladium 173
  - bimetallic catalysts 449, 528 ff

- clusters 376
- chemical vapor deposition 448 f
- deposition–precipitation 482
- films 448
- precursor preparation 562
- spreading/wetting 505, 512
- zeolite metal clusters 396, 401
- palladium–silicon alloys 24
- palladium–zirconium alloys 22
- pan granulation, catalyst forming 583 f
- parasitic reactions, industrial catalysts 4
- parent catalysts 526
- particle growth, matrix damage 402
- particle size, supported metal clusters 371
- pelletizing, catalyst forming 583
- pellets
  - industrial catalysts 4
  - supported catalysts activation 556
- pentachlorides 436
- pentane
  - anchoring 352
  - solid superacids 489
- pentasil chains 273
- perchlorate, deposition–precipitation 476
- performances, industrial catalysts 8
- perovskite catalysts 129
- pH level changes
  - deposition–precipitation 470 f
  - precipitation 73
- pH value
  - carbons 195
  - oxide supports 332
- phase diagrams
  - Al–Cu–Ni system 39
  - Al–Ni system 32
  - pyrosulfate vanadium oxide system 20
  - solid-state reactions 113
- phase transformations, solid superacids 491
- phase transitions, carbons 154
- phenol groups
  - carbons 199
  - IR absorption frequencies 210
- phenylacetylene, sol–gel process 92
- photoemission spectroscopy, metallic glasses 48
- phthalic anhydride 496
- phthalocyanines
  - NMR data 418
  - zeolite-entrapped metal complexes 406
- physical properties 3 ff, 62
  - carbons 154
  - chemical vapor deposition precursors 429
  - high-surface transition metal carbides/nitrides 139
  - oxide surfaces 328
  - pillared clays 297
  - skeletal copper catalysts 36, 40
  - skeletal nickel catalysts 33
  - sol–gel process 85
  - spreading/wetting 504
- physicochemical interactions, supported phases 544
- physiochemical properties 8
  - fumed oxides 101
- physisorption, metal complexes on oxide surfaces 343
- pill-box model, spreading/wetting 511, 514
- pillared clays 284 ff, 296 ff
  - enzyme heterogenization 360
- pillars 290
- pK value
  - carbons 203
  - solid superacids 487
- plasma-enhanced chemical vapor deposition 455
- plating, metallic glasses 43
- platinum
  - bimetallic catalysts 527 ff
  - precursor preparation 562
  - spreading/wetting 505
  - supported catalysts activation 555
  - underpotential deposition shifts 536
  - zeolite metal clusters 396
- platinum ammine complexes 375
- platinum black 174
- platinum catalysts 173
- platinum clusters, supported 376, 385
- platinum desorption, aluminum surfaces 335
- platinum–gold bimetallic catalysts 530
- platinum-modified metal oxides 487 f
- platinum raft 216
- poisoning, carbons 226
- poisons 4, 70
- polarization dependent total reflection fluorescence (PTRF) 442
- polyacrylonitrile (PAN) 171
- polycations, precipitation 67
- polyethylene 206
- polymeric oxoanions 240
- polymerization 4
  - carbons 168
- polymolybdates 552
- polymorphic crystallization, metallic glasses 55
- polyoxomethalates 240
- polystyrene 357
- polyvinylalcohol 206
- population balance, precipitation 64
- pore diffusion, zeolite metal clusters 400
- pore structure
  - additives 74
  - leaching temperature 30
  - skeletal copper catalysts 36, 41
  - sol–gel process 93

- pore volume
  - deposition–precipitation 464
  - skeletal nickel catalysts 33
  - titanium oxide supports 105
- porous glass, enzyme heterogenization 365
- porous polysulfate (PSF) 258
- potassium pyrosulfate, vanadium pentoxide system 19
- potassium salts 257
- powder microgranules, catalyst forming 579
- precipitation 60 ff
  - deposition–precipitation 467
  - from acidic solutions 67
  - from homogeneous solution (PFHS) 66
  - from solution 61
  - fused catalysts 13 f
  - HT type catalysts 135
  - solid-state reactions 109 ff
- precursor dispersion effects, supported catalysts activation 556
- precursor preparation 557
- precursor support interactions 324, 544
- precursors 3 ff, 557
  - amorphous 128
  - chemical vapor deposition 428
  - deposition–precipitation 460 f
  - final catalysts 541 ff
  - flame hydrolysis 99 f
  - fused catalysts 11
  - graphene 179
  - iron oxides 12
  - metallic glasses 49, 55
  - precipitation 63
  - sol–gel process 85
  - spreading/wetting 516
  - supported catalysts 317 f
  - supported metal clusters 373, 377
  - zeolites 263
- prehydrolysis, sol–gel process 94
- preparation methods 8
  - bimetallic catalysts 526
  - catalyst forming 579
  - deposition–precipitation 460 ff
  - final catalysts 541 ff
  - formed supports 104 f
  - fused catalysts 12
  - heteropoly compounds 240 ff
  - heteropolyanion-supported metals 255
  - high-surface transition metal carbides/nitrides 139 ff
  - heteropolyacids 247, 251
  - layered double hydroxides 256
  - metal complexes on oxide surfaces 342
  - metallic glasses 43
  - mixed-coordinated HPAs 252
  - monometallic reforming catalysts 334
  - oxide monolayers 517
  - precipitation 60
  - sol–gel process 85
  - solid-state reactions 117 f
  - solid superacids 488 f
  - supported HPAs 258
  - supported metal clusters 373
  - supports 315, 326
  - zeolite metal clusters 390
  - zeolites 282
- preshaped support bodies, deposition–precipitation 484
- pressure, precursor support interaction 324
- pressure drop, industrial catalysts 4
- production methods 9, 541 ff
  - deposition–precipitation 462
  - reduction–sulfidation 567
- promoted gold–zirconia catalysts, glassy alloys 52
- promoted skeletal copper catalysts 37
- promoted skeletal nickel catalysts 34
- promoters
  - precursor preparation 561
  - reduction–sulfidation 565
  - skeletal cobalt catalysts 35
  - spreading/wetting 502
- propane 381
- propene
  - chemical vapor deposition 436
  - heteropolyacids 242
  - metallic glasses 45
- prophyrins 420
- proton acid site, pyridine 492
- protonated intermediates, HPAs 245
- protonic metal oxidation, zeolite metal clusters 398
- protons
  - heteropolyacids 249
  - pillared clays 304
  - zeolite metal clusters 391
- pseudoboehmite
  - support materials 79
  - zeolites 263
- pyridine
  - heteropolyacids 245
  - solid superacids 492, 499
- pyridinium resin 358
- pyrogenic silica
  - flame hydrolysis 103
  - zeolites 262
- pyrolysis
  - chemical vapor deposition 428
  - fused catalysts 13
- pyrone 198
- pyrophyllite 286
- pyrosulfate promoter, fused catalysts 19 f

- quenching
  - fused catalysts 19
  - graphitization 178
  - metallic glasses 43
- quinone–hydroquinone system 532
- quinones
  - carbons 200
  - IR absorption frequencies 210
- radiotracer, carbons 174
- Raman spectra 520
- Raney alloys
  - catalyst forming 586
  - skeletal metal catalysts 28 ff
- Raney metals 463
  - copper 528
  - nickel 555, 574
- rapid cooling 11
- rapid quenching 178
- rapid solidification, fused catalysts 15
- rare gas clusters, zeolites 389
- raw materials, precipitation 70
- reactive surface area (RSA), carbons 185
- reactivity, metallic glasses 44
- reactors, industrial catalysts 4
- redispersion, spreading/wetting 502, 509, 512 f
- redox amphoteric behavior, carbons 218
- redox bifunctionality 242
- redox properties, HPAs 250
- redox reactions, bimetallic catalysts 526 f
- reducing agents 564
- reduction 61, 541
  - bimetallic catalysts 526, 531
  - metallic glasses 45
  - supported catalysts activation 553
  - zeolite metal clusters 392
- reduction–sulfidation 553 ff, 565
- reference hydrogen electrode (RHE) 536
- regenerability, industrial catalysts 5
- regioselectivity, zeolite-entrapped metal complexes 421
- relaxation time, precursor support interaction 325
- removal, selective 463
- reproducibility, industrial catalysts 5
- resins, enzyme heterogenization 357
- rhodium 398, 505
  - rhodium catalysts, carbons 173
  - rhodium clusters, zeolites 389
  - rhodium–tin/SiO<sub>2</sub> catalyst 449
- ribbons, fused catalysts 11
- rings, industrial catalysts 4
- ripening 582
  - spreading/wetting 508, 512
  - zeolites 263
- ruthenium
  - bimetallic catalysts 527 ff
  - chemical vapor deposition 448
  - graphite surfaces 219
  - spreading/wetting 505
  - transition metal-substituted polyanions 254
- salts
  - bimetallic catalysts 526
  - crystalline complex 128
  - heteropolyacids 247 f
  - supported metal clusters 371, 379
- saponite 288, 301, 306
- scaling up
  - deposition–precipitation 472
  - fusion processes 14
- scanning electron microscopy (SEM)
  - fused catalysts 25
  - metallic glasses 50
- scanning tunneling microscopy (STM)
  - chemical vapor deposition 446
  - metallic glasses 46
- Schiff bases 406 f
- secondary building units (SBU) 265
- seeding 278
- segregation
  - metallic glasses 46, 50, 55
  - precursor–support interactions 551
  - solid-state reactions 110
- selective catalytic reduction (SCR) 226
- selective doping 331
- selective leaching 398
  - carbons 150, 225
  - metallic glasses 55
- selective removal, deposition–precipitation 463
- selectivity 3
- self-assembly 456
- self-gasification 195
- self-gelation, solid-state reactions 132
- self-supporting inorganic membranes 96
- ship-in-the-bottle method 408
- silane, enzyme heterogenization 366
- silanol groups, flame hydrolysis 104
- silica
  - chemical vapor deposition 452
  - deposition–precipitation 460, 474
  - enzyme heterogenization 365
  - precursor–support interactions 545
  - support materials 75
- silica–alumina beads 582
- silica gels
  - enzyme heterogenization 366
  - sol–gel process 93
- silica pillars 295
- silica supports, anchoring 347

- silicate pillars 295  
 silicates, supported catalysts 318  
 silicomolybdic acids, precursor–support interactions 552  
 silicon alkoxides, zeolites 262  
 silicontetrachloride, flame hydrolysis 101  
 siloxane groups, flame hydrolysis 104  
 silver, deposition–precipitation 482  
 silver oxides 216  
 Silverton type structure 240 f  
 single file diffusion, zeolite metal clusters 400  
 single ion exchange, supported catalysts 320  
 sintering  
   – deposition–precipitation 460  
   – sol–gel process 90  
   – spreading/wetting 502, 512  
 size-selected gas phase metal clusters 375  
 skeletal isomerization 487  
 skeletal metal catalysts 28 ff  
 smectics 285, 300  
 sodium aluminosilicate, zeolites 279  
 sodium hydroxide 474  
 sodium nitrite 471, 484  
 sodium vermiculite 287  
 sol–gel preparation, fused catalysts 12  
 sol–gel process 85 ff  
   – silica supports 75  
 solid acid catalysts, oxide-based 175  
 solid–solid gas interphase, spreading/wetting 503  
 solid solution formation 548  
 solid-state diffusion 542  
 solid-state ion exchange, zeolites 523  
 solid-state reactions 109 ff, 542  
 solid superacids 487 ff  
 solidification, fused catalysts 11, 14, 18  
 solubility  
   – deposition–precipitation 469  
   – solid-state reactions 113  
 solution methods  
   – fused catalysts 13  
   – sol–gel process 85  
 solution pH, oxide supports 332  
 solvent effects, precipitation 71  
 soot 151, 169  
 spreading, supported catalysts 501 ff  
 spiking, reduction–sulfidation 565, 570  
 spillover hydrogen 562, 566  
 spinels  
   – fused catalysts 14  
   – precursor–support interactions 549  
   – spreading/wetting 511 f  
 spinning, metallic glasses 44  
 sponge metal catalysts *see*: skeletal metal catalysts  
 spray calcination 121, 127  
 spray drying  
   – catalyst forming 580  
   – solid-state reactions 121  
 spray granulation, formed supports 106  
 spray pyrolysis 99  
 spreading, precursor–support interactions 551  
 sputter deposition, metallic glasses 43  
 stability 4  
   – extrusion 584  
   – metallic glasses 54  
   – supported materials 94  
   – zeolite-entrapped metal complexes 418  
 stacked graphenes 169  
 stacking faults 79  
 stacking sequences, carbons 155, 160  
 standard redox potentials, bimetallic catalysts 528  
 steam reforming 172  
 stearic acid 583  
 step sequences, manufacturing 567  
 stereates, catalyst forming 583  
 stereoselective oxidation 422  
 stirring  
   – solid-state reactions 120  
   – supported catalysts 323  
 storage, skeletal metal catalysts 31  
 Strandberg type structure, heteropoly compounds 240  
 Stranski–Krastanov mechanism 505  
 strengths 5  
   – high-surface transition metal carbides/nitrides 139  
 strong metal support interaction (SMSI) 502, 511  
 structural properties  
   – carbons 151  
   – metallic glasses 44, 53  
   – solid superacids 493  
   – supported metal clusters 376  
 structure directing agents (SDA) 263, 274  
 structures  
   – fused catalysts 13  
   – heteropoly compounds 240  
   – high-surface transition metal carbides/nitrides 139  
   – surface groups 197  
 substrate–adatom system 535  
 substrate-to-product conversion, fused catalysts 16  
 succinates 123  
 sulfuric acid catalysts 19 f  
 sulfates  
   – poisoning 70  
   – solid superacids 487 f  
   – valencies 122  
 sulfidation 541, 553 f

- sulfides
  - carbon formation 173
  - reduction–sulfidation 570
  - thioacetamine 66
- sulfoxides, chiral 310
- sulfur functional groups 193
- sulfuric acid 224
- superacids, solid 487
- superconductors, flame hydrolysis 99
- supercooling, fused catalysts 15
- supercritical drying, sol–gel process 90
- superlattices 163
- supersaturation
  - precipitation 66, 71
  - solid-state reactions 120
  - zeolites 266
- supersolubility 469
- support chemistry, precursor preparation 560
- support materials, carbon 150
- support pretreatment, metal complexes on oxide surfaces 342
- supported catalysts 315–540
- supported heteropoly compounds 257
- supported liquid phase (SLP) 12
- supported metal catalysts 511
- supported metal cluster catalysts 371 ff
- supported nickel catalysts 432
- supported oxide catalysts 516
- supported phases, interactions 544
- supported solid phase (SSP) 356
- supports
  - bulk 11–98
  - carbon 216
  - enzyme heterogenization 356
  - formed 104 f
  - high-surface transition metal carbides/nitrides 148
  - materials 75 f
  - precipitation 62
- supramolecular ligands, oxide surfaces 328
- surface area
  - chemical vapor deposition 443
  - deposition–precipitation 460
  - leaching temperature 30
  - solid superacids 491
- surface chemistry, carbon 150, 180, 188 f
- surface defects, metallic glasses 46
- surface hydroxy groups, enzyme heterogenization 360
- surface melting 510
- surface multimetal sites 441
- surface oxidation, metallic glasses 55
- surface oxygen groups, carbons 195
- surface properties
  - skeletal metal catalysts 33 ff
  - solid superacids 490
  - spreading/wetting 504, 507
- surface redox reactions, bimetallic catalysts 526
- surface segregation, metallic glasses 44 f, 55
- surface transport, spreading/wetting 510
- surface type heterogeneous catalysis, heteropoly compounds 242
- surfaces, smectic 300
- surfactants, precipitation 74
- suspended supports, deposition–precipitation 466, 470
- swelling, pillared clays 285
- syneresis
  - silica 76
  - sol–gel process 88
- synthetic routes
  - carbons 169
  - nanotubes 168
  - zeolite-entrapped metal complexes 405 ff
- talc 286
- Tammann temperature
  - solid-state reactions 116
  - spreading/wetting 504
- tartaric acid
  - alumina surfaces 336
  - complexation 128
- tartrates 123
- telomerization 362
- temperature programmed desorption (TPD)
  - carbons 174, 189
  - heteropolyacids 248
  - solid superacids 487, 499
- temperature programmed reduction (TPR)
  - activation processes 564
  - high-surface transition metal carbides/nitrides 147
  - interface movement 543
  - nickel nitrate 473
  - precursor chemistry 558
  - zeolite metal clusters 392
- temperatures
  - activation 568
  - calcination 557
  - carbons 231
  - leaching 30
  - oxide supports 331
  - spreading/wetting 504, 507
  - zeolites 274
- templates, zeolites 274 f
- terephthalaldehyde, CVD 451
- terephthalic acid, solid superacids 496
- ternary gold containing glassy alloys 52
- tetraalkylammonium 275
- tetraethylorthosilicate (TEOS) 87
- tetrahydrofuran 242

- tetramethylammonium (TMA) 275 f  
 tetrapropylammonium (TPA) 282  
 textures  
   – industrial catalysts 3, 7 f, 579  
   – pillared clays 287  
 thermal activation *see*: activation  
 thermal decomposition *see*: decomposition  
 thermal properties *see*: physical properties  
 thermal stability *see*: stability  
 thermal treatment  
   – carbons 164  
   – fused catalysts 16  
 thermodynamics  
   – fused catalysts 17 f  
   – high-surface transition metal carbides/nitrides 139  
   – spreading/wetting 502  
   – supported catalysts 322  
 thermoform catalytic cracking (TCC) 582  
 thermogravimetric analysis (TGA) 23  
 thermoions 170  
 thick films, spreading/wetting 506  
 Thiele modulus 400  
 thiny chloride 193  
 thioacetamine, precipitation 66  
 thiophenes  
   – chemical vapor deposition 436  
   – reduction–sulfidation 569  
 thixotropy, extrusion 584  
 time scales  
   – fused catalysts 12, 18  
   – zeolites 274  
 tin 447  
 titania 474  
 titania aerogels 92  
 titania pillars 295  
 titania–silica system 94  
 titanium 445  
 titanium oxides  
   – enzyme heterogenization 366  
   – formed supports 105  
 titration 205  
 toluene 381  
 tosylchloride 366  
 total surface area (TSA), carbon 185  
 tracer methods, solid superacids 495  
 transformation degree, solid-state reactions 543  
 transition layer attachment 545  
 transition metal carbides/nitrides 139 ff  
 transition metal clusters, zeolites 389  
 transition metal complexes, zeolite-entrapped 411  
 transition metal ions, supported 326  
 transition metal oxide pillars 294  
 transition metal substituted heteropolyanion (TMSP) 253 f  
 transition states, zeolite metal clusters 399  
 transport restrictions, zeolite metal clusters 399  
 tresylchloride 366  
 2-(trichlorosilyl)ethylpyridine (TCSEP) 295  
 trichlorotriazine 366  
 triethylpropylammonium (TEPA) 282  
 trimethylbenzene (TMB) 248  
 trimethylpentane (TMP) 454  
 tungsten-based catalysts, spreading/wetting 522  
 turbostratic stacking, carbon 163  
 turn over frequency (TOF)  
   – carbons 185  
   – iridium clusters 380  
 ultraviolet photoelectron spectroscopy (UPS), metallic glasses 51  
 underpotential deposition (UPD), bimetallic catalysts 526, 534 f  
 unrolling carpet mechanism, spreading/wetting 510  
 unsupported fused catalysts 11  
 urea 66  
   – deposition–precipitation 471, 484  
   – formed supports 105  
   – solid superacids 490  
 urease enzyme, deposition–precipitation 471  
 UV electron excitation, zeolite-entrapped metal complexes 413  
 V/P/O catalysts, butane oxidation 82  
 vacancies, spreading/wetting 510  
 valence band, carbon 155  
 valence state changes  
   – deposition–precipitation 470  
   – precursor ions 481  
 valencies, precursors 122  
 van der Waals bonds  
   – carbons 152  
   – oxide surfaces 351  
   – pillared clays 304  
   – precursor–support interactions 545  
 vanadia–molybdena, solid-state reactions 110  
 vanadium  
   – chemical vapor deposition 442  
   – deposition–precipitation 479  
   – mixed-coordinated heteropolyacids 253  
 vanadium-based catalysts, spreading/wetting 521  
 vanadium pentoxides  
   – fused catalysts 12  
   – potassium pyrosulfate 19  
   – precursor–support interactions 550  
 vanadium phosphate catalysts 574  
 vapor deposition, metallic glasses 43

- vapor phases
  - heteropolyacids 242
  - oxide surfaces 348
- vaporization, solid-state reactions 118
- vermiculite, pillared clays 287 f
- viscosity, extrusion 584
- (VO)HPO<sub>4</sub> · 0.5 H<sub>2</sub> precursor 72
- volatile agents, industrial catalysts 4
- volatile alcoholates 99
- volatile products, precipitation 70
- Volmer–Weber growth 505
- vulcanization 193
  
- washing, oxide supports 333
- water gas shift (WGS), skeletal copper–zinc catalysts 38, 42
- water solvent, precipitation 71
- weak bonds, carbons 152
- weak forces, precursor–support interactions 545
- wetting
  - carbons 220
  - fused catalysts 14 f
  - solid-state reactions 119
  - supported catalysts 501 ff
- whetlerite, carbons 216
- wustite, fused catalysts 13
  
- X-ray diffraction (XRD)
  - deposition–precipitation 475
  - heteropolyacids 246
  - solid superacids 495
  - zeolite metal clusters 393
  - zeolites 266
- X-ray photoelectron spectroscopy (XPS)
  - metallic glasses 51
  - oxygen chemisorption 230
  - reduction–sulfidation 567
  - solid-state reactions 116
  - solid superacids 493
  - zeolite-entrapped metal complexes 415
- xerogels
  - silica 76
  - sol–gel process 85, 90
- xylenes, chemical vapor deposition 451
  
- Young equation 503
- Young–Laplace law 325
  
- zeolite catalysts, ion exchange 133
- zeolite-entrapped metal complexes 405 ff
- zeolite metal clusters 379, 388 ff
- zeolite supports, spreading/wetting 521
- zeolites 262 ff
  - carbons 150, 175 f
  - chemical vapor deposition 435
  - enzyme heterogenization 360, 365
  - H-ZSM-5 498
  - LTL/KLTL 385
  - metal ion fixation 322
  - spreading/wetting 521
  - supported catalysts 318
  - supported metal clusters 373
- zeozymes 420
- zerovalent state, zeolite metal clusters 389
- zeta potential, gibbsite 319
- Ziegler hydroxides 79
- Ziegler–Natta catalysts 72
- zinc, deposition–precipitation 474, 480
- zinc chromite, solid-state reactions 110
- zirconia 498
- zirconia aerogels 92 f
- zirconia hydroxypolymers 293
- zirconium 445